

AD A 122 168

2

AGARD-CP-323

AGARD-CP-323

AGARD

ADVISORY GROUP FOR AEROSPACE RESEARCH & DEVELOPMENT

7 RUE ANCELLE 92200 NEUILLY SUR SEINE FRANCE

AGARD CONFERENCE PROCEEDINGS No. 323

Problems in Bearings and Lubrication



NORTH ATLANTIC TREATY ORGANIZATION



DISTRIBUTION AND AVAILABILITY

DISTRIBUTION STATEMENT A

ON BACK COVER

82 12 08 029

DTIC FILE COPY

2

AGARD-CP-323

NORTH ATLANTIC TREATY ORGANIZATION
ADVISORY GROUP FOR AEROSPACE RESEARCH AND DEVELOPMENT
(ORGANISATION DU TRAITE DE L'ATLANTIQUE NORD)

AGARD Conference Proceedings No.323
PROBLEMS IN BEARINGS AND LUBRICATION

DTIC
DEC 7 1982
H

DISTRIBUTION STATEMENT A
Approved for public release;
Distribution Unlimited

THE MISSION OF AGARD

The mission of AGARD is to bring together the leading personalities of the NATO nations in the fields of science and technology relating to aerospace for the following purposes:

- Exchanging of scientific and technical information;
- Continuously stimulating advances in the aerospace sciences relevant to strengthening the common defence posture;
- Improving the co-operation among member nations in aerospace research and development;
- Providing scientific and technical advice and assistance to the North Atlantic Military Committee in the field of aerospace research and development;
- Rendering scientific and technical assistance, as requested, to other NATO bodies and to member nations in connection with research and development problems in the aerospace field;
- Providing assistance to member nations for the purpose of increasing their scientific and technical potential;
- Recommending effective ways for the member nations to use their research and development capabilities for the common benefit of the NATO community.

The highest authority within AGARD is the National Delegates Board consisting of officially appointed senior representatives from each member nation. The mission of AGARD is carried out through the Panels which are composed of experts appointed by the National Delegates, the Consultant and Exchange Programme and the Aerospace Applications Studies Programme. The results of AGARD work are reported to the member nations and the NATO Authorities through the AGARD series of publications of which this is one.

Participation in AGARD activities is by invitation only and is normally limited to citizens of the NATO nations.

The content of this publication has been reproduced directly from material supplied by AGARD or the authors.

Published August 1982

Copyright © AGARD 1982
All Rights Reserved

ISBN 92-835-0318-9



PROPULSION AND ENERGETICS PANEL

Chairman: Professor E.E.Covert
 Department of Aeronautics and
 Astronautics
 Massachusetts Institute of Technology
 Cambridge, Massachusetts 02139, US

Deputy Chairman: Professor Ch. Hirsch
 Vrije Universiteit Brussel
 Dienst Stromingsmechanica
 Pleinlaan 2
 1050 Brussel, Belgium

PROGRAM COMMITTEE

Professor Dipl-Ing. F.Wazelt (Chairman)
 Lehrstuhl für Flugantriebe
 Technische Hochschule Darmstadt
 Petersenstrasse 30
 Darmstadt, Germany

Professor D.Dini
 Università degli Studi
 Istituto di Macchine
 Via Diotisalvi 3
 56100 Pisa, Italy

Mr A.J.B.Jackson (Acting Chairman)
 Rolls Royce Ltd., Aero Division
 PO Box 31
 Derby DE2 8BJ, UK

M. l'Ingénieur Général A.Journeau
 Haut Conseiller Technique
 ONERA
 29 Avenue de la Division Leclerc
 92320 Châtillon sous Bagneux, France

Mr A.J.Acurio
 Director, Propulsion Laboratory
 US Army Research & Technology Labs.
 (AVRADCOM)
 21000 Brookpark Road
 Cleveland, Ohio 44135, US

Dr N.Sandsmark
 Det Norske Veritas
 Veritasveien 1
 1322 Høvik, Norway

Dr R.B.Whyte
 Fuels and Lubricants Laboratory
 Division of Mechanical Engineering
 National Research Council
 Ottawa, Ontario K1A 0R6, Canada

HOST NATION COORDINATOR

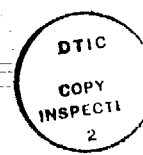
Dr R.B.Whyte

PANEL EXECUTIVE

Dr-Ing. E.Riester
 AGARD-NATO
 7 rue Ancelle
 92200 Neuilly sur Seine
 France

ACKNOWLEDGMENT

The Propulsion and Energetics Panel wishes to express its thanks to the Canadian National Delegates to AGARD for the invitation to hold its 59th Symposium in Ottawa, and for the personnel and facilities made available for this meeting.



Accession For	
NTIS SPA&I	<input checked="" type="checkbox"/>
DTIC TAB	<input type="checkbox"/>
Unannounced	<input type="checkbox"/>
Justification	
By	
Distribution/	
Availability Codes	
Dist	Special
A	

CONTENTS

	Page
PANEL AND PROGRAM OFFICERS	iii
TECHNICAL EVALUATION REPORT by W.J.Anderson	vii
	Reference
KEYNOTE ADDRESS -- BEARINGS: TECHNOLOGY AND NEEDS by W.J.Anderson	K-1
<u>SESSION I -- ROLLING BEARINGS</u>	
Paper 1 cancelled	
DETECTION AND DIAGNOSIS OF BEARING DETERIORATION IN AIRCRAFT PROPULSION SYSTEMS BY WEAR DEBRIS ANALYSIS by C.A.Waggoner	2
INCREASING THE WEAR LIFE OF GAS TURBINE ENGINE ROLLER BEARINGS by F.Brown, L.J.Dobek, M.J.Carrano, R.A.Valori and R.D.Dayton	3
CONDITION MONITORING OF BEARINGS -- (A MEASURING TECHNIQUE IN AN EXPERIMENTAL STAGE) by M.J.W.Schouten	4
SILICON NITRIDE BEARING ELEMENTS FOR HIGH-SPEED HIGH-TEMPERATURE APPLICATIONS by L.B.Sibley	5
LIGHTWEIGHT MATERIALS FOR ROLLING ELEMENTS IN AIRCRAFT BEARINGS by R.T.Cundill and F.Giordano	6
<u>SESSION II -- LUBRICATION</u>	
THE OIL/AIR SYSTEM OF A MODERN FIGHTER AIRCRAFT ENGINE by J.Schmidt, W.K.Hank, A.Klein and K.Maier	7
LUBRICATION OF 35-MILLIMETER-BORE BALL BEARINGS OF SEVERAL DESIGNS AT SPEEDS TO 2.5 MILLION DN. by H.R.Signer and F.T.Schuller	8
MITIGATION OF THERMAL HAZARDS IN ROLLING CONTACT BEARINGS THROUGH CORRELATED COMPUTER ANALYSIS by V.A.Schwarz and B.R.Reason	9
ELASTOHYDRODYNAMIC LUBRICATION OF ELLIPTICAL CONTACTS by B.J.Hamrock	10
EPAISSEUR DU FILM ET FORCE DE FROTTEMENT EN REGIME ELASTO HYDRODYNAMIQUE DANS LE CONTACT BILLE-CHEMIN DE BAGUE D'UN ROULEMENT par G.Dalmaz et N.Gadallah	11
THE LUBRICATION OF RIGID ELLIPSOIDS BY A PIEZO-VISCOUS FLUID by D.Dowson, J.F.Dunn and C.M.Taylor	12
REGIMES OF FLUID FILM LUBRICATION AT THE RIB-ROLLER CONTACT IN A TAPERED ROLLER BEARING by C.L.Swingler	13

THE INFLUENCE OF THE SHEAR THINNING EFFECTS OF NON-NEWTONIAN OILS ON THE PERFORMANCE OF FINITE LENGTH JOURNAL BEARINGS
by M.Vermeulen and H.S.Yoo 14

GLISSEMENT DANS LES ROULEMENTS A ROULEAUX. INFLUENCE DU LUBRIFIANT
par D.Berthe et L.Flamand 15

A DETAILED TREATMENT OF TWO-DIMENSIONAL, STARVED LUBRICATION IN THE VICINITY OF TWO COUNTER-ROTATING CYLINDERS
by R.A.Medrow and L.R.Shipers 16

THE BEHAVIOR OF VARIOUS ROLLING BEARING MATERIALS UNDER UNFAVORABLE LUBRICATION CONDITIONS
by H.K.Lorösch, P.Dreschmann and R.Weigand 17

GEOMETRY AND STARVATION EFFECTS IN HYDRODYNAMIC LUBRICATION.
by D.Brewe and B.J.Hamrock 18

Paper 19 cancelled

LUBRICANT EFFECTS ON EFFICIENCY OF A HELICOPTER TRANSMISSION
by A.M.Mitchell and J.J.Coy 20

THE DYNAMIC PERFORMANCE OF THE SELF-REGULATED HYDROSTATIC OPPOSED-PAD BEARING
by R.Bassani and B.Piccigallo 21

SESSION III - JOURNAL BEARING AND GEAR PHENOMENA

COMPORTEMENT DYNAMIQUE D'UN PALIER LISSE. CRITERES DE STABILITE
par J.Frene, D.Nicolas et N.A.Wahed 22

THE COMPUTER AIDED DESIGN ENTITY (C.A.D.E.). A NEW APPROACH TO JOURNAL BEARING DESIGN
by A.H.Siew and B.R.Reason 23

AN EXPERIMENTAL METHOD FOR THE DETERMINATION OF JOURNAL BEARING COEFFICIENTS
by M.Akkök 24

AN ANALYTICAL STUDY OF THE HEAT BALANCE FOR A JOURNAL BEARING
by P.K.Hansen and J.W.Lund 25

BEHAVIOR OF AIRCRAFT ENGINE OILS AT HIGH TEMPERATURE
by E.Jantzen 26

EXPERIMENTAL AND ANALYTICAL DETERMINATION OF GEAR TOOTH TEMPERATURES WITH OIL JET LUBRICATION
by D.P.Townsend and L.S.Akin 27

SESSION IV - ADVANCED BEARING APPLICATIONS

AN ADVANCED METHOD FOR PREDICTING HYBRID BEARING PERFORMANCE
by R.Colsher, I.Anwar and S.Katsumata 28

ETUDE THEORIQUE ET EXPERIMENTALE D'UN PALIER MAGNETIQUE AXIAL DU TYPE ACTIF^{*}
par M.Kant et R.Kessou 29

LE PALIER MAGNETIQUE ACTIF 'ACTIDYNE'
par H.Habermann 30

^{*}This paper was not presented.

AN INVESTIGATION OF SQUEEZE-FILM DAMPERS IN FLEXIBLE SUPPORT STRUCTURES

by R.Holmes and M.Dogan

31

SQUEEZE-FILM BEARING SUPPORT ANALYSIS

by F.A.P. Da Silva

32

UNCENTRALIZED SQUEEZE-FILM DAMPER BEARINGS APPLIED TO AN OVERHUNG DISC/ROTOR SYSTEM

by R.A.Cookson and X-H.Feng

33

Paper 34 cancelled

AERODYNAMIC COMPLIANT BEARINGS FOR SMALL TURBO-ENGINES

by M.Ehinger, J.Glienicke and H.Hunger

35

HIGH TEMPERATURE (649°C/1200°F) COATINGS FOR GAS-LUBRICATED FOIL BEARINGS OF THE NAVY'S ADVANCED AUXILIARY POWER UNIT CONCEPTS

by F.J.Suriano, R.J.Keiser, F.G.Woessner and R.Valori

36

EVALUATION OF ANTI STICK-SLIP BEHAVIOUR OF BRONZE FILLED PTFE AS BEARING MATERIAL

by Ö.Anlağan

37

APPLICATION OF DYNAMIC GAS BEARINGS TO CRYOGENIC COMPRESSORS AND TURBINES

by G.Nardi

38

TECHNICAL EVALUATION REPORT

by

W.J. Anderson
Bearings and Lubrication
North Olmsted, Ohio, US

1. INTRODUCTION

The key role which bearings play in the performance and durability of engines and transmissions has long been recognized by designers. Although dramatic advances have been made in bearing and lubrication technology during the past few decades, there continue to be problems, both in performance prediction and in performance limitations. These problems are manifest in the life and durability of engines and transmissions in current use, and also in the limits they place on the design of future engines and transmissions.

It was for the purpose of addressing these problems that the 59th AGARD Propulsion and Energetics Panel Meeting, a Symposium on Problems in Bearings and Lubrication, was held at the Lester B. Pearson Building in Ottawa, Canada, 31 May - 3 June, 1982.

The Symposium was divided into four sessions. Thirty five invited papers and one short presentation were given. A very broad scope of subjects was covered. These include:

- (1) Rolling element bearings-design, materials and lubrication
- (2) Gear lubrication
- (3) Elastohydrodynamics
- (4) Hydrodynamic, hydrostatic and hybrid bearing design and lubrication
- (5) Squeeze film dampers
- (6) Lubricant deposition studies
- (7) Gas film bearings
- (8) Magnetic bearings
- (9) Diagnostics and health monitoring of lubrication systems
- (10) Rotor dynamics
- (11) Engine lubrication system design
- (12) Helicopter transmission efficiency as influenced by lubricant composition

2. TECHNICAL CONTENT

Ten papers (3, 7, 8, 9, 17, 20, 26, 27, 31 and 33)* report experimental data on rolling element bearings, gears, dampers, oils and transmissions. These papers contain highly relevant information on improved high speed roller bearing design (3), high speed cage design (8), the criticality of the bearing thermal environment (7, 9), the influence of material and lubrication on bearing life (11), power losses in a helicopter transmission as influenced by the lubricant (20), oil characteristics at high temperatures (26), temperature profiles in both bearings (7), and gears (27), and viscous damper performance (31, 33).

Some of the more significant implications of these data are:

- (1) The lubrication and cooling system used in both rolling element bearings and gears can significantly influence the temperature profiles of these components. Careful attention must therefore be given to the design of the lubrication and cooling system to avoid thermal distortion. These could conceivably destroy the original precision geometry of these elements with a possible detrimental influence on performance and life.
- (2) A single thermocouple at a bearing or gear location or a single pyrometer reading is not adequate to describe the thermal environment. Significant axial temperature gradients or difference in inner and outer race temperatures can be present, again with the implication of a detrimental influence on performance.

*Throughout the discussion, numbers in parenthesis refer to paper numbers assigned to each contribution to the symposium.

- (3) Simulation of the conditions in the actual application may be critical to an accurate assessment of lubricant behavior at elevated temperatures. The startling differences in lubricant deposition character under static and dynamic conditions in (26) attests to this.
- (4) Lubricant composition can cause variations in helicopter transmission power losses as high as 50 percent, although the differences in efficiency are small (20). A 50 percent increase in power loss would require a comparable increase in size and weight of cooling system.
- (5) Where conditions of unfavorable lubrication are present in a bearing, high temperature resistant steels such as T-1 and M-50 have life expectancies superior to that of 52100 steel (17). Locally severe temperatures not detectable by a thermocouple measuring bulk bearing temperature have a far greater detrimental effect on 52100 steel than they do on either T-1 or M-50.
- (6) Cylindrical roller bearing design and quality control for ultra high speed applications should be reassessed, based on the results of (3). In particular, roller balance is critical, and rollers with shorter length/diameter ratios than are now standard should be considered.

Six papers (10, 11, 12, 13, 16 and 18) deal with elastohydrodynamics. The regimes of EHL lubrication, elastic or rigid, isoviscous or viscous, and fully flooded or starved are discussed in (10) and (12). Sliding and spinning effects influence traction more than film thickness (11). An application of EHL analysis to the cone rib contact in a tapered roller bearing is presented in (13). Starvation is treated (10, 16 and 18), but not in a way that can be directly applied to multiple body assemblages such as ball and roller bearings.

Papers (5) and (6) are concerned with advanced low density high temperature rolling element bearing materials. Both of these papers deal with critical needs which must be met for a material such as silicon nitride before it can be considered a viable material for bearings. These are:

- (1) Quality control, specifically non-destructive inspection techniques which can reliably separate good from bad material. The increasing use of advanced analytical physics tools to accomplish this is particularly encouraging.
- (2) Improved manufacturing. The systematic attack on manufacturing methods as reported in (6), is mandatory.

The very important subjects of diagnostics and health monitoring are treated in papers (2) and (4). These are important subjects because they deal with the realities of actual applications. Good design and proper installation and operation are necessary to achieve good service life, but not sufficient in themselves. Imperfections in the total engineering system and variances in operating environments can introduce unforeseen hazards to reliability. There is a need for health monitoring of operating systems, but the monitoring equipment must be reliable and the personnel who interpret the data must be properly trained. The advent and use of several new tools from analytical physics has greatly enhanced the potential of system health monitoring.

With the steady trend toward higher and higher speeds, rotor dynamics, including methods for predicting instability thresholds, and the use of viscous dampers for attenuating rotor vibrations, has become an increasingly important area of research. Papers (22), (24), (31) and (33) deal with rotor dynamics and vibration attenuation. Rotor dynamics and related topics could well be the subject of a future conference.

Papers (21), (23), (25) and (28) present new approaches, through analysis and design, for hydrodynamic, hydrostatic and hybrid fluid film bearings. The use of CADE (23) in the design of journal bearings, with the capability of handling misalignment, is a step forward. Further incorporation of flexibility in the bearing and its support utilizing finite element structural analysis would probably be required to truly represent a bearing application. The advanced hybrid bearing design approach (28) is needed because the intricate geometries of hydrostatic-hybrid bearings demand special fluid flow analysis techniques.

More attention is now being given to compliant types of gas film bearings rather than rigid geometry bearings because of their lesser sensitivity to contaminant particles in the gas, occasional high speed rubs and human error. Paper (35) reports results on both foil type and tilting pad bearings. Paper (36) deals with advanced surface coatings for foil bearings, a necessary element in their successful use, especially at extreme temperatures. Paper (38) reports operating experience with several types of gas film bearings in small cryogenic turbo-compressors. The experimental work in these papers is especially welcome.

Feasible magnetic bearings have long been sought as a possible solution to specialized bearing problems. Paper (30) is a very comprehensive treatment of a number of successful applications of active magnetic bearings. It is quite apparent that they will prove to be advantageous in many situations where size and weight are not critical, and where cost is not the dominating factor.

3. CONCLUSIONS AND RECOMMENDATIONS

The symposium successfully addressed a number of topics related both to improving presently operational systems and to advancing design capability for future systems. Bearings and lubrication encompass a multitude of technologies,

however, and it is not possible to discuss all of them in any depth in a single symposium. As with any major technology area, research on bearings and lubrication ranges from very fundamental studies involving first principles in fields such as physics, mechanics, stress analysis, chemistry and rheology, to applied studies of complete systems. Well directed fundamental research supplies the foundation for later applied research. The various technical societies effectively provide forums for the discussion and critical review of the more fundamental research, and the journals which constitute the permanent written record of the work. Our present efforts at disseminating the results of applied research and development, both component and systems oriented, which can be of direct use to operations and design engineers, is much less effective. The Propulsion and Energetics Panel, partly because of its international makeup, is ideally structured to improve the interchange of applied research and development information.

It is recommended that in future symposia more stress be placed on the presentation of research and development results which can be immediately put to use by designers. To that end symposia titles which include the specific application such as aircraft turbine and turboshaft engines, and rotorcraft/turboprop transmission would encourage the submission of more applied papers.

In regard to this symposium and its technical content the following additional comments are offered:

- (1) The several papers on elastohydrodynamics are almost totally concerned with film thickness on a macro scale. More information on micro-elastohydrodynamics of real surfaces is needed, particularly as it relates to future progress in bearing and gear life prediction and enhancement. The criticality of surface finish and texture, and of system cleanliness and filtration level, and their influence on bearing life and system reliability need to be emphasized and placed in balance with all of the research on film thickness. The role played by lubricant chemistry also needs to be explored to learn why some systems operating with asperity contact successfully run in, and why others do not. This is particularly critical in gear lubrication, and in low speed, highly loaded rolling element bearings.
- (2) The papers on squeeze film dampers offer a significant body of information. Non-central dampers may be sensitive to shaft attitude so experiments at various shaft attitudes other than the horizontal are encouraged. Even in civilian aircraft, takeoff, landing and in-flight maneuvers can produce markedly different results.
- (3) A future symposium on rotor and structural dynamics is recommended. The subject needs to be treated in depth. In particular, flexible or supercritical rotors, the prediction of damped critical speeds, vibration attenuation and prediction and control of instability thresholds are subjects vital to the design of future high speed turbomachinery.
- (4) Continuance of the types of research with high potential for the development of design tools is recommended. Paper (15) on cage slip, (23) on journal bearing design, and (27) on improved gear lubrication are good examples.

REFERENCES

See Contents pages iv - vi.

BEARINGS: TECHNOLOGY AND NEEDS

by

William J. Anderson
 Consulting Engineer - Bearings & Lubrication
 5031 Devon Drive
 North Olmsted, Ohio 44070 USA

ABSTRACT

A brief status report on bearing technology and present and near-term future problems that warrant research support is presented. For rolling element bearings a material with improved fracture toughness, life data in the low Λ region, a comprehensive failure theory verified by life data and incorporated into dynamic analyses, and an improved corrosion resistant alloy are perceived as important needs. For hydrodynamic bearings better definition of cavitation boundaries and pressure distributions for squeeze film dampers, and geometry optimization for minimum power loss in turbulent film bearings are needed. For gas film bearings, foil bearing geometries that form more nearly optimum film shapes for maximum load capacity, and more effective surface protective coatings for high temperature operation are needed.

LIST OF SYMBOLS

C radial clearance, m (in)
 D diameter, m (in)
 E modulus of elasticity, N/m² (psi)
 E' modified modulus of elasticity,

$$\frac{2}{\frac{(1 - \nu_1^2)}{E_1} + \frac{(1 - \nu_2^2)}{E_2}}$$

F normal applied load, N (lb)
 G dimensionless material parameter, E'/P_s
 H_{min} dimensionless minimum film thickness, h/R_x
 h film thickness, m (in.)
 k ellipticity parameter, a/b
 L length, m (in)
 R radius m (in)
 r radius of curvature, m (in.)
 R_x, R_y effective radius of curvature, m (in.)
 $\frac{1}{R_x} = \frac{1}{r_{1x}} + \frac{1}{r_{2x}} ; \frac{1}{R_y} = \frac{1}{r_{1y}} + \frac{1}{r_{2y}}$
 U dimensionless speed parameter, (u μ_a)/(E'R_x)
 u surface velocity in x direction, m/sec (in./sec)
 W_p dimensionless load parameter, F/(E'R_x²)
 Λ lubricant film parameter, h/ σ
 μ_a dynamic viscosity, N sec/m² (lb sec/in.²)
 ν Poisson's ratio
 σ composite surface roughness, micrometers (μ in.)
 σ_1, σ_2 surface roughness of bodies 1 and 2, micrometers (μ in.)

Subscripts:

1, 2 bodies 1 and 2
 x, y coordinate directions
 b bearing
 p preload

INTRODUCTION

In these days of intensive research efforts in a multiplicity of high technology areas which result in a steady stream of products unknown only a few years ago, one would think that anything as prosaic as bearings, which have been with us since the dawn of civilization, would long since have been relegated to R&D dormancy. That is not the case, however, because we find a continued high level of research and development activity in bearings and other mechanical components. A continued level of substantial support for bearing related R&D activity is a result of the recognized key role that bearings play in rotating machinery. Thus we find that advances in rotating machinery technology have necessitated parallel advances in bearing technology.

Large aircraft gas turbine engines, and transmissions and gear boxes for rotorcraft and turboprops have, for example, been a principal driver for improvements in rolling element bearings. The general demand for greater power density in rotating machinery has led to ever increasing speed demands on both rolling element and fluid film bearings. High speeds have intensified rotor dynamic problems, forcing greater attention on the stability aspects of fluid film bearings and rotor-bearing systems. They have brought about an increas-

ingly wide use of non-circular, whirl resistant journal bearings and of viscous dampers configured as non-rotating journal bearings for vibration attenuation.

High sliding speeds in fluid film bearings can also result in super laminar flow accompanied by sharply increased levels of frictional power loss. In large power generating equipment bearing power loss may reach several thousand kilowatts so bearing power loss is of major concern, especially in today's atmosphere of energy conservation. Accordingly, the development of a better understanding of super laminar flow and of bearing designs which minimize power loss without degrading load capacity should have high priority.

The development of gas film bearings continues with a steadily broadening scope of applications. The obvious benefits are a simpler lubrication system, less mechanical complexity and higher operating temperature capability because of the elimination of organic lubricants. Research has concentrated on compliant types of bearings, many incorporating flexible foils, because of their relatively forgiving nature. Wear resistant coatings are also under intensive development for completely self-acting bearings.

It is not the objective of this paper to present an in-depth treatise on the state of the bearing art. Such an attempt would result in a compendium of encyclopedic proportions. Rather, the objective is to present highlights illustrating where we are and what problems are most urgently in need of solution. A few key references, some of which contain extensive bibliographies, are presented.

ROLLING ELEMENT BEARINGS

The principal driver has seen the need for bearings with higher speed capability and improved endurance in aircraft propulsion systems, most notably large gas turbine engines, and transmissions and speed reducers for rotorcraft and turboprops. Aircraft turbine engine designers want bearings with 3 million DN and even higher speed capability coupled with extended endurance life. Gear box designers want bearings with 2+ million DN, and high combined thrust and radial load carrying capability, again with extended endurance life and high reliability.

Liquid Lubrication - Parker (1) presents a thorough review of rolling element bearing lubrication. During the mid 1960's it became apparent that jet lubrication of large bore mainshaft ball and roller bearings would not be adequate for DN values beyond 2.3 to 2.5 million. As speeds increase centrifugal effects make it increasingly difficult for oil to penetrate to the critical interior surfaces of the bearing when directed from jets at the sides of the bearing. Brown (2) first presented the concept of underrace lubrication, figure 1. Underrace lubrication allows oil to be metered at controlled flow rates directly into the bearing with an option to use part of the flow exclusively for cooling by bypassing the bearing. Underrace lubrication offers several advantages for extreme speed applications. Churning losses can be kept to a reasonable level by feeding directly into the bearing only enough oil to satisfy the internal lubrication and cooling requirements. By-passed oil flow serves exclusively as a coolant. With underrace lubrication, centrifugal effects assist in pumping oil into the critical areas requiring lubrication. In (3) jet lubrication was found to be ineffective at 2.5 million DN in experiments with 120 mm bore ball bearings, figure 2. Underrace lubrication is effective, in contrast, at DN values to 3 million (4).

Underrace lubrication has also been applied to small bore (35-mm) ball bearings operating at DN values to 2.5 million (5), and to highly loaded tapered roller bearings operating at DN values to 2.4 million (6). It has proven to be particularly effective in solving lubrication problems associated with the cone rib flange in high-speed tapered roller bearings.

It can reasonably be said that the concept of underrace lubrication, in its various forms, constitutes a major advance in the lubrication and cooling of very high speed bearings. Lubrication and the control of frictional heat generation and bearing temperature no longer constitute a problem or limiting factor in high speed bearings.

Elastohydrodynamics - Beginning with the work of Grubin (7), and followed by both analytical and experimental work of numerous other investigators, most notably Dowson and Higginson (8), Archard and Cowking (9), and, most recently, Hamrock and Dowson (10, 11), the calculation of elastohydrodynamic film thickness has become an integral part of rolling bearing analysis and design. An easily used equation for minimum film thickness in either point and line contacts (10) is.

$$H_{\min} = 3.63 U^{0.68} G^{0.49} W_p^{-0.073} (1 - e^{-0.68K})$$

H_{\min} is a dimensionless minimum film thickness and K is a function of the contact ellipticity.

$$K = 1.03 \left(\frac{R_y}{R_x} \right)^{0.64}$$

The influence of elastohydrodynamic films on bearing performance is determined by the now widely accepted EHD film parameter, Λ , which is the ratio of film thickness, h , to composite surface roughness, σ , where

$$\sigma = \sqrt{\sigma_1^2 + \sigma_2^2}$$

σ_1 and σ_2 are the RMS roughnesses of the two surfaces in contact. Tallian, et.al., (12, 13) first investigated the relationship between Λ and bearing performance. As shown in figure 3, there is a high probability that surface distress in the form of superficial glazing, smearing and micropitting will occur at $\Lambda \leq 1$, figure 4. The frequency of asperity contact in this Λ region is high. At $0.9 \leq \Lambda \leq 1.5$ surface distress may occur. If surface distress does occur it will probably result in early bearing failure due to wear out and/or surface initiated fatigue. At $\Lambda > 3$ very little asperity contact occurs, and the surfaces are, for practical purposes, completely separated. In this region the bearing can be expected to run to its full endurance life expectancy.

In the Λ range between 1 and 3, where many bearings operate, successful operation depends on additional factors such as the boundary lubricating characteristics of the lubricant with the bearing materials involved, bearing kinematics such as spin-roll ratios, temperature and surface texture (other than rms surface finish).

It is in the low Λ region where the departure of bearing life from that predicted by classical fatigue theory becomes the greatest. Tallian and his coworkers have recognized the need for a much broader theory of bearing failure, based on several competing modes of failure (13, 14, 15). The theory allows for material, lubrication and surface topography effects and goes considerably beyond the consideration of Λ alone. This is especially needed in the low Λ range where the scatter in the little available life data is greatest, figure 5, (15). Bearing endurance data are needed in the Λ range up to 2 with controlled values of asperity slopes and traction in order to demonstrate the validity of the theory.

A second lubrication related factor for which better predictive methods are required is starvation. The influence of lubricant availability in front of the contact (in terms of inlet distance) on the ability of the rolling system to develop an elastohydrodynamic film has been mathematically described by Hamrock (11) and lubricant starvation has been observed experimentally by Wedeven, et al., (16) and Wolveridge, et al., (17) in simple ball and cylinder contacts. The problem of observing and predicting starvation in full scale bearings operating at high speeds is considerably more complex than developing mathematical models and conducting simple experiments.

Chiu (18) developed a film replenishment model which incorporates a speed-viscosity parameter and a starvation parameter dependent on oil-air surface tension and rolling element spacing. Experimental data are needed to verify Chiu's model and to assist in developing more effective predictive techniques. The importance of starvation in ball and roller bearings is not well understood. It appears to be significant in gyro bearings and may very well influence the operation of other high speed bearings. Pemberton and Cameron (19) conducted experiments with a cylindrical roller bearing operating at approximately 0.2 million DN and had difficulty producing starvation. The method of lubricating a bearing as well as the operating DN of the bearing may be critical to the onset of starvation, and that hasn't been studied.

Computerized Analysis and Design Methods - The availability of accurate elastohydrodynamic film thickness and traction predictive methods has made possible the development of both quasi-static and dynamic ball and roller bearing analyses which can accurately predict bearing performance. The evolution of large high speed computers has made the use of complex computer programs practical as design and performance prediction tools.

The first widely used ball bearing analysis was conceived by Jones (20, 21). Coulomb friction was assumed to exist in the ball-race contacts. Jones' analysis predicted life quite well but had shortcomings in predicting skidding and slip. Harris (22) first incorporated elastohydrodynamics into a ball bearing analysis. Harris used Archard and Cowking's (9) film thickness equation and an exponential viscosity pressure relationship. As shown in figure 6, Harris' analysis predicted cage slip better than did Jones' earlier race control theory.

A revised version of Harris' computer program called SHABERTH was developed incorporating experimental traction data. Further revisions by Coe (23) resulted in a program which predicted bearing temperatures reasonably well (figure 7).

The development of analytical tools for predicting the performance and life of cylindrical roller bearings parallels that for ball bearings. Harris (24) first introduced elastohydrodynamics into a roller bearing analysis. Since then increasingly reliable programs have evolved through the introduction of more precise traction relationships. Poplawski (25) and Rumbarger (26) generated programs which predicted roller bearing skidding with increasing accuracy, figure 8.

Quasi-static analyses have also been developed for tapered and spherical roller bearings. These programs are being continually updated with more efficient subroutines, especially thermal subroutines which can produce reliable estimates of bearing temperatures.

The quasi-static analyses are suitable only for describing steady-state bearing operation since they tacitly assume that an equilibrium of forces exists at all times. Evidences of transient behavior and instabilities have been observed in gyro bearings, and unsteady state behavior has probably been responsible for numerous high speed bearing failures. These have provided the stimuli for full scale dynamic analyses, such as Gupta (27-30). Even with a high speed digital computer, however, a full dynamic analysis is costly and time consuming, as such a program can only be used very selectively. Quasi-static programs have proven to be very effective engineering design tools. Dynamic analyses may prove of real value in the diagnosis of bearing failures, many of which follow in the wake of the onset of unsteady state dynamic conditions.

Bearing life prediction is presently based on the Lundberg and Palmgren theory with several life multiplying factors applied as suggested in (31). These factors include corrections for materials and lubrication. The lubrication factor is developed from experimental data relating bearing life and Λ . An "average" curve such as that of figure 9 is recommended for use, but we have already seen the wide scatter in fatigue lives at low Λ 's (figure 5) and, as stated earlier, we lack a good understanding of the factors that control bearing life in the low Λ region of operation. At high values of Λ the lubrication factor recommended in (31) is probably valid although even there it may be overly simplistic, based on Tallian's work on competing failure modes (13, 14, 15) and the dramatic advances that have been made in the quality of bearing materials. It may be argued with some validity that the advent of double vacuum melted steels and superior processing techniques has greatly diminished the incidence of classical subsurface fatigue, upon which the Lundberg-Palmgren theory is based. Advanced life-prediction methods should, therefore, recognize the many failure modes that are possible, and incorporate physical and chemical factors in addition to surface texture effects. These should then be incorporated into computer programs for more realistic life prediction.

Materials - A broad scope, in-depth discussion of the state of the art of rolling element bearing materials is given in (33). As stated above, dramatic improvements in bearing endurance life have resulted from modi-

fications in melting and processing techniques applied to existing iron base bearing alloys (as opposed to the development of new alloys). Bearing endurance life improvement realized through the evolution of AISI M-50 bearing steel, for example, is shown in figure 10 (from 33). The extended bearing endurance life resulting from improved alloys has made bearings more susceptible to other failure modes (such as surface initiated fatigue). This, together with an increasing awareness of elastohydrodynamic and other lubrication effects, has made the development of a more comprehensive life (or failure) prediction method even more relevant.

The dramatic improvement in iron base bearing alloys has also made it possible to achieve adequate endurance life at extreme speeds, despite the high cycling rate and the detrimental centrifugal effects (34). With the aforementioned developments in undertrace lubrication, computerized design, and now adequate material endurance, one might be tempted to think that all aspects of the 3 million DN bearing problem have been solved. Such is not the case, however, as reported in (34) because fatigue spalling at 3 million DN was followed by crack propagation through the rotating inner ring. This quickly precipitated catastrophic failure (figure 11). At moderate bearing speeds, spalling is a benign type of failure, but at extreme speeds the hoop stress in the rotating ring coupled with inadequate fracture toughness of the ring material combine to make the failure catastrophic. A number of research efforts are presently directed toward obtaining bearing materials with improved fracture toughness. Some of the more promising approaches are discussed in (33). These are critically needed efforts, because fracture toughness presently constitutes a barrier problem preventing rolling element bearing operation at DN values beyond 2.4 million, figure 12.

Bearing ring fracture is also a problem in anti-skid roller bearings (35). These bearings frequently utilize non-circular raceways designed to produce preload or "roller pinching" at points within the bearing. Inner ring flexing can occur in these bearings resulting in fatigue cracks which propagate radially outward from the initiation site at the bore. Similar problems occur in hollow rollers when that approach is used to produce bearing preload. It is clear from this discussion that bearing materials with improved fracture toughness are required to solve several critical bearing problems. This is a major challenge for the bearing materials researcher.

Other areas of bearing materials research which are particularly relevant to present and near future needs and problems are corrosion resistant ferrous alloys, powder-metallurgy produced materials, and ceramics. A large number of conventional oil-lubricated bearings are rendered unserviceable each year because of corrosion, Table 1, (36). Therefore, there is a genuine need for a cost competitive, corrosion resistant alloy with endurance characteristics equivalent to vacuum processed M-50 and AISI 52100. One promising alloy under development is AMS 5749, a martensitic stainless steel. AMS 5749 has shown fatigue characteristics which compare favorably with those of M-50 in bench fatigue tests (37). Endurance tests of full scale bearings should be run to properly assess the potential of AMS-5749.

Powder-metallurgy-produced materials have been under investigation as potential bearing materials for a number of years. Among the P/M alloys under investigation are M-50, T-15 and CRB-7 (an alloy similar to AMS-5749) (38, 39). The potential for producing a fine-grained material with fine, evenly dispersed carbides is recognized and provides the incentive for this research. A viable P/M material might also lead to lower cost bearings through the reduction of waste in processing bearing parts. Results so far have been promising but somewhat erratic. An integral part of the problem is quality control in both making and processing the powders. Continued research is needed to establish good quality control so that the ultimate potential of P/M materials can be assessed.

Ceramics have also been the subject of much research as potential bearing materials since the 1950's. A successful ceramic material would find application in high temperature bearings, and bearings for corrosive and non-lubricating environments. A summary of ceramic bearing materials research is given in (33). Much of the early work proved disappointing; quality control was erratic and the endurance characteristics were generally poor. Recent emphasis has shifted to silicon nitride, which has shown considerable promise in both hybrid (silicon nitride rolling elements coupled with ferrous alloy races) and in all ceramic bearings, (40). It has demonstrated endurance characteristics comparable to those of a good quality forged bearing alloy (41). Its low density, excellent high temperature properties and excellent corrosion resistance insure that it will someday find use in bearings requiring a material with one or more of these properties. Research on silicon nitride should continue with strong emphasis on manufacturing quality control.

Solid Film Lubrication - Operation of rolling element bearings at extreme temperatures, either very high or low, or in vacuum usually precludes the use of conventional oil or grease lubricants. Solid film lubrication can often be used in these unusual environments, and in systems where the life requirements are short and simplicity of mechanical design is of premium importance.

The use of solid film lubrication generally limits bearing life to a small fraction of its full endurance life potential with oil lubrication. Solid lubricants are most often used in the form of bonded films or as transfer films. Gas entrained loose powders of molybdenum disulfide, lead monoxide and graphite have been evaluated in experiments, but to the writer's knowledge have not found use in actual applications (42).

Polytetrafluoroethylene base materials have found considerable use in cryogenically cooled bearings in high energy rocket engine turbopumps (43). Feasibility studies of very thin ($\approx 5000 \text{ \AA}$) sputtered films of hard nitrides and carbides as surface protectants in gyro and turbine engine bearings with short-life requirements are presently being made (44). Thin films are probably more suitable for use in Hertzian contacts than are thick films.

The ultimate utility of solid film lubricants in rolling element bearings is probably limited by the nature of their stressed contacts and kinematics, but one of the factors limiting the success achieved to date may lie in the bearing designs used. Bearings designed for use with liquid lubricants have been the vehicles employed in evaluating solid lubricants. Careful studies to optimize surface texture and bearing design have never been done. Such studies would enhance the level of success with solid lubricants.

HYDRODYNAMIC BEARINGS

The analytical and experimental foundation for hydrodynamic bearing design began with the work of Osborne Reynolds and Beauchamp Tower before the turn of the present century. In contrast, rolling element bearing analysis does not predate the work of Lundberg and Palmgren in the 1940's. A reasonably good level of technical understanding of hydrodynamic bearings was, therefore, established before a comparable understanding of rolling element bearings was developed. Probably for this reason the level of research activity on hydrodynamic bearings in recent years has been somewhat lower than that on rolling element bearings. There appear to be several rather select areas in which research on hydrodynamic bearings, directly relevant to visible needs and problems, is being carried on. These include:

1. Non-circular journal bearings for vibration suppression in high speed rotating machinery.
2. Non-rotating journal bearings as squeeze film dampers, for suppression of vibrations in high speed rotors supported on rolling element bearings.
3. Turbulent flow bearings for more efficient design and energy conservation.

As mentioned earlier the trend toward higher speed, higher power density rotating machinery has made mandatory steady advances in both rolling element and fluid film bearing technology. Higher operating speeds have aggravated problems associated with vibrations due to critical speeds, unbalance and stability. Several of the bearing types developed to combat these problems are discussed in (45). These include multilobe (figure 13), pressure dam and tilting pad bearings.

A critical element in the design and selection of anti-whirl bearings for high speed systems is the ability to predict the instability threshold speed, or the onset of subsynchronous, potentially dangerous, vibration frequencies. In investigations reported in (45) bearing coefficients were determined using finite elements and the flexible rotor was modeled using lumped rotor masses. Theoretical predictions compared reasonably well with experiments, as shown in figure 14. More work is needed to establish more realistic boundary conditions for the solution of the relevant differential equations, and to incorporate real geometry effects (runout, out-of-round, minor unbalance) into the theoretical model. Additional experiments would then be required to test the degree of correlation.

The ability to predict the stiffness and damping coefficients of squeeze film dampers has been limited partly by an inability to properly characterize film cavitation. Recent analytical attempts (46, 47) utilizing more sophisticated extensions of the short-bearing theory have produced some interesting film boundaries. Experimental studies (48) indicate that significant pressure variations may occur in cavitated regions, contrary to the usual assumption of constant pressure.

Additional experimental work in which film shapes can be observed over a range of eccentricity ratios, frequencies, supply pressures, end conditions, etc., needs to be done to obtain data for correlation with, and possible feedback into existing analyses. Squeeze film dampers are an important component of high speed bearing-rotor systems. The ability to accurately predict their performance is vital to continued advancements in rotating machinery technology.

The occurrence of turbulent or superlaminar flow in liquid film bearings has been recognized for over three decades (49). Superlaminar flow is accompanied by greater than expected load capacity, power loss and temperature rise together with reduced flow. Interest of late has centered around large bearings in electric power generating machinery. These bearings have very considerable power losses which, together with the escalating cost of energy, has stimulated research on more energy efficient bearings (50). An in-depth discussion of the state of the art of turbulent bearings and of their economic importance is given in (51). Turbulent lubrication theories, although somewhat empirical in nature, are well developed and have been translated into usable design procedures (52, 53, 54).

There remain, however, areas where further research gains could be translated into significant economic savings. From a fundamental point of view the nature of the flow over a wide range of Reynolds' numbers immediately beyond the laminar flow region is not well understood. Vortex flow appears to persist over a wide range of Reynolds' numbers up to the development of fully turbulent flow, if, in fact, the latter ever comes about (51). It is in this "transition" region where discrepancies occur among the various theories. Further analytical and experimental studies are needed. In the practical arena lubricant supply effects and parasitic churning losses need to be better defined and translated into design guides. Much can probably be done, by way of power loss and energy saving, through studies of the portions of the thin film regions in both journal and thrust bearings that don't contribute appreciably to load capacity. Elimination or minimization of non-productive thin film regions could result in reduced levels of power loss.

GAS FILM BEARINGS

Air or, more generally, gas film bearings have evolved into practical entities used in a fairly broad scope of machinery and mechanisms. Gas bearings can be found in gyros, magnetic recording heads, microcircuit pattern generators, metrology instruments, load transportation pallets, textile spinning rings, space power turboalternators and air cycle machines. The pattern of gas bearing development has been interesting. At first rigid geometry bearings were applied; of late, compliant bearings, most of which incorporate foils of various designs, have been finding more widespread use. Compliant gas bearings have greater tolerance to contaminants and shock loads than rigid geometry bearings.

Foil bearings which have been developed to the point of application include tensioned foil bearings, figure 15, (55), cantilevered foil bearings, figure 16, (56), and bump foil bearings, (57). A more recent version of a bump foil journal bearing, being developed by Mechanical Technology, Inc., is shown in figure 17. A

journal bearing that utilizes a telescoped foil within a rigid shell (58) and a thrust bearing that utilizes a spirally grooved membrane on a compliant back (59) were successfully evaluated in experiments conducted with a high speed rotor. Schematic diagrams of these bearing concepts are shown in figures 18 and 19.

Development work is continuing on both the cantilevered and bump foil bearing types to achieve geometries closer to the optimum for both load capacity and stability. Continued research on these bearings is fully warranted by their promise as rotor support systems superior to conventional oil lubricated bearings for a variety of high speed turbomachines. Their advantages are obvious - the complete elimination of conventional lubrication systems and operating temperature capability limited only by the properties of the bearing materials rather than those of organic lubricants.

All of these bearings are completely self-acting which means that their surfaces are in contact at startup, shutdown and perhaps momentarily at high speeds. Wear resistant surface coatings are therefore mandatory on both the foils and the journal or the thrust runner. Foil coatings must be very thin and resilient, adherent, possess good wear properties and be stable at temperatures up to the maximum operating temperature. Foil bearing coatings are under development (60); the ultimate success of gas bearings depends heavily on the degree of success achieved in coating development.

SUMMARY

A brief status report on bearing technology, present and near-term future problems that warrant research support has been presented. Some selected research needs are the following:

1. Rolling Element Bearings

- a. Bearing materials with improved fracture toughness to allow bearing operation to at least 3 million DN without catastrophic failures.
- b. Ball and roller bearing life data in the low Λ region with carefully controlled surface textures and lubrication factors for correlation with and feedback into a bearing life or failure theory which recognizes competing failure modes.
- c. A comprehensive bearing life or failure theory that goes beyond Lundberg-Palmgren and incorporates competing failure modes.
- d. Bearing experiments at high DN values for assessment of starvation effects.
- e. Incorporation of advanced life prediction methods into bearing dynamic analyses.
- f. An improved corrosion resistant bearing alloy.
- g. Improved thin film surface protective coatings for unlubricated short life bearings.
- h. Optimization of bearing surface texture and geometry for solid film lubrication.

2. Hydrodynamic Bearings

- a. Experiments with non-rotating short journal bearings subjected to oscillating loads to establish the boundaries of cavitated films and pressure distributions in both the film and cavitated regions for prediction of squeeze film damper performance.
- b. Analysis and experiments to determine lubricant supply effects and parasitic churning losses in turbulent flow bearings.
- c. Analysis and experiments to determine optimum geometries for minimum power loss in turbulent flow bearings.

3. Gas Film Bearings

- a. Foil bearing geometries that form more nearly optimum film shapes for maximum load capacity.
- b. Surface protective coatings for use in compliant bearings at temperatures to 1200°F.

REFERENCES

1. Parker, R. J., "Lubrication of Rolling Element Bearings", in Bearing Design - Historical Aspects, Present Technology and Future Problems. ASME, publication H00160, 1980, pp 87-110.
2. Brown, P. F., "Bearings and Dampers for Advanced Jet Engines", SAE Paper No. 700318, April 1970.
3. Zaretsky, E. V., Signer, H., and Bamberger, E. N.: "Operating Limitations of High-Speed Jet-Lubricated Ball Bearings", Journal of Lubrication Technology, Vol. 98, No. 1, Jan 1976, pp 32-39.
4. Signer, H., Bamberger, E. N., and Zaretsky, E. V., "Parametric Study of Thrust Loaded 120-mm Bore Ball Bearings to 3 million DN", Journal of Lubrication Technology, Vol. 96, No. 3, July 1974, pp 515-524.
5. Schuller, F. T., and Signer, H. R., "Effect of Three Lubrication Methods on the Characteristics of a High-Speed 35-Millimeter-Bore Ball Bearing", NASA TP- , 1980.

6. Parker, R. J., Pinel, S. I., and Signer, H. R., "Performance of Computer-Optimized Tapered-Roller Bearings to 2.4 million DN", Journal of Lubrication Technology, Vol. 103, No. 1, January 1981, pp 13-20.
7. Grubin, A. N., "Fundamentals of the Hydrodynamic Theory of Heavily Loaded Cylindrical Surfaces", Investigation of the Contact of Machine Components, K. F. Ketova, ed., Translation of Russian, Book No. 30, Central Scientific Institute for Technology and Mechanical Engineering, Moscow, 1949, Chapter 2. (Available from Department of Scientific and Industrial Research, Great Britain, Transl. CTS-235 and Special Libraries Association, Transl. R-3554.)
8. Dowson, D., and Higginson, G. R., Elastohydrodynamic Lubrication - The Fundamentals of Roller and Gear Lubrication, Pergamon Press, Oxford, 1966.
9. Archard, J. F., and Cowking, E. W., "Elastohydrodynamic Lubrication of Point Contacts", Proc. Inst. Mech. Eng., Pt. 38, Vol. 180, pp 47-66.
10. Hamrock, B. J., and Dowson, D., "Isothermal Elastohydrodynamic Lubrication of Point Contacts. Part III - Fully Flooded Results", Journal of Lubrication Technology, Vol. 99, No. 2, April 1977, pp 264-276.
11. Hamrock, B. J., and Dowson, D. "Isothermal Elastohydrodynamic Lubrication of Point Contacts. Part IV Starvation Results", Journal of Lubrication Technology, Vol. 99, No. 1, January 1977, pp 15-23.
12. Tallian, T. E., et. al., "Lubricant Films in Rolling Contact of Rough Surfaces", ASLE Transactions, Vol. 7, No. 2, April 1964, pp 109-126.
13. Tallian, T. E., "On Competing Failure Modes in Rolling-Contact", ASLE Transactions, Vol. 10, No. 4, October 1967, pp 418-439.
14. Tallian, T. E., Chiu, Y. P. and Van Amerongen, E., "Prediction of Traction and Microgeometry Effects on Rolling Contact Fatigue Life", Journal of Lubrication Technology, Vol. 100, No. 2, April 1978, pp 156-166.
15. Tallian, T. E., "Rolling Bearing Life Modifying Factors for Film Thickness, Surface Roughness and Friction", Journal of Lubrication Technology, Vol. 103, No. 3, October 1981, pp 509-520.
16. Wedeven, L. E., Evans, D., and Cameron, A., "Optical Analysis of Ball Bearing Starvation", Journal of Lubrication Technology, Vol. 93, No. 3, July 1971, pp 349-363.
17. Wolveridge, P. E., Baglin, K. P., and Archard, J. G., "The Starved Lubrication of Cylinders in Line Contact", Proc. Inst. Mech. Eng. (London), Vol. 185, No. 1, 1971, pp 1159-1169.
18. Chiu, Y. P., "An Analysis and Prediction of Lubricant Film Starvation in Rolling Contact Systems", Trans. ASLE, Vol. 17, No. 1, January 1974, pp 22-35.
19. Pemberton, J. C. and Cameron, A., "An Optical Study of the Lubrication of a 65mm Cylindrical Roller Bearing", Journal of Lubrication Technology, Vol. 101, No. 3, July 1979, pp 327-337.
20. Jones, A. B., "Ball Motion and Sliding Friction in Ball Bearings", Journal of Basic Engineering, Vol. 81, 1959, pp 1-12.
21. Jones, A. B., "A General Theory for Elastically Constrained Ball and Radial Roller Bearings Under Arbitrary Load and Speed Conditions." Journal of Basic Engineering, Vol. 82, 1960, pp 309-320.
22. Harris, T. A., "An analytical Method to Predict Skidding in Thrust-Loaded, Angular Contact Ball Bearings", Journal of Lubrication Technology, Vol. 93, No. 1, January 1971, pp 17-24.
23. Coe, H. H., and Zaretsky, E. V., "Predicted and Experimental Performance of Jet-Lubricated 120-mm Bore Ball Bearings Operating to 2.5 million DN". NASA TP-1196, 1978.
24. Harris, T. A., "An Analytical Method to Predict Skidding in High Speed Roller Bearings", Trans. ASLE, Vol. 9, 1966, pp 229-241.
25. Poplawski, J. V., "Slip and Cage Forces in A High Speed Roller Bearing", Journal of Lubrication Technology, Vol. 94, 1972, pp 143-152.
26. Rumbarger, J. H., and Filetti, E. G., and Gubernick, D., "Gas Turbine Engine Mainshaft Roller Bearing - System Analysis", Journal of Lubrication Technology, Vol. 95, 1973, pp 401-416.
- 27.-30. Gupta, P., K., "Dynamics of Rolling-Element Bearings,
 Part I - Cylindrical Roller Bearing Analysis
 Part II - Cylindrical Roller Bearing Results
 Part III- Ball Bearing Analysis
 Part IV - Ball Bearing Results".
Journal of Lubrication Technology, Vol. 101, No. 3, July 1979, pp 293-326.
31. Bamberger, E. N., et. al., "Life Adjustment Factors for Ball and Roller Bearings - An Engineering Design Guide", American Society of Mechanical Engineers, New York, 1971.
32. Skurka, J. C., "Elastohydrodynamic Lubrication of Roller Bearings", Journal of Lubrication Technology, Vol. 92, No. 2., April 1970, pp 281-291.

33. Bamberger, E. N., "Materials for Rolling Element Bearings", in Bearing Design-Historical Aspects, Present Technology and Future Problems. ASME, publication H00160, 1980. pp 1-46.
34. Bamberger, E. N., Zaretsky, E. V., and Signer, H., "Endurance and Failure Characteristics of Mainshaft Jet Engine Bearings at 3×10^6 DN", Journal of Lubrication Technology, Vol. 98, No. 4, October 1976, pp 580-585.
35. Brown, P. F., et. al., "Development of Mainshaft Cylindrical Roller Bearings for Gas Turbine Engines", NAPC Report FR-11453, October 1978.
36. Cunningham, J. S., and Morgan, M. A., "Review of Aircraft Bearing Rejection Criteria and Cause", ASLE, Lubrication Engineering, Vol. 35, No. 8, August 1979, pp 435-441.
37. Parker, R. J., and Hodder, R. S., "Rolling Element Fatigue Life of AMS 5749 Corrosion-Resistant High Temperature Bearing Steel", Journal of Lubrication Technology, Vol. 100, No. 2, April 1978, pp 226-235.
38. Brown, P. F., and Potts, J. R., "Evaluation of Powder Processed Turbine Engine Ball Bearings", Interim Report AFAPL TR-77-26, June 1977.
39. Brown, P. F. and Potts, J. R., "Evaluation of Powder Processed Turbine Engine Ball Bearings", Final Report, AF Contract F33615-75-C-2009, 1980.
40. Reddecliff, J. M. and Valcri, R., "The Performance of a High Speed Ball Thrust Bearing Using Silicon Nitride Balls", Journal of Lubrication Technology, Vol. 98, No. 4, October 1976, pp 553-563.
41. Parker, R. J., and Zaretsky, E. V., "Fatigue Life of High-Speed Ball Bearings With Silicon Nitride Balls", Journal of Lubrication Technology, Vol. 97, No. 3., July 1975, pp 350-357.
42. Wilson, D. S., et. al., "The Development of Lubricants for High Speed Rolling Contact Bearings Operating at 1200° F Temperature", WADC TR-59-590, Wright Air Development Center, Ohio, 1959.
43. Seibbe, H. W., "Bearings and Seals For Cryogenic Fluids", SAE Paper No. 680550, October 1968.
44. Anon., "Solid Lubricated Rolling Element Bearings", Semiannual Status Report No. 6, DARPA Order No. 3576, October 1981.
45. Allaire, P. E., and Flack, R. D., "Journal Bearing Design For High Speed Machinery", in Bearing Design Historical Aspects, Present Technology and Future Problems. ASME, publication H00160, 1980, pp 111-159.
46. Pan, C. H. T., "An Improved Short Bearing Analysis for the Submerged Operation of Plain Journal Bearings and Squeeze Film Dampers", Journal of Lubrication Technology, Vol. 102, No. 3, July 1980, pp 320-332.
47. Pan, C. H. T., and Ibrahim, R. A., "Cavitation in Short Bearing with Pressurized Lubricant Supply", Journal of Lubrication Technology, Vol. 103, No. 3, July 1981, pp 337-349.
48. Etsion, I., and Ludwig, L. P., "Observation of Pressure Variation in the Cavitation Region of Submerged Journal Bearings", NASA TM-81562, 1981.
49. Wilcock, D. F., "Turbulence In High Speed Journal Bearings", Trans. ASME, Vol 72, 1950, pp 825-834.
50. Wilcock, D. F., "Design of Efficient Turbulent Thrust Bearings", Journal of Lubrication Technology, Vol. 99, No. 1, January 1977, pp 113-121.
51. Taylor, C. M., "Turbulent Flow Bearings: Design and Energy Losses", in Bearing Design-Historical Aspects, Present Technology and Future Problems. ASME publication H00160, 1980, pp 161-185.
52. Garner, D. R., Jones, C. J. and Martin, F. A., "Turbulent Journal Bearings: Design Charts for Performance Prediction", Transactions ASLE, Vol. 3, 1977, pp 221-232.
53. Jones, C. J. and Martin, F. A., "Turbulent Journal Bearings: Dimensionless Steady-State Performance Charts for the Two-Axial Groove Case", Transactions ASLE, Vol. 23, 1980, pp 163-174.
54. Martin, F. A., "Tilting Pad Thrust Bearings: Rapid Design Aids", Proceedings Institution of Mech. Engrs., Vol. 184, Pt. 3L, 1970, pp 120-138.
55. Licht, L., Branger, M., and Anderson, W. J., "Gas Lubricated Foil Bearings for High Speed Turbo-alternator -Construction and Performance", Journal of Lubrication Technology, Vol. 96, No. 2, April 1974, pp 215-223.
56. Emerson, T. P., "The Application of Foil Air Bearing Turbomachinery in Aircraft Environmental Control Systems", ASME Paper 78-ENAS-18.
57. Gray, S., Sparks, S., and McCormick, J., "The Application of Gas-and-Oil Lubricated Foil Bearings for the ERDA/Chrysler Automotive Gas Turbine Engine", ASME Paper No. 76-GT-115, March, 1976.
58. Licht, L., Anderson, W. J., and Doroff, S., "Dynamic Characteristics of a High-Speed Rotor with Radial and Axial Foil-Bearing Supports", Journal of Lubrication Technology, Vol. 103, No. 3, July 1981, pp 361-372.

59. Licht, L., Anderson, W. J., and Doroff, S., "Design and Performance of Compliant Thrust Bearings With Spiral-Groove Membranes on Resilient Supports", Journal of Lubrication Technology, Vol. 103, No. 3, July 1981, pp 373-388.

60. Anon., "36th Monthly R&D Status Report-APU Gas-Lubricated Turbine End Foil Bearing Development and Performance Verification", A. F. Contract No. F33615-78-C-2044, August, 1981.

TABLE I. - AIRCRAFT BEARING REJECTIONS BY CAUSE (FROM (36))

CATEGORY	PERCENT OF TOTAL		
	1969	1971	1977
DIMENSIONAL DISCREPANCIES	15	10	18
CORROSION/PITTING	32	30	29
IMPROPER INSTALLATION, DAMAGED DURING REMOVAL OR HANDLING	7	5	6
WEAR, EXCESSIVE INTERNAL CLEARANCES	--	15	8
FATIGUE, SURFACE OR SUBSURFACE INITIATED	2	3	1
CAGE WEAR	2	3	--
INDENTATIONS/CONTAMINANTS (NICKS, SCRATCHES, DENTS)	14	19	20
OTHER - CHANGE IN DIRECTIVES, SPEC'S, TIME COMPLIANCE, ETC.	28	15	18

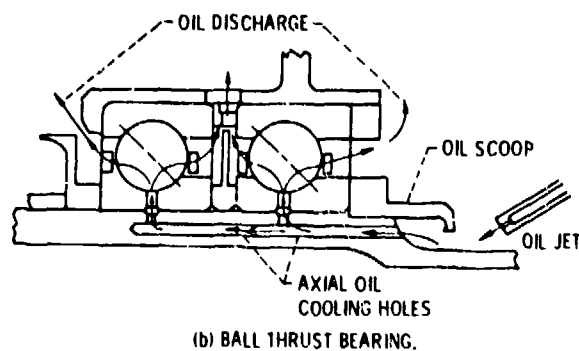
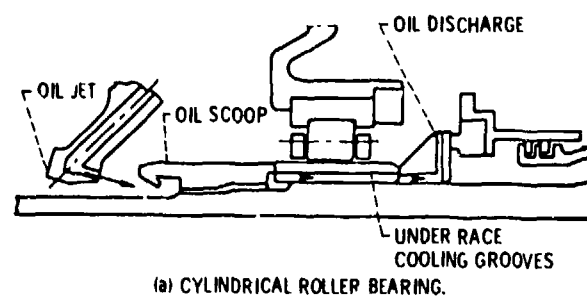


Figure 1. - Underrace oiling system for main shaft bearings on turbofan engine. (From ref. 2.)

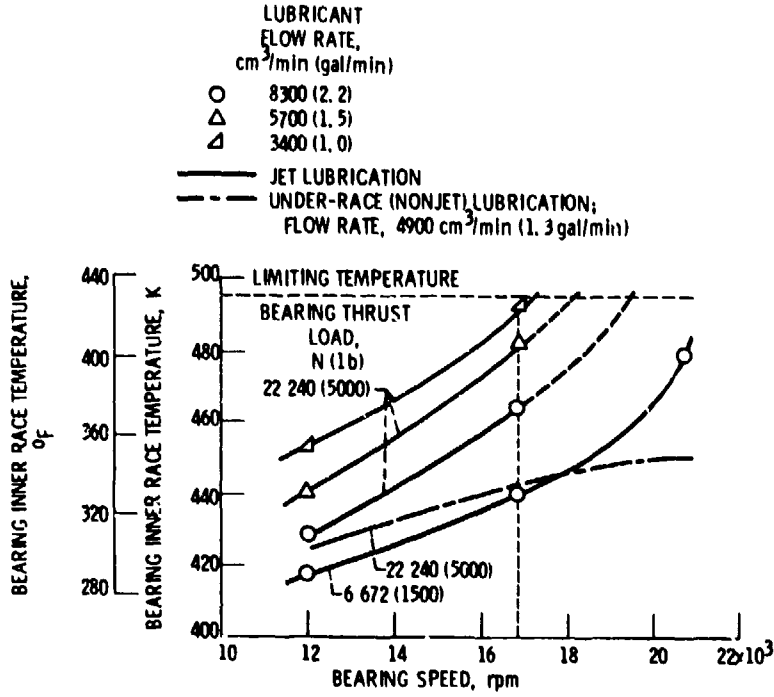


Figure 2. - Effectiveness of under-race lubrication with 120 mm-core angular contact ball bearings. (Oil-in temperature, 394 K (250° F), (From ref. 3.)

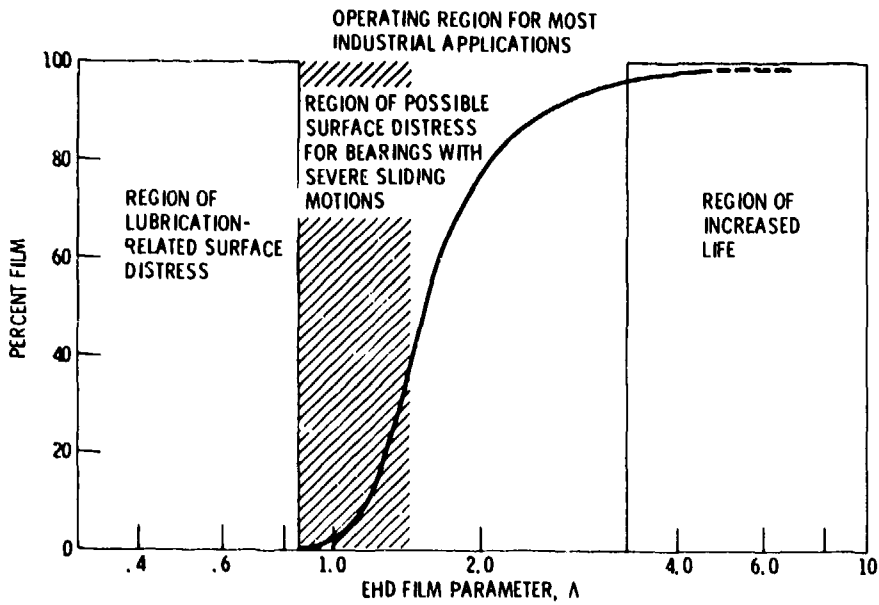


Figure 3. - Percent film as a function of EHD film parameter. (From ref. 13.)

59. Licht, L., Anderson, W. J., and Doroff, S., "Design and Performance of Compliant Thrust Bearings With Spiral-Groove Membranes on Resilient Supports", Journal of Lubrication Technology, Vol. 103, No. 3, July 1981, pp 373-388.

60. Anon., "36th Monthly R&D Status Report-APU Gas-Lubricated Turbine End Foil Bearing Development and Performance Verification", A. F. Contract No. F33615-78-C-2044, August, 1981.

TABLE I. - AIRCRAFT BEARING REJECTIONS BY CAUSE (FROM (36))

CATEGORY	PERCENT OF TOTAL		
	1969	1971	1977
DIMENSIONAL DISCREPANCIES	15	10	18
CORROSION/PITTING	32	30	29
IMPROPER INSTALLATION, DAMAGED DURING REMOVAL OR HANDLING	7	5	6
WEAR, EXCESSIVE INTERNAL CLEARANCES	--	15	8
FATIGUE, SURFACE OR SUBSURFACE INITIATED	2	3	1
CAGE WEAR	2	3	--
INDENTATIONS/CONTAMINANTS (NICKS, SCRATCHES, DENTS)	14	19	20
OTHER - CHANGE IN DIRECTIVES, SPEC'S, TIME COMPLIANCE, ETC.	28	15	18

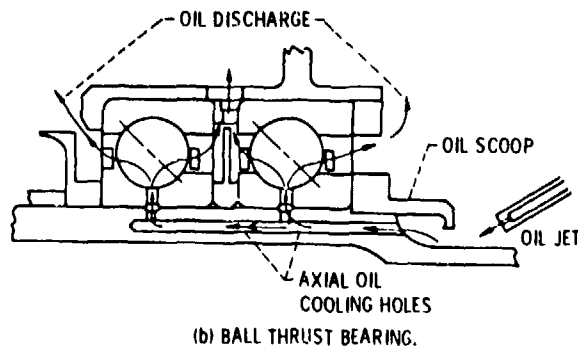
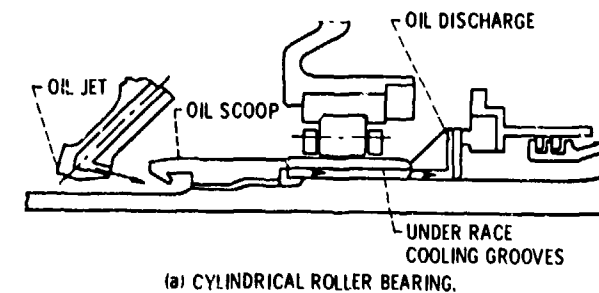


Figure 1. - Underrace oiling system for main shaft bearings on turbofan engine. (From ref. 2.)

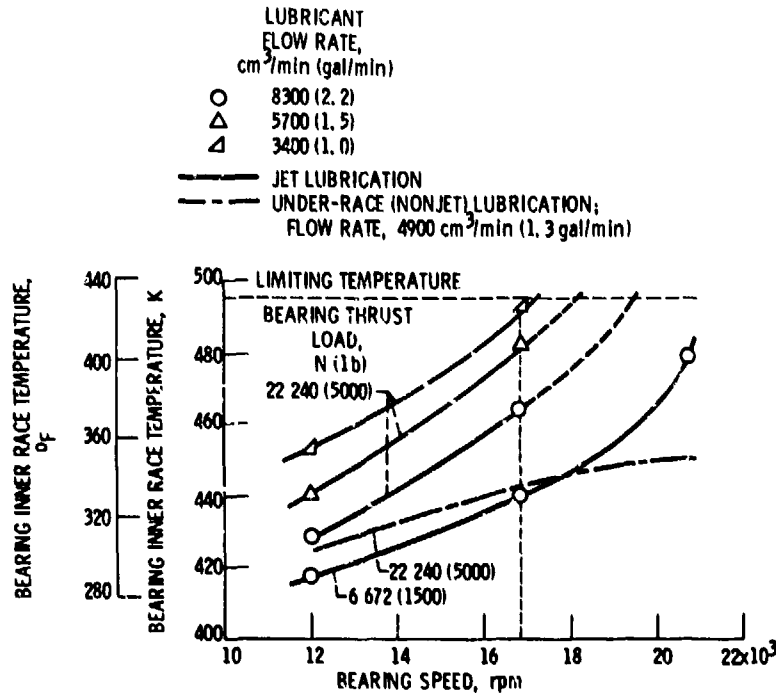


Figure 2 - Effectiveness of under-race lubrication with 120 mm-bore angular contact ball bearings. (Oil-in temperature, 394 K (250° F), (From ref. 3.)

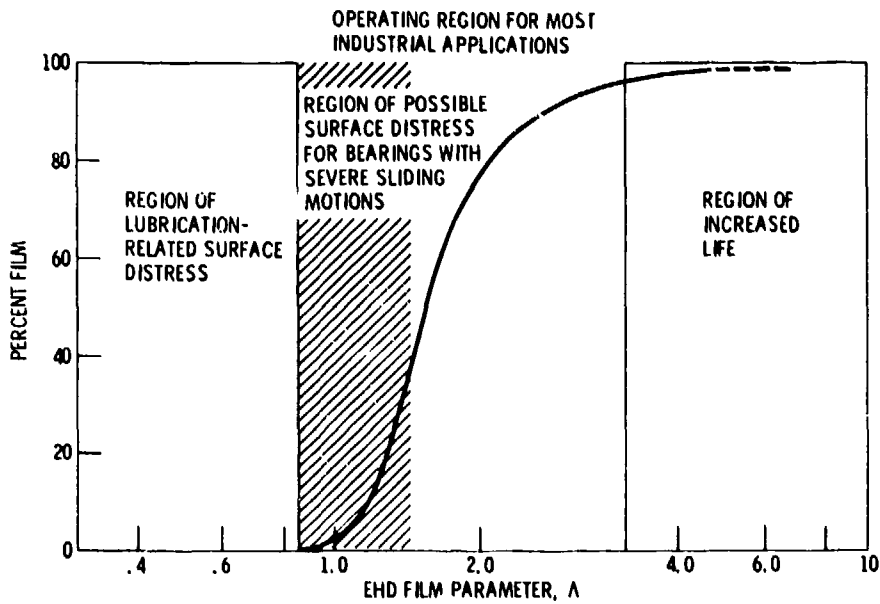
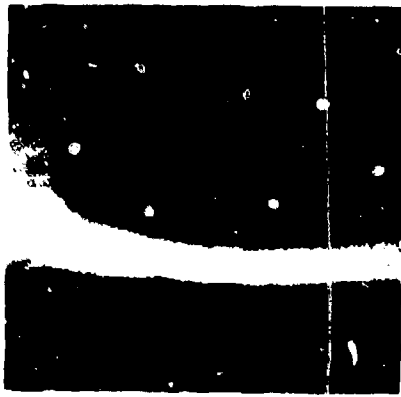
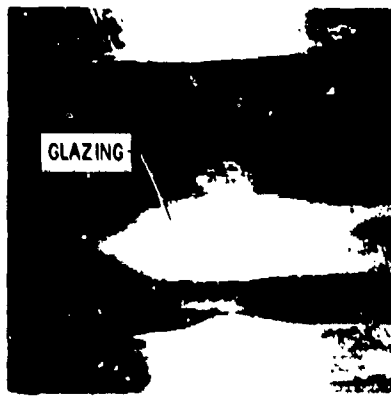


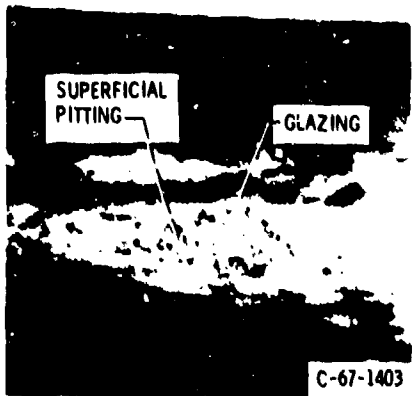
Figure 3 - Percent film as a function of EHD film parameter. (From ref. 13.)



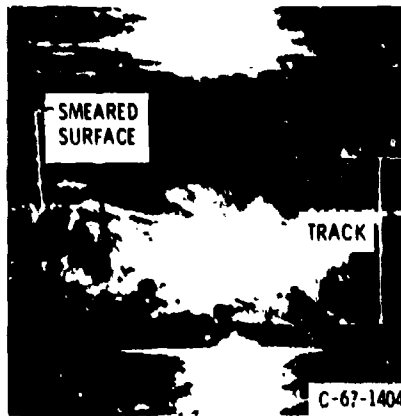
(a) NORMAL RACE APPEARANCE AFTER BEING RUN WITH FULL ELASTOHYDRODYNAMIC LUBRICATION.



(b) RACE APPEARANCE AFTER GLAZING.



(c) RACE APPEARANCE AFTER GLAZING AND SUPERFICIAL PITTING.



(d) RACE APPEARANCE AFTER SMEARING.

Figure 4. - Effect of EHD lubrication on surface damage to bearing raceways. (From 1,)

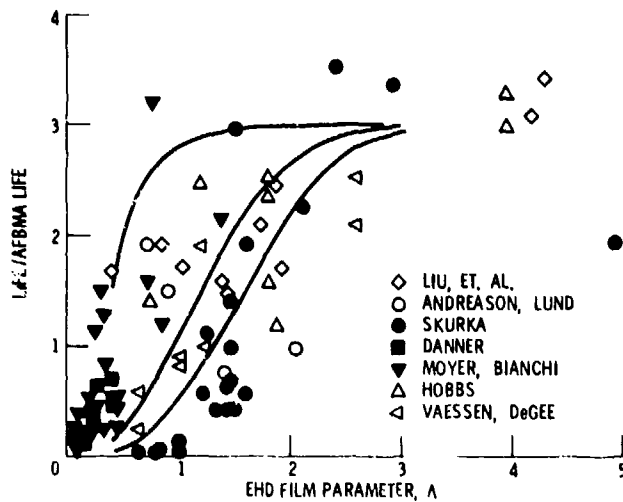


Figure 5. - Effect of λ -ratio on life. (From ref. 15,)

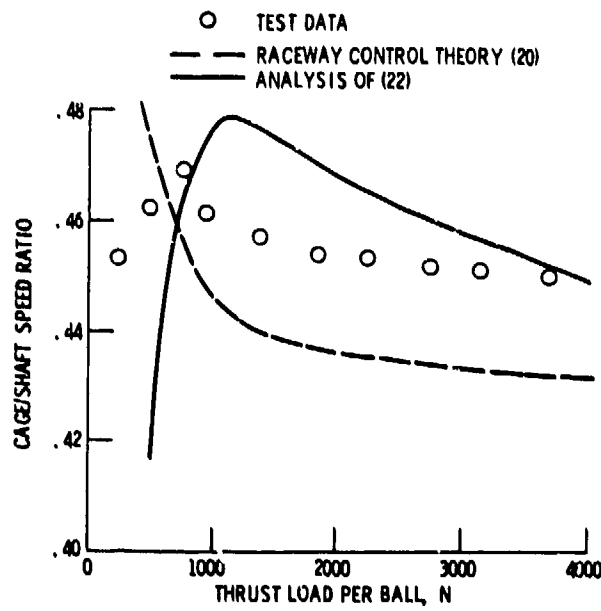


Figure 6. - Cage/shaft speed ratio versus thrust load per ball. (From ref. 22.)

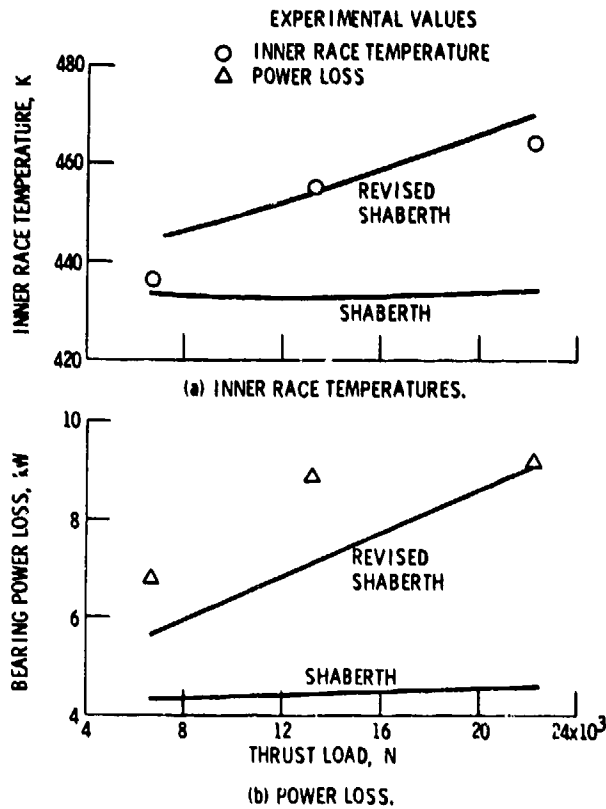


Figure 7. - Comparison of measured and calculated values of bearing operating characteristics as functions of thrust load using two versions of SHABERTH. Shaft speed, 16 700 rpm; lubricant flow rate, 8.3×10^{-3} cubic meter per minute (2.2 gal/min); volume of lubricant, 2 percent. (From ref. 23.)

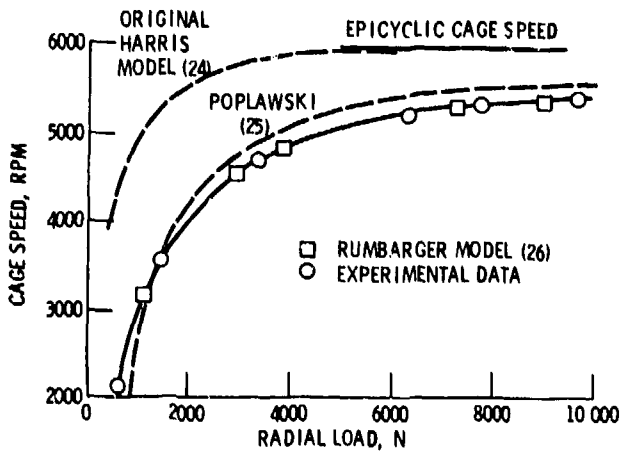


Figure 8. - Roller bearing cage speed correlation.

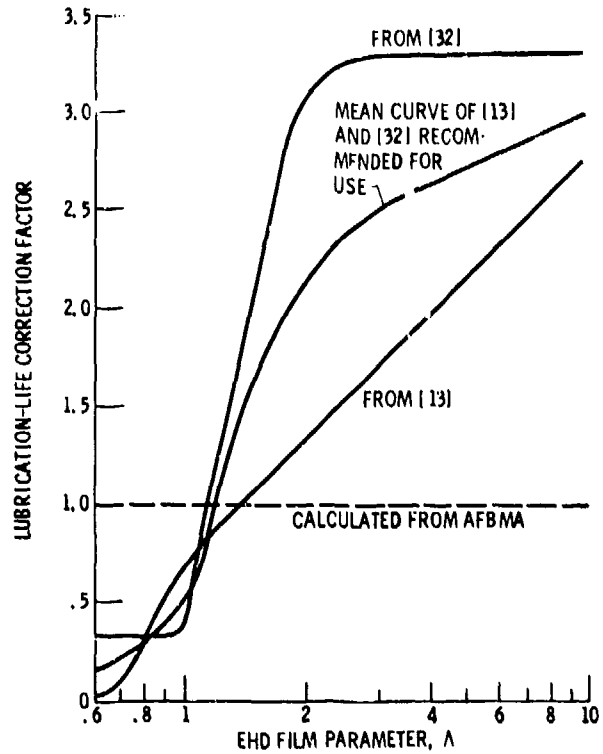


Figure 9. - Lubrication-life correction factor as a function of lambda, (From ref. 31.)

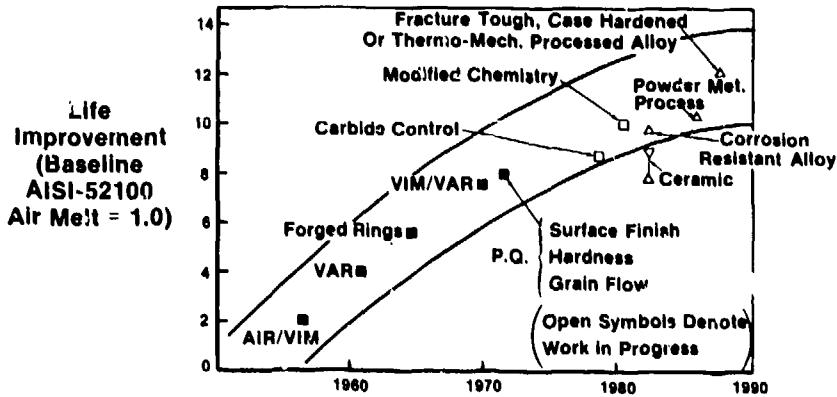


Figure 10. - Evolution of A, I, S, I M-50 bearing steel, (From ref. 33.)

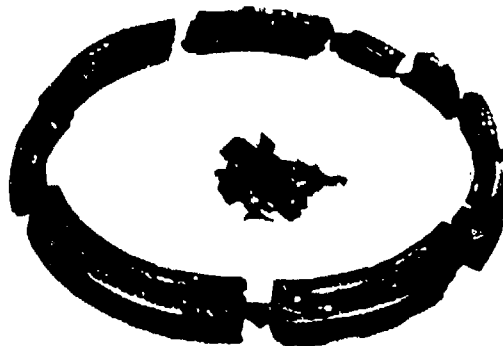


Figure 11. - Fractured bearing inner race initiated by a rolling-element fatigue spall, (From ref. 34.)

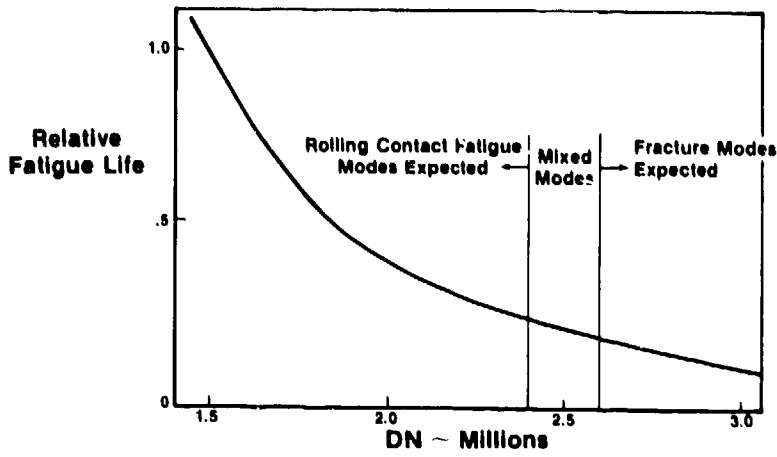


Figure 12. - Mainshaft bearing lives and expected failure mode as a function of speed for a constant bore size. (From ref. 33.)

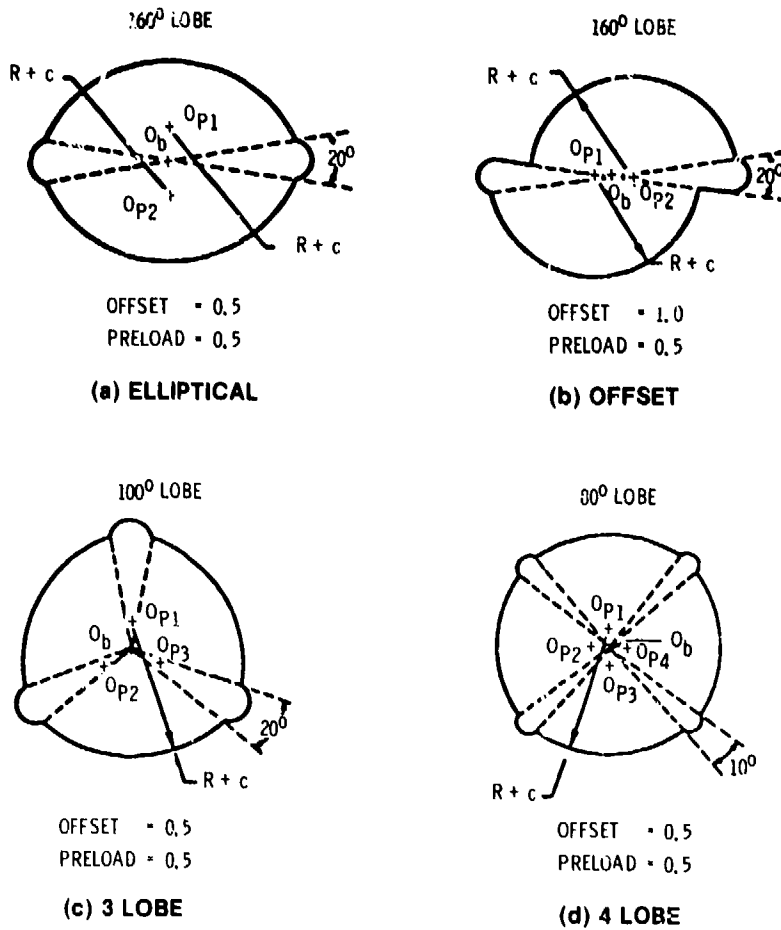


Figure 13. - Multilobe bearing geometry. (From ref. 45.)

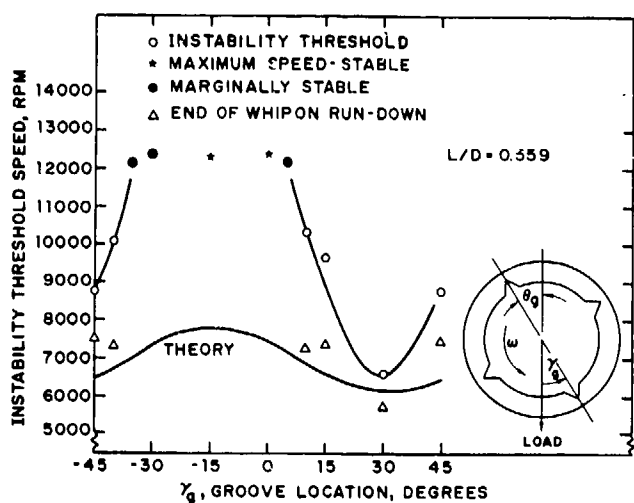


Figure 14. - Summary of correlation of instability threshold speed with γ_g . (From ref. 45.)

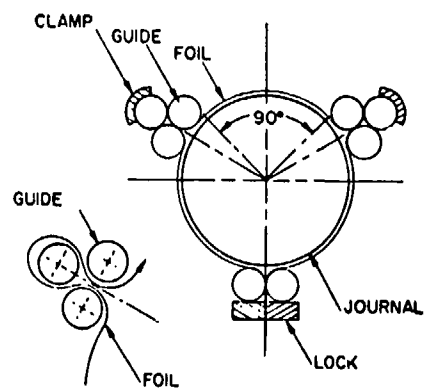


Figure 15. - Schematic diagram of tensioned foil-bearing. (From ref. 55.)

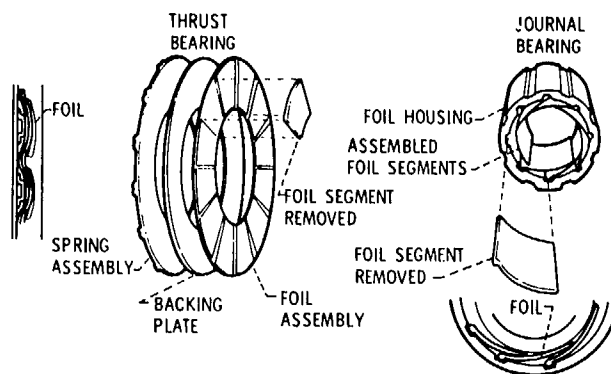


Figure 16. - Cantilevered foil bearings (Garrett Corp.). (From ref. 56.)

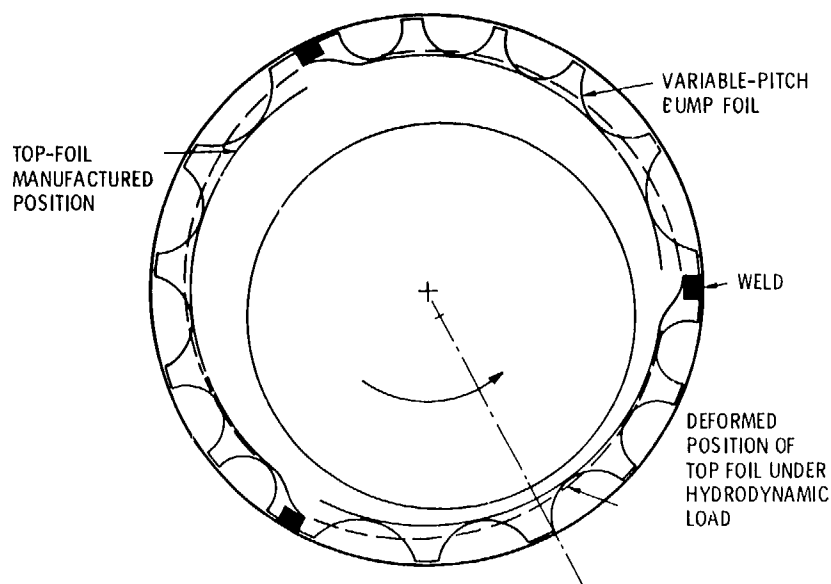


Figure 17. - A three sector bump foil journal bearing with variable pitch bump foils. (Mechanical Technology, Inc.)

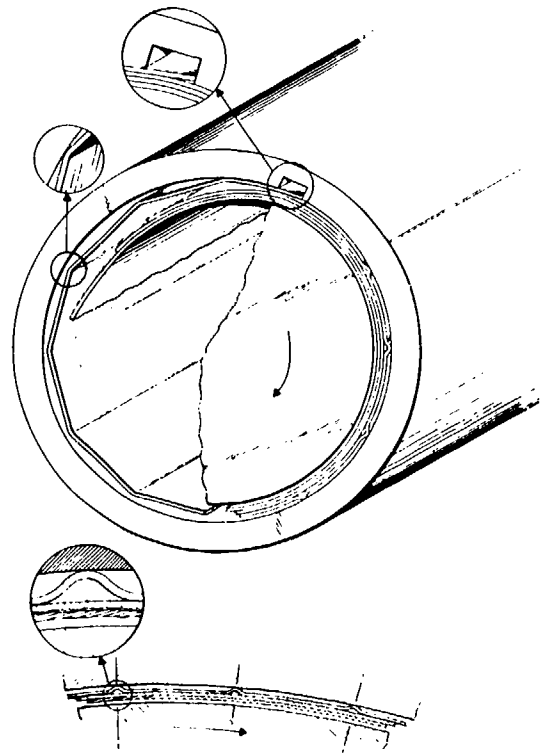


Figure 18. - Schematic drawing of journal foil-bearing (Design B). Structure before and after insertion of journal is depicted. Details illustrate rounded vertices and retaining groove. (From ref. 58.)

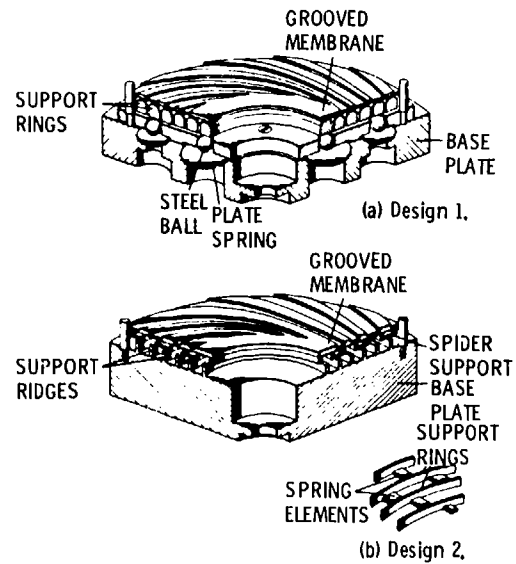


Figure 19. - Isometric drawings of thrust bearings. (From ref. 59.)

DISCUSSION

D.G.Astridge, Westland Helicopters, Yeovil, UK

Concerning the low $\Lambda (= h/R)$ region for rolling element bearings (and gears), much attention is being given to improvement of film thickness, as evidenced by the number of papers at this conference. Much attention is also being given to the analysis and modelling of the influence of surface roughness characteristics on film thickness (h). It should be remembered, however, that surface roughness (R) is just as influential and further work is required to establish the required characteristics of optional surface finish, and the means of producing this. Also, the influence of filtration on the size of build or wear debris particles entrained in these contacts should be noted -- of the three factors discussed, h , R , and particle size, the latter is the one which we can address most readily. The program carried out by the US Army on 50 UH-1 helicopters has demonstrated the powerful influence of fine filtration on the life of bearings and gears in engines and transmissions. The optimum value of 3 mm absolute may appear magical at first sight, in terms of its universal applicability to aircraft gears and bearings, and in the fact that at this filtration level normal wear processes appear to be arrested, I am sure that both can be explained by EHL theory (film thickness virtually independent of load - temperatures and surface speeds not too different) and by surface roughness characteristics of ground bearings and gears). I found your survey very valuable, but would make a plea for implementation of fine filtration and improved surface finishes.

Author's Reply

It is fully agreed that factors such as surface roughness, surface texture and lubricant cleanliness are critical to system life and reliability. Further work needs to be done on those aspects of achieving improved system performance and durability.

E.Covert, MIT, US

Is there any discussion of cryogenic application of bearings?

Author's Reply

No. Although this is certainly a relevant topic for review.

C.Brownridge, Pratt & Whitney, Ca

What is the maximum D. N. Value used today in Engines today?

Author's Reply

Approximately 2.2 to 2.3 million.

DETECTION AND DIAGNOSIS OF BEARING DETERIORATION
IN AIRCRAFT PROPULSION SYSTEMS BY WEAR DEBRIS ANALYSIS

C.A. Waggoner
Defence Research Establishment Pacific
Victoria, B.C. Canada VOS 1B0

ABSTRACT

Because of high investment and maintenance costs for various types of propulsion equipment, such as aircraft gas turbine engines and transmission systems, considerable interest exists in nondestructive methods of monitoring mechanical condition to forestall costly failures, increase reliability, and maximize useful operating life. Various methods have evolved by which wear debris can be effectively utilized to diagnose wear condition and reveal imminent mechanical failure. Spectrometric trend monitoring of wear metals in lubricating oils is the predominant method in current use. In recent years new methods, such as ferrography and scanning electron microscopy coupled with X-ray microanalysis, have been applied to extract additional diagnostic information from wear debris. As a consequence, the nature and severity of mechanical wear in oil-lubricated components can now be more completely characterized. Aspects of wear revealed by advanced analytical methods, and the manner in which these methods are being successfully applied to detect and diagnose bearing deterioration in aircraft propulsion machinery are reviewed.

INTRODUCTION

In the management of military aircraft operation, maintenance of propulsion machinery accounts for a major proportion of life cycle costs. Considerable effort is therefore expended in finding ways to facilitate and minimize maintenance, and improved tools and techniques for performance assessment and condition monitoring are continually being sought to ensure dependability and forestall costly failures.

Monitoring the condition of dynamic components such as bearings presents special problems. Apart from effectiveness, fault sensing techniques must be nondestructive, and must not unduly disrupt equipment operation. While numerous monitoring concepts have been proposed, no single method meets all requirements for satisfactory failure detection and diagnosis. Present practice, therefore, is to use mutually supportive procedures proven by experience to reduce maintenance costs.

A well-known concept that has met with some success is wear debris analysis.^{1,2} Although this procedure is well-established for military aircraft, there is ample evidence that its effectiveness could be greatly improved by the application of newer methods which are better suited to utilizing the diagnostic information available from wear debris. This paper reviews some current advances and trends in wear debris analysis with emphasis on bearing failures in aircraft propulsion equipment.

BACKGROUND

Bearing failure continues to be a primary cause of aircraft machinery malfunction and, consequently, is the focus of extensive research and development into improved diagnostic techniques, as well as into more wear-resistant materials. Experience in current wear debris monitoring programs has shown that existing procedures are in many cases ineffective or only marginal in the timely detection of bearing deterioration. For example, Figure 1 illustrates the breakdown of a turbo-jet engine bearing that was barely detected in time to avoid complete destruction. The quantity of debris subsequently recovered from an oil sample taken prior to detection was unusually large (Figure 2) and included coarse fragments representative of the severe pitting and spalling evident on the races and balls. A surprising aspect of the analytical results was the discovery, on more accurate analysis of the sample, that the detection was made on the basis of little more than one-third of the actual iron content because of method

deficiencies. Consequently, this case and others of similar nature have pointed to an obvious need for critical review of conventional analytical procedures and the prospects of utilizing wear debris to better advantage.

The merits of potential analytical methods are judged on the basis of their capabilities with respect to failure detection, diagnosis, and prognosis. The time available to carry out these separate actions is defined by the lead-time allowed by the particular type of failure. Prospective methods must therefore be capable of providing accurate data as early as possible if failure is to be properly diagnosed and avoided. The variety of wear debris analysis methods now available can be classed basically as "in-line" or "off-line" in application and detective or diagnostic in function. The most economic and effective monitoring program would combine reliable in-line real-time fault sensing for early detection of incipient bearing failure and precise off-line diagnostic procedures to predict life expectancy. However, proven real-time sensors are not yet available and present aircraft monitoring programs still rely primarily on off-line detection techniques. Since these techniques give only limited data concerning component wear, more informative analytical procedures are being applied increasingly to ensure correct diagnosis of the nature and extent of deterioration. Prognosis, or the prediction of remaining life following detection of an abnormality, is dependent on the quality of diagnostic data and background experience relating to characteristic failure trends. At present, further understanding of failure processes and refinement of diagnostic procedures are necessary before prognoses can be made with full confidence.

WEAR DEBRIS ANALYSIS

The use of wear debris in lubrication systems for monitoring machinery health has a long history, particularly as it relates to spectrometric oil analysis. However, only in the last decade has the concept been recognized in its broadest context, which includes the physical as well as the chemical characteristics of wear particles. With the development and adaptation of new methods of analysis, such as ferrography and electron microscopy, new perspectives on wear mechanisms have evolved, and the prospects of more cost-effective monitoring have greatly improved.

In the application of wear debris analysis, significant advantages and some disadvantages are evident, as follows:

Advantages

- minimal interference with machinery operation
- independent of operating parameters
- failing components identifiable
- wear mode and severity determinable
- high sensitivity to wear rate change
- verification of results readily done
- indicates cleanliness of lubrication system

Disadvantages

- requires substantial lead time to detect failure
- requires skilled personnel for effective application
- high instrumentation and monitoring costs
- labor-intensive
- moderate potential for judgmental errors

In view of the limited availability of other suitable diagnostic methods for monitoring dynamic components, the advantages of wear debris analysis presently outweigh the disadvantages and this approach continues to be one of the more attractive options for aircraft machinery.

In recirculatory systems, wear debris samples are generally available from three sources: the lubricating oil, magnetic plugs, and the pressure filter (Figure 3). Oil sampling is done from the return or scavenge line before filtration to obtain debris representative of current condition. Magnetic plugs, also located in the scavenge line, cumulatively sample a portion of the debris within a pre-determined time frame. The pressure filter contains virtually all debris generated over a given time span, which is thus representative of the total wear for the period. The oil sample normally contains wear particles finer than the filter pore size, commonly in the 30 to 50 μm range. Since 15 to 25 μm particles are indicative of accelerating wear, debris from this source permits the earliest detection of bearing deterioration. Coarser particles (>100 μm) are collected by the magnetic plug and a substantial time interval may be required to accumulate sufficient debris for visual or microscopic examination of wear severity. Fine (pressure) filters are an excellent source of accumulated wear debris of broad size range and have yet to be fully exploited for wear diagnosis.

The current trend to finer oil filtration ($\approx 3 \mu\text{m}$) in aircraft engines to extend useful life by removing damaging abrasive debris suggests that oil samples will become an outmoded source of debris in future. Chip detectors and filters of improved design are therefore likely to become more important sources of debris for diagnostic monitoring.

Wear debris contains a wealth of information about the state of component wear in mechanical equipment. For example, debris and wear particle data of importance, and the respective diagnostic significance, are as follows:

<u>Parameter</u>	<u>Interpretation</u>
Quantity (volume or metal content)	degree and rate of wear
Composition (general)	characteristic wear metals and contaminants
Composition (particulate)	material specification, component source
Particle Size	stage of wear and possible severity
Particle Morphology	modes and severity of wear

Several analytical methods and procedures highly suited to the recovery of this information for diagnostic application are now available.

METHODOLOGY

The simplest methods of wear debris analysis are based on visual or microscopic examination to obtain elementary clues about machinery condition. However, the most informative methods are based on more complex analytical instrumentation which provides appreciably greater insight into the character and severity of wear and thus, the actual condition of equipment. The more advanced methods in current use and undergoing further evaluation and improvement are: alternative spectrometric analysis techniques, ferrography, electron microscopy, and X-ray microanalysis. Spectrometric analysis is widely used as a primary method, while the remaining methods are presently used in supporting roles.

Spectrometric Oil Analysis (SOAP)

This method has been moderately effective in identifying deterioration of aircraft bearings and associated components. Two analytical procedures are in common use on military bases, one based on direct-reading atomic emission spectrometry (AE), and the other on atomic absorption spectrometry (AA). The former has the advantages of minimum sample preparation and fast, automatic read-out, and documentation of results when coupled with modern data processing techniques. The AA method is less costly but more time-consuming and, though more sensitive for some significant wear metals, eg. silver, it is likely to be used for only small monitoring programs in future. Two alternative spectrometric methods - X-ray fluorescence spectrometry and plasma spectrometry - show promise of quantitative superiority but are expensive and need further development. Plasma spectrometry has exceptionally high sensitivity and offers the prospect of identifying the material specification and thus, the origin of isolated particles.

Because of speed and the ability to cope with large numbers of oil samples, spectrometric oil analysis is the most effective off-line method for the early detection of wear anomalies. Its applicability for detecting aircraft bearing deterioration is greatly enhanced by the special materials used in bearing assemblies. For example, alloy-rich tool steel bearings, such as M50, and high nickel (Incoloy) bearing housing alloys facilitate identification, and bronze and steel bearing cages with silver platings enable ready spectrochemical diagnosis of cage wear. Other component materials of singular composition, eg. graphite seal debris, are identifiable by complementary techniques such as X-ray diffractometry.

Although SOAP has enjoyed moderate success as a preventive maintenance procedure, shortcomings are frequently evident in cases in which typical failures are not detected. This has prompted critical examination of spectrometric procedures which has revealed limitations in accuracy due to insensitivity to larger wear particles (>5 μm) of primary diagnostic importance. As previously mentioned, studies have shown that more than half the wear debris in a sample may be overlooked in an analysis. It has been demonstrated that if more accurate analysis was done, fewer failure oversights would occur and earlier detections would be possible. A refinement of the method in which wear debris is isolated by microfiltration of the sample and dissolved in acids prior to analysis has been shown to improve accuracy and yield supplementary information concerning the size distribution and significance of wear particles.

Ferrography

Ferrography, a method of wear particle analysis that appeared in the early 1970's,³ has stimulated new interest in mechanical wear phenomena and the potentialities of machinery condition monitoring. Although simple in concept, this method uniquely reveals the nature of wear and is very sensitive to changing wear conditions. The method has proven particularly effective for the characterization of aircraft turbine engine bearing deterioration.

In principle, ferromagnetic wear debris in an oil sample is isolated magnetically on a glass slide (Figure 4) and particles are separated into large (>5 μm) and small (<5 μm) size fractions. The entry deposit on the resulting ferrogram contains the larger particles which are of primary diagnostic interest based on the observation that wear particle size increases as wear progresses. By examination of the debris in a bichromatic illumination microscope and optical measurement of particle density, much can be learned about the qualitative and quantitative aspects of wear processes.

Particle features observed at high magnification (1000 X) reveal the various modes of material failure, and the measured area or density ratio of large to small particles provides an index of wear severity. Non-ferrous particles, such as copper and aluminum, are also retained on the ferrogram and are distinguishable by color or random alignment.

Wear caused by the dynamic surface interaction of rolling bearing components produces particles with distinctive features characteristic of the mechanisms by which they were formed. Surface fatigue, induced by such factors as subsurface stresses, surface flaws, and cyclical loading, is the classic failure mode in ball and roller bearing components. This type of failure is evidenced by surface pitting and spalling. The majority of particles generated in advanced bearing wear will therefore be in the form of irregularly shaped flat platelets representative of these mechanisms.⁴ Associated particle forms indicative of bearing surface fatigue are thin laminar fragments, apparently produced by interfacial sandwiching, and small spheres (<3 μm dia.) believed to be generated by ultrafine particle agglomeration during fatigue crack propagation. Other common wear modes may also be evident in debris originating from rolling bearings or associated components. Rubbing (adhesive) and cutting wear often precede fatigue wear, for example, and particle contamination produced by these mechanisms may, in fact, initiate surface fatigue. As wear progresses, clearances and abrasive contaminant levels increase and, as a consequence, secondary damage occurs as other components begin to wear and generate identifiable characteristic particles.

To gauge the significance of wear, optical measurements can be made from the ferrogram deposit or with a direct-reading ferrograph which magnetically separates large (A_L) and small (A_S) particles as the oil sample flows through a glass tube and numerically measures the relative density of the fractions by parallel densitometers. An index of wear severity (I_S) is calculated from area measurements by an arbitrary relationship $I_S = A_L^2 - A_S^2$, which correlates debris quantity and particle size distribution. This index increases sharply as debris quantity and particle size increase with advancing wear. Since aircraft engine wear debris is comparatively free of interfering non-metallic contaminants, the index can be an effective indicator of the rate of bearing deterioration.

Scanning Electron Microscope/X-ray Microanalysis

The scanning electron microscope coupled with an X-ray microprobe analyser adds a further dimension to ferrography for wear particle analysis,⁵ and facilitates the study of surface wear phenomena in failure diagnosis. For wear particle examination the ferrogram serves as an ideal sample when coated with an electrically conductive carbon film. Outstanding advantages gained with this instrumentation are: 1) the extension of the optical microscope magnification limit of 1000 X by several orders of magnitude with high resolution and large depth of focus, and 2) the ability to utilize characteristic X-ray signals to perform elemental chemical analyses on individual wear particles. Particle form and surface topography can thus be more precisely correlated with wear mode and the location of abnormal wear can be determined from material specifications. Facilities of this kind are therefore invaluable diagnostic aids in the characterization of bearing failures. Despite high initial costs, their use is expanding as potentialities are recognized and military requirements warrant more cost-effective machinery condition monitoring.

CASE HISTORY

To illustrate the manner in which the above methods can improve the detection and diagnosis of bearing deterioration, a case history relating to a General Electric T58 helicopter engine is reviewed. Impending failure of the engine was predicted by conventional spectrometric oil analysis and confirmed by filter examination. Oil samples therefore contained meaningful wear debris that could be used as a basis for evaluating the above methods and establishing whether further relevant diagnostic information was available.

The detection of the apparent abnormality was based on wear metal trends in five samples preceding bearing failure. Incipient wear was indicated by small increases in iron, copper, and silver, but prescribed caution guidelines had not been reached. Engine failure was averted on discovery of excessive wear debris in the filter. Inspection revealed that the front bearing was in an advanced state of deterioration.

Retrospective analysis by the procedures discussed above provided an enlightening failure diagnosis. Comparative spectrometric data are shown in Figure 5. In the original analysis (lower profiles) sudden increases in iron to 8 ppm and copper to 2 ppm were noted after 140 operational hours. By applying the more accurate technique involving microfiltration and acid dissolution of the wear debris prior to spectrometric analysis, substantially higher results (24 ppm iron and 8 ppm copper) were obtained (upper profiles). Further, it was noted that iron content had actually increased fivefold in the preceding sample taken 13 hours earlier. Application of ferrography confirmed these results (Figure 6), indicating the early increase followed by the sharp increase as bearing deterioration progressed. This profile of wear rate reflects the significant growth in particle size as surface pitting and spalling developed. Confirmation of these events was then revealed by scanning electron microscopy and X-ray microanalysis (Figure 7). The large particle, verified as AISI type 52100

bearing steel, is typical of surface fatigue spalling. Cutting wear particles, evident at the lower right, were observed by ferrography in the early samples before spalling occurred, and are a possible cause of the surface fatigue that led to failure. Positive identification of silver-plated brass particles by X-ray microanalysis also confirmed that cage wear was much more severe than indicated by the original copper determination.

It is clear, therefore, that the initial detection of this failure could have been made more positively, and probably earlier, had more accurate and comprehensive analysis of the wear debris been possible. Similar results observed in other bearing failures confirm that the diagnostic information available from wear debris is not being fully or adequately exploited by present methods, and that monitoring programs could be appreciably more cost-effective if appropriate combinations of analytical procedures were employed.

FAILURE DIAGNOSIS

An important aspect of any evaluation of new non-destructive methods with potentialities for wear detection or diagnosis is the correlation of observed results with actual damage to machinery components. It is essential, therefore, to identify the symptoms by which abnormal wear can be recognized at progressive stages if reliable judgments of mechanical condition are to be made. Retrospective in-depth investigation of failures occurring in service equipment offers an expedient course if components are not too severely damaged and useful diagnostic evidence is not obliterated. However, to properly understand and define the sequence of wear mechanisms it is necessary to examine the wear process from its initiation rather than its termination. This can only be done systematically with test machinery in which normal operating parameters can be simulated. For example, observation of one stage of roller bearing deterioration under controlled conditions has identified the stages of wear at which detection and diagnosis become feasible.

Rollers in gas turbine engine bearings have a common tendency to wear excessively on their front ends (Figure 8). In the early stage smooth polishing wear occurs, accelerating in depth as fine abrasive particles are generated, and producing a sharp, pronounced ridge at the boundary of the roller end contact with the race flange. As clearances increase, slackness and skewing of the roller develops, causing high stress contact which initiates fatigue pitting on both the roller end face and the opposing inner race flange surface (Figure 9). With increasing roller skewing, secondary damage begins by rubbing contact of the roller end and the roller surface extremities with the bronze cage walls. Deep circular tracks develop in the sidewalls and dumbbell-shaped wear scars form on the cage ribs (Figure 10). In the latter case, the wear mode changes from fine rubbing action to fatigue spalling (flaking) with a corresponding increase in particle size ($>20 \mu\text{m}$). Deterioration then proceeds rapidly to final destruction of the bearing.

From the perspective of wear debris analysis, events in the course of the failure that provide diagnostic evidence are the initial removal of fine particulate steel debris, the proportional increase in particle size as fatigue pitting develops, and the generation of fine particulate bronze, followed by coarse fatigue wear particles, as cage wear progresses. With conventional procedures this bearing deterioration would be detected only after substantial cage wear had occurred and failure was imminent. By using the more refined methods described above, the failure could be detected with the onset of the fatigue pitting of the roller, which would allow time for subsequent diagnosis and prognosis as failure progressed. Thus, with precise foreknowledge of the mechanisms of bearing deterioration, the prospects for life prediction and failure prevention could be greatly enhanced.

SUMMARY AND CONCLUSIONS

Recent developments in methodology suggest that wear debris analysis will continue to be an important procedure for the detection and diagnosis of bearing deterioration in aircraft propulsion machinery. Retrospective analysis of samples representative of bearing failures has shown that diagnostic information available from wear debris can be used more effectively in condition monitoring. Earlier detection of incipient bearing failure is possible by more precise spectrometric analysis and the advanced methods of ferrography and electron microscopy/X-ray spectroscopy enable more positive diagnosis of wear trends and severity. These and related developments indicate that future condition monitoring programs will be more precisely controlled by the complementary application of reliable real-time sensors to detect incipient failure and off-line diagnostic procedures to monitor subsequent deterioration and accurately predict remaining bearing life.

REFERENCES

1. Beerbower, A. "Mechanical Failure Prognosis Through Oil Debris Monitoring", USAAVLABS TR74-100, U.S. Army Air Mobility Research and Development Laboratory, Fort Eustis, VA, 1974.
2. Parr, N. L. and Ritchie, J. "Wear Debris Analysis", AGARD Lecture Series No. 103, Non-Destructive Inspection Methods for Propulsion Systems and Components, April, 1979.
3. Seifert, W. W. and Westcott, V. C. "A Method for the Study of Wear Particles in Lubricating Oil", Wear, 21, pp. 27 - 42, 1972.
4. Bowen, E. R. and Westcott, V. C., Foxboro Trans-Sonics, Inc., Wear Particle Atlas, July 1976.
5. Scott, D. and Mills, G. H. "Debris Examination in the SEM: A Prognostic Approach to Failure Prevention", Scanning Electron Microscopy/1974, (Part IV), ITT Research Institute, April, 1974.

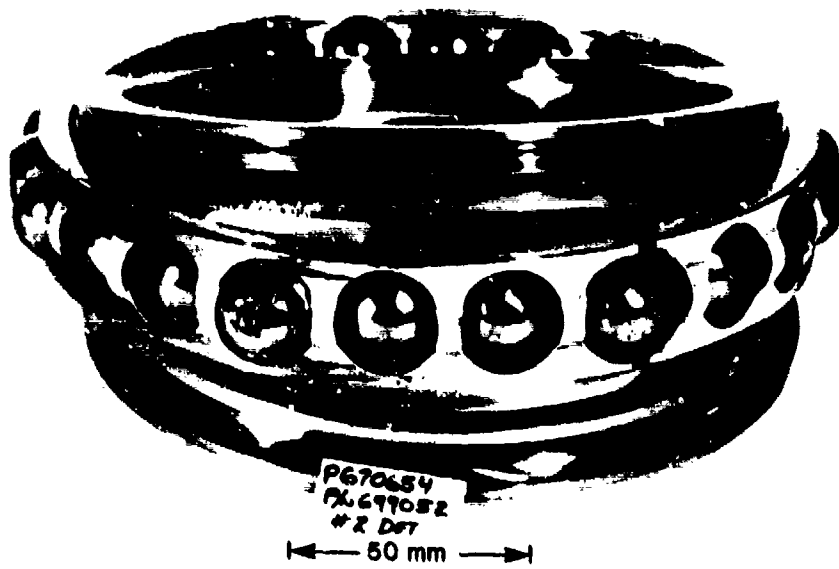


Fig. 1. Advanced Failure of Aircraft Engine Bearing Detected by Wear Debris Analysis



Fig. 2. Particulate Wear Debris Representative of Fatigue Pitting and Spalling of Bearing in Fig. 1.

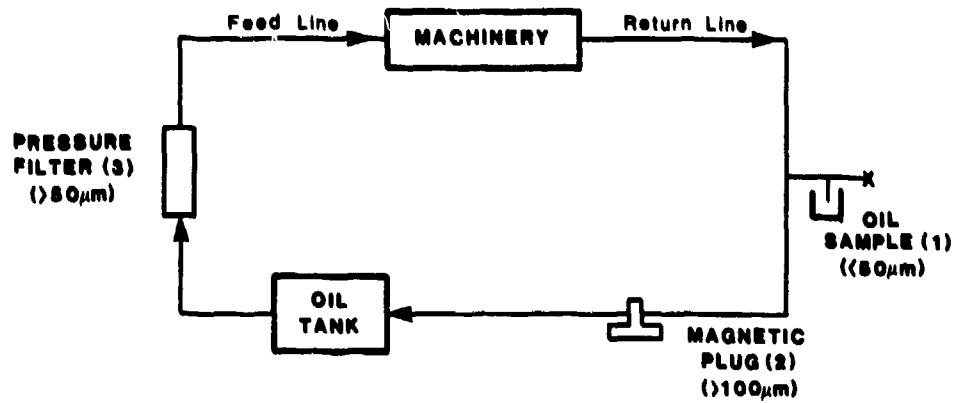


Fig. 3. Sources and Size Ranges of Particulate Wear Debris In Recirculatory Lubrication Systems

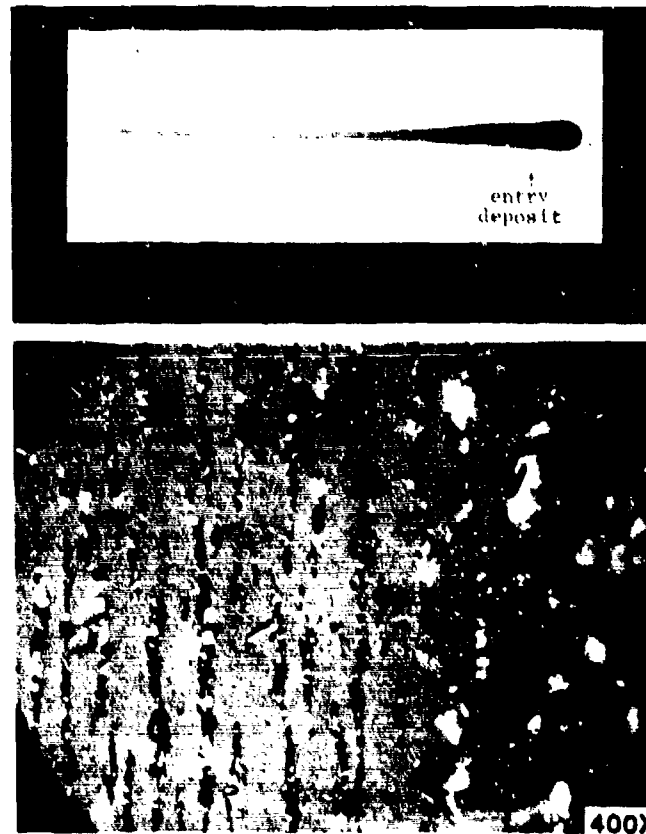


Fig. 4. Ferrograms Illustrating Wear Debris Deposition

Top - General Deposition
 Bottom - Bearing Wear Particle
 Distribution Near Entry Deposit

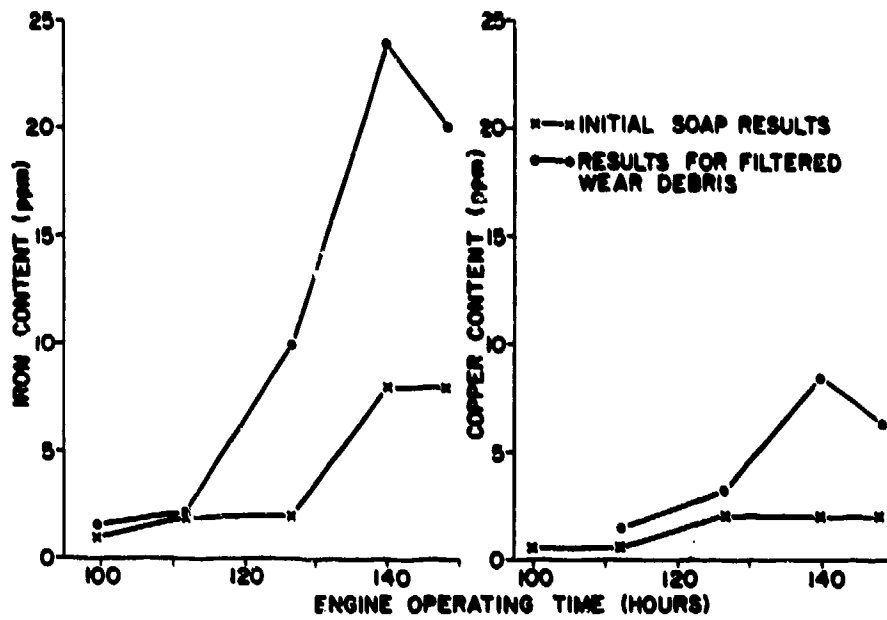


Fig. 5. Wear Profiles of Bearing Failure Based on Spectrometric Analysis Data

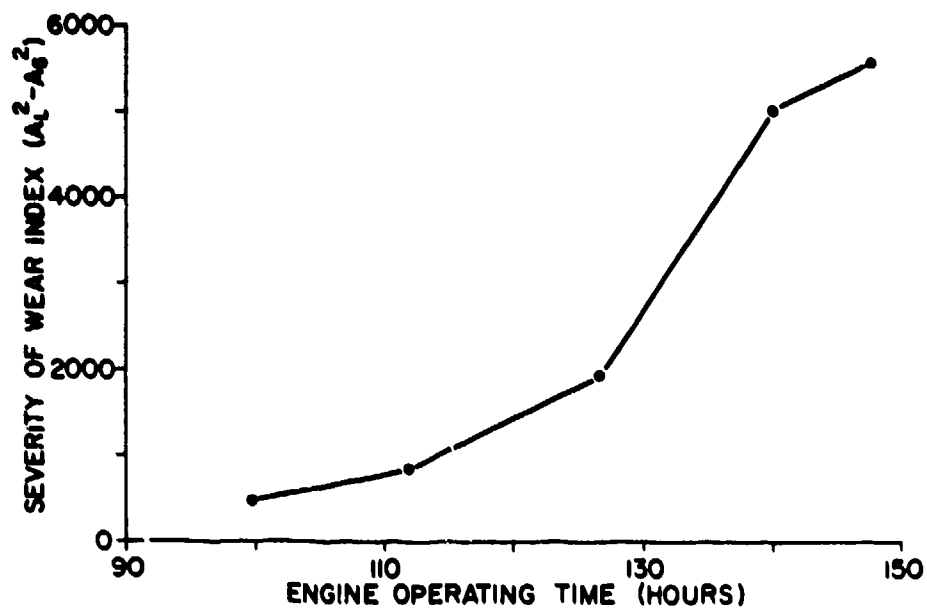


Fig. 6. Wear Profile of Bearing Failure Based on Ferrographic Data



Fig. 7. Bearing Particles Representative of Cutting and Surface Fatigue Wear Mechanisms

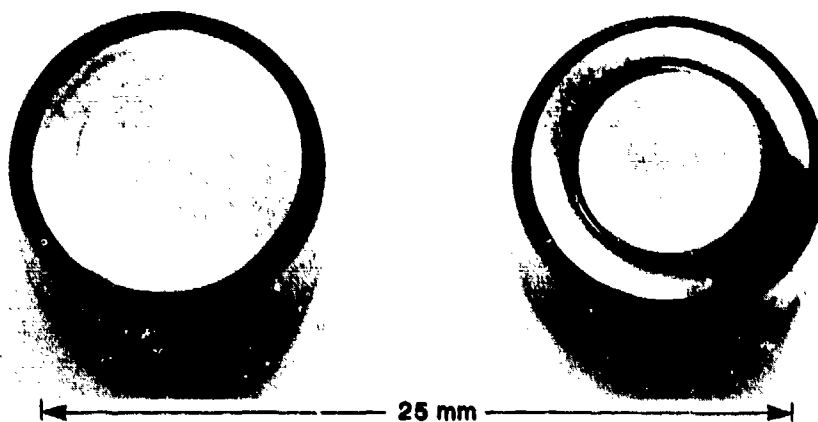


Fig. 8. Excessive Roller End Wear (Right) Causing Roller Skewing and Eventual Destruction of Bearing
Left - Minor Wear on Opposite End of Roller

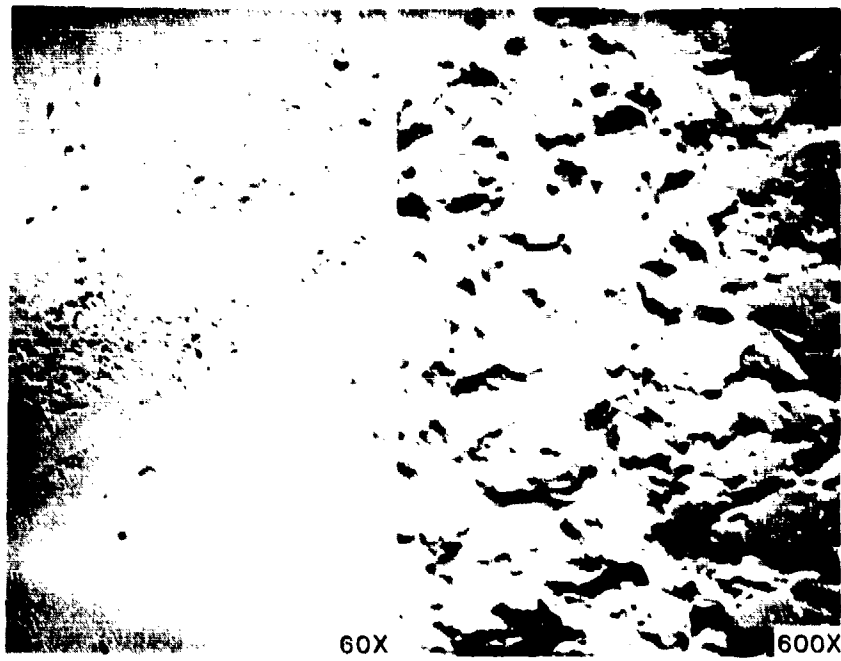


Fig. 9. Fatigue Pitting (Right) on Roller End (Left) Caused by High Stress Contact With Inner Race Following Extensive Rubbing (Polishing) Wear (Left-Lower Right)

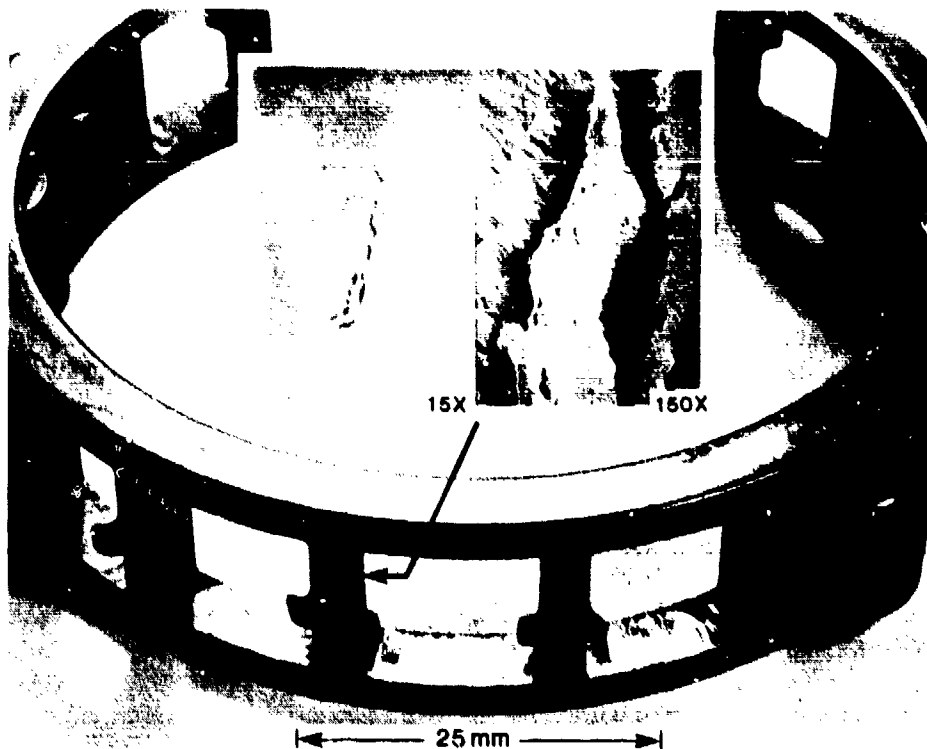


Fig. 10. Circular Grooves in Cage Sidewall Caused by Contact With Ridged Roller End
Inset - Fatigue Fracture of Rib Wall (Arrow) by High Stress Contact With Roller Surface

DISCUSSION

W.E.A.Fries, Ministry of Defense, Ge

Is use of the latest USAF method, which is based upon bringing into solution all wear particles in an oil sample by utilizing a known mixture of acids (nitric acid and hydrofluoric acid)?

The method is especially useful for particles in the range of 25–50 which the rotating disc spectrometer does not see.

Author's Reply

Yes, we are aware of the USAF method in question, and have confirmed its analytical accuracy when applied to the determination of titanium wear metal in oil samples. Since implementation of the method requires modification of existing procedures and introduces a potential acid handling hazard, it has not been adapted for field use.

E.Saibel, USARO, Research Triangle Park, North Carolina, US

Instead of using Severity of Wear Index ($A_L^2 - A_S^2$) along with debris quantity, a non-dimensional quantity having a rational basis should be established.

Author's Reply

Thank you for your suggestion. The severity of wear index referred to is a programmatic approach devised by the originators of the method which utilizes the measureable parameters of debris quantity and particle size distribution. Variants of this index have been applied by different investigators in attempts to achieve more meaningful correlations between wear debris and component surface damage. As you suggest the theory of non-dimensional parameters will be explored to determine the feasibility of this approach.

E.Jantzen, DFVLR, Ge

Have you established border lines (for severe bearing failures) for the lab numbers e.g., ppm, or wear index for the different engine types, and where are these border lines?

Author's Reply

In the day-to-day monitoring of aircraft engines by spectrometric oil analysis, atomic absorption and atomic emission guideline levels in ppm are specified for each type of engine. Similar wear index guidelines based on ferrography have not yet been established. Preliminary work is in progress to determine the wear characteristics and threshold wear levels for each type of engine and, from this information, the feasibility of using wear index data. Engine types have been observed to exhibit appreciably different degrees and rates of wear and some are more amenable to condition monitoring by wear debris analysis than others.

D.G.Astridge, Westland Helicopters Ltd, Yeovil, UK

Whilst paying tribute to the useful work of those who have developed the equipment and application techniques that the author has described, implementation of 3 mm filtration in engines and transmissions – shown to be necessary for extending bearing life – nullifies most oil sampling methods. Wear debris may, of course, be extracted from the filter for examination, but this involves a significant penalty in maintenance workload. The loss of oil analysis capability would not be regretted by aircraft operators, however, if any effective alternative can be found. I believe that such an alternative does exist, combining the experience gained from the US Army program on the UH-1 helicopter, and Westland's experience with the TEDECO QDM system on the Westland 30 helicopter transmission. I would advocate:

- (a) *Engines*: 3 mm absolute filters; magnetic chip collectors with relatively low catch efficiency in each bearing scavenge line (for fault location – only to be inspected following master sensor “amber” alert); a quantitative debris monitoring system (e.g., TEDECO QDM) in a full flow high catch efficiency arrangement in the common scavenge line upstream of the fine filter.
- (b) *Gearboxes with recirculating oil systems*: 3 mm filter; quantitative debris monitoring sensors in highest catch efficiency (transport efficiency) location – this may be inside the gearbox or in an external scavenge line, depending upon this particular gearbox design.
- (c) *Gearboxes – Splash Lubricated*. Quantitative debris monitoring system with sensor in position giving highest catch efficiency (less important than on circulating oil system).

Whatever the principles of operation employed in the wear sensor, I believe that particle size detection thresholds will be of order 0.01 gms of metal. In my experience of failures occurring in helicopter transmissions and engine bearings, in service and in rig tests, such a threshold size is perfectly adequate for detecting failure progression early enough for maintenance planning purposes, without jeopardizing flight safety. I believe that detection of wear phenomena at a very early stage in the failure progression can be disadvantageous (it is likely to result in an increase in premature rejections) when fine filters are fitted these can prevent secondary damage. Visual inspection of such a sensor fitted in a quick-release, self-sealing housing can quickly reveal the likely source of debris – whether build

or wear debris, and whether from gears or bearings, with a level of skill commensurate with aircraft service engineers. Maintenance workload for wear monitoring is reduced to a minimum – regular recording of numbers accessible in an avionics compartment, or processing by a centralized maintenance processor system being suggested for aircraft of the future.

INCREASING THE WEAR LIFE OF GAS TURBINE ENGINE ROLLER BEARINGS

F. F. Brown, Sr. Staff Project Engineer*
 L. J. Dobek, Project Engineer*
 M. J. Carrano, Senior Engineer*
 R. A. Valori, Bearings Program Manager**
 R. D. Dayton, Group Leader Lubrication Systems***

SUMMARY

The objective of this analytical and experimental program is to develop a long life bearing for operation at 3.0 MDN. Life limiting roller end wear of the eccentric type, which ultimately results in cage failure, was demonstrated in high speed rig tests to levels of 3.0 MDN. Seventeen parameters having the potential for influencing the skew action of the roller and its end wear were selected for experimental evaluation on a series of 124 mm experimental roller bearings. The corresponding statistical test plan is described and the essentials of a mathematical model are covered that ultimately defines the motion of the roller and its interaction with other parts of the bearing. The test results showed roller corner radius runout as having the most influence on wear with roller length to diameter ratio and end clearance demonstrating modest effects.

INTRODUCTION

Background

Increasing thrust-to-weight ratios for aircraft turbine propulsion systems realized in recent decades require that main shaft engine bearings operate reliably at ever increasing severity levels of speed and load. In addition to increased rotor speeds which are needed to achieve maximum gas dynamics performance and minimize engine size and weight, larger shaft diameters are required because of greater bending and torsional stiffness requirements. These factors result in requiring high levels of bearing DN, which is a severity parameter defined as the product of the bearing bore in millimeters and the rotor speed in revolutions per minute. Rummel and Smith (1) have shown that even at today's service engine DN levels, main shaft engine bearing failures are a major cause of accidents and unscheduled removals. Therefore, a continuous upgrading of bearing technology is necessary for advanced and current day engines.

Valori (2) conducted a study which identified the need to advance the technology of high speed cylindrical roller bearings from a state-of-the-art of about 2 million DN to a level of 3 million DN. Bearing research and development at the time concentrated heavily on the development of high speed ball thrust bearings to the point where they operated successfully for thousands of hours at 3 million DN in test rigs (3). In contrast cylindrical roller bearings technology had lagged to the point where it became the limiting factor in the design of high speed bearing systems. At that time, both field and development data indicated that bearing performance was very sensitive to roller instabilities. These instabilities are aggravated by high DN operation and cause roller skewing which is identified by rapid eccentric wear on the end surfaces of some or all of the rolling elements of a bearing. Figure 1 shows the eccentric wear pattern on one end of a roller with the other end having a similar pattern but 180 degrees out of phase. This condition can exist undetected until bearing failure occurs. Figure 2 shows a typical example of bearing failure precipitated by eccentric end wear of but one roller element.

Related to skewing, and apparently influenced by many of the same forces which induce it is roller skidding. Currently, skidding is considered to be of secondary importance compared to roller end wear. Roller skidding occurs when bearing radial loads are light and rotational speeds are high. A concept commonly used to supplement the external load is a two-point radial preload design. However, as speeds increase, the ability to maintain control of the internal clearance to prevent skidding damage becomes increasingly dependent upon accurate knowledge of the internal heat generated by the bearing. The heat generated must be known to control the operating clearance so as to maintain the roller loading at a level that successfully inhibits roller skidding.

Attempts at operating roller bearings at high DN levels using bearings of novel designs such as the Dual Diameter Roller Bearing by Rumbarger, et al (4) have met limited success. Zwicker's (5) work on conventional roller bearings demonstrated the importance of geometrical and tolerance factors on bearing performance even at speeds below 2 million DN. The work described herein was aimed at developing an analytical tool for

* Pratt & Whitney Aircraft, Commercial Products Division, EB3SW East Hartford, Conn.
 USA 06108

** Naval Air Propulsion Center PE72, RV, P.O. Box 7176, Trenton, New Jersey 08628

*** Air Force Wright Aeronautical Laboratory, Aero-Propulsion Laboratory, AFWAL/POSL
 Wright Patterson AFB, Ohio 45433

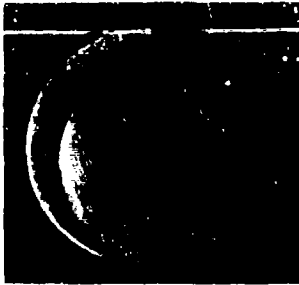


Figure 1 Typical Eccentric Roller End Wear Pattern Indicating Dynamic Instability



Figure 2 Typical Bearing Failure Attributable to Eccentric Roller End Wear

designing conventional cylindrical roller bearings for operation up to 3 million DN with particular emphasis on the elimination of surface damage due to roller skewing and skidding. The program involved developing a dynamic, i.e. time transient, analysis and generating correlative experimental data to verify and modify the analysis as required. Tests were conducted on bearings with variations in those geometrical and tolerance parameters which would most likely affect roller wear.

Program Approach

Future engine design requirements dictate roller bearings that can operate at DN levels to 3 million. To develop these bearings, considerable analytical and experimental effort must be undertaken to investigate the effects of increased DN levels on critical design parameters. In addition to the conventional parametric studies involving fatigue life, stresses, temperature, fits, clearances, alignment, lubrication, and rotor dynamic response, special attention must be given to roller skidding and skewing motions which have been identified as likely problem areas for high DN operation. Proper analysis of these effects requires development of a new computer program which considers the complete dynamic motion of each element in the roller assembly.

The effort under this program was directed towards formulating a viable generalized roller bearing analytical design system. The program was based on an integrated analytical/experimental effort. The resulting design system, in the form of a computer program, provides the bearing design engineer with a useful tool for studying the static as well as dynamic characteristics of high DN roller bearings for future aircraft engine main-shaft applications. This design system could be used in a parametric study which would establish basic design criteria, select important variables, predict the effect of each controllable design factor, and would substantially reduce the number of costly test programs in the early phase of new bearing development. The design system could also be used to assist in the diagnosis of roller bearing failures in service engines.

Program Scope

This program encompassed both analytical and experimental activity. However, emphasis will be given to the experimental effort and only a brief description of the analytical aspects of the program will be given. Analytically, a computer program was developed which describes the roller bearing dynamics, loads, stresses, deflections, deformations, thermal conditions, heat generation, lubrication, and operating parameters.

The experimental effort comprised a series of rig tests conducted on thirty 124 mm bore roller bearings tested in four separate groups in accordance with a statistically designed test plan. The bearings were designed to permit evaluation of the effect of a number of geometric, dimensional tolerances and operating variables on thermal, wear and skidding performance. Pre- and post test measurements made on each bearing included roller weights and angles of skew which provided data necessary to refine the roller bearing dynamics computer program.

Roller Bearing Analytical Model

General Approach

The basic roller bearing analytical modeling requirement was divided into two major areas; first, a static analysis to compute roller load distribution and to determine optimum bearing geometry and oil flow for maximum B-10 life, and second, a dynamic analysis to predict bearing component behavior when influenced by time varying load conditions. Both the static and dynamic analyses consisted of smaller "sub-analyses" which were combined into a computer program.

The static analysis consisted of a basic elasticity analysis to determine roller load distribution, a preload/outer ring out-of-roundness calculation, and a roller geometry and oil flow optimization procedure. The roller load distribution analysis included the effects of ring and structural flexibility as well as misalignment and moment loading.

The dynamic analysis used the results of the static analysis as part of its input. Other analyses were developed to determine roller and cage loads at other interfaces, including the cage bore and inner ring land, roller OD and outer raceway ID surfaces, roller OD and inner raceway OD surface, roller end and guide flange faces and roller end and cage pocket walls.

Static Analysis

The purpose of the static analysis was fourfold; (1) to determine values of key geometry parameters which result in optimum bearing fatigue life, (2) to calculate roller load distribution for both determination of fatigue life and further identify dynamic loads, (3) to determine the fatigue life of the optimized bearing design and (4) to provide a means by which the bearing stiffness can be determined for use in rotor dynamics analyses.

Bearing performance is influenced by the combined effects of fits, thermals, and operating conditions, as well as the design of the support structure. Ideally, the bearing internal geometry should be designed to achieve the maximum possible fatigue life under these conditions without violating any theoretical or experience-based design criteria. The oil flow level chosen for lubricating and cooling the bearing should be such that the temperature of the bearing rings will never cause a complete loss of bearing clearance or result in a temperature level that exceeds the capability of either the ring material or the oil itself. Initial fits must also be set so that they never reduce the bearing clearances to zero, yet remain tight at speed and temperature. Since the determination of factors such as the optimum oil flow, bearing fits, raceway out-of-roundness, and fatigue life is a laborious task involving many iterations within each and among all of the bearing performance analyses, the optimization process is usually not fully implemented. However, with the development of the analyses described in this report, full optimization of any or all of these parameters can be more readily accomplished from a quasi-static point of view.

The static analysis was developed to permit two distinct operating modes - checkout and optimization. In the checkout mode, an analysis was made of an existing bearing design whose critical geometric parameters were already established. This bearing was analyzed to determine its roller load distribution, preload, contact stress and fatigue life at operating conditions. If the bearing was in its early stages of design, the static analysis would be used in its optimization mode. The objective of this system was to determine the optimum roller bearing geometry for maximum bearing fatigue life. The program calculated optimized values of internal radial clearance and out-of-roundness with respect to input preload and race temperature criteria. Also, all bearing fits were optimized with regard to fit pressure requirements. After establishing the bearing internal geometry, the program then calculated values of roller flat length and crown radius for maximum bearing life at acceptable levels of roller edge stress.

Dynamic Analysis

The dynamic analysis used the output of the static analysis along with other input to determine all the forces acting on the bearing cage and rollers, including those due to contact between the inner ring and cage, rollers and cage, and rollers and inner race. The equations of motion of the interacting elements were solved as a function of time to determine the dynamic behavior of the cage/roller system under the action of the external forces.

The motion of the rollers was due to the action of a complex force/moment system as shown in Figure 3. This system included elasto-hydrodynamic (EHD) traction force at the inner and outer race, centrifugal force due to orbiting of the roller mass center, imbalance force due to geometrical imperfection of the rollers, aerodynamic drag on rolling elements, external loading transmitted through the roller/race contact and gravity forces due to the roller mass. Other important forces considered in the system were contact forces at the cage pocket walls and guide flanges as well as fluid shear drag forces.

A bearing cage is similarly subjected to the combined effect of a force/moment system, as shown in Figure 4, which consists of hydrodynamic forces, inertial forces, aerodynamic forces, shear drag forces and roller impact forces.

It is apparent that the motion of the rollers is affected by the motion of the cage, and vice versa, as a result of forces and moments transmitted through the various interfaces. In a loaded bearing, an individual rolling element and the cage may take turns driving each other. This motion may result in intermittent contact between the moving elements. Intuitively, the contacting process may involve one or a combination of the modes listed below:

1. Hydrodynamic contact occurring when the roller is far enough away from the wall of the cage pocket so that a hydrodynamic oil film is maintained at the interface.
2. Elasto-hydrodynamic contact which always exists when the contacting surfaces are extremely close and the pressure generated in the interposed lubricant film is sufficient to cause simultaneous elastic deformation of the surfaces, and
3. Elastic action in the contact mode which exists when the approach velocity is such that contact occurs before the lubricant film has sufficient time to develop or when the roller forces are large enough to break through an existing oil film.

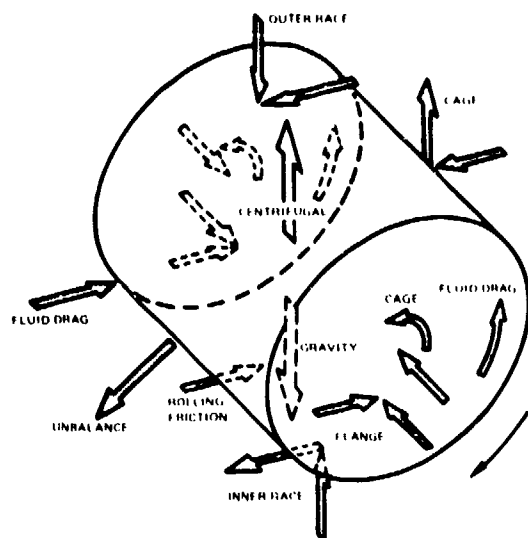


Figure 3 Roller Motion is Dictated by a Complex Force and Moment System

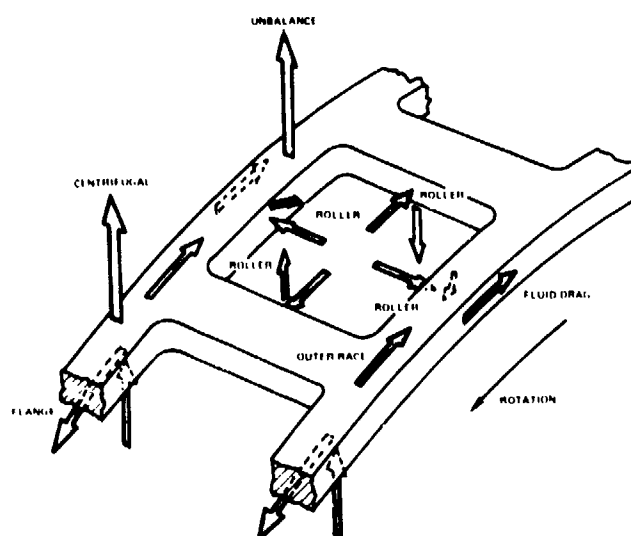


Figure 4 Cage Force and Moment System is Complex

Furthermore, the motion of the rollers and the cage is influenced by the ambient fluids. Determination of the roller and cage motion requires simultaneous solution of their respective equations of motion. Once the analyses were developed and tested, they were combined into a large scale computer program, TRIBO I, for solution. The name TRIBO is derived from the word "tribology".

Organization of the Computer Program

TRIBO I is a state-of-the-art cylindrical roller bearing design tool capable of accomplishing both static and dynamic phases of the design process. The program is composed of two basic modules - STATIC and SYSDYN. The module SYSDYN is composed of the modules CADYN and RODYN. Figure 5 shows the relationship of the modules to each other and to the complete TRIBO I program. STATIC contains the structural analysis of the bearing due to loads resulting from a quasi-static equilibrium. RODYN analyzes roller dynamic behavior without the influence of the element retainer or cage. CADYN analyzes the cage dynamic behavior without the influence of the rollers. SYSDYN analyzes the complete system dynamic behavior allowing for full interaction among the rollers, the cage, and the two raceways. The complete program, TRIBO I is invoked by running STATIC and SYSDYN together so that the output from STATIC is used as input to SYSDYN. STATIC may also be run to provide input for RODYN.

The TRIBO I output consisted of the quasi-static design parameters mentioned previously, along with the motion of each roller in the bearing, as well as the cage, expressed as a function of time. Since the forces acting on the roller ends were known, it was possible to estimate the amount of wear on each roller for a given set of operating conditions. The computer program predictions of end wear were correlated with the test data obtained from the experimental program.

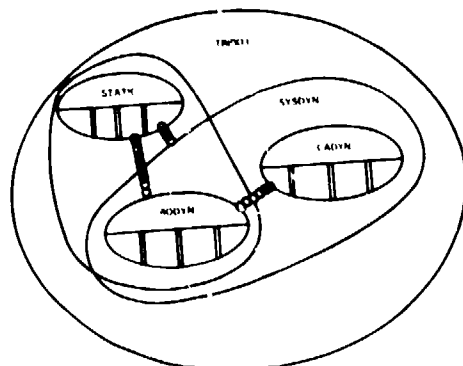


Figure 5 TRIBO I Modular Program Construction

Parameter Selection, Experimental Program

The main obstacle to advancing high speed roller bearing technology is related to roller element skewing and skidding. It was the objective of this experimental portion of this program to quantify those variables having an influence on roller skew and skid. Thirty separate variables were identified and are shown in Table 1. Operational variables, such as bearing speed, externally applied load, and lubricant temperature were not counted in this total. The basic categories considered were design geometries that included internal lubrication arrangements, manufacturing tolerances, and quality control variables.

Table 1. Relative Ranking of Roller Bearing Variables

Category I (Most effect on wear)	Category II (Moderate effect)	Category III (Least effect)
1. Roller Length/Diameter Ratio	15. Roller Clamping Load	23. Roller Length Variation
2. Roller Unbalance - (Nonhomogeneous material, roller corner runout, crown radius runout)	16. Flange Face Runout	24. Cage Pocket Offset
3. Preload	17. Roller Crown Radius Runout	25. Roller End Surface Finish
4. Cage Unbalance	18. Extended Roller Flat Length	26. Flange Surface Finish
5. Roller Flat Centrality	19. Flange Face Waviness	27. Raceway Surface Finish
6. Roller End Circular Runout	20. Flange Layback Angle	28. Cage Pocket Squareness
7. Roller End Shape	21. Roller-Cage Pocket Clearance	29. Raceway Waviness
8. Raceway Taper	22. Flange Contour	30. Roller Taper
9. Roller End Clearance		
10. Roller Diameter Variation		
11. Lubrication		
12. Flange Height		
13. Raceway Angular Misalignment		
14. Percent Flat Length of Roller		

It was apparent that an evaluation of all 30 variables required some judgment be made as to the relative importance of these variables. Therefore, these were divided into three categories as shown in Table 1. Category I included 14 variables that were considered to have the greatest influence on the roller bearing wear phenomena. Category II consisted of eight variables considered to have less impact on wear. Category III was composed of eight variables judged to have the least effect. The criteria employed in making these assessments, although somewhat subjective, were based on experience available from experimental test results, field service reports, analytical studies, manufacturing surveys, and an understanding of the physical phenomena affecting fundamental bearing behavior.

Four groups of bearings, A, B, C and D identified by parameter groupings in Table 2, were selected for evaluation in a statistically designed experiment. Each group incorporated parameters from Table 1 which could be varied. By varying the parameters in the statistical experiments, it was possible to isolate and rank the effect of any parameter on surface damage due to roller skidding and skewing.

Table 2. Identification of Parameters Evaluated in Each of the Four Bearing Test Groups*

Group A (8 Bearing Designs)	Group B (8 Designs)	Group C (5 Designs)	Group D (6 Designs)
1. Bearing preload	1. Roller length/diameter ratio	1. Guide flange layback	1. Roller end clearance
2. Roller coupled corner runout	2. cage imbalance	2. Guide flange contour	3 levels
3. Roller end circular runout	4. Extended roller clearance	3. Guide Flange runout	2. Roller end circular runout
4. Inner race taper	4. Roller end shape	4. Extended roller flat length	3. Roller flat centrality
5. Roller flat centrality	5. Flange height		4. Flange height variations
6. Outer ring angular misalignment	6. Roller diameter variations		
7. Lubrication flow.	7. Roller flat length		

*Each parameter was tested at two levels unless otherwise indicated.

A statistically designed test program incorporating the fractional factorial method was selected. Table 3 shows the number of main effects and the number of interactions that can be determined with programs consisting of 5, 6 and 8, bearing designs with variations in the number of bearing parameters to be studied. For each parameter the level of variation was maintained at two. The combination of eight test bearing designs was chosen for Groups A and B. Seven parameters were chosen for investigation in each of the two groups so that the maximum number of main effects could be evaluated. The parameters which were studied with these two groups of bearings were all selected from, and comprise the entire list of the Category I variables shown in Table 1.

The scope of that portion of the program in which the Group C bearings were evaluated limited its size to five designs. Four parameters is the maximum number for which the main effects can be investigated when employing five designs. The four parameters in this group are listed in Table 2 and were selected from Category II which corresponds to the parameters that were anticipated to have only a moderate effect on roller wear.

Table 3. Parametric Study Combinations

No. of Test Assemblies	No. of Parameters of Two Levels	Effects Determined
8 (Groups A & B)	7	Main
	6	Main and one interaction
	5	Main and two interactions
6 (Group D)	5	Main
	4	Main and one interaction
5 (Group C)	4	Main

The parameters selected for evaluation in the fourth group of bearings, Group D, provided additional data on four variables from Category I. Since five designs appear in this group, only four main effects can be determined. It should be noted that two of these variables, roller end circular runout and roller flat centrality, were also evaluated in the Group A bearings, and the two other variables, roller end clearance and flange height, were also evaluated in the Group B bearings.

Design of Parametric Bearings

The roller bearing selected as the basis for the design of the parametric bearings is shown in Figure 6. This bearing is used in the No. 5 mainshaft position of the TF30 model production engine and has accumulated many thousands of hours of successful rig and engine operation. In addition, this design includes geometric and tolerance control features directed at minimizing roller skewing and skidding.

Using the partial factorial statistically designed experiment approach, a test matrix was prepared for each of the four groups of program bearings. As an example, the matrix for Group C bearings is presented in Table 4. This matrix is for the design of 5 bearings, incorporating four variables with two levels of variation each. In this table the two levels are represented by the symbols H and L, for high and low. The actual levels of the parameter variation for each of the Group C designs, as well as the basic or baseline bearing, are presented in tabular form in Figure 9. These levels were established on the basis of experimental, analytical, manufacturing, and production experience. The parameters of the Group C bearings which were not being studied were maintained at the level used in the basic bearing. Figure 9 assigned a specific identification number to each bearing design in Group C. A similar tabular description of the parameter levels chosen for the Group A, B and D bearings are shown in Figures 7, 8 and 10, respectively. Again, for each group, the parameters not being studied were maintained at the level used in the basic bearing.

TABLE 4 TEST MATRIX - GROUP C PARAMETRIC BEARINGS

VARIABLE "M"		VARIABLE "N"		VARIABLE "J"		VARIABLE "K"		
H	L	H	L	H	L	H	L	
L	L	L	L	L	L	L	L	1
L	L	L	L	L	H	L	L	2
L	L	L	L	L	L	L	H	3
L	L	L	L	L	L	L	L	4
L	L	L	L	L	L	L	L	5
L	L	L	L	L	L	L	L	6
L	L	L	L	L	L	L	L	7
L	L	L	L	L	L	L	L	8
L	L	L	L	L	L	L	L	9
L	L	L	L	L	L	L	L	10
L	L	L	L	L	L	L	L	11
L	L	L	L	L	L	L	L	12
L	L	L	L	L	L	L	L	13
L	L	L	L	L	L	L	L	14
L	L	L	L	L	L	L	L	15
L	L	L	L	L	L	L	L	16
L	L	L	L	L	L	L	L	17
L	L	L	L	L	L	L	L	18
L	L	L	L	L	L	L	L	19
L	L	L	L	L	L	L	L	20
L	L	L	L	L	L	L	L	21
L	L	L	L	L	L	L	L	22

3 ROLLER BEARING DESIGNS
4 BEARING VARIABLES
2 LEVELS OF VARIATION
= L LOW
= H HIGH

NUMBERS IN MATRIX INDICATE BEARING IDENTIFICATION NUMBERS

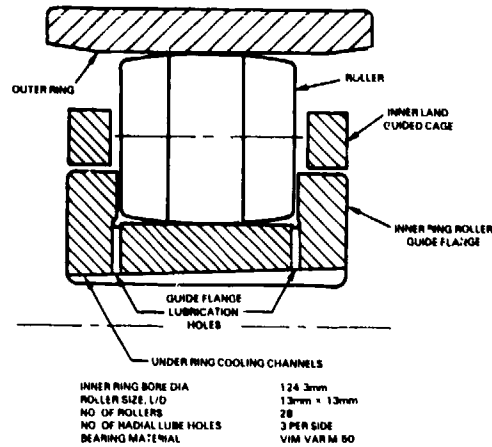
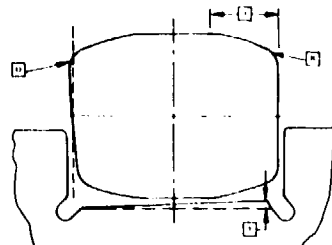


Figure 6 Basic Bearing for Parametric and Verification Testing



Identifi- cation No.	Bearing Prelim. M	Max Coupled Corner Runout mm, A	Roller End R/O in Roller O-D, mm, D	Inner Bore Taper, Minutes	Roller Flat Centrality, mm, I	Runway Angular Misalign- ment, Degrees	Lubrication Flow, g/min
Baseline	2224	0.0254	0.001048	0.8	0.254	0	5.0
1	2224	0.1270	0.004572	0.8	1.270	0	5.0
2	2224	0.0254	0.001270	3.58	0.254	0	13.15
3	0	0.1270	0.001270	3.58	0.254	0.5	5.0
4	0	0.0254	0.004572	0.8	1.270	0.5	13.15
5	0	0.0254	0.004572	3.58	1.270	0	5.0
6	0	0.1270	0.001270	0.8	0.254	0	13.15
7	2224	0.0254	0.001270	0.8	0.254	0.5	5.0
8	2224	0.1270	0.004572	3.58	1.270	0.5	13.15

Figure 7 Group A Parametric Bearing Designs

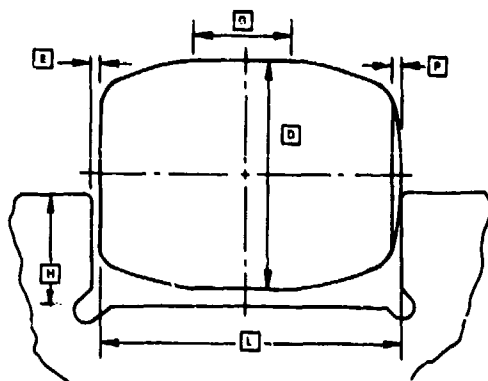


Figure 8 Group B Parametric Bearing Designs

Identifi- cation No.	Roller Length/ Diameter Ratio, mm/mm	Cage Imbalance, Gram Centimeter	Roller End Clearance, mm	Roller End Shape, Max. Protrusion, mm	Flange Height, % of Roller Diameter	Roller Dia. Variation, Per Bearing, mm	Roller Flat Length, Percent of Roller Length C
	L/D		E	P	H		
Baseline	1.0	3.0	0.0254	0.00127	25	0.00127	40
11	1.0	8.0	0.0254	0.00127	20	0.00127	0
12	1.0	1.0	0.0254	0.01016	20	0.00127	50
13	0.77	8.0	0.0254	0.01016	20	0.01270	0
14	0.77	1.0	0.0254	0.00127	20	0.01270	50
15	0.77	1.0	0.1270	0.01016	30	0.00127	0
16	0.77	8.0	0.1270	0.00127	30	0.00127	50
17	1.0	1.0	0.1270	0.00127	30	0.00127	0
18	1.0	8.0	0.1270	0.01016	30	0.01270	50

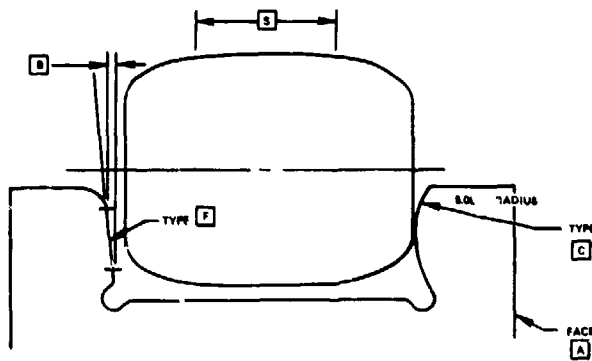


Figure 9 Group C Parametric Bearing Designs

Identifi- cation No.	Extended Roller Flat, % of Roller Length, S	IR Guide Flange Layback, mm B	IR Guide Flange Contour, F or C	IR Guide Flange Runout to Face A, mm Max
Baseline	40	0.00635 Max.	Type F	0.0102
21	48	0.00635 Max.	Type F	0.0102
22	67	0.02286-0.02794	Type F	0.0508
23	67	0.02286-0.02794	Type C	0.0102
24	67	0.00635 max	Type C	0.0508
25	46	0.02286-0.02794	Type C	0.0508

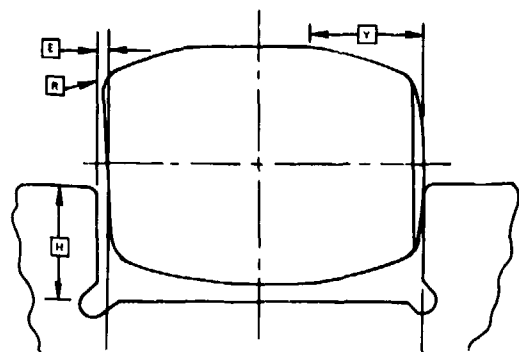


Figure 10 Group D Parametric Bearing Designs

Identifi- No.	Roller Coupled Corner Runout to Roller OD, mm E	Roller Flat Centricity, mm Y	Roller End Clearance, mm E	Guide Flange Height, % Roller Dia. H
Baseline	0.007048	0.254	0.0254	25
27	0.002540	1.270	0.0254	20
28	0.005080	0.254	0.0254	30
29	0.005080	1.270	0.0508	20
30	0.002540	1.270	0.0508	30
31	0.002540	0.254	0.1270	20
32	0.005080	1.270	0.1270	30

Procurement of Bearing Hardware

The Split Ballbearing Co. (SBB), Division of MPB Corporation, was selected to fabricate the parametric bearings. SBB is a producer of the basic No. 5 mainshaft position roller bearing used in production of TF30 engines and has supplied experimental hardware which has been successfully evaluated in tests to speeds of 3.0 MDN.

A total of 10 Group A parametric bearings were manufactured for testing. One each of the eight designs shown in Figure 7 and two duplicate bearings for repeat testing were procured. The bearings selected for repeat testing were numbers 7 and 8 shown in Figure 7. A total of eight bearings were manufactured in Group B, six in Group C with one bearing identified as No. 26 being a duplicate bearing for repeat testing, and six bearings manufactured for parametric Group D.

For each of the bearings, detailed dimensional measurements of the bearing components were made and recorded by SBB. This was done to ensure the tight quality control required as dictated by the demands of any statistically planned program and to assist in the post-test analysis of the experimental results.

The inspection data which accompanied each of the bearings were reviewed and with rare exceptions no significant deviations compared to the design specifications were uncovered. Since the inspection results for each bearing consisted of 94 pages, only a summary of inspection results for the rollers in bearing No. 1 in Group A is presented in Table 5 which is representative of the data obtained for all 30 bearings in this program. For simplification, averages are presented since 28 separate roller measurements were made.

Table 5. Typical Manufacturing Inspection Data for Bearing Number 1 Rollers, Group A

Length, mm	12.99845
Diameter, mm	12.99616
Surface Finish AA, nm	88.9
Coupled Corner Runout, mm	0.0940
Crown Radius, cm	76.2
Cylinder Length, mm	5.200
Cylinder Flatness, nm	304.8
Cylinder Off-Set, mm	1.27
Crown Profile R.O., nm	4064
End Circular R.O., nm	0.006223
Crown Drop, mm	1.524
Hardness, R _c	60

Pretest Bearing Preparation and Inspection

Preparation of the parametric bearings for test included instrumenting each outer ring with a strain gage to permit measurement of roller pass frequency during test which determined whether or not the roller elements were skidding for each of the program test combinations imposed. Each roller was weighed before and after test to determine the amount of roller mass loss attributable to wear. Also, each of the rollers was measured for static skew angle-of-turn allowed by the inner raceway guide flanges. Table 6 shows typical pretest roller weight and static skew angle measurements for the Group A bearings.

Table 6. Group A Bearings - Pretest Wear Related Measurements

Identification No.	Avg. Roller Weight, Grams	Avg. Skew Angle, Minutes
1	13.2457	14.94
2	13.2918	11.95
3	13.2417	14.19
4	13.2755	13.71
5	13.2768	13.43
6	13.2411	14.98
7	13.2866	10.87
8	13.2446	14.47
9	13.2999	13.96
10	13.3340	15.10

In addition to the bearing manufacturer's pretest inspection data, in-house inspection measurements were made and recorded during installation of the bearings into the test rig. These measurements included the fits of the inner ring on the shaft and the outer ring in the support housing, the installed internal radial clearance of the test bearing and the axial misalignment of the installed outer ring.

Test Rig and Instrumentation

The test rig used for the experimental evaluation of the parametric bearings is shown in Figure 11. Relatively trouble-free operation was experienced with this rig in more than 5000 hours of testing, of which over 250 hours were at speeds of 3.0 MDN.

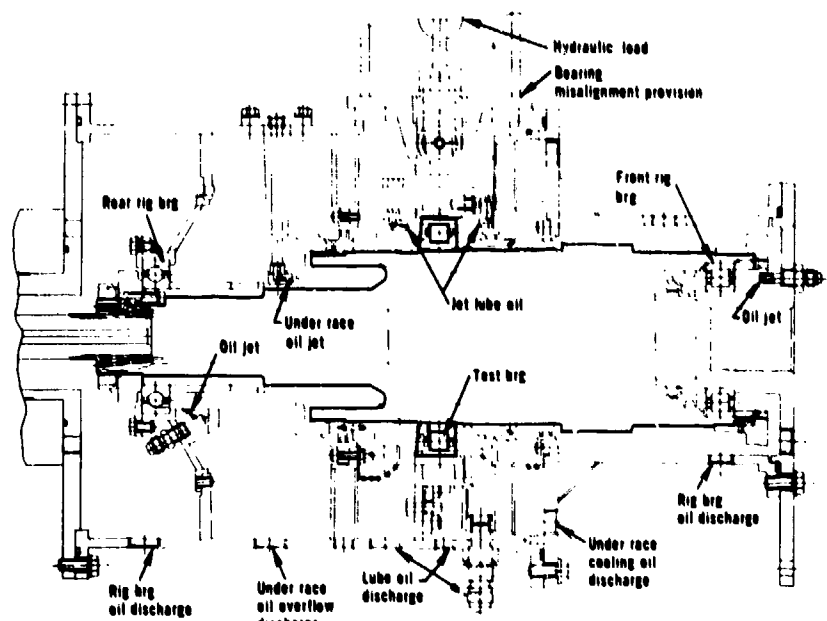


Figure 11 High Speed Roller Bearing Test Rig

The test rig consisted of a cylindrical housing with a hydraulic load cylinder located centrally on top of the housing to apply a radial load to the test bearing. Three bearings were located on a common shaft assembly in the rig. The two bearings nearest the ends of the shaft assembly were rigidly mounted to the housing. The center or test bearing was mounted in a carrier attached to the load cylinder piston and was radially guided by tracks in the housing.

Radial load applied to the test bearing by the load cylinder was transmitted through the shaft assembly to the end bearings and then through the end bearing carriers to the housing. These bearings were equally spaced from the center bearing and each carried half the load applied to the center bearing. This arrangement maximized alignment control among the bearings. Axial location of the shaft assembly was controlled by the ball thrust bearing mounted at the drive end.

Lubrication and cooling oil was supplied to the test bearing by directing jet oiling into both sides of the bearing cavity. Oil was also supplied separately to axial slots located under the rotating inner ring. Radial holes intercepting a number of axial slots directed lubrication to the inner ring roller guide flanges.

The test rig was serviced by a lubrication system that supplied: 1) oil to the test bearings as well as to the rig slave bearings for lubrication and temperature control, 2) oil to the speed increaser gearbox for lubrication of the gearbox bearings and gears, 3) pressurizing oil to the hydraulic load cylinder of the rig to radially load the test bearing, and 4) controlled and monitored the temperature, pressure and flow of oil supplied to each part of the system.

The lubrication system included an oil reservoir which supplied oil to two pressure pumps. The high-capacity pump supplied oil filtered to a level of 15 microns absolute to the test rig internals and to the gearbox. The low-capacity pump supplied oil to the load cylinder which provided the radial load to the test bearing. The temperature of the oil to the test rig was controlled by a heat exchanger. Three delivery branches supplied oil to the test bearing. Two of the branches supplied the bearing with primary lubrication and provided outer ring temperature control. The third branch supplied oil to the test bearing for inner ring temperature control and lubrication of the inner ring guide flanges.

Instrumentation was provided to measure the imposed test conditions, bearing operating conditions, and operating conditions of the test rig. Table 7 lists the measurements obtained. Manual recordings of all measurements were made every 10 minutes during the calibration portion of the experimental program and once every 20 minutes during the endurance running.

Table 7. Instrumentation

<u>Imposed Test Conditions:</u>	
o Applied radial load	o Rig shaft speed
o Test bearing oil flow	o Oil supply temperature
<u>Test Bearing Operating Conditions:</u>	
o Outer and inner ring temperature	o Cage speed or slip
o Discharge oil temperature	o Horsepower and torque
<u>Rig Operating Conditions:</u>	
o Slave bearings oil flow	o Slave bearing temperatures
o Vibration	

Experimental Program Plan

The 10-hour test program that was followed during the rig evaluation of each parametric bearing is shown in Table 8 and was designed to obtain both calibration and endurance data. The calibration section consisted of 30 separate test combinations which were designed to obtain bearing operational data with variations of speed, oil flow, radial load, and oil temperature. The imposed conditions were maintained at each test combination for 10 minutes. From the operational test data obtained, the following performance parameters were determined for each bearing; heat generation, horsepower and torque, roller skid, inner and outer ring thermal stability, outer-to-inner ring thermal gradient, and axial and circumferential thermal gradients.

TABLE 8. Test Program

	Under Race	Supply Oil Flow, Kg/min		°C	Applied Bearing Load, N	Speed, MDN/Point No.					Test hr	
		Each Jet*	Total			1.0	2.0	2.5	2.75	2.9		3.0
Calibration	4.536	2.268	9.072	107	1112	1	4	7	10	13	16	
					2224	2	5	8	11	14	17	3
	2.268	1.814	5.897	107	4448	3	6	9	12	15	18	
					2224	19	20	21	22	23	24	1
	4.990	4.082	13.154	135	2224	25	26	27	28	29	30	1
Steady State Endurance												
Group A	2.268 or 4.990	1.814 or 4.082	5.897 or 13.154	107	2224	Endurance at 3 MDN					4	
Groups B, C, D	4.536	2.268	9.072									
Cyclic Speed												
Group A	2.268 or 4.990	1.814 or 4.082	5.897 or 13.154	107	1112	2.0/2.75 MDN Accels-Decels 1						
Groups B, C, D	4.536	2.268	9.072									

*Two jets, one directed at each side of bearing.

Once the calibration portion of the program was completed, endurance testing was conducted in order to assess the extended operating performance and roller wear durability of each bearing design. The first 4 hours of endurance running were conducted at the 3.0 MDN steady-state condition noted in Table 8. For a specific bearing test within Group A, the level of the oil flow variation of either 5.897 or 13.154 kg/min was determined from the Group A bearing design chart shown in Figure 7. The oil flow for the Group B through D bearings was maintained at the baseline level of 9.072 kg/min. In the fifth hour of the endurance testing, the bearing speed was cycled between the two speed levels indicated in Table 8. A total of 30 acceleration-deceleration cycles were completed on each bearing, simulating the type of transient operation found in gas turbine engines where accelerated bearing wear due to skidding and skewing may be encountered due to the rapid accelerations experienced by the roller elements.

At the completion of each 10-hour test, the experimental data was reduced to obtain the individual performance parameters for each bearing. Each roller element was weighed and also measured for the static angle of turn that is allowed within the inner ring guide flanges. Roller wear by weight loss and roller and guide flange wear by change in static skew angle were determined using pretest and the post-test measurements.

Experimental Evaluation

A total of 26 parametric bearings was tested including a baseline bearing described in Figures 7-10. The bearing was rig evaluated in accordance with the test program outlined in Table 8. It performed smoothly throughout the 10-hour test.

Performance was stable both thermally and mechanically with no indication of roller element skidding. Visual examination of the rollers showed them to be free of any eccentric end wear. However, several of the rollers were found to have some concentric end wear, providing an indication that these particular rollers experienced the greatest amount of weight loss during test. The average weight loss of each roller was 0.0004 gram. The static skew angle for the baseline bearing was not measured since the roller static skew angle inspection equipment was not yet available. It was used later in the program on other bearings.

Of the total of nine bearings experimentally evaluated in Group A, bearing No. 7 was first selected for test since No. 9, a duplicate bearing, was available for repeat testing. This permitted back-to-back tests of a similar design at the beginning of the program so that testing repeatability could be assessed. Both bearings performed in a stable manner throughout their respective 10 hour tests. No thermal instabilities or significant raceway axial thermal gradients were noted.

Post-test inspection of both bearings indicated a similar overall appearance with all of the bearing components in good condition and showed no evident distress. All of the rollers in both bearings were free of any eccentric end wear, however, they exhibited moderate levels of concentric wear on both ends. Post-test inspection measurements revealed similar low levels of wear for each bearing. Roller weight measurements indicated an average roller weight loss of 0.0003 grams for bearing No. 7 and 0.0007 grams for bearing No. 9. Post-test static skew angle measurements indicated an average increase of 1.26 minutes for bearing No. 7 and 1.79 minutes for bearing No. 9.

The experimental results obtained from tests of bearings No. 7 and 9 demonstrated adequate repeatability, allowing testing of the remainder of the Group-A designs to be pursued.

During the ten hour test, four of these bearings failed because of rapid roller end wear which allowed the rollers to skew excessively. In each instance, this caused the cage to break. These failures occurred with the No. 1, 3, 6 and 8 bearings, and as seen in Figure 7, they contained rollers with a high level of coupled corner radius runout or dynamic imbalance. Another group of four bearings exhibited continuous skidding over the speed range from 1.0 to 2.5 million DN, however, at the 2.75 million DN level and above no skidding was measured. These bearings were No. 3, 4, 5 and 6, and, as seen in Figure 7, were all designed without preload. A graphical representation of the skidding performance typically experienced is shown in Figure 12 for bearing No. 4. The cage-to-shaft speed ratio is shown increasing, i.e., less skidding, with increased applied load in the 1.0 to 2.5 MDN range. No obvious skid damage was observed on any of the rollers and raceway surfaces of bearings No. 4 and 5. These bearings contained low imbalanced rollers and successfully completed the 10-hour test. Stable operation was obtained with bearings No. 2, 7 and 9, which were of a preloaded design and contained rollers with a low level of coupled corner radius runout. Thermal performance was similar for each of the Group-A bearings tested. Figure 13 presents typical bearing outer ring and heat generation results obtained for bearings operating at opposite ends of the roller wear spectrum. Although bearing No. 7, as shown in Figure 10, performed with low roller wear and bearing No. 8, which contained rollers with a high level of corner runout, showed heavy end wear, no significant difference in outer ring thermal performance or heat generation was observed.

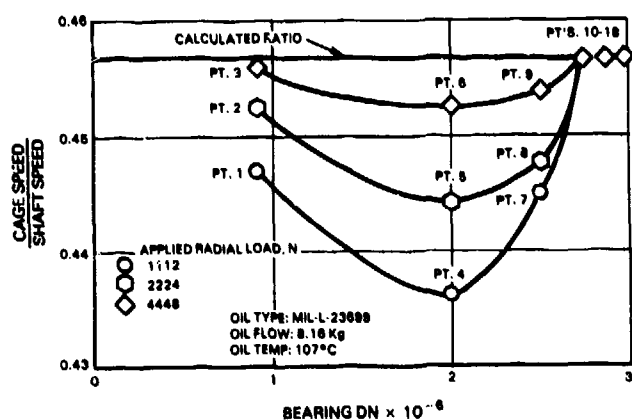


Figure 12 Test of Group A Unpreloaded Bearing, No. 4. Shows Decreased Skid as Load is Increased with no Skid Beyond 2.75 MDN

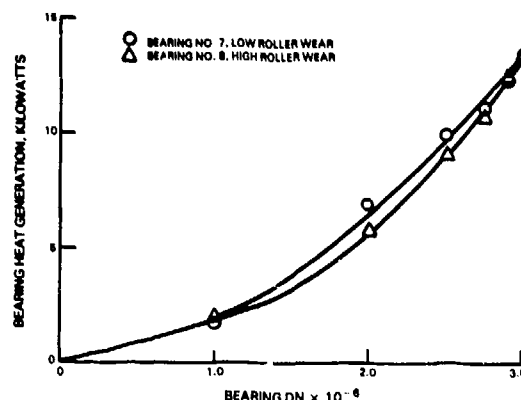
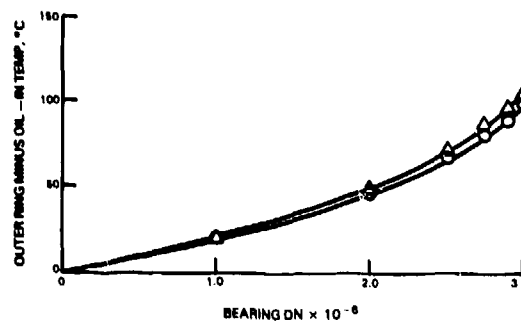


Figure 13 Extreme Roller End Wear not Reflected in Bearing Thermal Performance

Testing was subsequently conducted on the Groups B, C and D bearings in a similar manner to that performed on the Group A bearings. A total of eight bearings were evaluated in Group B, five in Group C and six in Group D. Stable operation and performance were observed with each bearing except for No. 21 of Group C which experienced an inner ring fracture while running at 2.75 MDN, point No. 11 in the test sequence shown in Table 8. The total running time at failure was only 1.75 hour. The rollers were severely edge damaged but free of eccentric end wear. Metallurgical analysis conducted at the site of the inner ring break indicated a transverse fracture which had progressed in a tensile manner. It was concluded that the fracture originated at the inner diameter of the ring in the vicinity of the intersection of a radial oil hole and an axial oil slot.

The thermal performance data for Groups B, C and D bearings was determined to be similar to that previously observed for the Group-A bearings as shown in Figure 10. Post test bearing wear related measurements, roller weight and skew angle, were obtained where possible. The resultant changes from pretest values are presented in Table 9. Included here are the wear results obtained for the four groups of bearings as well as for the baseline bearings.

Analysis of Test Results

The statistical analysis of the wear results obtained in the experimental evaluation of the four groups of bearings was accomplished using regression and correlation analyses. The parameters listed in Table 2 were evaluated and ranked using the roller weight loss and static skew angle change measurements. Procedures outlined by Draper and Smith (6) were followed in the analysis where the "T value" provides a measure of the relative magnitude of the influence of the test variable being analyzed.

TABLE 9 Experimental Wear Data

	Bearing Identification	Roller Weight Loss, Grams	Roller Skew Angle Change, Minutes
	Baseline	0.0004	not measured
Group-A	1	0.0311	73.06
	2	0.0001	1.20
	3	0.0188	60.64
	4	0.0003	1.70
	5	0.0001	1.62
	6	excessive wear	excessive wear
	7	0.0003	1.26
	8	0.0136	71.05
	9	0.0007	1.79
Group B	11	0.0008	1.02
	12	0.0000	3.48
	13	0.0001	1.17
	14	0.0001	1.15
	15	0.0005	3.97
	16	0.0014	14.14
	17	0.0046	24.40
	18	0.0031	20.65
Group C	21	0.2094	60.24
	22	0.0001	0.79
	23	0.0002	1.75
	24	0.0002	2.09
	25	0.0001	1.10
Group D	27	0.0022	9.86
	28	0.0003	0.93
	29	0.0004	5.27
	30	0.0003	1.17
	31	0.0061	32.43
	32	0.0022	11.41

The analysis of the roller weight change results tabulated in Table 9 showed that roller coupled corner runout or imbalance has the strongest effect on roller weight change. The regression analysis produced a T value for roller coupled corner runout that was at least an order of magnitude larger than for any of the other variables. Its effect is positive, i.e., increasing the level of coupled corner runout increases roller weight loss. A typical graphical display of the roller weight loss regression model using a least squares fit is shown in Figure 14 for the variable roller coupled corner runout. Therefore, based on the roller weight loss analysis, for minimum roller wear, the lower level of runout evaluated in this test program should be specified for high speed roller bearing design. Other variables tested that also indicated a significant effect on roller weight change are tabulated in Table 10. Included is the direction of their effect as well as the recommended variable design level for minimum wear.

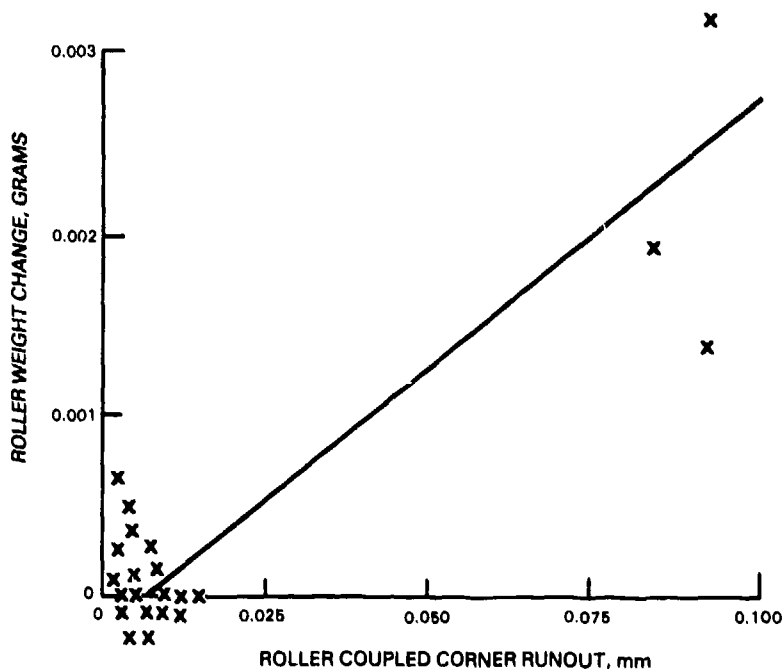


Figure 14 Typical Regression Model Analysis-Roller Coupled Corner Runout shows a Significant Positive Effect on Roller Weight Change

Table 10. Parameters That Influence Roller Weight Loss

<u>Level of Significance</u>	<u>Independent Variable</u>	<u>Direction of Effect</u>	<u>Recommended Level for Minimum Wear</u>
Important	Roller coupled corner runout	Positive	0.00254 mm
Moderate	Inner race taper	Negative	3.5 min
	Outer raceway misalignment	Negative	0.5 deg
	Roller L/D	Positive	0.77
Slight	Roller end clearance	Curvilinear	0.0508 mm
	Roller end circular runout	Negative	0.004572 mm
	Roller flat centrality	Negative	1.27 mm
	Inner ring guide flange runout	Negative	0.0508 mm
	Roller preload	Negative	2224 N

The remaining parameters were determined not to be statistically important in contributing to the roller weight change for the range of parameter variations evaluated. These parameters consist of lubrication, cage imbalance, roller end shape, guide flange height, roller diameter variation, roller flat length, inner ring guide flange layback and inner ring guide flange contour.

The regression analysis of the alternate dependent variable, roller skew angle change, also showed that roller coupled corner runout or imbalance had the most significant impact on wear. The T-value for this variable was again greater than that for any of the other variables evaluated. The variables along with the direction of their effect and the recommended design levels are listed below:

Table 11. Parameters That Influence Roller Skew Angle Change

<u>Level of Significance</u>	<u>Independent Variable</u>	<u>Direction of Effect</u>	<u>Recommended Level for Minimum Wear</u>
Important	Roller coupled corner runout	Positive	0.00254 mm
Moderate	Roller L/D	Positive	0.77
	Roller end clearance	Positive	0.0254 mm
	Guide flange height	Negative	30%
Slight	Roller end circular runout	Negative	0.004572mm
	Inner Race taper	Negative	3.58 min
	Roller diameter variation	Positive	0.001270 mm

The regression analysis further determined that the following variables were not statistically important for the range of parameter variations evaluated; roller preload, roller flat centrality, outer raceway misalignment, lubrication, cage imbalance, roller end shape, roller flat length, inner ring guide flange layback, inner ring guide flange contour and inner ring guide flange runout.

CONCLUSIONS AND RECOMMENDATIONS

An experimental program using full scale 124 mm roller bearings was successful in providing a reliable means of evaluating the parameters affecting roller end wear, one of the primary concerns in high speed cylindrical roller bearing operation. The experimental test running time duration and operating conditions produced roller end wear levels of sufficient magnitude to allow correlation of the wear results with the roller bearing test parameters.

Although a wide range of wear was observed in the parametric testing, similar thermal characteristics were measured for each bearing. Thus bearing temperature monitoring cannot be employed as a means of detecting roller wear. Also, extreme amount of roller slippage did not result in any unusual thermal behavior, nor did it produce obvious skid damage or distress in the test environment imposed and over the duration of the test runs.

The experimental portion of this program established that roller coupled corner radius runout or imbalance has the most significant influence on roller end wear as determined by roller weight loss and skew angle change measurements. High speed roller bearings should therefore be designed with the lowest possible levels of roller corner runout. The experiments also identified roller end clearance and length-to-diameter ratio (L/D) as being parameters of significance albeit to a lesser degree than that for roller corner runout. As established by both the roller weight loss and skew angle change measurements, these parameters should be designed into high speed roller bearings to the lower levels evaluated.

The experimental roller wear data obtained in this program was used successfully to correlate the computerized analytical model, TRIBO I. Substantiation of the capability of TRIBO I to provide an optimum prototype bearing design at least for short term service was successfully demonstrated in a separate 60 hour rig test. A description of this work is beyond the scope of this paper but was done in conjunction with the program described herein. This 60 hour test provided additional wear data allowing some extension of the capabilities of TRIBO I. Currently, tests on additional bearings are being conducted, under the auspices of a related U.S. Air Force contract that will provide wear data under extended rig endurance conditions. In this effort a pair of bearings, designed with use of TRIBO I, are being tested for 1000 hours with all of this time spent in the 2.5 to 3.0 million DN speed range. When the wear data becomes available from this test, the TRIBO I computer model will be updated accordingly. The result will be a design system with improved capability for providing high DN roller bearing with extended wear life for main shaft application in aircraft gas turbine engines.

REFERENCES

- (1) Rummel, K. G., Smith, H. J. "Investigation of Reliability and Maintainability Problems Associated with Army Aircraft Engines" Eustis Directorate, U.S. Army Air Mobility Research and Development Laboratory, Fort Eustis, Va., Contract DAAJ02-71-C-0055 Boeing Vertol Co., August 1973.
- (2) Valori, R. "State-of-the-Art Review, Mainshaft Turbine Engine Bearings" Naval Air Propulsion Center Report No. NAPTC-PE-44, October 1974.
- (3) Signer, H., Bamberger, E. V. and Zaretsky E.V. "Parametric Study of the Lubrication of Thrust Loaded 120 mm Bore Ball Bearings to 3 Million DN" ASME Paper No. 73-LUB-24, 1973.
- (4) Rumbarger, J. et al "Dual Diameter Roller Bearing - 3.5 Million DN - 600°F", Air Force Aero Propulsion Laboratory Report No. AFAPL-TR-23 May 1973, Contract F33615-71-C-1883, Franklin Institute Research Laboratory.
- (5) Zwicker, V. M. "Evaluation of Geometry Factors in Roller Bearings" U.S. Army Aviation Material Laboratories, Report EDRC772 contract DAAJ02-68-C-0107 Detroit Diesel Allison Division, General Motors, November 1970.
- (6) Draper, N., Smith, H. "Applied Regression Analysis," First Edition, USA, John Wiley & Sons, Inc., 1966, pp. 104-123.

ACKNOWLEDGEMENTS

The following employees of Pratt & Whitney Aircraft made significant contributions to the success of this program. Dr. Frederick Hsing as Analytical Program Manager in the formative stages of TRIBO I; Robert McFadden, Ronald Edelstein, Gene Tsai, Ming Shen and Arthur Fine for analytical modeling; Walter Grube for computer programming; Edward Tobiasz and Richard Fair for experimental bearing testing assisted by Robert Cohan and Frederick Danser for statistical analysis. Special mention is made for A.B. Jones, Consulting Engineer, whose earlier analytical work was utilized in portions of TRIBO I.

DISCUSSION

D.G.Astridge, Westland Helicopters Ltd, Yeovil, UK

- (1) Do you consider that bearing manufacturers can achieve a cost effective improvement in corner radius runout?
- (2) In view of the considerable (excellent) experimental effort expended by you and your team to determine the ranking of so many parameters, do you consider that detailed design of bearings for high speed applications is beyond the scope of the bearing manufacturers, and needs to be undertaken by the engine/transmission designers -- yourselves in this case?

Author's Reply

- (1) Yes, they are doing it now.
- (2) From an aircraft engine manufacturer's point of view cooperation between the bearing manufacturer and the engine manufacturer is essential in engineering successful high technology aircraft engine bearings. The bearings represent the edge of technology, requiring extensive expenditures of R&D effort. On a purely economic basis this effort solely on the part of the bearing manufacturers is probably not justified because aircraft bearings do not represent that significant a total market. The importance factors here are that the effort be cooperative, that nothing be done in a void as regards either party, and that a mutual know how be developed.

C.Brownridge, Pratt & Whitney, Ca

When you started the program you felt that the four most important parameters were corner radius runout, end face runout, clearance and L/D ratio. Could you tell us why you now think that, of these four, only corner radius runout is important?

Author's Reply

The level of unbalance that results from corner radius runout is much more significant than that for end face runout. End face runout has proved to be important but in those cases where it has been critical it has developed after the wear process has started.

C.Brownridge, Pratt & Whitney, Ca

What about clearance -- was that important?

Author's Reply

End clearance is important. It was listed among the second group that had a lesser effect. If end clearance is too low or too large, rapid wear results.

C.Brownridge, Pratt & Whitney, Ca

The last one was L/D ratio.

Author's Reply

The bearing industry has persisted in using L/Ds of 1 to 1.3, usually to obtain higher load capacity. Load capacity is not the problem in these applications. Roller design should be looked upon like that of a flywheel. If you have an L/D ratio of 0.86 or less, then the roller will continue to want to operate stably and rotate about its axis of symmetry. If the L/D ratio is greater than that, the roller will want to turn over and rotate about its transverse axis, just as a gyro would.

J.F.Chevalier, SNECMA, Fr

Do you measure the inner and outer race temperatures during test and was there a correlation between these and wear?

Author's Reply

We did, in most cases, especially early in the program. Operating temperatures were consistent from one bearing group to another and there was no correlation with wear.

Condition monitoring of bearings
(A measuring technique in an experimental stage)

M.J.W. Schouten

Eindhoven University of Technology
Department of Mechanical Engineering
P.O. Box 513, 5600 MB Eindhoven / Netherlands

Several methods of bearing monitoring have been developed in the last 15 years. Important stages in this technique are: the measurement of a representative signal, processing of the signal, comparison of the measured result with a model in order to come to conclusions on the health of the bearing.

Two measuring techniques, which are being developed now, are described in this paper. The bases of those two methods: the thermodynamic measurement and the measurement with thin film transducers, are presented briefly. For other applications, both were already used under laboratory conditions.

Condition monitoring

From the point of view of economy, rotating mechanical constructions can be divided into three groups:

- simple consumption products as e.g. electric shavers: they run until failure and then are replaced by a new product: there is no maintenance.
- more expensive consumption products like motor cars: under normal maintenance they run until a component fails and then the component is replaced.
- expensive professional machinery where failure of a component gives expensive repair procedures, loss of production, or a dangerous situation. Examples are aeroplanes or big production machines.

It is interesting to have a monitoring system for the last group of machinery, so that a signal could be had from critical components some time before damage would occur, and a repair or a replacement of a part could take place during the next standstill of the machinery.

A monitoring system can be used, if

- the failure mechanisms are known and well understood
- the influence of different parameters is known, as well as the influence of the critical parameters and their limitations and gradients in the safe regions
- a measuring technique for those critical parameters is available
- a mechanism by which the operating conditions of the machine can be influenced is available.

During the last ten years, monitoring systems based on the measurement of various machine parameters have been developed and are already used in practice.

The following signals referring to the condition of the machinery can be made use of:

- vibrations
- radial movements of a rotating shaft
- wear particles in the oil
- temperature of components
- leakage measurements
- etc.

A survey of monitoring systems is given by /1/ and /2/.

Condition monitoring of bearings

Most of the monitoring techniques used for complete machine systems can also be used for condition monitoring of bearings.

When monitoring a bearing during action, the primary function for which the bearing is applied should be checked. The following primary demands are made upon the bearing, and these demands should be made upon the entire load-speed area:

- right shaft position
- low friction
- sufficient long life

Therefore, monitoring means: measuring these magnitudes as directly as possible, and comparing the signal with the permissible limiting values as mentioned beforehand.

- The shaft position can be measured directly with respect to fixed points of the housing of the bearing.
- As a result of increase of friction a rise in temperature occurs which can be worked with indirectly as a measure.
For bearings with a full lubricant film the thickness of this film is indirectly a measure for friction and for the functioning of the bearing.
- The degree to which a part of the life has passed can be found by the registration of wear. This can be done directly by measuring the worn-off thickness of the coating, through which the position of the shaft changes, but also indirectly, by vibration measurements. By this both increase of clearance and the occurrence of cracks or pittings in bearing surfaces can be observed.

Measuring determining magnitudes in a bearing

With the various types of bearing several shapes of wear may occur. Furthermore, the various types of bearing cannot, all of them, be approached to the same degree for the measurement of critical parameters.

As with measurements of complete machines, also with the bearing attention may be drawn to either "over all" magnitudes or values which appear in the critical place themselves. An example of the "over all" magnitudes is the rise in temperature for the entire bearing, from which conclusions with respect to the critical places have to be drawn through a model. An example of the values which appear in the critical places themselves are the occurring lubrication film thickness on the spot of the narrowest clearance. Measurement of temperatures on the spot in the most loaded places of the bearing belongs to this latter category too. By this, information about the sought magnitudes is obtained immediately. Detailed information is given because there is a chance that the average temperature does not rise alarmly, whereas in consequence of another distribution of the heat sources yet locally inadmissibly high values occur. However, detailed measurement of critical magnitudes in the bearing itself means a miniaturization of the signal transducers to be used. Figure 1 shows this schematically.

When measuring the "over all" magnitude, above all the conversion of the measured signal into the condition of the critical place is a problem. When measuring the magnitude in the critical place directly the signal transducer usually is the biggest problem.

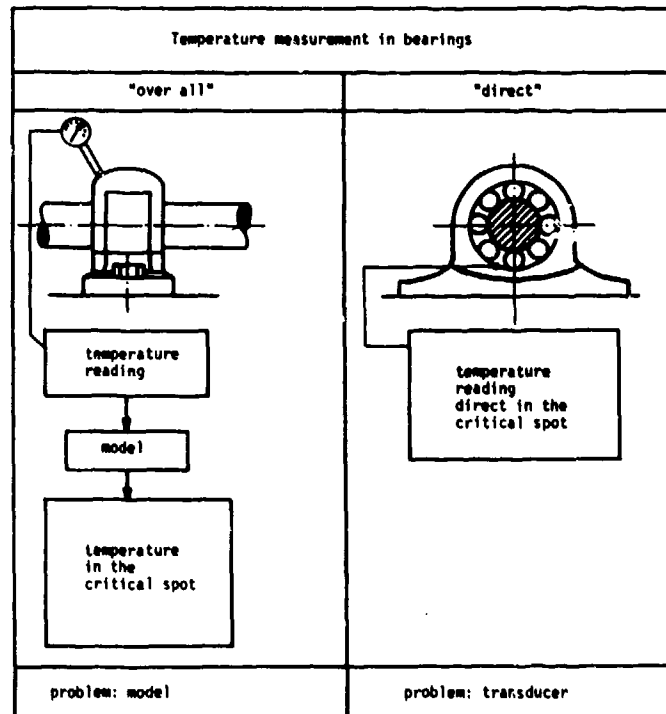


Fig. 1

A survey of critical parameters which can be measured in various types of bearings is shown in figure 2.

In principle, with all bearings mentioned the possibility exists to determine on the spot temperatures in the bearing surface. In bearings with a lubricant film a measuring technique developed for this purpose may give an insight into the distance between the bearing surfaces in the most critical places.

parameter / signal	dry or porous plain bearings	rolling element bearings	hydrodynamic bearings	hydrostatic bearings
location of shaft				
vibration				
(local) temperature				
filmthickness				

Fig. 2 Critical parameters used as a monitoring signal

Measuring technique for temperature registration (on the spot and "over all" values) and the registration of lubricant filmthickness. An experimental stage.

Two measuring techniques are being developed now:

- A • The thermodynamic measuring technique applied to the bearings in which a fluid flow through the bearing takes place.

Especially with hydrostatic bearings is this the case, but with hydrodynamic and rolling element bearings, as well, the fluid can be circulated through the bearing.

The fluid appears to be an outstandingly pleasant machine-element, which cannot only be replaced in a simple way, but also can act as a supplier of information about the condition of the bearing.

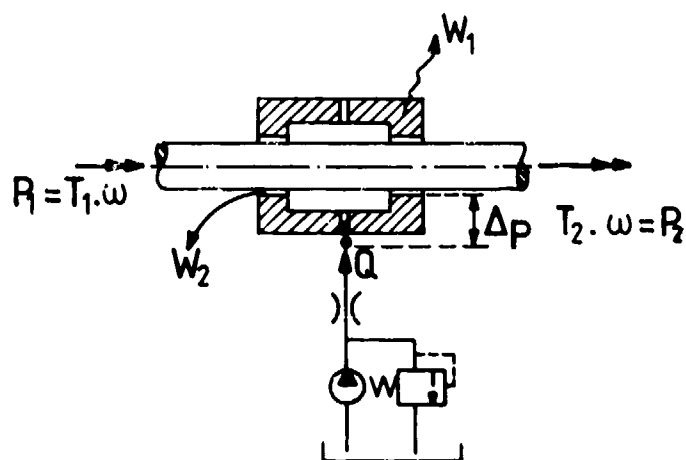


Fig. 3

- Hydrostatic bearings

The energy-balance for the bearing is as follows, figure 3:

Mechanical: $P_1 - P_2 = (T_1 - T_2) \cdot \omega = T_W \cdot \omega = \text{frictional power}$

Hydraulic: $\Delta p \cdot Q = \text{flow power where } \Delta p \text{ is the pressure drop of the fluid}$

W_1 is the radiated heat and the heat which is carried off by conduction.

W_2 is the heat which is carried off by the liquid.

This means: $W_2 = T_W \cdot \omega + \Delta p \cdot Q - W_1$

The rise in temperature of the liquid can be determined from:

$$T_W \cdot \omega + \Delta p \cdot Q - W_1 = Q \cdot \rho \cdot c \cdot (\Delta\theta)$$

For a known liquid the rise in temperature as a result of the pressure drop can be read from the enthalpy-entropy (i-s)-diagram, as shown in figure 4.

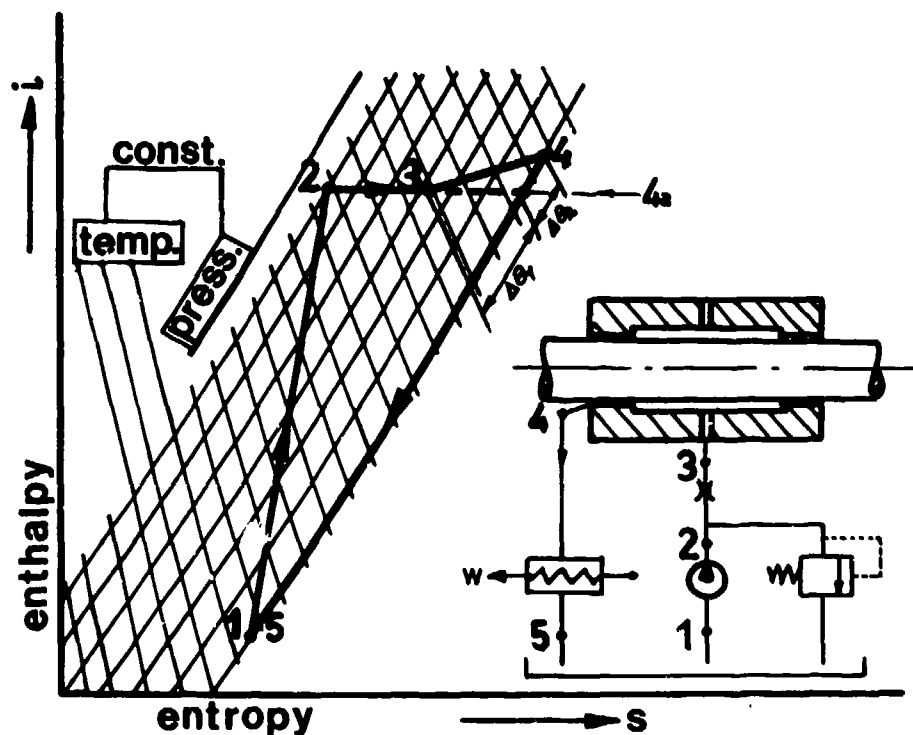


Fig. 4

Witt /3/ derived this both theoretically and experimentally for the hydrostatic transmission. Doing this, on the strength of these measuring methods an accurate monitoring system for hydrostatic transmissions was obtained /4/.

For an isolated bearing $W_1 = 0$.

In case of doubling of friction $T_W \cdot \omega$ becomes twice as large.

- Hydrodynamic bearings and roller-element bearings.

Though the mechanisms on which these bearings are based are different in principle, in case of monitoring through measurement of temperature on the outside of the bearing, this difference as to action will not be visible.

In order to carry out measurements as to differences in temperature, it is necessary that a volume-flow of a lubricant will run through the bearing, thus conducting away the produced frictional heat. The scheme is as follows, figure 5:

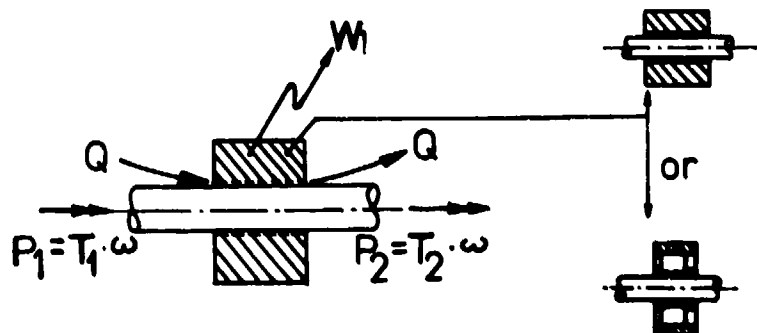


Fig. 5

$$P_1 - P_2 = (T_1 - T_2) \omega = T_w \cdot \omega = \text{frictional power}$$

In the case of heat W_1 radiated and carried off by conduction, it holds that:

$$Q \cdot \rho \cdot c \cdot (\Delta\theta) = T_w \cdot \omega - W_1$$

Should the bearing be isolated, in consequence, we find:

$$\Delta\theta = \frac{T_w \cdot \omega}{Q \cdot \rho \cdot c}, \text{ so that the rise in temperature is directly proportional to the friction that occurs.}$$

Doubling of the coefficient of friction also gives a doubling of the difference in temperature. With the help of the present-day temperature transducers this rise in temperature can be recorded accurately.

B • Measurement of local temperature and filmthickness.

If the rise in temperature on the outside is defined as an average, with the above method of monitoring sometimes there is insufficient certainty about the value of the local temperature in the bearing. Figure 1 shows this difference in measuring methodology schematically. At present, technically the possibility exists to measure in the critical places in the bearing both the rise in temperature and the thickness of the lubricant film directly.

In order to attain this end, a measuring technique is applied which had been made use of earlier for laboratory experiments by among others /5/ and /6/. Further development of this technique is now taking place, so that monitoring may occur for a longer period.

In developing this measuring technique a measuring method is aimed at by which in highly loaded bearing surfaces between which a lubricant film is to be found, pressure, temperature and filmthickness are estimated directly.

The transducer is made as a combination of a vapour deposited or sputtered layer of insulating material and a metal film, as is shown in figure 6a. The dimensions of the layer are small compared with the dimensions of normal contacting zones in rolling element bearings. The thickness of the metal part of the transducer is small compared with normal filmthickness in bearings.

Pressure or temperature is measured as the change of the electrical resistance of a pressure-sensitive material (NiCr - or manganin) or a temperature-sensitive material (Ti). The resistance is mounted in a Wheatstone-bridge. Values of pressure and temperature-influence on the electrical resistance of those metals are given in table 1.

Filmthickness is measured as a change in capacitance between the transducer surface and the mating surface; the lubricant film is the dielectric material, figure 6b. As for the normal parallel capacitor the capacity C is written as:

$$C = \frac{\epsilon_r \cdot \epsilon_0 \cdot A}{h}$$

ϵ_0 is the permittivity in vacuum. (Fm^{-1})

ϵ_r is the dielectric constant for the lubricant under the conditions of the measured part of the film. (-)

A is the area of the transducer. (m^2)

h is the filmthickness. (m)

Table 1	electrical resistance		
	specific resistance	temperature sensitivity	pressure sensitivity
	ρ $(\frac{\Omega \cdot \text{mm}}{\text{m}})$	$\frac{\Delta \rho}{\rho \Delta \theta}$ $(\frac{\%}{\text{°C}})$	$\frac{\Delta \rho}{\rho \Delta p}$ $(\frac{\%}{\text{bar}})$
Ti	0,5	$2,3 \cdot 10^{-3}$	$-0,1 \cdot 10^{-6}$
85% Cu, 10% Mn, 5% Ni (Manganin)	0,4	$\pm 0,01 \cdot 10^{-3}$	$2,2 \cdot 10^{-6}$
80% Ni; 20% Cr NiCr	1,1	$0,085 \cdot 10^{-3}$	$20 \cdot 10^{-6}$

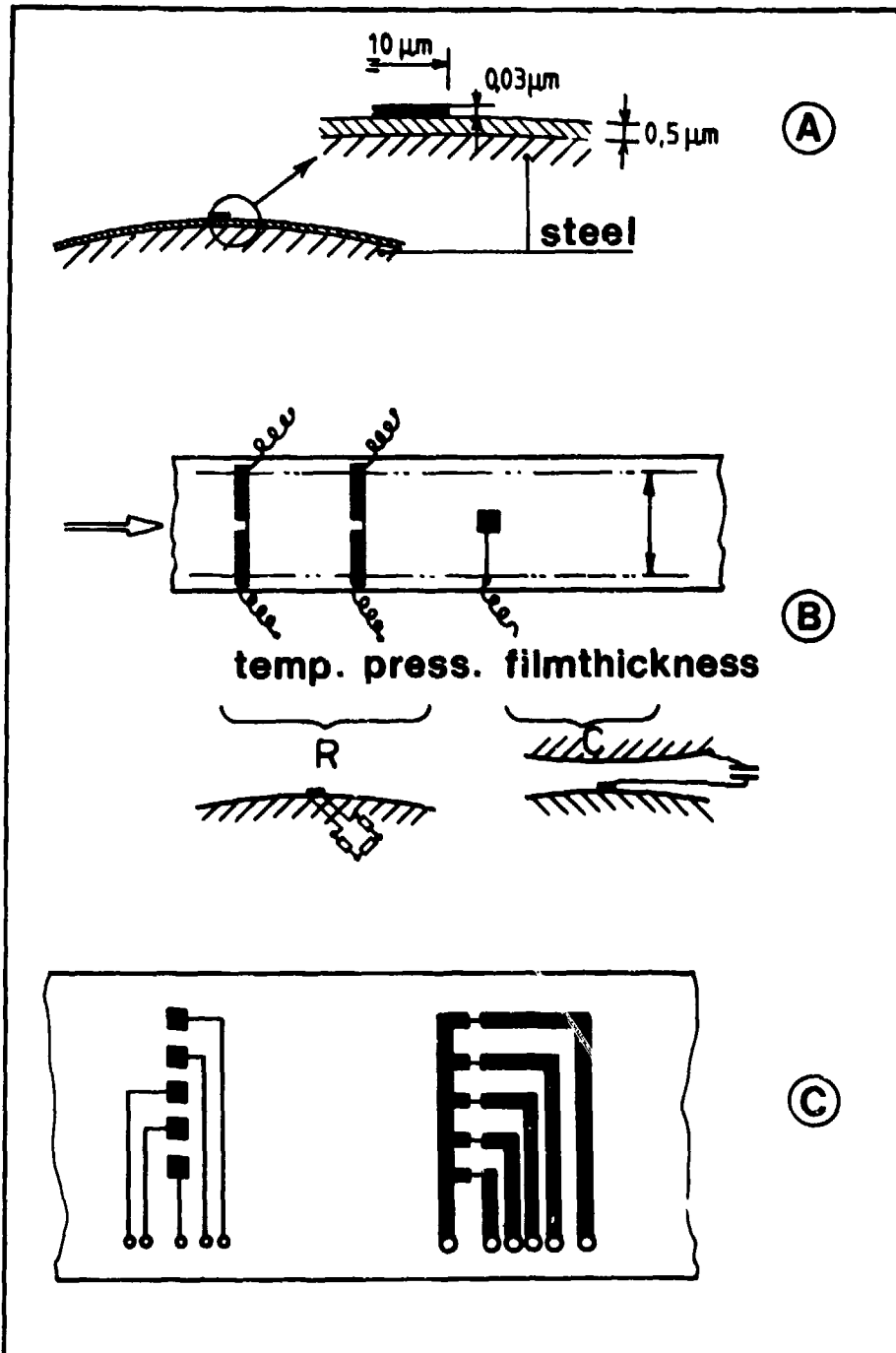


Fig. 6

The dielectric constant of a mineral oil is shown in figure 7. Values under other pressures or temperatures are estimated, using Clausius - Mosottis law:

$$\frac{\kappa - 1}{\kappa + 2} \cdot \frac{1}{\rho} = \text{constant}$$

ρ is the specific gravity of the fluid.

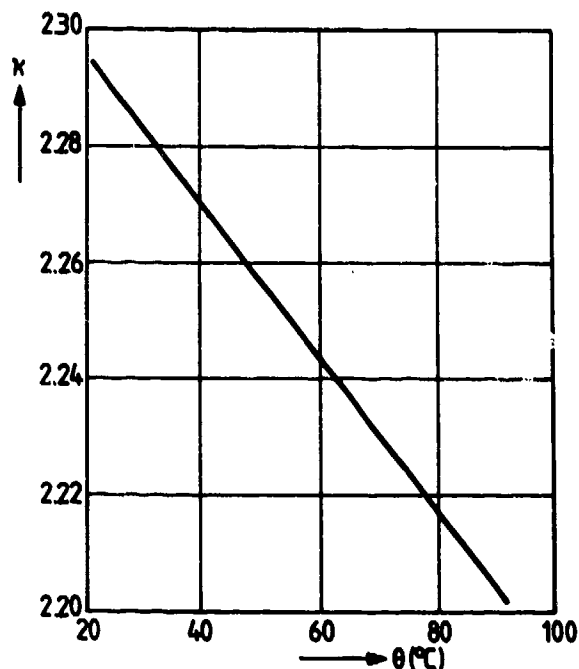


Fig. 7

A set of 5 pressure- or temperature-transducers and 5 filmthickness transducers is shown in figure 6c.

Measured results of pressure, temperature and filmthickness between steel surfaces with full-film elastohydrodynamic lubrication are given in figure 8.

Figure 9 shows filmthickness measurements between the lip of a lip-seal and rotating shaft taken in the axial direction of the shaft.

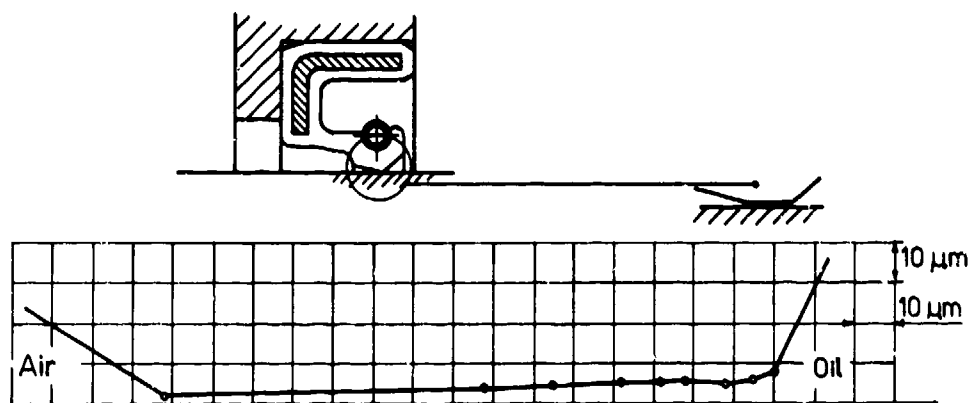
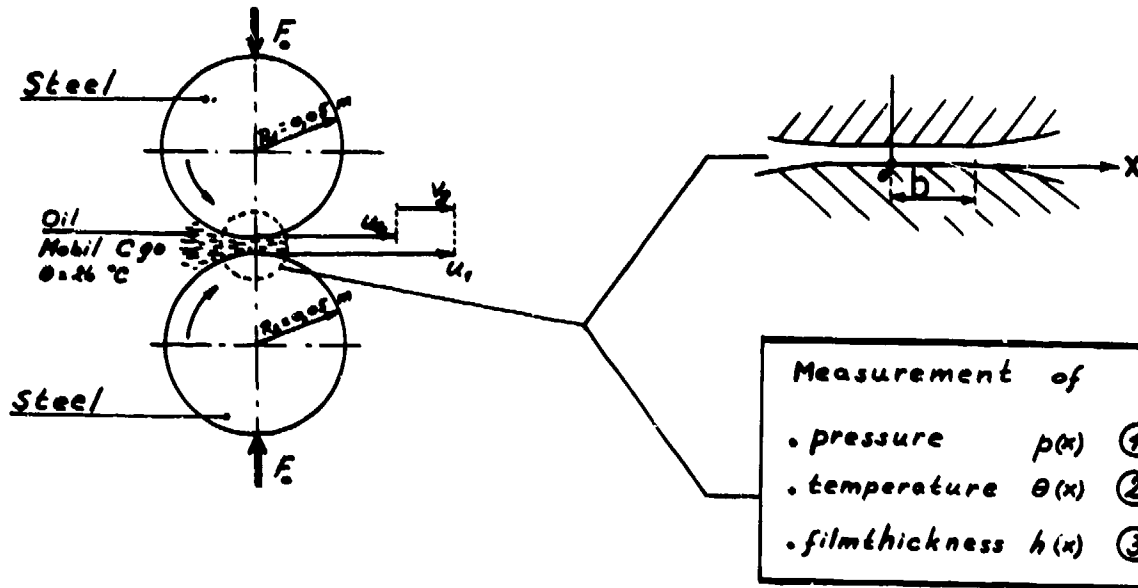


Fig. 9

Those readings were published in /7/ and /8/ as a result of two research projects on elastohydrodynamic lubrication.

Investigation of the lubricating conditions was the main topic in those projects; monitoring of a lubricated contact or a bearing was not. Transducers of this type were used up to pressures of 1300 N/mm², surface-speed of 10 m/s and sliding speed of 2,5 m/s.

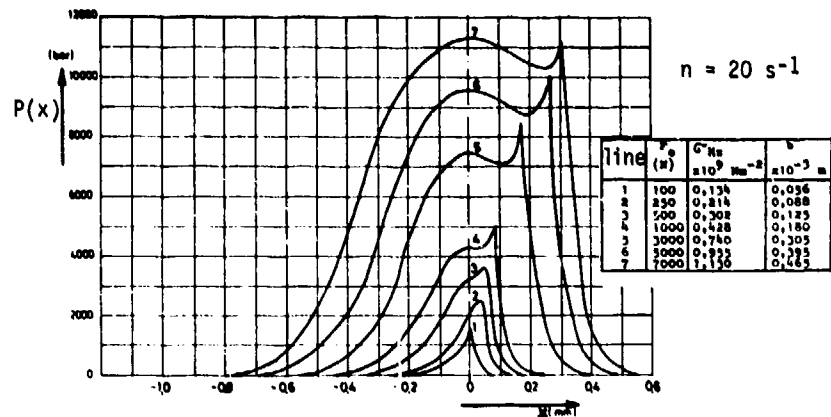
At this moment special attention is paid to the further development of a "second generation" of transducers for pressure, temperature and filmthickness under heavily loaded conditions, so that a reading of those values during a long time of running can be used in a monitoring system.



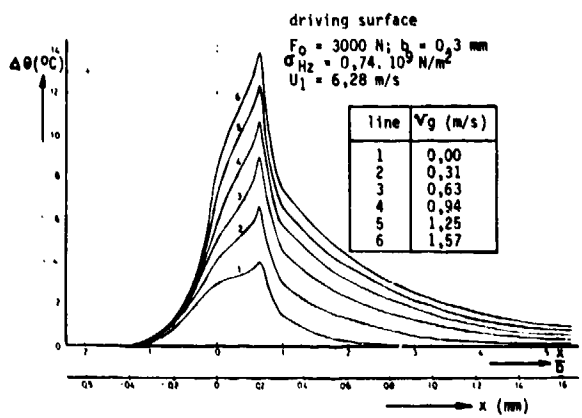
①



$n = 20 \text{ U/s}$, $F_0 = 5500 \text{ N}$, $\sigma_{Hz} = 10.000 \text{ bar}$
 $x = 50 \mu\text{s/cm}$, $y = 2 \text{ mV/cm}$; DC 100 kHz



②



③

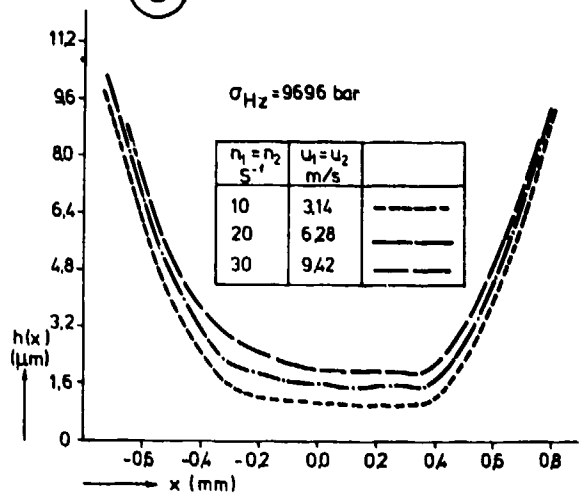


Fig. 8

Conclusion

Two measuring techniques, the thermodynamic method for the total temperature difference measurement and the thin film transducer technique for the measurement of pressure, temperature and filmthickness between lubricated surfaces are presented briefly. With all measurements coming up for discussion here, the oil acts as an intermittent medium.

Both methods are being used under laboratory conditions, the first as an accurate technique for the estimation of the total efficiency of hydrostatic components, the second as a tool in research of elastohydrodynamic lubrication.

Further development of both methods is carried out in order to bring those techniques to the level, necessary for a reliable monitoring technique for full-film lubricated bearings.

References:

- /1/ Collacott, R.A.: Mechanical Fault Diagnosis and condition monitoring. Chapman and Hall, London 1977.
- /2/ Neale, M.: A Guide to the condition monitoring of Machinery. London 1977.
- /3/ Witt, K.: Druckflüssigkeiten und Thermodynamisches Messen. Thesis, Eindhoven University of Technology (1974).
- /4/ Witt, K.: Thermodynamisches Messen in der Ölhydraulik. (Thermodynamic measurements in hydraulic systems). (In German). Ölhydraulik und Pneumatik. 1976 Nr. 6 and 9; 1977 Nr. 1, 2, 3, 9, 12; 1978 Nr. 1.
- /5/ Kannel, J.W. and Dow, T.A.: The evaluation of Surface pressure and Temperature measurement techniques for use in the study of lubrication in metal rolling. Journal of Lubrication Technology, Trans. ASME. Vol. 96, no. 4, 1974.
- /6/ Schouten, M.J.W.: Einfluss elastohydrodynamischer Schmierung auf Reibung, Verschleiss und Lebensdauer von Getrieben. Thesis, Eindhoven University of Technology, 1973 FKM - Forschungsheft Nr. 24 (1973) Maschinenbau Verlag GmbH, Frankfurt/Main.
- /7/ Schouten, M.J.W.: Elastohydrodynamische Schmierung. Theoretische und experimentelle Untersuchungen zur Erweiterung der EHD - Theorie auf praxisnahe und instationäre Bedingungen (in German). FKM - Forschungsheft Nr. 34 (1976) Maschinenbau Verlag GmbH, Frankfurt/Main.
- /8/ Schouten, M.J.W. and M.J. Gawlinski: Seals as an elastohydrodynamic problem. Contribution to the 6th International Sealings Conference. Dresden 10 - 12 april 1978.

DISCUSSION

F.Snyder, University of Waterloo, Ca

In regard to measuring EHD film thickness:

- (1) What kind of detection circuit do you use to measure the gap capacitance?
- (2) Have you obtained reasonable agreement with EHL theory by using the Clausius-Mosottis law?
- (3) Since the dielectric constant of an oil is *also* a function of the applied frequency, at what frequency (and voltage) were your measurements taken at?

Author's Reply

- (1) The capacitance-transducer is mounted in a bridge. This bridge and an amplifier are rotating, mounted on the disk. Slip-rings are used.
- (2) Good agreement was found between theory and measurement, where the Clausius-Mosottis Law was used to make corrections of the dielectric constant as a function of pressure.
- (3) No influence was found of the frequency on the dielectric constant of a 5 mm filtrated oil.

SILICON NITRIDE BEARING ELEMENTS FOR
HIGH-SPEED HIGH-TEMPERATURE APPLICATIONS

by

Lewis B. Sibley
President, Tribology Consultants, Inc.
504 Foxwood Lane
Paoli, PA 19301
USA

SUMMARY

Progress to date in the use of silicon nitride ceramics for critical high-speed high-temperature ball and roller bearings is reviewed. The properties of silicon nitride are presented that make it an attractive bearing material compared to steel, such as high hardness, excellent high-temperature performance and low density which reduces high-speed bearing centrifugal loads and skidding. Design procedures are demonstrated for bearing applications using computer analysis codes to evaluate the cross-coupled effects of these material properties and bearing operating characteristics.

Silicon nitride processing, inspection criteria and rolling-contact fatigue performance are reviewed. Successful test results are presented for an oil-lubricated hybrid silicon nitride bearing (silicon nitride balls with tool steel rings) in a 93,500 rpm turbine application. Solid lubricant development studies are reviewed, demonstrating low bearing wear at operating temperatures over 500°C. Therefore, it is expected that solid lubricated silicon nitride rolling bearings will find increasing application in future high-speed high-temperature aircraft systems.

INTRODUCTION

Modern turbine machines operate at very high speeds with desired high time between overhaul (TBO). One of the most critical items limiting the TBO is the shaft support bearing system. Angular-contact ball bearings and cylindrical roller bearings are usually selected by designers because of their low starting torque, low power loss, and their ability to support combined loads and to provide good control of blade and seal clearances. However, a compromise is made between a low enough shaft speed to obtain the desired bearing life and reliability and the optimum (higher) speed for maximum compressor efficiency, the optimum speed being curtailed in favor of longer bearing life and reduced susceptibility to thermal imbalance failure. Thus, improved bearing fatigue life and resistance to skidding and lubrication distress could maintain the desired reliability while permitting a higher shaft speed and thus improvement in the overall efficiency of the turbine power unit.

The recent awareness of the need for energy conservation has resulted in an increased emphasis on higher efficiency for all rotating machinery. The maximum efficiency of an engine is directly related not only to shaft speed but also to the maximum temperature in the combustion chamber. Properties of conventional materials often impose maximum speeds and temperatures and thus limit the unit efficiency.

One of the predominant forces acting on bearings and reducing their fatigue life in high-speed applications is the centrifugal force generated by the orbital velocity of the balls or rollers. A substantial portion of this loss in fatigue life can be regained if light-weight balls or rollers are used. Low density bearing materials, therefore, offer great potential in high-speed turbo-machinery.

Low density balls or rollers also reduce the tendency for skidding damage in high-speed bearings, since the inertial forces on the ball or roller-cage assembly are substantially reduced. Ball or roller skidding, for example during high shaft accelerations, is known to cause premature bearing failure in high-speed machines.

One candidate material class from which bearing elements with significantly lower density and higher temperature capability can be made is ceramics. Early efforts at screening a wide variety of available ceramic materials for bearing applications met with only limited success due to the inherent porosity and lack of homogeneity of the then available materials (1,2)*. However, recent advances in the processing of ceramic materials has made it possible to manufacture fully dense components. This is true especially with silicon nitride where the processing technology now is in the most developed stage.

PROPERTIES OF BEARING QUALITY SILICON NITRIDE

Recent developments in ceramic material processing has produced improved silicon nitride products with respect to density, homogeneity, and strength, suitable for use in ball and roller bearings. Figure 1 shows a comparison of high-temperature tensile strength between bearing quality silicon nitride and M50 steel, which is now commonly used for turbine bearings. Table 1 is a selected list of properties for these two bearing materials, showing the higher temperature capability and lower density of silicon nitride. Testing

* Numbers in parentheses refer to the References at the end of this paper.

Table 1. Selected Physical and Thermal Properties of Silicon Nitride and M50 Steel

Property	Silicon Nitride	M50 Steel
Hardness, R_c at 20°C	78	64
Maximum Useful Temperature*, °C (°F)	1200 (2200)	320 (600)
Density, g/cm ³	3.2	7.6
Elastic Modulus at 20°C, GPa (10 ⁶ psi)	310 (45)	190 (28)
Poisson's Ratio	0.26	0.28
Thermal Conductivity at 20°C, Cal/s m °C	7.3	13.4
Coefficient of Thermal Expansion, 10 ⁻⁶ /°C	2.9	12.3

* Maximum operating temperature when used for rolling bearings based on a minimum hot hardness of R_c 57 after long-term soaking at temperature, compared to a maximum temperature of 180°C (360°F) for 52100 steel.

also has shown that bearing quality silicon nitride usually is superior in rolling-contact fatigue resistance to bearing steels, as given in the endurance data plotted in Figure 2, taken from (3).

Thus it can be expected that high-speed ball and roller bearings utilizing improved silicon nitride elements will result in an improvement in bearing life and performance over all-steel bearings. In isolated cases where early failures of silicon nitride bearing elements have occurred, the cause has been traced to material defects such as porosity and excessive surface damage produced by inadequately controlled surface finishing processes (4). Basic lapping technology for silicon nitride balls has resulted in substantial increases in fatigue life of silicon nitride finished by improved ball lapping and polishing processes (5).

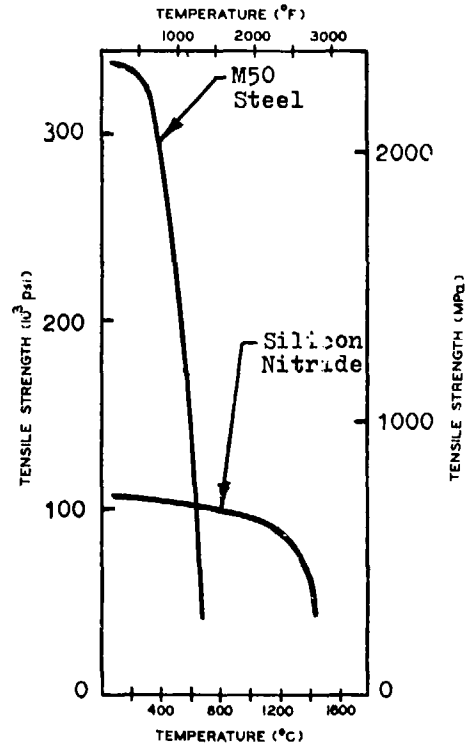


Figure 1. Comparison of High-Temperature Tensile Strength of Silicon Nitride and M50 Steel

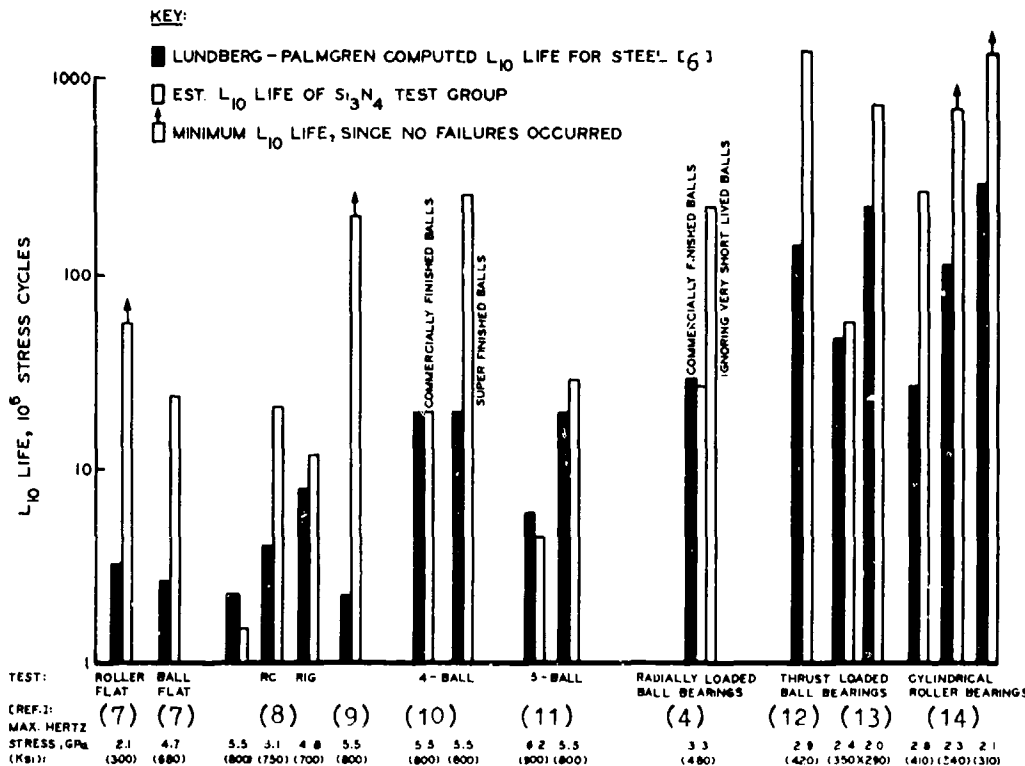


Figure 2. Rolling-Contact Silicon Nitride Spalling Fatigue Test Results

BEARING DESIGN ANALYSIS

The most recent computer analysis codes for computing the performance of high-speed ball and roller bearings are used to optimize the design of silicon nitride bearings. In all of the computer programs used, the bearing fatigue life is calculated using the Lundberg-Palmgren theory (6). In the case where silicon nitride material is used, adjustments are needed in the computer programs to account for the differences in properties of this material from steel, as given in (3). The reduced density and Poisson's ratio and increased Young's modulus of silicon nitride are used properly in the computer programs to calculate the reduction in centrifugal forces and redistribution of the loads between the balls or rollers in the bearing resulting from these changes in material properties. However, an adjustment to the computer calculated fatigue lives is required by the need to account for the change in contact stress and stressed volume resulting from the change in elastic properties of the silicon nitride material from those of steel.

As an example, Table 2 is a summary of the results of a computer analysis of an optimum design ball bearing for an oil-lubricated high-speed turbine application using silicon nitride balls. This tabulation illustrates the advantages of predicted bearing life to be obtained by properly accounting for the properties of silicon nitride compared to steel. Rig testing of this hybrid bearing demonstrated successful operation without failure at speeds up to 115,000 rpm (15).

Table 2. Application of Silicon Nitride Balls to High-Speed Turbine Bearings

Basic 7001 size (12-mm bore) angular-contact ball bearing under 220 N total thrust and preload and 70 N radial load at 93 500 rpm shaft speed with circulating 3.5 cs ester lubricant			
	CURRENT ALL-STEEL BEARING	Si ₃ N ₄ BALLS AND STEEL RINGS	
		SAME DESIGN AS ALL-STEEL BRG	OPTIMIZED DESIGN & PRELOAD
Max. Hertz stress, GPa	1.66	1.72	1.24
Computed L ₁₀ fatigue life, h	3000	1500	10 000
Heat generation rate, watts	60	42	40

The tendency of the bearings to skid in this turbine unit in service was analyzed by setting the bearing designs at their extremes of closest ring groove conformities and largest radial clearances expected for the tolerance ranges and mounting fits specified. These tolerance extremes were used as input in computer program SHABERTH for the SHAFT/BEARING/Thermal analysis of the turbine rotor system. Also, the lubricant cavity percentages and film replenishment layers were adjusted to simulate a copious oil flow rate which is expected to help induce ball skidding. Figure 3 is a plot of the computed cage speeds from a series of runs at 93 500 rpm preloads.

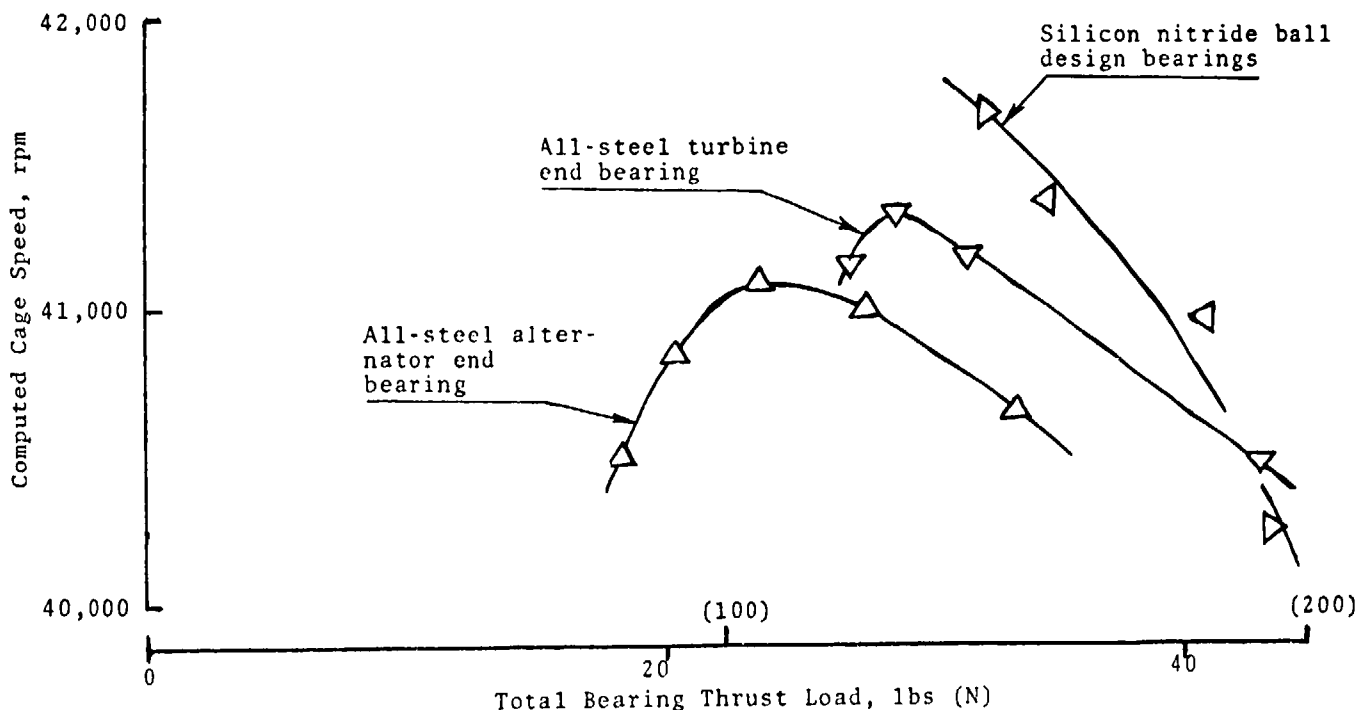


Figure 3. Program SHABERTH Predicted Cage Speeds in a Turbine Unit for All-Steel Bearing Design and Improved Silicon Nitride Ball Bearing Design at Tolerance Extremes

Although the data in Figure 3 is useful for comparison with rig test results, no clear indication of skid tendency is apparent. Skid behavior can best be analyzed by dividing the computed cage speed by the cage speed calculated for the computed operating contact angles assuming that no gross slip occurs, in other words the "epicyclic" cage speed. This cage speed ratio is given as part of the output of program SHABERTH and is plotted over a wide range of designs and operating conditions in Figure 4. Although the

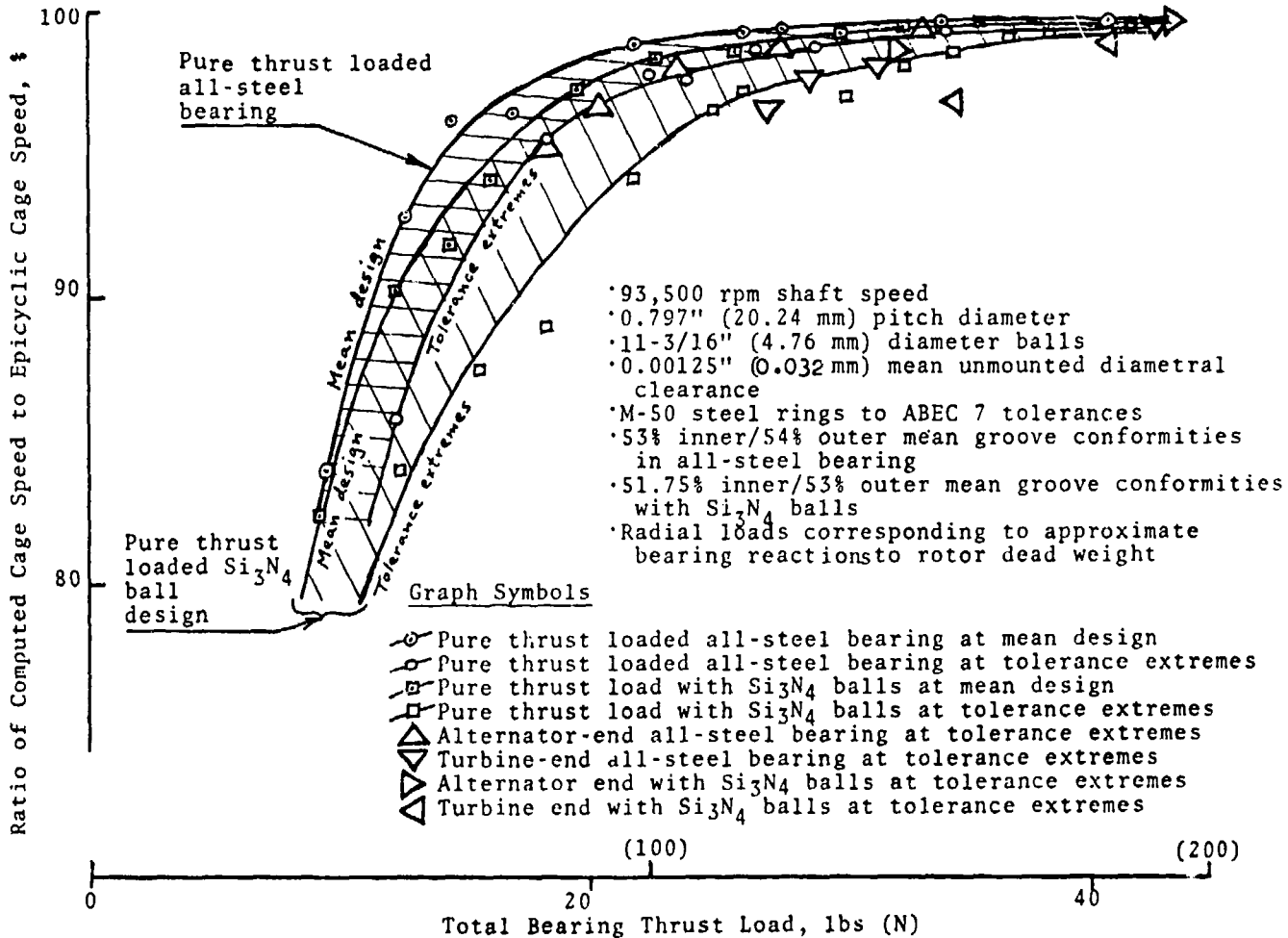


Figure 4. Summary of Program SHABERTH Predictions of Skidding in Turboalternator Bearings of Improved Silicon Nitride Ball Design Compared to Current All-Steel Design

spread in cage speed ratio between the mean designs and the tolerance extremes at any given preload level is slightly greater for the silicon nitride ball bearing than for the all-steel bearing (as expected for the higher elastic modulus silicon nitride), the skid tendency ranges of the silicon nitride and all-steel designs overlap and do not seem to be significantly different. Skid-free operation would appear to be possible with either type bearing down to at least 20-25 lbs (about 100 N) thrust preload. In addition, since the silicon nitride balls have only 40% of the mass of the steel balls, their ability to follow the transient motions imposed on them during operation under the combined radial and thrust loads in the turboalternator must be greater for the silicon nitride balls than the steel balls. For this reason, therefore, it is expected that the selected silicon nitride ball bearing design should be more skid resistant than the present all-steel bearing design.

Comparison of the predicted bearing fatigue lives at the same preload level of 32 lbs (145 N) after adjusting the silicon nitride bearing life as described above, shows a predicted life of the silicon nitride bearing about three times that of the all-steel bearing. Therefore, this selected silicon nitride bearing design was finalized for the application.

SILICON NITRIDE PROCESSING AND INSPECTION CRITERIA

Acceptable performance of silicon nitride rolling bearings depends critically on the use of raw material that is sufficiently free of failure inducing defects. Also, it is just as important to finish the load-carrying surfaces of silicon nitride bearings without

producing surface originated failure inducing defects. Silicon nitride bearing development projects conducted over the past decade have resulted in an extensive backlog of non-destructive evaluation (NDE) data, as well as other material and surface inspection data, correlated with bearing performance criteria. This experience is summarized here with some typical examples of NDE results and their interpretation.

The most successful silicon nitride material used in bearings to date is produced in the form of hot pressed billets, roughly 150 mm square by whatever thickness is required to obtain the bearing part needed. Machining bearing parts from hot pressed billets is very expensive, so efforts have been made to make bearing quality silicon nitride material in near net shapes (NNS). Figures 5, 6 and 7 compare the responses of 2 mm thick sections cut from three such candidate NNS spherical blanks to scanning laser acoustic microscopy (SLAM). The NC132 blanks gave very long fatigue spalling life when tested, whereas the 147Y and GTE blanks had excessive wear in rolling contact from the high porosity indicated in these alternative materials.

An NDE method of detecting surface damage on silicon nitride bearing parts is by radiographic gas penetrant, as illustrated in Figure 8. The finishing surface defect that was detected was quite small as shown, demonstrating the high sensitivity of this method. An especially useful NDE method is the fluorescent die penetrant technique. Figures 9, 10 and 11 show three different kinds of material defects found on NC132 ball surfaces by this method.

The critical size, shape and composition of material or surface defects in silicon nitride depends on their ability to initiate wear, cracking or fatigue spalling failures in rolling bearings. Figure 12 shows several NC132 silicon nitride balls that failed by fatigue spalling in ball bearing endurance tests. Closer examination and analysis of one such spall in Figures 13 and 14 showed that a structurally affected area about 150 μm in size, caused by graphite inclusions in the material from the hot pressing mold, resulted in a spalling life of about half the theoretically expected 90% survival life (L_{10}) in this endurance test. In a similar manner, the void of about 25 μm in size shown in Figure 15 also resulted in about half the expected spalling life. When silicon nitride material free of such large defects is used, spalls occur at much longer lives and are initiated from surface defects often manifested as Hertz cracks at the initiation point.

TURBINE BEARING TEST RESULTS

A number of tests have been conducted on silicon nitride bearings with oil lubrication at high speeds. In a typical high-speed turbine application, a 12-mm-bore hybrid bearing with silicon nitride balls, M50 steel rings and standard brass cage was developed (15) to replace the present all-steel angular-contact ball bearings which were limited in life and speed capabilities. Six hybrid bearings have successfully completed over 4000 hours of testing to date (a single bearing exceeding 1600 hours) in oil environment at 190°C, 93,500 rpm, maximum radial load of 67 N and maximum thrust load of 220 N.

During the course of this turbine testing, the unit was disassembled after 790 hours of successful running to inspect the bearings which were found in excellent condition. Upon reassembly, however, it was discovered later that the locknut on the forward end of the rotor was not returned to its precise balanced condition, so that excessive vibration occurred during subsequent testing at speed. After 23 additional hours running at 93,500 rpm with high vibration but no failure, the unit was disassembled again and the aft end bearing was found in the condition shown in Figure 16, with the cage partially fractured. The cage in the forward end bearing, shown in Figure 17, was completely missing, apparently having been broken up and the pieces discharged out the turbine exhaust, so that the bearing continued to operate successfully without a cage and with somewhat less than a full complement of balls.

Bearings in this turbine application with steel balls have seized under similar conditions. However, the silicon nitride balls suffered almost no damage, as shown in Figure 18, and the steel raceway tracks showed only the normal expected amount of microwear, which was somewhat greater in the forward bearing as expected, and as shown in Figure 19.

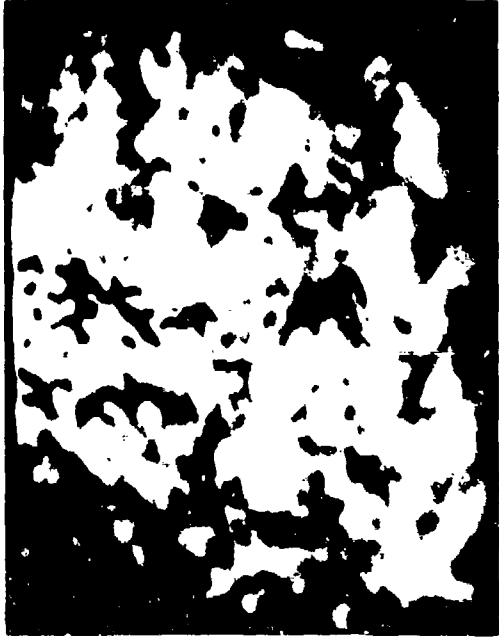
SOLID LUBRICATED SILICON NITRIDE

The major advantage of using a ceramic such as silicon nitride as a rolling bearing material is its potential for operating at much higher temperatures than is possible with bearing steels. Since the maximum temperature capabilities of silicon nitride are well beyond the temperature limits of all available liquid hydrocarbon-base lubricants, it is imperative that engineering principles be developed for operating silicon nitride bearings with no external lubrication or with dry lubricants having temperature capabilities in the order of 540°C (1000°F) or higher.

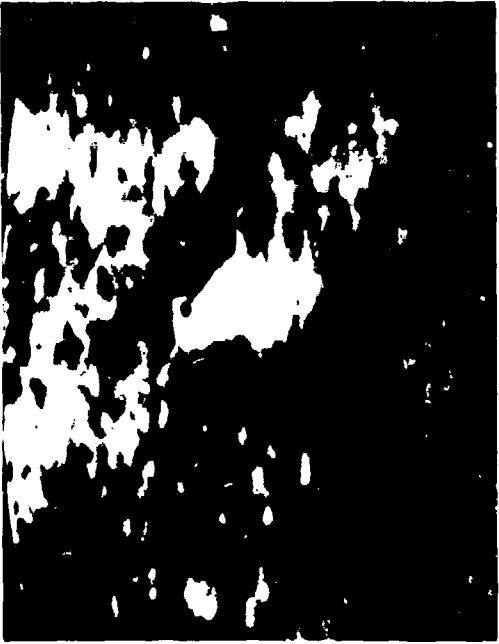
A large amount of information exists on the dry film lubrication of bearing metals and some ceramics, mostly under sliding, rather than rolling contact conditions (16-21). The ability of candidate solid lubricant and bearing materials to produce successful self-lubricated surfaces can only be determined by tests run under conditions simulating the intended bearing application service conditions as closely as possible.



77 592



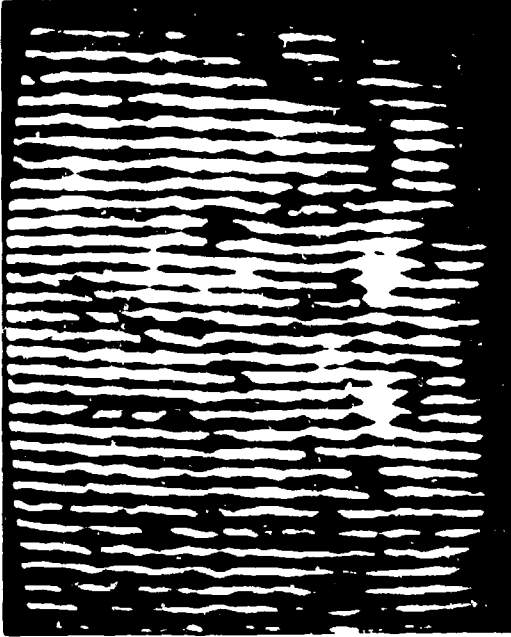
77 593



77 594



77 595



77 596



77 597

Figure 5. Transmission Scanning Laser Acoustic Micrograph (SLAM) of a Section from a Norton NC132 Rough Sphere

Figure 6. Transmission Scanning Laser Acoustic Micrograph (SLAM) of a Section from a Ceramloy 147Y Rough Sphere

Figure 7. Transmission Scanning Laser Acoustic Micrograph (SLAM) of a Section from a GTE Sylvania Rough Sphere



Figure 8. Surface Defect on NC132 Ball Detected by Gas Penetrant Inspection (Qual-X)

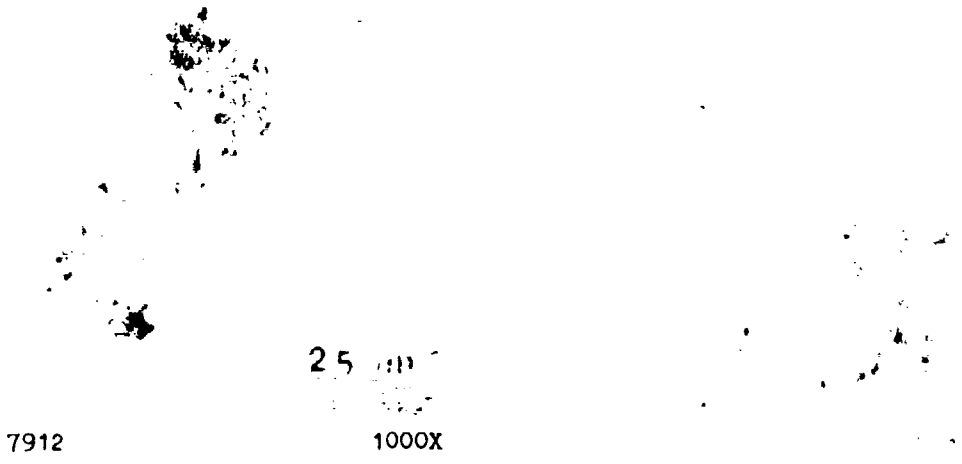


Figure 9. Material Defect (Porosity) Detected on NC132 Surface by Fluorescent Die Penetrant Inspection

Optical Micrograph 500X

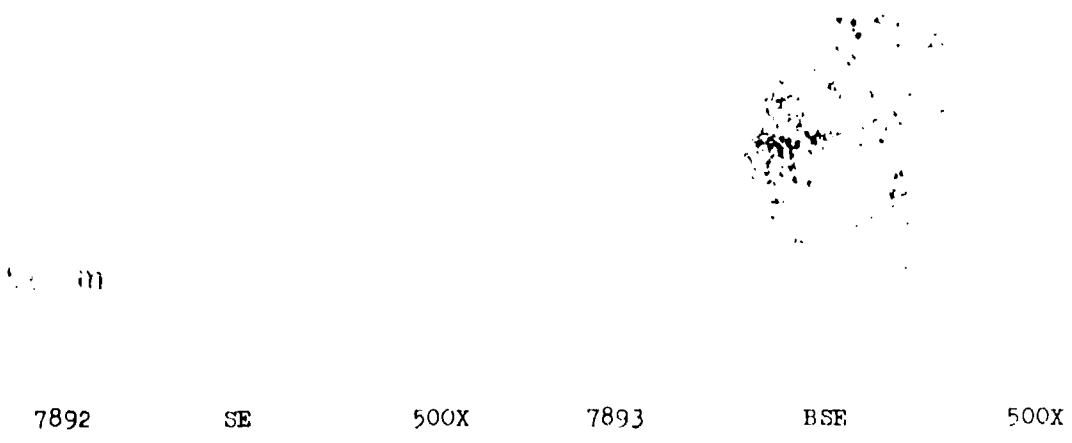


Figure 10. Material Defect (Silicon Inclusion) Detected on NC132 Surface by Fluorescent Die Penetrant Inspection



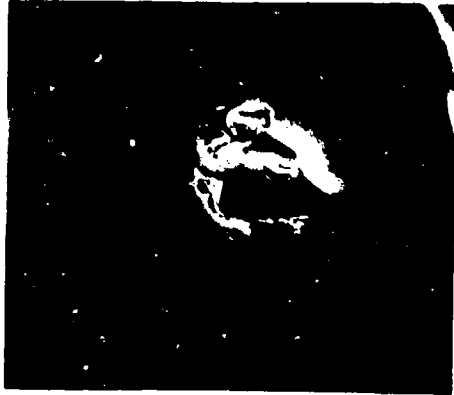
Bearing 104



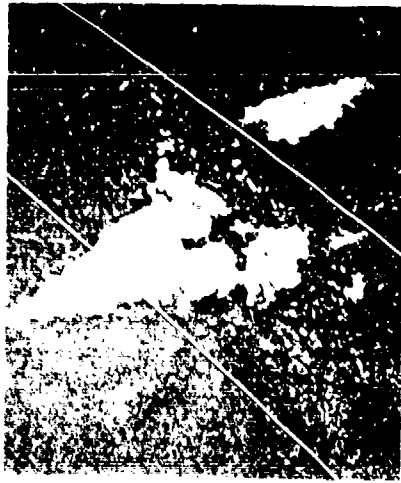
Bearing 102



Bearing 108



Bearing 105



7886 BSE 250X



7889 Fe Map 740X



7885 SE 250X



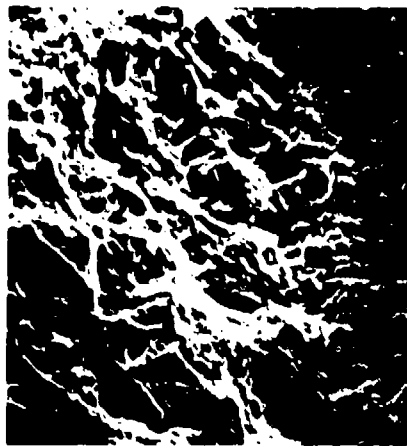
7888 740X

Figure 11. Material Defect (Iron Silicide) Detected of NC132 Surface by Fluorescent Die Penetrant Inspection

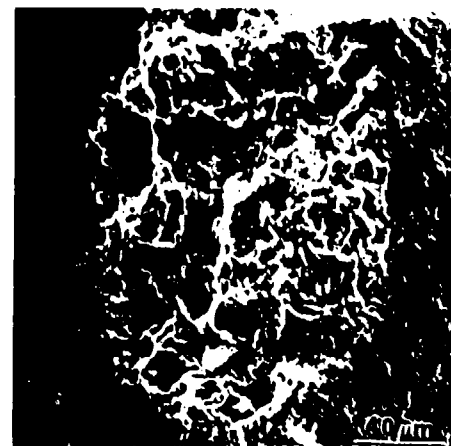
Figure 12. Typical Spalls Encountered on NC132 Silicon Nitride Balls Tested in Ball Bearings



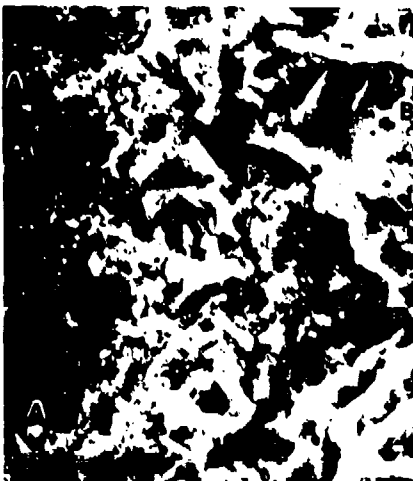
7782 60X
Spall Origin Indicated
by Arrows



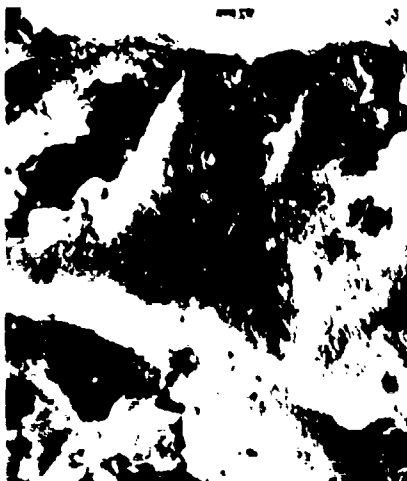
7787 680X
Coarse Grain Structure Noted
at Spall Origin



7783 SE 400X



7785 1600X
Interface Between Typical
Hot Pressed Si_3N_4 "A" and
Spall Origin "B"



7792 5000X
Microstructure at Fracture
Origin



7784 BSE 400X
Arrows Indicate Metal Contami-
nation From Bearing Ring
"C" Arrows Indicate Probable
Carbon Contamination

Figure 13. Inclusion Type Spall Origin Found in NC132 Silicon Nitride Ball Endurance Tested Under 2.4 GPa (350,000 psi) Maximum Hertz Stress to Half the Lundberg-Palmgren L_{10} Life

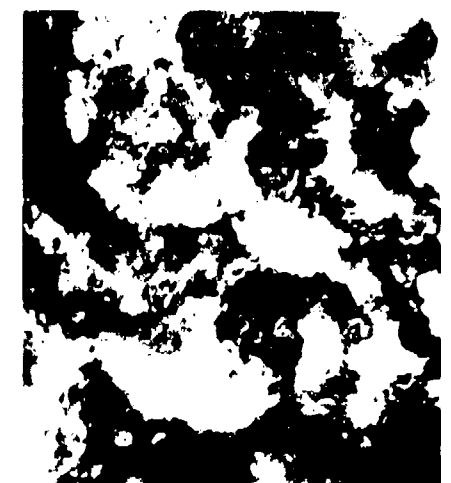
Figure 14. Secondary Electron (SE) and Back Scattered Electron (BSE) Image of Spall Origin on Ball in Figure 13



7776 40X
Arrows Depict Crack Propaga-
tion Direction



7777 400X
Arrow Points to Suspected
Fracture Origin



7780 5000X
Microstructure at Fracture
Origin

Figure 15. Void Type Spall Origin Found in NC132 Silicon Nitride Ball Endurance Tested Under 2.4 GPa (350,000 psi) Maximum Hertz Stress to Half the Lundberg-Palmgren L_{10} Life



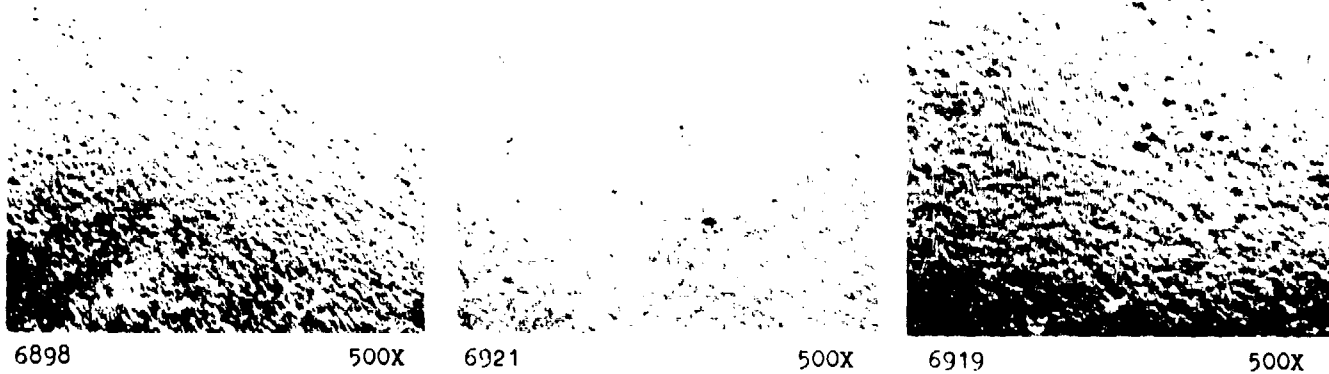
78 043

Figure 16. Aft End 12-mm Bore Turbine Bearing with Silicon Nitride Balls, M50 Steel Rings and Brass Cage After 813 Hours Running at 93,500 rpm Under 55 lbs. (240 N) Thrust Load with Excessive Unbalance Radial Load Imposed on Forward End During Last 23 Hours of Test, Showing Initial Cage Fracture but Excellent Condition of Balls and Rings



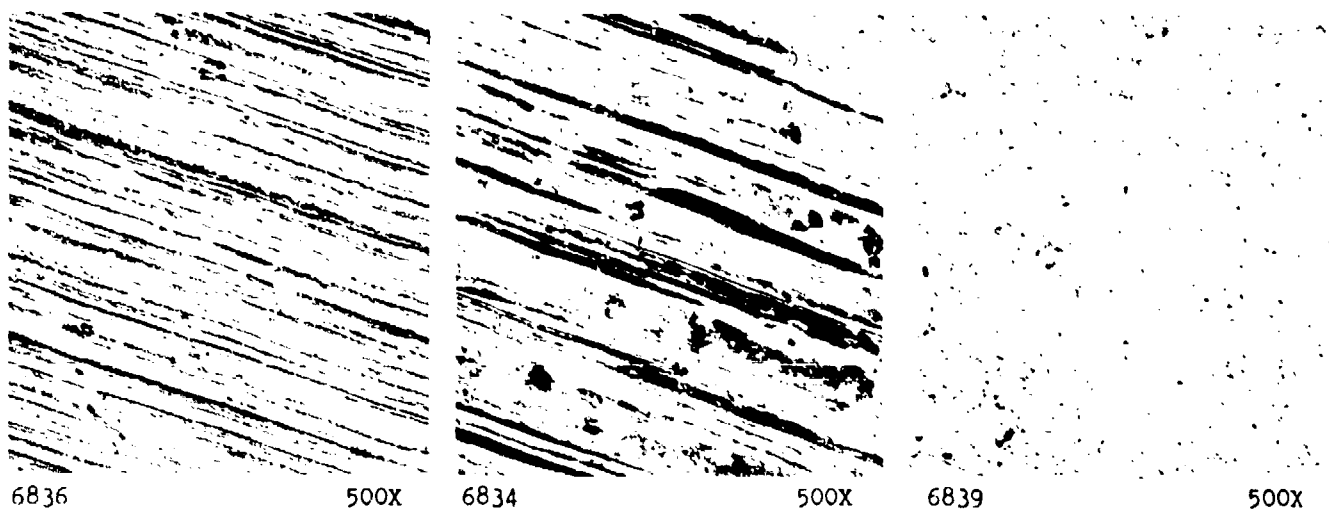
78 043

Figure 17. Forward End 12-mm Bore Turbine Bearing with Silicon Nitride Balls, M50 Steel Rings and Brass Cage After 813 Hours Running at 93,500 rpm Under 45 lbs. (200 N) Thrust Load with Excessive Unbalance Radial Load Imposed During Last 23 Hours of Test, Showing Complete Destruction of Cage (Pieces Blown Out Turbine Exhaust) but Excellent Condition of Balls and Rings



6898 500X Unrun Ball Surface 6921 500X Aft Bearing Ball After Test 6919 500X Forward Bearing Ball After Test

Figure 18. Scanning Electron Micrographs of Silicon Nitride Balls Before and After Running 813 Hours at 93,500 rpm in 12-mm Bore Turbine Bearings with Excessive Unbalance Radial Load and Broken or Missing Cages During the Last 23 Hours



6836 500X Unrun Surface of Ball Groove 6834 500X Center of Aft Bearing Track After Test 6839 500X Center of Forward Bearing Track After Test

Figure 19. Scanning Electron Micrographs of M50 Steel 12-mm Bore Turbine Bearing Inner Ring Ball Tracks Before and After Running 813 Hours at 93,500 rpm with Excessive Unbalance Radial Bearing Load and Broken or Missing Cages During Last 23 Hours.

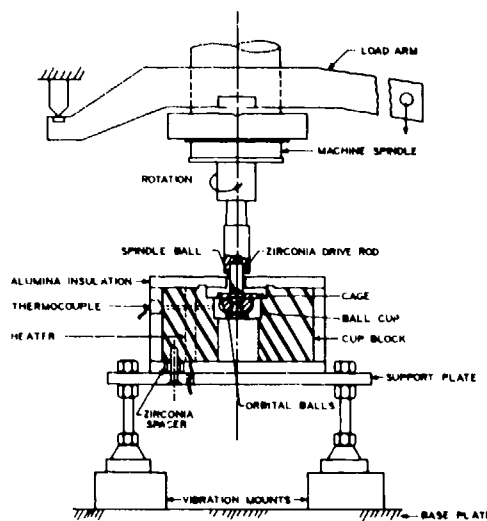


Figure 20. Schematic of High-Temperature Rolling Four-Ball Tester

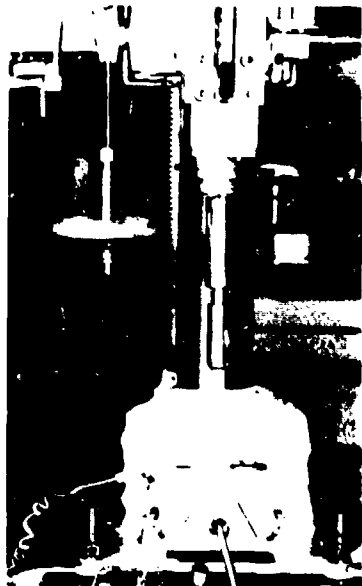


Figure 21. Photograph of High-Temperature Test Rig Showing Insulated Cup Block

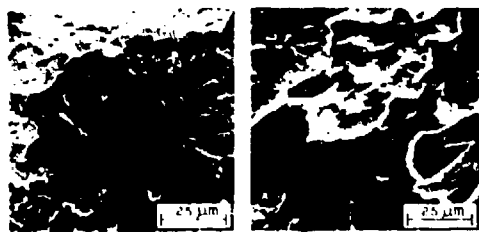


Figure 22. SEM Micrographs of Solid Lubricant Coating on Ball Supplied by Cage at 540°C for 187×10^6 Cycles



NEW AFTER 258 HOURS, 540°C Figure 23. Cage Before and After Tests

A convenient screening test machine for dry lubrication tests is the rolling four-ball machine used for similar tests for a number of years and shown in Figures 20 and 21. The test specimens are in the form of bearing balls which are manufactured of silicon nitride to very close tolerances and reproducibility of the wear surfaces by the unique statistical characteristics of the ball manufacturing process, thus giving good test reproducibility. Since these tests were run dry the ball separator was made from a composite salt-impregnated mixture of carbon and graphite which provides self-lubrication to the cage rubbing contacts, as well as transfer film lubrication to the ball-ball and ball-cup contacts. The cups are made of either silicon nitride or AISI M1 grade tool steel to accommodate the high temperature of the tests.

The tests were conducted at 10,000 rpm with a Hertzian contact stress of 2.76 GPa (400 ksi) maximum at the rolling contacts between the balls. Most tests were conducted at 540°C and continued until excessive wear occurred. Silicon nitride wear volumes and wear coefficients were estimated by analysis of both weight loss measurements and diamond stylus traces perpendicular to the wear track.

A number of high-temperature carbon graphite materials (P3310, AFX-5QE, P2003, 56HT and CJPS) and WSe₂-In-Ga composite were tested. The lowest wear was achieved by a P3310 cage up to 315°C and a P2003 cage up to 540°C. The wear coefficient of the silicon nitride spindle ball using the P2003 cage was measured to be 2×10^{-7} . Figure 22 shows the scanning electron micrograph of a partial solid-lubricant transfer film on the support balls after 139 hours of operation. The film was so thin that it could not be detected by x-ray wavelength spectroscopy. Figure 23 shows graphite cages before and after four-ball testing at 540°C. The cage has a noticeably white, fluffy surface after high-temperature testing. The wear coefficient for silicon nitride of 2×10^{-7} at 540°C is an order of magnitude lower than that measured for boundary lubrication of 52100 steel balls in the rolling four-ball tester with partial EHD lubrication (22). As a further comparison of typical wear coefficients from the literature (23), a mild steel (R_B 90 hardness) is reported to have a dry wear coefficient of about 7×10^{-3} . The tungsten carbide coefficient is about 10^{-6} , and therefore, both are higher than that measured for silicon nitride from room temperature to 540°C.

CONCLUSIONS

Silicon nitride is now available in sufficiently high quality to perform satisfactorily as a ball or roller bearing material. With two to three times the hardness (flow pressure) of bearing steels and by maintaining its strength and oxidation resistance up to 1200°C, silicon nitride holds particular promise as a high-temperature bearing material.

Even though the elastic modulus of silicon nitride is lower than that of most other ceramics, thus reducing bearing contact stresses, it is still half again higher than the modulus of bearing steels. With 40% of the density of steel, however, silicon nitride reduces the inertial loads in high-speed bearings, thus overcoming the effect of its higher elastic modulus on computed fatigue life. Rolling contact fatigue tests of silicon nitride have demonstrated one to two orders of magnitude longer life than the Lundberg-Palmgren rated life of bearing steel in 40% of the endurance groups reported, with a log average life for all groups at least five times greater than steel.

Prototype silicon nitride bearings have been applied successfully in critical machinery such as high-speed turbines, using oil lubrication. Impregnated graphite cages reduced the wear of dry silicon nitride rolling-spinning contacts to a wear coefficient of 2×10^{-7} , an order of magnitude lower than oil boundary lubricated steel. It is expected, therefore, that solid lubricated silicon nitride bearings will find increasing application in future aircraft systems.

REFERENCES

1. Sibley, L. B., et al, "A Study of Refractory Materials for Seal and Bearing Applications in Aircraft Accessory Units and Rocket Motors," WADC Technical Report 58-299(1958).
2. Taylor, K. M., Sibley, L. B., Lawrence, J. C., "Development of a Ceramic Rolling Contact Bearing for High Temperature Use," *Wear*, 6, pp 226-40 (1963).
3. Bhushan, B., and Sibley, L. B., "Silicon Nitride Bearings for Extreme Operating Conditions," ASLE Preprint No. 81-LC-4C-2 (1981).
4. Dalal, H. M., et al, "Surface Endurance and Lubrication of Silicon Nitride Ball Bearings," Final Report on U. S. Navy Contract No. N00019-75-C-0216 (1975), AD-A022157.
5. Dalal, H. M., Rosenlieb, J. W., and Sibley, L. B., "Effect of Lapping Parameters on Generation of Damage on Silicon Nitride Ball Surfaces," Final Report on U. S. Navy Contract No. N00019-76-0147 (1976), AD/A037485/LLC.
6. Lundberg, G. and Palmgren, A., "Dynamic Capacity of Rolling Bearings," *Acta Polytechnica* No. 196 (1947). See also No. 210 (1952).
7. Dalal, H. M., et al, "Effect of Surface and Mechanical Properties on Silicon Nitride

Bearing Element Performance," Final Report on Naval Air Systems Command Contract No. N00019-74-C-0168 (1975), AD-A006917.

8. Baumgartner, H. R., "Evaluation of Rolling Bearings Containing Hot-Pressed Silicon Nitride Rolling Elements," Proc. of Second Army Materials Science Conf. on Ceramics for High Performance Applications, Hyannis, Mass. (1973).
9. Valori, R., "Rolling Contact Fatigue of Silicon Nitride," NAPTC Report No. PE-42, August (1974).
10. Dalal, H. M., "Machining of Ceramics for Bearing Applications," Proc. of the Fifth Army Materials Technology Conf., Newport, R. I. March (1977).
11. Parker, R. J., and Zaretsky, E. V., "Fatigue Life of High Speed Ball Bearings with Silicon Nitride Rolling Elements," Trans. ASME, J. Lub. Tech., 97, pp 350-357 (1975).
12. Lorosch, H. K., et al, "Fatigue Strength of Silicon Nitride for High-Speed Rolling Bearings," ASME Paper No. 79-GT-83, March (1979).
13. Morrison, F. R., and Yonushonis, T., "Establishment of Engineering Design Data for Hybrid Steel/Ceramic Ball Bearings, Phase II," SKF Report No. AT80T042, September (1980).
14. Baumgartner, H. R., "Ceramic Bearings for Turbine Applications," Proc. of the Fifth Army Materials Technology Conf., Newport, R. I., March (1977).
15. Morrison, F. R., and Sibley, L. B., "Phase I Final Report on the Application of Ceramic Ball Bearings to the MERADCOM 10 KW Turbine," SKF Report No. AL77T033, June (1977).
16. Sibley, L. B., et al, "A Laboratory Evaluation of Some Ceramic and Cermet Materials for Bearing and Seal Applications in Aircraft Auxiliary Power Units and Liquid Rocket Motors," WADC TR 57-4 (1956).
17. Wilson, D. C., Gray, S., Sibley, L. B., et al, "The Development of Lubricants for High-Speed Rolling Contact Bearings Operating at 1200°F Temperature," WADC TR 59-790 (1959).
18. Cosgrove, S. L., Sibley, L. B. and Allen, C. M., "Evaluation of Dry Powdered Lubricants at 1000°F in a Modified Four-Ball Wear Machine," ASLE Trans., 2 (2), 217-224 (1960).
19. Sibley, L. B., and Allen, C. M., "Friction and Wear Behavior of Refractory Materials at High Sliding Velocities and Temperatures," Wear, 2, 312 (1962).
20. Campbell, M. E., and Thompson, M. B., "Lubrication Handbook for Use in the Space Industry, Part A - Solid Lubricants," NASA Marshall Space Flight Center Contract NAS8-27662 (1972).
21. Lipp, L. C., Van Wyk, J. W., and Williams, F. J., "Development of Solid Lubricant Compact Bearings for the Supersonic Transport," Lubrication Engineering, 29 (3), 108-115 (1973).
22. Tallian, T. E., McCool, J. I., and Sibley, L. B., "Partial Elastohydrodynamic Lubrication," Paper No. 14, Inst. Mech. Engrs., London (1965).
23. Archard, J. F., and Hirst, W., "The Wear of Metals Under Unlubricated Conditions," Proc. Roy. Soc., Series A, 236, pp 397-410 (1956).

ACKNOWLEDGMENTS

Portions of the research reported here were sponsored by the Naval Air Systems Command, the Army Mobility Equipment Command, Norton Company, and Solar International. The author acknowledges the facilities and support of SKF Industries, Inc., under whose auspices this research was conducted.

DISCUSSION

E.Jantzen, DVFLR, Ge

- (1) Have you conducted any investigations of boundary lubrication with liquid lubricants (effect of wetting, adhesion and surface reaction of lubricants)?
- (2) Is the carbon cage the only lubricant in the dry lubrication investigation? (e.g., is the lubrication of surfaces (bearing rings) solely by lubricant in the retainer?)

Author's Reply

The boundary lubrication of silicon nitride is the same as steel. Measurements of boundary lubricated friction of silicon nitride compared to other ceramics and M-50 steel using either hydrocarbon or synthetic ester or silicone base liquid lubricants are given in Reference (3) of the paper as well as in ASLE Transactions, 18 (3) 211-221 (1975), the latter of which also includes surface wetting tests. In the dry lubrication studies, solid film coatings on the silicon nitride balls sometimes were used as well as the solid lubricant cages, but very little effect of the coatings tested was detected. Apparently, the main dry lubrication mechanism is by transfer of a solid lubricant film from the cage to ball surfaces in the cage pockets. The dry coefficient of friction of silicon nitride is only one-third that of steel.

D.G.Astridge, Westland Helicopters Ltd, Yeovil, UK

In view of the poor tensile strength of silicon nitride compared with tool steel, and the large difference in thermal expansion coefficient between Si_3N_4 and steels/nimonic commonly used in engines, are you aware of any rolling contact fatigue tests with Si_3N_4 bearings on steel shafts (or hybrid bearings) in which start-stop cycles have been simulated?

Author's Reply

Since the thermal expansivity of silicon nitride is less than that of steel, special designs must be used to mount silicon nitride bearing rings on steel shafts and in steel housings. For small turbomachines, the best arrangement often is to use a ceramic shaft. In all cases, and especially with hybrid bearings, all possible engine operating extremes should be analyzed with modern computer codes to account for these property differences in the design. Reference (3) of the paper gives references to thermal cycling tests, most of which have been conducted on silicon nitride turbine blades.

B.R.Reason, Cranfield Institute of Technology, Cranfield, UK

The author has presented an interesting review of silicon nitride ceramics for high-temperature rolling bearings, particularly regarding its advantages over conventional bearing steel in this environment. Has the author or his colleagues carried out any in-site bearing testing with this material under conditions of transient mechanical shock and, if so, how does it compare with the more compliant bearing steels?

What reaction has silicon nitride with the type of polar charged additions used in mineral oils to produce metallic soap films on ferrous surfaces in conditions of boundary lubrication?

Author's Reply

Wettability studies have been conducted. Those are covered in several references in the paper. With standard ester base or mineral oil lubricants indications are that the same type of EHD films are formed as with steels. We do not know whether anti-wear additives will work as well as with steels. There may, however, be substitutes for use with silicon nitride. There is always a layer of silica, probably monomolecular, on the surface of silicon nitride and this is known to be a high temperature lubricant in the metal working industry. The dry, clean coefficient of friction of silicon nitride against silicon nitride is only .17, whereas with M-50 steel it would be .5.

B.Courage, Rolls Royce Ltd, Aero Division, Bristol, UK

Could the author confirm the Lundberg-Palmgren L_{10} values used as baseline comparators for the silicon nitride performance in Figure 2 are not factored up to represent current tool steel performance levels. If this is the case we clearly still require a significant and consistent improvement to be demonstrated by the silicon nitride before it can be used to replace tool steel balls and thereby permit high operating speeds in mainshaft ball bearings. Unless there is parity between silicon nitride and current tool steels the present maximum permissible stress levels would have to be reduced which would inhibit the maximum thrust capacity due to overstressing of the balls at the inner race contact. This situation will arise because bearings have to be optimized to carry high thrust loads at takeoff, when the centrifugal load is not dominant as well as the lower load cruise conditions when the centrifugal load does become dominant.

Author's Reply

All of the fatigue life data that I was able to find in the literature are on the bargraph in the paper. The log average of all that life data is 5 times Lundberg-Palmgren. So in that sense it's comparable if you are using a factor of 5 or so for M-50. It's important to note that that data represents all that's in the literature for the last ten years, and that

improvements are being made all the time. If we took 40 percent of the groups with the longest life on the bargraph we get between 10 and 100 times Lundberg-Palmgren life, which I think is significantly better than M-50.

M.A.H.Sequeira, Portuguese Oil Co., Po

I would like to know if you could use synthetic oils instead of petroleum oils. Do you have any experience with these?

Author's Reply

Yes, I mentioned ester base oils. Most of the endurance test data were obtained with military specifications ester base synthetic oils.

LIGHTWEIGHT MATERIALS FOR ROLLING ELEMENTS IN AIRCRAFT BEARINGS

by R.T. Cundill, Head of Material Development,
SKF Engineering and Research Centre,
Postbus 50, 3430 AB Nieuwegein, Netherlands.
and
F. Giordano, Assistant Laboratory Manager,
RIV-SKF Industrie S.p.A., 10060 Airasca (To), Italy.

SUMMARY

Using in-house experience with powder metallurgy, SKF has followed two approaches in the development of lightweight rolling elements. Balls have been made from both silicon nitride and a proprietary composite material using process routes based on hot isostatic compaction. The composite material consisted of titanium carbide in a superalloy matrix and the finished balls had densities of 5.4 - 5.75 g/cc with hardness values above 1500 Hv.

The performance of silicon nitride balls was compared with that of T1 tool steel balls in a test in which two mainshaft bearings were run at progressively increasing loads and speeds. Inspection after testing showed that there was much less distortion of raceway profiles in the bearing with silicon nitride balls indicating better kinematic behaviour. As a consequence, the silicon nitride balls showed little change in physical form, whereas there was marked deterioration of the tool steel balls for the bearing design and test conditions considered.

INTRODUCTION

The efficiency of gas turbine engines can be improved by increasing the rotational speeds and combustion temperatures. In principle, an increase in combustion temperature should have little interaction with the bearing system provided that there is a sufficient flow of lubricant to maintain the bearing at a suitable running temperature. However, the extent to which shaft rotational speeds can be increased is significantly affected by the centrifugal forces from the rolling elements acting on the bearing outer rings. At very high speeds, the centrifugal loading can exceed that caused by the applied load and lead to extensive skidding and/or overload of the outer ring. One solution to this problem is to reduce the density of the material used for the rolling elements and thereby decrease the centrifugal loading. Using in-house experience with powder metallurgy techniques, including cold and hot isostatic pressing, SKF in Europe has followed two approaches in the development of lightweight materials for aircraft engine bearings. Examples of these are given for two different types of bearing applications.

Titanium carbide/superalloy composite materials are being developed and evaluated for balls to be used in bearings in thrust-reverser motors. These units are located alongside the afterburner section and are driven by air from the compressor stage. Consequently, the operating temperature can exceed 500°C and the bearings run dry; i.e., without any liquid lubricant. During the development and proving of these bearings, it was found that the best available ball material was tungsten carbide-cobalt hardmetal. Although the motors operate intermittently and the required life in terms of total number of revolutions is very low, accelerations are high - 0 to 18000 rpm in 0.6 seconds, with corresponding decelerations. The high density of the tungsten carbide balls leads to high inertial forces which can cause the cage to fracture. The requirement for this application was for a material of moderately low density with high strength, hardness and oxidation resistance at temperatures up to 550°C.

The other approach has been to use silicon nitride which has a density approximately 40% that of tool steels. The physical, mechanical and bearing properties of silicon nitride are such that it is the leading, if not the only, contender for use in future high speed/high temperature bearings. It is now opportune that more consideration should be given to the manufacturing processes and economics for the production of bearing components from this material. So far, virtually all silicon nitride rolling elements and complete bearings, that have been tested, have been made from hot pressed material. The cutting and shaping of bearing elements from hot pressed slabs or billets by either diamond machining or ultrasonic machining is expensive and time consuming. This is particularly so in the case of balls.

What is required is a manufacturing method that can give near-net-shape blanks or preforms of sufficient accuracy so that finishing operations are minimized. Two such processes are under development - hot isostatic pressing (HIP) (1-3) and pressureless sintering (4-6). As the name implies, densification in the pressureless sintering process is achieved through the application of heat alone. This is potentially the cheapest manufacturing method for silicon nitride components. However, the materials developed to date have residual porosity levels such that it is doubtful whether they can withstand the high stresses in an aircraft bearing. HIP is similar to hot pressing in that both heat and pressure are used to densify the material, but has the additional capability of producing near-net-shape components. The main part of this paper, therefore, describes the manufacture of silicon nitride balls by a HIP process and the subsequent comparative testing of these balls in a mainshaft bearing.

TITANIUM CARBIDE/SUPERALLOY COMPOSITE MATERIALS

During the mid 1970's, a number of composite materials consisting of metal carbides in a nickel or cobalt based superalloy matrix were investigated at the SKF Engineering and Research Centre. The aim of this work was to develop improved tool materials for metal cutting using the high temperature strength of superalloys to give increased hot hardness. One of these composite materials - titanium carbide in a Udimet 700 matrix - was considered to be the most promising substitute for tungsten carbide balls in the bearing application referred to previously. This combined the advantages of the low density of the titanium carbide and the high temperature strength of the superalloy. Furthermore, the manufacturing process, which is outlined below, is essentially similar to that used in the hardmetal industry and could be readily applied in practice.

The TiC/Udimet composite material was used to manufacture balls of 7,938 mm (5/16") final size. From previous work, it was known that a 70 wt% TiC + 30 wt% Udimet 700 composition would give a material with high hardness. However, a second batch of material of 60% TiC + 40% Udimet was also processed to provide a material with higher toughness.

Powder Preparation

Normal commercially available, high purity powders were used as raw materials. The superalloy powder was produced by inert gas atomization. This process gives relatively coarse spherical particles which are unsuitable for die compaction. Therefore, the gas atomized powder was cryogenically disintegrated by the Coldstream process to give a fine, irregularly shaped powder. Median particle sizes of the carbide and superalloy powders were 4 μm and 15 μm respectively. The powders were blended together in ball mills which also further reduced the particle size. To avoid oxidation, this operation was carried out in petroleum ether which was evaporated afterwards. The optimum milling or blending time was 12 hours. After milling, 2% paraffin wax was mixed into the powder to ensure that the fine powder would have satisfactory flow properties for die compaction. The paraffin wax also acted as lubricant during compaction.

Preform Compaction

Ball blanks were compacted by a hydraulic press using a simple die set with hemispherically shaped punches (Fig. 1). The balls were pressed with an equatorial band, since in practice it is not possible to compact true spheres by die pressing without damaging the punches. Using such a die system inevitably leads to density variation throughout the compact. Therefore, control of compaction pressure and filling height was critical. Too high a pressure led to lamination and cracking across the mid-section; but, at low pressures, the compacted balls were too fragile to be handled. Since the hemispherical sections of the ball blanks had lower densities than in the equatorial region, there was correspondingly more shrinkage during sintering along the vertical axis of the balls. Therefore, the filling height had to be carefully adjusted so that the compacted ball blanks were elongated; but, reverted to a more spherical shape after sintering. The compaction pressure used was 490 MPa which resulted in densities of about 3.5 g/cc.

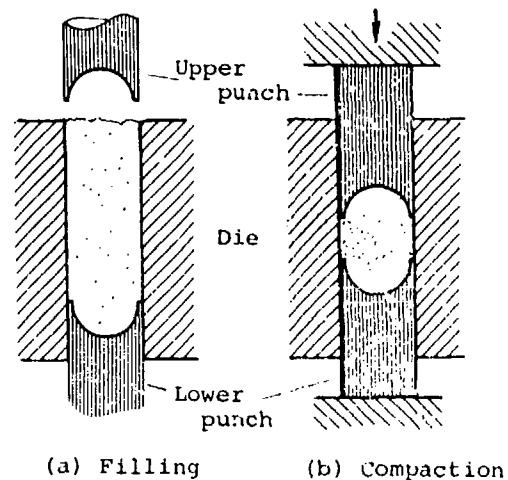


Fig. 1

Compaction of ball blanks

Dewaxing and Sintering

After compaction, the paraffin wax binder was removed by heating the ball blanks to 550°C in nitrogen. The blanks were then sintered in hydrogen at 1500°C for 1 hour. The sintering temperature was controlled to within $\pm 2^\circ\text{C}$ to ensure consistency between the several batches of balls. Lower sintering temperatures led to incomplete densification and non-uniform structures, whereas higher temperatures caused excessive growth of the titanium carbide particles. After sintering, the densities of the two compositions were as follows.

60% TiC + 40% Udimet	5.4-5.5 g/cc
70% TiC + 30% Udimet	5.2-5.3 g/cc

These were equivalent to relative densities of 94-96%.

Hot Isostatic Pressing

The balls were HIPed after sintering to eliminate residual porosity. This process is also applied to cobalt-bonded tungsten carbide components intended for high duty applications. The equipment used consisted of a wire-wound pressure vessel with an integral resistance heater, thermally insulated from the pressure vessel walls. The vessel could be pressurized up to 2000 Bar (200 MPa) by argon gas with a maximum operating temperature of 1450°C. Although this was a laboratory press, the internal dimensions, which limit the work load, were 160 mm diameter x 600 mm high. The HIP unit is shown schematically in Fig. 2. The pressure vessel was located in a wire-wound frame, which held the end closures in place during pressing.

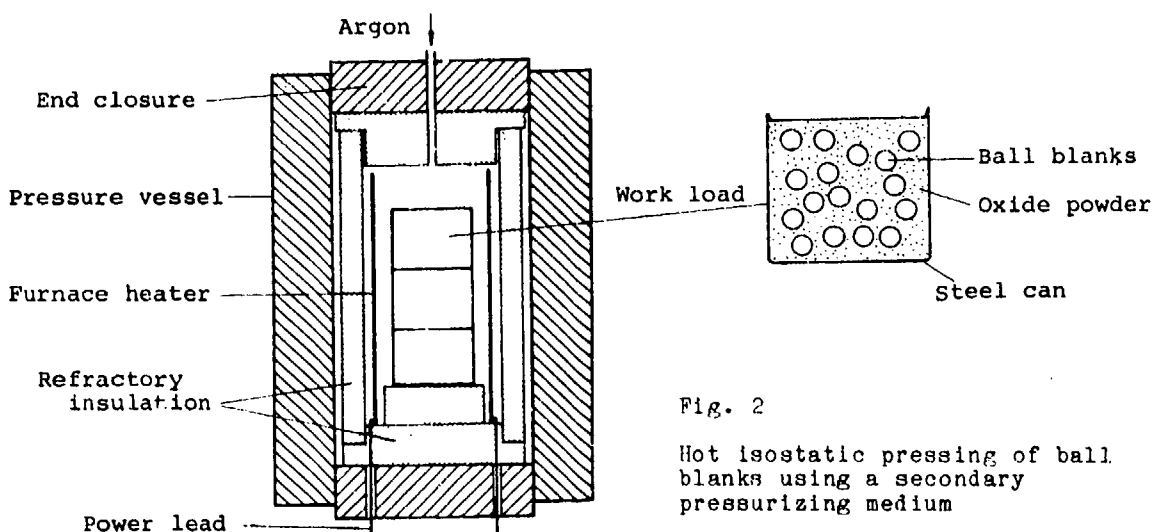


Fig. 2

Hot isostatic pressing of ball blanks using a secondary pressurizing medium

Since a gas is used as the pressurizing medium, it is not possible to densify materials with interconnected porosity without some form of encapsulation. To avoid having to encapsulate each ball separately, the method shown in Figure 2 was used. A number of balls was packed in a ceramic oxide powder inside a steel can. The filled can was then evacuated to remove air and the lid was electron-beam welded in place. During the hot pressing cycle, the oxide powder acted as a secondary pressurizing medium. Due to friction between the oxide particles, true isostatic conditions are not achieved by this method, which may result in some slight distortion. Since the balls were not true spheres, this was not a problem for this application. Batch encapsulation was simpler and quicker than individual encapsulation in metal foils or glass and would be more economical for production quantities.

Several different HIP cycles were investigated and two of these were selected for the composite balls.

Temperature	Maximum Pressure	Pressing Time
1160°C	200 MPa	30 minutes
1190°C	200 MPa	30 minutes

Although the compaction time was relatively short, the overall cycle time was about 8 hours due to the time required for heating, cooling and decompression. With industrial HIP units, the cycle time is substantially reduced by heating and cooling the charge in separate furnaces outside the unit.

Grinding and Finishing

The HIPed balls were ground in conventional ball grinding machines. Originally it was intended to use diamond as the grinding medium; but, it was found that this led to smearing of the superalloy phase. Therefore, silicon carbide was used instead, which although lengthening the grinding and polishing times, resulted in a satisfactory surface finish.

Structure and Properties

The structures of both sintered and HIPed balls consisted of a network of titanium carbide particles in a metallic matrix phase (Fig. 3). Median carbide particle sizes were in the range 5-10 μm for both types of composite material.

20 μm

20 μm

Fig. 3

Sintered (left) and HIPed (right) structures of TiC/Udimet composite

Density and hardness values of balls made from the two material compositions by both HIP cycles are given in Table 1 below. The higher hot pressing temperature had a marginal effect on density, but gave a significant increase in hardness with the 70% titanium carbide composition.

Table 1

Density and hardness values of TiC-Udimet composite balls.

Composition	Hot Pressing Temperature °C	Density (g/cc)	Hardness HV
60% TiC; 40% Udimet	1160	5.740	1530
	1190	5.744	1535
70% TiC; 30% Udimet	1160	5.435	1640
	1190	5.521	1720
Tungsten Carbide Balls	-	14.98	1600

Although the densities of the composite balls were only 25-30% lower than those of tool steels, they were less than 40% of the density of the tungsten carbide balls used in the thrust-reverser bearing. Since the manufacturing route was very similar to that used for tungsten carbide balls, any difference in cost would depend mainly on the relative costs of the raw materials. It is planned to test the lightweight composite balls in test rigs which simulate the actual operating conditions of the bearings.

HOT ISOSTATICALLY PRESSED SILICON NITRIDE BALLS

HIP has been used on a commercial basis for a number of years for the consolidation of superalloy and high alloy steel powders. Recently the process has been extended to high duty engineering ceramics and silicon nitride in particular. There are some important differences in the consolidation of metal powders and ceramic powders. Unlike metal powders, silicon nitride cannot be densified by heat and pressure alone. It is necessary to add a sintering aid which forms a liquid phase at the pressing temperature. Full densification of silicon nitride occurs only at temperatures above 1700°C whereas most HIP units in operation today are limited to maximum operating temperatures of 1400-1500°C. Therefore, new designs of HIP units have had to be developed for processing silicon nitride and similar engineering ceramics. As a consequence of the high operating temperatures required, new methods and materials for encapsulation have also had to be developed.

For these reasons, the application of HIP to silicon nitride is still at an early stage. Nevertheless, the obvious advantages of producing near-net-shape components which require a minimum of 'hard machining' are such that the process can be expected to achieve widespread use in future, particularly for ceramic components for gas turbine engines. The manufacture of 17 mm (final size) balls by a HIP process and subsequent bearing performance tests are outlined below.

Material Preparation

High purity silicon nitride powder was mixed and milled with 6 wt% yttrium oxide and an organic binder material. Yttrium oxide, like magnesium oxide, is used as a sintering additive for silicon nitride. The blended powder was cold isostatically pressed into bars, 130 mm long and 25 mm nominal diameter, using polyurethane rubber moulds. The bars were pre-sintered to remove the binder and also to improve the green strength. Since the cold isostatically pressed bars had non-uniform diameters, they were turned to a diameter of 21.2 mm. At this stage the material density was 2.10 - 2.12 g/cc.

Soft Machining

Several 'soft machining' methods were investigated for shaping the bars into balls. The best result was achieved by profile grinding the bars using a bonded diamond wheel. The sequence of operations is shown in Fig. 4. The first stage was to profile grind most of the ball shape, followed by parting off. The incomplete section of the ball was then shaped in a subsequent grinding operation. Ball diameters of 150 balls produced by this method were in the range 20.1 ± 0.5 mm. The various stages in the process are illustrated in Fig. 5.

It should be emphasized that this method of producing ball blanks by soft machining was used because a relatively small number of balls was required.

The method was more suited to the manufacture of ring blanks, for which hollow bars could be produced by cold isostatic pressing. There are several processes which could be used to produce ball blanks without the need for soft machining - cold isostatic pressing of balls, die pressing (as described for the composite balls) and injection moulding. However, one advantage of using cold isostatically pressed bars as a starting material, which became apparent later, was that the density of the ball blanks was more uniform than could be achieved by other methods. This meant that there was very little distortion of the ball shape during hot compaction.

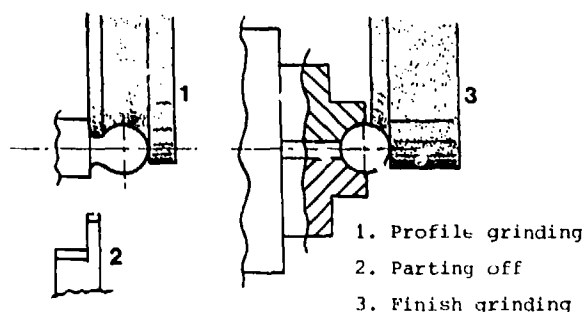


Fig. 4

Soft machining of ball blanks

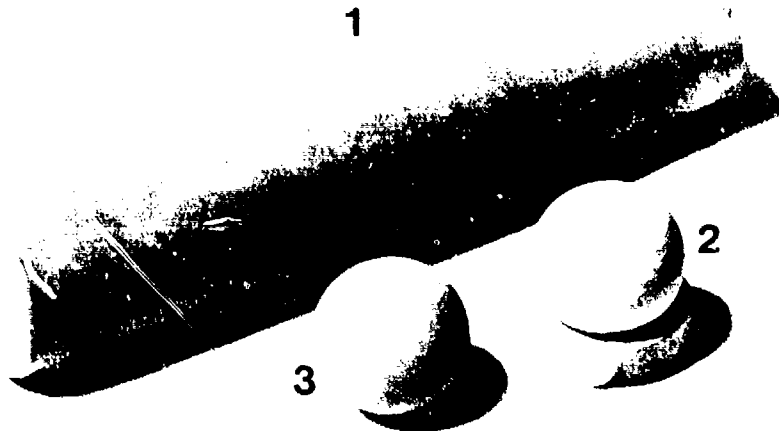


Fig. 5

Stages in the soft machining of ball blanks.

1. Cold isostatically pressed bar
2. Profile grinding
3. Finish grinding

Hot Isostatic Pressing

As mentioned previously, encapsulation is a problem when HIP is carried out at high temperatures. Gastight containers have to be made from either refractory metal foils or high melting point glasses. For the silicon nitride balls, a proprietary encapsulation method developed by ASEA AB, Sweden, (7) was used. This involved spraying the ball blanks with a glass powder to form a porous glass coating. The balls were then heated in a specially designed furnace under vacuum to remove air from the material. At a certain temperature, the glass softened and formed an impermeable layer. After controlled cooling, the coated balls were transferred to the HIP unit. In principle, this coating process could be incorporated into the HIP cycle.

The balls were hot compacted at a temperature of 1750°C for 2 hours using argon at a pressure of 250 MPa. The pressure was maintained during the first stage of cooling. Then, while the glass was still in a plastic condition, the pressure was released. The internal nitrogen pressure was sufficient to inflate the glass envelope, which facilitated the stripping of the glass from the balls after full cooling. Densities of the hot pressed balls were 3.315 ± 0.005 g/cc and the hardness was in the range 1600-1700 Hv.

Grinding and Finishing

The shape and surface condition of the HIPed balls were such that rough grinding was not necessary. The balls were finished by a single grinding operation followed by lapping. Grinding was carried out in a conventional ball grinding machine using ceramic-bonded silicon carbide wheels. To prevent overload of individual silicon nitride balls, some steel balls were added to the batch to take up the initial working pressure. Diamond paste (0.25 μ m particle size) was used for lapping.

Inspection and Dimensions

All balls were visually inspected. No cracks were observed in any of the balls, but some surface defects originating from the soft machining were detected. This led to the rejection of a small number of balls. The remaining balls were all measured and the results are summarized in Table 2.

	Diameter (Reference = 17.000 mm)	Diameter Variation (Ovality)	Out of Roundness (Talysond)	Surface Roughness Ra
Minimum	+1.9	0.2	0.18	0.025
Maximum	+2.7	0.3	0.36	0.030
Mean	+2.21	0.222	0.23	0.028
Standard Deviation	0.22	0.042	0.048	0.001

Table 2

Dimensional and surface roughness measurements on HIPed silicon nitride balls. All values given in micrometres (μ m).

The balls were within the appropriate specifications for diameter, ovality and roundness for Class I, aviation quality balls. Eighteen balls were selected for comparative tests in a mainshaft bearing.

TESTING OF HOT ISOSTATICALLY PRESSED SILICON NITRIDE BALLS

The aim of the tests was to determine whether hot isostatically pressed silicon nitride balls could operate successfully under conditions of high loads and speeds in a full size mainshaft bearing. At the same time it was intended to make a qualitative assessment of the kinematic and dynamic behaviour of the silicon nitride balls in relation to that of tool steel balls. The test bearings were identical to those used for the low pressure turbine bearings in a modern military engine. The bearings were tested on a rig that had been built to the customers' specifications for the initial proving and acceptance tests for these bearings. This rig allowed two bearings to be run under the same conditions, so that by substituting silicon nitride balls for tool steel balls in one of the bearings, a direct comparison could be made.

Test Bearings

The bearings used in the tests were of the three-point angular contact type. Main dimensions of the bearings are shown in Fig. 6 and other details are given below.

Number of balls	- 18
Ball diameter	- 17 mm
Outer ring radius	- 8.69 mm
Inner ring radii	- 8.69 mm
Initial contact angle	- 35°
Radial clearance	- 0.115-0.125 mm
Axial play (max.)	- 0.360 mm

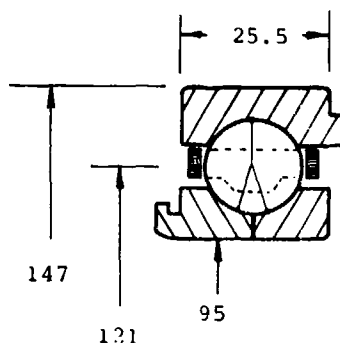


Fig. 6

Bearing dimensions (mm)

Two such bearings were used in the tests. The inner and outer rings of both bearings were made from AISI T1 tool steel (18-4-1). Balls made from T1 tool steel were used in one bearing and the HIPed silicon nitride balls in the other. Both bearings were subjected to the same inspection and quality control procedures that were applied to production bearings.

The same ring geometry was used with both types of balls. Since silicon nitride has a higher elastic modulus than tool steels, this means that contact stresses would be higher in the bearing with silicon nitride balls.

An initial contact angle of 40° was originally specified for this bearing type. However, during the initial proving tests, the heat generated when running under conditions of high speeds and loads, was considered to be too high. In addition, high relative cage speeds were observed and there were indications that the contact ellipse had been truncated under extreme running conditions. The bearing was re-designed with a lower contact angle. This type of bearing, therefore, was considered to be well suited for tests with silicon nitride balls.

Test Rig

The test machine consisted of two bearings mounted on a shaft driven centrally by an asynchronous electric motor through a pulley system. The arrangement is shown schematically in Fig. 7. The inner rings were shrink fitted to the shaft. The outer rings were located in a housing which allowed axial movement. Load was applied to the outer rings by a pneumatic cylinder through multiplying levers. The bearings were lubricated by oil flowing through the hollow ends of the shaft into the lubricating holes in the inner rings. The oil flow to each bearing could be controlled independently, but for these tests both bearings were given the same flow rate. The input oil temperature was measured as was the outlet oil temperature from both sides of each bearing (positions 2 and 3 in Fig. 7). Shaft and cage speeds were measured by tachometers and the outer ring temperature was also monitored.

Only axial loading was applied to the bearings; the radial load being that of the weight of the shaft and the pull from the drive system. The maximum shaft speed for testing according to the customers' test specifications was 15500 rpm. Typical test conditions for endurance tests were 900 kg axial load at a shaft speed of 11650 rpm.

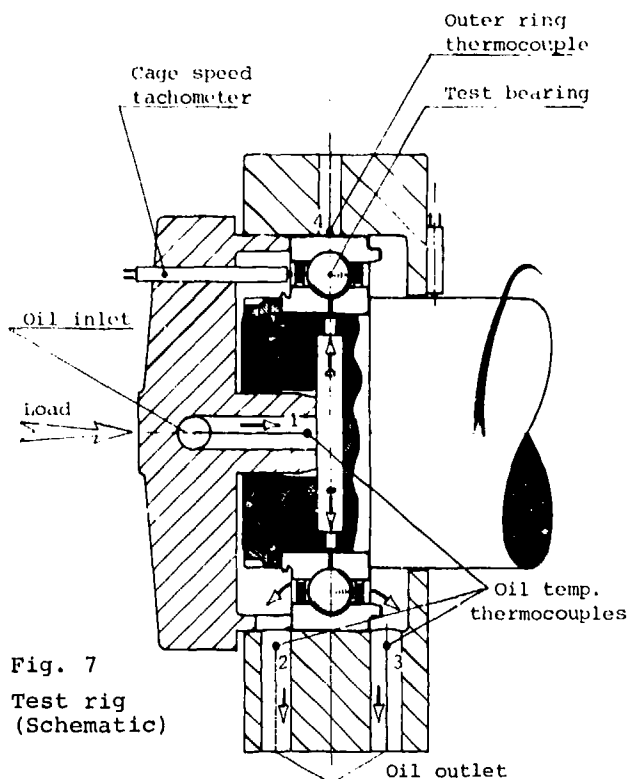


Fig. 7

Test rig (Schematic)

Test Program and Conditions

Originally it was planned to test the bearings at medium and high speeds with axial loads increasing from 250 kg to 2500 kg according to the schedule shown in Table 3. Tests 1-5 proceeded without incident, but when the speed was increased to 20670 rpm, oil exit temperatures did not stabilise. It proved to be beyond the capacity of electric motor to drive the bearings at this speed with a load of 1000 kg. Since the motor was already showing signs of distress at the lower loads and the bearing outer ring temperatures were above 200°C, the tests were discontinued. Total running time up to this point was 40 hours, representing 6 hours running under stable conditions for tests 1-5 and shorter times for tests 6 and 7. The lubricant used was Esso Turbo Oil 2380 (according to MIL-L-23699) and the flow rate was 1 litre/ minute to each bearing.

Test	Speed (rpm)	Axial Load (kg)
1	11500	250
2	"	500
3	"	1000
4	"	2000
5	"	2500
6	20670	250
7	"	500
8	"	1000
9	"	2000
10	"	2500

Table 3
Planned test conditions

After the first test series, the bearings were dismantled and inspected. The rings and cages of both bearings were in good condition. Inspection and measurement of the silicon nitride balls showed no signs of deterioration. Therefore, the bearings were reassembled and a second test was carried out under the following conditions.

Speed - 15 000 rpm Axial Load - 1000 kg Time - 50 hours Oil Flow - 1 litre/min.

On completion of this second test, the bearings were inspected again and surface profiles of balls and rings were measured.

TEST RESULTS

Temperatures

Details of the oil and bearing outer ring temperatures during the first test series are given in Table 4.

TEST CONDITIONS			BEARING WITH TOOL STEEL BALLS				BEARING WITH SILICON NITRIDE BALLS			
Test	Speed (rpm)	Load (kg)	Oil Temperatures °C			Outer ring Temperature °C	Oil Temperatures °C			Outer ring Temperature °C
			Inlet (1)	(2)	Outlet (3)		Inlet (1)	(2)	Outlet (3)	
1	11500	250	30	95	90	110	30	92	84	95
2	"	500	"	112	60	116	"	100	90	105
3	"	1000	"	114	60	120	"	105	95	112
4	"	2000	"	130	80	145	"	124	114	130
5	"	2500	"	150	100	165	"	120	110	130
6	20670	250	"	-	-	200	"	-	-	200
7	"	500	"	-	-	212	"	-	-	205

Table 4
Oil and ring temperatures during the first test series (See Fig. 7 for oil outlet positions).

It was apparent that the bearing with silicon nitride balls ran at consistently lower temperatures and that there was less difference in outlet oil temperature from the two drain positions. This was an indication that the variations in the dynamic contact angle with silicon nitride balls had been lower than with the tool steel balls.

In the second test when the bearings ran for 50 hours, the outer ring temperature of the bearing with silicon nitride balls was 170°C compared with 180°C for the standard bearing.

Cage Speed

During most of the tests, the cages of both bearings ran at steady speeds. There were indications that the cage speed with silicon nitride balls was lower than that with tool steel balls; but, this difference was too small to be quantified. During the last 15 hours of the 50 hour test, the cage speed of the bearing with tool steel balls became uneven and fluctuated.

Visual Inspection

Visual examination of the rings that had run with silicon nitride balls showed no evidence of deterioration. The load transmitting areas of the rings with tool steel balls contained polished wear bands, indicative of extensive skidding or sliding during running. There were also marked differences in the condition of the balls after testing. The tool steel balls had a variety of surface textures; but, the silicon nitride balls actually had a better appearance after the test than before. Microscopic examination showed that this was due to pick-up of metal which had improved reflectivity and decreased surface roughness.

Metrological Examination

Details of clearance and ball variations before and after testing are given in Table 5 below.

	Tool Steel Balls		Silicon Nitride Balls	
	Before	After	Before	After
Radial Clearance	122	126	122	120
Axial Play	325	340	330	335
Radial Movement				
Outer Ring	2	8	2	3
Inner Ring	2	7	2	4
Axial Movement				
Outer Ring	2	12	2	3
Inner Ring	2	10	2.5	6
Ball Diameter				
V_{DWL}	<0.25	3.8	0.22	0.4
V_{3DWL}	<0.5	1.25	<0.5	0.5

Table 5

Bearing clearances and ball diameter variations before and after testing (All values given in micrometres - μm).

Comparisons of the Talysurf and Talysond profiles for rings from both bearings are given in Figs. 8-11. For simplicity, traces are given only for the load transmitting inner rings and the directly loaded sections of the outer rings. These results show the extensive distress or damage of the bearing with tool steel balls and the good condition of the rings that were used with the silicon nitride balls. Figure 12 compares the condition of the balls after the tests.

CONCLUSIONS

Although limited in scope, this preliminary test demonstrated that HIPed silicon nitride balls could run satisfactorily in mainshaft bearings under conditions which caused marked deterioration of a standard bearing with tool steel balls. This was in spite of the fact that the conformity had not been optimized for the silicon nitride balls and therefore contact stresses were higher with this bearing. The lower operating temperatures and absence of damage in the bearing with silicon nitride balls were indications of better kinematic behaviour. It can be inferred that there was less variation in dynamic contact angles with silicon nitride balls and lower spin friction losses. This gives added confidence in silicon nitride as a bearing material and in HIP as a manufacturing method for bearing components.

REFERENCES

1. High Pressure Science and Technology, Vol. 2 (1979), p651, Plenum, New York.
2. Hot Isostatic Pressing of Silicon Base Ceramics. Final Report AFWAL-TR-80-4193 (1981).
3. Yeh, H.C. and Sikora, P.F. Ceramic Bulletin, Vol. 58, No. 4, (1979).
4. Engineering, Vol. 220, No. 9, p1009 (1980).
5. Giachello, A. et al. Journal of Materials Science, 14, p2825, (1979).
6. Lewis, M.H. et al. 'Sialons: Composition, Structure, Properties and Uses'. To be published in Journal of the British Ceramic Society.
7. U.S. Patents 4112143 and 4256688.

ACKNOWLEDGEMENTS

The authors wish to thank R.J. Smalley and A. Hoffmann for their work on the development of the manufacturing processes and D.Ferrero who carried out the testing.

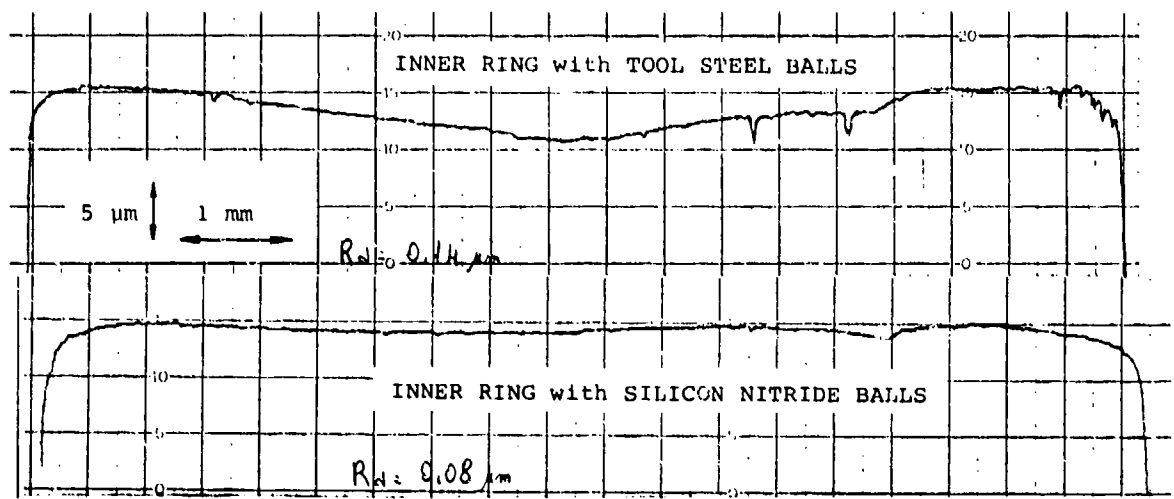


Fig. 8
Talysurf traces of inner rings

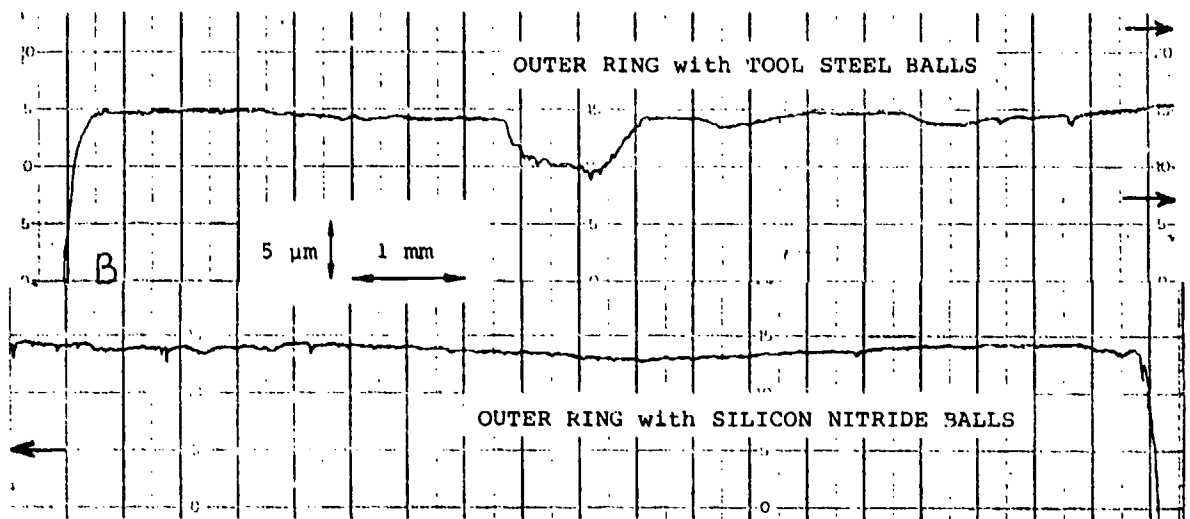


Fig. 9
Talysurf traces of outer rings

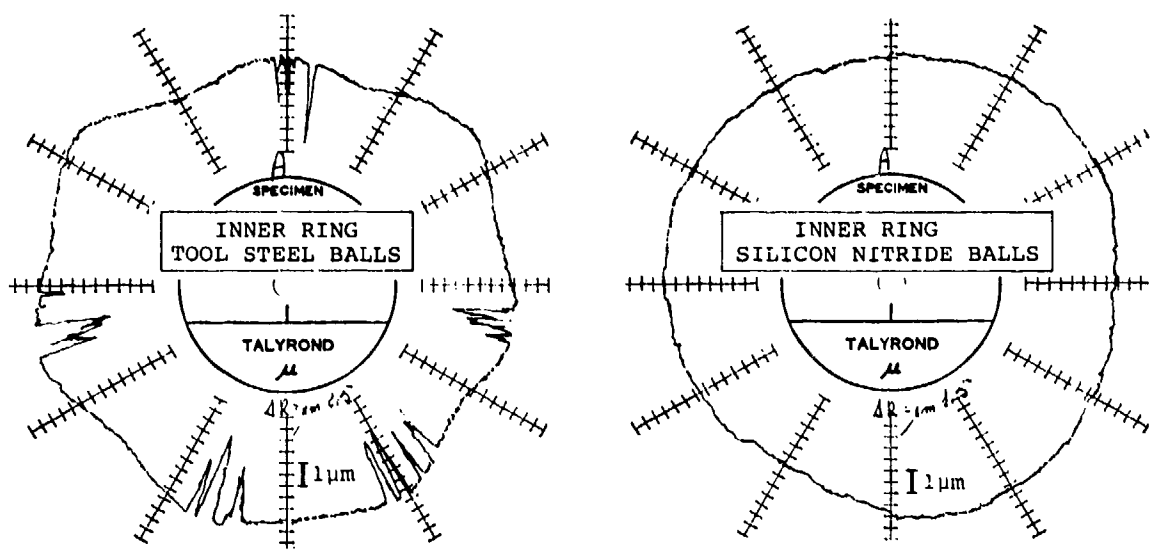


Fig. 10
Talyrond profiles of inner rings

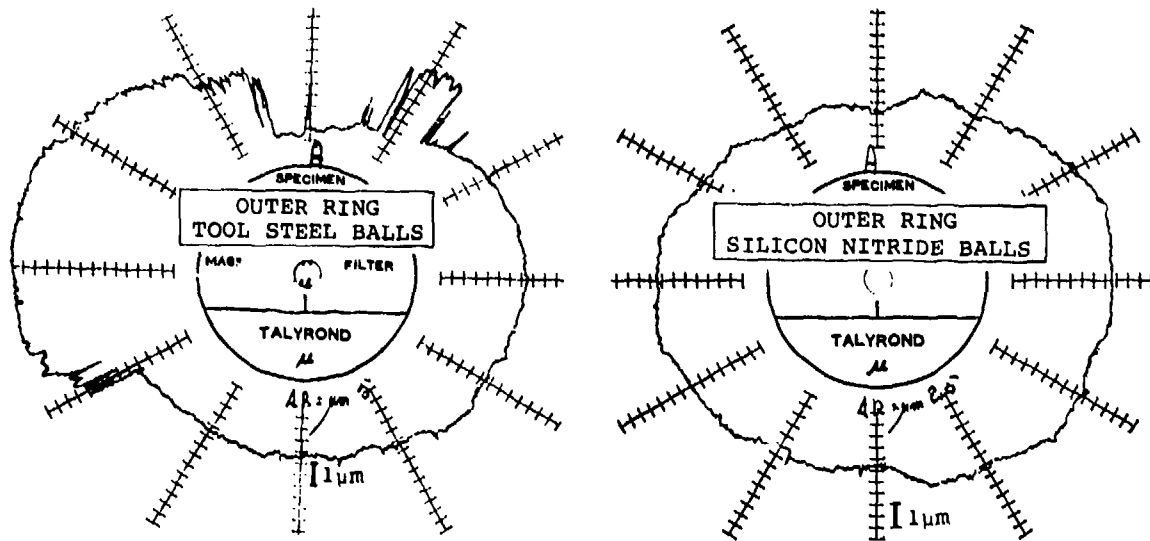


Fig. 11
Talyrond profiles of outer rings

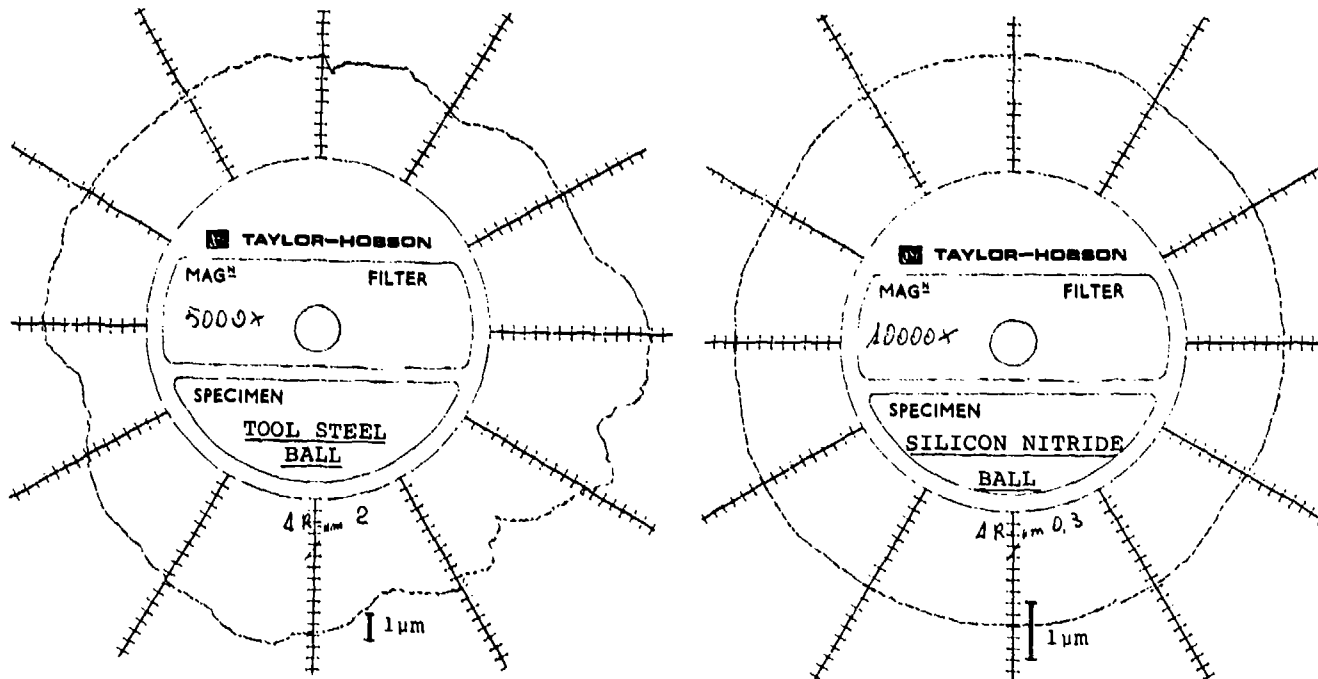


Fig. 12
Talyrond profiles of balls. (Note difference in magnification)

DISCUSSION

D.G. Astridge, Westland Helicopters Ltd, Yeovil, UK

- (1) How would cost of production quantities of Silicon Nitride bearings compare with tool steel bearings?
- (2) In view of the poor tensile strength of silicon-nitride compared with tool steel, and the great difference in coefficient of thermal expansion between SiNi and steels/nimonics, are you aware of any rolling contact fatigue tests with SiNi bearings on steel shafts (or hybrid bearings) in which thermal cycling has been incorporated to simulate engine start-stop cycles?

Author's Reply

At this stage, it is not possible to give any estimates of the costs of silicon nitride rolling elements or complete bearings. As you are aware, inspection and quality control costs account for a high proportion of the total cost of an aircraft bearing and these are material independent. However, I can give you some information about pressureless sintered silicon nitride. Tool tips made from this material are currently being sold at twice the price of equivalent Tungsten carbide tips. It is thought that pressureless sintered components should cost no more to produce than Tungsten carbide -- on a volume rather than weight basis. To put this in perspective, aircraft quality Tungsten carbide balls 5/16" diameter are currently sold at about \$3.25 each.

With regard to your second question, I am not aware of any tests involving thermal cycling. I can only repeat what Mr Sibley has said about the excellent thermal shock resistance of silicon nitride. Thermal cycling in the temperature regime of aircraft engine bearings should not present any problems.

THE OIL/AIR SYSTEM OF A MODERN FIGHTER AIRCRAFT ENGINE

J. Schmidt, W. K. Hank, Dr. A. Klein, Dr. K. Maler
 MTU Motoren- und Turbinen Union München GmbH
 Dachauerstr. 665, 8000 München 50

Summary:

Current experience has shown that the oil/air system of a modern fighter aircraft engine determines to a considerable extent the capabilities of the aircraft. To illustrate this point, first of all the specification requirements of such an oil/air system are defined and interpreted. Fulfillment of these requirements necessitates a variety of considerations, of which a few are highlighted in this paper.

Taking a three-spool engine as an example, the basic features of the design and functioning of the oil/air system are explained. The importance of the sealing air system and of its reliable computation is demonstrated. The advantages and disadvantages of interconnected and separated bearing chambers are pointed out. Attention is drawn to the vent system and to some special conditions of the turbine bearing chamber.

Problems of highly loaded bearings are dealt with in some detail in view of a long bearing life, in particular the optimization of the oil supply and the bearing behaviour in the event of an oil supply interruption. Finally, the reasons and consequences of a possible bearing chamber overheating are described as well as means to avoid such overheating.

1. Introduction

When designing a new aircraft engine, first of all, the cycle, performance data of the individual components and the construction are decided on, based on the requirements made of the aircraft. In this, the emphasis in the investigations is laid on the areas of turbine and compressor aerodynamics, turbine cooling techniques, component strength and the vibration characteristics of critical parts.

It has been common practice in the past to deal with the oil/air system only at a rather late stage of engine development. For modern fighter engines this procedure is no longer justified: attention to certain basic features of the oil/air system should be paid already at the early design stage. This is mainly due to the high temperatures and rotational speeds (high specific thrust) encountered in modern fighter engines in conjunction with severe space limitations (high thrust to weight ratio).

The requirements of the oil/air system of a fighter aircraft are determined by the missions, the necessary degree of serviceability and operational safety under extreme operation conditions, as well as an appropriately long engine life, for minimizing the life-cycle costs (see Fig. 1). The following requirements have a decisive influence on the layout of the oil/air system:

- Continuous oil supply under extreme flight conditions,
- sufficiently low mission oil consumption,
- as low as possible heat transfer to the oil,
- effective sealing of the bearing chambers under all flight conditions,
- avoidance of bearing chamber overheating, which could lead to oil fires and excessive oil consumption, and
- as long as possible life of the bearings.

Of these requirements only the last three are gone into some detail in this paper.

2. Design Considerations

Modern fighter aircraft engines have been built with two spools as well as with three spools. Because of the high cycle temperatures and pressures both types of engines need a careful consideration of the oil/air system at an early design stage. Three-spool engines, however, have to be designed with a larger number of seals. Therefore the design activities for the oil/air system are more elaborate and require a greater computational as well as development effort. Therefore the three-shaft system is dealt with in greater detail in this paper.

Fig. 2 shows schematically a three-spool engine with separate low-, intermediate- and high-pressure sections. In this example it has been possible, by clever arrangement of the bearings, to provide the engine with only three bearing chambers. As will be explained later on, this has certain consequences for the oil/air system.

Another important feature of the example of Fig. 2 is the fact that the three bearing chambers are interconnected. In comparison with unconnected bearing chambers, this design has the advantage that intershaft seals, which are problematical to design, can be omitted. This simplifies the layout of the engine and reduces the number of parts. However, for the oil/air system this means a complication for balancing the pressure differences required across the bearing chamber seals, since any changes in one bearing chamber automatically affect the other chambers in a system in which the bearing chambers are interconnected.

The schematic arrangement of the bearing chambers and their seals of the three-spool engine of Fig. 2 together with the sealing-air system with its seals is shown in Fig. 3. The front bearing chamber houses the bearing for the LP-compressor (bearing No. I), the centre bearing chamber houses the thrust bearings of the HP- and IP-compressors (bearings No. II and III), and the rear bearing chamber houses the thrust bearing of the LP-compressor (bearing No. VI) as well as the intershaft bearing (No. IV), which is necessary with this arrangement and which is somewhat offset from the actual rear chamber for design reasons. The IP- and LP-shafts rotate in the same direction, whereas the HP-shaft rotates in the opposite direction.

Oil is prevented from escaping from the bearing chambers by labyrinth seals, which are pressurized by sealing air tapped downstream of the IP-compressor. This sealing air enters the bearing chambers via the bearing chamber seals (Fig. 3) and leaves them through the vent lines, carrying a certain quantity of oil from the bearing chambers with it. The sealing air is discharged overboard after passing through a breather to separate the oil. The amount of air discharged must be kept to a minimum, because

- it represents a loss of engine power,
- the flow rate of the air and the quantity of oil entrained in the vent system increase with increasing air flow; both cause a greater oil loss at the breather,
- the problem of oil overheating (heat to oil) becomes the greater, the greater the amount of hot air flowing into the bearing chambers.

On the other hand, small quantities of air discharged or passing through the vent lines result in small pressure differences across the bearing chamber seals, which can lead to oil leakage. Calculations and experiments have shown that these pressure differences are subject to a limit, on account of the fact that oil must be prevented from escaping from the bearing chambers throughout the operating range of the engine, even after a large number of engine running hours.

Oil escaping from the rear bearing chamber would form a mixture with the sealing air, which would ignite on contact with hot turbine discs, leading to oil fire. Oil leaking from the front and centre bearing chambers, on the other hand, could contaminate the cabin air. This is because for reasons of space, in modern fighter aircraft the cabin air is sometimes tapped from the compressor casing, and not at the compressor hub as in civil applications. This means that oil mixed with the main flow of compressor air inevitably passes into the cabin air, since it is centrifuged outwards at the compressor blades.

3. Particulars of the Air System

According to the explanations given above, one of the important goals of designing the internal air system of an engine is (in addition to the supply of appropriate quantities of cooling air to the turbine blades and to other hot parts of the engine) to make sure that the pressure differences across the bearing chamber seals are large enough to completely avoid oil leakage, but not larger than absolutely necessary. It is therefore necessary to accurately calculate the pressure differences across the bearing chamber- and sealing air-seals when designing an engine. Particulars are given in what follows.

3.1 Sealing Air System

An example of the sealing air conditions calculated for a system according to Fig. 3 is shown in Fig. 4. In addition to the pressure differences across the bearing chamber seals, normalized with the pressure difference across the rear bearing chamber seal marked "B" in Fig. 3, the figure also shows the quantities of air flowing into and out of the chambers as well as those flowing between the chambers through the shafts, as a percentage of the total flow rate in each case.

The results shown in Fig. 4 include the calculation of the bearing chamber pressure as well as a calculation of the sealing air system pressures that are effective at the bearing chamber seals. These pressures depend on the operating condition of the engine and on the clearances of the seals, which separate the sealing air system from the rest of the engine.

In the example given here, the sealing air pressure at the front bearing chamber depends, above all, on seals 1 and 2 (Fig. 3), and that at the rear bearing chamber on seals 6 and 7. The effects of a deterioration of seals 6 and 7 are shown in Figs. 5 and 6 (corresponding considerations apply to seals 1 and 2). Here it has been assumed that with nominal clearances of these seals a pressure drop across rear bearing chamber seal B (see Fig. 4) is produced of a magnitude, which just avoids oil leakage through this seal at all operating conditions, including idling and transients. This pressure drop is taken as 100% in Fig. 5. With an increase of the clearances of air seals 6 and 7, by running-in for in-

stance, the pressure drop across seal B will sink below the permissible value in a way shown in Fig. 5.

In order to retrieve the required pressure difference, the bearing chamber pressure must be reduced and hence the amount of air discharged overboard must be increased. According to Fig. 6, an increase of 20% is necessary in order to compensate a seal degradation of 160% under unfavourable circumstances. However, this results also in a 30% increase in breather oil consumption (Fig. 6). Optimum design of the sealing air system thus calls for a very high degree of dimensional accuracy of the air seal clearances. It requires excellent thermal matching of the seal-rotors and stators and the choice of suitable abradable coatings.

A certain amount of seal deterioration and hence of overboard-flow increase must be accepted to be unavoidable. The breather therefore must be designed in such a manner that its oil consumption nevertheless meets the specification. Also, for safety reasons one will choose the pressure drop across seal B to be always somewhat higher than the limiting value of 100% assumed in Figs. 5 and 6. In any case it is important that the behaviour of all the air seals and its effects on sealing air pressures can be correctly simulated in the computations.

3.2 Vent System

The calculated pressure drops across the bearing chamber seals are meaningful in designing the system only, when the bearing chamber pressures in addition to the sealing air pressures can be calculated with sufficient accuracy. In the second case this calculation is made difficult because of the uncertainty as to the true running clearances of the air seals. In the first case it is complicated by the complex flow conditions in the vent system.

Because of the high shaft speeds of modern aero engines, the idea that pure oil will be present in the bottom section of a bearing chamber and pure air in the top, no longer holds true. Instead, the bearing chambers contain a more or less uniform oil/air mixture. Therefore an oil/air mixture flows through the vent lines. This two-phase flow of a compressible fluid does not easily lend itself to theoretical analysis. Because of these uncertainties, when designing an engine, the vent cross sections must be amply dimensioned and the lines must be provided with replaceable restrictors (see Fig. 3), which can be used to set the bearing chamber pressure and, consequently, the pressure drop across the seals (and hence the overboard flow) within certain limits.

3.3 Rear Bearing Chamber Conditions

The rear bearing chamber with the LP-thrust bearing (No. VI) and the intershaft bearing (No. IV) is shown in detail in Fig. 7. As is seen in Fig. 4, the pressure difference across seal B of the rear bearing chamber is lower than the one across the other bearing chamber seals. The explanation is, that in the present example the sealing air is supplied to the rear bearing chamber seals via the HP-shaft (see Figs. 2 and 7). In so doing, the air receives a strong swirl from the rotating shaft and, as a result, suffers a major pressure loss, additional to the pressure loss of the flow along the shaft, as it flows through the contra-rotating holes, marked "A" in Figs. 2 and 7. This leads to the low pressure drop across seal B, shown in Fig. 4. The reason, why the sealing air pressure further downstream is higher again and hence the pressure drop across seal C (Figs. 2 and 7) is larger than that across seal B, is easily understood: Due to the swirl, the pressure increases as the air, after having passed seal B, proceeds to a larger radius (Fig. 7); since subsequently the swirl is removed by the struts supporting the bearing chamber, the pressure then remains nearly constant as the air flows towards seal C.

The reduced pressure drop across seal B, as compared with that of the other rear bearing chamber seals, is thus a consequence of the sealing air supply arrangement discussed here for the three-spool concept shown. The inflow through the other two seals thus being higher than required, the overboard flow also is somewhat higher, and the breather must be designed accordingly.

This slight disadvantage could be avoided, would the sealing air be supplied to the rear bearing chamber through pipes fitted in the engine's bypass duct instead of via the HP-shaft. This complication of additional supply lines would, however, be chosen only if dictated by other stringent requirements, in particular by an unacceptably high (with regard to overheating) heat pick-up of the air as it proceeds along the HP-shaft. A reliable calculation of this heat pick-up already at the design stage, therefore, belongs to the important tasks of the systems engineer. It is the basis for the decision as to the type of air supply for the rear bearing chamber.

A final point is made in this connection. With the relatively simple arrangement of Fig. 3, the pressure drops across and hence the inflows through the seals of the centre bearing chamber will be much higher than for the other seals, as can be seen in Fig. 4. This is a direct consequence of the relatively large pressure loss the air encounters as it flows towards the rear via the HP-shaft, since the minimum pressures at the rear bearing chamber seals must be maintained. As a result, the overboard flow would again be higher than required. This can be remedied by introducing suitable flow restrictions upstream of the centre bearing chamber seals and/or by improving these seals. In the case of the front bearing chamber this is accomplished by the holes marked "D" in Fig. 3.

The best air system will be one where the pressure drops across all the bearing chamber seals throughout the engine are approximately the same and as small as possible, to just guarantee good sealing of the bearing chambers under all running conditions of the engine.

3.4 Measures and Development Tasks for Improving the Air System

The future engine development will lead to higher temperatures and pressures in the oil/air system of the engines. For this reason in addition to others the following tasks should be given priority to meet the requirements as specified in Fig. 1:

- Development of better sealing devices (air/air and air/oil), which exhibit only slight deterioration with running time,
- investigation and theoretical treatment of two-phase flows (oil/air), as encountered in vent systems,
- reduction of the flow rate of the air discharged overboard (the sealing-air pressure differences across all the bearing chamber seals should be approximately the same),
- reduction of the sealing-air temperatures by cooling the sealing air of the rear bearing chamber or by redesigning the air supply lines to prevent the air from becoming heated.

4. Highly-loaded Bearings

As shown in Fig. 8, the highly-loaded thrust bearings II and III of the high- and intermediate-pressure sections of the three-spool engine are located in the centre bearing chamber. Labyrinth seals, pressurized by sealing air from the IPC, prevent oil from leaking out of the bearing chambers.

Large quantities of the oil are threshed around by the bevel gears of the radial drive, located in this bearing chamber, and become mixed with the sealing air entering the bearing chamber. The churning effect of the bearings, the threshing of the air/oil mixture and the relatively large quantities of hot sealing air entering the bearing chambers cause a considerable temperature rise of the oil/air mixture in the bearing chambers.

It must be possible for the thrust bearings to function properly in this hot oil/air environment. In addition to the need for long life, even under extreme operating conditions, the parameters given in Fig. 9 must be borne in mind when designing the bearings. The dimensions of the bearings represent a compromise between the contradictory requirements for compactness and high running speed, on the one hand, and high thrust loads on the other. Only by having a very close ball/race conformity was it possible to guarantee the required life with the dimensions chosen.

The bearings are of the angular contact ball bearing type, a design that is best suited to meet the requirements for this application.

The oil supply to thrust bearings II and III is optimized to

- minimize churning,
- improve cooling of the outer and inner races, and
- ensure clearance maintenance.

Some of the knowledge gained from the bearing tests is presented below.

4.1 Determination of Lubrication Oil Flows

The determination of the lubrication oil flows to the bearings is of fundamental importance and one of the first tasks for the development of the engine to solve. Therefore some research has been conducted to define those oil flows. All rig testing of the bearings has been done at typical shaft speeds, oil temperatures and axial loads.

In order to attain the required long life (Fig. 1) and operational reliability, the oil flow Q through the inner races for cooling the bearings must be considerably greater than would be required for forming a load-bearing film of lubricant. On the other hand, if the oil flow is excessive, the heat to oil problem, mentioned earlier, will be aggravated because of the high churning losses.

The outer race temperature T_{Or} of bearing No. III and the heat generation P of the bearing are shown in Fig. 10 in relation to the lubrication oil flow Q . The oil supply has to be so chosen that an acceptable operating temperature of 250°C of the outer race is not exceeded. The heat generation P (kW) of this bearing design rises with increased oil flow and was measured as 7 kW at the design oil flow.

4.2 Optimization of the Lubrication Oil Flows

The experiments for determining the lubrication oil flows have shown that the method often used in engine construction of passing the oil through the inner race (under-race lubrication as for example for bearing III, Fig. 9) leads to considerable temperature differences between the inner and outer races (Fig. 12, left). These differences become striking when high speeds and the resultant centrifugal forces cause the load equilibrium to shift to the disadvantage of the outer race. The temperature differences reveal that under-race lubrication, at least as far as cooling is concerned, can in no way be described as optimal. Undesirable consequences of these temperature differences are

- non-uniform thermal stressing of the bearing races (to the detriment of the life),
- widening of the clearance in operation (reduced margin with respect to overspeed and overload).

To avoid these problems, an improved lubrication system has been developed, which influences the temperature distribution in the bearing (inner and outer race) and makes more economical use of the cooling potential of the oil. The oil is supplied to the bearing cage from the sides L and R, whence it passes to the contact points in the bearing (under-cage lubrication - Fig. 11, right). However, optimum conditions are achieved only with a suitable ratio between the flows from L and R. The correct split was determined in a series of measurements, in which the ratio L:R was varied in steps, whilst observing the change in the shape and position of the temperature profiles T_{A-D} at the loaded halves of the tracks (Fig. 11, bottom). A split of $L = 4/5 Q$ and $R = 1/5 Q$ was shown to be the optimum. It produces the smallest temperature differences between the outer and inner race and reduces the peak temperature by the greatest amount. However, the optimum value varies slightly according to the operation conditions. The predominance of the flow rate L, which is injected against the direction of thrust load F_{ax} , is attributable to the kinematics of the angular contact ball bearing.

In addition to the reduction of the temperature differences in the bearing, under-cage lubrication is characterized by the following advantages:

- A saving of about 10% of the oil supply, thanks to the more balanced cooling. This represents a useful, even if modest, contribution towards relieving the oil system.
- Deletion of lubrication openings underneath the inner race, which weaken the race, have a deleterious effect on the roundness of the track and increase the danger of insufficient lubrication, because of their tendency to become blocked by rubbings and dirt.

4.3 Significance of Squeeze Film for Bearing Cooling

Bearing II has a squeeze film at the outer race (Fig. 9). Detailed measurements have shown that the squeeze film makes a significant contribution towards cooling of the outer race. In the present case, it brings about a temperature reduction in the region of 30°C (Fig. 12).

Further to its actual purpose, namely the absorption of rotor vibrations, it consequently has a really good cooling effect on the bearings. It reduces the marked temperature differences between the outer and inner races, already mentioned, and allows the amount of lubrication oil Q supplied to the bearing to be reduced. This holds true for bearings with under-race and under-cage lubrication. Due to the reduction of the oil flow Q the churning as well as the amount of heat to oil decrease.

4.4 Bearing Behaviour in Event of Oil Supply Interruption and Reduction of Lubrication Oil Flows

4.4.1 Reaction of Thrust Bearings to Oil Supply Interruption (Emergency Case)

The dependence of highly-loaded thrust bearings on the supply of lubrication oil becomes clear when the supply fails completely, for example due to a leak in the oil tank or rupture of an oil feed pipe. It is then revealed that, with high bearing loads F_{ax} , the emergency (dry-running) reserve of the high-speed bearings quickly runs out, with consequent imminent damage. The behaviour of the bearings in the event of oil supply failure can be seen in Fig. 13 and 14.

Normally, as a result of centrifugal forces, the contact between the rolling elements and the outer race is closer than that between the elements and the inner race. Consequently, the elements run under outer-race control. During the initial phase (t_1) of oil supply interruption the bearings continue to run smoothly, since the film of lubricant is still present, actually with less power absorption than under full lubrication, owing to the reduction in churning. However, the temperature of the bearings begins to rise steadily (Fig. 13).

The lubrication conditions appear to deteriorate more quickly at the rotary, convex inner race than at the stationary, concave outer race. The result will be that the bearing

will go from outer to inner race control, recognizable by a drop of the cage speed and by strong audible reactions of the balls and the cage (peak of the heat generation curve in Fig. 13). Increased power absorption and accelerated heating of the bearing in the next phase (t 2) are indications that the running conditions have now deteriorated drastically. The oil film has disappeared. Dry friction between the rolling elements and races has set in, leading to increased tangential stresses in the tracks, which finally produce cracks in the contact areas, resulting in bearing seizure. The time this sequence of events takes to occur, naturally, depends greatly on the degree of loading of the bearing.

In addition to the above phenomena, a cage damage can occur. The mechanism is already known [1], so there is no need for an explanation here.

4.4.2 Reduction of Lubrication Oil Flow

It is well known that the oil feed pressure and consequently the oil flow to the bearing can be reduced by leakages in the feed system, failures of the pressure pump and sticking of a recirculation valve which avoids excessive oil flow under certain conditions. The bearings II and III have been tested with reduced oil flow (50% of design flow) and the results are shown in Fig. 15. It can be seen that the bearings can sustain a longer time. However, as illustrated in Fig. 15, the temperature of the bearings and consequently of the complete bearing chamber rises steadily, resulting in the possibility of overheating the bearing chamber and subsequent oil fire.

4.4.3 Measures for Avoiding Damage of Bearings

According to [1] there are some simple measures to prevent the last-mentioned damage to the cage. Unfortunately, the same cannot be said for the damage to balls and races. Only those measures which contribute to reducing the bearing loading hold promise. From Fig. 14 it can be seen how the permissible dry running times increase as the axial load is reduced. Therefore, the following measures for improving the dry running properties of bearings are suggested:

- Optimum design and balancing of the air system to achieve minimum bearing thrust load,
- thrust load to be absorbed by two bearings,
- use of lighter materials, e. g. ceramics, for rolling elements, in order to reduce centrifugal forces.

5. Bearing Chamber Overheating and Oil Fire

One of the most harmful effects of high temperatures in the oil/air system of an aircraft engine is oil fire in bearing chambers. High temperature of the oil or oil/air mixture in the rear bearing chamber (Fig. 16), which is located in the hot section of the engine, can have various reasons:

- Interruption of oil supply (emergency case): cooling of the bearing is reduced and bearing friction increased, both causing bearing temperature rise,
- inflow of large quantities of hot sealing air via the damaged or worn out bearing-chamber seals into the bearing chamber,
- heating of bearing-chamber walls and heat conduction through the bearing chamber's supporting structure, which is exposed to hot turbine gases,
- excessive residence time of the oil/air mixture in the bearing chamber (oil hiding).

Tests have shown that the presence of an inflammable air/oil mixture in the bearing chamber is unavoidable, if the oil supply is interrupted, and that ignition of this mixture in the chamber can occur in various ways.

5.1 Spontaneous Ignition

Spontaneous ignition of an oil/air mixture can occur in bearing chambers only when an inflammable mixture stays in the bearing chamber for a period longer than the ignition delay time. In addition, there have to be temperature conditions which are conducive to a combustion reaction that becomes stabilized. Such conditions can occur under certain circumstances in areas of low velocity zones in the rear bearing chamber, e. g. in the bearing chamber sump (Fig. 16). For working out countermeasures, it is of vital interest to know how prone engine oils are to spontaneous ignition. As the definitions of the spontaneous ignition temperature (SIT) of engine oils in the specifications (DERD 2479 or 0-160) to ASTM and DIN are not usable for practical applications, tests were carried out under static and dynamic conditions. Of particular interest was the dependence of the SIT on high pressure. For these investigations, oil was injected into a calorific bomb (volume 500 cc), which was then heated. The sudden rise in pressure in the bomb indicated that the temperature at which the stoichiometric oil/air mixture ignites had been reached. The results of tests with the three engine oils to specification 0-160 are given in Fig. 17. The tempera-

tures in this case are probably not very far off the SIT values for an ideal, steady-state oil vapour/air mixture. The influence of pressure and of oil type is slight.

Dynamic tests were carried out to simulate the engine conditions (Fig. 18). The test equipment consisted of a pressure vessel fitted with an inspection window and containing a small oil sump, the bottom of which was heated and over which air flowed. The tank was fitted with a perforated plate for increasing the residence time of the air through flow.

Spontaneous ignition temperatures in the region of 320°C were determined for the above oils by varying the air flow ratio, the thickness of the oil film, the residence time and the mixture ratio.

5.2 External Ignition

Ignition, for instance spark ignition in bearing chambers, can occur even at low temperatures in the presence of an inflammable mixture. The sparks are produced by rubbing of bearing chamber seals, such as during surging. This wears away the abradable coating of the stationary part of the seal.

Initial experiments, using the above dynamic test equipment (Fig. 18), were conducted with an inflammable mixture of oil mist (generated by oil injection) and air. Ignition was provided by sparks from a plug. As expected, appreciably lower ignition temperatures were found than those with spontaneous ignition, namely as low as 120°C.

5.3 Effects of High Oil Temperatures in Bearing Chambers on Lubricating Oil Properties

Oil fires are accompanied by high temperatures in bearing chambers, which can affect the quality of the engine oil and, thus, the operational reliability of the bearings. Analysis of engine oil samples, taken after certain running times in the oil fire simulation tests to get information on the behaviour of the system under oil off conditions (duration of oil fire: several minutes), provided the following results:

- Marked decomposition of the oil, verified by analysis of the acid number and the viscosity (Fig. 19, middle), as well as by differential thermo-analysis,
- increase in the formation of residues, mainly soot from combustion (Fig. 19, middle),
- the percentage decrease in the phenothiazine is a measure for the degradation of the additives (Fig. 19, bottom); the same effect is found for tricresyl-phosphate,
- decrease in the load-carrying capability (Fig. 19, bottom) is shown by the results with the four-ball apparatus/modified wear test.

The shape of the curves in Fig. 19 is determined, in the first place, by the number of oil fires and, in the second place, by the amount of oil added after each test, i. e. the improvement in the properties of the oil after certain running times (Fig. 19, middle and bottom) is due to topping up with fresh oil.

The results show that damage to bearings and gears, caused by degradation of the properties of the lubricating oils and increased formation of residues, is to be expected after extensive running times.

5.4 Measures for Avoiding Spontaneous Ignition of Engine Oils in Bearing Chambers

As demonstrated in the tests, the lowest ignition temperatures occur with external ignition and on reaching a stoichiometric oil vapour/air mixture. In addition, spontaneous ignition depends on the residence time of an inflammable mixture, as well as on the wall temperature of the bearing chamber.

Measures for preventing ignition are:

- Adjustment of the oil/air ratio to avoid an inflammable mixture during steady-state and transient conditions, and to ensure adequate cooling of the bearing chamber walls by the oil,
- optimum design to achieve as low as possible residence times of the oil/air mixture in the bearing chamber,
- selection of suitable materials for the abradable coatings to avoid sparks,
- avoidance of hot spots on bearing-chamber walls by efficient cooling of the walls.

No great improvements of oil properties can be expected in the near future, because non-inflammable or virtually non-inflammable oils do not yet meet the requirements of engine oils with regard to lubrication and bearing life.

6. Flight Attitudes

To maintain the oil supply at all flight attitudes including negative "g"- and zero "g"- conditions for the durations specified in Fig. 1 is by no means an easy task. This is, however, essentially a design problem.

This problem is twofold:

- The pressure pump must be in a position to supply oil with every combination of attitude and acceleration the aircraft may encounter.
- The oil must return immediately from the engine to the oil tank with every possible combination of attitude and acceleration.

Essentially three approaches exist towards the solution of this problem which have been developed to a stage that they meanwhile are proven technology:

- a) One has to provide a sufficient number of suction and scavenge ports, respectively, at various locations in the oil tank, the bearing chambers and the external gear box. A system of valves may then be required to ensure that always oil is sucked or scavenged instead of air. The tank, gear box and the bearing chambers must be cleverly designed so that the number of ports and valves does not become too large.
- b) Suction and scavenging is ensured by use of moveable pipes, connected to the inlet of the pressure and scavenge pumps, which, under the action of the "g"-forces, follow the inclination of the oil level.
- c) Pressurized air, artificially created "g"-loads and/or additional pumps are employed to produce a continuous flow of oil to the pumps during adverse flight conditions. Only this approach will guarantee continuous oil supply with zero "g"-conditions.

In the bearing chambers usually approach a) suffices and can be optimized in such a manner that additional valves are not necessary. For the tank and gear box, approaches b) or c) or combinations thereof are the most reasonable ones. The final solution must be thoroughly matched to the exact requirements of the particular aircraft. If, for example, the zero "g" specification is less severe than shown in Fig. 1, an interruption of the oil supply for these durations may be allowable and a solution using the methods of approach b) is adequate.

The designer has to keep the volumes of bearing chambers, gear boxes, pipes, filter etc. to a minimum to ensure a quick and sufficient return of the oil to the tank and that oil hiding cannot occur.

7. Future Prospects

Current production fighter aircraft engines meet the requirements shown in Fig. 1. However, the need for higher thrust to weight ratios and better mission fuel consumption for future aircraft engines will lead to higher system pressures and temperatures. In the same way the sealing air pressures and temperatures, i. e. the temperatures of the engine components and the bearing chambers, will increase. It is therefore necessary to improve the present concepts so that adverse effects are avoided which otherwise would be encountered in particular with respect to

- heat generation,
- oil consumption,
- bearing life (especially in emergency cases),
- oil fire behaviour,
- oil degradation with running time.

Improvements under development comprise, among others:

- Better sealing devices (for example face seals),
- rolling elements of bearings made from ceramics,
- better, high temperature resistant oils,
- cooling of the sealing air and better insulation of the bearing chamber structure.

There is no doubt that with improved technology future fighter aircraft engines will also meet the requirements of Fig. 1, in spite of their elevated system temperatures and pressures.

To conclude, the engineer is challenged by a wide field of future activities.

Reference: [1] Paul F. Brown, Bearing Retainer Material for Modern Jet Engines, ASLE Transactions 13, 1970, 225-239.

- Low mission oil consumption
- Low heat to oil
- No oil leakage
(external and internal)
- No overheating of bearing chambers
- High bearing life and reliability
(B 10 (DIN 622) ~ 3000-5000 hrs at adverse conditions)
- Reasonable life of bearings at oil off conditions
(emergency cases)
- Oil supply at all flight attitudes







Flight condition		Attitude g-load	Duration
Level flight		—	Continuous
Climb		$\alpha = +30^\circ$ $\alpha = +105^\circ$	Continuous 1 min
Dive		$\alpha = -30^\circ$ $\alpha = -90^\circ$	Continuous 1 min
Push over		0g	≥ 10 sec
Terrain following		$0g \pm 0,5g$	≥ 5 sec
Inverted flight		—	≥ 60 sec

Fig. 1:
Specification Requirements for an
Oil-Air System

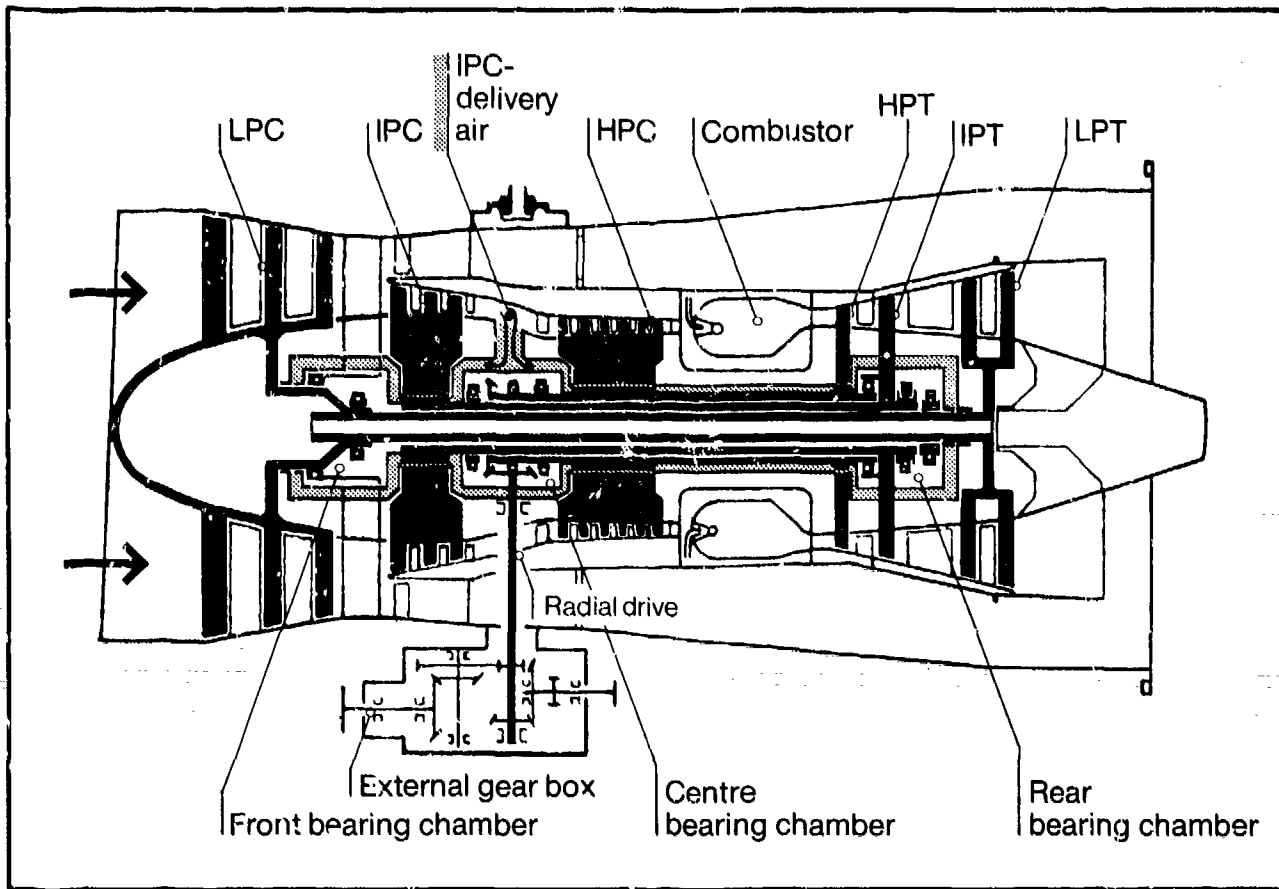


Fig. 2:
Three Spool Engine General
Arrangement

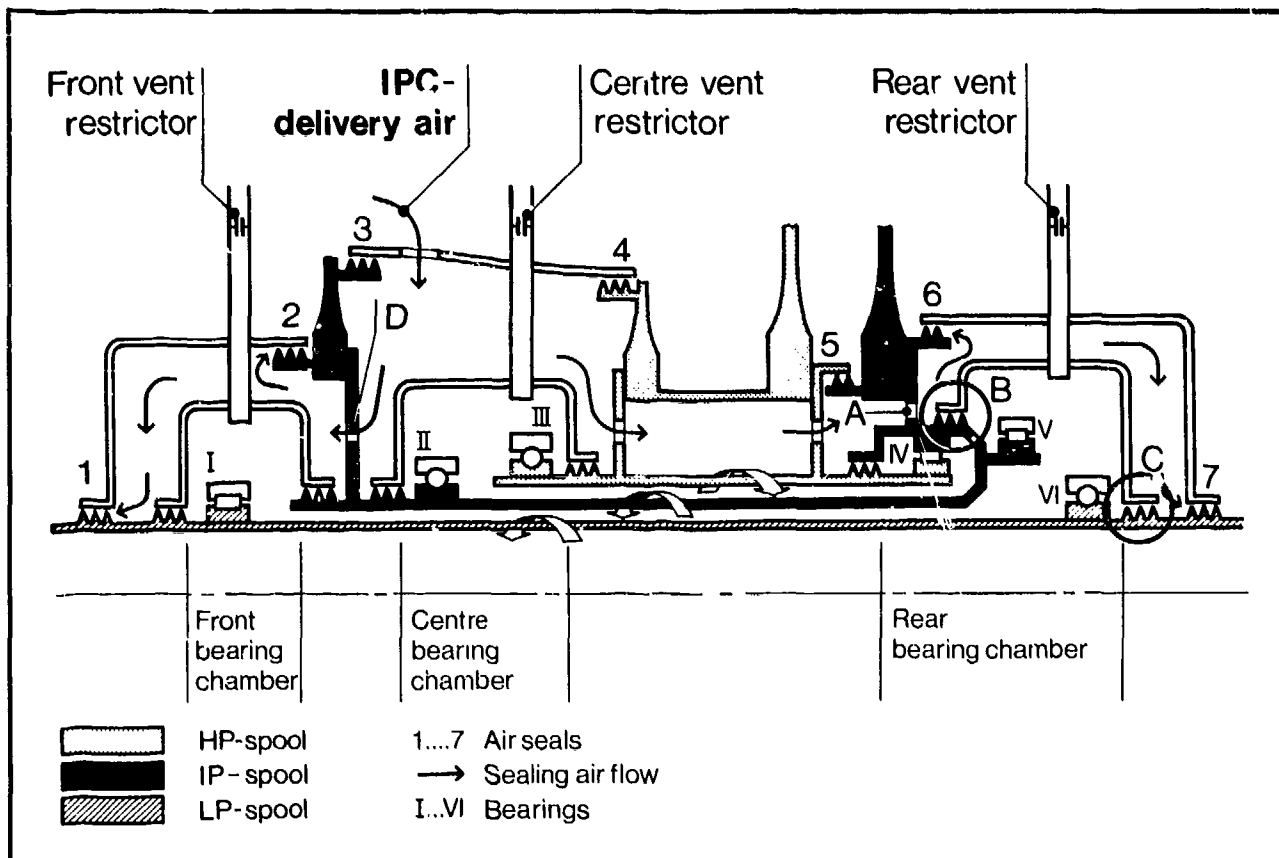


Fig. 3:
Bearing Chamber Pressurization Air System

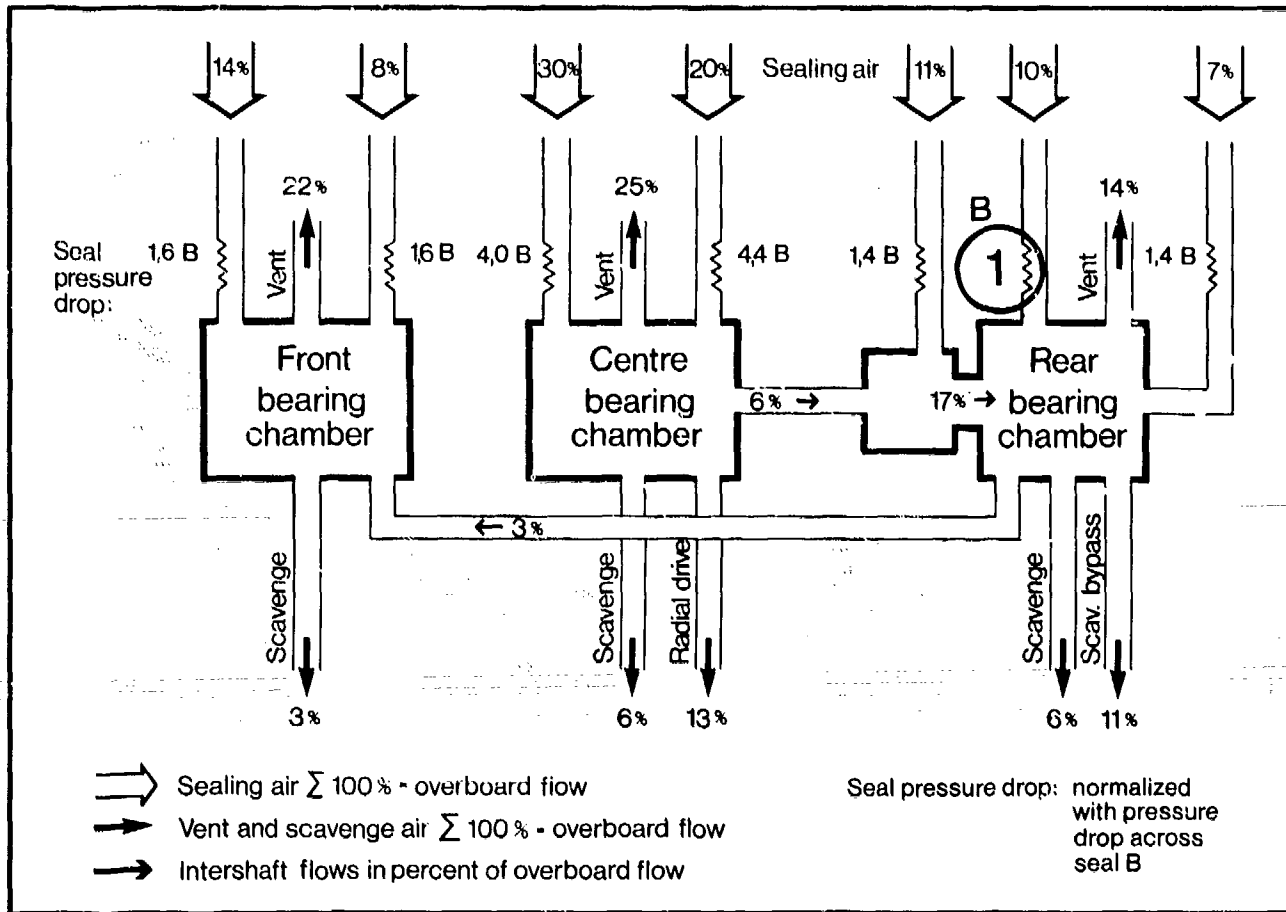


Fig. 4: Bearing Chamber Flow Diagram

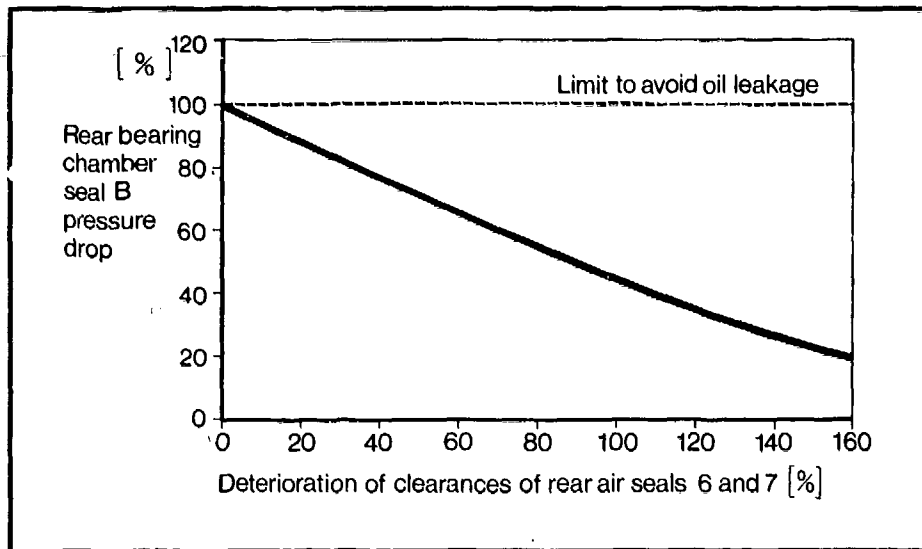


Fig. 5: Pressure Drop across Rear Bearing Chamber Seal B versus Air Seal Deterioration

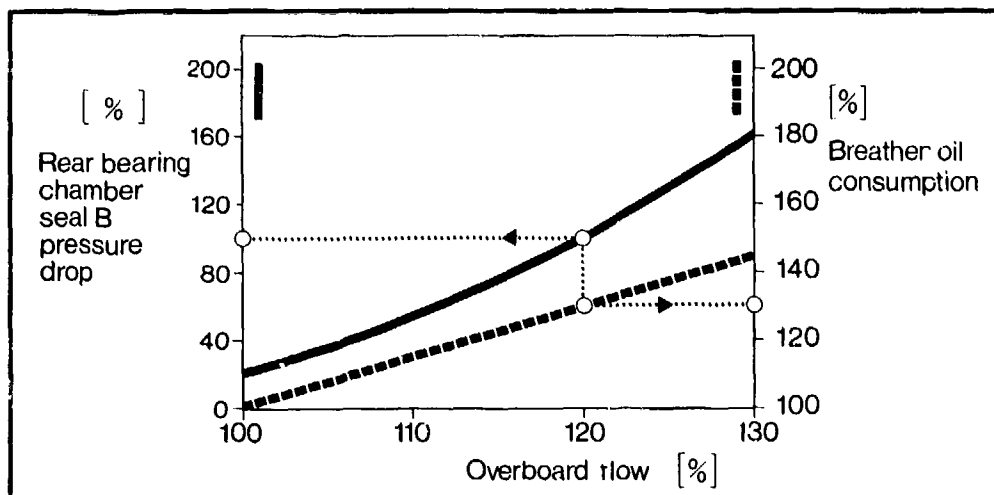


Fig. 6: Pressure Drop across Rear Bearing Chamber Seal B and Breather Oil Consumption versus Overboard Flow

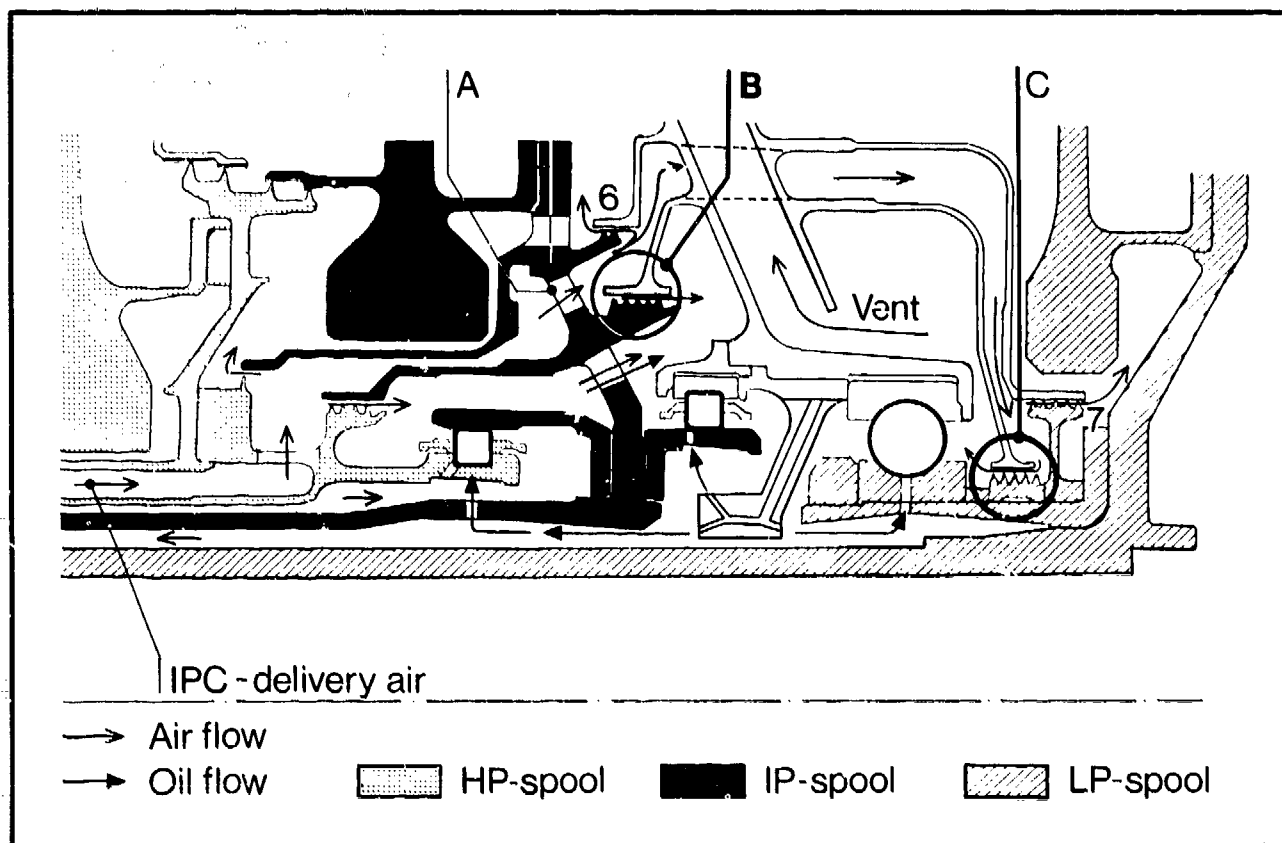


Fig. 7:
Rear Bearing Chamber

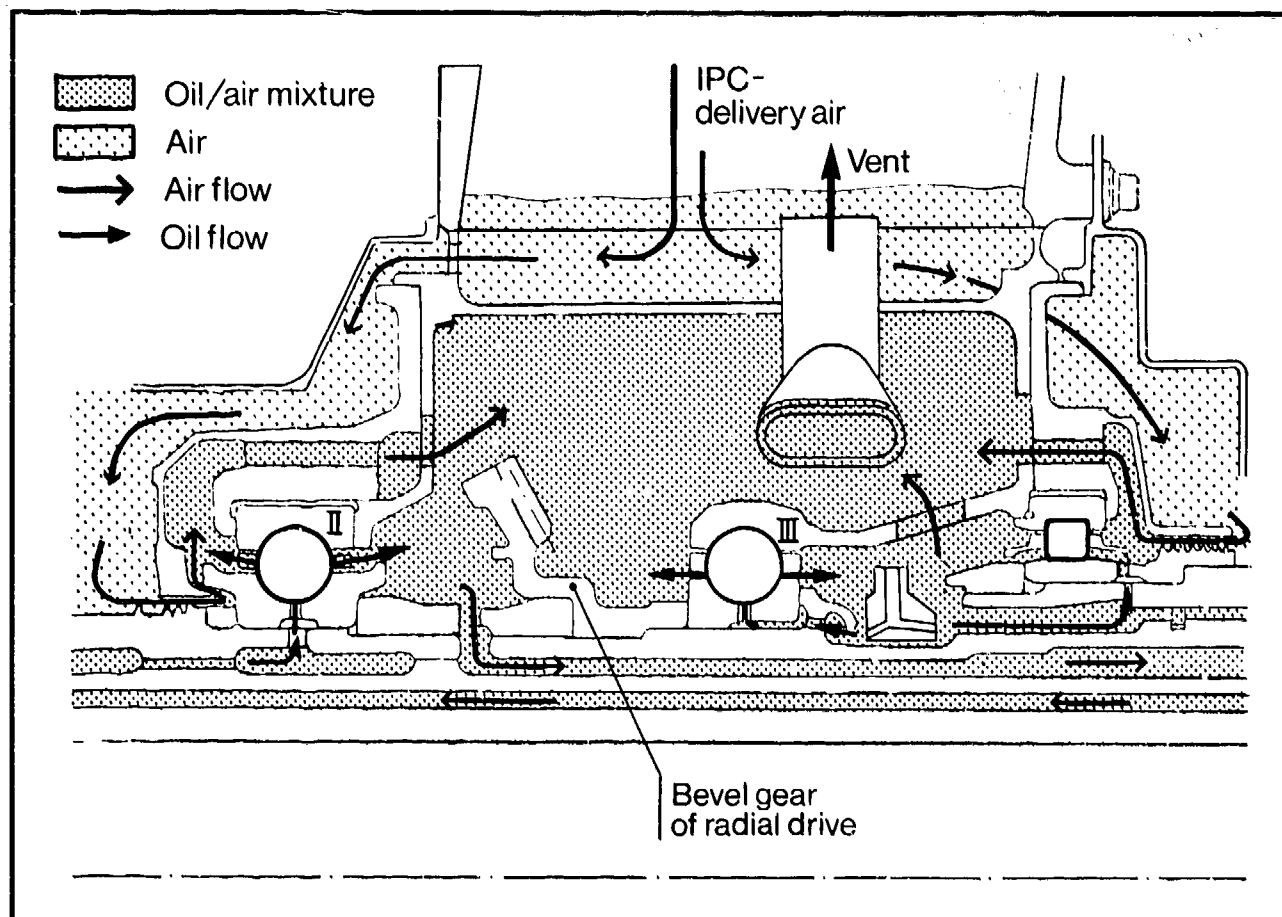


Fig. 8:
Centre Bearing Chamber

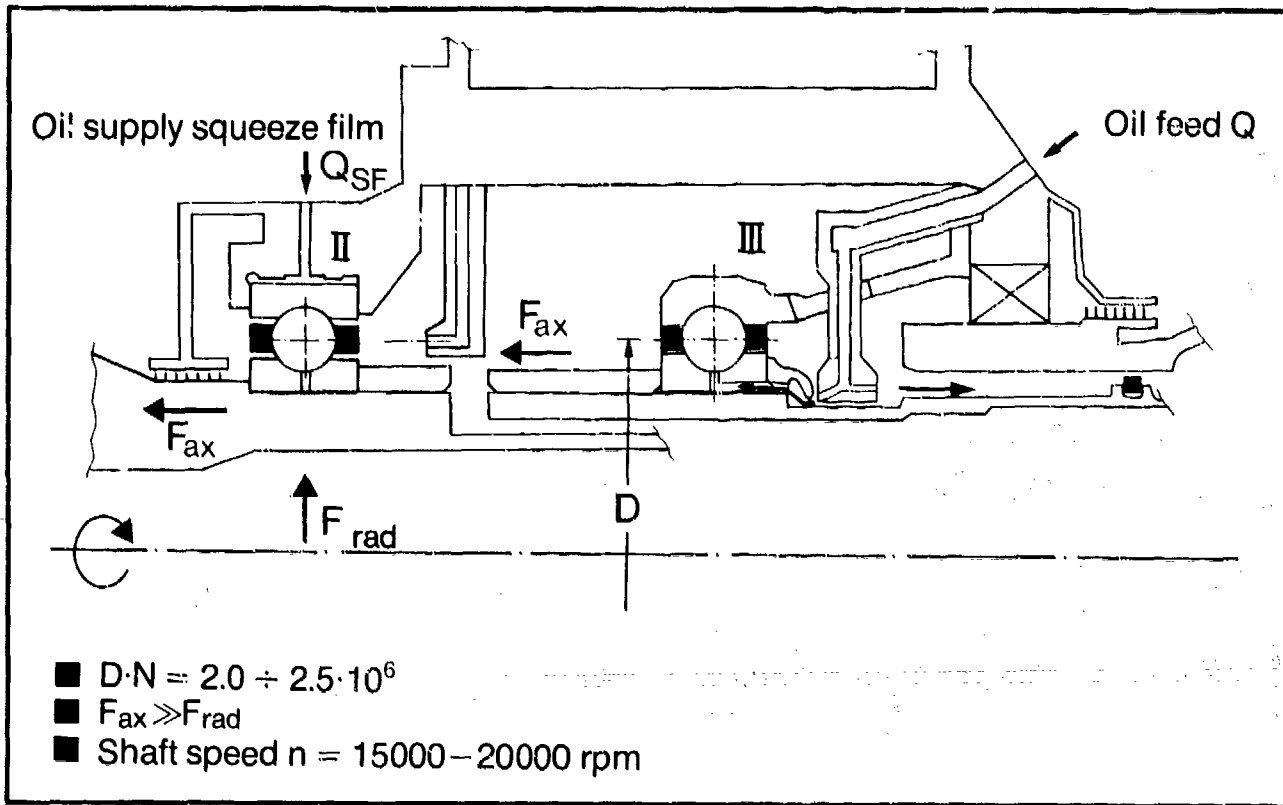


Fig. 9:
Main Design Features for Thrust Bearing II and III

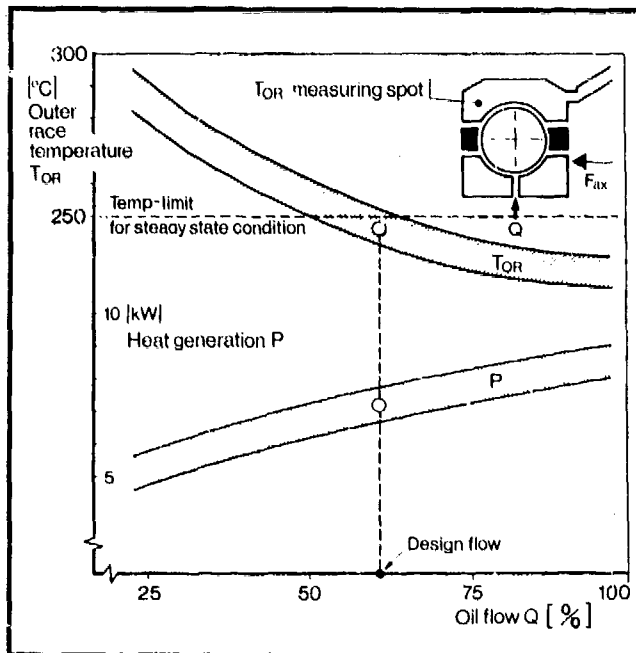


Fig. 10:
Thrust Bearing No. III
Influence of Oil Flow on Bearing Temperature and Heat Generation

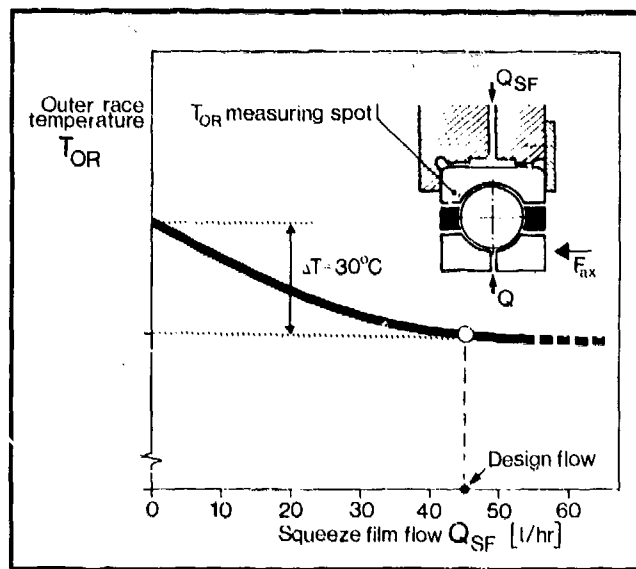


Fig. 11:
Thrust Bearing No. II
Contribution of Squeeze Film to Outer Race Cooling

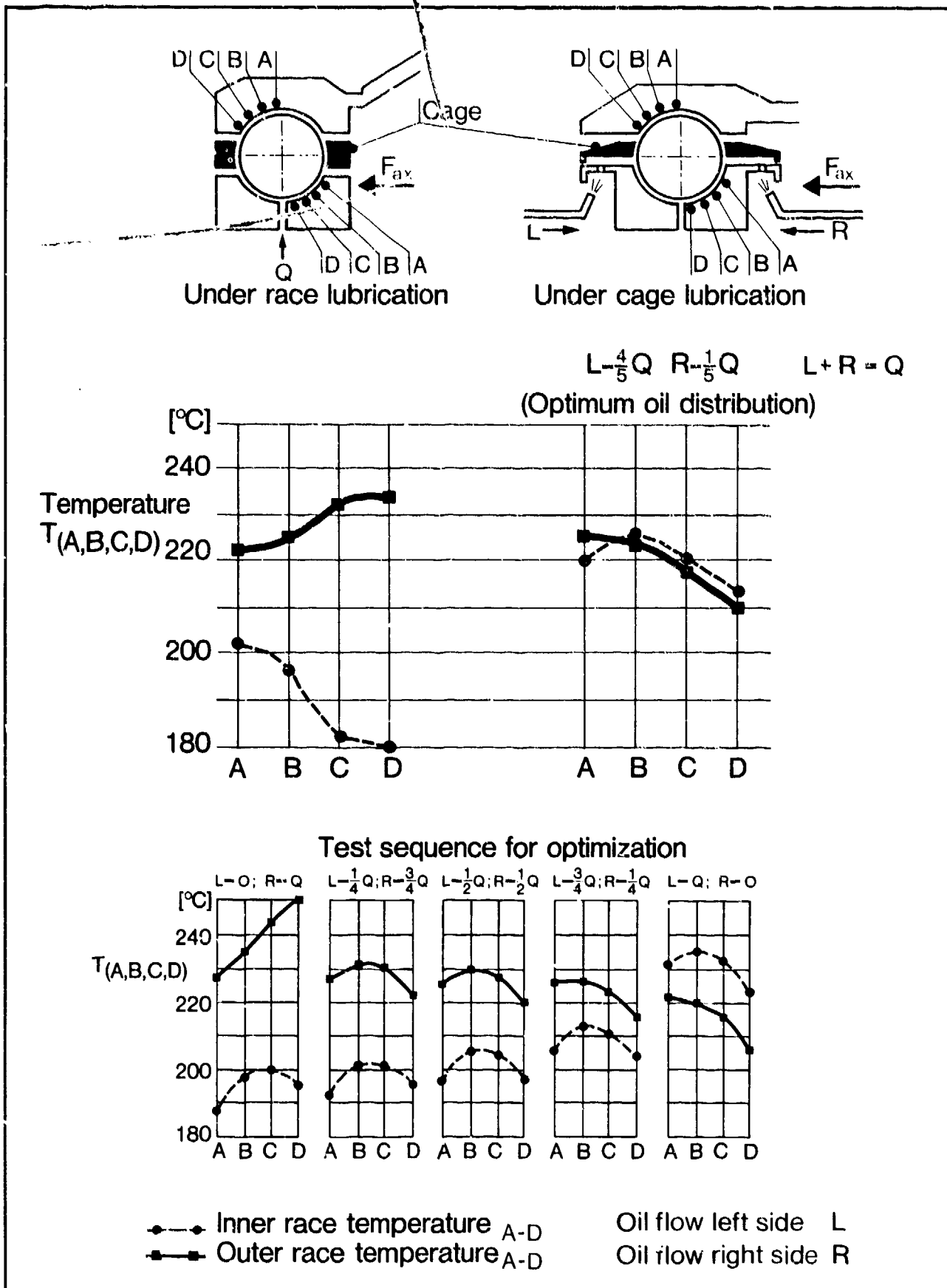


Fig. 12:
Thrust Bearing No. III
Optimization of Lubrication

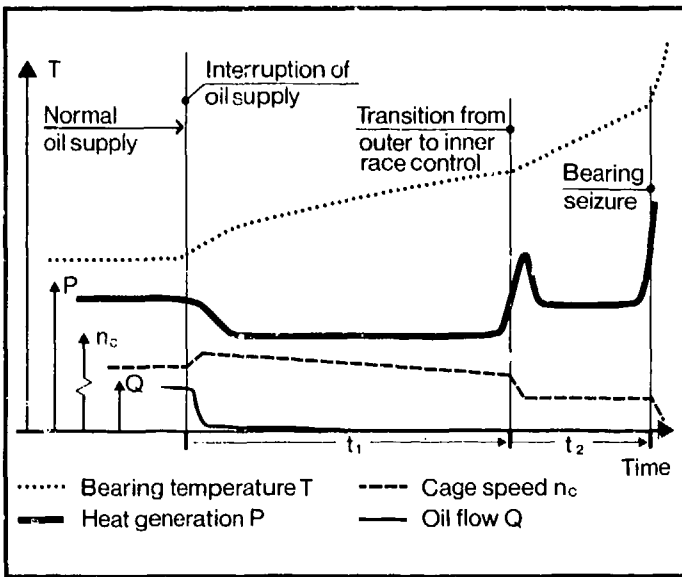


Fig. 13:
Bearing Reaction to
Oil Interruption

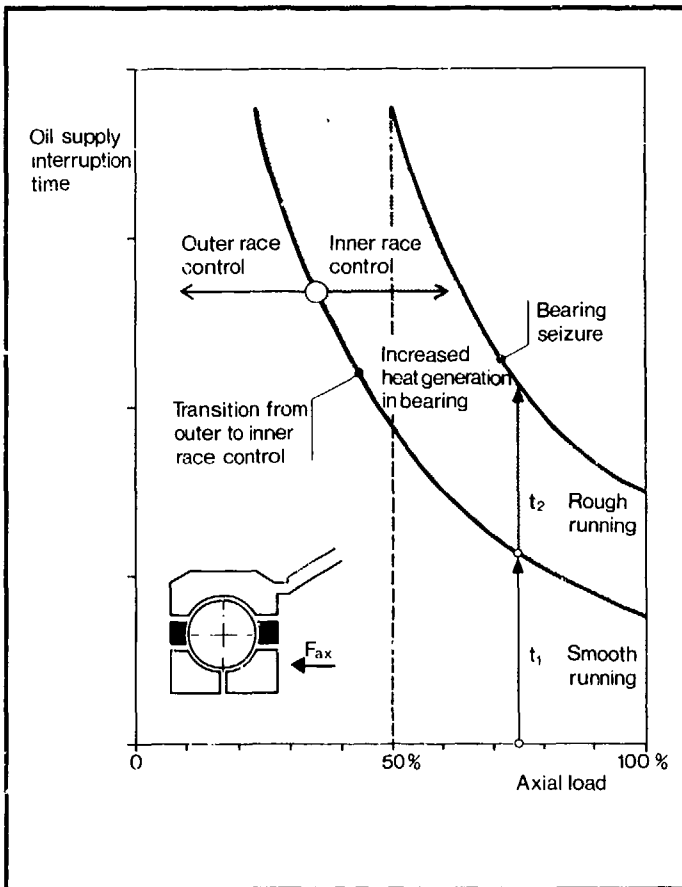


Fig. 14:
Thrust Bearing No. III
Permissible Oil
Interruption Time (Rig results)

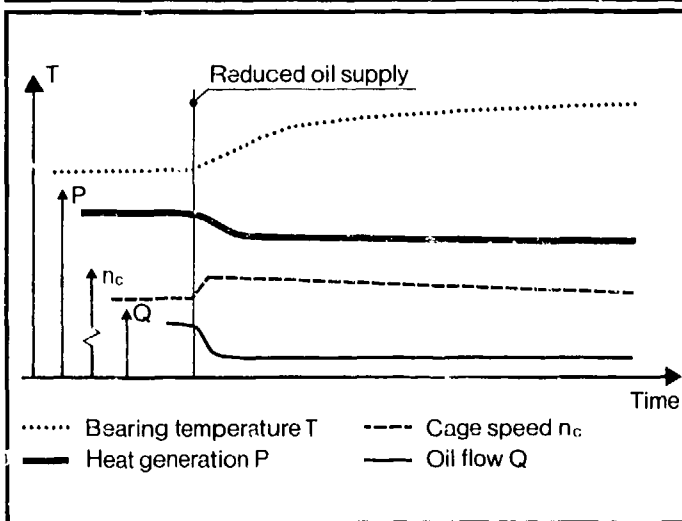


Fig. 15:
Bearing Reaction to
Reduced Oil Flow

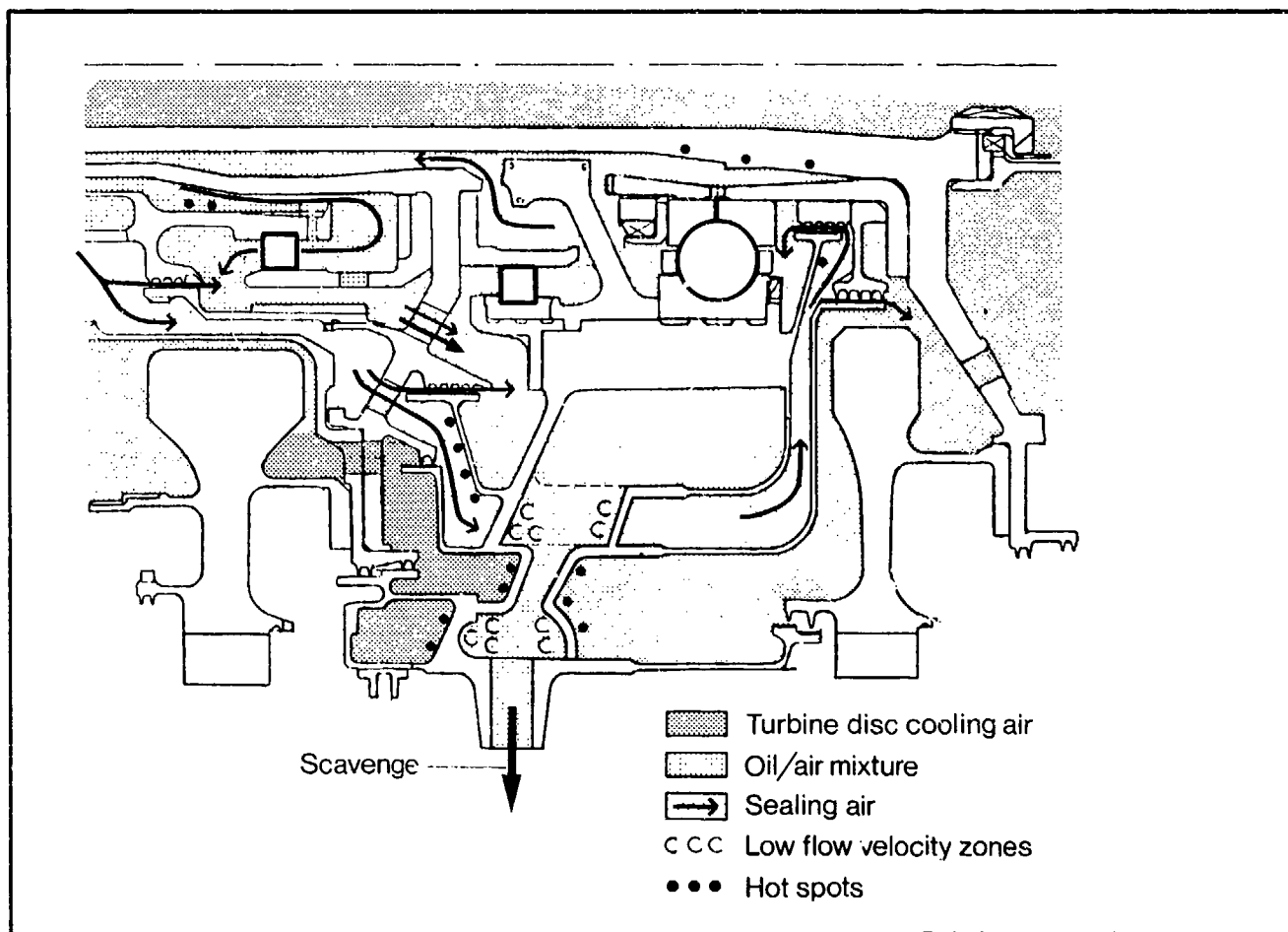


Fig. 16:
Rear Bearing Compartment with Oil Sump

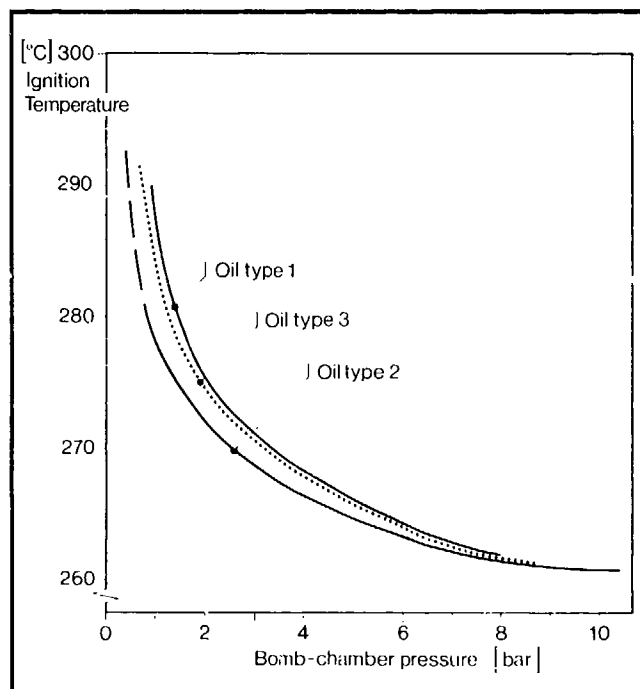


Fig. 17:
Influence of Pressure on the Spontaneous Ignition Temperature of 0-160 Oils under Static Conditions

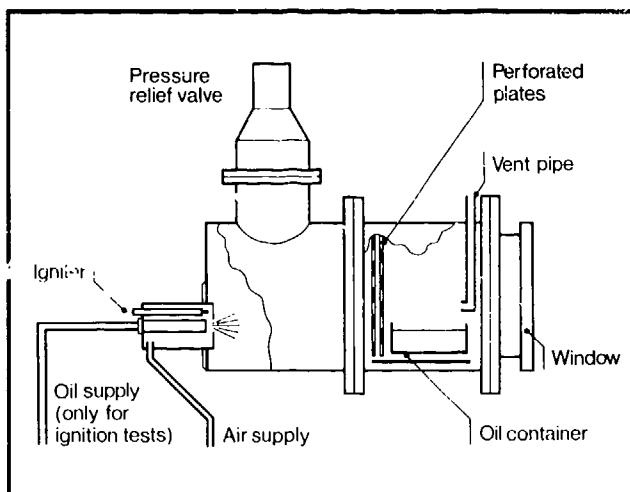


Fig. 18:
Dynamic Test Rig for Spark Ignition and Spontaneous Ignition Investigations

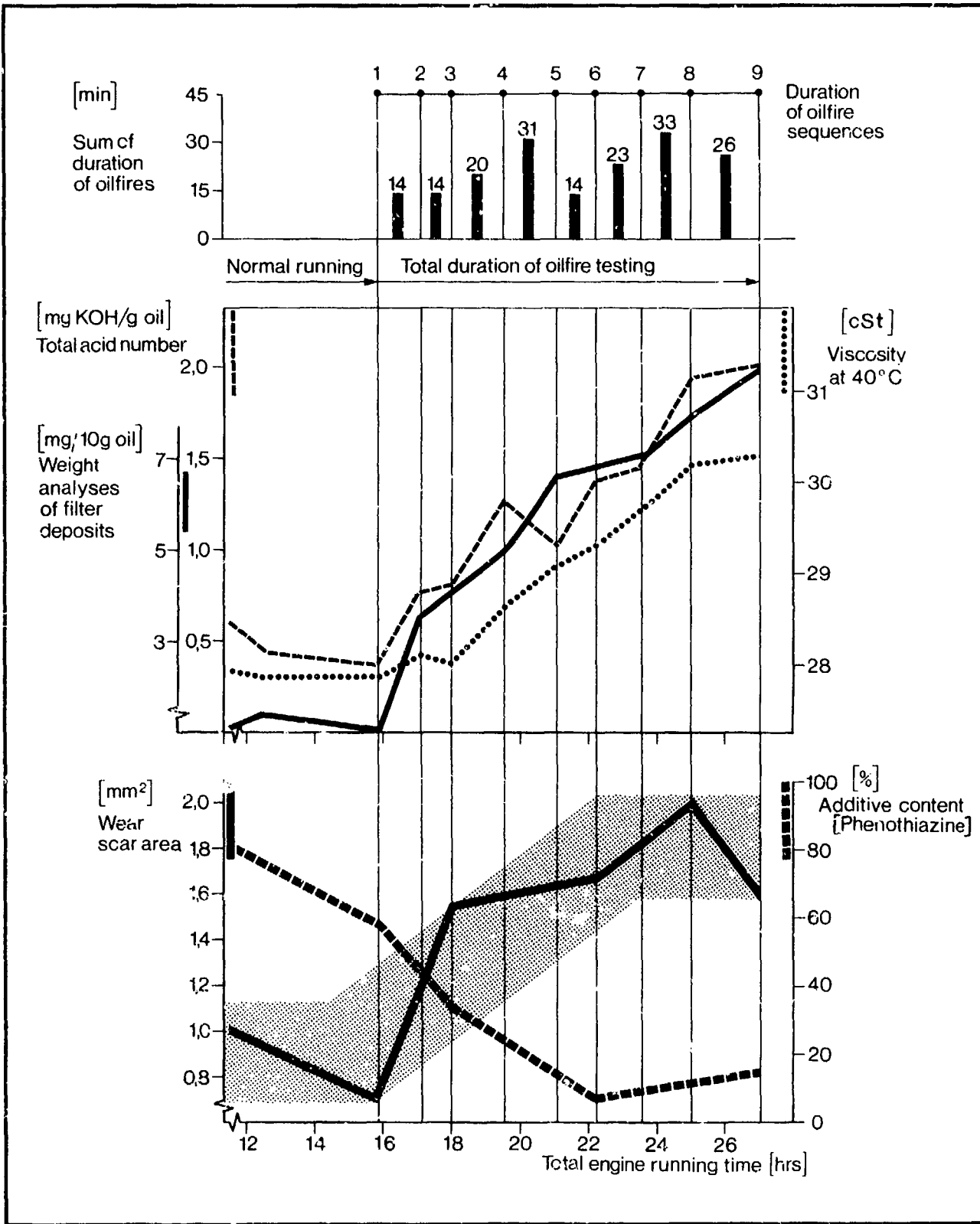


Fig. 19: Changes in Oil Quality due to Spontaneous Ignition Investigated in a Test Engine

- Reduction of internal cooling air and overboard air
- Reduction of bearing chamber temperatures and pressures (Cooling of sealing air and development of new sealing systems)
- Reduction of mission oil consumption (Low vent and scavenge airflows)
- Improvement of bearing capability (Introduction of new materials (ceramics))
- Optimization of air and oil system design (Reduced bearing loads and residence time of oil /air mixture in bearing chambers)
- Improvement of lubrication oils (Stability at high temperatures)

Fig. 20:
Future Development Tasks

DISCUSSION

J.F.Chevalier, SNECMA, Fr

In your proposals for improvements you mentioned the cooling of the sealing air for the rear chamber. Why do you not propose to have a bigger flow?

Author's Reply

I think your question has been how do you design the system to get air, not internally down the shafts to the rear bearing chamber, but outside. You trap the air at the same position here in the intermediate case and put the air in downstream. You cool it with cooler and then you guide the air inside the core engine, to the rear bearing chamber.

V.Bruno, Pratt & Whitney, Ca

The temperature distribution diagrams in Figure 12 show measurements taken at very close locations along the raceways. How were these measurements made and were the locations on each single race angularly offset?

Author's Reply

The holes were drilled from the outside and the thermocouples inserted from the outside. The distance between the surface of the outer race and the temperature couple is approximately half a millimeter. We have accounted for this and we have a correlation between the actual temperature in the oil film and the thermocouple temperature.

LUBRICATION OF 35-MILLIMETER-BORE BALL BEARINGS OF SEVERAL DESIGNS AT SPEEDS TO 2.5 MILLION DN.

by

HANS R. SIGNER
INDUSTRIAL TECTONICS, INC.
COMPTON, CALIFORNIA 90224

and

FREDRICK T. SCHULLER
NASA-LEWIS RESEARCH CENTER
CLEVELAND, OHIO 44135

SUMMARY

Parametric tests were conducted with 35mm bore, angular contact ball bearings with either a single or double-outer-land-guided cage. The bearings were either lubricated by oil jets or employed inner ring lubrication. Outer ring cooling was added in selected tests.

Test conditions were a radial load of 222 N (50 lb) and/or a thrust load of 667 N (150 lb), shaft speeds to 72,000 rpm, and an oil inlet temperature of 394 K (250°F). Lubricant flow to the bearing ranged from 300 to 1900 cm³/min (0.08 to 0.50 gal/min).

All bearings were successfully run at speeds to 2.5 million DN. Increasing the lubricant flow decreased bearing ring temperatures but increased bearing power loss. The power loss and race temperatures of a jet lubricated bearing with double-outer-land-guided cage were always higher than those of the single-land-guided design at similar test conditions. The lowest bearing operating temperatures were achieved when inner ring lubrication and outer ring cooling were combined. Cage slip of a double-outer-land-guided cage was approximately twice that of a single-outer-land-guided cage.

INTRODUCTION

Small advanced turbine engines, 0.5 to 4.6 kg/sec (1 to 10 lb/sec) total air flow, require bearings that can operate in the speed range of 2.5 million DN (product of the bearing bore in millimeters and the shaft speed in rpm) and at high temperatures. Bearing designs and lubrication techniques must be refined and optimized for reliable engine performance and long bearing life.

The conventional method of lubricating small high-speed ball bearings uses oil jets. Due to centrifugal forces and windage which prevent the oil from effectively lubricating and cooling the cage and rolling contacts, reliable operation is limited to about 2.5 million DN. Proper cage design and adequate oil flow can increase the speed as described in ref. 1 where 2.85 million DN was achieved with a 30mm bore, jet lubricated deep groove ball bearing.

Large-bore ball and roller bearings have been successfully tested at speeds to 3.0 million DN (refs. 2 to 5). In these tests the lubricant was fed to the bearings through radial holes in the inner ring. Inner ring lubrication also shows promise for reliable operation of smaller bearings at high speeds. This is especially true when it is combined with external cooling of the bearing ring surfaces, as reported in references 2 to 5 for large bearings.

One of the principal bearing elements is the cage, and its design greatly affects the limiting speed. For example, in reference 1, operation at 2.85 million DN caused a failure of the outer-land-guided cage, whereas an inner-land-guided cage was limited to a DN value to 1.65 million. As discussed in references 6 and 7, other investigators found most reliable bearing performance with outer-land-guided cages. The outer ring land surfaces are usually more thoroughly lubricated due to the centrifugal oil flow pattern within a bearing. For small, jet lubricated high-speed bearings, therefore, outer-land-guided cages are usually recommended.

The research reported herein was conducted to investigate the performance of 35mm bore, angular contact ball bearings at speeds to 2.5 million DN. The primary objectives were to (a) determine the operating characteristics under variable lubricant flow conditions at high speeds, (b) establish the effects of lubricant introduction methods using jet lubrication, inner ring lubrication and outer ring cooling, and (c) determine the effects of single- and double-outer-land-guided cage designs on high speed bearing performance.

APPARATUS

HIGH SPEED BEARING TESTER

A general view of the air-turbine-driven test machine is shown in figure 1. A sectional drawing is shown in figure 2. The shaft is mounted horizontally and is supported by two preloaded, angular-contact ball bearings. The test bearing is assembled into a separate housing that incorporates the hardware for lubrication, oil removal, thrust and radial load application, and instrumentation for cage speed measurement. Test bearing torque is measured with strain gages located near the end of an arm that prevents the housing from rotating. Thrust force is applied through a combination of a thrust needle bearing and a small roller support bearing which minimizes test housing restraint during torque measurements. Radial load is applied to the test bearing through knife-edge bearings.

The test bearing was lubricated either by dual jets or through the inner ring. The oil jets were located approximately 3.0mm (0.12 in.) from the non-loaded side of the inner ring face and were aimed at the inner raceway. In separate tests, not reported herein, it was determined that a 20 m/sec (66 ft/sec) jet velocity provided the most efficient lubrication of the test bearing. This velocity was used in all the tests.

When inner ring lubrication was used, oil was pumped by centrifugal force from the center of the hollow shaft through axial grooves in the test-bearing bore and through a series of radial holes to the bearing inner race. Cooling oil was supplied to the outer ring by means of holes and grooves in the bearing housing, shown in figure 2. Shaft speed (inner ring speed) was measured with a magnetic probe. Ball-pass frequency (cage speed) was determined by analyzing signals from a semiconductor strain gage mounted in a cavity of the test-bearing housing close to the bearing outer race. Two thermocouples were assembled in the shaft to measure inner ring temperatures through a rotating telemetry system. Outer ring temperatures were obtained by two thermocouples installed in the test-bearing housing. The high-speed bearing tester is described in detail in references 8 and 9.

TEST BEARINGS

The test bearings were ABEC-7 grade, 35mm bore, angular contact ball bearings with a double or single-outer-land-guided cage, as shown in figures 3(a) and 3(b). The effective land area of the double-outer-land-guided cage bearing was approximately three times that of the single-outer-land-guided cage bearing. It weighed 16 percent more than the single-outer-land-guided cage. The cage balance was within 0.05 g-cm.

One bearing design, fig 3(c), permitted lubrication through the inner ring by means of axial grooves machined in the bore. There were 16 axial grooves in the bearing bore. Eight 0.76mm (0.030 in.) diameter holes (one in every other axial groove) radiating from the bearing bore formed a flow-path for bearing lubrication. Therefore, it was assumed that 50 percent of the oil supplied to the inner ring lubricated the bearing and 50 percent flowed axially through those grooves that contained no radial holes and cooled the inner ring. In some tests, four of the eight radial holes were plugged to allow 25 percent of the total flow to be used for bearing lubrication and 75 percent for inner ring cooling.

A detailed specification of the test bearings is given in table I.

LUBRICANT

The lubricant used for the parametric studies was a neopentylpolyol (tetra) ester. This type II oil is qualified to the MIL-L-23699 specifications. The major properties of the lubricant are presented in table II.

TEST PROCEDURE

After warming the test machine by circulating heated oil and calibrating the torque measuring system, test loads were applied and the lubricant flow rate was set at 1900 cm³/min (0.50 gal/min). The shaft was then slowly brought up to the test speed. When bearing and test machine temperatures stabilized, the oil-inlet temperature and lubricant flow rate were set to the desired values. A test series was run by starting at the lowest speed, a nominal 48,000 rpm, and progressing through 65,000 and 72,000 rpm before changing the lubricant flow. Four lubricant flow rates to the bearing inner ring of 300 to 1900 cm³/min (0.08 to 0.50 gal/min) were used. In some tests, a separate run was made during which outer ring cooling oil flow was employed.

If it became apparent during the course of testing that a test condition would result in predictable distress of the test bearing or test rig, or generate a bearing temperature above 491 K (425°F), that test point was aborted or omitted.

RESULTS AND DISCUSSION

EFFECT OF CAGE DESIGN ON PERFORMANCE OF JET LUBRICATED BEARINGS

Parametric performance tests were conducted with jet-lubricated 35mm bore, angular contact ball bearings. Either a single or a double-outer-land-guided cage was used. Except for the cage design and the inside diameter of one outer ring land the two bearings were identical (fig. 3(a) and (b)). These tests were run with combined radial and axial loads of 222 N (50 lb) and 667 N (150 lb) respectively.

EFFECT OF CAGE DESIGN ON BEARING TEMPERATURE

The effect of lubricant flow rate on bearing temperature at three different speeds is shown in figure 4. The ring temperatures of bearings with either cage design decreased with increasing oil flow. The bearing with the double-outer-land-guided cage ran hotter at all speeds. The temperature difference between the two bearings increased with speed and reached 25 K (45°F) at 72,250 rpm at a flow rate of 1900 cm³/min (0.50 gal/min).

The higher temperatures of the bearing with the double-outer-land-guided cage are partially due to shearing of the oil over the larger land areas in this bearing. Also the lubricating oil becomes trapped by the extra land, adding heat due to churning within the bearing, whereas the single land allows a free evacuation of the oil.

EFFECT OF CAGE DESIGN ON BEARING POWER LOSS

Two approaches were used to determine bearing power loss. In the first, outer ring torque was measured. In the second, the heat rejected to the lubricant was determined. Bearing power loss is dissipated in the form of heat rejected to the lubricant and transferred by conduction, convection, and radiation to the surrounding environment. To obtain a measure of this heat rejection and, thus, power loss within the bearing, oil inlet and outlet temperatures were measured for all conditions of lubricant flow. The heat energy absorbed by the lubricant was obtained from the standard heat transfer equation.

$$Q_T = MC_p (t_{out} - t_{in})$$

where

Q_T total heat transfer rate to the lubricant, J/min (Btu/min)

M mass flow rate, kg/min (lb/min)

C_p specific heat, J/kg K (Btu/lb °F)

t_{out} oil outlet temperature, K (°F)

t_{in} oil inlet temperature, K (°F)

Power loss obtained from torque readings and as determined from heat rejected to the oil are plotted in figure 5 for both the single and the double-outer-land-guided cage bearings.

The disadvantage of a double-outer-land-guided cage becomes apparent when comparing power demands of the two cage designs. Figure 5 shows that power loss increases with increasing speed and lubricant flow for bearings with either cage configuration. However, the power losses of a double-outer-land-guided cage bearing are considerably higher and increase at a faster rate with increasing speed and/or with increasing lubricant flow to the bearing. Churning of the oil, which is entrapped by the double-outer-land-guided cage, and the drag in the larger separator land areas are believed to cause the increased power loss in this design.

Relatively good correlation was obtained between the power loss values obtained from torque measurements and those by calculating the heat transferred to the oil. In figure 5, both methods show identical trends. The heat transfer calculations yielded somewhat lower values, which may be explained by unaccounted heat losses to the environment.

When designing a power sensitive system, the highest lubricant flow rate may not be the most desirable choice, even though it produces the lowest bearing operating temperatures.

EFFECT OF CAGE DESIGN ON CAGE SLIP

To determine percent cage slip, the epicyclic cage speed C_{epi} at the various test shaft speeds was obtained from a computer program SHABERTH (ref. 10), which allows a complete mathematical simulation of a dynamic bearing system. However, thermal, lubricant and bearing fit effects were not considered in this solution of epicyclic cage speed. A subsequent calculation at the highest speed (72,300 rpm) and a thrust load of 667 N (150 lb), considering all the centrifugal growth effects on the inner ring, showed the epicyclic speed to change only from 33,000 rpm to 32,720 rpm. This resulted in the calculated slip changing from 7.0 to 6.2 percent for this point. Therefore, all the values of C_{epi} were not recalculated. The calculated epicyclic cage speeds were combined with the measured experimental cage speed C_{exp} to

$$\text{Percentage cage slip} = (1 - C_{exp}/C_{epi}) (100)$$

Figure 6 shows that percent cage slip increases with speed at about the same rate for each of the three lubricant flow rates tested. The double-outer-ring-guided cage bearing showed a higher percent cage slip than the single-outer-ring-guided cage at all speeds and lubricant flow rates. It also showed a higher change of cage slip with increasing flow. For all speeds and flow rates tested, the cage slip ranged from 1.0 to 10.2 percent for both bearing configurations. The small increase in slip with flow rate is primarily due to additional drag on the balls and cage. Percent cage slip for a double-outer-land-guided cage bearing ranged from 1.5 to 2.7 times that for a single-outer-land-guided cage bearing over the range of lubricant flow rates and speeds shown. The double-land-guided cage, because of its greater surface area, has more drag as it rotates against the outer ring. This increased drag and the oil churning reduce cage speed (increase slip) to a greater extent than with the single-outer-land-guided cage. The observed increase in cage slip with increasing shaft speed for both configurations could be expected due to centrifugal forces decreasing the ball load, and thus traction at the inner raceway contact. Increasing the shaft speed also increases the drag at the land area, especially with the double land cage design.

EFFECTS OF INNER RING LUBRICATION ON BEARING PERFORMANCE

Inner ring lubrication was studied in a series of tests with a 35mm angular contact ball bearing. The bearing, shown in figure 3(c), was fitted with the single-outer-land-guided cage which rendered superior performance in the tests previously described. The lubricant was supplied through passages at the inner ring. The tests were run with a thrust load of 667 N (150 lb).

EFFECT OF OIL FLOW DISTRIBUTION THROUGH THE INNER RING ON BEARING TEMPERATURE

The effects of lubricant distribution through the inner ring on bearing inner-and-outer ring temperature are shown in figures 7 and 8, respectively. Two oil flow schemes were tested. In the first one, 50 percent of the oil flowed through the bearing inner ring for lubrication and 50 percent flowed axially only, for inner ring cooling. In the second flow scheme, 25 percent was used for lubrication and 75 percent for cooling. As expected, the bearing temperature decreased with increasing lubricant flow to the bearing for all conditions investigated. The lube flow scheme using 75 percent of the oil to cool the inner ring and 25 percent to lubricate the bearing resulted in higher ring temperatures than the 50-50 percent distribution for all three shaft speeds. Apparently the 25-75 percent oil split supplied less than the "optimum" amount of lubricant to the bearing, and the added cooling flow through the axial grooves in the inner ring did not improve the cooling of this component. Hence, we find that an oil flow distribution of 50 - 50 percent for lubrication and inner ring cooling is more desirable.

EFFECT OF OUTER RING COOLING

In selected tests the exterior surfaces of the bearing outer ring were cooled with an oil flow of 1700 cm³/min (0.45 gal/min). Both, the cooling and lubricating oil inlet temperatures were maintained at 394 K (250°F). The results are shown in figures 7 and 8. At the lowest shaft speed of 47,200 (figure 7(a)) outer ring cooling reduced the outer ring temperature by about 36 to 8 K (65 to 14°F) as the total oil flow to the inner ring was increased from 300 to 1900 cm³/min (0.06 to 0.50 gal/min). At the higher speeds, figures 7(b) and (c), the outer ring temperature decreased by 42 to 16 K (75 to 28°F) as the total oil flow was increased from 580 to 1900 cm³/min (0.15 to 0.50 gal/min). The reduction in outer ring temperature with outer ring cooling was approximately equal for the 50-50 percent and 25-75 percent total oil flow distributions.

Outer ring cooling had little or no effect on the inner ring temperature (fig. 8). The reduction of the inner ring temperature varied from 0 to 6 K (0 to 11°F) over the entire range of oil flows, shaft speeds and with both oil distribution patterns.

EFFECT OF SPEED ON TEMPERATURES OF INNER RING-AND JET LUBRICATED BEARINGS

The effect of speed on the test bearing temperature for the 50-50 and 25-75 percent inner ring oil flow distribution patterns is shown in figure 9 and compared with that of the jet-lubricated bearing. With all lube schemes the bearing ring temperatures increased with increasing speed and decreased with increasing oil flow. Bearing lubrication through the inner ring produced lower inner ring temperatures and higher outer ring temperatures than jet lubrication at corresponding speeds and lube flow rates. This is not unexpected, since through-the-inner-ring lubrication cools the inner ring on its exterior surfaces, and only a portion (25 or 50 percent) of the inner ring oil flow enters the bearing to lubricate and cool the outer ring.

The effects of outer ring cooling, previously discussed and illustrated in figures 7 and 8, are cross-plotted onto figure 9. Only values for the 50-50 percent oil split and a constant outer ring cooling oil flow of 1700 cm³/min (0.45 gal/min) are shown. The outer ring temperature approached that of the inner when inner ring lubrication and outer ring cooling were combined, giving the lowest operating temperatures measured. The improved elastohydrodynamic film thickness associated with lower operating temperatures is known to increase bearing fatigue life (ref. 11).

POWER LOSS; INNER RING - AND JET LUBRICATED BEARINGS

Bearing power loss, determined from torque measurements, is plotted in fig. 10. Inner ring lubricated bearings with a 50-50 and a 25-75 percent oil flow split show almost identical power loss, ranging from 0.6 to 2.5 kW (0.8 to 3.4 hp) over the entire range of speeds and flow rates tested. The largest increase in power loss was about 1.27 kW (1.7 hp) at a total oil flow rate of 1900 cm³/min (0.50 gal/min) over a speed range of 47,000 to 72,000 rpm. The jet lubricated bearing showed slightly less power loss at the higher oil flow rates of 1300 and 1900 cm³/min (0.35 and 0.50 gal/min).

Figure 11 illustrates bearing power loss calculated from heat transferred to the lubricant. Correlation with the power loss values from torque measurements, fig. 10, is excellent over the entire range of speeds, flows and for all bearing configurations tested.

CAGE SLIP; INNER RING - AND JET LUBRICATED BEARINGS

For all lube schemes, the percent cage slip increased significantly with increasing inner ring speed, but only slightly with increasing lubricant flow rate as illustrated in figs 12 and 13. Only small differences in cage slip were detected between the inner ring lubricated bearings with a 50-50 and 25-75 percent oil flow split. At low inner ring speeds, the jet lubricated bearings showed higher cage slip than the inner ring lubricated bearing. But as the lube flow rate and speed increased, the difference in cage slip between the bearings diminished. The maximum cage slip of 7.0 percent occurred at 72,300 rpm, at a total oil flow rate of 1900 cm³/min (0.50 gal/min) with an oil flow distribution of 50-50 percent through the inner ring.

A visual examination of the bearing after running showed no damage to the raceway and ball surfaces, indicating that the measured cage slip was not of sufficient magnitude to affect satisfactory bearing operation. The silver plated land and ball pocket surfaces of the cage were lightly burnished but showed no signs of significant wear.

CONCLUSIONS

The performance of 35mm bore, angular contact ball bearings was investigated in parametric tests. The bearings had a nominal, unmounted contact angle of 24° and either a single- or a double-outer-land-guided cage. The investigation included lubrication by oil jets or through passages in the bearing inner ring. When inner ring lubrication was used, the oil was channeled through axial grooves and radial holes in the bearing inner ring. In some tests, 50 percent of the oil supplied to the inner ring was introduced into the bearing for lubrication and 50 percent cooled the inner ring exterior surfaces. In other tests the distribution was 25 percent lubrication and 75 percent cooling. In selected tests the bearing outside diameter was cooled with a constant oil flow of 1700 cm³/min (0.45 gal/min).

Test conditions included nominal shaft speeds from 48,000 to 72,000 rpm, a radial load of 222 N (50 lb) and/or a thrust load of 667 N (150 lb). Lubricant flow to the bearing ranged from 300 to 1900 cm³/min (0.08 to 0.50 gal/min) at an inlet temperature of 394 K (250°F). The following results were obtained:

1. All bearings were successfully run at speeds to 2.5 million DN. Generally, increasing the lubricant flow decreased bearing ring temperatures but increased bearing power loss.

2. Race temperatures and power loss of a jet lubricated bearing with double-outer-land-guided cage were always higher than those of the single-land-guided-design at equivalent test conditions.
3. Cage slip in a bearing with double-outer-land-guided cage was 1.5 to 2.7 times higher than in a bearing with a single-outer-land-guided cage, over the entire range of speeds and lubricant flow rates tested. The increase in cage slip with increasing lubricant flow rate was minimal, however, cage slip increased significantly with speed.
4. The inner ring lubricated bearing with an oil flow distribution pattern of 50 percent lubrication and 50 percent inner ring cooling ran slightly cooler than an equivalent bearing with a 25-75 percent oil distribution.
5. Without outer ring cooling, the inner ring of an inner ring lubricated bearing ran cooler and its outer ring temperatures were higher than in a jet lubricated bearing at equivalent operating conditions.
6. Outer ring cooling reduced the bearing outer race temperature significantly, but affected the inner race temperature only slightly. The outer ring temperature approached that of the inner when inner ring lubrication and outer ring cooling were combined, giving the lowest operating temperatures measured. The improved elastohydrodynamic film thickness associated with lower operating temperatures is known to increase bearing fatigue life.

ACKNOWLEDGMENTS

This test program was performed at the Industrial Tectonics, Inc. laboratory in Compton, California under contract with the NASA-Lewis Research Center, Cleveland, Ohio; contract NAS 3-19779.

Mr. F. T. Schuller was the NASA project manager. Mr. H. R. Signer was the program manager and Mr. S. I. Pinel was the project engineer at Industrial Tectonics, Inc.

REFERENCES

1. Miyakawa, Y.; Seki, K.; and Yokoyama, M.: Study on the Performance of Ball Bearings at High DN Values. NASA TTF-15017. Translation of "Koh dn Chi Ni Okeru Gyokujikujū No Seino Ni Kansuru Kenkyū." National Aerospace Laboratory, Tokyo (Japan), Report NAL-TR-284, May 1972, p. 120.
2. Signer, H.; Bamberger, E.N.; and Zaretsky, E.V.: Parametric Study of the Lubrication of Thrust Loaded 120-Millimeter Bore Ball Bearings to 3 Million DN. ASME Journal of Lubrication Technology, Vol. 96, No. 3, July, 1974, pp. 515-524.
3. Zaretsky, E.V.; Bamberger, E.N.; and Signer, H.R.: Operating Characteristics of 120-Millimeter-Bore Ball Bearings at 3×10^6 DN, NASA TN D-7837, 1974.
4. Bamberger, E.N.; Zaretsky, E.V.; and Signer, H.R.: Effect of Speed and Load on Ultra-High-Speed Ball Bearings. NASA TN D-7870, 1975.
5. Schuller, F.T.: Operating Characteristics of a Large-Bore Roller Bearing to Speeds of 3×10^6 DN. NASA TP-1413, 1979.
6. Matt, R.J.; Giannotti, R.J.: Performance of High Speed Ball Bearings with Jet Oil Lubrication. ASLE paper 66AM-1B4, August, 1966.
7. Anderson, W.J.; Macks, E.F.; and Nemeth, Z.N.: Comparison of Performance of Experimental and Conventional Cage Designs and Materials for 75-Millimeter-Bore Cylindrical Roller Bearings at High Speeds, NACA Report 1177, 1954.
8. Schuller, F.T.; Pinel, S.I.; Signer, H.R.: Operating Characteristics of a High-Speed-Jet-Lubricated 35-Millimeter-Bore Ball Bearing with a Single-Outer-Land-Guided-Cage NASA TP-1657, 1980.
9. Pinel, S.I.; Signer, H.R.: Development of a High-Speed, Small Bore Bearing Test Machine. (ITI P-1249, Industrial Tectonics, Inc.: NASA Contract NAS 3-17358). NASA CR-135083, 1976.
10. Crecelius, W.J.; Heller, S.; and Chiu, Y.P.: Improved Flexible Shaft-Bearing Thermal Analysis with NASA Friction Models and Cage Effects. SKF-AL-76P003, SKF Industries, Inc., February, 1976.
11. Bamberger, E.N.; et al.: Life Adjustment Factors for Ball and Roller Bearings - An Engineering Design Guide. American Society of Mechanical Engineers. 1971, pp. 8-16.

TABLE I. - TEST BEARING SPECIFICATION

Bearing dimensions, mm (in.):	
Bore	35 (1.3780)
Outside diameter.....	62 (2.4409)
Width.....	14 (0.5512)
Cage specifications:	
Diametral land clearance, mm (in.).....	0.406 (0.016)
Diametral ball-pocket clearance, mm (in.).....	0.660 (0.026)
Material.....	(a) AISI 4340, silver plated
Rockwell C hardness	28-36
Bearing ball specifications:	
Number.....	16
Diameter, mm (in.).....	7.14 (0.28)
Grade.....	10
Material.....	(b) CEVM M-50
Rockwell C hardness (minimum).....	60
Race conformity, percent:	
Inner.....	54
Outer.....	52
Race material:	
Inner and outer ring.....	(b) CEVM M-50
Rockwell C hardness (average).....	62
Assembly:	
Internal radial clearance, mm (in.).....	0.074 (0.0029)
Contact angle, deg.....	24

(a) AMS 6415; Ag platin, AMS 2412, 0.02-0.04mm (0.0008-0.0015 in.)
 (b) AMS 6490

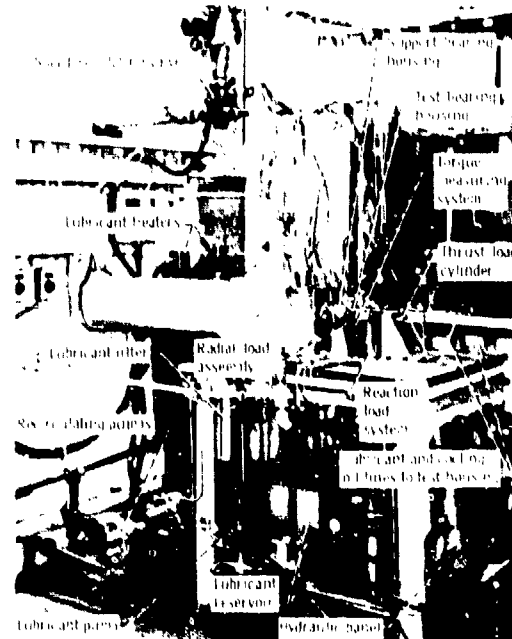


Figure 1. - High-speed, small-bore-bearing test machine.

TABLE II. - PROPERTIES OF TETRAESTER LUBRICANTS

Additives.....	Antiwear, corrosion and oxidation inhibitors, and antifoam
Kinematic viscosity, cS, at	
311 K (100°F).....	28.5
372 K (210°F).....	5.22
477 K (400°F).....	1.31
Flashpoint, K (°F).....	533(500)
Autogenous ignition temperature, K (°F).....	694(800)
Pourpoint, K (°F).....	214(-75)
Volatility (6.5 hr at 477 K (400°F)), wt%.....	3.2
Specific heat at 372 K (210°F) J/kg K (Btu/lb°F).....	2140 (0.493)
Thermal conductivity at 372 K (210°F) J/m sec K (Btu/hr ft °F).....	0.15 (0.088)
Specific gravity at 372 K (210°F).....	0.931

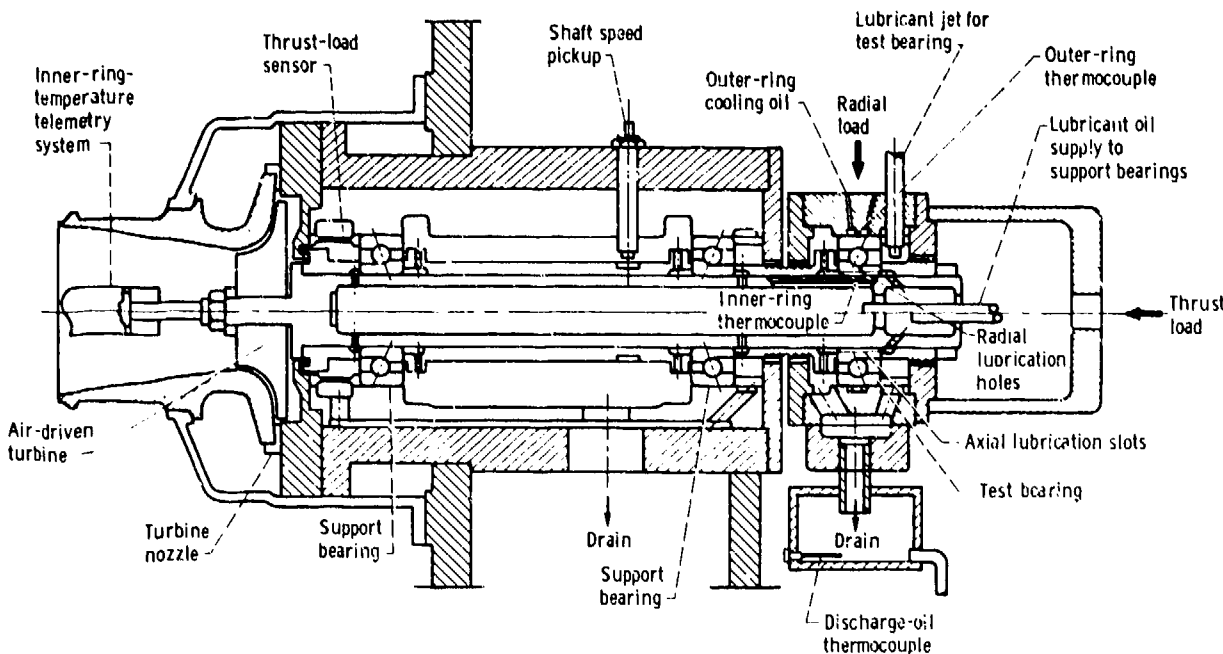


Figure 2. - Schematic of high-speed, small-bore-bearing test rig.

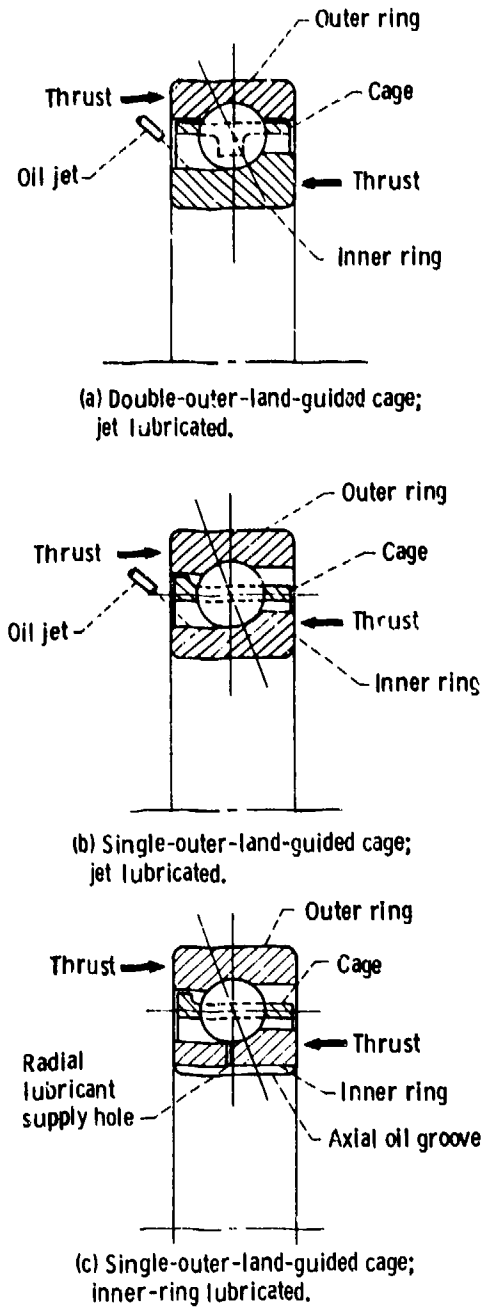


Figure 3. - Angular-contact ball bearing.

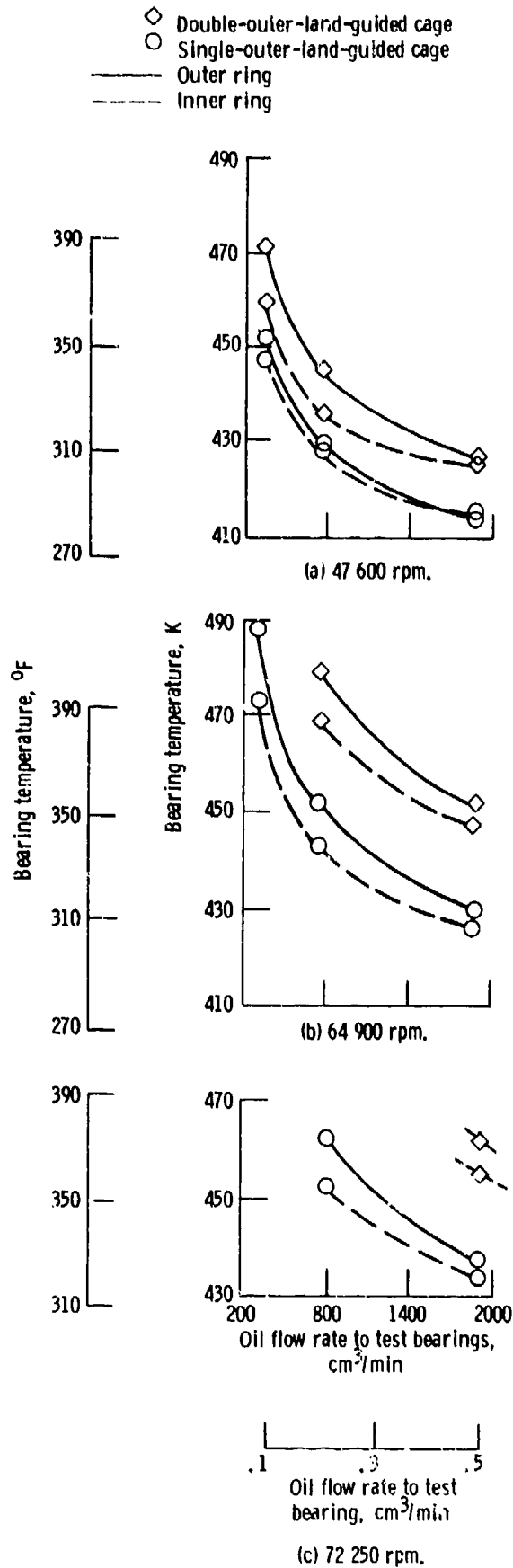


Figure 4. - Effect of oil flow on test bearing temperature for two bearing configurations. No outer-ring cooling; combined load: thrust, 667N (150 lb); radial, 222N (50 lb).

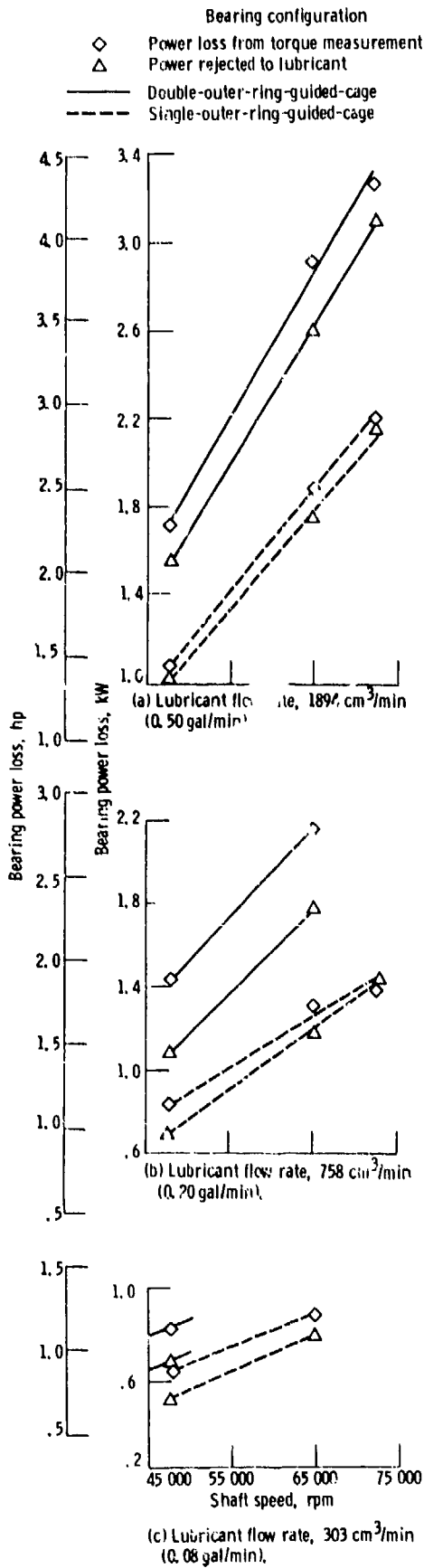


Figure 5. - Power loss as function of shaft speed for two bearing configurations. No outer ring cooling; combined load; thrust, 667 N (150 lb); radial, 222 N (50 lb).

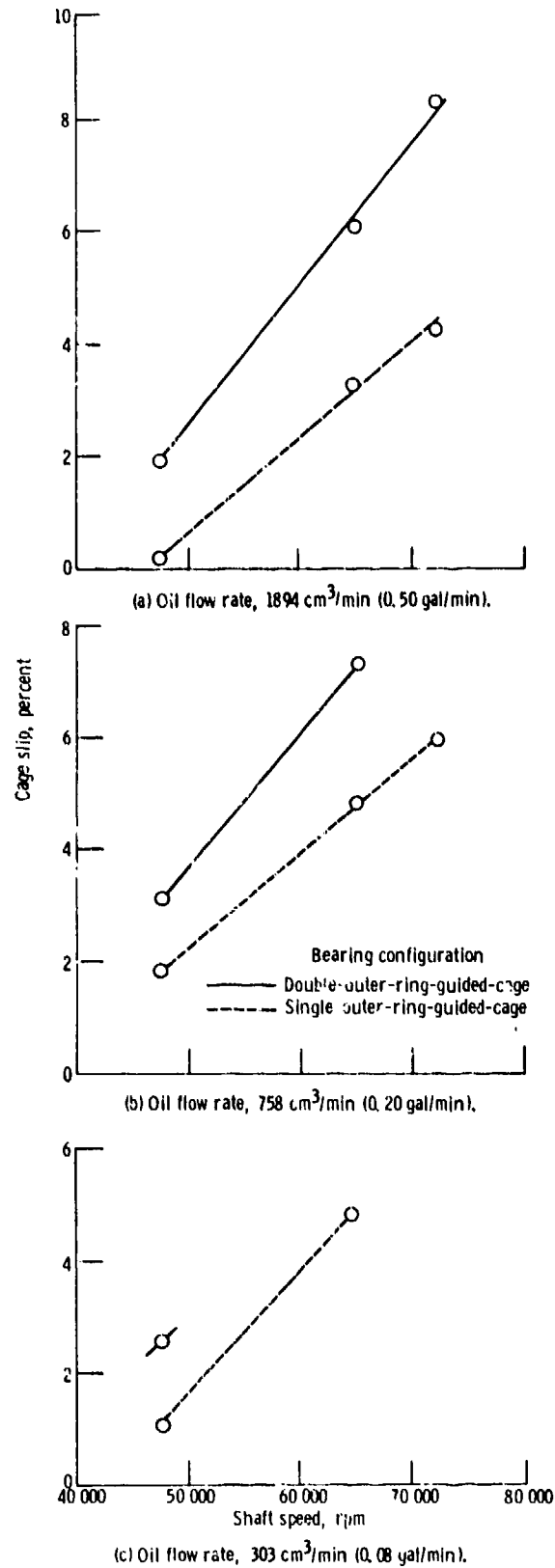


Figure 6. - Effect of shaft speed on cage slip for two bearing configurations with and without outer-ring cooling. Combined load; thrust, 667 N (150 lb); radial, 222 N (50 lb).

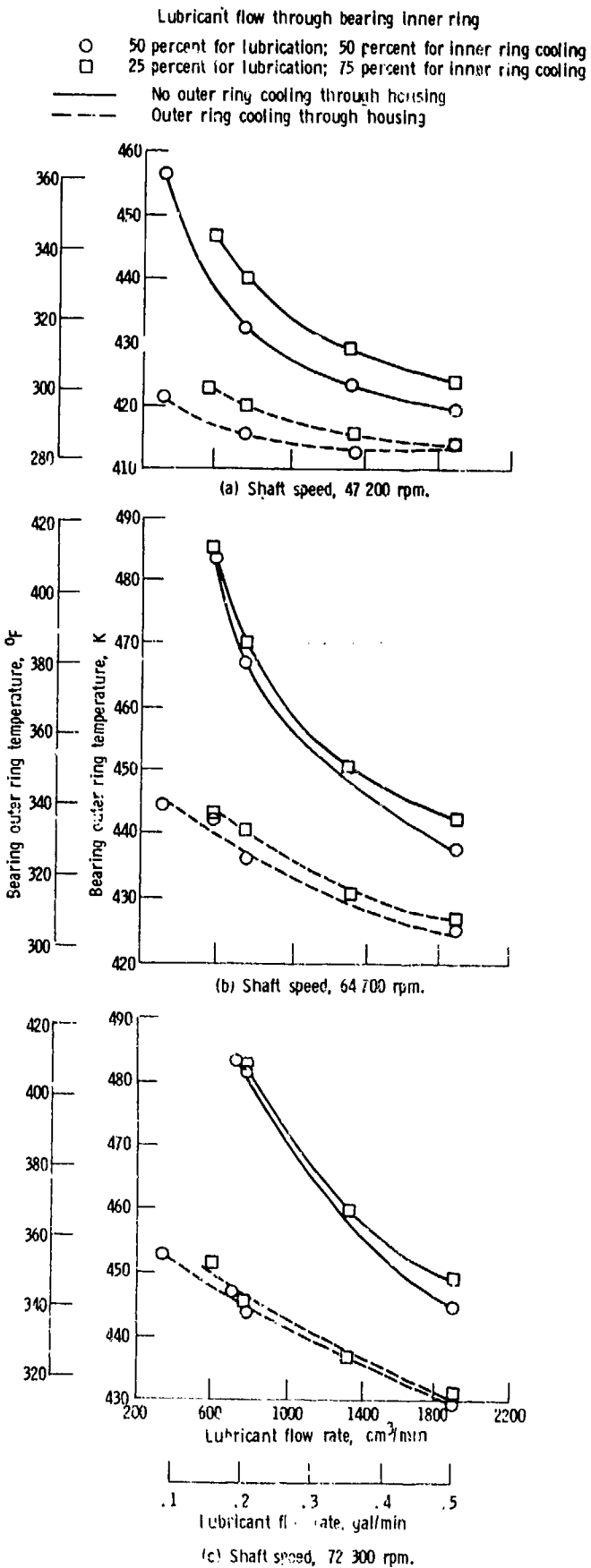


Figure 7. - Effect of lubricant flow rate on bearing outer ring temperature.

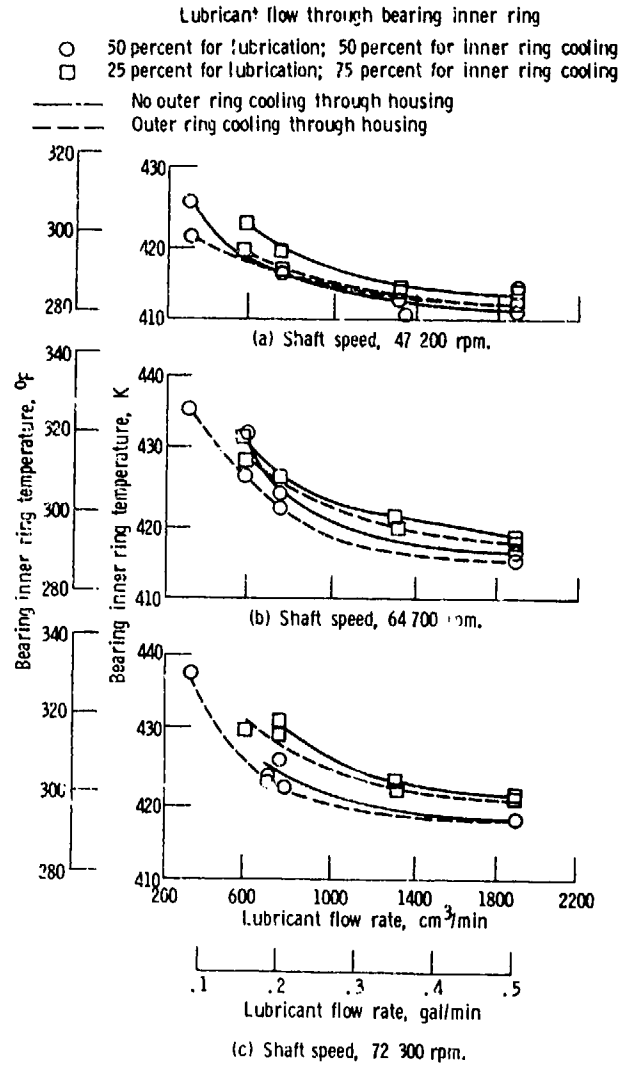


Figure 8. - Effect of lubricant flow rate on bearing inner ring temperature.

Lubricant flow through bearing inner ring

— 50 percent for lubrication; 50 percent for inner ring cooling
 - - - 25 percent for lubrication; 75 percent for inner ring cooling
 - - - Jet Lubrication
 ○ Outer ring
 □ Inner ring
 Solid symbols: outer ring cooling through housing; 50-50 percent

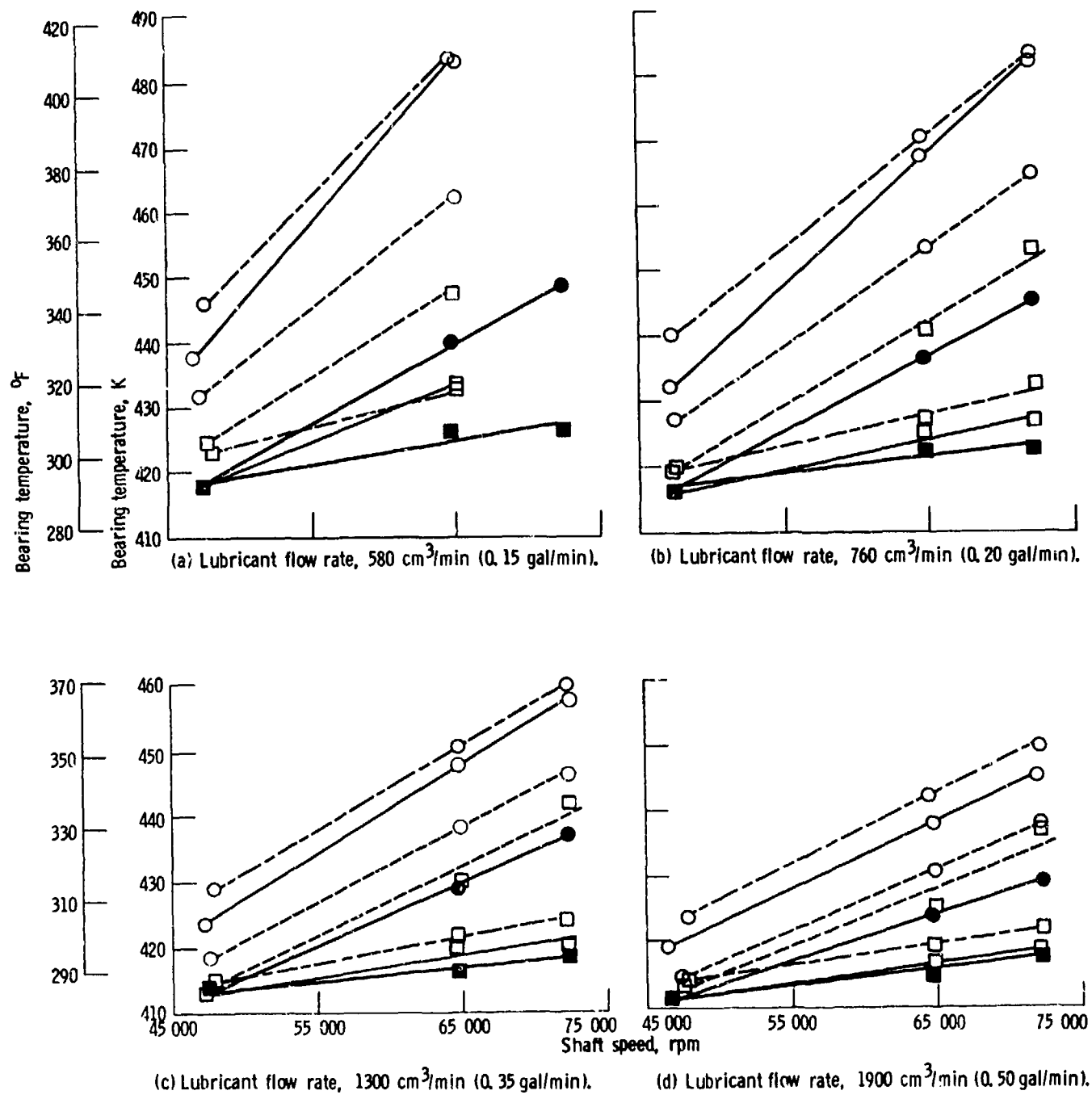


Figure 9. - Effect of shaft speed on test-bearing temperature for two different lubricant supply systems.

Lubricant flow through bearing inner ring
 50 percent for lubrication; 50 percent for inner ring cooling
 25 percent for lubrication; 75 percent for inner ring cooling
 Jet lubrication

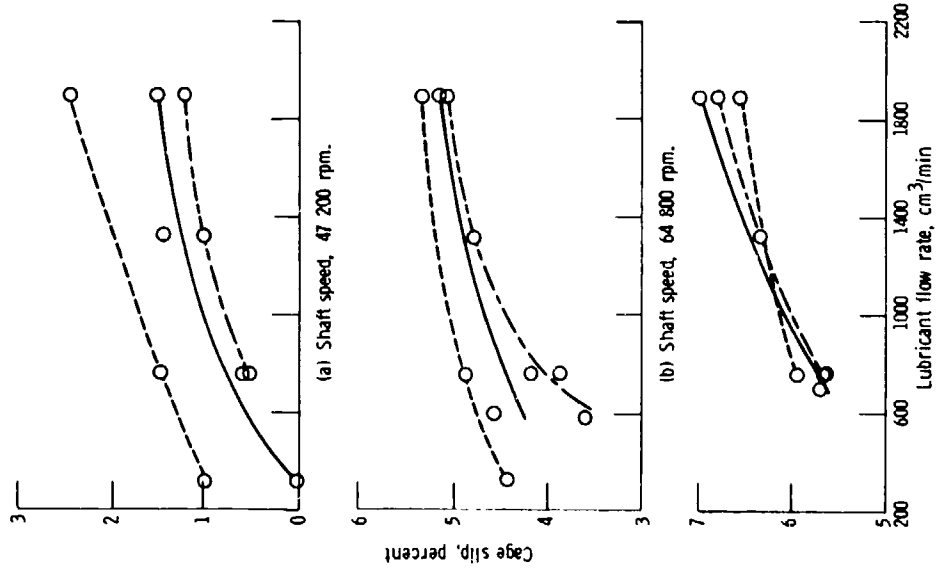


Figure 12. - Effect of lubricant flow rate on cage slip for two different lubricant supply systems. No outer ring cooling through housing.

Lubricant flow through bearing inner ring
 50 percent for lubrication; 50 percent for inner ring cooling
 25 percent for lubrication; 75 percent for inner ring cooling
 Jet lubrication

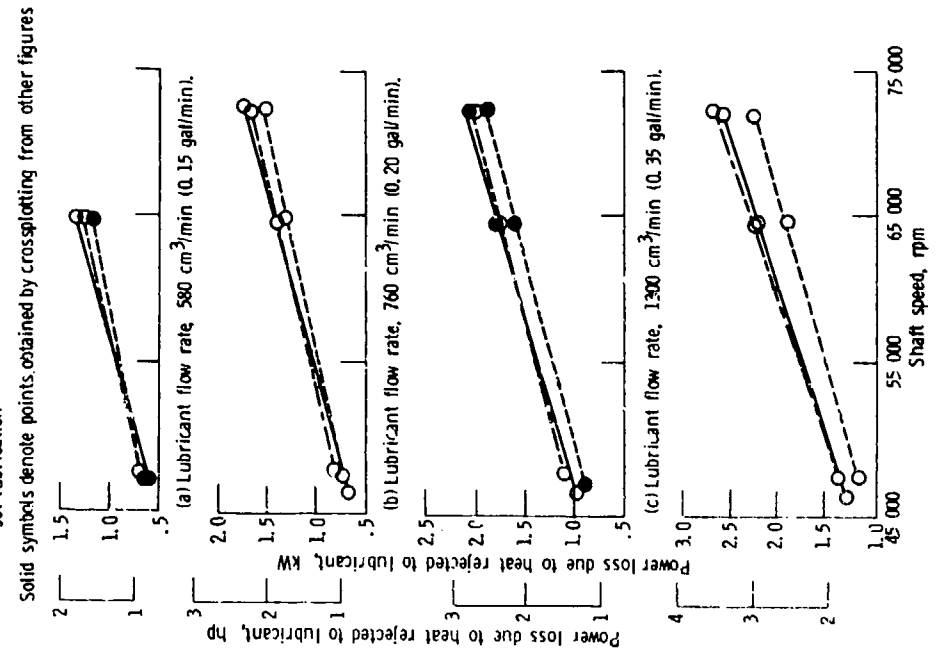


Figure 11. - Effect of shaft speed on power loss due to heat rejected to lubricant for two different lubricant supply systems. No outer ring cooling through housing.

Lubricant flow through bearing inner ring
 50 percent for lubrication; 50 percent for inner ring cooling
 25 percent for lubrication; 75 percent for inner ring cooling
 Jet lubrication

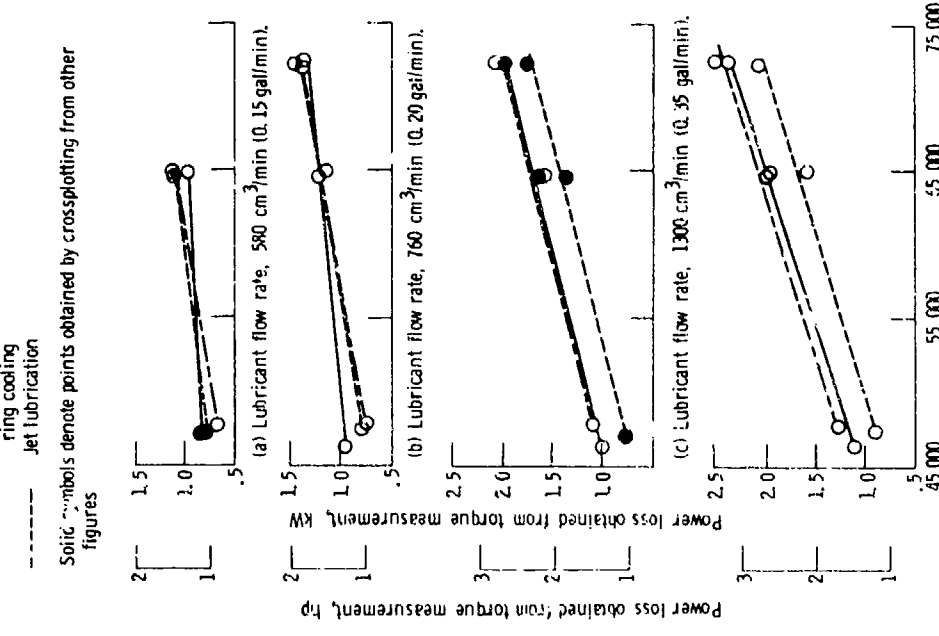


Figure 10. - Effect of shaft speed on power loss obtained from torque measurements for two different lubricant supply systems. No outer ring cooling through housing.

Solid symbols denote points obtained by crossplotting from other figures

Lubricant flow through bearing inner ring

- 50 percent for lubrication; 50 percent for inner ring cooling
- - - 25 percent for lubrication; 75 percent for inner ring cooling
- · - · Jet lubrication

Solid symbols denote points obtained by crossplotting from other figures

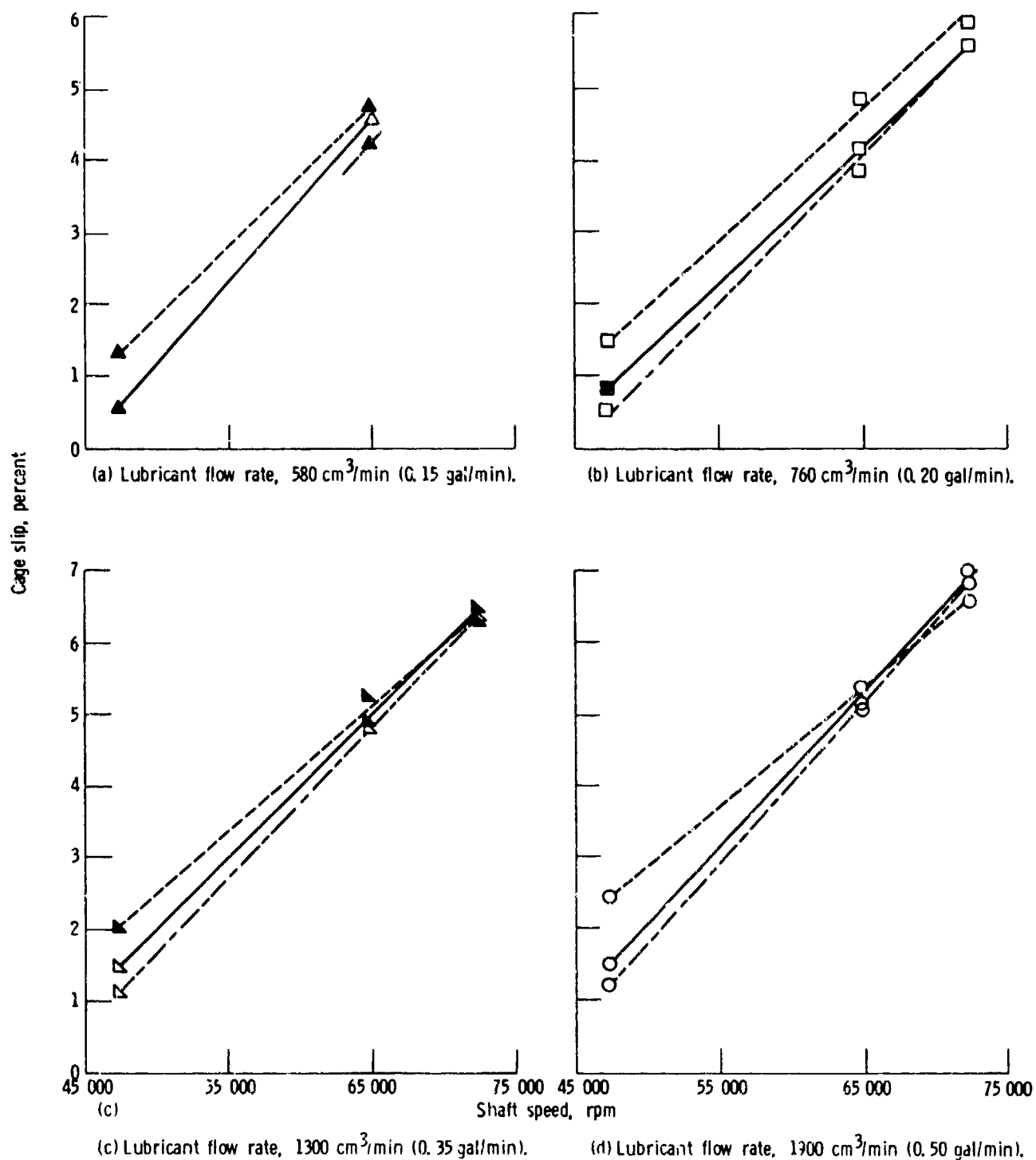


Figure 13. - Effect of shaft speed on cage slip for two different lubricant supply systems. No outer ring cooling through housing.

DISCUSSION

B. Courage, Rolls Royce Ltd, Bristol, UK

The reduction of power loss brought about by changing from a double to a single guiding land, as depicted in Figure 5(a) and (b) is a significant and very worthwhile achievement. Could the authors enlarge on the specific changes that bring this about, i.e., is it (a) the reduction of the total guide land surface, which seems unlikely, or (b) the change in cross-sectional shape of the cage which will clearly alter its general drag or churning potential, or (c) the increased bore diameter of the right-hand outer race shoulder which will reduce the volume of oil that can be entrained by the race, or (d) the overall increase in the exit path available for the oil. Some further testing would be of considerable value to isolate the major factors in order that more general advantage could be taken of this behaviour in future bearing designs.

Author's Reply

The single and double land guided cages had approximately the same masses. The land width of the double land guided cage was, of course, larger than that of the single land guided cage. Land clearances were the same, and they were all balanced for high speed operation. One shoulder of the outer race was relieved about .005 inches in the bearing with the single land guided cage. This is not considered significant. The center tabs in the double land guided cage were slightly larger so that it contacted the balls in the same place as in the single land guided cage.

D.G. Astridge, Westland Helicopters Ltd, Yeovil, UK

- (1) The authors' comment that no wear was observed with cage slip up to 7% is not surprising in the light of work carried out at Rolls Royce Derby (reported by C.F. Smith c. 1962) which demonstrated that it was the combination of cage slip and dynamic loading which resulted in skid-wear. Cage slip as high as 60% was possible without wear, with a well balanced shaft.
- (2) Some of the trends plotted (e.g., Figures 6, 13) look a little disconcerting relative to a zero speed origin. Have the authors tried plotting the data on paper with zero origins?

Author's Reply

- (1) The comment is self explanatory.
- (2) The plots are expected to go through zero origin. As an example, Figures 13(b) and (d) were complemented showing applicable data points from test runs at 27,600 rpm, not previously published in this paper. The point added in Figure 13(b) applies to lubrication through the inner ring, 50/50%. In Figure 13(d) points were added for the jet and the 50/50% inner ring lubricated bearings. The plots were then extrapolated through zero.

(See page 8-15 for diagrams)

P.T. Cornish, SNFA Bearings Ltd, UK

- (1) Cage designs used for 1 and 2 land guidance are radically different - different cross sectional shapes and different land widths - and therefore I cannot accept the statement that differences in results are entirely attributable to the number of guiding lands.
- (2) In your estimates of cage slip were all temperature and other effects, e.g., centrifugal, interference, taken into account in assessing the D.C. (Diametral Clearance)?
- (3) Did the change from 2 to 1 land guidance show any effect on cage dynamic stability?
- (4) In the experiments on the effect of oil flow distribution through the inner ring was the actual oil flow distribution measured at all and, if it was measured, was this done during the actual tests?
- (5) What is the error on the estimates of cage slip?

Author's Reply

- (1) Objective was to investigate bearings using "best" designs for single- and double-outer ring land guided cages. This approach demands some dimensional differences beyond "omitting one land". The single land cage was "L-shaped" to allow free evacuation of the oil. Mass of the cages was approximately equivalent.
- (2) The answer to this question is given on first para. of page 8-4.
- (3) Single land guided cages have run stable over hundreds of hours at speeds of 2.5 MDN.
- (4) Lube schemes are discussed in paragraph "Test Bearings" on page 8-2. Actual flow split at high speeds is very difficult to measure accurately and was not attempted.
- (5) The true "error" of cage slip values depends on the accuracy of the computer program (Reference 10).

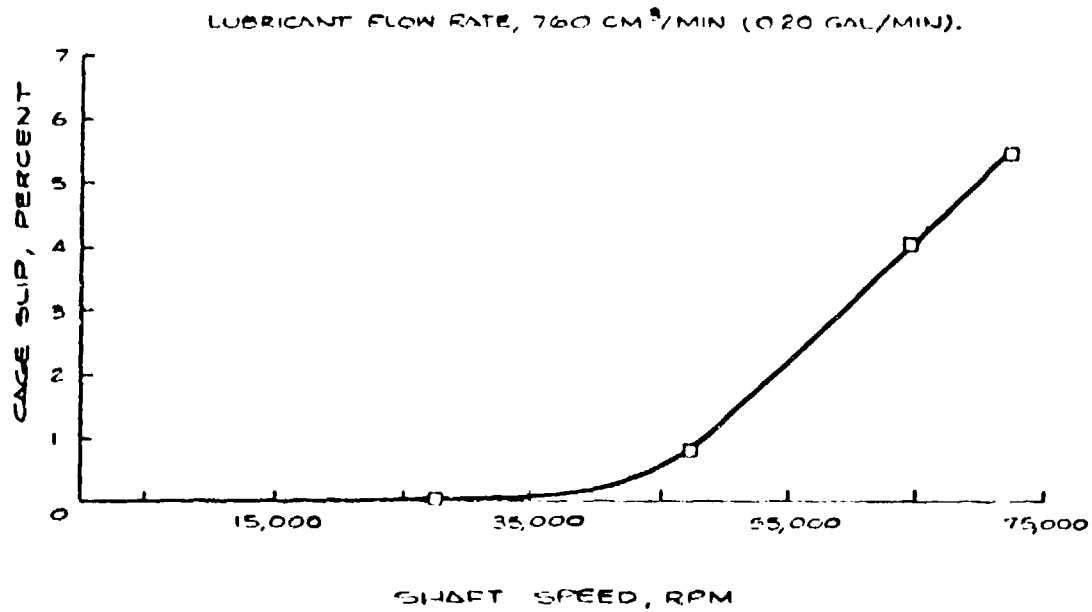


FIG. 13 (b) EXTENDED (I/R LUBRICATION, 50/50 %)

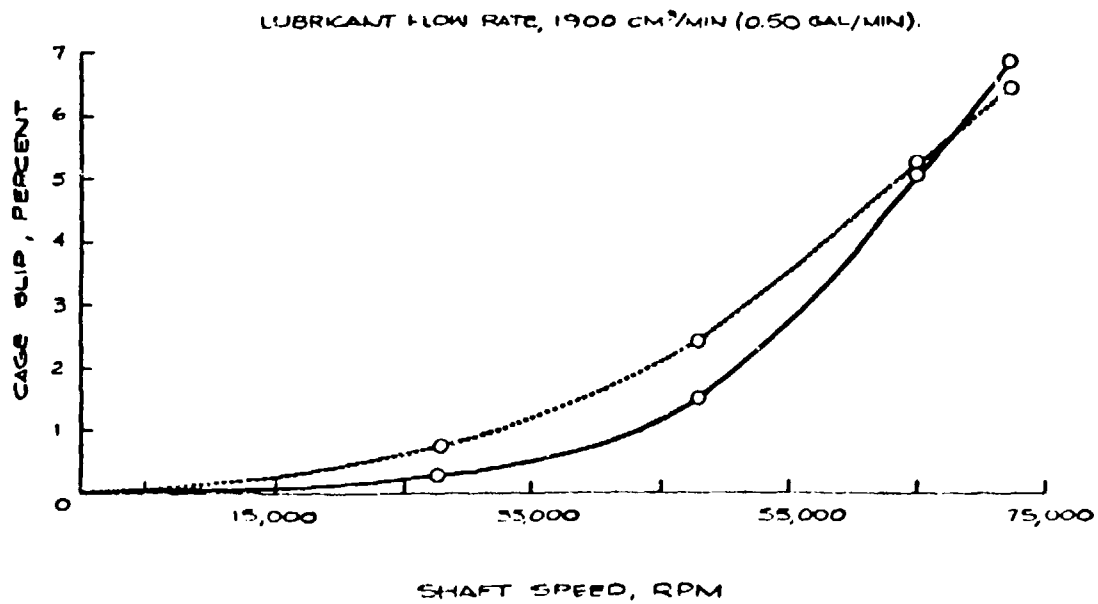


FIG. 13 (d) EXTENDED (JET-AND I/R LUBRICATION, 50/50 %)

MITIGATION OF THERMAL HAZARDS IN ROLLING
CONTACT BEARINGS THROUGH CORRELATED
COMPUTER ANALYSIS

V. A. SCHWARZ.
DOCTORAL STUDENT.

B. R. REASON.
SENIOR LECTURER IN TRIBOLOGY.

School of Mechanical Engineering
Cranfield Institute of Technology

Cranfield, Bedford MK43 0AL
England

SUMMARY

This paper presents an outline of investigations on the development of a predictive computer programme for establishing the likelihood of thermal hazards in rolling contact bearing assemblies.

Previous attempts at a tractable solution of the problem have been hampered by lack of practical knowledge on the division of generated heat in such bearings and on the formulation of suitable heat transfer coefficients.

Based on extensive experimental investigations carried out on a multi-capability test rig, the necessary data has been established, resulting in a programme capable of predicting spacial temperature distributions within bearing units operating under a wide variety of industrial conditions.

NOTATIONS

a	-	Length of larger side of a rectangular section	(m)
A	-	Area of a surface normal to heat flow	(m ²)
A _{1,2}	-	Area of surface 1, 2	(m ²)
b	-	Length of smaller side of rectangular section	(m)
b	-	Hertzian band width	(m)
C _{1,2,3,4}	-	Constants in the "Heat balance equations"	
C _{v,h}	-	Constants in the equations for the heat transfer coefficient	
D	-	Diameter of shaft	(m)
D _m	-	Mean diameter of bearing $D_m = \frac{D_o + D_i}{2}$	(m)
D _o	-	Outer diameter of bearing	(m)
D _i	-	Inner diameter of bearing	(m)
D _r	-	Roller diameter	(m)
E'	-	Reduced elastic modulus	(N/m ²)
		E' = 228 G P _a for bearing steels	
f	-	Geometrical factor $f = \frac{a}{b}$	
f _{0,1}	-	Friction torque coefficients, given by bearing manufacturers	
Fr	-	Radial load	(N)
h	-	EHL oil film thickness	(m)
h _{o,v}	-	Heat transfer coefficient	(W/m ² °C)
H _{min}	-	Minimum oil film thickness	(µm)
H _o	-	Thermal contact conductance	(W/m ² °C)
i, j	-	Subscript referring to Node i and j	
k	-	Thermal conductivity of a solid or a fluid	(W/m °C)
k _o	-	Thermal conductivity of an oil	(W/m °C)

$k_{1,2}$	-	Constants	
L	-	Length of heat transfer path	(m)
l	-	Roller effective length	(m)
M	-	Total bearing torque	(N.m)
M_o	-	Viscous friction torque	(N.m)
M_i	-	Load dependent torque	(N.m)
n	-	Shaft rotational speed	(r.p.m.)
N	-	Number of temperature Nodes	
Nu	-	Nusselt Number $Nu = \frac{h_c X}{k}, \frac{h_v D}{k}$	
Q	-	Heat flowing from a surface to a fluid	(W)
Q_e	-	External heat input to bearing assembly	(W)
Q_{i-o}	-	Heat conducted from inner to outer surface	(W)
Q_{i-j}	-	Heat conducted from surface 'i' to surface 'j'	(W)
Q_{Gen}	-	Heat generated in the bearing	(W)
Q_s	-	Heat flowing through contacting surfaces	(W)
R	-	Radius of housing bore	(m)
$RC(I)$	-	Residuals, in computer programme I = 1,2,.....N	
Re	-	Reynolds number $Re = \frac{w D}{v}, Re = \frac{v X}{v}$	
R_i	-	Inner radius of bearing ring	(m)
R_o	-	Outer radius of bearing ring	(m)
R'	-	Effective radius of cylinders in contact	(m)
		$R' = \frac{R_r R_{i,o}}{R_r + R_{i,o}}$	
R_r	-	Roller radius	(m)
t	-	Temperature	(°C)
$t_{r,t}$	-	Roller and track temperatures	(°C)
$t_{i,j}$	-	Temperature of Node 'i' and Node 'j'	(°C)
t_s	-	Surface temperature	(°C)
s_{1-2}^t	-	Temperature of surfaces 1 and 2	(°C)
$t_{f,a}$	-	Fluid temperature and air temperature	(°C)
T	-	Absolute temperature	(K)
T_{i-j}	-	Absolute temperatures of surfaces 'i' and 'j'	(K)
u	-	Combined surface velocity	(m/s)
		$u = \frac{1}{2} (u_{i,o} + u_r)$	
u_r	-	Roller surface velocity	(m/s)
$u_{i,o}$	-	Inner and outer race surface velocity	(m/s)
v	-	Linear velocity	(m/s)
w'	-	Load per unit length' in roller bearing	N/m
ω	-	Angular velocity	(rd/s)
X	-	Characteristic dimension of a heat transfer path eg: width, length or height of a surface or diameter of a cylinder	(m)
Z	-	Total number of rollers in a bearing	
β	-	Pressure coefficient of viscosity	(m ² /N)
ϵ	-	Effective "emissivity" between surfaces 'i' and 'j'	
σ	-	Stefan/Boltzmann constant = 5.76×10^{-8}	(W/m ² K ⁴)
ν	-	Kinematic viscosity of a fluid	(mm ² /s)
λ	-	Lubricant film parameter $\lambda = \frac{h}{\sigma}$	
η_o	-	Absolute viscosity of lubricant	(N.sec/m ²)
σ'	-	Composite roughness of two surfaces in contact	(µm)
		$\sigma' = (\sigma_r^2 + \sigma_t^2)^{\frac{1}{2}}$	
$\sigma_{r,t}$	-	Surface roughness of roller and track	(µm)

1. INTRODUCTION

The question of the prediction of the onset of thermal hazards in rolling contact bearing assemblies is of growing importance in modern industrial design as greater demands are made on the integrity of operating components and, with increased power output from prime movers, operating temperatures imposed on lubricating fluids continue to escalate.

A particular example of this is in the development of gas turbines for both commercial and military applications where operating bearing temperatures are reaching limits which create ultimate demands on bearing materials and lubricant capability. (Ref.1).

For specified operating conditions such as bearing load, speed and bulk lubricant temperature it is, clearly, of prime importance to the bearing designer if he could predict local spot temperature in the bearing, per se, together with a general spacial distribution of temperature in the complete assembly ie: shaft, seals, housing and other components.

Unfortunately, a tractable solution of the theoretical problem has not so far been forthcoming due, primarily, to a paucity of information on the spacial division of heat flux between component parts of the bearing assembly, together with the degree of heat 'take-up' by the lubricant itself.

This situation is further complicated, for theoretical purposes, by the limitation of available data on heat transfer coefficients, bearing in mind that, in all but the simplest cases, this information rests on pragmatical foundations.

As a means of circumventing the impasse created by this lack of measured data it was decided to construct an experimental test rig capable of accommodating a wide variety of bearing and housing configurations and to use this as an experimental datum against which predicted results from any theoretical model might be tested; the final objective being the creation of a viable computer programme for design application purposes.

From the standpoint of the mitigation of thermal hazards in rolling contact bearings this approach, it was thought, would appeal to the bearing designer, since not only would he have a new technique at his disposal for the prediction of spacial or localised temperatures, but he would be further secure in the knowledge that the veracity of the programme predictions had been corroborated experimentally.

The aim of the present paper is, therefore, both to present such a system and to illustrate to the user/designer the degree of correlation between experimental results and the computer suite predictions.

2. EXPERIMENTAL STUDY

2.1 Object

The test rig design was orientated specifically to the theoretical programme requirements and gave the following capabilities:-

- (1) Measurement of bearing load (radial and axial).
- (2) Variation of test shaft rotational speed.
- (3) Measurement of individual bearing power loss.
- (4) Variation of test bearing types.
- (5) Variation of bearing type combinations.
- (6) Variation of bearing housing configurations.
- (7) Measurement of input power to the system.
- (8) Choice of quantity and nature of lubricant.
- (9) Variation of bedplate mounting conditions.
- (10) Capability for spacial temperature measurement within bearing components; shafts, housings and at specific points within the bedplate/foundations.
- (11) Option of free or forced convective heat transfer.
- (12) Automatic data acquisition, processing and display.

2.2 Bearing Test Rig

(a) General

A full description of the test rig and instrumentation is given in Ref.2. and therefore only a cursory outline will be presented here.

Fig 1. indicates the general arrangement and illustrates two typical bearing options on the central section. By employing a generally symmetrical arrangement about the rig centre line, power losses could be measured on one bearing (through hydrostatic mounting systems) whilst temperature measurement could be conducted on a bearing of identical configuration at the opposite end of the test shaft; load being applied hydraulically. Power was supplied to the system from a three-phase electric motor of 3 HP via a hydraulic speed variator unit.

(b) Temperature Measurement System

For purposes of assessing the spacial temperature distribution throughout the bearing unit and its housing an array of Chromel/Constantan thermocouples is used each couple being located at a specific nodal point (see Fig.2.)

Thermocouple and transducer output signals are transmitted to a 'Fluke' 2200B' sixty-channel data-logger for capture and signal conditioning. The makers specified an accuracy of $\pm 0.1^{\circ}\text{C}$ between $0-100^{\circ}\text{C}$. This was confirmed on laboratory calibration.

Thermocouples for non-rotating nodal points are connected directly to the data logger. Rotating component signals are passed through high-quality silver/silver-graphite slip rings; the rings being air-cooled to negate thermal drift.

The data logger was programmable for various thermocouple combinations and included an electronic cold junction. Cyclic nodal scanning was a further feature of the unit.

3. TEST LUBRICANTS

3.1 Lubricants

Since mineral oil is employed as the lubricant in the vast majority of bath lubricated rolling contact bearing assemblies this was adopted; grades SAE 20 W, 30 and 50 oils were selected to produce a reasonably wide range of test viscosities.

The viscosity/temperature characteristics of the lubricants were established by laboratory measurement and these found to be expressible with excellent accuracy by the A.S.T.M. (or Walther) equation over all the range of experimental work ie:

$$\log \log (v + 0.6) = k_1 \log T + k_2 \quad (1)$$

The constants 'k₁' and 'k₂' were calculated for the three lubricants as follows:-

Oil	k ₁	k ₂
SAE 20 W	-3.6338	9.3356
SAE 30	-3.5022	9.0432
SAE 50	-2.3924	8.8435

3.2 Bearings

The basic bearing type, used herein as a representative example, is a Cylindrical Roller Bearing, type MRJ 1 $\frac{1}{2}$, the bearing details being as follows:-
Bore 44.45 mm (1.750 ins), Outer Diameter 107.95 mm (4.250 ins), Radial Clearance 0.0127 mm (0.0005 ins), Width 26.9875 mm (1.0625 ins). The flange configuration is as shown in Fig. 2, the cage, of machined brass, riding on the inner ring.

Surface roughness measured after testing was as follows:-

- (i) inner raceway 0.16 μm RMS
- (ii) outer raceway 0.17 μm RMS
- (iii) roller 0.09 μm RMS

4. TESTING PROCEDURE

4.1 General Testing

After initial 'running-in' of the bearings, tests were carried out at a series of speeds under a fixed load, after thermal equilibrium of the system had been attained (typically after five hours running). Speed was incremented in steps of 500 rpm from 500 to 5000 rpm, each increment usually taking about one hour running to stabilise.

Data capture was initiated upon thermal equilibrium being attained, the whole procedure being recapitulated for each fixed load value.

4.2 Specific Testing (Influence of Adjacent Bearings)

To study, in some detail, the influence of the adjacent bearings on the operating torque and temperature distribution of the front cylindrical roller bearing, three series of tests were repeated under the same conditions of speed, radial load, and lubricant, but with different conditions for the central bearing assembly, as follows:

- (a) Light axial preload (finger tight on the loading nut), applied to the twin taper roller bearings 'B' (Fig. 1).
- (b) Increased axial preload (3 KN), applied to the twin taper roller bearings.
- (c) Taper roller bearings 'B' replaced by the double row self-aligning spherical roller bearing 'C' (see Fig. 1 - below C.L.).

5. EXPERIMENTAL RESULTS

5.1 Effect of Adjacent Bearings on Temperatures and Torque

Fig. 1 illustrates, directly, the temperature distributions and operating torque of the cylindrical roller bearings. Each three-boxed temperature values and the three torque magnitudes correspond to the three different central bearing assembly conditions specified under Section 4.2.

5.2 Experimental and Theoretical Correlation

Fig. 2 shows typically measured temperatures for the front bearing unit. Predicted theoretical values, given by the computer programme at relevant nodal points, are included to indicate the correlation with the experimental results. The degree of agreement is noteworthy.

5.3 Effect of Speed on Torque and Nodal Temperatures

Fig. 3 indicates, as a typical case, the general trend of torque and nodal temperatures with varying speed. The particular example is taken at a constant radial load of 4000 N, using an SAE 20 oil.

6. THEORETICAL PREDICTION OF SPACIAL TEMPERATURES AND HEAT GENERATION

6.1 Mode of Heat Transfer

In studying the thermal equilibrium of the bearing assembly and its surrounding, the three basic modes of heat-transfer were employed, namely conduction, convection and radiation. These may be separately considered as follows:-

- (I) Conduction
(a) Solid

For radial conduction within the bearing rings and shaft the modified standard Fourier expression was employed viz:

$$Q_{i-o} = \frac{2\pi k W (t_i - t_o)}{\ln \left[\frac{R_o}{R_i} \right]} \quad - (2)$$

This expression was modified by Wong (3), as follows, for conduction from the inner circular surface of the bearing housing to its horizontal and vertical planar surfaces viz:

$$Q_{i-o} = \frac{2\pi k W (t_i - t_o)}{\ln \left[\frac{f \cdot a}{R} \right]} \quad - (3)$$

The thermal conductivity 'k' used in the above expression is a function both of the material and its temperature. The latter variation is of second-order importance and was therefore neglected.

- (b) Interfacial (Thermal Contact Resistance)

Conduction through a joint or surface interface in intimate contact is inhibited both by the limited area of the true contact and surface contamination at the interface.

These, in combination, act as a thermal resistance to heat transmission. The heat transfer may be expressed as:

$$Q_s = H_c A (t_1 - t_2) \quad - (4)$$

where 'H_c' is known as the "Thermal Contact Conductance" (the inverse of the Thermal Resistance).

In bearing assemblies thermal contact resistance is manifest at the contacting surfaces between the shaft and inner ring, outer ring and housing, and the housing and machine base proper.

- (c) Through the EHL oil film

It has been shown by Crook (4), Cheng (5), and Christensen (6) that heat transfer by conduction across the oil film is the chief heat transfer mechanism in an EHL contact, convection being negligible.

The heat transfer from a loaded roller to the inner and outer raceways can be calculated by using the following simple equation for heat transfer viz:

$$Q = k_o \frac{A}{h} (t_r - t_t) \quad - (5)$$

The lubricant's thermal conductivity 'k_o' is a function of temperature. Typically, the thermal conductivity of the SAE 30 testing oil varies with temperature as follows:-

$$k_o = 0.130 - 0.00007 t \quad - (6)$$

The heat flow area in equation (5) is given by the product of the roller effective length in the contact zone and the Hertzian flat width, viz:

$$A = l \cdot b \quad - (7)$$

The Hertzian band width 'b' may be expressed as:-

$$b = 6.691(10)^{-6} \left(\frac{4.08 F_r R'}{1Z} \right)^{0.5} \quad - (8)$$

In establishing the total heat flow area, the number of rollers under load must be determined.

It has been shown by Harris (7), Dowson and Higginson (8), and by Münnich et al. (9) that the load, acting on each roller within the Stribeck zone, varies with the angular position of the roller. Münnich et al. showed that the number of rollers under load, (and thus the load distribution) is dependent upon the housing configuration and on the thickness of the housing walls.

To simplify the analysis, i.e. to produce an averaging effect for purposes of heat transfer calculations, it was assumed that the radial load applied to the bearing is evenly distributed amongst the loaded rollers and that one quarter of the total number of rollers is supporting the load.

The length of heat transfer path 'h' in equation (5) is given by the EHL oil film thickness at the roller/raceway contacts. This is discussed in Section 7.

(II) Convection

Newton's law of cooling describes convective heat flow, viz:

$$Q_{s-f} = h_c A (t_s - t_f) \quad - (9)$$

'h_c' the "heat transfer coefficient", sometimes called the "film coefficient", is a complex function dependent upon the geometry and temperature of the heated surfaces and the temperature flow characteristics and physical properties (viscosity, thermal conductivity and density) of the convecting fluid.

Few analytical expressions exist for the heat transfer coefficients, empirical equations, obtained by combining experimental results with dimensional analysis, being employed. Thus the coefficients often appear as relationships between dimensionless number groups such as Nusselt (N_u), Reynolds (R_e), Grashof (G_r) and Prandtl (P_r) (depending on whether free or forced convection pertains). For free convection N_u = f(G_r, P_r) and for forced N_u = f(R_e, P_r) are used.

In the present analysis the following expressions for 'h_c' given by Fujii and Imura (10) and simplified by the authors, were employed:

For horizontal plates and cylinders facing upward:

$$h_c = 1.398 \left(\frac{t_s - t_a}{X_m} \right)^{0.25} \quad - (10)$$

and for similar vertical situations:

$$h_c = 1.452 \left(\frac{t_s - t_a}{X_h} \right)^{0.25} \quad - (11)$$

No completely reliable expressions for heat transfer coefficients between bearing components and lubricant could be found by the authors, although expressions are given by Bjordlund and Kays (11) and Gazley (12) pertaining to concentric cylinders. The existence of the rollers and cage between the bearing rings, however, tends to negate any analogy.

An expression used by Harris for heat flow across a flat plate, although of limited accuracy, was finally used in the present analysis, viz:

$$h_c = 0.332 \frac{k}{X} (R_e)^{1/2} (P_r)^{1/3} \quad - (12)$$

Characteristic terms in the previous equation were obtained as suggested by Harris (7).

The following expressions for additional heat transfer coefficients were employed, additionally, in the present analysis.

(a) For a rotating cylinder in air (after Dropkin and Carmi (13)):

$$\frac{h D}{k} = N_u = C_v P_r^{0.7} \quad - (13)$$

$$C_v = 0.076 \text{ for } 8000 < Re < 15000$$

$$C_v = 0.073 \text{ for } Re > 15000$$

(b) For a rotating disc in air (after Oehlbeck and Erian (14))

$$h_v = C_d \cdot k \cdot \left(\frac{\omega}{v} \right)^{1/2} \quad - (14)$$

where the coefficient ' C_d ' is mainly dependent on the geometry of the system.

(III) Radiation

Heat transfer by radiation between a small enclosed structure and a large surface may be expressed by a modified form of the Stefan/Boltzmann law viz:

$$Q = \sigma \epsilon A_1 (T_1^4 - T_2^4) \quad - (15)$$

Values of the emissivity ' ϵ ' between 0.6 and 0.8 are suggested by Jakob and Hawkins (15)

6.2 Heat Generation

Generated heat in rolling contact bearings is dependent on several factors. Chiefly these are rotational speed and lubricant viscosity and, to a lesser extent, applied load and bearing geometry. Loading effects, however, become much more important if the bearings are pre-loaded.

Specifically, the heat generated is a function of the bearing speed and torque. The latter, however, may be considered as the summation of the viscous friction torque M_o and the load dependent torque M_1 .

The following empirical equation were produced by Palmgren (16) for these torques ie:

$$M_o = f_o (Vn)^{\frac{2}{3}} D_m^3 \times 10^{-1} \quad \text{N.m.} \quad - (16)$$

$$M_1 = f_1 \cdot F_r \times D_m \quad \text{N.M.} \quad - (17)$$

6.3 Distribution of Generated Heat

Based on results produced by Garneil (17), Astridge and Smith (18) and work of the authors, the following distribution of generated heat was incorporated into the present programme.

(a) Roller Contacts at the Outer Raceway	20-40%
(b) Roller Contacts at the Inner Raceway	20-40%
(c) Roller Contacts in the Cage Pockets	8-12%
(d) Cage Contacts at the Land Riding Ring	8-12%
(e) Viscous Churning of Lubricant	8-40%
(f) Roller Guide Flange Contacts	0.1-0.8%

6.4 Temperature Prediction Technique

The so-called "Heat Balance Method" was employed as the foundation of the programme. The method, which is used where spacial temperature distributions are required in structures, is given in several textbooks on advanced heat transfer, a good description being that given by Welty (19).

Basically, the method involves the thermal equilibrium between a given point or 'node' and its surrounding nodes and is achieved by equating the total heat influx and efflux to and from the node (including any thermal energy generated at the node).

An initial step involves the spacial selection of nodes throughout the structure, the accuracy of the analysis being dependent on both the number of nodes and their position. Fig. 2 shows the nodes selected in the front bearing assembly, together with the measured and predicted nodal temperatures under the particular conditions of the test.

As a second step the "Heat Balance Method" is applied to each node, all modes of heat transfer being considered. For a bearing assembly these may be typically listed as follows:

- (a) Convective heat transfer from outer surface of the housing to the environment.
- (b) Radiation of heat from the outer housing surface to the surroundings.
- (c) Conductive heat transfer from the housing base to the foundations.
- (d) Conductive heat transfer from the bearing outer ring to the housing.
- (e) Conductive heat transfer from the bearing inner ring to the shaft.
- (f) Axial heat transfer by conduction along the shaft, including extraneous heat inputs outside the bearing system proper.
- (g) Convective heat transfer from the rotating shaft (and fins) to the surrounding fluids.
- (h) Convective heat transfer from the bearing components to surrounding fluid/fluids inside the housing.
- (i) Conductive heat transfer at the EHL contacts between the rollers and raceways.
- (j) Heat generation produced between surfaces in relative motion ie. roller contacts with bearing raceways, ring shoulders and cage pockets, cage contact with ring ribs, together with heat generation from viscous churning.

As an illustration of the method consider Fig. 4 as a typical bearing system with the following arbitrary selection of nodal points:

- Node 1 - Air surrounding housing - temperature 't₁'
 Node 2 - Outer surface of the housing - temperature 't₂'
 Node 3 - Inner surface of the housing - temperature 't₃'
 Node 4 - Bottom surface of the housing - temperature 't₄'

Applying the "Heat Balance Method" to Node '2' gives:

$$Q_{3-2} - Q_{2-4} - Q_{2-1} = 0 \quad - (18)$$

(For convenience it is assumed that the heat influx to Node 2 is positive).

'Q₃₋₂' and 'Q₂₋₄' illustrate conductive heat transfer from Node '3' to Node '2' and Node '2' to Node '4' respectively, whilst 'Q₂₋₁' illustrates convective and radiative heat transfer from Node '2' to Node '1'.

Equations (9), (3), (10) and (15), when simplified and applied to these nodes, yield:

$$Q_{3-2} = C_1(t_3 - t_2) \quad - (19)$$

$$Q_{2-4} = C_2(t_2 - t_4) \quad - (20)$$

$$Q_{2-1} = C_3(t_2 - t_1)^{1.25} + C_4(t_2 + 273.15)^4 - (t_1 + 273.15)^4 \quad - (21)$$

Substituting equations (19), (20) and (21) into equation (18) gives:

$$C_1(t_3 - t_2) - C_2(t_2 - t_4) - C_3(t_2 - t_1)^{1.25} - C_4(t_2 + 273.15)^4 + (t_1 + 273.15)^4 = 0 \quad - (22)$$

This final equation (22) is, therefore, the result of applying the "Heat Balance Method" to Node 2 for the specified conditions and illustrates a typical nodal equation.

It is obvious from the foregoing that similar equations will pertain for each nodal point giving a system of non-linear equations to be solved whose number is governed by the number of nodes selected.

The third and final step of the process is to obtain a simultaneous solution to the set of non-linear equations erected, which will then represent the predicted nodal temperatures. This was accomplished by use of the computer programme briefly described in Section 8.

7. E.H.L OIL FILM THICKNESS

The ability to predict the elastohydrodynamic lubrication (EHL) oil film thickness in a rolling contact bearing is clearly of importance both for the designer and the bearing user. Tallian (20), Bolton (21) and many other researchers showed that bearing fatigue life is directly related to the EHL oil film thickness, or, more specifically, to the lubricant parameter 'λ'.

$$\lambda = \frac{h}{\sigma} \quad - (23)$$

Bolton (21) proposed guidelines for the development of a simplified EHL oil film thickness formula for rolling contact bearings, to be expressed as a function of the bearing pitch diameter, rotational speed and kinematic viscosity of the lubricant.

Investigations by Dyson et al. (22) and by Wilson (23) showed that EHL oil film thicknesses calculated by the 'isothermal' theories correlate well with experimental values (provided the oil film thicknesses are less than 1μm).

Limited experimental information in the literature indicate that EHL oil film thicknesses in rolling contact bearings are usually < 0.7μm, examples of this being given by Pemberton and Cameron (24) and Wilson (25).

On the basis of the available information it was decided to develop a simplified EHL oil film thickness equation for the cylindrical roller bearings, based on the isothermal formula derived by Cheng (26), viz:

$$\frac{h}{R} = 1.987 \left[\frac{\eta_0 \beta U}{R'} \right]^{0.74} \left[\frac{W'}{E' R'} \right]^{-0.11} \quad - (24)$$

The product of the lubricant dynamic viscosity 'η₀' and the pressure viscosity coefficient 'β' may be conveniently expressed solely as a function of the kinematic viscosity 'ν', according to Bamberger et al. (27), i.e. (for mineral oils):

$$(\eta_0 \beta) = 8.5 \times 10^{-12} \nu^{1.18} \quad - (25)$$

Thus $(\eta_0 \beta)^{0.74} = 6.424 \times 10^{-9} \nu^{0.873} \quad - (26)$

The load parameter W' is given by Dowson and Higginson (8) as follows:

$$W' = \frac{a F_r}{Zl} \quad - (27)$$

The constant 'a' can be assumed, in general, as being equal to 4 to 5 for rolling contact bearings of conventional clearances (Ref. 8).

It can further be easily shown that:

$$\left(\frac{u}{R'}\right)_{i,o} = \frac{\pi}{60} \left(\frac{1 \pm s}{s}\right)n \quad - (28)$$

where $s = \frac{D_r}{D_m}$ - (29)

(The sign preceding 's' in the above equation relates to the speed parameter considered relative to either the inner or outer ring).

Substituting the above equations into eq. (24) the oil film thickness equations for the inner and outer race contact points are expressed as:

$$h_{i,o} = C_{i,o} \times D_m \times n^{0.74} \times v^{0.873} \times F_r^{-0.11} \quad - (30)$$

where $C_i = 3.052 \times 10^{-9}$
 $C_o = 3.512 \times 10^{-9}$

The lubricant kinematic viscosity ' ν ' in the above equation must be calculated from a mean between the roller and inner (or outer) race temperature, based on the fact that the EHL oil film thickness is governed by the lubricant properties (η_0, β) in the entry region of the EHL contact. Additionally, the following property, demonstrated by Crook (4) and other investigators, was taken into consideration:

"In considering the effect of lubricant viscosity upon film thickness, it is the viscosity of the oil at the temperature of the contacting surfaces which is the controlling factor and that the temperature of the oil supply has no influence, except insofar as it may affect the operating temperature of the solids in contact".

Thus the prediction of the oil film thickness between the rolling elements and raceways is only possible if the temperatures of the contacting surfaces can be measured or predicted with some degree of certainty. Conversely the calculation of the rolling element and races temperatures requires the calculation of these oil film thicknesses.

Therefore, the simultaneous calculations of the operating temperatures and EHL oil film thicknesses requires the service of a computer.

8. THE COMPUTER PROGRAMME

8.1 Programme Capability

At its present state of development the computer programme has the following capability.

- (a) Prediction of spacial temperature distribution at twenty nodes; these including bearing raceways, rollers, cage, housing, shaft and lubricant bath temperatures.
- (b) Calculation of lubricant viscosity at the operating temperature of the oil bath.
- (c) Reactive bearing torque and total heat generated.
- (d) EHL oil film thicknesses between a roller and raceways.

8.2 Programme Description

The computer programme was derived from a "Fortran" subroutine given by Powell (28). The package consists of hybrid solution method combining the "Newton Raphson" method and the so-called "Method of Steepest Decent". The former provides for the linearisation of the non-linear equations whilst the latter ensures a smooth and rapid convergence. Writing equation (22) in the form $RC(1) = f(\Delta t)$ then similarly, the remaining heat balance equations may be written as residuals $RC(2), RC(3) \dots RC(N)$.

The method of solution is iterative and requires an initially guessed input for the nodal temperatures. The computer routine then calculates the residuals $RC(I)$, these approaching zero as iteration proceeds. On reaching a specified convergence criterion, programme iteration ceases, the computed solutions being then obtained as a final print-out.

A monitor sub-routine programme is incorporated in the package which displays current nodal temperatures and residuals in print-out format, thereby enabling the convergence rate of the master programme to be studied. This optimises computer time utilisation and checks out any programme errors as iteration proceeds.

9. THEORETICAL RESULTS

9.1 Theoretical Temperature Distribution

Fig. 2 shows theoretical and experimental temperature distributions for the front bearing assembly (see Section 5.2).

9.2 'Heat Generation' and 'Heat Dissipation'

Fig. 5 shows both 'Heat Generation' and 'Heat Dissipation' curves plotted against temperature for two mineral oils, an SAE 50 and an SAE 30. Torque is also plotted on the ordinate. Since heat generation is a function of lubricant viscosity which is itself an inverse function of temperature, heat generation decreases with increasing temperature. The two 'Heat Generation' curves clearly show this effect.

Three 'Heat Dissipation' curves are plotted; the 'Total Heat Dissipation' corresponding to the sum of the 'Heat Dissipation through the Housing' and the 'Heat Dissipation through Shaft/Fins'.

9.3 Effect of Speed on Temperatures, Torque and Oil Film Thicknesses

Fig. 6 shows the effect of shaft speed on the bearing roller and rings temperatures, torque, and the EHL oil film thicknesses between the heaviest loaded roller and the inner and outer raceways. The particular example is plotted from a computer print-out taken for a constant radial load of 8000 N and for an SAE 20 W oil.

9.4 Effect of Load on Temperatures, Torque and Oil Film Thicknesses

The variation of the above factors, with load, is shown in Fig. 7 (for a constant shaft speed of 4000 rpm and a SAE 30 oil) and in Fig. 8 (for a constant shaft speed of 50 rpm and a SAE 50 oil).

10. DISCUSSION OF THE RESULTS

10.1 Experimental Results

(a) The influence of the heat dissipation potential

The effect of the housing configuration and heat dissipation potential is illustrated in Fig. 1 by the higher operating temperatures of the rear bearing, relative to the corresponding values for the front bearing, even though identical conditions of speed, radial load, and lubrication apply for the two bearings.

Essentially, convection and radiation are the chief heat dissipation mechanisms for the rear bearing housing (the only conduction path to the bedplate being via the twin loading pillars).

For the front housing, however, an appreciable amount of heat is conducted out of the bearing from the housing base to the bedplate. This conclusion is based on the significant temperature gradients found in the lower part of the housing (see Figs. 1 and 2). Calculations based on those values showed that some 45% of the total heat generated is dissipated in this way. Similar calculations showed that about 25-30% of the total heat generated is dissipated through the rotating shaft/fins assembly.

A further effect of the housing/bedplate arrangement and heat dissipation potential is illustrated by the spacial temperature distribution above and below the horizontal centre-line (see Fig. 2); the upper half of the system being at higher temperatures. This could not be attributed, solely, to the direction of the radial load, since earlier tests carried out by the authors (loads being applied in the opposite direction) on the same bearing unit showed the same effect, i.e. temperatures being higher for points above the horizontal centre-line.

In the light of the discussion on the influence of conductive heat transfer through the housing base, it can be concluded that this is the controlling factor; heat conduction through the base outweighing heat lost from the outer surface of the housing by radiation and convection to produce the asymmetrical temperature profile.

This was confirmed on measuring temperatures on the rear roller bearing housing. The temperatures of points above the horizontal centre-line being lower than those of the corresponding points below that line (see Fig. 1) irrespective of oil flow between the hydrostatic bearing surfaces. Although this trend is exactly the opposite of that for the front bearing housing, the explanation lies with the larger surface areas for convective and radiative heat dissipation above the horizontal centre-line.

(b) The effect of the adjacent bearings on the operating temperature and torque of the test bearing.

From the temperature distributions shown in Fig. 1 it can be seen that the front cylindrical roller bearing temperatures varied by as much as 50%, even though the speed, radial load, and lubrication conditions applied to that bearing were the same for the three 'boxed' temperatures corresponding to each nodal point.

Similarly, as shown in Fig. 1, the operating torque of the rear cylindrical roller bearing was appreciably affected by the different operating temperatures of the adjacent bearings, i.e. the higher the adjacent bearing temperatures the lower the operating torque. This can be easily explained by both the lubricant viscosity decrease, consequent on the increased temperature, and the high dependence of torque on lubricant viscosity.

The operating temperature of the twin taper roller bearing assembly is strongly dependent on the axial preload (see Fig. 1). This, together with correlated phenomena observed by the authors, will be discussed in a further paper.

(c) The effect of speed on operating temperature and torque

Not surprisingly, the bearing operating temperatures increased with shaft speed, as shown in Fig. 3; the inner ring temperature being usually about 12% higher than that of the outer ring. Bearing torque increased with speed, for speeds < 2000 rpm, but tended to remain constant, or even to decrease, for speeds above that value. This can be explained on the basis of the viscosity/temperature characteristics of the lubricant and the torque/lubricant viscosity relationship.

10.2 Theoretical Results

(a) Thermal balance

Fig. 5 shows the relationship between the total generated heat (including any external input) and the total heat dissipated, plotted against the mean operating temperature, for two test oils - an SAE 30 and an SAE 50. A corresponding ordinate for the friction torque has also been included. The condition is for a fixed load of 2090 N at an operating speed of 4000 rpm.

Points of interception of the 'Heat Generation' and 'Heat Dissipation (TOTAL)' curves give thermal equilibrium and indicate both the relevant temperature and friction torque for this condition.

It is immediately obvious that the choice of the thinner oil would result in a lower operating temperature and reduced power loss in the bearing unit. It is to be appreciated that a lower operating temperature implies increased oil change periods, since oil oxidation rate is lowered. Fig. 5 shows the importance of an accurate prediction of heat dissipation rate from the unit. If this is underestimated (for example, if the 'Heat Dissipation through the Shaft/Fins' is neglected), there is an apparent anomaly in that the predicted temperature is higher than the experimental one whilst the calculated friction torque is less than the corresponding measured value. This phenomenon is readily explained, however, on the basis of the rapid decrease of the lubricant viscosity with temperature. If the heat dissipation is underestimated in the programme, the predicted bearing temperature will, obviously, be higher, giving a lower operating viscosity. Since the friction torque equation used in the programme itself contains a viscosity term, the result will be a predicted friction torque lower than the measured value.

Apparently, this effect was experienced by Schwartz (29), the experimental and theoretical findings reported in his paper giving a similar 'contradiction' in the two parameters.

The effect was demonstrated, somewhat dramatically for the authors, during early development work on the programme. In normal running, after thermal equilibrium is reached, an appreciable amount of heat is conducted out of the bearing from the housing base to the bedplate as already discussed (Section 10.1). This was, initially, underestimated in the earlier programmes the resultant temperatures being, in certain cases, almost 50% higher than those experimentally measured whilst the calculated torques from the programme were, unexpectedly, less than those measured on test.

The problem was finally resolved when thermocouples were placed at the base of the housing. These gave a true picture of the extent of the conduction heat transfer. It is to be inferred, therefore, in the light of this, that close attention to foundation conduction is highly relevant when assaying thermal problems in bolted-down bearing housings.

(b) Theoretical and Experimental Temperature Correlation

When the proper extent of the conduction heat dissipation through the housing base to the bedplate was considered in the computer programme, a good correlation was obtained between theoretical and experimental results (see Fig. 2).

A further important aspect was that roller temperatures predicted by the programme were some 10%-20% higher than those predicted at the inner ring (see Fig. 2). Since roller temperatures were not measured in the test rig, current literature was searched for some substantiation of this result. Experimental confirmation of this prediction was found in the results obtained by Norlander and Stackling (30), who, in bearing tests, measured rolling element temperatures some 18% higher than those measured at the inner ring.

(c) EHL Oil Film Thicknesses Results

The EHL oil film thicknesses, calculated by the computer programme simultaneously with the temperature distributions, are in good agreement with the experimental results obtained by Pemberton and Cameron (Ref. 24) and by Wilson (Ref. 25). In particular, the variation of oil film thickness with shaft speed (see Fig. 5) follows closely the experimental trend reported in Ref. 24, both in magnitude and shape of the plotted curve.

For the reasons pointed out in Section 7, the mean between the roller and raceway temperature was considered when calculating lubricant viscosity and the corresponding oil film thicknesses. It is to be inferred that the high roller temperature (relative to the raceways temperature) has, therefore, a significant effect upon oil film thicknesses.

Predicted oil film thicknesses between the rollers and the inner race are lower than those between the rollers and the outer race. This is due, not only to the better degree of conformity and larger equivalent radius for the outer raceway contact, but also because the outer race temperature is lower than that of the inner raceway. Typically, as shown in Fig. 6, oil film thicknesses increased rapidly with speed (up to about 500 rpm) and then decreased gradually with speed (for speeds above that value). This is due to the significant decrease of both the lubricant viscosity and the pressure-viscosity coefficient as temperature increased with speed.

Figs. 7 and 8 shows the variation of oil film thicknesses, temperatures and torque with applied load. It can be seen that oil film thicknesses decreases by about 20% for a load increase of 100%. This dependence on load is slightly in excess of that found by Crook, as reported in Ref. 8. Oil film thicknesses decreases with load not only due to the load parameter in eq. (24) but also due to the effect of load upon the operating temperatures (see Figs. 7 and 8).

11. CONCLUSIONS

11.1 General Programme Utilisation

It has been demonstrated that a viable computer programme based on analytical heat transfer techniques may be developed, which is capable of predicting spacial temperature distributions, power loss and EHL oil film thickness in rolling contact bearing assemblies and that the predicted results yield close correlation with experimentally measured values.

From the standpoint of the industrial user/designer the programme capability can be utilised in several ways:

(a) Optimum lubricant selection, commensurate with the bearing duty, may be obtained at the design state to ensure minimum power loss.

(b) For a lubricant already specified the designer can quantify any critical thermal situation from a knowledge of both the spacial distribution of temperature and the prediction of any localised temperature. This is of particular importance when temperature effects induce dimensional changes.

(c) Since different bearing geometries may be catered for in the programme, the designer can study the effect of differing housing configurations on spacial temperature distribution and heat dissipation. Foundation effects can also be catered for.

(d) For bearing assemblies already in operation the industrial user can assess potential energy saving through lubricant viscosity changes, together with the effects of extended oil change periods when bearing temperatures have been lowered.

11.2 Specific Design Considerations

If thermal analysis indicates that bearing cooling is necessary, particular attention should be paid to which components should be specifically cooled.

External cooling of the housing will, in general, reduce dimensions between inner and outer rings if the shaft temperature itself is not appreciably affected. The resulting reduction in element clearances may produce an increase in power loss tending to invoke a thermal spiral. In extreme cases this may produce bearing seizure.

Since it has been shown that a significant percentage of heat is conducted through the housing base to the foundations, excessive conduction in the area may produce similar effects to those outlined above.

Good surface contact at the interface is important. Variations in surface flatness may produce large variations in local contact resistance with a concomitant variation in conductive heat transfer. Thermal distortions arising from this effect may be passed to the bearing with a consequent reduction in its useful life.

Shaft cooling will undoubtedly increase radial clearances between rollers and rings of plain roller bearings. However, in pre-loaded assemblies axial contraction of the shaft may increase the pre-load, dependent upon the mounting arrangement, particularly in taper-roller bearings with "indirect" mounting. Such a situation may incur high local temperatures between rollers and guide flanges. Overcooling of a shaft can, additionally, initiate inner ring creep or even slippage.

It is seen from the foregoing that variations of temperature within a bearing assembly are capable of producing exceedingly complex effects and this highlights the importance, to the designer, of having a thermal analysis programme capable of predicting local temperatures.

Such a programme, it may be inferred, not only mitigates any propensity towards premature mechanical failure initiated from thermal sources but, from the standpoint of basic design and subsequent in-service duty, provides a further step towards an optimum level of total energy conservation.

The economic implications of such an approach, particularly in the long-term aspect, are deemed worthy of consideration.

11.3 EHL Oil Film Thickness

It has been demonstrated that EHL oil film thickness between rollers and raceways of both lubricated rolling contact bearings decreases gradually with speed (in the moderate and high speed range). This is due to the significant effect of temperature on both the lubricant viscosity and the pressure-viscosity coefficient.

It has also been demonstrated that the effect of load on EHL oil film thicknesses can be considerable in both lubricated rolling contact bearings.

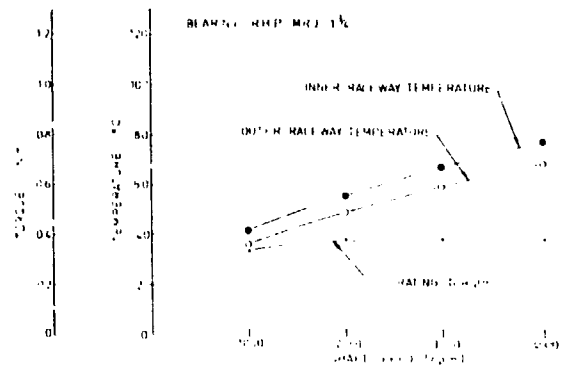
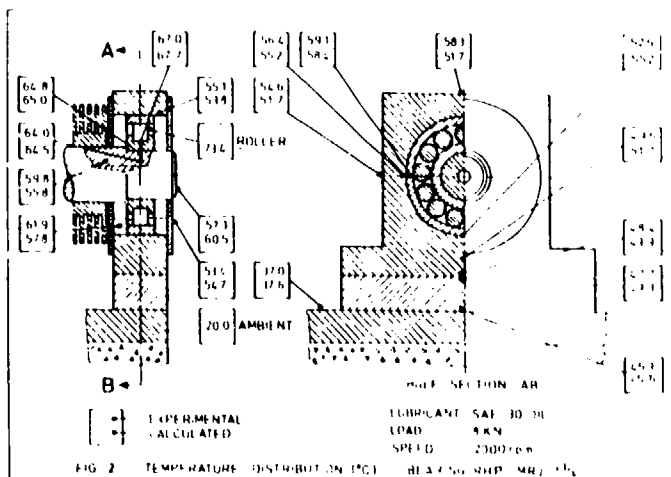
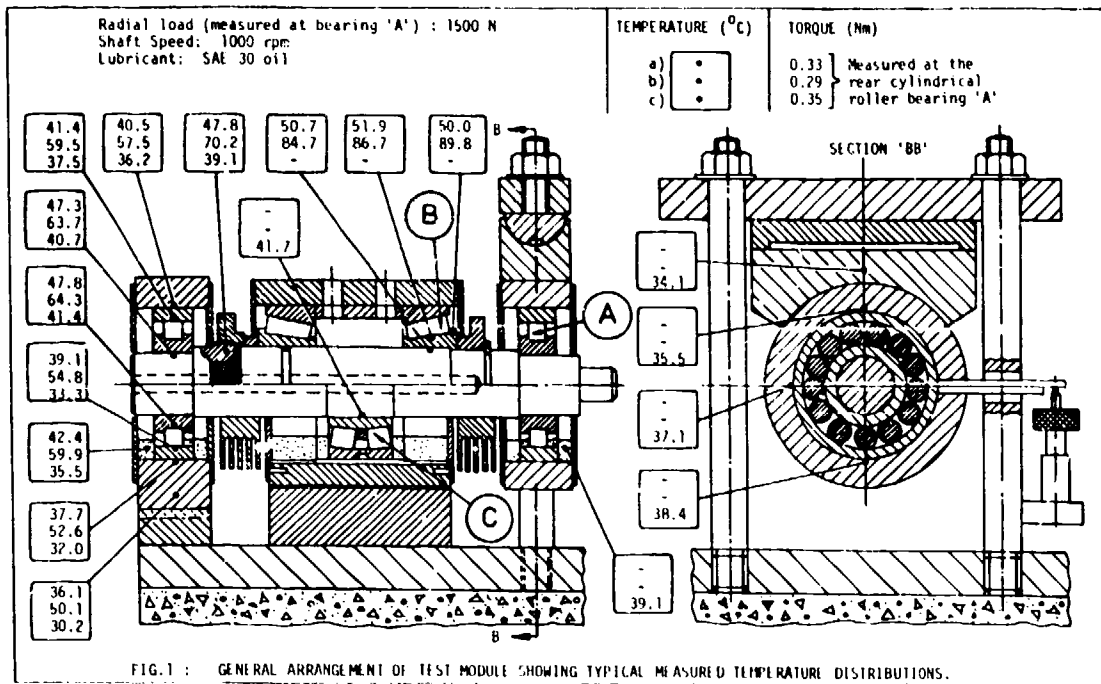
REFERENCES

1. BISSON, E.E. and ANDERSON, W.J. 'Advanced Bearing Technology', NASA, Washington D.C., 1964.
2. REASON, B.R. and SCHWARZ, V.A. 'Thermal Prediction Technique for Extending In-Service Life of Roller Bearing Assemblies', Symposium on 'Innovation for Maintenance Technology Improvements' Mechanical Failures Prevention Group - National Bureau of Standards, Gaithersburg, Washington D.C., U.S.A., 1981.
3. WONG, H.Y. 'Heat Transfer for Engineers' Ed. Longman Inc., New York, 1977, 18-22.
4. CROOK, A.W. 'The Lubrication of Rollers - IV. Measurements of Friction and Effective Viscosity', Phil. Trans., Series A255, 1963.
5. CHENG, H.S. 'A Refined Solution to the Thermal-Elastohydrodynamic Lubrication of Rolling and Sliding Cylinders', ASLE Transactions, 8, 1965, 397-410.
6. CHRISTENSEN, H. 'Starvation and Collapse of E.H.L. Films', Elastohydrodynamic and Related Topics, Proc. 5th. Leeds-Lyon Symposium on Tribology, 1978, Paper II(iii), 28-34.
7. HARRIS, T.A. 'Rolling Bearing Analysis' Ed. John Wiley and Sons, Inc., New York, 1966, 452-474.
8. DOWSON, D. and HIGGINSON, G.R. 'Elasto-Hydrodynamic Lubrication' SI. Edition, Pergamon Press, 1977.
9. Münnick, H. et al. 'The Effect of Elastic Deformation on Load Distribution in Rolling Bearings', The Ball Bearing Journal No. 155, 1968, 3-12.
10. FUJII, T. and IMURA, H. 'Natural Convection Heat Transfer from a Plate with Arbitrary Inclination', Int. J. Heat and Mass Transfer, Vol. 15, 1972, 755-767.
11. BJORKLUND, I.S. and KAYS, W.M. 'Heat Transfer between Concentric Rotating Cylinders', Trans. ASME, Journal of Heat Transfer, August 1959, 175-186.
12. GAZLEY, C. 'Heat Transfer Characteristics of the Rotational and Axial Flow between Concentric Cylinders', Trans. ASME, Vol. 80, 1958, 79-90.
13. DROPKIN, D. and CARMI, A. 'Natural Convection Heat Transfer from a Horizontal Cylinder Rotating in Air, Trans. ASME, May 1957, 741-749.
14. OEHLBECK, D.L. and ERIAN, F.F. 'Heat Transfer from Axisymmetric Sources at the Surface of a Rotating Disc', Int. J. Heat and Mass Transfer, Vol. 22, 1979, 601-610.
15. JAKOB, M. and HAWKINS, G.A. 'Elements of Heat Transfer' Ed. John Wiley and Sons, 1957.
16. PALMGREN, A. 'Ball and Roller Bearing Engineering', 3rd. ed., S.H. Burbank and Co. Inc. Philadelphia, 1959.
17. GARNELL, P. 'Further Investigations of the Mechanics of Roller Bearings', Proc. Inst. Mech. Engrs., Vol. 181, pt. 1, No. 16, 1966-67, 339-348.
18. ASTRIDGE, D.G. and SMITH, C.F. 'Heat Generation in High-Speed Cylindrical Roller Bearings', Elastohydrodynamic Lubrication 1972, Inst. Mech. Engrs., London, 83-94.
19. WELTY, J.R. 'Engineering Heat Transfer', Ed. John Wiley and Sons, New York., 1974, 38-65.
20. TALLIAN, T.E. 'On Competing Failure Modes in Rolling Contact', ASLE Transactions, 10, 1967, 418-439.
21. BOLTON, W.K. 'Elastohydrodynamics in Practice', International Symposium on 'Rolling Contact Fatigue: Performance Testing of Lubricants', The Institute of Petroleum, London, Pub. Heyden and Son Ltd., London, 1976, 17-25.
22. DYSON, A. et al. 'The Measurement of Oil-Film Thickness in Elastohydrodynamic Contacts', Proc. Inst. Mech. Engrs., Vol. 180 Pt. 3B, 1965-66, 119-134.
23. WILSON, A.R. 'An Experimental Thermal Correction for Predicted Oil-Film Thicknesses in Elastohydrodynamic Contacts', Thermal Effects in Tribology, Paper VII(i), I. Mech. E., 179-190.
24. PEMBERTON, J.C. and CAMERON, A. 'An Optical Study of the Lubrication of a 65 mm Cylindrical Roller Bearing', Journal of Lubrication Technology, Trans. ASME, Vol. 101, July 1979, 327-337.
25. WILSON, A.R. 'The Relative Thickness of Grease and Oil-Films in Rolling Bearings', Proc. Inst. Mech. Engrs., Vol. 193, 1979, 185-192.

26. CHENG, H.S. 'A Numerical Solution of the Elastohydrodynamic Film Thickness in an Elliptical Contact'. Journal of Lubrication Technology, Trans. ASME, January 1970, 155-162.
27. BAMBERGER, E.N. et al. 'Life Adjustment Factors for Ball and Roller Bearings. An Engineering Design Guide', The American Society of Mechanical Engineers, 1971.
28. POWELL, M.J.D. 'A Fortran Subroutine for Solving Systems of Non-Linear Algebraic Equations', from 'Numerical Methods for Non-Linear Algebraic Equations', by RABINOWITZ, P. Ed. Gordon and Breach, 1970, 115-161.
29. SCHWARTZ, J.I. 'Friction-Induced Heating in Axially Loaded Ball Bearings', Trans. ASME, Journal of Lubrication Technology, January 1970, 105-112.
30. NORLANDER, G. and STACKLING, H. 'A New Way to Measure Temperature', Ball Bearing Journal 172, 1972, SKF, 1-6.

ACKNOWLEDGEMENTS

The authors would like to thank the staff of the Cranfield S.M.E. Instrumentation Laboratory for their invaluable assistance. In addition, V.A. Schwarz gratefully acknowledges the sponsorship from Escola Federal de Engenharia de Itajuba, and CAPES, Brazil, under which it was possible to carry out this study.



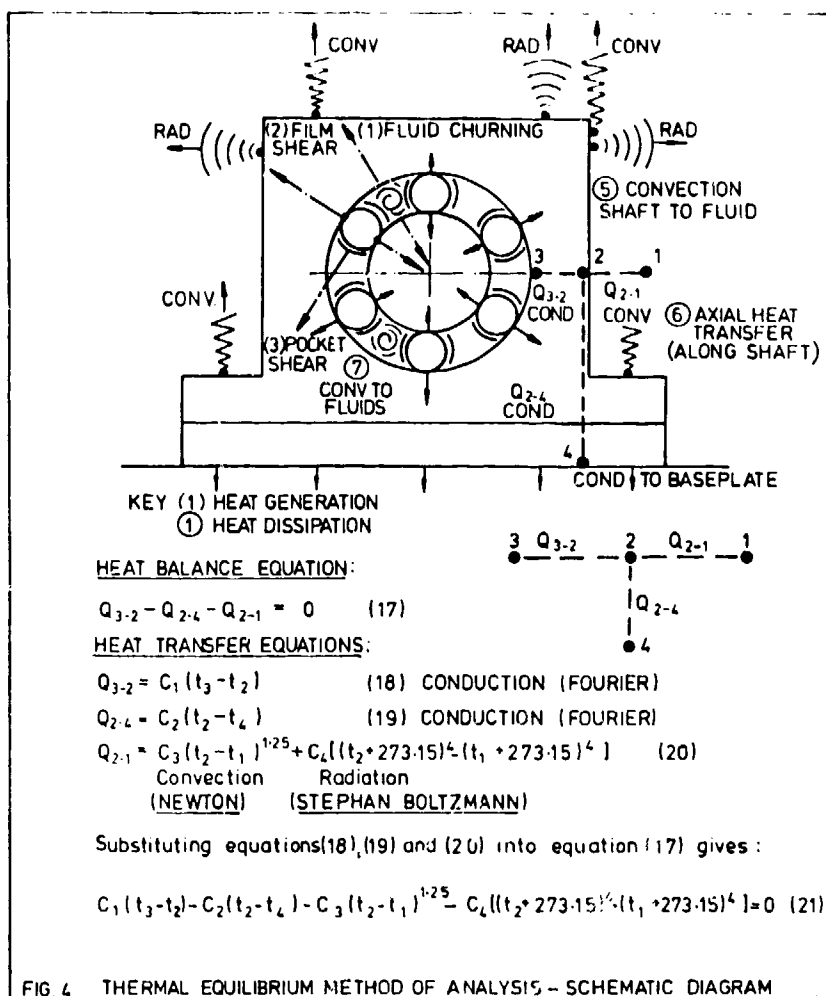
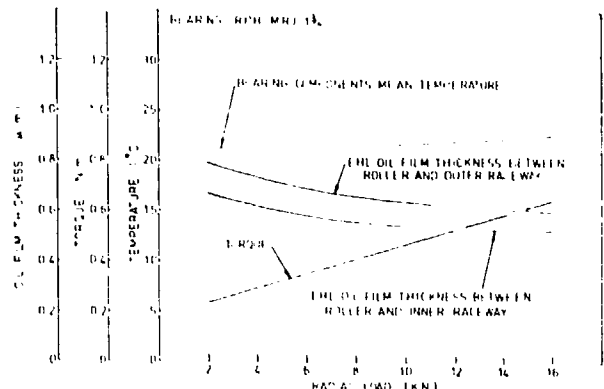
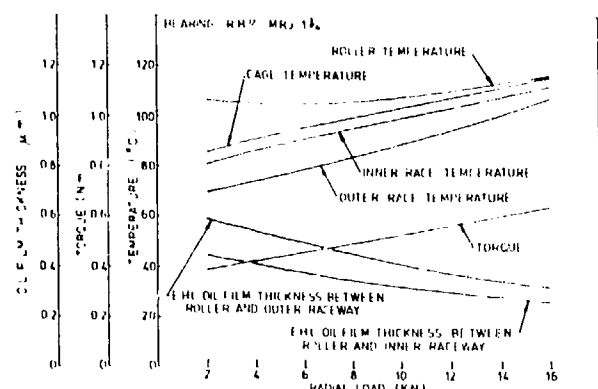
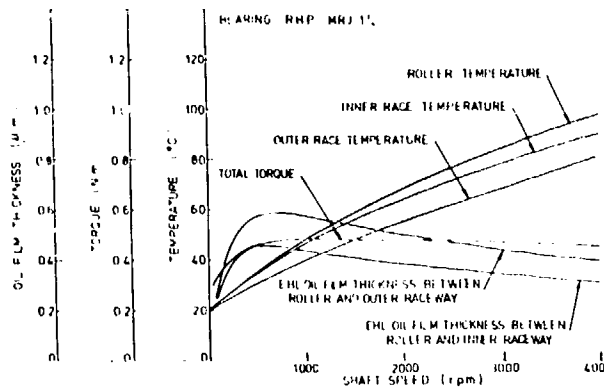
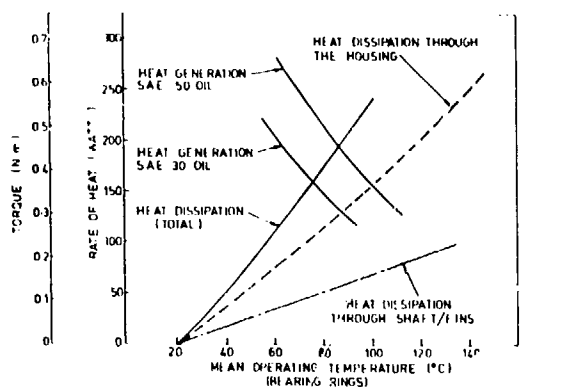


FIG. 4 THERMAL EQUILIBRIUM METHOD OF ANALYSIS - SCHEMATIC DIAGRAM



DISCUSSION

M.A.H. Sequeira, Portuguese Oil Co., Po
Did you use an SAE 20 or 20W oil?

Author's Reply

We used a 20W oil. There is a typing error but the graph is correct.

K.J. Brown, Ontario Hydro, Toronto, Ca

First, I would like to offer encouragement for your planned efforts to determine experimental heat transfer coefficients of bearing housings. I would also like to suggest that the effects of dirty or coated housing more typical of an industrial environment be considered. Regarding your model - can it be used to study the possibility of thermal "runaway" during start-ups. This can happen in the case of an inner race being hotter or getting hotter more rapidly than the outer race or bearing housing. Also, can the model do cases in which a parameter is changed. This could be the case when cooling water is discontinued and it is desired to know the time to reach a limiting or alarm value.

Author's Reply

As it now stands, the model cannot be used to study transients. That is a much more difficult problem than the steady state, and we feel that we would rather crawl before we try walking. At the moment we are looking at getting thermal equilibrium first of all. We will look at transient conditions later on.

ELASTOHYDRODYNAMIC LUBRICATION OF ELLIPTICAL CONTACTS*

Bernard J. Hamrock
 NASA Lewis Research Center
 21000 Brookpark Rd.
 Cleveland, Ohio 44135 U.S.A.

SUMMARY

The emphasis of the first part of the paper is on fully flooded, elastohydrodynamically lubricated, elliptical contacts. A fully flooded conjunction is one in which the film thickness is not significantly changed when the amount of lubricant is increased. The relevant equations used in the elastohydrodynamic lubrication (EHL) of elliptical contacts are briefly described. The most important practical aspect of the elastohydrodynamic theory is the determination of the minimum film thickness within the contact. The maintenance of a fluid film of adequate magnitude is an essential feature of the correct operation of lubricated machine elements. The results to be presented show the influence of contact geometry on minimum film thickness as expressed by the ellipticity parameter and the dimensionless speed, load, and materials parameters. Film thickness equations are developed for materials of high elastic modulus, such as metal, and for materials of low elastic modulus, such as rubber. The solutions for materials of high elastic modulus are sometimes referred to as "hard EHL," and the solutions for materials of low elastic modulus as "soft EHL." In addition to the film thickness equations that are developed, plots of pressure and film thickness are presented. These theoretical solutions for film thickness have all the essential features of previously reported experimental observations based on optical interferometry.

In the second part of the paper a theoretical study of the influence of lubricant starvation on film thickness and pressure in hard and soft elliptical elastohydrodynamic contacts is presented. From the results for both hard and soft EHL contacts a simple and important dimensionless inlet boundary distance is specified. This inlet boundary defines whether a fully flooded or a starved condition exists in the contact. It is also found that the film thickness for a starved condition can be written in dimensionless terms as a function of the inlet distance parameter and the film thickness for a fully flooded condition. Contour plots of pressure and film thickness in and around the contact are shown for fully flooded and starved conditions. The theoretical findings are compared directly with results obtained experimentally.

INTRODUCTION

Elastohydrodynamic lubrication is a form of fluid-film lubrication where elastic deformation of bearing surfaces becomes significant. It is usually associated with highly stressed machine components of low conformity, such as gears and rolling-element bearings. This lubrication mechanism is also encountered with soft bearing elements, such as rubber seals and tires. The common factor in these applications is that local elastic deformation of the solids provides coherent fluid films and thus asperity interaction is prevented.

Historically, elastohydrodynamic lubrication may be viewed as one of the major developments in the field of tribology in the twentieth century. It not only revealed the existence of a previously unsuspected regime of lubrication in highly stressed and nonconformal machine elements, such as gears and rolling-element bearings, but it brought order to the understanding of the complete spectrum of lubrication ranging from boundary to hydrodynamic.

CONFORMAL AND NONCONFORMAL SURFACES

Hydrodynamic lubrication is generally characterized by surfaces that are conformal. That is, the surfaces fit snugly into each other with a high degree of geometrical conformity, so that the load is carried over a relatively large area. Furthermore the load-carrying surface area remains essentially constant while the load is increased. Fluid-film journal and slider bearings exhibit conformal surfaces. In journal bearings the radial clearance between the shaft and the bearing is typically one-thousandth of the shaft diameter; in slider bearings the inclination of the bearing surface to the runner is typically one part in a thousand.

Many machine elements have contacting surfaces that do not conform to each other very well. The full burden of the load must then be carried by a very small contact area. In general the contact areas between nonconformal surfaces enlarge considerably with increasing load but are still small compared with the contact areas between conformal surfaces. Some examples of these nonconformal surfaces are mating gear teeth, cams and followers, and rolling-element bearings.

*Previously presented as a lecture for First Symposium INTERTRIBO '81, Stvbske Pleso, Czechoslovakia, April 27-29, 1981 (NASA TM-81647).

The load per unit area in conformal bearings is relatively low, typically only 1 MN/m^2 and seldom over 7 MN/m^2 . By contrast, the load per unit area in nonconformal contacts, such as those that exist in ball bearings, will generally exceed 700 MN/m^2 , even at modest applied loads. These high pressures result in elastic deformation of materials such that the elliptical contact areas are formed for oil film generation and load support. The significance of the high contact pressures is that they result in a considerable increase in fluid viscosity. Inasmuch as viscosity is a measure of a fluid's resistance to flow, this increase greatly enhances the lubricant's ability to support load without being squeezed out of the contact zone.

The undeformed geometry of contacting solids can be represented in general terms by two ellipsoids. The two solids with different radii of curvature in a pair of principal planes (x and y) passing through the contact between the solids make contact at a single point under the condition of zero applied load. Such a condition is called point contact and is shown in figure 1, where the radii of curvature are denoted by r 's. It is assumed throughout the paper that convex surfaces, as shown in figure 1, exhibit positive curvature and concave surfaces, negative curvature. Therefore, if the center of curvature lies within the solid, the radius of curvature is positive; if the center of curvature lies outside the solid, the radius of curvature is negative. It is important to note that if coordinates x and y are chosen such that

$$\frac{1}{r_{ax}} + \frac{1}{r_{bx}} > \frac{1}{r_{ay}} + \frac{1}{r_{by}} \quad (1)$$

coordinate x then determines the direction of the semiminor axis of the contact area when a load is applied and y , the direction of the semimajor axis.

RELEVANT EQUATIONS

The relevant equations used in elastohydrodynamic lubrication of elliptical contacts are as follows:

Lubrication equation (Reynolds equation)

$$\frac{\partial}{\partial x} \left(\frac{\rho h^3}{\eta} \frac{\partial p}{\partial x} \right) + \frac{\partial}{\partial y} \left(\frac{\rho h^3}{\eta} \frac{\partial p}{\partial y} \right) = 12u \frac{\partial}{\partial x} (\rho h) \quad (2)$$

where
$$u = \frac{u_a + u_b}{2}$$

Viscosity variation

$$\eta = \eta_0 e^{\alpha p} \quad (3)$$

where η_0 is the coefficient of absolute or dynamic viscosity at atmospheric pressure and α is the pressure-viscosity coefficient of the fluid.

Density variation (for mineral oils)

$$\rho = \rho_0 \left(1 + \frac{0.6 p}{1 + 1.7 p} \right) \quad (4)$$

where ρ_0 is the density at atmospheric conditions.

Elasticity equation

$$w = \frac{2}{E'} \iint_A \frac{p(x,y) dA}{\sqrt{(x-x_1)^2 + (y-y_1)^2}} \quad (5)$$

where

$$E' = \frac{2}{\left(\frac{1-v_a^2}{E_a} + \frac{1-v_b^2}{E_b} \right)} \quad (6)$$

Film thickness equation

$$h = h_0 + S(x,y) + w(x,y) = h_0 + \frac{x^2}{2R_x} + \frac{y^2}{2R_y} + w(x,y) \quad (7)$$

where

$$\frac{1}{R_x} = \frac{1}{r_{ax}} + \frac{1}{r_{bx}} \quad (8)$$

$$\frac{1}{R_y} = \frac{1}{r_{ay}} + \frac{1}{r_{by}} \quad (9)$$

The problem is to calculate the pressure distribution in the contact and at the same time allow for the effects that this pressure will have on the properties of the fluid and on the geometry of the elastic solids. The solution will also provide the shape of the lubricant film, particularly the minimum clearance between the solids. A detailed description of the elasticity model used is given in Dowson and Hamrock (1976), and the complete EHL theory is given in Hamrock and Dowson (1976).

DIMENSIONLESS GROUPING

The variables resulting from the isothermal elliptical contact theory developed in Hamrock and Dowson (1976) are

E'	effective elastic modulus, N/m^2
F	normal applied load, N
h	film thickness, m
R_x	effective radius in x (motion) direction, m
R_y	effective radius in y (transverse) direction, m
u	mean surface velocity in x direction, m/s
α	pressure-viscosity coefficient of fluid, m^2/N
η_0	atmospheric viscosity, $N \cdot s/m^2$

From these variables the following five dimensionless groupings were established:

Dimensionless film thickness

$$H = \frac{h}{R_x} \quad (10)$$

Ellipticity parameter

$$k = \frac{a}{b} = 1.03 \left(\frac{R_y}{R_x} \right)^{0.64} \quad (11)$$

Brewe and Hamrock (1977) used a linear regression by the method of least squares to obtain the simplified equations given in equation (11). That is, for given sets of pairs of data $\{(k_j, (R_y/R_x)_j)\}$, $j = 1, 2, \dots, n$, a power fit using a linear regression by the method of least squares resulted in obtaining equation (11).

Dimensionless load parameter

$$W = \frac{F}{E' R_x^2} \quad (12)$$

Dimensionless speed parameter

$$U = \frac{\eta_0 u}{E' R_x} \quad (13)$$

Dimensionless materials parameter

$$G = \alpha E' \quad (14)$$

The dimensionless film thickness can thus be written as a function of the other four parameters

$$H = f(k, U, W, G) \quad (15)$$

The influence of the dimensionless parameters k , U , W , and G on minimum film thickness H_{\min} is presented later for both hard and soft contacts.

The set of dimensionless groups $\{H, k, U, W, G\}$ is a useful collection of parameters for evaluating the results presented in this paper. It is also comparable to the set of dimensionless parameters used in the initial elastohydrodynamic analysis of line contacts, and it has the merit that the physical significance of each term is readily

apparent. However, a number of authors, for example, Moes (1965-66) and Theyse (1966), have noted that this set of dimensionless groups can be reduced by one parameter without any loss of generality.

FULLY FLOODED HARD-EHL RESULTS

By using the numerical procedures outlined in Hamrock and Dowson (1976) the influence of the ellipticity parameter and the dimensionless speed, load, and materials parameters on minimum film thickness has been investigated for hard-EHL, fully flooded contacts (Hamrock and Dowson, 1977b). The ellipticity parameter k was varied from 1 (a ball-on-plate configuration) to 8 (a configuration approaching a rectangular contact). The dimensionless speed U was varied over a range of nearly two orders of magnitude, and the dimensionless load parameter W over a range of one order of magnitude. Situations equivalent to using solid materials of bronze, steel, and silicon nitride and lubricants of paraffinic and naphthenic oils were considered in an investigation of the role of the dimensionless materials parameter G . The 34 cases used to generate the minimum-film-thickness formula are given in table 1. In the table H_{\min} corresponds to the minimum film thickness obtained from the EHL elliptical contact theory given in Hamrock and Dowson (1976). The minimum-film-thickness formula obtained from a least-squares fit of the data was first given in Hamrock and Dowson (1977b) and is given here as

$$\tilde{H}_{\min} = 3.63 U^{0.68} G^{0.49} W^{-0.073} (1 - e^{-0.68k}) \quad (16)$$

In table I \tilde{H}_{\min} is the minimum film thickness obtained from equation (16). The percentage difference between \tilde{H}_{\min} and H_{\min} is expressed by

$$D_1 = \left(\frac{\tilde{H}_{\min} - H_{\min}}{H_{\min}} \right) 100 \quad (17)$$

In table I the values of D_1 are within ± 5 percent.

A representative contour plot of dimensionless pressure is shown in figure 2 for $k = 1.25$, $U = 0.168 \times 10^{-11}$, $W = 0.111 \times 10^{-6}$, and $G = 4522$. In this figure and in figure 3, the + symbol indicates the center of the Hertzian contact zone. The dimensionless representation of the X and Y coordinates causes the actual Hertzian contact ellipse to be a circle regardless of the value of the ellipticity parameter. The Hertzian contact circle is shown by asterisks. On the figure is a key showing the contour labels and each corresponding value of dimensionless pressure. The inlet region is to the left and the exit region is to the right. The pressure gradient at the exit end of the conjunction is much larger than that in the inlet region. In figure 2 a pressure spike is visible at the exit of the contact.

Contour plots of film thickness are shown in figure 3 for $k = 1.25$, $U = 0.168 \times 10^{-11}$, $W = 0.111 \times 10^{-6}$, and $G = 4522$. In this figure two minimum-film-thickness regions occur in well defined side lobes that follow, and are close to, the edge of the Hertzian contact ellipse. These results reproduce all the essential features of previously reported experimental observations based on optical interferometry (Cameron and Gohar, 1966).

The variation of pressure and film thickness in the direction of rolling quite close to the X-axis near the midplane of the conjunction is shown in figure 4 for three values of U . The values of the dimensionless load, materials, and ellipticity parameters were held constant at $k = 6$, $W = 0.737 \times 10^{-6}$, and $G = 4522$. In figure 4(a) the dashed line corresponds to the Hertzian pressure distribution. This figure shows that the pressure at any location in the inlet region rises as the speed increases, a result that is also consistent with the elastohydrodynamic theory for line or rectangular contacts. Furthermore, as the speed decreases, the height of the pressure spike decreases and the hydrodynamic pressures gradually approach the semielliptical form of the Hertzian contact stresses. Note that the location of the pressure spike moves downstream toward the edge of the Hertzian contact ellipse as the speed decreases. For nominal line or rectangular contacts Dowson and Higginson (1966) showed results similar to those in figure 4(a).

The typical elastohydrodynamic film shape with an essentially parallel section in the central region is shown in figure 4(b). There is little sign of a reentrant region in this case, except perhaps at the lowest speed. Also, there is a considerable change in the film thickness as the dimensionless speed is changed, as indicated by equation (16). This illustrates most clearly the dominant effect of the dimensionless speed parameter U on the minimum film thickness in elastohydrodynamic contacts.

The variation of pressure and film thickness in the direction of motion along a line close to the midplane of the conjunction is shown in figure 5 for three values of dimensionless load parameter. The values of the dimensionless speed, materials, and ellipticity parameters were held fixed at $U = 0.168 \times 10^{-11}$, $G = 4522$, and $k = 6$. Note from figure 5(a) that the pressure at any location in the inlet region falls as the load increases. For the highest load ($W = 1.106 \times 10^{-6}$), figure 5(b), the film thickness rises between the central region and the outlet restriction. This reentrant effect is attributed to lubricant compressibility. Note also that at $W = 0.5228 \times 10^{-6}$ the film thick-

ness is slightly smaller than at $W = 1.106 \times 10^{-6}$. This somewhat curious result is linked to the fact that the location of the minimum film thickness also changes drastically over this load range. At the lower load the minimum film thickness is located on the midplane of the conjunction downstream from the center of the contact; at the higher load it moves to the side lobes as described earlier.

FULLY FLOODED SOFT-EHL RESULTS

The earlier studies of elastohydrodynamic lubrication of conjunctions of elliptical form are applied to the particular and interesting situation exhibited by materials of low elastic modulus (soft EHL). The procedure used in obtaining the soft-EHL results is given in Hamrock and Dowson (1978). The ellipticity parameter was varied from 1 (a ball-on-plate configuration) to 12 (a configuration approaching a nominal line or rectangular contact). The dimensionless speed and load parameters were varied by one order of magnitude. Seventeen different cases used to generate the minimum-film-thickness formula are given in table II. In the table H_{min} corresponds to the minimum film thickness obtained from applying the EHL elliptical contact theory given in Hamrock and Dowson (1976) to the soft-EHL contacts. The minimum-film-thickness formula obtained from a least squares fit of the data was first given in Hamrock and Dowson (1978) and is given here as

$$\tilde{H}_{min} = 7.43 U^{0.65} W^{-0.21} (1 - 0.85 e^{-0.31k}) \quad (18)$$

In table II \tilde{H}_{min} is the minimum film thickness obtained from equation (18). The percentage difference between H_{min} and \tilde{H}_{min} is expressed by D_1 , given in equation (17). The values of D_1 in table II are within the range -8 to 3 percent.

It is interesting to compare the equation for materials of low elastic modulus (soft EHL, eq. (18)) with the corresponding equation for materials of high elastic modulus (hard EHL) given in equation (16). The powers of U in equations (18) and (16) are similar, but the power of W is much more significant for low elastic-modulus materials. The expression showing the effect of the ellipticity parameter is of exponential form in both equations, but with different constants.

A major difference between equations (18) and (16) is the absence of a materials parameter G in the expression for low-elastic-modulus materials. There are two reasons for this. One is the negligible effect of pressure on the viscosity of the lubricating fluid, and the other is the way in which the role of elasticity is simply and automatically incorporated into the prediction of conjunction behavior through an increase in the size of the Hertzian contact zone corresponding to changes in load. As a check on the validity of this, case 9 of table II was repeated with the material changed from nitrile to silicone rubber. The results of this change are recorded as case 17 in table II. The dimensionless minimum film thickness calculated from the full numerical solution to the elastohydrodynamic contact theory was 181.8×10^{-6} , and the dimensionless minimum film thickness predicted from equation (18) turned out to be 182.5×10^{-6} . This clearly indicates a lack of dependence of the minimum film thickness for low-elastic-modulus materials on the materials parameter.

The variation of the ratio $H_{min}/H_{min,r}$ is shown in figure 6, where $H_{min,r}$ is the minimum film thickness for rectangular contacts, with the ellipticity parameter k for both high and low-elastic-modulus materials. If it is assumed that the minimum film thickness obtained from the elastohydrodynamic analysis of elliptical contacts can only be obtained to an accuracy of 3 percent, we find that the ratio $H_{min}/H_{min,r}$ approaches the limiting value at $k = 5$ for high-elastic-modulus materials. For low-elastic-modulus materials the ratio approaches the limiting value more slowly, but it is reasonable to state that the rectangular-contact solution will give a very good prediction of the minimum film thickness for conjunctions in which k exceeds about 11.

FULLY FLOODED - STARVED BOUNDARY

The computing area in and around the Hertzian contact is shown in figure 7. In this figure the coordinate X is made dimensionless with respect to the semiminor axis b of the contact ellipse, and the coordinate Y is made dimensionless with respect to the semimajor axis a of the contact ellipse. The ellipticity parameter k is defined as the semimajor axis divided by the semiminor axis of the contact ellipse ($k = a/b$). Because of the dimensionless form of the coordinates X and Y the Hertzian contact ellipse becomes a Hertzian circle regardless of the value of k . This Hertzian contact circle is shown in figure 7 with a radius of unity. The edges of the computing area, where the pressure is assumed to be ambient, are also denoted. In this figure the dimensionless inlet distance \tilde{m} , which is equal to the dimensionless distance from the center of the Hertzian contact zone to the inlet edge of the computing area, is shown. Lubricant starvation can be studied by simply changing the dimensionless inlet distance \tilde{m} . A fully flooded condition is said to exist when the dimensionless inlet distance ceases to influence the minimum film thickness to any significant extent.

The value at which the minimum film thickness first starts to change when \tilde{m} is gradually reduced from a fully flooded condition is called the fully flooded - starved boundary position and is denoted by \tilde{m}^* . Therefore lubricant starvation was studied by using the basic elastohydrodynamic lubrication elliptical contact theory developed earlier in the paper and by observing how reducing the dimensionless inlet distance

affected the basic features of the conjunction. The next two sections make extensive use of the work presented by Hamrock and Dowson (1977a) and Hamrock and Dowson (1979).

STARVED HARD-EHL RESULTS

Table III shows how changing the dimensionless inlet distance affected the dimensionless minimum film thickness for three groups of dimensionless load and speed parameters. All the data presented in this section are for hard-EHL contacts that have a materials parameter G fixed at 4522 and the ellipticity parameter, at 6. It can be seen from table III that, as the dimensionless inlet distance \tilde{m} decreases, the dimensionless minimum film thickness H_{\min} also decreases.

Table IV shows how the three groups of dimensionless speed and load parameters considered affected the location of the dimensionless inlet boundary distance m^* . Also given in this table are the corresponding values of dimensionless central and minimum film thickness for the fully flooded condition as obtained by interpolating the numerical values. The value of the dimensionless inlet boundary position m^* shown in table IV was obtained by using the data from table III when the following equation was satisfied:

$$\frac{H_{\min} - (H_{\min})_{\tilde{m}=m^*}}{H_{\min}} = 0.03 \quad (19)$$

The value of 0.03 was used in equation (19) since it was ascertained that the data in table III were accurate to only ± 3 percent.

The general form of the equation that describes how the dimensionless inlet distance at the fully flooded - starved boundary m^* varies with the geometry and central film thickness of an elliptical elastohydrodynamic conjunction is given as

$$m^* - 1 = A^* \left[\left(\frac{R_x}{b} \right)^2 H_{\min} \right]^{B^*} \quad (20)$$

The right side of equation (20) is similar in form to the equations given by Wolveridge, et al. (1971) and Wedeven, et al. (1971). By applying a least-squares power fit to the data obtained from table III we can write

$$m^* = 1 + 3.34 \left[\left(\frac{R_x}{b} \right)^2 H_{\min} \right]^{0.56} \quad (21)$$

A fully flooded condition exists when $\tilde{m} \geq m^*$, and a starved condition exists when $\tilde{m} < m^*$.

Having clearly established the limiting location of the inlet boundary for the fully flooded conditions (eq. (21)) we can develop an equation defining the dimensionless film thickness for elliptical conjunctions operating under starved lubrication conditions. The ratio between the dimensionless minimum film thickness in starved and fully flooded conditions can be expressed in general form as

$$\frac{H_{\min,s}}{H_{\min}} = C^* \left(\frac{\tilde{m} - 1}{m^* - 1} \right)^{D^*} \quad (22)$$

Table V shows how the ratio of the dimensionless inlet distance parameter to the fully flooded - starved boundary $(\tilde{m} - 1)/(m^* - 1)$ affects the ratio of minimum film thickness in the starved and fully flooded conditions $H_{\min,s}/H_{\min}$. A least-squares power curve fit to the 16 pairs of data points

$$\left[\left(\frac{H_{\min,s}}{H_{\min}} \right)_i, \left(\frac{\tilde{m} - 1}{m^* - 1} \right)_i \right], \quad i = 1, 2, \dots, 16$$

was used in obtaining values for C^* and D^* in equation (22). For these values of C^* and D^* the dimensionless minimum film thickness for a starved condition can be written as

$$H_{\min,s} = H_{\min} \left(\frac{\tilde{m} - 1}{m^* - 1} \right)^{0.25} \quad (23)$$

Therefore, whenever $\tilde{m} < m^*$, where m^* is defined by equation (21), a starved lubrication condition exists. When this is true, the dimensionless minimum film thickness is expressed by equation (23). If $\tilde{m} > m^*$, where m^* is defined by equation (21), a fully flooded condition exists. Expressions for the dimensionless minimum film thickness for a fully flooded condition H_{\min} are given in equation (16).

Figures 8 to 11 explain more fully what happens in going from a fully flooded to a starved lubrication condition. As in the earlier part of the paper the + symbol indicates the center of the Hertzian contact, and the asterisks indicate the Hertzian contact circle. Also on each figure the contour labels and each corresponding value are given.

In figures 8(a), (b), and (c) contour plots of dimensionless pressure ($P = p/E'$) are given for group 1 of table III and for dimensionless inlet distances \tilde{m} of 4, 2, and 1.25, respectively. In these figures the contour values are the same in each plot. The pressure spikes are evident in figures 8(a) and (b), but no pressure spike appears in figure 8(c). This implies that as the dimensionless inlet distance \tilde{m} decreases, or as the severity of lubricant starvation increases, the pressure spike is suppressed. Figure 8(a), with $\tilde{m} = 4$, corresponds to a fully flooded condition; figure 8(b), with $\tilde{m} = 2$, to a starved condition; and figure 8(c), with $\tilde{m} = 1.25$, to even more severe starvation. Once lubricant starvation occurs, the severity of the situation within the conjunction increases rapidly as m is decreased and dry contact conditions are approached.

Contour plots of the dimensionless film thickness ($H = h/R_x$) for the results shown in group 1 of table III and for conditions corresponding to the three pressure distributions shown in figure 8 are reproduced in figure 9. It is clear that the film shape in the central region of the elastohydrodynamic conjunction becomes more parallel as lubricant starvation increases and that the region occupied by the minimum film thickness becomes more concentrated. Note also that the values attached to the film thickness contours for the starved condition (fig. 9(c)) are much smaller than those of the film thickness contours for the fully flooded condition (fig. 9(a)).

STARVED SOFT-EHL RESULTS

By using the theory and numerical procedure mentioned earlier in the paper, we can investigate the influence of lubricant starvation on minimum film thickness in starved, elliptical, elastohydrodynamic conjunctions for low-elastic-modulus materials (soft EHL). Lubricant starvation is studied by simply moving the inlet boundary closer to the center of the conjunction, as described in the previous section.

Table VI shows how the dimensionless inlet distance affects the dimensionless film thickness for three groups of dimensionless load and speed parameters. For all the results presented in this section the dimensionless materials parameter G was fixed at 0.4276, and the ellipticity parameter k was fixed at 6. The results shown in table VI clearly indicate the adverse effect of lubricant starvation in the sense that, as the dimensionless inlet distance \tilde{m} decreases, the dimensionless minimum film thickness H_{\min} also decreases.

Table VII shows how the three groups of dimensionless speed and load parameters affect the limiting location of the dimensionless critical inlet boundary distance m^* . Also given in this table are corresponding values of the dimensionless minimum film thickness for the fully flooded condition, as obtained by interpolating the numerical values. By making use of table VI and following the procedure outlined in the previous section, we can write the critical dimensionless inlet boundary distance at which starvation becomes important for low-elastic-modulus materials as

$$m^* = 1 + 1.07 \left[\left(\frac{R_x}{b} \right)^2 \tilde{H}_{\min} \right]^{0.16} \quad (24)$$

where \tilde{H}_{\min} is obtained from the fully flooded soft-EHL results in equation (18).

Table VIII shows how m^* affects the ratio of minimum film thickness in the starved and fully flooded conditions $\tilde{H}_{\min,s}/H_{\min}$. The dimensionless minimum film thickness for a starved condition for low-elastic-modulus materials can thus be written as

$$\tilde{H}_{\min,s} = H_{\min} \left(\frac{\tilde{m} - 1}{m^* - 1} \right)^{0.22} \quad (25)$$

Therefore, whenever $\tilde{m} < m^*$, where m^* is defined by equation (24), a lubricant starvation condition exists. When this is true, the dimensionless minimum film thickness is expressed by equation (25). If $\tilde{m} \geq m^*$, a fully flooded condition exists, and the expression for the dimensionless minimum film thickness for a fully flooded condition H_{\min} for materials of low elastic modulus is given in equation (18).

REFERENCES

- Brewe, D. E. and Hamrock, B. J. (1977) "Simplified Solution for Elliptical Contact Deformation Between Two Elastic Solids," J. Lubr. Technol. 99 (4), 485-487.
- Cameron, A. and Gohar, R. (1966) "Theoretical and Experimental Studies of the Oil Film in Lubricated Point Contact." Proc. R. Soc. (London) 291A (1427), 520-536.
- Dowson, D. and Hamrock, B. J. (1976) "Numerical Evaluation of the Surface Deformation of Elastic Solids Subjected to a Hertzian Contact Stress." ASLE Trans. 19 (4), 279-286.
- Dowson, D. and Higginson, G. R. (1966) Elasto-Hydrodynamic Lubrication - The Fundamentals of Roller and Gear Lubrication. Pergamon Press, Oxford.
- Hamrock, B. J. and Dowson, D. (1976) "Isothermal Elastohydrodynamic Lubrication of Point Contacts. Part I - Theoretical Formulation," J. Lubr. Technol. 98 (2), 223-229.
- Hamrock, B. J. and Dowson, D. (1977a) "Isothermal Elastohydrodynamic Lubrication of Point Contacts. Part IV - Starvation Results," J. Lubr. Technol., 99 (1), 15-23.
- Hamrock, B. J. and Dowson, D. (1977b) "Isothermal Elastohydrodynamic Lubrication of Point Contacts. Part III - Fully Flooded Results," J. Lubr. Technol. 99 (2), 264-276.
- Hamrock, B. J. and Dowson, D. (1978) "Elastohydrodynamic Lubrication of Elliptical Contacts for Materials of Low Elastic Modulus. Part I - Fully Flooded Conjunction," J. Lubr. Technol., 100 (2), 236-245.
- Hamrock, B. J. and Dowson, D. (1979) "Elastohydrodynamic Lubrication of Elliptical Contacts for Materials of Low Elastic Modulus. Part II - Starved Conjunction," J. Lubr. Technol., 101 (1), 92-98.
- Moes, H. (1965-66) "Communication, Elastohydrodynamic Lubrication," Proc. Inst. Mech. Engr., London, Part 3B, 180, 244-245.
- Theyse, F. H. (1966) "Some Aspects of the Influence of Hydrodynamic Film Formation on the Contact Between Rolling/Sliding Surfaces," Wear, 9, 41-59.
- Wedeven, L. E., Evans, D., and Cameron, A. (1971) "Optical Analysis of Ball-Bearing Starvation," J. Lubr. Technol., 93 (3), 349.
- Wolveridge, P. E., Baglin, K. P., and Archard, J. G. (1971) "The Starved Lubrication of Cylinders in Line Contact," Proc. Inst. Mech. Eng. (London), 185 (1), 1159-1169.

TABLE I. - DATA SHOWING EFFECT OF ELLIPTICITY, LOAD, SPEED, AND MATERIALS PARAMETERS ON MINIMUM FILM THICKNESS FOR HARD EHL CONTACTS

Case	Ellipticity parameter, k	Dimensionless load parameter, W	Dimensionless speed parameter, U	Dimensionless materials parameter, b	Minimum film thickness		Difference between H_{min} and H_{min} , U ₁ , percent	Results
					Obtained from EHL elliptical contact theory, H_{min}	Obtained from least-squares fit, H_{min}		
1	1	0.1106x10 ⁻⁶	0.1683x10 ⁻¹¹	4522	3.367x10 ⁻⁶	3.514x10 ⁻⁶	+4.37	Ellipticity
2	1.25	↓	↓	↓	4.105	4.078	-0.66	
3	1.5	↓	↓	↓	4.565	4.554	-0.24	
4	1.75	↓	↓	↓	4.907	4.955	+0.98	
5	2	↓	↓	↓	5.255	5.294	+0.74	
6	2.5	↓	↓	↓	5.755	5.821	+1.15	
7	3	↓	↓	↓	6.091	6.196	+1.72	
8	4	↓	↓	↓	6.636	6.662	-0.24	
9	6	↓	↓	↓	6.969	7.001	+0.46	
10	8	↓	↓	↓	7.048	7.091	+0.61	
11	6	0.2211	0.1683x10 ⁻¹¹	4522	6.492	6.656	+2.53	Load plus case 9
12	↓	.3686	↓	↓	6.317	6.412	+1.50	
13	↓	.5528	↓	↓	6.268	6.225	-0.69	
14	↓	.7371	↓	↓	6.156	6.095	-0.99	
15	↓	.9214	↓	↓	6.085	5.997	-1.45	
16	↓	1.106	↓	↓	5.811	5.918	+1.84	
17	↓	1.290	↓	↓	5.657	5.851	+3.43	
18	6	0.7371	0.08416	4522	3.926	3.805	-3.08	Speed plus case 14
19	↓	↓	.2525	↓	8.372	8.032	-4.06	
20	↓	↓	.3367	↓	9.995	9.769	-2.26	
21	↓	↓	.4208	↓	11.61	11.37	-2.07	
22	↓	↓	.5892	↓	14.39	14.29	-0.69	
23	↓	↓	.8416	↓	18.34	18.21	-0.71	
24	↓	↓	1.263	↓	24.47	24.00	-1.92	
25	↓	↓	1.683	↓	29.75	29.18	-1.92	
26	↓	↓	2.104	↓	34.58	33.96	-1.79	
27	↓	↓	2.525	↓	39.73	38.44	-3.25	
28	↓	↓	2.946	↓	43.47	42.69	-1.79	
29	↓	↓	3.367	↓	47.32	46.76	-1.18	
30	↓	↓	4.208	↓	54.57	54.41	-0.29	
31	↓	↓	5.050	↓	61.22	61.59	+0.44	
32	6	0.7216	0.3296	2310	6.931	6.938	+0.10	Materials plus case 9
33	6	.7216	.9422	3691	17.19	17.59	+2.33	
34	6	.2456	.1122	6785	6.080	6.116	+0.59	

TABLE II. - DATA SHOWING EFFECT OF ELLIPTICITY, LOAD, SPEED, AND MATERIALS PARAMETERS ON MINIMUM FILM THICKNESS FOR SOFT EHL CONTACTS

Case	Ellipticity parameter, k	Dimensionless load parameter, W	Dimensionless speed parameter, U	Dimensionless materials parameter, G	Minimum film thickness		Difference between H _{min} and H _{min} , D ₁ , percent	Results
					Obtained from EHL elliptical contact theory, H _{min}	Obtained from least-squares fit, H _{min}		
1	1	0.4405x10 ⁻³	0.1028x10 ⁻⁷	0.4276	88.51x10 ⁻⁶	91.08x10 ⁻⁶	+2.90	Ellipticity
2	2	↓	↓	↓	142.5	131.2	-7.93	
3	3	↓	↓	↓	170.4	160.8	-5.63	
4	4	↓	↓	↓	186.7	182.4	-2.30	
5	6	↓	↓	↓	206.2	209.8	+1.75	
6	8	↓	↓	↓	219.7	224.6	+2.23	
7	12	↓	↓	↓	235.2	236.0	+0.34	
8	6	0.4405x10 ⁻³	0.05139	0.4276	131.8	133.7	+1.44	Speed plus case 5
9	↓	↓	.1542	↓	268.1	273.1	+1.86	
10	↓	↓	.2570	↓	381.6	380.7	-.24	
11	↓	↓	.05139	↓	584.7	597.3	+2.15	
12	6	.2202	0.1028	0.4276	241.5	242.7	+0.37	Load plus case 5
13	↓	.6607	↓	↓	190.7	192.7	+1.05	
14	↓	1.101	↓	↓	170.5	173.1	+1.52	
15	↓	1.542	↓	↓	160.4	161.3	+0.56	
16	↓	2.202	↓	↓	149.8	149.7	-.07	
17	6	0.1762	0.06169	1.069	181.8	182.5	+0.39	Material

TABLE V. - EFFECT OF DIMENSIONLESS INLET DISTANCE ON DIMENSIONLESS CENTRAL- AND MINIMUM-FILM-THICKNESS RATIOS FOR HARD EHL CONTACTS

TABLE III. - EFFECT OF STARVATION ON MINIMUM FILM THICKNESS FOR HARD EHL CONTACTS

Dimensionless Inlet Distance, m	Group		
	1	2	3
Dimensionless Load Parameter, W			
0.3686x10 ⁻⁶	0.7371x10 ⁻⁶	0.7371x10 ⁻⁶	
Dimensionless Speed Parameter, U			
0.1683x10 ⁻¹¹	1.683x10 ⁻¹¹	5.050x10 ⁻¹¹	
Minimum Film Thickness, H _{min}			
6	29.75x10 ⁻⁶	61.32x10 ⁻⁸	
4	6.317x10 ⁻⁶	29.27	57.50
3	6.261	27.84	51.70
2.5	-----	26.38	46.89
2	5.997	23.46	39.91
1.75	-----	21.02	34.61
1.5	5.236	-----	27.90
1.25	3.945	-----	-----

Group	Dimensionless Inlet Distance, m	Film Thickness Ratios for Starved and Flooded Conditions		Inlet Boundary Parameters	
		Central, H _{c,s} /H _c	Minimum, H _{min,s} /H _{min}	Critical, $\frac{\bar{m}-1}{m^* - 1}$	Wedeven, et al. (1971), $\frac{\bar{m}-1}{m_W - 1}$
1	2.62	1	1	1	0.9895
	2	.9430	.9640	.6173	.6108
	1.5	.7697	.8417	.3086	.3054
	1.25	.5689	.6341	.1543	.1527
2	3.71	1	1	1	0.8281
	2	.9374	.9534	.7380	.6111
	2.5	.8870	.9034	.5525	.4584
	2	.7705	.8034	.3690	.3056
3	1.75	.7151	.7199	.2768	.2292
	5.57	1	1	1	0.8498
	4	.9348	.9439	.6565	.5579
	3	.8335	.8487	.4376	.3719
2.5	2.5	.7440	.7697	.3282	.2789
	2	.5223	.6551	.2188	.1860
	1.75	.5309	.5681	.1641	.1395
	1.5	.4155	.4580	.1094	.0930

TABLE IV. - EFFECT OF DIMENSIONLESS SPEED AND LOAD PARAMETERS ON DIMENSIONLESS INLET DISTANCE AT FULLY FLOODED - STARVED BOUNDARY FOR HARD EHL CONTACTS

Group	Dimensionless Parameters			Fully Flooded Film Thickness		Dimensionless Inlet Boundary, m
	U	W	R _x /b	Central, H _c	Minimum, H _{min}	
1	0.1683x10 ⁻¹¹	0.3686x10 ⁻⁶	205.9	7.480x10 ⁻⁶	5.211x10 ⁻⁶	2.62
2	1.683	.7371	163.5	33.55	29.29	3.71
3	5.050	.7371	163.5	70.67	60.92	5.57

TABLE VI. - EFFECT OF STARVATION ON FILM THICKNESS FOR SOFT EHL CONTACTS

Dimensionless Inlet Distance, \tilde{m}	Group		
	1	2	3
Dimensionless Load Parameter, W			
	0.4405×10^{-3}	0.2202×10^{-3}	0.4405×10^{-3}
Dimensionless Speed Parameter, U			
	0.5139×10^{-8}	0.1027×10^{-7}	0.5139×10^{-7}
Dimensionless Minimum Film Thickness, H_{min}			
1.967	131.6×10^{-6}	241.8×10^{-6}	584.7×10^{-6}
1.833	131.2	238.6	572.0
1.667	129.7	230.8	543.1
1.500	125.6	217.2	503.0
1.333	115.9	199.3	444.9
1.167	98.11	120.8	272.3
1.033	71.80	120.8	272.3

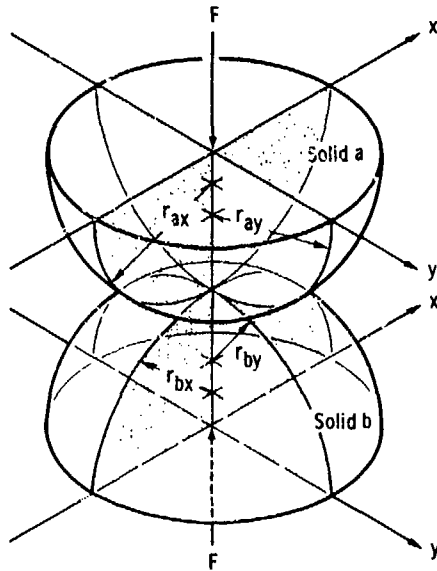


Figure 1. - Geometry of contacting elastic solids.

TABLE VII. - EFFECT OF INLET DISTANCE ON MINIMUM-FILM-THICKNESS RATIO FOR SOFT EHL CONTACTS

Group	Dimensionless Inlet Distance, \tilde{m}	Ratio of Minimum Film Thicknesses for Starved and Flooded Conditions, $H_{min,s}/H_{min}$	Critical Inlet Boundary Parameter, $(\tilde{m} - 1)/(\tilde{m}^* - 1)$
1	1.661	1	1
	1.500	.9828	.7584
	1.333	.9069	.5038
	1.167	.7677	.2526
	1.033	.5618	.0499
2	1.757	1	1
	1.667	.9842	.6811
	1.500	.9282	.6605
	1.333	.8499	.4399
	1.167	.7207	.2206
3	1.850	1	1
	1.667	.9575	.7847
	1.500	.8868	.5882
	1.333	.7844	.3918
	1.167	.6761	.1965
1.033	.4801	.0388	

TABLE VIII. - EFFECT OF INLET DISTANCE ON FILM THICKNESS FOR SOFT EHL CONTACTS

Group	Dimensionless Parameters			Fully Flooded Minimum Film Thickness, H_{min}	Dimensionless Inlet Boundary, \tilde{m}
	U	W	R_x/b		
1	0.5139×10^{-8}	0.4405×10^{-3}	19.41	127.9×10^{-6}	1.661
2	$.1027 \times 10^{-7}$.2202	24.45	234.5	1.757
3	.5139	.4405	19.41	567.2	1.850

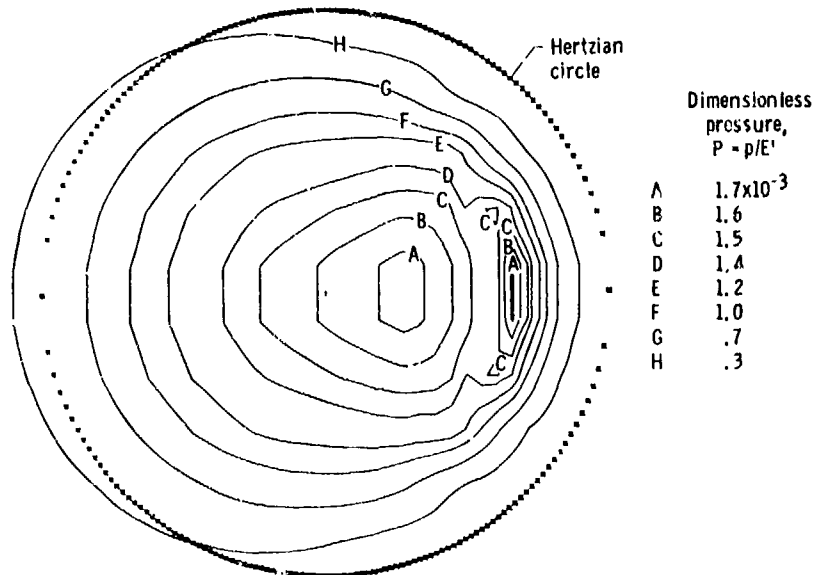
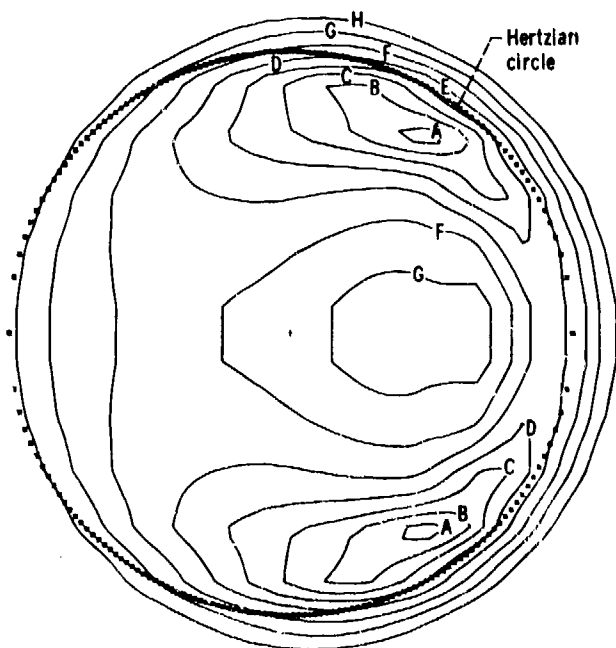


Figure 2. - Contour plot of dimensionless pressure. $k = 1.25$, $U = 0.168 \times 10^{-11}$, $W = 0.111 \times 10^{-6}$, and $G = 4522$.



Dimensionless film thickness, $H = h/R_x$

A	4.3×10^{-6}
B	4.6
C	5.0
D	5.5
E	6.0
F	6.6
G	7.4
H	8.2

Figure 3 - Contour plot of dimensionless film thickness, $k = 1.25$, $U = 0.168 \times 10^{-11}$, $W = 0.111 \times 10^{-6}$, and $G = 4522$.

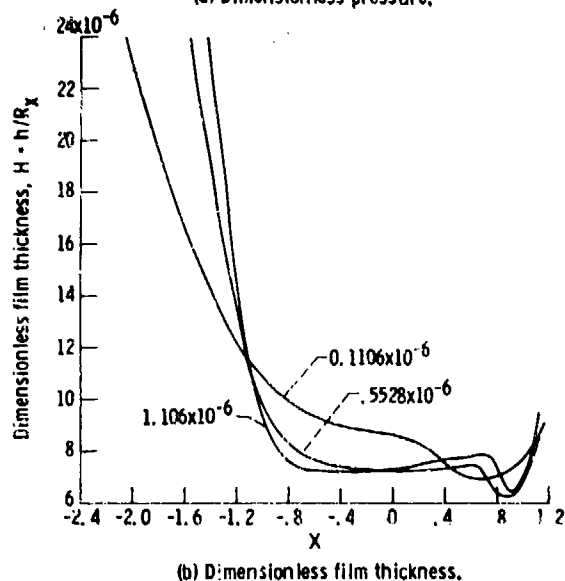
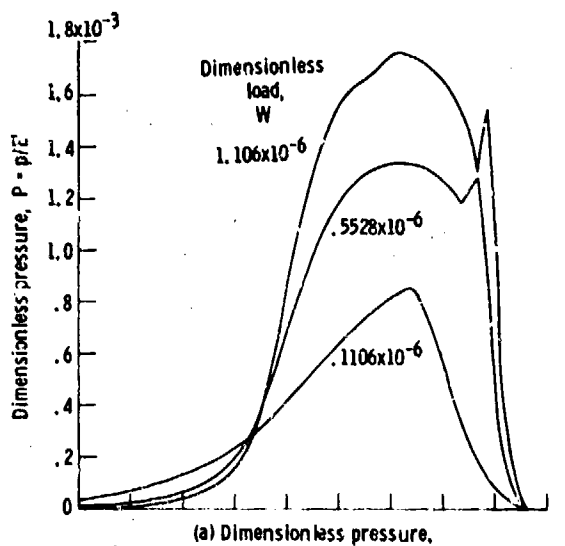


Figure 5 - Variations of dimensionless pressure and film thickness on X-axis for three values of dimensionless load parameter. The value of Y is held fixed near axial center of contact.

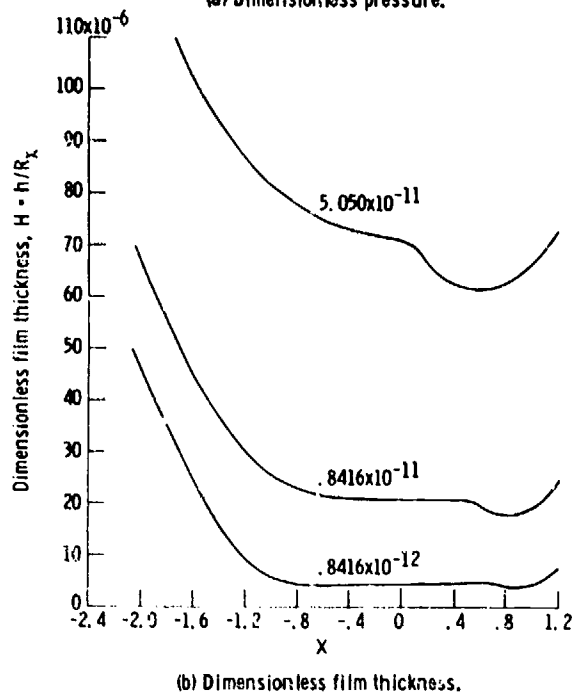
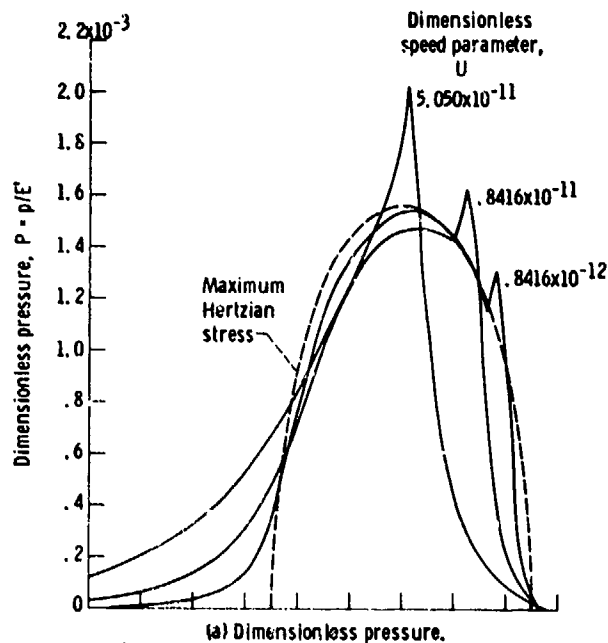


Figure 4 - Variation of dimensionless pressure and film thickness on X-axis for three values of dimensionless speed parameter. The value of Y is held fixed near axial center of contact.

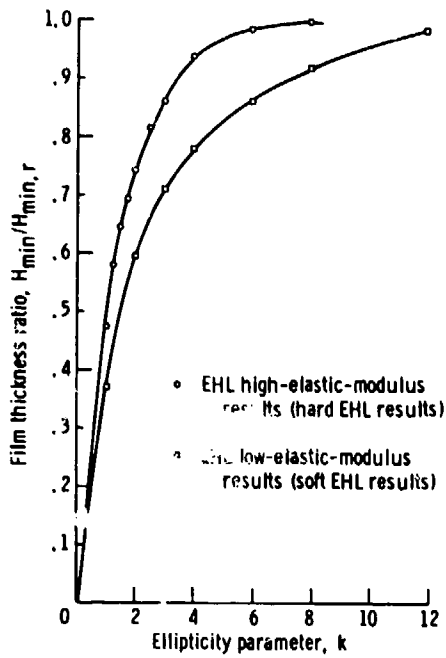


Figure 6. - Effect of ellipticity parameter on ratio of dimensionless minimum film thickness to dimensionless minimum film thickness for a line contact, for EHL high- and low-elastic-modulus analyses.

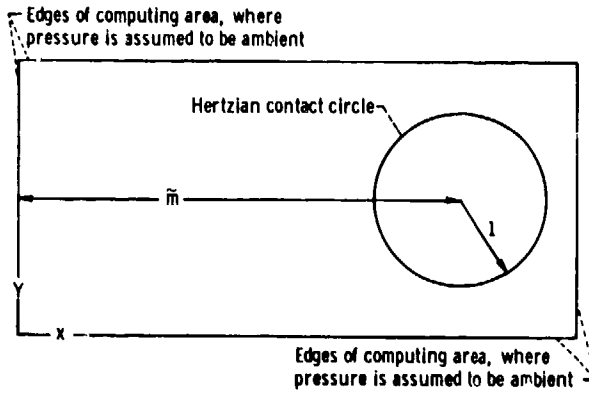


Figure 7. - Computing area in and around Hertzian contact zone.

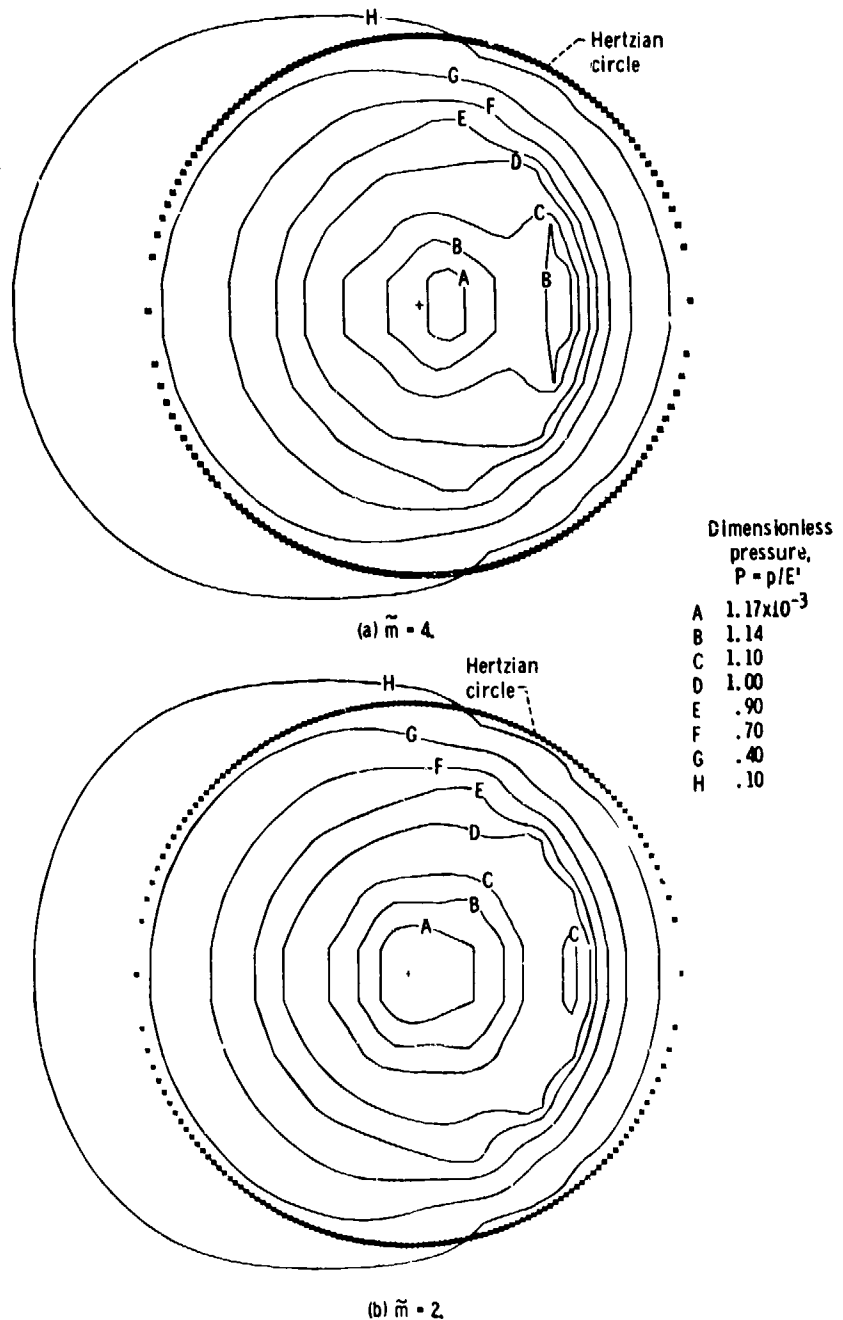


Figure 8. - Contour plots of dimensionless pressure for dimensionless inlet distances \tilde{m} of 4, 2, and 1.25 and for group 1 of table 2.

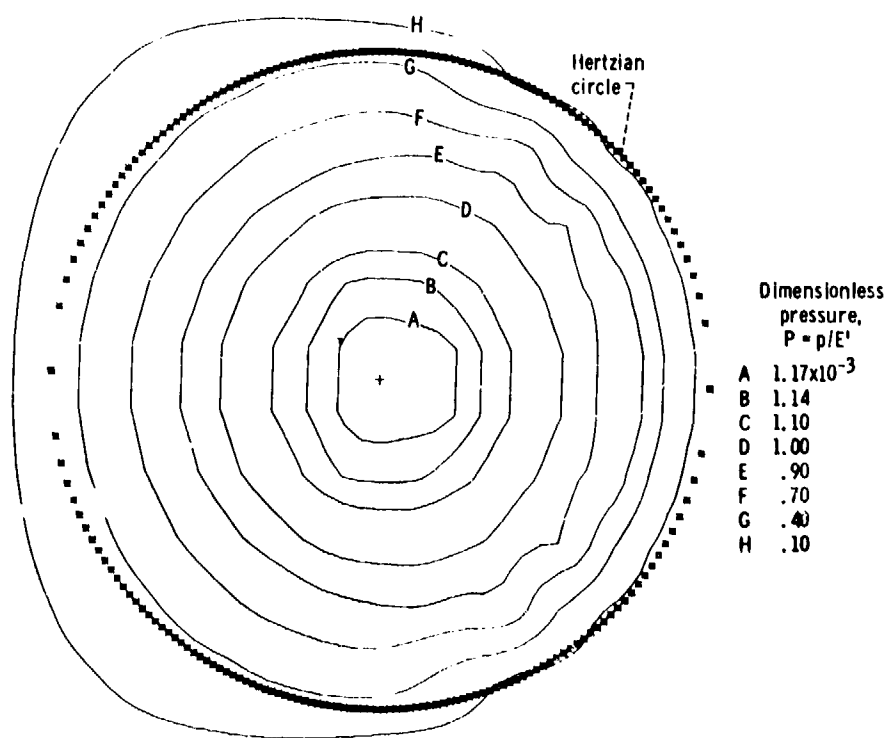
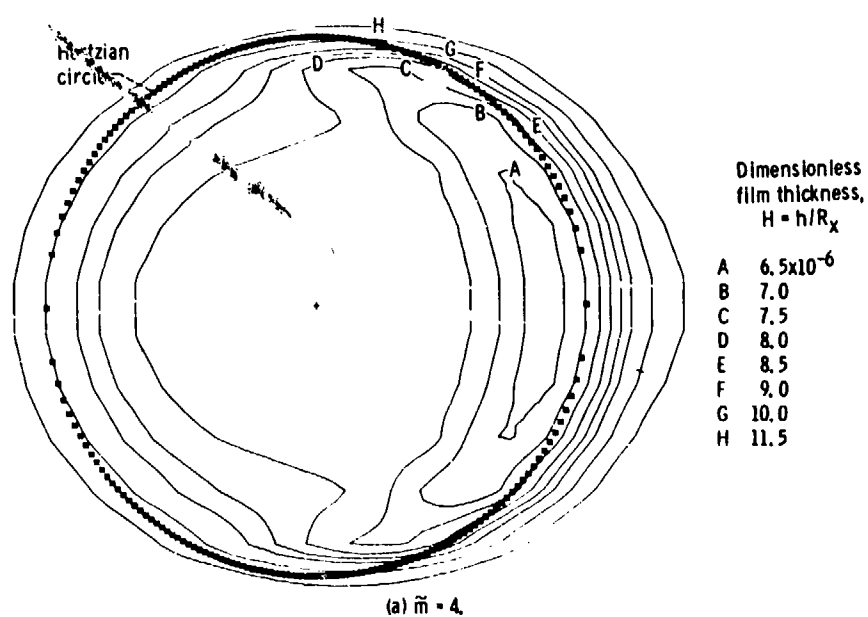
(c) $\tilde{m} = 1.25$.

Figure 8. - Concluded.

(a) $\tilde{m} = 4$.Figure 9. - Contour plots of dimensionless film thickness for dimensionless inlet distances \tilde{m} of 4, 2, and 1.25 and for group 1 of table 2.

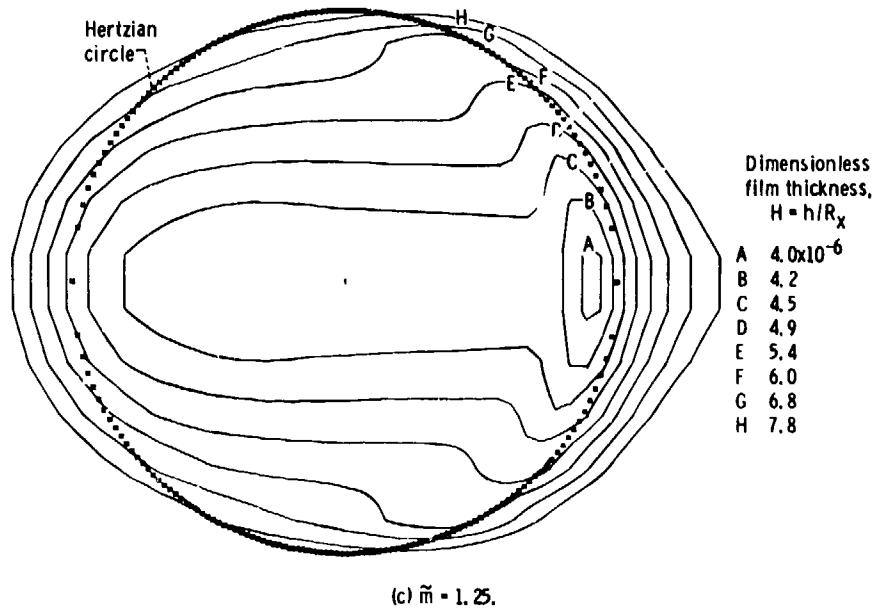
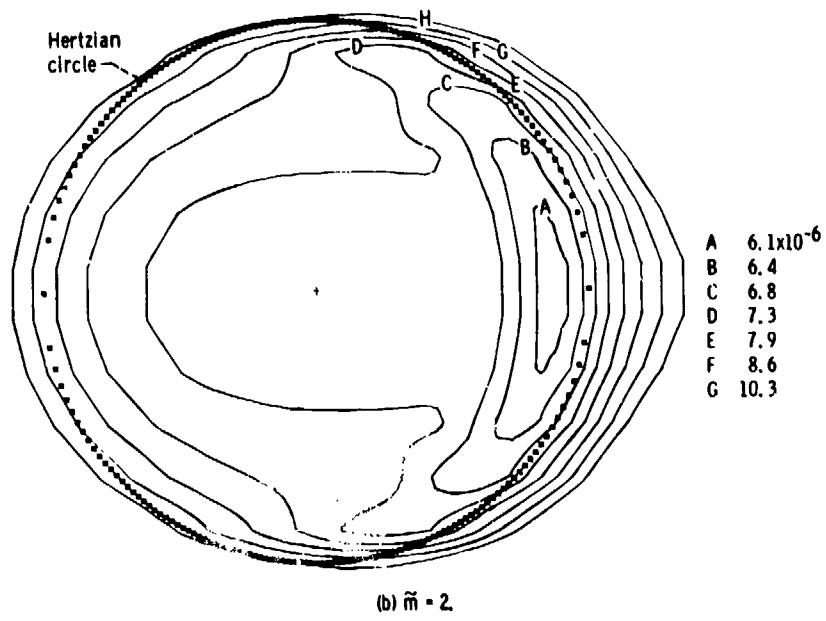


Figure 9. - Concluded.

DISCUSSION

D.G.Astridge, Westland Helicopters, Yeovil, UK

Could the author confirm that the major axis considered is perpendicular to the rolling axis, and, if so, has he considered the implications of major axis parallel to the rolling axis, as occurs in our conformal tooth gears.

Author's Reply

The considerations in obtaining the minimum film thickness formula are valid for ellipticity parameters greater than one. Ellipticity parameters less than one have not been considered by me, but are presently being considered by Professor Dowson, Dr Taylor and Mr Durn at the University of Leeds.

J.B.Medley, University of Waterloo, Ca

Were there any regions in your regime charts that numerical instability made solutions for minimum film thickness difficult to obtain?

Author's Reply

Numerical instabilities are definitely present in high load situations.

EPAISSEUR DU FILM ET FORCE DE FROTTEMENT EN RÉGIME ELASTOHYDRODYNAMIQUE
DANS LE CONTACT BILLE-CHEMIN DE BAGUE D'UN ROULEMENT

par

Gérard DALMAZ , Professeur
Nabil GADALAH, Docteur-Ingénieur

Laboratoire de Mécanique des Contacts
Institut National des Sciences Appliquées de Lyon.
20, avenue Albert Einstein
69621 Villeurbanne - France

RESUME

La lubrification élastohydrodynamique des contacts elliptiques, tels qu'ils existent entre une bille et un chemin de bague de roulements à contacts obliques, a été étudiée sur un dispositif de simulation original de haute précision spécialement construit. Ce dispositif permet de mesurer simultanément, à température ambiante, la charge normale, la force de frottement tangentielle, les vitesses et l'épaisseur du film par une méthode interférométrique (0,05 à 1 μm).

Les résultats expérimentaux montrent que, pour une huile minérale, la théorie élastohydrodynamique peut être étendue aux très fortes pressions (2 GPa). Les effets des vitesses de glissement et de pivotement superposées aux vitesses de roulement ont peu d'influence sur l'épaisseur du film mais diminuent considérablement la force de frottement. Dans ces conditions, le film se comporte comme un solide amorphe.

Le calcul théorique de la force de frottement a été effectué en régime élastohydrodynamique en utilisant le modèle isotherme non linéaire de Maxwell, de Johnson et Tevaarwerk. Les résultats théoriques et expérimentaux obtenus pour des pressions de 1 à 2 GPa concordent aux faibles taux de glissement, (< 5 %). Les effets thermiques, qui ne sont plus négligeables à forts taux de glissement, sont considérés en utilisant d'une part le modèle thermo-viscoélastique de Daniels qui tient compte de la conduction de chaleur au travers de l'épaisseur du film, et d'autre part le modèle thermique de Tevaarwerk qui tient compte également de la convection dans le cas du pivotement. Ces deux modèles qui sont discutés donnent des résultats satisfaisants.

1. INTRODUCTION

Cette étude concerne la détermination expérimentale de l'épaisseur du film et de la force de frottement au voisinage de la température ambiante, d'un contact elliptique lubrifié par une huile minérale de faible viscosité sur un dispositif de simulation de contact bille-chemin de bague de roulement.

Les charges appliquées entraînent des pressions maximales de Hertz qui atteignent 2 GPa et des vitesses de glissement et de pivotement sont introduites au voisinage du roulement pur. Ces conditions correspondent à celles qui existent dans les roulements à billes à contacts obliques.

Les épaisseurs de film mesurées par la technique interférométrique sont comparées aux valeurs calculées par la théorie élastohydrodynamique de Hamrock et Dowson [1]. La force de frottement qui est mesurée simultanément dans la direction du roulement est interprétée et comparée à celle calculée à partir du modèle non linéaire de Maxwell de Johnson et Tevaarwerk [2] en régime isotherme, du modèle thermique de Daniels [3] et du modèle thermique plus complet de Tevaarwerk [4].

2. DISPOSITIF, CONDITIONS D'ESSAIS ET MESURES

Un dispositif original de très hautes performances capable de simuler en vraie grandeur un contact hertzien elliptique tel qu'il existe entre une bille et un chemin de bague d'un roulement à billes à contacts obliques a été construit. Ce dispositif de haute précision permet de mesurer simultanément, au voisinage de la température ambiante, la charge normale, la force de frottement tangentielle dans la direction du roulement, les vitesses de roulement, de glissements et de pivotement, et de déterminer l'épaisseur du film par une méthode interférométrique.

2.1. Dispositif expérimental

Le dispositif expérimental a été détaillé par ailleurs [5]. Le montage utilisé dans ces essais est schématisé figure 1. Le disque en saphir est entraîné en rotation avec une vitesse angulaire variable de 30 à 3000 tr/mn et le tonneau en acier tourne avec une vitesse qui varie de 5000 à 45000 tr/mn. Le déplacement axial du palier hydrostatique permet de mesurer la force de frottement et le déplacement angulaire, d'appliquer et de mesurer la charge. Le changement de position de l'axe de rotation du tonneau produit au point de contact un pivotement (angle λ) ou un glissement latéral (angle β). L'huile est déposée sur la surface inférieure du disque par le tube d'alimentation. La planéité et le voile du disque sont inférieurs à 0,5 μm et le faux rond de l'éprouvette en forme de tonneau inférieur à 0,6 μm . Les rugosités des surfaces du disque et du tonneau sont respectivement 0,005 μm et 0,01 μm CLA. La surface inférieure du disque en saphir est également recouverte d'une couche mince de chrome de 150 Å qui améliore le contraste des franges d'interférence.

2.2. Conditions d'essais

Les essais sont réalisés au voisinage de la température ambiante entre 25 et 30°C, avec une huile minérale et pour un contact elliptique formé par un disque plan en saphir et une éprouvette en acier

en forme de tonneau dont les rayons de courbure principaux sont : $R_x = 1,34$ mm et $R_z = 9,7$ mm. L'huile utilisée a une viscosité de 32 mPa.s à 25°C. Le coefficient de piézo-viscosité α a été déterminé avec un viscosimètre à chute de bille pour des pressions variant de 10^5 à 5×10^8 N/m². La viscosité varie avec la pression suivant la loi : $\mu = \mu_0 \exp(\alpha(p-p_0))$ et à 25°C, $\alpha = 16,5 \times 10^{-9}$ Pa⁻¹. Le coefficient de thermo-viscosité η tel que $\mu = \mu_0 \exp(-\eta(\theta-\theta_0))$ est déterminé entre 20 et 50°C à pression atmosphérique p_0 , $\eta = 0,0435^\circ\text{C}^{-1}$.

Les essais sont effectués pour des valeurs de la pression maximale de Hertz P et des vitesses de roulement U_1+U_2 maintenues constantes. Les vitesses de rotation des éprouvettes et les charges appliquées qui dépendent également des angles λ et β sont modifiées pour respecter ces conditions.

Dans chaque essai, pour des éprouvettes et un lubrifiant donnés, nous imposons et contrôlons donc la charge normale au contact, les vitesses angulaires du disque et de l'éprouvette en forme de tonneau, et les deux angles λ et β . Le programme expérimental comprend les différentes conditions cinématiques suivantes :

- roulement pur pour $1 < U_1 + U_2 < 12$ m/s,
- glissement U_1-U_2 dans la direction Ox pour des valeurs constantes de la vitesse de roulement U_1+U_2 dans l'intervalle $-0,3 < U_1-U_2/U_1+U_2 < +0,3$,
- pivotement $\Omega = \omega_{2y} - \omega_{1y}$ autour de l'axe Oy en changeant l'angle λ de -1° à 18° ,
- glissement latéral W_1 dans la direction Oz en changeant le point de contact défini par l'angle β dans l'intervalle $-10^\circ < \beta < +10^\circ$.

Pour chacune des conditions cinématiques, nous fixons quatre pressions maximales de Hertz. Les valeurs de la pression maximale P et de la pression moyenne \bar{P} de Hertz du demi petit axe a et du demi grand axe c de l'ellipse de contact sont données table 1. Ces valeurs correspondent à un contact dont la géométrie est définie pour $\lambda = 2^\circ$ par les rayons de courbures locaux $R'_x = 1,336$ mm et $R'_z = 9,7$ mm, pour le couple de matériaux saphir-acier de module d'élasticité équivalent $E = 2,95 \times 10^{11}$ N/m² et pour les quatre charges appliquées de 2, 4, 8 et 16 N.

\bar{P} GPa	P GPa	a μm	c μm
0,636	0,954	16,5	60,1
0,801	1,202	20,7	75,7
1,009	1,514	26,1	95,4
1,272	1,907	32,9	120,2

Table 1

2.3. Précisions des mesures

Les mesures simultanées de la température de l'huile, de la charge normale, des vitesses de rotation de chacune des éprouvettes, de la force de frottement tangentielle sur le tonneau dans la direction du roulement, de l'étendue du film et de l'épaisseur du film par une technique interférométrique sont réalisées.

La charge et la force de frottement sont mesurées avec une précision de $\pm 2\%$ et la mesure de la force de frottement est significative pour les valeurs supérieures à 0,01 N. Les vitesses de rotation des éprouvettes sont contrôlées à $\pm 0,1\%$. La température de l'huile est mesurée à $\pm 0,5^\circ\text{C}$ à la sortie du tube d'alimentation.

Les épaisseurs de film comprises entre 0,05 et 1 μm sont déterminées par la technique interférométrique décrite précédemment [5], tant en lumière blanche qu'en lumière monochromatique. La précision des mesures dépend principalement de la valeur de l'indice de réfraction de l'huile dans la zone de contact. Or, la relation de Lorenz-Lorentz permet de relier l'indice de réfraction à la masse volumique dans le cas d'une substance isotrope. Les variations de la masse volumique avec la pression, la température et le temps étant connues, les valeurs vraisemblables retenues pour cette huile dont l'indice de réfraction à température et pression ambiante est $n_0 = 1,476$ sont respectivement $n = 1,54$ et $n = 1,57$ pour les pressions de 1 GPa et 2 GPa. Les mesures d'épaisseurs de film entre 0,1 et 0,5 μm sont ainsi obtenues avec une précision de l'ordre de $\pm 0,02$ μm.

2.4. Discussion

Ce dispositif permet de réaliser la simulation des conditions de fonctionnement proches de celles rencontrées dans un roulement réel [6]. Cependant, la correspondance n'est pas complète.

Le dispositif ne simule qu'un seul contact, les effets dus aux passages des différentes billes et de la cage de roulement ne peuvent pas être reproduits. Les conditions d'alimentation en lubrifiant du contact et les échanges thermiques sont également très différents.

Le verre ou le saphir qui constitue le disque du dispositif ont des caractéristiques mécaniques et thermomécaniques différentes de celles des aciers. Remarquons cependant que le module d'Young et le coefficient de Poisson ont dans ce cas une importance secondaire et qu'ils ne modifient pratiquement pas les résultats en régime élastohydrodynamique.

3. EPAISSEUR DU FILM

L'épaisseur du film dépend des conditions d'alimentation de la région d'entrée du contact qui peuvent être caractérisées par la position du ménisque d'entrée air-huile déterminée expérimentalement. L'abscisse d'entrée x_e qui définit la position du ménisque air-huile décroît de $10a$ à $1,5a$ lorsque la

vitesse de roulement augmente. Dans les conditions expérimentales rencontrées dans cette étude, nous constatons que l'abscisse d'entrée n'a pratiquement plus d'influence sur l'épaisseur de film lorsque $x_e \geq 5a$.

3.1. Formulation théorique

L'épaisseur du film au centre du contact tonneau plan en fonction des paramètres sans dimension caractéristiques de l'épaisseur du film $H = h/R_x$, de la charge $W_* = \omega/ER_x^2$, de la vitesse $U_* = \mu(U_1+U_2)/ER_x$ et du matériau $G_* = \alpha E$, en régime élastohydrodynamique isotherme sans pivotement ni glissement latéral, s'écrit :

$$H_0 = k U_*^a G_*^b W_*^c$$

Les valeurs du coefficient k et des exposants a , b et c correspondants aux solutions élastohydrodynamiques approchées de Archard et Cowking [6] et de Cheng [7] et de la solution élastohydrodynamique exacte de Hamrock et Dowson [1] sont données table 2 pour la géométrie particulière des éprouvettes utilisées dans cette étude.

Auteur Référence	k	a	b	c
Archard et Cowking, [6]	1,15	0,74	0,74	- 0,074
Cheng, [7]	1,34	0,739	0,739	- 0,0727
Hamrock et Dowson, [1]	1,62	0,67	0,53	- 0,067

Table 2

L'épaisseur minimale du film est donnée uniquement par la solution élastohydrodynamique exacte de Hamrock et Dowson et s'écrit pour cette géométrie particulière :

$$H_m = 2,08 U_*^{0,68} G_*^{0,49} W_*^{-0,073}$$

Les effets thermiques dans la région d'entrée entraînent une réduction de l'épaisseur du film qui peut être estimée par le facteur de réduction thermique [8]. La progression du ménisque d'entrée vers le centre du contact observée à haute vitesse entraîne un aplatissement de la zone de contact et une diminution de l'épaisseur du film qui peut être calculée par l'expression proposée par Hamrock et Dowson lorsque la position du ménisque d'entrée est connue, [9].

3.2. Résultats

Les variations de l'épaisseur du film au centre du contact h_0 et de l'épaisseur minimale du film h_m en fonction de la concordance de roulement U_1+U_2 , pour les quatre pressions de Hertz retenues, figures 2.a) et b) montrent une concorde très surprenante entre les épaisseurs de films calculées et mesurées. La diminution de l'épaisseur de film observée aux hautes vitesses correspond à la progression du ménisque d'entrée vers le centre du contact. Cette diminution correspond bien à celle obtenue théoriquement lorsque l'abscisse du ménisque d'entrée qui est mesurée dans chaque essai, est introduite dans les calculs.

La réduction de l'épaisseur du film due aux effets thermiques est de l'ordre de 10 % pour les plus grandes vitesses.

Ces résultats montrent que les épaisseurs de film calculées à partir des solutions élastohydrodynamiques isothermes sans pivotement, ni glissement latéral, s'appliquent jusqu'aux très fortes pressions de 2 GPa.

Les figures 3.a), b) et c) montrent que le glissement U_1-U_2 dans la direction Ox , le glissement latéral W_1-W_2 dans la direction Oz et le pivotement $\Omega = \omega_{2y} - \omega_{1y}$ autour de l'axe Oy ont peu d'effet sur l'épaisseur du film pour une vitesse de roulement U_1+U_2 constante.

Toutefois, remarquons que les intervalles de variation des paramètres de glissement U_1-U_2/U_1+U_2 , de glissement latéral W_1/W_1+U_2 et de pivotement $\Omega/\sqrt{ac}/U_1+U_2$ sont très différents.

Les résultats expérimentaux montrent, qu'en roulement pur, l'épaisseur du film au centre du contact h_0 et l'épaisseur minimale du film h_m sont en accord avec celles calculées à partir de la nouvelle théorie élastohydrodynamique exacte de Hamrock et Dowson. La progression du ménisque d'entrée vers le centre du contact observée à haute vitesse (12 m/s) entraîne un aplatissement de la zone de contact et une diminution de l'épaisseur du film de 30 %. Les valeurs typiques des épaisseurs de film mesurées sont $h_0 = 0,26 \mu\text{m}$ et $h_m = 0,22 \mu\text{m}$ pour une vitesse de roulement de 12 m/s et une pression maximale de Hertz de 2 GPa. L'étendue du film à l'entrée du contact n'a plus d'influence sur l'épaisseur du film lorsque le ménisque d'entrée est situé à une distance supérieure à $5a$ si $2a$ est le petit axe de l'ellipse de contact. La superposition de faibles vitesses de glissement et(ou) de pivotement aux vitesses de roulement n'a que peu d'effet sur l'épaisseur du film.

4. FORCE DE FROTTEMENT

La force de frottement est mesurée sur le tonneau dans la direction Ox , pour plusieurs vitesses de roulement $\bar{U} = 1/2(U_1+U_2)$ maintenues constantes, pour les quatre pressions de Hertz retenues P , d'abord avec un glissement $\Delta U = U_1-U_2$ dans la direction Ox , ensuite avec un glissement latéral $\Delta W = W_1-W_2$ dans la direction Oz et enfin avec un pivotement $\Delta \Omega = \omega_{2y} - \omega_{1y}$ autour de l'axe Oy . La force de frottement est toujours très faible dans ces essais et les valeurs obtenues qui sont de l'ordre de 0,005 N sont comparables à la sensibilité du dispositif. Pratiquement nous réglons le système de mesure pour avoir une force de frottement nulle en roulement pur et nous obtenons les courbes de frottement en augmentant le

glissement, la vitesse de roulement restant constante.

L'étude des forces de frottement dans un contact lubrifié en régime élastohydrodynamique a été effectuée par de nombreux auteurs [10 à 15]. Les différentes lois de comportement rhéologique proposées tentent de prendre en compte les pressions très élevées existant dans le film (1 à 2 GPa), les temps de passage très courts dans le contact (10^{-4} à 10^{-6} s), des gradients de vitesse pouvant atteindre 10^7 s $^{-1}$ et des variations de température locales de l'ordre de 100°C . L'analyse de Johnson et Tevaarwerk [2] conduit à un modèle simple non linéaire de Maxwell qui permet en régime isotherme d'expliquer la plupart des résultats expérimentaux. Cependant pour des vitesses de glissement, de glissement latéral et(ou) de pivotement élevées, les effets thermiques ne sont plus négligeables.

Le calcul des forces de frottement dans un contact élastohydrodynamique nécessite la connaissance de la géométrie et de la cinématique du contact, de la pression, de l'épaisseur du film, de la température, de la loi de comportement rhéologique et des propriétés caractéristiques du fluide. Tous ces paramètres ne sont pas indépendants. Les effets thermiques n'étant pas négligeables lorsque des vitesses de glissement et de pivotement importantes se superposent aux vitesses de roulement, l'énergie dissipée dans le film du lubrifiant et dans les solides qui bordent le contact devra également être calculée. Nous retenons les hypothèses suivantes :

- la répartition des pressions dans la zone de contact hertzien elliptique, et les dimensions de l'aire de contact sont données par la théorie de Hertz.
- l'axe de l'ellipse du contact coïncide à la direction des vitesses de roulement.
- la variation des contraintes de cisaillement suivant l'épaisseur du film est négligée.
- les taux de déformation sont calculés en négligeant les changements des rayons dus aux déformations de Hertz ainsi que les déformations de l'aire du contact.
- l'épaisseur du film d'huile est constante dans la zone du contact et égale à l'épaisseur au centre du contact h_0 .
- les forces de frottement de roulement, créées à l'entrée et à la sortie de la zone du contact sont négligées. La condition aux limites qui permet de résoudre les équations différentielles suppose que les contraintes de cisaillement soient nulles sur le bord de l'ellipse du contact.

L'épaisseur du film au centre du contact utilisée dans les programmes de calcul est l'épaisseur de film mesurée. Pour éviter le défaut d'alimentation observé aux hautes vitesses, et qui correspond à la progression du ménisque d'entrée vers le centre du contact, nous choisissons des vitesses de roulement plus faibles, afin de ne pas introduire un paramètre supplémentaire caractéristique des conditions d'alimentation.

4.1. Formulation théorique

4.1.1. Modèle isotherme

Johnson et Tevaarwerk [2] ont montré que le comportement rhéologique en cisaillement d'un film d'huile dans un contact élastohydrodynamique peut être décrit simplement en régime isotherme par le modèle non linéaire de Maxwell :

$$\dot{\gamma} = \dot{\gamma}_{\text{élastique}} + \dot{\gamma}_{\text{visqueux}} = \frac{1}{G} \frac{d\tau}{dt} + \frac{\tau}{\tau_e} \frac{\tau_0}{\mu} \sinh \left(\frac{\tau_e}{\tau_0} \right)$$

où $\dot{\gamma}$ est le gradient de vitesse total, τ est la contrainte, G le module d'élasticité en cisaillement, τ_0 la contrainte représentative au dessus de laquelle le comportement devient non linéaire et τ_e la contrainte locale équivalente. Dans les axes Oxz , si $dt = 2dx/U_1 + U_2 = dx/\bar{U}$, les équations s'écrivent :

$$\dot{\gamma}_x = \frac{\bar{U}}{G} \frac{d\tau_x}{dx} + \frac{\tau_x}{\tau_e} \cdot \frac{\tau_0}{\mu} \sinh \left(\frac{\tau_e}{\tau_0} \right)$$

$$\dot{\gamma}_z = \frac{\bar{U}}{G} \frac{d\tau_z}{dx} + \frac{\tau_z}{\tau_e} \cdot \frac{\tau_0}{\mu} \sinh \left(\frac{\tau_e}{\tau_0} \right)$$

avec : $\tau_e = \sqrt{\tau_x^2 + \tau_z^2}$, $\dot{\gamma}_x = (\Delta U + \Delta \Omega z)/h$ et $\dot{\gamma}_z = (\Delta \omega - \Delta \Omega x)/h$.

La résolution de ces équations nécessite donc la connaissance de trois paramètres caractéristiques du fluide : sa viscosité μ , son module d'élasticité G et une contrainte de référence τ_0 . Ces paramètres sont des fonctions de la pression, de la température et du temps de passage du fluide dans le contact. L'intégration du système d'équation différentiel en τ_x et τ_z devient simple si des valeurs moyennes des paramètres \bar{G} , $\bar{\mu}$ et $\bar{\tau}_0$ sont retenues. La forme des courbes de frottement dépend du nombre de Deborah :

$$D_e = \frac{\bar{\mu} \bar{U}}{\bar{G} a}$$

qui compare le temps de relaxation du fluide $\bar{\mu}/\bar{G}$ au temps de passage du fluide dans le contact a/\bar{U} .

Pour de faibles valeurs de D_e associées à de faibles pressions et(ou) de faibles viscosités, le comportement du fluide est visqueux aux faibles gradients de vitesse et visqueux non linéaire à forts gradients de vitesse. Pour les moyennes et grandes valeurs de D_e obtenues avec des pressions, des viscosités et(ou) des coefficients de piézo-viscosité élevés, le comportement du fluide qui est élastique aux faibles gradients de vitesse devient visqueux non linéaire pour les gradients de vitesse élevés. Dans le cas où $D_e \gg 1$ le comportement élastique devient rapidement plastique et une contrainte limite de cisaillement dans le fluide $\bar{\tau}_2$ peut être aussi définie. Ce modèle est peu différent du modèle proposé par Bair et Winer [16] dans lequel la contrainte limite $\bar{\tau}_2$ est introduite.

Dans les programmes de calcul nous utiliserons les valeurs de \bar{G} et de $\bar{\tau}_2$ déterminées à partir des

courbes de frottement expérimentales obtenues pour de grands nombres de Deborah. Aux faibles gradients de vitesse (10^3 s^{-1}), le module d'élasticité apparent \bar{G} est défini par l'expression :

$$\bar{G} = \bar{\tau} \frac{h_0 (U_1 + U_2)}{2a (U_1 - U_2)}$$

où a est le demi petit axe de l'ellipse de contact et $\bar{\tau}$ la valeur moyenne de la contrainte de cisaillement telle que : $\bar{\tau} = f_x / \pi a c$.

Les valeurs du module d'élasticité apparent \bar{G} sont obtenues en mesurant la pente dans la région linéaire qui correspond à : $0 < \bar{\tau} < 1/2 \bar{\tau}_l$ est une fonction de la pression moyenne \bar{P} qui pour l'huile utilisée s'écrit :

$$\bar{G} = 1,27 \bar{P} - 0,50$$

La contrainte limite moyenne $\bar{\tau}_l$, qui correspond à la contrainte maximale, est une fonction de la pression moyenne \bar{P} et de la température moyenne $\bar{\theta}$ qui suit la relation empirique proposée par Dyscn, [12] :

$$\bar{\tau}_l = \frac{0,3 \bar{P}}{2,52 + 0,024 \bar{\theta}} - 0,2 \times 10^8$$

La contrainte de référence $\bar{\tau}_0$ est difficile à calculer en pratique. Johnson et Tevaarwerk [2] évaluent la contrainte $\bar{\tau}_0$ sur la surface de l'ellipse de contact afin d'ajuster la valeur expérimentale à la valeur théorique dans le cas où $\tau \gg \tau_0$. Réchemon Conry et al [17] déterminent τ_0 plus précisément et montrent que l'effet de la variation de la température peut être négligée. La contrainte $\bar{\tau}_0$ peut donc être considérée comme une fonction de la pression moyenne \bar{P} seulement. Nous utilisons une méthode itérative pour calculer $\bar{\tau}_0$ afin d'obtenir en intégrant les équations différentielles une valeur de la contrainte maximale correspondant à la valeur expérimentale $\bar{\tau}_l$.

Les équations différentielles avec les conditions aux limites associées sont résolues numériquement dans l'ellipse de contact par la méthode d'Adams-Bashforth, [18].

4.2. Modèles thermiques

La répartition des températures à travers le film dépend de plusieurs paramètres qui comprennent :

- le cisaillement local du film qui est lui-même fonction de la température,
- la quantité de chaleur dissipée, son origine et sa localisation,
- les températures des parois qui varient avec la chaleur transmise vers les parois,
- les effets dus à l'histoire des températures des parois et du film.

4.2.1. Modèle thermique de Daniels

Daniels [3] a supposé que la chaleur est créée en chaque point de la zone du contact par le cisaillement visqueux d'un élément équivalent de lubrifiant ayant des propriétés qui sont fonctions de la pression et de la température. La température de cet élément est supposée uniforme à travers le film. Il définit également la température effective θ_{ef} de cet élément équivalent pour lequel, la chaleur créée est égale à celle d'un élément réel mais dont la température réelle peut être plus grande au milieu du film.

La chaleur est transmise aux parois par conduction. Les parois sont isothermes avec une température : $\theta_s = \theta_{s1} = \theta_{s2}$. Daniels suppose que la chaleur est créée au milieu du film où la température maximale est égale à θ_{max} . La température effective θ_{ef} est égale à $0,5 \theta_{max}$ pour une répartition triangulaire des températures à travers le film et s'écrit si K_f est la conductivité thermique du fluide :

$$\theta_{ef} = \theta_s + \frac{\tau_e \tau_0 h^2}{8K_f \mu} \sin h \left(\frac{\tau_e}{\tau_0} \right)$$

Les détails de la méthode de calcul des forces de frottement avec le modèle non linéaire de Maxwell et le modèle thermoviscoélastique de Daniels sont présentés dans les références [3] et [18].

4.2.2. Modèle thermique de Tevaarwerk

Tevaarwerk [4] donne une solution tridimensionnelle thermique semi-analytique, semi-numérique, applicable dans la région de la courbe de frottement où les gradients de vitesse sont très importants. Ils suppose que le cisaillement se produit dans un plan situé au milieu du film en se référant aux résultats de Johnson et Cameron [11]. Tevaarwerk [19] montre également que les vitesses de pivotement modifient de façon très significative le comportement du film dans le contact et qu'aux grandes valeurs de pivotement, l'effet thermique est très important.

Dans ce modèle, les échanges de chaleur par convection qui ne sont pas négligeables sont également considérés. Les températures des surfaces du contact sont égales et varient en tout point de la surface $\theta_{s1}(x, z) = \theta_{s2}(x, z)$.

La contrainte de cisaillement locale τ dans le fluide peut être calculée si les équations de l'énergie dans les solides et dans le fluide sont résolues simultanément.

L'équation de l'énergie dans un solide élastique isotrope semi-infini animé d'une vitesse \bar{U} et soumis en surface à une source de chaleur $q(x, z)$ s'écrit :

$$\frac{\partial^2 \theta}{\partial x^2} + \frac{a^2}{b^2} \frac{\partial^2 \theta}{\partial y^2} + \frac{a^2}{c^2} \frac{\partial^2 \theta}{\partial z^2} = \bar{U} a \alpha_s \frac{\partial \theta}{\partial x}$$

si : $X = x/a$, $Y = y/b$, $Z = z/c$ et α_s est la diffusivité du solide.

A la surface du solide $\partial\theta_s/\partial y = 0$ à l'extérieur de la surface de la source de chaleur et $\partial\theta_s/\partial y = -q(x,z)/K_s$ si K_s est la conductibilité thermique des solides sur la surface en contact avec la source. Le nombre de Péclet du solide $Pe_s = \bar{U} a \alpha_s$ détermine l'importance relative de la propagation de chaleur par convection et par conduction. Dans un contact élastohydrodynamique, Pe_s est grand et le transfert de chaleur dans le solide s'effectue principalement par convection.

L'équation de l'énergie dans le cas d'un film mince incompressible tel que $h \ll a$ ou c et qui contient le terme correspondant à la source de chaleur résultant essentiellement du cisaillement visqueux s'écrit :

$$\frac{\partial^2 \theta}{\partial y^2} + \frac{h^2}{K_f} \phi(X, Y, Z) = \frac{\bar{U} h^2 \alpha_f}{a} \frac{\partial \theta}{\partial X}$$

Le nombre de Péclet du fluide $Pe_{ef} = \bar{U} h^2 \alpha_f / a$ si α_f est la diffusivité du fluide permet de savoir si le transport de la quantité de chaleur produite dans le film se fait par conduction vers les solides lorsque Pe_{ef} est petit ou par convection dans le fluide lorsque Pe_{ef} est grand. A l'interface solide fluide $\theta_s = \theta_f$.

Nous retiendrons l'hypothèse émise par Johnson et Cameron [11] et reprise récemment par Tevaarwerk [4] dans laquelle le cisaillement se produit dans un plan situé au milieu du film. Cette hypothèse entraîne une condition au limite supplémentaire dans le plan milieu du film d'indice c .

$$\frac{\partial \theta_c}{\partial y} = - \frac{\gamma Q(x, y_c, z)}{K_f}$$

où γ est le coefficient de partage vers les deux parois solides et Q la quantité de chaleur produite par le cisaillement au milieu du film telle que :

$$Q = \tau_x \Delta U + \tau_z \Delta W$$

Cette hypothèse est d'autant mieux vérifiée que les glissements ΔU et ΔW sont importants et que la contrainte limite locale τ_l est atteinte. Lorsque le comportement du film fluide est entièrement dissipatif Q devient :

$$Q = \tau_l \sqrt{\Delta U^2 + \Delta W^2}$$

Nous utiliserons la méthode numérique itérative proposée par Tevaarwerk [4] pour résoudre ce problème difficile. L'ellipse de contact est découpée en bandes suivant la direction du roulement correspondant à l'axe x et de largeur élémentaire Δz . Chaque bande est ensuite divisée en éléments Δx . Lorsque le nombre de Péclet du solide est grand, le transfert de chaleur se fait essentiellement par conduction dans la direction x et la propagation latérale entre deux bandes dans la direction z peut être négligée. Le processus de calcul consiste à calculer $\theta_c(x)$, $Q(x)$ sur une bande et la température des surfaces des solides $\theta_s(x)$ correspondante. Le calcul est répété avec cette température de surface jusqu'à convergence. La technique utilisée et les détails de la solution sont précisés dans les références [4] et [18].

4.2. Résultats

Les forces de frottement f_x sont mesurées et calculées dans la direction du roulement en fonction du taux de glissement pour une vitesse de roulement $U_1 + U_2 = 6,74$ m/s.

La figure 4 représente la variation de f_x en fonction de $U_2 - U_1 / U_1 + U_2$ pour différentes charges sans glissement latéral ni pivotement. Les valeurs du coefficient de frottement obtenues sont toujours inférieures à 0,07. La forme des courbes de frottement permettent de penser que l'huile se comporte comme un solide amorphe à l'état vitreux dans la zone de contact [20]. En effet le diagramme 18 de la référence [20] tracé pour une huile semblable suggère que pour des pressions maximales de Hertz de 1 à 2 GPa et des températures de 35 à 55°C l'huile est à l'état vitreux dans une région pratiquement étendue à toute la surface de l'ellipse de contact. Ces résultats qui sont en accord avec ceux obtenus indépendamment par Bair et Winer grâce à un viscosimètre à très haute pression [16 et 21], montrent que l'huile se comporte comme un solide amorphe plastique caractérisé par sa contrainte limite moyenne τ_l .

La figure 5 représente la variation de f_x en fonction de $U_2 - U_1 / U_2 + U_1$ pour la charge de 16 N sans pivotement et plusieurs valeurs de l'angle β qui introduit le glissement latéral.

La figure 6 représente la variation de f_x en fonction de $U_2 - U_1 / U_2 + U_1$ pour la charge de 16 N, sans glissement latéral et plusieurs valeurs de l'angle λ qui introduit le pivotement.

La superposition d'un pivotement et (ou) d'un glissement latéral entraîne une diminution de la force de frottement f_x .

En comparant les résultats théoriques isothermes avec les résultats expérimentaux, nous constatons un très bon accord aux faibles gradients de vitesse au voisinage de roulement pur où le régime de fonctionnement est bien isotherme.

Pour les gradients de vitesse plus élevés, l'utilisation des modèles thermiques de Daniels et Tevaarwerk entraîne également une bonne concordance entre les résultats. Remarquons que les vitesses de pivotement considérées dans ces essais sont toujours faibles, et qu'en conséquence, la convection de chaleur n'a que peu d'effet sur les températures dans le contact et sur le comportement rhéologique du lubrifiant. L'utilisation du modèle thermique de Tevaarwerk contre qu'un très bon accord est obtenu tant en présence de pivotement que de glissement latéral.

4.3. Discussion

L'ensemble des calculs théoriques des forces de frottement effectués en régime élastohydrodynamique montre que le modèle non linéaire de Maxwell proposé par Johnson et Tevaarwerk, représente bien les transitions viscoélastiques du fluide dans le contact en régime isotherme, mais il ne donne pas la décroissante de la courbe de frottement obtenue expérimentalement aux grands taux de glissement. La prise en compte des effets thermiques devient alors nécessaire. Nous avons donc utilisé deux modèles thermiques : celui de Daniels qui considère seulement la conduction de chaleur à travers le film, et celui de Tevaarwerk qui tient compte également de la convection de chaleur. Ces deux modèles donnent des résultats qui sont en accord avec les résultats expérimentaux.

L'utilisation de ces différents modèles rhéologique et thermique repose sur le calcul précis des contraintes de cisaillement limite de Newton τ_0 . La table 3 montre la correspondance entre les valeurs de τ_0 calculées d'une part par la méthode de Conry et al [17] et d'autre part par notre méthode itérative, pour l'huile minérale utilisée dans nos essais, à la pression maximale de Hertz $P = 1.91$ GPa et pour différentes vitesses de pivotement.

	λ°	τ_0 (MPa)	
		Notre méthode numérique	Méthode de Conry et al
Modèle isotherme	2	2.20	2.40
	6	2.10	2.20
	18	2.03	2.10
Modèle de Daniels	2	2.30	2.50
	6	2.10	2.20
	18	2.05	2.10
Modèle de Tevaarwerk	2	2.35	2.55
	6	2.15	2.30
	18	2.07	2.17

Table 3

La force de frottement latérale f_y n'est pas mesurée sur le dispositif. Les valeurs calculées sont toujours très inférieures à celles de la force de frottement f_x dans la direction du roulement. Les courbes de frottement latérales calculées ont la même allure que celles données par Johnson et Tevaarwerk [2] et les mêmes ordres de grandeur sont obtenus. Ce résultat met en évidence l'importance du rôle des forces de frottement latérales dans le contact existant entre une bille et un chemin de bague de roulement à billes à contacts obliques.

5. CONCLUSION

Les résultats obtenus montrent que dans un contact hertzien fonctionnant en régime élastohydrodynamique jusqu'aux pressions très élevées de 2 GPa, l'épaisseur du film dépend essentiellement des caractéristiques du film dans la région d'entrée du contact où s'effectue la montée en pression et la force de frottement des contraintes de cisaillement sur les parois dans la zone centrale du contact correspondant à la surface de l'ellipse de contact donnée par la théorie de Hertz.

Les épaisseurs de film mesurées au voisinage du roulement pur sont en accord avec celles calculées à partir de la solution théorique élastohydrodynamique exacte de Hamrock et Dowson dans laquelle la viscosité du fluide varie avec la pression suivant une loi exponentielle. La superposition d'une vitesse de glissement, de glissement latéral ou de pivotement n'entraîne qu'une faible diminution de l'épaisseur du film.

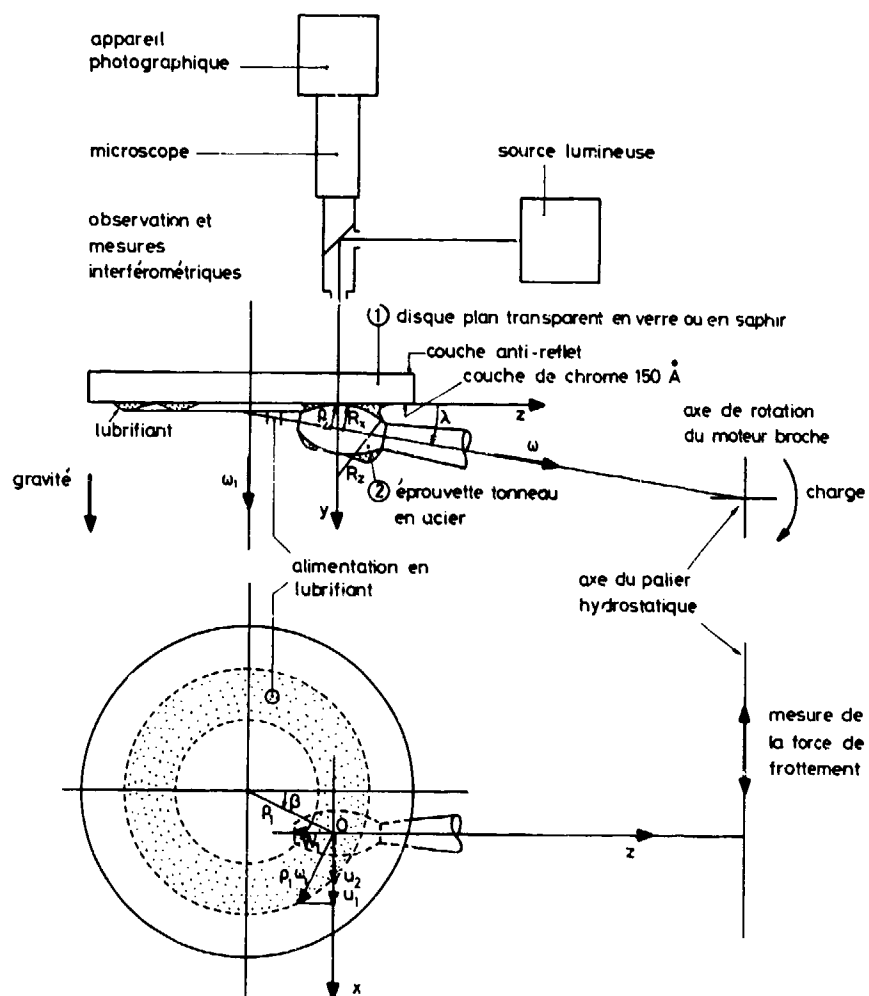
Les courbes expérimentales qui représentent la force de frottement en fonction du taux de glissement dans la direction du roulement, sans pivotement ni glissement latéral, montrent que la force de frottement croît, atteint un maximum puis décroît pour une charge et une vitesse de roulement constante. La forme typique des courbes de frottement obtenues suggère pour les pressions de 1 à 2 GPa, un comportement du film élastique-plastique. Le film se caractérise dans ce cas par un module d'élasticité moyen et par une contrainte limite moyenne qui sont des fonctions de la température et de la pression moyenne dans le contact. L'analyse des forces de frottement mesurées au voisinage de roulement pur dans ce contact soumis à de très fortes pressions montre que le modèle isotherme non-linéaire de Maxwell, de Johnson et Tevaarwerk est applicable. Le calcul des forces de frottement en régime isotherme, donne des résultats très satisfaisants pour les faibles gradients de vitesse, mais surestime les résultats aux forts gradients de vitesse qui correspondent à un régime de fonctionnement où les effets thermiques ne sont plus négligeables. Nous avons retenu deux modèles thermiques qui permettent de calculer l'énergie dissipée aux grands gradients de vitesses de glissement et de pivotement. Le plus simple de ces modèles thermiques est celui de Daniels qui considère des températures constantes sur les surfaces du contact et qui envisage le transfert de chaleur du film vers les parois du contact par la conduction seulement. Le deuxième modèle thermique plus complet est celui de Tevaarwerk qui considère un plan de cisaillement au milieu du film où la température est maximale, qui tient compte également du transfert de chaleur dans le film par convection et du changement des températures des surfaces du contact. Les deux modèles thermiques utilisés donnent des résultats satisfaisants par comparaison avec les résultats expérimentaux obtenus sur le dispositif expérimental de simulation du contact bille-chemin de bague de roulement à billes à contacts obliques.

REMERCIEMENTS

Cette étude a été financée par la Direction des Recherches et Moyens d'Essais, (contrat n° 73.7 0722), Paris, France.

REFERENCES

- 1 - HAMROCK, B.J. et DOWSON, D., "Isothermal elastohydrodynamic lubrication of point contacts. Part III - Fully flooded results", Trans. ASME, series F, vol.99, pp. 264-276, 1977.
- 2 - JOHNSON, K.L. et TEVAARWERK, J.L., "Shear behaviour of elastohydrodynamic oil films", Proc. Roy. Soc., London, series A, vol.356, pp. 215-236, 1977.
- 3 - DANIELS, B.K., "Non newtonien thermo-viscoelastic EHD traction from combined slip and spin", Trans. ASLE, vol.23, 2, pp. 141-154, 1980.
- 4 - TEVAARWERK, J.L., "Traction calculations using the shear plane hypothesis", Paper VII (iii), Proc. of 6th Leeds-Lyon Symposium on Tribology, pp.201-215, sept. 1979.
- 5 - DALMAZ, G., "Simulating angular ball bearing lubricated elliptical contacts. Film thickness and traction measurements", Tribology International, pp. 273-279, oct. 1978.
- 6 - ARCHARD J.F. et COWKING E.W., "Elastohydrodynamic lubrication at point contacts". Elastohydrodynamic lubrication symposium. Proc. Inst. Mech. Eng., vol.180, part 3B, pp. 47-56, 1965-66.
- 7 - CHENG H.S., "A numerical solution of the elastohydrodynamic film thickness in an elliptical contact". Trans. ASME, series F, vol.92, pp. 155-162, 1970.
- 8 - GREENWOOD J.A. et KAUZLARICH J.J., "Inlet shear heating in elastohydrodynamic lubrication". Trans. ASME, series F, vol.95, pp. 417-426, et discussion de Dyson A., p. 423, 1973.
- 9 - HAMROCK B.J. et DOWSON D., "Isothermal elastohydrodynamic lubrication of point contacts. Part IV : Starvation results". Trans. ASME, series F, vol.99, pp. 15-23, 1977.
- 10 - CROOK A.W., "The lubrication of rollers, III, A theoretical discussion of friction and the temperatures in the oil film", Phil. Trans. Roy. Soc., London, series A, vol.254, pp. 237-258, 1961.
- 11 - JOHNSON K.L. et CAMERON R., "Shear behaviour of elastohydrodynamic oil film at high rolling contact pressure", Proc. IME, vol.182, pp. 307-327, 1967-1968.
- 12 - DYSON A., "Frictional traction and lubricant rheology in elastohydrodynamic lubrication", Phil. Trans. Roy. Soc., London, vol.266, n° 1170, pp. 1-33, 1970.
- 13 - HIRST W. et MOORE A.J., "Non newtonien behaviour in elastohydrodynamic lubrication", Proc. Roy. Soc., London, series A, vol.227, pp. 101-121, 1974.
- 14 - JOHNSON K.L. et ROBERTS A.D., "Observations of viscoelastic behaviour of an elastohydrodynamic lubricant film", Proc. Roy. Soc., London, series A, vol.337, pp. 217-242, 1974.
- 15 - TRACHMAN E.G. et CHENG H.S., "Thermal and non newtonien effects on traction in elastohydrodynamic contacts", Proc. of the Second Symposium on Elastohydrodynamic Lubrication, IME, London, pp. 142-148, 1972.
- 16 - BAIR S. et WINER W.O., "Shear straight measurements of lubricants at high pressure", Trans. ASME, series F, vol.101, pp. 251-257, 1979.
- 17 - CONRY T.F., JOHNSON K.L. et OWEN S., "Viscosity in the thermal regime of EHD traction", Paper VIII(i), Proc. of 6th Leeds-Lyon Symposium on Tribology, pp. 219-227, sept. 1979.
- 18 - GADALLAH N., "Effets de la géométrie et de la cinématique sur l'épaisseur du plan et de la force de frottement dans un contact ponctuel lubrifié", Thèse de Docteur-Ingénieur, INSA, UCB et ECL de Lyon, n° ID 13-8114, 1981.
- 19 - TEVAARWERK J.L., "Traction drive contact performance prediction using the Johnson and Tevaarwerk traction model", NASA, Tech. Publication, TP. 1530, 1979.
- 20 - ALSAAD M., BAIR S., SANBORN et WINER W.O., "Glass transitions in lubricants : its relation to elastohydrodynamic lubrication", Trans. ASME, series F, vol.100, pp. 404-417, 1978.
- 21 - BAIR S. et WINER W.O., "A rheological model for elastohydrodynamic contacts based on primary laboratory data", Trans. ASME, series F, vol.101, pp. 258-265, 1979.



Paramètres du contact

$$\rho_1 ; \rho_2 = R_x - R_z (1 - \cos \lambda) ; \beta ; \lambda$$

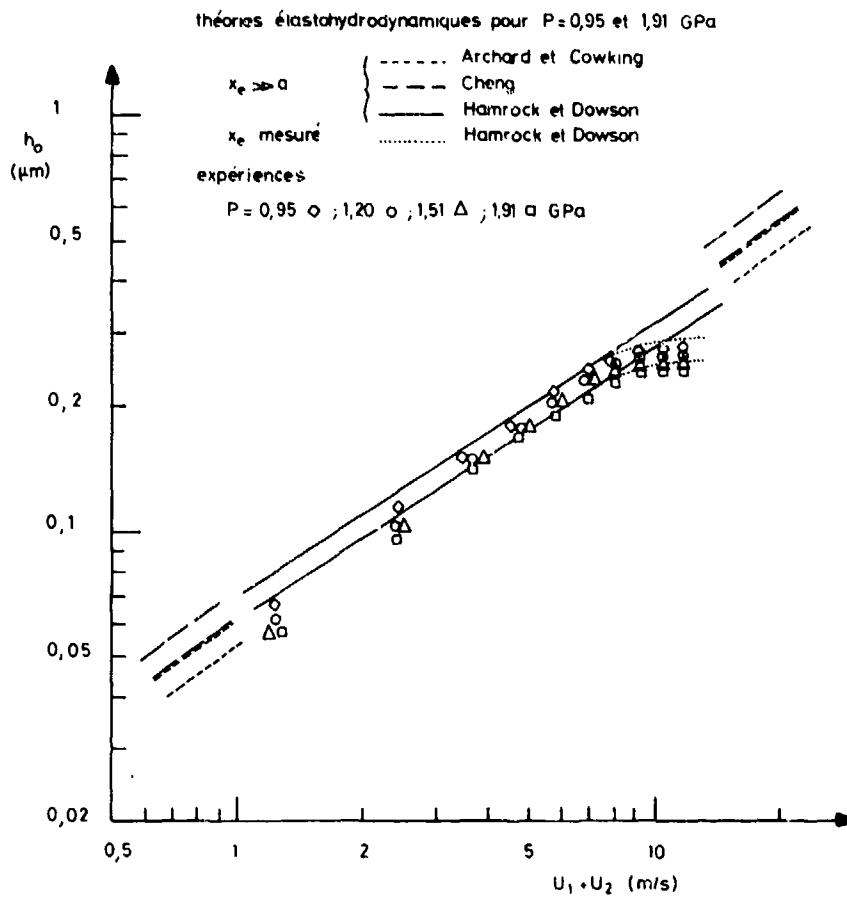
Rayons de courbure locaux

$$R'_x = \frac{\rho}{\cos \lambda} ; R'_z = R_z$$

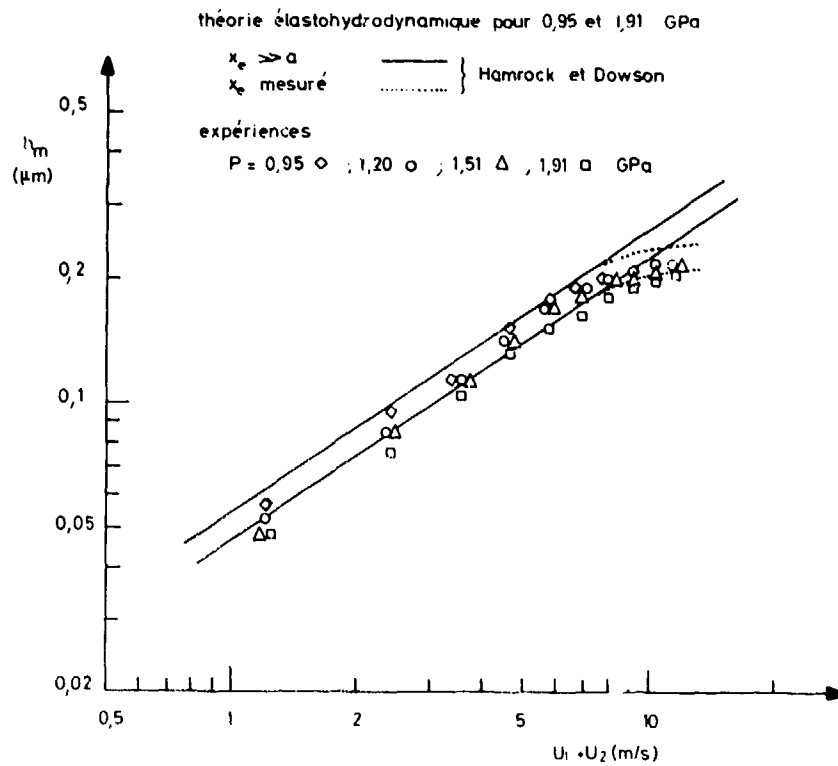
Composantes des vitesses dans les axes Oxyz

$$\begin{cases} U_1 = \rho_1 \omega_1 \cos \beta \\ W_1 = U_1 \operatorname{tg} \beta \end{cases} \quad \begin{cases} U_2 = \rho_2 \omega_2 \\ W_2 = 0 \end{cases} \quad \begin{cases} \omega_{1y} = \omega_1 \\ \omega_{2y} = \omega_2 \sin \lambda \end{cases}$$

Fig. 1 : Schéma de principe du dispositif tonneau-pian

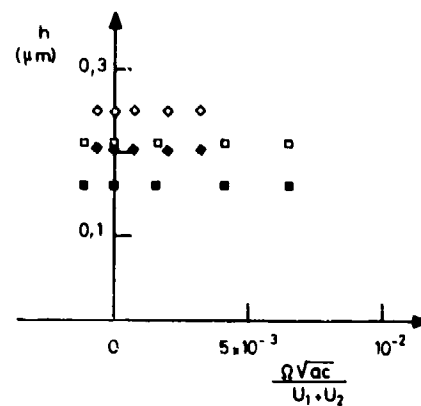
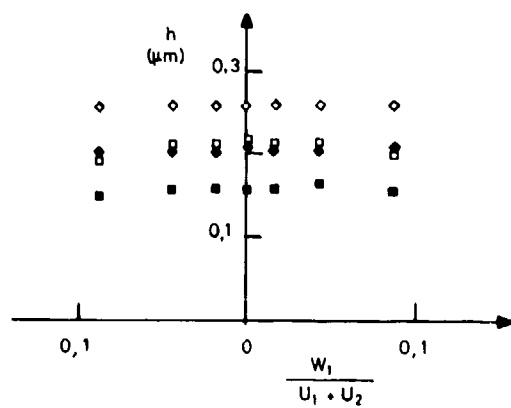
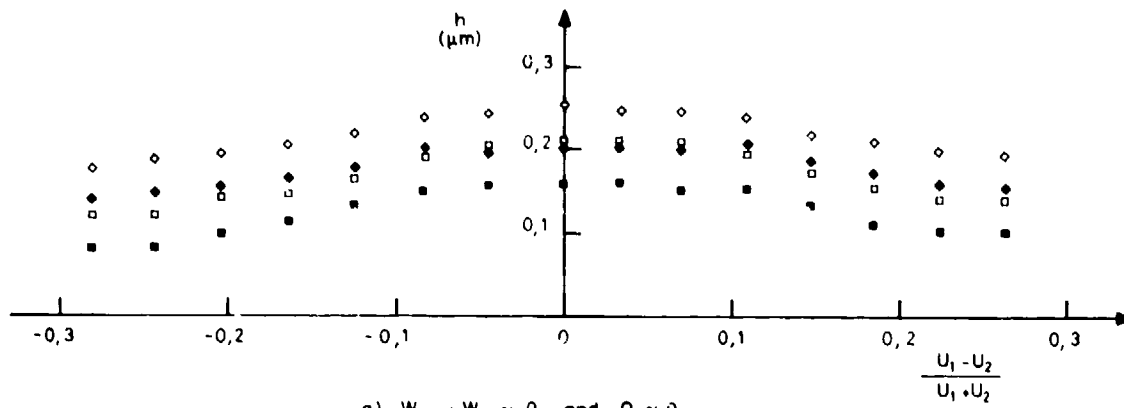


a) épaisseur du film au centre du contact



b) épaisseur minimale du film

Fig 2 Variation de l'épaisseur du film en fonction de la vitesse de roulement, sans pivotement ni glissement, pour différentes pressions maximales de Hertz



h_o : P = 0,95 \diamond et 1,91 \square GPa ; h_m : P = 0,95 \blacklozenge et 1,91 \blacksquare GPa

h_o : P = 0,95 \diamond et 1,91 \square GPa ; h_m : P = 0,95 \blacklozenge et 1,91 \blacksquare GPa

Fig. 3 : Variation de l'épaisseur minimale et de l'épaisseur du film au centre du contact en fonction des paramètres de glissement, de glissement latéral et de pivotement pour $U_1 + U_2 \approx 6,74$ m/s et deux pressions de Hertz

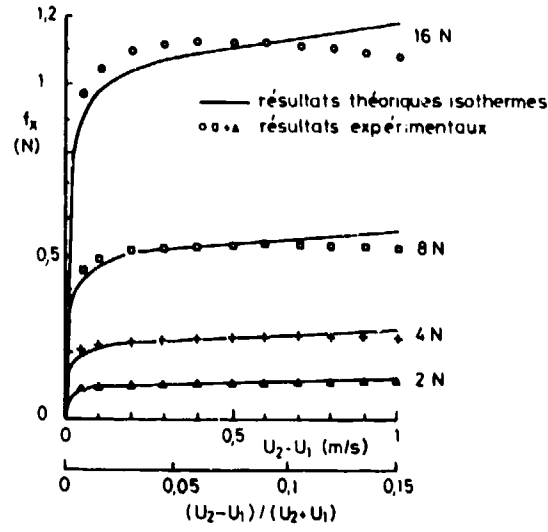


Fig. 4 : Variation de la force de frottement f_x en fonction de la vitesse de glissement pour $U_1 + U_2 = 6,74$ m/s sans pivotement ni glissement latéral et pour différentes charges

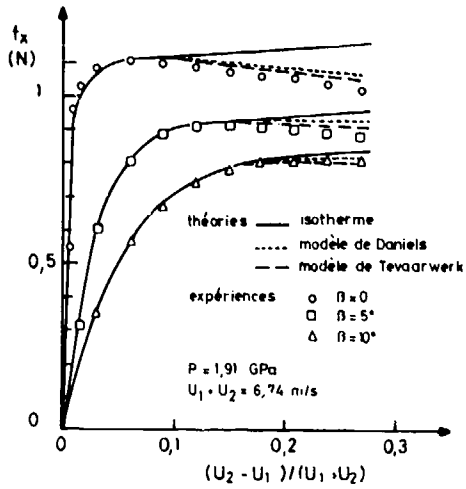


Fig. 5 : Influence du glissement latéral sur la force de frottement f_x lorsque $\lambda \neq 2^\circ$

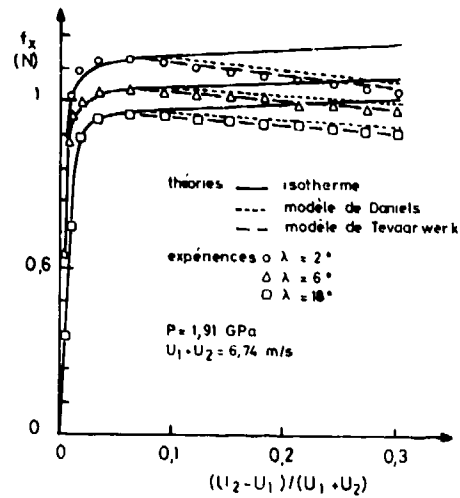


Fig. 6 : Influence du pivotement sur la force de frottement f_x lorsque $\beta = 0$

DISCUSSION

J.F.Chevalier, SNECMA, Fr

Les modèles que votre expérience valie pour des rayons de courbure très petits, sont-ils valables pour des grandes billes, avec de grands rayons de courbure?

Reponse d'Auteur

Différentes études expérimentales effectuées au laboratoire ou parues dans la littérature avec des rayons de courbure importants (10 mm $R_x < 20$ mm) ont établi la validité des théories élastohydrodynamiques (Ref. 1, 6, 7, 9). La confiance dans ces théories semble aujourd'hui bien établie, pour la cinématique, la géométrie et le comportement rhéologique pris en compte.

J.F.Chevalier

Avez vous essayé de mesurer la force transversale et le couple de frottement?

Reponse d'Auteur

Le dispositif a été modifié pour mesurer la force de frottement transversale, le couple ne pourra pas encore être mesuré. Des résultats seront publiés sous peu sur ce problème essentiel pour confirmer le bien fondé du comportement rhéologique du lubrifiant.

J.F.Chevalier

Avez vous essayé d'utiliser une huile plus fluide pour simuler une température plus élevée que l'ambiante?

Reponse d'Auteur

Compte tenu de la précision de la méthode interférométrique il est difficile de mesurer de très faible épaisseur de film d'huile.

B.J.Hamrock, NASA Lewis Research Center, US

Pouvez-vous donner plus de détails sur l'expression de la contrainte limite de cisaillement mentionnée dans l'article. Pouvez-vous également indiquer pour quel groupe de fluides cette expression est valable.

Reponse d'Auteur

La contrainte limite de cisaillement T_1 est l'une des caractéristiques du lubrifiant qui est fondamentale pour expliquer son comportement rhéologique dans les contacts très fortement chargés en régime élastohydrodynamique.

La valeur moyenne de la contrainte limite T_1 est déterminée directement à partir des courbes de frottement (fig.4). Les valeurs de T_1 obtenues pour l'huile minérale utilisée dans ces essais, pour des pressions maximales de Hertz de 1 à 2 GPa et des températures moyennes de 25 à 60°C correspondent bien à celles données par la relation empirique proposée par A.Dyson. Ces résultats sont également en accord avec ceux obtenus indépendamment par S.Bair et W.O.Winer qui mesurent la contrainte limite d'une huile semblable sur un viscosimètre à très hautes pressions.

Nous ne disposons pas actuellement de valeurs pour d'autres types de fluides mais nous pensons entreprendre des essais analogues pour d'autres lubrifiants.

THE LUBRICATION OF RIGID ELLIPSOIDS BY A PIEZO-VISCOUS FLUID

D. DOWSON, J.F. DUNN and C.M. TAYLOR

The Institute of Tribology,
Department of Mechanical Engineering,
The University of Leeds,
Leeds LS2 9JT
U.K.

SUMMARY

The lubrication of non-conformal contacts such as those occurring between gear teeth and the rolling elements and raceways of rolling bearings is influenced by two major physical effects. These are the extent to which the lubricant viscosity is enhanced due to the pressures to which it is subjected and the degree of elastic distortion of the bounding surfaces. Tribologists have defined four forms of fluid film lubrication depending on the extent of these effects, namely; rigid (solids) - isoviscous (lubricant); elastic-isoviscous; elastic-piezo-viscous; and rigid-piezo-viscous. The latter regime of lubrication has not previously been analysed for point contacts with the same general set of conditions as have been applied to the other forms. Such an analysis has been undertaken here and the results are presented in a formula enabling the limiting minimum film thickness to be calculated directly.

NOTATION

g'_e	dimensionless elasticity parameter for point contacts	$\left[= \frac{W'}{U^2} \right]^{8/3}$
g'_v	dimensionless viscosity parameter for point contacts	$\left[= GU \left(\frac{W'}{U} \right)^3 \right]$
h	film thickness	
k	ellipticity ratio for Hertzian contacts	
p	pressure	
q	reduced pressure	
u	entraining velocity	
x, y	Cartesian coordinates in plane of lubricating film	
G	dimensionless materials parameter (reference 4)	
H	dimensionless film thickness ($= h/R_x$)	
\hat{H}	dimensionless film parameter	$\left[= H \left(\frac{W'}{U} \right)^2 \right]$
R_x, R_y	principal radii of curvature of equivalent ellipsoid	
U	dimensionless speed parameter (reference 4)	
W'	dimensionless load parameter (reference 4)	
X, Y	dimensionless coordinates ($= x/R_x, y/R_x$)	
α	pressure viscosity coefficient	
δ	radius ratio (R_y/R_x)	
n	lubricant viscosity	
n_0	lubricant viscosity at atmospheric pressure	
ϕ	Vogelpohl substitution	

Subscript

o minimum film thickness

INTRODUCTION

The nature of the lubrication of a conjunction between two ellipsoids will be resolved by the degree to which two physical effects are influential. The variation of lubricant viscosity with pressure (the piezo-viscous effect) and the local deformation of the solids under the action of high pressure may or may not be important and this has prompted the recognition of four distinctive forms of fluid film lubrication normally described as,

- (i) rigid-isoviscous
- (ii) elastic-isoviscous
- (iii) elasto-variable viscosity (piezo-viscous)
- (iv) rigid-variable viscosity (piezo-viscous)

For the case of line contacts analytical or numerical solutions of each of these four lubrication regimes have been available for some time and this has enabled Johnson (1) to present a film thickness map. Such a map enables the dominant physical action to be clearly identified based on the operating conditions and also makes possible estimates of the appropriate minimum lubricant film thickness.

In the case of so called point contacts, where the boundary solids have curvatures in two principal directions, similar regimes of lubrication are possible and substantial computational effort has been directed towards obtaining numerical solutions predicting the film thickness. This is particularly true for the first three of the forms of lubrication mentioned above. Brewe et al (2) developed a formula for the prediction of minimum film thickness in the rigid-isoviscous regime and Hamrock and Dowson (3,4) examined the elastic-isoviscous and elastic-variable viscosity regions. The formulae developed for minimum film thickness may be presented as follows.

Rigid-Isoviscous (2)

$$\hat{H}_0 = H_0 \left(\frac{W'}{U} \right) = \left[1.482 \tan^{-1} \left(\frac{\delta}{2} \right) + 19.04 \right]^2 \frac{\delta}{\left[1 + \frac{2}{3\delta} \right]} \quad (1)$$

Elastic-Isoviscous (3)

$$\hat{H}_0 = H_0 \left(\frac{W'}{U} \right)^2 = 8.70 (g_e')^{0.67} \left[1 - 0.85e^{-0.31k} \right] \quad (2)$$

Elastic-Piezo-Viscous (4)

$$\hat{H}_0 = H_0 \left(\frac{W'}{U} \right)^2 = 3.42 (g_v')^{0.49} (g_e')^{0.17} \left[1 - e^{-0.68k} \right] \quad (3)$$

However, the rigid-piezo-viscous regime has not previously been analysed with the same general set of conditions for point contacts as have been applied to the other regimes of lubrication. Such an analysis has been undertaken to present the results given here. The rigid-piezo-viscous form of lubrication may be of importance, for example, in the rolling element/raceway contacts of high speed rolling bearings and also in the contacts between the rib/roller ends in taper roller and cylindrical roller bearings.

BACKGROUND

Noteworthy developments in the lubrication of rigid solids by a piezo-viscous lubricant were made in the decade following Gatcombe's contribution. Gatcombe (5) had demonstrated that the observed exponential increase in viscosity with pressure would have a beneficial effect upon film thickness at a given load, and this was confirmed for a parabolic viscosity-pressure relationship by Hersey and Lowdenslager (6).

McEwen (7) considered a viscosity-pressure relationship of the form $\eta = \eta_0 (1+p/k)^n$ and found that for values of (n) ranging from 6 to 11 and a Reynolds cavitation boundary condition, the theoretical load carrying capacity for a given minimum film thickness was increased above the Martin prediction by factors ranging from 2.8 to 2.4. This finding was endorsed by Blok (8) in an important discussion in which he pointed out that for an exponential viscosity-pressure characteristic there was limiting minimum film thickness at which the predicted maximum pressure became infinite. For this limiting condition and the geometry of a rigid cylinder near a plane, Blok predicted that piezo-viscous effects could account for a maximum increase in film thickness of about 131 percent.

A remarkable extension of classical hydrodynamic lubrication theory for counter-formal conjunctions was recorded by Kapitza (9), who presented an elegant analysis of both cylindrical and ellipsoidal solids lubricated by either iso-viscous or piezo-viscous fluids. In the case of cylindrical solids Kapitza was able to incorporate the Reynolds cavitation boundary condition. It was shown that the limiting film thickness discussed by Blok for a piezo-viscous lubricant could be written in a form equivalent to,

$$H_0 = \frac{h_0}{R_x} = \left[1.52 \frac{u \eta_0}{R_x} \sqrt{2} \right]^{2/3} = 1.666 [GU]^{2/3} \quad (4)$$

For the more general point contact geometry, Kapitza assumed that the film thickness could be expressed in quadratic form in terms of both x and y.

$$h = h_0 + \frac{x^2}{2R_x} + \frac{y^2}{2R_y} \quad (5)$$

Kapitza found it necessary to restrict pressure generation to the convergent film in order to make progress with the solution of the Reynolds equation for this quadratic film shape. He demonstrated that if a piezo-viscous fluid was permitted to develop pressure in the convergent film only, the pressure achieved an infinite value when the minimum film thickness was given by,

$$h_o = \frac{h_o}{R_x} = \left[1.3\sqrt{2} \text{ uan}_o \frac{1}{R_x \left(1 + \frac{2}{3} \left(\frac{R_y}{R_x} \right) \right)} \right]^{2/3} = 1.501 [\text{GU}]^{2/3} \left(\frac{1}{(1+2/3\delta)} \right)^{2/3} \quad (6)$$

Using the alternative notation involving the dimensionless elasticity and viscosity parameters developed by Johnson (1) equation (6) can be rewritten

$$\hat{h}_o = H_o \left(\frac{W'}{U} \right)^2 = 1.501 (g_v')^{2/3} \left(\frac{1}{1+2/3\delta} \right)^{2/3} \quad (7)$$

The prime objective of the work presented here was to evolve an expression for the limiting minimum lubricant film thickness equivalent to equations (6)/(7), but with the more precise Reynolds' cavitation boundary condition applied in the analysis rather than limiting pressure generation to the convergent film only.

It is worthy of note that Hamrock and Dowson (10) in developing film thickness contours for nominal point contacts adopted an interim measure by applying the elastic-piezo-viscous 'side leakage factor' from equation (3) to the expression for the limiting minimum film thickness for a line contact with rigid-piezo-viscous lubrication (equation (4)). Thus for nominal point contacts equation (4) was modified to

$$H_o = 1.666 (\text{GU})^{2/3} (1 - e^{-0.68k}) \quad (8)$$

or with the alternative normalization

$$\hat{H}_o = H_o \left(\frac{W'}{U} \right)^2 = 1.666 (g_v')^{2/3} (1 - e^{-0.68k}) \quad (9)$$

The expression developed here will enable the appropriateness or otherwise of this approximate approach to be evaluated.

THEORETICAL AND NUMERICAL ANALYSIS AND COMPUTATION

Fuller details of the theoretical formulation of the problem, the numerical analysis scheme adopted and the computational strategy can be found in Dowson et al (11). Some major features will be highlighted here.

(a) The film thickness between rigid ellipsoids was expressed in dimensionless form using the parabolic approximation.

$$H = H_o + \frac{X^2}{2} + \frac{Y^2}{2\delta}$$

(b) The Reynolds' equation was employed in a form enabling the influence of pressure on density (4) and viscosity to be investigated. The variation of viscosity with pressure was represented by the Barus relationship.

$$\eta = \eta_o e^{aP}$$

(c) The use of the exponential viscosity-pressure relationship permitted the Reynolds equation to be written in terms of a reduced pressure, q , such that

$$p = -\frac{1}{a} \ln(1-aq)$$

(d) A variable mesh size finite difference approximation to the governing Reynolds equation was adopted with a solution of the resulting system of equations by the Gauss-Seidel iterative technique with successive-over-relaxation. To minimise numerical problems associated with steep gradients of the dependent variable, the Vogelpohl substitution

$$\phi = qH^{3/2}$$

was adopted. The flow chart for the computer program developed is presented in Dowson et al (11). The computing strategy was to obtain a succession of solutions with decreasing minimum film thickness, for the same value of the dimensionless grouping, GU , until the limiting minimum film thickness for rigid-piezo-viscous lubrication was identified.

(e) Detailed studies of the required location of the inlet and side boundaries to the computing region to avoid starvation effects were undertaken (11). In addition the Reynolds cavitation boundary conditions

$$p = q = \frac{\partial q}{\partial X} = \frac{\partial q}{\partial Y} = 0$$

was adopted and achieved by setting negative film pressures to zero as the iterative solution proceeded.

RESULTS.

It is intended to present here the limiting minimum film thickness expression obtained for the lubrication of rigid ellipsoids by a piezo-viscous fluid. More comprehensive details and discussion are available in reference (11).

Both Blok (8) and Kapitza (9) have established that for the lubrication of counterformal contacts with a piezo-viscous fluid there exists a limiting minimum lubricant film thickness. The condition corresponds to the occurrence of an infinite pressure in the contact. In practice the effects of elastic distortion will of course become influential. The computations undertaken here have determined this limiting minimum film thickness for the general case of lubricated rigid ellipsoids with the Reynolds boundary condition taken to apply at rupture. A curve fitting technique was used to develop the following expression which has a maximum error of 7% over the range of variables considered.

$$H_0 = 1.666 (GU)^{2/3} \left(\frac{\delta}{1+\delta} \right)^{0.6} \quad (10)$$

which with the alternative dimensionless groupings becomes,

$$\hat{H}_0 = H_0 \left(\frac{W'}{U} \right)^2 = 1.666 (g_v')^{2/3} \left(\frac{\delta}{1+\delta} \right)^{0.6} \quad (11)$$

The formula has been developed for a range of GU extending over four decades from 10^{-9} to 10^9 and for values of δ , the ratio of the principal radii R_v and R_x , ranging from 0.2 to 8. The expression was so arranged such that it was consistent with equation (4) for line contacts when the radius ratio, δ , is infinite. Thus the term

$$\left(\frac{\delta}{1+\delta} \right)^{0.6}$$

is a 'side-leakage' factor.

DISCUSSION AND CONCLUSIONS.

Comparison of the predictions of the expression (10) developed for the limiting minimum film thickness with formulae given earlier in the paper leads to the following conclusions.

(i) The calculated film thickness is everywhere greater than that predicted by Kapitza's solution (equation (6)) and this is attributable to the inadequate half-Sommerfeld boundary condition used in the latter analysis. The difference ranges from 11% at a radius of ∞ to less than 1% for a radius ratio of 0.2. Such differences are consistent with the physical expectation of what would be the effect of a more precise consideration of cavitation. However, the accuracy of the Kapitza formula is strikingly good.

(ii) In contrast the adoption of the side leakage factor for elastic-piezo-viscous conditions by Hamrock and Dowson (equation (8)) considerably underestimates the limiting minimum film thickness for values of radius ratio of 2 and less. The error is 24% at a radius ratio of unity and 35% at 0.2.

(iii) Curvature of the ellipsoid in the direction perpendicular to motion has a profound effect upon film thickness. A sphere will develop only 66% of the film thickness generated by a cylinder near a plane under comparable conditions and a long slender ellipsoid having a radius ratio of 0.2 and its major axis aligned in the direction of motion can achieve only 52% of the film thickness developed by the sphere.

The results presented in this paper complete the analysis of four distinct regimes of fluid film lubrication which may be experienced by ellipsoidal solids near a plane. They yield an expression for minimum film thickness under rigid-piezo-viscous conditions which can be employed with similar confidence to that shared by existing expressions for the other three regimes of lubrication.

REFERENCES

- (1) Johnson, K.L. 'Regimes of Elastohydrodynamic Lubrication', Journ. Mech. Engrg. Sci., 12, (1), 1970, pp. 9-16.
- (2) Brewster, D.E., Hamrock, B.J. and Taylor, C.M. 'Effect of Geometry on Hydrodynamic Film Thickness', J. Lubn. Technol., 101 (2), 1979, pp. 231-239.
- (3) Hamrock, B.J. and Dowson, D. 'Elastohydrodynamic Lubrication of Elliptical Contacts for Materials of Low Elastic Modulus I - Fully Flooded Conjunction', Trans. A.S.M.E., Journal Lubn. Tech., 100, (2), 1978, pp. 236-245.
- (4) Hamrock, B.J. and Dowson, D. 'Elastohydrodynamic Lubrication of Point Contacts, Part III - Fully Flooded Results', Trans. A.S.M.E., Journ. Lubn. Technol., 99, (2), 1977, pp. 264-276.

- (5) Catcombe, E.K. 'Lubrication Characteristics of Involute Spur Gears - a Theoretical Investigation', Trans. Amer. Soc. Mech. Engrs., 67, 1945, pp.177.
- (6) Hersey, M.D. and Lowdenslager, D.G. 'Film Thickness Between Gear Teeth', Trans. A.S.M.E., 72, 1950, pp. 1035-1042.
- (7) McEwen, E. 'The Effect of Variation of Viscosity with Pressure on the Load Carrying Capacity of Oil Film Between Gear Teeth', Journ. Inst. Petrol., 38, 1952, pp 646.
- (8) Blok, H. Discussion of paper by E. McEwen, J. Inst. Petrol., 38, 1952, pp. 573-683.
- (9) Kapitza, P.L. 'Hydrodynamic Theory of Lubrication During Rolling', Zh. Tekh. Fiz., 25, (4), 1955, pp. 747-762.
- (10) Hamrock, B.J. and Dowson, D. 'Minimum Film Thickness in Elliptical Contacts for Different Regimes of Fluid Film Lubrication', Proceedings of the 5th Leeds-Lyon Symposium on Tribology (Elastohydrodynamics and Related Topics), Mechanical Engineering Publications, London, 1978, 22-27.
- (11) Dowson, D., Dunn, J.F. and Taylor, C.M. 'The Piezo-Viscous Fluid, Rigid Solid Regime of Lubrication', Submitted for Publication, 1982.

REGIMES OF FLUID FILM LUBRICATION AT THE
RIB-ROLLER CONTACT IN A TAPERED ROLLER BEARING
BY C. L. SWINGLER
Research Engineer
The Timken Company
Canton, Ohio 44706
U.S.A.

SUMMARY

A recent analysis for determining the regime of lubrication in elliptical contacts is applied to the rib-roller contact of axially loaded tapered roller bearings. The results indicate that the contact operates in either the isoviscous-rigid or isoviscous-elastic regimes depending on the conditions of load and speed. Although the corresponding calculated film thicknesses are an order of magnitude or more greater than those predicted by the traditionally adopted EHD theory, actual lubrication conditions may be marginal due to the effects of sliding and starvation at the rib.

NOMENCLATURE

a	minor axis of rib-roller contact ellipse
b	major axis of rib-roller contact ellipse.
$E_{1,2}$	modulus of elasticity of rib and roller materials.
E'	$2 \left(\frac{1-\nu_1^2}{E_1} + \frac{1-\nu_2^2}{E_2} \right)^{-1}$
F	normal load at rib-roller contact
G	$\alpha E'$
S_E	$W^{8/3}/U^2$
S_V	GW^3/U^2
H	$\bar{H} \left(\frac{W}{U} \right)^2$
\bar{H}	h/R_x
h	minimum film thickness
k	ellipticity parameter, $a/b = 1.03 \beta^{0.64}$
R_x	effective radius in rolling/sliding direction
R_y	effective radius perpendicular to rolling/sliding direction
U	$u \eta_0 / E' R_x$
u	mean surface velocity at rib-roller contact
W	$F/E' R_x^2$
α	pressure-viscosity coefficient of lubricant
β	R_y/R_x
η_0	lubricant viscosity at atmospheric pressure
$\nu_{1,2}$	Poisson's ratio
ϕ	$(1 + 2/3\beta)^{-1}$

INTRODUCTION

A positive axial force is required to retain and guide the rolling elements in a tapered roller bearing. This force is provided by a rib which is usually an integral part of the inner ring or cone. Conventionally, the rib face is a portion of the surface of a shallow cone centered on the bearing axis, while the roller end which runs against it is a portion of a sphere. If the roller end spherical radius is equal to the bearing apex length, AO in Figure 1, a line contact between the roller end and

the rib results. Such geometry is ideal from the point of view of providing excellent roller skew control, but unfortunately has the disadvantage of having poor film forming capabilities. This consideration has led to designs where the spherical end radius is some proportion of the apex length; typically between 75 and 95 percent. The resulting point contact deforms under load to give a long ellipse aligned in the direction of motion, see Figure 2.

In the past, it has been common practice to assume that the behaviour of this contact is represented by elastohydrodynamic theory. Wren and Moyer (1), Karnu (2) and Jamison et al. (3) have all used Archard and Cowking's theory (4) to calculate film thicknesses generated at the rib. The purpose of this study is to review this practice in the light of recent developments in the analysis of elliptical contacts and to suggest a more appropriate approach to this problem.

REGIMES OF LUBRICATION

During the development of elastohydrodynamic theory, it was realized that equal consideration had to be given to the effects of both elastic deformation and pressure dependent viscosity in order for the resulting film thickness equation to adequately represent counterformal steel components lubricated with mineral oil. It was also realized that certain situations exist where the influence of one of these factors far outweighed the other. For example, in the lubrication of a low elastic modulus component, such as a rubber seal, the effect of viscosity enhancement is negligible compared to the elastic deformation. Johnson (5) was one of the first to discuss this behaviour in a coordinated and comprehensive manner. To determine the relative effects of elastic deformation and pressure dependent viscosity he defined and compared two dimensionless parameters:

1. an elasticity parameter, $g_E = \frac{1}{\pi} \left(\frac{3}{2} \right)^{2/3} \left(\frac{q_f}{p_0} \right)$

in which p_0 is the peak Hertz contact pressure that the geometry would experience when loaded together in the absence of any lubricant;

- and 2. a viscosity parameter, $g_V = \alpha q_f$, where $1/\alpha$ is the pressure at which the viscosity has increased by a factor of e

It can be seen that both of these parameters are non-dimensionalized by a pressure, q_f . This is the peak hydrodynamic pressure that the geometry would generate if isoviscous-rigid conditions were assumed. Plotting g_E vs. g_V on logarithmic axes results in a map which can be divided into four different zones or regimes, depending on the relative influence of the viscous and elastic effects. The relationships governing friction and film thickness are different for each of these four regimes. Thus, the appropriate expression relating film thickness with material parameters, load, geometry and speed can only be determined by identifying the regime of lubrication operating at the contact. This is done by calculating g_E and g_V and plotting the contact on a regime chart.

It has been difficult to apply this technique to elliptical contacts because Johnson's detailed analysis was made for line contacts only. Recently, Hamrock & Dowson (6) removed this restriction on the majority of applications by extending their earlier work (7, 8) and the work of others (9) to provide a general regime analysis for elliptical contacts. In their analysis, they give a redefined non-dimensional minimum film thickness in terms of the viscosity and/or elasticity parameters g_V and g_E and the ellipticity parameter k :

isoviscous-rigid regime

$$H = 128g_V^2 \left[0.11 \tan^{-1} \left(\frac{\beta}{2} \right) + 1.66 \right]^2 \quad (1)$$

viscous-rigid regime

$$H = 1.66 g_V^{2/3} (1 - e^{-0.68k}) \quad (2)$$

isoviscous-elastic regime

$$H = 8.70 g_E^{0.67} (1 - 0.85 e^{-0.31k}) \quad (3)$$

viscous-elastic regime

$$H = 3.42 g_V^{0.49} g_E^{0.17} (1 - e^{-0.68k}) \quad (4)$$

where β and ϕ are geometry factors and

$$H = \bar{H} \left(\frac{W}{U} \right)^2$$

$$g_E = \frac{W^{8/3}}{U^2}$$

$$g_V = \frac{GW^3}{U^2}$$

For a given geometry k the boundaries separating adjacent regimes are defined by equating the appropriate expressions for film thickness H . In Figures 3 and 4, this procedure has been applied to the results recently published by Koye and Winer (10). Both sets of results are for narrow ellipses aligned in the direction of motion. In Figure 3 ($k = 0.305$) the low load results are set firmly within the viscous - elastic (EHD) regime, but move towards the viscous-rigid regime with increasing load. Figure 4 shows the results for the narrower geometry considered by Koye & Winer ($k = 0.117$). Despite the fact that the viscous-elastic regime has shrunk substantially in comparison to that of the previous figure, all the data falls within its boundaries.

In plotting the boundary lines separating the viscous-rigid, viscous-elastic and isoviscous-elastic regimes Hamrock has agreed (11) that one should extrapolate from the intersections with the isoviscous-rigid regime assuming a gradient of unity. This is due to the fact that round-up errors in various parameter exponents (Equations 2 to 4) would otherwise result in a slight boundary convergence and possible boundary intersection for very narrow contacts at high values of g_E and g_V .

Koye and Winer's experimental data, which were obtained using optical interferometry, clearly show the characteristic EHD deformation pattern within the contact. The fact that the corresponding data fall within the predicted EHD regime is central to this study, since it provides verification that the regimes analysis is applicable to narrow elliptical contacts. Theoretically, Hamrock and Dowson's work is restricted to contacts having ellipticity parameters between one (circular point contact) and infinity (line contact). Koye & Winer's study was primarily directed at showing that this limited range of application of Hamrock and Dowson's equations could be expanded to include narrow elliptical contacts aligned in the direction of motion. As a result of this, Koye and Winer suggest that the ellipticity parameter k be redefined as the ratio of the axis of the contact ellipse perpendicular to the direction of motion to the axis parallel with the direction of motion. This is the definition used in this study.

APPLICATION TO RIB-ROLLER CONTACTS

To illustrate the application of the above analysis, it has been applied to some of the results which form the basis of Reference 2. In these experiments, Karna used a separated rib machine to determine the speed dependence of the friction torque generated by the rib. For the purpose of this study, data obtained with the bearing denoted as X-2 is used (see Table 1) since this gave the largest range of load. The effective radius in the rolling-sliding direction R_x was 5.558 m (220 in.). Karna gave the contact geometry in terms of Archard & Cowling's side-leakage factor; $\phi^{0.74} = 0.15$. The equivalent value of the ellipticity parameter used in equations 1 to 4 is $k = 0.1628$. The lubricant, an SAE 20 mineral oil, had a pressure viscosity index of $1.013 \times 10^{-8} \text{ Pa}^{-1}$ ($1.25 \times 10^{-4} \text{ psi}^{-1}$). Further details of the apparatus and experimental technique can be found in Reference 2.

The regime chart for a long elliptical contact where $k = 0.1628$ is shown in Figure 5. Note that the width of the viscous-elastic regime is between those depicted in figures 3 ($k = 0.305$) and 4 ($k = 0.117$). The eleven data points on the figure represent the dimensionless elasticity and viscosity parameters g_E and g_V corresponding to the conditions listed in Table 1. All but two of the points lie within the isoviscous-rigid (classical hydrodynamic) regime. As expected, the data approaches the boundary as load increases and speed falls. However, the general distribution of the data is such that it moves into the isoviscous-elastic rather than the viscous-elastic regime. One of the properties of a regime chart, evident from figure 5, is that while speed changes move along a gradient of unity, changes in load are subject to the slightly steeper gradient of 9/8. Consequently, the contact moves towards the viscous-elastic regime as load increases, but this is limited in tapered roller bearings by the excessive loads that would be required at the main raceway contacts.

Unfortunately, the apparatus used in these experiments was load limited. The maximum load shown in the data represents approximately 50 percent of the rated thrust capacity of the bearing. If an additional, hypothetical, load line at 8000 lbf bearing thrust load is added to Figure 5 it can be seen that an appreciable portion of the low speed operating conditions (say, up to 1000 rpm) would be in the isoviscous-elastic regime.

In Reference 2 Karna calculated the film thickness at this contact using EHD theory. The regime chart shows that most of the data can be represented by classical hydrodynamic theory except for two high-load/low-speed results where isoviscous-elastic theory is appropriate. To illustrate these differences the film thickness for the eleven data points have been calculated for each of the three regimes using equations (1), (3) and (4). These are plotted together in Figure 6. The isoviscous-elastic results show a similar speed dependence but an appreciably thicker film and an increase in load sensitivity ($h \propto F^{-0.2}$) when compared to viscous-elastic theory. As expected, the load and speed sensitivity is greatest for the isoviscous-rigid regime ($h \propto \left(\frac{u\eta}{F}\right)^2$).

The intersections between the isoviscous-rigid and isoviscous-elastic characteristics for the 2000 lbf and 4000 lbf load lines correspond to the boundary transitions in Figure 5. Therefore, it would seem reasonable to suggest that the film thickness behaviour should follow the bold lines indicated in Figure 6. Whether or not such behaviour would be observed in practice is open to question since one of the difficulties inherent in this analysis is that it is not clear how rapidly a transition in regime of lubrication occurs as a contact crosses a boundary.

A more specific restriction in this particular application is the fact that equations (1) to (4) are based on fully flooded, isothermal theory. These assumptions do not represent the conditions at the rib where there is typically a slide/roll ratio $\Delta u/u$ of 0.35 and fairly restricted lubricant availability. One would, therefore, expect measured film thicknesses in any regime to be thinner than indicated by the theory. Furthermore, starvation and thermal effects could cause a significant shift in the structure of the regime chart itself.

A possible method of gaining some insight into these phenomena would involve studying the response of the lubricant film thickness to changes in applied load, speed and starvation conditions. If the film thicknesses are not too great, the application of the technique of optical interferometric measurement would appear to be the most promising means of investigation.

CONCLUSIONS

1. The extension of Hamrock and Dowson's regime analysis to elliptical contacts having fractional ellipticity parameters has been justified using published data.
2. The regime analysis has been applied to the lubrication of the rib-roller contact of a tapered roller bearing. The results show that the contact operates in either the isoviscous-rigid or isoviscous-elastic regimes depending on the conditions of speed and load.
3. This application of the analysis is restricted due to the assumptions of fully flooded and isothermal conditions at the contact.

REFERENCES

1. Wren, F. J. and Moyer, C. A.
"Understanding Friction and EHL Films in Concentrated Contacts of a Tapered Roller Bearing", in "Elastohydrodynamic Lubrication: 1972 Symposium", Instn. Mech. Engrs., London.
2. Karna, C. L.
"Performance Characteristics at the Rib Roller End Contact in Tapered Roller Bearings", ASLE Trans, 1974, Vol. 17, No. 1, pp. 14-21.
3. Jamison, W. E., Kauzlarich, J. J. and Mochel, E. V.
"Geometric Effects on the Rib-Roller Contact in Tapered Roller Bearings", ASLE Trans., 1977, Vol. 20, No. 1, pp. 79-88.
4. Archard, J. F. and Cowking, E. W.
"Elastohydrodynamic Lubrication at Point Contacts", Proc. Instn. Mech. Engrs., 1965-66, Vol. 180, Pt 3B, pp. 47-56.
5. Johnson, K. L.
"Regimes of Elastohydrodynamic Lubrication", J. Mech. Engng. Sci., 1970, Vol. 12, No. 1, pp 9-16.
6. Hamrock, B. J. and Dowson, D.
"Minimum Film Thickness in Elliptical Contacts for Different Regimes of Fluid-Film Lubrication", NASA Technical Paper 1342, 1978.
7. Hamrock, B. J. and Dowson, D.
"Isothermal Elastohydrodynamic Lubrication of Point Contacts, Part III -Fully Flooded Results", J. Lub. Tech., Trans ASME, 1977, Vol. 99, pp. 264-176.
8. Hamrock, B. J. and Dowson, D.
"Elastohydrodynamic Lubrication of Elliptical Contacts for Materials of Low Elastic Modulus. Part I - Fully Flooded Junction", J. Lub. Tech., Trans. ASME, 1978, Vol. 100, pp. 236-245.
9. Brewe, D. E., Hamrock, B. J. and Taylor, C. M.
"Effect of Geometry on Hydrodynamic Film Thickness", NASA Technical Paper 1287, 1978.
10. Koye, K. A. and Winer, W. O.
"An Experimental Evaluation of the Hamrock and Dowson Minimum Film Thickness Equation for Fully Flooded EHD Point Contacts", J. Lub. Tech., Trans ASME, 1981, Vol. 103, pp. 284-294.
11. Hamrock, B. J.
Private communication.

Table 1 Experimental Conditions At The Rib-Roller Contact

Thrust Load (lbf)	F (N)	Speed (rpm)	u (m/s)	Rib Temperature (°C)	η_o (Pas) ($\times 10^3$)
1000	40.03	100	0.296	39.4	56.0
1000	40.03	250	0.740	39.4	56.0
1000	40.03	500	1.481	39.4	56.0
1000	40.03	1500	4.442	46.2	39.0
2000	80.06	100	0.296	41.7	50.3
2000	80.06	250	0.740	40.0	54.5
2000	80.06	500	1.481	40.0	54.5
2000	80.06	1500	4.442	46.7	39.5
4000	160.13	250	0.740	43.3	46.4
4000	160.13	500	1.481	42.8	47.6
4000	160.13	1500	4.442	48.3	36.5

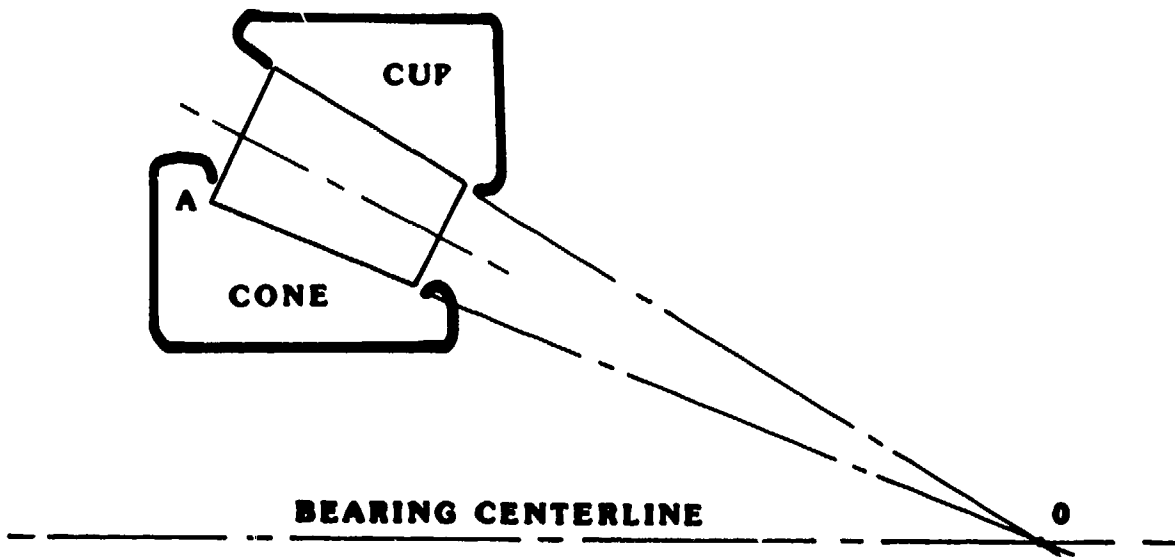


Figure 1 Tapered roller bearing geometry

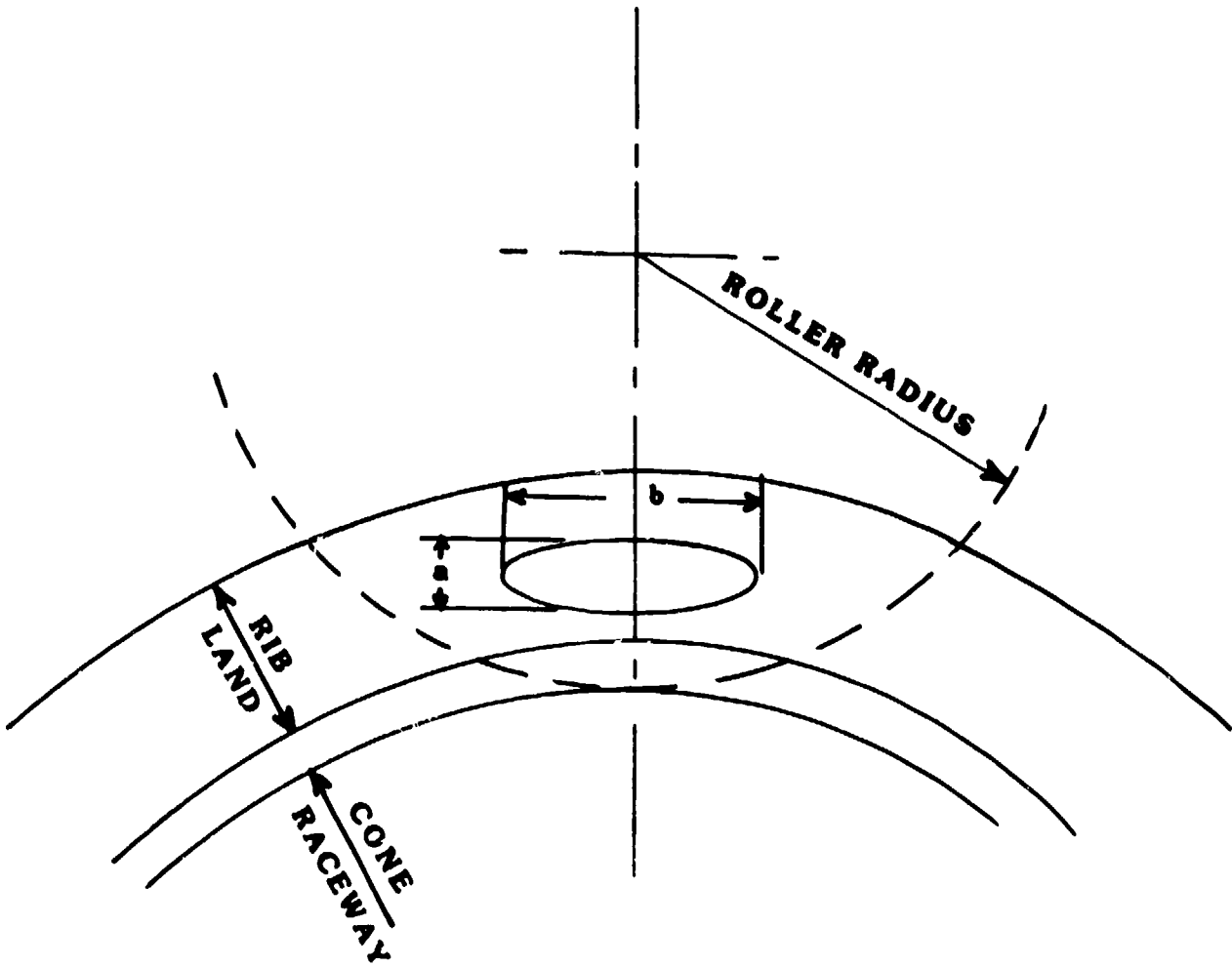


Figure 2 Projected rib-roller contact

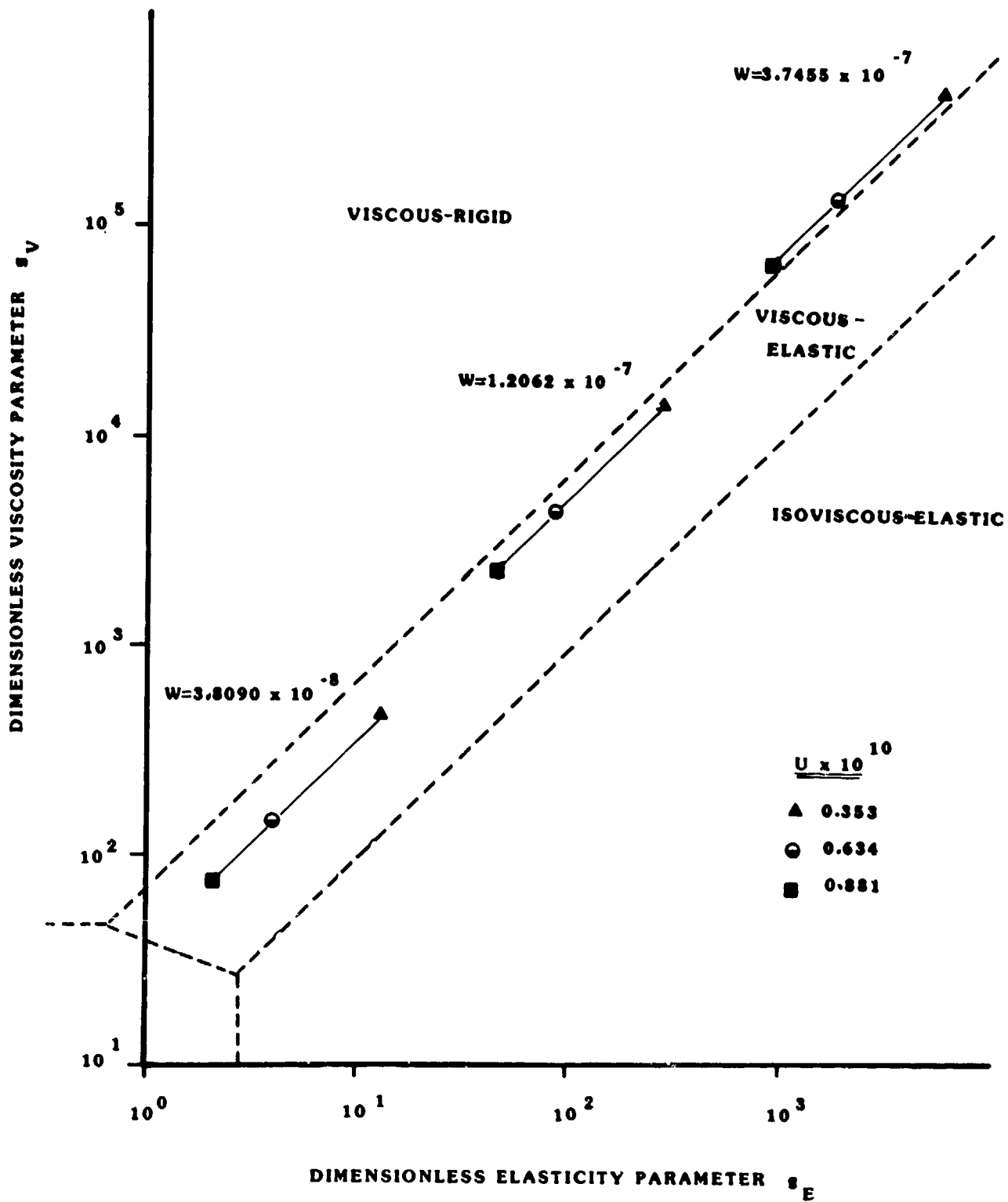


Figure 3

Regime chart of Koye and Winer's results for a narrow elliptical contact; $k = 0.305$

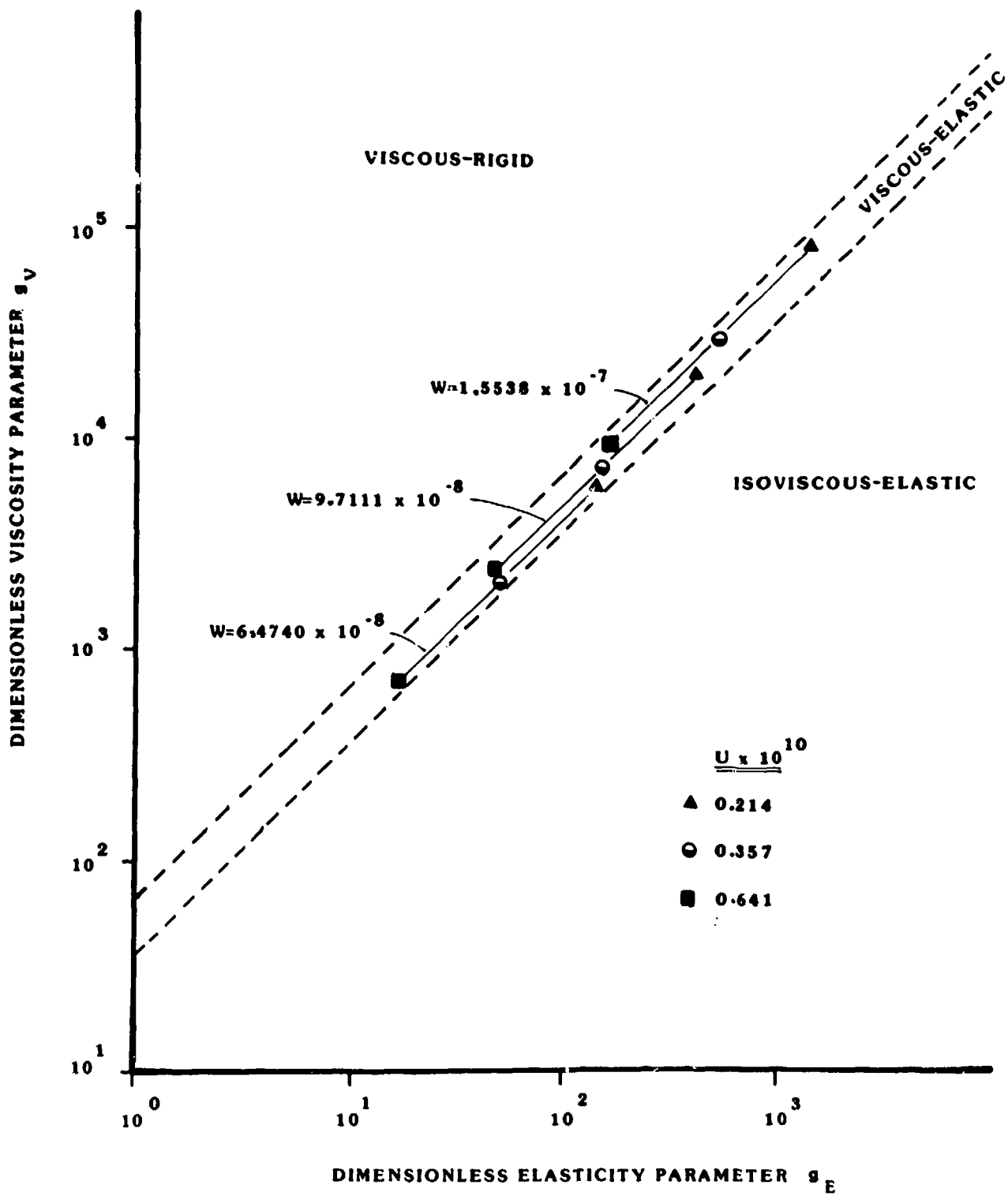


Figure 4 Regime chart of Koye and Winer's results for a narrow elliptical contact; $k = 0.117$

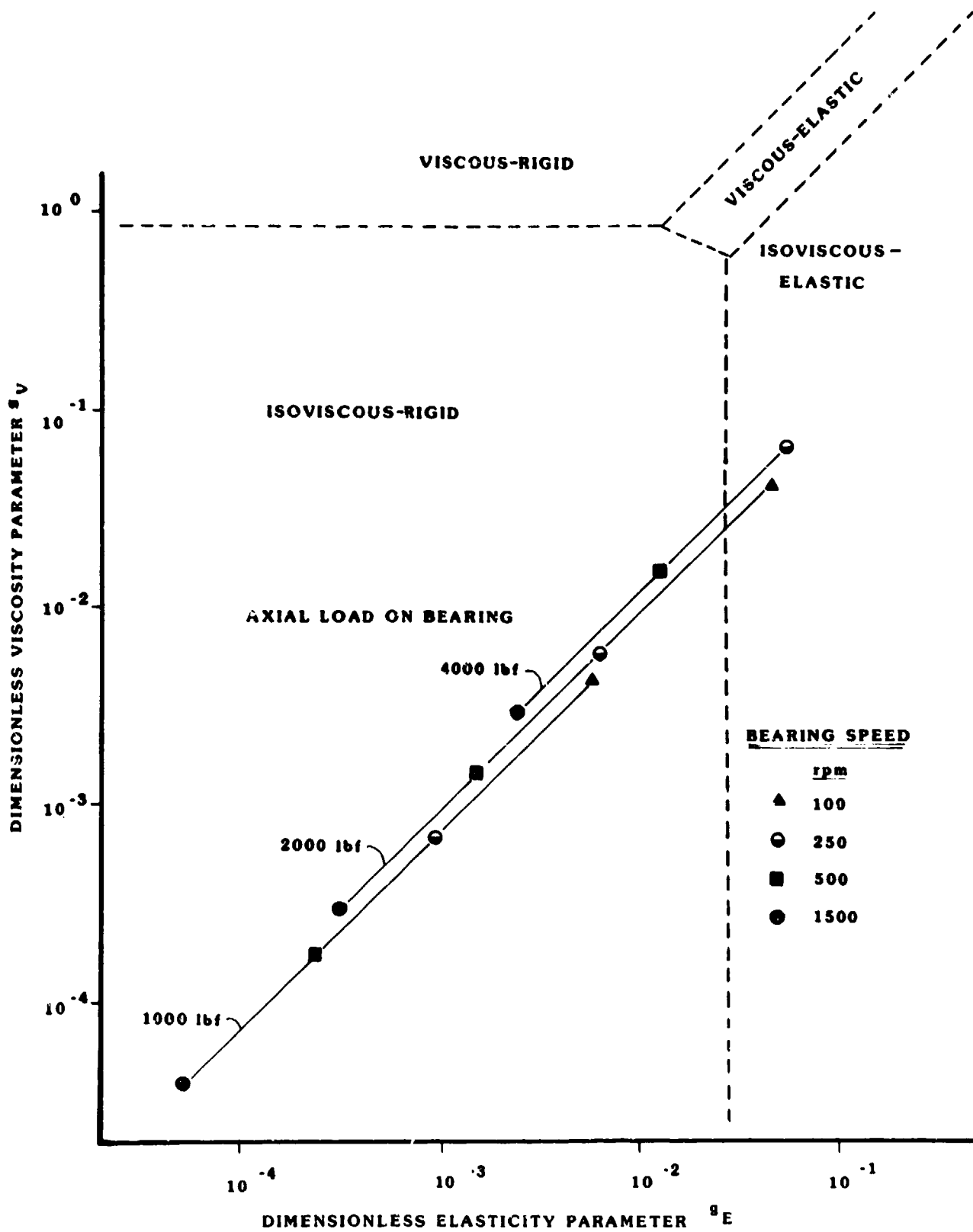


Figure 5

Regime chart of Karna's results for a rib-roller contact; $k = 0.163$

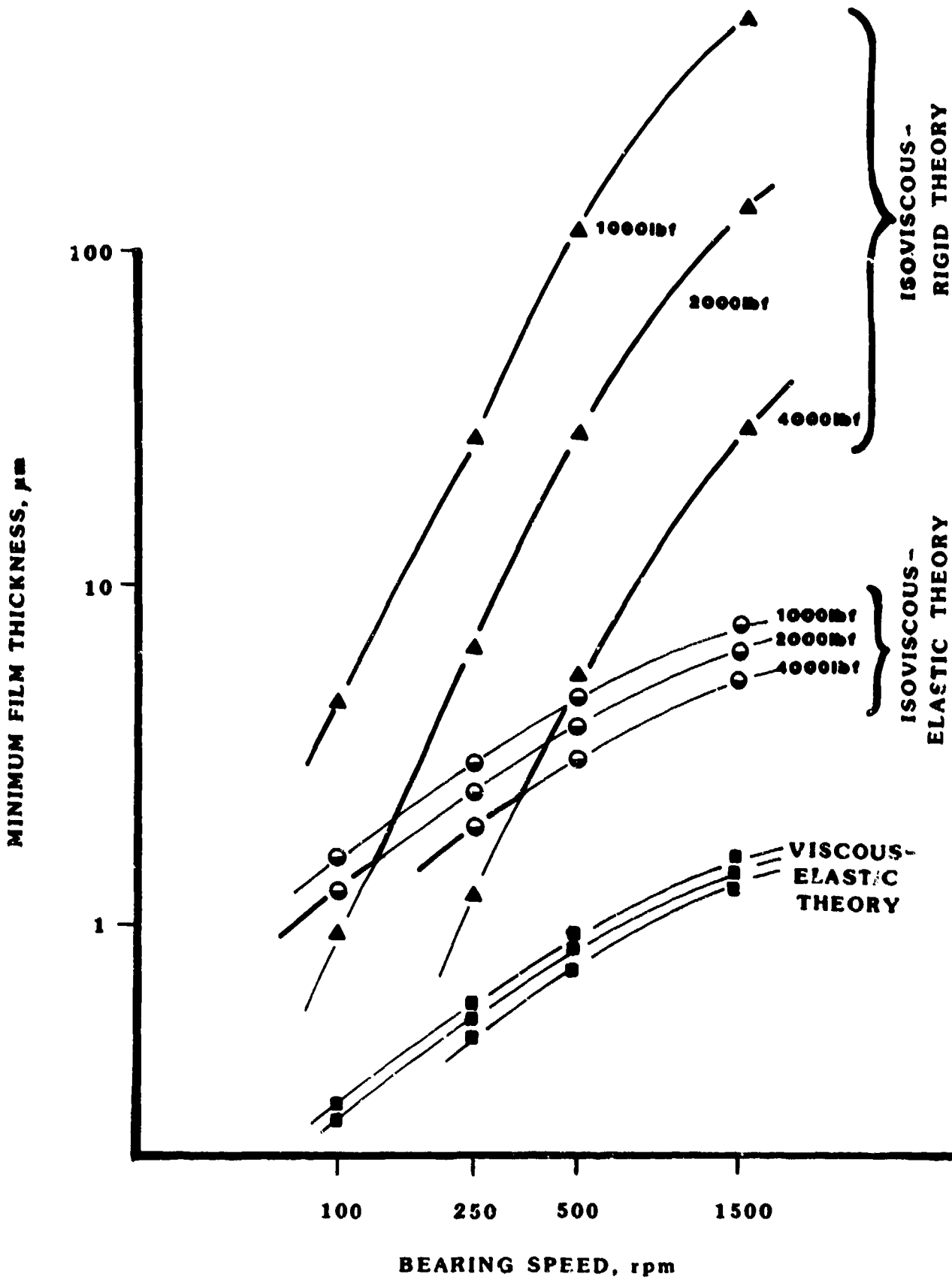


Figure 6

Rib-roller contact film thickness calculated using three different regime theories

DISCUSSION

D.G. Astridge, Westland Helicopters, Yeovil, UK

- (1) Two conceptual problems arise from the results:
 - (a) The suggestion of regime boundary lines imply a sudden change from say elastic behaviour to rigid behaviour for a small change in speed, viscosity, load etc.
 - (b) Figure 5 suggests that at higher loads film pressures are large enough to produce elastic deformation of steel, but not high enough to influence oil viscosity.
- (2) In common with contact conditions in conformal gears, the shape of the roller end/rib contact in taper roller bearings is a slightly distorted thin ellipse (with major axis in direction of rolling) approximating banana-shaped. To what extent do you consider that this distortion might influence film thickness calculations?

Author's Reply

- (1) (a) It is, of course, unrealistic to suggest that crossing a regime boundary results in a discontinuity in the response of the contact to external variables. However, at the present time we do not have any knowledge of the characteristics of contacts operating at regime boundaries. Consequently, any "blend" radius (for example, between the predicted isoviscous-rigid and isoviscous-elastic film thickness lines at 2000 lbf in Figure 6) would have to be arbitrary. It was decided that, from the point of view of clarity, a blend radius of zero would be used.
- (b) This behaviour appears at first to be a paradox. However, some insight into the possible mechanism involved can be gained if it is recalled that in EHL ("hard" or "soft") it is the conditions in the inlet of the contact that are of importance in determining film thickness. In the hard EHL of a line contact the generation of the film benefits both from the increased local radius of curvature due to deformation, and from the increase in viscosity due to the appreciable pressure build-up that precedes the Hertzian pressure profile. In contrast to this a long elliptical contact aligned in the direction of entrainment will suffer considerable side-leakage and hence pressure depletion in the inlet zone. Thus the contact is deprived of the high level viscosity enhancement common in contacts with little or no side flow in the inlet region. It will, however, benefit from the local increase in radius of curvature. The overall effect is an isoviscous-elastic response.
- (2) It would seem reasonable to suggest that the effect of contact distortion on film thickness will be considerably smaller than the effects of sliding and starvation.

E. Saibel, USARO, RTP, US

It would seem necessary to leave a model of the viscoelastic fluid from which a constitutive relationship could be derived and from which the author's Equation (4) could be derived; otherwise, this is simply a matter of curve fitting. This is not necessarily bad, but the element of uniqueness is lost.

Author's Reply

The construction of the regime chart is based on the four different film thickness equations corresponding to the four different regimes of lubrication. These equations are recast in terms of the non-dimensional elasticity and viscosity parameters. Equation (4) represents this form of Hamrock and Dowson's minimum film thickness equation for EHD (visco-elastic) conditions, and as such relies on their assumptions of fluid behaviour (see Reference 6).

D. Berthe, INSA Lyon, Fr

Nous avons effectué une étude de ce type de contact, sur le plan théorique en considérant un lubrifiant équi ou piézo-visqueux, des surfaces rigides, et sur le plan expérimental en introduisant la géométrie exacte des surfaces (inclinaison et hauteur du collet, courbure du flanc du rouleau . . .) et la cinématique très particulière qui comprend une vitesse due au pivotement du rouleau importante. L'étude expérimentale sur un dispositif qui reproduit cette cinématique et la géométrie a été effectuée, l'épaisseur du film est mesurée par une méthode interférométrique.

Les résultats montrent un effet prépondérant du paramètre 'alimentation' et en second lieu de la cinématique les deux effets n'apparaissent pas dans les relations que vous proposez. Pouvez-vous commenter ces 2 aspects?

Author's Reply

Reference to Figure 2 shows that the entrainment conditions for this contact are extremely complex. Lubricant supplied by the rib surface arrives at the inlet region at a different angle to that supplied by the roller spherical end. Prof. Berthe has accounted for this effect explicitly in his comprehensive analysis and has shown that the rib height is an important parameter since it defines the extent of the inlet zone. By comparison the calculations presented in the paper are rather crude since they take no account of the complex inlet shear and assume an infinite inlet boundary distance ('fully flooded' conditions). However, the object of the work was to provide a simple indication of the regime of lubrication at this contact. Berthe has assumed viscous-rigid conditions, apparently without justification, whereas this investigation shows that isoviscous-rigid or isoviscous-elastic conditions may be more appropriate.

It is conceivable that a more extensive regime analysis, based equations derived using Berthe's refinements, would give different results. The limited extent of the inlet zone would probably be significant, but it would affect each regime in a similar manner. This would appear to be a fruitful area for further study.

THE INFLUENCE OF THE SHEAR THINNING EFFECTS OF NON-NEWTONIAN OILS ON THE PERFORMANCE OF
FINITE LENGTH JOURNAL BEARINGS

VERMEULEN M., Dr. Ir., Assistant : State University of Gent
YOO H.S., M.Sc. * : Laboratory of Machines and Machine Construction
St Pietersnieuwstraat 41
B-9000 GENT, BELGIUM

SUMMARY

The behaviour of non-Newtonian lubricants in journal bearing is very complex. Previous results for considering the shear thinning phenomena were negative for non-Newtonian lubricants, which was not in agreement with experiments. In this paper we analyse this behaviour by assuming the same velocity profile for the non-Newtonian lubricants as the Newtonian one, splitting the viscosity into two parts η_x and η_y , which have relation with x and y directional velocity gradient respectively, and considering side leakage. The results are positive for the non-Newtonian lubricants, which agrees with experiments. The gains $((f_{New} - f_{non-New})/f_{New})$ are 3 - 10 % for most working ranges.

LIST OF SYMBOLS

n, A, B, a, b : constants
 m : fluid consistency ($N \cdot s^n/m^2$)
 p : pressure (N/m^2)
 r : radius of journal (m)
 L : bearing length (m)
 D : diameter of journal (m)
 u, v : fluid velocity in x, y direction (m/s)
 U : journal rotational velocity (m/s)
 x, y, z : spatial coordinates rotational, axial and film thickness direction
 G, Y : x, y directional step size
 h : lubricant film thickness (m)
 ϵ : eccentricity
 δ : radial clearance (m)
 $\eta, \eta^*, \eta_0, \eta_{base}$ } viscosity general, non-dimensional, at small rate of shear, base oil,
 $\eta_x, \eta_y, \eta_{sp}$ } x directional, y directional, $Lnd(\eta - \eta_{base})/\eta_{base}$
 ω : angular speed of journal (rad/s)
 γ : velocity gradient (1/s)
 θ : angular coordinate
 λ : = L/D
 ζ : coefficient of load carrying capacity
 ξ : coefficient of friction loss
 α : attitude angle
 f : coefficient of friction
 S : $\eta_{sp}/(\eta_{sp} \text{ at } 210^\circ)$

INTRODUCTION

It is well known that by the use of "additives" as modifiers of mineral lubricant performance, the modified oils exhibit non-Newtonian behaviour which does not exist in normal mineral oils. The exact behaviour of non-Newtonian lubricants in journal bearings is very complex. A lot of researchers have tried to solve this behaviour by considering the shear thinning phenomena of the lubricant [1], by elastico-viscous behaviour [2] [3] and by the cavitation properties [4].

* Permanent Address : Assistant Professor, Dept. of Mechanical Engineering,
INHA University, Incheon 160-01, Republic of Korea

The motivation of this research is to increase bearing performance and to save energy and materials; but up to now, the results were not completely satisfactory. In this paper we solve the non-Newtonian lubrication problem by considering the shear thinning and side leakage problem together.

Former researchers tried to solve the shear thinning effect with either infinitely long [5] or short [1] bearing assumption, and the results were negative for non-Newtonian lubricants. Our idea is to include the side leakage phenomena. Shear thinning means viscosity variation with variation of the velocity gradient. If the rotational velocity gradient is different from the axial one, then the rotational viscosity will differ from the axial one. Roughly, rotational velocity gradient will be larger than the axial one. Indeed, in the rotational direction the flow is induced by velocity and pressure, but the axial flow is only a pressure induced one. So, the rotational viscosity will be smaller than the axial one, and regarding the load capacity this has the same effect as an effective axial length of the bearing which is larger than the real geometrical length. This means an improvement of bearing characteristics when using non-Newtonian oils. As most engine bearings are short bearings ($L/D <$), the effect will be quite pronounced. Of course this temporary shear thinning phenomena is only one of the many non-Newtonian characteristics, so this paper will describe only partially the real bearing case.

DESCRIPTION OF PRINCIPLE

Experiments of viscosity variation with rate of shear (or shear stress) show that it is a very complex function of the rate of shear, but usually, the variation is very large between $10^3 - 10^4 \text{ s}^{-1}$ (rate of shear) [6] [7] : Fig. 1. At high rate of shear (up to 10^4 s^{-1}) the maximum viscosity loss is about 40 - 50 % [6] [7] [8] : Fig. 1 and 2. The viscosity variation with temperature is much less than for the Newtonian case [6] : Fig. 3. Therefore it is reasonable to consider viscosity variation with rate of shear only when we study non-Newtonian lubrication problems. Even in the Newtonian case, most researchers do not include the viscosity variation with temperature along and through the oil film.

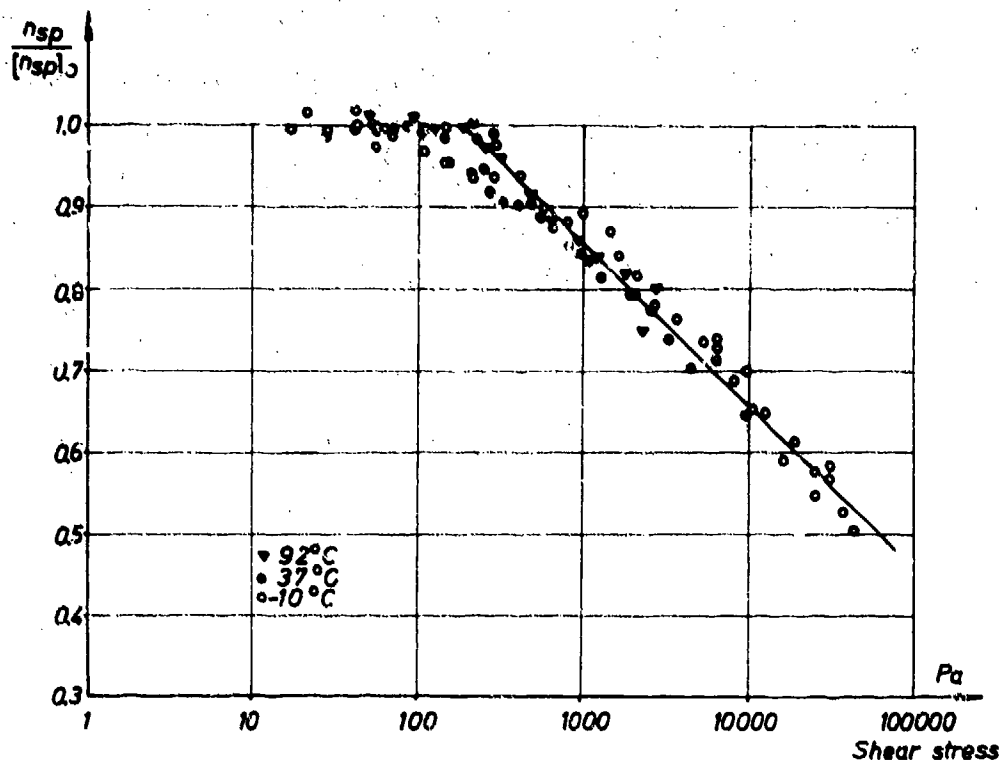


Fig. 1. Viscosity variation with shear stress (from [6])

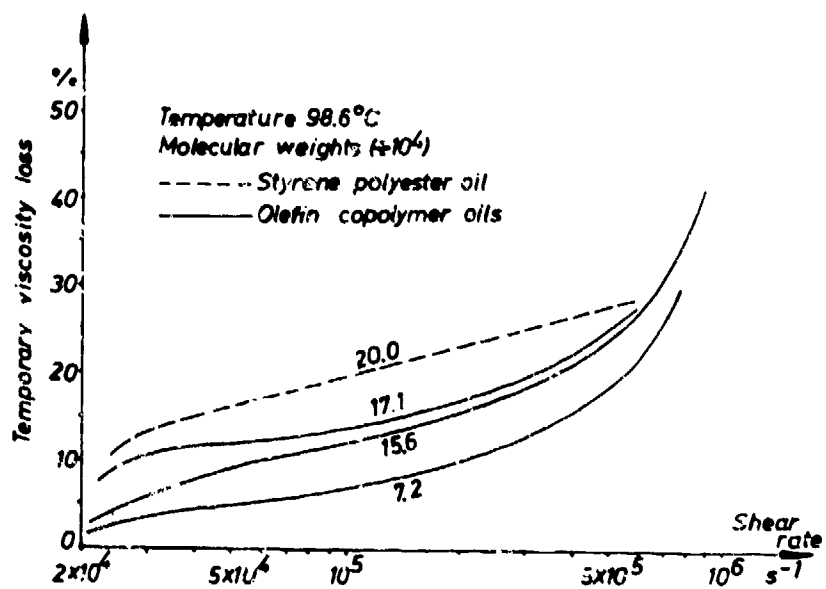


Fig. 2. Temporary viscosity on shear rate, from [7]

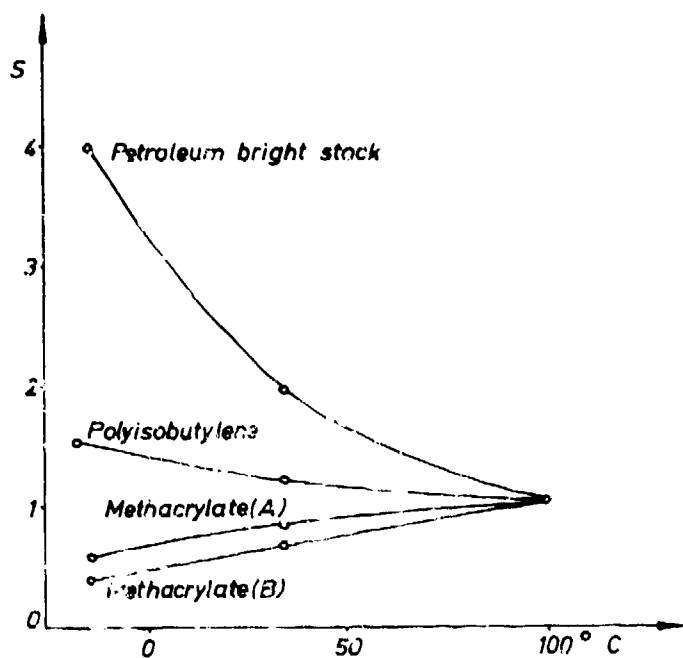
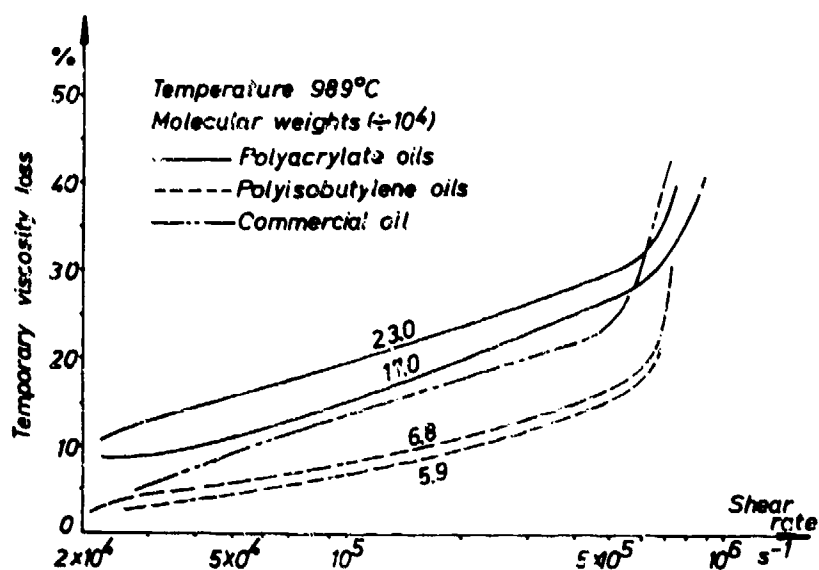


Fig. 4. Variation of specific viscosity with temperature (from [7])

Viscosity variation between $10^3 - 10^4 \text{ s}^{-1}$ is very important (diagrams showing viscosity - rate of shear relations are usually presented in log scale, but when showing this relation in a linear scale, the viscosity variations are very clear). The real values of journal bearing cases for rotational and axial rate of shear are mostly over the range of $10^3 - 10^4 \text{ s}^{-1}$. The gradient is still negative although it is very small.

MATHEMATICAL BACKGROUND

The classic Reynolds equation does not allow to take into account the viscosity variation, and for shear thinning lubricants we should modify the original Reynolds equation. A first problem to be solved is finding a valuable expression for the velocity. It is shown below that with very good accuracy the Newtonian expression can still be used.

Consider the journal bearing configuration outlined in Fig. 4, and for theoretical interpretation the viscosity variation of a lubricant can be expressed as a power law, Eq. 1.

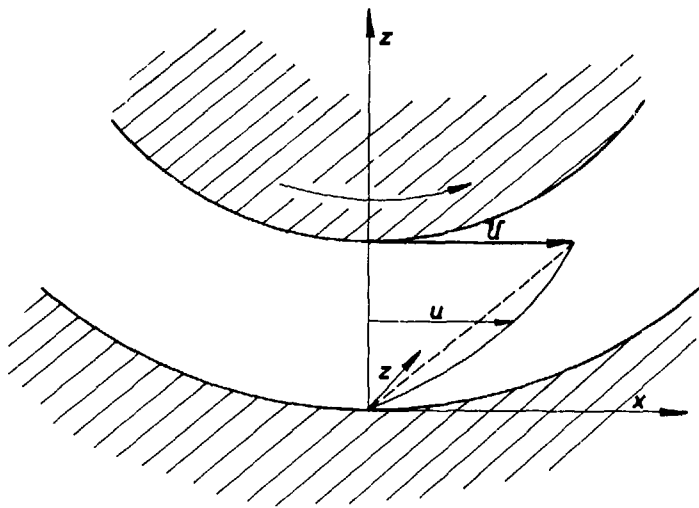


Fig. 4. Bearing geometry

$$\eta = m \dot{\gamma}^{n-1} \quad (1)$$

then the equation of motion becomes Eq. 2

$$\frac{dp}{dx} = \frac{d}{dz} \left(m \left(\frac{du}{dz} \right)^n \right) \quad (2)$$

and the corresponding velocity profile is

$$u = \frac{\left(\frac{1}{m} \frac{dp}{dx} z + C \right)^{\frac{n+1}{n}} - C^{\frac{n+1}{n}}}{\frac{1}{m} \frac{dp}{dx} \left(\frac{n+1}{n} \right)} \quad (3)$$

The constant C can be found from Eq. 4

$$U = \frac{\left(\frac{1}{m} \frac{dp}{dx} h + C \right)^{\frac{n+1}{n}} - C^{\frac{n+1}{n}}}{\frac{1}{m} \frac{dp}{dx} \left(\frac{n+1}{n} \right)} \quad (4)$$

The Eq. 3 is very complex to handle. However even for oils with 45 % shear thinning at 10^6 s^{-1} , the constant n is about 0.957 and the possible maximum error between Eq. 3 and the Newtonian expression Eq. 5 is about $\pm 4 \%$ with sign changes through bearing surfaces.

$$u = \frac{1}{2\eta} \frac{dp}{dx} (z(z-h)) + \frac{Uz}{h} \quad (5)$$

$$\frac{\text{velocity by Eq. 3} - \text{velocity by Eq. 5}}{\text{velocity by Eq. 5}} = -0.04 \sim 0.04$$

Therefore it is reasonable to use Newtonian parabolic velocity profile even for shear thinning lubricants.

So we can use Eq. 5 with variable viscosity for the shear thinning lubricant and Eq. 6 for axial flow.

$$u = \frac{1}{2\eta_x} \frac{dp}{dx} (z(z-h)) + \frac{Uz}{h} \quad (5')$$

$$v = \frac{1}{2\eta_y} \frac{dp}{dy} (z(z-h)) \quad (6)$$

Then the modified Reynolds equation becomes Eq. 7

$$\frac{\partial}{\partial x} \left(\frac{h^3}{\eta_x} \frac{\partial p}{\partial x} \right) + \frac{\partial}{\partial y} \left(\frac{h^3}{\eta_y} \frac{\partial p}{\partial y} \right) = 6U \frac{\partial h}{\partial x} \quad (7)$$

Let us use some parameters to non-dimensionalize the equation :

$$\begin{aligned} h &= \delta(1 + \epsilon \cos\theta^*) & p &= p^* \eta_0 \omega (r/\delta)^2 \\ x &= r\theta^* & \eta_x &= f(x) = \eta_0 \eta_x^* \\ y &= ry^* & \eta_y &= f(y) = \eta_0 \eta_y^* \end{aligned} \quad (8)$$

Substitute Eq. 8 to Eq. 7 and omitting asterisks *

$$\frac{1}{\eta_x} \left(\frac{\partial^2 p}{\partial \theta^2} \right) + \frac{1}{\eta_y} \left(\frac{\partial^2 p}{\partial y^2} \right) - \frac{\partial p}{\partial y} \left(\frac{\partial \eta_y}{\partial y} \right) \frac{1}{\eta_y^2} - \frac{\partial p}{\partial \theta} \left(\frac{\partial \eta_x}{\partial \theta} \right) \frac{1}{\eta_x^2} - \frac{\partial p}{\partial \theta} \frac{3\epsilon \sin\theta}{(1+\epsilon \cos\theta)} \frac{1}{\eta_x} + \frac{6\epsilon \sin\theta}{(1+\epsilon \cos\theta)^3} = 0 \quad (9)$$

Eq. 9 is the non-Newtonian form of the Reynolds equation; for the Newtonian case the second and third part of this equation will disappear.

For computing procedure, using 5 point finite difference method, and (9'), yields :

$$\begin{aligned} \theta &= iG \\ y &= jY \end{aligned} \quad (9')$$

$$\begin{aligned} \text{1st part} & \quad \frac{1}{G^2} (p(i+1,j) - 2p(i,j) + p(i-1,j)) \frac{1}{\eta_x(i,j)} \\ \text{2nd part} & \quad \frac{1}{Y^2} (p(i,j+1) - 2p(i,j) + p(i,j-1)) \frac{1}{\eta_y(i,j)} \\ \text{3rd part} & \quad - \frac{1}{2Y} (p(i,j+1) - p(i,j-1)) \left[\frac{1}{2Y} (\eta_y(i,j+1) - \eta_y(i,j-1)) \right] \frac{1}{\eta_y(i,j)^2} \\ \text{4th part} & \quad - \frac{1}{2G} (p(i+1,j) - p(i-1,j)) \left[\frac{1}{2G} (\eta_x(i+1,j) - \eta_x(i-1,j)) \right] \frac{1}{\eta_x(i,j)^2} \\ \text{5th part} & \quad - \frac{1}{2G} \frac{3\epsilon \sin\theta}{(1+\epsilon \cos\theta)} (p(i+1,j) - p(i-1,j)) \frac{1}{\eta_x(i,j)} \end{aligned} \quad (10)$$

From reference 6 (Fig. 1) the relation between viscosity and the rate of shear can be expressed by Eq. 11.

$$\left(\frac{\eta}{\eta_{\text{base}}} - 1 \right) = a - b \log \left(\eta \frac{du}{dz} \right) \quad (11)$$

However, this expression is cumbersome to use, because the viscosity is implicit, and Eq. 11 can be changed into Eq. 12 with very good accuracy. Maximum error is about $\pm 0.2\%$, and the sign changes from point to point in a bearing, therefore the total error will be negligible.

$$\eta = \eta_0 \left(A - B \log \left(\frac{du}{dz} \right) \right) \quad (12)$$

When we calculate non-Newtonian pressure, the velocity gradient and the viscosity are interconnected with the pressure, which leads to a lot of nested iterations with excessive computation time. Therefore in this paper we simplify the procedure from Eq. 13 to Eq. 14 for calculating the velocity gradient.

$$\frac{\partial u}{\partial z} = \frac{1}{\eta_x} \frac{\partial p}{\partial x} \left(z - \frac{h}{2} \right) + \frac{U}{h} \quad (13)$$

$$\frac{\partial v}{\partial z} = \frac{1}{\eta_y} \frac{\partial p}{\partial y} \left(z - \frac{h}{2} \right)$$

$$\frac{\partial u}{\partial z} = \frac{h}{2\eta_0} \frac{\partial p}{\partial x} + \frac{U}{h} \quad (14)$$

$$\frac{\partial v}{\partial z} = \frac{h}{2\eta_0} \frac{\partial p}{\partial y}$$

The accuracy of the simplification can be stated as following. Let us rearrange the Eq. 13 and Eq. 14

$$\frac{\partial u}{\partial z} = \frac{r\omega}{\delta} \left[\frac{1}{\eta_x^*} \frac{\partial p^*}{\partial \theta^*} h^* (1 + \epsilon \cos \theta^*) + \frac{1}{1 + \epsilon \cos \theta^*} \right] \quad (13')$$

$$\frac{\partial v}{\partial z} = \frac{r\omega}{\delta} \left[\frac{1}{\eta_y^*} \frac{\partial p^*}{\partial y^*} h^* (1 + \epsilon \cos \theta^*) \right]$$

where h^* is from $-1/2$ to $1/2$

$$\frac{\partial u}{\partial z} = \frac{r\omega}{\delta} \left[\frac{1}{2} \frac{\partial p^*}{\partial \theta^*} (1 + \epsilon \cos \theta^*) + \frac{1}{1 + \epsilon \cos \theta^*} \right] \quad (14')$$

$$\frac{\partial v}{\partial z} = \frac{r\omega}{2\delta} \frac{\partial p^*}{\partial y^*} (1 + \epsilon \cos \theta^*)$$

To show the difference between Eq. 13' and Eq. 14', following procedures are used :

1. Start with non-Newtonian pressure distribution by simplified equation 13'. This is reasonable because for both cases the distribution will have nearly same shape.
2. Calculate velocity gradient by iteration (Eq. 13') and viscosity expression Eq. 12.
3. Compare the results with Eq. 14'.

The results with the values of $\epsilon = 0.8$ and $L/D = 0.25$ are following :

$$\frac{\text{RVG. of Eq. 14}' - \text{RVG. of Eq. 13}'}{\text{RVG. of Eq. 13}'} = 0.012 \sim 0.131$$

$$\frac{\text{AVG. of Eq. 14}' - \text{AVG. of Eq. 13}'}{\text{AVG. of Eq. 13}'} = -0.031 \sim -0.013$$

where RVG. : rotational velocity gradient

AVG. : axial velocity gradient.

These values seem to be very big, but the effect on calculating the viscosity is much less. The viscosity variations corresponding the minimum and maximum values are :

$$\frac{\text{RV. of Eq. 14}' - \text{RV. of Eq. 13}'}{\text{RV. of Eq. 13}'} = -0.001 \sim -0.011$$

$$\frac{\text{AV. of Eq. 14}' - \text{AV. of Eq. 13}'}{\text{AV. of Eq. 13}'} = 0.002 \sim 0.001$$

where RV. : rotational viscosity

AV. : axial viscosity.

Above results show that the simplification is valid with high accuracy and it is in the safe side for calculating the bearing load; the simplification gives slightly less load capacity than using Eq. 13. To calculate the velocity gradient, we use Eq. 14' and the difference equations are given as Eq. 15

$$\frac{\partial u}{\partial z} = \frac{r\omega}{4\delta} \left[(1+\epsilon \cos\theta)(p(i+1,j) - p(i-1,j))/G + 4/(1+\epsilon \cos\theta) \right]$$

$$\frac{\partial v}{\partial z} = \frac{r\omega}{4\delta Y} (1+\epsilon \cos\theta)(p(i,j+1) - p(i,j-1)) \quad (15)$$

COMPUTATION PROCEDURE

For computation of the bearing performance, following models are used (Fig. 5).

Group A. Experimental viscosity relations of the form of Eq. 12

$$1. \eta^* = 1.45 - 0.15 \log \gamma$$

$$2. \eta^* = 1.30 - 0.10 \log \gamma$$

$$3. \eta^* = 1.15 - 0.05 \log \gamma$$

$$\text{and for } \gamma < 10^3, \eta^* = 1.0 \quad (16)$$

Group B. Power law relations as used in many theoretical analysis, which have same viscosity losses at 10^6 s^{-1} (45 %, 30 %, 15 %)

$$4. \eta^* = \gamma^{-0.043}$$

$$5. \eta^* = \gamma^{-0.026}$$

$$6. \eta^* = \gamma^{-0.0117}$$

$$\text{and for } \gamma < 1, \eta^* = 1.0 \quad (17)$$

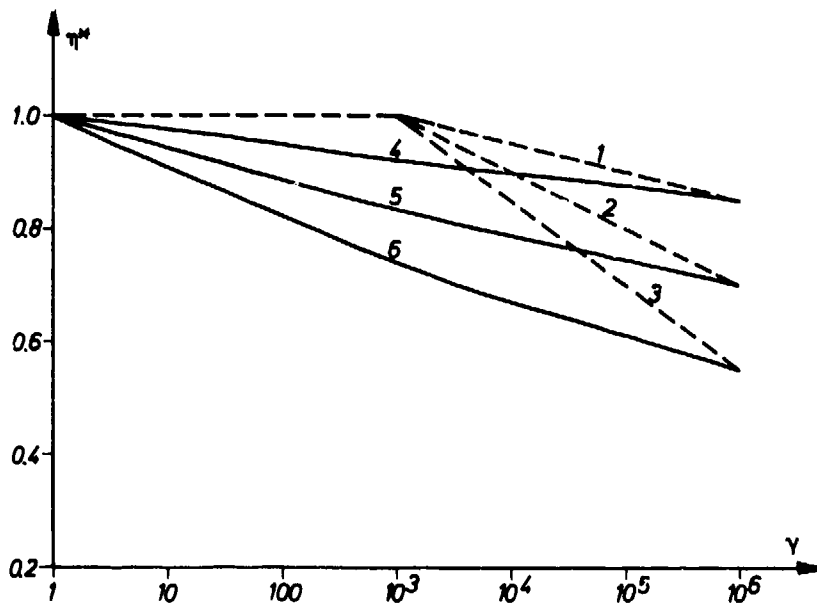


Fig. 5. Graphical representation of 6 models.

The computation of bearing performance is done in successive steps :

A. Pressure field

1. Calculate a Newtonian pressure field using 5 point finite difference iteration technique.
2. Find Newtonian velocity gradient field ($\partial u/\partial z$, $\partial v/\partial z$).
3. Find the viscosity fields (η_x , η_y).
4. Calculate a non-Newtonian velocity gradient field with modified coefficients in finite difference equations.
5. Find non-Newtonian velocity gradient fields.
6. Compare step 5 and 2, if the difference is larger than 0.1 %, send 5 values to 3 for recalculating the viscosity fields. Otherwise call performance subroutine.

B. Bearing parameters

1. Calculate total load, friction, attitude angle and the coefficient of friction by using performance subroutine.
2. The load-carrying capacity of the bearing can be determined from the expression :

$$W = \zeta \eta L D \omega \left(\frac{r}{\delta}\right)^2$$

where
$$\zeta = \frac{1}{4\lambda} (W_1^2 + W_2^2)^{1/2}$$

$$W_1 = \iint p(\theta, y) \sin\theta \, d\theta \, dy$$

$$W_2 = \iint p(\theta, y) \cos\theta \, d\theta \, dy$$

3. The frictional force

$$F = \xi \eta L D \omega \left(\frac{r}{\delta}\right)^2$$

where
$$\xi = \frac{1}{4\lambda} \iint (\eta_x \frac{\partial u}{\partial z}) \, d\theta \, dy \frac{1}{\omega} \left(\frac{\delta}{r}\right)^2$$

4. The coefficient of friction $f = \xi/\zeta$

5. The attitude angle $\alpha = \tan^{-1} (W_1/W_2)$

RESULTS

Computed results for bearing parameters are represented with figure 6 to 10. Lines indicated with E model (experimental) represent No. 1 of Eq. 16 and with P model (power law) represent No. 4 of Eq. 17. Fig. 6 shows that the attitude angle is nearly same for different models although there is a tendency that the value is a little large for large values of L/D. For the same L/D, the E model is the largest and the Newtonian is the smallest. Fig. 7 shows the pressure distribution of E model which is somewhat flatter than the Newtonian. The P model distribution is nearly the same as the E model. Fig. 8 represents the coefficient of load carrying capacity versus ϵ . The value of the E model is a little larger than the P model for most ranges, but for eccentricities > 0.9 it changes. Fig. 9 shows the coefficient of friction loss. There is a small tendency that the value is larger for large L/D even the difference is small. The E model shows higher values than the P model except at high eccentricity. Fig. 10 shows the coefficient of friction which is one of the most important factors for determining the bearing performance. From this logarithm diagram, it can be seen that the friction coefficient is smaller for non-Newtonian model, which means the non-Newtonian lubricant is better than the Newtonian one. The E model shows better characteristics than the P model.

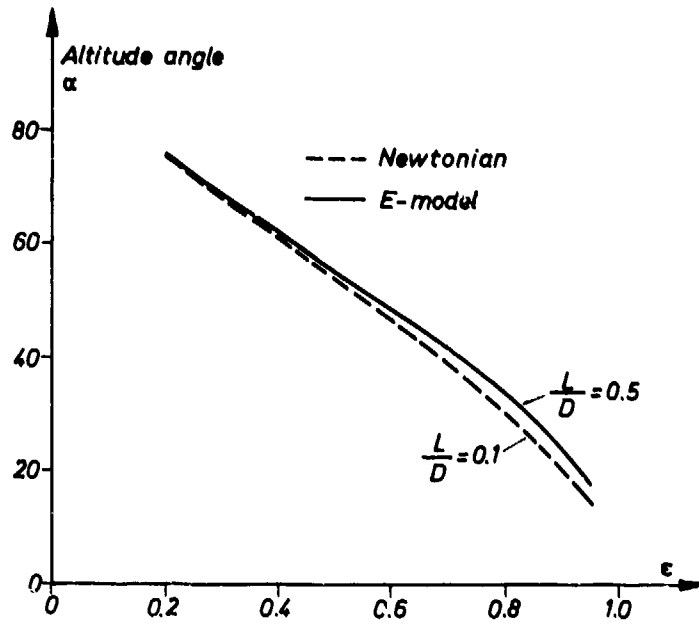


Fig. 6. Altitude angle versus eccentricity

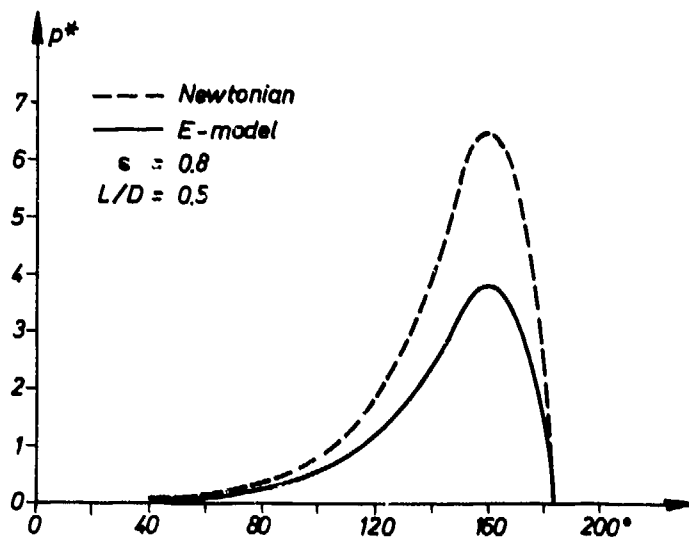


Fig. 7. Pressure distribution versus angle (on the mid plane)

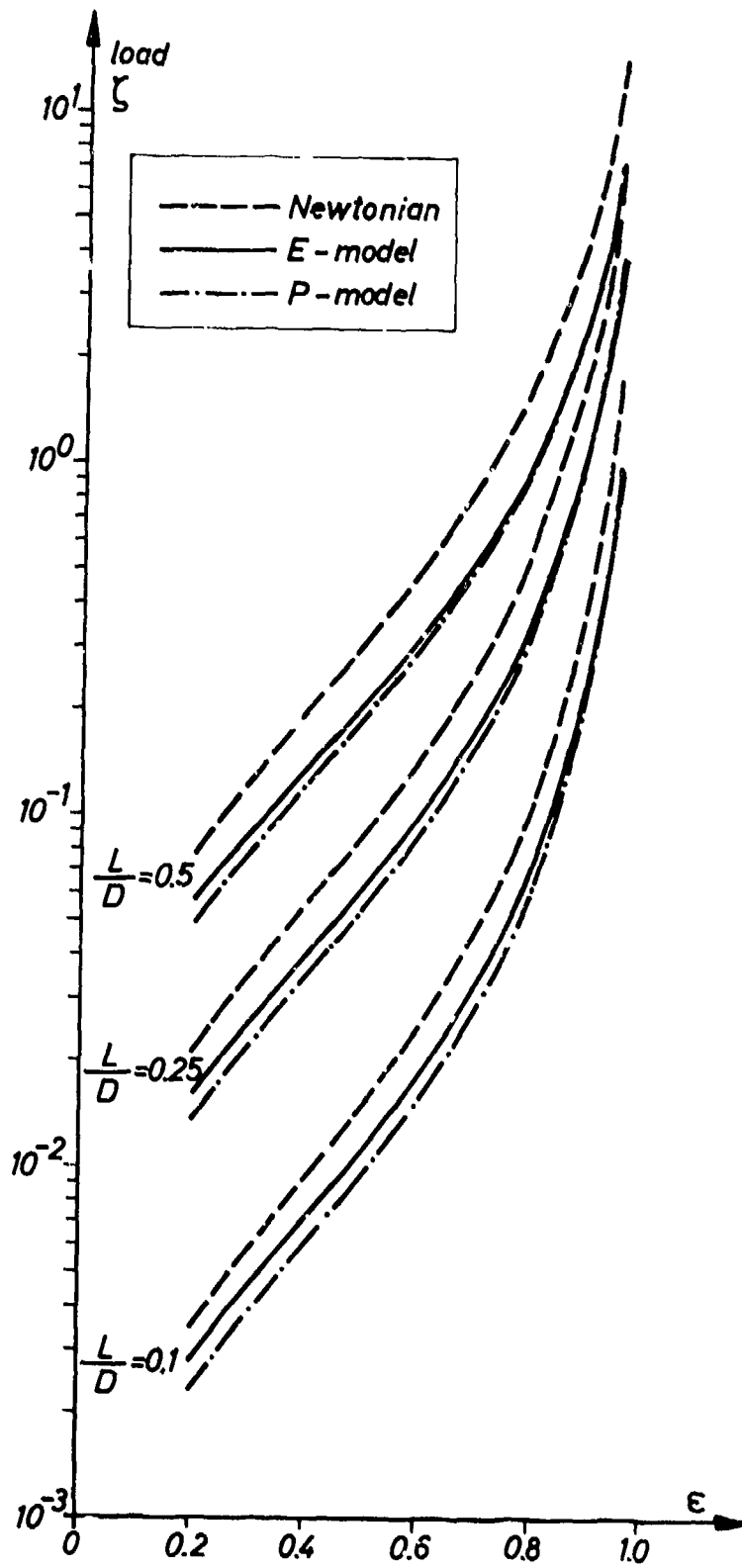


Fig. 8. The coefficient of load carrying capacity ζ versus eccentricity

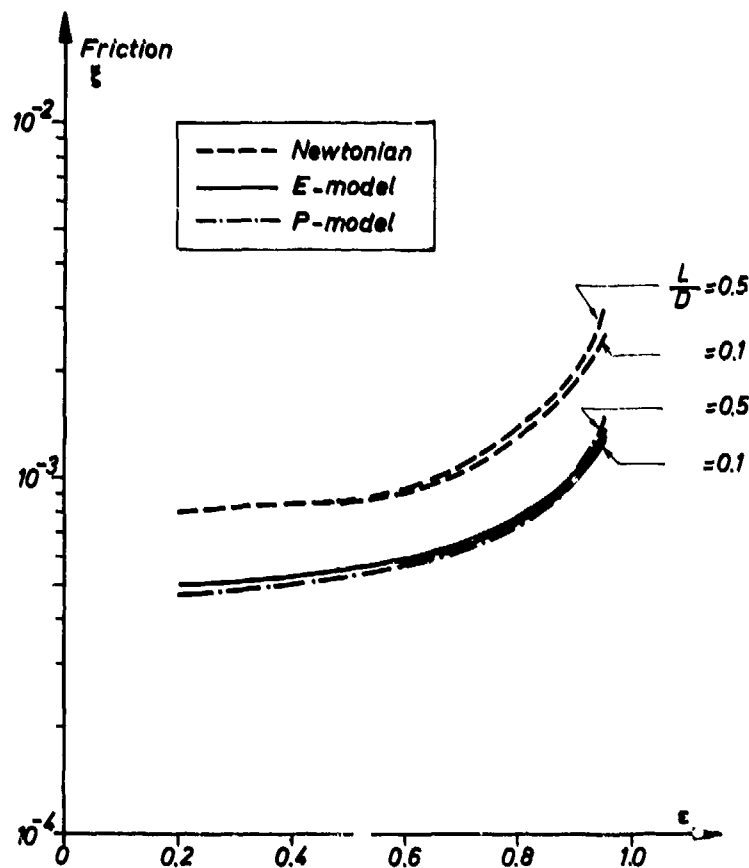


Fig. 9. The coefficient of friction loss ξ versus eccentricity

So, for a definite eccentricity ratio, non-Newtonian load capacity is lower than Newtonian which is in agreement with Pearson [5] who showed the shear thinning model without side leakage (long bearing assumption). As friction loss decreases even more than load capacity, the net result is quite positive. The gain, i.e. $(f_{New} - f_{non-New})/f_{New}$ is demonstrated in Fig. 11 to 13, for different values of bearing length ($L/D = 0.1, 0.25, 0.5$ respectively). The Fig. 11 to 13, the curves 1, 2, 3 represent No. 1, 2, 3 of Eq. 16 and the curves 4, 5, 6 represent No. 4, 5, 6 of Eq. 17. These important figures clearly show the benefit of non-Newtonian oils. The gain is a monotonically decreasing function of eccentricity for very short bearing ($L/D = 0.1$). For moderate bearing ratio ($L/D = 0.25$ to 0.5) the gain is again increasing at higher ϵ .

CONCLUSION

It has been clearly shown that the non-Newtonian lubricants are better than the Newtonian ones. For the interesting working ranges, such as eccentricity of about 0.9 and L/D of 0.1 to 0.25, the gains for oils with 45 % viscosity loss at 10^6 s^{-1} rate of shear, are about 5 to 10 % for the experimental Eq. 16 model and 3.3 to 4.6 % for power law model. As the experimental model is more realistic than the power law one, it will represent the best approach for bearing characteristics. The two-dimensional treatment of a modified Reynolds equation made it possible to incorporate the side leakage effect in the study of the shear thinning phenomena of non-Newtonian lubricants.

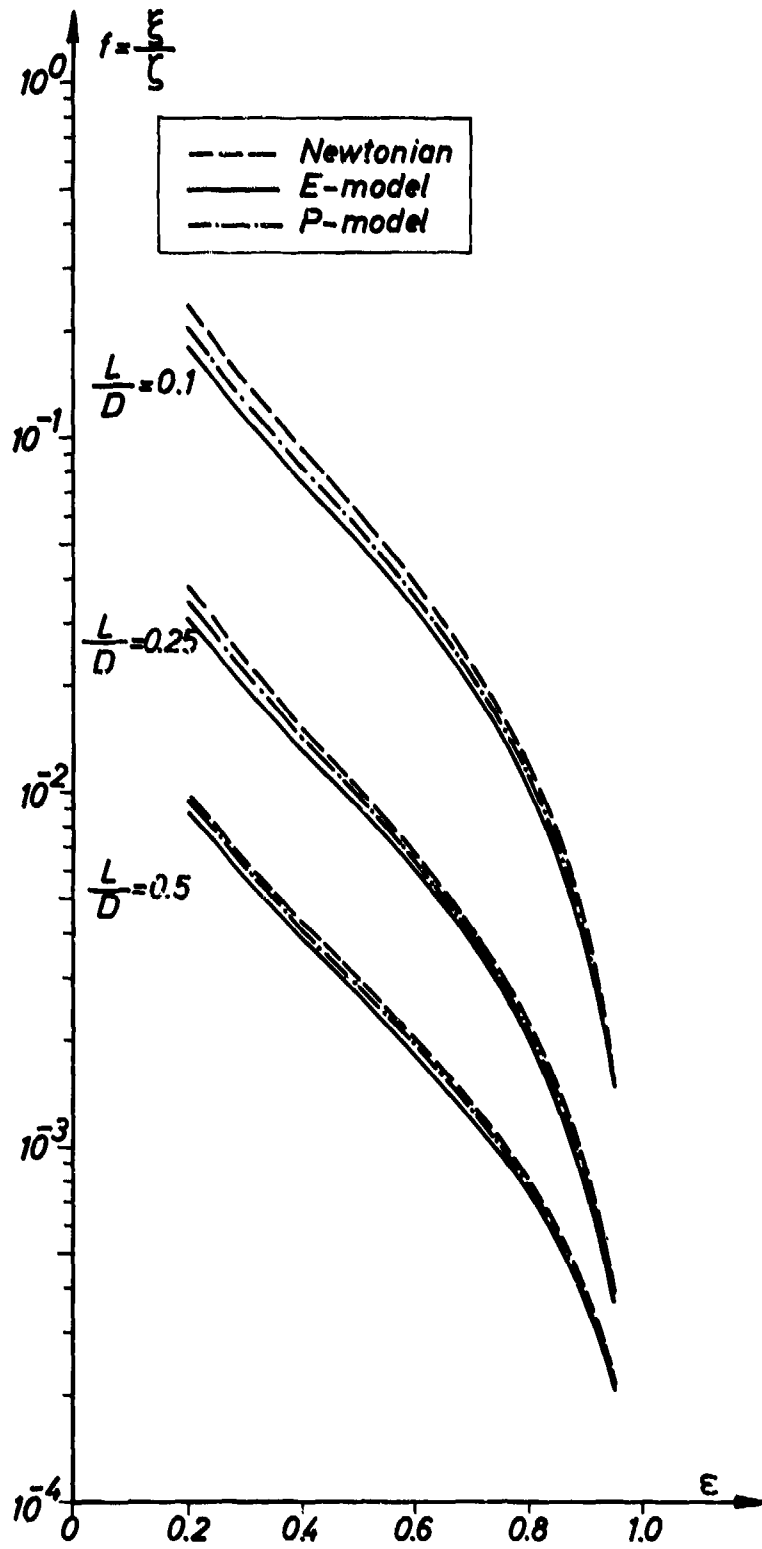


Fig. 10. The coefficient of friction f versus eccentricity

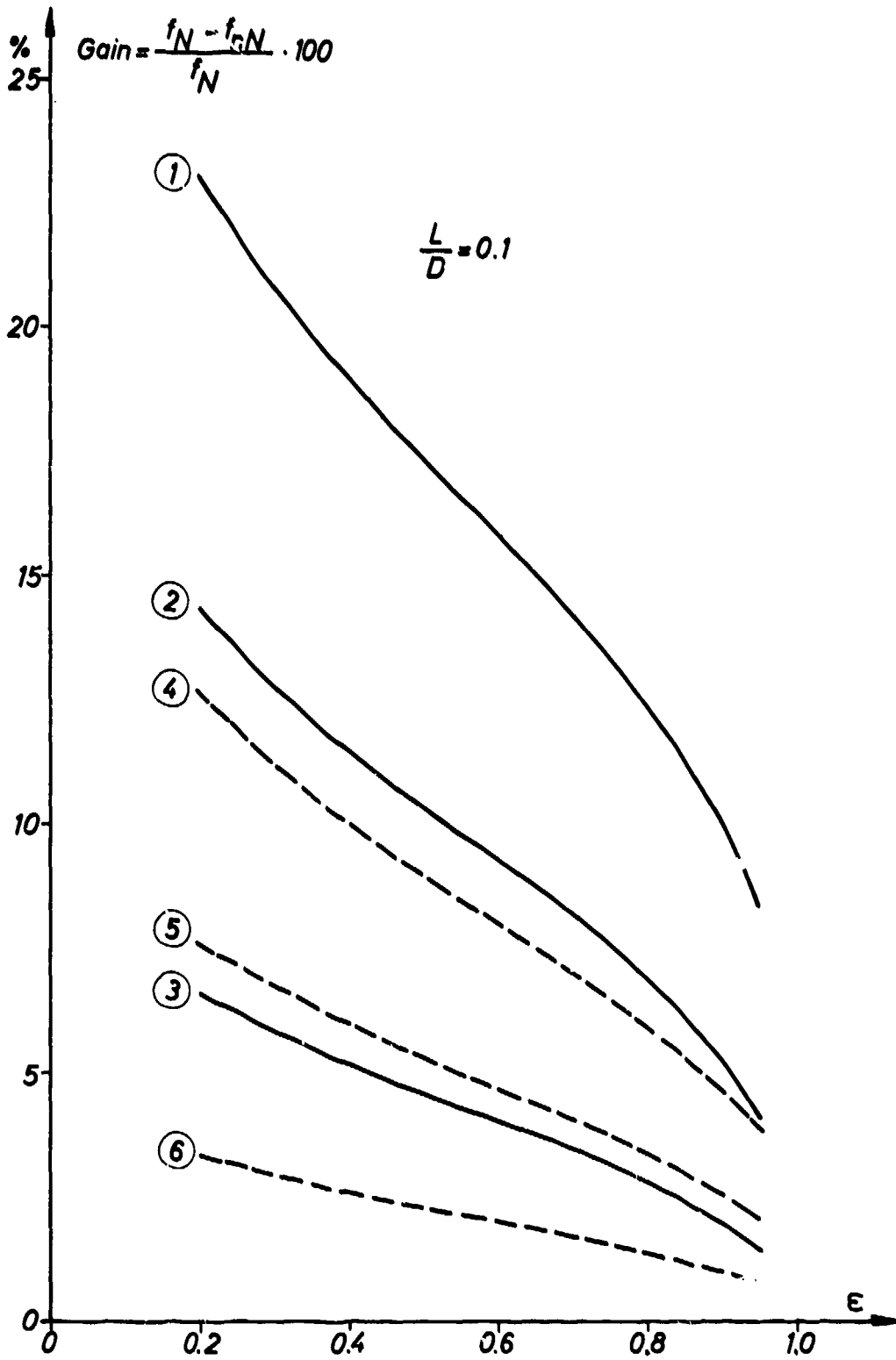


Fig. 11. Gain versus eccentricity

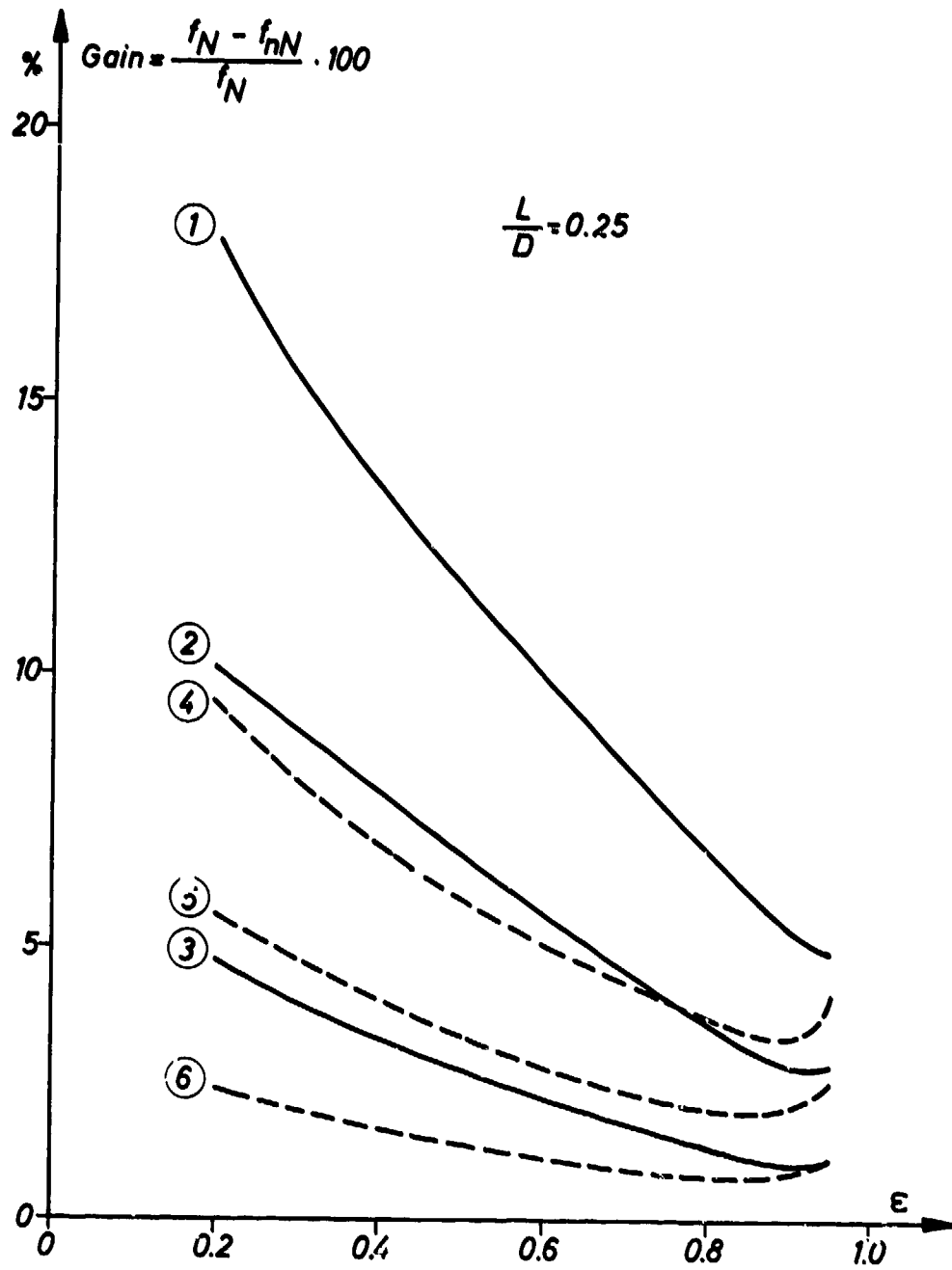


Fig. 12. Gain versus eccentricity

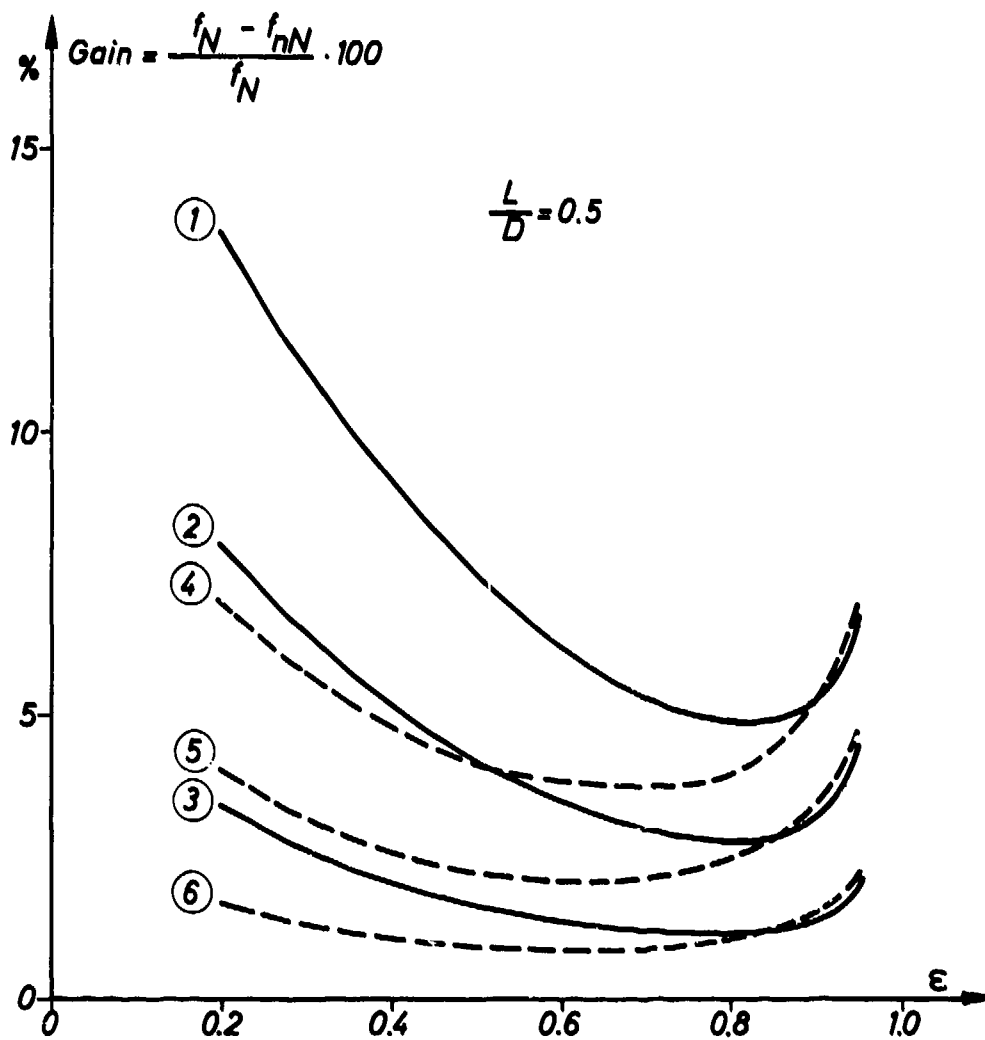


Fig. 13. Gain versus eccentricity

REFERENCES

1. R.I. Tanner, Study of Anisothermal Short Journal Bearings with non-Newtonian Lubricants, ASME Journal of Applied Mechanics, Vol. 32, Dec. 1965, pp. 781-787.
2. R.I. Tanner, Full Film Lubrication Theory for a Maxwell Liquid, Int. J. Mech. Sci., Vol. 1, 1960, pp. 206-215.
3. J.M. Davies, Elastico-Viscous Lubrication, Ph. D. thesis, University College of Wales, Wales, 1974.
4. F.F. Tao and W. Philippoff, Hydrodynamic Behaviour of Viscoelastic Liquids in a Simulated Journal Bearing, ASLE Trans., Vol. 10, 1967, pp. 302-315.
5. J.R.A. Pearson, The Lubrication Approximation Applied to non-Newtonian Flow Problems; a Perturbation Approach, Non-Linear Partial Differential Equations, ed. W.F. Ames, Academic, 1967, p. 73.
6. H.H. Horowitz, Predicting Effects of Temperature and Shear Rate on Viscosity of Viscosity Index-Improved Lubricants, Ind. and Eng. Chemistry, Vol. 50, No. 7, 1958, pp. 1089-1094.
7. M.L. McMillan and C.K. Murphy, Temporary Viscosity Loss and its Relationship to Journal Bearing Performance, SAE Transactions, Vol. 87, 1978, paper 780374.
8. S.R. Dobson, Analysis of High Shear Rate Viscosity Data for Engine Oils, Tribology International, Vol. 14, No. 4, August 1981, pp. 195-198.

DISCUSSION

C.M.Taylor, University of Leeds, UK

The introduction of different dynamic viscosities in the circumferential and axial directions implies different flow rates from the Newtonian condition. This in turn will influence the thermal equilibrium of the bearing. Could the author comment on the importance of thermal considerations in comparisons between predictions of their theoretical analysis and experimental results?

Author's Reply

The material presented is the result of the first study of this subject. Thermal effects, of course, will modify pressure distribution and shear rates, and so bearing performance.

The experimental results have to be treated statistically to find improvements for these kinds of oils; it means the gains are rather low (by some %). So this theoretical study shows gain of some higher % (but still low). Thermal effects could, of course, decrease the gain expected by the iso-thermal study.

A.Journeau, ONERA, Fr

Votre étude sur les fluides non-newtoniens est très intéressante. Les courbes présentées sont des résultats de calcul mais vous avez dit dans vos conclusions que les comparaisons avec l'expérience sont satisfaisantes. Peut on savoir avec quelle précision cette concordance se vérifie?

Reponse d'Auteur

Les résultats expérimentaux disponibles montrent une amélioration de seulement quelques 1 à 2%. Ces résultats ne sont qu'une partie des résultats totaux pour des moteurs à pistons.

Comme les résultats théoriques montrent un gain de = 5% pour des valeurs de ϵ normales ($\epsilon = 0,7-0,9$) et pour des huiles un 'peu normales' c'est-à-dire avec une perte de viscosité pas si grande peut-être des effets thermiques peuvent diminuer encore ce gain théorique, jusqu'aux valeurs expérimentales.

GLISSEMENT DANS LES ROULEMENTS A ROULEAUX.
INFLUENCE DU LUBRIFIANT.

par

Daniel BERTHE, Professeur
Louis FLAMAND, Maître-Assistant

Laboratoire de Mécanique des Contacts
Institut National des Sciences Appliquées de Lyon
20, avenue Albert Einstein
69621 Villeurbanne - France

1. POSITION DU PROBLEME

Dans les roulements à rouleaux cylindriques, la condition de roulement pur des corps roulants par rapport aux pistes n'est plus vérifiée lorsque les vitesses de rotation sont élevées et que les charges transmises sont faibles. Ce phénomène est connu sous le nom de skidding. Il convient de limiter ces glissements car ils peuvent être à l'origine d'échauffements importants et d'usure prématurée.

Dans ce but, on examinera les conditions d'équilibre mécanique des éléments constitutifs d'un roulement donné. La cinématique et en particulier les vitesses de glissement entre les corps roulants et les bagues sont déterminées à partir des actions normales et tangentielles transmises par le film lubrifiant. En conséquence, il est indispensable de prendre en compte le comportement rhéologique du lubrifiant.

Ce papier comporte trois parties :

- dans la première, on mettra en place les modèles rhéologiques utilisables pour des lubrifiants aéronautiques,
- dans la seconde, on modélisera les différents contacts rencontrés dans le roulement étudié,
- dans la dernière, on illustrera l'influence du lubrifiant sur l'équilibre global du roulement.

2. COMPORTEMENT RHEOLOGIQUE DES LUBRIFIANTS AERONAUTIQUES

2.1. Modèles rhéologiques

Différentes études [1,2] ont montré que sous des pressions élevées ou des temps de sollicitations courts, le comportement du lubrifiant ne peut plus être décrit par une loi newtonienne piézo-visqueuse. Des modèles plus complexes doivent être introduits, ils incluent une élasticité et une viscoplasticité du lubrifiant. Des modèles types Maxwell non linéaires décrivent bien les phénomènes.

$$(1) \quad \dot{\gamma} = \frac{1}{G} \frac{d\tau}{dt} + F(\tau)$$

G est le module de cisaillement, $\dot{\gamma} = (U_1 - U_2)/h$ est le gradient de vitesse de déformation, τ la contrainte de cisaillement, $F(\tau)$ est la composante de déformation visco-plastique ou visqueuse non linéaire.

Pour le fluide newtonien $\sigma(\tau) = \tau/\mu$ pour un non newtonien, différentes formes pour $F(\tau)$ ont été proposées, en particulier μ Ree-Eyring :

$$(2) \quad F(\tau) = \frac{\tau_0}{\mu} \operatorname{Sh} \frac{\tau}{\tau_0}$$

où τ_0 est une contrainte caractéristique du lubrifiant.

Le lubrifiant doit donc être caractérisé par trois paramètres : la viscosité μ , le module de cisaillement G , la contrainte caractéristique τ_0 et leurs variations avec la pression et la température.

Dans le cas particulier de faible valeur de contrainte, la relation (1) se réduit au modèle de Maxwell linéaire :

$$(3) \quad \dot{\gamma} = \frac{1}{G} \frac{d\tau}{dt} + \frac{\tau}{\mu}$$

Cette relation peut être intégrée dans le contact Hertzien lubrifié [3], il vient :

$$(4) \quad \tau = \mu \dot{\gamma} \left[1 - \exp \left(- \frac{(x+a)(U_1+U_2)}{\mu/G} \right) \right]$$

$\tau_0 = \frac{\mu}{G}$ est le temps de relaxation du lubrifiant et $\frac{x+a}{U_1+U_2}$ est le temps de sollicitation du lubrifiant, (fig.1).

Lorsque le temps de sollicitation est petit devant le temps de relaxation du lubrifiant, la relation (4) se réduit à :

$$(5) \quad \tau = G \dot{\gamma} \frac{x+a}{U_1+U_2} \quad \text{avec} \quad \dot{\gamma} = \frac{\partial u}{\partial y} \approx \frac{U_1 - U_2}{h}$$

le comportement est entièrement élastique.

2.2. Paramètres rhéologiques

Des mesures rhéologiques directes pour déterminer μ , G et τ_0 sont possibles mais très délicates à mettre en oeuvre [2] ; il semble plus aisé d'obtenir ces paramètres à partir d'expériences sur machines à disques dans lesquelles on simule le contact hertzien et on mesure le frottement en fonction de la vitesse de roulement, de la vitesse de glissement, de la pression et de la température. Les courbes de la figure 2 montrent l'allure des résultats obtenus. On détermine les paramètres μ , G , τ_0 par ajustement des résultats théoriques donnés par les équations (1) et (2) et les résultats expérimentaux, [4]. Des caractérisations de différents fluides aéronautiques sont disponibles dans la littérature [5], nous donnons ci-dessous les caractéristiques d'un seul lubrifiant MOBIL OIL JET II qui serviront dans la suite de cette étude :

$$\begin{aligned} \mu &= 2,33 \cdot 10^{-2} \exp \left[1,33 \cdot 10^{-8} p + 3800 \left(\frac{1}{T+273} - \frac{1}{313} \right) \right], \text{ Pa}\cdot\text{s} \\ G &= .1,68 \cdot 10^5 \exp \left[2,6 \cdot 10^{-9} p + 3800 \left(\frac{1}{T+273} - \frac{1}{313} \right) \right], \text{ Pa} \\ \tau_0 &= 6,02 \cdot 10^5 \exp (2,57 \cdot 10^{-9} p), \text{ Pa} \end{aligned}$$

2.3. Application pour le contact Hertzien et le roulement

Afin de définir les grandes tendances du comportement du lubrifiant, la table 1 donne le temps de relaxation du lubrifiant pour deux températures 20°C et 120°C et deux pressions 0,5 GPa et 16 GPa ;

p	GPa	0,5	0,5	1	1
T	°C	20	120	20	120
τ_l	s	$2,57 \cdot 10^{-5}$	$2,57 \cdot 10^5$	$6,95 \cdot 10^{-3}$	$6,95 \cdot 10^3$

Table 1

Compte tenu des vitesses importantes dans le roulement, les temps de sollicitations varient entre $5 \cdot 10^{-6}$ s et $20 \cdot 10^{-6}$ s. Dans ces conditions le comportement est essentiellement élastique plastique et la contrainte de cisaillement à faible déformation est donnée par la relation (5). On remarquera que cette contrainte est très largement inférieure à celle qui serait obtenue en supposant un comportement newtonien.

Lorsque la vitesse de glissement est importante, la déformation visco-plastique devient prépondérante, la relation (2) montre alors que la contrainte dans le film tend vers une limite τ_l égale à :

$$\tau_l = \alpha \cdot \tau_0 \cdot p$$

où α est le coefficient de piézoviscosité donné par la relation (6), τ_0 la contrainte caractéristique donnée par la relation (6) et p est la pression. La table 2, ci-dessous, donne des valeurs de cette contrainte limite pour différentes pressions.

p	GPa	0,2	0,5
τ_l	M.Pa	2,6	14,5

Table 2

Le fluide se comporte alors comme un corps plastique, la contrainte ici encore est très inférieure à celle qui serait obtenue en supposant un comportement visqueux.

3. MODELISATION DES CONTACTS DANS UN ROULEMENT

Pour calculer les forces de liaison entre les différents éléments constitutifs d'un roulement à rouleaux cylindriques, nous considérons trois types de contacts :

- 1 - le contact rouleau-bague extérieure,
- 2 - le contact rouleau-bague intérieure et rouleau-cage,
- 3 - les contacts cage-bagues.

A chaque fois, nous calculerons :

- l'épaisseur du film ou la répartition entre les surfaces,
- la force de frottement ou la contrainte tangentielle développées dans le film.

3.1. Contact rouleau-bague extérieure, (figure 3)

C'est un contact cylindre-cylindre chargé normalement par la force centrifuge agissant sur le rouleau et une éventuelle précontrainte. La pression hertzienne est de l'ordre de 0,3 GPa. Le fonctionnement est donc de type élastohydrodynamique.

La longueur du contact est donnée par la théorie de Hertz et l'épaisseur du film par la formule de Dowson et Higginson [6]. Elle fait intervenir le coefficient de piézoviscosité et la viscosité du lubrifiant, la vitesse des surfaces, les propriétés élastiques des matériaux, la géométrie et la charge normale par unité de longueur.

Les contraintes de cisaillement sont calculées à partir d'une loi rhéologique élastoplastique [1]. En effet, le temps de sollicitation est court devant le temps de relaxation pour la pression de fonctionnement. Cette contrainte fait intervenir la viscosité, le module de cisaillement, la contrainte d'écoulement,

la vitesse de déformation et le temps de sollicitation.

3.2. Contacts rouleau-bague intérieure et rouleau-cage (figure 4)

En l'absence de charge variable et de précontrainte, ce sont des contacts cylindre-cylindre ou cylindre-plan peu chargés. La charge hydrodynamique exercée dans ces contacts est environ cent fois plus faible que la force centrifuge. Nous considérons donc le corps roulant comme indéformable.

L'épaisseur du film est calculée par la solution de l'équation de Reynolds donnée par Martin [7]. Elle fait intervenir la viscosité, la géométrie, la vitesse des surfaces et la charge par unité de longueur.

Pour le calcul des forces de frottement, les temps de passage sont beaucoup plus grands que les temps de relaxation. Un comportement visqueux pur est donc utilisé pour calculer la contrainte de cisaillement. Elle s'exprime alors en fonction de la viscosité traditionnelle et de la vitesse de déformation.

3.3. Contacts cage-bagues (figure 5)

Ce sont des contacts entre deux cylindres centrés. Ils ne transmettent donc pas de charge radiale.

D'un point de vue hydrodynamique, ces deux contacts sont assimilés à des écoulements de Couette, le jeu et la longueur des génératrices sont définis par construction.

Pour le calcul des couples de frottement, une loi visqueuse pure est employée. La contrainte de cisaillement est fonction de la viscosité et de la vitesse de déformation.

3.4. Contact flanc de rouleau-cage ou bague

Nous les considérons comme des contacts plan-plan peu chargés.

D'un point hydrodynamique, ces contacts sont assimilés à des écoulements de Couette, dont la géométrie est définie par construction.

Les contraintes de cisaillement sont calculées à partir d'une loi visqueuse newtonienne habituelle en fonction de la viscosité et de la vitesse de déformation.

4. EQUILIBRE GLOBAL DU ROULEMENT

4.1. Position du problème

Nous étudions le comportement d'un roulement à rouleaux cylindriques soumis à des conditions représentatives du fonctionnement d'un palier arrière de petite turbomachine. Il s'agit d'un roulement de type 1010 dont la bague intérieure tourne à 20.000 tr/mn et dont la bague extérieure est immobile. Il est lubrifié par une huile synthétique, type NATO (5 cSt à 99°C). Il est soumis uniquement à une charge radiale résultant du poids et du balourd du rotor, qui sera négligé dans cette illustration.

Parmi les différents paramètres du fonctionnement, nous étudierons les glissements spécifiques rouleaux-bague extérieure et rouleaux-bague intérieure en fonction de :

- des jeux entre la cage et les bagues, (effet du centrage de la cage),
- du lubrifiant.

4.2. Hypothèses

Nous utilisons les hypothèses suivantes :

- 1/ le régime est permanent,
- 2/ chaque élément du roulement est à une température constante donnée,
- 3/ les charges radiales et axiales appliquées sont nulles ou négligées,
- 4/ chaque élément est infiniment rigide. Seules les déformations élastiques au contact sont prises en compte,
- 5/ les bagues et la cage sont concentriques.

4.3. Analyse mécanique

D'un point de vue cinématique puisque le régime est permanent, les corps roulants ne battent ni dans les alvéoles de la cage, ni dans la direction radiale. Deux degrés de liberté suffisent à cette analyse, (fig.6) :

- la vitesse de rotation de la cage autour de l'axe de symétrie du roulement ω_c ,
- la vitesse de rotation propre du rouleau autour de son axe ω_r .

L'équilibre de l'ensemble découle de l'équilibre d'une tranche de ce roulement d'ouverture égale au pas circonférentiel séparant deux corps roulants consécutifs et centrée sur une alvéole.

L'équilibre de cette tranche, qui tient compte de toutes les forces inter-éléments, c'est-à-dire des forces de liaisons et des forces d'inertie, conduit à un système de deux équations liant les deux vitesses de rotation ω_r et ω_c . La solution est calculée numériquement.

4.4. Résultats

Nous montrerons les variations des glissements spécifiques λ_i , λ_e pour les contacts rouleaux/bague intérieure d'une part, rouleaux/bague extérieure d'autre part en fonction :

- a) - du jeu entre la cage et la bague extérieure, (figure 7),
- b) - du jeu entre la cage et la bague intérieure, (figure 3).

Dans ces résultats, seuls les jeux varient ; par conséquent, l'épaisseur de la cage n'est pas obligatoirement constante. Ces résultats montrent le rôle essentiel des actions tangentielles développées par le film lubrifiant dans le centrage de la cage par rapport aux bagues. On constate que les glissements λ_e , λ_i diminuent lorsque le jeu extérieur augmente ou que le jeu intérieur diminue, ces deux actions vont dans le sens d'une équi répartition des efforts.

Les courbes de la figure 9 montrent les variations des glissements spécifiques λ_i , λ_e en fonction de la viscosité du lubrifiant. On constate que λ_i augmente et λ_e diminue légèrement avec la viscosité.

5. CONCLUSIONS

Une étude des différents types de contacts présents dans le roulement montre la nécessité d'une définition précise du comportement rhéologique du lubrifiant notamment aux contacts rouleaux-bagues. Les contraintes de cisaillement développées par le fluide dans ces contacts sont très inférieures à celles qui seraient obtenues en supposant un comportement visqueux classique ; le comportement du lubrifiant est alors essentiellement élasto-plastique.

Dans les roulements à rouleaux à grande vitesse, peu chargés, les actions aux contacts rouleaux-bagues restent faibles, et le rôle de la cage est essentiel sur la cinématique interne. Des solutions pour réduire les glissements passent par le développement de fluides susceptibles de provoquer des frottements plus importants, par un chargement du roulement ou par un dessin mieux adapté de la cage.

REMERCIEMENTS

Cette étude a été réalisée grâce à un financement D.R.E.T.

BIBLIOGRAPHIE

- 1 - JOHNSON K.L., TEVAARWERK J.L., "Shear behaviour of EHD oil films", Proc. Roy. Soc., London, series A, vol.356, 1977.
- 2 - BAIR S., WINER W.O., "A rheological model for elastohydrodynamic contacts based on primary laboratory data", A.S.M.E. JOLT, 258, vol.101, july 1979.
- 3 - BERTHE D., FLAMAND L., HOUPERT L., "Rheological parameters of lubricant under high speeds conditions", Proc. of Fifth Leeds-Lyon Symposium, Mec. Eng. Pub. Ltd., London, pp.188-196, 1978.
- 4 - HOUPERT L., FLAMAND L., BERTHE D., "Rheological and thermal effects in lubricated EHD contacts", A.S.M.E., JOLT, vol.103, pp.526-532, 1981.
- 5 - GUPTA P.K., FLAMAND L., BERTHE D., GODET M., "On the traction of several lubricants", A.S.M.E. JOLT, vol.103, pp.55-64, 1981.
- 6 - DOWSON D., HIGGINSON G.R., "Elastohydrodynamic lubrication", Pergamon Press, Oxford, First Ed., 1966.
- 7 - CAMERON A., "Principles of lubrication", Longmans Green, London, 1966.

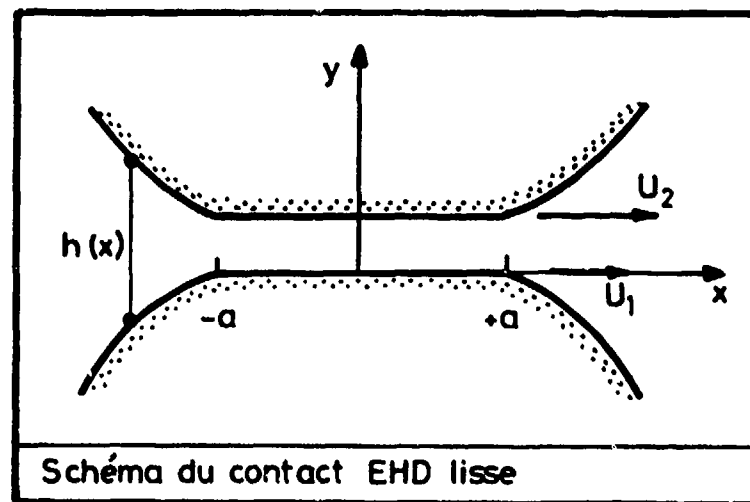


Fig. 1

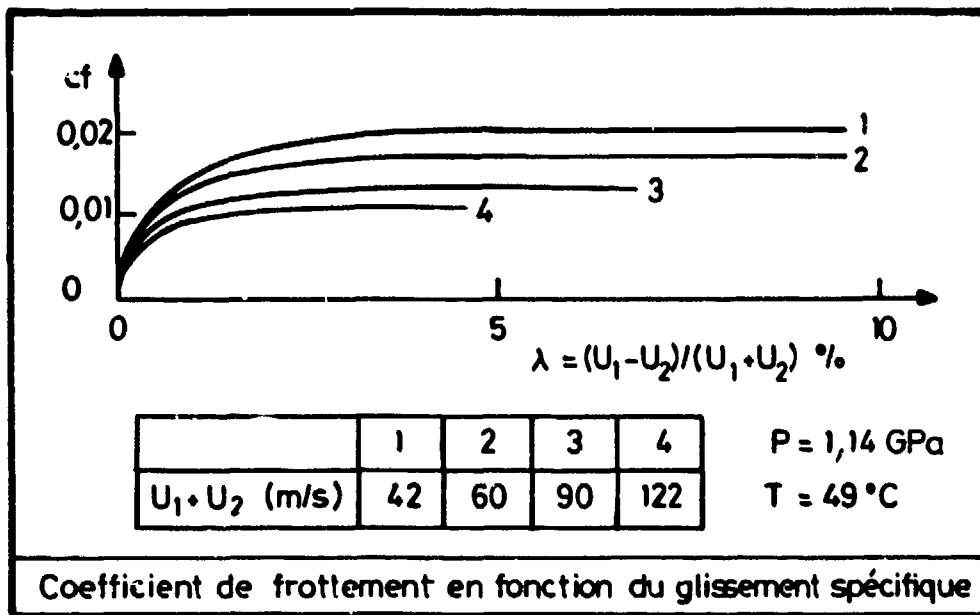


Fig. 2

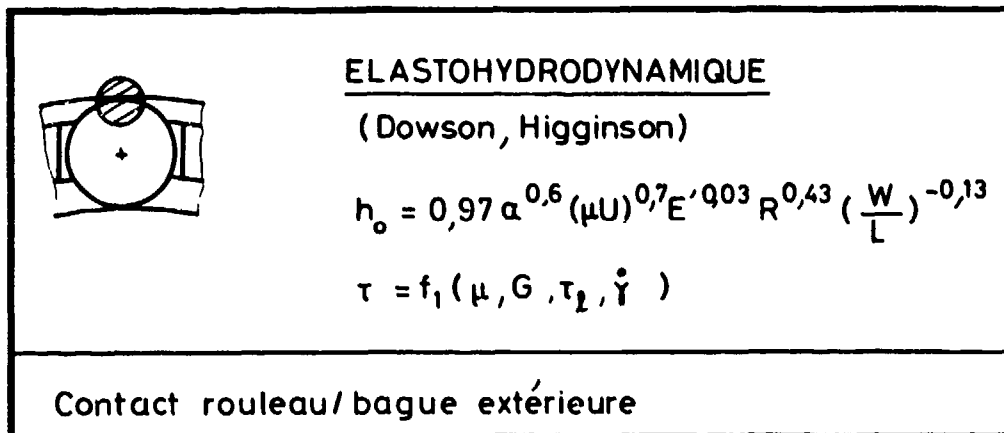


Fig. 3

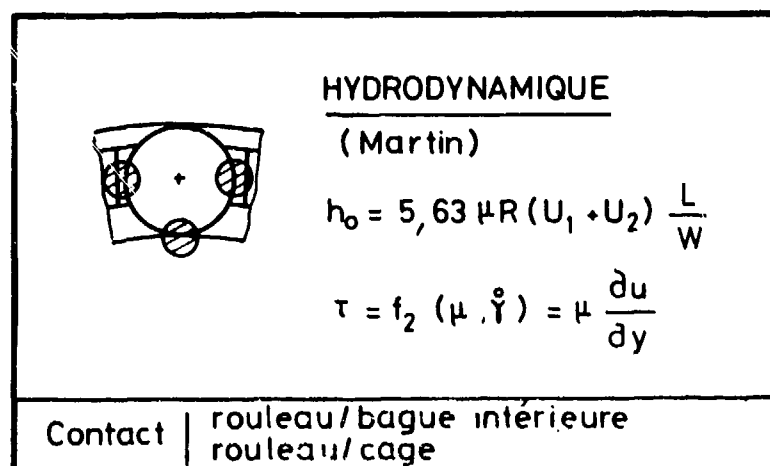
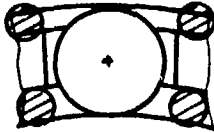


Fig. 4



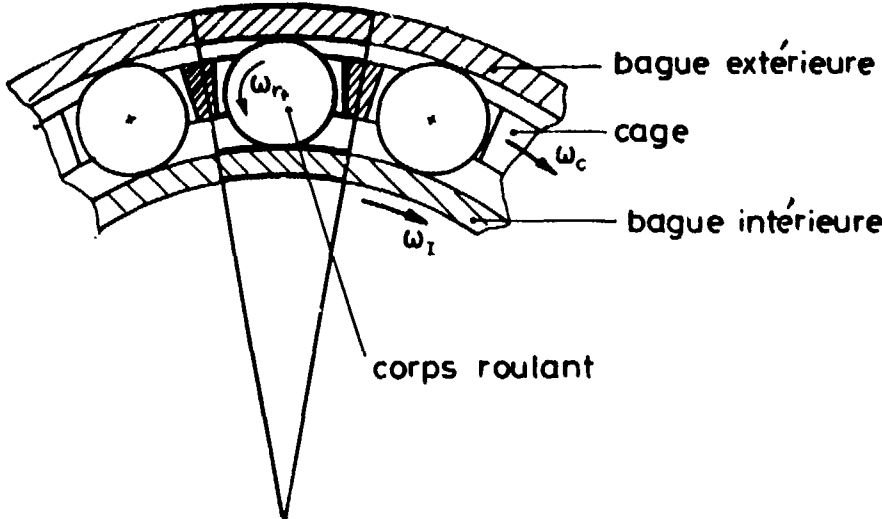
HYDRODYNAMIQUE
(Couette)

$h_0 = c$

$\tau = f_3(\mu, \dot{\gamma}) = \mu \frac{U_2 - U_1}{c}$

Contact cage/bagues

Fig. 5



ω_r

ω_c

ω_I

corps roulant

bague extérieure

cage

bague intérieure

Schéma d'un roulement à rouleaux cylindriques

Fig. 6

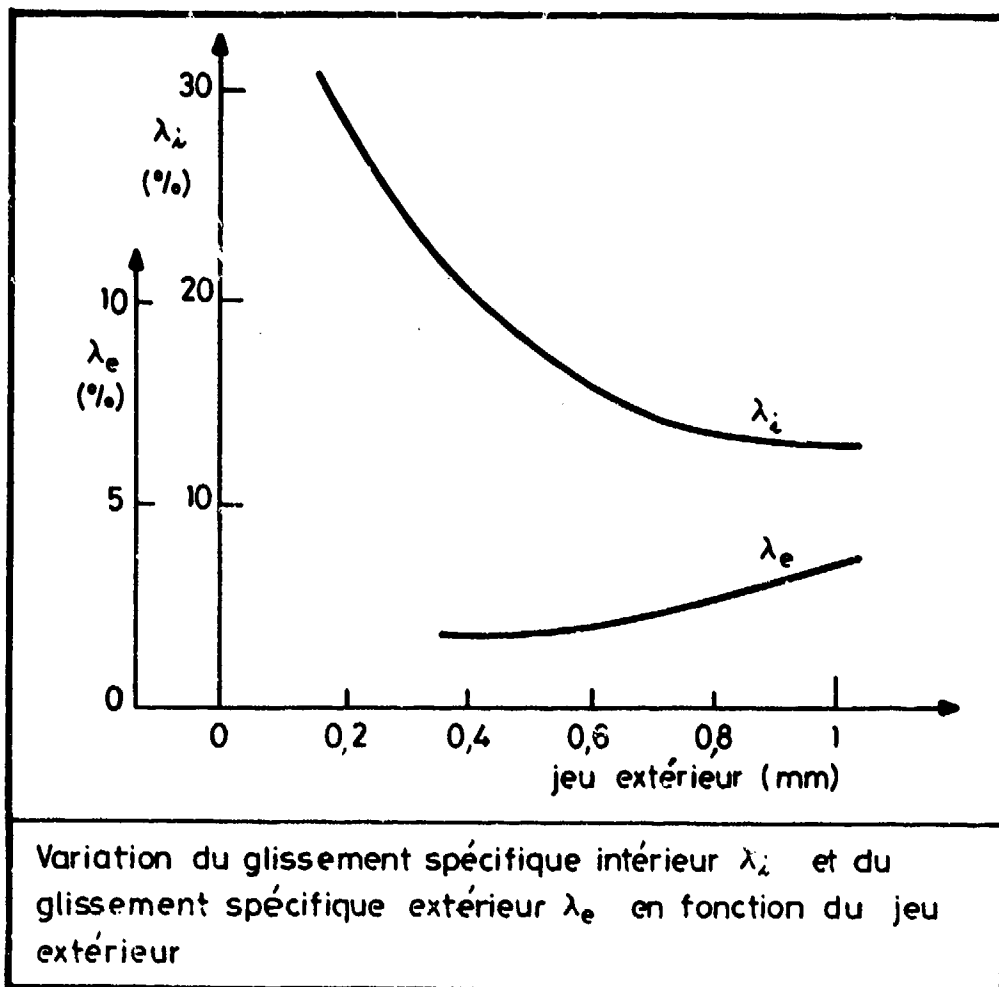


Fig. 7

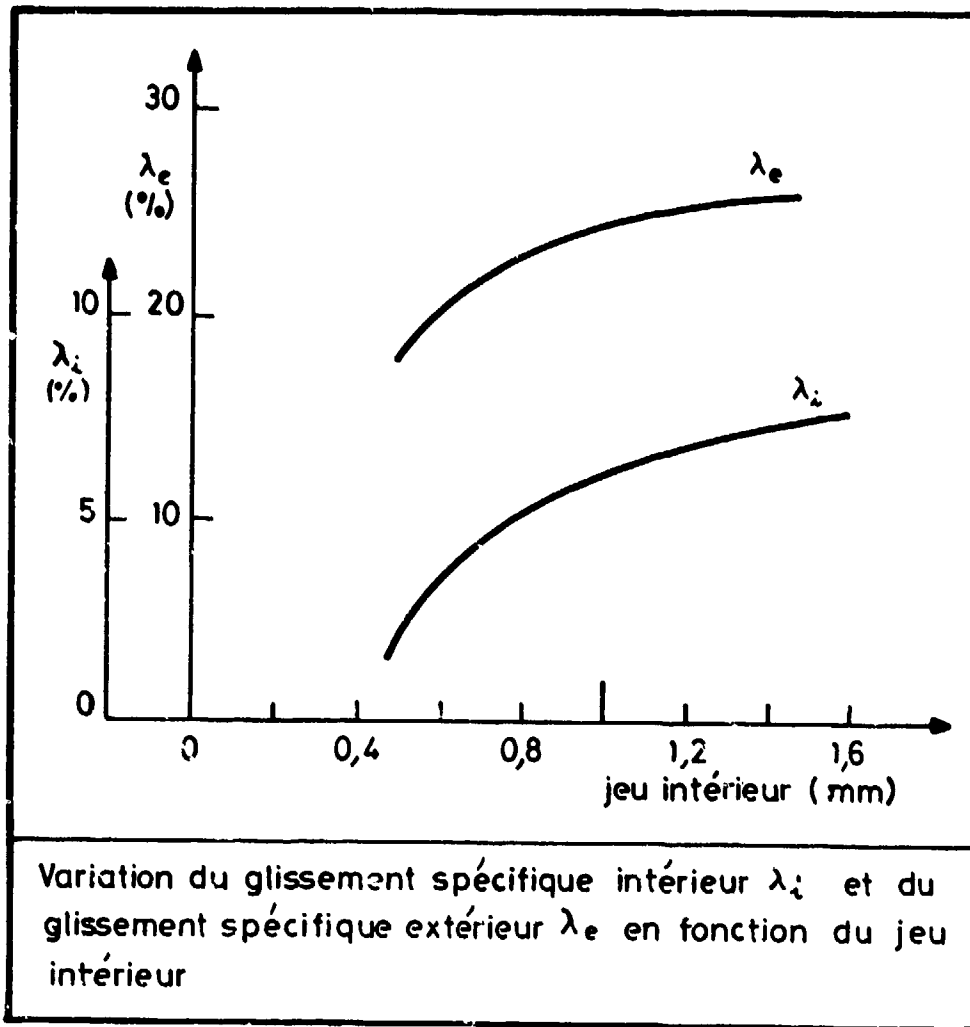


Fig. 8

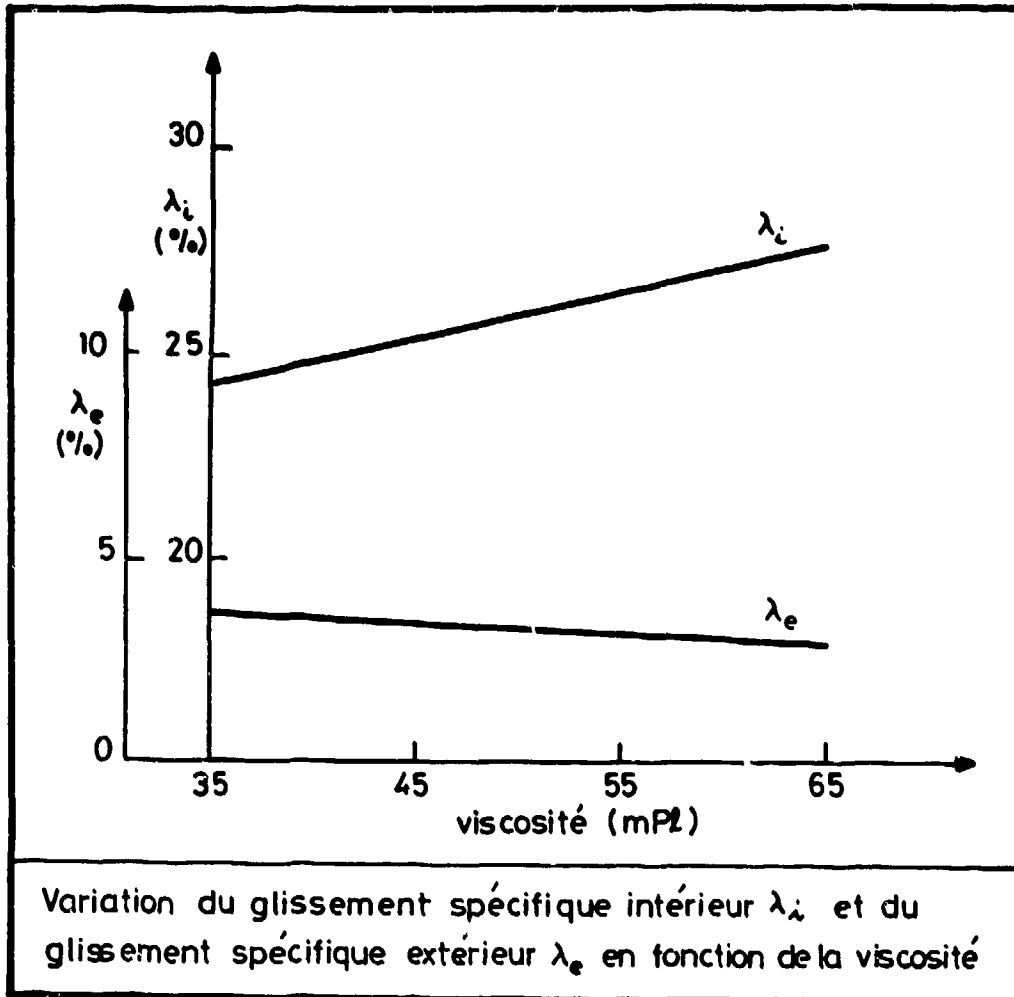


Fig. 9

DISCUSSION

D.G. Astridge, Westland Helicopters, Yeovil, UK

It was encouraging to see some progress being made in the modelling of high speed roller bearings. The basic treatment of the several contact situations was similar to that used earlier (Astridge and Smith 'Heat generation in high speed roller bearings' elasto-hydrodynamic lubrication, I. Mech. E., London 83 94, 1972), but a more advanced rheological model has been used for the EHL films at the roller/outer race contacts, together with more recently acquired oil traction data. It would be interesting to see the results of this latest treatment applied to bearing for which cage slip and heat generation have been measured (e.g. the reference quoted) to see if the accuracy of such analysis has been improved. Worthwhile objectives of work such as that contained in the paper are to provide a means of readily predicting cage slip and heat generation for a particular installation, and to execute parametric studies on a range of bearings/environmental conditions of interest.

Reponse d'Auteur

L'introduction de modèle rhéologique réaliste pour décrire le comportement du lubrifiant constitue une étape importante pour décrire l'équilibre du roulement. En effet, l'hypothèse de comportement newtonien peut entraîner sous forte pression une surestimation qui peut dépasser 100% des actions de frottement aux contacts corps roulants-bagues. Le second problème qu'il conviendrait de bien modéliser concerne l'alimentation des différents contacts (défaut d'alimentation, traînée des corps roulants . . .), une approche expérimentale semble indispensable pour décrire les phénomènes.

J.F. Chevalier, SNECMA, Fr

Avez vous vérifié sur moteur vos prévisions de glissement?

Reponse d'Auteur

Une corrélation complète avec des résultats obtenus sur moteur est encore délicate, en particulier parce que la modélisation implique la connaissance des domaines remplis d'huile, les jeux de fonctionnement pour les conditions thermiques existant dans le moteur, des essais sur un roulement seul dans ces conditions bien contrôlées sont en cours.

J.F. Chevalier

Avez vous calculé l'influence d'une charge radiale, induite par un balourd par exemple.

Reponse d'Auteur

La prise en compte d'un balourd a été faite pour des conditions quasi statiques uniquement, cet effet tend à diminuer les glissements spécifiques aux différents contacts.

A DETAILED TREATMENT OF TWO-DIMENSIONAL, STARVED LUBRICATION
IN THE VICINITY OF TWO COUNTER-ROTATING CYLINDERS

by
Robert A. Medrow
Associate Professor of Mechanical Engineering
and
Larry R. Shippers
Teaching Fellow
Department of Mechanical and Aerospace Engineering
University of Missouri-Rolla
Rolla, Missouri 65401
USA

SUMMARY

The problem of starved lubrication in the inlet region for the case of line contact between two non-deforming, equal radii cylinders rotating in opposite directions with equal surface speeds is considered. The lubricant is assumed to be a constant density, isoviscous, Newtonian fluid. The usual approach, which involves the use of Reynolds equation everywhere, is not followed. Instead, the situation is restricted to one in which the lubricant enters the contact region in thin films which adhere to the cylinders. Using Reynolds equation only at the line-of-centers and a suitable thin film approximation far from that point, the intervening region is treated as a general creeping flow region. Solutions, incorporating complete free surface boundary conditions, are obtained numerically. The hitherto unobtained results due to this approach include the existence of a unique free surface location for a fixed set of operating conditions.

LIST OF SYMBOLS

a_1, a_2, a_3, a_4	coefficients in Eq. (24)	u	velocity in x-direction
$A_{i,j}$	see Eq. (19)	U	surface velocity
D	d/dx	v	velocity in y-direction
$f_{r_{i,j}}, f_{\theta_{i,j}}$	see Eqs. (17) and (18)	v_r	velocity in r-direction
F	see Eq. (A10)	v_θ	velocity in θ -direction
h	thin film thickness	w	free surface velocity
h_0	one-half cylinder gap	x, y	Cartesian coordinates
h_∞	thin film thickness far from contact	X	x/h_∞
H	see Eq. (A10)	β	$2\gamma/\mu U$
i, j	nodal indexes	γ	surface tension
n, s	intrinsic coordinates	ζ	vorticity
p	pressure	ζ'	$R\zeta'/U$
p'	$p/\rho U^2$	λ	root of characteristic equation
q	volumetric flow rate per unit depth	μ	viscosity
r, θ	cylindrical coordinates	ρ	density
R	cylinder radius	σ	free surface angle
Re	Reynolds number ($\rho UR/\mu$)	ψ	stream function
		Ψ	ψ/UR

Superscripts: where not otherwise defined, denotes a quantity made dimensionless through division by U or R .

Subscripts: the subscript R denotes conditions at the cylindrical surface.

INTRODUCTION

Beginning with the 1966 publication of the experimental work of Lauder [1], the body of material devoted to the topic of starved lubrication has reached respectable dimensions. The works of a number of investigators [2-8] have served to demonstrate, for both line and point contacts, the extent to which bearing performance is altered when the amount of lubricant present in the inlet portion of the contact is insufficient to produce the fully-flooded situation. Ample motivation for this ongoing endeavor has been provided by the current awareness that, particularly with respect to many elasto-hydrodynamic contacts, starvation is the common condition.

In general, the analytical treatment of the starved lubrication problem has been based upon the use of Reynolds equation. The effect of starvation has been incorporated by causing the pressure rise to begin at various finite distances from the line or point of contact. The central problem with this approach is that there exists experimental evidence (e.g., Lauder [1] and Tipei [9]) that there do exist preferred interface locations. The usual basis for establishing the unique location of the start of pressure rise has been that which was first suggested by Lauder:

$$p = 0 \text{ where } u = \frac{\partial u}{\partial y} = 0 \quad (1)$$

As described by Dowson and Taylor [10], the general validity of this condition has yet to be established. If surface tension is ever a significant parameter this condition, along with the customary use of Reynolds equation itself, will then be inadequate. The great disadvantage of any alternative approach is that the situations considered will of necessity be more narrowly focussed. The purpose of this paper is to pose and to then explore one particular situation in some detail. In addition to the insights provided concerning this situation, it is hoped that this paper will also serve to illustrate the types of problems which must be overcome in performing a more detailed analysis.

PROBLEM SPECIFICATION AND METHOD OF SOLUTION

The situation to be considered is shown in Fig. 1. It is that of line contact between a pair of counter-rotating, non-deforming, equal radii, cylinders, each of which rotates with the same surface speed. Thin, equal thickness films on each cylinder supply lubricant to the contact. Far from the contact the film thickness is h_0 . This lubricant's temperature, viscosity, and density are all constant. Furthermore, it is supposed that the conditions of flow are such that inertial effects may be neglected throughout the entire flow.

This situation may be further identified as the complement to a common cavitation problem, thorough discussions of which have been presented by Dowson and Taylor [10] and Savage [11]. With regard to the present interest the basic character of the flow is such that no treatment of a solid-fluid interface is required. Coupled with the specified operating condition this situation also possesses a useful degree of symmetry.

Fig. 2 shows an enlarged view of the entrance region in which the lubricant flow field has been divided into three separate regions. Such a division of the flow was first suggested by Williamson [12]. It follows that if Reynolds equation is not to be used throughout the flow, and the actual conditions existing at the free surface of the lubricant are to be used, the truly two-dimensional character of the flow in at least a portion of the entrance region must be considered. That the governing equations of any general flow region will require numerical solution is inherent in the geometry of the flow. Considering the large number of times such a region must be solved, it then becomes desirable to restrict the dimensions of such a region as much as is possible.

Within region 1 the general applicability of Reynolds equation is well-established. When used with a specified gap, $2h_0$, this simplification of the problem allows the regions to either side of the line-of-centers to be treated separately. In practice, region 1 was restricted to just the line-of-centers. Region 2 involves a type of thin film flow which, in various contexts, has received considerable attention, particularly with regard to various chemical engineering applications. One may, therefore, reasonably expect some simplification of the flow equations to exist in this region. This leaves region 3 as the only one in which the full

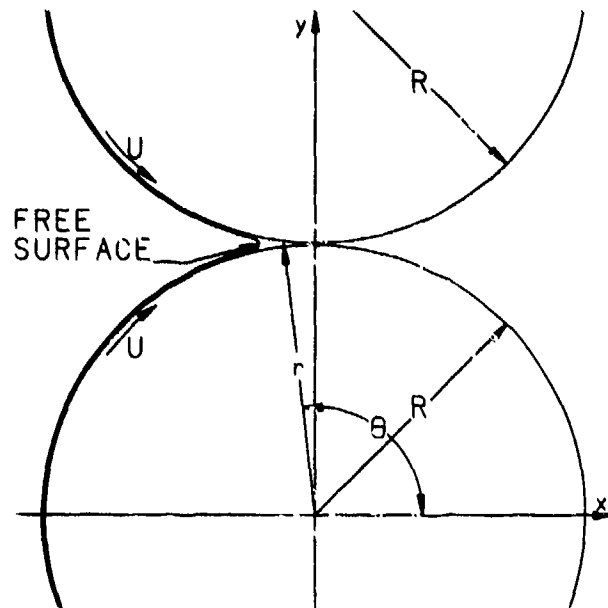


Fig. 1. Physical situation.

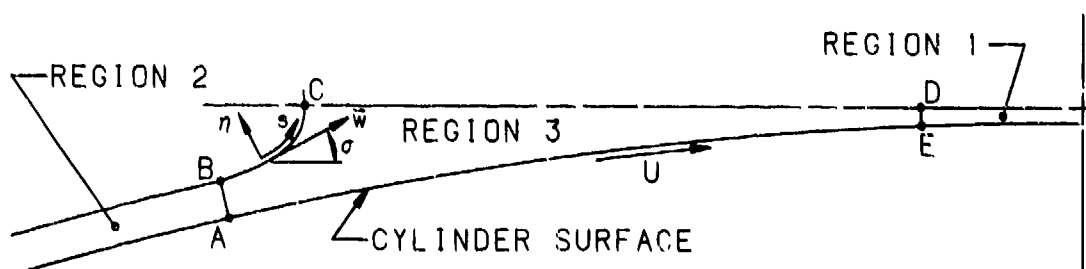


Fig. 2. Flow regions.

equation of creeping flow need be considered.

Practically, the two possible methods of approach to the numerical solution of the flow within region 3 are the finite element approach and the finite difference approach. The former has enjoyed considerable recent popularity, particularly with respect to free surface flows. However, recent developments in body-fitted coordinate systems as discussed for example, by Thompson, et al. [13], have made the finite difference approach quite competitive. In particular, the stream function - vorticity ($\psi - \zeta$) finite difference formulation allows a very elegant treatment of the free surface shear stress condition.

The fundamental source of complexity in this problem lies in the fact that, initially, the location of the free surface is unknown. Thus, any single solution of the flow within region 3 will be but one step in an iterative process in which the actual location of the interface is developed as part of the solution. The description of the method of solution is, therefore, divided into two parts. What is involved in finding a solution for region 3 when the extent of region 3 is completely specified forms the first part. The basis for determining the extent to which a particular set of region boundaries is unsatisfactory, and the ways in which they are then modified, makeup the second part.

Appropriately differentiated and combined to eliminate pressure the r - and θ -components of the equation of creeping flow become

$$\nabla^2 \zeta = 0 \quad (2)$$

where

$$\zeta = \nabla^2 \psi \quad (3)$$

for ψ defined by

$$v_\theta = -\frac{\partial \psi}{\partial r}, \quad v_r = \frac{1}{r} \frac{\partial \psi}{\partial \theta} \quad (4)$$

Boundary conditions concerning ψ and ζ are required on all surfaces which bound region 3. Along AB the values of these functions are found from the solution in region 2. A considerable body of literature exists on the behavior of a thin liquid film having a free surface, much of it, as in the fundamental work of Bretherton [14], based upon the use of Reynolds equation. While a solution for Reynolds equation which yields a steadily increasing film thickness in the direction of flow has been found to exist. Shivers [15] has demonstrated that the solution predicts results which are inconsistent with the assumptions of Reynolds equation. Currently, the approach used is that suggested by Coyne and Elrod [16], modified to overcome certain difficulties with that work. An outline of the development of the equations for boundary values of ψ and ζ is given in the Appendix.

From the definition of the two-dimensional stream function it follows that the change in value of ψ between AE and BCD is equal to q . Arbitrarily, ψ was set equal to zero on BCD, so that it must have the value of $-q$ on AE. Because of symmetry, $\zeta = 0$ along CD, but its values along BC and AE must be developed as part of the solution.

In terms of the intrinsic coordinate system shown in Fig. 2 the vorticity is given by

$$\zeta = \frac{\partial w}{\partial n} - w \frac{\partial \sigma}{\partial s} \quad (5)$$

However, the condition that shear stress vanish along BC is given by

$$\frac{\partial w}{\partial n} + w \frac{\partial \sigma}{\partial s} = 0 \quad (6)$$

so that, on a shear free streamline,

$$\zeta = -2w \frac{\partial \sigma}{\partial s} \quad (7)$$

where

$$\frac{\partial \sigma}{\partial s} = \frac{d^2 y}{dx^2} / \left[1 + \left(\frac{dy}{dx} \right)^2 \right]^{3/2} \quad (8)$$

The local magnitude of the surface velocity, w , was found from a first order finite difference approximation of the gradient in the stream function normal to the free surface.

On AE the relationship between ζ and ψ was found, to first order accuracy, by first writing a truncated series for ψ a distance Δr above the surface:

$$\psi_{R+\Delta r} \cong \psi_R + \left. \frac{\partial \psi}{\partial r} \right|_R \Delta r + \frac{1}{2} \left. \frac{\partial^2 \psi}{\partial r^2} \right|_R \Delta r^2 \quad (9)$$

and noting that

$$\zeta_R = \left. \frac{\partial^2 \psi}{\partial r^2} \right|_R + \frac{1}{R} \left. \frac{\partial \psi}{\partial r} \right|_R \quad (10)$$

where

$$\left. \frac{\partial \psi}{\partial r} \right|_R = U \quad (11)$$

Combining Eqs. (9) through (11) yielded

$$\zeta_R = \frac{2}{\Delta r^2} (\psi_{R+\Delta r} - \psi_R) - \frac{2U}{\Delta r} + \frac{U}{R} \quad (12)$$

In the vicinity of DE the velocity components were readily obtained from the general solution to Reynolds equation. At DE itself the necessary boundary conditions are

$$\psi' = \left(\frac{r - R - h_0}{R} \right) \left\{ 1 + \frac{3}{2} \left[1 - \frac{h_\infty}{h_0} \left(1 + \frac{h_\infty}{2R} \right) \right] \left[\frac{(r - R - h_0)^2}{3h_0^2} - 1 \right] \right\} \quad (13)$$

and

$$\zeta' = \frac{3R}{h_0^2} \left[1 - \frac{h_\infty}{h_0} \left(1 + \frac{h_\infty}{2R} \right) \right] (r - R - h_0) \quad (14)$$

The grid system used in region 3 is shown in Fig. 3. Radial spacings between $r = r_A$ and $r = r_B$ were uniform, as they were, although with a different step size, between $r = r_B$ and $r = r_C$. Angular locations were then established by the intersections of the lines of constant radius with BC and CD. Utilizing conventional finite difference formulations Eq. (2) is, in dimensionless form,

$$\zeta'_{i,j} = \frac{f_{\theta_{i,j+1}} \zeta'_{i,j+1} + f_{r_{i,j}} \zeta'_{i-1,j} + f_{\theta_{i,j}} \zeta'_{i,j-1} + f_{r_{i+1,j}} \zeta'_{i+1,j}}{f_{\theta_{i,j+1}} + f_{r_{i,j}} + f_{\theta_{i,j}} + f_{r_{i+1,j}}} \quad (15)$$

while Eq. (3) is

$$\psi'_{i,j} = \frac{f_{\theta_{i,j+1}} \psi'_{i,j+1} + f_{r_{i,j}} \psi'_{i-1,j} + f_{\theta_{i,j}} \psi'_{i,j-1} + f_{r_{i+1,j}} \psi'_{i+1,j} - A_{i,j} \zeta'_{i,j}}{f_{\theta_{i,j+1}} + f_{r_{i,j}} + f_{\theta_{i,j}} + f_{r_{i+1,j}}} \quad (16)$$

where

$$f_{r_{i,j}} = \frac{(r_i - r_{i-1})(\theta_{j-1} - \theta_{j+1})}{4(r_{i-1} - r_i)} \quad (17)$$

$$f_{\theta_{i,j}} = \frac{-(r_{i+1} - r_{i-1})}{2r_i(\theta_{j-1} - \theta_j)} \quad (18)$$

and

$$A_{i,j} = \frac{(r_{i-1} + 2r_i + r_{i+1})(\theta_{j+1} - \theta_{j-1})(r_{i+1} - r_{i-1})}{16R^2} \quad (19)$$

For a reason to be discussed in the second part of the description of the method of solution, the system of interior and boundary node equations was solved iteratively using the approach described by Roach [17]. Briefly, a new set of ζ'_{ij} values was calculated using Eq. (15) for all interior nodes based upon some initial guess of the ζ'_{ij} . These new values were then used, in conjunction with the known values of ψ' on all boundaries to solve Eq. (16) iteratively at each interior point. These new values of ψ' then made it possible to calculate new boundary values of ζ' along BC and AE using, respectively, Eqs. (7) and (12). A new cycle was then begun by calculating a revised set of ζ'_{ij} at all interior nodes. This process was continued until no calculated ζ'_{ij} or ψ'_{ij} value changed by more than 0.01 as a result of the last complete iterative step.

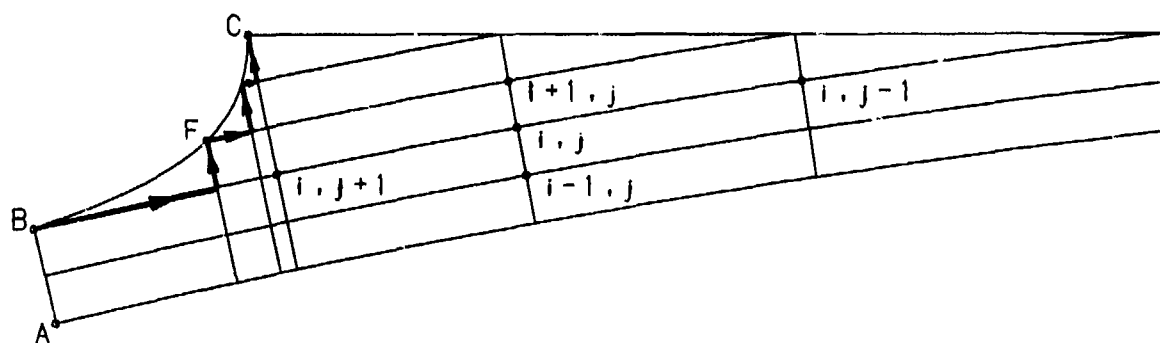


Fig. 3. Nodal distribution.

When the degree of convergence specified has been reached the results satisfy all but the normal stress condition along BC. This condition is, in terms of the intrinsic coordinate system shown in Fig. 2,

$$p + \gamma \frac{\partial \sigma}{\partial s} + 2\mu \frac{\partial w}{\partial s} = 0 \quad (20)$$

In dimensionless form this becomes

$$\text{Rep}' + \frac{\beta}{2} \frac{\partial \sigma}{\partial s'} + 2 \frac{\partial w'}{\partial s'} = 0 \quad (21)$$

To obtain values of Rep' along BC use was made of the fact that the r- and θ -components of the equation of creeping flow can be written as

$$\frac{\partial}{\partial r'}(\text{Rep}') = \frac{1}{r'} \frac{\partial \zeta'}{\partial \theta'} \quad (22)$$

and

$$\frac{1}{r'} \frac{\partial}{\partial \theta'}(\text{Rep}') = - \frac{\partial \zeta'}{\partial r'} \quad (23)$$

Since values of ζ' were known at every location within region 3 the gradients in ζ' , and, hence, in Rep' , were easily determined. In general, the use of such gradients to calculate the pressure field is subject to the criticism that the change in pressure between any two points will depend upon the path followed. In this situation, perhaps due to the nature of the problem, the calculation of pressures along BC, starting with the value of Rep' known at B from the thin film solution and using the path indicated in Fig. 3, produced results which differed insignificantly from those obtained by the more usual procedure.

Typically, the angular location first specified for AB and the initial representation of BC would fail to produce results which satisfied Eq. (21). The subsequent modification of region 3 was carried out in a two step process, and represents the second part of the solution procedure. The first step involved successive modifications of BC. The initial operation was to solve Eq. (21) for $\partial \sigma / \partial s'$ and to then calculate the surface curvature at each surface node as if the just found free surface velocity gradient and the pressure were correct.

What was done next is illustrated by considering point F (Fig. 3). At point B, in addition to its location, the values of σ and $\partial \sigma / \partial s'$ were known from the thin film solution. From the initial operation just described $\partial \sigma / \partial s'$ was assumed to be known at point F. These four conditions were then sufficient to fix the values of the four coefficients of the assumed relationship between x' and y' in the region between B and F,

$$x' = a_1 + a_2(y')^2 + a_3(y')^4 + a_4(y')^6 \quad (24)$$

if it was assumed that the new location of point F was at the same value of y' as was the original. This process was then repeated, from point to point, until the plane of symmetry was reached.

It was then necessary to recompute the node grid and to resolve the governing equations. With experience, the initial selection of region 3 was frequently good enough so that BC was not displaced significantly. In general, this resulted in a new grid having the same number of nodes as did the previous one. When this happened the values of ψ' and ζ' from the previous solution were used as the initial guesses for the new region. Typically, this reduced the computational time by an order of magnitude.

Commonly, four or five changes in BC were required to satisfy Eq. (21) along BC. When this had been accomplished the slope at point C was examined. If it was not vertical the location of AB was adjusted and a complete new cycle of computation was begun. This outermost iterative step was repeated until σ at C equaled 90° to within $\pm 0.25^\circ$.

RESULTS AND CONCLUSIONS

Up to this point solutions have been explored for β values in the vicinity of 10. This value was selected based upon consideration of the property values of typical lubricants, the general range of validity of a creeping flow assumption, and what appear to be some limits on the general applicability of the thin film analysis in an inlet flow.

Figure 4 shows a typical streamline plot. The volumetric flow rate between each pair of streamlines is $0.2q$. Neither in this nor in any other inlet flow situation was a recirculating flow region observed. While it is possible to lose such regions in a sufficiently coarse mesh, the use of approximately 25 radial locations between the cylinder and point C would require that such regions be extremely small. In contrast, preliminary work on the outflow side has generally shown the existence of recirculating regions of significant sizes.

Figures 5 and 6 illustrate the fundamental contribution of this type of analysis: that, for a given set of operating conditions, only one free surface location is possible. Figure 5 shows the way in which the distance from the line-of-centers to the closest approach of the free surface to the line-of-centers changes with β . Since β is directly proportional to γ this type of change can be thought of as being directly representative of the significance of surface tension changes when all other parameters are held constant. The results shown in Fig. 6 show how variations in the size of the gap between the cylinders influences the free surface location. This type of variation is analogous to that produced by a variation in load.

An obvious matter of concern in connection with an analysis of the type presented is the extent to which the results obtained agree with the results of an analysis based entirely upon the use of Reynolds equation. It is felt that a comprehensive comparison must await the completion of work concerned with behavior on the outflow side of the contact. However, in connection with the pressure variation plotted in Fig. 7, one comparison is possible. The range of θ shown is that from DE to AB. For each such set of results the pressure variation as predicted by Reynolds equation was calculated subject to the constraint that the pressure at A and that at E be the same as those predicted by the present analysis. In each case the Reynolds equation pressure distribution along the cylindrical surface coincided so closely with that of the present analysis that they are indistinguishable from one another on a plot drawn to the scale used in Fig. 7.

This result is most gratifying for two reasons. Firstly, it supports the use of the pressure determination method presented. Secondly, it provides a basis for confidence in the adequacy of the nodal mesh used, both with respect to its general configuration and to the number of nodes used.

In conclusion, the determination of a sound theoretical basis for the existence of unique interface locations for a given set of operating conditions has been established for a portion of the possible range of variation of operational parameters. While much still remains to be done, the results obtained should be considered encouraging.

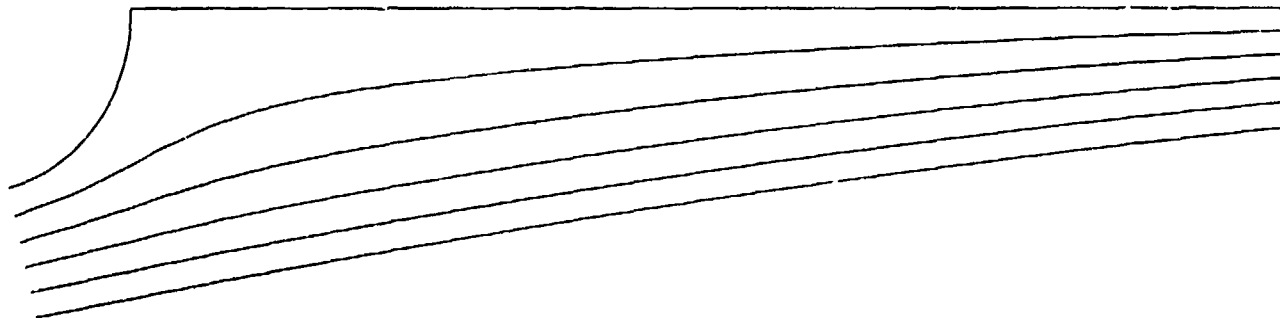


Fig. 4. Streamline plot for $\beta = 10$, $h_\infty/R = 0.01$, $h_0/h_\infty = 0.6$.

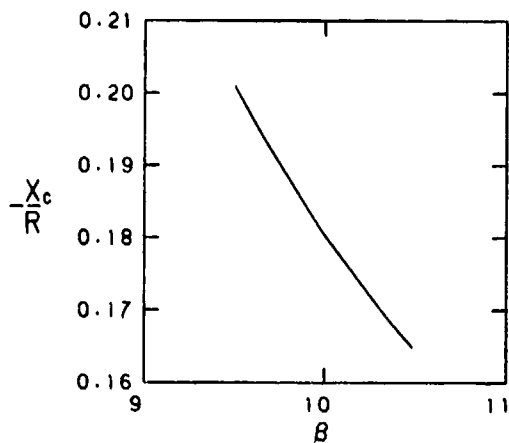


Fig. 5 Location of the free surface along the plane of symmetry as a function of β for $h_0/R = 0.01$, $h_0/h_\infty = 0.6$.

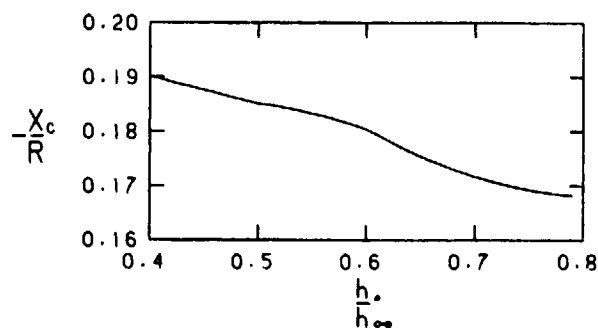


Fig. 6. Location of the free surface along the plane of symmetry as a function of h_0/h_∞ for $\beta = 10$ and $h_0/R = 0.01$.

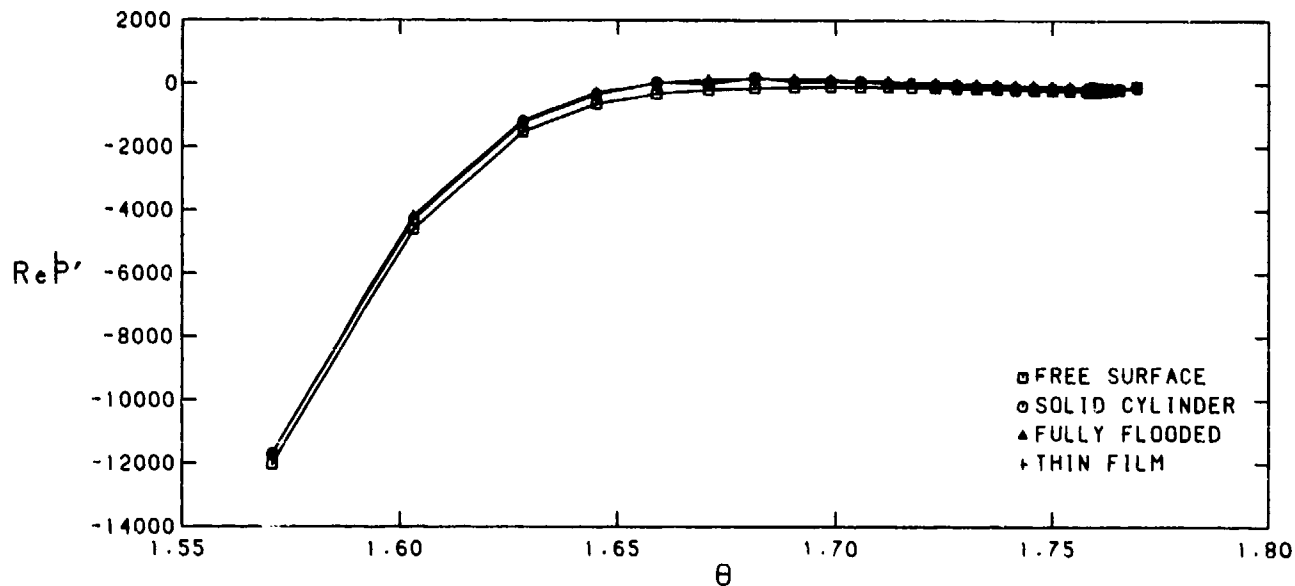


Fig. 7. Pressure distributions.

REFERENCES

1. Lauder, W., "Hydrodynamic Lubrication of Proximate Cylindrical Surfaces of Large Relative Curvature," Proc. Inst. Mech. Eng., V. 180, Pt. 3B, 1965-66, pp. 101-106.
2. Wedeven, L. D., Evans, D., and Cameron, A., "Optical Analysis of Ball Bearing Starvation," J. Lubr. Technol., Trans. ASME (Series F), V. 93, 1971, pp. 349-363.
3. Wolveridge, P. E., Baglin, K. P., and Archard, J. G., "The Starved Lubrication of Cylinders in Line Contact," Proc. Inst. Mech. Eng., V. 185, 1971, pp. 1159-1169.
4. Castle, P. and Dowson, D., "A Theoretical Analysis of the Starved Elastohydrodynamic Lubrication Problem for Cylinders in Line Contact," Elastohydrodynamic Lubrication Symposium, 1972, The Institution of Mechanical Engineers, 1972, pp. 131-137.
5. Archard, J. F. and Baglin, K. P., "Lubrication Effects in Elastohydrodynamic Contacts, Cavitation and Related Phenomena," Proceedings of the 1st Leeds-Lyon Symposium on Tribology, 1975, pp. 131-142.
6. Dowson, D., "The Inlet Boundary Conditions," Cavitation and Related Phenomena, Proceedings of the 1st Leeds-Lyon Symposium on Tribology, 1975, pp. 143-152.

7. Dalmaç, G., "The Influence of Air Entrainment on Fluid Supply Conditions in Lubricated Hertzian Contacts," Cavitation and Related Phenomena, Proceedings of the 1st Leeds-Lyon Symposium on Tribology, 1975, pp. 153-162.
8. Constantinescu, V., "On Some Starvation Phenomena in Fluid Films," J. Lubr. Technol., Trans. ASME (Series F), V. 99, 1977, pp. 441-448.
9. Tipei, N., Theory of Lubrication, Stanford University Press, Stanford, California, 1962.
10. Dowson, D. and Taylor, C., "Cavitation in Bearings," Ann. Rev. of Fluid Mech., V. 11, 1979, pp. 35-66.
11. Savage, M., "Cavitation in Lubrication. Part 1, On Boundary Conditions and Cavity-Fluid Interfaces," J. Fluid Mech., V. 80, 1977, pp. 743-755.
12. Williamson, A., "The Tearing of an Adhesive Layer Between Flexible Tapes Pulled Apart," J. Fluid Mech., V. 52, 1972, pp. 639-656.
13. Thompson, J., Thames, F., and Mastin, C., "Automatic Numerical Generation of Body-Fitted Curvilinear Coordinate System for Field Containing any Number of Arbitrary Two-Dimensional Bodies," J. Comp. Phys., V. 15, 1974, pp. 299-319.
14. Bretherton, F., "The Motion of Long Bubbles in Tubes," J. Fluid Mech., V. 10, 1961, pp. 166-188.
15. Shippers, L., "A Study of Thin Viscous Film with a Free Surface Boundary," M.S. Thesis, University of Missouri-Rolla, 1981.
16. Coyne, C. and Elrod, H. Jr., "Conditions for the Rupture of a Lubricating Film, Part I: Theoretical Model," J. Lubr. Technol., Trans. ASME (Series F), V. 92, 1970, pp. 451-456.
17. Roach, P., Computational Fluid Dynamics, Hermosa Publishers, Albuquerque, N.M., Second Edition, 1976, p. 17.

ACKNOWLEDGEMENTS

A portion of this work was supported by NASA under NASA NSG 3113.

APPENDIX

Figure A1 defines the system of interest. Provided that the film thickness is small with respect to the cylinder radius the fact of solid surface curvature can be ignored except as it affects the velocity profile far from the contact region. Since a major reason for considering a thin film region was to provide a vorticity distribution across the inflow boundary to region 3 it was essential that velocity gradients, as well as velocities themselves, be given correctly. Consistent with this idea, q was given by

$$q = Uh_{\infty} \left(1 + \frac{h_{\infty}}{2R} \right) \quad (A1)$$

where h_{∞} is the film thickness far from the contact.

Paralleling the approach pioneered by Coyne and Elrod [16] the momentum equations for creeping motion on the free surface were to be satisfied exactly, as were the stress conditions appropriate to a free surface above which lies a fluid of negligible density and viscosity. Here, however, the velocity profile assumed was normal to the solid surface rather than to the free surface. Thus, at $y = h$,

$$\frac{dp}{dx} = \frac{\partial p}{\partial x} + \frac{\partial p}{\partial y} \frac{dh}{dx} = \mu \left[\frac{\partial^2 u}{\partial x^2} + \frac{\partial^2 u}{\partial y^2} + \left(\frac{\partial^2 v}{\partial x^2} + \frac{\partial^2 v}{\partial y^2} \right) \frac{dh}{dx} \right] \quad (A2)$$

The form of u was assumed to be

$$u = U + f(x)y + g(x)y^2 \quad (A3)$$

Imposing the necessary condition that

$$q = \int_0^h u \, dy \quad (A4)$$

yields

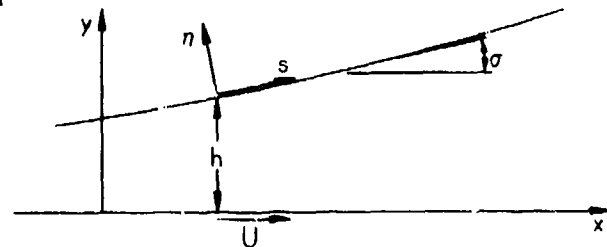


Fig. A1. System studied.

$$u = U + fy + \frac{3}{h^3} \left(q - \frac{fh^2}{2} - U_h \right) y^2 \quad (A5)$$

Then, from the continuity equation

$$v = \left[\frac{1}{h^4} \frac{dh}{dx} \left(3q - \frac{fh^2}{2} - 2U_h \right) + \frac{1}{2h} \frac{df}{dx} \right] y^3 - \frac{1}{2} \frac{df}{dx} y^2 \quad (A6)$$

The normal stress condition is given by

$$p = \frac{2\mu}{\left[1 + \left(\frac{dh}{dx} \right)^2 \right]} \left\{ \frac{\partial u}{\partial x} \left[\left(\frac{dh}{dx} \right)^2 - 1 \right] - \left(\frac{\partial u}{\partial y} + \frac{\partial v}{\partial x} \right) \frac{dh}{dx} \right\} - \gamma \frac{\partial \sigma}{\partial s} \quad (A7)$$

where

$$\frac{\partial \sigma}{\partial s} = \frac{d^2 h}{dx^2} / \left[1 + \left(\frac{dh}{dx} \right)^2 \right]^{3/2} \quad (A8)$$

The condition that the shear stress vanish at the free surface is given by

$$4 \frac{\partial u}{\partial x} \frac{dh}{dx} - \left(\frac{\partial u}{\partial y} + \frac{\partial v}{\partial x} \right) \left[1 - \left(\frac{dh}{dx} \right)^2 \right] = 0 \quad (A9)$$

where, in Eq. (A9) as in Eqs. (A2) and (A7), all of the partial derivatives are evaluated at $y = h$.

Eliminating p by differentiating Eq. (A7) with respect to x and setting the result equal to Eq. (A2) leads to an ordinary differential equation containing F and H as dependent variables, with X as the independent variable, and β as a parameter. F and H are defined by

$$f = \frac{U}{R} \left(1 + \frac{R}{h_\infty} F \right), \quad h = h_\infty (1 + H) \quad (A10)$$

Eq. (A9) contains, except for β , the same quantities. Considerable numerical experimentation has demonstrated that, within the requirements of the present investigation, the linearized forms of the combination of Eqs. (A2) and (A7) and of Eq. (A9) are sufficient. They are:

$$12H + 6F + 18D^2H = \beta D^3H - 3D^2F \quad (A11)$$

and

$$6H + 2F = D^2H \quad (A12)$$

where $D = d/dX$. Eliminating F yields

$$\frac{3}{2} D^4H - \beta D^3H + 12D^2H - 6H = 0 \quad (A13)$$

solutions to which are of the form

$$H = Ce^{\lambda X} \quad (A14)$$

where λ is a root of the characteristic equation

$$\frac{3}{2} \lambda^4 - \beta \lambda^3 + 12\lambda^2 - 6 = 0 \quad (A15)$$

For the β range of current interest λ has one positive real root, one negative real root, and a pair of complex conjugate roots. The first of these is the one of interest on the inlet side. Then, from Eq. (A12),

$$F = H \left(\frac{\lambda^2}{2} - 3 \right) \quad (A16)$$

In general, $X = 0$ was located at the point of inflection in the free surface, at which, approximately,

$$D^2H = \frac{h_\infty}{R} \quad (A17)$$

so that C is given by

$$\frac{1}{\lambda^2} \frac{h_\infty}{R} \quad (A18)$$

The value of X at the junction between regions 2 and 3 has generally been taken to be 0.75.

Consistent with what is done in the body of the paper, ψ is here given by

$$\psi = \int_0^y u \, dy - q \quad (A19)$$

so that the dimensionless stream function is, consistent with the linearization of the governing equations, given by

$$\psi' = \frac{r - R - h_{\infty}}{R} + \frac{1}{2R^2} \left[\left(1 + \frac{R}{h_{\infty}} F \right) (r - R)^2 - h_{\infty}^2 \right] - \left(H + \frac{F}{2} \right) \frac{(r - R)^3}{Rh_{\infty}^2} \quad (\text{A20})$$

Consistent with the assumption that $h_{\infty}/R \ll 1$ the vorticity is given by

$$\zeta = - \frac{\partial v}{\partial x} + \frac{\partial u}{\partial y} + \frac{u}{R} \quad (\text{A21})$$

so that the dimensionless vorticity is given by

$$\begin{aligned} \zeta' = & 2 + \frac{RF}{h_{\infty}} + \left(\frac{1}{R} - \frac{3RF}{h_{\infty}^2} - \frac{6RH}{h_{\infty}^2} \right) (r - R) \\ & + \left[\frac{R}{2h_{\infty}^3} \frac{d^2 F}{dX^2} - \frac{3}{h_{\infty}^2} \left(H + \frac{F}{2} \right) \right] (r - R)^2 - \frac{R}{h_{\infty}^4} \left(\frac{d^2 H}{dX^2} + \frac{1}{2} \frac{d^2 F}{dX^2} \right) (r - R)^3 \end{aligned} \quad (\text{A22})$$

DISCUSSION

H.G.Elrod, Dept. of Mech. Eng., Columbia University, New York, US

Would the authors kindly elaborate on why they chose a single eigenvalue for upstream influence, when two such eigenvalues permit vanishing at upstream infinity?

Also, a few additional comments would be appreciated on how the *local* normal stress condition at the surface was satisfied.

Author's Reply

The available photographic evidence showed a steadily increasing film thickness. Mr Shippers and I are of the opinion, however, that there is a more fundamental reason. The question is being studied.

In answer to the second question, experience showed that the pressure and the velocity gradient along BC did not change dramatically as the shape of BC was altered. Referring to Figure 3, in calculating a new location for the surface segment BF, the previous values of Rep' and $\partial w'/\partial s'$ were used to calculate a new $\partial\sigma/\partial s'$. With location, slope and curvature known at B there are then four conditions which must be satisfied at B or F. These conditions were used to obtain a_1 through a_4 (Eq. (24)) for the segment BF. This process was then repeated, segment by segment, until point C was reached.

J.F.Chevalier, SNECMA, Fr

Vous nous imposez la condition que l'arc BC soit perpendiculaire à l'axe de symétrie au point C. Ceci est vrai en écoulement stationnaire. Est-ce que physiquement on n'a pas un écoulement fluctuant au point C, ce qui n'exige plus la condition de perpendicularité?

Author's Reply

The analysis assumes that the free surface is stationary in space. Thus, from symmetry, point C is a stagnation point. The free surface above the line of symmetry is of course, then the mirror image of the free surface below this line. Any free surface angle at C other than the perpendicular one used results in an undefined set of conditions at point C.

J.Frene et D.Bonneau, Université de Poitiers, Fr

Dans votre analyse vous mentionnez que l'étude de la région d'entrée d'un contact ne peut être étudiée qu'à l'aide de 2 méthodes, la méthode des différences finies et la méthode des éléments finis. Il existe une troisième méthode particulièrement adaptée à ce problème, c'est la méthode des équations intégrales qui permet de déterminer la frontière à surface libre sans faire aucun calcul à l'intérieur du domaine. Le principe de cette méthode a été présenté au 2ème Congrès International du GAMNI sur 'Numerical Methods for Engineering', à Paris, en Décembre 1980 et les principaux résultats obtenus à l'entrée d'un contact en glissement pur ont été présentés à la 'Lubrication Conference of the ASME-ASLE' d'Octobre 1981 à La Nouvelle-Orléans (ASME paper n° 81 lub. 22).

Nous avons aussi effectué des calculs dans le cas précis que vous avez étudié et nous avons, dans certains cas, obtenu une zone de recirculation à l'entrée. Par ailleurs nous avons montré qu'il existe près des surfaces mobiles une zone de dépression. La valeur de cette dépression dépend essentiellement de la tension de surface à faible vitesse et du produit de la vitesse par la viscosité à grande vitesse. Avez vous obtenue une dépression de ce type?

Author's Reply

The authors had just received a copy of one of the references mentioned immediately prior to the conference, and have not as yet had an opportunity to examine it. A depression of the type mentioned has not been encountered in the inlet situations considered to this point.

The Behavior of Various Rolling Bearing Materials under Unfavorable Lubrication Conditions

Hans Karl Lorüsch, Peter Dreschmann, Rudolf Weigand
FAG Kugelfischer Georg Schäfer & Co., Schweinfurt/Federal Republic of Germany

The conventional rolling bearing material is the through-hardening chrome-alloyed steel 100Cr6 (SAE 52 100). Other materials for rolling bearings are case-hardening steels as well as high-alloy materials, among others so-called high-temperature resistant steels. Since the service life of rolling bearings is not only influenced by the material, but also very decisively by the lubrication, the behavior of various rolling bearing materials has been investigated in extensive field-like tests at elevated temperatures and under unfavorable lubrication conditions. In these tests rolling bearings made of the conventional rolling bearing steel 100Cr6 (SAE 52 100) and of the high-temperature resistant steels S18-0-1 (AISI T1) and M50 have been investigated.

These tests revealed that with increasingly unfavorable lubrication conditions the high-temperature resistant rolling bearing materials S18-0-1 (AISI T1) and M50 were superior to the conventional rolling bearing material 100Cr6 (SAE 52 100). With pronounced starved lubrication that is caused by lubricating only with the oil vapor produced at a temperature of 215 °C (488 K) and still reducing this oil vapor by exhaustion, the following results were found out: the bearings of high-temperature resistant rolling bearing materials still reached lives of more than 3 % of the rated L_{10} life, whereas bearings of 100Cr6 (SAE 52 100) steel could not be run any more under these conditions. Both high-temperature resistant materials turned out to be comparable under these marked conditions of starved lubrication. When the oil vapor was not exhausted, the bearings of S18-0-1 (AISI T1) reached the rated L_{10} life; the bearings of 100Cr6 (SAE 52 100), however, reached only a fraction of this life, that is approx. 2.5 %.

The results reveal that rolling bearings of the high-temperature resistant steels S18-0-1 (AISI T1) and M50 should not only be used at elevated operating temperatures, as it is the general rule, but also when it is important to obtain a higher operational reliability with starved lubrication conditions.

General

Rolling bearings are exposed to quite different conditions in machines and aggregates during operation. This certainly affects the bearing lubrication. Maximum bearing service life is reached, when the bearings are sufficiently supplied with lubricant and when the lubricant viscosity is high enough to separate the heavily loaded functional areas by a lubricating film. The innumerable running tests with a separating lubricating film carried out with rolling bearings show that the rolling contact fatigue strength of the frequently used through-hardened bearing steel 100Cr6 (SAE 52 100) is, on account of its advanced standard of quality, unequalled under normal operating conditions. High-alloy, high-temperature resistant steels turn out to be superior, because at elevated temperatures, as of approximately 200 °C (473 K), the hardness of the standard steel clearly declines.

There are only few expressive results on rolling bearings which ran under unfavorable lubrication conditions. The conditions are unfavorable, if the separating lubricating film cannot build up, since e. g. high temperatures lower the lubricant viscosity excessively or since the lubricant supply is insufficient on account of design deficiencies.

In order to find out the behavior of various rolling bearing materials under unfavorable lubrication conditions, tests were carried out at elevated temperatures. The temperature was, however, restricted to 215 °C (488 K) to ensure reliable operation of all investigated materials under the condition of a sufficient oil quantity.

In order to point out the capacity of the individual materials, a lubricant without EP and wear reducing additives was used. Moreover the lubricant quantity was reduced step by step until it could be seen that the bearing of the most unfavorable material variant could not be surely operated any more.

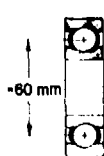
Test Bearings and Their Materials

For the tests deep groove ball bearings with the boundary dimensions 40 x 80 x 18 mm of the high-temperature resistant rolling bearing steels S18-0-1 (AISI T1) and M50, and bearings of the conventional bearing steel 100Cr6 (SAE 52 100) were used, figure 1.

The deep groove ball bearings of 100Cr6 (SAE 52 100) were heat-treated to ensure heat-stabilization up to a temperature of 250 °C (523 K). To allow disassembling of the bearings after the test runs in order to investigate the components, the two-piece steel cages were bolted and not riveted as usual.

Figure 2 contains data on the materials and their heat treatment. The rolling bearing material S18-0-1 (AISI T1) contains among others the alloying constituents vanadium and wolfram, the M50 steel molybdenum and vanadium. The conventional rolling bearing steel 100Cr6 (SAE 52 100) does not have these constituents.

1: Test Bearing Data



Test Bearings	Dimensions	Material	Internal Design
Deep Groove Ball Bearings	40 x 80 x 18 mm	S 18-0-1 (AISI T1)	Ball Diameter $d_b = 12.7$ mm Number of Balls $z = 9$ Ball / Raceway Conformity $\gamma_{BR} \geq 0.04$ Load Rating** $C = 32.5$ kN
Deep Groove Ball Bearings	40 x 80 x 18 mm	M50	Ball Diameter $d_b = 12.7$ mm Number of Balls $z = 9$ Ball / Raceway Conformity $\gamma_{BR} \geq 0.04$ Load Rating** $C = 32.5$ kN
Deep Groove Ball Bearings	40 x 80 x 18 mm	100Cr6* (SAE 52100)	Ball Diameter $d_b = 11.9$ mm Number of Balls $z = 9$ Ball / Raceway Conformity $\gamma_{BR} \geq 0.04$ Load Rating** $C = 29$ kN

* Heat-treated for an Operating Temperature $\leq 250^\circ\text{C}$

** Load Rating for FAG Bearings according to Determination of December 1, 1981

2: Test Bearing Materials

Material Designation	Material-No. (Steel-Iron List)	Other Designations
S 18-0-1	1.3355	AISI T1
M50	1.3551	80MoCrV4216
100Cr6	1.3505	SAE 52100

Material Designation	C	Si	Mn	Cr	Mo	Ni	V	W
S 18-0-1	0.7-0.78	< 0.45	< 0.4	3.8-4.5			1.0-1.2	17.5-18.5
M50	0.77-0.85	< 0.25	< 0.35	3.75-4.25	4.0-4.5	< 0.10	0.9-1.1	
100Cr6	0.95-1.1	0.15-0.35	0.25-0.45	1.4-1.65		< 0.3		

Material Designation	Austenitizing Temperature ($^\circ\text{C}$)	Annealing Temperature ($^\circ\text{C}$)	Hardness (HRC)
S 18-0-1	1250	550	62-65
M50	1100	540	60-64
100Cr6	850	280	56-59

Test Rig, Bearing Arrangement, Test Conditions

The tests were carried out on the high-temperature fatigue test rig L14. Figure 3 shows the principle of the test rig. Four test bearings on one shaft are tested at the same time. The two inner bearings are radially loaded and the two outer bearings take up this load as reaction force. The load is generated by Belleville spring washers. A bolt transmits the load onto a ring arranged between the two inner test bearings. In order to minimize the housing deformation within the loaded zone of the two inner bearings, the load enters at a point 180° offset to the loaded zone of the bearings. The test shaft is driven by a d.c. motor via belts, gears and a clutch of low thermal conduction. The test bearings are electrically heated; the resistance wires are arranged in the outer housing. The heating can be controlled with a temperature regulator. For measuring the temperature on the outer rings of the test bearings thermoelectric cells are used.

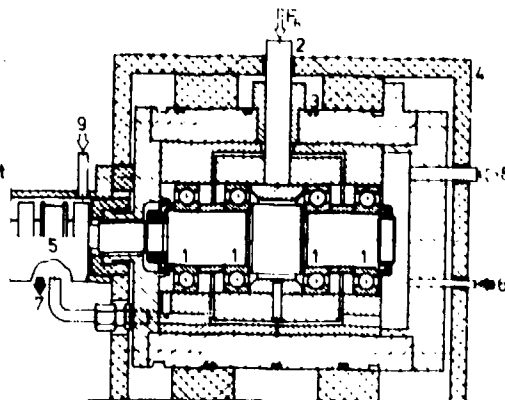
The test rig is equipped with a vibration control system. This system turns off the test rig, as soon as fatigue damage appears. The running periods are recorded on an hour counter.

The bearings are supplied with oil from a heated oil reservoir. The temperature can be controlled. The housing incorporates oil inlet and outlet bores. Other bores ensure that the oil level is the same for all four bearings. For regulating the oil level, a tube was used through which excessive oil can escape. For exhausting the oil vapor generated at the high temperature, an exhaustion pipe was mounted on the right side of the test rig. Exhaustion was assured by a fan. The depression was kept constant at 20 Torr (2,700 Pa).

To the exclusion of the lubrication, all other conditions such as loading, speed and temperature were kept constant for the tests.

3: High-Temperature Fatigue Test Rig L14

- 1 Test Bearings
- 2 Loading Pin
- 3 Heating
- 4 Insulation
- 5 Coupling
- 6 Oil Feed
- 7 Excessive Oil Outlet
- 8 Air Exhaust
- 9 Air Inlet



Three lubrication conditions were investigated:

Oil Sump Lubrication

The oil level was regulated by adjusting the height of the oil overflow pipe outlet. The lowest rolling element submerged up to its half. The oil quantity in the test rig was approximately 160 cm³. In order to avoid oil ageing, 40 cm³ oil per hour were continuously fed drop by drop. The excessive oil could escape from the overflow pipe.

Oil Vapor Lubrication

The oil level was lowered until the oil could not reach the rotating bearing parts any more. At the high operating temperature of 215 °C (488 K) an oil vapor was produced in the test rig which acted as lubricant.

By lowering the oil level to 2.5 mm below the outer ring shoulders, the oil quantity in the test rig was reduced to approximately 110 cm³. Since oil vapor escape is inevitable, a small quantity of preheated oil (approx. 40 cm³) was fed drop by drop in order to compensate for the loss. The oil overflow pipe outlet prevented the oil level from rising.

Lubrication by Exhausted Oil Vapor

The conditions were the same as for oil vapor lubrication, except for the oil vapor being exhausted in these tests with a fan. The depression in the exhaustion pipe was constantly approx. 20 Torr (approx. 2,700 Pa).

The test variants are summarized in figure 4.

- 4: Test Variants: Oil Sump Lubrication
 Oil Vapor Lubrication
 Lubrication by Exhausted Oil Vapor

Lubrication	Bearing - Materials		
	S18-0-1 AISI T1	M50	100Cr6 SAE 52100
Oil Sump Lubrication Oil Level to approx Middle of Rolling Elements	●		●
Oil Vapour Lubrication Oil Level below Outer Ring Shoulder	●		●
Lubrication by exhausted Oil Vapour	●	●	●

Test Bearings:

Deep Groove Ball Bearings
 40 x 80 x 18 mm
 Load $F = 8880 \text{ N}$
 Speed $n = 3000 \text{ min}^{-1}$
 Temperature $t = 215 \text{ °C}$
 (488 K) ± 6.5 K
 Lubricant Shell Turbo-Oil T32

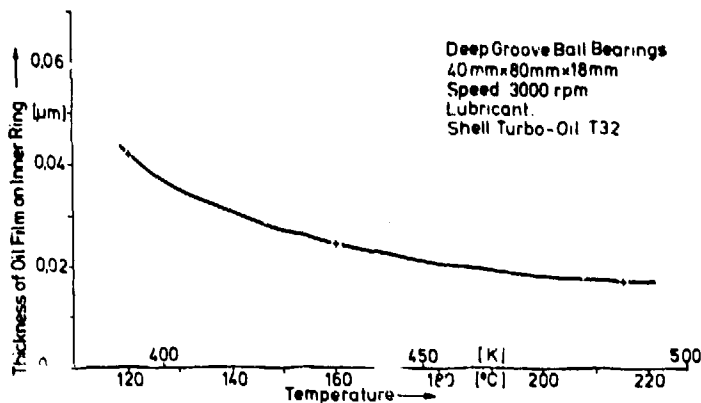
Lubricant

The bearings were lubricated with "Shell Turbo Oel T32". This is a mineral oil without any additives that increase the lubricant carrying capacity or reduce the wear. The kinematic oil viscosity is $34 \text{ mm}^2/\text{s}$ at $40 \text{ }^\circ\text{C}$.

Rated Lubricating Film Thickness

According to the general lubricating film theory there is no metal-to-metal contact in the heavily loaded contacts between rolling elements and raceways with a film thickness of approximately 0.3 micron . With the oil "Shell Turbo Oel T32" and with a speed of $n = 3,000 \text{ rpm}$ and a temperature of $215 \text{ }^\circ\text{C}$ the lubricating film thickness calculates according to Cheng only to $h_0 = 0.017 \text{ micron}$. This value applies to the test variant where the rolling elements submerge into the oil (oil sump lubrication). That means that even with sufficient oil supply of the contacts there is a permanent intense metal-to-metal contact. Accordingly, lubrication is considerably unfavorable in the other two cases.

5: Lubricating Film Thickness



Constant Test Data

Radial Load

In all tests the single test bearing was radially loaded with $F_r = 8,880 \text{ N}$. This load means a contact pressure of $p_0 \approx 2,900 \text{ N/mm}^2$ at the maximum loaded rolling element. Experience has shown that a contact pressure of this size does not cause any permanent deformations in bearings of 100Cr6 (SAE 52 100) under normal thermal load conditions. At the elevated temperature, however, there are already some slight permanent deformations occurring; this is not the case with the high-temperature resistant bearing steels S18-0-1 (AISI T1) and M50.

Speed

The bearing speed during the tests amounted to $n = 3,000 \text{ rpm}$. In some test runs carried out at the same time at $n = 6,000 \text{ rpm}$ no significant difference in the running time could be found out.

Test Temperature

All tests have been carried out at a temperature of $t = 215 \text{ }^\circ\text{C}$ ($t = 488 \text{ K}$) $\pm 0.5 \text{ K}$. The temperature was measured at the bearing outer rings.

Representation of the Results and Discussion

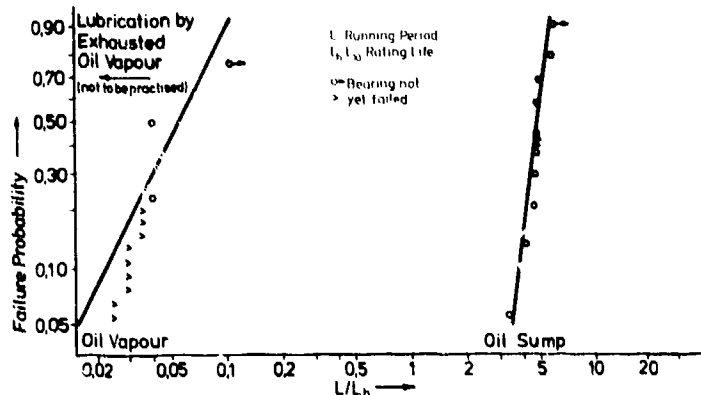
Running Periods

The running periods determined on the test rig were statistically analyzed according to the method described by G. Johnson in "The Statistical Treatment of Fatigue Experiments". When plotting the results into the Weibull failure probability chart, all bearings of the individual test bearing groups have been considered, that means, even bearings that had not yet shown any damage. The abscissa of the probability chart shows the ratio running period L to rated life L_{10} (L/L_{10}). The circles with arrows and the open arrows in the diagrams mean that the bearings finished the test run without any damage. Circles and squares represent the running periods of bearings which were damaged.

The diagrams of figures 6 and 7 show the failure distribution for bearings made of 100Cr6 (SAE 52 100) and S18-0-1 (AISI T1) for the three different test variants. It can be recognized that the different lubrication conditions have a considerable effect on the running periods; this effect is stronger for the bearings made of 100Cr6 (SAE 52 100) than for the bearings of S18-0-1 (AISI T1).

Bearings made of the conventional 100Cr6 (SAE 52 100) reach with oil sump lubrication the quadruple L_{10} life, in spite of the intense metal-to-metal contact in the contact areas. With oil vapor lubrication it is only approx. 2.5 % of the rated L_{10} life. The bearings fail already in the starting period, when the oil vapor is exhausted. The failure is marked by loud running noise caused by seizure marks.

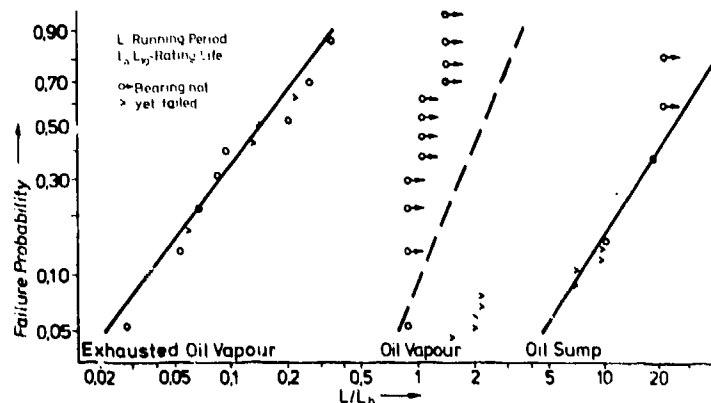
6: Results on Running Periods with Bearings of 100Cr6 (SAE 52 100) in Case of Starved Lubrication



With bearings of S18-0-1 (AISI T1) and oil sump lubrication a running period is reached which corresponds to approx. the sevenfold rated L_{10} life. With oil vapor lubrication at least the rated L_{10} life is reached, and with lubrication by exhausted oil vapor the bearings can still be operated for approx. 3.5 % of this life.

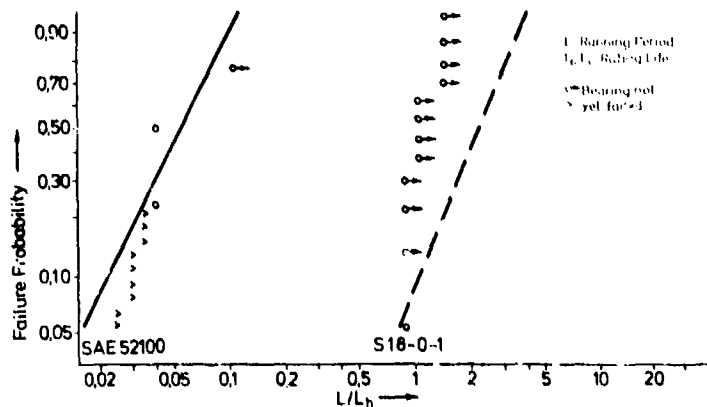
The figures 6 and 7 show that the running time losses resulting from increasingly worse lubrication conditions are considerably less severe for bearings made of the high-temperature resistant rolling bearing material S18-0-1 (AISI T1) than for bearings of the conventional bearing steel 100Cr6 (SAE 52 100). With regard to a failure probability of 10 %, the running times of bearings of 100Cr6 (SAE 52 100) are of a ratio of 5:0.025:0 if the starved lubrication condition deteriorates from oil sump lubrication to oil vapor lubrication by exhausted oil vapor. For bearings of S18-0-1 (AISI T1) this ratio is 7:1:0.035. This means for the bearings of 100Cr6 (SAE 52 100) a running time reduction by the factor 200 already when passing on from oil sump lubrication to oil vapor lubrication. The bearings of the high-temperature resistant steel S18-0-1 (AISI T1) still reached the rated life with oil vapor lubrication. Only when passing from oil sump lubrication to lubrication by exhausted oil vapor the running times were reduced by the factor 200.

7: Results on Running Periods with Bearings of S18-0-1 (AISI T1) in Case of Starved Lubrication

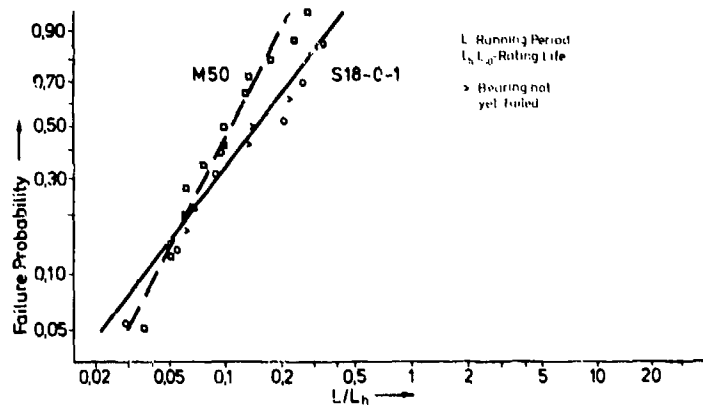


For direct comparison figure 8 represents the test results of bearings of 100Cr6 (SAE 52 100) and of S18-0-1 (AISI T1) in case of oil vapor lubrication. The bearings of the high-temperature resistant steel S18-0-1 (AISI T1) realized approx. the fortyfold running period (L/L_h) of bearings of 100Cr6 (SAE 52 100) under the same unfavorable operating conditions. Figure 9 shows the results achieved by bearings of the high-temperature resistant steels S18-0-1 (AISI T1) and M50. It can be seen that both steels supply comparable results.

8: Comparison of the Running Periods of Bearings of 100Cr6 (SAE 52 100) and of S18-0-1 (AISI T1) in Case of Oil Vapor Lubrication



9: Comparison of the Running Periods of Bearings of M50 and of S18-0-1 (AISI T1) in Case of Lubrication by Exhausted Oil Vapor



Damage Characteristics

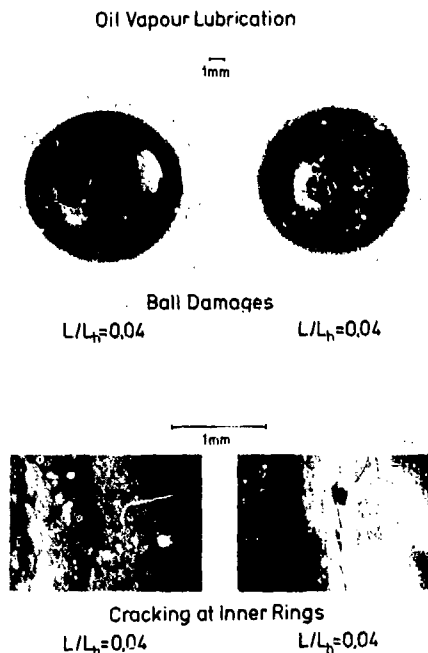
For bearings of high-temperature resistant steels damage exclusively arose on the raceways. In contrast thereto, rings and rolling elements of bearings of conventional bearing steel equally shared the failures.

With oil sump lubrication, bearings of S18-0-1 (AISI T1) and 100Cr6 (SAE 52 100) showed fatigue damage as known from bearing life tests in case of unfavorable lubrication conditions. In the initial damage phase micropittings appeared on the surfaces; these are minimum local grooves of low depth. If the bearings were run longer on the test rig, pittings of usual size and depth were also found.

During the tests with oil vapor lubrication, changes of the raceways occurred long before fatigue. Slight roughening of the raceways and wear could be observed. These changes meant a louder running noise. The changes were, however, considerably less for bearings of high-temperature resistant material than for bearings of the conventional bearing steel.

100Cr6 (SAE 52 100). Bearings of 100Cr6 (SAE 52 100) showed premature failure in case of oil vapor lubrication. Damage appeared on balls and inner rings; the raceways showed cracks all over the circumference. Figure 10 represents ball damage and raceway cracks of bearings of 100Cr6 (SAE 52 100) which were operated with oil vapor lubrication.

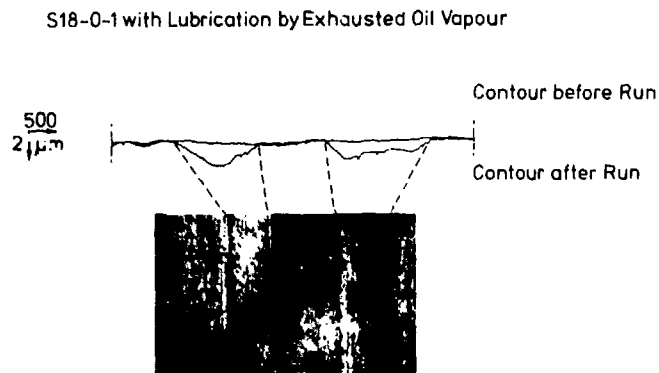
10: Ball and Inner Ring Damage
Bearings of 100Cr6 (SAE 52 100) in Case of Oil Vapor Lubrication



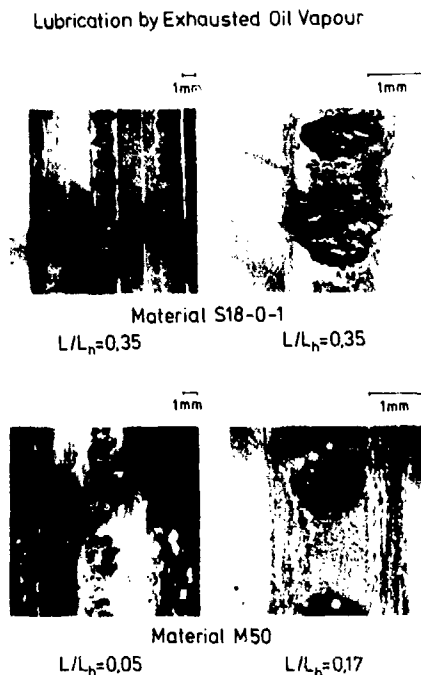
With lubrication by exhausted oil vapor the bearings fail, as already mentioned, already during the starting phase. The bearings of the high-temperature resistant bearing steels S18-0-1 (AISI T1) and M50 increasingly showed sliding and wear marks in the raceways.

The graphs compared in figure 11 - sensed transversally to the rolling direction - and the pertinent photo clearly show the wear. Wear mainly appears in the pressure ellipse where high sliding speeds occurred. Under the extreme starved lubrication conditions numerous small pittings appeared all over the circumference with the running period increasing, figure 12.

11: Raceway Wear
Bearings of S18-0-1 (AISI T1) in Case of Lubrication by Exhausted Oil Vapor



12: Typical Damage Patterns Lubrication by Exhausted Oil Vapor



With the damage progressing, the inner ring raceways also showed wider running marks at ball pitch. This is due to the fact that the load transmitted by the maximum loaded ball (apex ball) is reduced momentarily when cycling a larger pitting so that the neighboring rolling elements accommodate this load share.

Summary

In the tests deep groove ball bearings of the high-temperature resistant rolling bearing steel S18-0-1 (AISI T1) turned out to be long-lived with the test variant "Oil sump lubrication" and an operating temperature of 215 °C (288 K). It must, however, be considered that, in spite of sufficient lubricant quantities, an intense metal-to-metal contact at the rolling element/raceway contacts was given on account of the thin lubricating film. The running periods realized up to the sevenfold L_{10} life mean in practice that even under such conditions a considerable operating reliability can be achieved with bearings of S18-0-1 (AISI T1). The same can be expected for bearings of the M50 steel.

Even with the variant "Oil vapor lubrication" the bearings of the high-temperature resistant bearing steel achieved running times corresponding to the rated L_{10} life. For oil vapor lubrication the bearings were only lubricated with the oil vapor formed at 215 °C (488 K). This result can, however, only be applied to practice, if the operating conditions (load, speed) do not cause any additional temperature increase within the bearing.

Only if the oil vapor is reduced by exhaustion, the bearings of high-temperature resistant material S18-0-1 (AISI T1) and M50 become short-lived. But even with this extreme starved lubrication running periods of approx. 3.5 % of the L_{10} life are still reached. Both high-temperature resistant rolling bearing steels ensure comparable running times but with considerable wear.

In comparison to the high-temperature resistant rolling bearing steels the conventional bearing steel 100Cr6 (SAE 52 100) is considerably more sensitive to starved lubrication. With sufficient lubricant supply but an insufficient lubricating film thickness life decreases to approx. the quadruple rated L_{10} life; with oil vapor lubrication only 2.5 % of the L_{10} life are reached, and with lubrication by exhausted vapor the bearings of 100Cr6 (SAE 52 100) cannot be operated anymore.

References

- [1] Lorösch, H.-K.: Neue Erkenntnisse aus Ermüdungsversuchen an Wälzlagern ("New Findings on Rolling Bearing Fatigue Tests"), VDI-Bericht, No. 248, 1975, page 119...123
- [2] Lorösch, H.-K.: The Life of the Rolling Bearing under Varying Loads and Environmental Conditions, Ball and Roller Bearing Engineering 1981-1, page 17...23
- [3] Eschmann, P., Hasbargen, L., Weigand K.: Ball and Roller Bearings, R. Oldenbourg-Verlag München Wien, 1978
- [4] Johnson, L.G.: The Statistical Treatment of Fatigue Experiments, Elsevier Scientific Publishing Company, 1974

DISCUSSION

-.Dusserre-Telmon, SNECMA, Fr

Quelle est la taille du filtrage des particules dans votre essai?

Reponse d'Auteur

5 μm .

-.Dusserre-Telmon

Quelle était la pression de Hertz?

Reponse d'Auteur

2900 N/mm².

-.Dusserre-Telmon

Avez-vous essayé des pressions de Hertz plus faibles?

Author's Reply

All tests were performed under the same Hertzian contact stress.

P.Trudeau, DND, Ca

Please comment on 'the countour after run', ref. your slide para 11, page 17-7. How do you explain the 2 valleys which are not centered on the race?

Author's Reply

In the contact zone, because of specific geometrical relationship there is rolling and sliding contact occurring simultaneously and the load distribution is elliptical. In the area where there is sliding contact a higher wear rate under insufficient lubrication occurs even under mild contact conditions as for example on the edges of the contact zone. Small deviations in symmetry of the wear track is purely arbitrary.

R.J.Mather, Airworthiness Branch ABE/A, Ca

Were the test bearings subject to any pre-test treatment? for example, cleaning or running-in fully lubricated.

Author's Reply

No. Before the test, the bearings were not treated in any special way.

D.G.Astridge, Westland Helicopters, Yeovil, UK

Was any axial pre-load applied to the test bearings?

Author's Reply

No. The bearings were not axially pre-loaded.

D.G.Astridge

The operating conditions appear particularly severe, noting the calculated film thickness and the low L/Lh at .9 failure probability - it would be interesting to know if the life improvement factor, tool steel relative to 52100 steel is similar at less severe conditions (lower load, higher speed, EP oil) and with fine filtration (3 μm absolute or better).

Author's Reply

This question can be answered partially by the trends in the results. For the case of sump lubrication (plenty of oil) and a theoretical film thickness of 0.017 μm (extensive surface contact) a relative similar fatigue life is achieved for the 100Cr6 (SAE 52100) and S18-0-1 or M50.

With conditions of starved lubrication the difference in fatigue lives for the different materials becomes more pronounced. It is therefore to be expected that conditions of full lubrication leads to higher fatigue life and smaller differences in fatigue lives for different materials.

The effect of EP additives on the oil was not tested as part of this program.

D.G.Astridge

Was the same value of Lh used for all three steels?

Author's Reply

The fatigue life of all bearings was calculated using standard methods but small differences resulted due to small internal geometry differences between bearings of normal and temperature resistant steel.

W.J.Anderson, Bearings and Lubrication, North Olmsted, Ohio, US

The film thickness plot is evidently based on temperature conditions and not on any conditions of starvation present. In that case wouldn't the differences in film thickness for the 3 methods of lubrication be much greater?

Author's Reply

We agree with the observation. As already stated the film thickness with plenty of oil is inadequate to separate the contacting surfaces and an intensive metal to metal contact occurs. The lubricating conditions in the other two cases is substantially more severe.

Since the actual film thickness cannot be measured we have described the lubricating conditions and they were held constant for the duration of the test.

W.J.Anderson

Since the mode of failure in the bearings lubricated only with exhausted oil vapour was wear should the data be compared on weibull plots?

Author's Reply

All failures represented in the weibull plots were due to fatigue.

GEOMETRY AND STARVATION EFFECTS IN HYDRODYNAMIC LUBRICATION

by David Brewe
 Propulsion Laboratory
 AVRADCOM Research and Technology Laboratories
 Lewis Research Center
 Cleveland, Ohio

and

Bernard J. Hamrock
 Lewis Research Center
 Cleveland, Ohio

SUMMARY

Numerical methods were used to determine the effects of lubricant starvation on the minimum film thickness under conditions of a hydrodynamic point contact. Starvation was effected by varying the fluid inlet level. The Reynolds boundary conditions were applied at the cavitation boundary and zero pressure was stipulated at the meniscus or inlet boundary. A minimum-film-thickness equation as a function of both the ratio of dimensionless load to dimensionless speed and inlet supply level was determined. By comparing the film generated under the starved inlet condition with the film generated from the fully flooded inlet, an expression for the film reduction factor was obtained. Based on this factor a starvation threshold was defined as well as a critically starved inlet. The changes in the inlet pressure buildup due to changing the available lubricant supply are presented in the form of three-dimensional isometric plots and also in the form of contour plots.

NOMENCLATURE

C_0, C_1	= least-squares coefficients
D	= difference $[(\bar{H}_0 - H_0)/H_0] \times 100$, percent
H	= dimensionless film thickness, h/R_x
H_0	= dimensionless minimum (central) film thickness, h_0/R_x
\bar{H}_0	= dimensionless calculated minimum (central) film thickness
H_{in}	= dimensionless fluid inlet level, h_{in}/R_x
H_{in}^*	= dimensionless fluid inlet level (onset of starvation)
h	= film thickness, m
h_0	= minimum (central) film thickness, m
L	= reduced hydrodynamic lift, dimensionless
N	= direction normal to boundary
P	= dimensionless pressure, $pR_x/\eta_0 u$
p	= pressure, N/m^2
R	= effective radius of curvature, $R_x R_y / (R_x + R_y)$, m
W/U	= ratio of dimensionless load to dimensionless speed
u	= average surface velocity in x direction, $(u_A + u_B)/2$, m/s
w	= load capacity, N
X	= dimensionless coordinate, x/R_x
x	= coordinate along rolling direction, m
Y	= dimensionless coordinate, y/R_x
y	= coordinate transverse to rolling direction, m
α	= radius ratio, R_y/R_x
β	= film reduction factor
η_0	= fluid viscosity at standard temperature and pressure, Ns/m^2
ϕ	= Archard-Cowling side-leakage factor, $1/(1 + 2/(3\alpha))$
Subscripts	
cr	= critical
f	= flooded conjunction
x,y	= coordinate direction

INTRODUCTION

The effect of starvation in a hydrodynamically lubricated conjunction can be studied by systematically reducing the inlet supply and observing the resultant pressure distribution and film thickness. This starvation effect can have a significant role in the operation of machine elements. For example, roller-end wear due to roller skewing can be a critical problem for high-speed cylindrical roller bearings. It is desirable that the hydrodynamic film generated between the roller end and the guide flange provide stiffness and damping to limit the amplitude of the roller skewing motion. However, at high rotational speeds the roller end and the flange are often subjected to a depletion in the lubricant supply due to centrifugal effects. In such cases, the minute amount of lubricant available at the roller-end-flange conjunction might well represent an example of steady-state starvation. Starvation effects in hydrodynamically lubricated contacts are important also if one wishes to calculate the rolling and sliding resistance and/or traction encountered in ball and roller bearings [1]. In another example, the effect of restricting the lubricant to a roller bearing is seen experimentally and theoretically to reduce the amount of cage and roller slip [2]. The theoretical analysis was accomplished by changing the location of the boundary where the pressure begins to buildup and noting the effect on the hydrodynamic forces. Combining this with relative velocity expressions and equilibrium equations enabled the determination of the amount of cage and roller slip.

The location of the inlet and exit boundaries as well as the respective boundary conditions to be applied has been one of the most controversial issues concerning starvation of hydrodynamic contacts. The issue of the effect of the lubricant supply on the inlet boundary condition and its consequences to incipient pressure buildup began to materialize as a result of earlier studies applied to rigid cylinders [3,4]. Lauder [5] and Tipei [6] asserted an upstream limit of the fluid film where the pressure begins to rise as governed by the Reynolds equation. This limit according to Lauder is determined by applying reverse flow boundary conditions (i.e., $u = \partial u / \partial y = 0$). Tipei locates the upstream limit as defined by the line of centers of two bounded vortices that are observed for pure rolling. Both cases have been criticized because their analyses lead to one position of pressure buildup regardless of the oil supply [7]. Dowson [8] Floberg [9,10] and most dramatically, Wedeven, Evans, and Cameron [11] provide experimental evidence supporting the idea that the location of incipient pressure rise is determined by the oil supply. Further Wedeven, et al., using a Grubin type of EHD analysis, obtained very good correlation between experiment and the theory of starvation effects by choosing the start of the pressure buildup to occur at the meniscus boundary. Oteri [12], using stream function analysis for rolling rigid cylinders, showed that incipient pressure rise occurs at the meniscus boundary even in the presence of reverse-flow conditions. In view of this work, starvation effects in machine element applications can be predicted and relied on with a greater degree of confidence.

One of the more important manifestations of lubricant starvation is the reduction in film thickness. This topic has received a good deal of attention in the literature [11, 13-21]. With the exception of [13, 19-21], these references are applicable only to elastohydrodynamic situations. Most of the work concerned with rigid contacts has been devoted to line contact applications [13,20,21]. Dalmaz and Godet [19] analyze the effect of the inlet on the film reduction factor for a sphere against a plate. However, to the authors' knowledge, an effort that parallels that of Hamrock and Dowson [14,15] for the EHD contact is absent from the rigid contact theory. In those works, an expression was determined that relates the film reduction to the inlet distance.

The current study is a resumption of a previous rigid-contact analysis [22] to extend validity for the minimum-film-thickness equation derived there over a wider range of film thicknesses as well as to include the effects of starvation in this equation. The start of the pressure buildup as determined by the Reynolds equation is assumed to occur at the inlet meniscus. The location of the cavitation boundary was determined by applying the Reynolds boundary conditions as discussed in previous work [22]. The study applies to a wide range of geometries (i.e., from a ball-on-plate configuration to a ball in a conforming groove). Seventy-four cases were used to numerically determine (1) an equation relating minimum film thickness with the fluid inlet level as well as with the dimensionless load-speed ratio and geometry, (2) an equation predicting the onset of starvation, and (3) an equation predicting the onset of a critically starved conjunction. The resulting equations are valid for dimensionless minimum film thicknesses H_0 ranging from 5.0×10^{-5} to 1.0×10^{-3} . Further, contour isobar plots and three-dimensional isometric pressure plots are presented.

Numerical Procedure

The hydrodynamic effects on the central film thickness between two rigid solids in lubricated rolling and/or sliding contact are analyzed under conditions of lubricant starvation. The effects of starvation are determined by systematically decreasing the fluid inlet level. The Reynolds boundary conditions are applied at the cavitation boundary, and zero pressure is stipulated at the meniscus or inlet boundary. The lubricant is assumed to be an incompressible Newtonian fluid under laminar, isothermal, isoviscous, and steady-state conditions. The numerical approach follows that of a previous investigation [22]. There, a fully flooded film profile was specified and a pressure distribution satisfying the Reynolds equation was determined for a given speed, viscosity, and geometry. The analysis treats the two rigid bodies as having parallel principal axes of inertia. This enables one to make a simplifying transformation to an equivalent system of a rigid solid near a plane separated by a lubricant film (Fig. 1).

Relevant equations. - The same dimensionless expressions are used here as in [22], that is,

$$X = x/R_x, Y = y/R_x, H = h/R_x \quad (1)$$

also

$$p = pR_x/\eta_0 u, \alpha = R_y/R_x$$

The Reynolds equation

$$\frac{\partial}{\partial X} \left(H^3 \frac{\partial P}{\partial X} \right) + \frac{\partial}{\partial Y} \left(H^3 \frac{\partial P}{\partial Y} \right) = 12 \frac{\partial H}{\partial X} \quad (2)$$

is the governing equation within the conjunction.

We recognize that, when the inlet supply levels are increased to values much greater than the minimum film thickness, calculations as governed by the Reynolds equation are inherently in error far from the center of contact. The reason is that the Reynolds equation neglects curvature of the fluid film. Dowson [23] has pointed out that the errors involved in using this equation to determine the buildup of pressure in such regions are negligible. The predicted pressures are themselves so very much smaller than the effective load-carrying pressures in the region of closest approach of the solids. The dimensionless film thickness equation is given as

$$H = H_0 + 1 - \sqrt{1 - X^2} + \alpha \left[1 - \sqrt{1 - (Y/\alpha)^2} \right] \quad (3)$$

where H is bounded above by the dimensionless fluid inlet level H_{in} and below by the dimensionless minimum film thickness H_0 (i.e., $H_0 < H < H_{in}$, e.g., (Fig. 1). The fluid inlet level H_{in} is made dimensionless so that, if the inlet is completely filled, $H_{in} = 1$ and the conjunction is said to be fully flooded.

The Reynolds boundary conditions are used, that is, $P = \partial P / \partial N = 0$ at the cavitation boundary and $P = 0$ at the inlet boundary ($H = H_{in}$). A pressure distribution that satisfies these boundary conditions is then determined numerically by finite differencing with Gauss-Seidel successive over relaxation method. With this algorithm we are able to generate pressure distributions for given contact geometry, speed, viscosity, film thickness, and fluid inlet level.

Effect of inlet on pressure. - Figure 2 graphically portrays how a pressure distribution is affected by the lubricant supply for a dimensionless minimum film thickness of 1×10^{-4} . The two views, (a) and (b), are for a fully flooded contact ($H_{in} = 1.00$) and a starved contact ($H_{in} = 0.001$). The starvation effect on the pressure distribution might be considered rather moderate. That is to say, the effect of reducing the fluid inlet level has essentially had no effect on the magnitude of the peak pressure. Only the size of the load bearing region has been affected. The load bearing region is defined by the meniscus and the cavitation boundary.

We repeat this process of decreasing the fluid inlet level for a given minimum film thickness for a wide range of minimum film thickness values. Figure 3 illustrates a situation in which the starvation is more severe. The minimum film thickness here is ten times as thick as what is indicated in Fig. 2. Note that the pressure distribution of Fig. 3 is not as localized as in Fig. 2. Consequently decreasing the size of the load bearing region has a more noticeable effect on the load capacity. Starvation is more evident here since we also see that the peak pressure is noticeably reduced from the fully flooded condition. This sort of behavior takes place if the fluid inlet level is of the same order of magnitude as the minimum film thickness.

Generalized film thickness formula. - Now we've seen how starvation effects the pressure distribution for two different minimum film thickness values. In this analysis, we repeated this determination for minimum film thickness values ranging from 10^{-3} to 10^{-5} . In all, 74 different cases were analyzed to determine a minimum film thickness equation as a function of dimensionless load to speed ratio (W/U) and fluid inlet level.

The integration of the pressure distribution can be used in relating the hydrodynamic effects (i.e., load, speed, and viscosity) to the minimum (central) film thickness for a given fluid inlet level. In general, for a given H_0 and u the load capacity w and/or the dimensionless load-speed ratio is determined as follows:

$$w = \eta_0 u R_x \iint P \, dX \, dY$$

or

$$W/U = \iint P \, dX \, dY$$

where $W/U = w/\eta_0 u R_x$.

Kapitza [27], using half Sommerfeld boundary conditions derived the following relationship:

$$\frac{W}{U} = \frac{8\phi L \sqrt{2\alpha}}{\sqrt{H_0}} \quad (5)$$

where $L = \pi/2$ half-Sommerfeld B.C. (Ref. 27)

$$L = 0.131 \tan^{-1}(\alpha/2) + 1.683 \text{ Reynolds B.C. (Ref. 22)}$$

In a previous work [22], we found that if the problem is considered using Reynolds boundary conditions, then L required the above modification. But even then the equation was valid only if the pressure distribution was very localized in the case of thin films (i.e. $5 \times 10^{-5} \leq H_0 \leq 10^{-4}$). Consider, for example, a ball in rolling motion that is loaded against a flat plate. For a load-speed ratio W/U of 340, the numerically determined value (i.e., as determined by finite difference analysis) of the dimensionless film thickness is 10^{-3} (Table I). Equation (5) predicts the dimensionless film thickness to be 1.22×10^{-3} , which is in error of the numerical value by 22 percent. Consequently, we wish to revise Eq. (5) so that it is valid for the thicker films as well. This revised equation should reduce to Eq. (5) in the limit for thin films. Furthermore, the revised dimensionless film thickness should be expressed in such a way as to easily include the effects of starvation. This would then enable us to present one general expression to be presented for the dimensionless film thickness that can be used for the full range of film thicknesses for a starved conjunction as well as for a fully flooded conjunction. After the numerical analysis for each case was complete, the several curve fits or regression curves of H_0 on W/U were considered that would be consistent with these above requirements. The most suitable curve fit considered was in the form of a more general linear equation, that is,

$$\frac{1}{\sqrt{H_0}} = C_1 \frac{W}{U} + C_0 \quad (6)$$

Generalized film thickness formula (applicable to starved as well as fully flooded conjunctions). - The effect of lubricant starvation on the hydrodynamic film thickness was observed by varying the fluid inlet level to the contact and noting the effect on load capacity for five different film thicknesses for the ball-on-plate contact (i.e., $\alpha = 1.00$). In addition to the fully flooded data, 55 computer-generated data points were used to arrive at a family of equations having the form given in Eq. (6). An equation for each fluid inlet level was determined by performing a linear regression by the method of least squares. Table II lists for each fluid inlet level the values of the coefficients C_1 and C_0 , the coefficient of determination r^2 , and D_{\max} , the maximum percentage of error D defined as

$$D = \frac{\tilde{H}_0 - H_0}{H_0} \times 100 \quad (7)$$

Note that C_1 remains essentially unchanged, and can be determined from

$$C_1 = \frac{1}{\phi L (128\alpha)^{1/2}} \quad (8)$$

Furthermore, all of the effect of starvation is described in the value of C_0 . An expression for the coefficient C_0 as a function of the fluid inlet level H_{in} would enable determination of a generalized minimum-film-thickness formula that applies to starved as well as fully flooded conditions. A close examination of the variation of C_0 with H_{in} in Table II reveals that $C_0 \propto (2/H_{in})^{1/2}$ for the severely starved situations. As H_{in} approaches 1, C_0 approaches a value very nearly equal to e (i.e., the base of the natural systems of logarithms, 2.718). This suggests $e^{H_{in}}$ as a modulating factor. Further considerations for the nearly flooded inlet levels show that

$$C_0 e^{-H_{in}} \propto [(2 - H_{in})/H_{in}]^{1/2}$$

Finally for the full range of values, C_0 varies with H_{in} as follows:

$$C_0 = 1.11 e^{H_{in}} \left(\frac{2 - H_{in}}{H_{in}} \right)^{1/2} \quad (9)$$

Thus, our generalized minimum film thickness formula in terms of geometry (i.e., radius ratio α), load-speed ratio W/U , and fluid inlet level H_{in} , can be written as

$$\tilde{H}_0 = \left[\frac{W/U}{\phi L (128\alpha)^{1/2}} + 1.11 \left(\frac{2 - H_{in}}{H_{in}} \right)^{1/2} e^{H_{in}} \right]^{-2} \quad (10)$$

The measure of agreement between the calculated and input values of H_0 is represented by the value of D (Eq. (7)) and presented in Table I. Table I shows that, when the fluid inlet level is of the same order of magnitude as the minimum film thickness, the error that results from using Eq. (10) becomes larger. However, Eq. (10) can confidently be used for the full range of minimum film thickness if the fluid inlet level is such that $0.004 \leq H_{in} \leq 1.000$. For very thin films (i.e., $H_0 \leq 10^{-4}$) Eq. (10) can be useful throughout the full range of fluid inlet levels that were investigated (i.e., $0.001 \leq H_{in} \leq 1.000$). Note that the film thickness formula is intended to be used only for a range of speeds and loads in which piezoviscous and deformation effects are negligible. It was determined that these effects can be significant for minimum film thicknesses less than 5.0×10^{-5} .

Note also from Table I that excellent agreement is obtained for the near-line-contact applications (i.e., $\alpha = 36.54$) even though these data were not used in the determination of the above Eq. (10). Most of the predictions by Eq. (10) are within 3 percent of the numerically determined values and do not exceed 6 percent for any case.

Equation (10) is equally valid for the fully flooded conjunction as well as for the starved conjunction. That is, if we set $H_{in} = 1.00$, then Eq. (10) reduces to

$$\tilde{H}_{0,f} = \left(\frac{W/U}{\phi L \sqrt{128\alpha}} + 3.02 \right)^{-2} \quad (11)$$

Equation (11) should be used in place of Eq. (5) whenever a calculation is made for a fully flooded conjunction since it is valid for a broader range of film thicknesses (i.e., 5×10^{-5} to 1×10^{-3}). Table I shows that the error for the full range of minimum film thicknesses investigated (for $H_{in} = 1$) is less than 1 percent for $\alpha = 1$. For the near-line-contact geometry (i.e., $\alpha = 36.54$) the error does not exceed 3.36 percent.

Reduction in minimum film thickness. - It is now possible to determine the reduction in minimum film thickness from the fully flooded value if the fluid inlet level is known. This can be done by inserting Eq. (11) into Eq. (10).

$$\tilde{H}_0 = \left\{ \frac{1}{\sqrt{\tilde{H}_{0,f}}} + 3.02 \left[\sqrt{\frac{2 - H_{in}}{H_{in}}} e^{(H_{in}-1)} - 1 \right] \right\}^{-2} \quad (12)$$

Dividing both sides of the equation by H_0 gives

$$\beta \equiv \frac{\tilde{H}_0}{H_0} = \left\{ 1 + 3.02 \sqrt{\tilde{H}_{0,f}} \left[\sqrt{\frac{2 - H_{in}}{H_{in}}} e^{(H_{in}-1)} - 1 \right] \right\}^{-2} \quad (13)$$

where β is the reduction in minimum film thickness due to starvation.

RESULTS AND DISCUSSION

Effect of starvation on pressure distribution. - The discussion of lubricant starvation can be facilitated by focusing on one of the simplest geometric arrangements (i.e., a ball rolling and/or sliding against a flat plate) as shown in Fig. 2. The figure compares the pressure distribution determined numerically for the fully-flooded inlet with the most severely starved inlet ($H_{in} = 0.01$). The comparison is made for a constant minimum film thickness (i.e., $H_0 = 1.0 \times 10^{-4}$). Note that the pressure peak built up in the starved inlet is only slightly smaller than that of the fully flooded inlet. However, the area of pressure build-up is considerably smaller, and so the starved inlet is unable to support as much load for a given film thickness as the fully-flooded inlet.

Figure 3 provides the same sort of comparison but for a thicker minimum film (i.e., $H_0 = 1.0 \times 10^{-3}$). The significant difference between the two figures is that the starved inlet for the thicker film has a more pronounced effect on the pressure peak. The fluid inlet level ($H_{in} = 0.002$) for the thicker film represents a relatively more highly starved inlet since H_{in} is of the order of H_0 in this case. The other feature to be noticed in comparing Figs. 2 and 3 is that the pressure distribution is more evenly spread out for the thicker film. Thus, changes in the meniscus (or integration domain) are going to have a more noticeable effect on the load-carrying capacity. Note also that because of the boundary conditions the integration domain takes on a "kidney-shaped" appearance. This is more clearly shown in the isobaric contour plot shown in Fig. 4.

Minimum film thickness equation. - Thus far we have compared the pressure build up in a severely starved inlet with that in a fully flooded inlet for two minimum film thicknesses. Our investigation, however, included several fluid inlet levels for a variety of minimum film thicknesses. The results are summarized in Table I.

A generalized minimum film thickness formula (Eq. (10)) was derived from the results of Table I. Figure 5 indicates how well the equation represents the computer generated data in the table. It was not possible to display all these results in Fig. 5. However, the figure is representative of the overall results. The equation fits the data quite well except when the fluid inlet level is of the same order of magnitude as the minimum film thickness. Based on the discussion concerning peak pressure, it would seem that the formula holds well for those cases in which the degree of starvation is such that peak pressure is not significantly reduced.

Of course, it would be most desirable to compare the data in Table I with experimental data. To the authors' knowledge, the only available experimental data were obtained by Dalmaz and Godet [25]. To compare Eq. (10) with experiment, the data from [25] were replotted in Fig. 6. The experimental data were taken under lightly loaded (rigid contact), isoviscous conditions for pure sliding of a ball on a plate. The fluid inlet level in these experiments was reported to be 1 millimeter. The ball diameter was 30 millimeters; consequently the dimensionless fluid inlet level H_{in} was 0.067. The experimental data were presented as a plot of the dimensionless parameters H_0/WG versus $U/W^{1.5}G^{0.5}$. The materials parameter G in the plot was included so as to accommodate the elastohydrodynamic range in a more general way.

Here, we wish to compare our hydrodynamic starvation theory only with the hydrodynamic results of Dalmaz and Godet. To do this, the ordinate and abscissa were properly scaled (assuming a reasonable value of $WG = 4.5 \times 10^{-4}$), so that the minimum film thickness could be plotted against the dimensionless load-speed ratio as shown in Fig. 6. The solid line in Fig. 6 is a plot of Eq. (10) for $\alpha = 1$ and $H_{in} = 0.067$. The dashed line represents a previous theory [22] in which the reduced inlet level due to starvation was not considered. The present theory (Eq. (10)) shows better agreement with the experimental results than our previous theory [22] for lower values of W/U . This is because under conditions of low load and/or high speed, the pressures become more significant away from the center of the contact. Consequently, neglecting the size of the inlet introduces an increasing amount of error as W/U is decreased.

Although consideration of the size of the inlet domain improves the agreement of the theory with experiment for the thicker films, still further improvement is possible. It is believed that the effects of reverse flow in the inlet must be included in the theory to obtain better agreement. If reverse flow is considered, not all the available lubricant determined by the fluid inlet level will pass through the contact. The hydrodynamic contact would essentially see this as a reduction in supply from what actually is there. In other words, the inlet is more severely starved than we have taken into account. From Fig. 5, we see that increasing the severity of starvation has more effect on the load capacity for thicker films (i.e., $H_0 = 10^{-3}$) than it does for thinner films (i.e., $H_0 = 10^{-4}$). Consequently, reverse-flow considerations should improve agreement between theory and experiment for the thicker films while still maintaining good agreement in the thin-film range.

Lubricant film thickness reduction factor and onset of starvation. - Of practical importance to lubricant starvation is the reduction in minimum film thickness from the fully flooded value. Equation (13) is a derived expression for β in terms of the fluid inlet level and the fully flooded film thickness (also given by Eq. (11)). Figure 7 is a plot of β as a function of the fluid inlet level H_{in} for several values of $H_{0,f}$. It is of interest to determine a fully flooded-starved boundary (i.e., that fluid inlet level after which any further decrease causes a significant reduction in the film thickness). Hamrock and Dowson [14] determined this boundary for elastohydrodynamic (EHD) applications upon satisfying the following condition:

$$1 - \beta \Big|_{H_{in} = H_{in}^*} = 0.03 \quad (14)$$

The value of 0.03 was used in Eq. (14) since it was ascertained that the data in Table I were accurate to only ± 3 percent.

Thus, for a given value of $H_{0,f}$, one can solve for a value of H_{in}^* that satisfies Eq. (14). A suitable relationship between H_{in}^* and $H_{0,f}$ can be obtained by generating a table of values (e.g., Table III) and fitting a power curve by the method of least squares. This gives

$$H_{in}^* = 4.11(H_{0,f})^{0.36} \quad (15)$$

Thus, we have an equation that determines the onset of starvation. That is, for $H_{in} > H_{in}^*$ a fully flooded condition exists, whereas for $H_{in} < H_{in}^*$ a starved condition exists.

Critically starved inlet. - In certain bearing applications, the power loss resulting from churning of the oil may be higher than the power loss resulting from friction of the bearing alone [26]. These power losses can be minimized by reducing the lubricant supply until a loss in film thickness causes the friction losses to increase. According to the results shown in Fig. 7, the fluid inlet level can be decreased substantially without adversely affecting the minimum film thickness. Consequently, it might be advantageous to operate the bearing with a lubricant supply just sufficient to preclude any drastic reductions in minimum film thickness, as seen in the figure. Such a critical fluid inlet level might well be defined to occur at the knee of the curve, that is,

$$\left. \frac{d(\beta)}{dH_{in}} \right|_{H_{in} = H_{in,cr}} = 1 \quad (16)$$

Solutions to this expression for several values of minimum film thickness are listed in Table III. A power curve fit by the method of least squares gives

$$H_{in,cr} = 0.875(H_{o,f})^{0.2977} \quad (17)$$

The regression coefficient for this fit was determined to be 0.9999, indicating an extremely good fit.

CONCLUDING REMARKS

Numerical methods were used to determine the effects of lubricant starvation on the minimum film thickness under conditions of hydrodynamic point contact. Starvation was effected by varying the fluid inlet level. The Reynolds boundary conditions were applied at the cavitation boundary, and zero pressure was stipulated at the meniscus or inlet boundary. The analysis is considered valid for a range of speeds and loads for which thermal, piezoviscous, and deformation effects are negligible. It can be applied to a wide range of geometries (i.e., from a ball-on-plate configuration to a ball in a conforming groove). Seventy-four cases were used to numerically determine

(1) A generalized expression for the minimum film thickness as a function of dimensionless load-speed ratio, geometry, and fluid inlet level (Eq. (10)). The expression should be applied for film thicknesses in the range $1.0 \times 10^{-3} > H_0 > 1.0 \times 10^{-4}$ and for fluid inlet levels of $0.004 < H_{in} < 1.00$. For $5 \times 10^{-5} < H_0 < 10^{-4}$ the equation can be applied for a fluid inlet level of $0.001 \leq H_{in} \leq 1.00$.

(2) A film thickness reduction factor (Eq. (13)) expressed as a function of the degree of starvation (or fluid inlet level) for a given fully flooded film thickness value.

(3) An equation (Eq. (15)) that determines the onset of starvation.

(4) An equation (Eq. (17)) that determines a critically starved contact. Contour isobar plots and three-dimensional isometric plots also presented.

REFERENCES

1. Chiu, Y. P., "A Theory of Hydrodynamic Friction Forces in Starved Point Contact Considering Cavitation," ASME Journal of Lubrication Technology, Vol. 96, No. 2, Apr. 1974, pp. 237-246.
2. Boness, R. J. "The Effect of Oil Supply on Cage and Roller Motion in a Lubricated Roller Bearing," ASME Journal of Lubrication Technology, Vol. 92, No. 1, Jan. 1970, pp. 39-53.
3. Martin, H. M., "The Lubrication of Gear-Teeth," Engineering (London), Vol. 102, 1916, pp. 119-121.
4. Pepler, W., "Druckuebertragung und Geschmierten Zylindrischen Gleitund Waelzflaechen," V. D. I. Forschung., 1938, p. 391, Supp. to Forschung aug dem Gebiete des Ingenieurwesens, Vol. 9, No. 4, July-Aug. 1938.
5. Lauder, W., "Hydrodynamic Lubrication of Proximate Cylindrical Surfaces of Large Relative Curvature," Proc. Instn. Mech. Eng., Vol. 180, Part 3B, 1965-1966, pp. 101-106.
6. Tipei, N., "Boundary Conditions of a Viscous Flow Between Surfaces with Rolling and Sliding Motion," ASME Journal of Lubrication Technology, Vol. 90, No. 1, Jan. 1968, pp. 254-261.
7. Samen, W. Y., "A Study of Starved Elastohydrodynamic Lubrication with Particular Reference to Gyroscope Bearings," Ph.D. thesis, Inst. of Tribology, Leeds University, July 1974, p. 25.
8. Dowson, D., "Laboratory Experiments and Demonstrations in Tribology; No. 2 - The Principles of Hydrodynamic Lubrication," Tribology, Vol. 1, No. 2, Mar. 1968, pp. 104-108, and Vol. 1, No. 3, Aug. 1968, pp. 150-156.
9. Floberg, L., "On Hydrodynamic Lubrication with Special Reference to Subcavity Pressures and Number of Streamers in Cavitation Regions," Acta. Polytech. Scand., Series ME. 19, 1965.
10. Floberg, L., "Lubrication of Two Rotating Cylinders at Variable Lubricant Supply with Reference to the Tensile Strength of the Liquid Lubricant," ASME Journal of Lubrication Technology, Vol. 95, No. 2, Apr. 1973, pp. 155-165.

11. Wedeven, L. D., Evans, D., and Cameron, A., "Optical Analysis of Ball Bearing Starvation," ASME Journal of Lubrication Technology, Vol. 93, No. 3, July 1971, pp. 349-363.
12. Oteri, B. I., "A Study of the Inlet Boundary Condition and the Effect of Surface Quality in Certain Lubrication Problems," Ph.D. thesis, Leeds University, 1972.
13. Wolveridge, P. E., Baglin, K. P., and Archard, J. F., "The Starved Lubrication of Cylinders in Line Contact," Proc. Instn. Mech. Eng., Vol. 185, 81/71, 1970/1971, pp. 1159-1169.
14. Hamrock, B. J., and Dowson, D., "Isothermal Elastohydrodynamic Lubrication of Point Contacts, Part IV - Starvation Results," ASME Journal of Lubrication Technology, Vol. 99, No. 1, Jan. 1977, pp. 15-23.
15. Hamrock, B. J., and Dowson, D., "Elastohydrodynamic Lubrication of Elliptical Contacts for Materials of Low Elastic Modulus, II - Starved Conjunction," ASME Journal of Lubrication Technology, Vol. 101, No. 1, Jan. 1979, pp. 92-98.
16. Orcutt, F. K., and Cheng, H. S., "Lubrication of Rolling-Contact Instrument Bearings," Proceedings of the Gyro-Spin Axis Hydrodynamic Bearing Symposium, Vol. 2: Ball Bearings, Massachusetts Institute of Technology, 1966.
17. Castle, P., and Dowson, D., "A Theoretical Analysis of the Starved Elastohydrodynamic Lubrication Problem for Cylinders in Line Contact," Elastohydrodynamic Lubrication, Institution of Mechanical Engineers (London), 1972, pp. 131-137.
18. Wymer, D. G., and Cameron, A., "Elastohydrodynamic Lubrication of a Line Contact," Proc. Instn. Mech. Eng. (London), Vol. 188, No. 19/74, 1974, pp. 221-238.
19. Dalmaz, G., and Godet, M., "Effets des Conditions d'Alimentation sur l'Epaisseur du Film dans les Contacts Hertiens Lubrifies," Mec. Materiaux Elec. (France) No. 296-297, Aug.-Sept. 1974, pp. 25-34. (See NASA TM-75782, 1980, for Transl.)
20. Floberg, L., "Lubrication of a Rotating Cylinder on a Plane Surface, Considering Cavitation," Trans. Chalmers Univ. Techn. (Gothenburg), No. 216, 1959.
21. Floberg, L., "Lubrication of Two Cylindrical Surfaces, Considering Cavitation," Trans. Chalmers Univ. Techn. (Gothenburg), No. 234, 1961.
22. Brewe, D. E., Hamrock, B. J., and Taylor, C. M., "Effect of Geometry on Hydrodynamic Film Thickness," ASME Journal of Lubrication Technology, Vol. 101, No. 2, Apr. 1979, pp. 231-239.
23. Dowson, D., "The Inlet Boundary Condition, Cavitation and Related Phenomena in Lubrication," D. Dowson, M. Godet, and C. M. Taylor, eds., Mechanical Engineering Publications, Ltd., 1975, pp. 143-152.
24. Spiegel, Murray R., Schaum's Outline of Theory and Problems of Statistics, McGraw-Hill, 1961.
25. Dalmaz, G., and Godet, M., "Traction, Load, and Film Thickness in Lightly Loaded Lubricated Point Contacts," J. Mech. Eng. Sci., Vol. 15, No. 6, Dec. 1973, pp. 400-409.
26. Styri, H., "Friction Torque in Ball and Roller Bearings," Mech. Eng., Vol. 62, No. 12, Dec. 1940, pp. 886-890.
27. Kapitza, P. L., "Hydrodynamic Theory of Lubrication During Rolling," Zh. Tekh. Fiz., Vol. 25, No. 4, 1955, pp. 747-762.
28. Brewe, D. E., Hamrock, B. J., "Analysis of Starvation Effects on Hydrodynamic Lubrication in Nonconforming Contacts," AVRADCOM TR 81-C-17/NASA TM-82668, 1981.

TABLE I* - COMPARISON OF DIMENSIONLESS FILM THICKNESS VALUES FROM EQUATION (10) WITH DIMENSIONLESS FILM THICKNESS VALUES INPUT TO COMPUTER

Dimensionless fluid inlet level, H_{in}	Dimensionless minimum film thickness, H_0 ; radius ratio, a											
	$H_0 = 1 \times 10^{-3}; a = 1.00$			$H_0 = 1 \times 10^{-3}; a = 36.54$			$H_0 = 5 \times 10^{-4}; a = 1.00$			$H_0 = 1 \times 10^{-4}; a = 1.00$		
	Load-speed ratio, W/U	Equation (10) H_0	Error, D , percent	Load-speed ratio, W/U	Equation (10) H_0	Error, D , percent	Load-speed ratio, W/U	Equation (10) H_0	Error, D , percent	Load-speed ratio, W/U	Equation (10) H_0	Error, D , percent
1.000	339.57	0.9948×10^{-3}	-0.52	3646.70	0.9843×10^{-3}	-1.57	495.54	4.9644×10^{-4}	-0.71	1153.59	0.9906×10^{-4}	-0.94
.750	339.07	.9965	-.35				495.03	4.9703	-.59	1153.05	.9912	-.88
.500	336.70	1.0005	+ .05				492.68	4.9842	-.32	1150.64	.9925	-.75
.250	328.75	1.0050	+ .50				484.57	5.0029	+ .06	1142.56	.9941	-.59
.150	318.46	1.0121	+1.21				474.73	5.0194	+ .39	1132.68	.9956	-.44
.070	295.67	1.0253	+2.73				453.65	5.0326	+ .65	1106.41	1.0056	+ .56
.035	255.79	1.0361	+3.61				421.79	5.1078	+2.16	1077.99	1.0064	+ .64
.020	234.65	1.0345	+3.45				387.20	5.1703	+3.41	1044.01	1.0107	+1.07
.010	184.47	1.0141	+1.42				332.44	5.1886	+3.77	982.81	1.0235	+2.35
.004	89.74	.9481	-5.19				232.77	5.0363	+ .73	862.58	1.0462	+4.62
.002	25.96	.7170	-78.31				127.97	4.7331	-5.34	735.62	1.0563	+5.63
.001	4.54	.3990	-46.80				37.09	3.5855	-28.29	567.75	1.0489	+4.89

Dimensionless fluid inlet level, H_{in}	$H_0 = 1 \times 10^{-4}; a = 36.54$			$H_0 = 5 \times 10^{-5}; a = 1.00$			$H_0 = 1 \times 10^{-5}; a = 1.00$			$H_0 = 1 \times 10^{-5}; a = 36.54$		
	Load-speed ratio, W/U	Equation (10) H_0	Error, D , percent	Load-speed ratio, W/U	Equation (10) H_0	Error, D , percent	Load-speed ratio, W/U	Equation (10) H_0	Error, D , percent	Load-speed ratio, W/U	Equation (10) H_0	Error, D , percent
	1.000	12 430.93	0.9728×10^{-4}	-2.71	1646.74	4.9498×10^{-5}	-1.00	3706.19	1.0007×10^{-5}	+0.07	40 269.42	0.9664×10^{-5}
.750	12 428.08	.9730	-2.71	1646.28	4.9514	-.97	3705.65	1.0009	+ .09			
.500	12 403.78	.9740	-2.60	1643.92	4.9558	-.88	3703.29	1.0013	+ .13			
.250	12 373.86	.9746	-2.54	1635.68	4.9674	-.75	3695.02	1.0019	+ .19			
.150	12 224.02	.9752	-2.48	1626.06	4.9662	-.68	3685.42	1.0022	+ .22			
.070	12 042.07	.9698	-3.02	1606.17	4.9633	-.73	3665.43	1.0020	+ .20			
.035	11 552.18	.9994	-.06	1570.61	5.0085	-.17	3648.45	.9961	-.39			
.020	11 169.70	1.0069	+ .69	1536.34	5.0256	+ .51	3613.91	.9978	-.22			
.010	10 503.93	1.0216	+2.16	1474.84	5.0721	+1.44	3552.69	1.0017	+ .17			
.004	9 232.69	1.0422	+4.22	1372.16	5.0430	+ .86	3447.13	1.0005	+ .05			
.002	7 869.48	1.0535	+5.35	1221.52	5.2245	+4.49	3294.44	1.0176	+1.76			
.001	6 127.10	1.0378	+3.78	1041.53	5.2763	+5.53	3108.58	1.0253	+2.53			

TABLE II* - CONSTANTS APPEARING IN FILM THICKNESS EQUATION (EQ. (6)) FOR EACH FLUID INLET LEVEL

Dimensionless fluid inlet level, H_{in}	Least-squares coefficients		Coefficient of determination, r^2	Maximum percentage of error in film thickness determination (eq. (7)), D_{max}
	C_1	C_0		
1.000	0.08485	2.6511	0.99999	+1.67
.750	.08455	2.6931		+1.67
.500	.09455	2.8941		+1.67
.250	.08456	3.5720		+1.61
.150	.08454	4.4226		+1.78
.070	.08447	6.3850		+1.68
.035	.08414	9.2635	1.00000	-0.14
.020	.08418	12.0388	1.00000	-1.06
.010	.08440	16.6239	.99999	-3.51
.004	.08452	25.2892	.99990	-7.47
.002	.08630	33.5023	.99934	-21.72
.001	.08878	43.2636	.99737	-30.07

TABLE III* - DIMENSIONLESS FLUID INLET VALUES THAT DETERMINE STARVED - FULLY FLOODED BOUNDARY AND CRITICALLY STARVED BOUNDARY FOR SEVERAL VALUES OF MINIMUM FILM THICKNESS FOR A FLOODED CONJUNCTION

Dimensionless fluid inlet values	Dimensionless minimum film thickness, for a flooded conjunction, H_{0f}						
	5×10^{-5}	7.5×10^{-5}	1×10^{-4}	2.5×10^{-4}	5×10^{-4}	7.5×10^{-4}	1×10^{-3}
H_{in}^*	0.107	0.130	0.148	0.212	0.265	0.297	0.320
$H_{in,cr}$.046	.052	.056	.074	.091	.103	.112

* (From ref. 28).

* This value of W/U was determined using $H_0 = 7.5 \times 10^{-4}$, since $H_0 = H_{in}$ results in no load capacity.

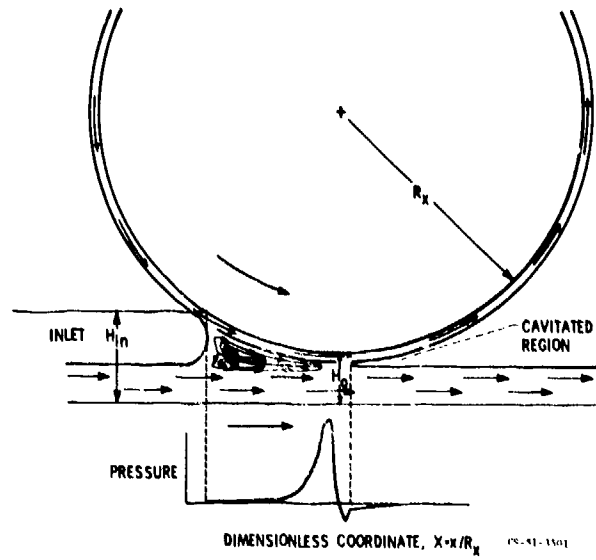


Figure 1. - Depiction of lubricant flow for a rolling/sliding contact and corresponding pressure build-up.

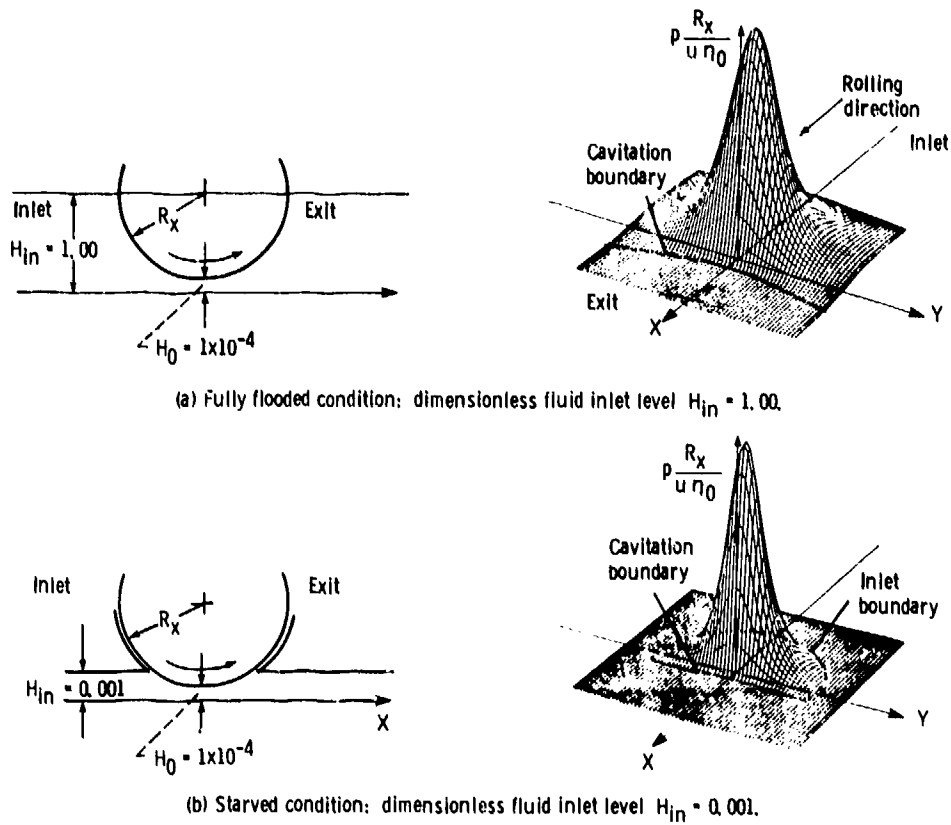
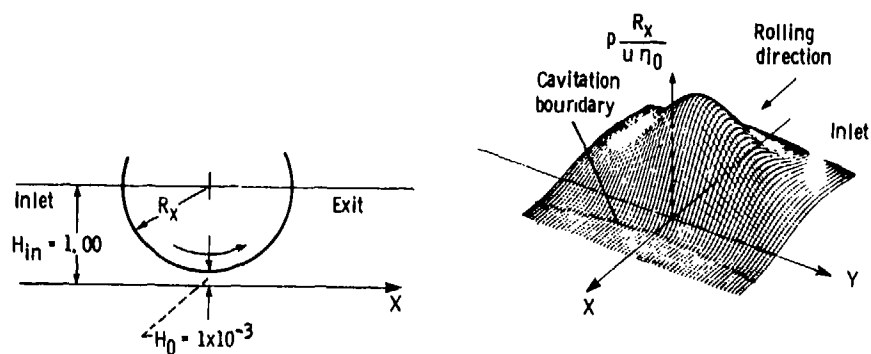
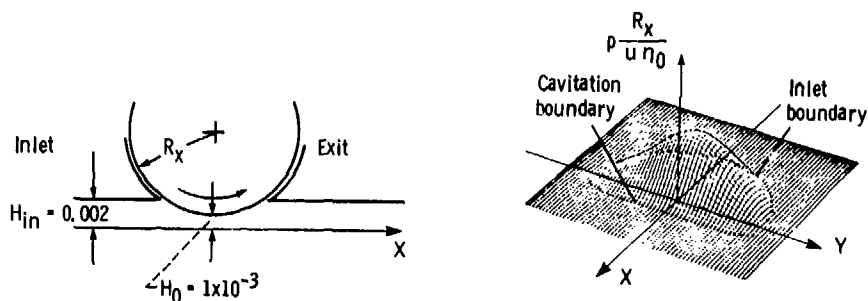


Figure 2. - Three-dimensional representation of pressure distribution, comparing starved with fully flooded conjunction for dimensionless minimum film thickness $H_0 = 1 \times 10^{-4}$.

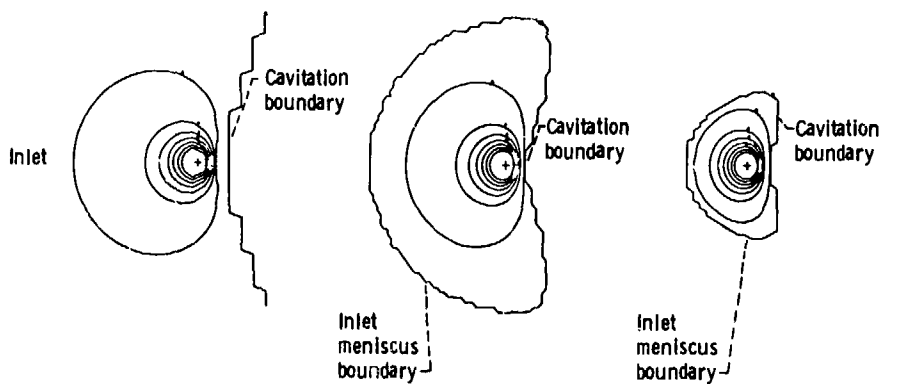


(a) Fully flooded condition: dimensionless fluid inlet level $H_{in} = 1.00$.



(b) Starved condition: dimensionless fluid inlet level $H_{in} = 0.002$.

Figure 3. - Three-dimensional representation of pressure distribution, comparing starved with fully flooded conjunction for dimensionless minimum film thickness $H_0 = 1 \times 10^{-3}$.



(a) Fully flooded condition: dimensionless fluid inlet level $H_{in} = 1.00$; dimensionless maximum pressure $P_{max} = 1.20 \times 10^6$; dimensionless load-speed ratio $W/U = 1153.6$.

(b) Starved condition: $H_{in} = 0.004$; $P_{max} = 1.19 \times 10^6$; $W/U = 862.6$.

(c) Starved condition: $H_{in} = 0.001$; $P_{max} = 1.13 \times 10^6$; $W/U = 567.8$.

Figure 4. - Isobaric contour plots for three fluid inlet levels for dimensionless minimum film thickness $H_0 = 1 \times 10^{-4}$.

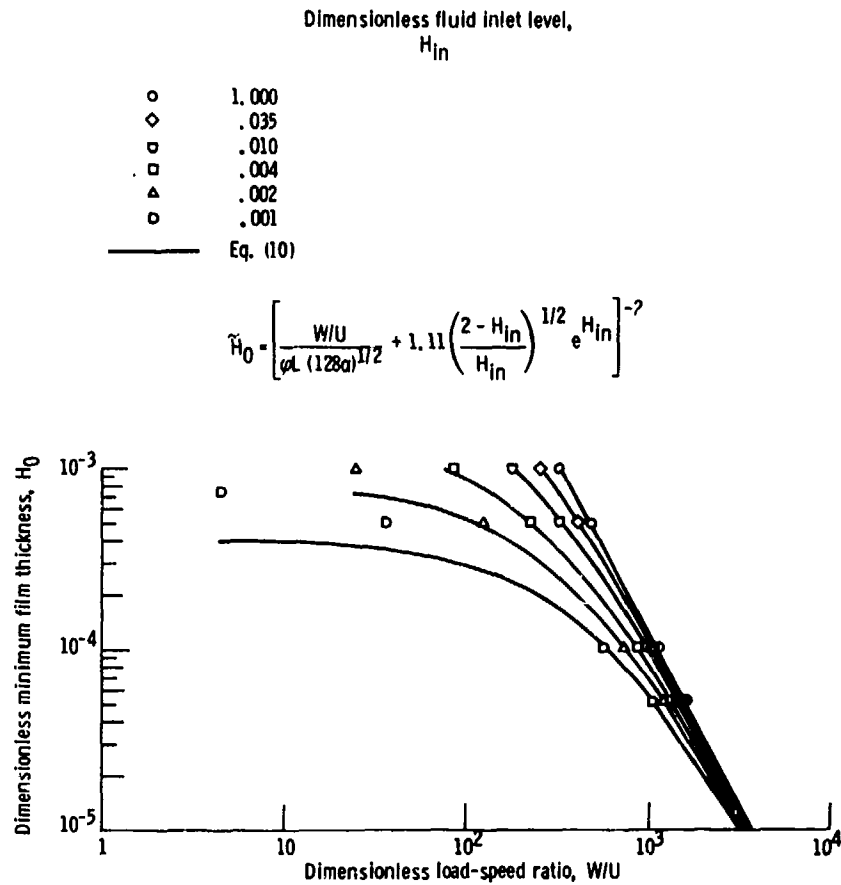


Figure 5. - Comparison of dimensionless minimum film thickness equation (eq. (10)) with computer-generated data as a function of dimensionless load-speed ratio for several values of dimensionless fluid inlet level.

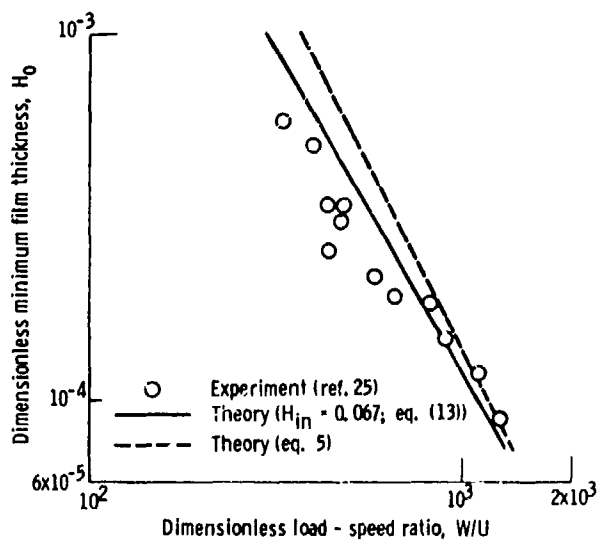


Figure 6. - Theoretical and experimental results.

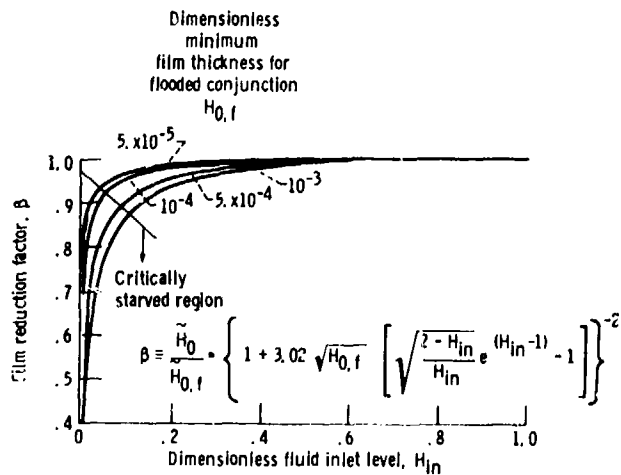


Figure 7. - Minimum film thickness reduction factor as a function of fluid inlet level for several values of dimensionless minimum film thickness for flooded conjunction.

DISCUSSION

D.G.Astridge, Westland Helicopters, Yeovil, UK

- (1) In determining the levels of starvation that one dare operate at in roller bearings it is important to consider the traction capability of the contacts as well as minimum film thickness. Have you attempted to predict the tractive capacity vs starvation characteristics.
- (2) How does your work differ from that of Archard and Baglin (1972)?

Author's Reply:

- (1) I must agree with you that it would have been equally desirable to calculate the effect of starvation on traction when determining a critical fluid inlet level.
- (2) Our work differs from Archard and Gablin (1972) in that their starvation analysis was for line contacts and included the EHD regime as well, whereas our results apply to a wide range of geometries but is restricted to rigid contacts (isoviscous, undeformed contacts).

C.M.Taylor, University of Leeds, UK

- (1) Have you checked your starvation data against that for cylinders published by Whitaker and Dowson in the early 1960s?
- (2) You suggest that at high Ho the discrepancy between the experimental results of Dalmaz/Godet and your predictions would be due to your reject of reverse flow in the inlet. However, does not your solution actually admit to reverse flow (if not, give the details) from the balance of Poiseuille/Couette effects?

Author's Reply

- (1) Prior to this we had not compared our starvation data against that for cylinders published by Whitaker and Dowson (1965). A quick check with their work shows that for a given fluid inlet level of $H_{in} = .01$, and $\alpha = 36.5$ (approaching line contact) the percent of load capacity to that when the inlet is fully flooded (i.e., $H_{in} = 1.00$) is about 85 percent. Whitaker and Dowson predict about 98 percent for a fluid inlet level corresponding to $H_{in} = .01$ ($\theta = -9^\circ$). This is understandable since the load bearing region for an elliptical contact per unit width would be less than that for a line contact per unit width. Further, our theory still allows for some side leakage even though $\alpha = 36.5$ (near line contact).
- (2) You are quite correct in pointing out that the Reynolds equation does account for reverse flow since it is derived from a flow balance. In my presentation, I have perhaps been careless to use reverse flow when it was intended to include the situation in which a circulation zone is set up downstream of the inlet meniscus without a net reverse flow. In this situation, the circulation represents a certain amount of fluid that does not pass through the contact and hence does not contribute to the load capacity. A bi-dimensional stream function analysis should be used to properly include the circulation effects on the inlet.

LUBRICANT EFFECTS ON EFFICIENCY OF A HELICOPTER TRANSMISSION

by

Andrew M. Mitchell
 NASA Lewis Research Center
 Cleveland, OH 44135

and

John J. Coy
 Propulsion Laboratory
 AVRADCOM Research and Technology Laboratories
 NASA Lewis Research Center
 Cleveland, OH 44135

SUMMARY

Efficiency tests were conducted using eleven different lubricants in the NASA Lewis Research Center's 500 hp torque regenerative helicopter transmission test stand. The test transmission was the OH58A helicopter main transmission. The mechanical power input to the test transmission was 224kW (300 hp) at 6060 rpm. Tests were run at oil-in temperatures of 355°K (180°F) and 372°K (210°F). The efficiency was calculated from a heat balance on the water running through an oil-to-water heat exchanger while the transmission was heavily insulated.

The following results were obtained.

1. Among the eleven different lubricants, the efficiency ranged from 98.3 to 98.8 percent, which is a 50 percent variation relative to the losses associated with the maximum efficiency measured.
2. For a given lubricant, the efficiency increased as temperature increased and thus as viscosity decreased. There were two exceptions which could not be explained on the basis of available data.
3. Between lubricants, efficiency was not correlated with viscosity. There were relatively large variations in efficiency with the different lubricants whose viscosity generally fell in the 5 to 7 centistoke range.
4. The lubricants had no significant effect on the vibration signature of the transmission.

INTRODUCTION

The mechanical efficiency of helicopter power train components is generally very high. As a rule of thumb, there is a loss of 3/4 percent for a planetary stage, and 1/2 percent for a single gear mesh. More specific estimates may be found in reference 1. An important step in development of the power transmission path in helicopters is to do everything possible to minimize power losses. Minimizing the power loss makes it possible to extend the performance envelope for the helicopter. Range, payload, and operating ceiling can be increased if efficiency is increased. With large, high power helicopter applications only a few tenths of one percent mechanical power loss can be the equivalent to the loss of hundreds of kilowatts. Compared with total power used this loss may seem trivial from an energy conservation viewpoint, but the effect on the operating envelope may be more significant. Since all mechanical power losses must be dissipated as heat, improvements in transmission efficiency will permit smaller and lighter weight cooling systems. This effect adds to increase the payload capacity of the helicopter.

The total power loss in a helicopter transmission is a function of many parameters. Sliding friction losses in the gears, bearings, and seals contribute a large effect. Sliding losses occur in whatever lubrication regime is present, whether the regime is hydrodynamic, elastohydrodynamic, boundary lubrication, or some mixture of these. Other large contributors to the losses are windage losses and lubricant churning losses in the rotating components. To a lesser extent rolling traction losses and material hysteretic losses are also contributors to total power loss. In a high speed transmission it is expected that a variety of physical and chemical characteristics of the oil influence the operating efficiency.

Martin (ref 2) presented a comprehensive review and bibliography of power loss calculations for friction between gear teeth. Martin (ref 3) concentrates on the problem of calculating the losses in the tooth contact. Anderson and Loewenthal (ref 4) give a more encompassing method of estimation of power losses which extends the calculation to partially loaded gear sets, including bearings. Bearing power loss was earlier addressed by Townsend, Allen, and Zaretsky (ref 5). Martin (refs 2 and 3) has pointed out that efficiency is important since it directly affects the cooling requirements of the gears. Townsend and Akin (refs 6 to 8) have studied gear tooth cooling and concluded that for best efficiency and cooling, the gears should be jet lubricated with radially directed jets on the exit side of the gear mesh.

Murphy, et al (ref 9) have studied the effect of lubricant traction on worm gear efficiency. They found that synthetic oils with lowest traction coefficients gave the best efficiency. This is to be expected since traction losses are the largest component of total loss in low speed worm gear sets which normally do not have much churning and windage losses.

In view of the above, the objective of the work presented herein was to measure the operating efficiency of a helicopter transmission with eleven different commercially available lubricants. A further objective was to examine the measured results for correlation with available physical property data on the lubricants and thereby determine reasons for the variability in efficiency from one lubricant to another.

APPARATUS, SPECIMENS, AND PROCEDURE

Transmission Test Stand

Figure 1 shows the NASA 500 HF helicopter transmission test stand, which was used to run the efficiency tests. The test stand operates on the "four-square" or torque regenerative principle, where mechanical power is recirculated around the closed loop of gears and shafting, passing through the test transmission. A 149kW (200hp) SCR controlled DC motor is used to power the test stand and control the speed. Since the torque and power is recirculated around the loop, only the losses due to friction have to be replenished.

A 11kW (15hp) SCR controlled DC motor driving against a magnetic particle clutch is used to set the torque in the test stand. The output of the clutch does not turn continuously, but only exerts a torque through the speed reducer gearbox and chain drive to the large sprocket on the differential gear unit. The large sprocket is the first input to the differential. The second input is from the upper shaft which passes concentrically through the hollow upper gear shaft in the closing end gearbox. The output shaft from the differential gear unit is the previously mentioned hollow upper gear shaft of the closing end gearbox. The torque in the loop is adjusted by changing the electrical field strength at the magnetic particle clutch. The 11kW (15hp) motor was set to turn continuously at 70 rpm.

The input and output shafts to the test transmission are equipped with speed sensors, torque meters, and slip rings.

Figure 2 is a schematic of the efficiency measurement system. The system allows the helicopter transmission to be operated in a thermally insulated environment with provisions to collect and measure the heat generation due to mechanical power losses in the transmission. In this schematic, the instrumentation used to measure torque and speed, and hence power input to the test transmission is not shown. The original oil-to-air heat exchanger which is standard flight hardware was replaced with an oil-to-water heat exchanger so as to allow more precise measurements of the heat rejection during an efficiency test run. By using the water to remove heat, any uncertainty of the correct value for specific heat of the oil was removed.

Figure 3 shows the test transmission mounted in the test stand. Figure 4 shows the test stand with the insulated housing around the test transmission. Thermocouples were placed at various locations inside the insulated housing to verify the adequacy of the insulation.

Test Lubricants

Tables 1 to 4 describe the lubricants used, their specification, physical properties and generic identification. All the lubricants were tested for physical properties, contaminants, and wear particles prior to and after completion of all test runs, as further described herein. Table 5 lists supplemental data related to the lubricants in this study which was gathered from references 10-12. All the lubricants were near to the 5-7 centistoke range in viscosity and were qualified for use or considered likely candidates for use in helicopter transmissions. Lubricants A and B are automatic transmission fluids (ref 13).

Test Transmission

The test transmission was the main rotor transmission from the U.S. Army's light observation helicopter (OH-58) as described in reference 14 and shown in figure 5. The transmission is rated for 201kW (270hp) continuous duty and 233kW (317 horsepower) at takeoff for 5 minutes. The 100 percent input speed is 354 rpm. The input shaft drives a 19 tooth spiral bevel pinion. The pinion meshes with a 71 tooth gear. The input pinion shaft is mounted on triplex ball bearings and one roller bearing. The 71 tooth bevel gear is carried on a shaft mounted in duplex ball bearings and one roller bearing. The bevel gear shaft drives a floating sun-gear which has 27 teeth. The power is taken out through the planet carrier. There are three planet gears of 35 teeth which are mounted on spherical roller bearings. The ring gear (99 teeth) is splined to the top case and therefore is stationary. The overall gear ratio is 17.44:1 reduction.

The planet bearing inner races and rollers are made of AISI M-50 steel. The outer races and planet gears, which are integral, are made of AISI 9310. The cage material is 2024-T4 aluminum. The gear shaft duplex bearing material is CVM 52CB. All other bearings are made of AISI 52100 with bronze cages. The sun gear and ring gear material is Nitralloy N (AMS6475). The input spiral bevel gear-set material is AISI 9310. Lubrication is supplied through jets located in the top case.

Test Procedure

Before the start of each efficiency test, the transmission and heat exchanger were cleaned out with solvent and the transmission components were visually inspected. Gear tooth surfaces were photographed. The transmission was then assembled and mounted in the test stand and filled with oil. The rig was run briefly to check for oil leaks. Then the loose fill insulation was added, filling the plexiglass box to completely surround and thermally insulate the test apparatus and transmission.

Efficiency test runs were made with the oil inlet temperature controlled to within less than one degree kelvin. Tests were run at oil inlet temperatures of approximately 355°K (180°F) and 372°K (210°F). The torque on the input shaft was 352 N-m (3118 lb-in) for each run. The input speed was 6060 rpm. This

corresponds to the full power condition on the test transmission. The oil inlet and oil outlet temperatures were monitored until equilibrium conditions were established, which generally took about 20-30 minutes. Then the efficiency test run was started. Water was collected in the weighing tank and data was recorded for total water weight, inlet and outlet temperatures for the water and oil, and flow rate for the water and oil. Vibration spectrum records were made for seven accelerometers mounted on the test transmission. Data logging records were taken once each minute for a total test time of approximately 30 minutes for each test temperature.

After the tests were completed the transmission was disassembled, cleaned and visually inspected for changes in the gear and bearing surfaces. Photographic records were made. The lubricant was saved for later analysis. The efficiency was later calculated from the heat balance on the water that flowed through the heat exchanger.

RESULTS AND DISCUSSION

The experimentally determined efficiencies are listed in table 6 and plotted against oil inlet temperature in figure 6. The range of efficiencies varied from 98.3 to 98.8 percent. This is an overall reduction in losses of almost 50 percent, relative to the losses associated with the maximum efficiency measured.

In general, the higher test temperature for a given lubricant yielded a higher efficiency. The exceptions were with lubricants E and C, which were different types of synthetic lubricant. Lubricant G, being more viscous than the other lubricants could not be tested at the targeted oil inlet temperature. This was because the heat generated could not be removed with the existing water/oil heat exchanger. The test temperature floated up to 378.5°K with the heat exchanger at full water flow capacity. At the higher temperature the efficiency for oil G was consistent with the efficiencies lower viscosity oils. The two automatic transmission fluids (A and B) and the Type I Synthetic Gear Lubricant (E) yielded significantly lower efficiencies as a group.

In figure 7 the efficiencies are plotted against the lubricant viscosity at the inlet temperature. This was done to determine if the efficiency is strongly dependent on the viscosity. By the plotted results, it is clear that viscosity variation is not the primary reason for the varying efficiencies between the different lubricants. But there is a general trend to higher efficiency for lower viscosity for all the lubricants except C and E. The slope of the aforementioned trend is identical for a large number of the lubricants.

The reason for the lower efficiency for lubricants A, B, and E is suspected to be related to higher traction coefficient characteristics, which would come into effect in the elastohydrodynamic regime of lubrication between the gear teeth. It is interesting to note that while the Mil-L-7808 lubricant was the lowest viscosity oil, the efficiency was no better than the Mil-L-23699 lubricants. This may also be related to an EHD tractional or frictional phenomenon. The reason for the reverse trends with viscosity for lubricants E and C is unknown at this time.

The vibration spectra were monitored during the tests with the various lubricants. The variations in amplitude were insignificant from one oil to the next. Figure 8 is a typical vibration spectrum measured by placing an accelerometer on the transmission case at the split line between the top and bottom cases.

Tables 7-10 give the comparison between the lubricant analyses performed before and after the efficiency test runs. It is noticed that lubricants A and C showed significant increases in the iron content (table 7). Also, lubricant E showed a strong acid value before and after the test runs (table 8). These three lubricants were among the ones giving deviant performances for efficiency.

The visual inspection of the transmission components after each test run showed no indications of wear or degradation. In fact, the black oxide coating which was placed on the gear surfaces during manufacturing was hardly worn off.

SUMMARY AND RESULTS

Efficiency tests were conducted using eleven different lubricants in the NASA Lewis Research Center's 500 hp torque regenerative helicopter transmission test stand. The test transmission was the OH58A helicopter main transmission. The mechanical power input to the test transmission was 224kW (300hp) at 6060 rpm. Tests were run at oil-in temperatures of 355°K (180°F) and 372°K (210°F). The efficiency was calculated from a heat balance on the water running through an oil-to-water heat exchanger while the transmission was heavily insulated.

The following results were obtained.

1. Among the eleven different lubricants, the efficiency ranged from 98.3 to 98.8 percent, which is a 50 percent variation relative to the losses associated with the maximum efficiency measured.
2. For a given lubricant, the efficiency increased as temperature increased and thus as viscosity decreased. There were two exceptions which could not be explained on the basis of available data.
3. Between lubricants, efficiency was not correlated with viscosity. There were relatively large variations in efficiency with the different lubricants whose viscosity generally fell in the 5 to 7 centistoke range.
4. The lubricants had no significant effect on the vibration signature of the transmission.

REFERENCES

1. Shipley, E. E.: Loaded Gears in Action, Gear Handbook, D. W. Dudley, ed., McGraw-Hill, 1962, pp. 14-1 to 14-60.
2. Martin, K. F.: A Review of Friction Predictions in Gear Teeth. *Wear*, Vol. 49, No. 2, Aug. 1978, pp. 201-238.
3. Martin, K. F.: The Efficiency of Involute Spur Gears. *ASME trans., J. Mech. Des.*, Vol. 103, No. 1, Jan. 81, pp. 160-169.
4. Anderson, N. E.; and Loewenthal, S. H.: Effect of Geometry and Operating Conditions on Spur Gear System Power Loss. *ASME trans., J. Mech. Des.*, Vol. 103, No. 1, Jan. 81, pp. 151-159.
5. Townsend, D. P.; Allen, C. W.; and Zaretsky, E. V.: Study of Ball Bearing Torque Under Elastohydrodynamic Lubrication. *ASME trans., J. Lub. Tech.*, Vol. 96, No. 4, Oct. 74, pp. 561-571.
6. Townsend, D. P.; and Akin, L. S.: Analytical and Experimental Spur Gear Tooth Temperature as Affected by Operating Variables. *ASME trans., J. Mech. Des.*, Vol. 103, No. 1, Jan. 81, pp. 219-226.
7. Townsend, D. P.; and Akin, L. S.: Study of Lubricant Jet Flow Phenomena in Spur Gears - Out of Mesh Condition. *ASME Trans., J. Mech. Des.*, Vol. 100, No. 1, Jan. 1978, pp. 61-68.
8. Akin, L. S.; and Townsend, D. P.: Cooling of Spur Gears with Oil Jet Directed Into the Engaging Side of Mesh at Pitch Point. paper b4, JSME proceedings, International Symposium on Gearing & Power Transmissions, Tokyo, 1981, Vol. 1, pp. 261-274.
9. Murphy, W. R.; et al.: The Effect of Lubricant Traction on Wormgear Efficiency. AGMA paper P254.33, Oct. 1981.
10. Willis, R. J.: General Electric Co. - Aircraft Engine Group, personal correspondence, July 15, 1980.
11. Mobil EHL Guidebook, Mobil Oil Corporation, Products Dept, 150 East 42nd St., New York, NY 10017, 1979.
12. Jones, W. R., Jr.; et al.: Pressure-Viscosity Measurements for Several Lubricants to 5.5×10^8 Newtons per Square Meter (8×10^4 psi) and 149°C (300°F). NASA TN D-7736, 1974.
13. Deen, H. E.; et al.: Bridging the Gap Between Dexron-II and Type F ATF. SAE paper 790019, 1979.
14. Townsend, D. P.; Coy, J. J.; and Hatvani, B. R.: OH-58 Helicopter Transmission Failure Analysis. NASA TM X-71867, 1976.
15. Evaluation of a Calorimetric Inc. Kit (CIK) as a Supplemental Oil Analysis Technique. U.S. Air Force Report AFWAL-TR-80-4022, 1980.
16. Greenberg, M. K.; and Newmann, F. K.: Application of Energy Dispersive X-Ray Fluorescence Spectroscopy to the Analysis of Contaminants in Fuels and Lubricants. U. S. Army Fuels and Lubricants Research Laboratory, Southwest Research Institute, San Antonio, TX, Report AFLRL No. 102, (AD-A062792), 1978.

Table 1
Test lubricant types

CODE NO.	SPECIFICATION	TYPE
A	DEXRON II GM 6137-M	Automatic Transmission Fluid
B	DEXRON II GM 6137-M	Automatic Transmission Fluid
C	MIL-L-23699	Turbine Engine Oil
D	MIL-L-23699	Type II Synthetic Gas Turbine Engine Oil
E		Type I Synthetic Gear Lubricant
F		Synthetic Paraffinic with Antiwear Additives
G	MIL-L-210 C MIL-L-4615	Synthetic Fleet Engine Oil
H	MIL-L-7808	Turbine Engine Oil
I	MIL-L-23699	Type II Turbine Engine Oil
J	MIL-L-23699	Type II Turbine Engine Oil
K		Turbine Engine Oil

Table 2
Specific Gravity Data According to ANSI/ASTM Specification D-1481,
API Gravity According to ANSI/ASTM *Specification D-1298

LUBRICANT	SPECIFIC GRAVITY @ LISTED TEMP			API GRAVITY 288°K
	313°K	355°K	373°K	
A	.8620	.8558	.8514	29.8
B	.8626	.8548	.8546	29.9
C	.9973	.9862	.9843	8.2
D	.9868	.9768	.9746	9.7
E	.9322	.9211	.9201	17.7
F	.8262	.8108	.8088	36.0
G	.8629	.8536	.8527	29.6
H	.9442	.9320	.9313	15.7
I	.9659	.9568	.9546	12.8
J	.9856	.9759	.9747	10.1
K	.9829	.9721	.9725	10.3

*ANSI/ASTM, American National Standards Institute/American Society for Testing and Materials

Table 3
Kinematic viscosity data according to
ANSI/ASTM Specification D-455

LUBRICANT	VISCOSITY @ LISTED TEMP, CSt		
	313°K	355°K	373°K
A	37.48	10.48	7.01
B	33.15	9.64	6.52
C	26.40	7.69	5.12
D	26.17	7.50	5.00
E	33.91	8.91	5.87
F	28.01	8.15	5.36
G	56.65	15.05	9.83
H	13.16	4.73	3.38
I	24.19	7.18	4.85
J	24.76	7.23	4.89
K	26.39	7.61	5.09

Table 4
Specific heat data according to
ANSI/ASTM Specification D-3947-80

LUBRICANT	SPECIFIC HEAT @ LISTED TEMPERATURE					
	313°K		373°K		413°K	
	Cp	σ	Cp	σ	Cp	σ
A	.42	.091	.42	.12	.44	.14
B	-	-	-	-	-	-
C	.33	.097	.32	.097	.32	.091
D	.33	.071	.34	.072	.34	.084*
E	.68	.11	.73	.13	.76	.20
F	.53	.12	.54	.13	.54	.14
G	.50	.091	.47	.058	.42	.059
H	.37	.036	.30	.037	.31	.094
I	.53	.060	.47	.039	.44	.075*
J	-	-	-	-	-	-
K	.44	.073	.38	.076	.34	.075

*For calculation of Cp and σ (std. deviation) one value, inordinately different from the others, was discarded. Thus, four values rather than five were used to determine these data.

Table 5
Pressure-viscosity coefficients for test lubricants
expressed as reciprocal asymptotic isoviscous pressures

LUBRICANT	RECIPROCAL ASYMPTOTIC ISOVISCIOUS PRESSURE, α^* , (N/m ²) ⁻¹ @ LISTED TEMPERATURE			SOURCE OF DATA
	311°K	372°K	422°K	
A	1.35x10 ⁻⁸	.951x10 ⁻⁸	.772x10 ⁻⁸	ref 11
B	a	a	a	
C	-	1.01x10 ⁻⁸	.832x10 ⁻⁸	ref 10
D	b	b	b	
E	-	-	-	
F	1.90x10 ⁻⁸	1.50x10 ⁻⁸	1.15x10 ⁻⁸	ref 12 ^c
G	1.42x10 ⁻⁸	1.02x10 ⁻⁸	.918x10 ⁻⁸	ref 11
H	-	.894x10 ⁻⁸	.731x10 ⁻⁸	ref 10
I	b	b	b	
J	b	b	b	
K	1.28x10 ⁻⁸	.987x10 ⁻⁸	.851x10 ⁻⁸	ref 12

^a most likely the same as A since they are similar lubricants

^b most likely the same as C or K since they are similar lubricants

^c estimate based on ref 12

Table 6
Measured efficiencies

LUBRICANT	EFFICIENCY	INLET TEMP, °K
A	.9840	361.5
	.9850	375.0
B	.9833	356.8
	.9843	375.0
C	.9876	356.4
	.9873	371.5
D	.9860	356.1
	.9874	370.1
E	.9835	361.0
	.9832	371.5
F	.9865	355.7
	.9877	372.0
G	.9873	378.7
H	.9870	355.6
	.9879	372.1
I	.9864	355.6
	.9882	372.2
J	.9864	355.6
	.9877	372.3
K	.9869	355.6
	.9882	372.3

Table 7
Total iron analysis by
calorimetric method (ref 15)

LUBRICANT	IRON CONTENT (ppm)	
	BEFORE TEST	AFTER TEST
A	1	4
B	<1	<1
C	1	6
D	<1	1
E	<1	1
F	<1	2
G	2	3
H	<1	1
I	<1	<1
J	<1	<1
K	<1	<1

Table 8
Lubricant acid analysis according to
ANSI/ASTM Specification D-664

LUBRICANT	TOTAL ACID NUMBER Mg KOH/g	
	BEFORE TEST	AFTER TEST
A	.54	.54
B	-	-
C	.01	.02
D	.07	.07
E	15.8*	15.7†
F	.42	.51
G	3.2	3.5
H	.34	.34
I	.34	.38
J	-	-
K	.48	.43

* Strong acid value = 7.1 on sample

† 6.2 acid value

Table 9
 Particulate contamination count according to
 SAE Aerospace Recommended Practice ARP 598A

LUBRICANT BEFORE AFTER	Number of Particles/100ml					
	Particle Sizes in Micrometers					
	5-15	15-25	25-50	50-100	100	Fibers
A	17 4	2 1	2 6	4 7	10 11	12 10
B	-	-	-	-	-	-
C	72 4	36 1	18 2	12 1	10 5	7 9
D	685 200	275 65	35 38	22 24	15 21	20 39
E	120 44	60 7	23 10	25 13	22 12	33 19
F	60 475	16 8	30 2	13 5	7 6	22 52
G	49 4740	39 10	45 11	38 9	34 6	78 34
H	1780 1850	72 118	45 108	40 60	25 52	32 62
I	54 840	23 660	17 450	16 210	4 80	19 120
J	-	-	-	-	-	-
K	185 105	175 48	100 35	70 21	35 20	45 22

Table 10
Wear metals test results using x-ray fluorescence filter method (ref 16)

LUBRICANT BEFORE AFTER	ELEMENTS (PPM)												LIMIT(3) OF DETECTION (PPM)
	Mg	Al	Cl	Fe	Ni	Cu	Pb	Zn(1)	P(2)	S(2)	Ca(2)	Ba(2)	
A	0.48 -	- 5.91	2.47 1.12	- 0.51	- 0.10	- 0.14	0.21 -	- 0.11	0.18 0.17	4.71 1.12	- -	0.23 0.12	0.11 0.09
B	-	-	-	-	-	-	-	-	-	-	-	-	-
C	0.28 -	- 2.97	0.73 1.04	0.13 2.19	- 0.21	- 0.12	- -	- 0.15	0.26 0.19	- 0.20	- -	- -	0.09 0.09
D	0.27 -	- 12.7	0.90 2.08	- 1.16	- 0.24	- 0.19	- 0.20	- 0.20	0.16 0.71	- 0.51	- -	- -	0.11 0.15
E	0.16 0.12	0.19 1.69	7.57 1.61	0.10 0.26	- -	- 0.11	1.28 -	7.27 3.71	2.15 0.94	13.01 4.29	0.29 -	10.16 2.43	0.09 0.09
F	0.31 5.36	- -	0.45 2.49	- -	- -	- -	- -	- -	0.19 2.42	7.08 51.0	- -	- -	0.10 0.55
G	1.31 0.39	- 0.67	4.91 1.49	- 0.22	- -	- -	- -	1.51 0.39	0.70 -	5.29 0.89	8.69 2.53	- -	0.43 0.13
H	0.29 0.67	- 4.68	3.81 16.68	0.11 0.74	- -	- 0.26	0.16 -	- 0.62	0.47 2.37	0.21 3.20	- 3.47	- -	0.10 0.25
I	0.33 0.34	- 1.18	0.56 0.85	- 0.58	- -	- -	0.11 0.12	- 0.13	0.58 0.46	- 0.16	- -	- -	0.10 0.11
J	-	-	-	-	-	-	-	-	-	-	-	-	-
K	0.60 1.26	- 0.39	9.80 7.30	0.28 0.56	- -	- -	- 0.65	- -	2.51 1.86	- -	- -	- -	0.24 0.37

(1) Zn could be due to wear when present with copper, or as an additive when present alone.

(2) P, S, Ca, Ba probably present as additives.

(3) Limit of detection for sample, when - shown, element is less than this value.

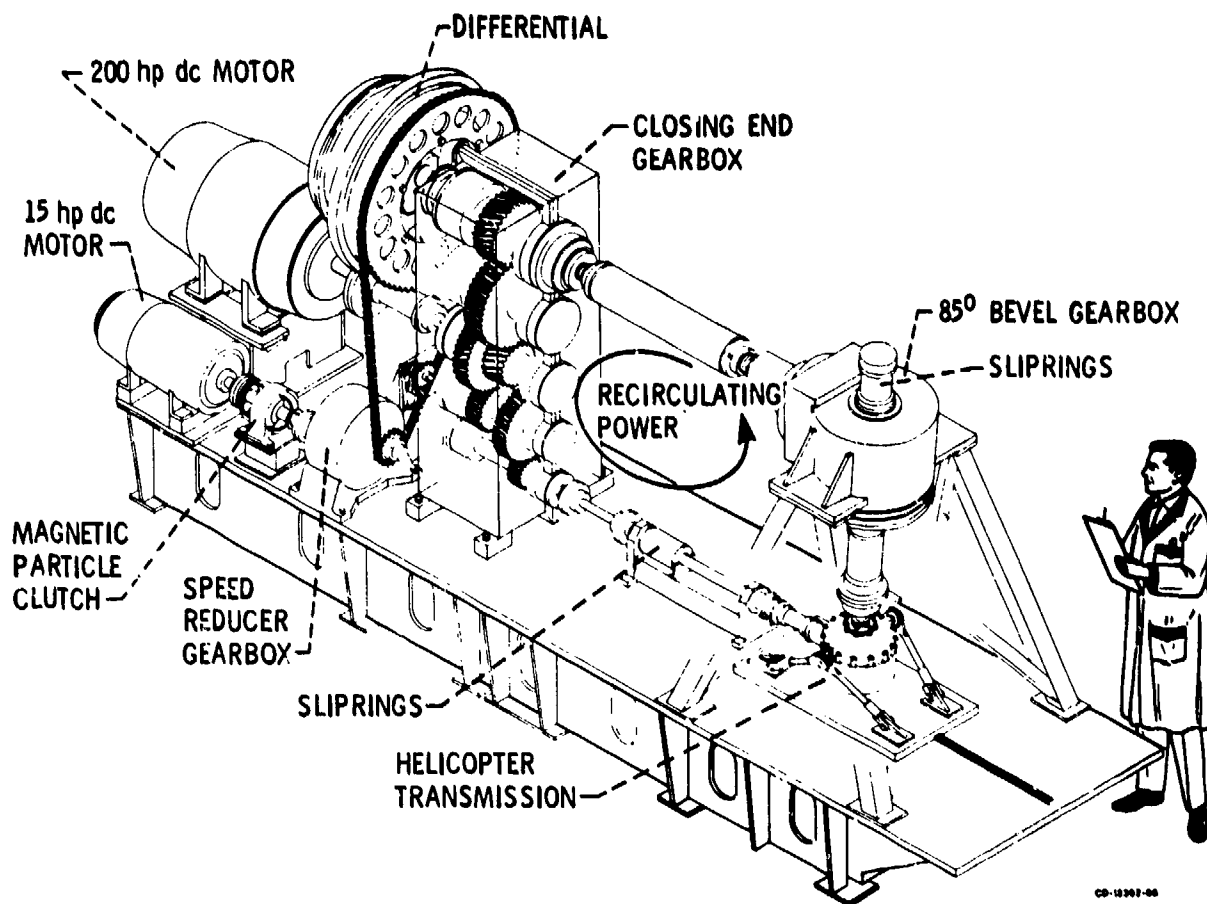


Fig.1 NASA 500 hp helicopter transmission test stand

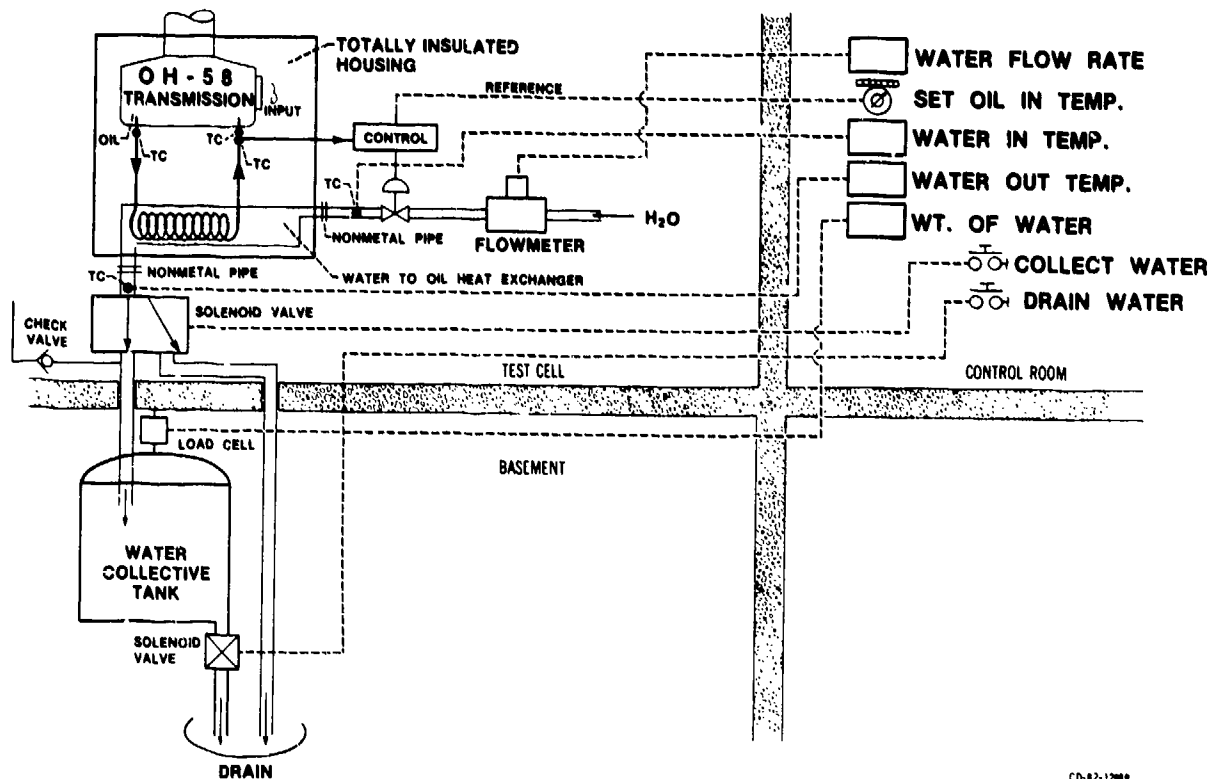


Fig.2 Schematic of measurement system

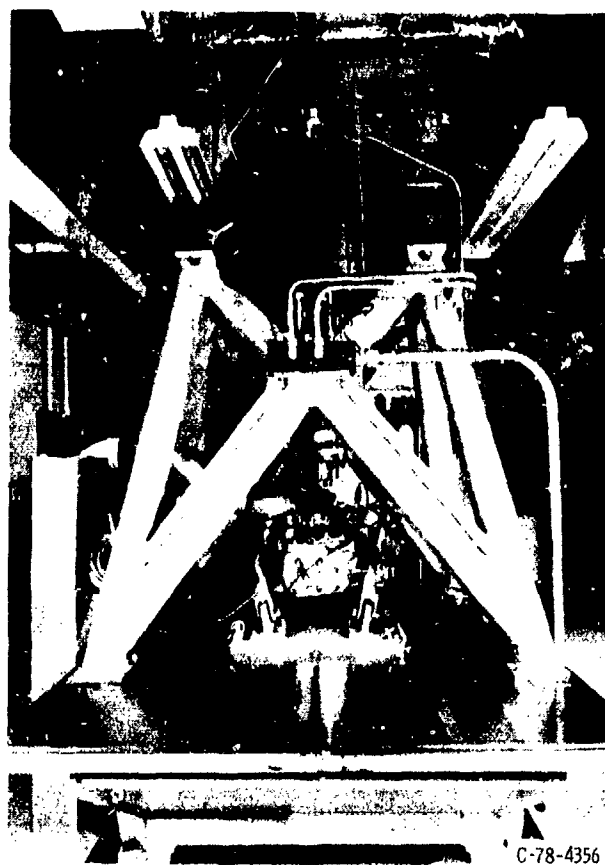


Fig.3 View of test stand showing OH-58 transmission installed

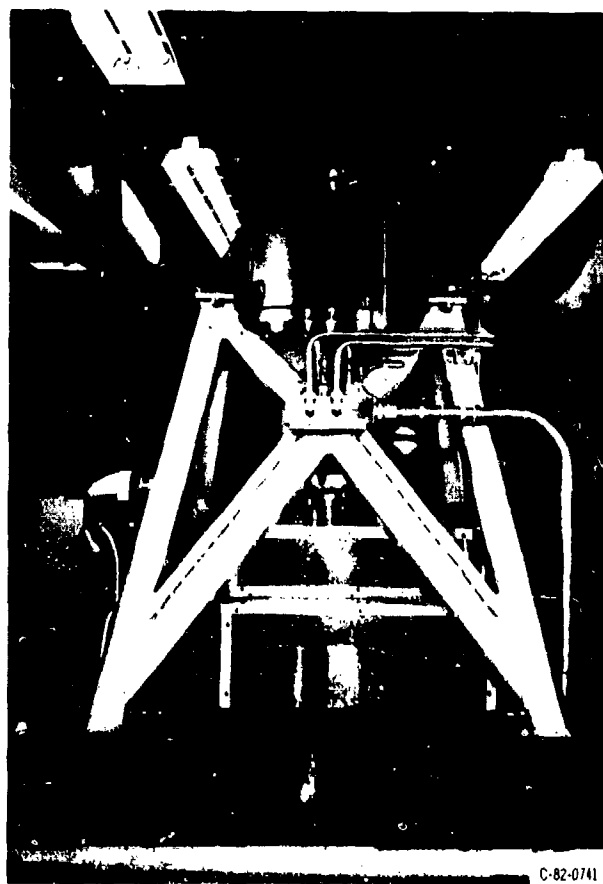


Fig.4 View of test stand showing insulated transmission housing

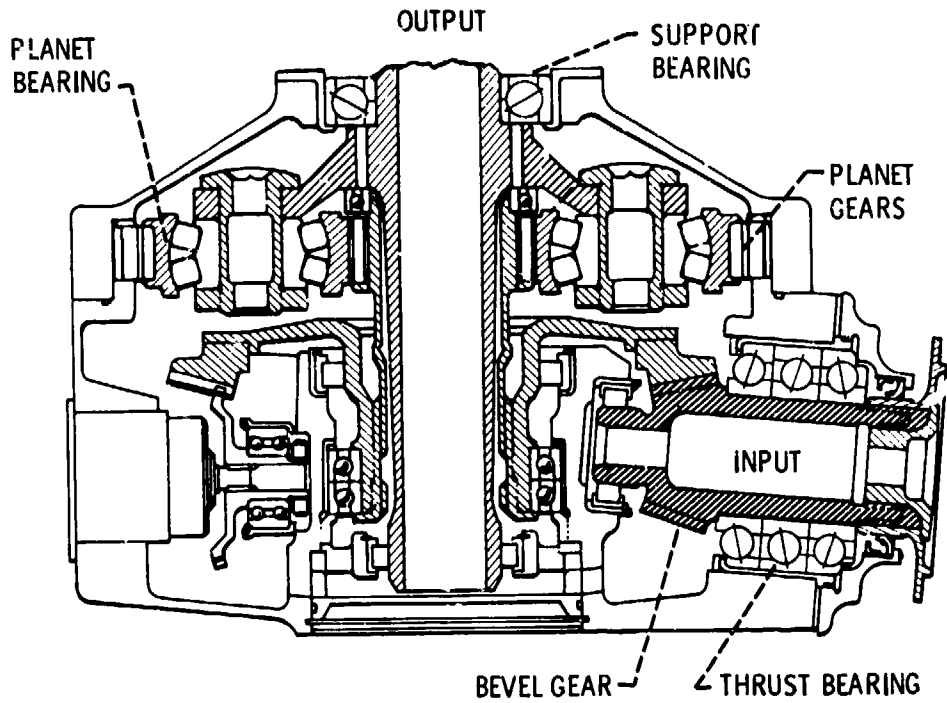


Fig.5 Cross section of OH-58 helicopter transmission

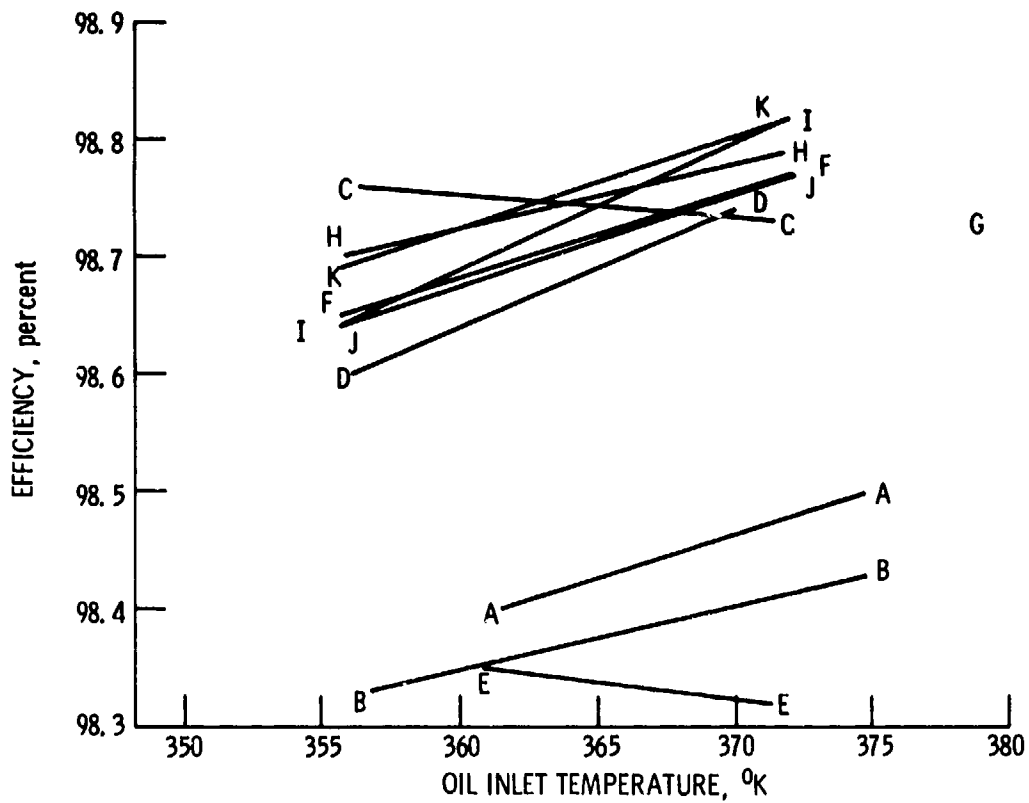


Fig.6 Experimental efficiency correlated with inlet oil temperature

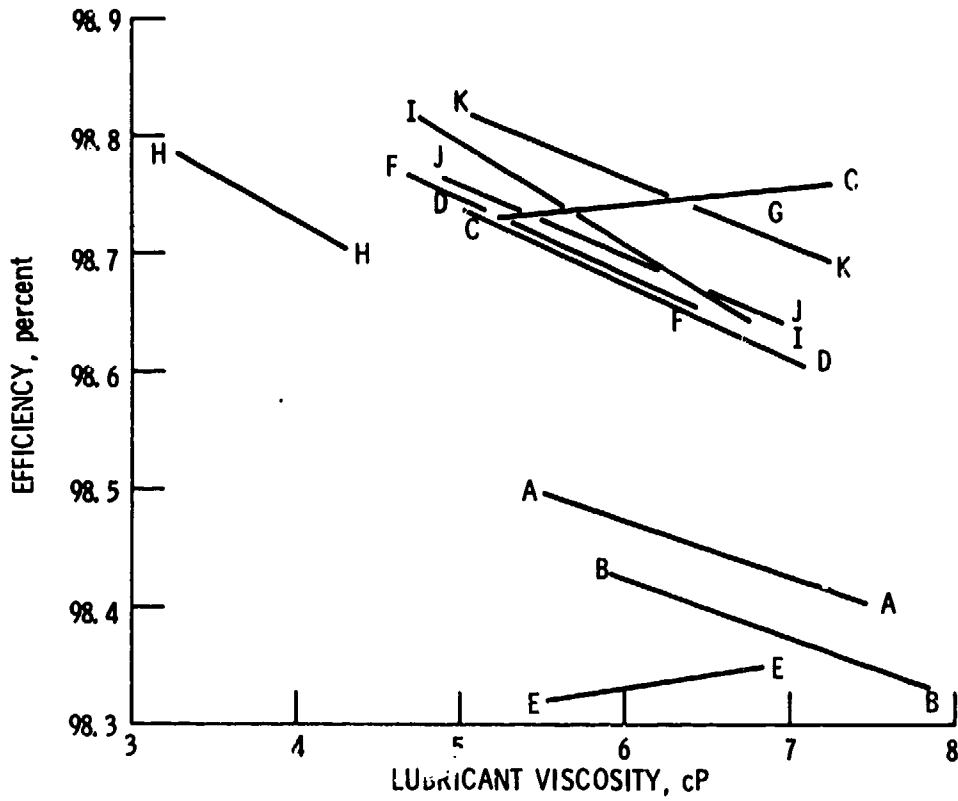


Fig.7 Experimental efficiency correlated with lubricant viscosity

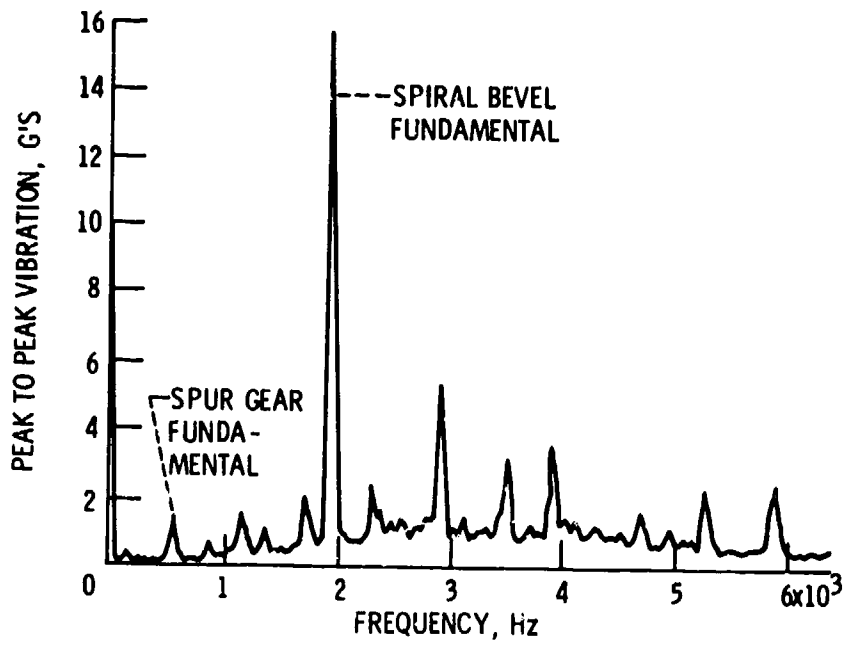


Fig.8 Typical vibration spectrum

DISCUSSION

P.T.Cornish, SNFA Bearings Ltd, UK

Was the effect of transmitted power level (both by change of torque and speed) on efficiency studied?

Author's Reply

Parametric explorations of efficiency were made to determine the effect of speed and torque. There was very little effect of speed, but with torque, beginning at less than about 90 percent of full load torque, the efficiency decreased sharply and continued to decrease as the torque decreased.

F.Snyder, University of Waterloo, Ca

- (1) What type of solvent did you use to clean the transmission?
- (2) In what order were the lubricants tested; and could the efficiency of lubricant "A" be reproduced after testing one of the lubricants with an anti-wear additive.

Author's Reply

- (1) The transmission and heat exchanger were taken apart and the parts were cleaned in trichlorethylene with a final rinse in alcohol.
- (2) The lubricants were tested in the order as listed in the tables. Lubricant C was the lubricant used in repeat testing as well as in other types of parametric tests. When the tests with this lubricant were repeated, the same results within 0.1 percent efficiency points were obtained. Tests were repeated on the same day as well as several months apart. The lubricant known to have the strongest additive package was tested last. The lubricant C was not run again after that. According to Mr Charles Braddock of Bell Helicopter, rehousing the gears is the only sure way to remove the surface reactants. This, of course, was not done in our program.

D.G.Astridge, Westland Helicopters, Yeovil, UK

- (1) What level of filtration was used?
- (2) Were any repeat tests done -
 - (a) Before and after gearbox strip -- influence of build?
 - (b) First oil repeated at end of test-influence of wear?

Author's Reply

- (1) The standard filter was used which I believe is 30-40 micron, nominal.
- (2) (a) There were no influences of build noticed, but the teardown between tests was only partial. The input bearings and pinion were not removed from the lower case between tests.
- (b) The question about repeating the test has been answered before. The tests were not long enough to cause significant changes in wear. The gearbox was well worn in before tests had begun, having approximately 100-200 hours on it.

W.E.A.Fries, Ministry of Defense, Ge

Did you monitor wear during the gear box tests, and, if so, which methods were used?

Author's Reply

Yes, two methods of wear analysis were used. For iron content before and after the test, please refer to Table 7; and for other wear metals see Table 10. Particle counts are reported also in Table 9. The oral presentation had to be brief and the materials presented in the tables could not be discussed. There is, however, much interesting data there for those who are inclined to study it closer.

B.Courage, Rolls Royce Ltd, Bristol, UK

Your tests were run with an internal lube pump. Do you have any data on the significance of oil flow rate from other tests and do you consider it likely that the viscosity or temperature influence may be exaggerated in practice because the flow rate will reduce as the temperature increases.

Author's Reply

The lubricant flow rate was monitored with a turbine type flow meter. In all, the observed flow rates fell in the range of 4.8 to 5.3 gal/min, with the higher flow at the higher temperature. No tests were run for the purpose of discovering the effect of lubricant flow rate, for a constant inlet temperature. I think this would be an excellent thing to do.

K.J. Brown, Ontario Hydro, Toronto, Ca

As you are reporting on very small differences in the efficiency could you please comment on the repeatability of the tests.

Also have the differences in the efficiency been compared to the pressure viscosity or traction coefficient of the various fluids used?

Author's Reply

These are very discerning questions. The question of repeatability has already been dealt with, but there is the aspect of the "small differences" in efficiency in this question. One must remember that when the heat balance method is used, the measurement is on the heat rejection and not on the total mechanical power. If the measurement accuracy on heat rejection is ± 10 percent repeatable and the total efficiency is near 99%, then the measurement for mechanical efficiency is 0.1% repeatable. I feel that the measurement accuracy on the heat rejection is better than 10% accurate and repeatable and, therefore, the measurement expressed as mechanical efficiency is better than 0.1% accurate. Laboratory accuracy in measurements of this type of 1% percent (of the quantity measured) are possible to achieve.

The pressure-viscosity coefficients and traction properties are currently being measured and will be reported in the near future. I am very anxious to get this data.

THE DYNAMIC PERFORMANCE OF THE SELF-REGULATED HYDROSTATIC OPPOSED-PAD BEARING

by

R. BASSANI* - B. PICCIGALLO**

* Professor, Dipartimento di Costruzioni Meccaniche e Nucleari, Università di Pisa, Via Diotisalvi, 2, 56100 Pisa,

** Assistant Professor, Gruppo Costruzioni, Accademia Navale, 57100 Livorno, Italy.

SUMMARY

The work deals with the behaviour, under dynamic loading, of a special hydrostatic opposed-pad bearing: the "self-regulated" bearing (capable of dividing the lubricant flow into two equal partial flows in the two recesses as a consequence of its own shape). The bearing is studied in a constant pressure system. The effect of a hydraulic resistance in series with the bearing is also considered. Consequences which may arise from dimensional inaccuracies due to tolerances are also accounted for.

Like the static performance, the dynamic performance of the self-regulated bearing is often better than that of conventional bearings; stiffness in particular is much greater. The influence of tolerances may not always be negligible.

The design of a standardizing self-regulated bearing is also presented.

LIST OF SYMBOLS

A	= effective area
C, C', C _d	= damping coefficients (see (2.10), (3.2), (3.3))
F	= external force
g _s = h _{s, I} + h _{s, II}	= axial play
g _i = h _{i, I} + h _{i, II}	= " "
g _c = h _{i, I} + h _{s, I}	= " "
h ₀	= design amplitude of clearances when P=0
h _{i, I} , h _{i, II} , h _{s, I} , h _{s, II}	= amplitude of clearances (see Fig. 1)
K	= linearized bearing stiffness
M	= moving mass
M	= mass parameter
P	= load capacity of the bearing
P _p ⁱ , P _p ⁱⁱ	= dimensionless static load capacity
P _d ⁱ , P _d ⁱⁱ	= dimensionless dynamic load capacity
p̄	= supply pressure (at the bearing inlet)
p̄	= constant pressure of feeding system
P _s , P _i	= recess pressures
Q	= supply flow rate
Q _p ⁱ , Q _p ⁱⁱ	= dimensionless static flow rate
Q _d ⁱ , Q _d ⁱⁱ	= dimensionless dynamic flow rate
R	= theoretical hydraulic resistance of the bearing, when ε = 0
R _{i, I} , R _{i, II} , R _{s, I} , R _{s, II}	= hydraulic resistance of bearing clearances
R̄	= feeding restrictor resistance
r _n	= bearing radii (see Fig. 1)
r _f	= r ₂ /r ₅
r _u	= r ₂ /r ₃ = r ₄ /r ₅
z	= bearing displacement from steady unloaded states
β	= restrictor parameter for conventional bearings
γ	= restrictor parameter for self-regulated bearings
Γ _p ⁱ , Γ _p ⁱⁱ	= dimensionless static supply pressure
Γ _d ⁱ , Γ _d ⁱⁱ	= dimensionless dynamic supply pressure
δ	= damping parameter
ε = z/h	= eccentricity
ε _s , ε _c	= vibration amplitudes for self-regulated and conventional bearing
η _{i, I} , η _{i, II} , η _{s, I} , η _{s, II}	= dimensionless clearance thickness, for P=0
μ	= lubricant viscosity
Π _p	= ratio between static load capacities of conventional and self-regulated bearings
Π _d	= the same, for dynamic load capacity
φ	= dimensionless external force

1. INTRODUCTION

The features of hydrostatic lubrication are well known: especially high load capacity and stiffness, even at zero speed, and low friction, even at high speed /1/. In addition, such lubrication may prove to be useful in special environmental conditions, for example, at extreme temperatures, that suggest the use of bearing materials with poor wear properties: in such cases, hydrodynamic lubrication may not prevent galling and surface welding.

Such features are already sufficient hydrostatic lubrication to be considered advantageous in the field of aerospace: in propulsion, control and experimental apparatuses /2/.

It is also known that there are typical supply systems of hydrostatic pairs: the constant flow system and the constant pressure system; the latter involves less load capacity and stiffness than the former, but it is simpler.

Furthermore, a recent type of hydrostatic lubrication must also be borne in mind: "self-regulated hydrostatic lubrication" the properties of which are better than those of conventional lubrication /3/.

The principle of self-regulation for incompressible flow, is explained in Fig. 1, with reference to an opposed pad thrust bearing, under static load. The principle is valid apart from the supply system (in Fig. 1 a constant pressure system is shown). The

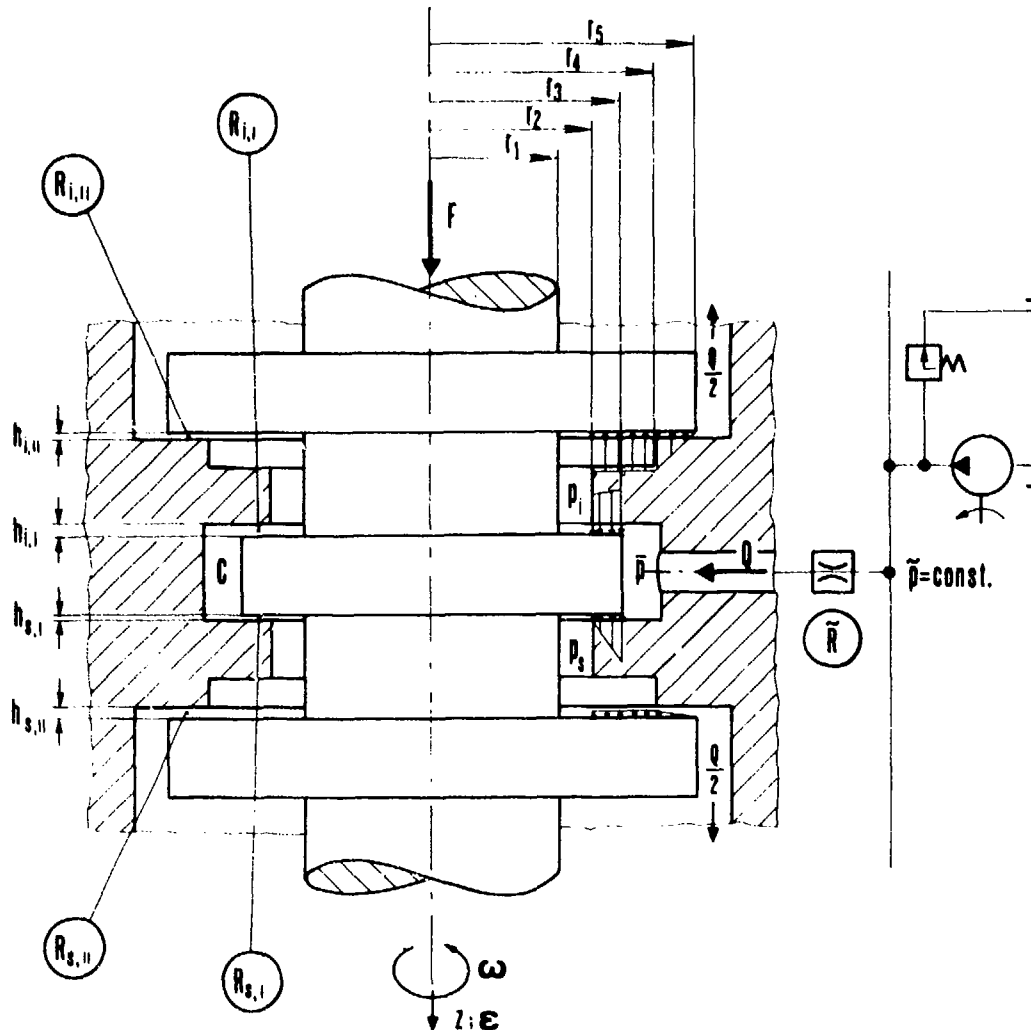


Fig. 1 - The self-regulated hydrostatic opposed-pad thrust bearing.

total flow rate Q supplied to the central annular cavity C is divided into two parts. One part Q_s passes first through one and then through the other of gaps (hydraulic resistances) $R_{s,I}$ and $R_{s,II}$ of the upper semibearing, and the other part Q_i passes in the same way through gaps $R_{i,I}$ and $R_{i,II}$ of the lower semibearing. The hydraulic resistances of the aforesaid semibearings are respectively $R_s = R_{s,I} + R_{s,II}$, $R_i = R_{i,I} + R_{i,II}$.

If the load is zero, symmetry requires:

$$R_s = R_i$$

(1.1)

and the two partial flow rates Q_s and Q_i are equal to $Q/2$.

If, furthermore, the relation

$$r_4 / r_5 = r_2 / r_3 \quad (1.2)$$

is satisfied, then $R_{s,I} = R_{s,II}$, $R_{i,I} = R_{i,II}$ and, therefore, also

$$R_{s,I} = R_{i,II}, \quad R_{i,I} = R_{s,II} \quad (1.3)$$

If the load is not zero, the shaft moves in relation to the bearing, but (1.3) and consequently (1.1) are still valid, and the two partial volume flow rates are still equal to $Q/2$. The load is supported by the resultant of the pressures in the two semibearings.

The principle has been applied both to opposed pad bearings /4,5/, and to other pairs /6,7/, under static loads: they are more efficient than the corresponding conventional hydrostatic pairs.

An opposed-pad hydrostatic self-regulated bearing in a constant flow system has also been studied under dynamic loads /8/. It is more efficient than the conventional bearing, as far as load capacity, stiffness and damping are concerned.

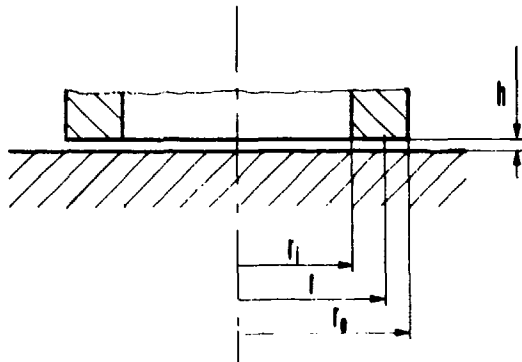
In this paper the aforesaid bearing in a constant pressure system, the most widely used in practice, is studied under dynamic loads. The effect of a hydraulic resistance (capillary restrictor) in series with the bearing is also considered. Consequences arising from dimensional inaccuracies due to tolerances are also accounted for. The behaviour of the bearing is compared with that of a conventional bearing. A standardized type of such a bearing and its dynamic features are given.

2. ANALYSIS

2.1

For an annular gap (Fig. 2), it is found on the basis of Stokes equation, and making suitable assumptions, that:

$$\frac{\partial p}{\partial r} = - \frac{6\mu}{\pi h^3 r} q \quad (2.1)$$



where q is the rate of flow of lubricant through the cylindrical surface at radius r ; q is stated to be positive when flowing from the inner edge r_i to the outer edge r_e . From (2.1) and the continuity equation:

$$\frac{\partial q}{\partial r} = -2\pi r h \dot{h} \quad (2.2)$$

the Reynolds equation is obtained for the annular gap:

$$\frac{h^3}{12\mu} \left[\frac{\partial^2 p}{\partial r^2} + \frac{1}{r} \frac{\partial p}{\partial r} \right] = \dot{h} \quad (2.3)$$

By integrating (2.3) with suitable boundary conditions, the pressure pattern in the gap may be obtained. So if p and q are known at the inner radius r_i

$$p(r) = p(r_i) - \frac{6\mu}{\pi h^3} \left[q(r_i) \ln \frac{r}{r_i} - \pi \dot{h} \left(\frac{r^2 - r_i^2}{2} - r_i^2 \ln \frac{r}{r_i} \right) \right] \quad (2.4)$$

If the inner and outer pressure are known:

$$p(r) = p(r_i) - \frac{\ln \frac{r}{r_i}}{\ln \frac{r_e}{r_i}} \left[p(r_e) - p(r_i) \right] + \frac{3\mu \dot{h}}{h^3} \left[(r_e^2 - r_i^2) \frac{\ln \frac{r}{r_i}}{\ln \frac{r_e}{r_i}} + r^2 - r_i^2 \right] \quad (2.5)$$

In the same way, from (2.2), the flow pattern may be obtained

$$q(r) = q(r_i) - \pi \dot{h} (r^2 - r_i^2) = q(r_e) + \pi \dot{h} (r_e^2 - r^2) \quad (2.6)$$

2.2

The load capacity for the annular gap is obtained by integrating pressure on the total pad area: if outer and inner pressures are known and (2.5) is integrated, load capacity is given by:

$$P = \pi(r_e^2 - r_i^2)p(r_i) + \frac{\pi}{2} [p(r_e) - p(r_i)] \left[2r_e^2 + \frac{r_e^2 - r_i^2}{\ln \frac{r_i}{r_e}} \right] - \frac{3}{2} \pi \frac{\mu \dot{h}}{h^3} \left[r_e^4 - r_i^4 + \frac{(r_e^2 - r_i^2)^2}{\ln \frac{r_i}{r_e}} \right] \quad (2.7)$$

For a given pad, P turns out to be the sum of a "static" term depending on edge pressures, and of a "dynamic" term depending on the clearance and the relative velocity of the surfaces.

2.3

With the aid of the expressions obtained in the previous paragraphs, it is now possible to study the static and dynamic behaviour of the self-regulated bearing (SRB), which is outlined in Fig. 3 from a hydraulic point of view. The four annular gaps are reduced to four hydraulic resistances; \bar{p} is the pressure in the main cavity C and \bar{p} the supply pressure; if \bar{R} (the hydraulic resistance of the feeding system) is negligible, it is obvious that $\bar{p} = \bar{p}$. Concerning k , it must be noted that it is sometimes useful to insert a suitable restrictor in series with the bearing to reduce the lubricant flow rate with a certain loss in stiffness under light and medium loads) /9/.

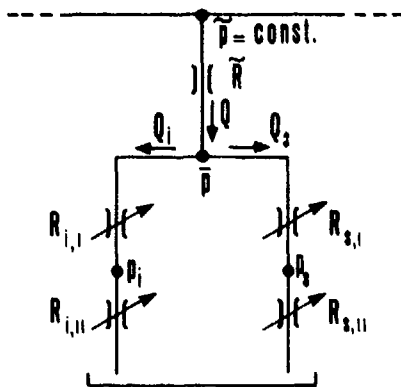


Fig. 3 - Hydraulic pattern of the self-regulated bearing.

As long as the self-resultating condition is present, it requires the four pad clearances to be equal when there is no external load. Due to tolerances, it can only occur in an approximate way. If the design value of the clearances in the centered (no-load) status is called h_0 (h_0 therefore equals half the designed bearing axial play), and the axial displacement from the centered position is called z , the four bearing clearances may be written as follows:

$$\left. \begin{aligned} h_{i,I} &= h_0(\eta_{i,I} + \epsilon) & h_{i,II} &= h_0(\eta_{i,II} - \epsilon) \\ h_{s,I} &= h_0(\eta_{s,I} - \epsilon) & h_{s,II} &= h_0(\eta_{s,II} + \epsilon) \end{aligned} \right\} \quad (2.8)$$

where $\epsilon = z/h_0$. The $\eta_{j,K}$ are dependent on geometry: in the "ideal" case, all $\eta_{j,K}$ values equal 1 (see App. A.1). Calling γ the \bar{p}_0/\bar{p} ratio (where \bar{p}_0 is the \bar{p} pressure in the steady unloaded status), since \bar{p} and \bar{R} are

not dependent on flow rate, it is found (see App. A) that pressure \bar{p} , flow rate, and load capacity are:

$$\begin{aligned} \bar{p} &= \bar{p} \Gamma'_p \Gamma''_p + h_0 R A \Gamma'_d \Gamma''_d \dot{\epsilon} \\ P &= \bar{p} A P'_p P''_p + C_d P'_d P''_d \dot{\epsilon} = \bar{p} A \Gamma'_p \Gamma''_p P'_p P''_p + A^2 R h_0 P'_p P''_p \Gamma'_d \Gamma''_d \dot{\epsilon} + C_d P'_d P''_d \dot{\epsilon} \\ Q &= \frac{\bar{p}}{R} Q'_p Q''_p - A h_0 Q'_d Q''_d \dot{\epsilon} \end{aligned} \quad (2.9)$$

In the above expressions certain constants appear: A (bearing effective area), R (bearing hydraulic resistance when $\epsilon = 0$, $\dot{\epsilon} = 0$, $\eta_{j,K} = 1$), C_d (bearing damping when $\epsilon = 0$, $\eta_{j,K} = 1$, $\gamma = 1$), whose values are:

$$A = - \frac{\pi r_5^2}{2} \frac{\left(1 - \frac{r_f'^2}{r_u'^2}\right) (1 - r_u'^2)}{\ln r_u'} \quad (2.10)$$

$$R = - \frac{6\mu}{\pi h_0^3} \ln r_u' \quad C_d = \frac{3}{2} \frac{\pi \mu r_5^4}{h_0^2} (1 - r_u'^2)$$

Functions P'_p , Q'_p , Q'_d depend solely on ϵ ; P'_d also depends on geometrical ratios r'_f and r'_u , and Γ'_p , Γ'_d depend on ϵ and γ . Expressions of these functions are given in App. A whereas their pattern is shown in Fig. 4. In Fig. 4-a "static" functions Γ'_p , Q'_p , P'_p are versus ϵ and in Fig. 4-b the "dynamic" functions Γ'_d , Q'_d , P'_d are versus ϵ . P'_d is calculated for some values of r'_f , while r'_u is assumed to suit the relevant "optimal" value, from the point of view of pumping power /4/.

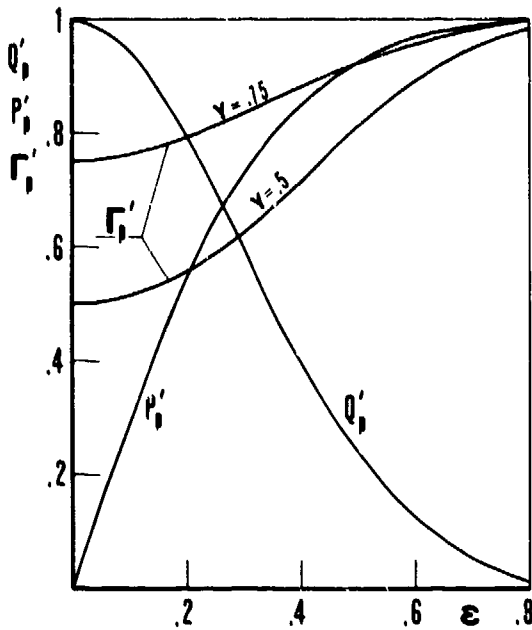


Fig. 4a) - "Static" values of flow rate Q'_p , load capacity P'_p .

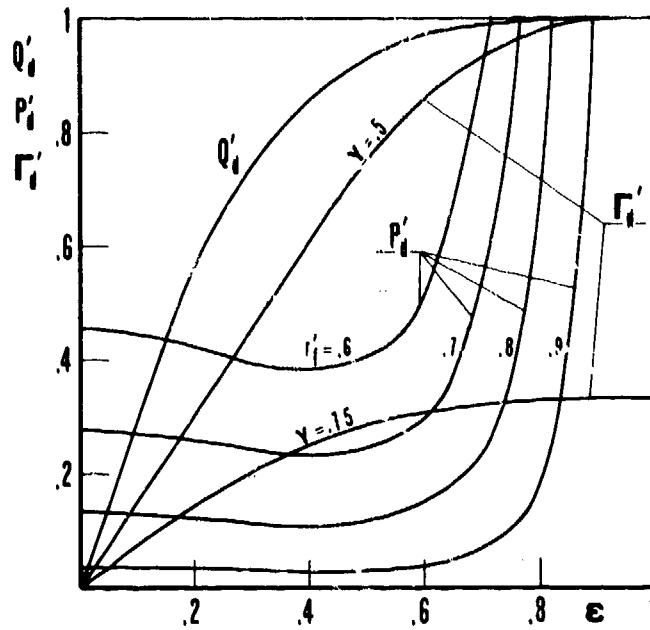


Fig. 4b) - "Dynamic" values P'_d , Q'_d and Γ'_d as functions of ε .

Two-apices functions depend on the same parameters, but the η_{jk} are also accounted for, and are identical to 1 when there are no clearance errors; their expressions are given in App. A.

The influences of η_{jk} on the static performance of the bearing are treated in /9/; the main points stated there are the following:

- it is advisable to assign manufacture tolerances in such a way that axial play is always less than (or equal to) $2h_0$;
- the load capacity pattern may become asymmetrical, that is $-P(-\varepsilon)$ may differ from $P(\varepsilon)$;
- due to reduction in axial play, the maximum load may be considerably less than the theoretical value $\bar{p}A$;
- stiffness for low ε values (<0.5) may be considerably more or less than the ideal case;
- the maximum rate of flow proves, in general, to be less than the ideal case.

In most cases, the most dangerous condition occurs when $g_s = g_i = 2h_0$ and $g_c < 2h$, in which the highest stiffness loss occurs.

In Fig. 5 P''_p , Γ''_p , Q''_p , P''_d , Γ''_d and Q''_d are plotted for $g_c = 1.6h_0$ hence $\eta_{i,I} = \eta_{s,I} = 0.8$; $\eta_{i,II} = \eta_{s,II} = 1.2$ and $g_c = 1.4h_0$ ($\eta_{i,I} = \eta_{s,i} = 0.7$; $\eta_{i,II} = \eta_{s,II} = 1.3$).

2.4

In order to help in evaluating the SRB performance, a comparison is made in Fig. 6 between the above and the conventional bearings regulated by capillary restrictors (see App. B).

Before making the comparison it must be noted that:

- all geometrical parameters (r_5 , h_0 , r_f , r'_u) must agree;
- both bearings are supplied at the same constant pressure \bar{p} with the same lubricant at the same temperature;
- in the conventional assembly, restrictors have to be set in such a way that the maximum flow rate is equal to the self-regulated flow rate: hence it must be $\beta = 0.25\gamma$.

In Fig. 6, Π_p (the ratio between the static load capacities of conventional and self-regulated bearings) and Π_d (the ratio between dynamic load capacities) are shown for $\gamma = 1$ and $\beta = 0.25$ (Π_d proves to be virtually independent from r'_p).

SRBs show better static performance. The stiffness pattern of the SRB remains better if even great errors in clearance values are tolerated, as in Fig. 5 (moreover, it should be considered that, in such a case, the maximum flow rate requirements are greatly reduced too). Concerning flow rate, it must be noted that, for SRBs, this rate greatly decreases under higher loads, whereas, for conventional bearings, it actually remains unchanged.

Damping properties prove to be better for the SRB in the case of amplitudes corresponding to low and medium static loads ($\varepsilon < 0.25$).

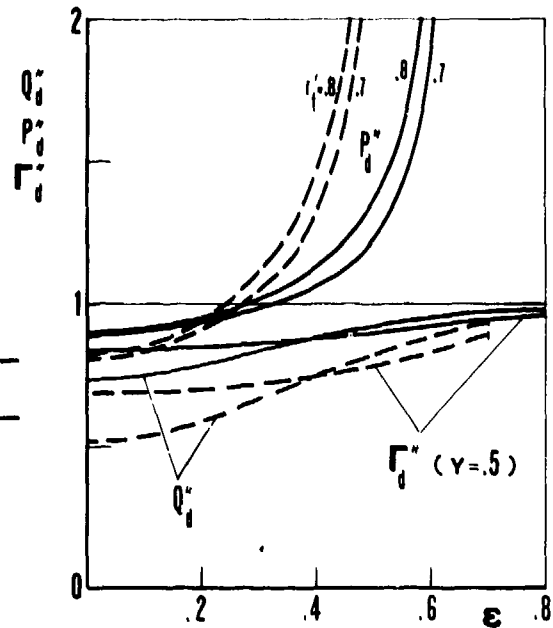
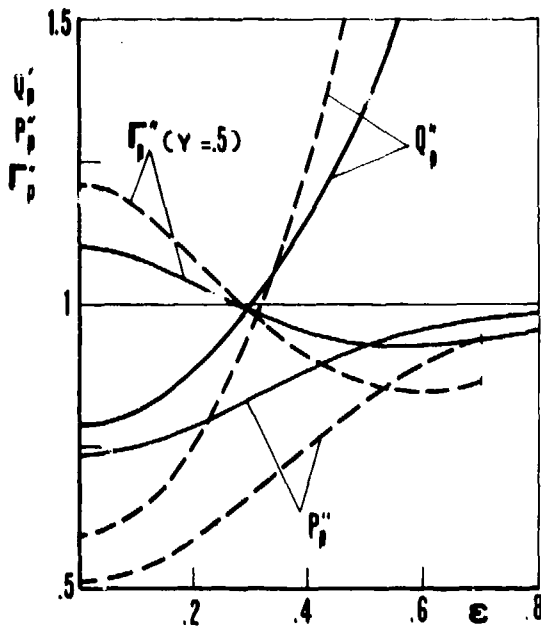


Fig. 5a) - "Static" values Q_p'' , P_p'' and Γ_p'' as functions of ϵ , in the presence of errors due to tolerances.

Fig. 5b) - "Dynamic" values Q_d'' , P_d'' and Γ_d'' as functions of ϵ , in presence of errors due to tolerances.

3. DYNAMIC BEHAVIOUR

3.1

The equation of motion for a bearing of the above type is:

$$M h_0 \ddot{\epsilon} + C_d C' \dot{\epsilon} + \bar{p} A P_p' P_p'' \Gamma_p' \Gamma_p'' = F(t) \tag{3.1}$$

where it is stated:

$$C' = P_d' P_d'' - \frac{\left(1 - \frac{r_f'^2}{r_u'^2}\right)^2 \left(1 - r_u'^2\right)}{\ln r_u'} P_p' P_p'' \Gamma_d' \Gamma_d'' \tag{3.2}$$

In the case of small vibrations around a suitable equilibrium point ϵ_0 , (3.1) can easily be linearized; if we state:

$$K = P_p''(\epsilon_0) \left[\frac{dP_p'}{d\epsilon} \right]_{\epsilon=\epsilon_0} \Gamma_p'(\epsilon_0) \Gamma_p''(\epsilon_0) \tag{3.3}$$

$$C = C_d C'(\epsilon_0) / (\bar{p} A)$$

$$\Phi(t) = \frac{F(t)}{\bar{p} A} - P_p'(\epsilon_0) P_p''(\epsilon_0) \Gamma_p'(\epsilon_0) \Gamma_p''(\epsilon_0)$$

$$\zeta = \epsilon - \epsilon_0 \quad M = \frac{M h_0}{\bar{p} A}$$

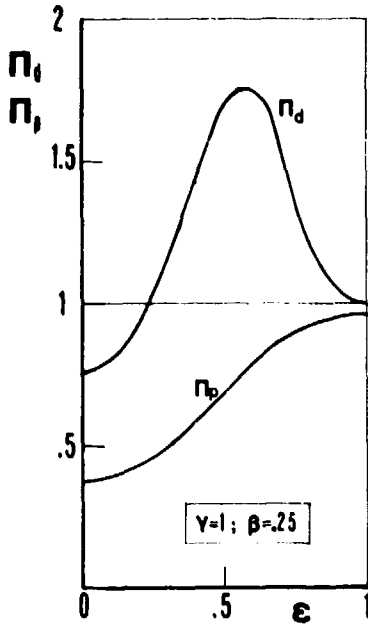


Fig. 6 - Ratios Π_p between static loads and Π_d between dynamic loads of a conventional and of a self-regulated bearing.

we obtain:

$$M \ddot{\zeta} + C \dot{\zeta} + K \zeta = \Phi(t) \tag{3.4}$$

3.2

From Fig. 4 it can be seen that, for $\eta_{jk} \approx 1$ and $\epsilon_0 = 0$, (3.4) can be used in a wide range of load values.

In Fig. 7 values for A , C_d , and $C' (\epsilon = 0) \approx P_p'(0)$ are given and the gain function ϵ_{max}/Φ_0 is calculated for a sinoidal excitation with Φ_0 amplitude and ω pulsatace (in

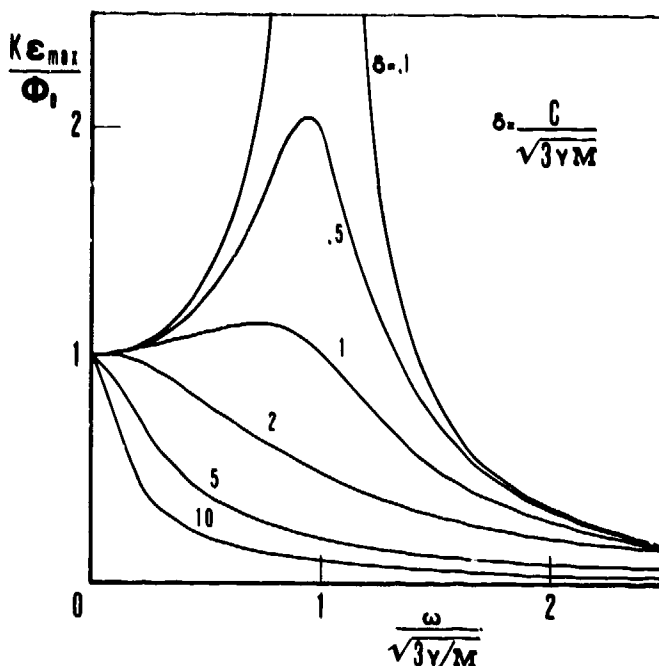
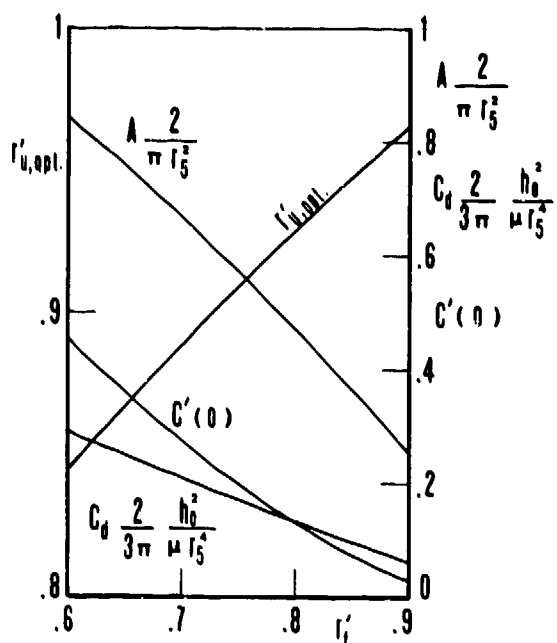


Fig. 7a) - Optimal values of $r'_u=r_2/r_3$ (minimum pumping power), and related values of A and of C_d as functions of r'_1 .

Fig. 7b) - Amplitude versus frequency curves (linearized model).

Fig. 7 r'_{11} is always assumed to be the "optimum" value, while $K = 3\gamma$).

It must be noted that, with the same bearing size and static load capacity, dynamic performance varies greatly in relation to h_0 , μ and M parameter. For example, for a bearing with $r_5 = 50$ mm, $r'_1 = 0.8$, $\bar{p} = 5$ MPa, $\gamma = 1$, the damping parameter $\delta = C / \mu \omega_n$ may range from $\delta = 22$ ($\mu = 0.1$ Nsec/m², $h_0 = 20$ μ m, $M = 100$ Kg) to $\delta = 0.14$ ($\mu = 0.02$, $h_0 = 50$, $M = 1000$), as the resonance frequency varies from $f_n = 590$ Hz to $f_n = 120$ Hz. Hence the opportunity, in most cases, of reducing h_0 , and values as the moving mass if often a design constraint. In the same way, a larger bearing has greater damping properties than a smaller one (fed at higher pressure to ensure equal static performances).

3.3

In Fig. 8, a comparison is made between SRBs and usual bearings (as above $\beta = \gamma/4$ to ensure that the same rates of flow are used): the ratio of vibration amplitudes for self-regulated (ϵ_s) and conventional (ϵ_c) bearings, under the same pulsating load, is plotted against pulsance.

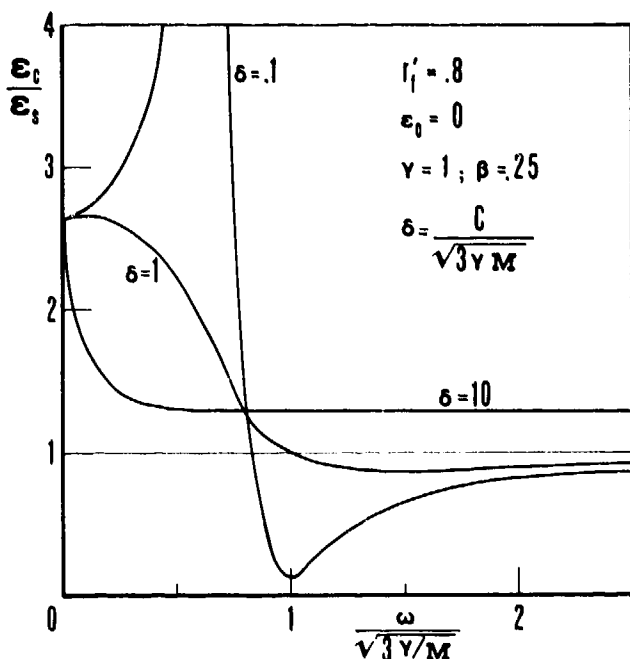


Fig. 8 - Ratio ϵ_c/ϵ_s between vibration amplitudes of a self-regulated and a conventional bearing.

Due to the greater stiffness, SRBs show a higher resonance frequency and lower vibration amplitudes for $\omega < \omega_n$. In the region of upper resonance frequencies, amplitudes become comparable.

It must be pointed out that Fig. 8 is only valid when $r'_1 = 0.8$ and for small vibrations around $\epsilon_0 = 0$. While r'_1 has no great influence on ϵ_c/ϵ_s , ϵ_0 has especially for lower frequencies: at higher ϵ_0 values, the stiffness of conventional bearing tends to become almost the same as that of the SRB (see Fig. 6), while damping properties become better, so the amplitude ratio becomes less unfavourable for the conventional bearing.

When vibration amplitude

3.4

When vibration amplitude

increases, numerical integration of (3.1) becomes necessary. Since many parameters are involved, it is not possible to have a synopic chart, as in Fig. 7, which shows an overall solution to the problem. Several examples of the behaviour of the bearing are given in Figs. 9 and 10. The effect of a step load is examined in Fig. 9: The maximum displacement reached when the load suddenly rises from C to F is plotted against the δ parameter for several F, γ , and g_c values (g_s and g_i are assumed to be equal to $2h_0$): it should be remembered that $\bar{p}A$ is the maximum theoretical load.

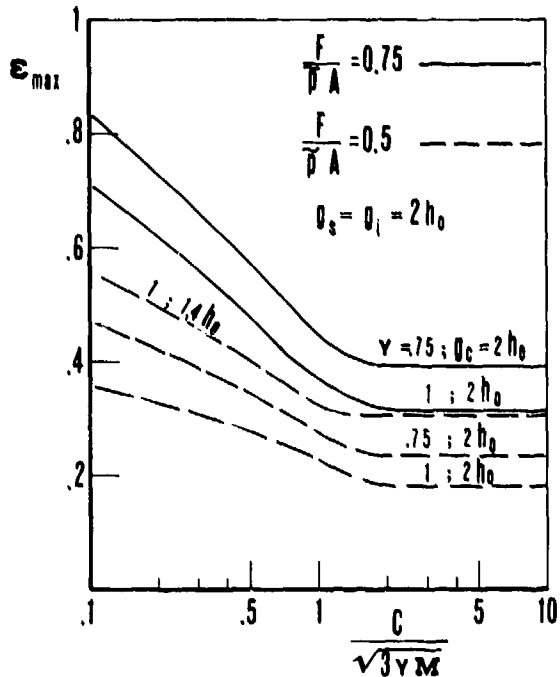


Fig. 9 - Maximum amplitudes values ϵ_{max} as a function of the damping factor for step loads.

In Fig. 10, eccentricity amplitudes under oscillating loads are plotted against the forced pulsatance: when damping is low, the typical pattern of nonlinear systems with "softening" stiffness can be recognized. It appears that, when great oscillations are expected in the load, bearing design parameters (especially h_0) must be carefully selected to avoid resonance phenomena: it must, however, be noted that a low value (such as $\delta = 0.1$) for the damping parameter can only occur when a great moving mass is combined with a large amount of axial play.

4. DESIGN EXAMPLE

Self-regulated bearings can be designed in such a way as to fit the dimensional standards of thrust roller bearings; Fig. 11 contains an example of an SRB whose dimensions are equal to the double effect ball bearing shown in the same figure.

This example is taken from /9/ where static calculations are made: when fed at 7 MPa, through a restrictor ($\gamma = .5$), the

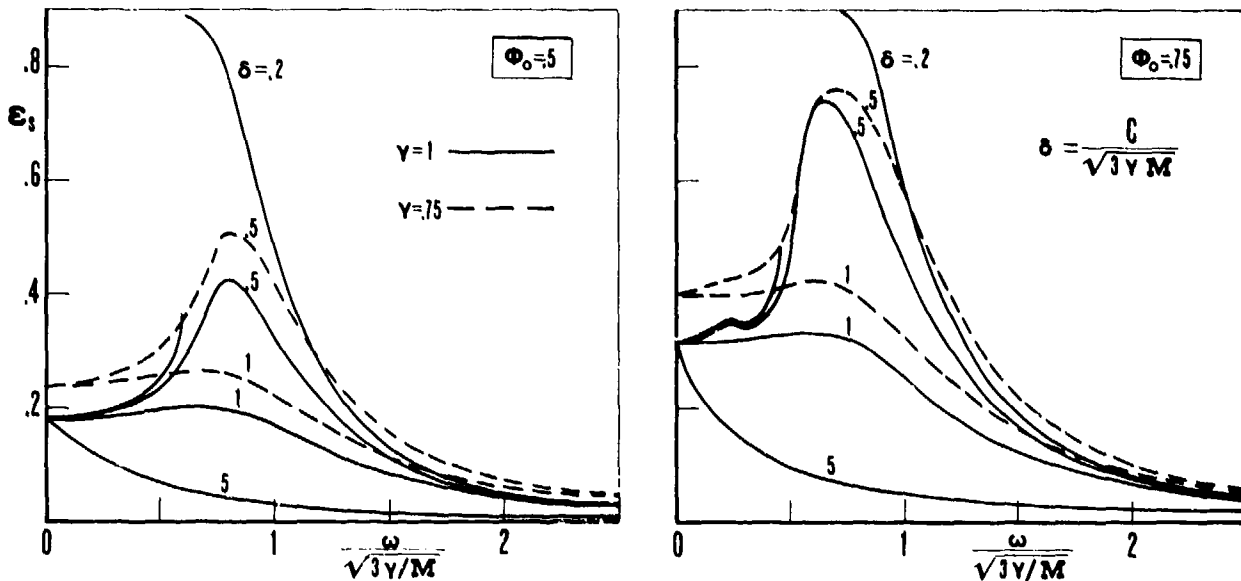


Fig. 10 - Amplitude versus frequency curves for two values of sinoidal load (non linearized model).

maximum theoretical load $\bar{p}A$ proves to be greater than 17 KN; the clearance design value is $h_0 = 29 \mu m$ and tolerances are assigned in such a way that axial plays g_c, g_s, g_i can vary between 40 and 58 μm : thus a 10 KN load can be sustained with a displacement (in the worst condition) of about 15 μm ; if lubricant viscosity is $\mu = 30 \cdot 10^3 N/sec m^2 (=5^\circ E)$, the maximum total flow rate is, in theory, less than 1 l/min (in practice it turns out to be lower).

It is worth noting that an equivalent roller bearing /12/ under a 10 KN load at 500

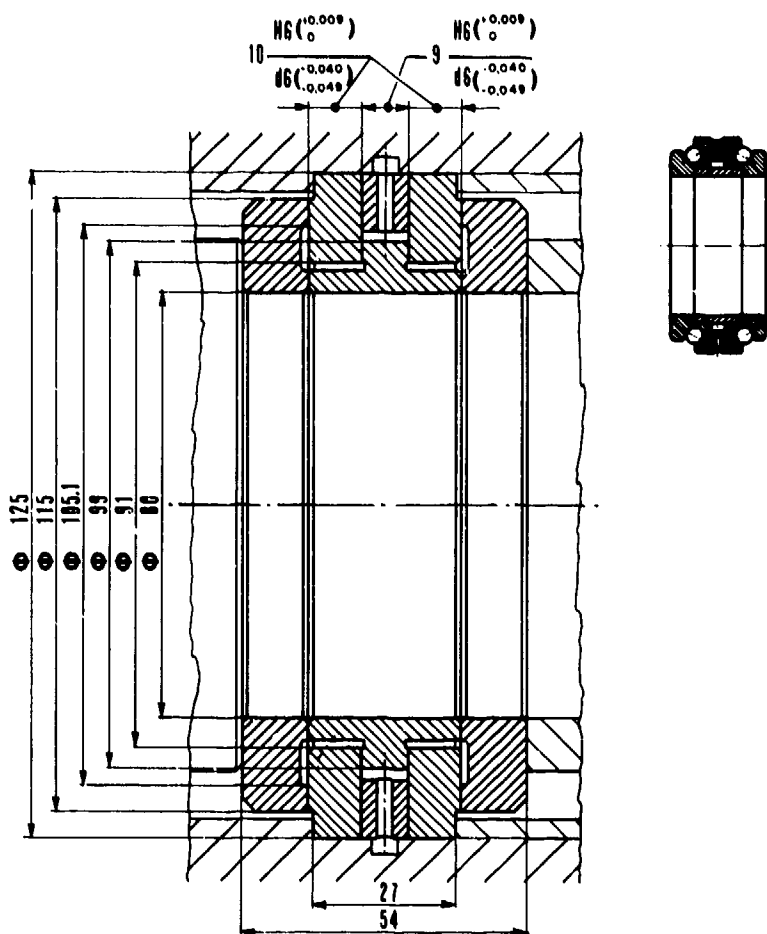


Fig. 11. - A standardized self-regulated bearing.

An example is given of a self-regulated bearing of "standardized" dimensions that may substitute a ball-bearing of the same size.

REFERENCES

- /1/ Halling J. "Principles of Tribology", London, The Macmillan Press Ltd, 1975, 308-358.
- /2/ Koevermans W.P., Jansen C.J. "Design and Performance of the Four-Degree-of-Freedom Motion System of NRC Research flight Simulator", AGARD-CP-198, The Netherlands, 1975.
- /3/ Bassani R. "Ricerche sulla lubrificazione idrostatica presso l'Istituto di Meccanica Applicata e Costruzione di Macchine dell'Università di Pisa", Tribologia e Lubrificazione, Vol. IX, n. 4, Settembre 1974, 173-184.
- /4/ Bassani R. "A New Opposed-Pad Hydrostatic Bearing: the Flow Self-Regulating Bearing", Meccanica, Vol. X, n. 2, 1975, 107-113.
- /5/ Bassani R. "Il cuscinetto idrostatico di spinta a doppio effetto autoregolatore della portata di lubrificante, alimentato a pressione costante", Atti Ist. Mecc. Appl. Costr. Macch. Università di Pisa, AIM 78-5, Novembre 1978.
- /6/ Bassani R. "Self-Regulated Hydrostatic Pads", Wear, 61, 1980, 49-68.
- /7/ Bassani R. "The Flow Self-Regulating Hydrostatic Screw and Nut", ASME, J. Lubr. Tech., Vol. 101, n. 3, July 1979, 364-375.
- /8/ Bassani R., Paladini M., Piccigallo B. "Studio sul comportamento dinamico di un cuscinetto idrostatico autoregolatore", Ist. Mecc. Appl. Costr. Macch., Internal Report, 1981.
- /9/ Bassani R., Piccigallo B. "Effetto delle tolleranze di fabbricazione sulle prestazioni di coppie idrostatiche autoregolate", Il progettista Industriale, Novembre 1981, n. 7.
- /10/ Koenigberger F., Cowley A. "Dynamic of Hydrostatic Bearing Systems", J. Mech. Eng., J. Prod. Eng., 1972, 284-307.
- /11/ Bassani R. "Cuscinetti idrostatici di spinta sottoposti a variazioni dinamiche del carico", II Congr. Naz. AIMETA, Vol. III, 1974, 225-236.
- /12/ RIV-SKF, Catalogo Generale, 28000-1, Agosto 1970.

rpm has a life expectancy of 2000 hours and relatively fast wear, while hydrostatic bearings have virtually no wear.

Concerning dynamic performance it can easily be seen that the damping parameter of the aforesaid bearing is $\delta = 4.4 \pm 1.4$ and the resonance frequency $f_n = 500 \pm 150$ Hz, when the moving mass varies from 100 to 1000 Kg.

5. CONCLUSIONS

The self-regulated hydrostatic opposed pad thrust bearing has been studied under dynamic loads (step loads and sinoidal loads) in a constant supply pressure system.

The damping of the bearing increases if film thickness decreases and if radial dimensions increase.

If the bearing is fed through a hydraulic resistance (capillary), damping may further increase, especially in presence of large displacements.

Dimensional inaccuracies due to tolerances may sometime reduce stiffness, but they generally increase the damping.

Comparison with conventional hydrostatic opposed-pad thrust bearings, supplied through capillary restrictors, demonstrated that the performance of the self regulated bearing is generally better because of its greater stiffness.

APPENDIX A

A.1

In a steady state, if no external load is applied, p_s must be equal to p_i , thus, if we call the hydraulic resistances of the four gaps $R_{j,K}$ (see Fig. 1)

$$\frac{R_{i,II}}{R_{i,I} + R_{i,II}} = \frac{R_{s,II}}{R_{s,I} + R_{s,II}} \quad (A.1)$$

Lubricant viscosity and r'_u may be considered to be equal for all the gaps, so hydraulic resistances turn out to be proportional to the -3 power of the respective clearance heights. Hence, if we call the clearance thickness in steady unloaded condition $h_{j,K}$, and assume $h_{j,K} = h_0 \eta_{j,K}$, it follows (see Fig. 1) that:

$$\begin{aligned} \eta_{i,I} &= \frac{g_s \cdot g_c}{h_c (g_s + g_i)} & \eta_{i,II} &= \frac{g_s (g_s + g_i - g_c)}{h_o (g_s + g_i)} \\ s_{,I} &= \frac{g_i \cdot g_c}{h_o (g_s + g_i)} & \eta_{s,II} &= \frac{g_i (g_s + g_i - g_c)}{h_o (g_s + g_i)} \end{aligned} \quad (A.2)$$

and when a relative axial displacement is imposed by external loads, clearance are expressed by (2.8).

A.2

With reference to the outline of the bearing (Fig. 3), it is possible, if \bar{p} and Q_s are known, and on the basis of (2.5), to calculate the rate at which the lubricant is flowing out from the s,I clearance; the rate flowing into the s,II clearance shall be equal to the latter multiplied by -1, with the addition of the term $\pi h_o (r_3^2 - r_4^2)$, due to recess squeeze. When flow rates are known as a function of Q_s , p_s can be obtained as a function of Q_s and \bar{p} by applying (2.4) to the s,I clearance:

$$p_s = \bar{p} + \frac{6\mu}{\pi h_{s,I}^3} \left[Q_s \ln r'_u + \pi h_o r_3^2 \ln r'_u \dot{\epsilon} + \frac{\pi h_o}{2} (r_3^2 - r_4^2) \dot{\epsilon} \right] \quad (A.3)$$

In the same way, may be expressed p_i as a function of Q_i and \bar{p} . Using (2.4) and (A.3), and assuming that $p(r_5) = 0$, Q_s , Q_i and hence Q may be obtained: see (2.9) in which:

$$\begin{aligned} Q'_p Q''_p &= \frac{(\eta_{s,I} - \epsilon)^3 (\eta_{s,II} + \epsilon)^3}{(\eta_{s,I} - \epsilon)^3 + (\eta_{s,II} + \epsilon)^3} + \frac{(\eta_{i,I} + \epsilon)^3 (\eta_{i,II} - \epsilon)^3}{(\eta_{i,I} + \epsilon)^3 + (\eta_{i,II} - \epsilon)^3} \\ Q'_d Q''_d &= \frac{1}{\left(1 - \frac{r_f^2}{r_u^2}\right)} \left[\frac{(r_f^2/r_u^2) (\eta_{s,II} + \epsilon)^3 + (\eta_{s,I} - \epsilon)^3}{(\eta_{s,I} - \epsilon)^3 + (\eta_{s,II} + \epsilon)^3} - \frac{(r_f^2/r_u^2) (\eta_{i,II} - \epsilon)^3 + (\eta_{i,I} + \epsilon)^3}{(\eta_{i,II} - \epsilon)^3 + (\eta_{i,I} + \epsilon)^3} \right] \end{aligned} \quad (A.4)$$

When all axial plays are identical to $2h_c$, Q'_p and Q'_d must be equal to 1, thus:

$$\begin{aligned} Q'_p &= \frac{2(1 - \epsilon)^3 (1 + \epsilon)^3}{(1 - \epsilon)^3 + (1 + \epsilon)^3} \\ Q'_d &= \frac{(1 + \epsilon)^3 - (1 - \epsilon)^3}{(1 - \epsilon)^3 + (1 + \epsilon)^3} \end{aligned} \quad (A.5)$$

A.3

When flow rates are known, pressures in the recesses may be calculated from (A.3):

$$p_s = \bar{p} \left[1 - \frac{(\eta_{s,II} + \epsilon)^3}{(\eta_{s,I} - \epsilon)^3 + (\eta_{s,II} + \epsilon)^3} \right] - \frac{3\mu r_5^2 [1 - r_u^2] [1 - (r_f^2/r_u^2)]}{h_o^3 (\eta_{s,I} - \epsilon)^3 + (\eta_{s,II} + \epsilon)^3} \dot{\epsilon}$$

$$p_i = \bar{p} \left[1 - \frac{(\eta_{i,II} - \epsilon)^3}{(\eta_{i,I} + \epsilon)^3 + (\eta_{i,II} - \epsilon)^3} \right] + \frac{3\mu r_s^2 [1 - r_u'^2] [1 - (r_f'^2/r_u'^2)]}{h_o^2 (\eta_{i,I} + \epsilon)^3 + (\eta_{i,II} - \epsilon)^3} \dot{\epsilon}$$

and hence, from (2.7), the total force that the lubricant applies to the two members of the bearing can be assessed. Load capacity is expressed in the second formula of (2.9), where:

$$\frac{P'_p P''_p}{P' P''} = \frac{(\eta_{s,II} + \epsilon)^3}{(\eta_{s,I} - \epsilon)^3 + (\eta_{s,II} + \epsilon)^3} - \frac{(\eta_{i,II} - \epsilon)^3}{(\eta_{i,II} - \epsilon)^3 + (\eta_{i,I} + \epsilon)^3} \quad (A.7)$$

$$P'_d P''_d = \left(1 + r_u'^2 + \frac{1 - r_u'^2}{\ln r_u'^2} \right) \left\{ \frac{r_f'^4}{r_u'^4} \left[\frac{1}{(\eta_{i,I} + \epsilon)^3} + \frac{1}{(\eta_{s,I} - \epsilon)^3} \right] + \frac{1}{(\eta_{i,I} - \epsilon)^3} + \frac{1}{(\eta_{s,II} + \epsilon)^3} \right\} +$$

$$- \frac{1 - r_u'^2}{\ln r_u'^2} \left(1 - \frac{r_f'^2}{r_u'^2} \right)^2 \left[\frac{1}{(\eta_{i,I} + \epsilon)^3 + (\eta_{i,II} - \epsilon)^3} + \frac{1}{(\eta_{s,I} - \epsilon)^3 + (\eta_{s,II} + \epsilon)^3} \right]$$

When all the $\eta_{j,k}$ equal 1, is $P''_p = P''_d = 1$, hence:

$$P'_p = \frac{(1 + \epsilon)^3 - (1 - \epsilon)^3}{(1 + \epsilon)^3 + (1 - \epsilon)^3} \quad (A.8)$$

$$P'_d = \left(1 + r_u'^2 + \frac{1 - r_u'^2}{\ln r_u'^2} \right) \left(1 + \frac{r_f'^4}{r_u'^4} \right) \left[\frac{1}{(1 - \epsilon)^3} + \frac{1}{(1 + \epsilon)^3} \right] - 2 \frac{1 - r_u'^2}{\ln r_u'^2} \left(1 - \frac{r_f'^2}{r_u'^2} \right)^2 \left[\frac{1}{(1 + \epsilon)^3 + (1 - \epsilon)^3} \right]$$

A.4

In previous expressions, \bar{p} has been taken to be constant. Actually, if the hydraulic resistance \bar{R} of the feeding ducts is not negligible, \bar{p} varies with ϵ and $\dot{\epsilon}$. If \bar{R} and supply pressure \bar{p} are constant, it may be written $\bar{p} = \bar{p} - QR$; thus, the first of (2.9) is easily obtained, in which γ is intended to be the value of the \bar{p}/\bar{p} ratio when the bearing is in an unloaded steady status, and:

$$\Gamma'_p \Gamma''_p = \frac{\gamma}{\gamma + (1 - \gamma) Q'_p Q''_p \left(\frac{\eta_{s,I}^3 \eta_{s,II}^3}{\eta_{s,I}^3 + \eta_{s,II}^3} + \frac{\eta_{i,I}^3 \eta_{i,II}^3}{\eta_{i,I}^3 + \eta_{i,II}^3} \right)} \quad (A.9)$$

$$\Gamma'_d \Gamma''_d = \frac{(1 - \gamma) Q'_d Q''_d \left(\frac{\eta_{s,I}^3 \eta_{s,II}^3}{\eta_{s,I}^3 + \eta_{s,II}^3} + \frac{\eta_{i,I}^3 \eta_{i,II}^3}{\eta_{i,I}^3 + \eta_{i,II}^3} \right)}{\gamma + (1 - \gamma) Q'_p Q''_p \left(\frac{\eta_{s,I}^3 \eta_{s,II}^3}{\eta_{s,I}^3 + \eta_{s,II}^3} + \frac{\eta_{i,I}^3 \eta_{i,II}^3}{\eta_{i,I}^3 + \eta_{i,II}^3} \right)}$$

as above $\Gamma''_p = \Gamma''_d = 1$ if all clearances are equal, so:

$$\Gamma'_p = \frac{\gamma}{\gamma + (1 - \gamma) Q'_p} \quad (A.10)$$

$$\Gamma'_d = \frac{(1 - \gamma) Q'_d}{\gamma + (1 - \gamma) Q'_p}$$

APPENDIX B

For a conventional bearing (see Fig. 12), defining the ratio of recess pressures and supply pressure \bar{p} , when $\epsilon = \dot{\epsilon} = 0$, as $\beta = \beta_i = \beta_s$, the expressions for load capacity and flow rates are:

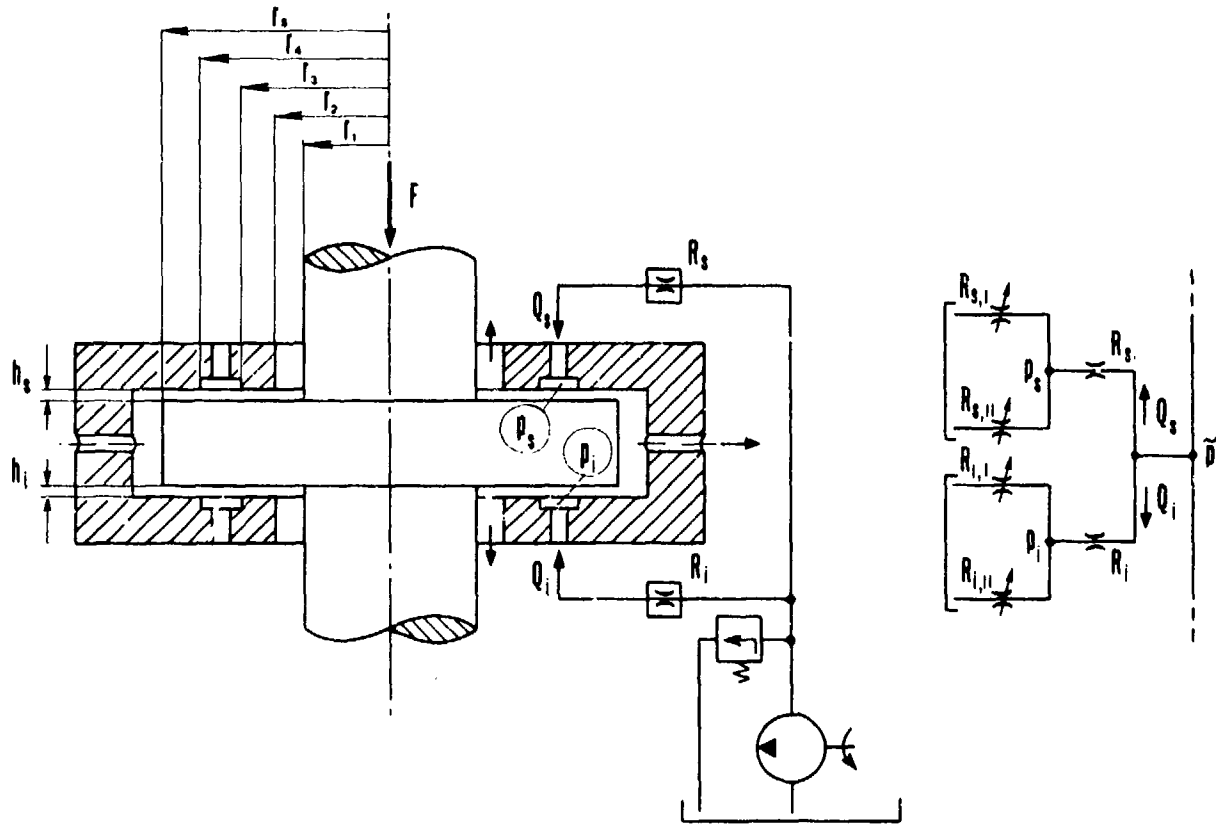


Fig. 12 - A conventional hydrostatic opposed-pad thrust bearing.

$$\begin{aligned}
 P &= A \beta \bar{p} \left[\frac{1}{\beta + (1-\beta)(1-\epsilon)^3} - \frac{1}{\beta + (1-\beta)(1+\epsilon)^3} \right] + \\
 &- C_d (1-\beta) \left[1 - \frac{r_f^2}{r_u^2} \right] \dot{\epsilon} \left[\frac{1-r_u'^2}{2 \ln r_u'} \left(1 + \frac{r_f^2}{r_u'^2} \right) + \frac{r_f^2}{r_u'^2} (1+r_u'^2) \right] \left[\frac{1}{\beta + (1-\beta)(1-\epsilon)^3} + \frac{1}{\beta + (1-\beta)(1+\epsilon)^3} \right] + \\
 &+ C_d \left[(1+r_u'^2) + \frac{1-r_u'^2}{\ln r_u'} \right] \left(1 + \frac{r_f^4}{r_u'^4} \right) \dot{\epsilon} \left[\frac{1}{(1-\epsilon)^3} + \frac{1}{(1+\epsilon)^3} \right] \\
 Q_i &= \frac{2(1-\epsilon)^3}{1 + \frac{1-\beta}{\beta} (1-\epsilon)^3} \left\{ \frac{\bar{p}}{R} - \frac{1}{2} \frac{1-\beta}{\beta} \pi h_o r_s^2 \left[\frac{1-r_u'^2}{2 \ln r_u'} \left(1 + \frac{r_f^2}{r_u'^2} \right) + \frac{r_f^2}{r_u'^2} (1+r_u'^2) \right] \dot{\epsilon} \right\} + \\
 &+ \pi r_s^2 h_o \left[\frac{1-r_u'^2}{2 \ln r_u'} \left(1 + \frac{r_f^2}{r_u'^2} \right) + \frac{r_f^2}{r_u'^2} (1-r_u'^2) \right] \dot{\epsilon} \\
 Q_s &= \frac{2(1+\epsilon)^3}{1 + \frac{1-\beta}{\beta} (1+\epsilon)^3} \left\{ \frac{\bar{p}}{R} + \frac{1}{2} \frac{1-\beta}{\beta} \pi h_o r_s^2 \left[\frac{1-r_u'^2}{2 \ln r_u'} \left(1 + \frac{r_f^2}{r_u'^2} \right) + \frac{r_f^2}{r_u'^2} (1+r_u'^2) \right] \dot{\epsilon} \right\} + \\
 &- \pi r_s^2 h_o \left[\frac{1-r_u'^2}{2 \ln r_u'} \left(1 + \frac{r_f^2}{r_u'^2} \right) + \frac{r_f^2}{r_u'^2} (1-r_u'^2) \right] \dot{\epsilon}
 \end{aligned}$$

The equation of motion is:

$$M\ddot{\epsilon} + \frac{P(c, \dot{\epsilon})}{\bar{p}A} = \phi(t)$$

COMPORTEMENT DYNAMIQUE D'UN PALIER LISSE
CRITERES DE STABILITE

par

J. FRENE, D. NICOLAS et N. ABDUL WAHED

Université de Poitiers
Laboratoire de Mécanique des Solides
40, Avenue du Recteur Pineau
86022 POITIERS Cedex
FRANCE

I.N.S.A. de Lyon
Laboratoire de Mécanique des Contacts
20, Avenue Albert Einstein - Bt 113
69621 VILLEURBANNE
FRANCE

RESUME

Le comportement dynamique d'un palier dépend non seulement de sa géométrie mais aussi des conditions de fonctionnement auxquelles il est soumis. Il est donc important de prévoir les domaines pour lesquels le fonctionnement du palier est stable, c'est-à-dire de définir les critères de stabilité. Par ailleurs en régime dynamique il faut obtenir la réponse du palier, c'est-à-dire calculer la trajectoire du centre de l'arbre à l'intérieur du coussinet.

Dans ce travail nous abordons essentiellement l'étude de la stabilité du palier à partir des coefficients dynamiques calculés en utilisant la théorie linéaire. Les conditions de stabilité de différents types de palier de géométrie fixe sont présentées sous forme d'abaques appelés cartes de stabilité.

L'influence sur la stabilité du palier de la valeur de chacun des coefficients dynamiques est examinée en utilisant le critère de Routh-Hurwitz : ceci permet de montrer que le critère de stabilité de Lund conduit à des résultats identiques alors que le critère de stabilité statique de Smith conduit dans certains cas à des résultats erronés. Ce dernier point est confirmé par l'étude en régime transitoire d'un palier particulier pour lequel le critère de Routh prévoit des conditions de fonctionnement stables en contradiction avec celles obtenues à partir du critère de Smith. Cette étude dynamique du palier est effectuée en utilisant la théorie non linéaire.

1. INTRODUCTION

Depuis les travaux de Newkirk et Stodola [1, 2, 3] on sait qu'un palier ne peut pas être considéré comme un simple guide mais qu'il constitue, associé avec le rotor, un système dynamique complexe. La position de l'arbre à l'intérieur du coussinet et la raideur du film lubrifiant ont une influence sur les vitesses critiques tandis que l'amortissement intervient principalement sur la sensibilité aux diverses excitations. Par ailleurs, il peut être lui même générateur d'instabilité.

Dès 1919, Harrisson [4], après avoir remarqué que dans un palier infiniment long non cavité la force hydrodynamique est toujours orthogonale au déplacement, concluait que le centre de l'arbre devait décrire une orbite à l'intérieur du jeu radial. Cette hypothèse fut confirmée par l'étude de stabilité de Robertson [5] qui montra qu'un palier circulaire totalement rempli d'huile était toujours instable. Burwell [6], prenant en compte l'écoulement axial en introduisant un terme correctif, arrive aux mêmes conclusions que Robertson. Ces résultats théoriques ne concordaient pas entièrement avec les observations expérimentales qui mettaient en évidence l'existence de plages de fonctionnement stables. Ces différences de comportement furent par la suite attribuées à l'existence, dans le palier, d'une région où le film lubrifiant est rompu. Cette hypothèse n'a pu être vérifiée que plus tard grâce aux observations effectuées en Laboratoire [7, 8] et au développement des moyens et des techniques de calcul numérique qui ont alors permis de déterminer les coefficients dynamiques d'un palier en tenant compte de la rupture du film [9, 10, 11]. Ainsi, l'extension des moyens de calcul, associée aux observations expérimentales a permis une meilleure compréhension des phénomènes vibratoires et a conduit à l'élaboration de paliers plus stables tels que les paliers à patins oscillants et les paliers à lobes.

Dans cette étude après une description élémentaire des différents types de fouettement rencontrés dans un palier, nous aborderons l'étude de la stabilité, en utilisant le critère de Routh-Hurwitz, à partir des coefficients dynamiques calculés à l'aide de la théorie linéaire.

2. DESCRIPTION DU FOUETTEMENT DANS UN PALIER

Considérons un rotor rigide, parfaitement équilibré, supporté par un palier. En l'absence de toutes perturbations, le centre du rotor occupe une position d'équilibre O_0 telle que la force hydrodynamique \vec{F}_0 engendrée par le film lubrifiant est égale et opposée à la charge extérieure \vec{W}_0 appliquée au rotor (Fig. 1) :

$$(1) \quad \vec{F}_0 + \vec{W}_0 = 0$$

Supposons maintenant que, pour une raison quelconque, le centre du rotor se trouve déplacé de sa position d'équilibre statique O_{0s} en O_0 . Dans ce cas, la résultante hydrodynamique \vec{F}_d n'est plus égale et opposée à la charge extérieure \vec{W}_0 . La force hydrodynamique additionnelle $\vec{f} = \vec{F}_d - \vec{F}_0$ due au déplacement $O_{0s}O_0$, va engendrer un mouvement du centre de l'arbre à l'intérieur du coussinet qui sera contré par l'amortissement de type visqueux du à l'existence du film lubrifiant. Selon les conditions expérimentales trois types de trajectoires peuvent être observées :

(a) L'arbre regagne sa position d'équilibre statique ; la position d'équilibre statique est dite stable,

- (b) Le centre de l'arbre décrit une orbite fermée autour de la position d'équilibre statique : la position d'équilibre statique est dite marginale ou orbitalement stable,
- (c) Le centre de l'arbre s'éloigne de la position d'équilibre en décrivant une orbite divergente ; la position d'équilibre statique est dite instable. Dans la pratique, l'amplitude de l'orbite est limitée par l'enveloppe intérieure du coussinet et nous observons une orbite fermée telle que l'épaisseur minimale du film lubrifiant est très petite ; ceci provoque de très grandes forces hydrodynamiques et donc des vibrations très sévères.

Les deux derniers cas correspondent à une vibration auto-excitée due à l'existence du film lubrifiant. La fréquence ν de cette vibration est fonction de la vitesse à laquelle l'arbre peut pomper le fluide et maintenir la distribution de pression qui produit la force F_d .

En 1946 Haag [12] a montré à partir de la continuité du débit que, dans un palier infiniment long non chargé, l'arbre décrit une orbite circulaire à une fréquence égale à la moitié de la fréquence de rotation, d'où le terme de demi fréquence de fouettement.

Ce phénomène de fouettement décrit précédemment de façon qualitative pour le cas d'un rotor rigide existe également avec des arbres flexibles. Les premières observations expérimentales de ce phénomène ont été effectuées par Newkirk et Taylor [2] qui ont remarqué qu'un arbre flexible supporté par des paliers hydrodynamiques entrainé en vibration sévère pour une vitesse de rotation proche du double de la vitesse critique de l'arbre sur appuis rigides. Dans ce cas, la fréquence de fouettement est en effet égale à la fréquence critique de l'arbre. Ce fouettement à la résonance entraîne généralement la destruction du mécanisme.

La figure 2 met en évidence les différents types de fouettement qui peuvent exister dans un système rotor-palier hydrodynamique. Comme la raideur des paliers est fonction de la vitesse de rotation de l'arbre la vitesse critique n'est pas constante. Elle décroît lorsque la vitesse de rotation augmente. On peut rencontrer :

- (a) Le fouettement synchrone qui se produit avec un arbre non équilibré, rigide ou flexible à n'importe quelle vitesse de rotation et avec une fréquence égale à la fréquence de rotation de l'arbre. Ce type de vibration synchrone est présent dans toutes les machines tournantes à cause des balourds résiduels. Ici, le palier joue un rôle bénéfique car, grâce à l'amortissement qu'il fournit au système, il facilite le passage des vitesses critiques.
- (b) La demi-fréquence de fouettement qui apparaît lorsque les conditions de fonctionnement sont telles que le palier est générateur d'instabilité. Cette instabilité vibratoire peut se produire pour n'importe quelle vitesse de rotation et possède en général une fréquence proche de la moitié de celle de la rotation. Ici, le palier joue un rôle néfaste car il est initiateur du fouettement. Ce type de fouettement existe tant que sa fréquence est différente de la fréquence critique de l'arbre.
- (c) Le fouettement à la résonance qui se produit lorsque le mouvement de demi-fréquence de fouettement engendré par le palier entre en résonance avec la fréquence propre de l'arbre. A ce moment, la fréquence de fouettement est égale à la fréquence critique de l'arbre. Ce phénomène se produit pour une vitesse égale à environ deux fois la vitesse critique du système. Ce type de fouettement est le plus dangereux car lorsqu'il se produit il correspond à une véritable vibration.

Cette description qualitative des phénomènes de fouettement met en évidence la nécessité d'une modélisation dynamique du palier afin que le spécialiste en vibration puisse prédire le comportement dynamique des rotors.

3. MODELISATION LINEAIRE D'UN PALIER EN REGIME VIBRATOIRE

Dans l'analyse dynamique d'une ligne d'arbre de machine tournante le rôle du palier est caractérisé par les forces hydrodynamiques engendrées dans le film lubrifiant, qui s'opposent au mouvement de l'arbre. Dans le cas général celles-ci sont obtenues par intégration du champ de pression calculé à partir de l'équation de Reynolds écrite en régime dynamique. Ces forces étant des fonctions non linéaires de la position et de la vitesse du centre de l'arbre, l'analyse exacte d'un système rotor-paliers est donc très complexe puisqu'elle nécessite la résolution simultanée des équations relatives au mouvement du rotor et de l'équation relative au comportement hydrodynamique des paliers. Cette étude peut néanmoins être largement simplifiée si on suppose le rotor parfaitement rigide et si on se limite aux petits déplacements au voisinage d'une position d'équilibre statique. La première hypothèse permet de comparer entre elles différentes configurations de paliers, tandis que la seconde hypothèse permet une approche de la limite de stabilité du palier.

Sous l'hypothèse des petits déplacements, on peut effectuer un développement limité des composantes de la force hydrodynamique \vec{F} et écrire :

$$(2) \quad \begin{pmatrix} f_x \\ f_y \end{pmatrix} = \begin{pmatrix} F_x - F_{x0} \\ F_y - F_{y0} \end{pmatrix} + \begin{bmatrix} \frac{\partial F_x}{\partial x} & \frac{\partial F_x}{\partial y} \\ \frac{\partial F_y}{\partial x} & \frac{\partial F_y}{\partial y} \end{bmatrix} \begin{pmatrix} x \\ y \end{pmatrix} + \begin{bmatrix} \frac{\partial F_x}{\partial \dot{x}} & \frac{\partial F_x}{\partial \dot{y}} \\ \frac{\partial F_y}{\partial \dot{x}} & \frac{\partial F_y}{\partial \dot{y}} \end{bmatrix} \begin{pmatrix} \dot{x} \\ \dot{y} \end{pmatrix}$$

où F_{x0} et F_{y0} sont les composantes de la force hydrodynamique \vec{F}_0 à l'équilibre, x et y représentent des déplacements élémentaires au voisinage de la position d'équilibre statique et \dot{x} , \dot{y} les vitesses de déplacement.

On définit ainsi par dérivation des composantes de la force hydrodynamique, les coefficients de raideur : $a_{ij} = -\partial F_i / \partial x_j$ et d'amortissement : $b_{ij} = -\partial F_i / \partial \dot{x}_j$ du palier. L'existence de termes croisés traduit le fait que dans un palier, en général, la force hydrodynamique n'est pas colinéaire au déplacement.

Le calcul des coefficients dynamiques est effectué à partir de l'équation de Reynolds [13] que l'on résoud d'une part pour les conditions de fonctionnement statique, ce qui permet de calculer F_{x0} et F_{y0} , et d'autre part en imposant successivement des petits déplacements et des vitesses de déplacement dans les directions x et y . Les coefficients dynamiques sont alors obtenus par des relations approchées déduites des développements limités de Taylor. Ainsi dans le cas d'un petit déplacement x , il vient :

$$(3) \quad a_{xx} = \frac{F_{x0} - F_{xx}}{x}$$

$$a_{yx} = \frac{F_{y0} - F_{yx}}{x}$$

Les autres coefficients dynamiques sont donnés par des relations semblables écrites pour un petit déplacement y et pour des vitesses de déplacement \dot{x} et \dot{y} , ce qui nécessite de résoudre 5 fois l'équation de Reynolds.

Remarques

- Une diminution importante du volume des calculs peut être obtenue en effectuant la détermination des coefficients dynamiques dans le système d'axes en coordonnées cylindriques ϵ_0 et ϕ_0 .
- Une meilleure précision sur la valeur des coefficients dynamiques peut être obtenue en remplaçant la formule de Taylor qui a permis d'écrire les relations (3) par des relations aux différences finies centrées, mais cela conduit à doubler le volume des calculs.
- Une étude précise [13] de la valeur des coefficients d'amortissement permet de montrer que quel que soit le type de palier hydrodynamique les coefficients croisés d'amortissement sont toujours égaux : $b_{xy} = b_{yx}$.

4. STABILITE D'UNE POSITION D'EQUILIBRE

4.1 Critère de Routh-Hurwitz

Pour comparer le comportement dynamique de différents types de paliers, l'étude de la stabilité d'une position d'équilibre est effectuée dans le cas d'un rotor rigide symétrique (Fig. 3) de masse $2m$, supporté par 2 paliers identiques dont la charge statique est W_0 . Le système linéaire associé s'écrit :

$$(4) \quad m \begin{pmatrix} \ddot{x} \\ \ddot{y} \end{pmatrix} + \begin{bmatrix} a_{ij} \end{bmatrix} \begin{pmatrix} x \\ y \end{pmatrix} + \begin{bmatrix} b_{ij} \end{bmatrix} \begin{pmatrix} \dot{x} \\ \dot{y} \end{pmatrix} = 0$$

où x et y sont les composantes, dans le repère fixe, du déplacement du centre de l'arbre à partir de la position d'équilibre statique O_{as} .

Pour généraliser les calculs on emploie les variables sans dimension suivantes :

$$M = \frac{m C \omega^2}{W_0} ; A_{ij} = \frac{a_{ij} C}{W_0} ; B_{ij} = \frac{b_{ij} C \omega}{W_0} ; X = \frac{x}{C} ; Y = \frac{y}{C}$$

$$\dot{X} = \frac{\dot{x}}{C\omega} ; \dot{Y} = \frac{\dot{y}}{C\omega} ; \ddot{X} = \frac{\ddot{x}}{C\omega^2} ; \ddot{Y} = \frac{\ddot{y}}{C\omega^2}$$

par ailleurs la recherche d'une solution de la forme

$$(5) \quad \begin{aligned} X &= \bar{X} e^{\lambda \omega t} \\ Y &= \bar{Y} e^{\lambda \omega t} \end{aligned} \quad \text{avec } \lambda = \eta + i\gamma$$

conduit au système homogène

$$(6) \quad \begin{bmatrix} M \lambda^2 + B_{xx} \lambda + A_{xx} & B_{xy} \lambda + A_{xy} \\ B_{yx} \lambda + A_{yx} & M \lambda^2 + B_{yy} \lambda + A_{yy} \end{bmatrix} \begin{pmatrix} \bar{X} \\ \bar{Y} \end{pmatrix} = 0$$

Ce système admet une solution si le polynôme caractéristique

$$(7) \quad f(\lambda) = A_0 \lambda^4 + A_1 \lambda^3 + A_2 \lambda^2 + A_3 \lambda + A_4$$

est nul. Avec

$$\begin{aligned}
 A_0 &= M^2 \\
 A_1 &= M (B_{xx} + B_{yy}) = M \text{ tr. } (B_{ij}) \\
 (8) \quad A_2 &= M (A_{xx} + A_{yy}) + B_{xx} B_{yy} - B_{xy} B_{yx} = M \text{ tr. } (A_{ij}) + \text{Det. } (B_{ij}) \\
 A_3 &= B_{xx} A_{yy} + B_{yy} A_{xx} - B_{xy} A_{yx} - B_{yx} A_{xy} \\
 A_4 &= A_{xx} A_{yy} - A_{xy} A_{yx} = \text{Det. } (A_{ij})
 \end{aligned}$$

Le critère de Routh-Hurwitz indique que toutes les racines du polynôme (7) ont des parties réelles négatives si et seulement si les inégalités suivantes sont respectées :

$$(9) \quad A_0 \Delta_1 > 0 ; \Delta_2 > 0 ; \Delta_3 > 0 ; \Delta_4 > 0$$

où Δ_i représente le déterminant de Hurwitz d'ordre i :

$$(10) \quad \Delta_i = \begin{vmatrix} A_1 & A_3 & A_5 & A_7 & \dots \\ A_0 & A_2 & A_4 & A_6 & \dots \\ 0 & A_1 & A_3 & A_5 & \dots \\ 0 & A_0 & A_2 & A_4 & \dots \\ \dots & \dots & \dots & \dots & \dots \\ \dots & \dots & \dots & \dots & A_i \end{vmatrix} \text{ avec ici } A_k = 0 \text{ pour } k > 4$$

Dans le cas considéré ici $A_0 = M^2 > 0$, ce qui conduit aux inégalités suivantes :

$$(11) \quad \begin{aligned}
 A_i &> 0 \quad i = 0 \text{ à } 4 \\
 A_1 A_2 A_3 - A_1^2 A_4 - A_0 A_3^2 &> 0
 \end{aligned}$$

ces conditions correspondent au cas d'un comportement stable du système rotor rigide-paliers.

La stabilité d'une position d'équilibre est donc fonction des coefficients dynamiques relatifs à cette position et de la masse de rotor M attribuée au palier et qui joue ici le rôle d'un paramètre.

Dans le cas où l'inégalité (11b) se réduit à une égalité, c'est-à-dire à la limite de stabilité, les déterminants d'Hurwitz d'ordre 3 et 4 sont nuls. La formule d'Orlando [14] précise alors que le polynôme caractéristique a au moins une paire de racines opposées imaginaires pures. Compte tenu des relations entre les coefficients A_i et les racines de l'équation (7) les deux autres racines peuvent être, soit des complexes conjugués à partie réelle négative, soit des réels négatifs. Cette solution représente le cas marginal de stabilité pour lequel le centre de l'arbre décrit une orbite fermée : il y a fouettement et la valeur de la masse pour laquelle ce mouvement prend naissance est appelée masse critique.

Ainsi lorsque :

- (a) La masse de l'arbre est inférieure à la masse critique : le point de fonctionnement est stable
- (b) La masse de l'arbre est égale à la masse critique : l'équilibre est marginal, le centre de l'arbre décrit une orbite fermée, il y a fouettement. La fréquence de fouettement peut être déterminée à partir des relations entre les coefficients des racines de l'équation (7), il vient

$$(12) \quad \gamma_g^2 = A_3/A_1$$

- (c) La masse de l'arbre est supérieure à la masse critique : l'équilibre est instable, le centre de l'arbre s'éloigne de la position d'équilibre statique. Dans ce cas, seule la résolution du problème non linéaire permet d'étudier le mouvement ultérieur.

4.2 Recherche directe de la frontière de stabilité

En 1965 Lund [15] a proposé une approche plus directe mais moins générale du problème ; celle-ci suppose l'existence d'un seuil de stabilité pour lequel le mouvement est un mouvement orbital de la forme :

$$(13) \quad \begin{aligned}
 X &= \bar{X} e^{i\gamma\omega t} \\
 Y &= \bar{Y} e^{i\gamma\omega t}
 \end{aligned}$$

où γ est un nombre réel. Cette approche conduit à un polynôme caractéristique dont on peut séparer directement partie réelle et partie imaginaire et écrire :

$$(14) \quad \begin{aligned}
 A_1 \gamma^3 - A_3 \gamma &= 0 \\
 A_0 \gamma^4 - A_2 \gamma^2 + A_4 &= 0
 \end{aligned}$$

la première équation admet $\gamma = 0$ et $\gamma^2 = A_3/A_1$ comme solutions. La solution $\gamma = 0$ est incompatible avec la seconde équation puisque A_4 est différent de zéro. Le report de $\gamma^2 = A_3/A_1$ dans la seconde équation conduit à la relation :

$$(15) \quad A_0 A_3^2 - A_2 A_3 A_1 + A_4 A_1^2 = 0$$

qui correspond au cas limite de l'inégalité (11b). On retrouve ainsi les relations établies en utilisant le critère de Routh-Hurwitz. Il faut remarquer que par cette méthode on ne possède pas de renseignements sur les deux autres racines et en particulier sur le signe des parties réelles, seule l'étude du signe des coef-

coefficients A_i , permet de répondre à cette question. Cette étude est omise par la plupart des auteurs ce qui peut partiellement se justifier car dans toutes les configurations de paliers que nous avons étudiées jusqu'ici, les coefficients A_i sont toujours positifs de par la valeur des coefficients de raideur et d'amortissement.

Les relations (8), (12) et (15) permettent d'exprimer la fréquence de fouettement γ_s et la masse critique M_c en fonction des coefficients dynamiques du palier. Il vient :

$$(16) \quad \begin{aligned} \gamma_s^2 &= \frac{(A_{xx} - A_s)(A_{yy} - A_s) - A_{xy} A_{yx}}{B_{xx} B_{yy} - B_{xy} B_{yx}} \\ M_c &= A_s / \gamma_s^2 \\ A_s &= \frac{A_{xx} B_{yy} + A_{yy} B_{xx} - A_{xy} B_{yx} - A_{yx} B_{xy}}{B_{xx} + B_{yy}} \end{aligned}$$

Ainsi pour un palier de géométrie donnée la masse critique adimensionnée est uniquement fonction du nombre de Sommerfeld puisque les coefficients dynamiques sans dimension ne dépendent que de ce nombre. On notera également que la vitesse de rotation intervient dans le dimensionnement de la masse : la détermination d'une masse critique est ainsi équivalente à la détermination d'une vitesse critique de rotation.

Remarquons que pour établir les relations (16) nous avons supposé l'existence d'un seuil de stabilité ; si celui-ci n'existe pas, c'est-à-dire si le palier est stable, cela se traduit au niveau du calcul par un coefficient γ_s^2 négatif. A l'opposé, si la masse adimensionnée M_c est négative, pour un coefficient γ_s^2 positif cela signifie une instabilité du palier pour toute valeur de la masse du rotor.

5. CARTES DE STABILITE

La courbe de variation de la masse critique adimensionnée M_c en fonction du nombre de Sommerfeld S forme ce que l'on appelle la carte de stabilité. Cette courbe divise le plan en deux régions : une région stable et une région instable. Sur la figure 4 nous avons représenté la carte de stabilité et l'évolution de la fréquence de fouettement relative à différents types de paliers.

La carte de stabilité caractérise exclusivement le palier ; elle permet d'une part de déterminer si un point de fonctionnement est stable ou non et d'autre part de calculer au-delà de quelle masse de rotor ou de quelle vitesse de rotation le fouettement apparaît.

On constate que dans le cas d'un palier chargé, il n'existe pas de conditions de fonctionnement totalement instables. Par contre aux grandes excentricités c'est-à-dire aux très fortes charges la stabilité est indépendante de la masse. De même la fréquence de fouettement adimensionnée γ_s , qui est voisine de 0,5 aux charges faibles et modérées, tend rapidement vers zéro lorsqu'on approche de la zone où le palier est infiniment stable.

Dans le cas d'un rotor flexible, la fréquence de fouettement est plus significative que la masse critique car l'instabilité apparaît lorsque la pulsation naturelle du système ω_n est égale à la pulsation de fouettement c'est-à-dire lorsque la pulsation réelle est égale à ω_n / γ_s .

6. ROLE DES COEFFICIENTS DYNAMIQUES VIS A VIS DE LA STABILITE

Les relations (8) et (11) qui permettent de définir les conditions de stabilité du palier ne font pas toutes intervenir la masse du rotor. Ainsi selon les valeurs respectives des coefficients dynamiques il est possible de rencontrer des cas où le système est instable ou stable quelque soit la valeur de la masse M du rotor et des cas où le système est stable pour certaines valeurs de M . On peut donc étudier la contribution des différents coefficients dynamiques sur la stabilité.

6.1 Coefficients de raideur et instabilité statique

Dans le cas où les termes d'amortissement B_{ij} sont nuls, le système linéaire (4) se réduit à :

$$(17) \quad m \begin{Bmatrix} \ddot{X} \\ \ddot{Y} \end{Bmatrix} + \begin{bmatrix} A_{xx} & A_{xy} \\ A_{yx} & A_{yy} \end{bmatrix} \begin{Bmatrix} X \\ Y \end{Bmatrix} = 0$$

Si les termes de couplage A_{xy} et A_{yx} sont nuls le point de fonctionnement n'est stable que si les termes directs A_{xx} et A_{yy} sont tous positifs et cela quelque soit la masse.

L'existence d'un couplage en raideur est généralement source d'instabilité. Dans ce cas le système est stable quelque soit la valeur de la masse si les 3 conditions suivantes déduites de l'étude des racines de l'équation caractéristique associée au système (17) sont vérifiées

$$(18) \quad \begin{aligned} A_{xx} + A_{yy} &> 0 \\ A_{xx} A_{yy} - A_{xy} A_{yx} &> 0 \\ (A_{xx} - A_{yy})^2 + 4 A_{xy} A_{yx} &> 0 \end{aligned}$$

Remarquons que l'un des termes de raideur directe peut être négatif à condition qu'il soit inférieur, en valeur absolue, à l'autre ; dans ce cas un et un seul des termes de raideur croisée doit être négatif. Ceci est en contradiction avec l'hypothèse avancée par Smith [16] selon laquelle la stabilité statique impose que A_{xx} et A_{yy} soient positifs. Ce point sera confirmé dans le paragraphe 7. Par ailleurs lorsque les deux coefficients directs sont positifs un terme de raideur croisée négatif facilite l'insta-

bilité.

Dans le cas où le système est conservatif c'est-à-dire si $A_{xy} = A_{yx}$ les conditions (18) se réduisent à :

$$(19) \quad \begin{aligned} A_{xx} &> 0 \\ A_{yy} &> 0 \\ A_{xx} A_{yy} - A_{xy} A_{yx} &> 0 \end{aligned}$$

L'instabilité statique aura lieu à partir de certaines valeurs des termes de couplage et cela quelque soit la valeur de la masse.

6.2 Coefficients de raideur et d'amortissement

Si les termes de couplage en raideur et en amortissement sont nuls les conditions de stabilité déduites des inéquations (11) seront en particulier satisfaites si tous les coefficients directs sont positifs. Ainsi la condition suffisante, qui s'écrit $A_{ii} > 0$, $B_{ii} > 0$ et $A_{ij} = B_{ij} = 0$ si $i \neq j$ conduit à une stabilité qui n'est pas influencée par la masse.

Dans le cas où il existe un couplage en raideur mais non en amortissement, les conditions de stabilité (11) imposent :

$$(20) \quad \begin{aligned} A_i &> 0 \\ -M [B_{xx} B_{yy} (A_{xx} - A_{yy})^2 + A_{xy} A_{yx} (B_{xx} + B_{yy})^2] &< (B_{xx} + B_{yy}) (B_{xx} A_{yy} + B_{yy} A_{xx}) (B_{xx} B_{yy}) \end{aligned}$$

Soit encore

$$(21) \quad -M (\alpha B_{xx} B_{yy} + \beta A_{xy} A_{yx}) < \delta B_{xx} B_{yy}$$

où α , β et δ sont des coefficients positifs. Dans le cas usuel où les amortissements directs sont tous deux positifs, la relation (21) montre que la stabilité est assurée quelque soit la valeur de la masse si :

$$(22) \quad (\alpha B_{xx} B_{yy} + \beta A_{xy} A_{yx}) > 0$$

soit encore

$$(23) \quad -A_{xy} A_{yx} < \frac{B_{xx} B_{yy}}{(B_{xx} + B_{yy})^2} (A_{xx} - A_{yy})^2$$

le rapport $B_{xx} B_{yy} / (B_{xx} + B_{yy})^2$ étant toujours inférieur ou égal à 0,25 cette condition est plus restrictive que celle relative au cas statique et donnée par la relation (18). Ainsi la présence de l'amortissement direct facilite l'instabilité. Cependant si celle-ci se produit elle peut être supprimée en réduisant la masse.

Dans le cas où un seul terme d'amortissement direct devient négatif, le mouvement n'est pas obligatoirement instable, mais les contraintes sur les valeurs respectives des coefficients sont plus restrictives que celles établies précédemment.

Dans le cas général les conditions de stabilité sont données par les relations (11) et il est quasi impossible d'examiner séparément l'effet des 8 coefficients dynamiques. Cependant il convient de signaler que les coefficients directs d'amortissement facilitent la destabilisation du système.

6.3 Conclusion

Les résultats présentés ici, qui peuvent paraître évident pour un spécialiste en vibrations, montrent que l'instabilité de fouettement trouve son origine dans les termes croisés de raideur et que contrairement à certaines affirmations trouvées dans la littérature :

- (a) L'équilibre stable n'impose pas que les termes directs de raideur soient tous deux positifs, ceci est illustré pour un cas particulier dans le paragraphe suivant,
- (b) Les termes directs d'amortissement ne permettent pas de repousser le seuil de stabilité mais au contraire ils facilitent l'apparition de l'instabilité.

Par ailleurs un palier, dont les coefficients directs de raideur et d'amortissement sont tous positifs et dont les termes de couplage sont nuls est toujours stable. Ce cas est représentatif de certains paliers à patins oscillants bien connus pour leur très grande stabilité.

7. ETUDE NON LINEAIRE D'UN PALIER

Lorsque le point de fonctionnement appartient à la région instable ou lorsque la charge appliquée au palier est fonction du temps, le comportement du palier ne peut être étudié, en toute rigueur, qu'à l'aide de la théorie non linéaire. Les équations du mouvement s'écrivent :

$$(24) \quad \begin{aligned} m \ddot{x} &= W_x(t) + F_x(x, y, \dot{x}, \dot{y}, t) \\ m \ddot{y} &= W_y(t) + F_y(x, y, \dot{x}, \dot{y}, t) \end{aligned}$$

où W_x et W_y sont les composantes de la charge appliquée à l'arbre, et où F_x et F_y sont obtenus par la résolution de l'équation de Reynolds. L'intégration de ce système différentiel non linéaire est effectuée en utilisant une méthode directe de type Euler dont la validité a été prouvée par ailleurs [13, 17].

A titre d'exemple nous présentons les résultats obtenus dans le cas d'un palier à deux lobes préchargés (palier citron), soumis à une charge statique, pour deux valeurs différentes de la masse du rotor, l'une correspondant au domaine stable, l'autre au domaine instable. Les caractéristiques adimensionnées du palier sont les suivantes :

- Rapport de la longueur au diamètre du palier $L/D = 1$
- Précharge géométrique $m = 0,5$
- Excentricité de fonctionnement statique $\epsilon = e/C_B = 0,1$

Pour ce point de fonctionnement les coefficients adimensionnés de raideur et d'amortissement sont :

$$\begin{aligned} A_{xx} &= 38,74 & A_{xy} &= 22,65 & A_{yx} &= -22,38 & A_{yy} &= -1,22 \\ B_{xx} &= 78,92 & B_{xy} &= B_{yx} &= -28,21 & B_{yy} &= 18,79 \end{aligned}$$

ce qui conduit à une masse critique et à une fréquence de fouettement adimensionnées de :

$$M_c = 17,38 \quad \gamma_s = 0,61$$

Les figures 6 et 7 représentent en trait plein le lieu des positions d'équilibre statique du centre de l'arbre à l'intérieur du coussinet et en traits discontinus la trajectoire décrite par le centre de l'arbre à partir d'une position choisie de façon arbitraire (point B), pour deux valeurs de la masse du rotor $M_1 = 4,33$ et $M_2 = 39$. On remarque, Fig. 6, que lorsque le point de fonctionnement appartient au domaine stable de la figure 4, le centre de l'arbre rejoint de manière asymptotique la position d'équilibre statique A. Ceci confirme les résultats obtenus par l'analyse linéaire et infirme l'hypothèse avancée par Smith puisque l'un des coefficients de raideur directe est négatif ($A_{yy} < 0$). Par contre dans le cas où le point de fonctionnement appartient au domaine instable de la fig. 4, le centre de l'arbre décrit une orbite fermée de grande amplitude (Fig. 7) dont les caractéristiques ne peuvent pas être obtenues à partir de la théorie linéaire. La fréquence moyenne de fouettement adimensionnée est voisine de 0,44, valeur différente de celle prévue par la théorie linéaire. Par ailleurs ce mouvement orbital entraîne des forces hydrodynamiques importantes ce qui conduit parfois à la rupture du palier.

8. CONCLUSION

La théorie linéaire permet de prédire les limites de stabilité d'un palier c'est-à-dire la masse critique et la fréquence de fouettement. Son application à différents types de paliers montre que le palier circulaire classique est le moins stable. Les modifications du profil du coussinet qui assurent une précharge géométrique ont généralement un effet stabilisant. Par ailleurs, la réalisation de paliers pour lesquels les termes de raideur croisées sont nuls conduit à des mécanismes très stables (par exemple les paliers à patins oscillants).

La validité de la théorie linéaire a été confirmée par l'étude du comportement dynamique d'un palier à 2 lobes pour deux conditions de fonctionnement correspondant respectivement à un point de fonctionnement stable et instable. Dans le domaine instable le centre de l'arbre décrit une orbite fermée de grande amplitude ce qui engendre de très grandes forces hydrodynamiques nuisibles au bon fonctionnement du mécanisme.

9. REFERENCES

- [1] NEWKIRK B.L., "Shaft whipping". General Electric Review, 1924-p. 169.
- [2] NEWKIRK B.L. and TAYLOR H.D., "Shaft whipping due to oil action in Journal bearings". General Electric Review, 1925, p. 559.
- [3] STODOLA A., "Kritische Wellenstörung Infolge der Nachgiebigkeit des Oelpolsters im Lager". Schweizerische Bauzeitung 1925 85, p. 265.
- [4] HARRISON W.J., "The hydrodynamic theory of the lubrication of a cylindrical bearing under variable load, and of a pivot bearing". Trans. Edinburgh philosophical Soc., Edinburgh, Scotland, 1919 22, p. 373.
- [5] ROBERTSON D., "Whirling of a journal in a sleeve bearing". Phil. Mag., Series 7, 1933, 15, p. 113.
- [6] BURWELL J.T., "The calculated performance of dynamically loaded sleeve bearings ; J. Appl. Mech., 3 (1947).
- [7] BOEKER G.F. and STERNLICHT B., "Translatory fluid whirl in vertical machines". Trans. ASME, 78 (1956), p. 17.
- [8] COLE J.A. and HUGHES C.J., "Discussion de la référence 7 .
- [9] HAAG A.C. and SANKEY G.O. "Elastic and damping properties of oil film journal bearings for application to unbalance vibration calculations". J. Appl. Mech. Trans. ASME, 1958, 80, p. 141.
- [10] STERNLICHT B., "Elastic and damping properties of cylindrical journal bearings". J. basic Eng., Trans. ASME, Series D, 1959, 81, p. 101.
- [11] LUND J.W. and STERNLICHT B. "Rotor bearing dynamics with emphasis on attenuation". J. Basic Eng., Trans. ASME Series, D, 1962, 84, 4, p. 491.

- |12| HAAG "The influence of oil film journal bearings on the stability of rotating machines". Journal of Applied Mech. Trans. ASME, Sept. 1946, p. 211.
- |13| ABDUL-WAHED N., "Comportement dynamique des paliers fluides, étude linéaire et non linéaire". Thèse de Doctorat ès Sciences, Lyon 1982.
- |14| GANTMACHER F.R., "Théorie des matrices", Tome 2, Dunod Paris 1966, p. 193.
- |15| LUND, J.W. "The Stability of an elastic rotor in journal bearings with flexible damped supports". ASME Journal of Appl. Mechanics, Dec. 1965, 87, p. 911.
- |16| SMITH, D.M. "Journal bearings in Turbomachinery" Chapman-Hill Ltd, 1969, p. 100.
- |17| CASTELLI, V. and ELROD, H.G., "Solution of the stability Problem of 360 deg. Self-acting Gas Lubricated bearings". ASME Journal of basic Engineering, Vol. 87, n° 2, June 1965, p. 199.

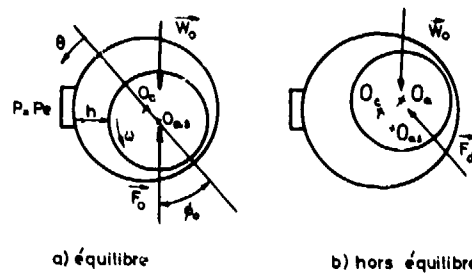


Fig. 1 : Schématisation du palier

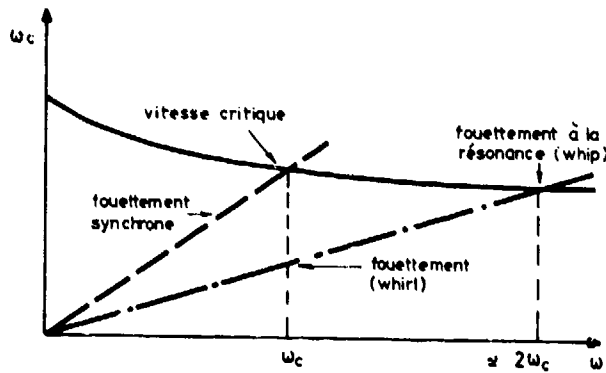


Fig. 2 : Différents types de fouettement

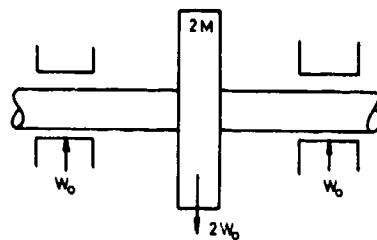


Fig 3 : Schématisation du rotor

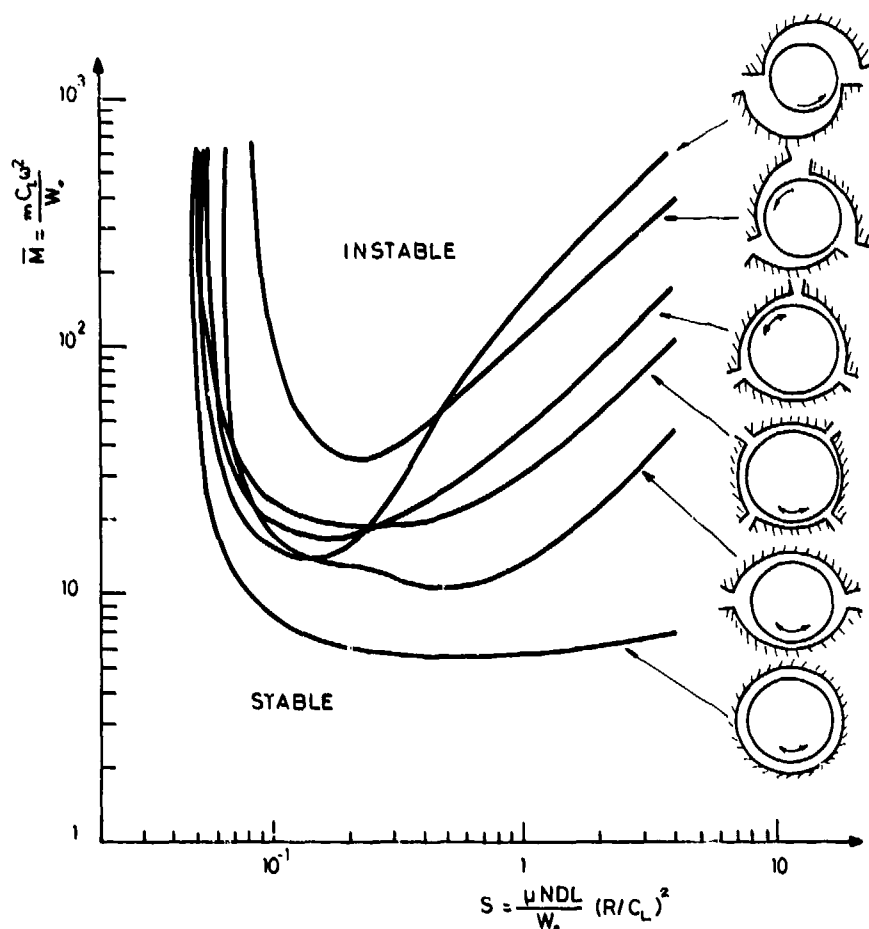


Fig. 4 : Carte de stabilité des différents paliers à géométrie fixe (L/D=1)

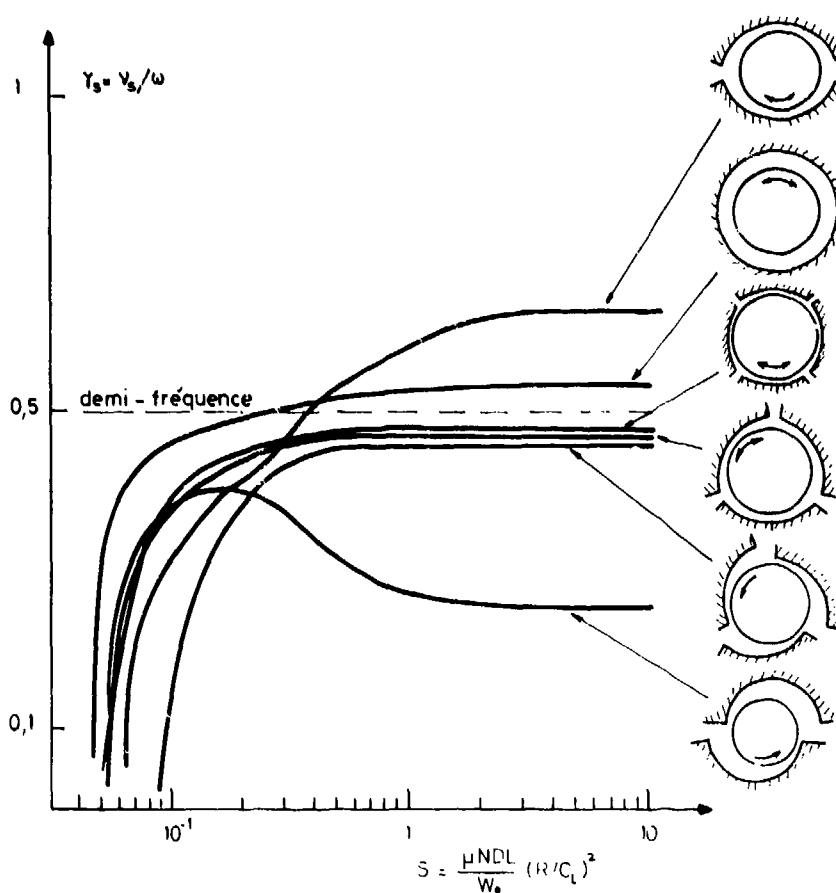


Fig. 5 : Fréquence de fouettement

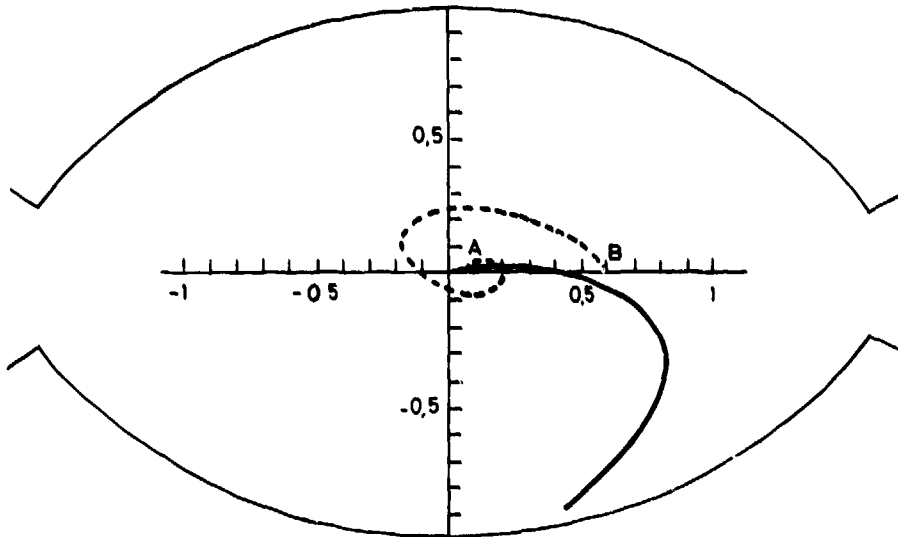


Fig. 6 : Position d'équilibre stable , palier à 2 lobes

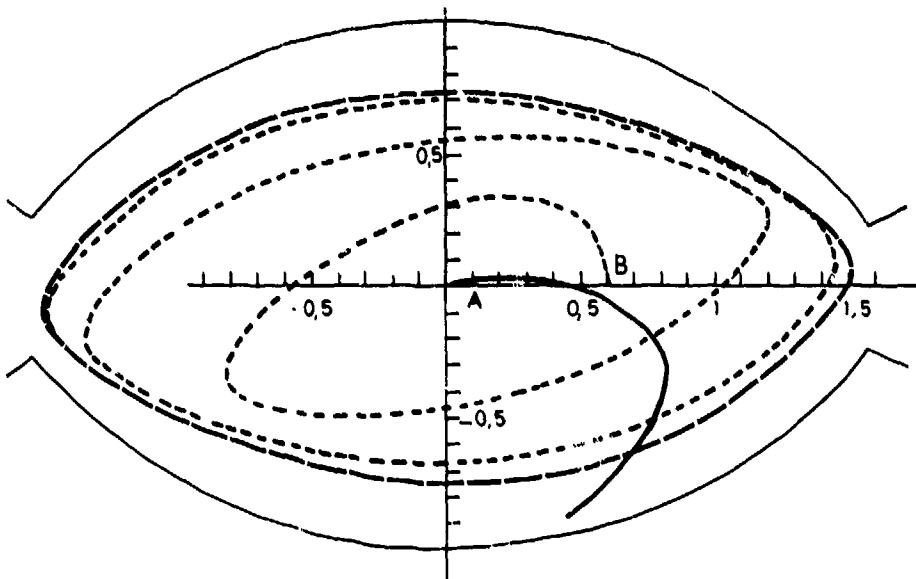


Fig. 7 : Position d'équilibre instable palier à 2 lobes

DISCUSSION

M.Akkök, Middle East Technical University, Tu

It is well known that, in non-circular bearings the groove angle between the arcs and the positions and the preload of arc centres with respect to the bearing centre have strong effect on the stability and whirl frequency. Therefore could you define the non-circular geometries in Figures A, 5 and 6 more specifically in terms of groove angles, positions and preloads on the bearing arcs?

Reponse d'Auteur

Les caractéristiques géométriques des différents types de paliers dont les cartes de stabilité sont présentées figure 4 données dans le tableau ci-dessous

Type de Palier	angle d'amplitude du lobe β_1	angle d'amplitude de la rainure γ_1	angle d'origine du 1 ^{er} lobe σ_1	Coefficient d'asymétrie α	Coefficient de précharge m
2 lobes	160°	20°	100°	0,5	0,5
2 lobes décollés	160°	20°	100°	1	0,5
3 lobes	110°	10°	5°	0,5	0,5
3 lobes décollés	110°	10°	5°	1	0,5
4 lobes	80°	10°	50°	0,5	0,5

Pour chacun des paliers les différents lobes sont identiques.

J.F.Chevalier, SNECMA, Fr

Quand vous calculez les coefficients dynamiques du palier, êtes vous obligé de faire des hypothèses simplificatrices, en particulier sur la corrélation?

Reponse d'Auteur

La valeur des coefficients dynamiques d'un palier dépend évidemment des conditions aux limites utilisées pour intégrer l'équation de Reynolds. Dans l'étude présentée ici, nous avons employé les conditions aux limites de Reynolds. Une comparaison des résultats obtenus pour différents paliers dans le cas où il n'existe pas de rupture du film a été effectuée par ailleurs (ref. 13). Les résultats obtenus montrent que les paliers cylindriques et à lobes symétriques sont généralement moins stables lorsque le film d'huile est complet. Ceci peut exister dans le cas de paliers fortement pressurisés.

J.Fabri, ONERA, Fr

Vous avez montré qu'il existe deux fréquences de fouettement: l'une à la fréquence de l'arbre, l'autre à fréquence moitié. Pourquoi seule la seconde est-elle dangereuse.

Reponse d'Auteur

La première fréquence de fouettement qui correspond à la fréquence de rotation de l'arbre est due aux balours résiduels; dans ce cas la force hydrodynamique dans le film du palier joue un rôle bénéfique et limite l'amplitude du mouvement de l'arbre. Par contre, la demi-fréquence de fouettement est une instabilité vibratoire propre au palier hydrodynamique et qui se développe quand le palier fonctionne dans la zone instable de la figure 4. Dans ce cas le palier est générateur de vibrations. Quand la fréquence de cette vibration entre en résonance avec la fréquence critique du rotor, le palier agit comme un excitateur. Les forces hydrodynamiques dans le film ne s'opposent plus au mouvement de l'arbre mais au contraire ont tendance à l'amplifier, ce qui peut entraîner la destruction du palier.

M.Verneulen, University of Gent, Be

Vous avez présenté des résultats pour des géométries fixes. Avez-vous aussi étudié les paliers à patins oscillants? Est-ce que ces résultats sont disponibles?

Reponse d'Auteur

Oui, nous avons aussi calculé les caractéristiques statiques et dynamiques de différents types de paliers à patins oscillants. Dans ce cas les calculs sont plus complexes car les caractéristiques dynamiques ne dépendent pas seulement de la géométrie du palier et du nombre de sommerfeld mais aussi de la fréquence d'excitation des patins.

Par ailleurs, le frottement au pivot, dont il est très difficile de tenir compte de façon réaliste, modifie ces caractéristiques. Les résultats de ces études sont en partie publiés et font par ailleurs l'objet d'une partie de la thèse de N. Abdul Wahed (ref.13).

R. Holmes, University of Sussex, UK

Even though a journal may be initially unstable, it is conceivable that this instability may be curved into a limit cycle well within the clearance limit. Have any of your computations shown this and have you been able to assess the effects of mass unbalance in this respect?

Reponse d'Auteur

L'étude effectuée ici concerne le comportement dynamique d'un palier supportant un rotor rigide parfaitement équilibré. Ainsi dans l'équation (2), $W_x(t) = W_0$ et $W_y(t) = 0$. Dans ce cas en régime instable, le centre de l'arbre décrit une orbite fermée d'amplitude voisine à celle du cercle de jeu, à une fréquence nettement inférieure à celle de la rotation de l'arbre (fig.7). La force additionnelle due à un balourd a évidemment une fréquence égale à celle de la rotation; elle peut ainsi dans certains cas jouer un rôle stabilisant. Le mouvement orbital de l'arbre est toujours différent de celui présenté figure 7 et l'amplitude de cette orbite varie selon la valeur du balourd.

THE COMPUTER AIDED DESIGN ENTITY (C.A.D.E.)
A NEW APPROACH TO JOURNAL BEARING DESIGN

A.H. Siew
Doctoral Student

B.R. Reason
Senior Lecturer in Tribology

School of Mechanical Engineering
Cranfield Institute of Technology
Cranfield, Bedford MK43 0AL
England

SUMMARY

This paper outlines the main features of a newly developed software suite dealing with the steady-state performance of solid and porous journal bearings. Variable bearing geometry, groove configuration, oil-supply pressure, matrix permeability (for the porous case) and journal misalignment are all within the capabilities of the suite.

The suite developed is design-orientated and circumvents many of the existing bearing design problems. It is particularly suitable for:

1. Analysis and performance prediction of the journal bearings' behaviour under conventional and newly established boundary conditions.
2. Optimisation of bearing performance by progressive modification through direct computer/user interaction whilst observing, in real-time, the effect both numerically and graphically on a direct visual display.

Good agreement has been found between the results from the use of 'C.A.D.E.' and the experimental findings from various sources.

NOTATIONS

C	Radial clearance	U_0	Slip velocity at the film/matrix interface in the x-direction
C_d	Diametral clearance	V_1	Radial velocity component at the journal/film interface
C_m	Couple variable	V_0	Radial velocity component at the film/matrix interface
C_n	Capacity number, $\mu N'(D/C_d)^2(L/D)^2/P$	W	Applied load
D	Journal diameter	W_0	Slip velocity at the film/matrix interface in the z-direction
D_m	Degree of misalignment, $\epsilon'/\epsilon'_{max}$	c	Specific heat
J	Mechanical equivalent of heat	e	Bearing eccentricity
L	Bearing length	e_0	Central eccentricity
L_r	Load ratio, S/S_e	e'	Projected length of the misaligned journal onto the bearing mid-plane
M	Resultant couple from the oil film	e'_{max}	Maximum value of e'
M_x	Component of M about the x-axis	h	Local film thickness
M_y	Component of M about the y-axis	h^*	Film thickness at the film breakdown boundary
N	Journal speed, rpm	h_{min}	Minimum value of h
N'	Journal speed, rps	l	Axial length of oil groove
P	Non-dimensional pressure $P/\omega\eta(R/C)^2$	P	Local film pressure
P_{max}	Maximum value of P	P_0	Oil supply pressure
P	Specific bearing pressure, W/LD	r_i	Inner porous bearing radius
Q_x	Circumferential flow	r_o	Outer porous bearing radius
Q_z	Axial leakage flow	t_i	Oil-inlet temperature
R	Journal radius (R_j)	t_o	Oil-outlet temperature
R_b	Bearing radius	x	Circumferential co-ordinate
S	Sommerfeld number, $\eta N'(R/C)^2/P$	y	Radial co-ordinate
S_e	Equivalent Sommerfeld number due to misalignment as defined by the authors of Ref. 31, $\eta N'(R/C)^2/PL_r$		
T	Bearing wall thickness		
T_{av}	Average temperature (defined in Ref.29)		
U	Journal surface velocity (U_1)		

z	Axial co-ordinate	δ	Small change
\bar{z}	Non-dimensional axial co-ordinate, z/L	ϵ	Eccentricity ratio, e/C
Δ	Duty parameter, $W/\omega\eta RL(R/C)^2$	ϵ_0	Central eccentricity ratio, e_0/C
Δt	Temperature rise, $t_0 - t_1$	η	Lubricant viscosity
Δx	Mesh interval in the x -direction	κ	Angle in degrees subtended by the breadth of the groove to the bearing centre
Δz	Mesh interval in the z -direction	λ	Some angle before the position of maximum clearance where film pressure starts
Φ	Matrix permeability	μ	Coefficient of friction
ψ	Permeability factor, $\Phi r_i / C^3$	θ	Circumferential co-ordinate, $2\pi\bar{x}$
α	Some small angle after π where film pressure terminates	θ_{pmax}	Position of the peak pressure
β	Angle between the central eccentricity vector and the projected journal axis	ϕ	Bearing attitude angle
γ	Weight/unit volume of lubricant	ϕ_0	Angle of the line of centres
γ	Angle between the resultant couple vector and the y -axis	ω	Angular velocity, $2\pi N'$

1 INTRODUCTION

The advent of the digital computer has given the modern bearing designer a reliable and exceedingly powerful tool for establishing optimum designs or evaluating the existing bearing potential.

Although conventional "desk top" design methods have their rightful place where bearing problems are of a relatively straightforward nature, there are design situations where such an approach is not possible, a typical example being one which requires an iterative procedure in order to reach a satisfactory solution.

Today, computers are playing an increasingly important role both in the generation of new design data and in the optimisation of bearing designs. This trend is likely to continue unabated within the foreseeable future.

2 LITERATURE SURVEY

A survey of the literature concerning the application of digital computers to journal bearing design reveals one of the earliest outstanding publications to be that of Christopherson (1), dated 1941, in which the author presented the first elegant numerical solution of the Reynolds equation based upon the "Relaxation Technique" devised by Southwell (2). By using a finite difference representation, this author demonstrated that the fluid-film governing equation for the finite journal bearing could be solved with relative ease; he further showed the new solution technique to be feasible even if oil viscosity was treated as a variable in terms of temperature and pressure. Examples of other notable contributions which may be cited in the published literature concerning the application of this method of solution to the journal bearing problem include the work of Cameron and Wood (3), Walther and Sassenfeld (4), Raimondi and Boyd (5) and Pinkus (6).

Whilst valuable bearing design data were being produced with the help of digital computers which could subsequently be incorporated into the "desk top" design methods, suitable computer programs were also developed to facilitate the analysis and design of journal bearings. Furthermore, computers were being increasingly employed not only to perform the tedious and time-consuming design calculations, but as design tools in ascertaining the effect of changing the various design parameters in order to achieve the desirable design objectives or to establish a compromise among a set of conflicting requirements. Hence, the term "COMPUTER AIDED BEARING DESIGN" was introduced, a typical example being the computer program developed by Lloyd and McCallion (7) for reciprocating engine bearings.

Woolacott and Singh (8,9) illustrated the computer-aided design technique they developed at the National Physical Laboratory; this was later adopted by the Engineering Sciences Data Unit as Item No. 69002 (10) to provide a computer service to industry. The need for computer-aided bearing design was discussed by Rippel (11) whilst Parker and Vickery demonstrated the use of a small computer in engine bearing analysis. A useful survey of computerized bearing design programs was conducted by Taylor (12) in 1971; this survey indicated clearly the availability of computer service to industry and also the gaps that need to be filled.

With the progress made in computer technology, the modern design trend appears to be in programming the computer in such a way that it can make 'value judgements' and 'decisions' automatically in order to achieve the best possible design so that time and effort are both at a minimum. Among those who have explored this novel approach are Seirez and Ezzat (13), Dowson and Ashton (14) and Dowson et al. (15).

3 OUTLINE OF THE APPROACH

This paper outlines the main features of a newly developed software suite dealing with the steady-state performance of solid and porous journal bearings. The study, besides aiming at obtaining accurate basic design data on a broad basis, essential for a sound bearing analysis or design, is also orientated towards achieving the following objectives:

- a) To assist the bearing designer in the prediction of bearing performance characteristics or in ascertaining the effect on performance of an existing bearing through a change of operating parameters.
- b) To simplify the bearing design process, particularly in the optimisation of bearing performance based upon the constraints imposed.

There are a number of good reasons for adopting the present "broad-brush" approach towards the journal bearing problem. Firstly, the available design data for the steady-state performance of journal bearing is generally scattered throughout the literature and very few contributions appear to be aimed at providing design guidance on a broad basis to the industrial designer. Secondly, the information presented is often incomplete, whereas the design data from different sources is usually so incompatible as to be of no direct use owing to the different basic assumptions used, solution techniques employed and the way in which the final results are presented. In order to achieve consistency in data presentation, a consistent method of design chart arrangement was employed by the present authors, as illustrated in reference 16. Thirdly, the study of the various aspects such as boundary conditions, journal misalignment or oil-inlet conditions not only helps to establish the validity of the basic assumptions made and reject the over-simplified ones, but also enables some of the "neglected variables" to be incorporated in the solution thus enabling more realistic bearing data to be produced. This is, perhaps, best illustrated by the comparisons between the computed data from the use of 'C.A.D.E.' and the experimental findings from various sources shown later in the paper.

4 THE SOFTWARE SUITE

The developed software suite consists of a number of computer programs, each capable of performing a specific task or in providing certain information, as outlined in the following sections.

4.1 Computer Programs for Examining the Boundary Conditions of Fluid Film

The use of correct boundary conditions governing the extent and shape of the generated pressure film is of importance in the solution of the Reynolds equation. Under the 'Full Sommerfeld Condition', a full fluid film is assumed to exist continuously around the bearing. The resulting pressure distribution is, therefore, positive in the converging bearing space for $0 \leq \theta < \pi$ and asymmetric negative in the diverging clearance sector for $\pi < \theta < 2\pi$. Although oil may sustain some tensile stresses, as shown by Dyer and Reason (17) if the journal eccentricity is smaller than some critical value, it usually breaks down once the gas expulsion pressure is reached. For a full journal bearing this normally occurs beyond the position of minimum film thickness where the clearance gap diverges. As a result of this departure in the boundary conditions the experimental bearing results are at considerable variance with theory. A typical example being the locus of the shaft centre which, observed from experiments, is nearly a semi-circle whereas the theoretical locus, obtained under this boundary condition, is always at right angle to the load line. It was not until 1957 that Floberg (18) demonstrated experimentally that a full Sommerfeld pressure curve could be maintained if an oil-groove is located at the position of minimum film pressure and that the bearing is operating under high ambient pressures. Thus, this particular boundary condition is only applicable to bearings operating under special circumstances, as employed by Raimondi and Boyd (5) in evaluating the performance characteristics of bearings used in atomic power installations and pumps where the ambient pressure is considerably higher than the atmospheric.

By assuming film pressure exists only for $0 \leq \theta < \pi$ and neglecting the negative or sub-atmospheric pressure, Gumbel and Everling (19) circumvented the main problem of the 'Full Sommerfeld Condition'. The new boundary condition is commonly referred to in the literature as the 'Gumbel Boundary Condition' or simply as the 'Half Sommerfeld Condition'. The main drawback of 'Gumbel Boundary Condition' is that it involves an abrupt change of pressure gradient at $\theta = \pi$, which is unrealistic for obvious reasons. Nevertheless, this boundary condition is frequently employed by researchers because of its simplicity and the fact that the predicted load capacity under this boundary condition is sufficiently accurate for most of the operating eccentricities.

A widely accepted film terminating condition which overcomes the difficulty of pressure discontinuity is the 'Reynolds Boundary Condition' (20). With this boundary condition, film pressure is assumed to continue until both the value of P and $\partial P / \partial x$ have fallen to zero; whilst the commencement of the film pressure is taken to be at the position of maximum clearance. Swift (21), on the basis of the stability of the lubricating film in journal bearings, and Stieber (22), from a consideration of the continuity of flow, provide justifications for the condition $P = \partial P / \partial x = 0$ at the film breakdown boundary. The 'Swift-Stieber Condition', as it is sometimes called, has been shown analytically by Cameron and Wood (3) to be the one which corresponds to the condition of minimum potential energy and maximum load. Christopherson (23) further showed that

this film terminating condition coincides with the minimum friction condition.

The assumption that film pressure starts at the position of maximum clearance implies that a full-width film begins at $\theta=0$. In an actual bearing, however, the commencement of the film pressure depends very much upon the supply pressure and oil-inlet configuration. Thus, it does not appear unreasonable to use the same boundary condition ($P = \partial P / \partial x = 0$) as that at breakdown. Such a condition provides a 'free' boundary and eliminates the restriction that film pressure begins specifically at the position of maximum clearance. This is, clearly very useful when dealing with journal misalignment as the film thickness now varies not only circumferentially, but also axially along the bearing length. Some experimental justifications for this boundary condition have been provided by Dyer (24) who found that film pressure may begin in the diverging clearance region before the position of maximum film thickness, particularly for smaller clearance bearings or when bearings operate at high eccentricities.

The behaviour of film rupture in the cavitated region has been studied by Jakobsson and Floberg (25). From a consideration of the continuity of flow a new boundary condition governing the reformation of film pressure was postulated. This film build-up boundary condition is probably the best currently available, but, unfortunately, it is difficult to implement in the solution.

From experimental observations of film rupture and separation of fluid on transparent bearings, a 'separation' boundary condition at the trailing edge of the lubricant film has been suggested by Mori et al (26). The criterion employed is that the separation of the film from the bearing surface takes place when the pressure and the velocity gradients perpendicular to the surface both become zero. The theoretical solution based on this approach shows some agreements with the experimental results, but, as this boundary condition leads to negative pressure after the position of minimum film thickness, it is only recommended by the authors for lightly-loaded bearings, otherwise the negative pressure in the cavitated region may become excessive.

An analysis showing the conditions for the rupture of a lubricating film and taking into account the effects of gravity, inertia and surface-tension was given by Coyne and Elrod (27). These authors derived the boundary conditions based on a theoretical model which assumes that, at film rupture, a partial film spreads across the clearance space adhering only to the moving surface with a quadratic tangential velocity distribution.

It is not within the scope of the present study to give detailed comparisons and show the effect upon the various bearing operating parameters arising from the use of each of the aforementioned boundary conditions but, nevertheless, some of the more popular ones have been examined and are enumerated below:

Boundary Conditions 1 {See Fig. 1(a)}

Film pressure begins at the position of maximum clearance and continues for the converging portion of the bearing. (Gümbel Boundary Condition)

$$P = 0 \text{ at } \theta = 0, \pi \text{ and } \pi \leq \theta \leq 2\pi$$

Boundary Conditions 2 {See Fig. 1(b)}

Film pressure and pressure gradients are both equal to zero at the commencement and termination of the pressure curve.

$$P = 0 \text{ at } \theta = \pi + \alpha, 2\pi - \lambda \text{ and } \pi + \alpha \leq \theta \leq 2\pi - \lambda$$

$$\partial P / \partial x = 0 \text{ at } \theta = \pi + \alpha, 2\pi - \lambda \text{ and } \pi + \alpha \leq \theta \leq 2\pi - \lambda$$

where

α - an angle after π where film pressure terminates

λ - an angle before the position of maximum clearance where film pressure starts

Boundary Conditions 3 {See Fig. 1(c)}

Film pressure begins at the position of maximum clearance and continues until both the pressure and pressure gradients have fallen to zero. (Reynolds Boundary Condition)

$$P = 0 \text{ at } \theta = 0, \pi + \alpha \text{ and } \pi + \alpha \leq \theta \leq 2\pi$$

$$\partial P / \partial x = 0 \text{ at } \theta = 0, \pi + \alpha \text{ and } \pi + \alpha \leq \theta \leq 2\pi$$

Boundary Condition 4

The film build-up boundary is established from a consideration of the flow-balance as suggested by Jakobsson and Floberg (25) whilst allowing for the oil-inlet conditions. The film breakdown boundary is assumed to be at the position where both the pressure and pressure gradients are zero.

$$\left(\frac{h^3 U}{2}\right) \Delta z = \left(\frac{hU}{2} - \frac{h^3}{12\eta} \frac{\partial P}{\partial x}\right) \Delta z + \left(\frac{h^3}{12\eta} \frac{\partial P}{\partial z}\right) \Delta x \quad (\text{Film build-up boundary condition})$$

$$P = \partial P / \partial x = 0 \text{ at } \theta = \pi + \alpha \quad (\text{Film breakdown boundary condition})$$

Since the numerical solution employing Boundary Conditions 4 takes into account the presence of supply pressure and oil-inlet grooving, it will be treated separately, as shown later in Section 4.3.

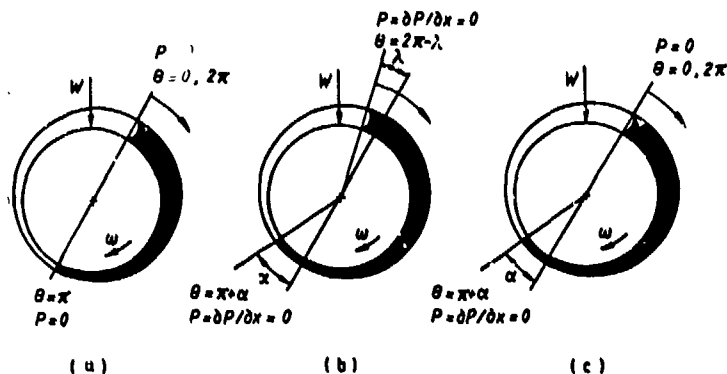


Fig.1 Boundary conditions of fluid film

The computer programs developed, employing the above boundary conditions, are capable of giving the following information:

- Bearing Load Parameter (Δ)
- Sommerfeld Number (S)
- Attitude Angle (ϕ)
- Journal Friction Parameter ($\mu R/C$)
- Minimum Film Thickness Parameter (h_{min}/C)
- Entrainment Flow ($Q_x/RCN'L$)
- Axial Leakage Flow ($Q_z/RCN'L$)
- Flow Ratio (Q_z/Q_x)
- Temperature Rise Parameter ($J\gamma\Delta t/P$)
- Peak Pressure (P_{max})
- Position of Peak Pressure (θ_{pmax})

Fig.2 shows a comparison of the central pressure profiles obtained under the aforementioned boundary conditions together with the experimental curve of McKee et al., (28). The theoretical bearing eccentricity ratios were deduced from the operating Sommerfeld numbers employing the representative oil viscosity values, as given in the reference.

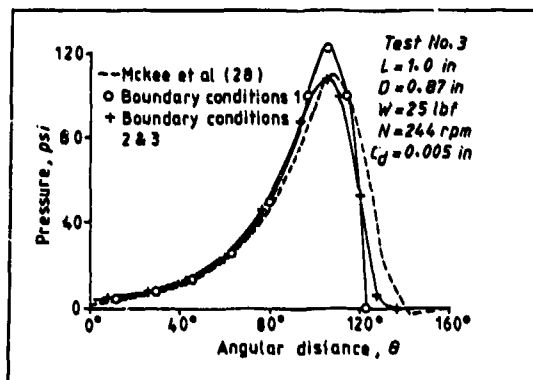


Fig.2 A comparison of the central pressure profiles

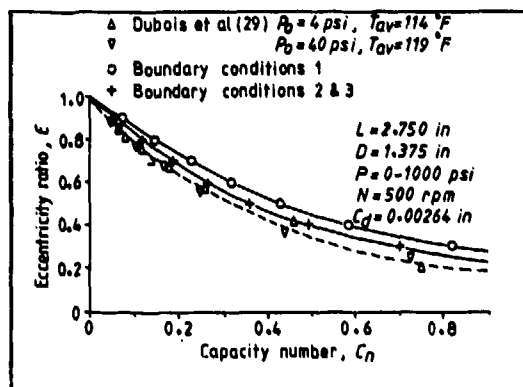


Fig.3 A comparison of E versus C_n at $L/D=2.0$

As shown in Fig. 3 - Fig. 5, the predicted results of eccentricity ratio versus capacity number, bearing frictional variable versus capacity number and eccentricity ratio against attitude angle agreed with the experimental findings of Dubois et al., (29). It is apparent from these direct comparisons that the theoretical results obtained with Boundary Conditions 2 and Boundary Conditions 3 are indistinguishable. These computed results correlated better with the experimental data than those obtained with Boundary Conditions 1.

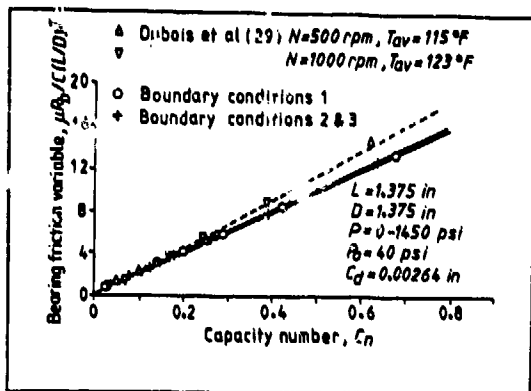


Fig. 4 A comparison of the bearing friction variable against capacity number at $L/D=1.0$

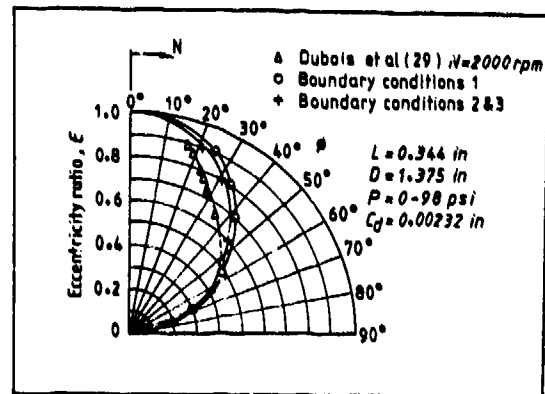


Fig. 5 A comparison of ϵ versus ϕ at $L/D=0.25$

As axial leakage flow is expected to be influenced considerably by the oil-supply pressure and the type of groove configuration present in the bearing which were neglected in the numerical solution employing Boundary Conditions 1, 2 or 3, the computed oil flow and, consequently, the temperature rise parameter can only be considered approximate in nature. Further treatment of this problem is given in Section 4.3.

4.2 A Computer Program for the Misaligned Journal Bearings

A consideration of the problem of journal misalignment and its effect upon the various performance characteristics is important in bearing design in view of the fact that elastic deflection, thermal distortion, asymmetrical loading and inaccuracies in component production and assembly frequently occur in practice. Although the subject has received attention since the early thirties, there is still a paucity of design information in the available literature. Undoubtedly, one of the major difficulties in obtaining an analytical solution for the misaligned journal bearing is the overall intractability of the problem, this being highlighted by the major simplifying assumptions that have been resorted to.

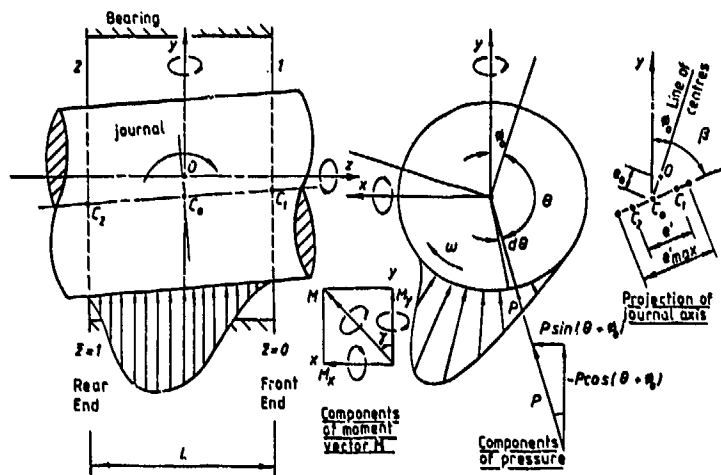


Fig. 6 Co-ordinate system for the misaligned journal bearing

The numerical solution, outlined herein, overcomes this difficulty and allows for bi-planar misalignment to any degree including the case when contact between the journal and bearing occurs. Fig. 6 shows the co-ordinate system used for the misaligned journal bearing. The computer program, developed as a result of this study, is stable and is capable of accepting any practical bearing L/D and eccentricity ratio. Extensive design data have already been obtained upon which a variety of design charts were constructed enabling the effect of misalignment on the various performance parameters to be better appreciated. Additionally, interactive computer graphical techniques were also implemented. This allows a designer to readily cognize the overall effect of misalignment in practical situations. As an example, Fig. 7(a) shows the pressure distribution of a perfectly aligned journal bearing ($L/D=0.25$) operating at $\epsilon_0=0.7$. Fig. 7(b) shows the pressure distribution when the journal is tilted to $D_m=0.4$ and finally Fig. 7(c) illustrates the extreme misaligned condition when contact between the journal and bearing just occurs.

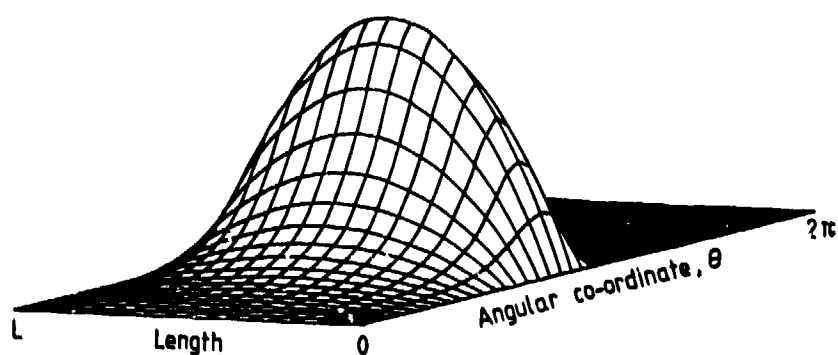
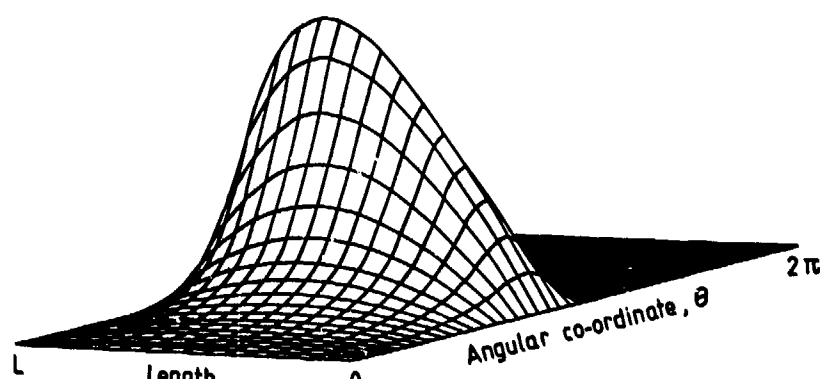
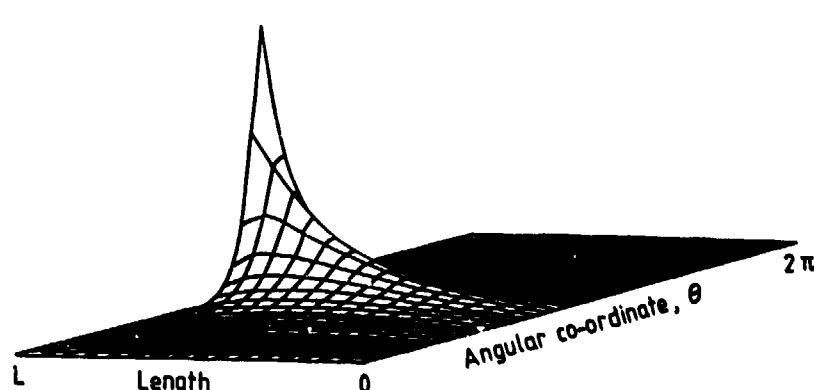
(a) A perfectly aligned case ($D_m=0.0$)(b) A typical misaligned case ($D_m=0.4$)(c) A maximum misaligned case ($D_m=1.0$)

Fig.7 The effect of misalignment upon the film pressure distribution ($L/D=0.25$, $\epsilon_g=0.7$, $\beta=0.0$)

As reported previously (16), good correlation has been found between the present computed results and the experimental findings of Dubois et al. (30 and 31). Figs. 8 (a)-(b) are samples of the comparison showing the validity of the computed data. A further noteworthy feature of the present computer program is that it has predicted twin peaks in the film pressure distribution under some conditions of 'twisting' misalignment (i.e. misalignment in a horizontal plane about the y-axis), this is in agreement with the observations made by Dubois et al. (30). It is believed that this is the first theoretical verification of this phenomenon reported in the literature.

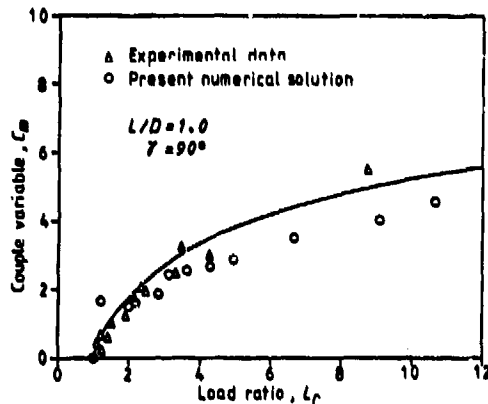


Fig. 8(a) A comparison of C_m versus L_r between the present numerical solution and the experimental results of Dubois et al (Ref. 31) for axial misalignment

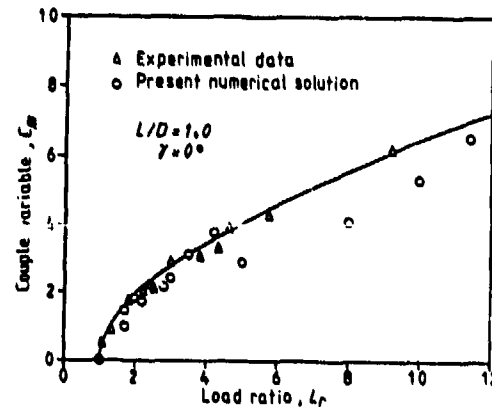


Fig. 8(b) A comparison of C_m versus L_r between the present numerical solution and the experimental results of Dubois et al (Ref. 31) for twisting misalignment

4.3 Computer Programs for Forced-Feed Journal Bearings

Forced-feed journal bearings are widely used in high speed machinery where effective cooling is essential. The main and connecting rod bearings of internal combustion engines are almost universally fed with oil under pressure. These bearings are also commonly employed in heavy machinery such as turbines, industrial gears and compressors.

Hitherto, most of the available bearing design studies have been obtained by neglecting the presence of a supply pressure and inlet configuration of some kind. The assumptions, frequently employed in the solution of the Reynolds equation, are:

- a) Film rupture does not occur.
- b) Oil is supplied to the bearing at ambient pressure through an imaginary axial groove at the line of maximum film thickness.
- c) Pressure and pressure gradients are both zero at the film breakdown boundary and film reformation takes place only along the line of maximum film thickness.

In practice, however, none of these assumptions may be considered completely satisfactory. As a result of the inaccuracy of these assumptions, predicted bearing parameters such as oil flow can be at variance with the experimentally measured values, this being highlighted earlier in Section 4.1.

To tackle this problem, a vigorous analysis of forced-feed journal bearings was carried out. This study led, eventually, to the development of a number of computer programs which are capable of giving the following information:

- a) The effect of supply pressure on bearing performance characteristics
- b) The effect of varying the groove size on various bearing performance parameters.
- c) The comparison of performance characteristics computed for bearings with either an oil hole, an axial groove, twin axial grooves or a full circumferential oil groove.

In conjunction with this study, two types of boundary conditions were examined. These were Boundary Conditions 2 and Boundary Conditions 4, elucidated earlier. The former, and more conventional one, assumes that film rupture does not occur (but discards any negative pressure), whereas the latter allows for film rupture, to take into account the presence of cavitation in the diverging clearance region.

Fig. 9 shows a typical film pressure distribution computed with Boundary Conditions 4 for a bearing with twin axial grooves subjected to a feed pressure of $P_0 = 0.1P$. The grooves, extending over $3/4$ of the bearing length, are diametrically opposite to each other and at $\pm 90^\circ$ to the load line. As can be observed from this plot, the film build-up boundary begins almost at the groove, which is appreciably later than the position of maximum clearance as commonly assumed. Since bearing leakage flow is dictated by the axial pressure gradient $\partial P / \partial z$, this plot provides a convincing explanation for the profound lack of agreement in oil flow between the conventional theory (which employs either Boundary Conditions 1, 2 or 3) and the experimental results.

Fig. 10 is another example of the film pressure distribution, computed for a bearing which has a full central circumferential oil groove. It is noteworthy that, for bearings with this particular type of groove configuration, the film pressure distribution is divided into two halves. The magnitude of the film pressure distribution is markedly reduced and therefore the associated load-carrying capacity would be considerably lower than the ungrooved type. Hence, the operating eccentricity of this particular type

of bearing would be higher for a given load.

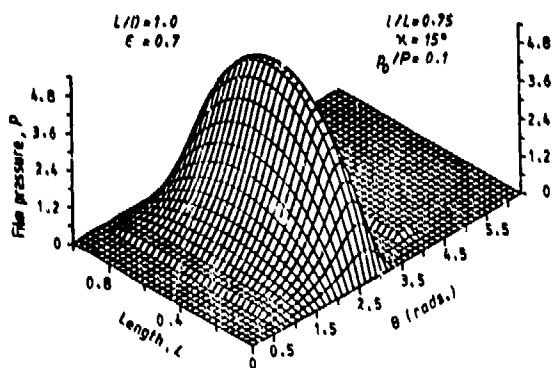


Fig. 9 Film pressure distribution computed for a bearing with twin axial oil grooves

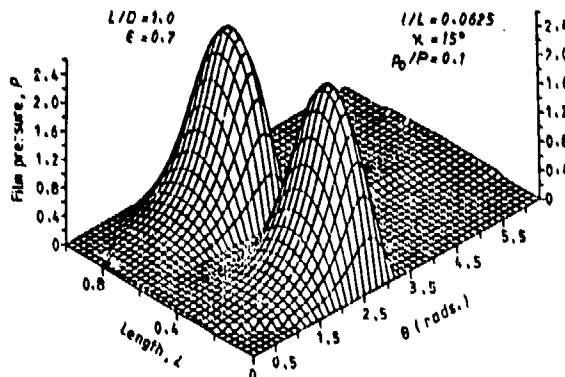


Fig. 10 Film pressure distribution computed for a bearing with a full circumferential oil groove

It is apparent from Fig. 10 that the film build-up boundary, established by using the flow-balance conditions, curves forward considerably at both sides of the central groove before a full-width film is attained, this is in agreement with the experimental observations of Cole et al (32) carried out on transparent bearings. Hence, the calculated axial leakage flow, based on the newly implemented Boundary Conditions 4, is expected to be more realistic. This is, perhaps, best illustrated by the correlations found (Fig. 11 and Fig. 12) between the present computed results and the experimental findings of McKee (33) and Woolacott (34). In the former case, the numerical results were computed on the basis of a 'same load' parameter employing the effective viscosity of the oil recommended by the author whereas, in the latter, they were based directly on the operating eccentricity ratios reported experimentally.

Further analysis of the results has shown that the use of Boundary Conditions 4 not only enables better correlated oil flow and friction values to be predicted, but also provides an explanation for the inadequacy of the conventional film boundary conditions (viz. Boundary Conditions 1, 2 and 3).

It is not intended to deal with the analysis here, nor to show the extent of the design data obtained as this will be presented in a separate paper in the near future.

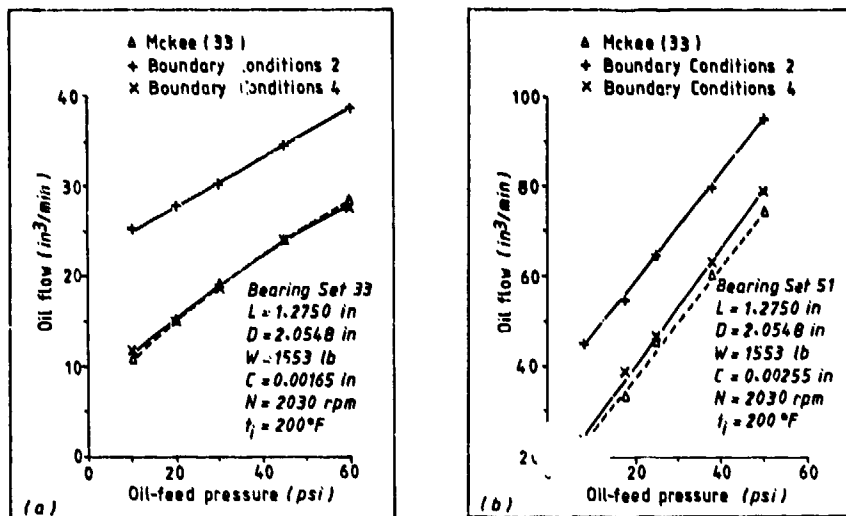


Fig. 11 Comparisons of oil flow for bearings with an oil hole between the present computed results and the experimental findings of McKee (33)

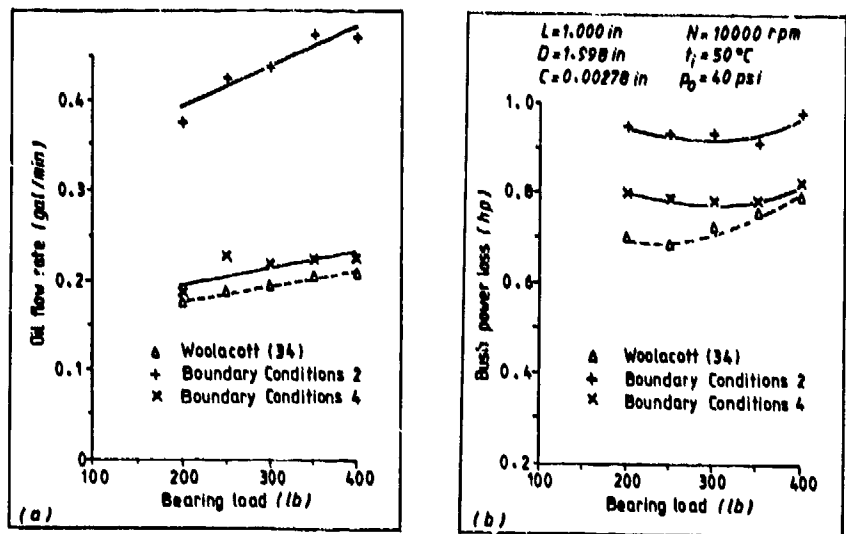


Fig. 12 A comparison of oil flow rate and bush power loss for a bearing with twin axial grooves between the present computed results and the experimental findings of Woolacott (34)

4.4 A Computer Program for the Porous Journal Bearings

Porous journal bearings are usually mass produced and are extensively used in a variety of devices, such as, electric motors, fan heaters and hair dryers. These bearings are made of sintered metal and are impregnated with lubricating oil before being put into service.

Basically, the solution to the fluid flow problem in a porous journal bearing entails the simultaneous solution of two distinct equations. The first being the modified Reynolds equation, which describes the hydrodynamic behaviour of the fluid film between the journal and bearing, whilst the second, the Poisson/Laplace equation, governs the flow of the fluid within the porous matrix.

Although a solution to this pair of simultaneous equations can be obtained by closed analytical methods, this approach is, so far, not satisfactory owing to the drastic approximations that have to be resorted to in order to achieve a solution.

The newly developed computer program, outlined herein, circumvents this problem. The solution was based on a finite difference technique and employed the boundary conditions $P=\partial P/\partial x=0$. Additionally, the interfacial slip across the pore mouth was accounted for by the Darcy expression. Fig. 13 shows the porous bearing configuration used in the analysis and Fig. 14 illustrates the velocity components in the oil film. The full analysis has been reported (35) and need not be repeated here.

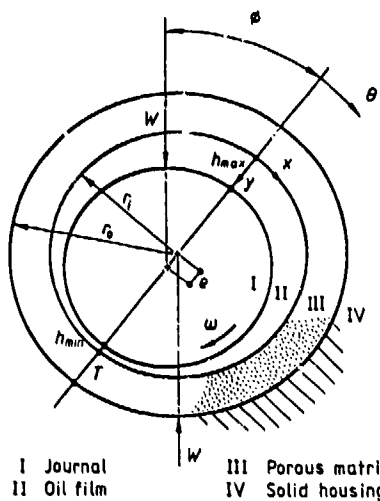


Fig.13 Porous bearing configuration

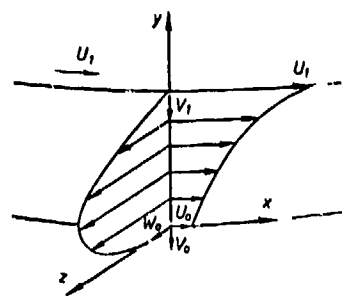


Fig.14 Velocity components in the oil film

The predicted bearing results, based upon the present computer program, have been shown to be accurate. A further attractive feature of the present numerical solution is the adoption of cylindrical co-ordinates. This makes it possible for the accuracy of the computed bearing results to be maintained for increasing T/D ratios; thus allowing for an unrestricted T/D ratio in bearing design. The computer program developed is general in structure permitting the performance characteristics of any combination of L/D, T/D and ψ encountered in practice to be computed. Useful design information has already been obtained upon which design charts have been constructed to provide the industrial designer with a compact format from which a bearing design may be quickly optimised for a set of operating conditions.

5 SOME COMPUTER-AIDED BEARING DESIGN TECHNIQUES

During the development of the software suite, a number of useful computer-aided design techniques were developed and implemented in order to make the task of bearing performance analysis or design as straightforward as possible. Some of these techniques are briefly discussed below:

a) Input Data Checking

Each input datum is automatically checked by the computer to ensure that its magnitude is within the practical range of the production bearings:

$$\begin{aligned} \text{e.g. } 0.20 \leq L/D \leq 2.00 \\ 0.05 \leq \epsilon \leq 0.95 \end{aligned}$$

All incorrect input data or typing errors at the computer terminal keyboard are immediately rejected by the computer. Should this occur, the user is then warned through the presentation of an error message and subsequently requested to re-supply the correct data. This simple computational technique prevents spurious output data being produced, ensures the reliability of the final results and most importantly avoids unnecessary computational work being executed.

b) Interactive Graphical Display Technique

The implementation of this graphical display technique into the various computer programs has proved to be fruitful because it gives, as an immediate visual display on the console screen, the effect of changing certain design parameters, pictorially, in a readily understandable form. Such a technique is particularly useful in predicting the performance of a bearing. Sample results portraying the utility of this technique can be seen in Fig. 7 for the mal-distribution of fluid film pressure under varying degrees of journal misalignment, whilst Fig. 9 and Fig. 10 illustrate clearly the effect on film pressure distribution through the employment of two distinctly different types of oil-inlet groovings.

c) Computer/User Interaction

Since the software suite developed is intended to be used for both bearing performance analysis and design, it becomes apparent that it would be beneficial to keep the structure of each individual program as flexible as possible. For this reason, parameters such as the bearing geometry, groove configuration, oil-supply pressure, permeability factor and the operating eccentricity ratio are all deliberately left open to be chosen by the user in order that the effect of changing any of these design parameters upon the various performance characteristics can readily be made apparent. Thus, by progressively altering the bearing configuration or any design parameter at one's discretion and observing in real-time the result of such a change, a satisfactory design can be produced. To facilitate the interaction mode between the user and the computer, optional choices, such as a scan over a range of operating eccentricity ratios or a view at the graphical output, were built into the computer programs. What the user is required to do is merely to indicate his own subjective response with a single letter 'Y' for 'yes' and letter 'N' for 'no'. By abbreviating the optional reply in this manner, both the typing and possible typing errors are reduced to a minimum.

6 CONCLUDING REMARKS

The broad approach adopted in the present study has undoubtedly made the task much more challenging but, nevertheless, rewarding. During the development of this software suite, each individual computer program was carefully tested and the accuracy of the computed results checked. In addition, some effort was also devoted to correlating the numerical results from the use of 'C.A.D.E' with established experimental findings from various sources. This measure was taken in order to justify the bearing design data obtained and for the results to be of use to the industrial designer.

By opting for a numerical approach, no drastic approximation needed to be made which could otherwise lead to serious error. This factor, together with the refinements made in the film boundary conditions, has made it possible for more accurate and realistic design data to be obtained.

Finally, the work reported herein, has clearly demonstrated both the capability and suitability of the digital computer as a powerful design tool. This trend towards computer-aided bearing design is expected to accelerate owing to a greater awareness of

its potential and also the general availability of computer systems and software packages. It is, however, to be emphasised that the computer solution to bearing design problems should always be considered in relation to the complexity of the information required and total integrated effort. By such an approach 'sledge hammers will not be applied to the problem of cracking nuts!'

7 REFERENCES

- (1) Christopherson, D.G. 'A new mathematical method for the solution of film lubrication problems', Proc. Inst. Mech. Engrs., Vol. 146, 1941, pp 126-135
- (2) Southwell, R.V. 'Relaxation Methods in Engineering Science', Clarendon Press, Oxford, 1940
- (3) Cameron, A and Wood, W.L. 'The full journal bearing', Proc. Inst. Mech. Engrs., Vol. 161, 1949, pp 59-72
- (4) Walther, A. and Sassenfeld, H. 'Pressure distribution and load in a 360° journal bearing, for values of the characteristics B (Ratio of diameter to length) from 0 to 8, and eccentricity C = 0.1 to 0.95', Dept. of Scientific and Ind. Research, Sponsored Research (Germany), Report No. 11, 1950, IPM. Report No. 8
- (5) Raimondi, A.A. and Boyd, J. 'A solution for the finite journal bearing and its application to analysis and design: I, II, III', Trans. A.S.L.E., Vol. 1, 1958, pp 159-209
- (6) Pinkas, O. 'Solution of Reynolds equation for finite journal bearings', Trans. Am. Soc. Mech. Engrs., Vol. 80, 1958, pp 858-864
- (7) Lloyd, T. and McCallion, H. 'A computer program for the design of reciprocating engine bearings', Proc. Instn. Mech. Engrs., Vol. 182 Pt. 3L, 1967 - 68, pp 193-205
- (8) Woolacott, R.G. 'Computer-aided tribological design', Tribology, Jan. 1968, pp 21-22
- (9) Singh, S. 'Conversational techniques in computer-aided bearing design', 1949 NEL Report 429, pp 12-22
- (10) ESDU, 'Computer service for prediction of performance of steadily loaded pressure fed hydrodynamic journal bearings', Engineering Sciences Data Unit, Item 69002, Inst. Mech. Engrs. London, 1969
- (11) Rippel, H.C. 'Designing fluid-film bearings by computer', Mech. Engineering, June 1970, pp 30-41
- (12) Taylor, C.M. 'A survey of computerized bearing design programmes', Tribology, May 1971, pp 87-93
- (13) Seirez, A. and Ezzat, H. 'Optimum design of hydrodynamic journal bearings', Trans. A.S.M.E., J. Lub. Tech., July 1969, pp 516-523
- (14) Dowson, D. and Ashton, J.N. 'Optimum computerized design of hydrodynamic journal bearings', Int. J. Mech. Sci., Vol. 18, 1976, pp 215-222
- (15) Dowson, D., Blount, G.N. and Ashton, J.N. 'Optimisation methods applied to hydrodynamic bearing design', Int. J. for Numerical Methods in Engineering, Vol. 11, 1977, pp 1005-1027
- (16) Reason, B.R. and Siew, A.H. 'A numerical solution for the design and performance evaluation of journal bearings with misalignment', Inst. Mech. Engrs., 1982, C9/82, pp 77-85
- (17) Dyer, D. and Reason, B.R. 'A study of tensile stresses in a journal-bearing oil film', J. Mech. Eng. Sci., Vol. 18, 1976, pp 46-52
- (18) Floberg, L. 'Attitude-eccentricity curves and stability conditions of the infinite journal bearing', Trans. Chambers Univ. Technol. No. 235, Gothenburg, Sweden, 1961
- (19) Gumbel, L. and Everling, E. 'Reibung und Schmierung im Maschinenbau', Krayn, Berlin, 1925
- (20) Reynolds, O. 'On the theory of lubrication and its application to Mr Beauchamp Tower's experiments, including an experimental determination of the viscosity of olive oil', Phil. Trans. Roy. Soc., London, Vol. 177, Pt. I, 1886, pp 157-234
- (21) Swift, H.W. 'The stability of lubricating films in journal bearings', Proc. Inst. Civil Eng., Vol. 233, 1931, pp 267-322

- (22) Stieber, W. 'Das Schwimmlager', Krayn, Berlin, 1933
- (23) Christopherson, D.G. 'Boundary conditions in lubricating films', The Engineer, Vol. 203, 1957, pp 100
- (24) Dyer, D. 'Theoretical and experimental studies of the effect of clearance and geometry in hydrodynamic journal bearings', Ph.D. Thesis 1974, School of Mech. Eng., Cranfield Inst. of Tech., Cranfield, England.
- (25) Jakobsson, B. and Floberg, L. 'The finite journal bearing considering vaporization', Trans. Chambers Univ. Technol., Gothenburg, Sweden, 1957
- (26) Mori, H., Yabe, H. and Fujita, Y. 'On the separation boundary condition for fluid lubrication theories of journal bearings', Trans. A.S.L.E., Vol. 11, 1968, pp 196-203
- (27) Coyne, J.C. and Elrod, H.G. 'Conditions for the rupture of a lubricating film', Part I: Theoretical model, Trans. A.S.M.E., Vol. 92, Series F, No. 3, 1970, pp 451-456, Part II: New boundary conditions for Reynolds equation, Trans. A.S.M.E., Vol. 93, Series F, No. 1, 1971, pp 156-167
- (28) McKee, S.A. and McKee, T.R. 'Pressure distribution in oil films of journal bearings', Trans. A.S.M.E., Vol. 54, 1932, pp 149-165
- (29) Dubois, G.B. and Ocvirk, F.W. 'Experimental investigation of eccentricity ratio, friction and oil flow of short journal bearings', N.A.C.A. Tech. Note 2809, 1952
- (30) Dubois, G.B. Mabie, H.H. and Ocvirk, F.W. 'Experimental investigation of oil film pressure distribution for misaligned plain bearings', N.A.C.A., Tech. No. 2507, 1951
- (31) Dubois, G.B., Ocvirk, F.W. and Wehe, R.L. 'Experimental investigation of misaligned couples and eccentricity at ends of misaligned plain bearings', NACA, Tech. No. 3352, 1953, 1-81
- (32) Cole, J.A. and Hughes, C.J. 'Oil flow and film extent in complete journal bearings', Proc. Instn. Mech. Engrs., Vol. 170, 1956, pp 499-510
- (33) McKee, S.A. 'Oil flow in plain journal bearings', Trans. A.S.M.E., Vol. 74, 1952, pp 841-848
- (34) Woolacott, R.G. and Macrae, D. 'The performance at high speeds of complete plain journal bearings with two axial oil-inlet grooves', 1967, N.E.L. Report No. 326
- (35) Reason, B.R. and Siew, A.H. 'A numerical solution to the coupled problem of the hydrodynamic porous journal bearing', Int. Conf. on Numerical Methods for Coupled Problems, Univ. of Swansea, U.K., Sept. 1981, pp 769-780

8 ACKNOWLEDGEMENTS

The authors would like to thank the staff at the Cranfield Computing Centre for their assistance. In addition, A. H. Siew gratefully acknowledges support from the Science Research Council in providing a 'Case Award' under which it was possible to carry out this extensive research programme.

DISCUSSION

P.G. Astridge, Westland Helicopters, Yeovil, UK

The suite of design programs described would be welcomed by transmission designers in general. As the author mentioned that the package represents a first stage, and that extensions are envisaged, I would make a plea for further programs to aid the aero-engine designer. Plain journal bearings used in reduction gearing, whether for propeller drives, or for helicopter gearbox drives, tend to operate at very high eccentricity ratios, local pressures, and surface tractions. Local plastic flow of the whitmetal, and elastic deformation of steel substrates appear inevitable. It would be useful if (a) the analysis could be extended to cover this, and (b) that the various design criteria be addressed, one of which is the shear stress/strength ratio in the whitmetal.

the oil film shape and the damping coefficients arise from the squeeze film considerations.

The linearized model has proved extremely useful in rotor bearing system analysis. It is possible to carry out the most sophisticated analysis of rotor behavior by using the eight linearized coefficients of bearing. It has been analytically found that the damped natural frequency is not greatly affected by the bearing coefficients but the damping characteristics of the system which are very important for instability and unbalance response are sensitively affected [4]. Therefore, it is necessary to have an accurate knowledge of the fluid film bearing coefficients for dynamic conditions.

The theoretical derivations of these coefficients are now well known, many being based on the finite difference solutions of the Reynolds equation with constant viscosity. Although linearization is valid only for small amplitudes, Lund and Thomsen [5] state that, in practice, it had been found to hold for amplitudes of up to one half of the clearance. However, considering the highly non-linear oil film forces with respect to the eccentricity ratio, it is much more appropriate to mention the limitation in terms of the minimum film thickness as proposed by Lund and Orcutt [6]. They state that the linearization represents the actual oil film force also for large amplitudes with surprisingly good accuracy as long as the minimum film thickness during the vibration does not become less than approximately 25% of the radial clearance.

Using various analytical approximations for the relationships between the oil film force and the position and velocity of the journal for circular bearings, many authors have predicted shaft behaviour under dynamic conditions [7,8,9]. Although these approximate analytical solutions may be helpful in explaining the behaviour of systems with circular bearings, for bearings with non-circular profile which have been found to have greater stability they are not applicable.

METHODS OF DETERMINATION OF BEARING COEFFICIENTS

Although the analysis of rotor bearing systems is considerably simplified by the eight linearized bearing coefficients, unless the coefficients can be measured experimentally such an analysis is of limited value. There are two basic methods available for the determination of the coefficients experimentally. These are classified according to the use of the static and dynamic response characteristics of the bearing.

The stiffness coefficients can be derived from the static testing of the journal locus curve. The definite relationship between the load and the eccentricity and the attitude angle is given by Morrison [3]. The other method given by Mitchell et al [10] is termed the incremental loading method, which is based on the measurements of the quasi-static equilibrium positions under the small changes of the imposed component of the load.

The eight coefficients can also be determined from the dynamic response of bearings. The technique of exciting the bearing sinusoidally in two mutually perpendicular directions, and in each case measuring the amplitude and phase angle of the resulting motions was adapted by Glienicke [11] for a series of tests on 120 mm diameter bearings. Full-scale bearing tests with this method were presented by Morton [12].

With the known values of the stiffness coefficients, the damping coefficients were calculated by Woodcock et al [13] from the measurements of the vibration amplitudes and phase angles relative to the unbalance force. Morton [14] has developed a transient technique which involves a step change in the force applied to a rotating shaft and presented the test results for a full-scale bearing.

It is to be recalled that the oil film coefficients are used in the dynamic situation. Therefore, it has great importance to calculate these coefficients from the dynamic response of the bearing and not from the quasi-static conditions.

The first attempt to determine the eight linearized coefficients directly from the response was adopted by Glienicke [11]. His technique involved the synchronous excitation of the bearing sinusoidally in two mutually perpendicular directions. In each case, the measurements of the vibration amplitudes and phase angles of the resulting motion in the two directions gave the necessary eight equations for the solution of the coefficients. However, he stated that "due to the accumulation of error in the calculations, an accuracy of measurement of about 1% in amplitude and of 10° phase angle resulted in about 5% error in the experimental coefficients, even if the measuring methods are optimised". However, the mean error of his results was about 20% to 30%, and in some coefficients it was about 50%. Morton [12] measured the coefficients with the same method but excited the bearing at a frequency non-synchronous with the running frequency. The error in his calculations was much higher than Glienicke's results.

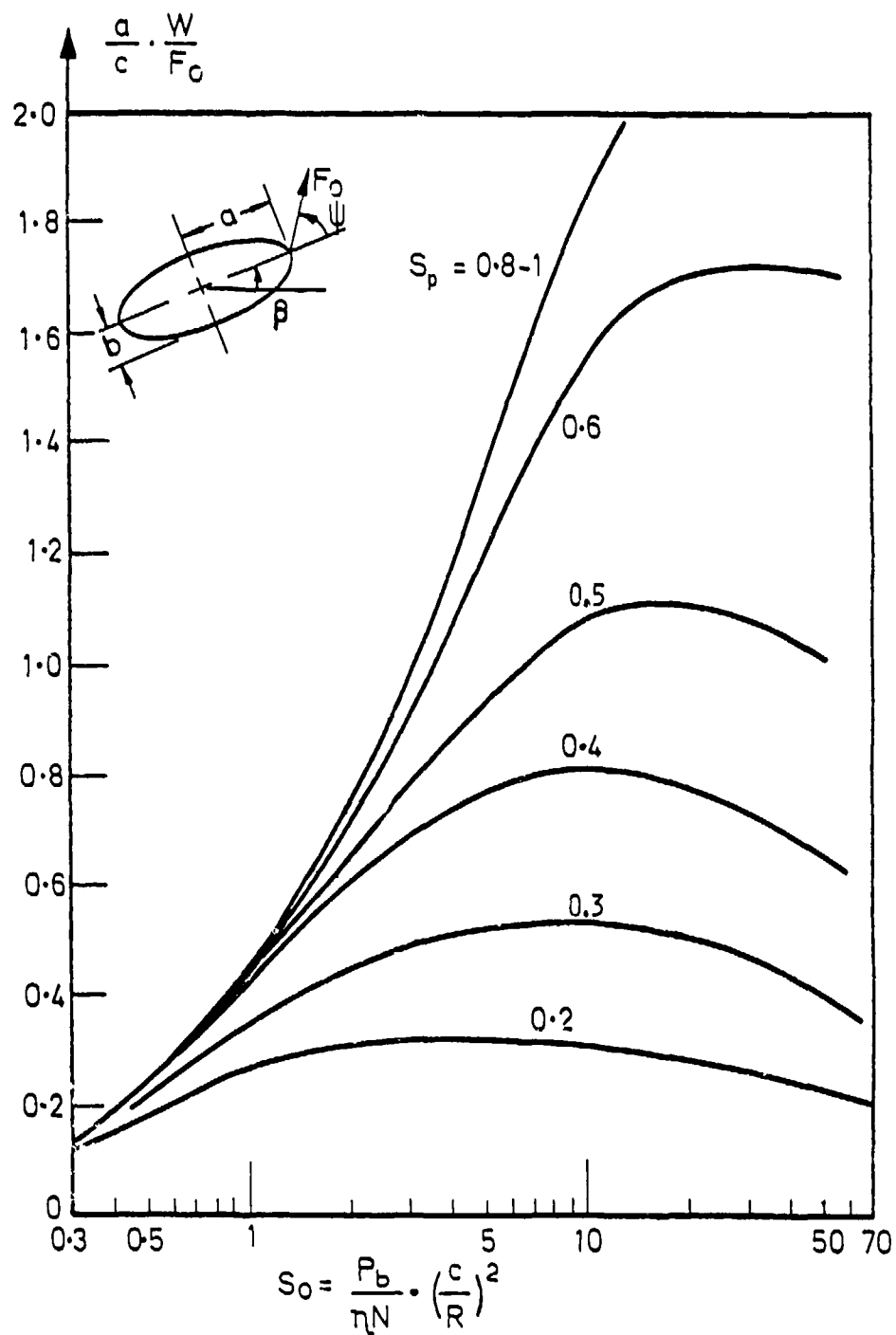
In all these methods, it is generally accepted that the coefficients derived from static testing data are extremely sensitive to measurement errors. The sensitivity of dynamically derived coefficients is more difficult to assess due to the ill-conditioning of the matrix formed in the evaluation of the coefficients. In particular, the cross-coupling stiffness coefficients, one of which always changes sign over the loading range, affect strongly the accuracy of the calculations.

THE DYNAMIC ANALYSIS OF A RIGID ROTOR BEARING SYSTEM

The linearized analysis is used, assuming a stiff symmetric rotor of mass $2M$ running in two identical journal bearings. The journal is supported eccentrically by the oil film at a stable equilibrium position under the application of a static load W . The equations of motion are derived considering the translational motion of the shaft about the equilibrium position in the bearing.

In practice, excitation at synchronous speed, ω , is always present due to run-out or unbalance. Excitation at some other frequency, $n\omega$, is often present, for example, due to shaft ovality in flexible systems, where $n=2$. In test apparatuses it is quite difficult to eliminate synchronous excitations due to run-out. Therefore, in order to keep the generality of the equations it is necessary to develop the equations for excitations at two frequencies.

If the geometric centre of the journal is not concentric with the rotation centre due to the run-out, r_0 , the journal will be excited at the synchronous speed. At the same time if the journal is excited by a



(a) The amplitude of major semi-axis

Figure 1. The response of circular bearing to synchronous excitation.

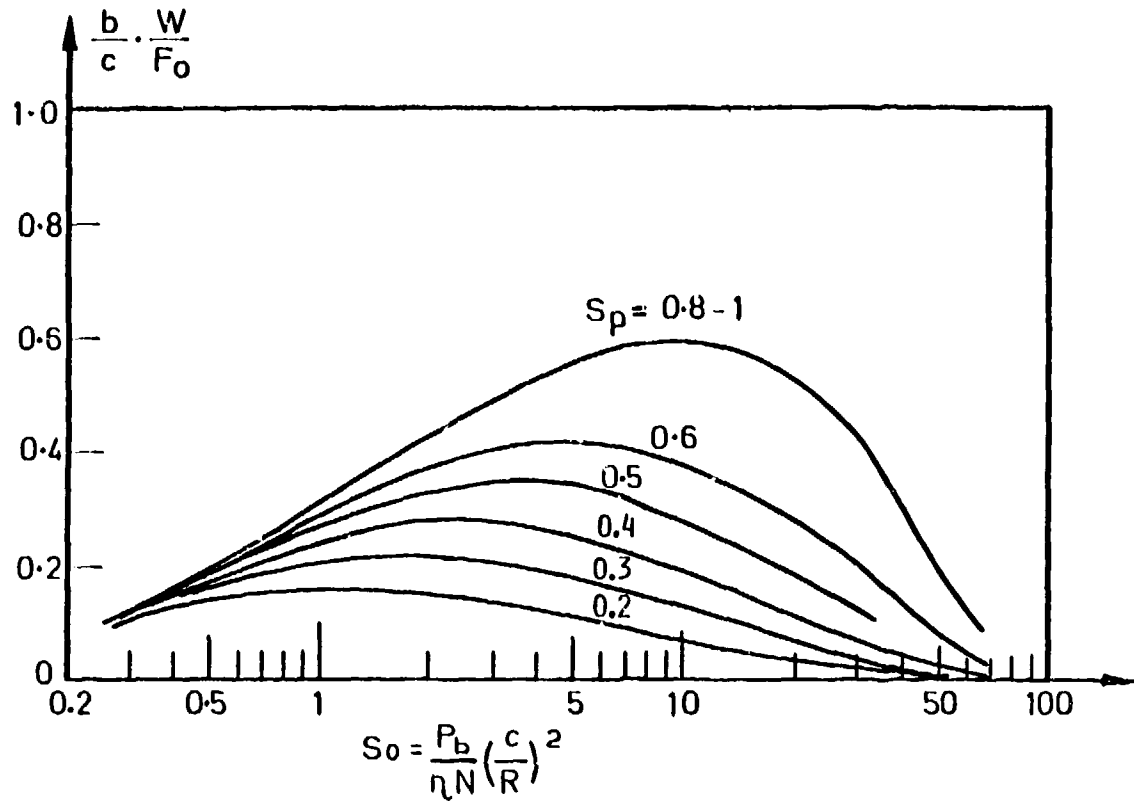
constant rotating force, F_0 , at a speed of Ω , then there will be a phase difference, β , between these forces at time $t=0$. Then by expressing the oil film forces in relative quantities the equations of motion of the journal about the equilibrium position can be expressed as follows:

$$\frac{1}{S_p} \begin{vmatrix} \ddot{x} \\ \ddot{y} \end{vmatrix} + \begin{vmatrix} C_{XX} & C_{XY} \\ C_{YX} & C_{YY} \end{vmatrix} \begin{vmatrix} \dot{x} - \dot{x}_0 \\ \dot{y} - \dot{y}_0 \end{vmatrix} + \begin{vmatrix} K_{XX} & K_{XY} \\ K_{YX} & K_{YY} \end{vmatrix} \begin{vmatrix} x - x_0 \\ y - y_0 \end{vmatrix} = \frac{F_0}{W} \begin{vmatrix} \cos nT \\ \sin nT \end{vmatrix} \quad (1)$$

where:

$$\begin{vmatrix} x_0 \\ y_0 \end{vmatrix} = R_0 \begin{vmatrix} \cos(T - \beta) \\ \sin(T - \beta) \end{vmatrix}$$

Thus, for a bearing operating at a certain equilibrium eccentricity, the response will be determined by the excitation force, frequency and the stability parameter.



(b) The amplitude of minor semi-axis

Figure 1. The response of circular bearing to synchronous excitation.

Due to the cross-coupling damping terms, it is much easier to express all the state variables as complex quantities. Since there are two excitations at frequencies ω and $n\omega$, the solutions can be assumed as superposition of the harmonic functions at these frequencies:

$$X = X_R + X_F = X_1 e^{i(T-\phi_{X1})} + X_n e^{i(nT-\phi_{Xn})}$$

$$Y = Y_R + Y_F = Y_1 e^{i(T-\phi_{Y1})} + Y_n e^{i(nT-\phi_{Yn})}$$

The real part of these equations are the solutions and X_1 , Y_1 , X_n and Y_n are real quantities. The derivatives are:

$$\dot{X} = i X_R + i n X_F, \quad \dot{Y} = i Y_R + i n Y_F$$

$$\ddot{X} = -X_R - n^2 X_F, \quad \ddot{Y} = -Y_R - n^2 Y_F$$

Substituting into equation (1) and expressing the external and run-out excitations as parts of complex numbers, the equations can be separated into the two frequencies as:

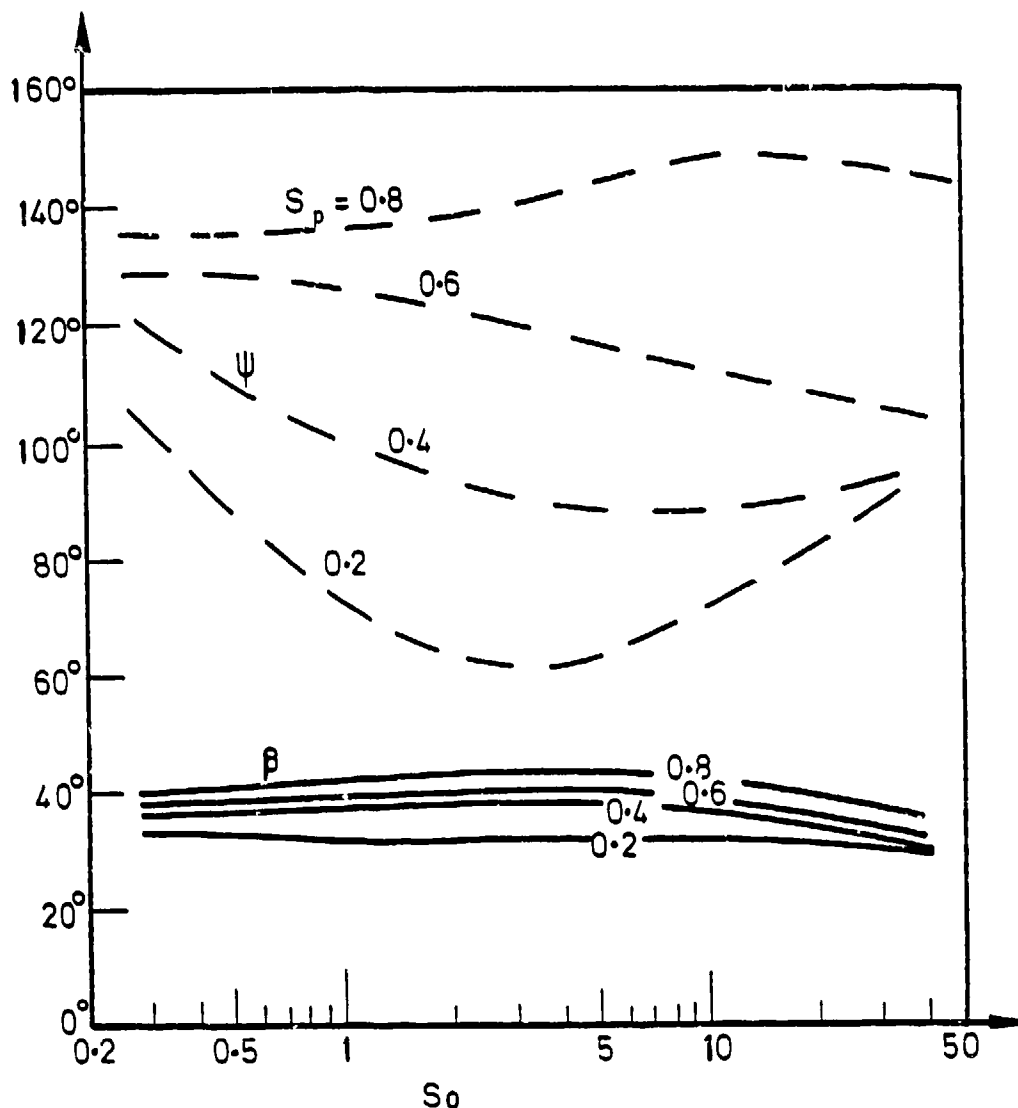
$$\left[[Z]_1 - \frac{1}{S_p} [I] \right] \begin{Bmatrix} X_R \\ Y_R \end{Bmatrix} = R_0 e^{i(T-\beta)} [Z]_1 \begin{Bmatrix} 1 \\ -i \end{Bmatrix} \quad (2)$$

$$\text{and: } \left[[Z]_n - \frac{n^2}{S_p} [I] \right] \begin{Bmatrix} X_F \\ Y_F \end{Bmatrix} = \frac{F_0}{W} e^{i n T} \begin{Bmatrix} 1 \\ -i \end{Bmatrix} \quad (3)$$

where $[Z]_n$ is the complex dynamic stiffness matrix or the impedance of the oil film and elements are:

$$Z_{XX_n} = K_{XX} + i n C_{XX}, \quad Z_{XY_n} = K_{XY} + i n C_{XY}$$

$$Z_{YX_n} = K_{YX} + i n C_{YX}, \quad Z_{YY_n} = K_{YY} + i n C_{YY}$$



(c) The phase angle and angle of inclination

Figure 1. The response of circular bearing to synchronous excitation.

It is to be noted that the oil film impedance is frequency dependent and subscript 1 refers to the synchronous impedance.

The amplitudes of the response and the phase angles can be solved by inverting equations (2) and (3):

$$\begin{vmatrix} X_1 & e^{-i\phi_{X1}} \\ Y_1 & e^{-i\phi_{Y1}} \end{vmatrix} = R_0 e^{-i\beta} [Z]_{11}^{-1} \begin{Bmatrix} [Z]_1 & 1 \\ & -1 \end{Bmatrix} \quad \text{and} \quad \begin{vmatrix} X_n & e^{-i\phi_{Xn}} \\ Y_n & e^{-i\phi_{Yn}} \end{vmatrix} = \frac{F_0}{W} [Z]_{nn}^{-1} \begin{Bmatrix} 1 \\ -1 \end{Bmatrix} \quad (4)$$

where: $[Z]_{11} = [Z]_1 - \frac{1}{S_p} [I]$, $[Z]_{nn} = [Z]_n - \frac{n^2}{S_p} [I]$

As it may be seen, the response variables are expressed as complex variables at the two excitation frequencies, and the amplitudes and the phase angles are given in equations (4). Since the responses are harmonic functions, a stationary orbit can be obtained if the excitation frequency is an integer number. If the external excitation frequency is half of the shaft speed, a double-loop orbit can be obtained. This orbit converges to a single-loop elliptical orbit if there is no run-out (or its response is negligibly small compared to the external excitation response); or if there is no synchronous external excitation. Since the vibration amplitudes are linearly dependent on the unbalance force to static load ratio, the response can be presented as the product of the non-dimensional major or minor axis and the static to unbalance force ratio. For an elliptical orbit the major and minor semi-axes, their direction of inclination and the phase angle between the excitation force and the major semi-axes are of interest for comparison with experiment and are derived in Appendix A.

The theoretical response curves are plotted in Figures 1 and 2 for two different bearing bore geometries against their load capacities. They showed fairly common characteristics. At low loads, the major axis amplitude increases with increase in the load capacity. At higher loads, for circular bearings,

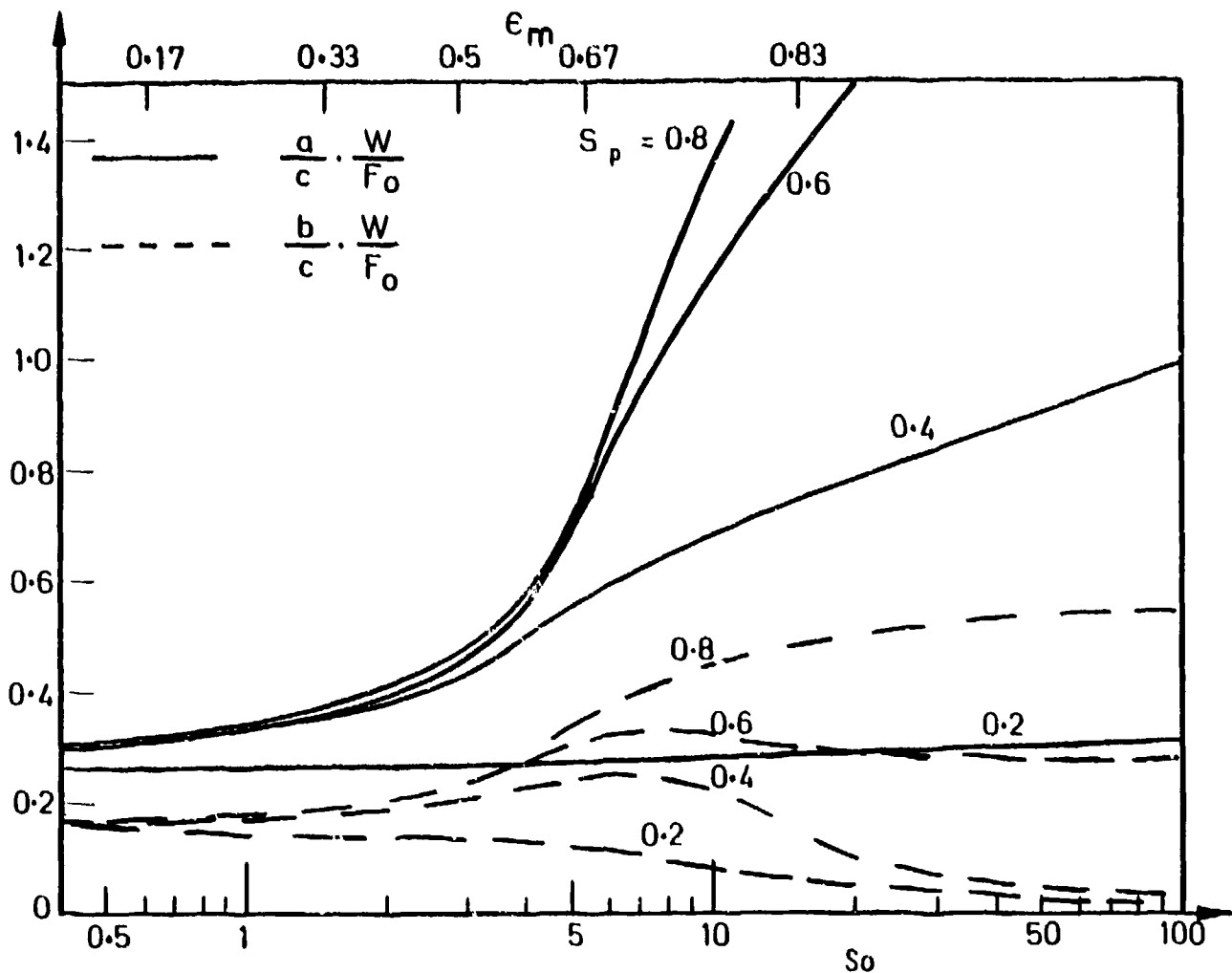


Figure 2. The response of elliptical bearing to synchronous excitation ($\delta = 0.4$).

the amplitudes may decrease or stay at the same level, but for elliptical bearings, it increases with the load. The minor axis amplitude increases at low loads and decreases at higher loads. But, again, for elliptical bearings it keeps increasing at a low rate. The stability parameter which can be considered as a measure of damping in the bearing has a strong effect on the vibration amplitudes. It is to be noted that as the stability parameter approaches to the corresponding threshold value (i.e. as the load decreases or the shaft speed increases), the F_0/W ratio increases; therefore, the real vibration amplitudes a/c or b/c increase.

CALCULATION OF THE COEFFICIENTS FROM THE RESPONSE

Experimental methods can be devised for the determination of the coefficients by means of the equations of motion. From a practical point of view, unbalance excitation is the simplest way of applying synchronous sinusoidal excitation. If the equations of motion given in equation (3) are considered with the unbalance excitation, then from measurements of the amplitudes and phase angles of the resulting motion in the two directions give four equations. In order to obtain the missing four equations, experiments must be carried out under varied conditions. The value of unbalance force, F_0 , cannot be changed because it will not produce linearly independent equations, and the experiments cannot be carried out with different values of ω , c or W , because they all determine the operating condition of the bearing at which the coefficients are sought. The only parameter that can be changed is the vibrating mass, M , in the stability parameter. The experiments can be carried out at substantially different values of the mass in order to obtain reliable results. However, as it is seen in Figures 1.a and 2 for different bearing geometries, there is a range of eccentricity and stability parameter for which the amplitudes of response converge to the same value. Therefore, substantially different values of response for different values of M (i.e. for different values of S_p), for practical reasons, are limited to high eccentricities and low stability parameters (which, of course, should be well above the threshold value).

At a certain operating condition, response to excitation at a non-synchronous frequency gives a set of four equations. For the determination of the second set of equations, the oil film is to be excited at a different frequency in order to obtain a substantially different response. For practical purposes, it is advantageous to have stationary response orbits. This can be achieved at half of the shaft speed. Response to external excitation at half of the shaft speed is given in Figure 3 for comparison with the synchronous response in Figures 1.a and 1.b. They show different characteristics. In practice, these two excitations may be applied simultaneously. Synchronous excitation occurs due to run-out and half-synchronous excitation from an external exciter. In this case, it is necessary to separate out the response to non-synchronous forcing from the synchronous vibration. In order to reduce the effect of measurement error, it is desirable

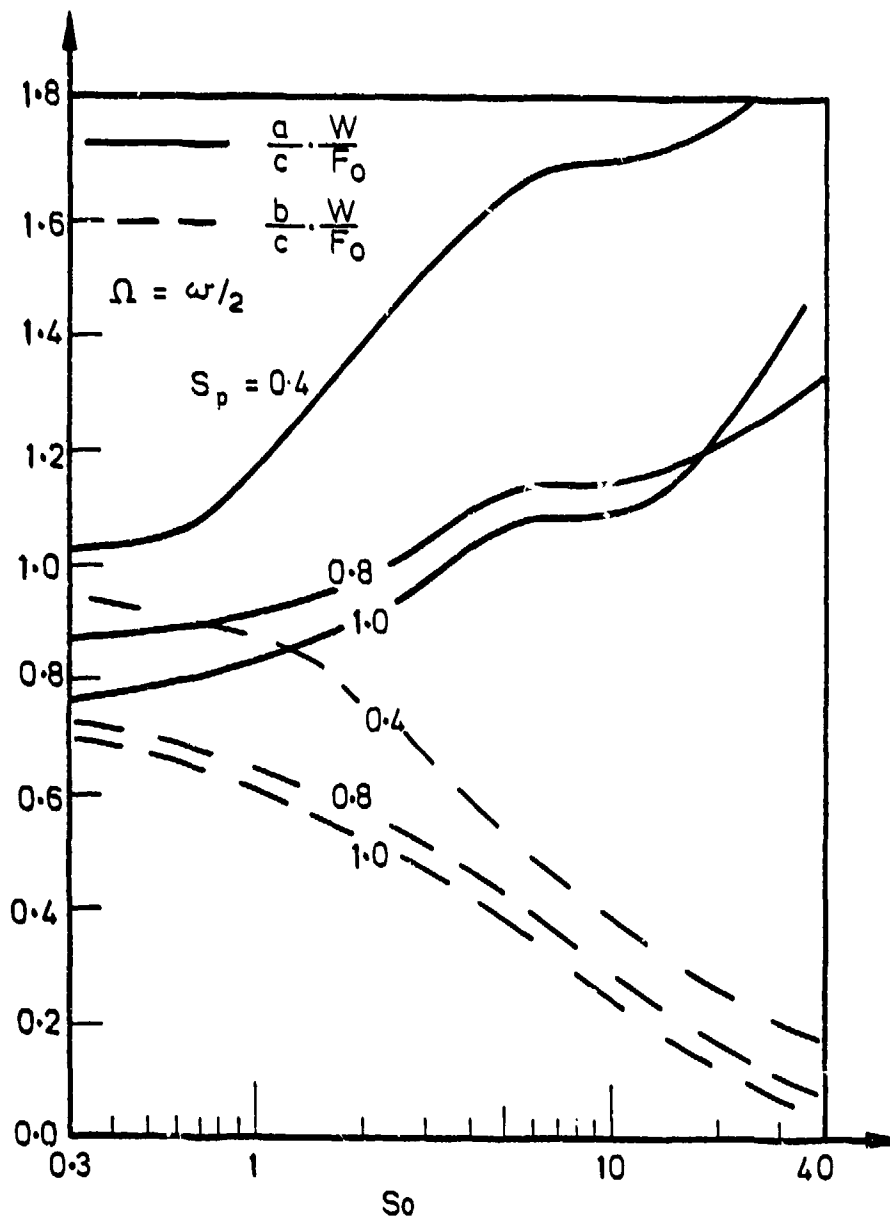


Figure 3. The response of circular bearing to half-synchronous excitation.

to have deliberate run-out to obtain a large response orbit and in half-synchronous excitation the force amplitude should be kept small enough due to low damping of the fluid film bearing at this frequency ratio. The overall response amplitude should be small enough in order not to violate the assumption of the linearization of the oil film forces. Further, the monitoring equipment for vibration orbit must be accurate in order to avoid misleading results. If there is no run-out, then by exciting at synchronous and half-synchronous frequencies the necessary eight equations can be obtained. In test apparatus, in order to avoid the effect of gravity on bearing loading, the stationary shaft axis is to be mounted vertically so that the bearing and its housing can be excited in the horizontal plane. In this case, the bearing housing is to be supported in the horizontal plane by hydrostatic air bearing which gives negligible resistance to vibration. If the amplitudes and phase angles of the resulting motions in the two directions are measured, then the vibrations can be expressed as complex equations. By substituting these equations into (2) and (3), respectively, and writing the impedances as unknowns gives two sets of four equations, then the coefficients can be solved (see Appendix B).

The bearing coefficients are found from the linearization of the oil film forces about the equilibrium running position. This can be expressed mathematically as a first order Taylor expansion. The Reynolds equation is solved by means of the finite difference method using the Reynolds boundary condition. The oil film forces are calculated from integration of the pressure distribution obtained for small displacements about the equilibrium position of the journal center. The gradients of these forces with respect to the perturbations give the bearing coefficients, the first index being the force direction and the second index the perturbation direction.

The effect of measurement errors on the calculations of the coefficients with this method is also investigated. For circular and elliptical bearings, the errors in the coefficients are calculated for +10% errors in amplitude of all measurements (i.e. in the elements of [AZ] and on the right hand sides of equations(B.1) and the results are shown in Figures 4 and 5 as dashed lines. In equations(B.1), the parameters are taken as $F_0/W = 0.2$, $S_p = 1.0$, $R_0 = 0.4$, $\alpha = 30^\circ$ and $\beta = 60^\circ$. Although the errors are small at high values of the coefficients, for low values of the coefficients (less than about 2.0) the errors can reach higher percentages.

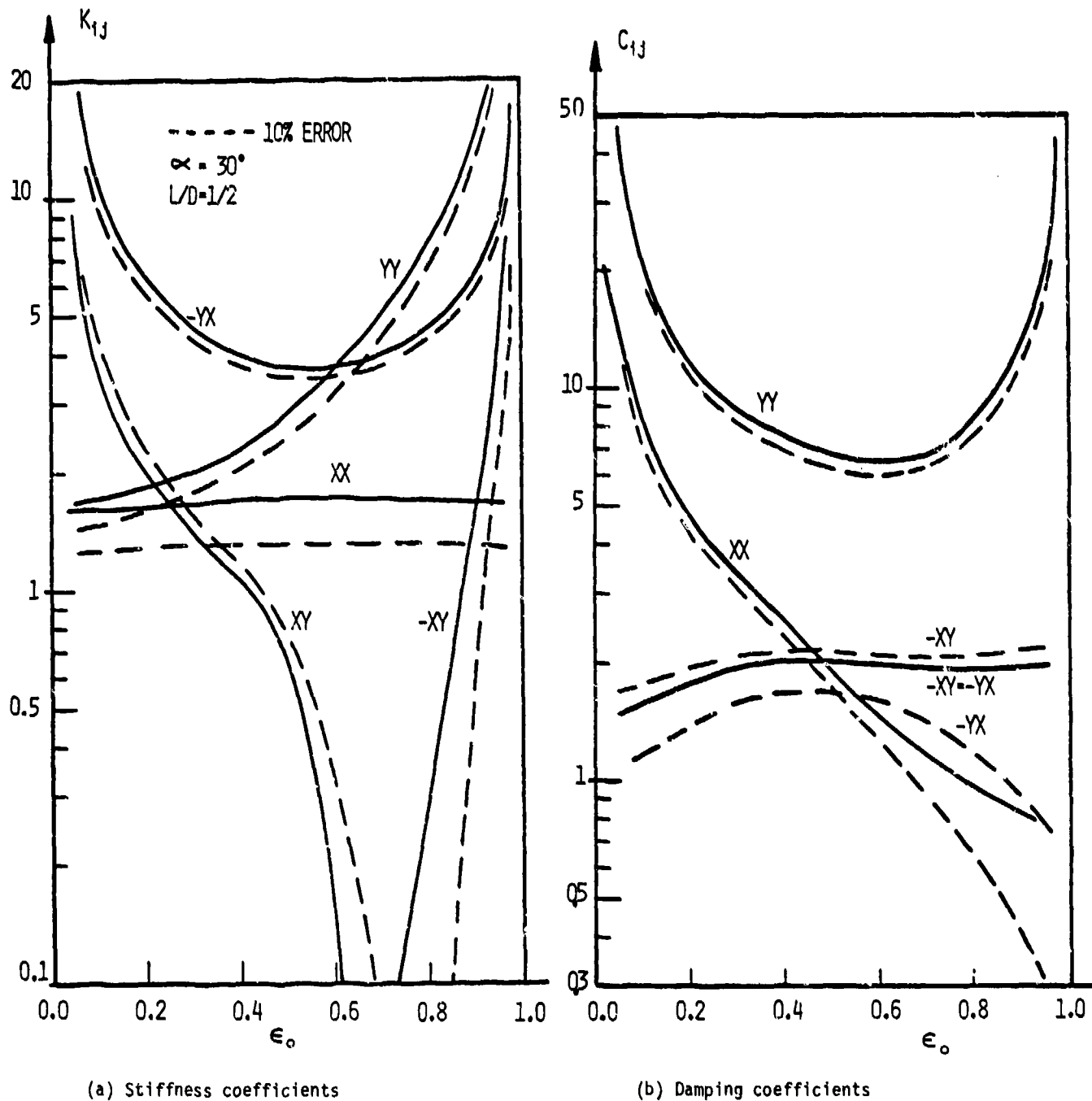
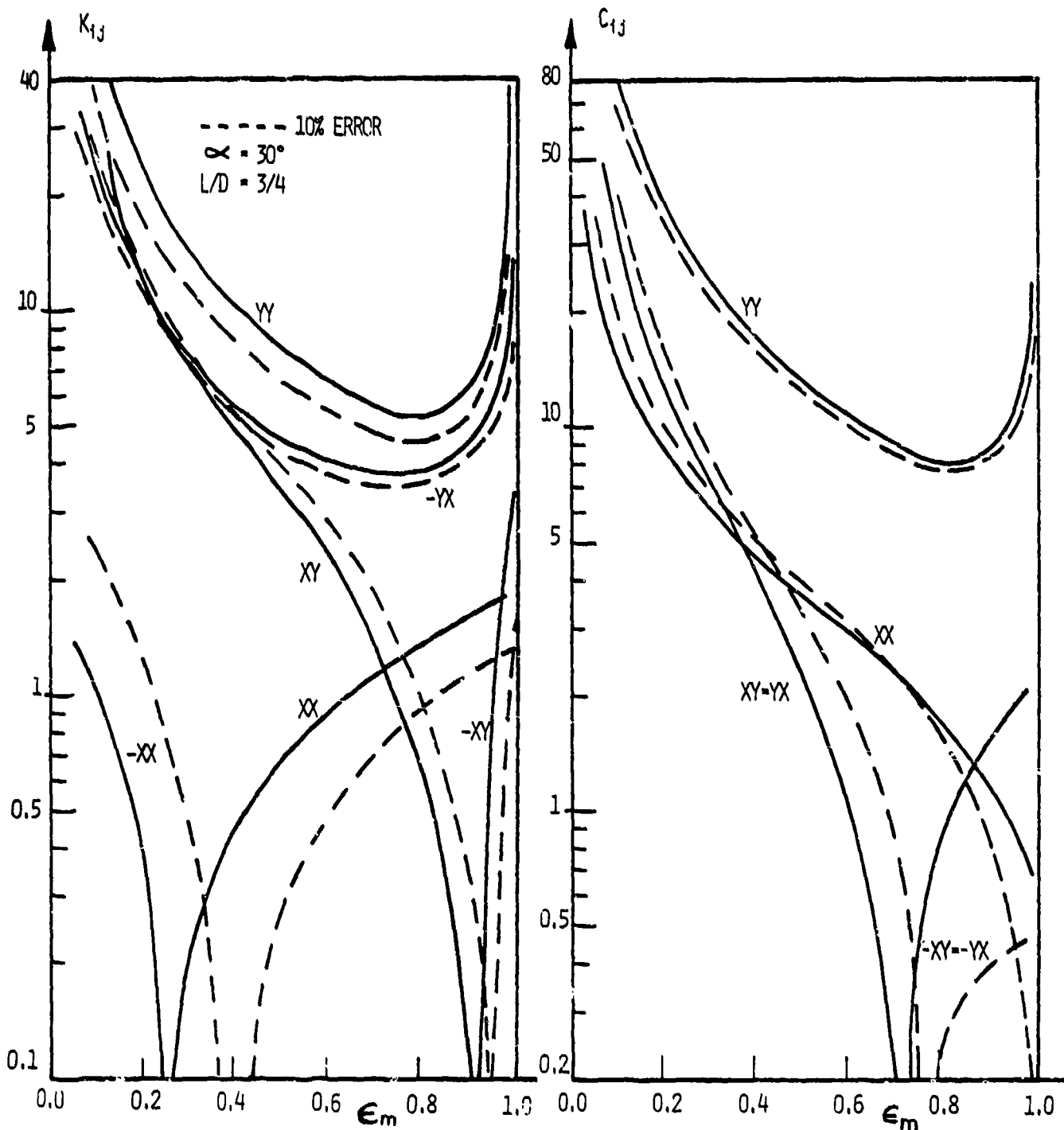


Figure 4. Variation of the errors in the coefficients of a circular bearing.

CONCLUSIONS

Although several methods exist for the determination of the eight bearing coefficients, from the foregoing considerations, it has been shown that the coefficients obtained from the dynamic response of the journal is extremely sensitive to the method of calculation. The oil film impedances which depend on the excitation frequency make it possible to get completely different response when it is excited at two frequencies. Therefore, the test apparatus is to be designed such that the bearing and its housing are to be allowed to vibrate in the horizontal plane while the shaft is to rotate about its stationary vertical axis. With this arrangement the excitation forces can be applied easily to the bearing housing. The coefficients obtained from the forced response can be predicted with high accuracy. Although the percentage errors are quite small for higher values of coefficient the errors can go higher values for the coefficients which change sign over the eccentricity range.



(a) Stiffness coefficients

(b) Damping coefficients

Figure 5. Variation of the errors in the coefficients of an elliptical bearing.

REFERENCES

- [1] STERNLICHT, B., "Elastic and damping properties of cylindrical journal bearings", Trans. ASME, J. Basic Eng., 1959, Vol. 81, No. 1, p. 101.
- [2] HOLMES, R., "The vibration of a rigid shaft on short sleeve bearings", J. Mech. Eng. Sci., 1960, Vol. 2, No. 4, p. 337.
- [3] MORRISON, D., "Influence of plain journal bearings on the whirling action of an elastic rotor", Proc. Inst. Mech. Engrs., 1962, Vol. 176, No. 22, p. 452.
- [4] IWATSUBO, T., "Error analysis of vibration of rotor-bearing system", Conf. on Vibrations in Rotating Machinery, I. Mech. E., September 1976, p. 87.
- [5] LUND, J.W., and THOMSEN, K.K., "A calculation method and data for the dynamic coefficients of oil-lubricated journal bearings", Topics in Fluid Film Bearing and Rotor Bearing System Design and Optimization, presented at the ASME Design Engineering Conference and Shows, Illinois, April 1978, p. 245.

- [6] LUND, J.W., and ORCUTT, F.K., "Calculations and experiments on the unbalance response of a flexible rotor", Trans. ASME, J. Eng. Ind., 1967, Vol. 89, p. 785.
- [7] HOLMES, R., "Oil whirl characteristics of a rigid rotor in 360° journal bearings", Proc. Inst. Mech. Engrs., 1963, Vol. 177, No. 11, p. 291.
- [3] KIRK, R.G., and GUNTER, E.J., "Transient journal bearing analysis", NASA CR-1549, June 1970.
- [9] BADGLEY, R.H., and BOOKER, J.F., "Rigid-body rotor dynamics: Dynamic unbalance and lubricant temperature changes", ASME Paper No. 69-Lub-14, October 1969.
- [10] MITCHELL, J.R., HOLMES, R., and VAN BALLYGOOYEN, H., "Experimental determination of a bearing oil-film stiffness", Proc. Inst. Mech. Engrs., 1965-66, Vol. 180 (3K), p. 90.
- [11] GLIENICKE, J., "Experimental investigation of the stiffness and damping coefficients of turbine bearings and their application to instability prediction", Proc. Inst. Mech. Engrs., 1966-67, Vol. 181 (3B), p. 116.
- [12] MORTON, P.G., "Measurements of the dynamic characteristics of large sleeve bearings", Trans. ASME, J. Lub. Tech., 1971, Vol. 93, p. 143.
- [13] WOODCOCK, J.S., and HOLMES, R., "The determination of the dynamic properties of a turbo-rotor bearing oil-film", Proc. Inst. Mech. Engrs., 1969-70, Vol. 194 (3L), p. 111.
- [14] MORTON, P.G., "The derivation of bearing characteristics by means of transient excitation applied directly to a rotating shaft", IUTAM Symp., Dynamics of Rotors, Lyngby, Denmark.

APPENDIX A

An elliptical whirl orbit, in general, can be expressed in terms of complex variables as:

$$X = \operatorname{Re} \{ \bar{X} e^{i(T - \bar{\phi}_X)} \} = \operatorname{Re} \{ (X_C - iX_S) e^{iT} \}$$

$$Y = \operatorname{Re} \{ \bar{Y} e^{i(T - \bar{\phi}_Y)} \} = \operatorname{Re} \{ (Y_C - iY_S) e^{iT} \}$$

or in terms of real variables as:

$$X = \bar{X} \cos (T - \bar{\phi}_X) = X_S \sin T + X_C \cos T$$

$$Y = \bar{Y} \cos (T - \bar{\phi}_Y) = Y_S \sin T + Y_C \cos T \quad (\text{A.1})$$

where: $\bar{X} = (X_C^2 + X_S^2)^{1/2}$, $\bar{Y} = (Y_C^2 + Y_S^2)^{1/2}$

$$\bar{\phi}_X = \tan^{-1} \left(\frac{X_S}{X_C} \right), \quad \bar{\phi}_Y = \tan^{-1} \left(\frac{Y_S}{Y_C} \right)$$

If the X-Y coordinate is rotated such that it coincides with the major and minor semi axes of the ellipse, as in Figure A.1, then the motion can be expressed as:

$$X' = A \cos (T + \psi), \quad Y' = B \sin (T + \psi) \quad (\text{A.2})$$

where A and B are non-dimensional major and minor semi-axes, respectively, and ψ is the phase angle between the exciting force and the major semi-axis.

If β is the angle between the major semi-axis and the X axis, then using the following transformation equations:

$$\begin{vmatrix} X' \\ Y' \end{vmatrix} = \begin{vmatrix} \cos \beta & \sin \beta \\ -\sin \beta & \cos \beta \end{vmatrix} \begin{vmatrix} X \\ Y \end{vmatrix}$$

and equating the coefficients of $\sin T$ and $\cos T$ terms by the use of equations (A.1) and (A.2) gives:

$$A \cos \psi = X_C \cos \beta + Y_C \sin \beta \quad (\text{A.3a})$$

$$-A \sin \psi = X_S \cos \beta + Y_S \sin \beta \quad (\text{A.3b})$$

$$B \sin \psi = -X_C \sin \beta + Y_C \cos \beta \quad (\text{A.3c})$$

$$B \cos \psi = -X_S \sin \beta + Y_S \cos \beta \quad (\text{A.3d})$$

Eliminating ψ and β between the equations in two ways gives:

$$A^2 + B^2 = X_C^2 + Y_C^2 + X_S^2 + Y_S^2 \quad (\text{A.4})$$

$$\text{and: } (A + B)^2 = (X_C + Y_S)^2 + (Y_C - X_S)^2 \quad (\text{A.5})$$

From equations (A.4) and (A.5), one can deduce that:

$$B = \frac{X_C Y_S - Y_C X_S}{A} \quad (\text{A.6})$$

Substituting equation (A.6) into equation (A.4) gives:

$$A^4 - (X_C^2 + X_S^2 + Y_C^2 + Y_S^2) A^2 + (X_C Y_S - Y_C X_S)^2 = 0$$

then:

$$A = \left\{ \frac{1}{2}(X_C^2 + X_S^2 + Y_C^2 + Y_S^2) + \sqrt{\frac{1}{4}(X_C^2 + X_S^2 + Y_C^2 + Y_S^2)^2 - (X_C Y_S - Y_C X_S)^2} \right\}^{1/2}$$

The attitude angle of the elliptical orbit, β , can be obtained by eliminating A and B and ψ between the equations (A.3) and gives:

$$\beta = \frac{1}{2} \tan^{-1} \left[\frac{2(X_C Y_C + X_S Y_S)}{X_C^2 + X_S^2 - (Y_S^2 + Y_C^2)} \right]$$

Then, the phase angle between the excitation force and the major semi-axis can be solved by using any one of equations (A.3).

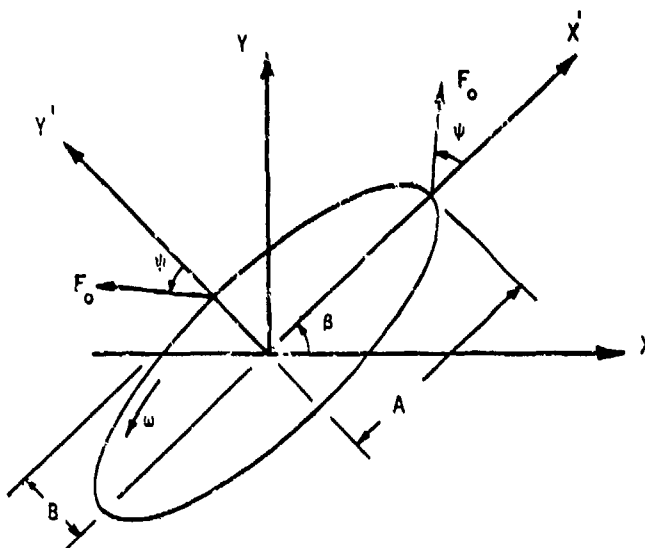


Figure A.1. Dynamic load orbit

APPENDIX B

The vibration in the two directions can be expressed as:

For synchronous response:

$$X_R = X_1 e^{i(T-\phi_{X1})} = X_{R1} e^{iT}$$

$$Y_R = Y_1 e^{i(T-\phi_{Y1})} = Y_{R1} e^{iT}$$

For half-synchronous response:

$$X_F = X_n e^{i(nT-\phi_{Xn})} = X_{Fn} e^{inT}$$

$$Y_F = Y_n e^{i(nT-\phi_{Yn})} = Y_{Fn} e^{inT}$$

where $n = 1/2$.

If these equations are substituted into equations (2) and (3), respectively, and keeping the terms including the impedances on the left hand side gives:

$$[Z]_1 \begin{vmatrix} X_{R1} & -R_o e^{-i\beta} \\ Y_{R1} & +i R_o e^{-i\beta} \end{vmatrix} = \frac{1}{S_p} \begin{vmatrix} X_{R1} \\ Y_{R1} \end{vmatrix}$$

$$[Z]_n \begin{vmatrix} X_{Fn} \\ Y_{Fn} \end{vmatrix} = \frac{F_o}{W} \begin{vmatrix} 1 \\ -i \end{vmatrix} + \frac{n^2}{S_p} \begin{vmatrix} X_{Fn} \\ Y_{Fn} \end{vmatrix}$$

If these equations are written with the impedances as unknowns:

$$\begin{vmatrix} X_{R1} - R_o e^{-i\beta} & Y_{R1} + i R_o e^{-i\beta} & 0 & 0 \\ 0 & 0 & X_{R1} - R_o e^{-i\beta} & Y_{R1} + R_o e^{-i\beta} \end{vmatrix} \begin{vmatrix} Z_{XX1} \\ Z_{XY1} \\ Z_{YX1} \\ Z_{YY1} \end{vmatrix} = \frac{1}{S_p} \begin{vmatrix} X_{R1} \\ Y_{R1} \end{vmatrix}$$

$$\begin{vmatrix} X_{Fn} & Y_{Fn} & 0 & 0 \\ 0 & 0 & X_{Fn} & Y_{Fn} \end{vmatrix} \begin{vmatrix} Z_{XXn} \\ Z_{XYn} \\ Z_{YXn} \\ Z_{YYn} \end{vmatrix} = \begin{vmatrix} \frac{F_o}{W} + \frac{n^2}{S_p} * X_{Fn} \\ -i \frac{F_o}{W} + \frac{n^2}{S_p} * Y_{Fn} \end{vmatrix}$$

These equations are to be written as real variables for the solutions of the eight coefficients; then the two sets of four equations are:

$$[AZ] \begin{vmatrix} K_{XX} \\ C_{XX} \\ K_{XY} \\ C_{XY} \end{vmatrix} = \begin{vmatrix} 0 \\ 0 \\ F_o/W \\ 0 \end{vmatrix} + \frac{1}{S_p} \begin{vmatrix} \text{Re}(X_{R1}) \\ \text{Im}(X_{R1}) \\ n^2 \text{Re}(X_{Fn}) \\ n^2 \text{Im}(X_{Fn}) \end{vmatrix} \quad \text{and} \quad [AZ] \begin{vmatrix} K_{YX} \\ C_{YX} \\ K_{YY} \\ C_{YY} \end{vmatrix} = \begin{vmatrix} 0 \\ 0 \\ 0 \\ -F_o/W \end{vmatrix} + \frac{1}{S_p} \begin{vmatrix} \text{Re}(Y_{R1}) \\ \text{Im}(Y_{R1}) \\ n^2 \text{Re}(Y_{Fn}) \\ n^2 \text{Im}(Y_{Fn}) \end{vmatrix} \quad (B.1)$$

where $n = 1/2$, and:

$$[AZ] = \begin{vmatrix} \text{Re}(X_{R1} - R_o e^{-i\beta}) & -\text{Im}(X_{R1} - R_o e^{-i\beta}) & \text{Re}(Y_{R1} + i R_o e^{-i\beta}) & -\text{Im}(Y_{R1} + i R_o e^{-i\beta}) \\ \text{Im}(X_{R1} - R_o e^{-i\beta}) & \text{Re}(X_{R1} - R_o e^{-i\beta}) & \text{Im}(Y_{R1} + i R_o e^{-i\beta}) & \text{Re}(Y_{R1} + i R_o e^{-i\beta}) \\ \text{Re}(X_{Fn}) & -n * \text{Im}(X_{Fn}) & \text{Re}(Y_{Fn}) & -n * \text{Im}(Y_{Fn}) \\ \text{Im}(X_{Fn}) & n * \text{Re}(X_{Fn}) & \text{Im}(Y_{Fn}) & n * \text{Re}(Y_{Fn}) \end{vmatrix}$$

Then the coefficients can be solved by inverting equation (B.1) for given values of operating parameters F_o/W and S_p .

DISCUSSION

K.J. Brown, Ontario Hydro, Toronto, Ca

Could you please comment on the comparison of your experimental results with calculated values in the literature and whether you have done or know of any work that has been done on calculating the coefficient when air is entrained in the oil.

Author's Reply

In this paper, I have presented a method for the determination of the coefficients experimentally. From the error analysis, it has been shown that by using this method, the effect of measurement errors on the coefficients can be considerably reduced. The effect of air entrainment in the oil has not been considered. Since the vibration amplitudes are small the effect of air in the oil has been neglected in all the previous works like in the computation of static bearing performance.

J. Frene, Université de Poitiers, Fr

Les coefficients dynamiques sont obtenus dans le cadre de la théorie linéaire qui suppose des déplacements et des vitesses de déplacement infiniment petits. Dans le mouvement orbital que vous imposez, pour réaliser la mesure, les déplacements sont finis. Pouvez vous commenter cet aspect?

Author's Reply

Every non-linear problem can be linearized about the point under consideration. Depending on the system characteristics the linearization region can be small or large. Actually, in References (5) and (6), it has been shown that the linearization region for journal bearings can go up to about half of the clearance of the bearing. Therefore, if the amplitudes of responses to excitation are within the linearization range, the linearized coefficients can be determined from the finite amplitude responses as described in the paper.

AN ANALYTICAL STUDY OF THE HEAT BALANCE FOR A JOURNAL BEARING

P.K. Hansen
 Department of Machine Elements
 Det norske Veritas
 P.O. Box 300
 N-1322 Høvik
 Norway

J.W. Lund
 Department of Machine Elements
 The Technical University of Denmark
 DK-2800 Lyngby
 Denmark

SUMMARY

The thermo-hydrodynamic lubrication problem for a journal bearing is studied. Special emphasis is given to the heat balance for the bearing. The flow is assumed to be laminar, the lubricant is Newtonian and incompressible. Allowance is made for the viscosity-temperature dependence. The shaft surface temperature is taken to be constant, and at the outer surface of the bearing bush the temperature is determined from heat flux continuity.

NOMENCLATURE

c	= viscosity-temperature coefficient	T_j	= journal temperature
c_p	= heat capacity, J/kgC	T_h	= groove temperature
C^p	= radial clearance, m	T_m	= mean temperature across film thickness
D	= diameter of journal, m	T_{mi}	= mean inlet temperature
e	= eccentricity, m	T_o	= inner bush surface temperature
E	= powerloss, W	u, v, w	= velocity components in circumferential-, radial- and axial directions, respectively, m/s
E^*	= $E/(2\mu_o R^4 \omega^2 / C)$	\bar{u}	= $u/(R \omega)$
$f(\xi, \zeta)$	= inlet temperature distribution	\bar{v}	= $v/(R \omega)(C/R)$
f_r, f_t	= hydrodynamic fluid-film forces	\bar{w}	= $w/(R \omega)$
h	= film thickness, m	x	= circumferential coordinate in the direction of rotation, m
\bar{h}	= h/C	y	= radial coordinate through the film-thickness measured from bush surface, m
k_o	= thermal conductivity of lubricant, W/mC	z	= axial coordinate measured from bearing centerline, m
k_s	= thermal conductivity of bush, W/mC	ϵ	= e/C , eccentricity ratio
K	= hot oil carry-over coefficient	ζ	= z/R , axial coordinate
L	= bearing length, m	θ	= x/R , circumferential coordinate, measured from maximum film thickness
m	= viscosity-temperature coefficient	θ'	= circumferential coordinate, measured from loadline, see fig. 1.
N	= rotational speed, rpm	κ_r, κ_z	= heat transfer coefficients, W/m ² C
p	= pressure, N/m ²	μ	= viscosity, Pas
p^*	= $p/(6\mu_o \omega(R/C)^2)$	μ_o	= reference viscosity, Pas
p_b	= specified boundary pressure	$\bar{\mu}$	= mean viscosity across film thickness
p_{bc}	= $k_o/(\rho c_p \omega C^2)$	μ_m	= viscosity, cSt
q	= flow	ν	= y/C , radial coordinate through the film thickness
q_c	= Couette flow	ξ	= ξ/\bar{h}
q_{θ}, q_z	= flow in circumferential and axial direction, respectively	ρ	= density of lubricant, kg/m ³
r	= radial coordinate, m	ϕ	= attitude angle, see fig. 1
\bar{r}	= r/R	ω	= angular velocity, rad/sec.
R	= inner bush radius, m	q_s	= side leakage
R_1	= outer bush radius, m		
\bar{R}_1	= R_1/R		
S	= Sommerfeld number		
T	= temperature, C		
T_f	= T/T_f		
T_a	= ambient temperature		
T_f	= $(6\mu_o \omega(R/C)^2)/(\rho c_p)$, T ⁻¹		

INTRODUCTION

During the last decades, and especially within the last few years, a number of articles, describing the thermohydrodynamic lubrication problem, has appeared. These articles have, however, rarely considered the energy-balance, or heat-balance, related to the stationary operating conditions for the bearings. It is, therefore, the intention of this paper to illustrate the dependence of the temperature and heat balance on the most significant bearing parameters.

The evaluation of the lubricant temperature in a hydrodynamic bearing is based on the solution of the energy equation which, in this case, forms a parabolic differential equation. The initial conditions for this equation is the temperature at the inlet to a bearing sector from a groove. Additionally, the temperature of the bearing surfaces form the boundary conditions to the equation.

Both the radial temperature distribution at the inlet and the temperature of the bearing surfaces have a decisive influence on the solution of the energy equation and Reynolds equation, and thereby on the operating conditions for the bearing.

The general energy equation is very complicated and difficult to solve. Approximations to this equation is thus of great interest. In this work several approximations have been investigated, and comparisons between them have been made to clarify the influence of the temperature on the stationary operating conditions.

GOVERNING EQUATIONS

Using the procedure published by Dowson /1/, with the conventional assumptions of thin film lubrication, and introducing dimensionless variables, the fluid velocities can be expressed as

$$\bar{u} = 6 \frac{\partial \bar{p}}{\partial \theta} \int_0^{\xi} \frac{\xi}{\bar{\mu}} d\xi + \left(\frac{1}{\bar{F}_0} - 6 \frac{\bar{F}_1}{\bar{F}_0} \frac{\partial \bar{p}}{\partial \theta} \right) \int_0^{\xi} \frac{d\xi}{\bar{\mu}} \tag{1}$$

$$\bar{w} = 6 \frac{\partial \bar{p}}{\partial \zeta} \int_0^{\xi} \frac{\xi}{\bar{\mu}} d\xi - 6 \frac{\bar{F}_1}{\bar{F}_0} \int_0^{\xi} \frac{d\xi}{\bar{\mu}}$$

and Reynolds equation becomes

$$\frac{\partial}{\partial \theta} (\bar{F}_2 \frac{\partial \bar{p}}{\partial \theta}) + \frac{\partial}{\partial \zeta} (\bar{F}_2 \frac{\partial \bar{p}}{\partial \zeta}) = \frac{1}{6} \frac{\partial}{\partial \theta} (\bar{h} - \frac{\bar{F}_1}{\bar{F}_0}) \tag{2}$$

where \bar{F}_2 , \bar{F}_1 and \bar{F}_0 are given by

$$\bar{F}_2 = \int_0^{\bar{h}} \frac{\xi}{\bar{\mu}} (\xi - \frac{\bar{F}_1}{\bar{F}_0}) d\xi \tag{3}$$

$$\bar{F}_1 = \int_0^{\bar{h}} \frac{\xi}{\bar{\mu}} d\xi \tag{4}$$

$$\bar{F}_0 = \int_0^{\bar{h}} \frac{d\xi}{\bar{\mu}} \tag{5}$$

The boundary conditions connected with Reynolds equation are

$$\bar{p} = \bar{p}_0 \tag{6}$$

or

$$\bar{p} = \frac{\partial \bar{p}}{\partial \theta} = \frac{\partial \bar{p}}{\partial \zeta} = 0 \tag{7}$$

The functions \bar{F}_0 , \bar{F}_1 and \bar{F}_2 in Reynolds equation depends on the viscosity and, thereby, on the temperature distribution in the lubricant. In dimensionless variables, the appropriate energy equation becomes

$$\frac{\partial}{\partial \theta} (\bar{u}\bar{T}) + \frac{\partial}{\partial \xi} (\bar{v}\bar{T}) + \frac{\partial}{\partial \zeta} (\bar{w}\bar{T}) = Pe \frac{\partial^2 \bar{T}}{\partial \xi^2} + \frac{\bar{\mu}}{6} \left[\left(\frac{\partial \bar{u}}{\partial \xi} \right)^2 + \left(\frac{\partial \bar{w}}{\partial \xi} \right)^2 \right] \tag{8}$$

The boundary conditions for (8) are

$$\xi = 0, \quad \bar{T} = \bar{T}_0(\theta, \zeta) \tag{9a}$$

$$\xi = \bar{h}, \quad \bar{T} = \bar{T}_h \tag{9b}$$

$$\theta = \theta_0, \quad \bar{T} = f(\xi, \zeta) \tag{9c}$$

$$\zeta = 0, \quad \frac{\partial \bar{T}}{\partial \zeta} = 0 \tag{9d}$$

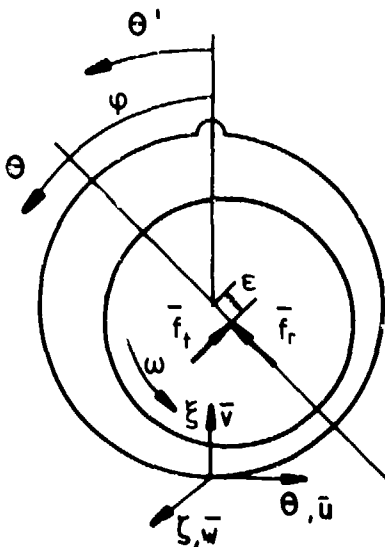


Fig. 1. Geometry and coordinate system of a radial bearing.

Description of the temperature distribution, eq. (9c), at the inlet to a bearing pad is a complex problem. Several authors have studied this problem /3,4,5/, and provided a rather good knowledge about the mean inlet temperature, but detailed information about the temperature profile at the inlet is lacking.

It is therefore usually suggested that the inlet temperature is uniform /7, 11/. However, when studying the heat balance, this can give severe problems by causing discontinuities in the temperature distribution of the bearing surfaces and the lubricant.

In the examples shown in this work, the temperature is assumed to be distributed according to a function $f(\theta, \zeta)$ which gives a continuous temperature distribution in the transition zones between the bearing solids and the fluid. The mean value of $f(\theta, \zeta)$ equals the mean inlet temperature calculated from a hot oil carry-over coefficient

Equation (9b) expresses the temperature at the surface of the rotating shaft. At the outer surface of the stationary bearing sleeve, convection takes place, and at the interface between the lubricant and the solid, continuity of temperature exists.

The heat conduction equation is

$$\frac{\partial}{\partial \bar{r}} \left(\bar{r} \frac{\partial \bar{T}}{\partial \bar{r}} \right) + \frac{1}{\bar{r}} \frac{\partial^2 \bar{T}}{\partial \theta^2} + \bar{r} \frac{\partial \bar{T}}{\partial \zeta^2} = 0 \quad (10)$$

$$\bar{r} = \bar{r}_1, \quad 0 < \theta < 2\pi, \quad 0 \leq \zeta \leq \frac{L}{D} : \frac{\partial \bar{T}}{\partial \bar{r}} = - \frac{\kappa_r R_i}{k_s} (\bar{T} - \bar{T}_a) \quad (11a)$$

$$1 \leq r \leq \bar{r}_1, \quad 0 < \theta < 2\pi, \quad \zeta = 0 : \frac{\partial \bar{T}}{\partial \zeta} = 0 \quad (11b)$$

$$1 \leq r \leq \bar{r}_1, \quad 0 < \theta < 2\pi, \quad \zeta = \frac{L}{D} : \frac{\partial \bar{T}}{\partial \zeta} = - \frac{\kappa_c R_i}{k_s} (\bar{T} - \bar{T}_a) \quad (11c)$$

$$\bar{r} = 1, \quad 0 < \theta < 2\pi, \quad 0 \leq \zeta \leq \frac{L}{D} : \frac{\partial \bar{T}}{\partial \bar{r}} = \frac{k_o R_i}{k_s C} \frac{\partial \bar{T}}{\partial \xi} \quad (11d)$$

Equation (11a) and (11c) expresses the convection boundary condition at the outer surface. Since the bearing is assumed to be symmetric, (11b) expresses the symmetry conditions. (11d) expresses the heat flux continuity condition at the fluid-solid interface.

To express the viscosity-temperature dependency the standard Walther-ASTM equation is used,

$$\nu = -0.6 + 10^{10(c+m \log_{10} T)} \quad (12)$$

where the temperatures in this equation are absolute.

APPROXIMATIONS

The equations given above provide a basis for a complete description of the stationary thermohydrodynamic behaviour of a journal bearing. To solve these equations is a cumbersome and expensive job. It is necessary to use numerical methods involving a large number of variables. A reduction of the number and complexity of the equations to be solved and thereby the cost involved, is therefore highly desirable.

Only approximations to the energy equation will be considered since the approximations to the Reynolds - and the heat conduction equation will follow as a natural consequence of the approximations given for the energy equation.

Energy equation independent of the film height

Here it is assumed, that the viscosity is constant across the film thickness and evaluated at the local mean temperature.

Integrating the left-hand side (LHS) of eq. (8) across the thickness and using the above given assumptions together with the continuity equation, gives,

$$\text{LHS} = \bar{q}_\theta \frac{\partial \bar{T}}{\partial \theta} + \bar{q}_\zeta \frac{\partial \bar{T}}{\partial \zeta} \quad (13)$$

$$\bar{q}_\theta = \int_0^h \bar{u} d\xi \quad (14)$$

$$\bar{q}_\zeta = \int_0^h \bar{w} d\xi \quad (15)$$

Using equation (1) with constant viscosity $\bar{\mu}_m$ and integrating the right-hand side (RHS) of eq. (8), yields,

$$\text{RHS} = \text{Pe} \frac{\partial \bar{T}}{\partial \xi} \left|_0^{\bar{h}} + \frac{\bar{\mu}_m}{\sigma} \left[\frac{1}{\bar{h}} + \frac{3\bar{h}^3}{\bar{\mu}_m^2} \left[\left(\frac{\partial \bar{p}}{\partial \theta} \right)^2 + \left(\frac{\partial \bar{p}}{\partial \zeta} \right)^2 \right] \right] \right|_0^{\bar{h}} \quad (16)$$

To evaluate the heat conduction at the fluid-solid interface, it is assumed that the flow is pure Couette flow and that

$$\frac{\partial \bar{T}}{\partial \theta} = \frac{\partial \bar{T}}{\partial \zeta} = \frac{\partial \bar{T}}{\partial \xi} = 0 \quad (17)$$

Used on eq. (8) this gives

$$Pe \frac{\partial^2 \bar{T}}{\partial \xi^2} = - \frac{\bar{\mu}_m}{\sigma} \left(\frac{\partial \bar{u}}{\partial \xi} \right)^2 \quad (18)$$

Integrating this twice with respect to ξ gives

$$\bar{T}(\xi) = \bar{T}_o + (\bar{T}_h - \bar{T}_o) \frac{\xi}{h} + \frac{\bar{\mu}_m}{12Pe} \frac{1}{h^2} (h\xi - \xi^2) \quad (19)$$

Obtaining the mean temperature \bar{T}_m from

$$\bar{T}_m = \frac{1}{\bar{q}_c} \int_0^{\bar{h}} \bar{u}(\xi) \bar{T}(\xi) d\xi \quad (20)$$

where both \bar{q}_c and \bar{u} are evaluated from Couette flow only, gives

$$\bar{T}_m = \frac{1}{3} \bar{T}_o + \frac{2}{3} \bar{T}_h + \frac{\bar{\mu}_m}{72} \frac{1}{Pe} \quad (21)$$

Using (21) to eliminate $\bar{\mu}_m$ from (19) gives

$$\bar{T}(\xi) = \bar{T}_o + 3(2\bar{T}_m - \bar{T}_o - \bar{T}_h) \frac{\xi}{h} - 2(3\bar{T}_m - \bar{T}_o + 2\bar{T}_h) \frac{\xi^2}{h^2} \quad (22)$$

For usual running conditions the energy dissipation in eq.(16), caused by the Couette term, is much greater than that caused by the Poiseuille term. When (22) is introduced in (16) the energy equation becomes,

$$\bar{q}_\theta \frac{\partial \bar{T}_m}{\partial \theta} + \bar{q}_\zeta \frac{\partial \bar{T}_m}{\partial \zeta} = 4Pe(\bar{T}_o + 2\bar{T}_h - 3\bar{T}_m) + \frac{\bar{\mu}_m}{6h} \quad (23)$$

As is seen from eq. (22), the temperature distribution across the thickness is parabolic. By solving eq. (23), Reynolds and the heat conduction equation together, the temperature distribution in the lubricant can be found. Reynolds equation will in this case be simplified compared to eq. (2) - (5), since the viscosity is expressed at the mean temperature.

Assuming that the convective as well as the dissipative terms can be expressed by Couette flow only, and that the bearing is infinitely long, the energy equation takes the following form

$$\frac{\partial \bar{T}_m}{\partial \theta} = \frac{8Pe}{h^2} (\bar{T}_o + 2\bar{T}_h - 3\bar{T}_m) + \frac{\bar{\mu}_m}{3h^2} \quad (24)$$

Since eq. (24) is independent of the pressure distribution in the film, only iteration between eq. (24) and the heat conduction equation needs to be considered.

A still more simplified version of the energy equation can be obtained if it is assumed that the shaft and bush are adiabatic. Then,

$$\frac{\partial \bar{T}_m}{\partial \theta} = \frac{\bar{\mu}_m}{3h^2} \quad (25)$$

For the energy equations given by eq. (23) - (25), the inlet temperature must be specified as a mean temperature across the thickness.

Energy equation independent of the film length

Next it is assumed that the temperature in the lubricant is constant in the axial direction, and allowed to vary across the thickness. /14/ has considered this situation for a bearing with pure Couette flow. The appropriate energy equation is then as eq. (8), except for the third term which is left out. In order to make the numerical treatment of the energy equation more convenient, the bearing gap is transformed into a rectangular domain by the substitution /14/.

$$\bar{\xi} = \frac{\xi}{h} \quad (26)$$

Eq. (8) then takes the form

$$\bar{u} \frac{\partial \bar{T}}{\partial \theta} + \bar{u} \bar{\xi} c \frac{\sin \theta}{h} \frac{\partial \bar{T}}{\partial \xi} + \frac{\bar{v}}{h} \frac{\partial \bar{T}}{\partial \xi} = \frac{Pe}{h^2} \frac{\partial^2 \bar{T}}{\partial \xi^2} + \frac{\bar{\mu}}{6h^2} \left[\left(\frac{\partial \bar{u}}{\partial \xi} \right)^2 + \left(\frac{\partial \bar{w}}{\partial \xi} \right)^2 \right] \quad (27)$$

An expression for \bar{v} in the rectangular solution domain can be obtained from the continuity equation and the well known expressions for the lubricant velocity under isothermal conditions.

$$\bar{v} = \frac{\partial \bar{h}}{\partial \theta} (\bar{\xi} \bar{u} + \bar{z}^2)(1 - \bar{\xi}) \quad (28)$$

Insertion of eq. (28) into (27) yields

$$\bar{u} \frac{\partial \bar{T}}{\partial \theta} + \bar{\xi}^2 (1 - \bar{\xi}) \frac{1}{h} \frac{\partial \bar{h}}{\partial \theta} \frac{\partial \bar{T}}{\partial \xi} = Pe \frac{\partial^2 \bar{T}}{\partial \xi^2} + \frac{\bar{\mu}}{6h} \left[\left(\frac{\partial \bar{u}}{\partial \xi} \right)^2 + \left(\frac{\partial \bar{w}}{\partial \xi} \right)^2 \right] \quad (29)$$

Since \bar{v} in eq. (28) is expressed in terms of isothermal parameters, eq. (29) will not be valid in the general case of temperature dependent velocities. The error is however, small and the advantages are obvious.

THE ENERGY BALANCE

The heat generated by the dissipation in the lubricant is removed in several ways. Some of it goes to the bush and the shaft, the rest to the axial boundaries or to the inlet groove. From a design point of view, the relative magnitude of these contributions to the energy balance are of interest. A similar experimental analysis has been carried out in /2/. The reduced film length in the diverging zone is taken into account when the energy balance is set up.

Most of the heat, generated by dissipation in the bearing, will be removed by convection. Some of the lubricant will, mainly depending on the eccentricity ratio, be recirculated to the inlet groove. In the groove, a mixing of the incoming fresh lubricant and the recirculating one takes place. Hence, at the inlet to a bearing segment, the temperature will be dependent on the mixing and temperature conditions in the groove. Attempts to describe these phenomena analytically as well as experimentally are mainly done in /3,4,5/. The results obtained are expressed by a hot oil carry-over coefficient, which relates the mean inlet temperature at the bearing segment to the temperature of the incoming fresh lubricant and the temperature of the shaft.

$$\bar{T}_{mi} = \bar{T}_g + K(\bar{T}_h - \bar{T}_g) \quad (30)$$

SOLUTION METHODS

Several different numerical techniques have been employed to solve the equations involved.

The Reynolds equation is solved by the Finite Element Method /10/. Since Reynolds equation with it's boundary conditions expresses a well-posed elliptic boundary value problem, it can be cast into an equivalent variational form, suitable for the usual FEM. Six node isoparametric triangular elements are used.

The energy equations (8) and (29) are solved by Implicit Finite Difference Methods, /9,15/.

Eq. (23), where the mean temperature across the thickness is introduced, is solved by the Galerkin Method, which is one of the Weighted Residual Methods, WRM. The mesh used for the solution of Reynolds equation by FEM, can be employed again for the solution of eq. (23) by the WRM, /10/.

To solve eq. (24) and (25) which are ordinary differential equations, a Predictor-Corrector Method is used, /8/.

The heat conduction equation (10) is solved by a usual Finite Difference Method.

To evaluate the governing equations at the same points, regardless of solution method, the same grid, in axial and circumferential direction, has been used for all three types of equations in one calculation.

RESULTS

The results are all obtained for the same bearing to make comparisons easier. The numerical data for the bearing are given in the following list.

$R = 50 \cdot 10^{-3} \text{ m}$ $R_1 = 100 \cdot 10^{-3} \text{ m}$
 $C = 71 \cdot 10^{-6} \text{ m}$ $k_B = 50 \text{ W/mC}$
 $\kappa_r = \kappa_t = 50 \text{ W/m}^2\text{C}$ $T_h = 77 \text{ C}$
 $T_r = 20 \text{ C}$ $N = 4800 \text{ rpm}$

and for the lubricant

$\rho = 850 \text{ kg/m}^3$ $C_p = 2000 \text{ J/kgC}$
 $T_g = 50 \text{ C}$ $k_o = 0.150 \text{ W/mC}$

The coefficients in the viscosity-temperature relation are found from the following values, $\nu = 20 \text{ cSt}$ at 50C and $\nu = 6.55 \text{ cSt}$ at 90 C . $\nu = 20 \text{ cSt}$ is taken to be the reference viscosity. The simplest version of the energy equation is given in eq. (25). From the solution to this equation, the temperature distribution is shown in figure 2. Since eq. (25) is independent of the pressure distribution, the results are presented for constant attitude angle $\phi = 0$.

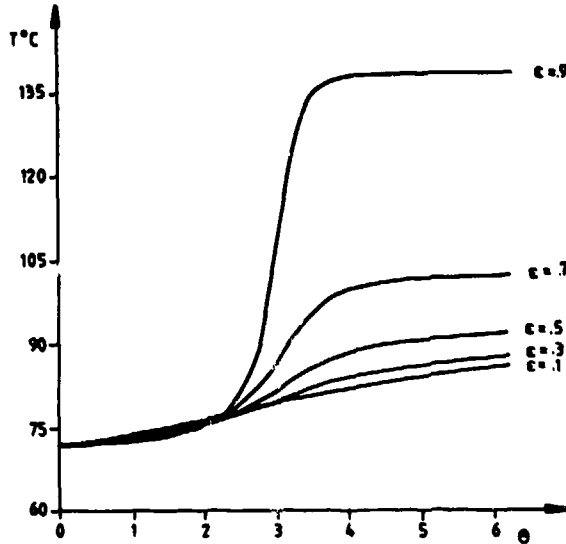


Fig. 2. Mean temperature distribution in the lubricant, attitude angle fixed at $\phi=0$. $L/D=\infty$. Inlet temperature constant. Adiabatic bearing surfaces.

The curves show that the temperature rises sharply in a narrow band around minimum film thickness and it is seen that the eccentricity ratio has a strong influence on the temperature rise. Eq. (25) is also solved, assuming that the viscosity is constant. With this assumption, the temperature rise is three times as high, for $\epsilon = 0.9$, as it is with variable viscosity.

If heat conduction to the shaft and the bush is allowed, the energy equation is given by eq. (24). Again the attitude angle has been fixed at $\phi = 0$. Figure 3 shows the results. The highest value of the mean temperature is now lowered considerably compared to the results obtained in figure 2. The temperature at the lubricant-bush interface, and the shaft temperature are shown on the figure too. Along most of the circumference, the bush surface temperature is higher than the mean temperature. As the eccentricity ratio is increased, the hottest spot is moved closer to the point of minimum film thickness. Figure 4 shows the radial temperature distribution corresponding to the results obtained in figure 3. The radial temperature distribution is described by parabolas at each circumferential position, as given by eq. (22). If a lower value of the hot oil carry over coefficient is taken, the temperature will be almost the same in the diverging zone, whereas both the mean temperature and the bush surface temperature will be lower in the converging film zone. This effect also influences the heat balance for the bearing.

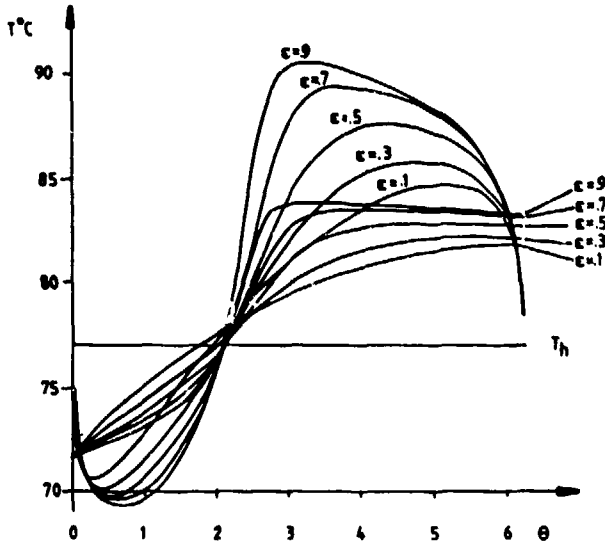


Fig. 3. Mean temperature in the lubricant and bearing surface temperatures. Attitude angle fixed at $\phi=0$. $L/D=\infty$. Radial temperature distribution on fig. 4 for $\epsilon = 0.7$.

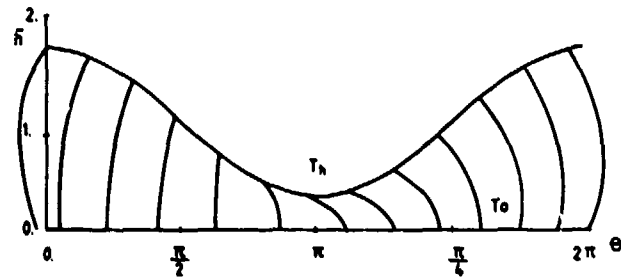


Fig. 4. Parabolic temperature distribution across film thickness for $\epsilon = 0.7$.

For the two-dimensional energy equation, eq. (23), a solution was obtained including also an evaluation of the pressure distribution. This means that besides the iterations to obtain a correct temperature distribution, an additional iteration procedure is employed to find the correct attitude angle. With the boundary conditions given above, the temperature variation in the axial direction, in the lubricant, was about 0.2 C for $\epsilon = 0.7$. Figure 5 and table 1 shows the results. It is seen that the hottest spot at the bush surface is located close to the point of minimum film thickness for all eccentricity ratios. The parameters in table 1 are evaluated from:

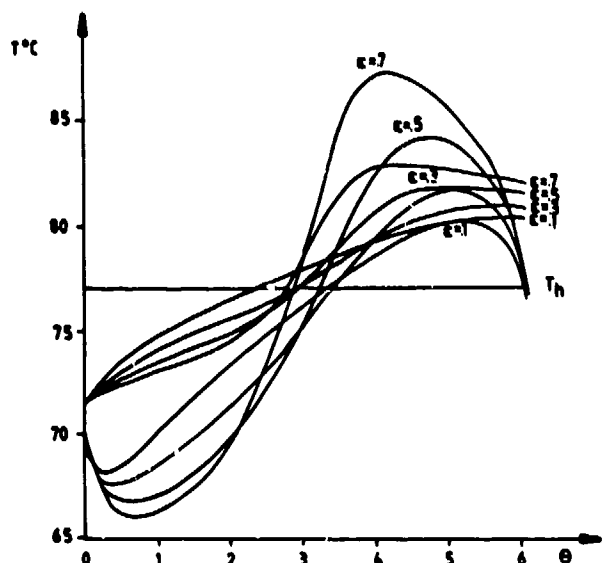


Fig. 5. Distribution of mean temperature in the lubricant and bearing surface temperature. $L/D = 0.3$.

Table 1. Steady state running parameters as a function of the eccentricity ratio.

S	ϵ	ϕ	\bar{q}_s	\bar{E}
0.95	0.7	41.51	0.39	0.99
2.71	0.5	56.25	0.28	0.89
6.68	0.3	69.76	0.17	0.85
24.36	0.1	83.42	0.06	0.87

balance for the two models, since the bush temperature in the latter case is generally higher. While about 10% of the dissipated energy goes into the bush in the latter case, it is only about 5% for the case given in figure 3. An interesting fact which is valid for both cases, is that the relative amount of heat to the bush is almost independent of the eccentricity ratio. The isotherms in the bush and the lubricant are shown on figure 8 for $\epsilon = 0.7$. Figure 9 indicates the radial temperature distribution. Although the temperature may vary freely, the curves on figure 4 and 9 are very similar.

When the energy equation (29), Reynolds equation and the heat conduction equation are solved simultaneously by an iterative procedure, the results are as shown by the following figures and tables. The distribution of the mean temperature in the lubricant on figure 10 is very similar to that obtained in figure 5, while the bush surface temperature is remarkably higher in the inlet zone for the results in figure 10. The heat balance, figure 11, is

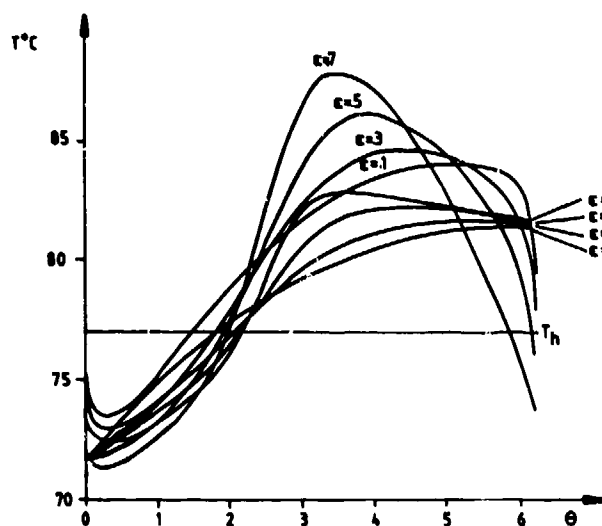


Fig. 6. Mean temperature in the lubricant and bearing surface temperatures. Attitude angle fixed at $\phi = 0$. $L/D = \infty$. The same results are presented in figures 7, 8 and 9.

$$S = (\bar{f}_r^2 + \bar{f}_t^2)^{-1/2} \quad (31)$$

where

$$\left. \begin{matrix} \bar{f}_r \\ \bar{f}_t \end{matrix} \right\} = \frac{6\pi}{L/D} \int_0^{L/D} \int_0^{2\pi} \bar{p} \begin{matrix} -\cos(\theta' - \phi) \\ -\sin(\theta' - \phi) \end{matrix} d\theta d\xi \quad (32)$$

and

$$\bar{q}_s = \int_0^2 -12\bar{F}_2 \frac{\partial \bar{p}}{\partial \xi} d\theta \quad (33)$$

and

$$\bar{E} = \int_0^{L/D} \int_0^{2\pi} \bar{u} \left. \frac{\partial \bar{u}}{\partial \xi} \right|_{\xi=\bar{h}} d\theta d\xi \quad (34)$$

S is the Sommerfeld number, \bar{q}_s the side leakage and \bar{E} the powerloss.

In the cases demonstrated below, the energy equation will be given as eq. (29), i.e. the temperature is now allowed to vary freely in the radial direction.

To compare the results in figure 3 and 4 with the corresponding results for the case of temperature variation across the thickness it is assumed that the flow is pure Couette flow, and that $\phi = 0$. The results are given in figure 6, 7, 8 and 9. When figure 3 and 6 are compared, it is seen that the mean temperature in the oil film is almost the same, but that the bush surface temperature distribution is different as expected. This difference influences the heat

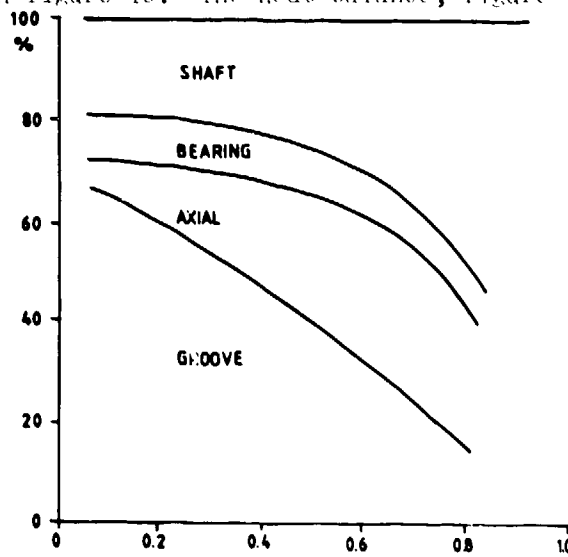


Fig. 7. Heat balance for the bearing. Couette flow.

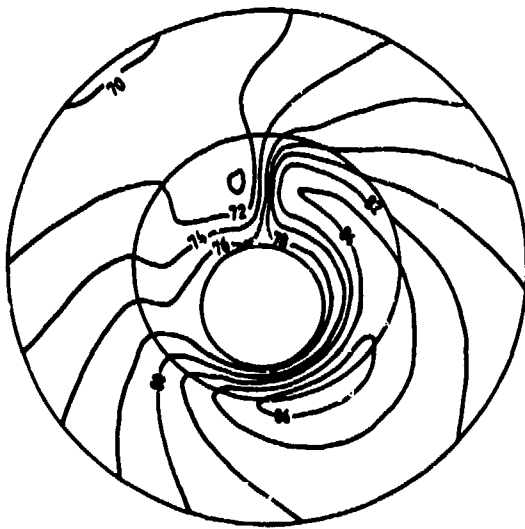


Fig. 9. Isotherms in the lubricant and in the bush. $\epsilon = 0.7$.

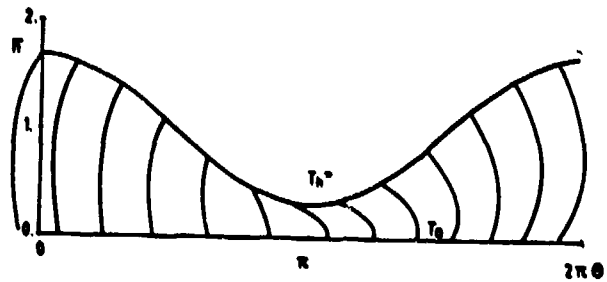


Fig. 9. Radial temperature distribution in the lubricant. $\epsilon = 0.7$.

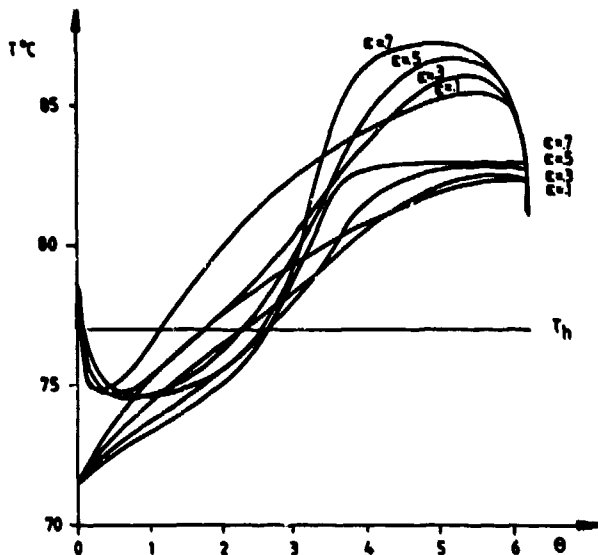


Fig. 10. Mean temperature in the lubricant and bearing surface temperatures.

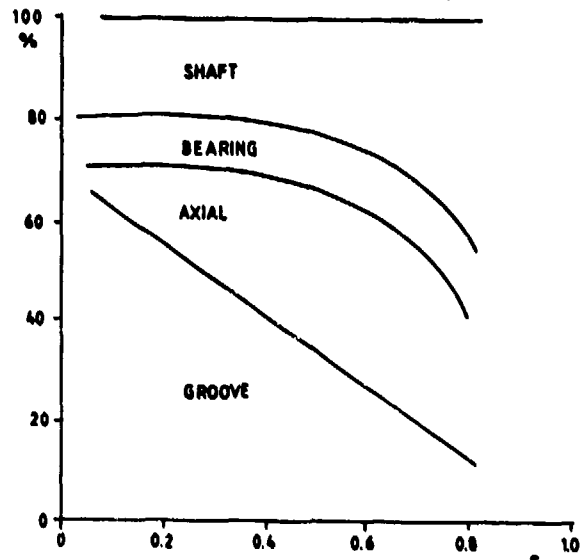


Fig. 11. Heat balance for the bearing.

Table 2. Steady state running parameters as a function of the eccentricity ratio.

S	ϵ	ϕ	\bar{q}_s	\bar{E}
0.51	0.8	34.15	0.43	1.06
0.97	0.7	40.84	0.39	0.94
2.91	0.5	56.31	0.28	0.83
7.45	0.3	70.26	0.16	0.80
31.74	0.1	82.51	0.05	0.80

almost the same as for the case of pure Couette flow given in figure 7, but generally the amount of heat to the bush is greater in the latter case. Table 2 lists the main steady state running parameters as a function of the eccentricity ratio.

A fully three-dimensional thermohydrodynamic solution was obtained by solving eq. (8), Reynolds equation and the heat conduction equation. The maximum axial temperature variation was less than 1 C for $\epsilon = 0.7$, and the temperature distribution on the bush surface was essentially the same as for figure 10.

It should be emphasized, that the results presented in this paper are related to a particular lubricant and bearing geometry. It is not possible, to make the results independent of the bearing dimensions and lubricant properties by means of a single dimensionless parameter as can be done in the isothermal case through the use of the Sommerfeld number.

For a particular bearing, with thermal boundary conditions specified, it is possible to set up an overall heat transfer coefficient as a function of, for example, the eccentricity ratio or the rotational speed. As this coefficient, however, still depends on the geometry and boundary conditions, there seems to be no advantage in introducing such a concept.

CONCLUSION

- The viscosity-temperature dependence has a pronounced influence on the temperature level
- Heat conduction to the bearing sleeve and the shaft must be taken into account
- The temperature variation across the fluid film thickness is significant
- The mean temperature in the lubricant is well represented by the parabolic approximation
- Under normal operating conditions the axial temperature variation is negligible.

REFERENCES

- /1/ Dowson, D.: "A Generalized Reynolds Equation for Fluid-Film Lubrication", Int. J. Mech. Sci., Vol. 4, 1962, pp. 159-170.
- /2/ Dowson, D., Hudson, J.D., Hunter, B., March, C.N.: "An Experimental Investigation of the Thermal Equilibrium of Steadily Loaded Journal Bearings", P. Instn. Mech. Engrs., Vol. 181, Pt. 3B, 1966-67, pp. 70-80.
- /3/ Ettles, C.: "Solutions for Flow in a Bearing Groove". P. Instn. Mech. Engrs., Vol. 182, Pt. 3 N, 1967-68, pp. 120-131.
- /4/ Ettles, C.M.M., Cameron, A.: "Considerations of Flow in a Bearing Groove", J. Lub. Techn., January 1968, pp. 312-319.
- /5/ Ettles, C.: "The Development of a Generalized Computer Analysis for Sector Shaped Tilting Pad Thrust Bearings", ASLE Trans., Vol. 19, 2, 1976, pp. 153-163.
- /6/ Ezzat, H.A., Rohde, S.M.: "A Study of the Thermohydrodynamic Performance of Finite Slider Bearings", J.Lub. Techn., July 1973, pp. 298-307.
- /7/ Frene, J., Boncompain, R.: "Thermohydrodynamic Analysis of Finite Journal Bearings Static and Dynamic Characteristics". 6. Leeds-Lyon Symposium, 1979.
- /8/ Gear, C.W.: "Numerical Initial Value Problems in Ordinary Differential Equations". Prentice-Hall, 1971.
- /9/ Hornbeck, R.W.: "Numerical Marching Techniques for Fluid Flow with Heat Transfer". NASA SP-297, 1973.
- /10/ Huebner, K.H.: "Application of Finite Element Methods to Thermohydrodynamic Lubrication". Int. J. Num. Methods in Eng., Vol. 8, 1974, pp. 139-165.
- /11/ Huebner, K.H.: "A Three-Dimensional Thermohydrodynamic Analysis of Sector Thrust Bearing". ASLE Trans., Vol. 17, 1, 1974, pp. 62-73.
- /12/ Håkansson, B.: "The Journal Bearing Considering Variable Viscosity". Trans. Chalmers University of Technology, Sweden, Nr. 298, 1965.
- /13/ Lund, J.W., Arwas, E.B.: "A Simultaneous Solution of the Lubrication and the Energy Equations for Turbulent Journal Bearing Films". Mechanical Technology Inc., No. MTI 64TR31, 1964.
- /14/ McCallion, H., Yousif, F., Lloyd, T.: "The Analysis of Thermal Effects in a Full Journal Bearing". J.Lub. Tech., October 1970, pp. 578-587.
- /15/ Richtmeyer, R.D.: "Difference Methods for Initial-Value Problems". Wiley, Sec.ed.
- /16/ Tipei, N., Nica, A.: "On the Field of Temperature in Lubricating Films", J.Lub. Tech., October 1967; pp. 483-492.
- /17/ Tipei, N.: "Flow Characteristics and Pressure Head Build-Up at the Inlet of Narrow Passages". J. Lub. Tech., Vol. 100, January 1978, pp. 47-55.
- /18/ Vohr, J.H.: "Prediction of the Operating Temperature of Thrust Bearings".

DISCUSSION

J.B. Medley, University of Waterloo, Ca

Can you comment on difficulties encountered in the application of the sophisticated numerical techniques you used in your solution procedures?

Author's Reply

Two main numerical problems emerged in the solution of the energy equations described.

For the general energy equation 1 Eq. (8), and for Eq. (29) numerical problems arise for high eccentricity ratios. The system of finite difference equations will no longer be positive definite. The physical explanation for this is, that backflow appears in the high pressure region. To evaluate the temperature at an arbitrary circumferential position in the lubricant film the results already obtained upstream are used. The appearance of backflow means that downstream temperatures must be taken into account. This cannot be done in a usual finite difference discretization of a parabolic equation.

When solving the energy equation given by Eq. (23) the above mentioned problems caused by backflow will not appear. Instead, at least when the WRM is used, the system of equations obtained will be nonsymmetric and indefinite.

J. Frene, Université de Poitiers, Fr

Pouvez-vous donner des détails sur la façon dont vous prenez en compte les transferts thermiques dans la zone de cavitation?

Author's Reply

For the energy Equations (8) and (22) where axial temperature variation in the lubricant is taken into account the Peclet number in the diverging film zone is adjusted according to the reduced film length

$$(7) \quad Pe^x = Pe \frac{l}{L}$$

In this work it is assumed that the lubricant will be supplied to the bearing at the groove only. From continuity considerations it is seen that

$$\frac{l}{L} = \frac{h_0^-}{h^-(0)}$$

l is the reduced film length in the diverging film zone.

h_0^- is the film height at the circumferential position where cavitation first appears.

For the energy Equations (24) and (29), the Peclet number is assumed to be the same in the converging film zones. But, when the heat balance is set up, the reduced film length in the diverging film zone is taken into account.

J.F. Chevalier, SNECMA, Fr

Avez-vous fait les mêmes calculs pour un squeeze film, et avez-vous fait les mêmes calculs pour un contact roulant?

Author's Reply

Unfortunately we have not made the same analysis for squeeze film bearings and rolling element bearings.

Probably the assumption of parabolic temperature distribution across the film height could be used in the analysis of squeeze film bearings.

For the case of EHL it should be emphasized that the temperature gradients can be several orders of magnitude higher than in the usual hydrodynamic lubrication situation. It may therefore be difficult to express the temperature gradients sufficiently accurate in the EHL situation.

C.H.T. Pan, Columbia University, US

In a related study, "Finite-Element Method for Heat Transfer Problems in Hydrodynamic Lubrication" by Dr Kwang June Bai, which is being released as US DOD Report No. DTNSRDC/SPD-1043-01, the numerical procedure required to compute the temperature field in the lubricant film was considered. In view of the recent trend of increased use of computers in engineering work (CAD, CAM etc.), an accurate and trouble-free numerical procedure to determine the lubricant temperature field is needed because lubricant viscosity is sensitive to temperature, because thermo-elastic distortion of bearing surface is important for certain bearing types, and because intense local heating is expected in mixed lubrication. A three-domain problem was formulated. A parabolic domain (combined convection-conduction with internal heating) is sandwiched between two elliptic domains (conducting solids). It is known that numerical instability would develop if Galerkin type finite element method is applied to calculate a single domain parabolic field. However, no numerical instability was encountered when the three-domain

problem was so treated. Two model problems were solved. In the first model problem, an analytically known field was computed by the FEM. Residual errors, measured by the deviations of the numerical result from the analytical field were correlated with mesh size. Converging type power law dependence of residual errors on the mesh size was established for a wide range of the Peclet number. A second problem considered dealt with a situation which closely approximates the realistic physical conditions of an actual bearing. The results indicate a strong dominance of wall effects. Temperature gradients in the conducting solids are of moderate magnitudes. The lubricant temperature rises quickly to correspond to the wall temperatures. Although the transverse temperature gradient in the lubricant film is quite high, the actual transverse temperature variation is relatively modest. Heat capacity associated with "hot oil carryover" is deemed to be of secondary importance in comparison with the amount of viscous heating. A large fraction of the temperature rise can be attributed to the thermal resistance between the solid bodies and the ambient.

BEHAVIOR OF AIRCRAFT ENGINE OILS AT HIGH TEMPERATURE**Dr. E. Jantzen****Deutsche Forschungs- und Versuchsanstalt
für Luft- und Raumfahrt e.V.
Institut für Technische Physik
Pfaffenwaldring 38-40, 7000 Stuttgart 80
F.R. Germany****SUMMARY**

Higher temperatures in current and future aircraft engines lead to a stronger thermal and oxydative attack of the engine oils. In this paper the reversible and irreversible change of the engine oil will be reported and the reasons discussed. Furthermore the influence of hot surfaces on aircraft engine oils as determined by different laboratory simulation equipment used in Germany will be shown. Moreover, different types of deposits, their properties, and the current knowledge about the influencing parameters will be reported. Finally, possibilities to avoid deposit formation will be shown.

1. Introduction

This topic will discuss a problem as old as aviation with motor aircraft. During the first world war people concerned with aircraft engine operation had to contend with the so-called "piston ring sticking" problem. The reason was the formation of resin-type deposits around the piston rings due to the high temperature in the engine and the low stability of the engine oil. The problem still exists at hot walls of our current aircraft engines. The reason for the existence of this problem over a long period of time is the continuous increase of engine temperatures, despite the much better engine oils available today. The further rise of engine temperature in the near future is a rather certain situation: Higher turbine inlet temperature can be used to reduce the fuel consumption or can raise the thrust of an engine. The consequence is that aircraft engine oils will also be under strong thermal attacks in the future.

2. Behavior of the Oil at High Temperature

If we speak about 'behavior' of an engine oil at high temperature, we have to remember that reversible and irreversible changes are possible. Reversible change means no chemical reaction but variation of physical behavior, e.g.

- ° viscosity
- ° specific gravity
- ° vapour pressure
- ° conductivity
- ° surface tension
- ° foaming
- ° elastomer change

Irreversible change is the consequence of chemical reactions, e.g.

- ° splitting of the molecules
- ° oxydation of the molecules
- ° combination of the molecule parts or reaction compounds.

By molecules we refer to the base oil and the additives, which react in different ways.

The above mentioned chemical reactions can have strong consequences on the character and behavior of the original engine oil. The extent of this oil change is dependent on the factors:

- ° temperature
- ° reaction time
- ° oxygen amount
- ° type of catalysts (e.g. metals, water, acids)

3. Influencing Factors on Aircraft Engine Oils

Lubrication means mechanical stress of the engine oils. Aircraft engine oils overcome this stress rather well. Stronger influencing factors are high temperatures in the presence of air and metals. Hot air is widely used in aircraft engines as sealing air and thus comes into intensive contact with the engine oil. Furthermore, it is taken into account that an extended oil surface leads to a stronger attack and change of the oil. Such extended surfaces are quite common when generating thin films in the bearings and several other oil wetted parts, or as small droplets or foam. Another essential factor for the reaction is the time which an oil molecule has to stay at a certain high temperature. In chemistry we speak about the reaction time. Finally, the oil change in an engine is influenced very often by certain materials, which can promote as catalysts the reaction in very small amounts. These catalysts can be especially metals (e.g. wear particles), but also water, acids, and some other compounds.

4. Reversible Change at High Temperature

As mentioned, certain reversible changes are of great importance to people developing and using engines. One of them is the viscosity. In this connection may I mention that in certain aircraft engines the oil viscosity can be as low as the viscosity of water at room temperature, e.g.:

	MIL 7808 oil	DEng RD 2497 oil
at 200 °C	1 cS*	1,3 cS
at 250 °C	0,76 cS	0,96 cS

* 1 cS = 1 mm²/s₂₀

These temperatures are possible in bearings and gears of several types of modern aircraft engines. The negative influence of such low viscosities on wear and life time of a machine element is well known.

The increase of vapour pressure can also be of some importance, e.g. under the aspect of high evaporation loss. In a mixture of base stocks under high temperature, a specific loss of the lower boiling components can occur, with the consequence of viscosity and pour point increase. It is also possible that a high evaporation rate leads to a loss of certain additives, reducing the service time of an oil. In most aircraft engines reversible and irreversible situations overlap.

5. Irreversible Change at High Temperature

At this time it is rather difficult to explain all steps in detail which can occur during splitting, oxydation, and combination of molecules. As a consequence of these reactions a change of properties is possible, e.g. viscosity, color, vapour pressure, density, acidity, pour point, lubrication, rubber swelling. Furthermore, a splitting and evaporation of certain additives is also possible. Figure 1 shows that this change can be rather small. The data is from a commercial, rather low operating temperature, aircraft engine. The situation can look quite different with engines which operate under high speed and high thrust, or with rather high temperatures in the back section of the engines. Furthermore plays the amount of oil which has to be added at certain interval an important role under this aspect. A rather high oil loss and, as consequence, a high amount of added oil can hold the total circulating oil in relatively good condition. If temperature or air amount exceed certain limits, strong changes of the oil are inevitable (Fig. 2). A strong polymerisation reaction of molecules leads to a higher viscosity. A higher density has the same basis. The darkening of color is caused by the splitting and oxydation reactions of the molecules, resulting in so-called chromophor groups (very well known in the organic dye industry). The increase of vapour pressure and acidity is due to a reaction of splitting and oxydation products. In some engines types these products will not be found despite high temperatures, because of the high amount of vent air which carries out most of the low molecular weight reaction products. Lubrication can be positively influenced by certain acids and also by higher molecular weight reaction compounds. This is investigated by wear tests and by gear tests.

6. High Temperature Behavior and Chemical Structure

The discussed behavior of aircraft engine oils has its foundation in the chemical nature of the baseoil and the antioxydation additives. At the beginning of a high temperature oxydation on an engine first, the high temperature additives shield the base stock against oxydation. So the first step under the aspect is destruction of the additives. This is easily controlled by modern analytical methods, e.g. HPLC, DTA and FT-IR (1,2). At the same time the color of the oil change to brown and dark, is explained by chemical reactions of the additives with oxygen under creation of colorintensive chromophor groups.

After destroying the antioxydation additives, the oxydation of the ester molecule starts. This reaction is similar for hydrocarbons and esters and proceeds by a free radical mechanism (3,4,5,6,7). In an initial reaction hydroperoxide is formed. This hydroperoxide molecule reacts further to form aldehydes and ketons. The aldehydes, as rather instable compounds, react easily with oxygen to form acids. Investigations in our laboratory with trimethylolpropan- and pentaerythritheptonoate at high temperature verify this reaction mechanism. Further gaschromatograph/masspektrograph investigations of the final splitting products show us a homologous row of acids from propion- to heptanoic-acid, these compounds being about 70 % of the splitting products. Another homologous row are ketons. A major question was the selectivity of the oxygen attack on an ester molecule under the aspect of improving the stability. Several workers have reported that the carbon-hydrogen bond closest to the ester group in the alcohol- and acyl-portion of the molecule undergoes an oxydative attack at a much slower rate than the other secondary carbon-hydrogen bonds (7,8,9,10). The secondary hydrogen atoms are oxydized about 15 times faster than the primary hydrogen atoms. These findings are in good agreement with that from aliphatic hydrocarbon oxydations (11).

7. Behavior of Thin Oil Films at High Temperature

Oil in form of a thin film reacts especially strongly in an air atmosphere at higher temperatures. Due to the reaction conditions in an engine, a broad range of deposits are possible. The first step - at the beginning of deposit formation - is a light brown sticky resin. The next step is a less sticky dark brown resin. Then follows a black non-sticky but elastic resin as a deposit. At higher temperatures and longer reaction times the resin becomes more brittle and of high hardness and deep black color. Figure 3 shows a hard, laquer-like deposit in an gasturbine engine developed under static conditions. Under the situation of oil droplets and vapours a more faint coal or coke like deposit occurs. This type of deposit generated in the diffuser case of an aircraft engine is shown in figure 4.

The temperature is between 280 and 400 °C in the region between burning chamber and turbine of an aircraft turbine engine. Thicker films and coke-like deposits are the consequence of longer service times. These thicker films are dangerous by reducing heat transfer (less cooling of engine parts), blocking of air and oil tubes and filters, with all the consequences.

8. Laboratory Investigations of Deposits

Over the years, a lot of laboratory investigations were done to solve this problem (12,13,14,15). A high number of test devices for static or dynamic simulation of similar situations as in aircraft engines, were developed. Our laboratory in Germany was especially involved in work with a modification of the so-called "panel coker", which was originally developed by the US-Air Force. This device simulates a dynamic situation, e.g. the permanent incidence of oil droplets on a hot surface. The nature of the deposits are very much dependent on the test parameters (oil amount, wall temperature and air amount). During this investigation we obtained all types of deposits, ranging from a brilliant surface like a hard laquer film to others which look faintly like carbon black (Figs. 5a,b). Furthermore, with the different modification of the "panel coker" we achieved a good reproducibility of the results.

As a second device we built up the so-called static deposition tester with assistance of the US-Air Force Propulsion Laboratory. With this device we study mainly the development of thin laquertype films (Figs. 6a,b). A third test which we use is the Rolls Royce cup deposit formation test. This test was also developed to study the laquer type deposits under static conditions. The cup has an outer diameter of 60 mm and an inner diameter of 50 mm. The inner height is 5 mm. The test temperatures for all these tests range from 260 to 390 °C. Test time varies normally between 3 and 24 hours.

9. Results of Deposit Formation Tests

The results, e.g. the amount of deposit or layer thickness depends to a large extent on the test parameters. First, some results about the influence of the oil amount on the amount of deposits. The results under dynamic condition show that the amount of deposits decrease with the amount of oil (thrown as droplets against the hot wall) (Figs. 7a,b). Under static conditions the opposite was found: The amount of deposits increases with the oil amount at the hot surface. The reason for this is the retention time. In the dynamic situation, the retention time of the oil molecules becomes shorter with higher oil amount: In an extreme case it can be a part of one second. In the static case, the retention time is as long as the overall test time, e.g. as long as a long distance flight.

The next interesting parameter is the temperature of the metal surface. Under dynamic conditions the deposit amount increases with the temperature (Fig. 8). Under static conditions we again found a quite different situation: The amount of deposits decreases with the wall temperature. The explanation for these opposite results again is the retention time on the surface. Under dynamic conditions, permanent new oil comes on the surface and generates, at high temperature, more deposits. Under static conditions with higher temperature, a higher degree of oil evaporation and cracking reaction leads to a smaller amount of deposits. The deposit film becomes thinner but harder with higher temperature.

The third important parameter is the air amount which flows over the oil film. Under dynamic conditions the amount of deposits increases with higher air amounts (Fig. 9). In the static situation, deposits decrease with the amount of air. An explanation for these opposite results is again that under dynamic condition a permanent "delivery" of new oil to the surface occurs. This oil can generate with higher air amount more deposits. Under constant conditions a higher air amount leads to a higher oil loss due to higher evaporation rates with the consequence of a lower deposit amount. Figure 10 shows some results from the aspect of layer amount and its hardness in relation to the flight- (= test)-time under static conditions. The amount of the deposit decreases over the time but the hardness increases to values as high as glass.

During investigations in this area, we made a high number of scanning electron microscope photographs of which four examples are shown here. Figure 11 is a deposition conducted in a static deposition tester. It shows eleven deposit layers, each produced by a new oil film in a three hour period at high temperature. Figure 12 shows a scanning electron-microscope photograph resulting under dynamic test conditions. The small balls have a size of about 1 to 2 microns. Figure 13 shows a microphotograph of an elastic resin deposit. The surface is scratched with a needle. Figure 14 shows a microphotograph of a brittle deposit. The conditions for both tests were the same: 3 hours at 290 °C, but the engine oil were from different sources.

10. Possibilities to influence deposit formation

If somebody desires to influence deposit formation, he has to clear the question as about dynamic or static oil situation first. For example, in a dynamic situation (oil droplets), a higher oil amount leads to a shorter retention time at the hot surface and so to less or no deposit. In a static situation, the oil amount should be as small as possible. Here, a higher air amount and a somewhat lower temperature of the hot surface are the answers. In the dynamic oil situation a lower air amount can lead to a lower deposit formation. A metal surface temperature as low as possible is a good method to reduce deposit formation. From our knowledge of MIL 7808 and MIL 23699 aircraft engine oils, a temperature lower than 250 °C is noncritical. With the DEngRD 2497 engine oils a higher surface temperature, about 50 °C, is possible.

Conclusions

Aircraft engine oils change reversible and irreversible under higher temperatures. Deposit formation depends on several parameters: Surface temperature, oil and air amount, and retention time on the surface (static or dynamic conditions). Also the type of engine oil can be of influence. Investigations under variation of the different parameters shows that a decrease of deposit formation can be achieved. Worldwide investigations concerning the reasons for this "aging" process show that an oxydation and reaction process of the shielding additives and the base-oil itself take place. The main influencing parameters are metal catalysts, air amount, temperature and reaction time in the high temperature zone. The reaction is frighly influenced by the extension of the oil surface, e.g. small droplets, oil/air foam or a thin oil layer.

References

- (1) Stavinoha, L.L., Fodor, G.E., Newman, F.M., Lestz, S.J.: "Analytical Characterisation of Synthetic Lubricants", ASLE Trans. Vol. 21, 3, 217-225 (1978).
- (2) Jantzen, E.: "Die Bestimmung des Alterungsverhaltens von Flugturbinenölen mit DTA", DFVLR-Forschungsbericht, Köln, FRG (Juli 1982).
- (3) Emanuel, N.M.: "The Oxydation of Hydrocarbons in the Liquid Phase", Pergamon Press Ltd., Oxford, England (1965).
- (4) Reich, I., and Stivela, S.S.: "Autooxydation of Hydrocarbon and Polyolefins", Marcel Dekker Inc., New York (1969).
- (5) Ali, A., Lockwood, F., Klaus, E.F., Tewksbury, F.J., and Duda, J.L.: "The Chemical Degradation of Ester Lubricants", ASLE Trans. Vol. 22, 3, 267-276 (1979).
- (6) Cuellar, J.P.: "Degradation Study of a Trimethylolpropane Triheptonoate Lubricant Basestock", Techn. Report AFAPL-TR-77-87 Wright Patterson Air Force Base (1977).
- (7) Sniegowski, D.J.: "Selectivity of the Oxydative Attack and Model Ester", ASLE Trans. Vol. 20, 4, 282-286.
- (8) Lockwood, F.E., and Klaus, E.E.: "Ester Oxydation under Simulated Boundary Lubrication Conditions", ASLE Trans. Vol. 24, 2, 276-284 (1981).
- (9) Brodnitz, M.H.: "Autooxydation of Saturated Fatty Acids", J. Agr. Food Chem. Vol. 16, 994 (1968).
- (10) Parson, B.I., and Hinshelwood, C.: "The Oxydation of Hydrocarbons and their Derivates", J. Chem. Soc. 1799 (1956).
- (11) Benton, J.L., Wirth, M.M.: "Position of Radical Attack During Oxydation of Long Chain Paraffins", Nature 171, 269 (1953).
- (12) Oberright, E.A., Leonardi, S.J., and Hepplewhite, H.L.: "Deposit Forming Tendencies of High Temperature Lubricants", ASLE Trans. Vol. 7, 64-72 (1974).
- (13) Salle, F.E., Smock, W.D., Lea, F.K.: "Deposition Characteristics of Lubricants Developed for Aircraft Gas Turbine Engines", J. Am. Soc. Lubr. Eng. Vol 28, 10, 357-364 (1972).
- (14) Cuellar, J.P.: "Mechanism of Turbine Engine Lubricant Deposition", Techn. Report AFAPL-TR-79-2037, Wright Patterson Air Force Base (1979).
- (15) Barber, B.D., Tyler, J.C., Valtierra, M.L.: "An Aircraft Gas Turbine Engine Simulator Test for Evaluating Lubricant Deposition and Degradation", Lubrication Eng. Vol. 34, 1, 22-30 (1978).

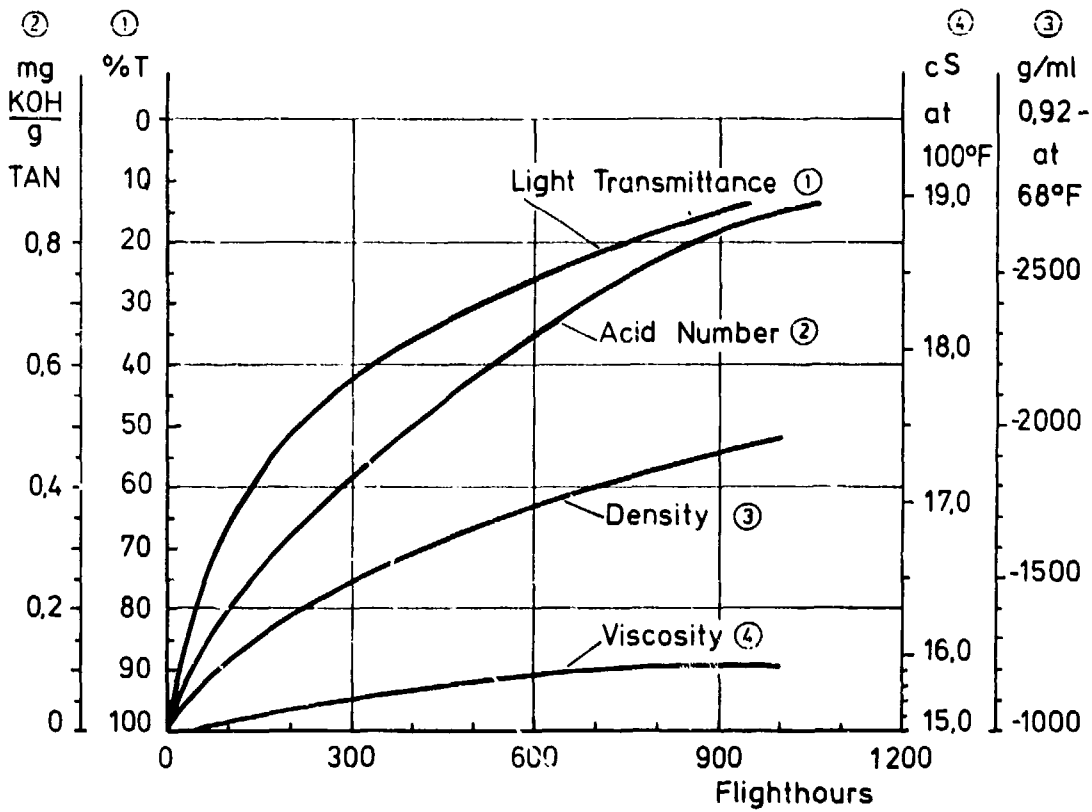


Fig. 1: Increase of test values as consequence of oxydation, splitting and polymerisation reactions. - Typical behavior of an engine oil in a long range transport aircraft.

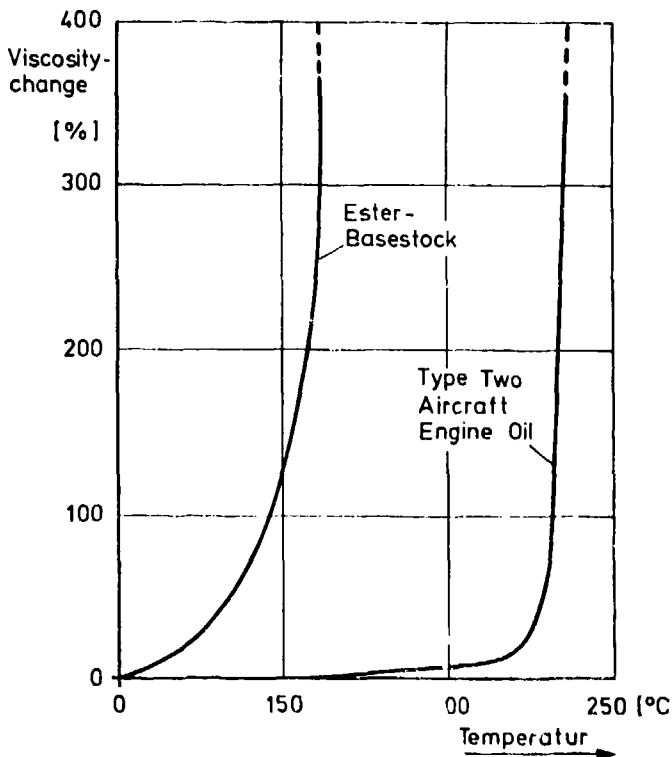


Fig. 2: Typical behavior of an aircraft engine oil and basestock at increasing temperature. At the inflection area the shielding additives are used up. The unshielded basestock shows a rather constant change of viscosity.



Fig. 3: Varnish-type deposits in a gas turbine engine, generated by liquid oil - static situation.

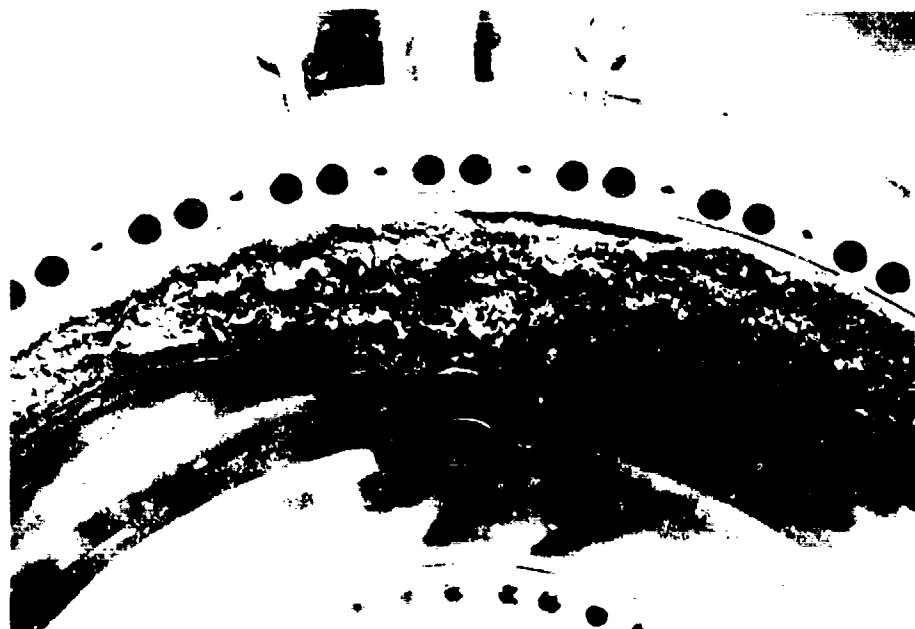


Fig. 4: Coal-type deposits in the diffuser case of an aircraft engine, generated by droplets and oil vapors - dynamic situation.

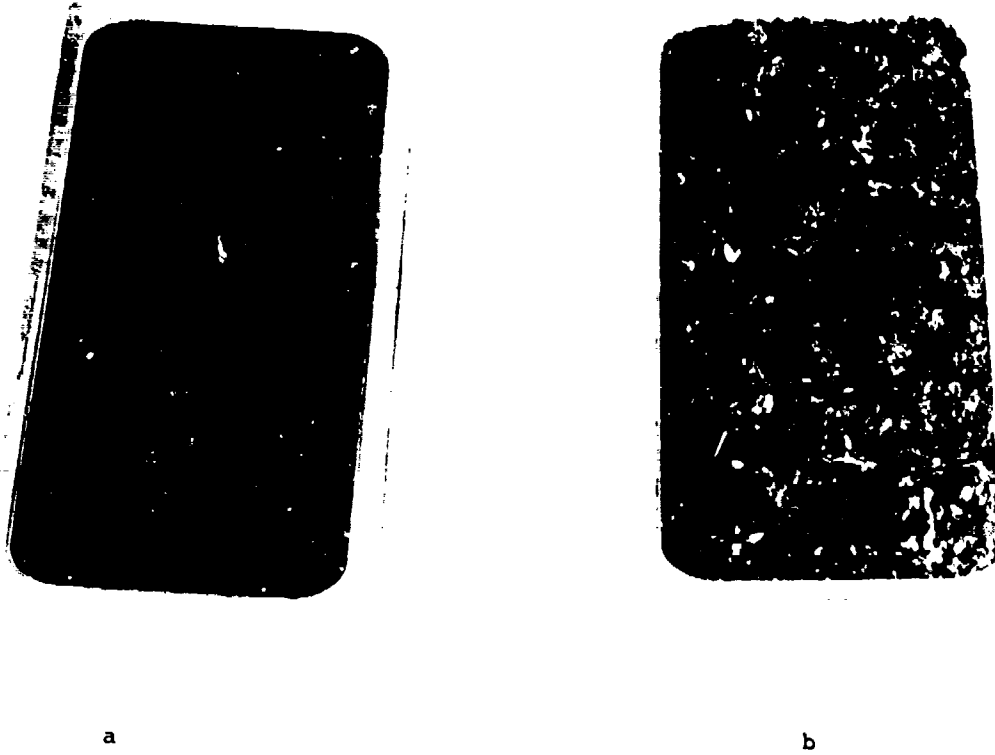


Fig. 5: Deposits - dynamic situation, generated by oil droplets

a) test	600 L air/h) at 320 °C	high splash rate
b) test	60 L air/h		low splash rate



Fig. 6: Deposits - static situation, generated by liquid oil

a) test temperature	260 °C
b) test temperature	350 °C

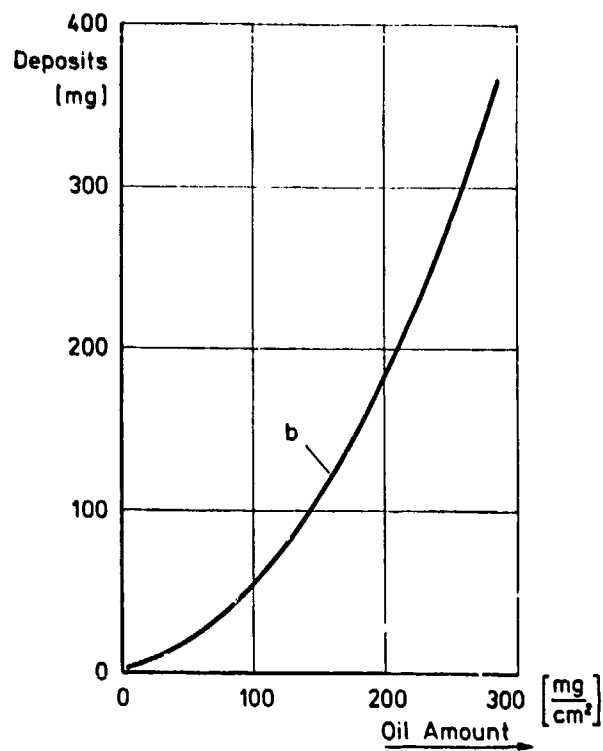
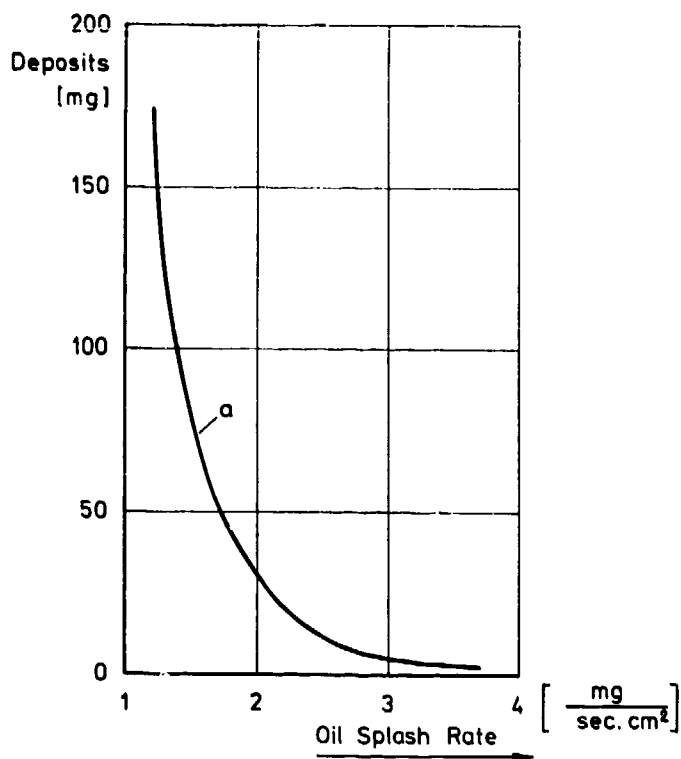


Fig. 7: Influence of oil amount to deposit formation
 a) dynamic conditions
 b) static conditions
 - MIL-L-23699 aircraft engine oil -

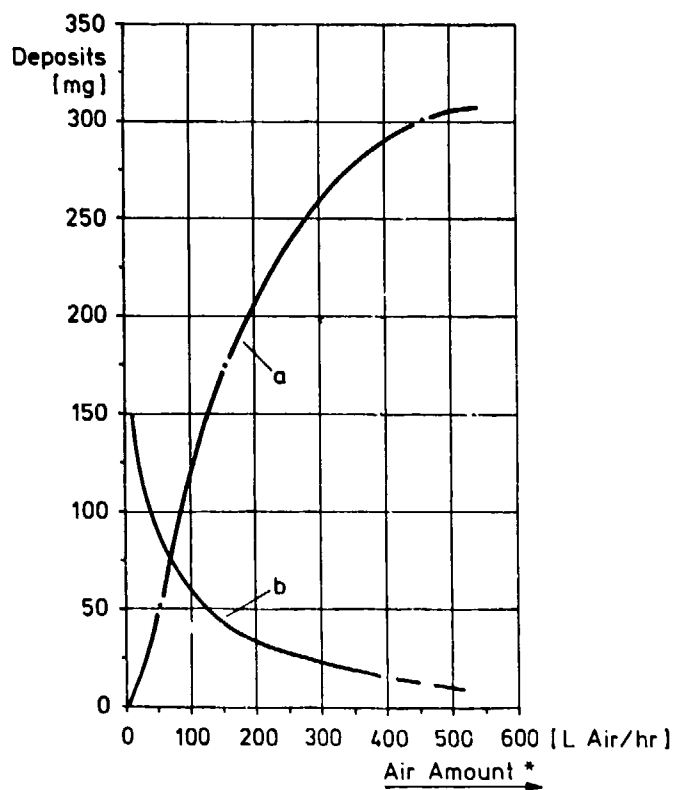
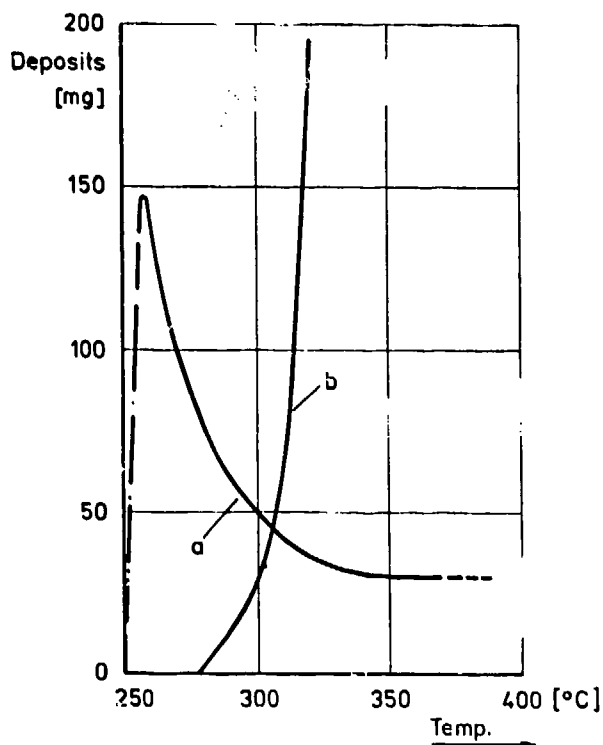


Fig. 3: Influence of surface temperature deposit formation
 a) static condition
 b) dynamic conditions

Fig. 9: Influence of air amount to deposit formation
 a) dynamic situation
 b) static situation

* for static results divided by ten

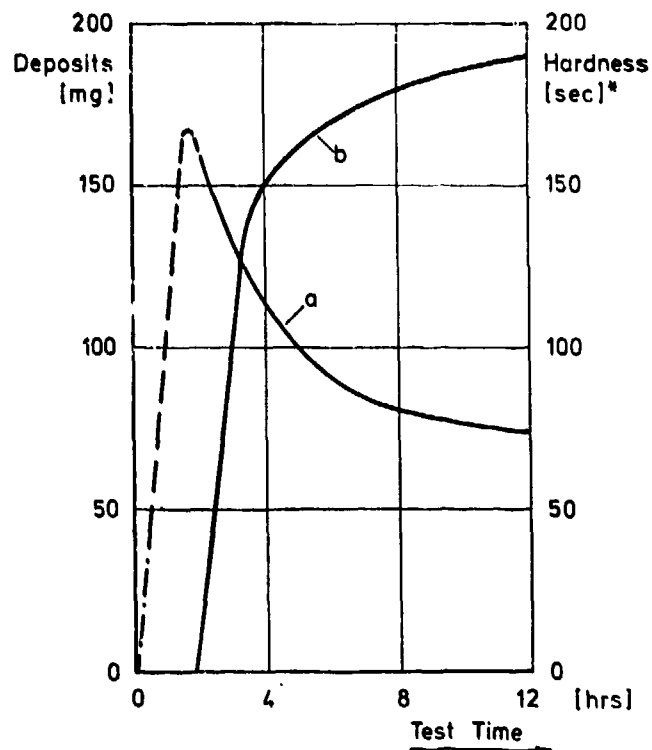


Fig. 10: Influence of test time to deposit formation
 a) amount of deposits
 b) hardness of layer

* damping time, pendulum test, DIN standard
 Method No. 53157 FRG



Fig. 11:

Varnish-type deposit, after 11 temperature/oil cycles - static test conditions. Surface temperature 290 °C, 3 hour test cycles. SEM, 200 x magnification



Fig. 12:

Coal-type deposit on a metal surface after 24 hours test time at 360 °C. SEM, 6000 x magnification.



Fig. 13:

Elastic, varnish-type deposit with
needle scratch - static condition
Surface temperature 270 °C
test time 3 hours
SEM, 50 x magnification.



Fig. 14:

Brittle varnish type deposit after metal-
plate bending - static conditions -
Surface temperature 290 °C
test time 3 hours
SEM 1000 x magnification.

DISCUSSION

E.Saibel, USARO, RTP, US

Among other factors, internal and external stress can affect the rate of chemical reaction at the surface. Also there is the possibility of electrochemical action developing in the lubricant. Both can augment or impede the rate of reaction.

Author's Reply

We agree that mechanical stress can have an influence on the oil. Two things are possible: splitting of high molecular weight component by shearing (well known in oils with v. i. - improvers, which are not allowed in aircraft turbine engine oils), the other major possibility is that by mechanical shearing more energy is brought into the oil which leads to an easier thermal or thermal-oxidation reaction. In this connection the influence of metallics through catalytical effects, on chemical reactions is important.

M.A.H.Sequeira, Portuguese Oil Company, Po

- (1) The increase of acidity is always a very dangerous situation that means sooner or later the replacement of the used oil. However, in pages 3 and 5 of your presentation you say, "lubrication can be positively influenced by certain acids . . .". This seems to be at least a very controversial opinion that I would like to see clarified.
- (2) Among several parameters you mentioned, such as viscosity, specific gravity, acidity, etc., I didn't see reference for the *Insolubles Content* (Pentane and Toluene). That gives us an idea about degradation of the oil (carbon residues as well as acid products).

Do you think that this characteristic is not important to your study?

Author's Reply

- (1) Acids in oils are a very complicated matter, due to the different types of acids (weak, medium, strong acids). Certain acids support lubrication, such as by reactions involving fatty acid esters as additives in different engine oils.
- (2) Thank you very much for mentioning the "Insolubles Content". We did two characterizations over a long period of time and it is indeed useful if an oil has developed high molecular weight compounds. In many cases it seems that the aircraft engine oil is highly stressed. For control of changes from the very beginning we use today more and more GC and the different possibilities of HPLC.

D.G.Astridge, Westland Helicopters, Yeovil, UK

Noting your reference to type classifications of oils could you please quote the reference to your classifications, or explain their basis. Some workers in this field classify oils by performance characteristics (e.g., A.Squires, Rolls-Royce, proposal to SAE 197?) whilst others appear to classify them on the basis of basestock ester type.

Author's Reply

Indeed it is possible to use several possibilities to classify engine oil under the aspect of high temperature behavior. The type of basestock plays an important role, but today most engine oils for aircraft turbine engines are made by so called steric hindered esters. Above this the additive package is important. As you can see, current MIL 7808 and MIL 23699 oils are very similar in their high temperature behavior. The D. Eng. R. D. 2497 oil has a higher c/o stability. Under the aspect of deposit formation rather large differences are possible. This has to be tested under different methods which should be as near to practical as possible.

EXPERIMENTAL AND ANALYTICAL DETERMINATION OF GEAR TOOTH
TEMPERATURES WITH OIL JET LUBRICATION†

Dennis P. Townsend
NASA Lewis Research Center
Cleveland, Ohio
Member ASME

and

Lee S. Akin*
Western Gear Corporation
Industry, California
Fellow ASME

SUMMARY

Experimental measurements of gear tooth average and instantaneous surface temperatures were made with a fast response infrared radiometric microscope, while operating at various speeds, loads and oil jet pressures. Increased oil jet pressure had a significant effect on both average and peak surface temperatures at all test conditions. Increasing the speed at constant load and increasing the load at constant speed causes a significant rise in average and peak surface temperatures of gear teeth. A gear tooth temperature analysis was conducted using a finite element method combined with a calculated heat input and oil jet impingement depth with estimated heat transfer coefficients based on the experimental data. Oil jet pressures required for adequate cooling at high load and speed conditions must be high enough get full penetration depth of the teeth. Calculated and experimental results were in good agreement.

SYMBOLS

a	diffusivity, $= \kappa / P C_p$, lb/in °F sec ^{1/2}
b	Hertzian contact width, m (in.)
c _p	specific heat, J/kg K (Btu/lb °F)
d _j	oil-jet impingement depth, m (in.)
f _e	effective face width, m (in.)
f	friction coefficient
h _j	heat-transfer coefficient for lubricated flank of gear, W/hr m ² K (Btu/hr ft ² °F)
h _s	heat-transfer coefficient sides of gear, W/hr m ² K (Btu/hr ft ² °F)
h _t	heat-transfer coefficient for unlubricated flank of gear, W/hr m ² K (Btu/hr ft ² °F)
J	heat conversion factor
k	infrared radiometric microscope constant
L _A	line of action length, m (in.)
L _t	length of tooth, m (in.)
m	module
N	number of teeth
ΔN	radiance
P _d	diametral pitch module (in ⁻¹)
q	heat flux, W/hr (Btu/hr)
q _t	total heat generated, W/hr (Btu/hr)
V	rolling velocity, m/sec (ft/sec)
ΔV	infrared radiometric microscope measured, V
V _g	gear pitch line velocity, m/sec (ft/sec)
V _j	oil-jet velocity, m/sec (ft/sec)
V _s	sliding velocity, m/sec (ft/sec)
W	normal tooth load, N (lb)
W _t	tangential tooth load, N (lb)
α	oil-jet angle from radial, deg
β	temperature coefficient of viscosity
δ _j	dimensionless impingement depth, d _j P _d , m ² (in.)
ε	emissivity
n	rotation angle, revolutions/sec
θ _s	temperature, K (°F)
θ _w	gear rotation angle from tip of tooth to impingement point, rad
κ	thermal conductivity, W/m K (Btu/ft °F)
Λ	partition constant
ν, ν ₀	kinematic viscosity
ν _j	dimensionless oil-jet velocity
ρ _j	density, kg/m ³ (lb/in ³)
ρ _{1,2}	involute radius of curvature, m (in.)
φ	pressure angle, rad
ω	angular velocity, rad/sec

†Material contained in this report is similar to material presented at the ASME Third International Power Transmission and Gearing Conference, San Francisco, California, August 18-22, 1980 (NASA TM-81419).

*Also, California State University, Long Beach, California.

INTRODUCTION

There are several methods of lubricating and cooling gear teeth: splash lubrication, drip feed, air/oil mist, and pressurized oil-jet flow. The method of successful lubrication usually depends on the operating conditions. For gears operating at moderate to high speed (above 5000 rpm), the pressurized oil jet becomes necessary to provide adequate lubrication and cooling and to prevent scoring of the gear-tooth surfaces. Scoring is a result of having a too thin elastohydrodynamic (EHD) oil film. This thin EHD film is usually caused by inadequate cooling rather than insufficient lubricant.

Of the three primary modes of gear tooth failure, scoring is the most common and the most difficult to analyze. A considerable amount of work has been done over the past four decades to produce quantitative analysis procedures to evaluate the risk of scoring in lubricated gear drives [1,2]. For the first 30 years of this time period, most of the concentrated effort had to do with developing a procedure to evaluate the incipient onset of the scoring phenomenon. It has only been in the last decade or so that a concentrated effort has been provided to evaluate the contribution of the gear tooth bulk temperature on the scoring phenomenon and to determine its contribution in bringing about the onset of this mode failure of [3,4].

A computer program was developed using a finite element analysis to predict gear tooth temperatures [5,6]. However, this program did not include the effects of oil-jet cooling and oil-jet impingement depth. It used an average surface heat-transfer coefficient for surface temperature calculation based on the best information available at that time.

In order to have a better method for predicting gear-tooth temperature, it is necessary to have an analysis that allows for the use of a heat-transfer coefficient for oil-jet cooling coupled with a coefficient for air/oil mist cooling for that part of the time that each condition exists. Once the analysis can make use of these different coefficients, it can be combined with a method that determines the oil-jet impingement depth to give a more complete gear temperature analysis program. However, both the oil-jet and air/oil mist heat-transfer coefficients are unknowns and must be determined experimentally.

The objectives of the work reported herein were to (a) further develop the gear temperature analysis computer program [5,6] incorporating different heat-transfer coefficients for air/oil and oil-jet cooling, (b) combine that program with a program developed to determine the impingement depths, and (c) experimentally measure gear-tooth temperatures to compare them with those predicted using the improved analysis.

APPARATUS AND PROCEDURE

Gear Test Apparatus

Gear-tooth temperature measurements were made using the NASA gear test shown in Fig. 1 and described in [7]. This test rig uses the four square principle of applying the test gear load so that the input drive needs only to overcome the frictional losses in the system.

The gear surface temperatures were measured with a fast-response infrared radiometric (IR) microscope that uses a liquid-nitrogen-cooled detector. The IR microscope can measure transient temperatures up to 20 000 Hz. All radiance measurements were made with a 1X lens that has a focal length of approximately 23 cm (9 in.) and a viewing spot size of 0.05 cm (0.020 in.) diameter. The test gear cover, viewing port, and lubrication jet as shown in Fig. 2 were used with the IR microscope.

Test Gears

The test gears were 8 DP, 28 teeth, 8.89-cm (3.5-in.) pitch diameter with a 0.635-cm (0.250-in.) face width. All gears had a nominal surface finish on the tooth flank of 0.406 μ m (16 μ in.), rms, and a standard 20° involute profile without tip relief. The test gears were manufactured from consumable electrode vacuum melted (CEVM) AISI 9310 steel. The gears were case carburized and hardened to a Rockwell C hardness of 60 before final grinding of the finished gear.

Test Lubricant

The test gears were lubricated with a single batch of synthetic paraffinic oil. The physical properties of the oil are summarized in Table I. Five percent of an extreme pressure additive, designated Lubrizol 5002 was added to the lubricant.

Test Procedure

After the test gears were cleaned to remove the preservative, they were assembled on the test rig. The test gears were run in a full face load condition on the 0.635-cm (0.250-in.) face width. The tests were run at four speeds, 2500, 5000, 7500, and 10 000 rpm; three tangential loads, 1895, 3736, and 5903 N/cm (1083, 2135, and 3373 lb/in.); five oil-jet pressures 96×10^4 , 69×10^4 , 41×10^4 , 27×10^4 , and 14×10^4 Pa (140, 100, 60, 40 and 20 psi); and two oil-jet diameters, 0.04 and 0.08 cm (0.016 and 0.032

in.). Inlet oil temperature was constant at 308 K (95° F). At each speed the lowest load was first applied with the maximum oil-jet pressure. At this load the oil-jet pressure was reduced in steps to the lowest pressure before the next load was applied. The oil jet was pointing in a radial direction and hitting the unloaded side of the gear tooth as it came out of the mesh zone. The 0.08-cm (0.032-in.) diameter jet is the size typically used in many applications for the maximum power conditions used herein. The 0.04-cm (0.016-in.) diameter jet was used to determine what cooling conditions could be obtained with considerably less oil flow and good oil-jet impingement depth. The temperature was measured by the IR scope at a location approximately 160° away from the mesh zone.

The IR scope operates in two modes. In the DC mode the average surface temperature of the gear tooth was read out on the meter supplied with the IR scope. The scope was calibrated before running the tests to determine the emissivity of the gear-tooth surface.

In the AC mode a voltage that varies with surface radiance according to the equation

$$\Delta V = \kappa \epsilon \Delta N \quad (1)$$

was measured from two signals on a dual trace cathode-ray oscilloscope (CRO). The upper signal in Fig. 4 was from the IR scope directly; the lower signal was filtered through a variable-band-pass filter to remove the 20-mV high-frequency noise. At the lower loads and at the high oil-jet pressure, the signal-to-noise ratio was approximately one. In the ac mode, only temperature variations on the surface are measured.

A 1X lens which had a focal length of 23 cm (9 in.) was used with the IR microscope and looked at a 0.05 cm (0.02 in.) diameter spot. The gear tooth surface was viewed by the IR scope as it passed in front of the lens. The tip of the tooth is seen first, the view then goes down the tooth surface until it is interrupted by the next tooth.

GEAR TEMPERATURE ANALYSIS

A gear-tooth temperature analysis was developed in [5,6] to calculate the gear-tooth temperature profile using a finite-element analysis. This analysis uses a finite-element mesh and calculates isotherms on the gear tooth. However, the following conditions are required to be determined or calculated before the program can calculate effective temperatures: (a) the frictional heat input at the gear-tooth working surface, (b) the different heat-transfer coefficients for the various gear-tooth surfaces and cooling methods, and (c) the oil-jet penetration onto the gear-tooth flank.

The frictional heat input to the gear-tooth working surface can be calculated using the following analysis: The instantaneous heat generated per unit area per unit time due to the sliding of the two gear teeth is given by

$$q = \frac{fW|V_s|}{bJ} = \frac{fW|\omega_1\rho_1 - \omega_2\rho_2|}{bJ} \quad (2)$$

where

$$W = W_t/F_e \cos \phi$$

Since W , V_s , and f are functions of the mesh-point location, the q will vary through the meshing cycle. The f varied from approximately 0.02 to 0.07 for the cases evaluated. The heat generated will be divided between the gear and pinion and may not be equally withdrawn by each, so that a partitioning function Λ is used. The heat withdrawn by the gear and pinion will then be

$$q_1 = \Lambda q \quad q_2 = (1 - \Lambda)q \quad (3)$$

For the test gears used in this paper Λ is assumed to be 0.5, so that

$$q_1 = q_2 \quad (4)$$

once the instantaneous heat flux to the gear surface is determined. The total time average heat flow per revolution can be calculated by the following equation from [6]

$$q_1 = \frac{b\omega_1\Lambda}{V_1^2\pi} = \frac{b\omega_2(1 - \Lambda)q}{V_2^2\pi} \quad (5)$$

where V_1 and V_2 are the gear and pinion rolling velocities. Substituting Eq. (2) into Eq. (5) gives

$$q_1 = q_2 = \frac{\Lambda f W \omega_1^2}{V_1 2\pi J} \left| \rho_1 - \frac{\omega_2}{\omega_1} \rho_2 \right| \quad (6)$$

substituting

$$\Lambda = 0.5, \quad \eta_1 = \frac{\omega_1}{2\pi}, \quad \frac{\omega_2}{\omega_1} = \frac{N_1}{N_2}, \quad \text{and} \quad V_1 = \omega_1 \rho_1$$

gives

$$q_1 = q_2 = \frac{f W \eta_1}{2J} \left| 1 - \frac{N_1}{N_2} \frac{\rho_2}{\rho_1} \right| \quad (7)$$

for the time-average heat flux. Using this expression, the instantaneous heat flux may be calculated at any position along the line of action by substituting the instantaneous profile radius, giving the heat input to the gear tooth surface at that location. Substituting $L_A - \rho_1$ for ρ_2 , where $L_A = \rho_1 + \rho_2$, and using instantaneous notation, Eq. (7) becomes

$$q_{i1} = \frac{f_i W \eta_1}{2J} \left| 1 - \frac{N_1}{N_2} \left(\frac{L_A - \rho_{i1}}{\rho_{i1}} \right) \right| \quad (8)$$

The heat-transfer coefficients (Fig. 3) for the sides, top land, and flanks of the gear teeth are different because of the different cooling regions. Also, the coefficient for the two flanks will be different, depending on whether they are cooled by the oil-jet hitting the surface or by air (no jet cooling). The heat-transfer coefficient for the sides of the gear teeth h_s can be estimated by the method of [9] for a rotating disk by

$$h_s = Nu \kappa \sqrt{\frac{\omega}{v}} \quad (9)$$

for air $Nu = 0.5$. However, the amount of oil mist present will have a considerable effect on this coefficient. The gear-tooth flanks not cooled by the oil jet will have a heat-transfer coefficient h_t for air or air/oil mist. Since there are no data available to determine this coefficient, an estimate somewhere between an air-cooled disk and jet cooling will be used until something better is developed experimentally.

The heat-transfer coefficient h_j for the jet-cooled tooth face and the tooth tip may be calculated [4,8] using the following

$$h_j = \left(\frac{2L_t}{m} \right)^{1/4} \left(\frac{v_o}{aN} \right)^{1/4} \frac{b_w^{1/2}}{2\pi} q_{tot} \quad (10)$$

where q_{tot} is a dimensionless factor [4,8]. Curve fitting the data [8] gives

$$q_{tot} = 0.98 - 0.32 \gamma + 0.06 \gamma^2 - 0.004 \gamma^3 \quad (11)$$

where

$$\gamma = \beta \theta_s \quad (12)$$

Using the above method for calculating the oil-jet heat-transfer coefficient gives temperatures that are much too high. For the results presented in this paper, an oil-jet heat-transfer coefficient was assumed that would give more realistic results. For future work a more realistic oil-jet heat-transfer coefficient will be determined based on experimental results reported in this paper and from future testing.

The oil-jet penetration onto the gear-tooth flank can be determined by the method of [10,11]. A more accurate analysis is being developed by the authors using a new kinematic radial model instead of the vectorial model used in [10]. The new model gives the oil-jet impingement depth for radially directed jet as

$$\delta_i = \frac{v_j \theta_w (N + 2) \cos \alpha}{4} \quad (13)$$

Using the above equation with a known jet velocity, the angle of rotation is assumed and must be iterated until the angle of rotation and impingement point coincide, since θ_w is a function of δ_j and α . A more usual case is when a specified design depth δ_j and θ_w are given, then Eq. (13) is rearranged as

$$V_j = \frac{4\delta_j}{\theta_w(N+2)\cos\alpha} \quad (14)$$

Once the heat generation and the oil-jet impingement depth have been calculated, the heat-transfer coefficients are either calculated or estimated. Then, the finite-element analysis is used to calculate the temperature profile of the gear teeth. The finite-element model has 108 nodes with triangle elements. The computer program calculates a steady-state temperature at all 108 nodes and prints these temperatures. The program also plots temperature isobars on the gear tooth profile and lists the temperatures of the isobars.

RESULTS AND DISCUSSION

Experimental Results

Transient and average gear-tooth surface temperatures were measured using a fast-response infrared (IR) radiometric microscope. The gear-tooth temperatures were measured at four speeds, three loads, five oil-jet pressures, and two oil-jet diameters. The test gears were 3.2 module (8 pitch), 8.89-cm (3.5-in.) pitch diameter with a 0.64-cm (0.25-in.) face width.

Figure 4(a) is a typical transient measurement of a gear tooth surface at 7500 rpm, 5903-N/cm (33.3-lb/in) tangential load, and 14×10^4 -Pa (20-psi) oil-jet pressure with a 0.041-cm (0.016-in.) diameter orifice. The change in surface temperature from the gear tooth tip to a point just below the pitch line was 32 K (58 F°). The pitch line where pure rolling occurs can be seen by the slight dip in temperature. The highest temperature is below the pitch line where the combination of high load with some sliding occurs.

Figure 4(b) is for the same load, speed, and oil-jet size condition but with an oil-jet pressure of 97×10^4 Pa (140 psi), which reduces the maximum temperature difference to 12 K (22 F°), with the peak temperature still occurring below the pitch line. The average surface temperature for these conditions was 423 and 391 K (302° and 244° F) for the 14×10^4 and 97×10^4 Pa (20 and 140 psi) oil pressure, respectively. Figure 5 is typical of what happens when scoring occurs. Here, the peak temperature is at the tip of the gear tooth and has reached a maximum temperature of 508 K (455° F) or 75 K (135 F°) above the average surface temperature of 433 K (320° F). Scoring temperatures as high as 603 K (626° F) were measured during the high-load, high-speed tests with reduced oil-jet pressure or orifice size. These temperatures would be somewhat lower than those at the contact point since they were measured 160° away from the contact and after oil-jet cooling. The scoring conditions occurred only at the 10 000-rpm test condition with intermediate loads and full or less oil-jet impingement depths.

Figure 6(a) is a plot of gear-tooth average surface temperature (solid line) with the high and low temperatures included (dashed lines) versus oil-jet pressure for three speeds, an oil-jet diameter of 0.04 cm (0.016 in.), and a load of 5903 N/cm (3373 lb/in.).

The high load and high speed with the small jet size could not be run except at the highest pressure because of scoring. From these plots the effect of different speed at constant load and the effect of oil-jet pressure on both average surface temperature and temperature variations can be seen. The increased speed causes a higher surface temperature and higher temperature variations. The oil-jet pressure also has a greater effect at the higher speed. The maximum oil pressure needed for a speed is also seen by the leveling of the curve at the lower speeds where increased oil pressure causes very little improvement in cooling.

Figure 6(b) is the same type of plot as Fig. 6(a) except the load is 3736 N/cm (2135 lb/in). The curves for 5000 and 2500 rpm are nearly identical. The effect of oil-jet pressure is considerably reduced because of the lower load. Here, the maximum change in average surface temperature is 35 K, and the maximum surface temperature difference is 45 K at the 13.8×10^4 Pa (20 psi) oil-jet pressure.

Figure 6(c) is a plot of gear-tooth average surface temperature versus oil-jet pressure with different loads at a speed of 7500 rpm. This figure shows the effect of load and oil-jet pressure on gear-tooth temperature at constant speed.

Figure 7 is a plot of load versus gear-tooth average surface temperature for the 7500 rpm condition and three oil-jet pressures. The effect of load and oil-jet pressure on gear-tooth surface temperature is clearly seen. Increasing the pressure from 14×10^4 to 97×10^4 Pa (20 to 140 psi) has about the same effect as reducing the load from 6000 to 2000 N/cm.

Figures 8(a) and (b) are plots of average surface temperatures with temperature variations and bulk gear temperature, respectively, versus oil jet pressure for three loads at 10 000 rpm and an oil jet size of 0.08 cm (0.032 in.). With the larger oil jet size the temperatures are reduced considerably from those for the smaller jet size. The bulk temperature of the gear does not increase as much as the average surface temperature. At the lower load and high jet pressure the surface and bulk temperatures are nearly identical.

Analytical Results

Calculations were made using the computer program to examine the effects of calculated heat inputs from the experimental test cases and estimated heat-transfer coefficients. The gear tooth differential temperature profiles are shown in Figs. 9 and 10. The differential profiles in these figures are the temperatures difference between the inlet cooling oil at 308 K (95° F) and the actual gear tooth temperatures.

The experimental tests were conducted with oil jet cooling on the unloaded side of the gear tooth. This was done to allow measurement of the surface temperature of the loaded side of the tooth by having the oil splash going away from the infrared observation window. Any oil splash on the window alters the gear surface temperature measurements.

The analytical program can allow for cooling on either side of the tooth. In many applications the oil jet cools the loaded side of one gear and the unloaded side of the mating gear. Figures 9(a) and (b) are the analytical results for gears with oil jet cooling on the unloaded side of the gear tooth. Both cases, Figs. 9(a) and (b) were for a speed of 10 000 rpm a load of 5903 N/cm (3373 lb/in.) and shows (□) the high and low experimentally measured temperatures near where they were measured. Figure 9(a) is for 33.5 percent oil jet impingement depth and shows a calculated differential temperatures at the high and low point of the working surface of 127 K (229° F) and 92 K (166° F) respectively. The corresponding measured temperatures were 123 K (221° F) and 96 K (173° F) which show very good agreement with the analytical results. Figure 9(b) is for an oil jet impingement depth of 75 percent of the tooth depth. The temperatures here are considerably reduced from the 33.5 percent impingement depth and shows the advantage of increased oil jet pressure. The computed differential temperatures at the high and low point on the working surface were 70 K (126° F) and 48 K (86° F) respectively. The corresponding measured temperatures were 63 K (113° F) and 49 K (88° F) which also show very good agreement with the analytical results.

Figures 10(a) and (b) are the analytical results for a gear speed of 10 000 rpm a load of 5903 N/cm (3373 lb/in) with the oil jet cooling on the loaded side of the gear teeth. Comparing this case to Figs. 9(a) and (b) it can be seen that the overall temperature of the gear teeth has been reduced only 2 or 3 K while the minimum and maximum surface temperature have been reduced by 10 K \pm 4 K indicating that the loaded side cooling is better, especially for surface maximum temperatures. However the unloaded side cooling is still very effective in removing the heat from the gear tooth when good penetration depth is obtained.

Table II shows the differential temperatures that were calculated and measured for the different impingement depths and different cooling sides of the gear teeth.

With the analytical results using backside cooling and the experimentally adjusted film coefficients, the calculated and experimental results are in very close agreement. With loaded side cooling the analytical results predict lower maximum surface temperatures than those obtained with unloaded side cooling.

SUMMARY OF RESULTS

A gear-tooth temperature analysis was performed using a finite-element method combined with a calculated heat input, a calculated oil-jet impingement depth, and estimated heat-transfer coefficients for the different parts of the gear tooth that are oil cooled and air cooled. Experimental measurements of gear-tooth average surface temperature and gear-tooth instantaneous surface temperature were made with a fast-response, infrared, radiometric microscope. The following results were obtained.

1. Increasing oil pressure has a significant effect on both average surface temperature and peak surface temperature at loads above 1895 N/cm (1083 lb/in) and speeds of 10 000 and 7500 rpm.
2. Both increasing speed (from 5000 to 10 000 rpm) at constant load and increasing load at constant speed cause a significant rise in the average temperature and in the instantaneous peak surface temperatures on the gear teeth.
3. The oil-jet pressure required to provide the best cooling for gears is the pressure required to obtain full gear-tooth impingement.
4. Calculated results for gear tooth temperatures were close to experimental results for various oil-jet impingement depths for identical operating conditions.

REFERENCES

1. Blok, H., "Lubrication as a Gear Design Factor," The Institution of Mechanical Engineers, Proceedings of the International Conference on Gearing, London, Sept. 23rd-25th, 1958.
2. Kelley, B. W. and Lemanski, A. J., "Lubrication of Involute Gearing," Institution of Mechanical Engineers, Proceedings (Fundamentals and Application to Design), Vol. 182, Pt. 3A, 1967-1968, pp. 173-184.
3. Akin, L. S., "An Interdisciplinary Lubrication Theory for Gears (With Particular Emphasis on the Scuffing Model of Failure)," ASME Journal of Engineering for Industry, Vol. 95, No. 4, Nov. 1973, pp. 1178-1195.
4. DeWinter, A. and Blok, H., "Fling-Off Cooling of Gear Teeth," ASME Journal of Engineering for Industry, Vol. 96, No. 1, Feb. 1974, pp. 60-70.
5. Wang, K. L. and Cheng, H. S., "A Numerical Solution to the Dynamic Load, Film Thickness, and Surface Temperatures in Spur Gears, Part II - Results," ASME International Power Transmission and Gear Conference, Chicago, Illinois, Sept. 28-30, 1977.
6. Patir, N. and Cheng, H. S., "Prediction of Bulk Temperature in Spur Gears Based on Finite Element Temperature Analysis," ASLE Preprint No. 77-LC-3B-2, Oct. 1977.
7. Townsend, D. P., Bamberger, E. N., and Zaretsky, E. V., "A Life Study of Aus-forged, Standard Forged, and Standard Machined AISI M-50 Spur Gears," ASME Journal of Lubrication Technology, Vol. 98, No. 3, July 1976, pp. 418-425.
8. Van Heijningen, G. J. J. and Blok, H., "Continuous as Against Intermittent Fling-Off Cooling of Gear Teeth," ASME Journal of Lubrication Technology, Vol. 96, No. 4, Oct. 1974, pp. 529-538.
9. Patir, N., "Estimate of the Bulk Temperature in Spur Gears Based on Finite Element Temperature Analysis," M.S. Thesis, Northwestern University 1976.
10. Akin, L. S., Mross, J. J., and Townsend, D. P., "Study of Lubricant Jet Flow Phenomena in Spur Gears," ASME Journal of Lubrication Technology, Vol. 97, No. 2, April 1975, pp. 283-288.
11. Townsend, D. P. and Akin, L. S., "Study of Lubricant Jet Flow Phenomena in Spur Gears -- Out of Mesh Condition," ASME Journal of Mechanical Design, Vol. 100, No. 1, Jan. 1978, pp. 61-68.

TABLE I. - LUBRICANT PROPERTIES

Property	Synthetic paraffinic oil plus additives ^a
Kinematic viscosity, cm ² /sec (cs) at:	
244 K (-20° F)	2500x10 ⁻² (2500)
311 K (100° F)	31.6x10 ⁻² (31.6)
372 K (210° F)	5.7x10 ⁻² (5.7)
477 K (400° F)	2.0x10 ⁻² (2.0)
Flash point, K (°F)	508 (455)
Fire point, K (°F)	533 (500)
Pour point, K (°F)	219 (-65)
Specific gravity	0.8285
Vapor pressure at 311 K (100° F), mm Hg (or torr)	0.1
Specific heat at 311 K (100° F), J/(kg)(K)(Btu/(lb)(°F)	676 (0.523)

^aAdditive, Lubrizol 5002 (5 percent volume): phosphorous 0.03 percent volume; sulfur, 0.93 percent volume.

TABLE II. - EXPERIMENTAL VERIFICATION

Depth δ	Cooled on loaded side		Cooled on backside	
	Hot spot	Cool spot	Hot spot calc/exper.	Cool spot calc/exper.
0.3346	121 K	Front 71 K Back 61 K	127 K / 123 K	Front 90 K / 95 K Back 58 K
0.7528	58 K	Front 34 K Back 21 K	70 K / 63 K	Front 42 K / 49 K Back 22 K

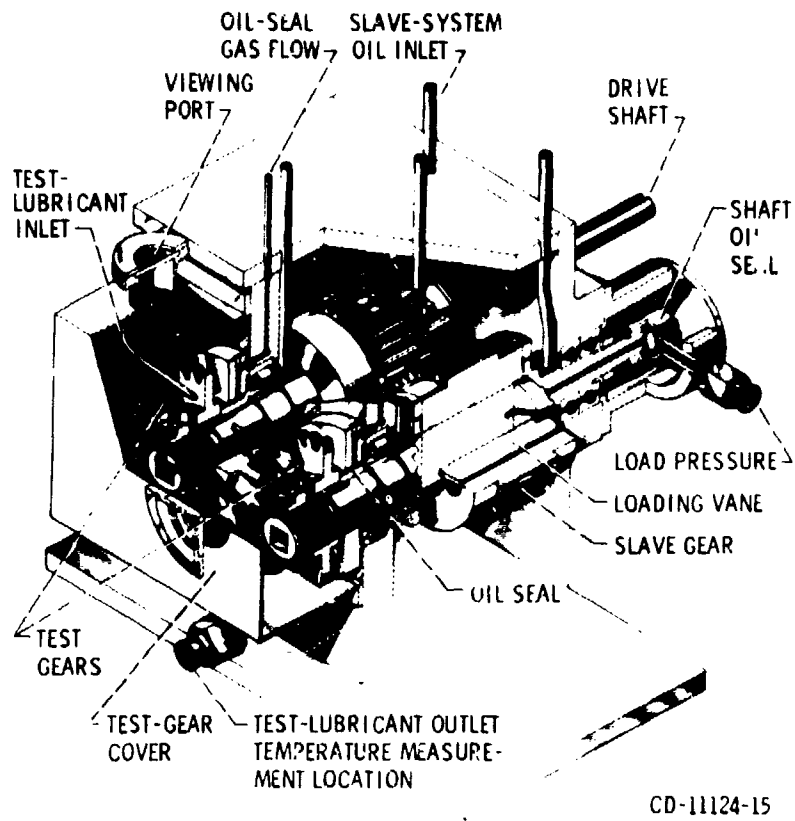


Figure 1. - NASA Lewis Research Center's gear fatigue test apparatus.

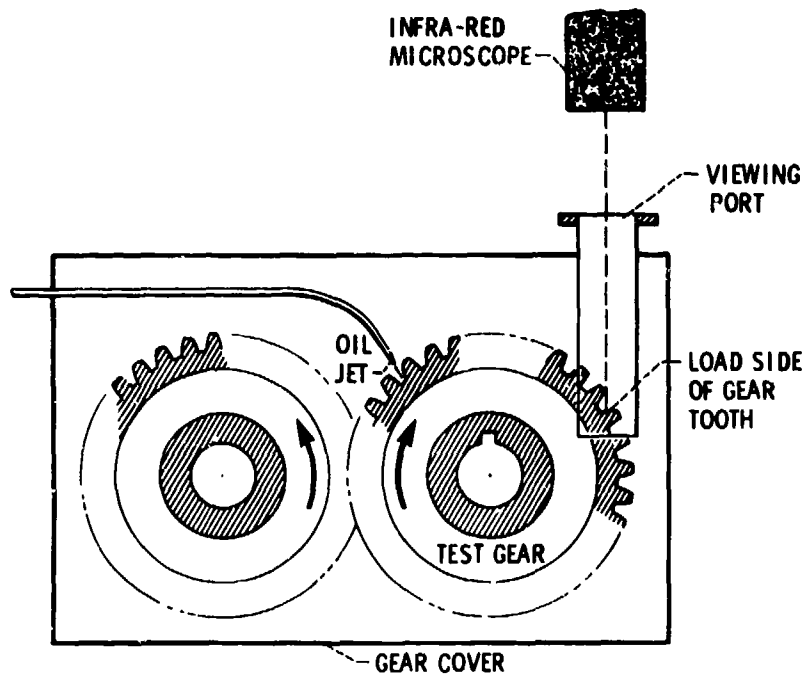
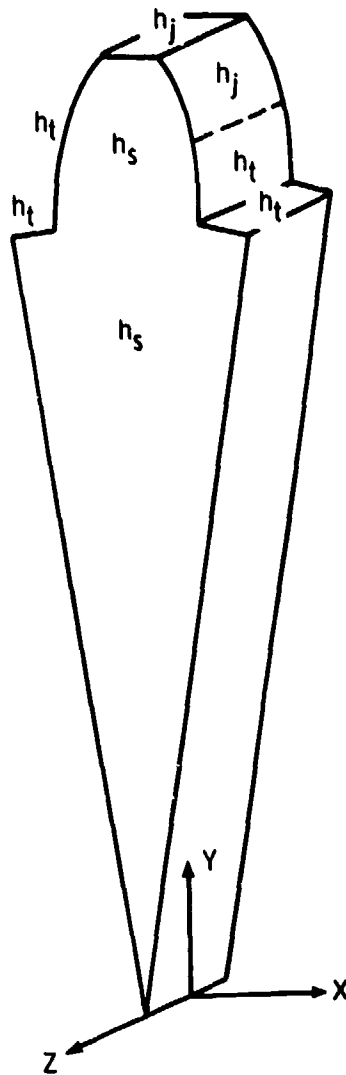


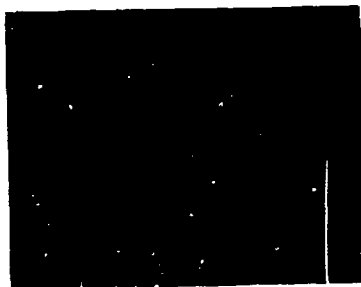
Figure 2. - Test setup for measuring dynamic gear tooth surface temperature.



h_s, h_j, h_t = DEFINITION OF
HEAT TRANSFER ZONES

Figure 3. - Geometry of problem.

7500 rpm; 3373 lb/in.



$14 \times 10^4 \text{ N/m}^2$ (20 psi), 0.05 V/DIV



$69 \times 10^4 \text{ N/m}^2$ (100 psi), 0.02 V/DIV

CS-80-3147

Figure 4. - I.R. microscope measurements of gear tooth surface temperature, speed; 7500 rpm load 5903 N/cm (3373 lb/in.) inlet oil temperature 308 K (95° F) oil jet diameter 0.04 cm (0.016 in.).

10 000 rpm; LOAD 3373 lb/in.



CS-80-3148

Figure 5. - I. R. microscope measurements of gear teeth scoring temperature 0.5 V/div speed 10 000 rpm load 5903 N/cm (3373 lb/in.) inlet oil temperature 308 °K (95° F) oil jet diameter 0.04 cm (0.016 in.).

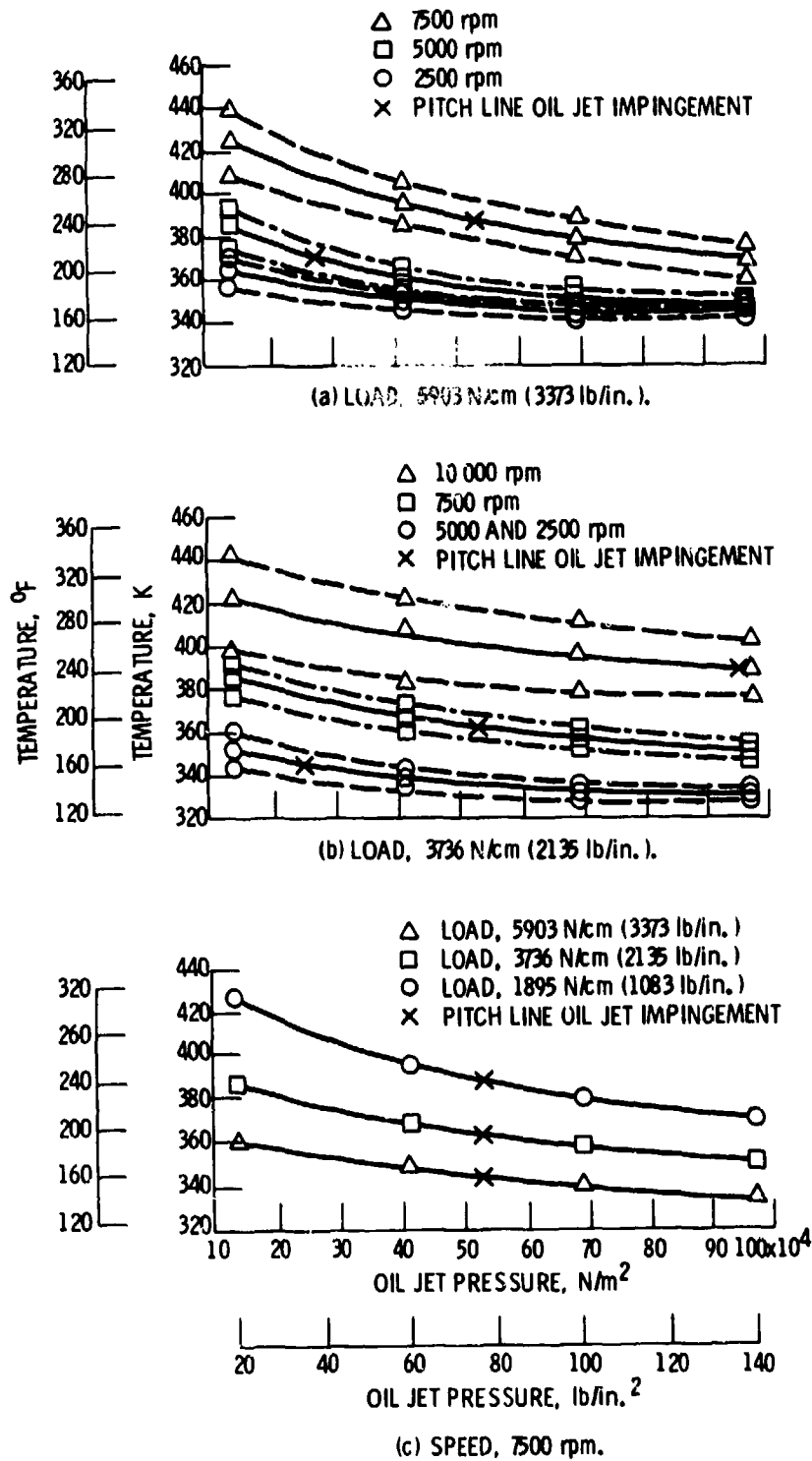


Figure 6. - I.R. microscope measurements of gear surface temperature versus oil jet pressure, inlet oil temperature 308 K (95° F), oil jet diameter 0.04 cm (0.016 in.).

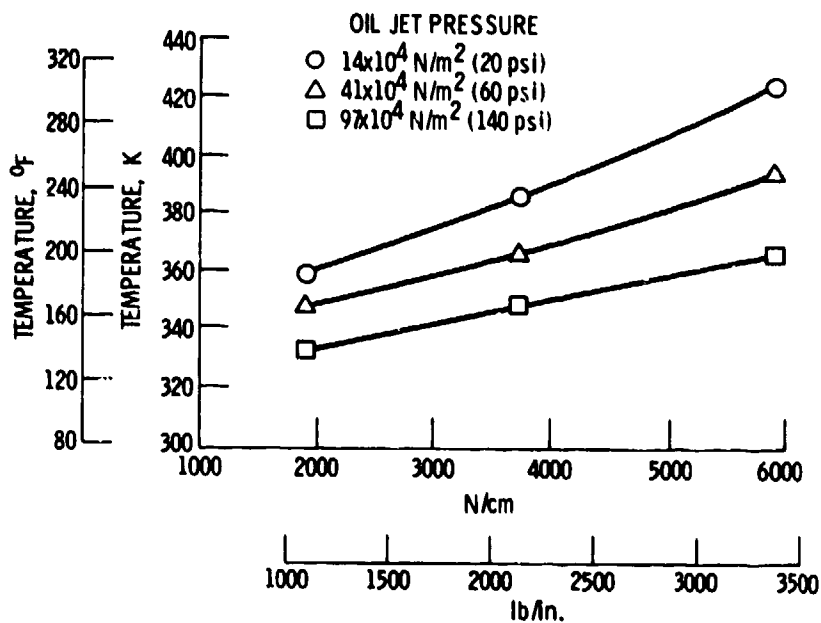


Figure 7. - I. R. microscope measurement of gear average surface temperature versus load for three oil jet pressures, speed 7500 rpm, oil jet diameter 0.04 cm (0.016 in.) inlet oil temperature 308 K (95° F).

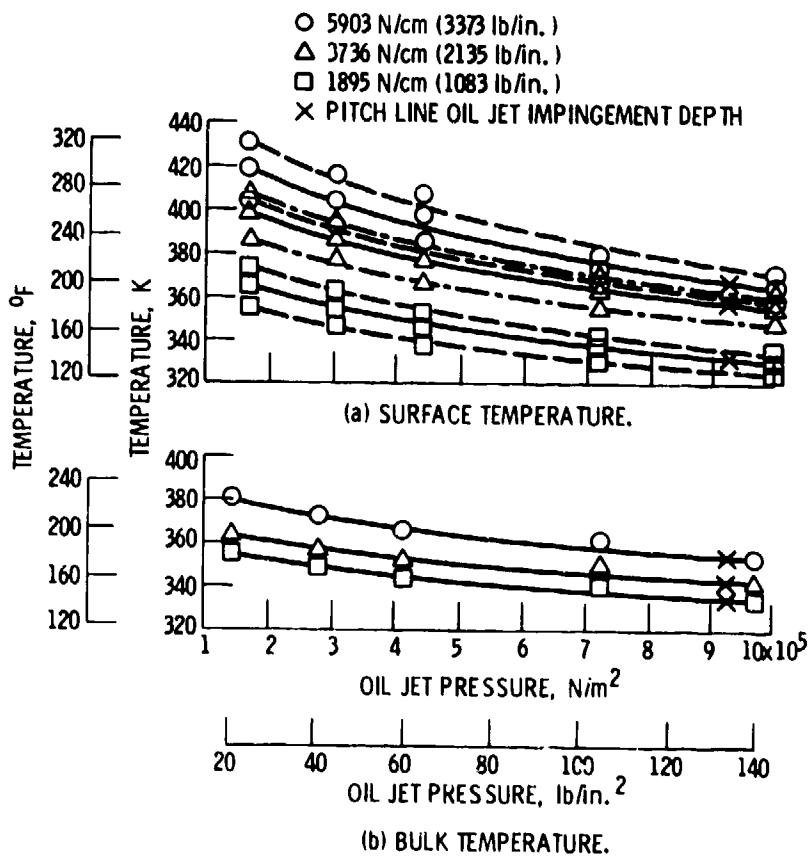
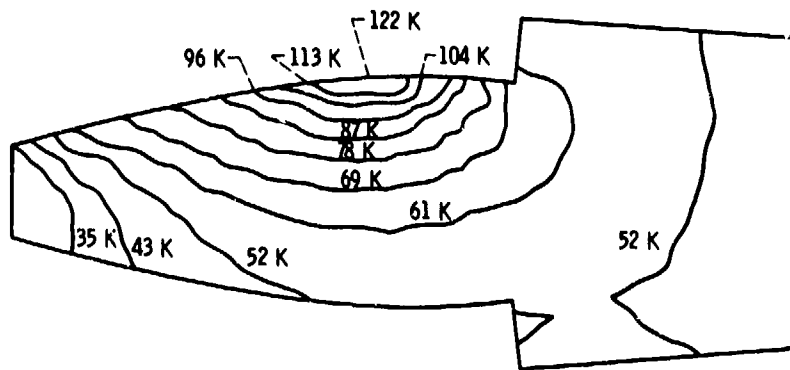
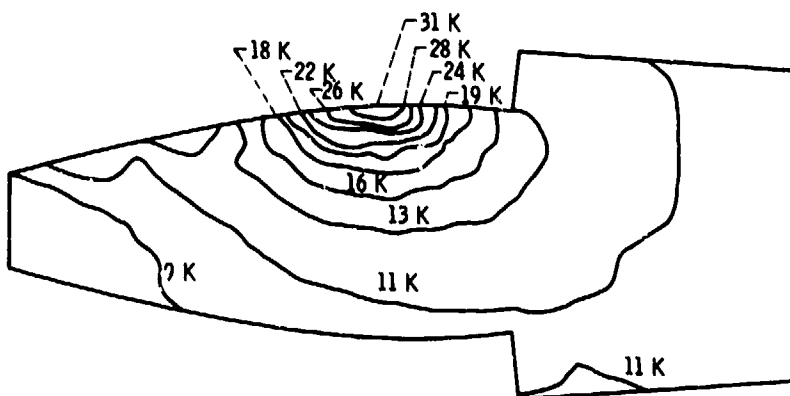


Figure 8. - I. R. microscope and thermocouple measurement of gear temperature versus oil jet pressure for three loads, speed 10 000 rpm, oil jet diameter 0.08 cm (0.032 in.). Inlet oil 308 K (95° F).

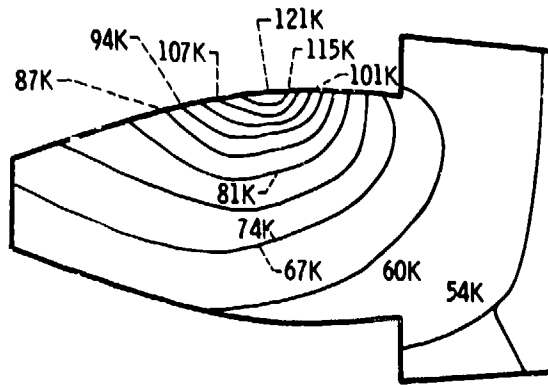


(a) ZERO IMPINGEMENT DEPTH.

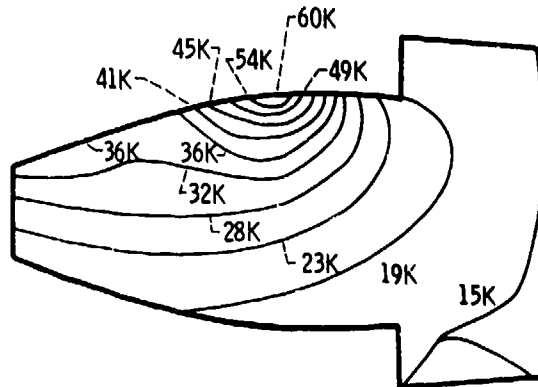


(b) 87.5 percent IMPINGEMENT DEPTH.

Figure 9. - Calculated gear tooth temperatures speed 10 000 rpm, load 5903 N/cm (3373 lb/in.).



(a) 33.5 PERCENT IMPINGEMENT DEPTH.



(b) 75.3 PERCENT IMPINGEMENT DEPTH.

Figure 10. - Calculated gear tooth temperature - cooled on loaded side (speed 10 000 RPM, load 5903 N/cm (3373 lb/in)).

DISCUSSION

D.G.Astridge, Westland Helicopters, Yeovil, UK

The beneficial influence of oil pressure is attractive, but care is required in reducing jet size to achieve this at constant flow. With high standard of build cleanliness plus fine filtration there should be no problem, but with typical filtration levels and build standards currently used, blockage of jets less than 1 mm diameter can be expected. Another possibility is the use of fine thread filters, well deburred, immediately upstream of the jets.

Author's Reply

For high speed and high loads the standard method of lubrication using low oil pressure and large jet orifice diameters needs to be re-evaluated. With increased oil pressure to get full depth impingement depth the oil jet diameter will generally have to be less than 1 mm. While a filter at the oil jet might be satisfactory it would be better to use a system filter that can be changed or cleaned at certain intervals. There are some gear and bearing users who are using oil pressures as high as 500 psi with oil jet diameters less than .025 cm (.010 in) with good results.

F.Snyder, University of Waterloo, Ca

One of your reasons for choosing two jet diameters was to examine the effect of "jet impingement depth" on the final tooth surface temperature. This variable is not explicitly isolated from the different jet flow rates as shown in Figures 6 to 8. Could you elaborate on this . . .

Author's Reply

The reason for choosing two oil jet diameters was to determine the effect of oil flow on the gear tooth temperatures. The oil jet diameter has no effect on penetration depth. The oil jet diameters and their different oil flow rates are accounted for by changing the heat transfer coefficient h_j in the computer program. Since this is an experimentally determined coefficient a test series would be needed to cover different oil jet sizes. The analytical coefficient proposed in Ref. (4, 8) by Blok does not have a variable for oil jet size. The analytical coefficient does not give results that match the test data.

J.B.Medley, University of Waterloo, Ca

- (1) Why didn't you locate the temperature measuring device (infra-red microscope) closer to the contact?
- (2) How did you determine the friction coefficient?

Author's Reply

- (1) It was necessary to keep the oil spray away from the area and window to prevent an error in I R temperature measurements. The best location was, therefore, the position where the gear teeth were moving away from the viewing window and was accessible to the placement of the I R microscope which had to be mounted in the vertical direction because of the liquid nitrogen dewar.
- (2) The question was also asked about the analytical method used to determine the influence of jet size on the cooling or temperature. *Answer.* The present analysis does not account for differences in oil flow except to change the h_j for different oil flows.
- (3) The friction coefficient was calculated by the method of Benedict and Kelley, Reference 12.

Reference 12: Benedict, G.H. and Kelley, B.W: Instantaneous Coefficients of Gear Tooth Friction. ASLE Trans, Vol.4, No.1, April 1961, pp.59-70.

AN ADVANCED METHOD FOR PREDICTING
HYBRID BEARING PERFORMANCE

by

R. Colsher
I. Anwar
S. Katsumata

Franklin Research Center
20th and Cherry Streets
Philadelphia, PA 19103

ABSTRACT

An advanced computerized technique has been developed to predict performance for hydrodynamic, hydrostatic and hybrid bearings operating with an incompressible lubricant.

The numerical technique utilizes the finite difference cell approach coupled with Gaussian elimination to solve the lubrication equation (Reynolds equation). The recess pressures, although unknown, are treated as boundary conditions and the lubrication equation is then solved in terms of the recess pressures. The recess pressure is then determined by coupling the recess flow conditions with the external lubrication supply system.

The numerical technique is very economical because the lubrication equations are only solved once. Also, the equations for the boundary pressures including the recess pressures are eliminated thus reducing the size of the matrix that must be solved.

An analysis performed on a ball mill is described.

NOMENCLATURE

c	= Radial clearance, m	P_{ref}	= Reference pressure, Pa
c_d	= Orifice discharge coefficient	P_S	= Supply pressure, Pa
d_c	= Capillary diameter, m	Q_r	= Recess flow, m^3/s
d_0	= Orifice diameter, m	Q_f	= Flow rate of restrictor, m^3/s
e	= Eccentricity, m	Q_S	= Supply flow, m^3/s
f_x	= Force in x-direction, N	r	= Shaft radius, m
F_x	= Non-dimensional force = $\frac{f_x}{P_{ref} L^2}$	R	= Non-dimensional radius = r/L
f_y	= Force in y-direction, N	S_K	= Restrictor constant
F_y	= Non-dimensional force = $\frac{f_y}{P_{ref} L^2}$	t	= Time, s
f_K	= Restrictor coefficient	T	= Non-dimensional time = $t \frac{\omega r}{2\Delta L}$
h	= Local film thickness, m	V	= Volume, m^3
H	= Non-dimensional clearance = h/c	\vec{V}	= Velocity vector, m/s
l	= Capillary length, m	V_θ	= Velocity component in θ -direction, m/s
L	= Bearing length, m	V_z	= Velocity component in z-direction, m/s
M	= Number of grid points in axial direction	x	= Horizontal direction, m
M_x	= Moment in x-direction, N-m	y	= Vertical direction, m
\bar{M}_x	= Non-dimensional moment = $\frac{M_x}{L^3 P_{ref}}$	Δz	= Length increment in axial direction, m
M_y	= Moment in y-direction, N-m	$\bar{\Delta z}$	= Cell length in axial direction, m
\bar{M}_y	= Non-dimensional moment in y-direction = $\frac{M_y}{L^3 P_{ref}}$	z	= Axial direction, m
N	= Number of grid points in circumferential direction	Z	= Nondimensional axial direction = z/L
p	= Local pressure, Pa	$\bar{\Delta \theta}$	= Cell width in circumferential direction, radians
P	= Non-dimensional pressure p/p_{ref}	θ	= Angular direction, radians
P_r	= Recess pressure, Pa	ϵ	= Eccentricity ratio = e/c
		Λ	= Speed parameter = $\frac{6\mu\omega r L}{c^2 P_{ref}}$
		μ	= Absolute viscosity = $N\cdot s/m^2$
		ρ	= Fluid density, kg/m^3
		ω	= Shaft speed, rad/s

1. INTRODUCTION

Hybrid bearing systems are finding wide acceptance in a variety of applications. These include the support of massive moving antenna structures, frictionless space-vehicle simulators, tumbling (ball) mills and for many types of machine tools and measuring equipment. Typically, the hydrostatic part of the system consists of multiple bearings positioned at supporting areas whose locations are governed by geometric and loading conditions.

The determination of performance parameters for multiple bearing arrangements can be a formidable task. It requires solution of a set of simultaneous equations equal to the number of separate bearing pads; further complication is introduced by the fact the equations are not always linear. If a number of bearing configurations, supply circuits, type of compensation, and loading conditions are to be investigated, hand computations become impractical and digital computer techniques are necessary [1-2].

The present paper describes an advanced computerized technique that has been developed to predict performance of hydrodynamic, hydrostatic and hybrid bearings. To demonstrate the developed technique, a study performed on a ball mill is described.

2. THEORETICAL FORMULATION

2.1 HYDRODYNAMIC

The bearing area is divided into a grid network that may have variable spacing between grid points. Figure 1 shows a typical section of the grid necessary to compute the pressure at the grid point L. The grid is laid out so that the circumferential intervals are distances between columns ($j = 1 \rightarrow N$) and the axial intervals are distances between rows ($i = 1 \rightarrow M$). The points are labeled sequentially by progressing down a column. The upper left hand corner grid point ($i = 1, j = 1$) is the first grid point while the lower right hand grid point ($i = M, j = N$) is the last grid point.

An imaginary cell surrounds the grid point and the distance to each leg of the cell perimeter from the grid point L is half the distance between the Lth grid point and its corresponding neighbor. The circumferential length of the cell is $r\Delta\theta$ and the axial length is Δz (see Figure 1 and 2).

The integral form of the continuity equation for the typical cell shown in Figure 1 is:

$$\frac{\partial}{\partial t} \int_V \rho dV + \int_S \rho \bar{v} \cdot \bar{n} dS = 0 \quad (1)$$

From lubrication theory, the fluid velocity in each direction is:

$$v_\theta = - \frac{\partial p}{r \partial \theta} \frac{h^2}{12\mu} + \frac{r\omega}{2} \quad (2)$$

$$v_z = - \frac{\partial p}{\partial z} \frac{h^2}{12\mu} \quad (3)$$

Equation (1) states that the mass flux leaving a cell must equal the mass flux entering the cell. The flow balance equation for a typical cell can be written

$$\gamma_V + \gamma_N + \gamma_S + \gamma_E + \gamma_W = 0 \quad (4)$$

where γ_V = Mass flow due to change in volume with time

$\gamma_N, \gamma_S, \gamma_E, \gamma_W$ = Mass flow due to pressure gradient and rotational velocity out of the north, south, east and west sides of the control volume.

The mass flow $\frac{\partial}{\partial t} \int_V \rho dV$ applied to the elemental volume can be written:

$$\gamma_V = \frac{\partial h}{\partial t} \Delta a \quad (5)$$

where Δa = area of the surface = $r\Delta\theta \Delta z$

Substituting the pressure and flow induced mass flows in equation (4) we obtain

$$\begin{aligned} \frac{\partial h}{\partial t} + \frac{h_n^3}{12\mu \Delta z} \left. \frac{\partial p}{\partial z} \right|_n - \frac{h_s^3}{12\mu \Delta z} \left. \frac{\partial p}{\partial z} \right|_s - \frac{h_e^3}{12\mu \Delta \theta r^2} \left. \frac{\partial p}{\partial \theta} \right|_e \\ + \frac{h_w^3}{12\mu \Delta \theta r^2} \left. \frac{\partial p}{\partial \theta} \right|_w + \frac{\omega}{2\Delta \theta} (h_e - h_w) = 0 \end{aligned} \quad (6)$$

In finite difference form, Equation (6) can be written as:

$$\begin{aligned} \frac{\partial h}{\partial t} + \frac{h_n^3}{12\mu \Delta z} \left(\frac{p_L - p_{L-1}}{\Delta z_1} \right) - \frac{h_s^3}{12\mu \Delta z} \left(\frac{p_{L+1} - p_L}{\Delta z_{1+1}} \right) \\ - \frac{h_e^3}{12\mu \Delta \theta r^2} \left(\frac{p_{L+M} - p_L}{\Delta \theta_{j+1}} \right) + \frac{h_w^3}{12\mu \Delta \theta r^2} \left(\frac{p_L - p_{L-M}}{\Delta \theta_j} \right) \\ + \frac{\omega}{2\Delta \theta} (h_e - h_w) = 0 \end{aligned} \quad (7)$$

The following non-dimensional quantities are defined:

$$\begin{aligned} r &= RL \\ h &= Hc \\ p &= P p_{\text{ref}} \\ t &= (2\Lambda L / \omega r) T \\ \Lambda &= 6\mu\omega r L / (p_{\text{ref}} C^2) \text{ where } p_{\text{ref}} \text{ is a reference pressure} \\ z &= ZL \end{aligned}$$

Introducing these expressions in Equation (7) we obtain

$$A P_L + N P_{L-1} + S P_{L+1} + W P_{L-M} + E P_{L+M} = G \quad (8)$$

where:

$$\begin{aligned} A &= \left[\frac{H_n^3}{\Delta z \Delta z_1} + \frac{H_s^3}{\Delta z \Delta z_{1+1}} + \frac{H_e^3}{R^2 \Delta \theta \Delta \theta_{j+1}} + \frac{H_w^3}{\Delta \theta R^2 \Delta \theta_j} \right] \\ N &= \left[\frac{-H_n^3}{\Delta z \Delta z_1} \right] & E &= \left[\frac{-H_e^3}{R^2 \Delta \theta \Delta \theta_j} \right] \\ S &= \left[\frac{-H_s^3}{\Delta z \Delta z_{L+1}} \right] & W &= \left[\frac{-H_w^3}{R^2 \Delta \theta \Delta \theta_j} \right] \\ G &= \left[\frac{-\partial H}{\partial T} - \frac{\Lambda L}{R \Delta \theta} (H_e - H_w) \right] \end{aligned}$$

Film Thickness

The film thickness for any grid point can be expressed as

$$h = c + e \cos\theta \quad (9)$$

where

c = Machined in radial clearance, m

e = eccentricity, m

Non-dimensionalizing the clearance with c results in

$$H = 1 + \epsilon \cos\theta \quad (10)$$

Structural deformation of the bearing members may be added to equation (10) to adjust the fluid film thickness.

Force and Moments

Forces (or loads) in x and y directions are obtained by integrating the pressure distribution over the area

$$\begin{aligned} f_x &= \iint -p(\cos\theta)rd\theta dz \\ f_y &= \iint -p(\sin\theta)rd\theta dz \end{aligned} \quad (11)$$

where: f_x = Force in x -direction

f_y = Force in y -direction

Non-dimensionalizing:

$$\begin{aligned} f_x &= \iint (P p_{ref})(\cos\theta)(RL)(d\theta)(LdZ) \\ f_y &= \iint (P p_{ref})(\sin\theta)(RL)(d\theta)(LdZ) \\ F_x &= \frac{f_x}{p_{ref} L^2} \\ F_y &= \frac{f_y}{p_{ref} L^2} \end{aligned} \quad (12)$$

Moments

Moments about x and y coordinates, located at the axial mid-point of bearing system are computed. These are:

$$\begin{aligned} M_x &= \iint p_z(\cos\theta)rd\theta dz \\ M_y &= \iint -p_z(\sin\theta)rd\theta dz \end{aligned} \quad (13)$$

Non-dimensionalizing:

$$\begin{aligned} M_x &= \iint (P p_{ref})(ZL)(\cos\theta)(RL)(d\theta)(LdZ) \\ M_y &= \iint (P p_{ref})(ZL)(\sin\theta)(RL)(d\theta)(LdZ) \\ \bar{M}_x &= \frac{M_x}{p_{ref} L^3} \\ \bar{M}_y &= \frac{M_y}{p_{ref} L^3} \end{aligned} \quad (14)$$

2.2 HYDROSTATIC & HYBRID

For the hydrostatic and hybrid mode of lubrication, information on the external lubrication supply system is required. This information can be in terms of lube oil supply pressure or flow or both. Figure 3 shows some typical external lubrication supply arrangements. Briefly they can be stated as follows:

- a. Figure 3(a) shows an arrangement where recess pressures are specified. This arrangement is used for preliminary calculations of bearing load capacity, flow, etc.
- b. Figure 3(b) shows an arrangement where recess flows are specified.
- c. Figure 3(c) shows an arrangement where two recesses are connected to a common lubrication supply pump. Each recess has its own restrictor, i.e., orifice or capillary.
- d. Figure 3(d) shows a multirecess arrangement. This arrangement combines the concept described in (c).

Several other lubrication supply arrangements are possible. These can be analyzed with the help of arrangements shown in Figure 3. The main purpose is to establish conditions on recess pressures. Therefore, the number of conditions required are the same as the number of recesses in the system. If the pressure values in the recesses are specified, then the problem is simple and solution can be readily obtained. For the other cases, conditions on recess pressures are specified indirectly either through conditions on flow or conditions on supply pressure. Generally, the flow conditions are less than the conditions required to solve the problem. Therefore, remaining conditions are obtained from the conditions on supply pressure. For a restrictor type feeding arrangement, flow through a restrictor is dependent on supply pressure, recess pressure and characteristic of the restrictor itself. This establishes a relationship between recess pressure and supply pressure. Using this relationship, additional conditions on recess pressures are established. This will complete the total number of conditions required to solve the problem.

3. SOLUTION APPROACH

The pressure equation (Equ. 8) is written for all grid points excluding boundary and recess points. Therefore, Equation 8 would be written for the nodes labeled grid points in Figure 4. For the hydrodynamic case once the boundary pressures are specified the resulting matrix equation can be readily solved using Gaussian elimination method.

For the hydrostatic mode of lubrication further manipulation of Equation (8) is carried out to incorporate an external lubrication oil supply system into the formulated problem. This is achieved by modifying Equation (8) for the grid points next to the recess. Since the recess pressure is not known it is treated as an unknown boundary condition whose value has to be found later. The approach adopted here is to express the pressure distribution in the bearing in terms of recess pressure. Therefore, the terms associated with the recess pressure are moved to the right hand side of Equation (8). The right hand side will have a constant term plus a term associated with Pr_1 for a single recess system. A system with two recesses will have three terms, a constant term, a term for Pr_1 and a term for Pr_2 . Since recess pressure is considered constant in the recess area, the pressure equations for the grid points in the recess area are eliminated. This reduces the number of equations to be solved.

Equation (8) in terms of matrix becomes

$$[A]\{p\} = \{B\} \quad (15)$$

where

$$\begin{aligned} \{B\} &= \left\{ G^0 + G^1 Pr_1 + G^2 Pr_2 \dots \right\} \\ &= [G] \begin{Bmatrix} 1.0 \\ Pr \end{Bmatrix} \end{aligned}$$

The pressure distribution in the bearing is given by

$$\{P\} = [A]^{-1}\{B\} = [A]^{-1}[G] \begin{Bmatrix} 1.0 \\ Pr \end{Bmatrix} \quad (16)$$

or

$$\text{Let } [C] = [A]^{-1}[G]$$

$$\{P\} = [C] \begin{Bmatrix} 1.0 \\ Pr \end{Bmatrix} \quad (17)$$

Flow Out of Each Recess

Flow out of each recess is given by

$$Q_r = Q_{r_{E\&W}} + Q_{r_{N\&S}} \quad (18)$$

where

$$Q_{r_{N\&S}} = \left\{ \left[\frac{h^3}{12\mu} \frac{\partial p}{\partial z} \right]_N + \left[\frac{h^3}{12\mu} \frac{\partial p}{\partial z} \right]_S \right\} r d\theta$$

$$Q_{r_{E\&W}} = \left\{ \left[\frac{h^3}{12\mu r} \frac{\partial p}{\partial \theta} + \frac{Uh}{2} \right]_E + \left[\frac{h^3}{12\mu r} \frac{\partial p}{\partial \theta} - \frac{Uh}{2} \right]_W \right\}$$

Expressing the pressure derivatives in terms of recess pressure and the pressure value next to the recess edge, the flow out of each recess (with the use of Equation (18)) may be expressed as

$$\begin{aligned} Q_{r_1} &= d_0^1 + d_1^1 P_{r_1} + d_2^1 P_{r_2} + \dots + d_m^1 P_{r_m} \\ Q_{r_2} &= d_0^2 + d_1^2 P_{r_1} + d_2^2 P_{r_2} + \dots + d_m^2 P_{r_m} \\ &\vdots \\ Q_{r_m} &= d_0^m + d_1^m P_{r_1} + d_2^m P_{r_2} + \dots + d_m^m P_{r_m} \end{aligned} \quad (19)$$

External Lubrication Supply System

The external lubrication supply system is coupled mathematically with the bearing through conditions on flow. The flow through recesses as given by Equation (19) must be equal to the flow supplied by the external supply system. The K^{th} recess flow from an external system may be written as:

$$Q f_K = f_K (P_S - P_{r_K})^{S_K} \quad (20)$$

For constant recess flow (flow control valve)

$$f_K = Q f_K \quad \text{and} \quad S_K = 0.0$$

For orifice compensated restrictor

$$f_K = c_d \frac{\pi d_0^2}{4} \sqrt{\frac{2}{\rho}} \quad \text{and} \quad S_K = 0.5$$

where

d_0 = orifice diameter, m

c_d = discharge coefficient $\approx .61$

ρ = lubricant density, Kg/m^3

For capillary compensated restrictor

$$f_K = \frac{\pi d_c^4}{128 \mu l_c} \quad \text{and} \quad S_K = 1.0$$

where

d_c = capillary diameter, m

l_c = capillary length, m

μ = lubricant viscosity, N-s/m^2

Equating the two flows given by Equations (19) and (20) we get

$$Qr_K = Qf_K$$

or

$$d_0^K + \left[\sum_{i=1}^m d_i^K Pr_i \right] - f_K (PS - Pr_K) S_K = 0 \quad (21)$$

where

K = recess number

m = total number of recesses

In matrix form Equation (21) may be written as

$$[D]\{Pr\} = \{C\} \quad (22)$$

where

$$[D] = \begin{bmatrix} 1 & & & \\ d_1^1 & \dots & & d_m^1 \\ \cdot & & & \cdot \\ \cdot & & & \cdot \\ \cdot & & & \cdot \\ d_1^m & & & d_m^m \end{bmatrix}$$

$$\{C\} = \left\{ f_K (PS - Pr_K) S_K - d_0^K \right\}$$

If the value of $S_K = 0$ or 1 Pr terms in $\{C\}$ are transferred to the left hand side, then the solution to the equation (22) is written as

$$Pr = [D]^{-1}\{C\} \quad (23)$$

Once Pr is known, the pressure distribution in the bearing is obtained with Equation (17).

If the value of $S_K = 1/2$, the terms of Pr can not be transferred to the left hand side easily. Therefore an iterative scheme based on Newton-Raphson method is used to obtain the solution.

4. SAMPLE PROBLEM

Figure 5 shows a typical large size 9.4m (31 ft.) diameter ball mill used for bulk processing. The large drum is supported by two fluid film journal bearings, one on each side of the drum. The cylindrical journals at each end of the drum (called "trunnions") are hollow and can be thought of as shells because of the thin walls used to allow maximum area for the material being processed to pass through the trunnions into and out of the drum.

The journal bearings are hydrostatically lubricated. The design specifications for the bearings are:

Bearing diameter	= 1.44m
Bearing length	= 0.48m
Load	= 1.5×10^6 N
Lubricant	= 0.132 N-s/m^2
Lubricant inlet temperature	= 38°C
Mill Operational speed	= 10 rpm

Figure 6 shows the bearing design and dimensions in detail. The external lubrication supply system is designed to maintain a fixed flow through the bearing. Figure 7 shows the external lubrication supply system.

4.1 RESULTS

Bearing load capacity analyses were conducted with the above described approach. Two trunnion configurations, rigid and deformed, were analyzed. The results for the rigid trunnion configuration were obtained first. Using these results structural deformations of the trunnion were computed. For computations a separate structural finite element computer program was used. The computed deformations were then read to the bearing computer program for performing the bearing performance analysis. The results are summarized in Figure 8 to 10.

Figure 8 shows the pressure distribution in the bearing for the rigid and distorted trunnion. In both cases the load capacity is the same. Significant changes occur in the pressure distribution in the axial direction due to uneven deformation of the trunnion. The hydrodynamic effects on the pressure distribution were found to be negligible due to low rotational speed.

The deformation of the trunnion at the design point load condition is shown in Figure 9. The deformation curve in rotational direction is symmetrical about the bearing mid-axis. The deformation in the axial direction is higher at the outboard side of the bearing. The deformation values are about 25 percent of the running clearance.

Figure 10 shows bearing load capacity as a function of the minimum clearance. The results are for the rigid and the deformed trunnion. As the minimum clearance is reduced, the load capacity increases. This is due to the fact that external lubrication supply system is maintaining a constant flow through the bearing. For a given load condition the minimum clearance for the deformed case is considerably less than the rigid case. Therefore structural deformations are extremely important when designing this type of equipment.

5. SUMMARY

1. An advanced computerized technique for analyzing hybrid type of bearings is described.
2. The technique is highly efficient which results in reducing computational time considerably. The following are key elements in the proposed technique.
 - o The pressure equations for the grid points over the bearing recess areas and boundary points are assumed known and are eliminated from the pressure matrix solution.
 - o The matrix solution for the fluid film equation at each grid point is performed only once in terms of the recess pressures. This solution is then saved and can be used for a variety of external feeding systems.
 - o Most types of external lubrication supply system can be analyzed.
3. The following conclusions are drawn from the analysis performed on a ball mill.
 - o The structural deformation of trunnion significantly reduces the minimum clearance between the journal and the bearing.

REFERENCE

1. H. C. Rippel, "Design of Hydrostatic Bearings", Part 1-10, Machine Design, Vol. 35, No. 18-28, 1963.
2. W. Shapiro, V. Castelli, and S. Heller, "Determination of Performance Characteristics of Hydrostatic Bearing System that Support a Rigid Body", ASLE Trans. 9, 272-282, 1966.

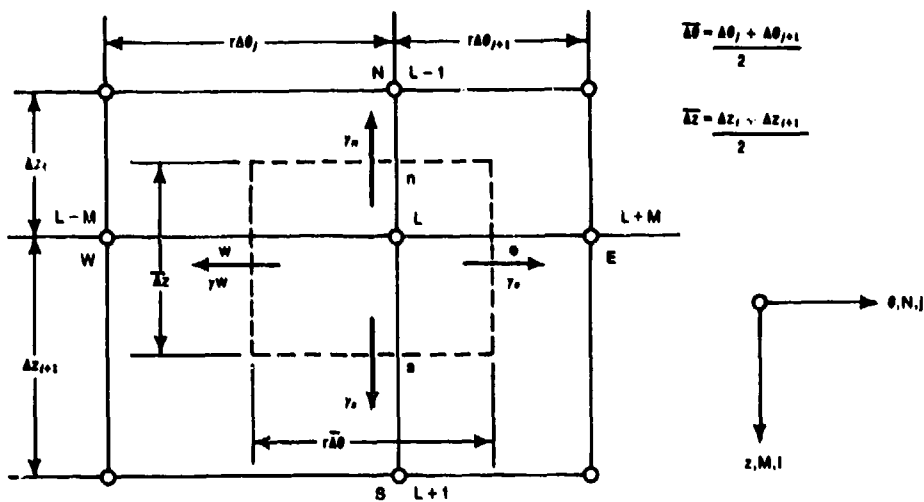


Figure 1 - Typical Flow Balance Cell

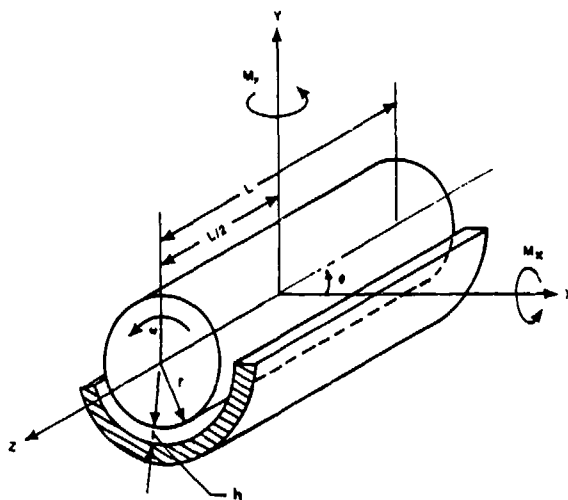


Figure 2 - Sign Convention for Bearing Forces and Moments

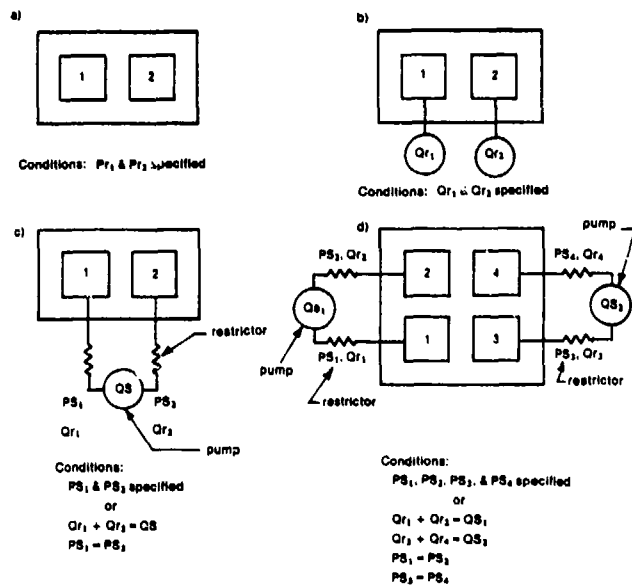


Figure 3 - Typical External Lubrication Supply System

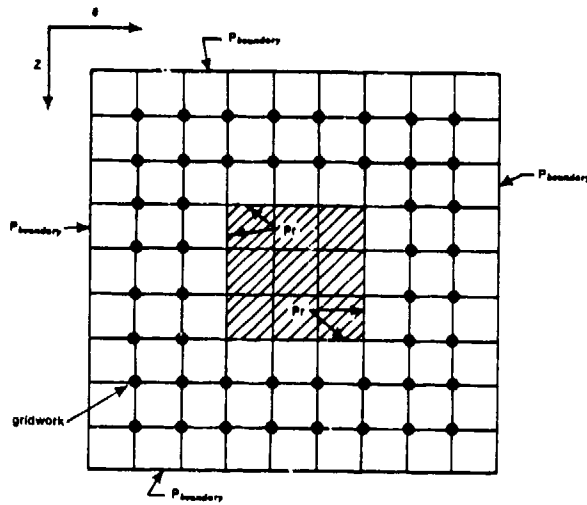


Figure 4 - Single Recess Pad

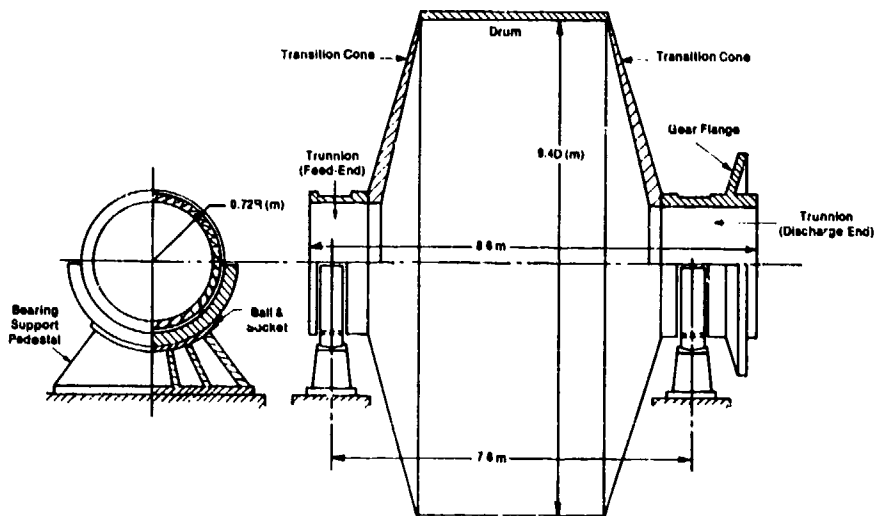


Figure 5 - Ball Mill and Bearing Support Structures

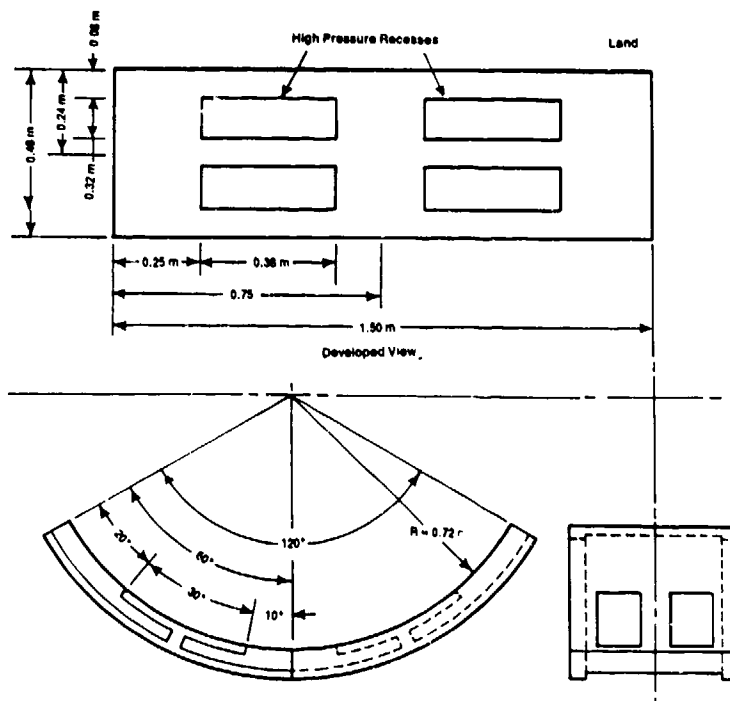


Figure 6 - Hydrostatic Bearing Configuration

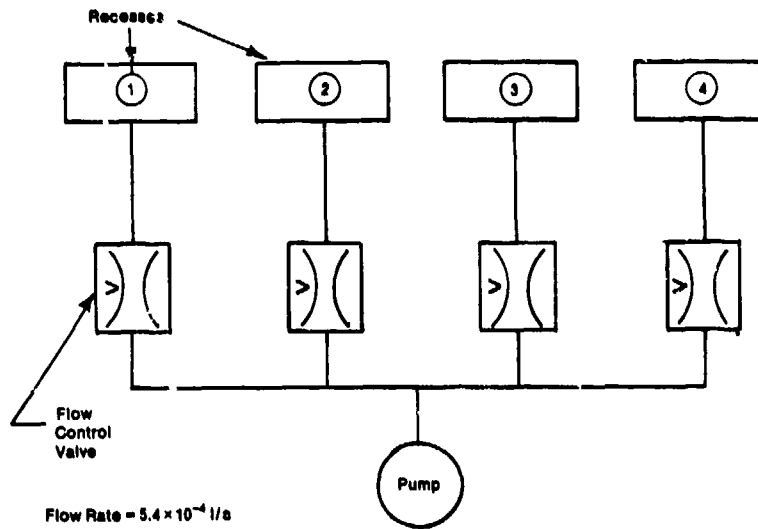


Figure 7 - Bearing External Lubrication Supply System

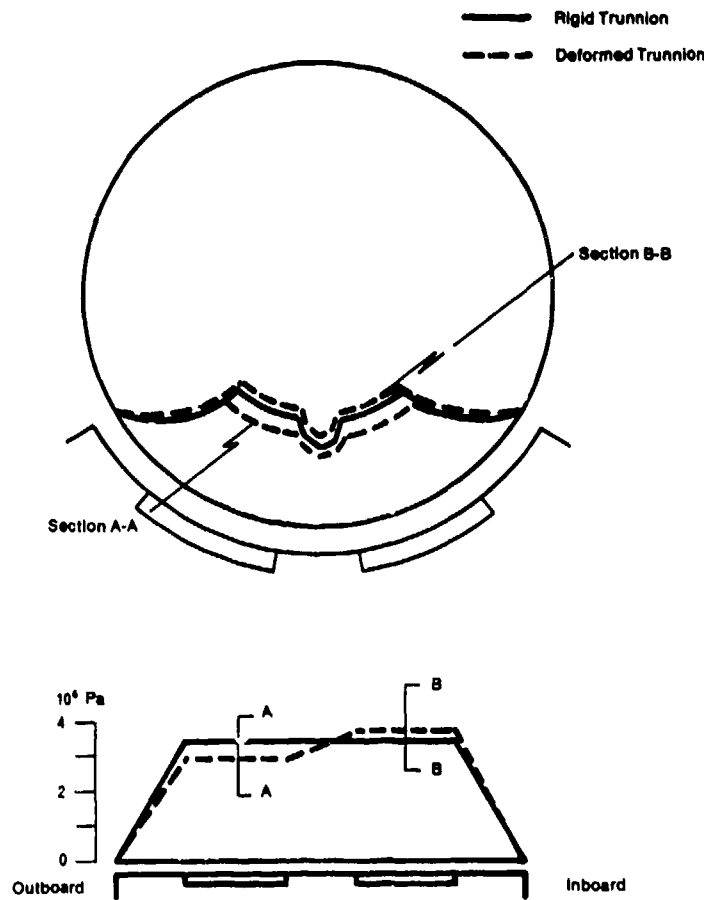


Figure 8 - Pressure Profile

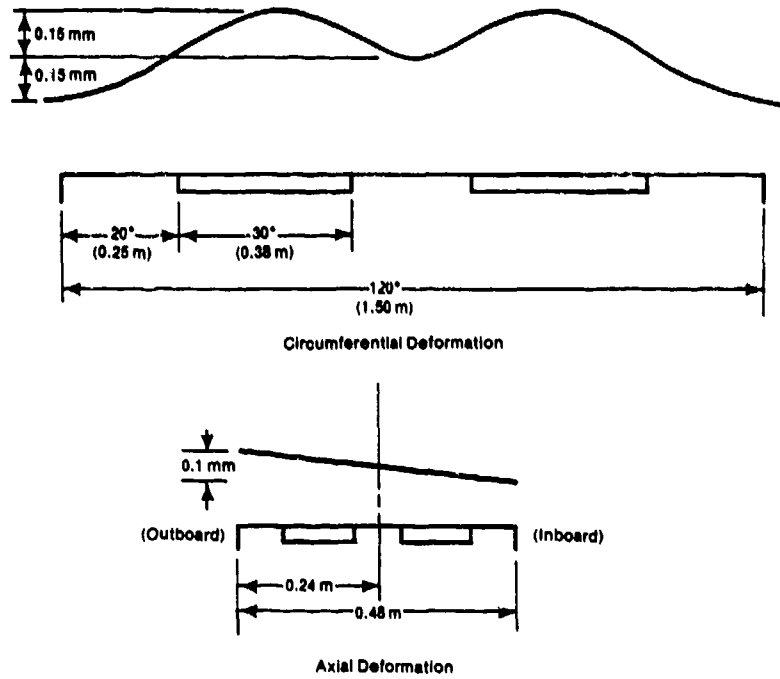


Figure 9 - Deformation of Trunnion

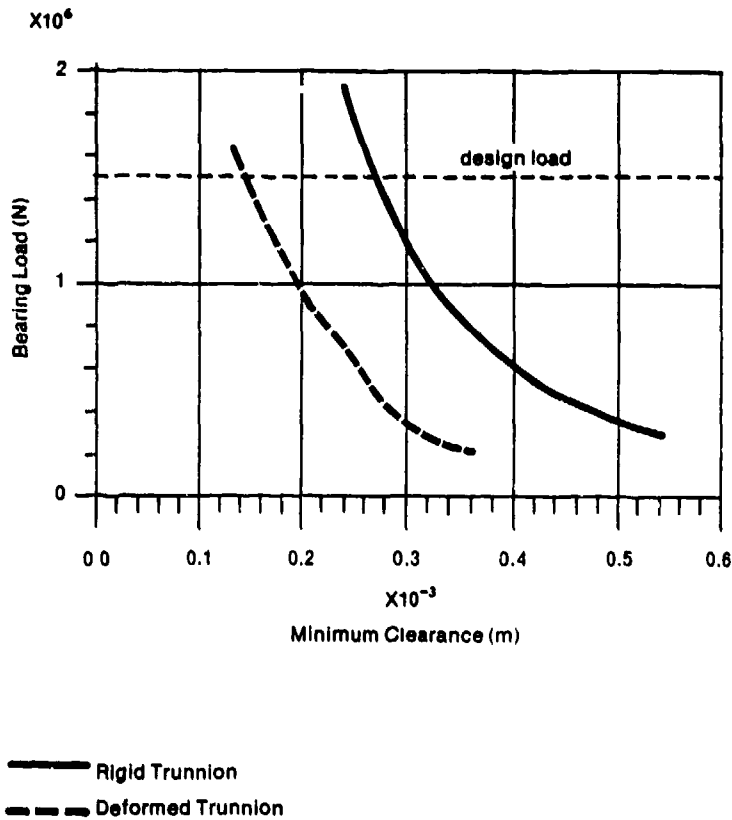


Figure 10 - Bearing Load Capacity VS. Minimum Clearance

DISCUSSION

H.S. Yoo, University of Gent, Be

You showed an application of these bearings in mainly hydrostatic conditions. If you have some more hydrodynamic action, for instance as in machine tool spindles, the speed can be higher. On some lands between the pockets you may have some cavitation. How can you deal with that situation?

Author's Reply

The example I showed was for a 10 rpm application. We have not tried to apply the method where the hydrodynamic situation is predominant, only where hydrostatic effects predominate.

W.B. Rowe, Liverpool Polytechnic, UK

I'm interested in your remarks on cavitation. We do find that cavitation does occur at moderate eccentricity ratios (about 0.6) with bearings that are optimized for minimum power dissipation, which means that there are not excessive amounts of hydrodynamic action. I imagine that this method would be similar to the superposition techniques described in the literature, with respect for cavitation. I was wondering whether the method you describe here is faster than the superposition technique or whether you think it would be similar in computation time.

Author's Reply

One of the objectives of our method was to obtain answers as quickly as possible. We were looking at problems from the design point of view. I'm not certain which method would be faster. We have to explore various conditions of cavitation and turbulence.

P. Kim, NRC, Ca

It looks like your bearing is of larger size. Is your computer program capable of dealing with elastic deformation of a pad bearing, i.e., a partial arc bearing?

Author's Reply

Yes, we have a finite element structural analysis program which is used for establishing deformation. It is not coupled, however, so we use an iterative procedure. The program forms the clearance distribution based on the structural deformation data. The programs could be coupled, but they are not at this time.

ETUDE THEORIQUE ET EXPERIMENTALE
D'UN PALIER MAGNETIQUE AXIAL DU TYPE ACTIF

Michel KANT, Roger KESSOU
Division Electromécanique
Université de Technologie de COMPIEGNE
B.P. 233 - 60206 COMPIEGNE CEDEX (FRANCE)

RESUME : Après un bref rappel historique des travaux concernant les paliers magnétiques actifs (PMA), on décrit le système de sustentation axiale, pouvant servir de butée tant verticale qu'horizontale. Le palier magnétique actif du type axial fonctionne selon le principe de ferro-attraction. La force d'origine électromagnétique, qui s'exerce entre la partie statorique bobinée (coussinet - inducteur) et la partie rotative en fer doux, est inversement proportionnelle au carré de la distance (entrefer), qui sépare ces deux parties ; ainsi, à force électromagnétique constante (courant continu dans les bobines statoriques par exemple), le fonctionnement dynamique du palier est instable. Pour stabiliser le palier, il convient d'asservir son courant inducteur à une consigne d'équilibre (valeur d'entrefer par exemple). Dans ce travail, on modélise le palier à l'aide de la méthode des éléments finis, qui permet, d'une part, de calculer les forces de sustentation et, d'autre part, d'identifier une chaîne d'asservissement optimale. La réalisation pratique de l'asservissement est basée sur un filtre numérique, constitué à partir d'un microprocesseur Z80A de ZILOG. Les résultats expérimentaux sur un PMA de 200 dN à 20 000 tours/min sont confrontés avec le calcul numérique.

I. INTRODUCTION

La suspension des pièces mobiles s'effectue classiquement par les paliers mécaniques, qui présentent un certain nombre d'inconvénients, parmi lesquels on peut citer : frottement, usure, complexité du système de lubrification. Pour toutes ces raisons, l'emploi des paliers mécaniques est limité au point de vue technologique, aussi bien en température qu'en charge et en vitesse. Pour remplacer le palier mécanique, dans certaines applications spécifiques, on propose actuellement plusieurs dispositifs : hydrauliques, aérodynamiques, magnétohydrodynamiques, ou purement magnétiques. Dans ce dernier domaine, on distingue deux catégories de paliers : paliers magnétiques passifs (PMP) et paliers magnétiques actifs (PMA). Les paliers magnétiques passifs sont basés sur le principe de répulsion entre les deux circuits électriques véhiculant généralement un courant primaire (inducteur) et un courant secondaire (induit) ; ces paliers, qui s'autoéquilibrent à l'aide d'énergie électrique fournie aux enroulements par un réseau extérieur, ont l'avantage de ne nécessiter aucun réglage mécanique ou/et électronique ; leur inconvénient réside dans une consommation élevée de l'énergie, qui, de plus, doit être dissipée en chaleur dans des volumes réduits. Les paliers magnétiques actifs, qui ne mettent en jeu, aux pertes Joule près, aucune énergie électrique ou mécanique, ont, à notre avis, les meilleures chances de trouver une application industrielle de plus en plus large. Le principe de ces paliers découle directement de l'expérience classique de Faraday sur la "suspension" d'une sphère en fer doux dans le champ d'un électro-aimant. Le palier magnétique axial (ou la butée magnétique) de la Figure 1 reproduit presque sans modification l'expérience de Faraday.

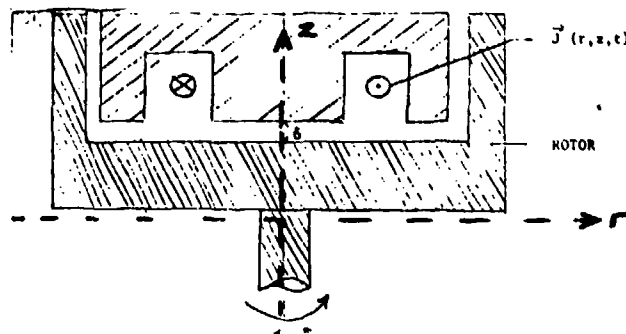


Figure 1 : Configuration générale d'un palier magnétique axial

Le courant, de densité \vec{J} , circulant dans les enroulements d'un électro-aimant cylindrique immobile (stator), engendre un flux magnétique, qui se ferme à travers une armature ferromagnétique mobile (rotor), formée par un autre cylindre, coaxial avec le précédent. Le rotor est attiré par le stator, de manière à minimiser l'énergie électromagnétique emmagasinée dans le système ou, ce qui revient pratiquement au même, à diminuer l'entrefer δ entre la partie mobile et immobile. L'équilibre, qui correspond à l'égalité entre la force de ferro-attraction et la charge s'exerçant sur le rotor, est continuellement instable. En effet, toute diminution de la charge provoque une diminution de l'entrefer et donc une augmentation de la force portante ; et inversement, toute augmentation de la charge conduit à une augmentation de l'entrefer et, par conséquent, à une diminution de la force d'attraction ; dans le premier cas, le rotor va "coller" au stator ; dans le deuxième, il va "décrocher". Pour qu'un palier de ce type puisse fonctionner d'une façon stable, sa force portante, et donc son courant, doivent être asservis à une consigne d'équilibre, basée par exemple sur une valeur précise de la variation de l'entrefer.

Les difficultés de mise en oeuvre des PMA sont donc liées essentiellement aux problèmes d'alimentation et de commande. La première tentative de concevoir une commande adaptée aux PMA date, à notre connaissance, de 1934 et est due à E.F.W. ALEXANDERSON¹, dont le dispositif, basé sur les tubes électroniques et les contacteurs mécaniques, n'a probablement jamais franchi le stade de la recherche universitaire.

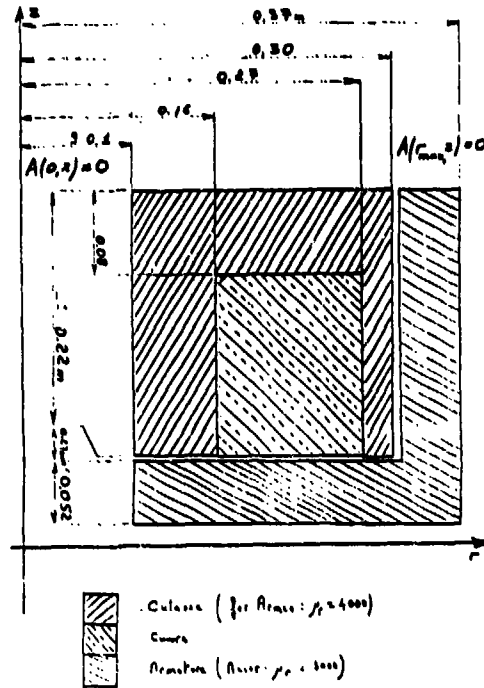


Figure 2 : Les dimensions du PMA : 200 dN à 20 000 tours/min, qui ont été prises en compte dans les calculs numériques

L'avènement de l'électronique de puissance moderne et des circuits logiques miniaturisés est à l'origine du regain de l'intérêt pour les paliers magnétiques actifs, qui ont franchi, entre 1965 et 1970, l'étape du développement scientifique, pour passer au stade de l'application industrielle, comme en témoigne notamment la publication ². Ce regain d'intérêt s'explique bien à l'aide des figures 3 et 4, donnant respectivement les courbes de consommation d'énergie et des vitesses limites pour les différents types de paliers.

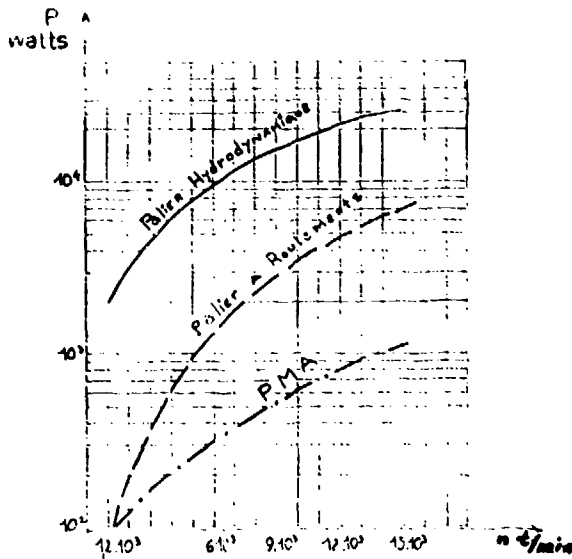


Figure 3 : Consommation énergétique des différents types de paliers

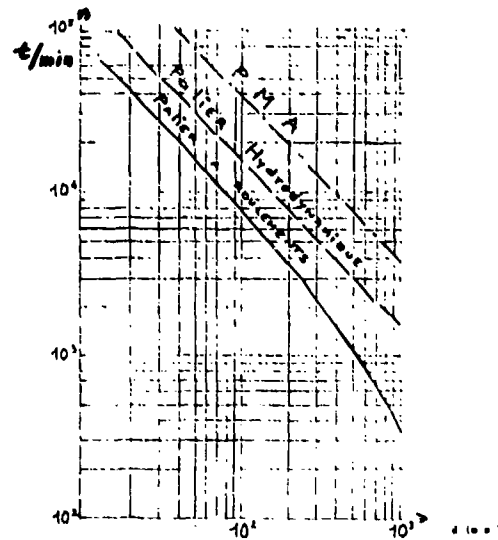


Figure 4 : Vitesses limites des différents types de paliers

Une des raisons pour laquelle le PMA ne trouve pas encore d'applications plus générales réside, d'une part, dans sa théorie très sommaire, qui limite les possibilités de conception des systèmes correspondants. D'autre part, les organes de commande proposés ne répondent pas toujours aux exigences des assemblages actuelles. La difficulté et l'intérêt des études sur le PMA résident dans la complexité des phénomènes mis en jeu, qui se situent au carrefour de l'électromécanique, l'automatique et l'électronique de puissance, pour ne nommer que les domaines les plus importants.

Dans notre travail, nous essayerons de montrer comment on peut établir une théorie plus précise des PMA, à l'aide de la méthode des éléments finis, et de proposer l'amélioration de son asservissement à l'aide d'un processeur digital.

Pour terminer ce chapitre introductif, rappelons les avantages des PMA :

- absence de contacts mécaniques, donc d'usure ;
- possibilité de fonctionner à très grande vitesse ;
- couple de frottement limité (dix à vingt fois plus petit que celui du palier hydrodynamique) ;
- consommation d'énergie active très faible ;
- absence de lubrification permettant le fonctionnement sous vide ou/et à température élevée ;
- possibilité d'asservissement en position ou/et en charge ;
- démarrage en charge .

II . ANALYSE ELECTROMAGNETIQUE DE LA BUTEE

Afin de pouvoir déterminer les caractéristiques mécaniques de la butée, nous déterminons, à chaque point de sa géométrie (cf Fig. 1), la valeur du champ magnétique \vec{B} ($B_r, B_z, 0$), en résolvant l'équation de diffusion en potentiel vecteur \vec{A} ($0, 0, A_\varphi$) de la forme :

$$\nabla \vec{A} = \vec{\mu} \vec{J}_{\text{tot}} \quad (1)$$

où la densité du courant total se décompose en :

$$\vec{J}_{\text{tot}} = \vec{J}_{\text{ex}} + \vec{J} = \vec{J}_{\text{ex}} - \gamma \left[\frac{\partial \vec{A}}{\partial t} + \vec{\nabla} \times \vec{B} \right] \quad (2)$$

Compte tenu de la géométrie circulaire de la butée et des hypothèses et développements de la référence ³, (1) et (2) se réduisent, dans les coordonnées cylindriques de la Figure 1, à :

$$-\frac{\partial}{\partial r} \left(\frac{1}{\mu} \frac{\partial A}{\partial r} \right) - \frac{\partial}{\partial z} \left(\frac{1}{\mu} \frac{\partial A}{\partial z} \right) - \frac{\partial}{\partial r} \left(\frac{1}{\mu} \frac{A}{r} \right) = J_{\text{ex}} - \gamma \frac{\partial A}{\partial t} + \gamma v_z \frac{\partial A}{\partial z} \quad (3)$$

où : μ, γ : respectivement perméabilité et conductivité électrique des matériaux

\vec{V} (v_r, v_z, v_φ) : vitesse mécanique du rotor

L'expression (3) a été résolue par la méthode des éléments finis (résolution pas à pas ; discrétisation temporelle + schéma d'Euler), mettant en jeu des éléments quadratiques selon les études résumées dans ⁴. Compte tenu de la symétrie axiale, l'étude a été effectuée pour la moitié de la Figure 1, présentée dans la Figure 2, où l'on a porté de plus les conditions aux limites correspondantes. Le système présente quatre zones géométriquement et magnétiquement différentes : l'entrefer, l'armature du rotor, l'encoche où est logé l'enroulement conducteur, l'armature magnétique du stator. L'armature du rotor et du stator sont en matériaux ferromagnétiques.

La connaissance du potentiel vecteur permet le calcul simple du champ magnétique \vec{B} ($B_r, B_z, 0$)

$$B_r = \frac{\partial A}{\partial z} \quad B_z = - \frac{\partial A}{\partial r}$$

et partant, de la force portante à partir du tenseur de Maxwell :

$$\vec{F}_z = \iint_{\Omega_1} (\mu \vec{H} (\vec{H} \cdot \vec{n}) - \mu/2 H^2 \vec{n}) d\Omega \quad (4)$$

Le champ magnétique \vec{H} , étant relié à \vec{B} par la loi du milieu $\vec{B} = \mu \vec{H}$

Pour assurer le fonctionnement du palier, on divise généralement l'enroulement du stator en deux parties, dont l'une alimentée en courant d'amplitude constante $J_{\text{ex}1}$ sert à suspendre le mobile et l'autre parcourue par le courant variable $\Delta J_{\text{ex}}(t)$ assure la stabilisation ;

$$\text{ainsi :} \quad \vec{J}_{\text{ex}} = \vec{J}_{\text{ex}1} + \Delta \vec{J}_{\text{ex}}(t) \rightarrow \vec{F}_z = \vec{F}_{z1} + \Delta \vec{F}_z \quad (5)$$

Dans certaines réalisations, les deux courants sont injectés dans un seul enroulement.

Des figures 5, 6, 7 représentant, pour le palier décrit dans l'Annexe, respectivement : la distribution de la composante B_z du champ dans l'entrefer, la courbe de la force portante en fonction de l'entrefer et la courbe de cette même force en fonction du courant d'excitation, on peut dégager les conclusions suivantes :

- les calculs correspondent assez bien avec les mesures ;
- la force portante est reliée à l'entrefer et au courant par une relation simple de type : $c \cdot e^{-I^2/\delta^2}$.

Pour le palier magnétique développant une force moyenne de 180 dN à 300 dN, le courant doit être compris entre 16 A et 23 A et l'entrefer entre 0,23 mm et 0,32 mm, tandis que la raideur est de 1,4 dN/ μm :

- la saturation joue un rôle non négligeable dans le fonctionnement du palier.

Remarquons que la méthode des éléments finis permet de tenir compte des courants induits dans la butée par le champ électrique $v_z \frac{\partial A}{\partial z}$; ce courant provoque une force de répulsion et contribue à la diminution

des performances du palier. L'utilisation de matériaux les plus perméables possible et de faible conductivité transversale (tôles feuilletées) permet d'annuler, en grande partie, l'effet parasite du courant induit.

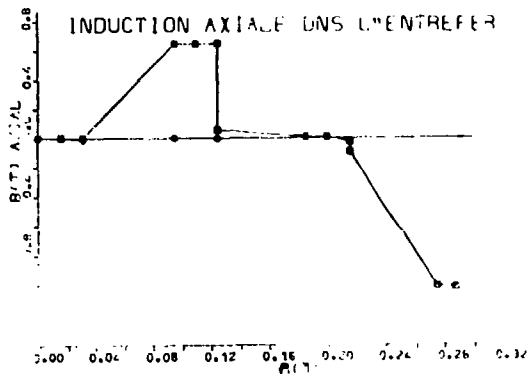


Figure 5 : Champ magnétique dans l'entrefer en fonction du rayon à $z = 0$ pour le courant de 5A

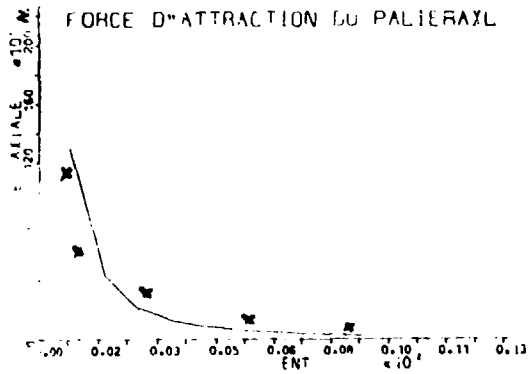


Figure 6 : Force portante du palier en fonction de la variation de l'entrefer pour le courant de 5A (λ : points de mesure)

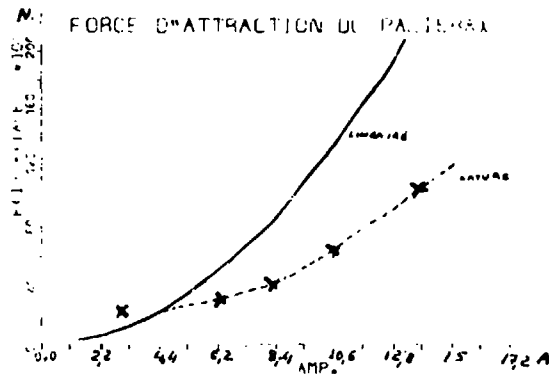


Figure 7 : Force portante du palier en fonction de la variation du courant (λ : points de mesure)

III. ETUDE D'ASSERVISSEMENT

La forme de la force portante du palier en fonction de l'entrefer (Fig.6) montre le caractère instable du PMA ; pour rendre le système stable, il est nécessaire de modifier l'allure de la force portante à l'aide d'un asservissement approprié. La modification de la force portante passe par une connaissance parfaite de la fonction de transfert reliant la bobine et le PMA. Cette fonction de transfert peut être obtenue :

- par des méthodes d'identification appliquées aux processus en temps réel ;
- par une modélisation mathématique du processus à asservir.

Dans le cas du PMA, étant donné l'impossibilité d'assurer une stabilisation pratique en boucle ouverte, seule la deuxième méthode peut être prise en compte.

La détermination d'un régulateur pour PMA peut s'opérer selon le schéma ci-après, où l'on envisage le choix d'un filtre, soit analogique, soit numérique. Dans nos réalisations, nous avons choisi cette dernière solution, qui, à notre avis, est la mieux adaptée aux paliers rapides ou/et à charge variable.

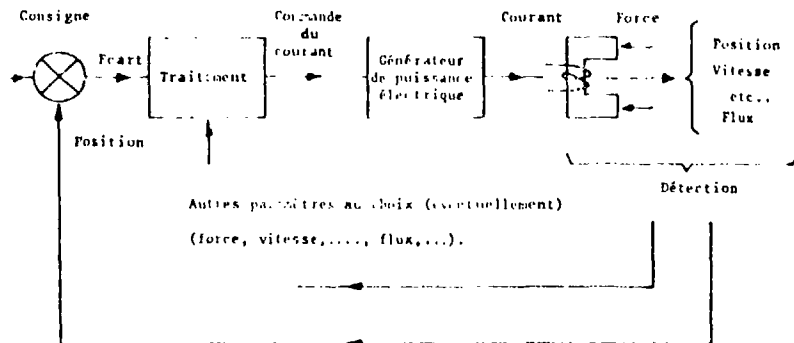
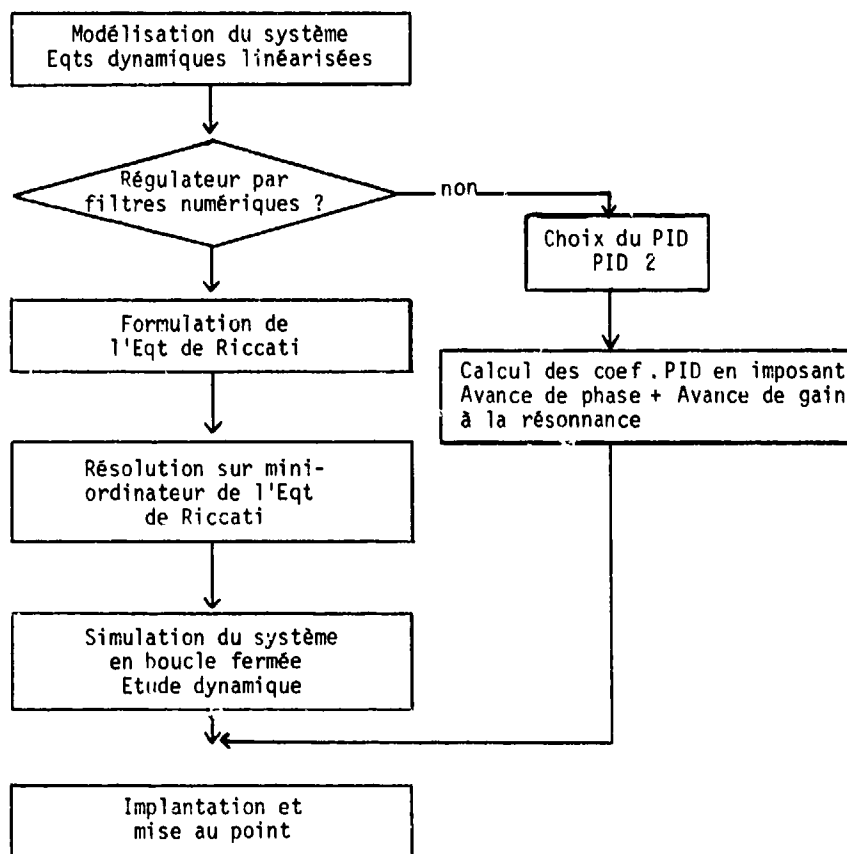


Figure 8 : Schéma de principe de commande et d'alimentation d'un PMA

La boucle d'alimentation et d'asservissement, schématisée sur la Figure 8, assure le contrôle du courant d'excitation, donc de la force électromagnétique (4) : ce qui permet de stabiliser le palier. En effet, l'état d'équilibre correspond à la loi de Newton :

$$[M] \dot{v} = F_z(t) - [M]g$$

avec : v : vitesse - $[M]$: matrice masse - t : temps - g : gravitation



Quelle que soit la méthode de contrôle choisie pour J_{ex} , donc $F_z(t)$, la boucle de retour de l'asservissement comportera les paramètres suivants : courant (i_{ex}), déplacement (z), vitesse (v). La prise en compte de $F(t)$ en fonction de ces paramètres peut s'effectuer par la méthode de discrétisation classique, correspondant notamment aux publications ^{5,6}, ou par la méthode continue de la résolution directe des équations (3). Cette dernière méthode a l'avantage de tenir compte de l'ensemble des phénomènes liés à la géométrie réelle du palier (saturation, courant induit...); son inconvénient réside dans la complexité des calculs par les éléments finis.

S'il paraît dérisoire de chercher actuellement des asservissements digitaux, basés sur la résolution à temps réel des équations (3) et (4), on peut néanmoins concevoir des fonctions approchées accessibles aux microprocesseurs existants : ce qui permet de remplacer la commande analogique par une commande numérique plus performante et plus souple. Ainsi, nous avons réalisé un palier axial, dont la commande a été structurée autour d'une carte-microprocesseur BLC 80/316 de l'ational Semiconductor.

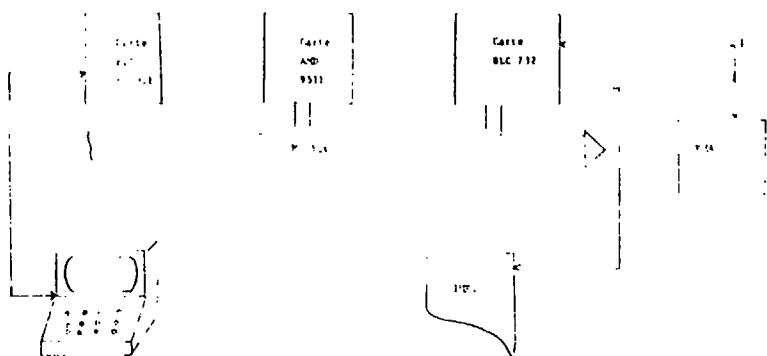


Figure 9 : Bloc digital d'asservissement d'un PMA

Conformément au schéma de la Figure 9, l'architecture de l'asservissement digital comporte :

- une carte BLC 80/316 articulée autour d'un microprocesseur Z80A de ZILOG ;
- une carte de calcul AMD 9511 de Advanced Microdevice ;
- une carte de conversion analogique/digital BLC 732 ;
- un moniteur vidéo et un moniteur de développement BLC 80-Z80 .

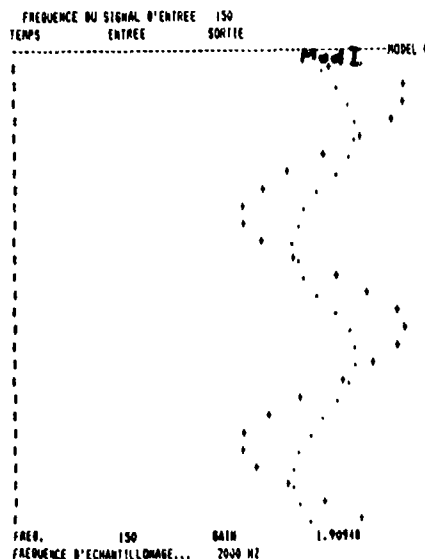


Figure 10 : Relation de la récurrence entre les coefficients calculés à partir de l'équation de Riccati (Model 0) et les coefficients du dispositif réellement réalisé (Model I)

La Figure 10 montre l'approximation de l'asservissement (Model I) par rapport à l'équation de Riccati, qui représente le guidage parfait du palier. Dans la réalisation pratique, la stabilisation du système a été obtenue avec un entrefer de 0,3 mm, pour une gamme de vitesse allant jusqu'à 20 000 tours/min et une charge nominale avoisinant 200 dR.

IV. CONCLUSION

Par rapport aux études des PMA préalablement effectuées, nous pensons avoir introduit les éléments suivants :

- l'application de la méthode des éléments finis, pour calculer et optimiser la géométrie des PMA ;
- la conception et la réalisation des asservissements, basés sur l'emploi des processeurs digitaux .

A la lumière des travaux effectués à ce jour, nous pouvons envisager l'emploi des paliers magnétiques actifs à des charges supérieures à quelques dizaines de tonnes, ayant des vitesses de rotation de plusieurs milliers de tours/min. Un palier de butée de 8 Tonnes à 40 000 trs/min, que nous avons étudié, peut, en tout point, rivaliser avec les dispositifs mécaniques ou hydrauliques .

Afin d'élargir l'application industrielle des PMA, il convient d'axer les recherches à venir sur :

- le perfectionnement de la commande numérique (en particulier, en ce qui concerne l'élaboration du régulateur d'état optimal) ;
- l'optimisation des caractéristiques géométriques et électromagnétiques par couplage des équations électromagnétiques et mécaniques .

V. BIBLIOGRAPHIE

1. E.F.W. ALEXANDERSON : "The thyatron bearing" - Electrical Engineering - Nov. 1934
2. H. HABERMAN, G. LIARD : "Paliers magnétiques actifs appliqués à l'industrie spatiale" - La Revue des Roulements - n° 194 - 1978
3. M. KANT, J. BARRAL : "General study of electromagnetic bearing" - Transactions of I.E.E.E. (Magnetics) - n° 9 - 1975
4. R. KESSOU : "Contribution à l'étude des paliers magnétiques actifs" - Thèse de Docteur-Ingénieur - Université de Technologie de COMPIEGNE - 1981
5. G. SCHWEITZER, R. LANGE : "Characteristics of magnetic rotor bearing for active vibration control" - Proceedings of I.M.E. - 1976
6. M. KANT, R. KESSOU : "Etude théorique préliminaire des paliers magnétiques à ferro-attraction" - Note Scientifique n° 1/80 de la Division Electromécanique - U.T.C. - 1980

ANNEXE

Les applications numériques du présent mémoire concernent un palier axial de 200 dr nominal à - 20 000 tours/min. Ce palier, dont les dimensions sont représentées sur la Figure 2, possède les caractéristiques suivantes :

- la partie statorique se compose de deux cylindres coaxiaux en tôles feuilletées ; autour du cylindre intérieur est placée une bobine de 3 x 100 spires ; chaque enroulement de 100 spires est indépendant et peut être alimenté séparément.
- la partie rotorique circulaire est en fer massif encoché dans le sens radial, de manière à augmenter la surface d'entrefer et diminuer les effets parasites des courants induits.

LE PALIER MAGNETIQUE ACTIF " ACTIDYNE "
 Helmut HABERMANN, Directeur Scientifique de la S 2 M
 Chemin Départemental 181-Forêt de Vernon-BP 431-F 27204 VERNON Cédex

Le palier magnétique actif est basé sur l'utilisation des forces développées par un champ magnétique pour soutenir un rotor en lévitation magnétique, sans contact mécanique entre la partie fixe et la partie mobile.

Des détecteurs de position repèrent la position du rotor et délivrent un signal d'erreur vers une boucle de contrôle électronique qui agit pour corriger le déplacement du rotor par rapport à sa position de référence.

SCHEMA DE PRINCIPE

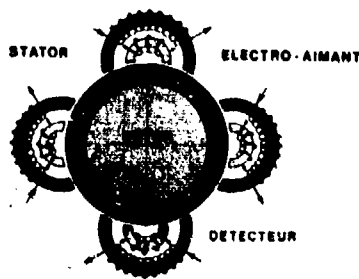
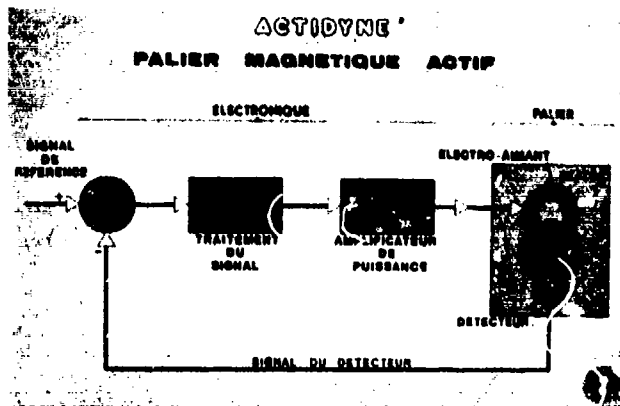


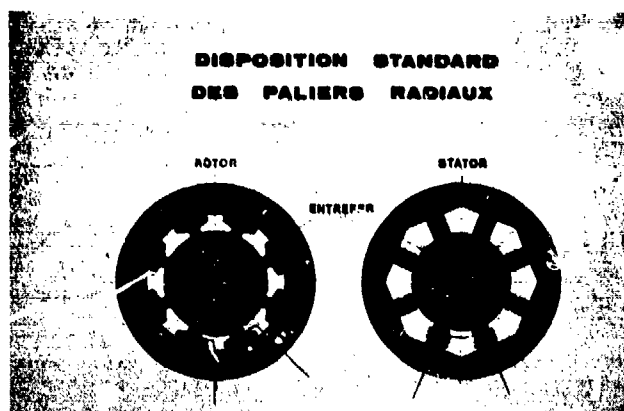
Schéma de principe

Pour contrôler un degré de liberté, deux électro-aimants sont nécessaires, ceux-ci travaillant uniquement en attraction. Pour un rotor complet où cinq degrés de liberté doivent être asservis, dix électro-aimants sont nécessaires.

Il est important de noter que ce palier fonctionne en attraction à l'inverse de tous les autres types de paliers. De plus, le contrôle est obtenu dès la mise sous tension et ne nécessite pas de "décollage par la vitesse".



Principe boucle d'asservissement



Disposition standard des paliers radiaux

Le palier magnétique actif, comme tout palier, se compose essentiellement de deux parties : le rotor et le stator.

Le rotor qui peut être intérieur ou extérieur est constitué par un empilage de tôles ferromagnétiques, sans encoche, ni bobinage.

Le stator, lui aussi fait de tôles empilées, encochées et bobinées, se compose de la partie électro-aimant du palier proprement dit et de la partie détecteur de position.

Les électro-aimants du stator maintiennent le rotor en lévitation magnétique, leur champ magnétique étant modulé en fonction de la position du rotor, elle-même surveillée par les détecteurs de position et comparée à la référence désirée.

Le détecteur de position qui utilise une porteuse haute fréquence élabore un signal dépendant de la position du rotor.

Ce signal est comparé à la consigne de l'asservissement (en général nulle si l'on veut un rotor centré).

La différence des signaux, appelée signal d'erreur, est traitée par l'asservissement en gain et en phase de manière à commander les amplificateurs de courant des électro-aimants pour assurer au palier sa rigidité et son bon amortissement. Le contrôle complet d'un rotor nécessite naturellement cinq asservissements, le sixième degré étant la rotation utile.

La technologie du palier magnétique actif est très proche de celle des moteurs à induction, type asynchrone.

Le rotor qui peut être intérieur ou extérieur est composé de tôles ferromagnétiques, sans encoches. L'épaisseur des tôles varie de 0,05 mm à 0,35 mm, suivant l'application et sont en général en Fe-Si, ce qui permet des vitesses linéaires de rotation jusqu'à 200 m/s.

Le stator utilise aussi des tôles ferromagnétiques de 0,35 mm d'épaisseur. Le matériau utilisé est en général du Fe-Si à 3%, non orienté. Avec ce matériau la capacité de charge spécifique du palier magnétique actif varie de 5 daN/cm² à 8 daN/cm².

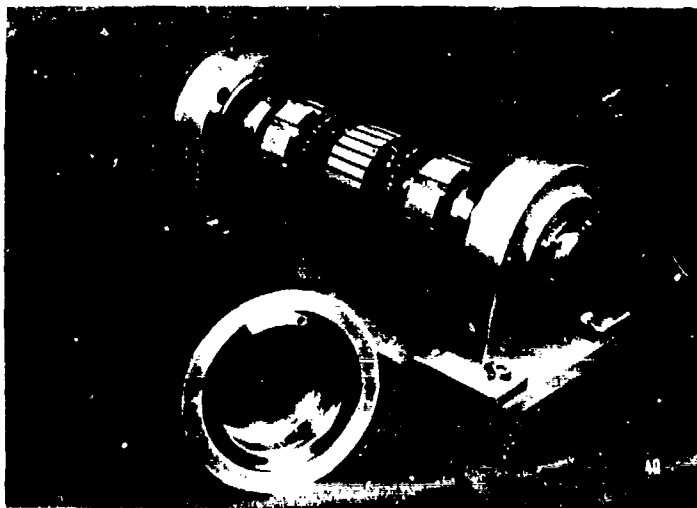


Éléments palier radial

Cette maquette portable permet de montrer les performances du palier magnétique actif ACTIDYNE.

On peut reconnaître les deux stators des paliers radiaux, les deux stators des détecteurs radiaux et au milieu un stator de moteur asynchrone.

A l'avant on peut voir le rotor extérieur.



Maquette de démonstration

Le contrôle axial des machines se fait généralement grâce à une butée à double effet.

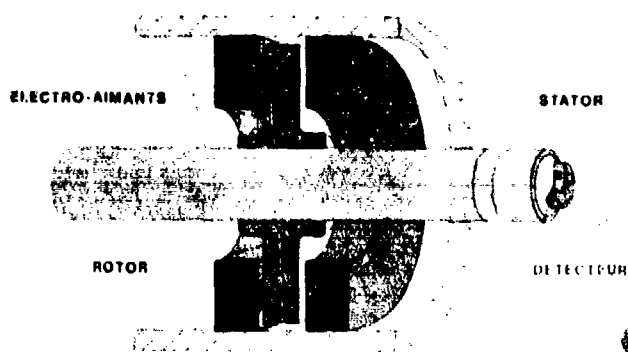
Dans le cas des paliers magnétiques, le stator de la butée est du type annulaire (parties rouges) ainsi que le bobinage. Le feuilletage de la butée est fait par sciage et remplissage des fentes par des tôles ferro-magnétiques.

Les valeurs d'entrefer sont similaires à celles de paliers radiaux.

Le rotor se compose en général d'un volant réalisé dans un matériau massif très résistant ce qui permet des vitesses linéaires jusqu'à 400 m/s. Le volant n'a pas besoin d'être feuilleté car la butée n'est pas le siège, en rotation, de changement de magnétisation, donc de pertes par courants de Foucault.

La charge spécifique est la même que pour les paliers radiaux avec, en plus, le fait que toute la surface est utilisée en projection (à l'inverse du palier radial qui est affecté par sa cambrure).

BUTÉE AXIALE A DOUBLE EFFET

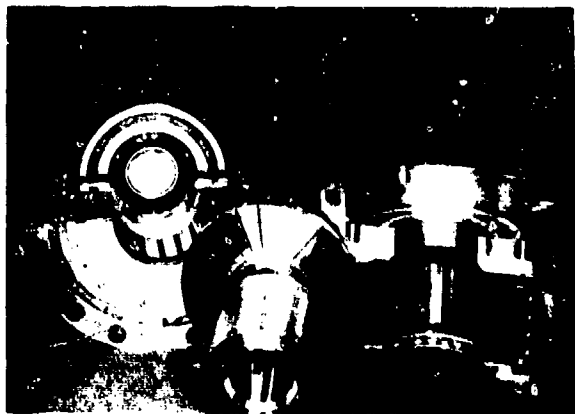


Coupe butée axiale

Pour quelques applications où la compacité de la machine doit être particulièrement soignée, on utilise des tôles en Fe-Co (51% Fe, 49% Co) qui permettent d'avoir des charges spécifiques de 8 daN/cm² à 14 daN/cm² (l'inconvénient majeur de ces tôles est leur prix).

Les entrefers des paliers magnétiques actifs varient de 0,3 mm à 1 mm ou plus, suivant le diamètre du palier (50 mm jusqu'à 1 000 mm). Ces valeurs, grandes par rapport à celles rencontrées dans d'autres paliers, ne nécessitent pas des usinages précis (une finition de tour est en général suffisante).

Les bobinages des électro-aimants, plus simples que ceux des moteurs électriques, utilisent néanmoins la même technologie et les mêmes classes d'isolation. Par contre, la simplicité de bobinage permet aussi d'utiliser des fils à isolation céramique pour les applications haute température (450°C).



Palier radial et axial type

La plupart des machines utilisent des paliers radiaux cylindriques et une butée axiale à double effet; néanmoins, dans certains cas où la compacité de la machine doit être poussée et où la charge axiale n'est pas très élevée (broches de machines-outils) on utilise des paliers coniques.

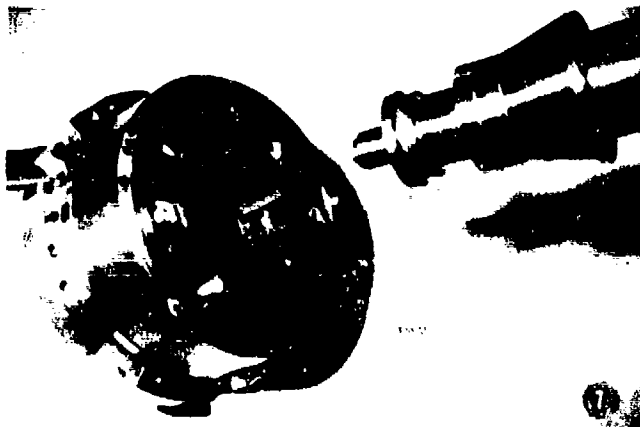
Dans ce cas on utilise les deux composants de la force magnétique pour réaliser simultanément le contrôle radial et axial. Par contre, la détection reste découplée.

Sur cette image on peut reconnaître l'ensemble technologique des paliers magnétiques actifs.

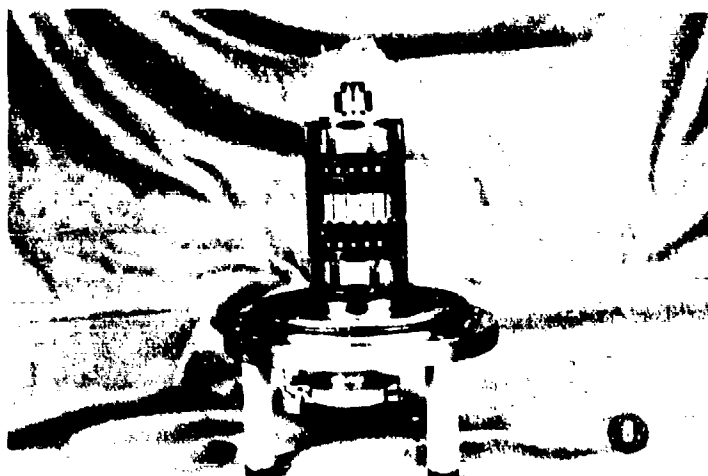
Le rotor du palier radial avec les tôles palier et détecteurs, et le volant de butée.

Le stator du palier radial est réalisé avec plan de joint pour des questions de montage ainsi que la couronne de détection.

On distingue dans le fond la butée axiale et son feuilletage et sur la droite une butée axiale en deux parties avec plan de joint et bobinage "haricot".

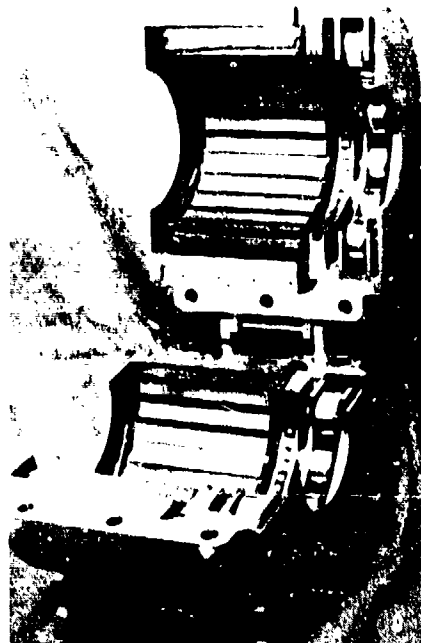


Palier conique



Roulements auxiliaires-Stator intérieur

Pour protéger les parties électromagnétiques pendant l'arrêt des machines ou en cas de panne de l'électronique, ou en cas de surcharge du palier, on utilise en général des paliers auxiliaires de secours.



Roulements auxiliaires-Galets

Ceux-ci sont le plus souvent des roulements à billes à cage massive et lubrifiés à sec. Naturellement, en fonctionnement nominal, ils sont immobiles, un jeu égal à la moitié de l'entrefer du palier magnétique les séparant du rotor.

A noter que ces dispositifs auxiliaires ne sont pas sollicités en cas de panne de secteur, le relais étant assuré par une batterie de secours.

Dans le cas de paliers avec plan de joint, les roulements sont alors remplacés par des galets eux-mêmes montés sur de petits roulements.



Armoire électronique

L'armoire électronique associée à la suspension magnétique présentée ici est du type E100, c'est-à-dire que les amplificateurs de puissance alimentant les bobines ont pour caractéristiques tension courant 80 V, 125 A, soit 10 kVA. Ces amplificateurs peuvent être associés à des paliers de charge jusqu'à 10 tonnes.

Dans le haut de l'armoire est située la partie traitement du signal. A gauche l'oscillateur alimentant les détecteurs puis les cartes asservissement et optimisation de la chaîne. En haut, à droite, le système d'équilibrage automatique et les surveillances.

Les amplificateurs de puissance, au nombre de 5 doubles, car 5 degrés de liberté sont des amplificateurs travaillant en commutation à 17 kHz; le courant est obtenu par modulation en largeur du découpage de la tension d'alimentation.

Dans la partie inférieure on trouve les alimentations ainsi que les batteries qui sont logées dans le tiroir tout en bas.

On distingue deux types d'avantages pour les paliers magnétiques actifs.

Dans un premier temps examinons les avantages dus au fait que le palier est un palier sans contact et sans fluide. Qui dit sans contact, dit naturellement absence d'usure et d'entretien d'où une grande durée de vie. Rappelons que le palier permet de grandes vitesses de rotation (200 m/s) et que les progrès dans les matériaux magnétiques laissent espérer un accroissement de ces vitesses.

L'échauffement provenant du palier est très faible (pertes Joule dans les bobinages inférieurs à 50 Watts) ainsi que la puissance consommée par frottement magnétique.

Dans le cas de machines verticales, le frottement magnétique du palier est quasi nul, la butée reprenant la charge ne créant pas de pertes par frottement magnétique.

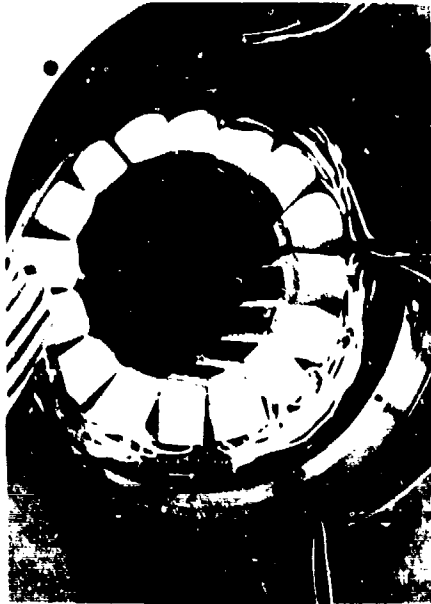
Du fait de l'absence de fluide, le palier peut fonctionner dans le vide ou dans une atmosphère corrosive sans étanchéités, ni lubrification; la seule précaution à prendre est de protéger les bobinages contre l'agressivité du milieu ambiant.

La gamme de températures couverte par le palier est très grande; nous avons même réalisé des essais de la technologie jusqu'à quelques degrés Kelvin.

Les pertes par frottement magnétique des paliers radiaux qui sont liées aux pertes par hystérésis et courants de Foucault sont très faibles (environ 10 à 100 fois inférieures à celles de paliers hydrauliques ou roulements à billes).

Enfin, du fait des entrefers confortables des paliers magnétiques et de la conception originale des détecteurs de position, la précision de fabrication des parties électromagnétiques ne nécessite pas d'usinage délicat et onéreux. En effet des tolérances inférieures au centième de millimètre ne sont jamais requises.

Palier haute température



Le palier présenté ici utilise des fils de bobinage à isolation céramique, le tout surmoulé dans un ciment réfractaire. Ce palier peut fonctionner en permanence à 450°C.

La deuxième série d'avantages que présente le palier magnétique est due au fait qu'il s'agit d'un asservissement et que l'on peut donc lui faire faire un certain nombre de choses intéressantes.

L'équilibrage automatique est la faculté qu'a le système de pouvoir fonctionner autour de son axe d'inertie plutôt qu'autour de son axe géométrique. En effet, la notion de balourd n'est rien d'autre qu'un mésalignement entre l'axe géométrique de la machine, donc des paliers, et son axe d'inertie.

L'électronique de calcul détecte les perturbations provoquées par le balourd car elles sont synchrones avec la vitesse de rotation du mobile. L'axe de rotation est automatiquement déplacé afin d'annuler ces forces perturbatrices. Le mobile tourne ainsi autour de son axe d'inertie, aucune vibration n'est transmise au stator. Ce procédé particulier a un très grand intérêt : il permet de maintenir en permanence la machine autour de son axe d'inertie même si le balourd évolue en fonction de la vitesse, de la température, du temps.

De plus l'information du détecteur de position pour la fréquence concernée correspond exactement à la distance entre l'axe géométrique des paliers et l'axe d'inertie, d'où surveillance permanente du balourd et de son évolution.

Le palier magnétique actif permet un franchissement aisé des vitesses critiques, en particulier des vitesses critiques d'arbre. En effet, lors de ces franchissements, il est nécessaire d'apporter à la machine un amortissement extérieur très important. Cet amortissement obtenu par avance de phase ne doit concerner que la vitesse de rotation; pour cette raison, on utilise le même dispositif synchrone piloté par la vitesse de rotation que précédemment mais cette fois on agit sur la phase et non sur le gain de l'asservissement.

La rigidité du palier magnétique est essentiellement liée au gain électrique de l'asservissement, élément réglable. En particulier la rigidité statique du palier magnétique est très grande; en effet, grâce à un contrôle intégral de l'asservissement, les rigidités statiques couramment atteintes sont de 50 daN/micron pour électrobroches de machines-outils jusqu'à plusieurs tonnes/micron pour des rotors lourds (poids supérieur à 100 kg).

L'asservissement électronique du palier magnétique permet de surveiller en permanence la machine. Les informations des détecteurs de position informent des mouvements du mobile dans une très large bande passante (du continu jusqu'à 2 000 Hz). Ces informations contiennent à la fois la position statique ou moyenne du rotor, son niveau de balourd et d'éventuelles autres fréquences dues soit à des perturbations aérodynamiques, soit à des perturbations extérieures (usinage dans le cas des électrobroches de machines-outils).

Les informations courant dans le palier sont naturellement une image parfaite des efforts appliqués au palier, poids ou perturbations extérieures. Par exemple la charge d'une butée axiale peut être surveillée et mesurée en permanence; les efforts appliqués aux paliers dans le cas de la machine-outil peuvent être utilisés pour la commande adaptative.

Le signal de référence de l'asservissement définit la position du rotor. La modification électronique de cette référence permet donc le déplacement du rotor dans son entrefer. Dans de nombreux cas d'usinage précis cette possibilité est très précieuse.

Dans le cas d'électrobroches de machines-outils on cherche à avoir la raideur la plus élevée possible que l'on atteint en augmentant au maximum la fréquence de résonance de l'asservissement.

Dans le cas de grosses machines, même si la fréquence de résonance n'est pas très élevée, la rigidité importante est obtenue grâce à la masse.

Exemples de raideur



Applications de paliers magnétiques réalisées à ce jour

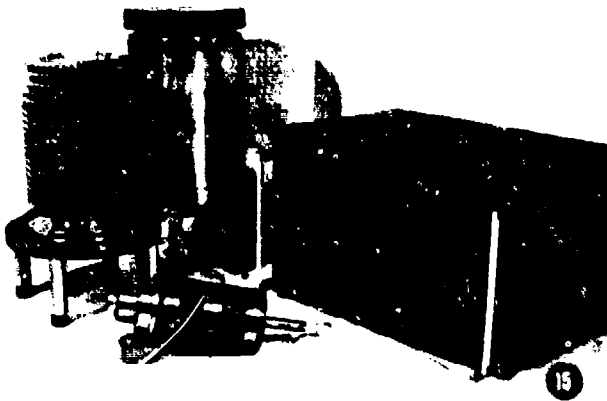
Volant d'inertie

Ici il s'agit d'un système de restitution d'images type VIZIR.

Sur le tambour est fixé un film photographique. Ce film est impressionné par un rayon laser modulé par les informations numériques en provenance des satellites ou de bandes magnétiques enregistrées.

La qualité de l'image, 15 000 lignes et 15 000 points par ligne pour un format 40 cm x 40 cm, nécessite une précision de rotation de 10^{-6} à 1 200 tr/mn. Les paliers magnétiques ont été choisis pour leur faible frottement et surtout pour la constance de ce frottement. L'asservissement de vitesse qui module la tension du moteur permet d'atteindre la précision demandée.

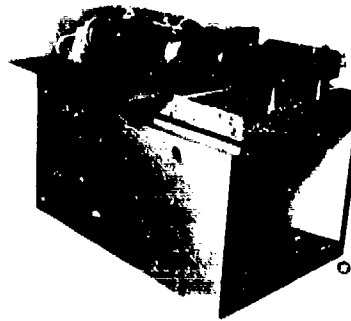
Une vingtaine de matériels de ce type sont actuellement utilisés dans le monde (Europe, Brésil, Inde, etc...) pour la météorologie et les applications de détection des ressources terrestres.

Pompe turbomoléculaire

Cette image présente un volant d'inertie réalisé pour une entreprise américaine. Pour piloter de gros satellites on a besoin de disposer de volant d'inertie à fort moment cinétique (100 Nms). Ce moment cinétique (produit $I\omega$) a intérêt à être obtenu avec ω élevé et I faible, chaque kg embarqué coûtant très cher.

Pour cela on a développé une roue de 3 kg en béryllium tournant à 12 000 tr/mn.

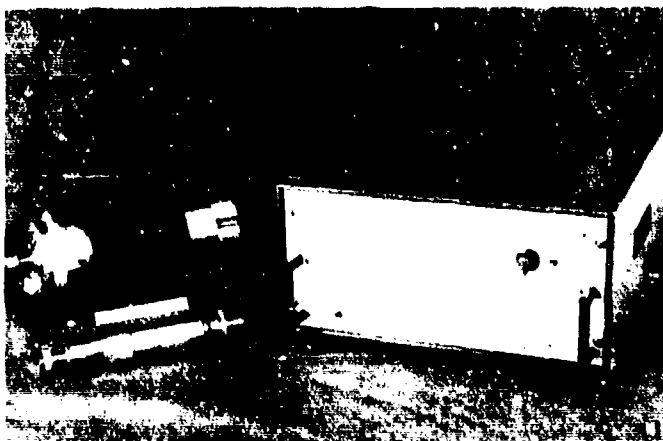
Le palier magnétique présente aussi l'avantage de fonctionner dans le vide et d'y avoir une grande fiabilité. Enfin la puissance consommée à pleine vitesse est de 15 Watts, valeur tout à fait intéressante.

V I Z I R

Pompe à vide à effet turbomoléculaire. Rotor vertical en alliage léger (8 kg) tournant à 30 000 tr/mn dans le vide. Fonctionnement à 120°C. Entraînement par convertisseur statique 520 Hz, 1 kVA.

Intérêt du palier magnétique : absence totale d'hydrocarbures pour les applications de spectrographie de masse. Absence totale de vibrations (déplacement du carter inférieur à 200 Å) pour les applications microscopie électronique. Augmentation du nombre d'étages de compression, de la vitesse de rotation d'où plus grande vitesse de pompage et plus grand taux de compression.

Ce matériel est fabriqué en série. 250 équipements de ce type ont été actuellement vendus.



Domaine de la machine-outil

Ce matériel est une électrobroche
75 000 tr/mn, 5 kW pour fraisage nid
d'abeilles ou rectification.

Electrobroche B 5/1250



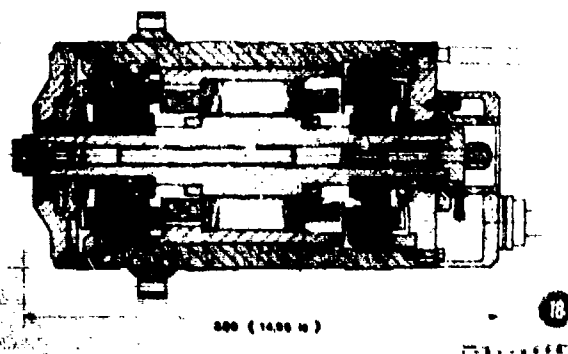
Electrobroche B10/1000

Pour le fraisage de l'aluminium à haute vitesse on a développé une électrobroche 60 000 tr/mn, 15 kW, que l'on aperçoit ici devant son armature de contrôle. La capacité de charge au nez de broche est de 35 daN dans toutes les directions, la raideur statique atteint 40 daN/micron.

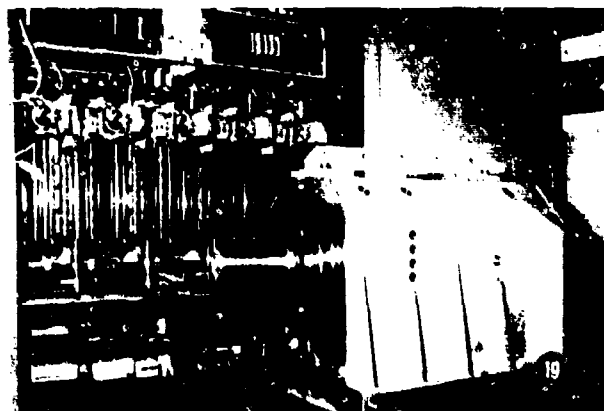
Sur le plan en coupe on distingue les paliers coniques de la machine. Le détecteur axial est situé près de l'outil pour laisser l'arbre se dilater librement vers l'arrière.

L'outil est fixé par un cône faible pente et une barre de rappel élastique.

Le moteur est refroidi par un circuit d'eau au stator et par un balayage d'air au rotor. Celui-ci pressurise la machine à 0,3 bar ce qui assure aussi la protection contre les entrées de copeaux.



Plan électrobroche B10/1000

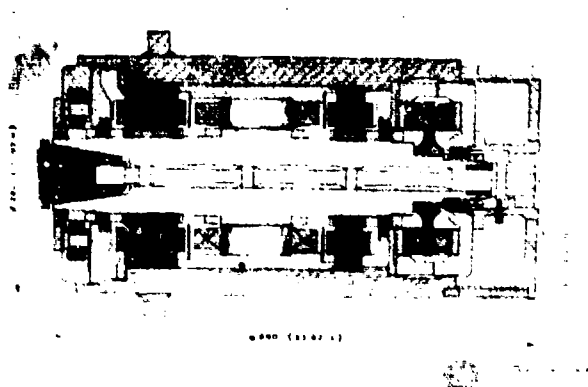


Electrobroche B20/500

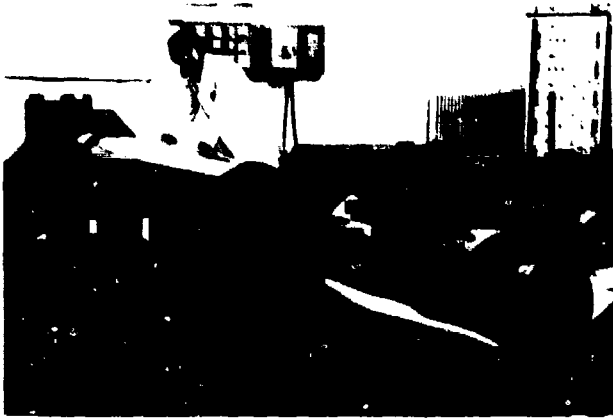
La troisième électrobroche standard appelée B20/500 a une vitesse nominale de 30 000 tr/mn et permet de monter des outils de \varnothing 30 jusqu'à 100 mm. La puissance disponible sur l'arbre est de 20 kW.

La coupe de la machine montre que cette version utilise des paliers cylindriques et une double butée. La charge maximale admissible au nez de broche est de 100 daN dans toutes les directions avec une rigidité statique voisine de 60 daN/micron en radial et de 200 daN/micron en axial.

L'attache de l'outil est une cône SA45.



Plan électrobroche B20/500



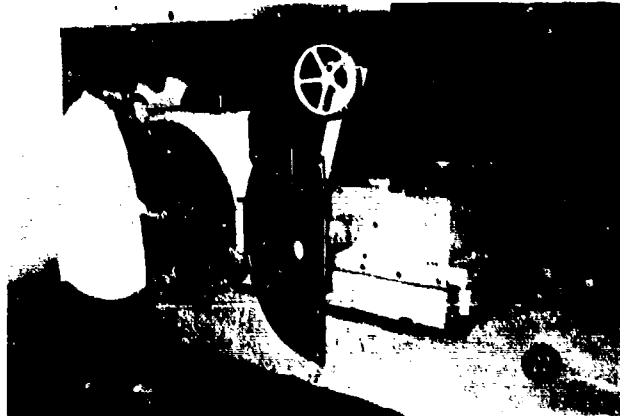
Tour de précision

Cette image représente un tour de précision pour l'usinage de cylindres d'imprimerie de 600 à 3 000 kg. Les détecteurs des paliers magnétiques qui sont clampés sur les extrémités du cylindre utilisent comme référence les bagues des roulements des paliers de rotatives. Quelle que soit la qualité du montage des paliers la précision de rotation du cylindre est voisine de 0,5 μ . De plus, l'absence d'échauffement du palier évite la mise en conicité du cylindre (vitesse de rotation 200 à 1 500 tr/mn).

La simplicité de montage et l'efficacité de la suspension magnétique associées à un usinage à l'outil diamant ont permis de réduire de 7 heures à 45 minutes le temps d'usinage d'un cylindre.

Intérêts du palier magnétique : grande fiabilité des paliers, grande précision de rotation, équilibrage automatique du porte-meule, déplacement électrique de l'axe pour usinage de bombés. Machine en cours d'essai de qualification.

Masse du rotor 300 kg plus la meule en porte-à-faux.



Porte-meule de rectification pour cylindre de laminoir

Cette vue montre la pivoterie à paliers magnétiques d'une soufflante d'hélium chaud réalisée avec des paliers fonctionnant à 450°C.

Cette soufflante est montée sur une boucle d'essais de matériels fonctionnant dans de l'hélium à 900°C destinés au réacteur nucléaire allemand HTR.

Le mobile pèse environ 260 kg et tourne à faible vitesse 1 800 tr/mn.

L'intérêt évidemment du palier magnétique est sa possibilité de fonctionnement à haute température par utilisation de bobinage à isolation thermique.



Soufflante haute température

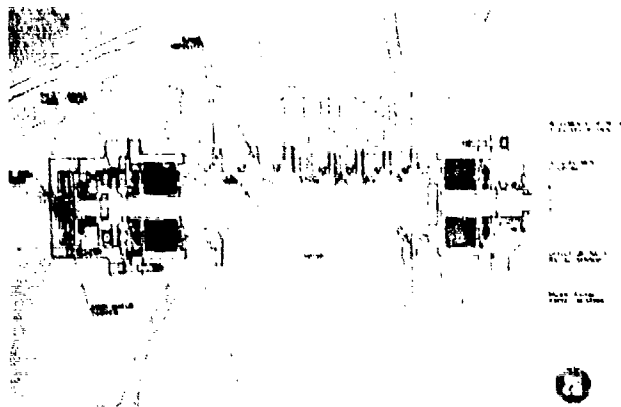
Il s'agit ici d'une réalisation de compresseur centrifuge.

Le rotor de 300 kg tourne à 1 300 tr/mn au-delà de sa troisième vitesse critique (10 000 tr/mn).

La puissance du compresseur utilisant Broues de compression est de 5 000 kW.



Compresseur centrifuge 5 MW-13 000tr/mn



Plan type de compresseur

Les intérêts du palier magnétique dans ce type d'application sont les suivants :

- suppression de l'huile et des problèmes qui s'y rattachent
- suppression de certains étanchéités
- grande vitesse de rotation pour des arbres très rigides
- franchissement aisé des vitesses critiques
- équilibrage automatique donc suppression des vibrations et des fatigues de structure
- surveillance permanente de la machine, charge de la butée, balourd, etc...

Le palier magnétique est particulièrement intéressant dans le cas d'applications machines tournantes moyennes type compresseur.

L'image représente la coupe de ce que pourrait être un compresseur centrifuge.

Côté gauche, côté haute pression, le palier radial et la butée sont directement dans le gaz de process, dans les conditions de température et de pression. Entre le palier et les étages de compression pas besoin d'étanchéités.

Côté basse pression, seule subsiste l'étanchéité de la sortie d'arbre.

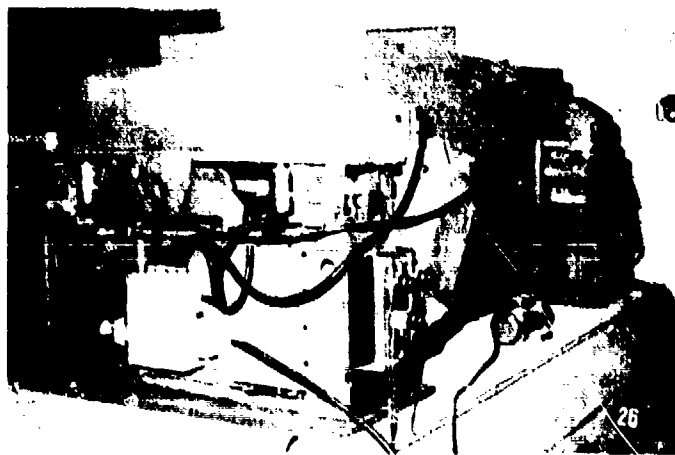


Table stabilisée dans l'espace

Table stabilisée dans l'espace.

Cette table sert de support à un cylindre réalisant le dépôt de gélatine sur les films photographiques.

Il était donc impératif de disposer d'un matériel très bien découplé du sol et pouvant résister aux efforts de traction du film.

L'asservissement de cette table de 6 tonnes utilise d'une part un asservissement de position contre le sol à très faible bande passante (2 à 3 Hz), ce qui permet d'être découplé environ 100 fois sur le 50 Hz venant des vibrations des machines électriques à proximité et d'autre part d'un asservissement contre l'espace par utilisation de capteurs accélérométriques montés sur la table.

DISCUSSION

W.B. Rowe, Liverpool Polytechnic, UK

Would you please comment on the requirement for safety in the case of overloading beyond the maximum design load. This is particularly important for a high speed spindle to prevent disastrous failure.

Author's Reply

As safety device there are first batteries (for 5 minutes or more) and against overload of the maximum design load there are conventional roller bearings specially designed to bear very high loads with high acceleration for a short time.

M.A.H. Sequeira, Portuguese Oil Company, Po

The magnetic bearing it seems to be the ideal solution for almost all problems. They don't need lubrication and we don't have wear problems, friction losses, etc.

However, there should be a problem - *The Cost*. Do you have any comparisons of costs of hydrodynamic and magnetic bearings?

Author's Reply

It is necessary to consider the cost on an economical point of view and also not only the product but the whole devices it is necessary to associate in order to let it run well (we think of oil installations, safety devices, cubicles, pipes... for oil bearings).

About the cost itself, the *price* is twice as much for small machines (< 1 ton) and in the same range for bigger shafts (the biggest is the best up to 10 tons today).

BUT as far as *working expenses* are concerned, the energy we need to let the bearings run and to overcome the "wear" and "friction" is negligible. For example the need for a 1 ton rotor running 10 000 rpm is 2 kW (1 kW for friction at 1 kW for the electronics) (about 80-100 kW for the same hydrodynamics bearings). Thus it is possible even to save up to a few percents in the efficiency of the machine.

J.B. Medley, University of Waterloo, Ca

Are you aware of any work on combining magnetic effects with liquid lubricant bearings?

Author's Reply

Combining magnetic effects with liquid lubricated bearings at the end of a long shaft improves damping when passing through critical speeds.

Application is a "S2M" 5 ton bearing designed for a long turbogenerator shaft.

K.J. Brown, Ontario Hydro, Toronto, Ca

Could you please comment on the use of those bearings in steam and water and also how the dynamic characteristics compare with cylindrical and tilting-pad journal bearings.

Author's Reply

- (1) Active magnetic bearings "ACTIDYNE" can work in steam and water only taking care of oxidation of magnetic metal sheets. In order to avoid it, it is possible to use stainless steel sheets or to protect stator polar surfaces or put in a jacket containing the rotor and fluid.
- (2) Dynamic characteristics are very good due to the fact that it is a controlled (electronically) and active (and no reactive) bearing. Both axes are decoupled and completely independently controlled. Thanks to the PID regulation there is a very good stiffness and very high damping coefficient (enabling to pass through critical speeds). Furthermore this stiffness is independent of rotation speed and direction.

AN INVESTIGATION OF SQUEEZE-FILM DAMPERS
IN FLEXIBLE SUPPORT STRUCTURES

Holmes, R. and Dogan, M.
University of Sussex
Brighton, U.K. BN1 9QJ

SUMMARY

Squeeze-film dampers are a means of reducing vibration amplitudes in rotating-shaft assemblies. Their efficiency depends very much on the condition of the oil, which in turn depends on inlet and outlet arrangements, on damper geometry and on the flexibility of the rotor and surrounding structure. The work discussed in this paper concerns rig investigations in which structural flexibility is included experimentally and comparisons are made between measured and predicted vibration results.

INTRODUCTION

In two previous papers (refs. 1 and 2), the performance of a squeeze-film damper unassisted by any retainer spring was examined between a rigid rotor and its rigid bearing pedestals. In many gas turbine applications, however, both rotor and pedestals are flexible, the latter to the extent that the first two rotor-pedestal critical speeds are essentially bounce modes, in which the rotor does not bend to any significant degree. Instead, on increase in speed the rotor often vibrates first in a symmetric and then in an anti-symmetric mode, while the pedestals are the only elements to show any appreciable degree of dynamic deflection. For such systems a squeeze-film damper interposed between one or more of the rolling-element bearings of the rotor and the pedestals can contribute a degree of damping which may enable the passage of the system through such critical speeds without vibration becoming excessive, and inhibit possible rotational instability.

It is not uncommon in gas turbines for the antisymmetric mode of vibration to exhibit a node near one of the rolling-element bearings. With such an application in mind, a test rig (fig. 1) was designed and built, which afforded the investigation of the squeeze-film damper 1 at one of its two rolling-element bearings 2, the other bearing 3 being of the self-aligning variety. This constituted a pivot about which an antisymmetric (i.e. conical) mode of vibration would occur, when the rotor 4 was acted upon by a force arising from rotation of the unbalance mass 5. The test rig was provided with flexible bars 6, which simulated the pedestal flexibility of an actual engine. Alternatively, the squeeze 7 could be pedaled by the special clamps 8 to avoid investigation of the squeeze-film damper alone. A heavy foundation block 9 was provided which represented ground and into which the flexible bars were screwed. Oil of 21 cp viscosity was supplied to the damper via three supply holes 10 and a central circumferential groove (fig. 2). End plates were attached at the ends of the outer element of the damper to afford some sealing, the extent of which could be varied by the insertion of spacing shims. The squeeze-film dimensions were set by the outer diameter of the rolling bearing (136 mm), the damper land length (9 mm) and its radial clearance (.216 mm).

Proximity vibration pickups were used to measure the vibration of the shaft relative to the pedestal and relative to ground. A pressure transducer was placed at a mid-land position at the base of the squeeze film to measure dynamic pressure in the oil under operating conditions and a thermocouple was also provided there to record oil-film temperature. The presence of the flexible bars allowed convenient recording of transmitted force by the provision of strain gauges.

This paper describes investigations into the performance of the damper and a comparison of experimental findings with numerical predictions. For the latter, the numerical method developed in reference (2) was used. This was based on the short-bearing approximation applied to the Reynolds equation to describe the pressure field in the squeeze film and required the clearance between the end plates and the inner member of the damper to be wide enough to enable the assumption of atmospheric pressure at the ends of the damper to be used.

In reference (2) it was shown that the independent parameters of the squeeze-film damper could be presented in terms of three non-dimensional groups, namely

$$Q = P/mc\omega^2$$

$$Q_c = P_c/mc\omega^2$$

and

$$\beta = \frac{\eta R}{m\omega} \cdot \left(\frac{\ell}{c}\right)^3,$$

in which P is the static load, usually provided by gravity, which for one land of the damper was 147 N, m is the effective mass of the rotor at each land (12.25 kg), c is the radial clearance in the damper (0.216 mm), R is the radius of the inner member of the damper (68 mm), ℓ the damper land length (9 mm) and η the oil viscosity (21 cp). ω is the rotational speed of the shaft carrying the unbalance mass, which provides the required dynamic force, P_c , causing vibration. An essential requirement in the numerical computations is the specification of a cavitation pressure below which the pressure field is curtailed. This pressure was found experimentally.

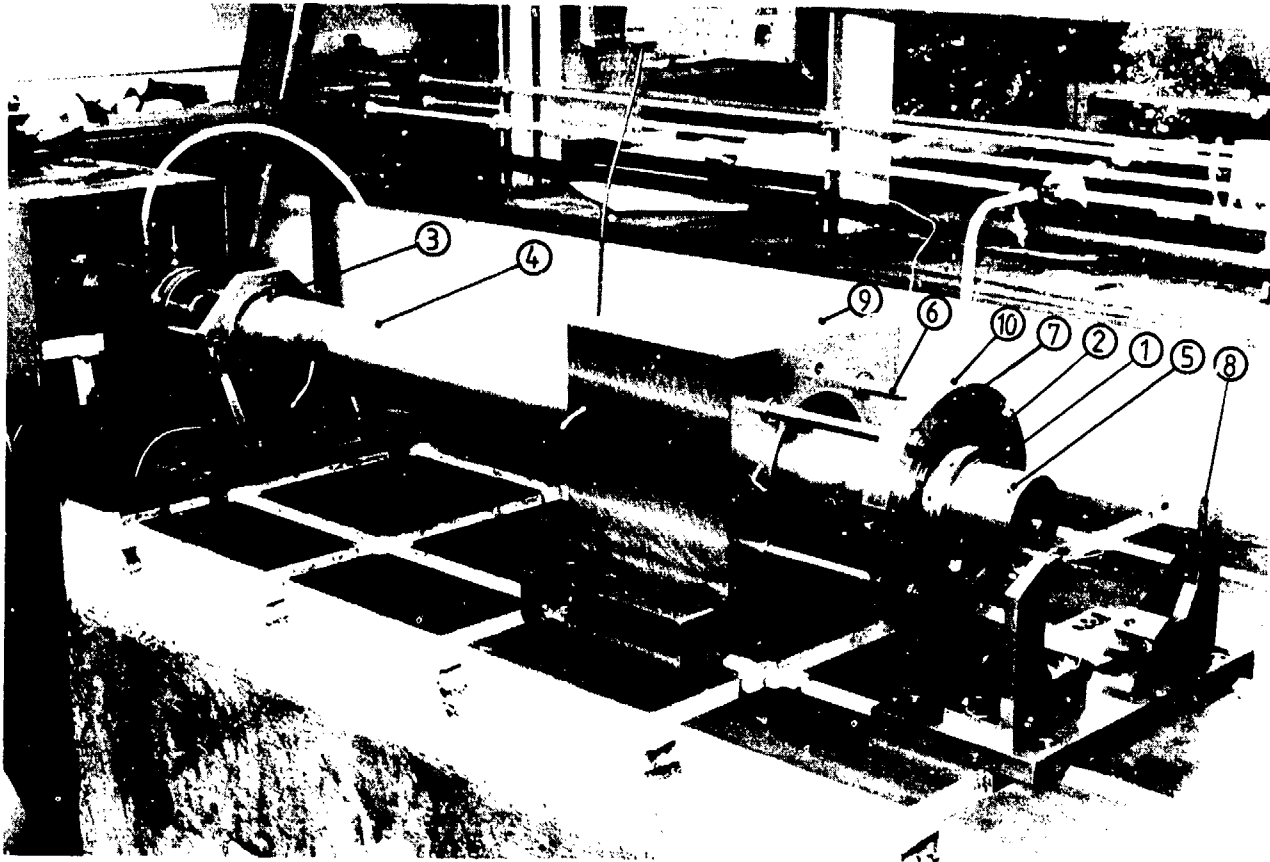


Fig. 1 : Damper Test Rig

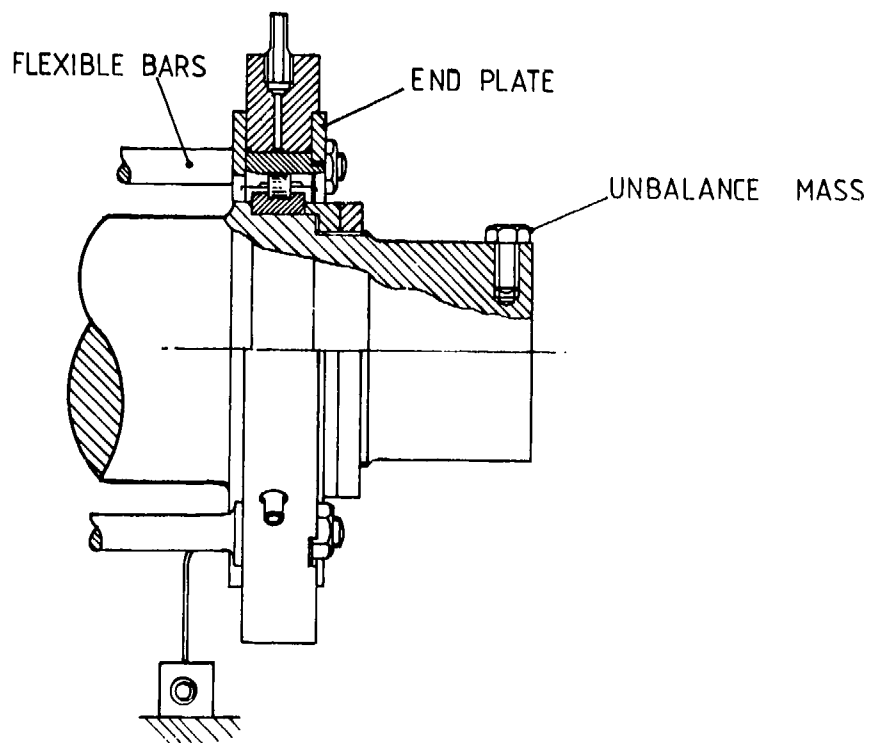


Fig.2 DETAIL OF DAMPER

TESTS WITH CLAMPED HOUSING

Firstly a series of tests was carried out with the housing clamped and details of these are given in Table 1.

TABLE 1

Tests with housing clamped

Q_c	Rotor speed rev/min		
0.229	4000	4500	5000
0.642	3000	3400	3750

As the value of Q_c was increased the top speed of the rig was successively reduced in order to avoid excessive vibration of the rolling-element bearing in the damper clearance space. The value of speed dictated the corresponding values of the non-dimensional groups Q and δ and these are given with the appropriate experimental recordings and numerical predictions shown later. An oil supply pressure of 34.48 KN/m^2 (5 lbf/in^2) was used throughout these tests to avoid excessive outflow from the ends of the damper through the rather wide end-plate clearances of 1.25 mm .

A set of experimental vibration orbits and pressure recordings is given in figure 3a for $Q_c = 0.229$. Fig. 3b shows the corresponding numerical predictions. Each numerical hydro-dynamic pressure distribution was curtailed at its experimentally-observed negative pressure limit before integration to obtain the squeeze-film forces which acted on the rotor to produce the orbit of vibration. Figures 4a and b show similar comparisons for a higher value of Q_c of 0.642 , and are typical of many others.

Some significant general observations can be made from these comparisons. In figure 3a, the general sizes and dispositions of the vibration orbits are well predicted, while both the experimental and numerical recordings show a reversal in position of the sharp 'tail' between 4500 and 5000 rev/min . The pressure waveforms also show good agreement in respect of general shape and height. The orbits of figure 4a are quite well predicted in general shape, size and disposition (even to the extent of showing a sudden increase in size between 3700 and 3750 rev/min). Whilst the experimental pressure waveform at 3000 rev/min is fairly well predicted, the waveform at 3400 rev/min does not show such good agreement in that numerical computations indicate a sharp positive pressure spike, which is not reproduced experimentally. It seems probable that the slightly shallower slopes of the experimental vibration orbits do not give rise to such pressures, which are very sensitive to orbit shape. An inspection of the second experimental pressure peak in a given cycle will, however, indicate a good comparison with the numerical prediction.

TESTS WITH FLEXIBLY-MOUNTED HOUSING

The housing was now unclamped, giving an undamped natural frequency of the system of about 4500 c/m . A series of tests was carried out using a Q_c value of 0.229 at speeds of 3500 , 3800 , 4200 and 4500 rev/min . In addition to obtaining vibration orbits of the rotor relative to the housing, orbits of the rotor relative to ground and polar diagrams of transmitted force were obtained. For such a configuration the mathematical model for the structure included the same damper model as previously, together with the stiffness of the bearing pedestal, but for speed of computation, neglected the relatively small housing mass which was only 14% of the effective rotor mass.

Comparisons of experimental and numerically predicted orbits are shown in figures 5 a,b and indicate good agreement. For the case of 3500 rev/min , a distorted figure of eight pattern is observed in both experimental and numerical recordings. The double loops visible in the other experimental recordings persisted over the entire periods of experimentation and those in the numerical predictions persisted up to a non-dimensional time ωt of 96 , that is about 15 revolutions, when the length of computing time became prohibitive. The general sizes, shapes and dispositions show good agreement, and the size at 4200 rev/min is observed to be larger than at the undamped natural frequency of 4500 rev/min . The pressure recordings of figure 5b also show fair agreement in shape and size. Negative 'spikes' are evident in figure 5a, indicating that the oil can temporarily support tensile forces. Such tensile forces have been discussed in reference 2.

Turning now to the vibration orbits of the rotor relative to ground (figs. 6a,b), very good agreement prevails both in size, shape and disposition and a peak vibration between 4200 and 4500 rev/min is again observed. This suggests that the squeeze-film damper has had some effect in reducing the critical speed of the system. The polar diagrams of total dynamic load transmitted from both lands show striking agreement in many respects, such as size, shape and disposition. In particular the kink in each experimental polar diagram for 3800 , 4200 and 4500 rev/min is predicted by numerical computation. These latter results give extra confidence in accepting the short bearing model of reference 2 for the squeeze film, albeit with a negative pressure curtailed at an experimentally-recorded limit.

Also shown in figure 6b are circles representing total displacements and transmitted forces when no damper is present. It can be seen that, at the lower speeds the damper is not really beneficial. However, at speeds approaching the critical speed, its benefits become apparent, especially at the undamped critical speed of 4500 rev/min where, without the damper the amplitudes of vibration and transmitted force would theoretically be

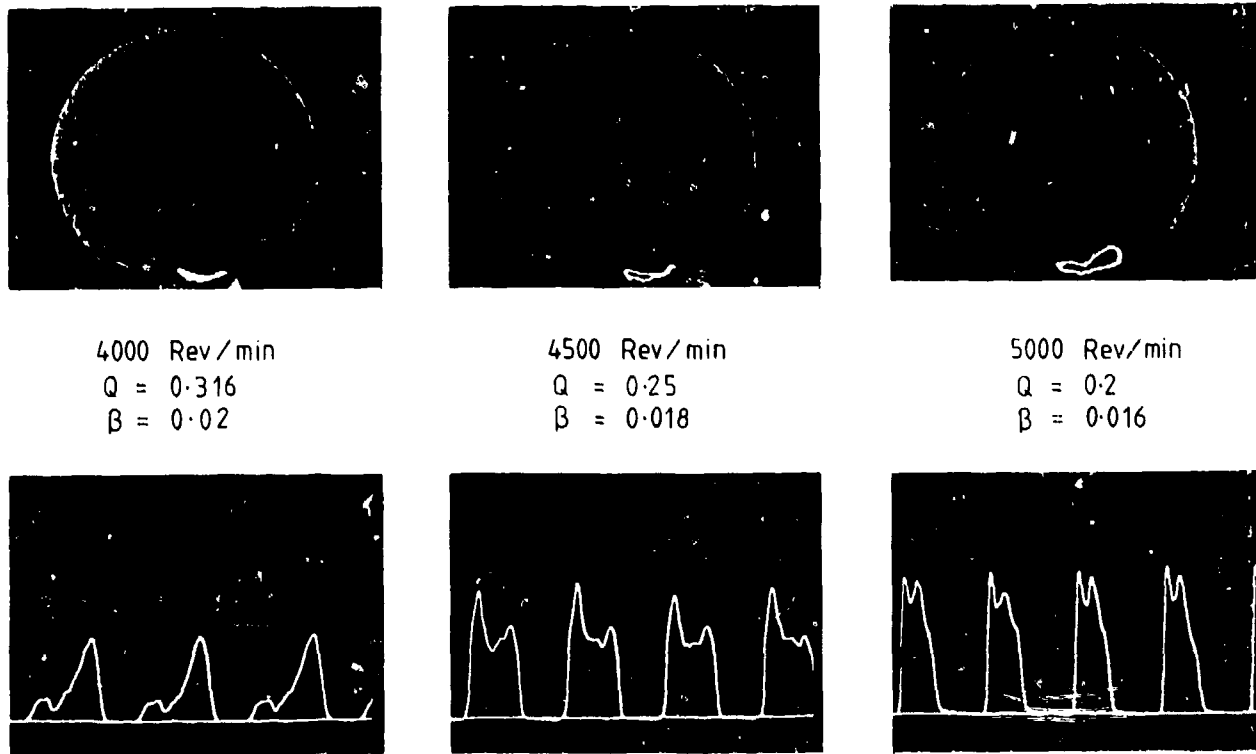


Fig 3a Experimental orbits and pressure recordings (1cm = 177 psi = 1220 kN/m²) $Q_c = 0.229$

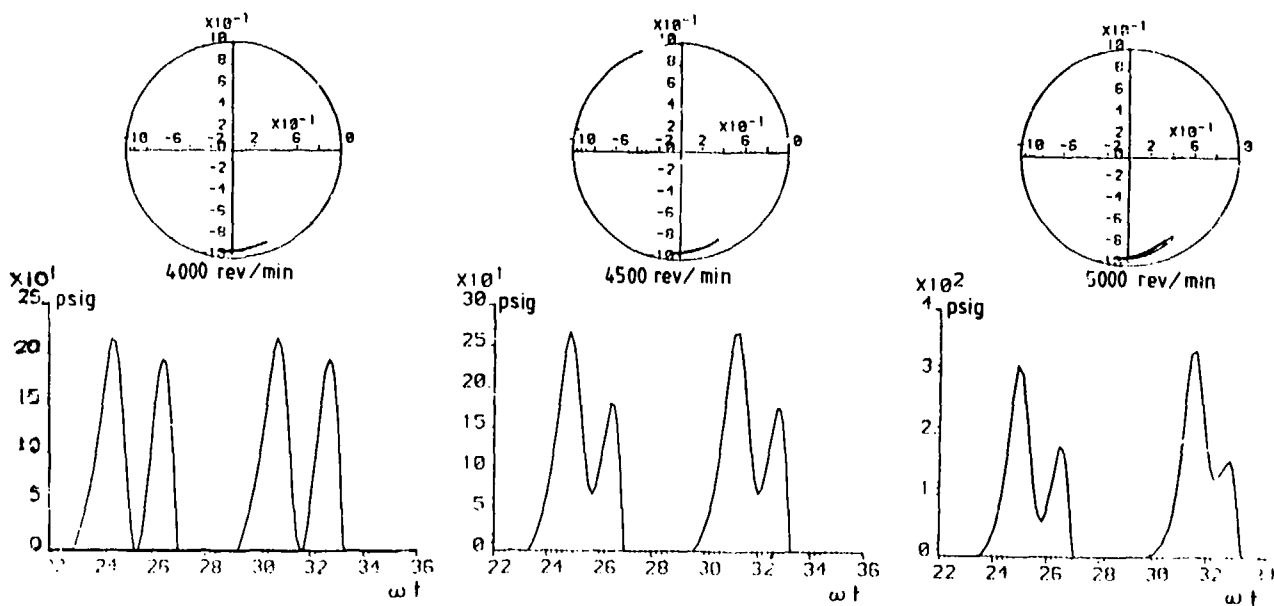


Fig 3b Numerical orbits and pressures, $Q_c = 0.229$

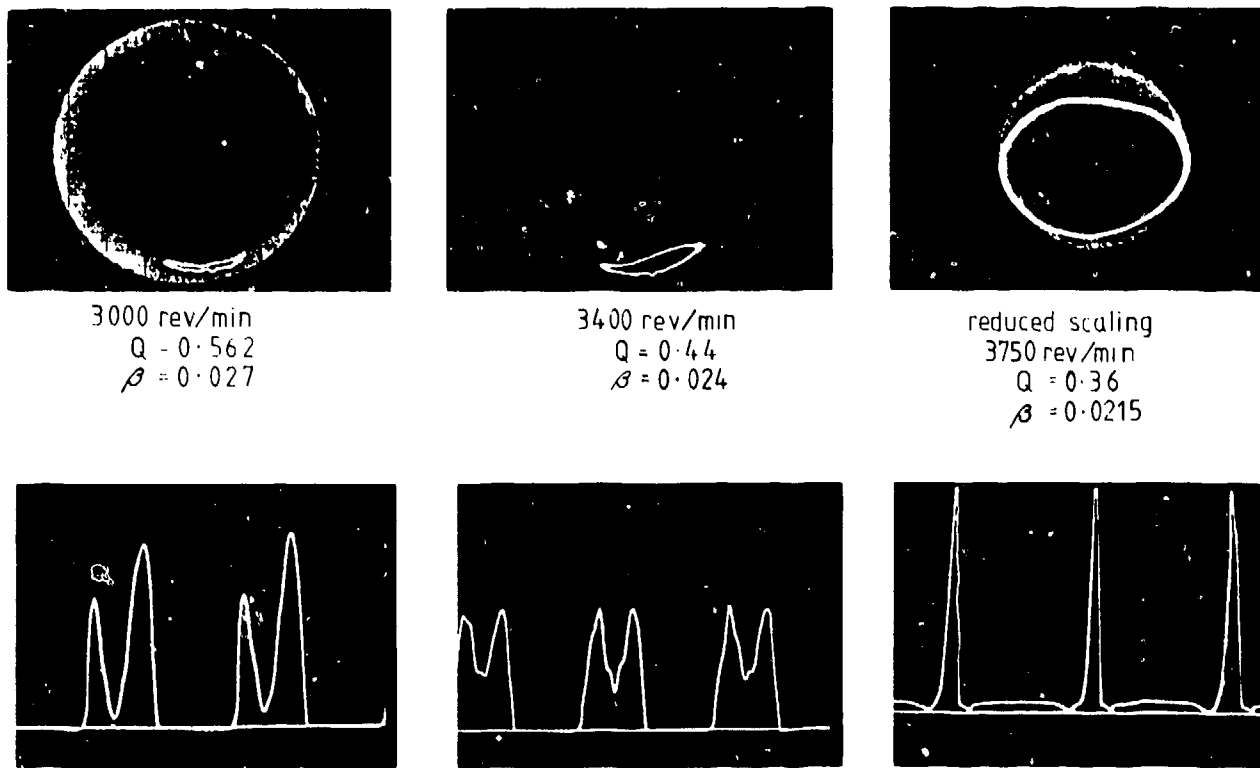


Fig 4a: Experimental orbits and pressure recordings (1cm = 177psi = 1220kN/m²) $Q_c = 0.642$

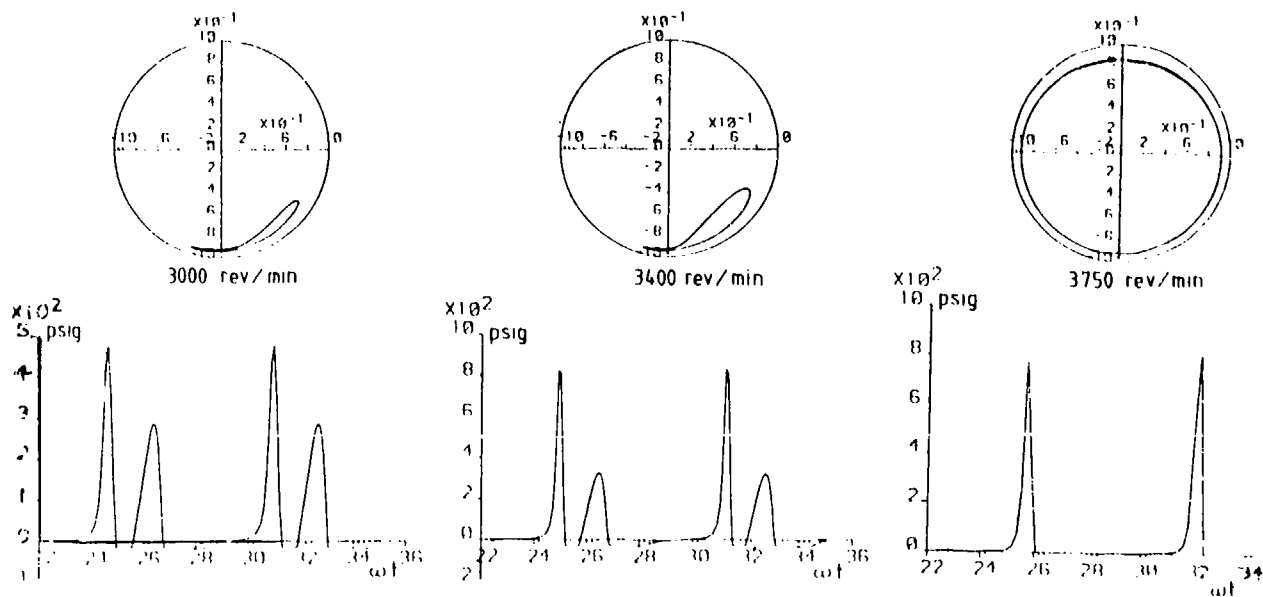


Fig 4b Numerical orbits and pressures $Q_c = 0.642$

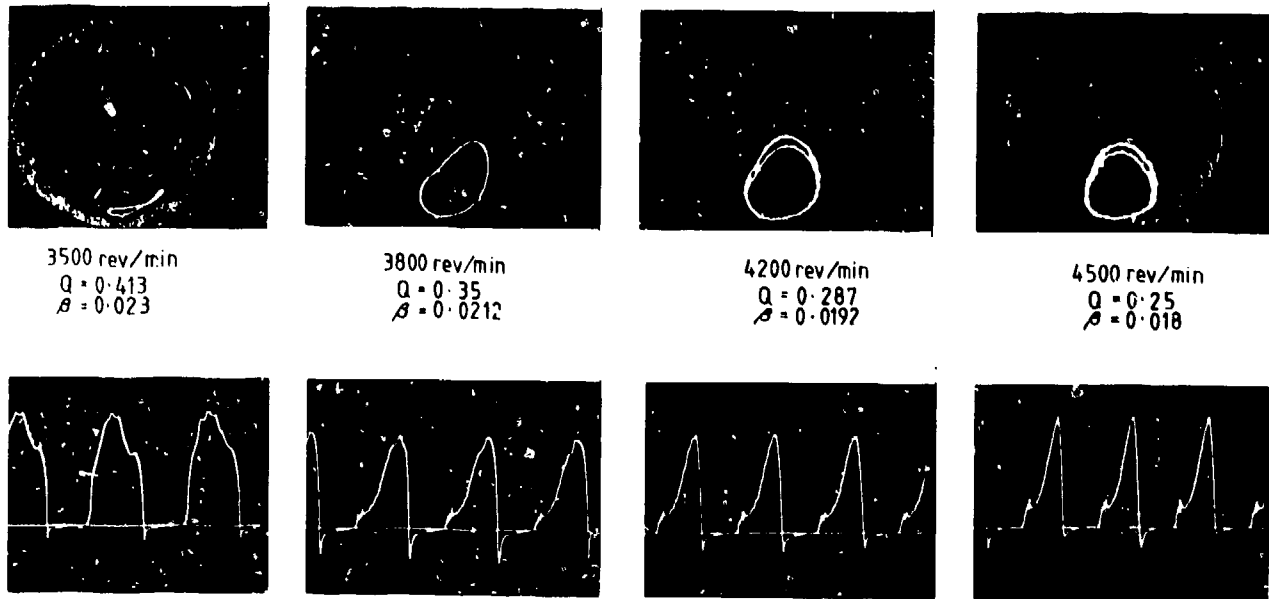


Fig 5a Experimental orbits and pressure recordings ($1\text{ cm} = 218\text{ psi} = 1510\text{ kN/m}^2$) $Q_c = 0.229$.

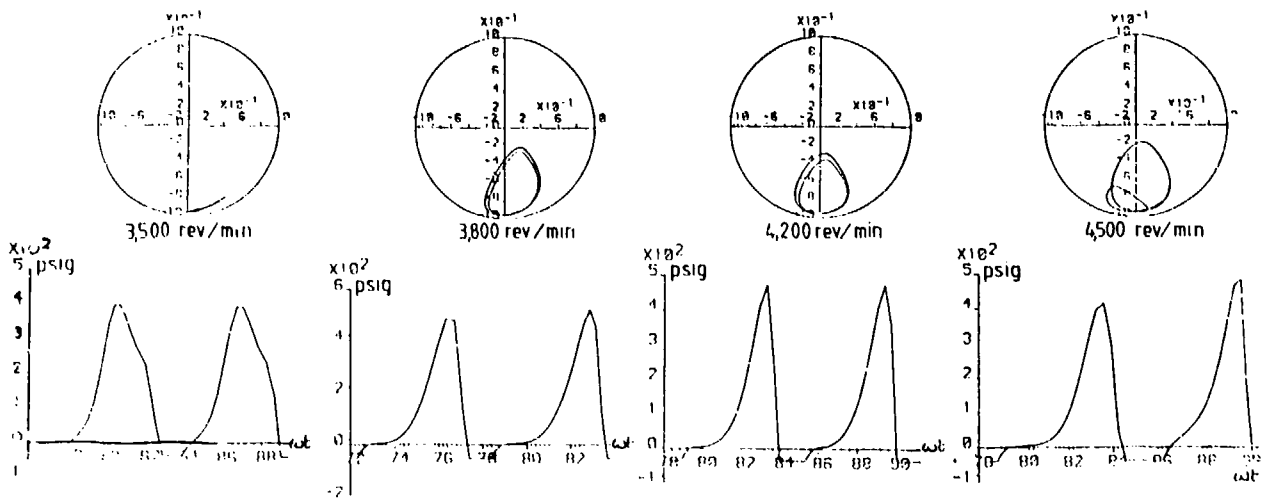
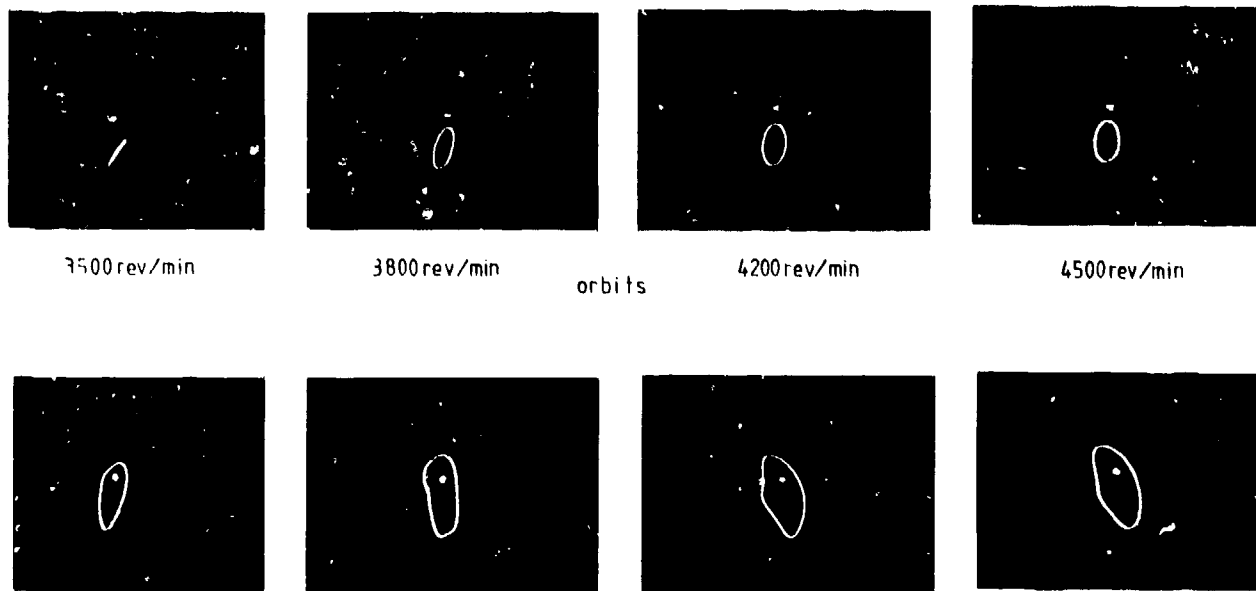


Fig 5b Numerical orbits and pressures, $Q_c = 0.229$



loads
 Fig. 6a Experimental orbits relative to ground and polar load diagrams $Q_c = 0.229$
 (1 cm = 0.65mm and 1 cm = 1290 N)

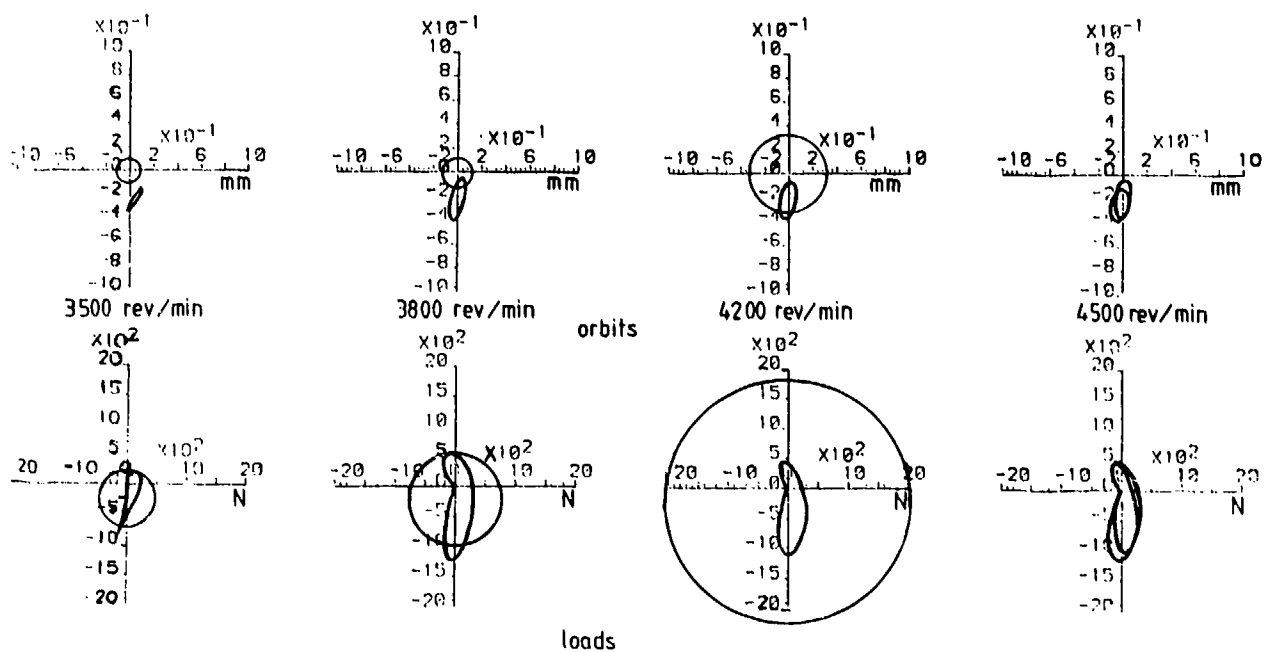


Fig. 6b Numerical orbits and loads, $Q_c = 0.229$

infinite.

CONCLUSIONS

Continuing on from experience gained on test rigs involving open-ended squeeze-film dampers interposed between rigid rotors and rigid bearing pedestals (refs.1,2), this paper has described experimental and numerical work on weakly-sealed dampers with flexible pedestals. Good agreement has been observed between experimental observations and numerical predictions over a wide range of operating parameters. These observations included vibration of rotor relative to bearing housing and relative to ground, dynamic pressure in the squeeze-film damper and transmitted force to ground. The work shows that, given the correct interpretation of boundary conditions in the damper, reliance can be placed on a mathematical model incorporating the short-bearing approximation. The benefits of such a damper can also be readily seen.

This work will shortly be extended to include the effect on the damper of tighter sealing and the use of higher supply pressures and very low oil viscosities, in keeping with present-day operational practice with gas turbines.

REFERENCES

1. Holmes, R. and Humes, B.: 'An investigation of vibration dampers in gas-turbine engines' AGARD Conference Proceedings No. 248 Propulsion and Energetics Panel's 52nd meeting, Cleveland, U.S.A., Oct. 1978, pp.17-1 to 17-10.
2. Holmes R. and Dede, M. : 'Dynamic pressure determination in a squeeze-film damper'. Proc. I.Mech.E. Paper C260/80. Second International Conference on Vibrations in rotating machinery, Cambridge, Sept. 1980, pp.71-75.

ACKNOWLEDGEMENTS

This work was performed under contract to Rolls Royce Ltd., U.K., to whom the authors are grateful for their financial support.

DISCUSSION

M. Vermeulen, State University of Gent, Be

Is the orbit influenced by the "short-time" absences of the negative pressures?

Would it be interesting to use some restrictors in the feed lines to the oil film?

(The use of restrictors would transfer to a kind of hydrostatic bearing so that the orbit will always be around the centre (even in tilted and vertical position).)

Author's Reply

The non periodic nature of the pressure waveform did not appear to cause a change in the orbit size or shape.

I agree that restrictors may prove to be beneficial if the extra hardware could be accommodated.

V. Bruno, Pratt & Whitney, Ca

(1) Would the dynamic behaviour of a vertical shaft be different from the horizontal?

(2) If so do you envisage the need for adjustable conditions of the oil supply on rotors subject to tilting maneuvers or "G" loads of various amplitude and direction?

Author's Reply

(1) The damping behaviour would be drastically altered by virtue of the change in the static-load parameter $P/mc\omega^2$, mentioned on page 31-1.

(2) While adjustable conditions may be beneficial in reducing vibration the extra complexity of hardware may be difficult to justify.

Paul Y. Kim, NRC, Ca

(1) You mentioned that the bar was locked so that only the squeeze film was activated. Could you please describe how you locked your bar?

(2) What was the critical speed of the rotor? and what was natural frequency of your support system?

(3) Your orbit seemed to be very clear. Did you use any filter? If so, what kind of filters or probes did you use?

Author's Reply

I would like to thank all the contributors for their interest in our work.

In answer to the questions of Mr Kim:

(1) The housing and bars were locked by the special clamps (8) in Figure 1, which were slid up around the housing (7).

(2) The undamped critical speed of the rotor and support system was 4500 rev/min, with some evidence of a slight reduction for certain operating conditions.

(3) No filters were needed to ensure the very clear orbits. The probes used were capacitive and manufactured by Wayne-Kerr in the UK.

B. Courage, Rolls Royce, Bristol, UK

Your tests with the bearing housing fixed in the rigid mode indicate a large orbit and presumably large transmitted locus at 3750 RPM. This implies that such a squeeze film can introduce an instability or resonance at a condition that would be stable without the film. Can a simple parameter be suggested to predict this particular phenomena and thereby avoid it?

Author's Reply

It should be emphasized that since this apparent resonance is recorded when the housing is damped, we do not have a realistic engine configuration. However, it is an important observation and it should be possible to predict when this will occur. We are at present conducting such an investigation, and it may be that some form of jump-up phenomena is manifesting itself.

W.B. Rowe, Liverpool Polytechnic, UK

A. Are restrictors used for the purposes of either:

(1) Feed of cooling oil from the squeeze film recesses to the rolling bearing.

(2) Supply of oil from the supply to the squeeze film recesses.

B. And would such restrictors be taken into account in the calculation of damping in the bearing system?

- C. Has there been any investigation of the employment of oil-fed and/or unposted recesses to promote lift-off in the uncentralized squeeze film configuration?

Author's Reply

- A. At the present time restrictors or recesses are not used to the author's knowledge for feeding rolling-element or squeeze-film bearings in aircraft gas-turbine engines. This is probably because the first priorities tend to be simplicity and reliability. However, a feasibility study would be of considerable interest.
- B. If such a bearing design were used then its damping would certainly be affected and would have to be taken into account in predicting engine vibration.
- C. To the author's knowledge no such investigation has been carried out.

SQUEEZE-FILM BEARING SUPPORT ANALYSIS

by

Prof. F.A.P. Da Silva
CEMUL
Avenida Rovisco Pais
Lisbon 1096, Portugal

SUMMARY

Squeeze film bearings operate on high frequency vibration of one the bearing surfaces. The time-averaged pressurisation effect is mainly due to the compressibility of the gas film and this degree of pressurisation depends on the amplitude and frequency of oscillation of the moving surface. If this supporting surface is sufficiently flexible, the amplitude of vibration is not uniform. An investigation on the effect of this non-uniformity on the performance of the squeeze film is presented. The characteristics of the supporting member are demonstrated to be critical as they dictated the frequency of operation at low input power. Cases considered respect discs and conical shapes. For discs a particular parameter, the ratio between the inner and the outer edges, is analysed.

1 INTRODUCTION

Squeeze film bearings cannot be considered as well established, even though work on the last fifteen years. The first reference to gas squeeze films is due to Tipler in 1954 (1). Later contributions referring to theoretical work and practical applications have been produced by Langlois (2) Sølbu (3) and Pan (4,5,6). Another research team, Beck and Strodman (7,8) also studied and provided theoretical conclusions on the influence of some parameters. Finally Cooke (9) presented a full discussion on the inclusion of grooves. However apart from a work from Huxley (10) no effort has been shown to relate the actual behaviour of the supporting member with the efficiency of this type of bearing.

2 SQUEEZE FILM BEARING COMPONENTS

A simple model for the parameters involved can be idealised as shown in Fig. 1 where the dotted lines mean an ideal boundary from which the supported member and the electric power supply are both excluded. In Fig. 2 it is shown an actual arrangement for a conical squeeze film bearing, which has been used in experiments described later. The most important elements are basically three:

- The electromechanical transducer,
- The supporting member that includes the bearing shape and any existing attachments to the electromechanical transducer
- The fluid

2.1 The Piezoelectric Transducer

The squeeze film bearing pressure effect relies on the high frequency oscillation of the supporting member. For this purpose a magnetic device was used in first applications but it was soon realised that piezoelectric ceramics were most suitable, because of the small weight and size, small power consumption, good temperature stability, low internal power losses and availability in several sizes and shapes. The only major inconvenience of piezoelectric ceramics is their mechanical instability, which causes small changes of the ceramic shape and partial loss of some of their properties with time.

The two major parameters associated with the ceramics are the type of ceramic (composition) and its shape. Materials that are currently in use are compositions of lead zirconate-barium titanate, commercially produced by the Clevite Company, Mullard and Philips.

The usual shapes for the piezoelectric ceramics are the simple disc for thrust bearings and the cylinder for the journal bearings. Cylindrical shapes require accurate tolerances and surface finish as they act directly as the supporting member. This means that the film thickness is directly dictated by the vibrational modes of the ceramic.

2.2 The Supporting Member

The mechanical expansion produced by the ceramic must usually be applied to a metallic shell acting as a moving member with the exception already mentioned.

Popular shapes have been simple discs, conical and spherical shapes, these providing radial as axial support. Conical shapes are easier to produce than the spherical ones and are a promising design in practical applications.

2.3 The Fluid

The lubricant fluid, in this case air, exist between the two bearing surfaces. Its behaviour is influenced by the clearance and the load of the supported member, and the motion of the supporting member that undergoes vibrational motion.

It dictates the main result of interest: the load capacity of the bearing.

3 EXPERIMENTAL DATA

Most authors assumed a rigid motion for the supporting member originating equal displacements along the bearing axis. Huxley (10) verified that it was not so with experiments both in conical and spherical bearings.

This brought up the question of the effect of the increased values of amplitude verified near the edge of these shapes. It is the investigation of this influence that will be now summarised:

3.1 Ceramic Characteristics

A dynamical model of the bearing is shown in Fig. 3 where the behaviour of the ceramic is that of a spring of equivalent stiffness K_c . Experiments were carried out to obtain the resonant frequency of the ceramic measuring its output signal with an applied sinusoidal force. A value of K_c of 7.73×10^{10} dynes/cm was obtained, much smaller than that predicted from the ceramic typical data, 2.28×10^{14} dynes/cm.

3.2 Conical bearing modal shapes and load capacity

An optical, non contacting device was used to measure the amplitudes of vibration along a generator. A typical station plot - Fig. 4 - shows that the frequency of resonance was 18 550 Hz with amplitudes decreasing considerably, in the range of ± 200 Hz. As the primary aim of this study was the determination of the influence of this elastic effect on the performance of the bearing axial load measurements were also made. For this purpose an externally pressurized thrust gas bearing was built. Simultaneous lift readings were also recorded by means of a wayne-kerr capacitance probe. For the low input power to the bearing it was noticed a very sharp working frequency band, (about ± 1 Hz) around 18,596 Hz. The measured values of film mean gap, load capacity and voltage applied to the piezoelectric ceramic are presented in Fig. 5.

3.3 Disc bearing experiments

Considering the close relationship between the resonant and lifting frequencies further experiments were conducted with disc shapes. Whilst this shape is of reduced interest in application considerable simplicity of manufacture with convenient surface finish control was a strong reason for its use.

Because it was interesting to obtain considerable variation of the frequency of resonance without change of shape, dimensions or masses three different specimen were used for amplitude measurements, as shown in Fig. 6, the only change consisted of a variation of the size of the small cylinder joining the supporting member to the base and designated by neck. The neck size is characterised in this study by the ratio of its radius, r_b , to the bearing radius, r_a , and designated as neck coefficient. Amplitude measurements were carried out with mild steel discs. The frequency of resonance for three cases is shown in the following Table 1

Neck Coefficient	FREQUENCY (C.P.S.)	
	Resonance	Lifting
.2	4002	4125
.4	6176	6260
.5	8567	no lift

TABLE 1

the neck coefficient values were arbitrary chosen, but it is evident the considerable stiffening effect as this ratio increases.

Lifting frequencies were recorded and also included in Table 1.

The disc with neck coefficient .5 didn't provide lift at any load but the two other cases show that resonant frequencies and lifting frequencies are closely related.

The mean gap was also measured for various power input values and applied loads, as indicated in Table 2.

4. THEORETICAL APPROACH

4.1 Conical Bearings

Full practical use if the previous findings depend on ability to predict the exact resonance frequencies of the referred bearing shapes.

For conical bearings two types of vibrations usually occur. The inextensional vibrations also called flexural vibrations with modal shapes having nodal lines coincident with the generators. When the middle surface of the shell undergoes extension the vibrations are called extensional.

The solutions of equations of motion for the combined extensional and inextensional vibrations have been first studied by Saunders at al (11). The theory was later developed by Plates (12), with the origination of a set of six equations governing the displacement of a point on the case middle plane. Integration can be performed using a procedure by Goldberg and others (13). A sliding - free edge condition was assumed. The receptance curve obtained shows that the predicted resonant frequency should occur at 17.700 Hz. The relative error between this and the actual value being 4,58%.

Neck coeff. ratio $\frac{r_a}{r_b}$	LIFT	LOAD	ELECTRICAL INPUT	
	Recorded gap at lift h_o (mm)	W (Kgf)	power (Watts)	voltage (Volts)
.2	10.0×10^{-2}	6.65×10^{-2}	.190	120
.4	22.0×10^{-2}	6.65×10^{-2}	.190	120
.4	18.5×10^{-2}	13.30×10^{-2}	.190	120
.4	17.5×10^{-2}	15.30×10^{-2}	.190	120
.5	No lift	-	.190	120

TABLE 2

4.2 Disc Bearings

For this case and because the modal shapes can be easily calculated using the theory developed by McLeod (14), a comparison between the experimental values of 3.3 and predicted load capacity was performed, Fig. 7.

To obtain the load capacity, W , from the instantaneous load capacity, W_{inst} , an integration in time must be made. As the instantaneous pressure, p , varies with the disc radius the value of W_{inst} is obtained according to (1):

$$W_{inst} = \int_0^{r_a} 2 \pi p r dr \quad (1)$$

Where p is the actual pressure value at a distance from the disc center, r , and r_a is the radius at the bearing (disc) outer edge.

Defining a nondimensional instantaneous load capacity, W_{inst}^* :

$$W_{inst}^* = \frac{W_{inst}}{\text{Atmospheric load pressure}} = \frac{W_{inst}}{\pi p_a r_a^2} \quad (2)$$

then,

$$W_{inst}^* = \frac{2}{p_a r_a^2} \int_0^{r_a} p r dr \quad (3)$$

or,

$$W_{inst}^* = \frac{2}{r_a^2} \int_0^{r_a} \frac{p}{p_a} r dr \quad (4)$$

Defining a nondimensional pressure as $p = \frac{p}{p_a}$ and the nondimensional coordinate

$$R = \frac{r}{r_a},$$

$$W_{inst}^* = 2 \int_0^1 p R dR \quad (5)$$

The time average of W_{inst}^* for one cycle of plate motion represents the nondimensional load capacity of the bearing, W^* . Using also the nondimensional variable $T = \omega t$, ω being the supporting member, and integrating for one cycle:

$$W^* = \frac{1}{2\pi} \int_0^{2\pi} W_{inst}^* dT \quad (6)$$

In terms of the actual load, W :

$$W = W^* \pi p_a r_a^2 \quad (7)$$

The usable load capacity, W_u , being:

$$W_u = W - \pi p_a r_a^2 = (W^* - 1) \pi p_a r_a^2 \quad (8)$$

The curves relating W_u with $H_c^* = \frac{h_0}{r_a}$ are shown in Fig. 8.

5. Conclusions

From the Fig. 8 the following conclusions can be drawn:

I - If the load has an imposed value, which means that the value of W^* is fixed, instead of h_0 , it is possible to conclude that the disc with 0.4 neck coefficient ratio will give the higher lift, i.e., the higher clearance between the bearing members. This is caused by the higher amplitudes of vibration for this particular neck coefficient which produce higher values of the excursion ratio, e .

II - Comparing now the behaviour of the two other cases, discs with coefficient .5 and coefficient .2, whilst the first case presents slightly higher amplitudes and therefore higher excursion ratio values, the behaviour of the .5 case is better from this point of view. The only explanation for this fact is the higher working frequency.

III - The experimental values of the load capacity, denoted by small triangles in Fig. 7.33, are lower than the theoretical ones for the same bearing clearance. One reason for this fact could be the damping effect of the air film on the disc amplitudes. Because the film thickness for the load capacity calculation is derived from the disc modal shapes, without the air film, and therefore the excursion ratio values result overestimated. This fact originates a higher load capacity than the actual one.

6. Acknowledgements

Acknowledgements are due to Dr. Ramsey Gohar of Imperial College and Mr. Huxley of A.C.O. (Slough) for unvaluable suggestions and guidance as well as the Calouste Gulbenkian Foundation (Portugal) and the S.R.C. (U.K.) for the support given and without whom this work would not have been possible.

7. References

- (1) TIPEI, N (1954) - Equatile Lubrificatiei cu Gaze - Comunicarile, Acad. P.R. Romine, 4, p. 699
- (2) LANGLOIS, W.E. (1962) - Isothermal Squeeze Films - Quart. Appl. Math., XX, (2), p131
- (3) SALBU, E.O.J. (1964) - Compressible Squeeze Films - Trans. ASME, (D) - J Basic Engineering, pp 355-364
- (4) PAN, C.H.T. (1964) - Analysis, Design and Prototype Development of Squeeze Film Bearings for AG-5 Gyroscope. MIT, Report 64-TR-66.
- (5) PAN, C.H.T. (1967) - On Asymptotic Analysis of Gaseous Squeeze Film Bearings, Trans. ASME, (F) - J. Lubric. Tech. 89, pp 245,253

- (6) PAN, C.H.T. and BROUSSARD, P.H. Jr. (1967) - Squeeze Film Lubrification. Gaz Bearing Symp., Univ. Southampton, Paper 12
- (7) BECK, J.V. and Strodman, C.L. (1967) Stability, of a Squeeze-Film Journal Bearing. Trans. ASME, (F), (J.Lub.Tech.), 89, pp 369-373
- (8) BECK, J.V. and Strodman, C.L. (1968), Load Support of Spherical Squeeze-Film Gas Bearing. ASME Paper 68, Lub 5-3
- (9) COOKE, D.D. (1974) Performance Comparisons Between Grooved and Ungrooved Squeeze Film Bearings. Royal Aircraft Establishment, Technical Report 74115
- (10) HUXLEY, A.S. (1972) Progress in Squeeze Film Technology. Paper 16, 5th Joint ONR/UK Gas Bearing Meeting
- (11) SAUNDERS, H. Winsniewski, E.J., and Paslay, P.R. (1960) Vibrations of Conical Shells. J. Acoust. Soc. Am., 32, (6), pp 765-772
- (12) PLATUS, D.H. (1965) Conical Shell Vibrations. NASA Technical Note TN-D-2767
- (13) GOLDBERG, J.E., Bogdanoff, J.L. and Marcus, L (1960) On the Calculation of the Axisymmetric Modes and Frequencies of Conical Shells. J. Acoust. Soc. Am., 32, (6), pp 738-742
- (14) MC LEOD, A.J. and Bishop, R.E.D (1965) The Forced Vibrations of Circular Plates, Mechanical Engineering Monograph No 1, March.

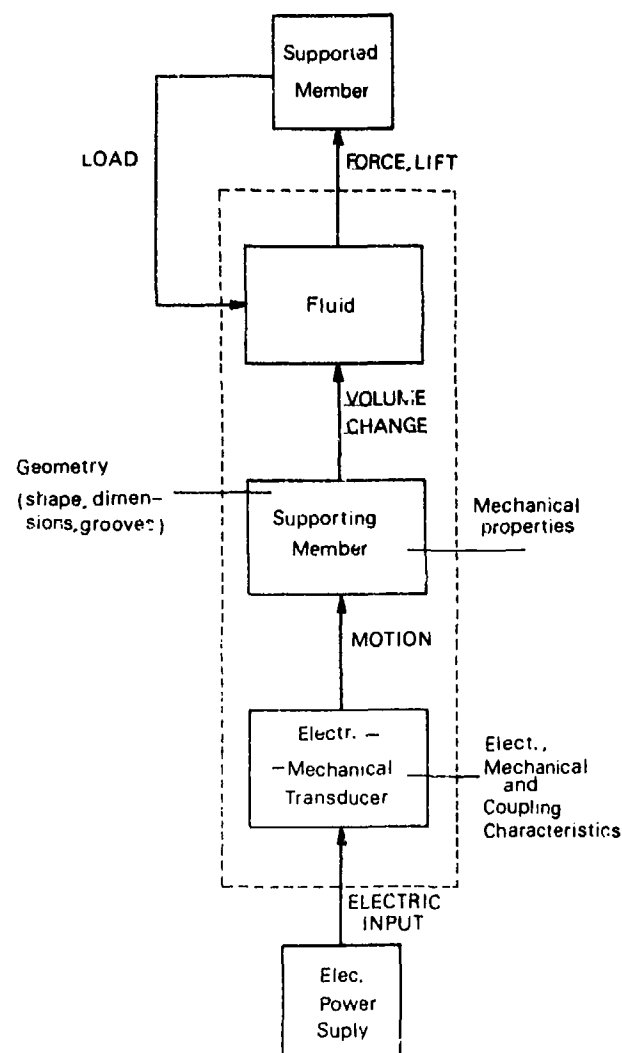
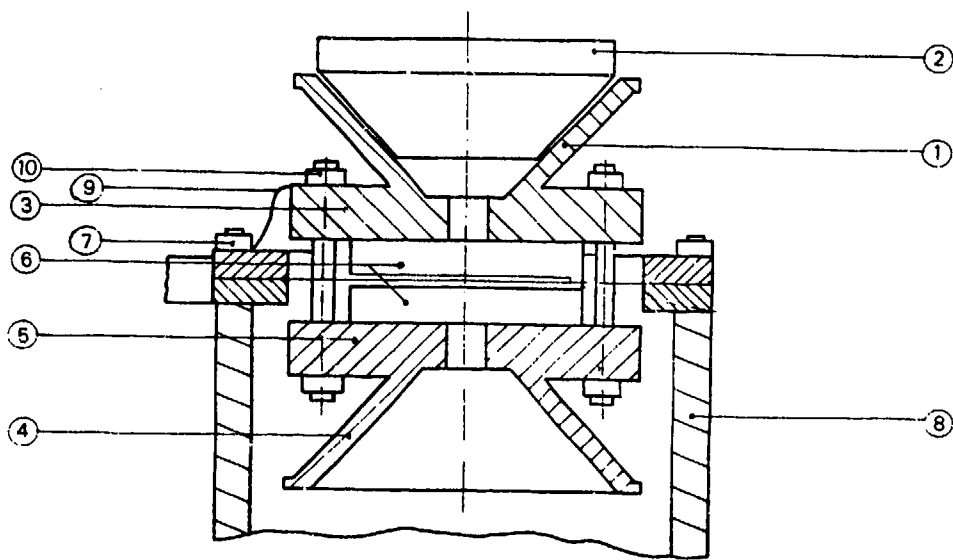


FIG. 1



Key for the figure:

1. Lower (supporting) member.
2. Upper (supported) member.
3. Supporting member base.
4. Element symmetric to (1).
5. Element symmetric to (3).
6. Piezoelectric ceramic crystal.
7. Fixing bolts.
8. Standing base (cylinder).
9. Connecting leads.
10. Bearing fixing bolts.

FIG. 2

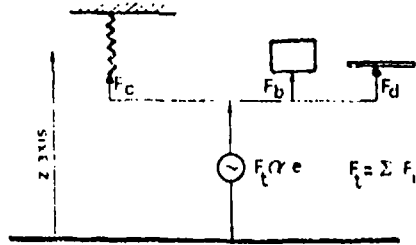


FIG. 3

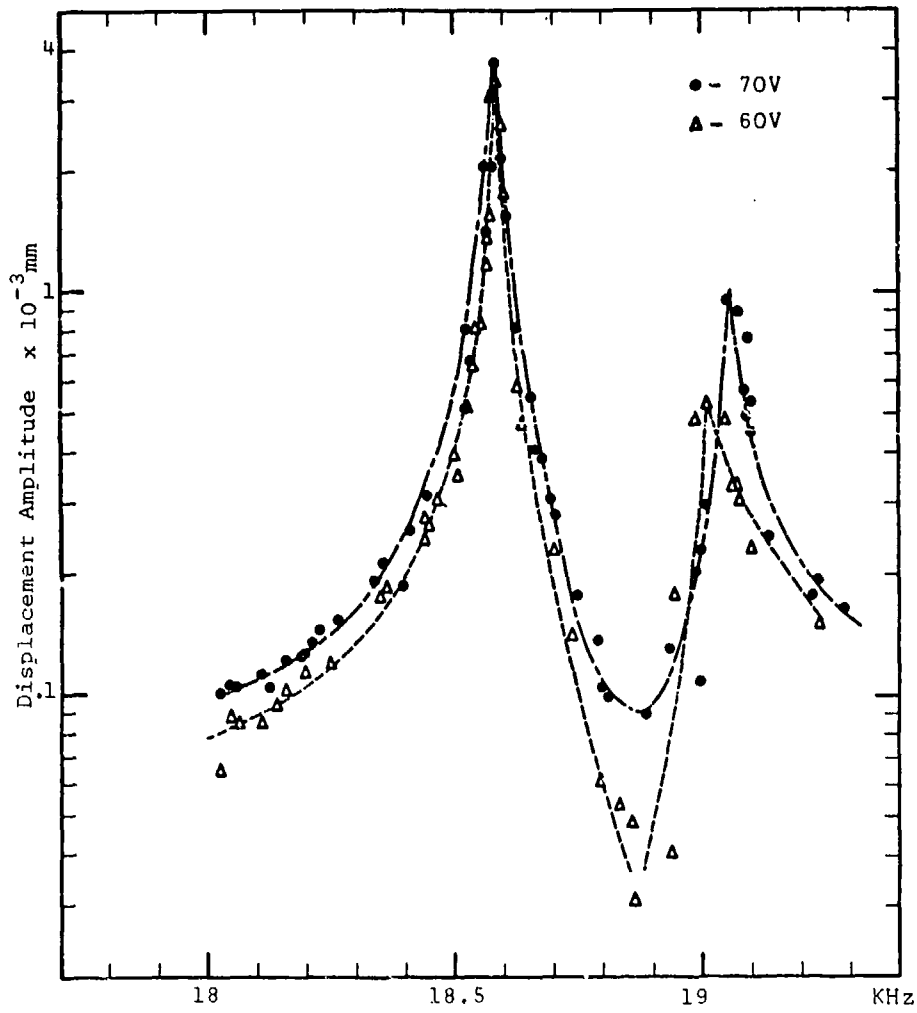


FIG. 4

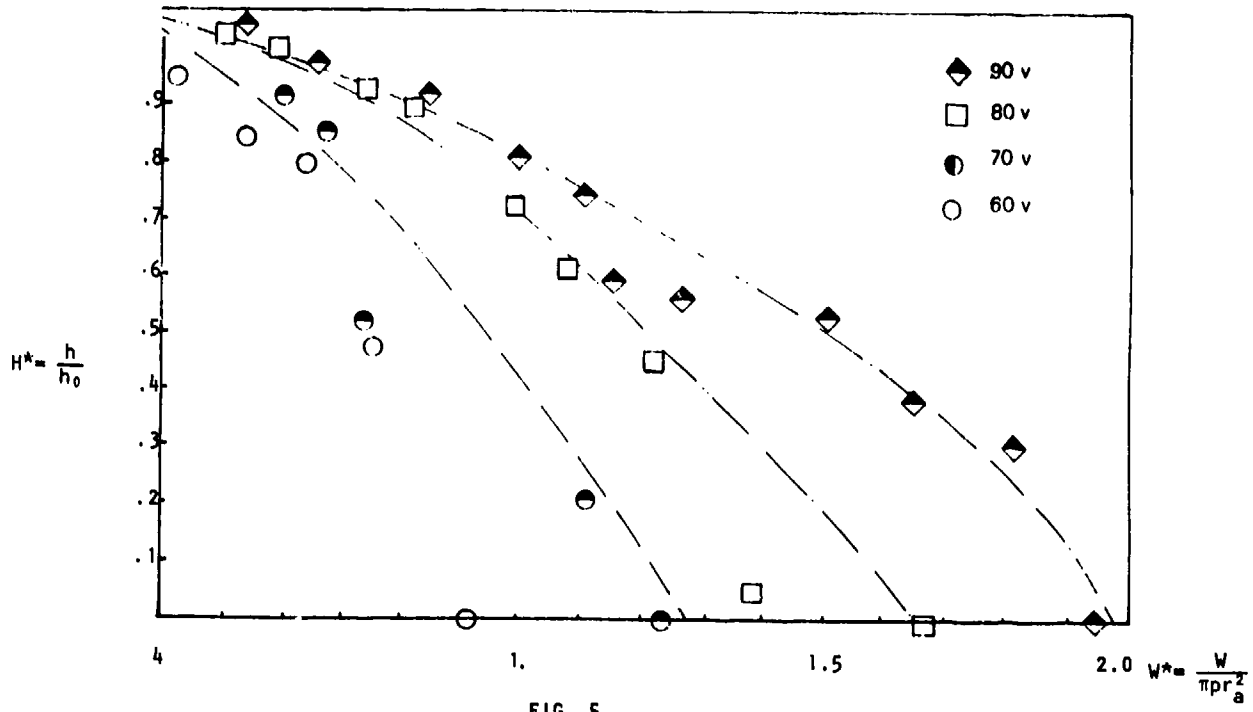


FIG. 5

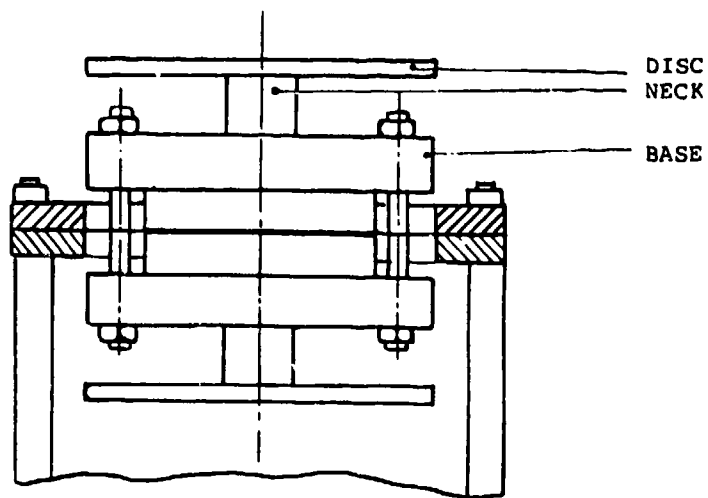


FIG. 6

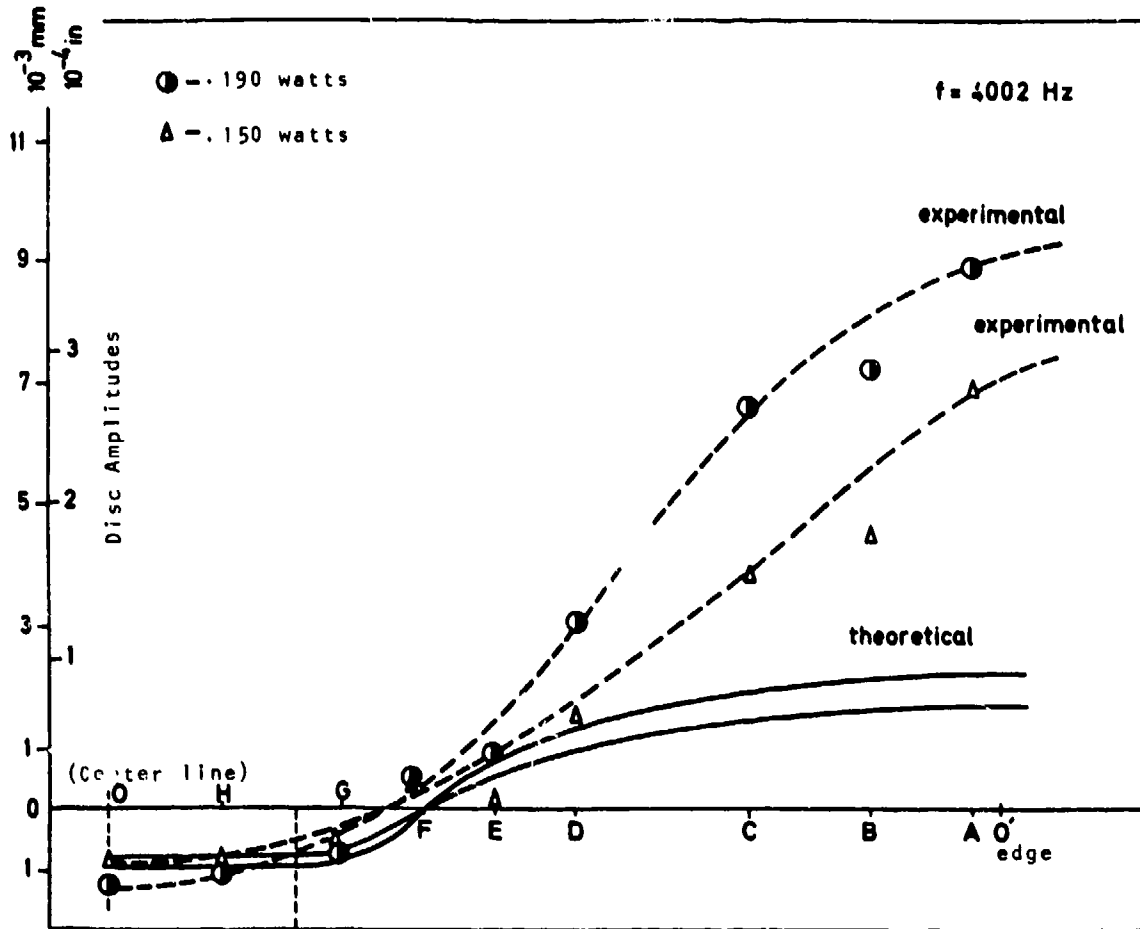


FIG. 7

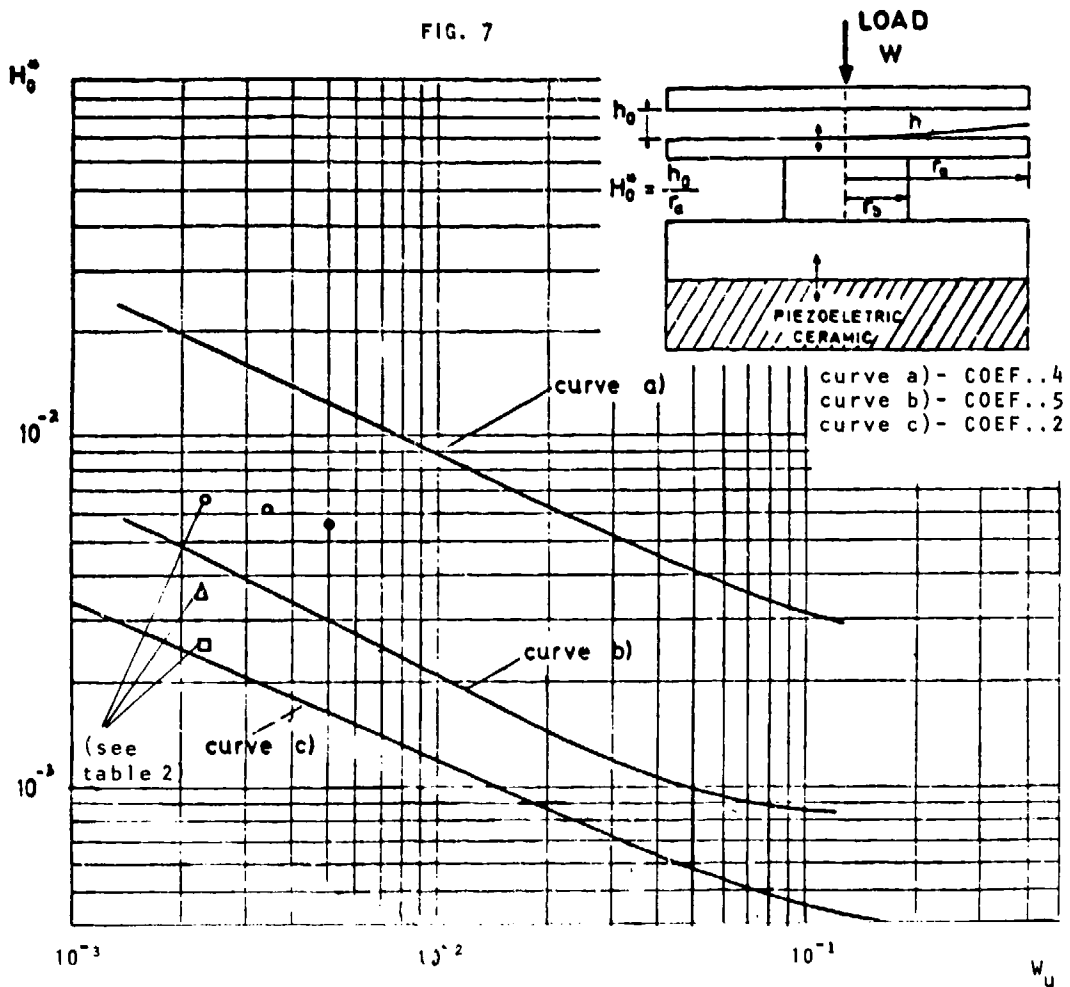


FIG. 8

UNCENTRALIZED SQUEEZE-FILM DAMPER
BEARINGS APPLIED TO AN OVERHUNG
DISC/ROTOR SYSTEM

R A Cookson
Head of Applied Mechanics
School of Mechanical Engineering
Cranfield Institute of Technology
Bedford MK43 OAL, UK

Xin-Hai Feng
Head of Vibration and Strength
Analytical Research Group
Aero Gas-Turbine Research Institute
Chinese Aeronautical Establishment
Peking, China

SUMMARY

Previous investigations at Cranfield have shown that the uncentralized squeeze-film damper, employed to support either rigid or flexible rotors, can be a very effective means of inhibiting the transmission of vibratory forces into the surrounding structure. These earlier studies also indicated that the performance of the squeeze-film damper could be optimised in terms of non-dimensional parameters which contained the basic bearing variables such as, land-length, radial clearance, fluid viscosity, unbalance, etc.

In the present report a shaft-disc system somewhat closer to a practical gas-turbine is considered. This model includes a disc (turbine) supported non-centrally between two squeeze-film damper bearings, and an overhung (fan) disc. The results included in this report again indicate that the forces transmitted into the support structure can be drastically reduced if a correct combination of damper parameters is chosen. Also, this investigation would appear to indicate that the design of squeeze-film damper commonly used by U.K. engine designers (uncentralized), is almost always more efficient, and never less efficient, than the squirrel-caged design usually employed in U.S. engines.

NOTATION

$A_{8,9}$	Amplitude of displacement at supports	(m)
$B_{6,7}$	Bearing parameter = $\{\mu RL_6^3/m_6 \omega_c^3\}$ or $\{\mu RL_7^3/m_7 \omega_c^3\}$	(-)
$c_{6,7}$	Radial clearance of squeeze-film damper	(m)
$c_{6,7}$	Ratio of damper clearances $\{c_7/c_6\}$	(-)
C_{di}	Rotor station transverse damping coefficient	(kg/s)
\bar{C}_{di}	Dimensionless damping = $\{C_{di}/m_6 \omega_c\}$	(-)
$C_{\theta i}$	Rotor station angular damping coefficient	(kg.m ² /s)
$\bar{C}_{\theta i}$	Dimensionless angular damping = $\{C_{\theta i}/m_6 c_6^2 \omega_c^2\}$	(-)
e_u	Unbalance eccentricity	(m)
F_x, F_y, F	Oil-film forces in x and y directions and resultant	(N)
\bar{F}_x, \bar{F}_y	Dimensionless oil-film forces = $\{F_{x,y}/m_6 c_6 \omega_c^2\}$	(-)
I_{ti}	Rotor station transverse moment of inertia	(kg.m ²)
\bar{I}_{ti}	Dimensionless transverse moment of inertia = $\{I_{ti}/m_6 c_6^2\}$	(-)
\bar{I}_{pi}	Rotor station polar moment of inertia	(kg.m ²)
\bar{I}_{pi}	Dimensionless polar moment of inertia = $\{I_{pi}/m_6 c_6^2\}$	(-)
K_A	Stiffness of centralizing spring (squirrel cage)	(N/m)
K_{si}	Rotor station transverse stiffness	(N/m)
\bar{K}_{si}	Dimensionless transverse stiffness = $\{K_{si}/m_6 \omega_c^2\}$	(-)
K_{ti}	Rotor station torsional stiffness	(Nm/RAD)
\bar{K}_{ti}	Dimensionless torsional stiffness = $\{K_{ti}/m_6 c_6^2 \omega_c^2\}$	(-)
l_1	Axial distance to bearing number 6	(m)
\bar{l}_1	Dimensionless distance to bearing 6 = $\{(l_1 - l_6)/c_6\}$	(-)
$\bar{l}_{7,6}$	Span parameter = $\{(l_7 - l_6)/c_6\}$	(-)

m_i	Rotor station mass	(kg)
\bar{M}_i	Dimensionless mass = $\{m_i/m_e\}$	(-)
R	Squeeze-film damper journal radius	(m)
TR_8, TR_9	Transmissibility at supports 8 and 9	(-)
u_i, v_i	Relative deflections	(m)
\bar{u}_i, \bar{v}_i	Dimensionless relative deflection = $\{u_i/c_e \text{ and } v_i/c_e\}$	(-)
U_i	Dimensionless unbalance = $\{e_{u1}/c_e\}$	(-)
\bar{W}	Dimensionless gravity parameter = $\{g/c_e \omega_c^2\}$	(-)
x_i, y_i, z_i	Body-fixed coordinate system	(m)
x'_i, y'_i, z'_i	Body-rotated coordinate system	(m)
u_{ij}	Influence coefficient, deflection at station i per unit force applied at station j	(m/N)
$\bar{\alpha}_{ij}$	Dimensionless influence coefficient = $\{\alpha_{ij} m_e \omega_c^2\}$	(-)
β_{ij}	Influence coefficient, deflection at station i per unit moment applied at station j	(m/Nm)
$\bar{\beta}_{ij}$	Dimensionless influence coefficient = $\{\beta_{ij} m_e c_e \omega_c^2\}$	(-)
ϕ_{ij}	Influence coefficient, slope at station i per unit force applied at station j	(RAD/N)
$\bar{\phi}_{ij}$	Dimensionless influence coefficient = $\{\phi_{ij} m_e c_e \omega_c^2\}$	(-)
γ_{ij}	Influence coefficient, slope at station i per unit moment at station j	(RAD/Nm)
$\bar{\gamma}_{ij}$	Dimensionless influence coefficient = $\{\gamma_{ij} m_e c_e^2 \omega_c^2\}$	(-)
θ, ψ, ϕ	Eulerian angles	(RAD)
$\hat{\theta}_x, \hat{\theta}_y$	Relative slope angles	(RAD)
ϕ_{oi}	Phase angle at station i between unbalance vector and x direction	(RAD)
μ	Absolute viscosity of damper fluid	(Ns/m ²)
ω	Rotor speed	(RAD/s)
ω_c	First (pin-pin) critical speed	(RAD/s)
Ω	Dimensionless speed ratio = $\{\omega/\omega_c\}$	(-)
($'$)	d/d $\{\omega t\}$	
($\dot{\quad}$)	d/dt	

INTRODUCTION

The life, reliability and general mechanical integrity of gas turbines can be seriously reduced by the presence of mechanical vibration. Mechanical vibration in this relatively flimsy structure can arise from several sources, for example, engine order excitations of discs and blades. However, one very serious source of vibration is the synchronous excitation produced by unbalance, present to some degree in all engines, but aggravated in service engines by thermal distortion (bowing) and material loss. Unbalance in this form can produce at one extreme rough-running of the engine at relatively low speeds, and at the other it can lead to a considerable increase in the amplitude of the forces which are transmitted into the surrounding structure when the engine approaches, or passes through a critical speed.

One method for reducing the effect of vibration in the gas-turbine is the inclusion of squeeze-film dampers, as proposed by Cooper (1), in its design. A squeeze-film damper can be simply an annular fluid-filled space surrounding the outer race of a rolling-contact bearing (see Figure 1). The radial clearance between the rolling-contact bearing and the bearing housing is usually of the order of 0.10mm to 0.25mm (0.004in to 0.010in), and the fluid within the clearance annulus is the oil employed in lubricating the rolling-contact bearing. The outer race of the rolling contact bearing is not usually allowed to rotate within the clearance circle, although in practice it will only rotate very slowly if unrestrained. However, it can move with fixed coordinates (orbit) within this space and it is this movement which produces the squeeze-film from which the device gets its name.

In most squeeze-film dampers oil is pressure fed into the annular groove shown in Fig. 1 and allowed to flow axially across the two symmetric bearing surfaces (lands). In many designs side-plates are fitted as flow restrictors and crude assumptions made

concerning the positioning of the bearing between the two side-plates. Even from the brief description included here, a number of design variables become apparent, for example, radial clearance, land width, inlet pressure, oil viscosity, side-plate clearance etc. However, the most significant variation in design exists between those squeeze-film dampers where the outer race of the rolling-contact is held centrally within the clearance circle, and those where it is assumed to fall to the bottom of the clearance circle until the unbalance forces become large enough to lift off and bring the squeeze-film effect into play. In this paper, where a comparison is made between the effectiveness of these two forms of squeeze-film damper, the terms "centralized" and "uncentralized" are used to describe them. Fig. 1 illustrates these two design forms.

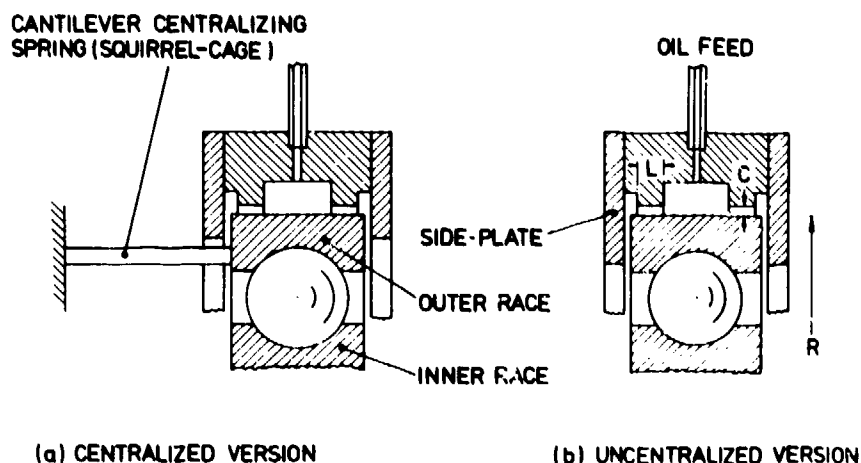


FIG. 1 Centralized and Uncentralized Squeeze-Film Dampers

It should be pointed out that the centralized squeeze-film damper, that is, the version where the bearing is held centrally by means of preloaded cantilevers (usually in the form of a squirrel-cage), is attempting to perform two functions. Firstly, the obvious reduction in vibration amplitude, and secondly "tuning" of the critical speed by varying the support stiffness. This centralized design is that usually employed by gas-turbine manufacturers in the U.S.A. (G.E., Pratt and Witney etc).

The uncentralized squeeze-film damper design is that usually employed in the U.K. (Rolls-Royce), and while it lacks the capability of varying the rotor critical speed, so that it can be moved (presumably) to some less sensitive sector of the operating speed range, it does lead to a simpler (cheaper) design, with a saving in space and the elimination of the possibility of fatigue failure at the squirrel-cage support.

It is almost certainly this emphasis in the U.S.A. on the centralized squeeze-film damper design, which led to the concentration by previous researchers (for example (2), (3) and (4)) on the case where rotor excursions would always take the form of a circular orbit around the equilibrium position. However, an investigation into the effectiveness of uncentralized squeeze-film dampers was begun at Cranfield and some results published in (5), (6) and (7). This previous work at Cranfield showed that the uncentralized squeeze-film damper is an effective means of reducing the vibratory forces transmitted to the structure surrounding an unbalanced rotor. Similarly, it was shown that the effectiveness of the device is a function of the design variables such as radial clearance, land-width, fluid viscosity etc., that these properties can be grouped together in non-dimensional form (bearing parameter B , gravity parameter W etc.), and that values for these non-dimensional groupings can be chosen so as to produce a high (if not optimum) squeeze-film damper performance.

For the work reported in references (5), (6) and (7) a simple two-bearing flexible shaft configuration, with a single centrally supported disc, was chosen. The results obtained with the aid of this simple rotor system indicated that uncentralized squeeze-film dampers could produce a significant reduction in the vibration amplitude, and that the greatest reductions were obtained when the bearing parameter B was about 0.1 and the gravity parameter W was about 0.05. In view of the elementary nature of the rotor model previously used, doubts must be raised concerning the applicability of these results to a model which is more representative of a real gas-turbine. For example, the values of the bearing and gravity parameters for optimum squeeze-film damper performance may not be the same as those previously determined, indeed there may not be a single value for these two parameters for optimum performance over the complete practical speed range.

As an extension of the research published in (5 to 7) a more representative experimental rig has been constructed and is currently under investigation. A theoretical model of this more advanced rig, which includes an overhung rotor (fan disc) and a second rotor (turbine) positioned non-centrally between two squeeze-film damper bearings, is shown in Fig. 2. Both of the bearings are attached to earth by means of springs intended to represent the stiffness of the supporting gas-turbine structure. A theoretical investigation of the vibratory characteristics of the model illustrated in Fig. 2 has been reported in (8).

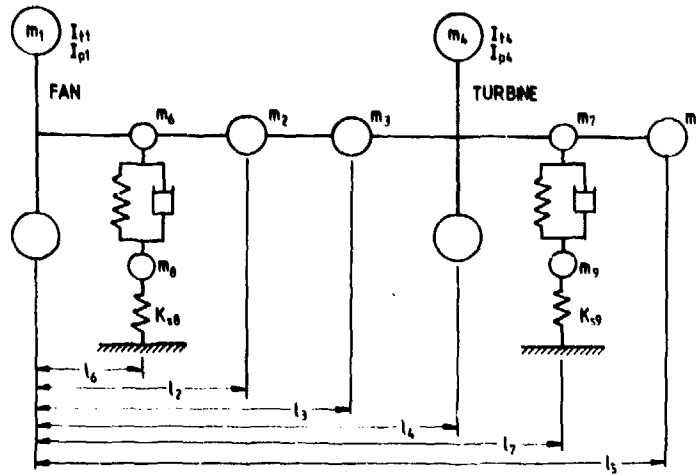


FIG. 2 Nine-mass Theoretical Model of Rotor System with Uncentralized Squeeze-Film Dampers

THEORY

From Fig. 2 it can be seen that the two-disc uncentralised squeeze-film damper system, which has been made the subject of our experimental investigations, is represented by a nine-mass theoretical model. Naturally, since a practical system could be considered to be made up of an infinite number of individual masses, it is to be expected that the accuracy of the results obtained from a particular model would improve with the number of lumped-masses included in that model. However, there is obviously a practical limitation to the complexity of any assumed theoretical model, and in the computer time available for obtaining a solution. Some trial calculations based upon a simpler six-mass model have been made and, from the limited evidence available, it would appear that the results obtained from such a model are not far removed from those reported here.

Masses m_1 and m_4 in Fig. 2 represent the overhung and inboard discs respectively, whilst masses m_2, m_3 and m_5 are lumped shaft masses. Masses m_6 and m_7 represent the squeeze-film housing masses. These latter masses are earthed through springs of stiffness K_8 and K_9 which represent the stiffness of the machine supporting structure.

For the analysis reported here it has been assumed that only discs m_1 and m_4 will have an associated gyroscopic effect, that rotor motion in the axial direction is negligible and that all vibratory amplitudes are relatively small. It has also been possible to include the effect of journal misalignment on the oil-film forces produced in the squeeze-film dampers, by means of a procedure reported in (9).

The equations of motion for the shaft supported masses can be expressed in the following form.

$$\begin{bmatrix} \ddot{x}_j \\ \dot{\theta}_{xj} \\ \ddot{y}_j \\ \dot{\theta}_{yj} \end{bmatrix} = \begin{bmatrix} \bar{B} & 0 \\ \text{---} & \text{---} \\ 0 & \bar{B} \end{bmatrix} \begin{bmatrix} -\ddot{u}_j + \sum_{i=1}^5 \bar{\alpha}_{ji} \bar{p}^*_{xi} + \sum_{i=1}^5 \bar{\beta}_{ji} \bar{m}^*_{yi} \\ -\dot{\theta}_{xj} + \sum_{i=1}^5 \bar{\phi}_{ji} \bar{p}^*_{xi} + \sum_{i=1}^5 \bar{\gamma}_{ji} \bar{m}^*_{yi} \\ -\ddot{v}_j + \sum_{i=1}^5 \bar{\alpha}_{ji} \bar{p}^*_{yi} - \sum_{i=1}^5 \bar{\beta}_{ji} \bar{m}^*_{xi} \\ -\dot{\theta}_{yj} + \sum_{i=1}^5 \bar{\phi}_{ji} \bar{p}^*_{yi} - \sum_{i=1}^5 \bar{\gamma}_{ji} \bar{m}^*_{xi} \end{bmatrix} \quad (1)$$

where

$$\ddot{x}_j = \begin{bmatrix} \ddot{x}_1 \\ \ddot{x}_2 \\ \ddot{x}_3 \\ \ddot{x}_4 \\ \ddot{x}_5 \end{bmatrix} \quad \dot{\theta}_{xj} = \begin{bmatrix} \dot{\theta}_{x1} \\ \dot{\theta}_{x2} \\ \dot{\theta}_{x3} \\ \dot{\theta}_{x4} \\ \dot{\theta}_{x5} \end{bmatrix} \quad \ddot{y}_j = \begin{bmatrix} \ddot{y}_1 \\ \ddot{y}_2 \\ \ddot{y}_3 \\ \ddot{y}_4 \\ \ddot{y}_5 \end{bmatrix} \quad \dot{\theta}_{yj} = \begin{bmatrix} \dot{\theta}_{y1} \\ \dot{\theta}_{y2} \\ \dot{\theta}_{y3} \\ \dot{\theta}_{y4} \\ \dot{\theta}_{y5} \end{bmatrix}$$

also

$$\bar{B} = \begin{bmatrix} B_1 & B_3 \\ B_2 & B_4 \end{bmatrix} \quad (2)$$

where $B_{1,ij} = \bar{\alpha}_{ij} \bar{M}_1 \Omega^2$ (i = 1 to 5) $B_{2,ij} = \bar{\beta}_{ij} \bar{M}_1 \Omega^2$ (i = 1 to 5)

$$B_{3,ij} = \begin{cases} \bar{\phi}_{ij} \bar{I}_{t1} \Omega^2 & (i = 1, 4) \\ \bar{\phi}_{ij} \bar{C}_{\theta 1} \Omega^2 & (i = 2, 3, 5) \end{cases} \quad B_{4,ij} = \begin{cases} \bar{\gamma}_{ij} \bar{I}_{t1} \Omega^2 & (i = 1, 4) \\ \bar{\gamma}_{ij} \bar{C}_{\theta 1} \Omega^2 & (i = 2, 3, 5) \end{cases}$$

Similarly, the equations of motion for the bearing-related masses m_6 to m_9 can be expressed as follows:

$$X_6'' = \frac{1}{\bar{M}_6 \Omega^2} \left\{ \frac{1}{\bar{l}_{76}} \left[\sum_{i=1,4} (-\bar{I}_{t1} \Omega^2 \theta_{x1}'' + \bar{M}_{Y1}^*) + \sum_{i=1,4} (-\bar{M}_1 \Omega^2 X_1'' + \bar{P}_{X1}^*) (\bar{l}_{76} - \bar{l}_1) \right. \right. \\ \left. \left. - \sum_{i=2,3,5} (-\bar{C}_{\theta 1} \Omega \theta_{x1}' + \bar{M}_{X1}^*) + \sum_{i=2,3,5} (-\bar{M}_1 \Omega^2 X_1'' + \bar{P}_{X1}^*) + (\bar{l}_{76} - \bar{l}_1) \right] + \bar{F}_{X6} \right\} \dots (3)$$

$$Y_6'' = \frac{1}{\bar{M}_6 \Omega^2} \left\{ \frac{1}{\bar{l}_{76}} \left[\sum_{i=1,4} (\bar{I}_{t1} \Omega^2 \theta_{y1}'' + \bar{M}_{X1}^*) + \sum_{i=1,4} (-\bar{M}_1 \Omega^2 Y_1'' + \bar{P}_{Y1}^*) (\bar{l}_{76} - \bar{l}_1) \right. \right. \\ \left. \left. + \sum_{i=2,3,5} (\bar{C}_{\theta 1} \Omega \theta_{y1}' + \bar{M}_{Y1}^*) + \sum_{i=2,3,5} (-\bar{M}_1 \Omega^2 Y_1'' + \bar{P}_{Y1}^*) (\bar{l}_{76} - \bar{l}_1) \right] + \bar{F}_{Y6} - \bar{W}_6 \right\} \dots (4)$$

$$X_7'' = \frac{1}{\bar{M}_7 \Omega^2} \left\{ \frac{1}{\bar{l}_{76}} \left[\sum_{i=1,4} (-\bar{I}_{t1} \Omega^2 \theta_{x1}'' + \bar{M}_{Y1}^*) + \sum_{i=1,4} (-\bar{M}_1 \Omega^2 X_1'' + \bar{P}_{X1}^*) \bar{l}_1 \right. \right. \\ \left. \left. + \sum_{i=2,3,5} (-\bar{C}_{\theta 1} \Omega \theta_{x1}' + \bar{M}_{X1}^*) + \sum_{i=2,3,5} (-\bar{M}_1 \Omega^2 X_1'' + \bar{P}_{X1}^*) \bar{l}_1 \right] + \bar{F}_{X7} \right\} \dots (5)$$

$$Y_7'' = \frac{1}{\bar{M}_7 \Omega^2} \left\{ \frac{1}{\bar{l}_{76}} \left[\sum_{i=1,4} (\bar{I}_{t1} \Omega^2 \theta_{y1}'' + \bar{M}_{X1}^*) + \sum_{i=1,4} (-\bar{M}_1 \Omega^2 Y_1'' + \bar{P}_{Y1}^*) \bar{l}_1 \right. \right. \\ \left. \left. - \sum_{i=2,3,5} (\bar{C}_{\theta 1} \Omega \theta_{y1}' + \bar{M}_{Y1}^*) + \sum_{i=2,3,5} (-\bar{M}_1 \Omega^2 Y_1'' + \bar{P}_{Y1}^*) \bar{l}_1 \right] + \bar{F}_{Y7} - \bar{W}_7 \right\} \dots (6)$$

$$X_8'' = \frac{1}{\bar{M}_8 \Omega^2} \left[-\bar{K}_{S8X} X_8 - \bar{F}_{X8} \right] \dots (7)$$

$$Y_8'' = \frac{1}{\bar{M}_8 \Omega^2} \left[-\bar{K}_{S8Y} Y_8 - \bar{F}_{Y8} - \bar{W}_8 \right] \dots (8)$$

$$X_9'' = \frac{1}{\bar{M}_9 \Omega^2} \left[-\bar{K}_{S9X} X_9 - \bar{F}_{X9} \right] \dots (9)$$

$$Y_9'' = \frac{1}{\bar{M}_9 \Omega^2} \left[-\bar{K}_{S9Y} Y_9 - \bar{F}_{Y9} - \bar{W}_9 \right] \dots (10)$$

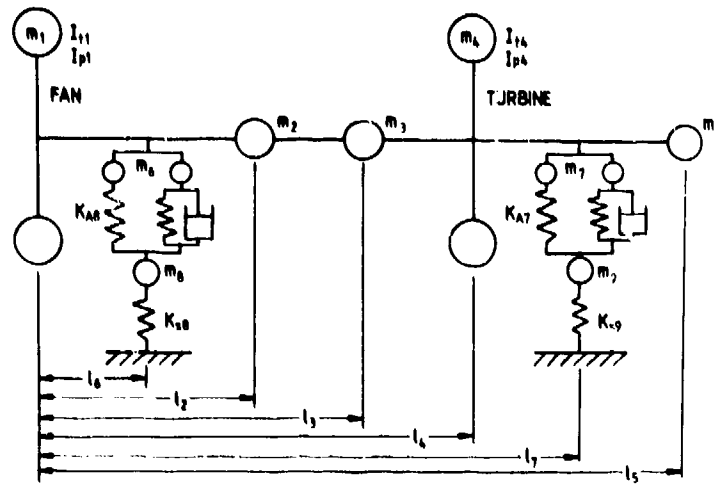


FIG. 3 Nine-Mass Theoretical Model of Rotor System with Centralized(Squirrel-Caged) Squeeze-Film Dampers

If centralizing springs (squirrel-cages) are included in the structure, as is the case in most of the aero-engines produced in the U.S., the system can be represented by Fig. 3. Similarly, equations 3 to 10 should be modified as follows. For the centralized case

$$X_6'' = X_6'' \text{ (EQ.3)} - \bar{K}_{a6x} (X_6 - X_8) \bar{M}_6 \Omega^2 \dots\dots (11)$$

$$Y_6'' = Y_6'' \text{ (EQ.4)} - \bar{K}_{a6y} (Y_6 - Y_8) \bar{M}_6 \Omega^2 \dots\dots (12)$$

$$X_7'' = X_7'' \text{ (EQ.5)} - \bar{K}_{a7x} (X_7 - X_9) \bar{M}_7 \Omega^2 \dots\dots (13)$$

$$Y_7'' = Y_7'' \text{ (EQ.6)} - \bar{K}_{a7y} (Y_7 - Y_9) \bar{M}_7 \Omega^2 \dots\dots (14)$$

$$X_8'' = X_8'' \text{ (EQ.7)} + \bar{K}_{a8x} (X_6 - X_8) \bar{M}_8 \Omega^2 \dots\dots (15)$$

$$Y_8'' = Y_8'' \text{ (EQ.8)} + \bar{K}_{a8y} (Y_6 - Y_8) \bar{M}_8 \Omega^2 \dots\dots (16)$$

$$X_9'' = X_9'' \text{ (EQ.9)} + \bar{K}_{a9x} (X_7 - X_9) \bar{M}_9 \Omega^2 \dots\dots (17)$$

$$Y_9'' = Y_9'' \text{ (EQ.10)} + \bar{K}_{a9y} (Y_7 - Y_9) \bar{M}_9 \Omega^2 \dots\dots (18)$$

where $X_1' = \frac{dX_1}{d(\omega t)} = \frac{\dot{X}_1}{\omega}$, $X_1'' = \frac{d^2X_1}{d(\omega t)^2} = \frac{\ddot{X}_1}{\omega^2}$ etc.

The generalised force terms for $i = 1$ and $i = 4$ are defined as follows

$$\bar{P}_{xi}^* = -\bar{K}_{si} X_i - \bar{C}_{di} \Omega X_i' + \bar{M}_i U_i \Omega^2 \cos(\omega t + \phi_{oi})$$

$$\bar{P}_{yi}^* = -\bar{K}_{si} Y_i - \bar{C}_{di} \Omega Y_i' + \bar{M}_i U_i \Omega^2 \sin(\omega t + \phi_{oi}) - \bar{W}_i$$

$$\bar{M}_{xi}^* = -\bar{I}_{pi} \Omega^2 \theta_{xi}' + \bar{K}_{ti} \theta_{yi} + \bar{C}_{\theta i} \Omega \theta_{yi}'$$

$$\bar{M}_{yi}^* = -\bar{I}_{pi} \Omega^2 \theta_{yi}' - \bar{K}_{ti} \theta_{xi} - \bar{C}_{\theta i} \Omega \theta_{xi}'$$

And for $i = 2, 3, \text{ and } 5$ the generalised force terms are given as

$$\bar{P}_{xi}^* = -\bar{K}_{si} X_i - \bar{C}_{di} \dot{X}_i$$

$$\bar{P}_{yi}^* = -\bar{K}_{si} Y_i - \bar{C}_{di} \dot{Y}_i - \bar{W}_i$$

$$\bar{M}_{xi}^* = -\bar{K}_{ti} \theta_{yi}$$

$$\bar{M}_{yi}^* = -\bar{K}_{ti} \theta_{xi}$$

It is clear that the oil fluid-film forces F_{x_8}, F_{y_8} and F_{x_9}, F_{y_9} , occurring at supports 8 and 9 respectively, are of considerable importance in determining the dynamic performance of a rotor system which includes squeeze-film damper bearings. By the same token it is clear that the calculated values of these forces (in the absence of experimental results) will depend to a great extent upon the fluid-film model adopted. In this report the π -film model has been chosen, although there is some evidence that this is not the most accurate model. It is proposed to publish a comparison of the results obtained from a number of film models at a later time.

In practice the effectiveness of a squeeze-film damper bearing is assessed in terms of its ability to reduce the amplitude of the vibratory forces transmitted from the rotor to the surrounding structure. In the same way the definition of squeeze-film damper effectiveness employed in this investigation is the ratio of the forces actually transmitted (K_{s_8}, A_8 and K_{s_9}, A_9), to the support reaction forces determined for the nine-mass system without squeeze-film dampers, at its first critical speed. A_8 and A_9 are the maximum displacements at the two supports and are equal to $(x_8^2 + y_8^2)^{0.5}$ and $(x_9^2 + y_9^2)^{0.5}$ respectively. This ratio is here called the transmissibility and is labelled TR8 and TR9 for the appropriate supports.

ANALYSIS

The set of first-order differential equations 1 to 10 have been produced from the equations of motion for the nine-mass representation of the rotor system shown in Fig. 2. Equations 1 to 10 have been numerically integrated using the modified Euler and Fourth-Order Runge-Kutta methods, although any appropriate technique could be used.

The initial displacements and velocities for all points within the system are specified at starting time t_0 . Hence, it is possible to obtain the acceleration rates at these points and subsequently to calculate the displacements and velocities at time $t_0 + \Delta t$.

In the present analysis the oil film forces F_x and F_y can be determined from any one of five possible fluid-film models (for example the π -film model), including one which takes account of shaft misalignment if it exceeds 0.5×10^{-3} (9). Since these fluid-film forces are introduced into the computation in generalized form it would be possible to introduce any other appropriate film model at a later date.

For the analytical investigation reported here only steady-state conditions are considered. In certain situations it is obvious that the transient conditions would be of importance, for example, the rotor response to sudden loading as would be met when a blade was shed. However, in the present circumstances the squeeze-film damper effectiveness under steady conditions is being evaluated, and consequently the initially assumed values of rotor velocity and displacement will have no influence on the final unique steady-state orbit. Whilst the transient path followed by the rotor centroid during the time-marching procedure is of no great significance in the present investigation, the choice of time interval adopted during the time-marching process was found to be very important indeed. If an unreasonably short time interval is chosen the computer costs become excessive. By the same token if the time interval is too great, the projected path of the rotor centroid can attempt to pass outside the clearance circle during a single time step, a condition which is clearly undesirable. Since the dynamics of the rotor centroid can vary considerably with operating conditions an optimum choice of time interval for each occasion is clearly desirable. The smallest time-step used for the present investigation was 0.0087266 radians, equivalent to 720 points for each cycle.

In the full theoretical study reported in (10) a wide range of system parameters were investigated. However, in the present paper only parameters appropriate to the associated experimental study have been chosen. These values are listed below in non-dimensional form.

Bearing parameter	B	Rigid, 3.8023, 0.5649, 0.1000
Gravity parameter	\bar{W}	0.1496
Unbalance parameter	U	0.2
Mass parameter	\bar{M}_1	$\bar{M}_1 = 1.1$; $\bar{M}_4 = 1.33$; $\bar{M}_{8,9} = 2.93$
Support stiffness	\bar{K}_s	12.66
Centralizing spring stiffness	\bar{K}_A	2.10
Transverse damping ratio	\bar{C}_d	0.01
Angular damping ratio	\bar{C}_θ	70.00
Phase angle	ϕ_{01}	0
Speed ratio	Ω	0.5 to 3.0

For the above analysis the initial conditions assumed at the beginning of each time-marching procedure were that the velocity of the rotor centroid was zero, and its displacement equivalent to that produced by the dead weight of the rotors.

The other physical properties of the experimental rig used in this analytical investigation are as follows. Mass of inboard disc equal to 9.70 kg, and the mass of the outboard disc equal to 8.04 kg. Distance between bearings 0.54 m.

RESULTS

Even for the limited range of system parameters listed above, the results of a full theoretical study would be too great to include in this paper. Consequently, only a few typical results are listed here, and since the influence of the bearing parameter B on the performance of a squeeze-film damper has been shown to be strong, some emphasis has been placed here upon the effect of varying that parameter.

In simple terms Fig. 4 illustrates the influence of the bearing parameter upon a system which includes uncentralized squeeze-film dampers, while Fig. 5 illustrates the influence, for a similar range of bearing parameters, upon a system where the bearings are supported on centralizing springs (squirrel-cages).

Both Fig. 4 and Fig. 5 illustrate the variation of the amplitude ratios at the two discs, two bearings, and two supports for different values of B. Both figures also include the transmissibilities determined at the two supports. Transmissibility, in this context, is defined as the force actually transmitted at each condition, relative to the force transmitted at the first critical speed in a system which has rigidly supported bearings.

The conditions, for which the results shown in Figs. 4 and 5 were determined, relate closely to the parallel experimental investigation currently being carried out at Cranfield. For example, the outboard and inboard disc masses are taken to be 8.04 kg and 9.70 kg respectively, and the distance between the bearing centres is fixed at 0.54 m. Similarly, the gravity parameter \bar{W} is fixed at 0.1496, the unbalance ratio U at 0.2, and the transverse and angular non-dimensional damping coefficients are assumed to be 0.01 and 70 respectively. The non-dimensional casing stiffness \bar{K}_s is assumed to be 12.66 (equivalent to 2.2×10^5 lbf/in. in imperial units), while the stiffness of the centralizing spring \bar{K}_A used in Fig. 5 is taken as 2.1, a value obtained from a typical U.S. engine.

The variation of the amplitude ratio and transmissibility with gravity parameter \bar{W} , stiffness parameter \bar{K}_s , unbalance parameter U, and mass parameter \bar{M} ($= m_1/m_0$), was also investigated and while there is not room in this paper to report on the effect of these parameters, they are covered fully in (1).

A comparison of the transmissibilities at the two supports, for the centralized and uncentralized cases, is shown in Fig. 6. Again the gravity parameter \bar{W} is taken to be 0.1496 (as in the experimental rig), U as 0.2, \bar{K}_s as 12.66, and \bar{K}_A as 2.1. Three values of the bearing parameter B are used, namely 0.1, 0.5649, and 3.8023, representing three of the cases which can be investigated experimentally.

The critical speeds, for the nine-mass rotor system operating without squeeze-film dampers, were calculated and the first two critical speeds were found to occur at 6113 and 12221 rpm respectively.

DISCUSSION

It is clear, from the diagrams which go to make up Figs. 4 and 5, that squeeze-film dampers can be effective in reducing the amplitude ratios and transmissibilities produced in the system under consideration. In general terms it can be seen that both the centralized and the uncentralized forms of the device can lead to reduced amplitudes of vibration, and reduced transmitted forces, and that the effectiveness of both types of squeeze-film damper increases with reducing bearing parameter. This general trend follows that discovered in our earlier investigations with a simpler model (6). In this

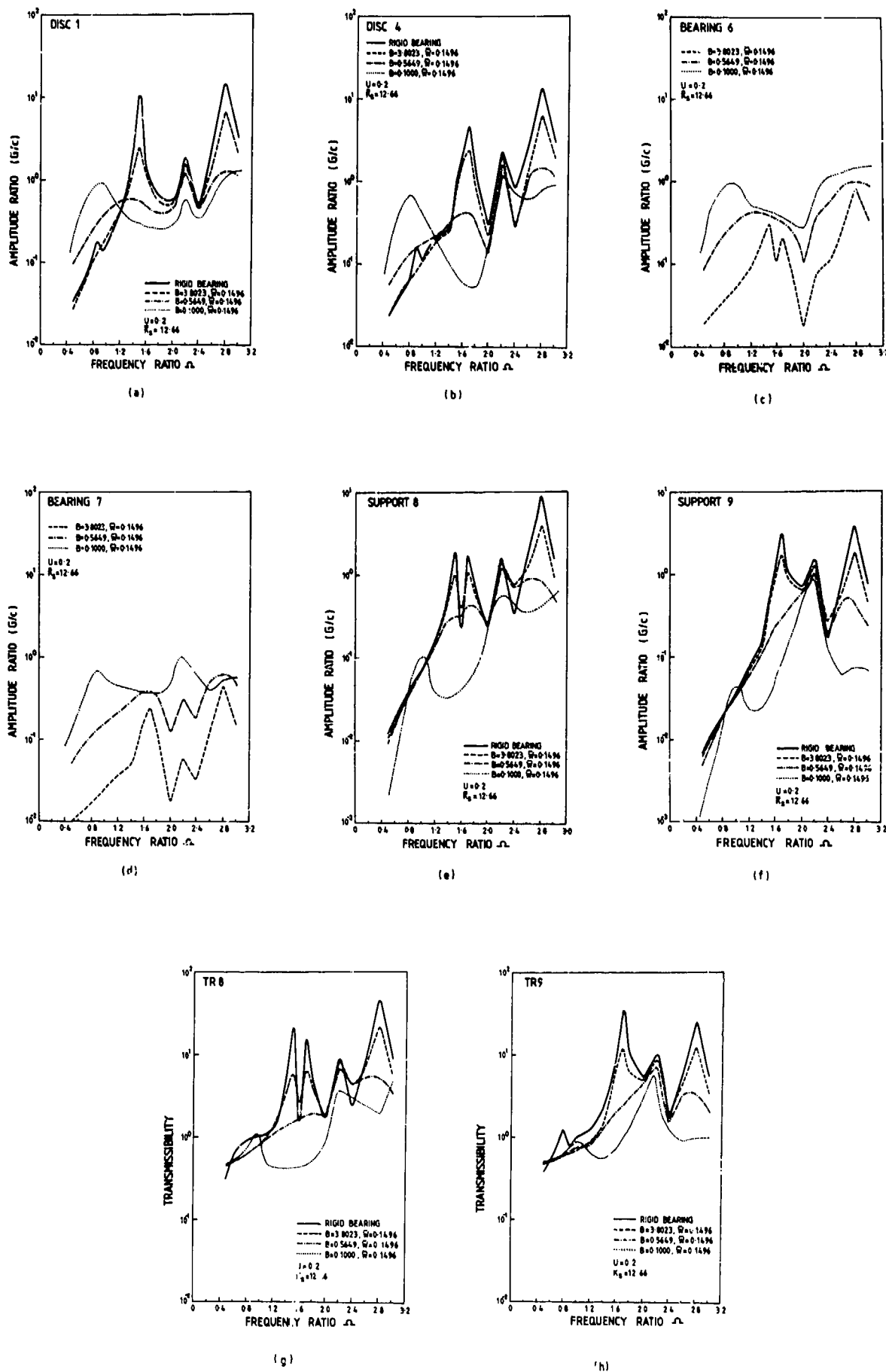


FIG. 4 Variation of Amplitude Ratios and Transmissibilities with Bearing Parameter for the Nine-Mass System with Uncanceled Squeeze-Film Dampers

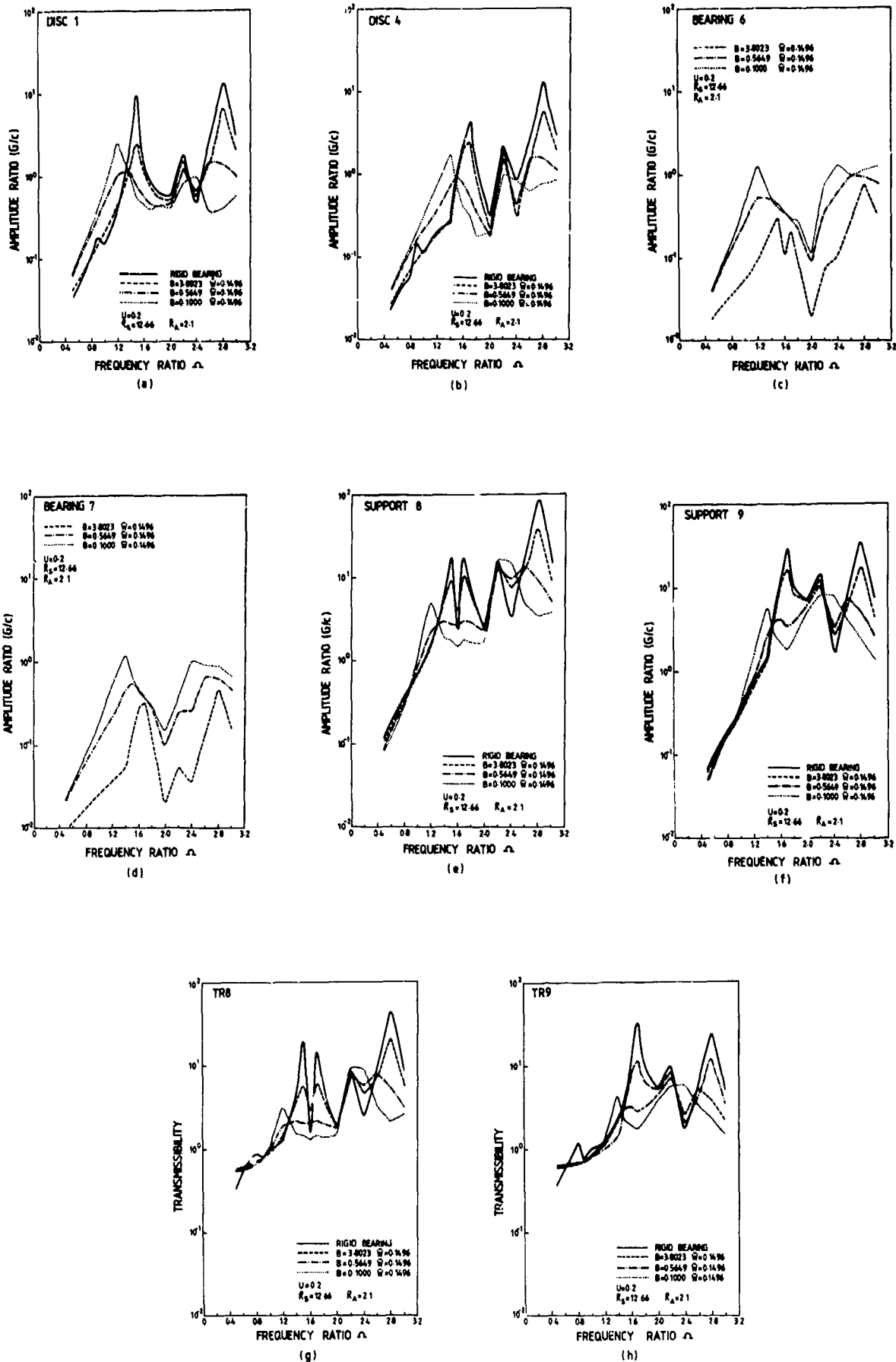


FIG. 5 Variation of Amplitude Ratios and Transmissibilities with Bearing Parameter for the Nine-Mass System with Centralized (Squirrel-Caged) Squeeze-Film Dampers

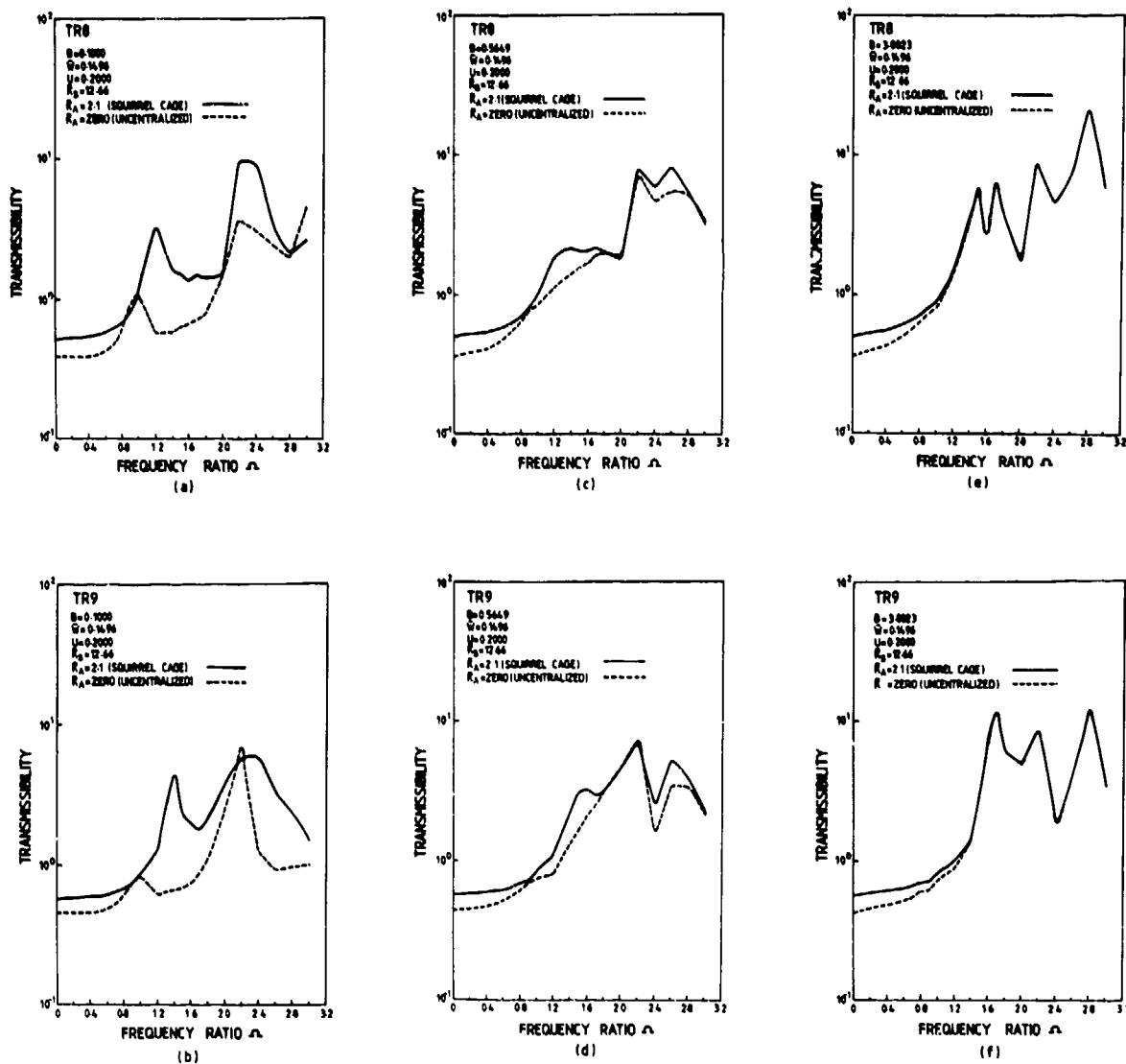


FIG. 6 A Comparison of the Effectiveness of Centralized (Squirrel-Caged), and Uncanceled Squeeze-Film Dampers

earlier work it was discovered that a value of about 0.1 for the bearing parameter B produced maximum attenuation of the vibratory properties (below about 0.1 instability could arise). However, a closer inspection of Figs. 4 and 5 reveals that, while a value of $B = 0.1$ produces a general reduction in the amplitude ratios and transmissibilities, in certain areas of the speed range this is not the case, in fact, in some instances values can exist which are significantly larger than those which would occur if the bearings were rigidly supported. For example, from Fig. 4 it can be seen that a bearing parameter of 0.1 can produce an amplitude of vibration of the fan disc, at around the first critical speed, which is ten times greater than that which would be expected if the bearings were rigidly fixed. By the same token, however, under the same conditions the force transmitted to the structure at support 8, at the second critical speed, would be one hundred times less than that which would exist if a squeeze-film damper had not been fitted. Hence, although it would be foolish to attempt to establish general rules from the limited data presented in this paper, it does appear to be difficult to choose one set of squeeze-film damper design parameters to give optimum performance over the whole speed range.

Not shown in Figs. 4 and 5 are the amplitude ratios and transmissibilities for the cases where the bearing parameter is low (for example $B = 0.01$ and 0.001). Values as low as this led to instability over part of the speed range in a similar manner to that reported in (6). This instability could be synchronous (eg: bi-stable), or non-synchronous.

Figs. 4(c), 4(d) and 5(c), 5(d) indicate that the movement of the squeeze-film damper journal increases with reducing bearing parameter. This would appear to support the suggestion made in (6) that in the region where the squeeze-film damper is most effective, the journal movement is greatest.

Having shown that both the centralized and the uncentralized forms of the squeeze-film damper can be effective, in reducing both the amplitude ratios and transmissibilities, in the system being investigated, the obvious next step is to compare the performance of the two designs. From Fig. 6 it can be seen that, for the vast majority of operating conditions, the uncentralized squeeze-film damper is more effective in reducing the force transmitted into the surrounding structure, than is the squeeze-film damper which is mounted in parallel with a centralizing spring. The difference between the two sets of transmissibilities is most marked where the bearing parameter is low (0.1), in some cases the transmissibility for the squirrel-caged version is ten times greater than that for the uncentralized version. Where the bearing parameter is high (3.8023) the difference between the two damper designs is much less. Hence, it is possible to say that an uncentralized squeeze-film damper is much more effective than a squirrel-caged model, in the region where squeeze-film dampers are most useful.

Naturally, if an uncentralized squeeze-film damper is incorporated in an engine design, the ability to tune the system (change the critical speed) by modifying the stiffness of the cantilever springs, is lost. However, as engine designers become more proficient at calculating critical speeds, it is possible that future engines will be designed such that their critical speeds do not occur in a troublesome sector of the speed range.

CONCLUSIONS

From the investigation described above it can be seen that both centralized, and uncentralized, squeeze-film damper bearings can be very effective in reducing the amplitude of vibration, and the forces transmitted into the surrounding structure, for the adopted theoretical model of a gas-turbine. In general it would appear that the optimum value of the bearing parameter is about 0.1. However, this investigation also indicates that a squeeze-film damper which leads to a fairly general reduction in transmissibility could also produce an increase in the vibration amplitude of some part of the system. Hence, care may be required in choosing the design parameters for a squeeze-film damper, so as to optimise its performance from all aspects. Alternatively, it may be desirable to design a squeeze-film damper which has properties which vary with engine speed.

This investigation would also appear to show fairly conclusively that the uncentralized squeeze-film dampers employed by U.K. engine designers, are more effective in reducing the forces transmitted from the rotor into the surrounding engine structure, than are the centralized (squirrel-caged) squeeze-film dampers favoured by U.S. engine designers. This advantage, of the uncentralized damper over the centralized, is particularly pronounced for designs where the bearing parameter is low, which is just the region where squeeze-film dampers are most effective. However, the squirrel-caged damper design does retain a capability for tuning the system, allowing critical speeds to be moved from some troublesome sector of the speed range.

ACKNOWLEDGEMENT

The authors wish to thank the Science and Engineering Research Council for their support of the above work through Research Grant GR B48307.

REFERENCES

1. COOPER, S - 'Preliminary Investigation of Oil-Films for the Control of Vibration'. Proceedings of the Lubrication and Wear Convention. I.Mech.E. 1963. London, England. pp 305-315.
2. WHITE, D C - 'The Dynamics of a Rigid Rotor Supported on Squeeze-film Bearings'. Inst.Mech.Engrs. Conference on Vibrations of Rotating Systems. pp 213-229, 1972.
3. MOHAN, S and HAHN, E J - 'Design of Squeeze-film Damper Supports for Rigid Rotors'. J.Engrg.Industry. Trans. ASME Series B. Aug. 1974. pp 976-982.
4. GUNTER, E J, BARRETT L E, and ALLAIRE, P E - 'Design and Application of Squeeze-film Damper for Turbomachinery Stabilization'. Report No. ME-4040-122-75. University of Virginia, 1975.
5. COOKSON, R A and KOSSA, S S - 'Theoretical and Experimental Investigations into the Effectiveness of Squeeze-film Damper Bearings without a Centralizing Spring'. Inst.Mech.Engrs. Meeting on Vibrations in Rotating Machinery, Churchill College, Cambridge, Sept. 1980.
6. COOKSON, R A and KOSSA, S S - 'The Vibration Inhibiting Properties of Uncentralized Squeeze-film Dampers, Supporting a Flexible Rotor'. J.Eng. for Power. Oct 1981. pp 781-787.
7. KOSSA, S S - 'Theoretical and Experimental Investigation of Uncentralized Squeeze-film Damper Bearings Supporting Flexible Rotors without a Centralizing Spring'. Ph.D. Thesis, Cranfield Institute of Technology 1980.
8. COOKSON, R A and FENG, X H - 'A Theoretical Investigation of an Overhung Flexible Rotor Mounted on Uncentralized Squeeze-film Damper Bearings and Flexible Supports'. Paper 82-GT-218. Amer.Soc.Mech.Eng. Gas Turbine Conference, London. April 1982 (To be published in J.Eng. for Power).

9. COOKSON, R A and FENG, X H - 'The Effect of Journal Misalignment on the Oil Film Forces Generated in a Squeeze-film Damper'. Paper 82-GT-285. Amer. Soc. Mech. Eng. Gas Turbine Conference, London. April 1982 (To be published in J.Eng for Power).
10. COOKSON, R A and FENG, X H - 'The Effectiveness of Uncentralized Squeeze-film Damper Bearings Supporting an Overhung Flexible Rotor - Theoretical Study'. Appl. Mech. Report AM 71, School of Mechanical Engineering, Cranfield Institute of Technology, Bedford, UK. 1981.

DISCUSSION

V. Bruno, Pratt & Whitney, Ca

Are your conclusions that the uncentralized squeeze film is superior to the squirrel cage affected by the presence of heavy axial loads?

Author's Reply

I have no knowledge of the effect of axial loads. Intuitively I would have expected the effect to be relatively low, but this is certainly a point worth investigating and I may try to incorporate axial loads in my experimental studies.

AERODYNAMIC COMPLIANT BEARINGS FOR SMALL TURBO-ENGINES

M. Ehinger, Dipl.-Ing.

J. Glienicke, Professor Dr.-Ing.

H. Hunger, Dipl.-Ing.

Institut für Maschinenkonstruktionslehre der Universität Karlsruhe

D 7500 Karlsruhe 1 (Germany)

Summary

This paper deals with theoretical and experimental investigations of aerodynamic spring bearings, the elastic bearing bushing structure of which can stand thermal deformations without any inadmissably large changes in the bearing clearance. Therefore, they seem to be suitable for the mounting of small turbo machines under extreme operating conditions. Based on the fundamental equations of aerodynamic bearing theory, a method was developed to determine the static and dynamic spring bearing characteristic curves and was applied to the tilting pad, "Garrett" and multiwedged spring bearing. To simplify matters the bearings are approximated by substitute models consisting of similar bearing elements. In the static and dynamic bearing characteristic curves determined in this way the parameters of the resilient bearing bushing structure are dominant over wide ranges. Rotor tests with rotational speeds up to 100,000 rpm prove the applicability of these bearings to extreme circumferential speeds and in general also the reliability of the calculated bearing characteristic values. For the material pairings graphite/steel and ceramic/hard metal coating, an adequate wearing strength could be proved by continuous starting tests (with 10,000 start-stop-cycles) up to a medium bearing load of 0.26 bar, at a temperature of 350° C.

1. Introduction

Substantial attributes of good spring bearings for small turbo machines with high speed rotors and extreme circumferential speeds and operating temperatures are the compliant structure of the bearing bushings, capable of compensating thermal deformations without any inadmissably large changes of the bearing clearance and a relative high damping in the external support of the bearing bushings guaranteeing a good stability and damping behaviour. Besides, the bearing surfaces need to have a high wearing strength because of the frequent starting under maximum load. Bearings for small gas turbines and exhaust gas turbo chargers must also stand high operating temperatures [1,2,3]. For a reliable construction of such bearings a special basis for calculation and special construction rules are necessary which are presented and discussed below.

Fig. 1 shows the three aerodynamic spring bearings with external bearing damping which were investigated. The tilting pad spring bearing [4] has bending resistant segments which are supported via a plate spring and have an adjustable clearance. In order to decrease the static journal eccentricity the segments are prestressed against stops at the side of the bearing housing. The "Garrett" spring bearing [3] has elastic foils which rest with one end in the stiff bearing bore and with the other end on the foil next to it. Here the foils are prestressed against the journal. This leads to an increased starting moment. The bearing surface and the external elasticity of the multiwedged spring bearing consist of thin walled cylindrical bushes which are elastically deformed via suitably arranged webs to a multiwedged profile. The required external bearing damping of all three spring bearing types is mainly produced by air squeeze films in the external gap.

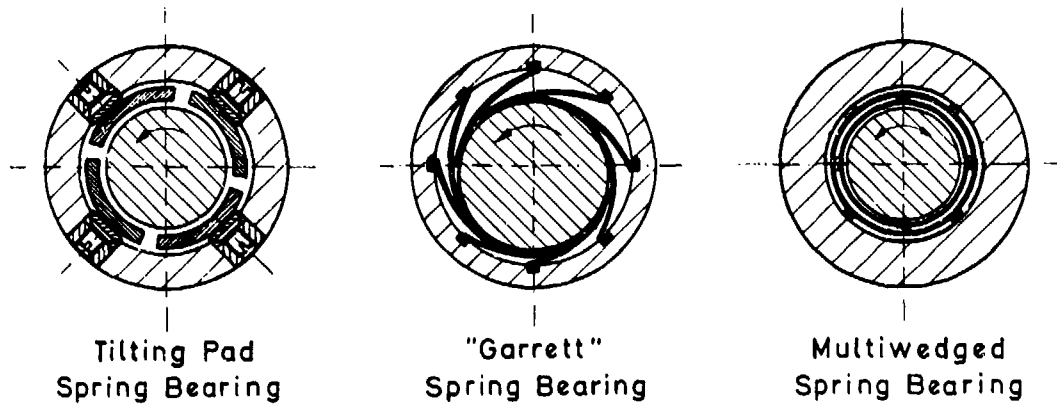


Fig. 1. Aerodynamic spring bearings investigated

2. Calculation Method for the Bearing Characteristic Curves

The direct calculation of the characteristic values of an aerodynamic spring bearing requires an extremely high calculation effort because of the complex bearing structure, the compressibility of the lubricant, and the coupling of the lubricant properties and the deformation of the bearing bushing. Therefore, systematic investigations for the development of a suitable model had to be carried out first. All three spring bearings could be related to a system of similar bending elastic bushing segments with an elastic and damping external support. The bushing elements of the investigated spring bearings differ substantially in the lubricant gap behaviour, in the position of the support points and in the angular mobility of the segments [5].

The calculation of the pure lubricant film characteristic value of a bearing element originates from the general Reynolds equation for compressible media

$$\frac{\partial}{\partial \psi} (PH^3 \frac{\partial P}{\partial \psi}) + \frac{\partial}{\partial \zeta} (PH^3 \frac{\partial P}{\partial \zeta}) = \Lambda \cdot \frac{\partial}{\partial \psi} (PH) + 2\Lambda \cdot \frac{\partial}{\partial \phi} (PH) \quad (1)$$

where $\psi, \zeta = z/(D/2)$ = the dimensionless coordinates in both circumferential and axial directions, D = journal diameter, $\phi = \omega \cdot t$ the dimensionless time, $P = p/p_a$ the dimensionless pressure (p_a = ambient pressure) and $\Lambda = 6\eta\omega/p_a\psi^2$ the compressibility number (η = dynamical viscosity, ω = angular velocity of the journal, $\psi = \Delta R/(D/2)$ = relative bearing clearance), H is the lubricant film width between the journal and the segments. In the general case, it depends on the eccentricity (ϵ, γ) of the journal center and also on the bearing bore form given by the construction, or on the lubricant gap function \bar{H} (distance of the bearing bore to the journal surface at central journal position) respectively. To simplify the calculation furthermore, the bearing bushing elements are approximated by circular segments. If the lubricant film width $H = H(\psi)$ remains constant over the bearing length, the following equation is valid

$$H(\psi) = \bar{H}(\psi) - \epsilon \cdot \cos(\psi - \gamma) \quad (2)$$

where $H = h/\Delta R$ and $\epsilon = e/\Delta R$ (ΔR = radial bearing clearance).

Contrary to hydrodynamical bearings, this partial differential equation of second order is nonlinear in the lubricant film pressure P . It describes the pressure built up $P(\psi, \zeta, \phi)$ in the lubricant gap in the case of a given compressibility number Λ and a given local and temporal gap behaviour $H(\psi, \zeta, \phi)$. In order to simplify the boundary conditions, it is assumed that an ambient pressure ($p = p_a$) dominates at all bearing segment edges (in circumferential and axial directions). This assumption is generally possible, if applied to air bearings, as in this case a certain negative pressure ($0 < p < p_a$) is also possible in the lubricant film.

The numeric solution of this differential equation was obtained by a suitable difference method. Because of the nonlinearity of the differential equation a transformation is carried out first by introducing a new variable $Q = P^2 H^2$. This transformation leads to a quasilinear differential equation whereby the hidden nonlinearity needs an additional iteration [6]. The static load capacity and the frictional force at the bearing element are the results of surface integration of pressure and of the shear stress. The nonlinear spring and damping properties of the lubricant film are approximated by stiffness and damping coefficients, as usual. These coefficients are calculated from the general Reynolds equation (1) for the nonsteady gas bearing by the perturbation "Ansatz"

$$P = P_0 + \left(\frac{\partial P}{\partial x}\right)_0 \Delta x + \left(\frac{\partial P}{\partial y}\right)_0 \Delta y + \left(\frac{\partial P}{\partial x}\right)_0 \Delta x' + \left(\frac{\partial P}{\partial y}\right)_0 \Delta y' \quad (3)$$

$$H = H_0 + \left(\frac{\partial H}{\partial x}\right)_0 \Delta x + \left(\frac{\partial H}{\partial y}\right)_0 \Delta y \quad (4)$$

For the pressure coefficient four additional linear differential equations are obtained which are also solved by a difference method [5]. The stiffness and damping coefficients finally result from a segment surface integration of the pressure coefficients. In order to calculate the bending elasticity of the bearing segments, a one-dimensional approximation (a board-like beam) is sufficient, as the elements of the investigated spring bearings are comparatively bending resistant. The bend up of the segment and the lubricant gap width of the stiff segment add up to the total lubricant gap width of the elastic segment. Generally, the stiffness of the external segment support can be calculated elementarily. The damping of the external air squeeze film is calculated from slightly modified perturbation differential equations, analogous to the damping of the inner lubricant film [5]. For further simplification it is assumed that the external elasticity and damping act on one point. The effective lubricant gap width is also influenced by the elastic and damping segment support. Therefore, the characteristic curves of a complete bearing element have to be calculated by iterative methods.

Fig. 2 explains this procedure by taking the element (index s) of a tilting pad bearing as a simple example. For the given segment dimensions (B/D , ψ_s , β_2 , β_1/β_2), the given compressibility number Λ_s and load \bar{F}_s the static operating point can be determined from the equilibrium of forces at the segment. The external load or the lubricant film pressure force \bar{F}_s respectively has to correspond with the force \bar{F}_F in the elastic support provided that $\bar{F}_s > \bar{F}_V^0$ is valid. This force results from the prestress force \bar{F}_V^0 and from the additional force $(k+H_p)\gamma_p$

$$\bar{F}_s \stackrel{!}{=} \bar{F}_F \quad \bar{F}_s = \bar{F}_s(\Lambda_s, \epsilon_s \cos \gamma_s), \quad \bar{F}_F = \bar{F}_V^0 + (k+H_p)\gamma_p \quad (5)$$

where

$$\bar{F}_s = 1 - \epsilon_s \cos \gamma_s, \quad \gamma_p = c_a \Delta R_s / (p_a B D), \quad \bar{F}_V^0 = F_V^0 / (p_a B D); \quad (6)$$

where c_a = the stiffness of the external segment support, F_V^0 = the elastic force prestressing the segment against the stop, and k is a geometric parameter of the complete bearing. The load capacity curves $\bar{F}_s(\Lambda_s, \epsilon_s \cos \gamma_s)$ of the pure lubricant film agrees with the known characteristic curves of a corresponding "fixed" segment [5,6]. The straight line $\bar{F}_F(\epsilon_s \cos \gamma_s)$ or $\bar{F}_F(H_p)$ for given \bar{F}_V^0 , k - and γ_p -values is obtained directly from equation (5). The static operating point $\epsilon_s \cos \gamma_s$ is clearly presented as the crossing point of these two curves. The static and dynamic characteristic curves of the complete bearing can be calculated approximately by a vectorial addition of the characteristic curves of all the bearing elements. Hereby the determination of the static equilibrium position (ϵ, γ) or of the static operating points $(\epsilon_s \cos \gamma_s)$ of all segments by iterative methods according to equation (5), is most important. First the parameters k or k_1 respectively depending on the parameters of the complete bearing explained in Fig. 3, have to

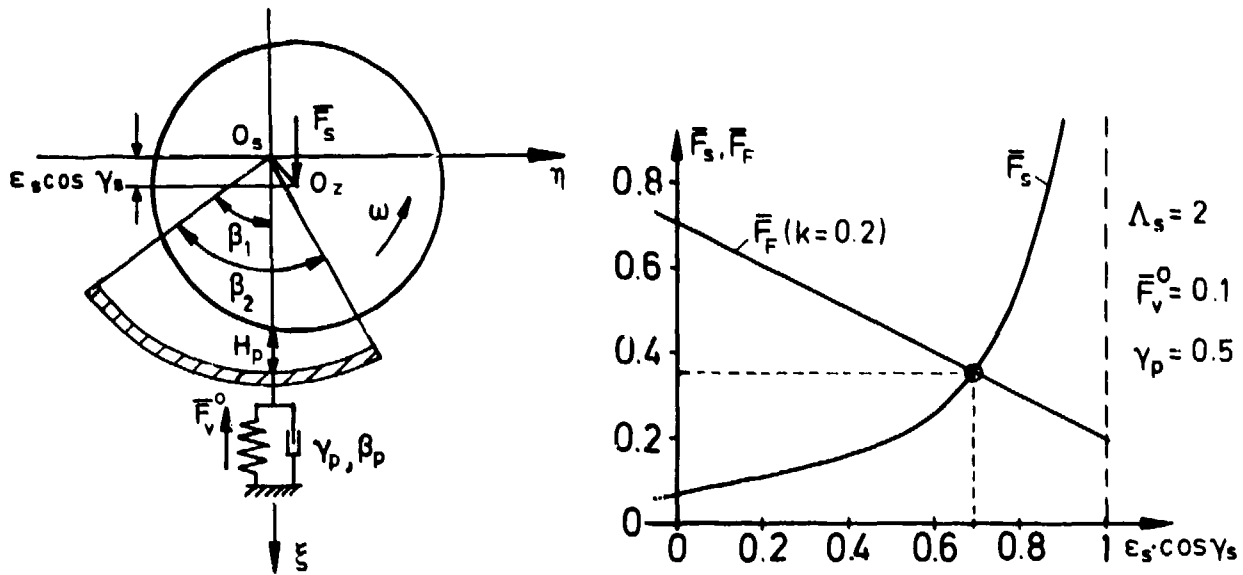


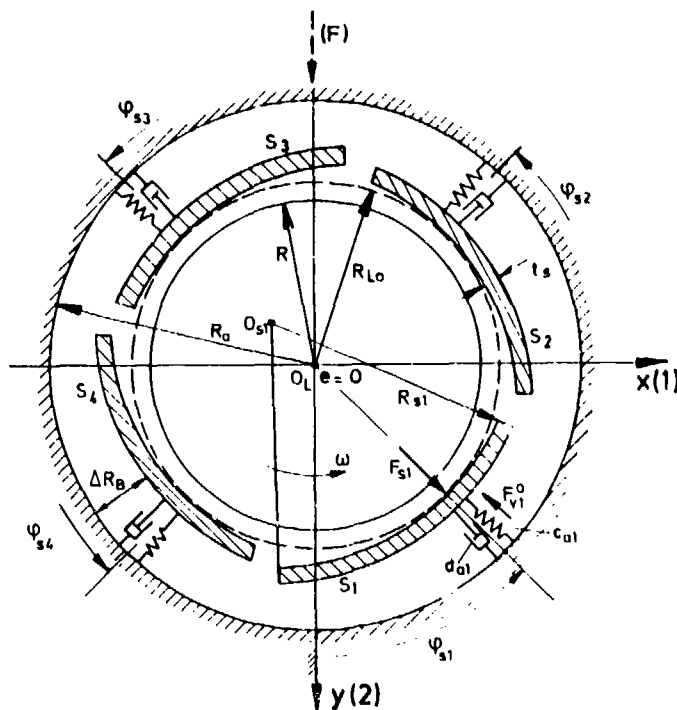
Fig. 2. Determination of the static operating point of an elastically supported tilting pad

be determined. F_{vi}^0 is the prestress force in the external spring at a bearing clearance (minimum clearance) of $\Delta R_o = R_{Lo} - R$, and in operation ($\omega \neq 0, F \neq 0$) the spring is additionally pressed about the amount of $h_{pi} + e \cdot \cos(\varphi_{si} - \gamma) - \Delta R_o$ when the prestress force is exceeded. If the dimensionless notation is used, the force F_{Fi} in the external spring amounts to

$$F_{Fi} = F_{vi}^0 + \left[h_{pi} + \frac{\epsilon}{\psi_{vi}} \cos(\varphi_{si} - \gamma) - \frac{1}{\psi_{vi}} \right] \gamma_{pi} \quad (7)$$

From equation (5) follows

$$k_1 = \left[\epsilon \cos(\varphi_{si} - \gamma) - 1 \right] / \psi_{vi} \quad (8)$$



$$\gamma_{pLi} = c_{ai} \Delta R_o / (p_a BD)$$

Fig. 3. Parameters of the tilting pad spring bearing

where $\psi_{vi} = (R_{si} - R) / \Delta R_o =$ relative bushing curvature. The distribution of the external load \bar{F} to the single segments is effected according to the equation

$$\bar{F} = \sum_{i=1}^8 \bar{F}_{si} \cos \psi_{si} \quad (9)$$

3. Calculation Results

As a high resilience of the segment support is required in operation, too large a static journal eccentricity can be avoided by choosing the correct prestress for the segment. It is recommended to choose the prestress forces of the segment \bar{F}_{vi} so that their vectorial sum is approximately in equilibrium with the given (constant) external load \bar{F}

$$\sum_{i=1}^8 \bar{F}_{vi} \cos \psi_{si} \approx \bar{F} \quad (10)$$

and also that all segments lift off before the operating rotational speed and the accompanying Λ_{si} -values respectively are reached.

Fig. 4 illustrates this principle by the symmetrical tilting pad bearing, as shown in Fig. 3 (four equal segments with $\beta_2 = 80^\circ$, $\beta_1/\beta_2 = 0.65$, $B/D = 1$). Plotted is the dimensionless load capacity \bar{F} as a function of the compressibility number Λ and the segment prestress; the two upper segments are prestressed with \bar{F}_v^{ou} , the two lower ones with \bar{F}_v^{oo} .

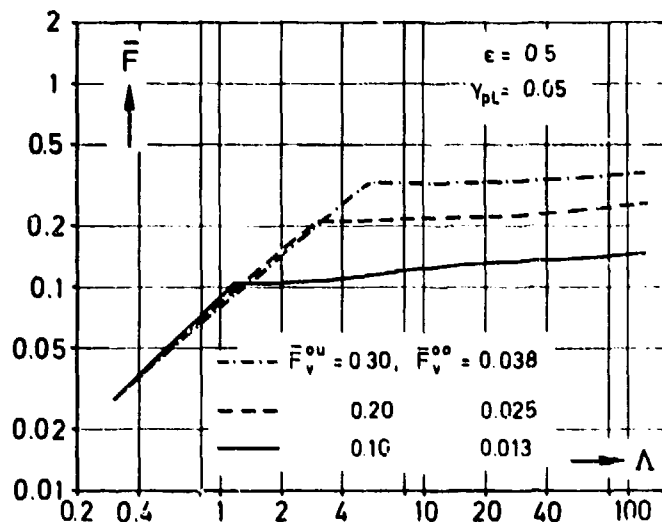


Fig. 4. Static load capacity $\bar{F}(\Lambda, \bar{F}_v^0)$ of a symmetric tilting pad spring bearing with four pads ($\beta_2 = 80^\circ$, $\beta_1/\beta_2 = 0.65$, $B/D = 1$, $\psi_v = 2$) prestressed against the housing

Here the static journal eccentricity ϵ and the stiffness of the segment support γ_{pl} are constant. Within the range of the rotational speed and the compressibility number Λ respectively, below the break point of the capacity load characteristic curve the bearing acts as it would do with a stiff segment support; there the bearing load capacity \bar{F} ascends (with $\epsilon =$ constant) with the compressibility number Λ (and the rotational speed). Above the break point the load capacity \bar{F} is determined only by the given static eccentricity ϵ and the prestress forces. An increase of the rotational speed and of the Λ -value leads mainly to an increase of the minimum lubricant gap height H_p . This characteristic spring bearing behaviour is shown by the "Garrett" bearing in a similar way. As shown in Fig. 5a the static load capacity \bar{F} increases with a given bearing ($B/D = 1$, $\bar{F}_v = 0.08$, $\gamma_{pg} = 0.05$) approximately proportionally to the static journal eccentricity ϵ ; here the compressibility number Λ_g is of little influence. The absolute minimum lubricant film height $H_{o,min}$ increases also considerably with the rotational speed and the compres-

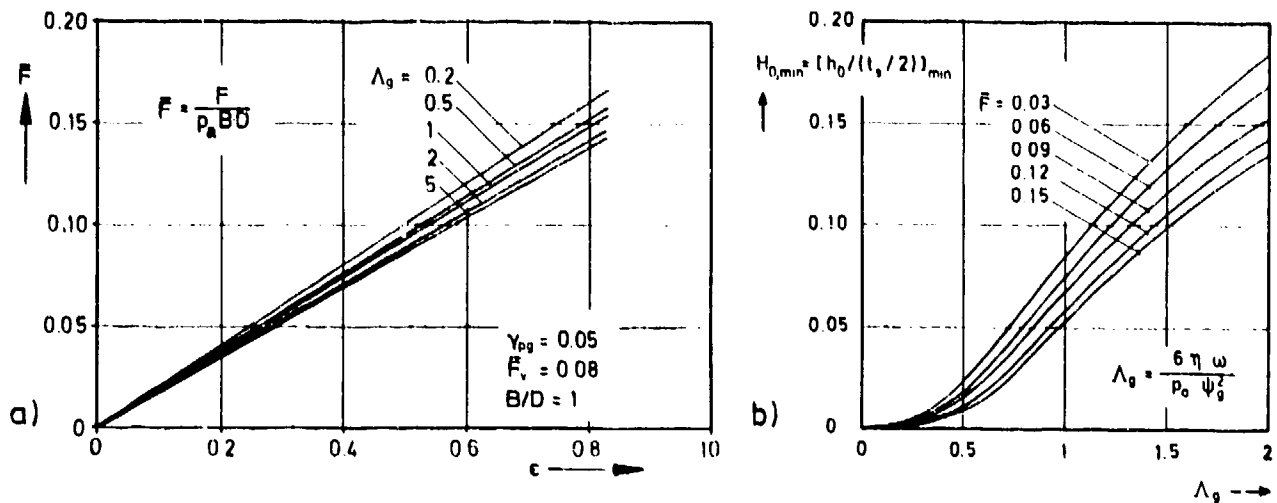


Fig. 5. Static load capacity $\bar{F}(\epsilon, \Lambda_g)$ and minimum lubricant gap width $H_{0,min}(\Lambda_g, \bar{F})$ of the "Garrett" spring bearing

stability number Λ_g , as shown in Fig. 5b, while the influence of the bearing load remains comparatively small. It should be noted that with the "Garrett" bearing, the compressibility number $\Lambda_g = 6\eta\omega/p_a\psi_g^2$ does generally not exceed the value 1, as the "reference clearance" $\psi_g = t_s/D$ is comparatively large by definition (t_s = thickness of the foils).

The static load capacity characteristic curves $\bar{F}(\epsilon)$ of the multiwedged spring bearing plotted in Fig. 6a show a stronger influence of the compressibility number Λ , resulting from the constructionally given bearing clearance ψ_{min} . According to Fig. 6b the minimum lubricant gap width H_0 ascends with the rotational speed (and with the compressibility number Λ) in the same way. The influence of the bearing load \bar{F} is here much stronger than that of the "Garrett" bearing, also because of the given bearing clearance ψ_{min} . From figures 5b and 6b the lift off rotational speed $\omega^* \sim \Lambda^*$ as a function of the load \bar{F} can be estimated for a given boundary value $H_0 \approx \epsilon R_2/\Delta R$ (ϵR_2 = sum of roughnesses).

Fig. 7 shows the dimensionless frictional force characteristic curves $F_R^*(\epsilon, \Lambda)$ for the "Garrett" and for the multiwedged spring bearing according to Fig. 5 and Fig. 6. Characteristic for the investigated spring bearing is the decrease of the frictional force F_R^* for large compressibility numbers Λ . The dependence of the static eccentricity is small in this range. For large Λ values the numerical values of the spring bearings are a little lower than those of air bearings with a stiff support and also lower than those of oil bearings.

For a given bearing and a given static eccentricity (ϵ, γ) , the stiffness and damping coefficients of the complete bearing can be calculated directly by a vectorial addition of the dynamic bearing forces and a transformation to the complete bearing system.

Fig. 8 shows the calculated stiffness and damping coefficients of the "Garrett" bearing according to Fig. 5 for a constant static load $\bar{F} = 0.13$ with a pure air squeeze film damping. In the stiffness coefficients γ_{11} , γ_{22} , the stiffness γ_{pg} of the external support or the bearing bushing structure respectively is dominant, therefore it depends only to a small extent on the compressibility number Λ_g (and on the rotational speed). The coupling coefficients β_{12} , β_{21} are in the technically interesting Λ_g -range negligibly small; therefore good stability properties of the bearing can be expected. The damping coefficients β_{11} , β_{22} first increase considerably with the compressibility number Λ_g (and rotational speed); having exceeded a maximum, they decrease (as with all air

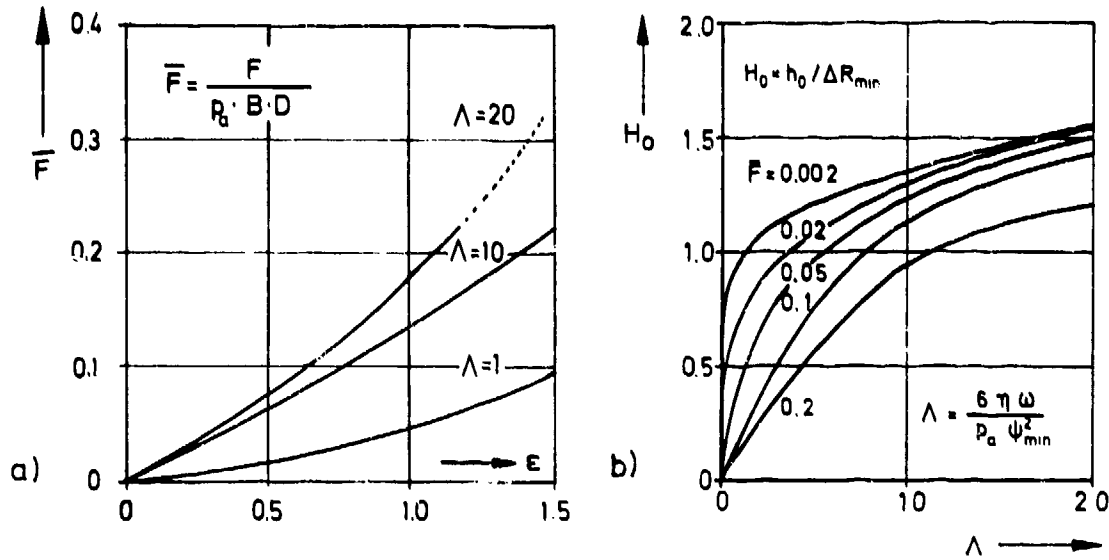


Fig. 6. Static load capacity characteristic curves $\bar{F}(\epsilon, \Lambda)$ and minimum lubricant gap width $H_0(\Lambda, \bar{F})$ of a multiwedged spring bearing

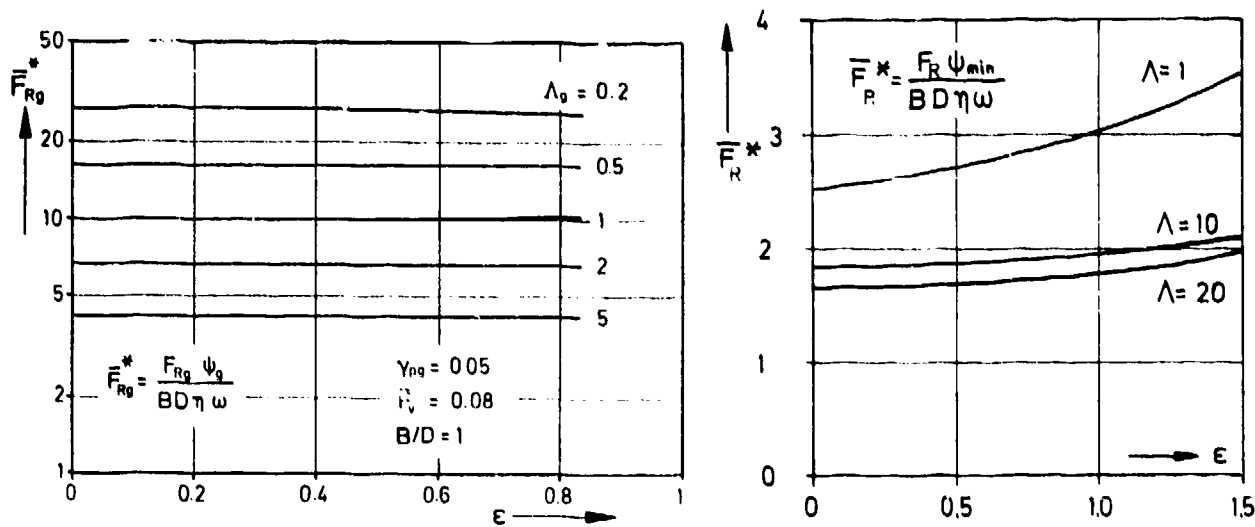


Fig. 7. Dimensionless friction force $\bar{F}_{Rg}(\epsilon, \Lambda_g)$ of the "Garrett" spring bearing and $\bar{F}_R^*(\epsilon, \Lambda)$ of the multiwedged spring bearing

bearings). The coupling coefficients β_{12} , β_{21} are negligibly small. In the range of the high rotational speeds ($\Lambda_g > 0.3$) the damping coefficients β_{11} , β_{22} are of the order of magnitude of the stiffness coefficients γ_{11} , γ_{22} , therefore a good damping capacity can be expected too. Fig. 9 shows also for a constant load $\bar{F} = 0.26$ the stiffness and damping characteristic curves of the tilting pad spring bearing according to Fig. 4. Above the lift-off point (i. e. after exceeding the prestress) they take a similar course as the curves of the "Garrett" bearing. The stiffness coefficients $\gamma_{11} = \gamma_{22}$ of the complete bearing are again in the order of magnitude of the stiffness of the complete support $2\gamma_{pL} = 0.12$ and depend only little on the compressibility number Λ . The damping coefficients $\beta_{11} = \beta_{22}$ first increase with the rotational speed (and with Λ) and decrease

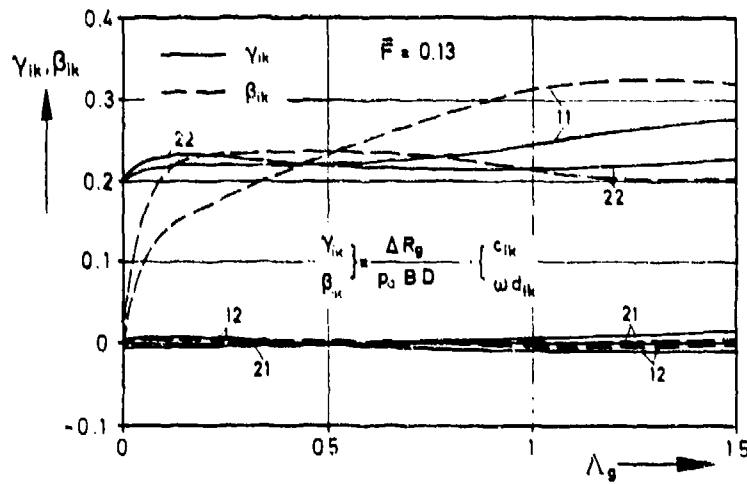


Fig. 8. Stiffness and damping coefficients of the "Garrett" bearing according to Fig. 5

with extreme Λ -values after having reached a maximum. In the technically interesting Λ -range the damping coefficients are influenced substantially by the gap width ψ_B of the external air squeeze gap. It should be mentioned, that for the idealized symmetrical tilting pad bearing all coupling coefficients become zero.

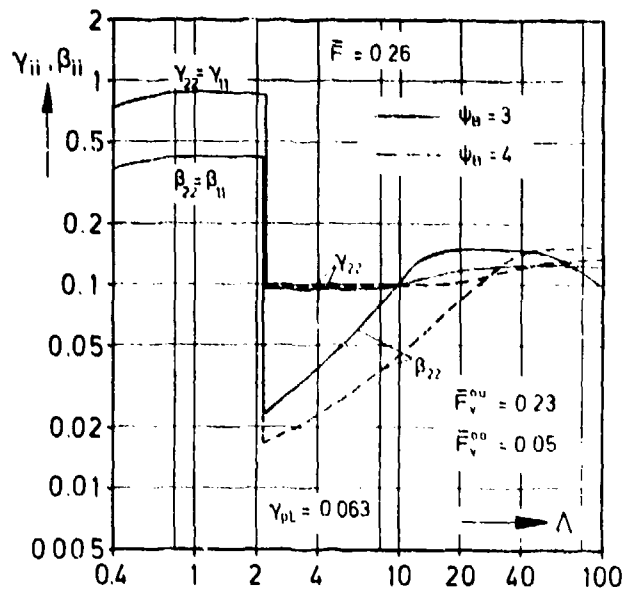


Fig. 9. Stiffness and damping coefficients of the tilting pad spring bearing according to Fig. 4 with an external damping by an air squeeze film and segments pre-stressed against a stop at the housing

4. Experimental Determination of the Stiffness and Damping Capacity of the Bearings

The calculated dynamical bearing characteristic values were determined, in general, by vibration measurements with complete rotor bearing systems. These measurements were carried out with a high speed rotor test stand with a variable rotational speed (maximum power 20 kW, maximum rotational speed 100,000 rpm) [4]. The measured quantities were the shaft vibration movement, the static journal eccentricity, deformations of the bearing bushing structure and temperatures in the bearing bushing. All tests were carried out with symmetrical rotors mounted in two identical bearings. In Fig. 10 the two test rotors are shown and their most important parameters are specified. The further substantial test parameters have been defined as follows: lubricant = ambient air (no compressed air supply), bearing length ratio $B/D = 1$, relative bearing clearance at a maximum rotational speed $\psi_{\min} \approx 0.5$ to 1‰ (self adjusting).

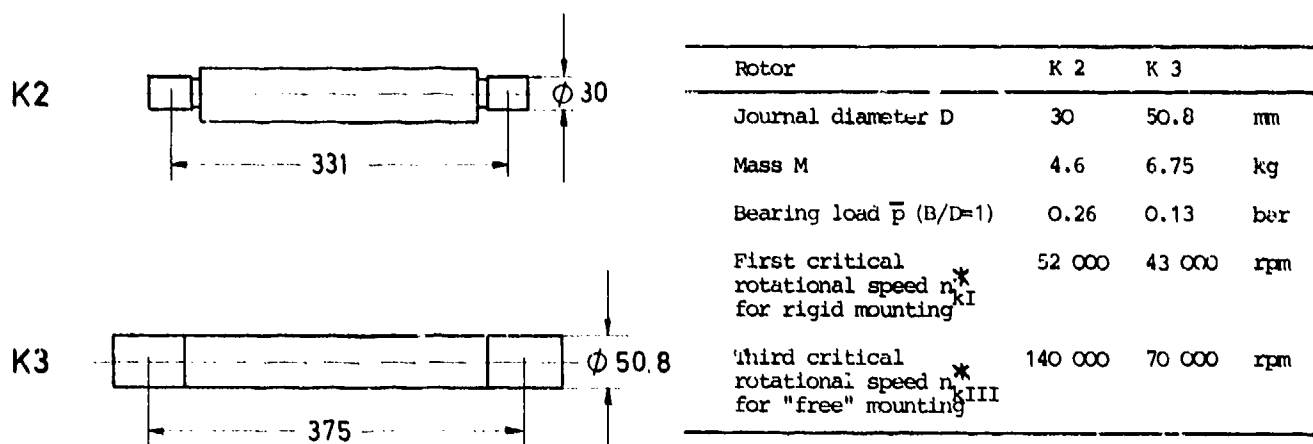


Fig. 10. Test rotors of the high-speed test stand

Fig. 11 shows for the combination rotor K3 with "Garrett" bearings according to Fig. 5 the measured vibration amplitudes A_I (amplitude A_I = greater semiaxis of the elliptical displacement of the free shaft-journal) plotted as a function of the shaft rotational speed. Curve parameter is the additional static unbalance or the eccentricity of the center of gravity Δp respectively. The amplitude curves $A_I(n)$ show exclusively in the range of the rotational speed from $n = 5,000$ to 9,000 rpm an evident amplitude increase, resulting from the first two critical rotational speeds. If the additional unbalance becomes too high, the vibration amplitude near the resonance increases substantially, while additionally subharmonic vibrations occur. The admissible range of the rotational speed is

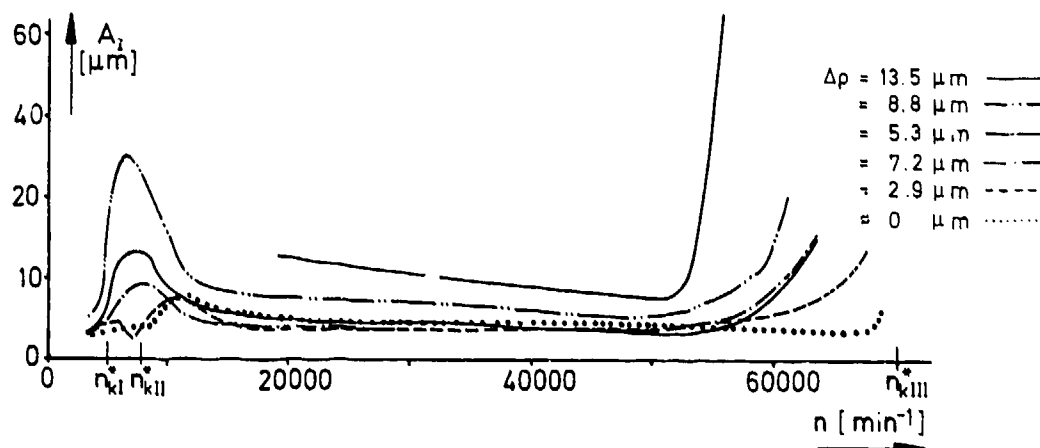


Fig. 11. Effects of a static unbalance Δp on the vibration amplitude A_I of the rotor K3 with "Garrett" spring bearings

limited by a substantial amplitude increase to the third critical rotational speed n_{kIII}^* , defined mainly by rotor data. In the wide range of the rotational speed between the first/second and third critical rotational speeds the vibration amplitudes are very small; self-excited vibrations did not occur within the complete rotational speed range. By comparison the calculation values of the first three critical rotational speeds n_{ki}^* are marked in Fig. 11. Measured and calculated values agree satisfactorily, hence the calculation values for the stiffness of the complete bearing are confirmed.

In Fig. 12 the influence of an additional unbalance on the vibration amplitude A_I of rotor K2, mounted in tilting pad spring bearings according to Fig. 4, is plotted analogously. With $\bar{p} = 0.26$ the bearing load is substantially higher. For small unbalances similar amplitude curves result as shown in Fig. 11. If a certain "boundary unbalance" is exceeded, the resonance amplitude increases super-proportionally with the magnitude

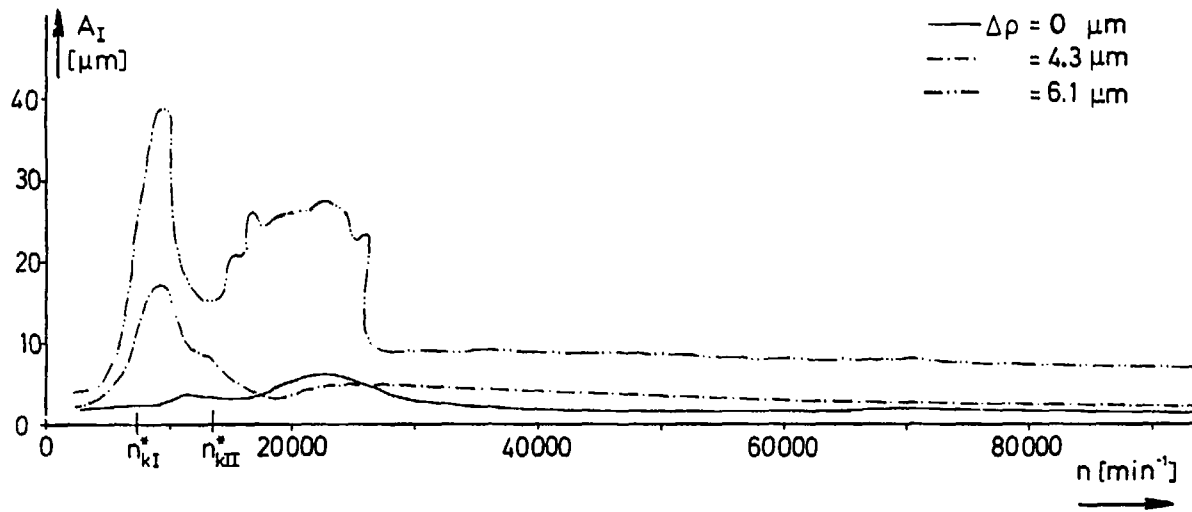


Fig. 12. Effects of a static unbalance $\Delta\rho$ on the vibration amplitude A_I of the rotor K2 with tilting pad spring bearings

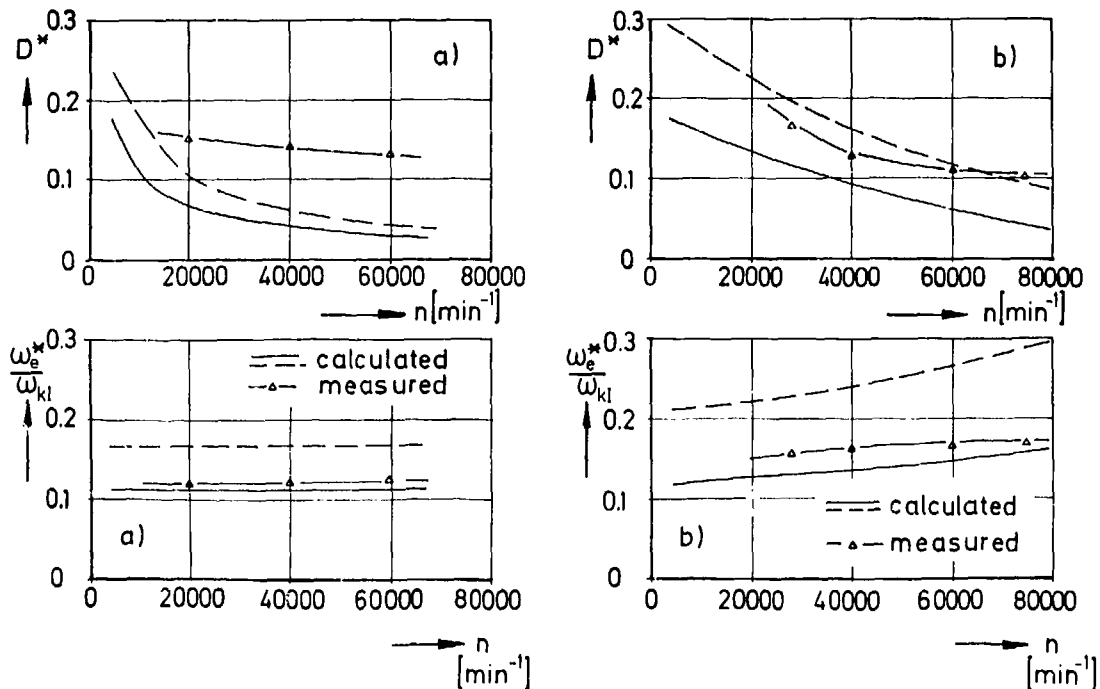


Fig. 13. Comparison between calculated and measured system dampings D^* and natural cyclic frequencies of the rotor K3 with "Garrett" spring bearings (a) and of the rotor K2 with tilting pad spring bearings (b)

of the unbalance. Besides, dangerous subharmonic vibrations may occur over large rotational speed ranges. The operating range is limited only by the maximum rotational speed of the test stand drive; the third critical rotational speed of rotor K2 is $n_{kIII}^* = 135,000$ rpm. The calculated first two critical rotational speeds n_{kI}^* and n_{kII}^* are marked in Fig. 12; they are confirmed by the measured values. Similar amplitude curves result with rotor K2 mounted in multiwedged spring bearings. With a dynamic unbalance the resonance amplitudes are significantly higher. Besides, the danger of subharmonic perturbation vibrations increases.

The theoretically determined damping capacity of the bearings can be experimentally checked best by measuring the system damping. Therefore, in operation with an electromagnet a contactfree shock of very short duration is applied to the center of gravity of the rotor and the impact transition function is measured. From its fading velocity or the time constant T_z respectively and the frequency ω_e^* , the system damping $D^* = 1/(T_z \omega_e^*)$ can be determined. Fig. 13a shows a comparison of the calculated and measured system damping D^* and the natural cycling frequency ω_e^*/ω_{kI} of rotor K3 with "Garrett" spring bearings according to Fig. 5. As the rotor bearing system answers in experiment only with the lowest natural vibration, a plotting of the first two calculated eigenvalues of the system is adequate.

The correspondence of measured and calculated values is satisfactory in respect of the manufacturing tolerances. The theoretically determined dynamical bearing characteristic values and also the substitute model are confirmed by the measured values. Fig. 13b shows the corresponding comparison for rotor K2 with tilting pad spring bearings according to Fig. 4. Here a satisfactory correspondence and therefore a confirmation of the calculated values results too. For all three spring bearings the system damping in the complete range of rotational speed remains positive therefore in normal operation there is no danger of self-excited vibrations coming from the bearing.

5. Starting Tests and Bearing Materials

By means of starting tests up to medium rotational speeds (about 30,000 rpm) first the function safety (low lift-off rotational speed, low friction, good damping capacity) for different material and construction variants has to be checked. It was considered as satisfactory provided the lift-off rotational speed was exceeded without disturbance, i. e. without excessive warming or substantial thermal deformations, and the first critical rotational speed of the rotor-bearing-system could be passed without inadmissably large vibration amplitudes. In order to reduce the efforts in manufacturing the bearings and in carrying out tests, the starting test stand shown in Fig. 14 has only one test bearing; the second bearing is a roller bearing. The bearing housing of the test bearing can be heated up to a maximum temperature of 350° C by a heating conductor surrounding the bearing. The test bearings had the same dimensions as used for the vibration measurements (30 mm journal diameter for the tilting pad spring bearing and the multiwedged spring bearing, and with $2'' = 50.8$ mm for the "Garrett" spring bearing); the bearing loads were the same as used for the vibration measurements ($\bar{p} = 0.13$ bar for the "Garrett" spring bearing, $\bar{p} = 0.26$ bar for the tilting pad spring bearing and for the multiwedged spring bearing). The wearing strength of the bearing materials in the starting range was proved by automatically controlled continuous starting tests with 10,000 start-stop-cycles. Fig. 15 shows the amplitude curves $A(n)$ of 10 start-stop-cycles for the tilting pad bearing. According to these the start and coast-down curves differ a little, but their temporal change during the complete test duration remains comparatively small. The requirements for the material selection were an adequate temperature resistance and a good emergency running behaviour (little scuffing tendency) in the starting range. It was found that ceramic materials to which in a wider sense also graphite belongs were most suitable. For use as air bearing materials only dense materials with a relatively good

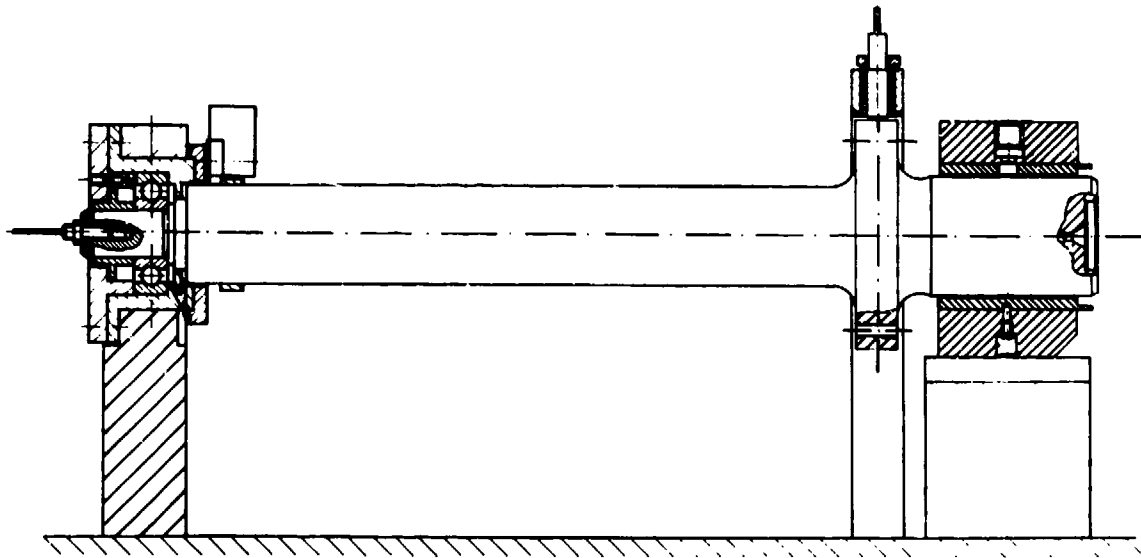


Fig. 14. Longitudinal section of the starting test stand

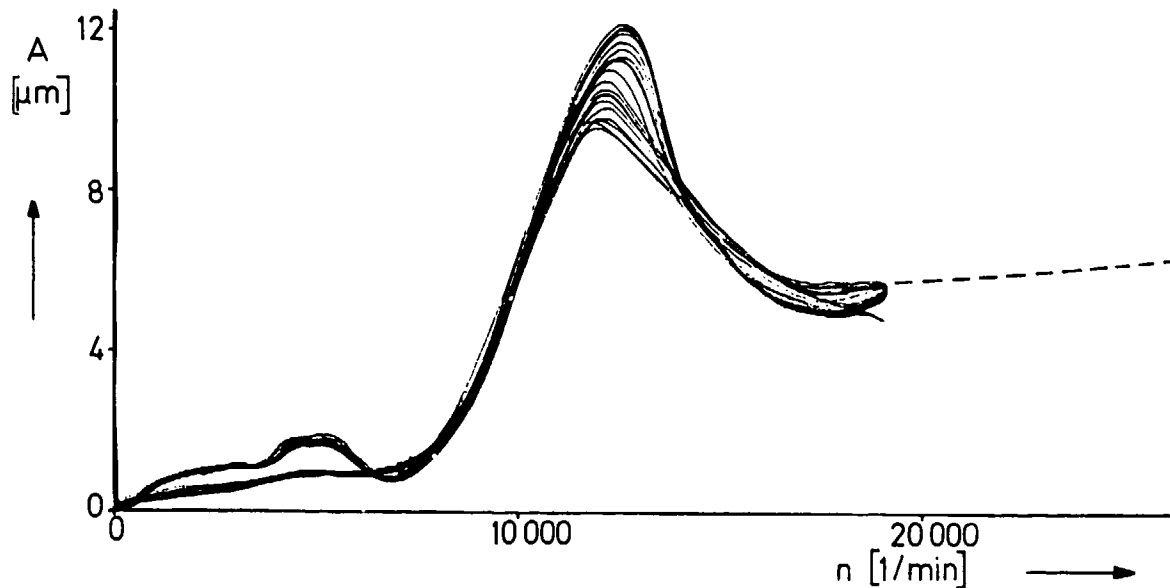


Fig. 15. Measured amplitude curves of starting tests with the tilting pad spring bearing

heat conduction capacity were suitable. For the material pairings graphite/steel and ceramic/hard metal coating, an adequate wearing strength was proved up to a medium bearing load of 0.26 bar, at a temperature of 350° C, by continuous starting tests (with 10,000 start-stop-cycles). At the moment these investigations are continued with higher temperatures up to 700° C, and with greater radial and axial temperature gradients. Finally, it can be concluded that with these three spring bearings investigated, an adequate load capacity and bearing damping can be achieved by a correct support design and a correct prestress of the segments. The necessary wearing strength and temperature resistance are only guaranteed by a correct material selection.

References

- [1] Morishita, T.: Experiments on Hydrodynamic Gas Bearing Applied to Automotive Gas Turbine. ASME Paper 74-GT-150 (1974)
- [2] Gray, S., Sparks, M. a. McCormick, J.: Application of Gas- and Oil-Lubricated Foil-Bearings for the ERDA/Chrysler Automotive Gas Turbine Engine. ASME Paper 76-GT-115 (1976)
- [3] Trippett, R. J.: Air Bearing Development for a GM Automotive Gas Turbine. SAE-Paper 790107, Feb. 1979
- [4] Glienicke, J., Domes, B. u. Ehinger, M.: Untersuchungen zur Schaffung von Auslegungsgrundlagen für aerodynamische Lager kleiner Turbomaschinen. 1. Teilabschlussbericht: Experimentelle Ergebnisse, Forschungsberichte Verbrennungskraftmaschinen, Heft 264, Frankfurt 1979
- [5] Glienicke, J. u. Hunger, H.: Untersuchungen zur Schaffung von Auslegungsgrundlagen für aerodynamische Lager kleiner Turbomaschinen. 2. Teilabschlussbericht: Theoretische Untersuchungen, Forschungsberichte Verbrennungskraftmaschinen, Heft 274, Frankfurt 1980
- [6] Wilcock, D. F. (Ed.): Design of Gas Bearings. Mechanical Technology Inc., Latham/ New York 1972

Acknowledgment

This report is the result of research commissioned by the Forschungsvereinigung Verbrennungskraftmaschinen e. V., Frankfurt am Main, and carried out at the Institut für Maschinenkonstruktionslehre der Universität Karlsruhe. The investigations were financially supported by the Bundesministerium für Wirtschaft over the Arbeitsgemeinschaft Industrieller Forschungsvereinigungen e. V. (AIF-Nr. 3596). The authors thank the Research Association and the Ministry for their valuable financial support. Thanks are also conferred to the team of the Forschungsvereinigung Verbrennungskraftmaschinen formed for the research task, which was under the direction of Dr.-Ing. D. Schmidt.

DISCUSSION

B.Courage, Rolls Royce (Aero Div) Ltd, Bristol, UK

Your analysis model assumes circular arc forms for the foil profiles or segments. Are you confident that the deformation during operation does not invalidate this assumption?

Author's Reply

All three spring bearings can be related to a system of similar circular segments. In an additional calculation the bending elasticity was taken into account.

M.A.H.Sequeira, Portuguese Oil Co., Po

Once there is no lubricant at all in these aerodynamic bearings, could you anticipate any kind of problems due to high percentages of humidity in the air?

The deposition of H_2O , due to vapour pressure that condenses during non working periods, couldn't attack the metal surfaces non-protected due to the absence of the oil film?

Author's Reply

We did not carry out any special investigations on the effect of humidity in the air on the metal surface. Changes of the surface due to this effect have not been obvious.

R.Holmes, University of Sussex, UK

This paper continues the fine tradition of the bearing work at Karlsruhe. What limitations would be imposed on the use of such bearings, e.g., size limitations or load limitations for adequate operation?

Author's Reply

With regard to the low viscosity of air, a pressure of $p = \frac{F}{B \cdot D}$ ($B = 1$) = 0.26 bar seems to be the upper limit.

D.K.Hennecke, MTU Munchen GmbH, Ge

Does your term "Garrett" bearing refer to a type or class of bearings or is it an actual bearing designed for a Garrett engine, and which engine is it?

Author's Reply

For our first investigations a bearing purchased from Garrett AiResearch has been used. This bearing type has PTFE-coated foils. In the next presentation Mr Suriano will report about an advanced bearing type.

V.Bruno, Pratt & Whitney, Ca

Is the coating of the surfaces rubbing during starts and stops, when no or insufficient lift is present, durable enough to allow applications on high cycles machines?

Author's Reply

The sufficient wear strength of the material pairings has been proved by 10,000 start-stop-cycles, whereby the speed range of no or insufficient lift has been exceeded every time.

**HIGH-TEMPERATURE (649°C/1200°F) COATINGS FOR
GAS-LUBRICATED FOIL BEARINGS OF THE NAVY'S ADVANCED
AUXILIARY POWER UNIT CONCEPTS**

Frank J. Suriano
Robert J. Keiser
Garrett Turbine Engine Company
A Division of The Garrett Corporation, Phoenix, Arizona, USA

Fred G. Woessner
Ray Valori
Naval Air Propulsion Center, Trenton, New Jersey, USA

SUMMARY

In a recent high-temperature foil bearing development effort(1) a separate materials task was directed at identifying and developing coatings and coatings combinations for use in a turbine-end journal foil bearing of an advanced design auxiliary power unit. The coatings were required to operate in thermal environments up to 649°C (1200°F). This paper describes that materials development task and the identified coatings.

INTRODUCTION

A study(2) for the definition of an advanced design auxiliary power unit (APU) applicable to modern Naval fighter/attack and V/STOL aircraft identified gas-lubricated foil bearings as a key component which would contribute to the increased efficiency, decreased weight and increased reliability of the APU. A foil bearing capable of operation in the turbine-end of this advanced design APU must sustain steady-state operating temperatures of 538°C (1000°F), potential transients to 649°C (1200°F), and loads equivalent to 20 + g's due to flight maneuvers. A high-temperature foil bearing development program(1) was undertaken to develop the foil bearing suitable for use in this advanced design APU, and the associated coating materials development is described herein.

The load-carrying capacity in a self-acting (hydrodynamic) fluid-film bearing is derived from the pressure generated in the film by the relative motion of two converging surfaces. The compliant foil journal bearing concept utilizes a rotating journal and a mating compliant foil as the converging surfaces (Figure 1). A certain relative speed between the surfaces is required to develop an adequate film, after which non-contact conditions between the journal and foil exist in the operating bearings.

Contact between the mating surfaces occurs when the journal speed is below that required to develop a supporting hydrodynamic film, such as a start-up and shut-down, or during bearing overload while operating. At these times, surface lubrication is provided in the form of a solid coating applied on the mating journal and foil surfaces. Foil bearings for low-temperature applications have been utilized in production turbomachinery for a number of years. The current dry-film coatings in these applications, such as Teflon, are limited to approximately 232°C (450°F) maximum operating temperature. Current low-temperature foil and journal coatings and coating combinations possess the following general characteristics:

- o Good wear resistance
- o Low friction coefficient
- o Chemical compatibility and good bondability with substrate material
- o Durability
- o Machinability
- o Availability
- o Low cost

For high-temperature applications, the coatings/combinations must possess all of the above characteristics up to higher temperatures, and also have:

- o Good oxidation resistance, or alternatively, the gradual formation of a soft lubricious oxide
- o Diffusional stability with the substrate
- o Adequate thermal conductivity
- o Thermal expansion coefficient compatible with the substrate material

The high-temperature foil bearing coatings development effort which was conducted is summarized in Figure 2. It was designed to reduce an initial coating combination candidate matrix to the two or three best suited coating combinations for the 649°C (1200°F) foil bearing application. The three principal steps in the materials development were:

Step 1 - Preliminary materials testing involving an inspection of incoming coatings for quality and mechanical integrity, followed by static oven screening to evaluate thermal fatigue and oxidation resistance.

Step 2 - Sliding friction measurements at three test temperatures conducted on a reduced matrix of shaft/foil coatings identified by the preliminary screen

Step 3 - Dynamic properties testing of a selected group of coating combinations on a materials test rig, and selection of final coating combinations for actual foil bearing testing.

CANDIDATE COATINGS AND COATINGS COMBINATIONS

A matrix of the ten candidate journal coatings and twelve candidate foil coatings was constructed (Table 1). The coating combinations exhibiting a high probability for successful foil bearing operation are identified by an "X". These coating combinations were selected on the basis of results from a prior Garrett high-temperature foil bearing program(3), results from a recent NASA/MTI foil bearing program(4), and input from miscellaneous recent literature.

The following brief discussion of the characteristics of each coating provides the basis for the coating selections.

Foil Coatings (IN718 substrate)

Kaman DES - Chemically adherent chrome oxide (Cr_2O_3) coating.

Kaman DES Plus Au Overcoat (Sputtered) - The gold overcoat is intended to improve foil surface quality and friction behavior.

Kaman DES Plus TiB_2 Overcoat (Sputtered) - TiB_2 offers excellent friction qualities.

Co-20 Ni (Electroplated) - Excellent as-plated surface finish, good friction qualities due to formation of lubricious cobalt oxide.

Co-20 Ni Plus TiB_2 Overcoat (Sputtered) - TiB_2 provides an oxidation-resistant and wear-resistant top coat for the soft cobalt-nickel substrate.

Co-20 Ni Plus Cr_2O_3 Overcoat (Sputtered) - Good oxidation and wear qualities of overcoat for soft cobalt-nickel substrate.

TiB_2 (Sputtered) - Excellent friction qualities, good wear capability, good oxidation resistance.

Cr_2O_3 (Sputtered) - Good oxidation and friction qualities. This permits a direct comparison with Kaman DES (chemically adherent Cr_2O_3).

TiC (Sputtered) - Good oxidation resistance and friction behavior.

B_4C (Sputtered) - Best overall oxidation resistance and friction behavior in the prior program(3).

Ion-Plated Cr-Au - Ion-plated Cr-Au is a two-layer coating system developed for anti-fret and wear applications.

Reactively Ion-Plated Cr_2O_3 - Ion-plated Cr_2O_3 coating was chosen to compare the reactive ion-plating process with sputtering and chemical bonding.

Shaft Coatings (IN718 Substrate)

Kaman SCA - Chemically adherent oxide composite ceramic containing Al_2O_3 , SiO_2 , and Cr_2O_3 .

Kaman SCA Plus TiB_2 Overcoat (Sputtered) - The TiB_2 overcoat improves the friction behavior of the SCA surface.

Kaman SCA Plus Ion-Plated Gold - The gold overcoat improves the friction response of the SCA material.

Co-20 Ni (Electroplated) - Excellent finish capability, good friction qualities.

Co-20 Plus Cr_2O_3 Overcoat (Sputtered) - The same reasoning as for the cobalt-nickel plus overcoat choices for the foils.

Co-20 Ni Plus TiB_2 Overcoat (Sputtered) - Same reasoning as combination above.

Tribaloy 400 (D-Gunned) - Tribaloy 400 is a cobalt base alloy containing a hard, wear-resistant intermetallic phase. Lubricity is derived from cobalt and molybdenum oxides.

Tribaloy 400 (D-Gunned) + Ion-Plated Gold - The gold overcoat provides low friction during the break-in period prior to formation of cobalt/molybdenum oxides.

Ni-Cr Bonded CrB_2 (Plasma-Sprayed) - This was one of the more successful coatings evaluated on a prior program(3).

NASA Lube PS-120 (Plasma Sprayed) - A composite material containing Tribaloy 400 for wear resistance, silver for low- to intermediate-temperature lubrication, embedability, and thermal conductivity, and calcium fluoride for high-temperature lubrication.

TABLE 1. HIGH-TEMPERATURE COATING CANDIDATES

Foil Coatings	Kaman DES Overcoat of:			Co-20 Ni Overcoat of:			Sputter Coatings Direct to Foil				Ion Plated	
	None	Au	TiB ₂	None	TiB ₂	Cr ₂ O ₃	TiB ₂	Cr ₂ O ₃	TiC	B ₄ C	Cr-Au	Cr ₂ O ₃
Journal Coatings												
Kaman SCA:												
No Overcoat	X	X			X	X	X	X	X	X	X	X
TiB ₂ Overcoat			X									
Au Overcoat	X											
Co-20 Ni:												
No Overcoat	X				X	X	X		X	X		X
Cr ₂ O ₃							X					
TiB ₂ Overcoat			X		X							
Tribaloy 400:												
No Overcoat	X			X				X	X			
Au Overcoat						X	X					X
Ni-Cr Bonded CrB₂												
No Overcoat								X	X			
NASA Lube PS-120 (Tribaloy/Silver/CaF ₂)	X			X								

Note: (Preferred combinations indicated by X.)

PRELIMINARY MATERIALS TEST PROCEDURES

Foil and journal coating test specimens were fabricated for preliminary testing. The foil specimens were fabricated by applying the candidate coating to both sides of an IN718 blank, which was 0.152 mm (0.006 inch) thick, 50.8 mm (2.0 inches) long and 25.4 mm (1.0 inch) wide. The journal specimens were fabricated by applying the candidate coating to a single side of a 3.75 mm (0.125 inch) thick IN718 blank, 114.3 mm (4.5 inches) long and 31.75 mm (1.25 inch) wide. The coated journal blanks were then aged and ground (as required) to the desired surface finish and coating thickness. All of the coatings in the initial test matrix were subjected to metallographic and SEM analysis to assess coating quality, uniformity and composition. SEM also was used whenever essential to assess a coating's response to the various tests performed on the coating.

The preliminary testing consisted of mechanical and oven screening tests designed to reduce the initial 10/12 matrix to a 6/6 matrix. The mechanical tests, which were performed both before and after the oven exposure tests, are described below:

- o Surface Finish
- o Bend Test (Foil Specimens) - Coating ductility and bond strength were tested by bending coated foil specimens through a 90-degree turn about a 3.175 mm (0.125-inch) mandrel. SEM analysis of the bent samples then was used to rank coating ductility and bond strength by measuring the average crack internal (spacing between cracks) and documenting any coating spallation
- o Hardness Test (Journal Specimens) - Knoop indentation on polished sections.
- o Scratch Test
- o Tape Test - A tape test was performed using 3-M, Number 150, pressure-sensitive tape to obtain a qualitative assessment of the adhesion between coating and substrate

After inspecting and testing the coating as described above, thermal exposure testing was conducted on the coated specimens. Separate oven tests were performed at 538°C (1000°F) and 649°C (1200°F) in an air atmosphere for a period of 500 hours. At the end of the 500-hour period, the specimens were cycled from their respective test temperatures to about 149°C (300°F) by withdrawal from the furnace and rapid air cooling. A minimum of ten cycles was accumulated.

Periodically during the thermal exposure testing, the specimens were withdrawn from the furnace, cooled to room temperature, ultrasonically cleaned in acetone, and weighed to determine the time dependence of coating oxidation.

After the 649°C (1200°F) thermal exposure testing, the coated specimens were retested with some of the same mechanical tests used prior to exposure.

PRELIMINARY SCREENING RESULTS--FOIL COATINGS

Talysurf profilometer surface finish readings were made on all incoming foils. The thin foil coatings generally reproduced the surface finish of the underlying substrate material, i.e., the surface finish was in the range of 3-6 microinches (RMS).

Bend test data for the coated foil specimens prior to thermal exposure are shown in Figure 3. The data in this Figure show that the coatings with metallic constituents offered the highest ductility. The data also show that even relatively brittle coatings such as Kaman DES can exhibit better surface quality when "top coated" with a ductile material such as gold.

Due to the subjectivity of the scratch test, a comprehensive breakdown from best to worst was not attempted. Instead, the foil coatings were grouped into four separate performance levels, as described briefly below:

<u>Rating</u>	<u>Description</u>
Excellent	No chipping, cracking, or coating breakthrough. Low friction, no abrasive wear debris.
Good	Limited chipping and/or cracking, local coating breakthrough. Some abrasive wear debris.
Fair	Moderate chipping and/or cracking. No crack branching or gross spalling.
Poor	Gross chipping and spalling.

Both visual and SEM observations contributed to the overall rating. Table 2 summarizes the ratings for the tested coatings.

Lastly, it is noted that all of the foil coatings candidates successfully passed the tape test.

Figures 4 and 5 present the weight change versus exposure time data for the coatings at exposure temperatures of 538°C (1000°F) and 649°C (1200°F), respectively. Ratings of the coatings thermal exposure performance, based on visual, SEM and weight change data, are presented in Tables 3 and 4 for the 538°C (1000°F) and 649°C (1200°F) testing, respectively. The relative rankings of the candidate coatings in Tables 3 and 4 are quite similar. A noticeable exception is ion-plated Cr-Au, which is ranked significantly higher at 649°C (1200°F) than it is at 538°C (1000°F).

TABLE 2. FOIL COATING SCRATCH TEST DATA

Coating	Comments	Rating
Ion Plated Cr-Au	Very low friction, no cracking, shipping or coated breakthrough. Some "plowing" at scratch edges.	Excellent
Kaman DES+Au	Very low friction, no breakthrough of Au, no plowing.	Excellent
Sputtered TiB ₂	Good bond, no chips, or cracks.	Good
Kaman DES	Very limited chipping at scratch edges. Some abrasive wear debris.	Good
Electroplated Co-20 Ni	Low friction, no breakthrough, some small cracks at scratch edges.	Good
Co-20 Ni + Sputtered Cr ₂ O ₃	Very hard. No cracks or chips, small amount of wear debris.	Good
Sputtered Cr ₂ O ₃	Localized chipping, no cracks, some abrasive wear debris.	Fair
Sputtered TiC	Localized chipping, no cracks, no wear debris.	Fair
Sputtered B ₄ C	Extremely hard (no coating breakthrough) although extensive chipping at scratch edges.	Fair
Co-20 Ni + Sputtered TiB ₂	Some spalling of TiB ₂ at scratch edges.	Fair
Ion plated Cr ₂ O ₃	Excessive spallation in and around scratch.	Poor
Kaman DES + Sputtered TiB ₂	Excessive TiB ₂ spallation in and around scratch.	Poor

TABLE 3. CANDIDATE FOIL COATINGS - 538°C (1000°F) THERMAL EXPOSURE PERFORMANCE RATING

Coating	Rating	Rating Designations
Kaman DES	Excellent	<u>Excellent</u> - No visual coating degradation. Stable weight change versus time behavior.
Sputtered TiC	Excellent	
Electroplated Co-20 Ni	Excellent	
Sputtered Cr ₂ O ₃	Good	<u>Good</u> - Localized areas of superficial attack not resulting in substrate exposure. Stable weight change versus time.
Kaman DES + Au	Good	
Sputtered B ₄ C	Fair	<u>Fair</u> - More pronounced degradation with some areas (less than 10%) of substrate exposure.
Ion Plated Cr-Au	Fair	
Kaman DES + TiB ₂	Poor	<u>Poor</u> - Excessive oxidation and/or spalling of coating. Unstable weight change versus time behavior.
Co-20 Ni + TiB ₂	Poor	
Co-20 Ni + Cr ₂ O ₃	Poor	
Sputtered TiB ₂	Poor	
Ion Plated Cr ₂ O ₃	Poor	

TABLE 4. CANDIDATE FOIL COATINGS - 649°C (1200°F) THERMAL EXPOSURE PERFORMANCE RATING

Coating	Rating	Rating Designations
Kaman DES	Excellent	<u>Excellent</u> - No visual coating degradation. Stable weight change versus time behavior.
Sputtered TiC	Excellent	
Ion Plated Cr-Au	Excellent	
Sputtered Cr ₂ O ₃	Good	<u>Good</u> - Localized areas of superficial attack not resulting in substrate exposure. Stable weight change versus time.
Kaman DES + Au	Good	
Electroplated Co-20 Ni	Good	
Sputtered B ₄ C	Fair	<u>Fair</u> - More pronounced degradation with some areas (less than 10%) of substrate exposure.
Sputtered TiB ₂	Fair	
Ion Plated Cr ₂ O ₃	Poor	<u>Poor</u> - Excessive oxidation and/or spalling of coating. Unstable weight change versus time behavior.
Kaman DES + TiB ₂	Poor	
Co-20 Ni + TiB ₂	Poor	
Co-20 Ni + Cr ₂ O ₃	Poor	

Figure 6 shows the results of the post-thermal exposure bend tests that were conducted on the coated foil specimens after the 649°C (1200°F)/500-hour oven exposure. In most cases, the thermal exposure tended to increase coating ductility and bond strength by promoting diffusion at the coating/substrate interface. Exceptions to this were the Co-20 Ni and ion-plated Cr₂O₃ coatings, which exhibited ductility decreases.

PRELIMINARY SCREENING RESULTS--JOURNAL COATINGS

Surface finish measurements were made on each journal coating candidate using a Talysurf profilometer. Since specimen warpage was experienced by some of the journal coating specimens, the Kaman SCA and Cobalt-20 Nickel coatings were tested in the as-processed, rather than ground, condition. The surface finish of these coatings ranged from 28 to 40 μ -in RMS. The surface finish for all the journal coating candidates is presented in Table 5.

Knoop microhardness tests were run on cross-sections taken through the journal coatings to determine coating hardness and assess cracking tendency. The hardness values are listed in Table 5. In the case of the Kaman SCA coating, an accurate measurement of hardness was difficult due to the composite nature of the coating, and coating porosity. This was also the case for the NASA-Lube PS-120 coating. The hardness values presented, therefore, are "apparent" microhardness values for these two materials.

The scratch test data for the journal coatings is presented in Table 5. The coatings were ranked in three categories as described below:

- Good - No chipping, cracking, or coating breakthrough. Low friction. Shallow scratch.
- Fair - Localized breakthrough, limited chipping and/or cracking.
- Poor - Heavy chipping and/or spalling of coating. Deep scratch or extensive breakthrough.

Generally, the hard ceramic coatings (SCA, TiB₂, Cr₂O₃) performed poorly in this test, exhibiting chipping and generating abrasive wear debris. Metallic coatings (Cobalt-Nickel, Tribaloy, Gold overcoat) performed well.

All of the journal coatings except Kaman SCA + ion-plated gold passed the tape test.

Figures 7 and 8 present the weight change versus exposure time data for the coatings at exposure temperatures of 538°C (1000°F) and 649°C (1200°F), respectively. Ratings of the coatings thermal exposure performance, based on visual, SEM and weight change data, are presented in Tables 6 and 7 for the 538°C (1000°F) and 649°C (1200°F) testing, respectively. The relative rankings of the candidate coatings in Tables 6 and 7 are similar. The most significant change in ranking was Cobalt-20 Nickel, which dropped from Excellent at 538°C (1000°F) to Poor at 649°C (1200°F), due to excessive oxidation.

TABLE 5. JOURNAL COATING TEST DATA

Coating	Composition	Deposition Method	Thickness mm (in)	Surface Finish, μ -in RMS	Knoop Hardness	Tape Test	Scratch Test
KAMAN SCA	SiO ₂ -Cr ₂ O ₃ -Al ₂ O ₃	Slurry	0.137 (0.0054)	36 (as coated)	482 (apparent)	Pass	Poor
KAMAN SCA + TiB ₂	SiO ₂ -Cr ₂ O ₃ -Al ₂ O ₃ plus TiB ₂ top coat	Slurry, sputtered top coat	0.114 (0.0045)	28 (as coated)	482 (apparent)	Pass	Poor
KAMAN SCA + Au	SiO ₂ -Cr ₂ O ₃ -Al ₂ O ₃ plus gold top coat	Slurry, ion plated top coat	0.152 (0.0060)	34 (as coated)	482 (apparent)	Fail	Good
Co-20 Ni	80% cobalt-20% nickel alloy	Electroplated	0.028 (0.0011)	30 (as coated)	491	Pass	Good
CO-20Ni + Cr ₂ O ₃	80% cobalt-20% nickel alloy plus Cr ₂ O ₃ top coat	Electroplate, sputtered top coat	0.043 (0.0017)	36 (as coated)	521	Pass	Poor
CO-20Ni + TiB ₂	80% cobalt-20% nickel alloy plus TiB ₂ top coat	Electroplated, sputtered top coat	0.038 (0.0015)	40 (as coated)	504	Pass	Poor
Tribaloy 400	62Co-28Mo-2Si-8Cr	Detonation gun	0.147 (0.0058)	6 (ground)	655	Pass	Good
Tribaloy 400 + Au	62Co-28Mo-2Si-8Cr plus gold top coat	Detonation gun, ion plated top coat	0.152 (0.0060)	7 (ground)	655	Pass	Good
Ni-Cr Bonded CrB ₂	20% Nichrome (80-20), 80% CrB ₂	Plasma sprayed	0.051 (0.0020)	TBD (ground)	-	Pass	Fair
NASA Lube PS-120	60% Tribaloy 400, 20% Silver, 20% CaF ₂	Plasma sprayed	0.122 (0.0048)	21 (ground)	103 (apparent)	Pass	Fair

TABLE 6. CANDIDATE JOURNAL COATINGS - 538°C (1000°F) THERMAL EXPOSURE PERFORMANCE RATING

Coating	Rating	Rating Designations
KAMAN SCA	Excellent	Excellent - No visual coating degradation. Stable weight change versus time behavior.
Cobalt-20 Nickel	Excellent	
Tribaloy-400	Excellent	Good - Localized areas of superficial attack no resulting in substrate exposure. Stable weight change versus time.
Tribaloy-400 + Au	Excellent	
Ni-Cr Bonded CrB ₂	Excellent	Fair - More pronounced degradation with some areas (less than 10%) of substrate exposure.
KAMAN SCA + Au	Good	
Cobalt-20 Nickel+Cr ₂ O ₃	Poor	Poor - Excessive oxidation and/or spalling of coating. Unstable weight change versus time behavior.
Cobalt-20 Nickel+TiB ₂	Poor	
KAMAN SCA + TiB ₂	Poor	
NASA Lube PS-120	Poor	

TABLE 7. JOURNAL COATINGS - 649°C (1200°F) THERMAL EXPOSURE PERFORMANCE RATING

Coating	Rating	Rating Designations
KAMAN SCA	Excellent	Excellent - No visual coating degradation. Stable weight change versus time behavior.
Tribaloy 400 + Au	Excellent	
Ni-Cr Bonded CrB ₂	Excellent	Good - Localized areas of superficial attack not resulting in substrate exposure. Stable weight change versus time.
KAMAN SCA + Au	Good	
Tribaloy 400	Good	Fair - More pronounced degradation with some areas (less than 10%) of substrate exposure.
KAMAN SCA+TiB ₂	Fair	
Cobalt-20 Nickel	Poor	Poor - Excessive oxidation and/or spalling of coating. Unstable weight change versus time behavior.
Cobalt-20 Nickel+Cr ₂ O ₃	Poor	
Cobalt-20 Nickel+TiB ₂	Poor	
NASA Lube PS-120	Poor	

PRELIMINARY SCREENING CONCLUSIONS

Reduction of the initial group of twelve foil coating candidates to a field of six relied heavily on oven screening results because coating durability at temperature is an absolute requirement for successful foil bearing operation. The metallographic and mechanical evaluations provided valuable information on coating quality and helped define the mechanisms of coating degradation after thermal exposure. The six coatings chosen for continued evaluation were:

Kaman DES
 Kaman DES + Au Overcoat (Sputtered)
 Co-20 Ni (Electroplated)
 Cr₂O₃ (Sputtered)
 TiC (Sputtered)
 B₄C (Sputtered)

The six journal candidates chosen for sliding friction evaluations were:

Kaman SCA
 Kaman SCA + Ion-Plated Gold
 Cobalt-20 Nickel (Electroplated)
 Tribaloy 400 (D-Gunned)
 Tribaloy 400 (D-Gunned) + Ion-Plated Gold
 Ni-Cr Bonded CrB₂ (Plasma Sprayed)

SLIDING FRICTION TEST PROCEDURE

Sliding friction measurements were made at room temperature, 316°C (600°F), 427°C (800°F) and 538°C (1000°F). Both static and dynamic friction coefficients were measured for each mating material combination in the six-by-six matrix of foil/journal coating combinations selected in the preliminary materials screening. Room-temperature tests only were conducted on as-coated specimens. All coatings were then pre-oxidized for one to two hours at 1200°F, and tested at all of the above temperatures. Room-temperature testing was conducted to assess coating performance during engine start up transients prior to foil lift-off, while elevated-temperature testing was conducted to evaluate friction coefficients to be expected during high speed runs and hot starts. A typical sliding friction data trace is shown in Figure 9, which also shows the data repeatability.

SLIDING FRICTION RESULTS

Table 8 is a compilation of the measured sliding friction coefficients at room temperature and elevated temperature for the 36 pre-oxidized coating combinations. Table 9 presents the sliding friction coefficients of as-coated and pre-oxidized coating combinations measured at room-temperature test conditions.

Results observed during the sliding friction tests are summarized below:

- o For the pre-oxidized coatings (Table 8), the mean measured static and dynamic friction coefficients at 24°C (75°F) were 0.53 and 0.26, respectively. At 538°C (1000°F) the mean static and dynamic friction coefficients were 0.88 and 0.73, respectively
- o In all cases, friction coefficients were found to increase when the test temperature was increased above 24°C (75°F), although in many instances the coefficients peaked at an intermediate temperature (i.e., less than 538°C (1000°F) and decreased slightly beyond this point
- o Compared as a group, the sliding friction coefficient of the as-coated combinations are quite similar to the pre-oxidized coating combinations (Table 9). The mean measured static and dynamic friction coefficients for the as-coated combinations were 0.55 and 0.25, respectively.
- o While, as a group, the performance of the as-coated and pre-oxidized combinations was similar, one coating combination responded to pre-oxidation of the coatings in a dramatic manner. When the coating combination of Kaman SCA on the journal and B₄C on the foils was pre-oxidized, the measured static and dynamic friction coefficients were 0.46 and 0.07, respectively, compared with the as-coated values of 0.79 and 0.59
- o Gold-gold combinations yielded extremely high friction coefficients

SLIDING FRICTION CONCLUSIONS

Selection of the four coating combinations to be carried forward for the dynamic properties testing relied on data from the sliding friction tests, as well as the earlier preliminary screening data. The material combinations selected and the rationale for the choices are presented in Table 10.

DYNAMIC PROPERTIES PROCEDURE AND TEST RIG

Previous investigations of high-temperature dry-film coatings for foil bearings(3)(4) tested the coatings utilizing foil and journal specimens that, essentially, were partial or total foil bearings. In this current program(1), to simplify the foil and journal specimens and facilitate both specimen fabrication and testing, the approach was based on using flat coating specimens in a test rig whose features are depicted in Figure 10.

The rotating wear ring, simulating the bearing journal, contacts a thin flat metal sheet simulating the bearing foil. Candidate journal and foil coatings are applied on the contact surfaces. The disk is driven by a variable speed motor, and is capable of axial translation along its axis of rotation. The disk can either be lifted off of the foil surface, or held against it with a controlled force, simulating the contact force in an actual bearing. Provisions are incorporated for measuring the torque created by the rotating disk contacting the foil specimen. Friction coefficients then are derived from the torque and load applied to the disk-foil interface. Since the foil specimen is supported on an undamped air bearing, only the dynamic friction coefficient is monitored with this rig.

The specimen portion of the dynamic properties test rig is in an oven capable of providing a controlled thermal environment in excess of 649°C (1200°F).

The procedure utilized for the rig simulated cold and hot starts and also developed wear rate data. The test procedure was designed to maximize information gained by testing to plausible conditions, rather than to test to extreme conditions, which would fail an excessive number of specimens, restricting information gained. The procedure is outlined in Table 11.

TABLE 8. STATIC AND DYNAMIC FRICTION COEFFICIENTS AT VARIOUS TEMPERATURES FOR PRE-OXIDIZED FOIL AND JOURNAL COATING COMBINATIONS

WEAR COUPLE (JOURNAL/FOIL)	TEST TEMPERATURE (°C ±5.55) (°F ±10)			
	24°C (75°F)	316°C (600°F)	427°C (800°F)	538°C (1000°F)
Cobalt-20 Nickel/Cobalt-20 Nickel	0.53/0.24	0.75/0.39	0.81/0.64	0.92/0.73
Cobalt-20 Nickel/Sputtered Cr ₂ O ₃	0.62/0.29	0.62/0.42	0.84/0.61	0.75/0.54
Cobalt-20 Nickel/Sputtered TiC	0.59/0.28	0.55/0.46	0.72/0.56	0.72/0.55
Cobalt-20 Nickel/Sputtered B ₄ C	0.50/0.17	0.62/0.44	0.83/0.61	0.92/0.68
Cobalt-20 Nickel/Kaman DES	0.28/0.18	0.66/0.44	0.64/0.44	0.72/0.50
Cobalt-20 Nickel/DES + Gold	0.50/0.28	0.73/0.48	0.77/0.40	0.73/0.39
Kaman SCA/Cobalt-20 Nickel	0.60/0.31	0.59/0.40	0.57/0.40	0.64/0.48
Kaman SCA/Sputtered Cr ₂ O ₃	0.69/0.40	0.92/0.81	0.94/0.75	0.86/0.73
Kaman SCA/Sputtered TiC	0.57/0.28	0.99/0.88	0.94/0.81	0.92/0.77
Kaman SCA/Sputtered B ₄ C	0.46/0.07	0.99/0.86	0.95/0.84	0.92/0.77
Kaman SCA/Kaman DES	0.40/0.29	0.90/0.77	0.83/0.72	0.86/0.79
Kaman SCA/DES + Gold	0.59/0.17	0.73/0.59	0.92/0.68	0.90/0.68
Tribaloy 400/Cobalt-20 Nickel	0.57/0.20	0.81/0.68	0.92/0.77	0.99/0.83
Tribaloy 400/Sputtered Cr ₂ O ₃	0.57/0.29	0.86/0.72	0.92/0.73	0.99/0.83
Tribaloy 400/Sputtered TiC	0.53/0.22	0.97/0.77	0.95/0.79	0.79/0.70
Tribaloy 400/Sputtered B ₄ C	0.44/0.17	1.05/1.05	1.05/0.99	1.01/0.92
Tribaloy 400/Kaman DES	0.38/0.26	0.81/0.68	0.90/0.73	1.01/0.84
Tribaloy 400/DES + Gold	0.61/0.18	0.88/0.72	0.97/0.81	0.94/0.73
Tribaloy 400 + Gold/Cobalt-20 Nickel	0.55/0.39	0.92/--	0.90/1.01	0.99/--
Tribaloy 400 + Gold/Sputtered Cr ₂ O ₃	0.50/0.29	0.81/0.70	1.01/0.94	0.94/0.94
Tribaloy 400 + Gold/Sputtered TiC	0.50/0.28	0.68/0.61	0.77/0.73	0.88/0.86
Tribaloy 400 + Gold/Sputtered B ₄ C	0.50/0.26	0.75/0.57	0.84/0.72	0.83/0.84
Tribaloy 400 + Gold/Kaman DES	0.53/0.42	0.81/0.77	0.99/0.84	0.95/0.92
Tribaloy 400 + Gold/DES + Gold	0.68/0.68	--	--	--
Nichrome-CrB ₂ /Cobalt-20 Nickel	0.51/0.22	0.70/0.50	0.72/0.55	0.72/0.51
Nichrome-CrB ₂ /Sputtered Cr ₂ O ₃	0.51/0.24	0.83/0.72	0.95/0.70	0.88/0.72
Nichrome-CrB ₂ /Sputtered TiC	0.50/0.35	0.92/0.70	0.95/0.70	0.90/0.68
Nichrome-CrB ₂ /Sputtered B ₄ C	0.44/0.17	0.88/0.70	0.90/0.68	0.86/0.68
Nichrome-CrB ₂ /Kaman DES	0.53/0.35	0.92/0.72	0.95/0.81	0.84/0.68
Nichrome-CrB ₂ /DES + Gold	0.57/0.22	0.94/0.72	0.86/0.66	0.95/0.72
Kaman SCA + Gold/Cobalt-20 Nickel	0.61/0.26	0.81/--	0.90/0.83	0.86/--
Kaman SCA + Gold/Sputtered Cr ₂ O ₃	0.51/0.20	0.72/0.52	0.77/0.57	0.94/0.75
Kaman SCA + Gold/Sputtered TiC	0.57/0.22	0.72/0.53	0.72/--	0.59/0.42
Kaman SCA + Gold/Sputtered B ₄ C	0.55/0.20	0.84/0.72	0.92/0.81	0.84/0.73
Kaman SCA + Gold/Kaman DES	0.44/0.24	0.70/0.44	0.66/0.44	0.86/0.64
Kaman SCA + Gold/DES + Gold	0.94/0.64	0.88/--	0.99/--	0.92/0.79

*NOTES:

- o Data Format: μ_s/μ_d (Static Coefficient/Dynamic Coefficient)
- o All Coatings Preoxidized at 649°C (1200°F) for 1 to 2 Hours
- o Unit Loading 25025 Newton/m² (3.63 psi), Sliding Velocity 0.3 to 0.6 m/sec (1 to 2 ft/sec)

TABLE 9. STATIC AND DYNAMIC FRICTION COEFFICIENTS AT ROOM TEMPERATURE FOR AS-COATED AND PRE-OXIDIZED FOIL AND JOURNAL COATING COMBINATIONS*

Wear Couple (Journal/Foil)	Test Temperature = 24°C (75°F)	
	As-Coated Condition	Pre-Oxidized
Cobalt-20 Nickel/Cobalt-20 Nickel	0.46/0.13	0.53/0.24
Cobalt-20 Nickel/Sputtered Cr ₂ O ₃	0.44/0.18	0.62/0.29
Cobalt-20 Nickel/Sputtered TiC	0.48/0.18	0.59/0.28
Cobalt-20 Nickel/Sputtered B ₄ C	0.40/0.18	0.50/0.17
Cobalt-20 Nickel/Kaman DES	-/-	0.28/0.18
Cobalt-20 Nickel/DES + Gold	0.50/0.28	0.50/0.28
Kaman SCA/Cobalt-20 Nickel	0.61/0.26	0.60/0.31
Kaman SCA/Sputtered Cr ₂ O ₃	0.64/0.37	0.69/0.40
Kaman SCA/Sputtered TiC	0.55/0.28	0.57/0.28
Kaman SCA/Sputtered B ₄ C	0.79/0.59	0.46/0.07
Kaman SCA/Kaman DES	-/-	0.40/0.29
Kaman SCA/DES + Gold	0.59/0.17	0.59/0.17
Tribaloy 400/Cobalt-20 Nickel	0.46/0.18	0.57/0.20
Tribaloy 400/Sputtered Cr ₂ O ₃	0.62/0.26	0.57/0.29
Tribaloy 400/Sputtered TiC	0.50/0.18	0.53/0.22
Tribaloy 400/Sputtered B ₄ C	0.51/0.18	0.44/0.17
Tribaloy 400/Kaman DES	-/-	0.38/0.26
Tribaloy 400/DES + Gold	0.61/0.18	0.61/0.18
Tribaloy 400 + Gold/Cobalt-20 Nickel	0.64/0.61	0.55/0.39
Tribaloy 400 + Gold/Sputtered Cr ₂ O ₃	0.53/0.26	0.50/0.29
Tribaloy 400 + Gold/Sputtered TiC	0.42/0.15	0.50/0.28
Tribaloy 400 + Gold/Sputtered B ₄ C	0.46/0.17	0.50/0.26
Tribaloy 400 + Gold/Kaman DES	-/-	0.53/0.42
Tribaloy 400 + Gold/DES + Gold	0.68/0.68	0.68/0.68
Nichrome-CrB ₂ /Cobalt-20 Nickel	0.44/0.28	0.51/0.22
Nichrome-CrB ₂ /Sputtered Cr ₂ O ₃	0.58/0.28	0.51/0.24
Nichrome-CrB ₂ /Sputtered TiC	0.57/0.28	0.50/0.35
Nichrome-CrB ₂ /Sputtered B ₄ C	0.57/0.35	0.44/0.17
Nichrome-CrB ₂ /Kaman DES	-/-	0.53/0.35
Nichrome-CrB ₂ /DES + Gold	0.57/0.22	0.57/0.22
Kaman SCA + Gold/Cobalt-20 Nickel	0.55/0.31	0.61/0.26
Kaman SCA + Gold/Sputtered Cr ₂ O ₃	0.51/0.20	0.51/0.20
Kaman SCA + Gold/Sputtered TiC	0.57/0.22	0.57/0.22
Kaman SCA + Gold/Sputtered B ₄ C	0.55/0.20	0.55/0.20
Kaman SCA + Gold/Kaman DES	-/-	0.44/0.24
Kaman SCA + Gold/DES + Gold	0.94/0.64	0.94/0.64

NOTES:

- o Data Format: μ_s/μ_d (Static Coefficient/Dynamic Coefficient)
- o Pre-Oxidation Conditions: 649°C (1200°F) for 1 to 2 Hours
- o Unit Loading 25025 Newton/m² (3.63 psi), Sliding Velocity 0.1 to 0.6 m/sec (1 to 2 ft/sec)

TABLE 10. FOUR COATING COMBINATIONS CHOSEN FOR DYNAMIC PROPERTIES TESTING

JOURNAL	FOIL	RATIONALE
Cobalt-20 Nickel	Sputtered TiC	Low friction. Good foil coating durability and oxidation resistance. Economical self-lubricating journal coating.
Tribaloy 400	Sputtered TiC	Stable sliding behavior. Good foil coating durability and oxidation resistance. Excellent journal coating durability; oxidation resistance.
Kaman SCA + Gold	Kaman DES	Low friction. Highly wear-resistant journal coating. Excellent foil/journal oxidation resistance. SCA open porosity provides reservoir for gold. Economical processes.
Tribaloy 400	Sputtered Cr ₂ O ₃	Stable sliding behavior. Excellent foil coating durability; oxidation resistance. Excellent journal coating durability; oxidation resistance.

TABLE 11. DYNAMIC PROPERTIES TEST SEQUENCE

Step	Condition	Temperature	Rig Speed ¹ (rpm)	Load Arm Load ²	Time (min)
1	Cold start Repeat 5 times minimum	Ambient	200-1600	2.224 Newton (0.5 Pound)	Accelerate as required, then decelerate
2	Hot Start Repeat 5 times minimum	427°C 649°C (800°F), (1200°F)	200-1600	2.224 Newton (0.5 Pound)	Accelerate as required
3	Wear test	Ambient, 427°C 649°C (800°F), (1200°F)	500 minimum	2.224 Newton (0.5 Pound)	60 at each temperature

NOTES:

- 1 Average wear ring surface speed:

at 200 rpm--0.43 m/sec (1.42 ft/sec)
at 1600 rpm--3.46 m/sec (11.35 ft/sec)

- 2 2.224 Newton (0.5-pound) load on load arm yields 6.672 Newton (1.5-pound) load at tested wear surfaces. The unit load is 7514 Newton/m² (1.09 psi).

DYNAMIC PROPERTIES TEST RESULTS

Dynamic properties tests were conducted on the four selected material combinations (Table 10). Figure 11 presents a typical data trace obtained during the start tests (Steps 1 and 2, Table 11) on the dynamic properties test rig. Table 12 presents the dynamic friction coefficient data from this portion of the dynamic properties tests. Typically, friction coefficients were found to decrease or stabilize with increasing sliding speed. Stick-slip behavior also was most pronounced at lower sliding speeds.

Friction coefficient and wear rate data for the wear test portion of the test sequence (Step 3) are presented in Table 13. The 649°C (1200°F) test was conducted first, followed by the 427°C (800°F), and 24°C (75°F) tests. Since oxide transfer, which occurred during the 649°C (1200°F) test, tended to mask wear rate trends that occurred at lower temperatures, the 649°C (1200°F) wear rate data are the most meaningful.

TABLE 12. DYNAMIC PROPERTIES RIG DATA - START/STOP TESTS*

Wear Couple (Journal/Foil)	DYNAMIC FRICTION COEFFICIENTS, C_F					
	24°C (75°F)		427°C (827°F)		649°C (1200°F)	
	At Maximum Speed	During Transients	At Maximum Speed	During Transients	At Maximum Speed	During Transients
Cobalt-Nickel/ TiC	0.35 to 0.40	0.35 to 0.40	0.50 to 0.60	Off scale [≥1.0 below 2.56 m/sec (8.4 ft/sec)]	0.35 to 0.40	[1.0 below 1.86 m/sec (6.1 ft/sec)]
T-400/TiC	0.18 to 0.20	0.18 to 0.20	0.50	0.5	0.20 to 0.40	0.20 to 0.40
Kaman SCA+Au/ Kaman DES	0.10 to 0.70 (INCREASES WITH TIME)	0.20 to 0.70	0.30	0.30 to 0.40	0.30	0.30 to 0.40
T-400/Cr ₂ O ₃	0.10 to 0.12	0.18 to 0.22	0.30 to 0.40	0.30 to 0.40	0.40 to 0.50	[1.0 below 2.32 m/sec (7.6 ft/sec)]

*Sliding velocity ranged from 0.56 m/sec (1.83 ft/sec) to 3.72 m/sec (12.22 ft/sec); unit load was 7514 Newton/m² (1.09 psi); air atmosphere; no lubrication.

TABLE 13. DYNAMIC PROPERTIES RIG DATA - STEADY STATE WEAR TEST*

Wear Couple (Journal/Foil)	WEAR (mg/304.8m (1000 ft) OF DISK TRAVEL)					
	24°C (75°F)		427°C (800°F)		649°C (1200°F)	
	Journal	Foil	Journal	Foil	Journal	Foil
Cobalt-Nickel/TiC	-0.2956	-0.0341	-0.0940	-0.0818	+0.0818	+0.4320
T-400/TiC	-0.0114	+0.1933	-0.0286	+0.0390	-0.0022	+0.0110
Kaman SCA+Au/Kaman DES	+0.1320	+0.0480	-	-	-0.1863	-0.1464
T-400/Cr ₂ O ₃	+0.0066	-0.0044	+0.1018	+0.1745	-0.1697	+0.9986

Wear Couple (Journal/Foil)	DYNAMIC FRICTION COEFFICIENTS (C_F)		
	24°C (75°F)	427°C (800°F)	649°C (1200°F)
	Cobalt-Nickel/TiC	0.44	0.50
T-400/TiC	0.40	0.55	0.35
Kaman SCA+Au/Kaman DES	0.55	-	0.55
T-400/Cr ₂ O ₃	0.22	0.20	0.14

*Sliding velocity ranged from 0.73 to 3.86 m/sec (2.40 to 12.68 ft/sec); unit load was 7514 Newton/m² (1.09 psi); air atmosphere; no lubrication.

Figure 12 shows the 649°C (1200°F) wear data in bar graph form for the four wear couples. The Cobalt-20 Nickel versus TiC data indicate Cobalt-Nickel oxide formation was rather excessive, with both samples gaining weight during the test (this material subsequently wore away at the lower test temperatures). The Tribaloy 400 versus TiC data reflect a slight weight loss of the Tribaloy sample with material transfer to the TiC sample. In the case of the Kaman SCA + Gold versus Kaman DES wear couple, both samples experienced abrasive wear. The Tribaloy 400 versus Cr₂O₃ combination experienced a much higher degree of adhesive wear than the Tribaloy 400 versus TiC combination, with heavier weight loss and transfer from the Tribaloy sample to the Cr₂O₃ sample. Table 14 presents a summary of post-test observations for the tested coating combinations.

Figure 13 compares the dynamic friction coefficient measured for one coating combination in the sliding friction test rig with that measured in the dynamic properties test rig. It is noted that reasonable agreement was obtained.

TABLE 14. DYNAMIC PROPERTIES RIG TESTS - POST-TEST OBSERVATIONS

Wear Couple (Journal/Foil)	Observations
Cobalt-Nickel/TiC	Cobalt-nickel shows considerable oxidation and loose material on the surface after hot wear tests. Heavy transfer of oxide from wear ring (Co-Ni) to TiC disk. Much oxide is removed during ambient wear test. Oxide is silver-grey and burnished smooth in many areas, although overall surface finish of both samples is relatively rough.
Tribaloy 400/TiC	Tribaloy 400 has blue heat-tinted areas plus adhesive patches of gold-brown material. Very fine crack patterns observable in Tribaloy 400 at 20X but no evidence of de-bonding. TiC sample shows patchy areas of oxide transfer from Tribaloy 400 wear ring. No evidence of coating failure. Both samples are extremely smooth.
Kaman SCA + Gold/Kaman DES	Uneven wear pattern on SCA + gold ring. In heavy wear areas SCA coating exhibits pulled out material which may have caused abrasion. Abrasive gouging of DES sample exposed substrate material, which is then smeared on top of DES coating.
Tribaloy 400/Cr ₂ O ₃	Tribaloy 400 wear ring is burnished to extremely smooth surface finish (2-3 μ-in RMS). Oxide formation and heavy transfer to Cr ₂ O ₃ sample created some relatively rough patchy areas of oxide buildup. Tribaloy 400 oxide tint varies from blue to gold to grey. Original lapping marks still evident in some areas. No evidence of coating breakthrough.

CONCLUSIONS AND FINAL COATING COMBINATION SELECTIONS

The materials development task conclusions are represented by selecting the prime coatings and coating combinations for use on the actual foil bearings for the rig and existing tests on the Reference (1) program. The selected coatings are:

Journal Coating

Tribaloy 400

Tribaloy 400

Foil Coating

Sputtered TiC

Sputtered Cr₂O₃

Alternatives: Kaman SCA

Kaman DES

Note that an alternate journal and alternate foil coating are also identified. These alternate coatings may be paired against each other, or with the other prime coatings selected. Of particular interest would be the combination of Kaman SCA and sputtered TiC, as both of these coatings have excellent wear properties. Table 15 provides some key overall comments on the performance of these coatings in the materials tests.

REFERENCES

- (1) Foil Bearing Development Program for Potential Application to Navy Advanced SPS/APU Program, Contract N00140-79-C-1294.
- (2) Power System Study, Advanced Fighter/Attack and V/STOL Airplanes, Garrett Turbine Engine Company Report No. 41-1906, December 1977.
- (3) Gas-Lubricated Foil Bearing Development Program for Advanced Turbomachines, Contract F33615-73-C-2058.
- (4) Hydrodynamic Air-Lubricated Compliant Surface Bearing in an Automotive Gas Turbine Engine, II - Materials and Coatings, NASA CR-135402, July 1978.

TABLE 15. BEST PERFORMING HIGH-TEMPERATURE COATINGS

Coating Combination (Foil/Journal)	Characteristics
Sputtered TiC/Tribaloy, 400	Both coatings offer good oxidation resistance up to 649°C (1200°F). Combination results in excellent wear behavior (low wear rates, good wear morphology) low to intermediate friction coefficients and very stable sliding behavior.
Sputtered Cr ₂ O ₃ / Tribaloy 400	Both coatings offer good oxidation resistance up to 649°C (1200°F). Combination results in good wear behavior, with low wear rates, (although slightly adhesive in nature) and low friction coefficients, although there was some stick-slip during transients.
Kaman DES/Kaman SCA* *Alternate foil and journal coatings. Not necessarily to be used as a couple.	Both coatings offer excellent oxidation resistance up to 649°C (1200°F). DES coating durability is somewhat lower than the sputtered coatings and in some cases exhibits local rub-through. Low to intermediate friction coefficients. Economical coating processes.

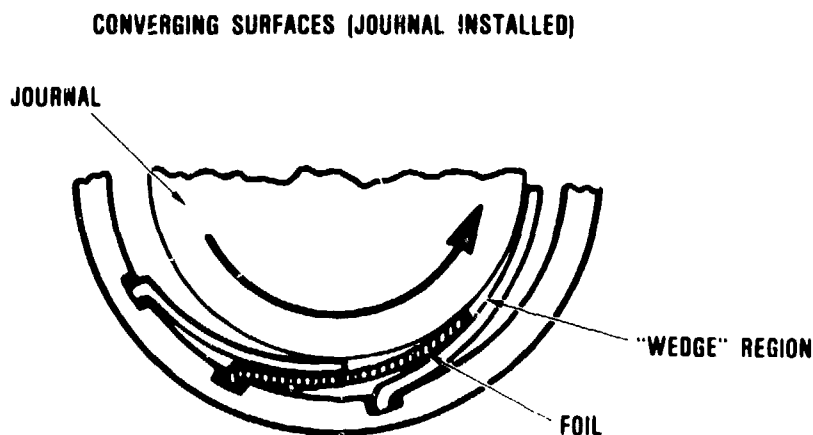


Figure 1. Self-Acting Gas-Lubricated Compliant Journal Foil Bearing Concept.

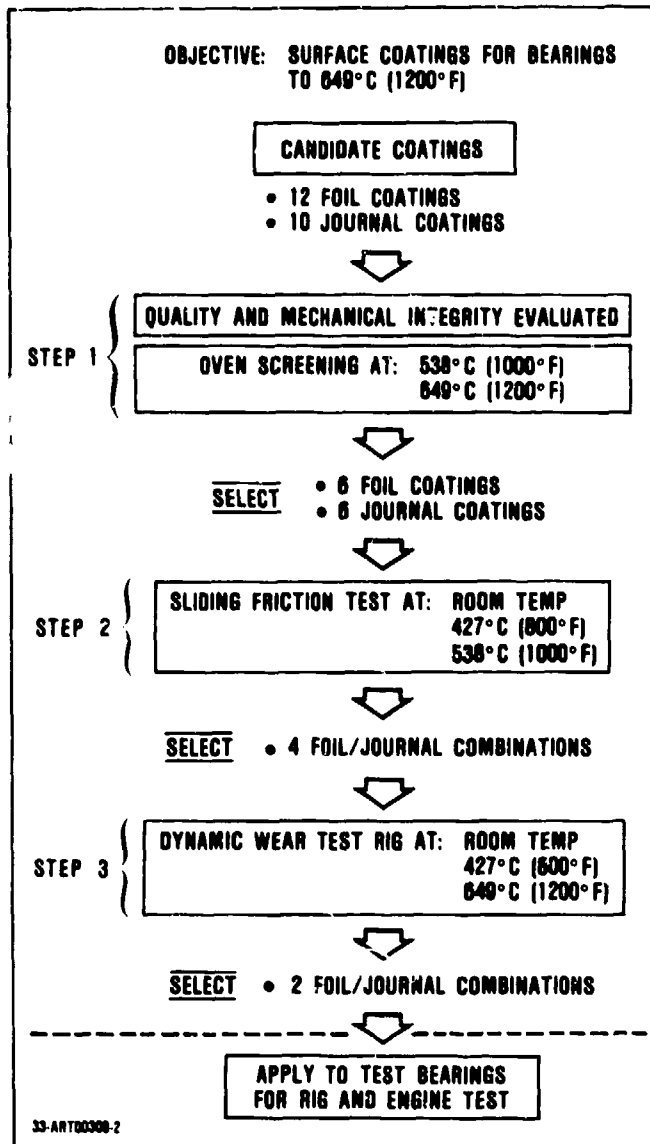


Figure 2. Foil Bearing Surface Coating Development

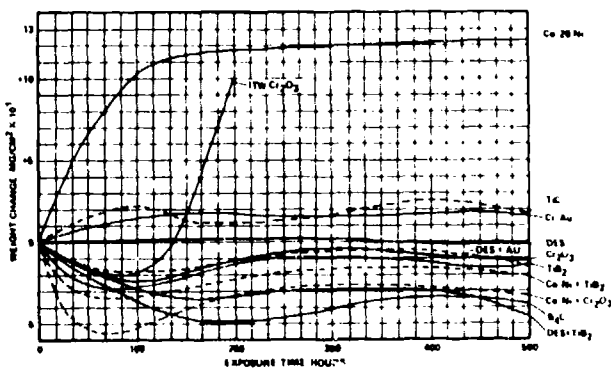


Figure 4. Foil Coating Candidates. Weight Change Versus Time at 538°C (1000°F) Exposure Temperature.

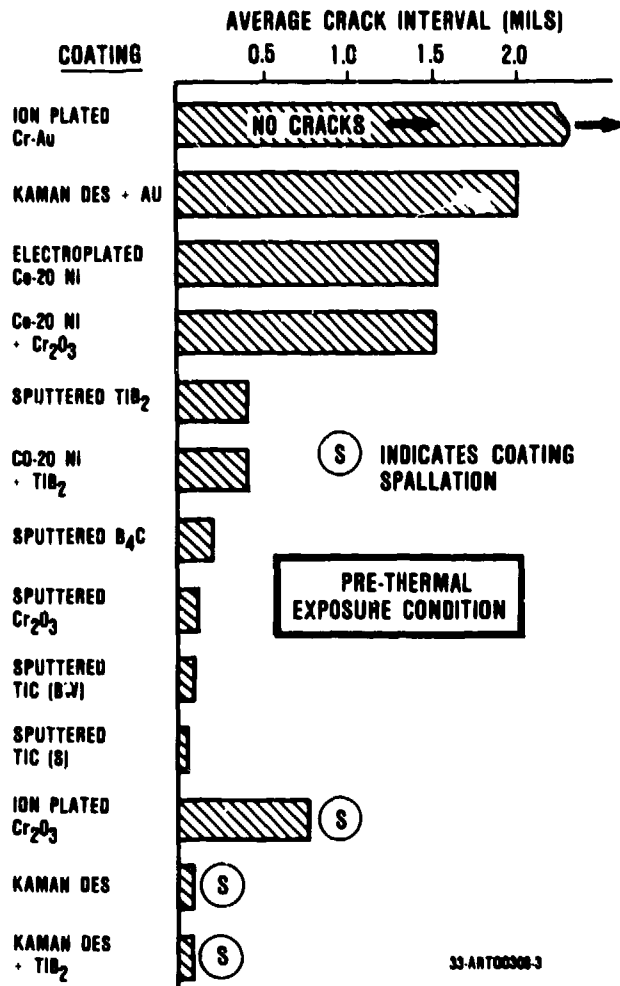


Figure 3. Foil Coating Ductility Comparison. Highest Values are Best.

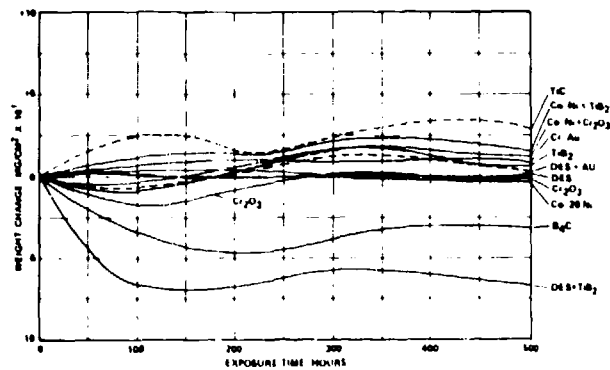


Figure 5. Foil Coating Candidates. Weight Change Versus Time at 649°C (1200°F) Exposure Temperature.

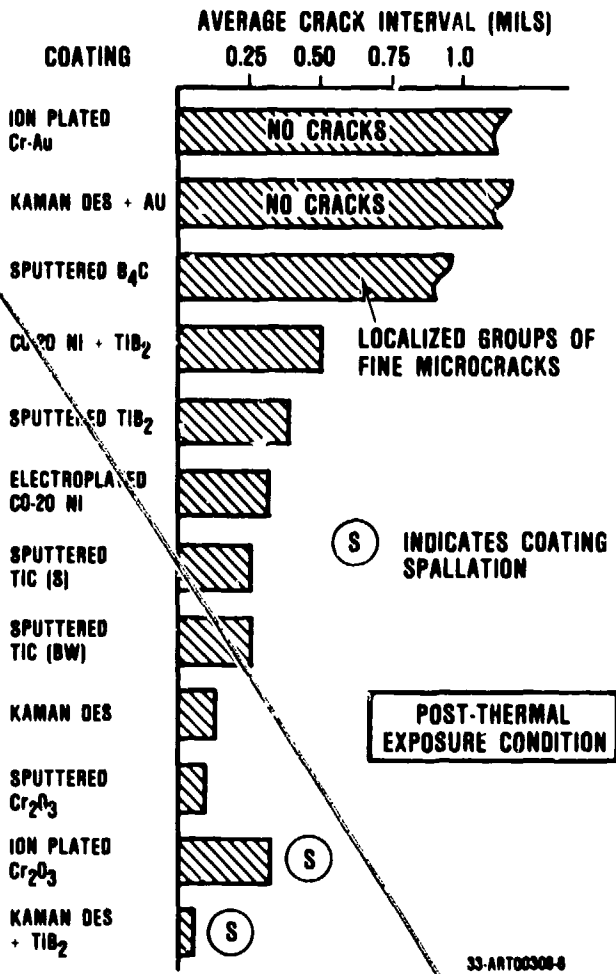


Figure 6. Foil Coating Ductility Comparison. Highest Values are Best.

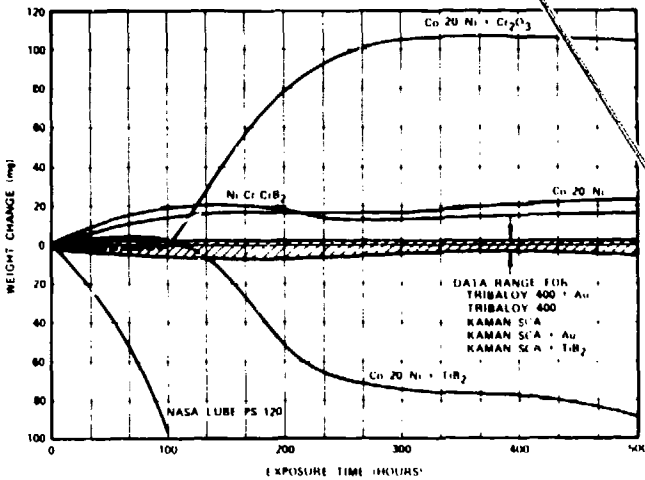


Figure 7. Journal Coating Candidates. Weight Change Versus Time at 538°C (1000°F) Exposure Temperature.

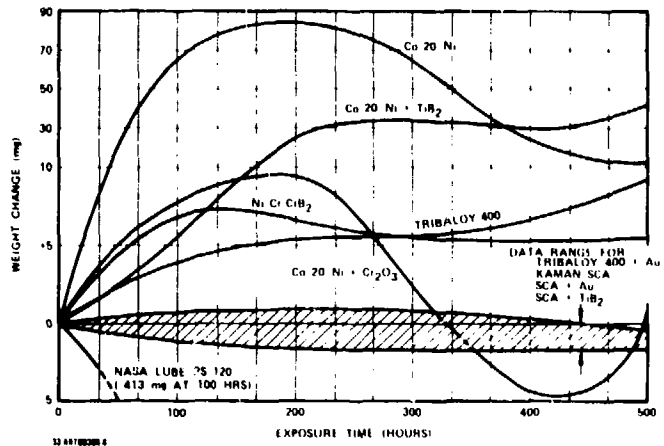


Figure 8. Journal Coating Candidates. Weight Change Versus Time at 649°C (1200°F) Exposure Temperature.

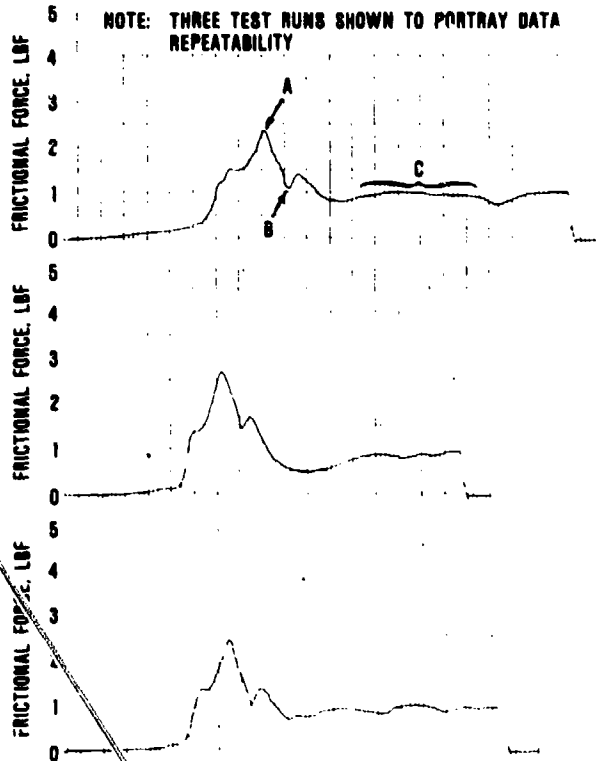


Figure 9. Sliding Friction Test Results, Triballoy 400 Versus B₄C (pre-oxidized) Showing Static Friction Spike A, Linkage Backlash B, Dynamic Friction Trace C. [Contact Force = 24.2 Newton (5.45 Pounds), Room Temperature].

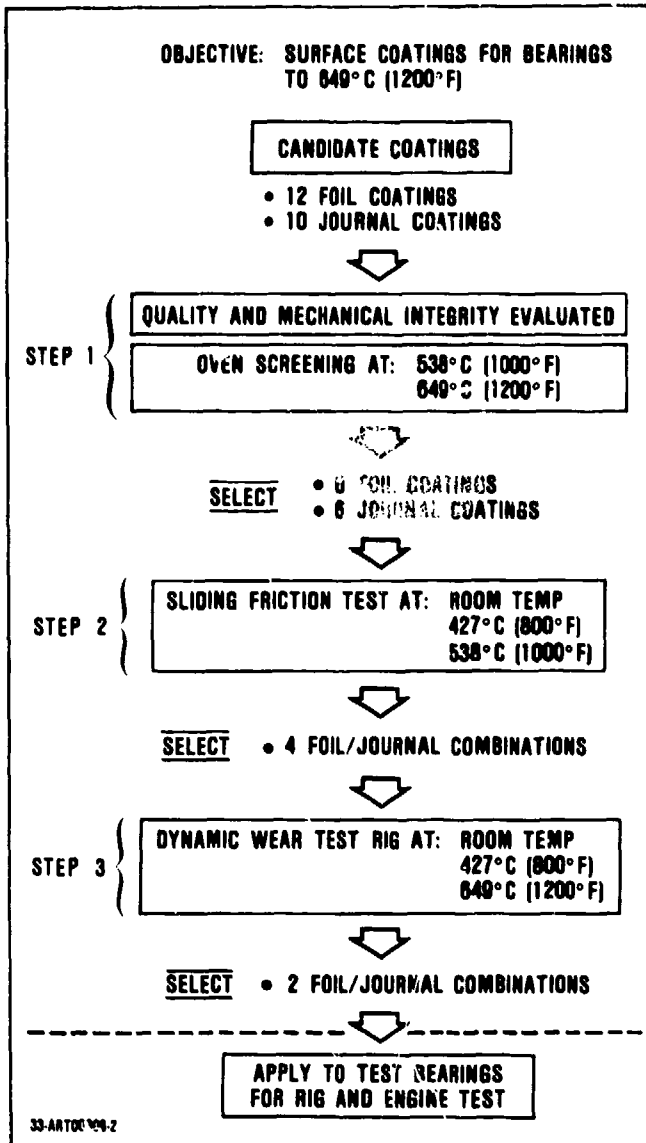


Figure 2. Foil Bearing Surface Coating Development

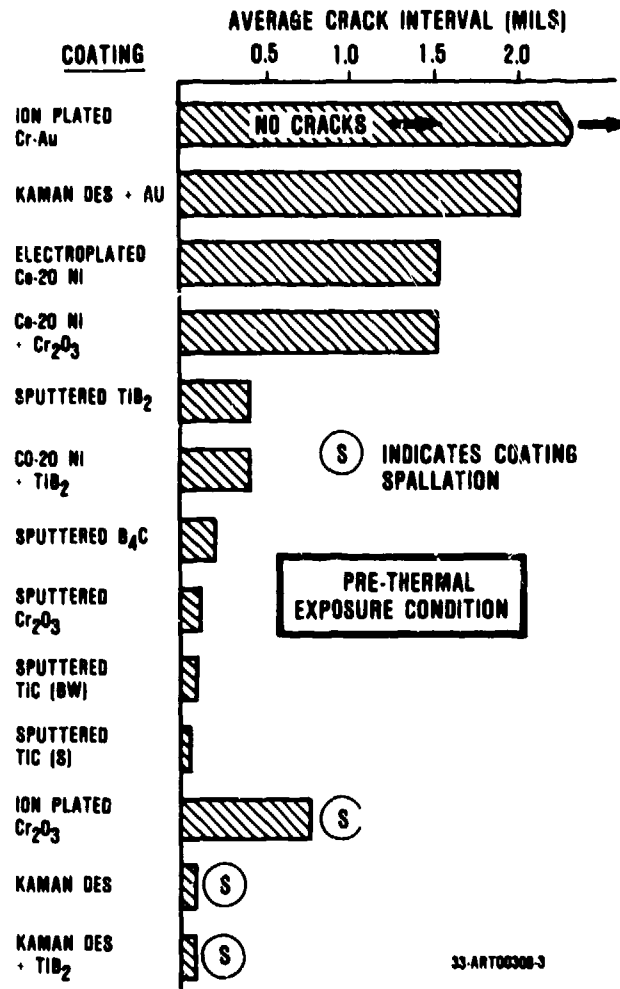


Figure 3. Foil Coating Ductility Comparison. Highest Values are Best.

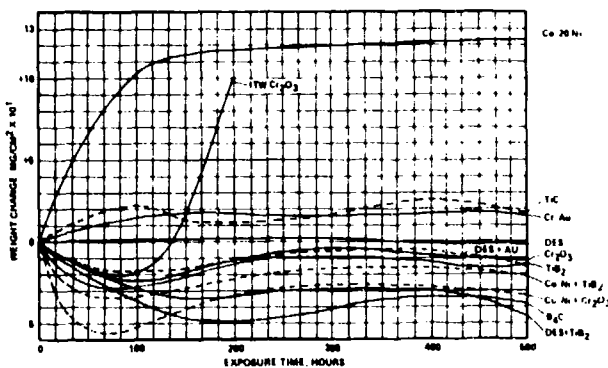


Figure 4. Foil Coating Candidates. Weight Change Versus Time at 538°C (1000°F) Exposure Temperature.

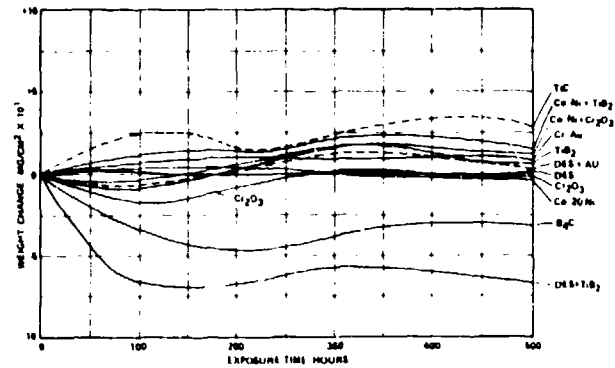


Figure 5. Foil Coating Candidates. Weight Change Versus Time at 649°C (1200°F) Exposure Temperature.

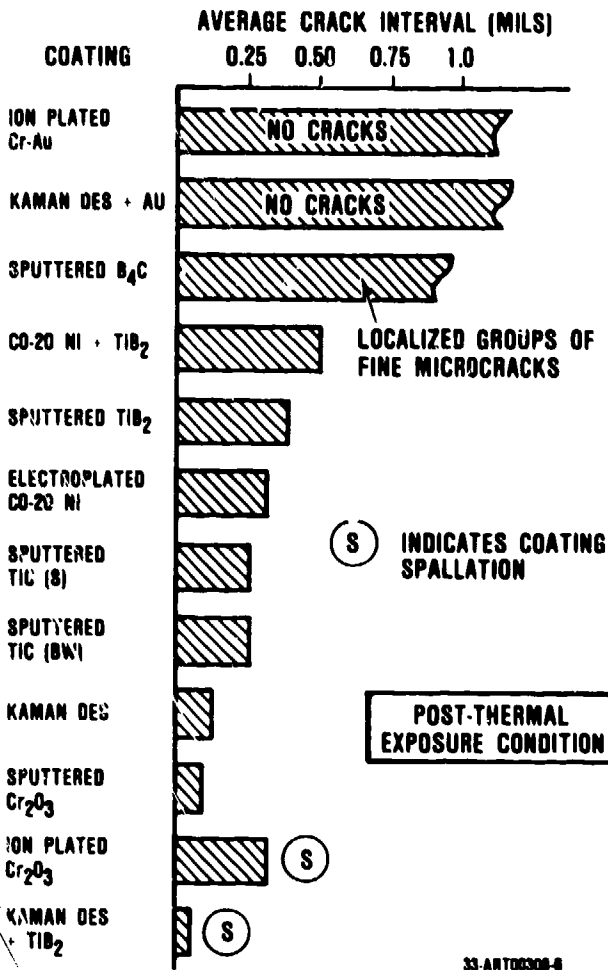


Figure 6. Foil Coating Ductility Comparison. Highest Values are Best.

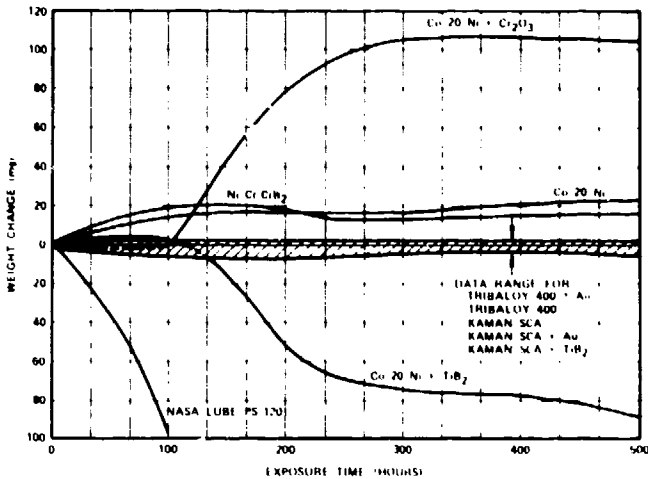


Figure 7. Journal Coating Candidates. Weight Change Versus Time at 538°C (1000°F) Exposure Temperature.

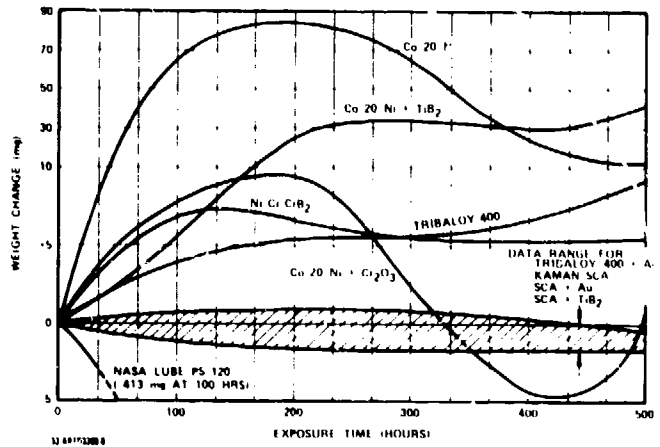


Figure 8. Journal Coating Candidates. Weight Change Versus Time at 649°C (1200°F) Exposure Temperature.

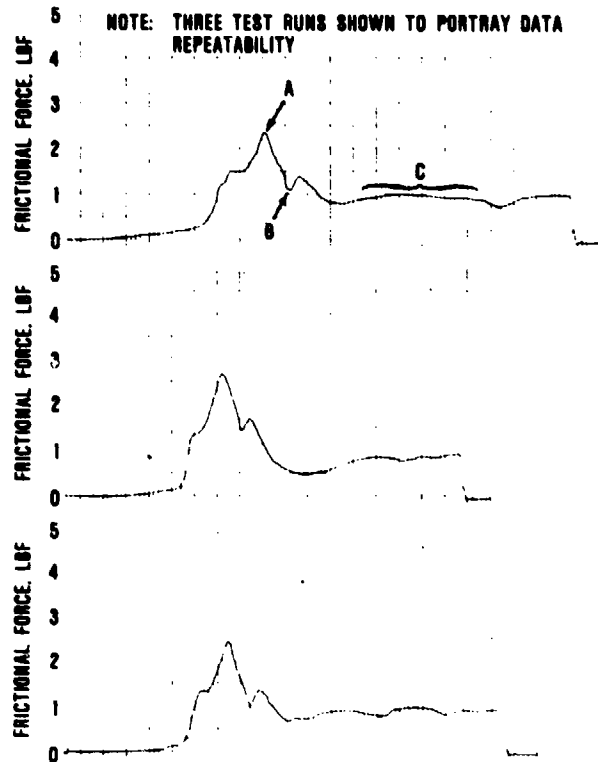


Figure 9. Sliding Friction Test Results, Triballoy 400 Versus B₄C (pre-oxidized) Showing Static Friction Spike A, Linkage Backlash B, Dynamic Friction Trace C. [Contact Force = 24.2 Newton (5.45 Pounds), Room Temperature].

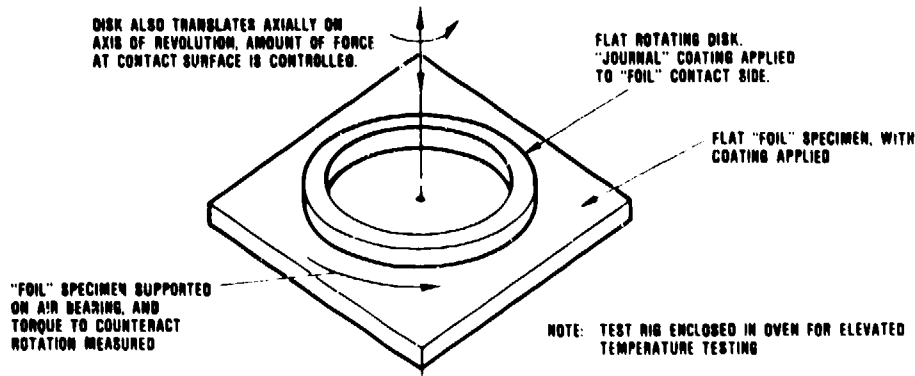


Figure 10. Sketch of Dynamic Properties Test Rig.

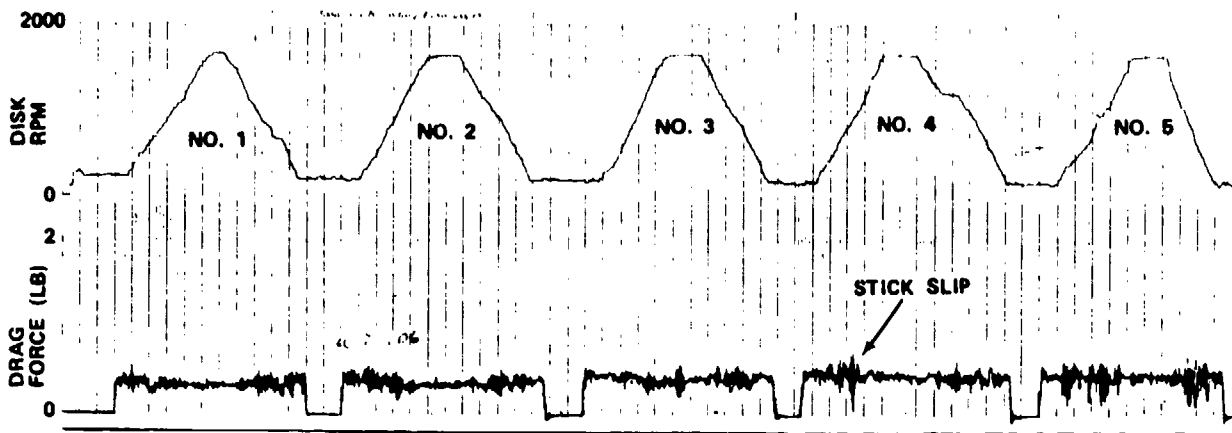


Figure 11. Typical Dynamic Friction Test Results (Steps 1 and 2, Table 11).

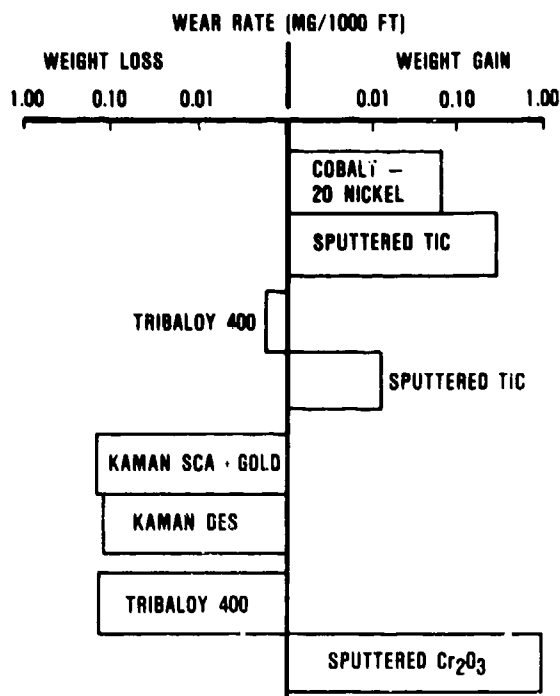


Figure 12. 649°C (1200°F) Wear Test Behavior of the Four Tested Wear Couples. Dynamic Properties Test Rig.

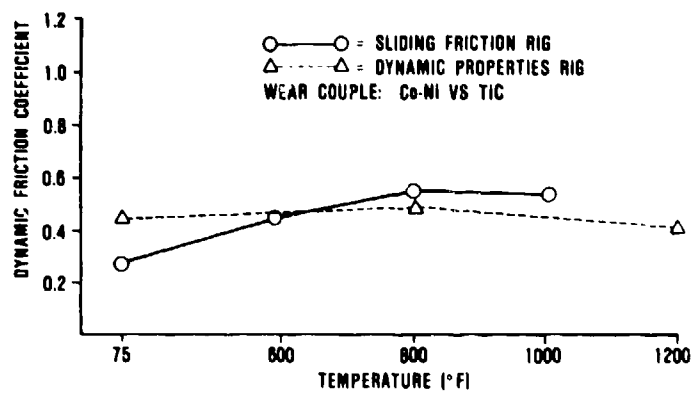


Figure 13. Comparison of Dynamic Friction Coefficient Data.

EVALUATION OF ANTI STICK - SLIP
BEHAVIOUR OF BRONZE FILLED PTFE
AS BEARING MATERIAL

by

Ö. Anlağan
Mechanical Engineering Department
Middle East Technical University
Ankara - Turkey

SUMMARY

PTFE based plastics have long been proved to be a good alternative group of materials used in bearings and guideways, where slow speed performance is important. Its good performance is backed up by relatively high wear resistance which provides reasonable bearing life expectancy comparable to the life of conventional bearing materials. However, deterioration in the slow speed performance of bronze filled PTFE is observed as wear progresses, that is, stick-slip occurs at low speeds.

The work reported in this paper is concerned with the evaluation of the performance of bronze filled PTFE at slow speeds. Experimental results are used to explain the mechanism involved in wear which is primarily responsible for the loss of slow speed performance. The behaviour change is attributed to the mechanical changes that takes place on sliding surface of plastic as wear progresses, which leads to change of friction-velocity profile from positive to negative.

INTRODUCTION

In bearings where boundary lubrication is inevitable, there is solid contact between sliding surfaces which may initiate an oscillatory motion called stick-slip. This kind of motion must be absolutely absent in bearing applications where accurate positioning is required, like in machine tools or in measuring instruments.

If a gradually increasing force is applied to a mass standing on a bearing surface, contacting surface asperities are tangentially deformed until the junctions are broken, then sliding starts; that is, static friction changes to kinetic friction. When there is an abrupt change from static to kinetic friction as the mass starts moving, energy stored in the elastic component of the drive unit which exerts force on to the mass is released after the static friction is overcome. The release of this energy may cause stick-slip oscillation. At low speeds, friction force is basically composed of solid and boundary frictions, which are functions of surface deflection. At higher speeds, the mass is lifted because of hydrodynamic effect, and consequently, the asperity deformation is changed, affecting the solid and boundary frictions. As speed increases, the viscous friction, which is caused by shearing of the lubricant film, and which is directly proportional to speed, becomes more significant.

The occurrence of stick-slip motion depends on: i) the frictional properties of bearing materials ii) the properties of lubricant used in the bearing and iii) the structural parameters of driving unit [1].

It is usually considered that friction is useful for damping unwanted oscillations in a system, but in the case of stick-slip oscillation, friction is the cause of instability. In general, materials have static coefficients of friction higher than kinetic coefficients of friction. Early works suggest that the ratio of static to kinetic friction determines the occurrence of stick-slip motion, but later works state that the friction-velocity profile is the effective factor [2]. If the kinetic coefficient of friction decreases as the sliding speed increases, the energy stored in the elastic component of drive unit will be introduced into the system in the form of kinetic energy when any increase in sliding speed takes place. Therefore the system stability is reduced. In other words, a negative friction-velocity profile represent a concept of negative damping which is the source of stick-slip oscillation [3] [4]. A positive friction-velocity profile indicate a stick-slip free motion.

The viscosity of lubricant applied to sliding surfaces is a factor affecting the stability of sliding motion. Hydrodynamic lift force, squeeze film force and viscous shear force depend on lubricant viscosity. Lift force separates sliding surfaces so that solid friction component is reduced, that means the negative damping is reduced. Since higher viscosity results higher lift force, stick-slip is reduced if a higher viscosity lubricant is employed. Viscous shear force which is proportional to the viscosity of lubricant, represents a positive damping in the system. So higher viscosity lubricant positive damping in the system due to higher viscous shear force. Critical velocity, that is, the sliding velocity beyond which the stick-slip motion is diminishes, can be reduced by employing higher viscosity lubricants [5].

It is a well known fact that polar lubricants (mineral oils containing a fatty acid as polar additive) inhibit stick-slip motion and reduce friction level. It is shown that when a polar lubricant is used between sliding surfaces, a friction-velocity profile with positive slope is obtained [4].

Bell and Britton [6] discuss the influence of polar lubricants on the stability of slideway systems. It is pointed out that the marginal instability can exist even in the presence of polar lubricants on large machine tools where low drive stiffness and low drive natural frequencies are common. Cockerham and Symmons [7] investigate the level of

positive viscous damping necessary to induce stability in a potential stick-slip situation. The results of this theoretical analysis show that smooth sliding is achieved by introducing a viscous damping system whose damping coefficient is equal to one-half of the negative friction damping coefficient value. It is suggested that the damping component might be adequately obtained by using a suitable polar lubricant, or a polymer material exhibiting high internal damping. It is also shown that as well as increasing the system stiffness, a reduction in the inertia of the system can reduce the amplitude of stick-slip oscillation.

The amount of energy stored in the elastic component of the drive actuator is an important factor influencing the stick-slip motion. Voorhes [8] proposes the energy concept to explain the stick-slip phenomenon. He suggests that there are two types of surface deformation, namely, elastic deformation of asperities where the slider remains stationary, and plastic deformation of asperities where sliding takes place. During elastic-plastic transition, the drive system releases an amount of energy which varies inversely with the drive stiffness. A soft drive accelerates the slider sufficiently to lower the meta-stable kinetic coefficient and triggers stick-slip. It is shown that a positive friction-velocity profile can be obtained by employing high stiffness drive. Hunt [9] works on elimination of stick-slip oscillations by normal excitation. He concludes that stick-slip is almost entirely eliminated when the slider is subjected to normal vibration at one of the resonant frequencies of the combined slider-slideway system. It is found that the amplitude of the oscillatory force required to overcome stick-slip can be as low as 4 percent of the static load. No effect on coefficient of friction by normal excitation is observed.

FRICITION OF BRONZE FILLED PTFE

PTFE has exceptionally good frictional characteristics which no other material has. Apart from having the lowest coefficient of friction compared with all the other materials when it slides against metals, its motion is free of stick-slip under any condition, and dry sliding application is possible. Despite all the satisfactory frictional behaviour, however, it has the lowest wear resistance compared with the others. The practical application of pure PTFE as a bearing material is limited due to its low wear resistance.

Use of filler materials in plastics to provide extra strength and wear resistance is a common application. Most of the commercially available PTFE bearing materials contain bronze particles as fillers. Bronze increases wear resistance especially at low and medium speeds. It also gives extra strength to PTFE and increase its thermal conductivity.

Turcite-B and Fluon VB-60, which are both commercially available bronze filled PTFE are tested for their frictional and wear characteristics. The mean size of bronze particles in Turcite-B is 23 μm whereas the mean size of bronze particles in Fluon VB-60 is 9 μm . Polished surface photographs of test specimens are shown in Fig.1.

Specimens are tested under dry and lubricated conditions. Dry test results suggest that Turcite-B has a brakeaway friction coefficient of about 0.12 and coefficient of friction increases as sliding speed increases. Introduction of lubricant between sliding surfaces reduces the brakeaway friction. Vitrea 27 and Vitrea 72 which are both mineral oils having viscosities of 22 Cs/50°C and 112 Cs/50°C respectively, reduce brakeaway friction to 0.1. Tonna 27 and Tonna 72 which are both polar oils having viscosities of 22 Cs/50°C and 112 Cs/50°C respectively, reduce brakeaway friction even further to 0.08. The classical effect of polar lubricants, that is, to create positive slope in the friction-velocity profile due to their boundary lubrication properties, is observed. No significant difference between friction test results of Turcite-B and Fluon VB-60, except that Fluon VB-60 has slightly lower dry brakeaway friction level than Turcite-B has, is observed (Fig.2).

Turcite-B and Fluon VB-60 are tested for their stick-slip performance. The experimental techniques are described elsewhere [1]. Neither Turcite-B nor Fluon VB-60 shows any tendency to stick-slip motion under dry or lubricated conditions.

WEAR OF BRONZE FILLED PTFE

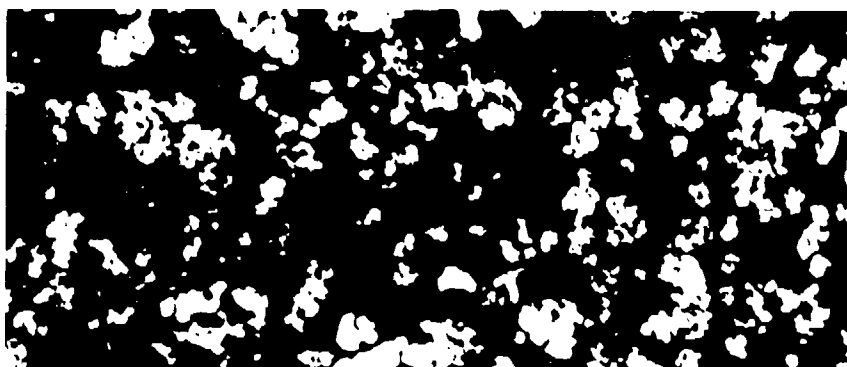
In the previous work [10], wear characteristics of Turcite-B and Fluon VB-60 were experimentally investigated. It is concluded that the dry wear resistance of bronze filled PTFE is much higher than that of cast iron. The use of lubricant has a dominant influence on bearing wear characteristics. Even with use of abrasive contaminant, the wear is 10 times less than that observed under dry conditions. The wear factor of tested specimens are shown in Table 1. It is concluded that the use of bronze filled PTFE as bearing material can give substantial improvements in wear and in the degree of gross damage inflicted on the bearing surfaces under poor working conditions. This is especially valuable where insufficient lubrication of sliding surfaces is inevitable.

Tests were performed on small scale specimens of 25 mm diameter to investigate the mechanical changes that take place on the surface of Turcite-B and Fluon VB-60 when they were sliding against steel surface. Surface of specimens were examined under microscope at certain stages of wear progress. Prior to wear tests, specimens were ground and mechanically polished.

The bronze particles in Fluon VB-60 have irregular shapes with sharp corners and wide variety of particle sizes. The bronze particles in Turcite-B are larger and they have spherical shape. As wear progresses, in the running-in period, friction tracks are observed on the particles and matrix surfaces. Surface scoring and longitudinal scratches are indication of abrasive wear on worn specimens. The particles become more irregular and more



a) Turcite-B (magnification is 400)



b) Fluon VB-60 (magnification is 400)

Fig.1. Polished surface photographs of Turcite-B and Fluon VB-60

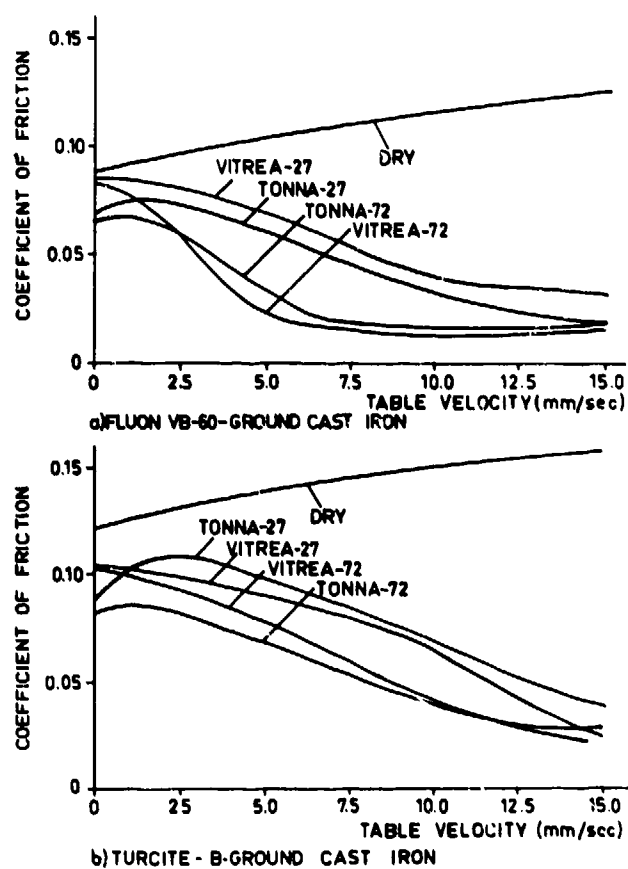


Fig.2. Steady state friction-velocity curves of Fluon VB-60 and Turcite-B sliding on ground cast iron.

Table I. Wear factors of Turcite-B and Fluon VB-60 when sliding against ground steel surface (contact pressure: 4 kg/cm², sliding velocity: 50 mm/sec)

MATERIALS	SLIDING CONDITIONS	WEAR FACTOR: $k_w \left(\frac{\mu\text{m}}{\text{kg/cm}^2 \cdot \text{km}} \right)$
TURUTE-B	dry	0.180
FLUON VB-60	dry	0.060
TURUTE-B	lubricated with contaminated lubricant	0.009

abrasive due to abrasive action and work hardening effect of the counterface.

After 10 km of sliding, due to polishing effect of the counterface and third bodies at the interface, smooth surface of individual particles were formed. They form an elevated "metallic plateau" like structure on the worn surfaces of the specimens, since the relatively soft matrix around bronze particles are worn with a faster rate by the abrasive action. At later kilometers, the total area of these plateaus gains importance on overall area of contacting surface. As the real contact area of bronze particles increases during sliding wear, more and more bronze comes into contact with counterface.

The surface photographs of Turcite-B show two types of scratch; thin and long scratches having almost uniform width, and dark scratches having a width comparable to the particle diameter. This suggests two different mechanisms for the formation of scratches. The first one is the abrasive effect of the steel counterface, the second is the flow of bronze particles in the soft PTFE matrix and in the direction of sliding. The second mechanism is also responsible for the detachment of particles from the polymer matrix. It appears that repeated movement of particles decreases the bonding effect of the matrix. The moving particles when encounter other particles are detached or detach weakly bonded particles. In case of Fluon VB-60 the number, the length and the depth of scratches are less. This is due to higher filler percentage and irregular shapes of particles which give maximum chance of being bonded.

The results, at the end of 40 km of sliding, show that an overall increase in particle proportion is obtained. In both specimens a rapid increase in particle proportion is observed in the running-in period. This is due to high transfer rate of PTFE during the running-in period. Then a decrease in particle proportion is observed. This is attributed to the fact that exposed particles are detached. These particles form third bodies or are transferred to the steel counterface together with PTFE. The transferred material gradually fills up the surface depressions of the counterface leading to a smoother surface. The new surface generated on the steel counterface is more resistant to particle penetration than the composite surface. Detached particles which penetrate in the PTFE matrix reincrease the particle area proportion of the composite. Percentage areas of bronze particles on the specimen surface are tabulated in Table II.

Table II. Percentage area of filled bronze particles and standart deviations from the mean values.

Sliding distance km	Turcite - B		Fluon VB - 60	
	% Area	Standard deviation	% Area	Standard deviation
0	10.5	3.1	18.6	3.
1	10.9	2.	20.5	2.8
5	12.	2.3	18.8	3.1
10	11.	2.1	20.5	3.9
20	10.6	2.	23.1	2.
27	11.5	2.	22.7	3.5
35	13.5	1.4	22.	3.2
40	13.9	3.4	23.2	1.9

EFFECT OF WEAR ON FRICTON OF BRONZE FILLED PTFE

Wear results two significant mechanical changes on the worn surface of bronze filled PTFE specimens. First, particle population between sliding surfaces increases as wear progress. That means the ratio of the metal to metal contact area to the plastic to metal contact area increases. This may effect the friction-velocity profile of original PTFE-metal pair. As a matter of fact, it is reported that the slope of friction-velocity profile

of bronze filled PTFE becomes negative after the sliding surface being subjected to wear [10]. The friction-velocity profiles of worn Turcite-B and worn Fluon VB-60 are shown in Fig.3. By comparing Fig.2 and Fig.3, one can easily observe that the slope of friction-velocity profile of bronze filled PTFE changes from positive to negative when sliding surfaces are subjected to wear.

Second, when sliding surfaces are subjected to wear, a non uniform wear progress on the surface of composite plastic because of the non homogeneity in the nature of composites and difficulty of sustaining a uniform contact pressure distribution over the sliding surface. Non uniform wear over the sliding surface of bronze filled PTFE is also emphasized in reference [10].

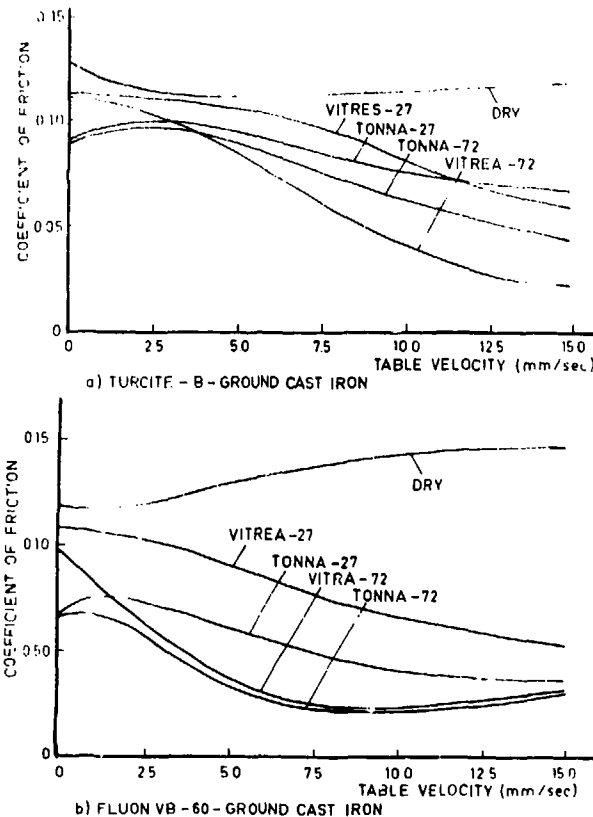
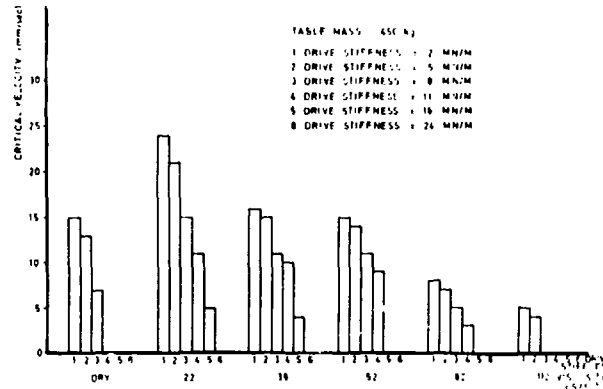


Fig.3. Steady state friction-velocity curves of worn Turcite-B and worn Fluon VB-60 sliding on ground cast iron.

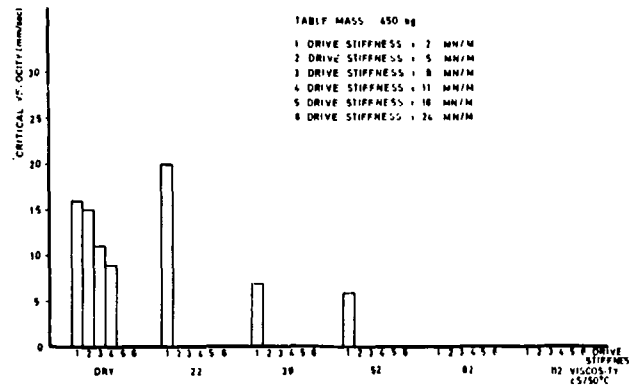
The stick-slip behaviour of bronze filled PTFE deteriorates as the bearing surface is worn. Deterioration of stick-slip performance is mainly due to the change of the friction-velocity profile from positive to negative. On the other hand in a theoretical investigation on the stick-slip phenomenon it is shown that high contact pressure increases the critical velocity of stick-slip motion [5]. Since it is obvious that non uniform wear results high local contact pressures, the occurrence of stick-slip on worn PTFE composite bearing surfaces is expected. The experimental results showing the critical velocities of worn Turcite-B and worn Fluon VB-60 are shown in Fig.4.

Critical velocity decreases when drive stiffness increases and also when lubricant viscosity increases. Overall stability picture of both worn specimens is more satisfactory when compared to the overall stability picture of cast iron which is presented in reference [11]. On the other hand, a comparative evaluation of stability behaviour of worn specimens suggests that Fluon VB-60 exhibits a better performance than Turcite-B. The use of polar lubricant in tests with worn Turcite-B and worn Fluon VB-60 prevent stick-slip motion under all experimental conditions.

Increase in the bronze particle population on the surface of worn specimens is observed. In Table II the percentage area of metal (bronze) is tabulated against the distance of sliding. After 40 km of sliding, a 30% of increase in the percentage area for Turcite-B and 25% of increase in the percentage area of Fluon VB-60 are measured. It is assumed that friction-velocity profile of bronze filled PTFE is composed of friction-velocity profiles of PTFE-metal and metal-metal pairs. As wear progresses the friction-velocity characteristics of metal-metal becomes dominant over the friction-velocity characteristics of composite PTFE. This is assumed to be the reason of the change of friction-velocity profile as wear progresses.



a) Turcite- sliding against ground cast iron



b) Fluon VB-60 sliding against ground cast iron

Fig.4. An overall view of the stability characteristics of worn Turcite-B and worn Fluon VB-60 showing the influence of drive stiffness and lubricant viscosity (contact pressure: 6×10^4 N/m²).

CONCLUSION

The friction-velocity profile of bronze filled PTFE has positive slope. Mainly due to this property, bronze filled PTFE does not exhibit stick-slip motion even under severe working conditions.

The wear resistance of bronze filled PTFE is high enough to provide an acceptable bearing life expectancy. Resistance against abrasive wear is especially superior over other conventional bearing materials. Use of small size bronze particles with irregular shape as fillers improve the wear resistance of composite PTFE.

Anti stick-slip performance of bronze filled PTFE deteriorates as the bearing surface is worn. Still the worn bronze filled PTFE exhibit better anti stick-slip performance than conventional bearing materials. The stick-slip motion can be completely eliminated by using a polar lubricant having an adequate viscosity.

Bronze filled PTFE is recommended as bearing materials if stick-slip free motion at low speeds under inadequate lubrication conditions is required.

REFERENCES

1. R. BELL and Ö. ANLAĞAN, The Friction Characteristics and the Sliding Stability of Machine Tool Slideways which Employ PTFE-Metal Composite Materials Proc. of 19th Int. M.T.D.R. Conference, 1978.
2. A.K. BENERJEE, Influence of Kinetic Friction on the Critical Velocity of Stick-Slip Motion Wear, Vol.12, 1968.
3. R. BELL and M. BURDEKIN, Dynamic Behaviour of Plain Slideways, Inst of Mech. Eng. Proc., Vol.184 Part 1, 1970.
4. D.R. BRITTON, Ph.D. Thesis, UMIST, 1976.
5. Ö. ANLAĞAN, Modelling of Friction Induced Instability in Machine Tool Slideways, Assoc. Professorship Thesis, METU, 1981.
6. R. BELL and D.R. BRITTON, Evaluation of Polar Lubricants for Machine Tool Slideways, 7th Machine Tool Conference, Budapest, 1972.
7. G. COCKERHAM and G.R. SYMMONS, Stability Criterion for Stick-Slip Motion Using a Discontinuous Dynamic Friction Model, Wear, Vol.4, 1976.
8. W.G. VOORHES, Investigation of Stick-Slip in Simulated Slideways, J.A.S.L.E., 1963.
9. J.B. HUNT, Research Note: Reduction in Relaxation Oscillation (Stick-Slip) Amplitudes, J. Mech. Eng. Sci., Vol.19, 1977.
10. Ö. ANLAĞAN and R. BELL, Wear Characteristics of PTFE-Metal Composites When Used Under Machine Tool Slideway Conditions, Proc of 21st Int. M.T.D.R. Conference, 1980.
11. R.D. BRITTON and R. BELL, The Influence of Design Parameters on the Stability of Sliding Motion of Machine Tool Feed Drives, Advances in Machine Tool Design and Research, 1971.

DISCUSSION

K.J.Brown, Ontario Hydro, Toronto, Ca

Could the stick-slip behaviour be related to the presence or thickness of the transferred PTFE layer on the steel?

Author's Reply

The friction and wear tests were performed at different test rigs. The worn specimens were tested in the friction test rig where the metal counterface was free of transferred PTFE. Therefore, the stick-slip behaviour of the worn specimen is not related to the transferred PTFE layer on the steel counterface.

APPLICATION OF DYNAMIC GAS BEARINGS TO
CRYOGENIC COMPRESSORS AND TURBINES

by

G. Nardi

Istituto di Macchine - Università di Pisa
56100 Pisa, Italy

SUMMARY

A particular design of dynamic gas bearing containing tilting pads, for cryogenic compressor and turbine applications, is discussed. The bearing system has no gas input during normal operation in order to prevent entirely the exchange of hot and cold gas. A pressure increase is generated in the wedge-shaped gas film between the shaft and the pad. A portion of the gas stream flowing through the wedge is introduced through the pad into the gas between the pad and the pad housing. In this manner, the pressure in the gap is a factor of the pressure in the wedge. The pad is completely surrounded by a gas film. It adjusts itself automatically in accordance with the equilibrium of the forces. The angle of incidence of the pads is determined by the equilibrium of torques relative to the axis of rotation of the pad.

It is shown that the gas bearings offer the advantage of improved reliability because no control system is necessary.

INTRODUCTION

Future aircraft and missiles will place severe requirements on the auxiliary power systems. As a result of high Mach number flight, approaching Mach 4 for current operational fighters and supersonic transport aircraft, hydrogen fuel may offer great promise. Hydrogen is cooled to 20 K to reach a state of liquefaction, stored in that form by well insulated tanks, and pressurized to feed the gas turbine combustion chamber. In order to avoid problems of priming and pre-cooling, the pumps is immersed in the liquid hydrogen tank. If the motor is placed outside the tank, a long, slender, shaft is required to drive the pump. There is also the problem of making safe the electric motor outside the tank, where gaseous hydrogen can surround it. However, when the pump runs there will be an appreciable hydrogen boiling away due to the inefficiency of the motor, which turns to heat, and the changes to gaseous state during the fueling operation. A submerged motor is preferable when hydrogen has to be rapidly pumped. The evaporated low temperature hydrogen, as a result of boiling at the pump suction and delivery, has to be used for auxiliary purposes in a cryogenic compressor and in a cryogenic turbine, respectively requiring and delivering power.

Cryogenic hydrogen pumps, compressors and turbines, are normal components, figure 1 and Rf. 1, in nowadays hydrogen liquefaction plants, for instance handling large quantities of gaseous hydrogen available at future air terminals, through pipelines from the production site. During the airplane fueling ground operation, and at any other time when the temperature and pressure exceed the conditions required to maintain hydrogen in its liquid state, some of the liquid hydrogen changes to gaseous state and must be collected and returned to the liquefaction plant for a cryogenic compression.

Thermal and environmental control systems in aircraft are more and more using nitrogen and helium loop heat exchangers to provide direct cooling of subsystems and equipment.

The present paper gives therefore a picture of some of the fields of present interest to problems in bearing and lubrication of cryogenic pumps, compressors and turbines. The uses of cryopumping with condensation surfaces at temperatures very low are increasing. The new superconducting electronic devices will need a whole new generation of refrigerators, too.

With the present state of development of superconductors and helium refrigerators, superconducting alternators may be used in aircraft. Between 500 kVA and 1 MVA, the superconducting machine becomes competitive, although direct liquid cooled alternators would probably be marginally lighter. Above 1 MW, the superconducting machine would be lighter than a conventional type, the weight advantage increasing as the rating increases. The predominant promise is that of the 4 K to 77 K refrigerator. This aspect could well be the major influence on the prospects for superconducting machines in aircraft, and emphasizes the need for the continued development of small, reliable, lightweight helium refrigerators with ratings up to approximately 8 to 10 Watts.

In a gas bearing cryogenic turbo-expander for refrigerators or liquefiers, the process gas (hydrogen, helium, nitrogen, etc.) may be expanded in a single-stage inward-flow turbine, driving a compressor seated on the same shaft. The hydrogen (or helium) turbine has radial and thrust dynamic gas bearings at ambient temperature, while the impeller operates at 20 K (or 4 K). The turbine with dynamic gas bearings, figure 2, neither needs bearing gas from the cycle compressor. Gas circulates in the bearing housing in a closed loop and does not effect the process stream.

Axial and centrifugal compressors with gas lubricated bearings have been developed in order to overcome the problem of oil contamination in hydrogen (or helium) refrigerators. The use of these compressors should permit the construction of practically maintenance free refrigerators.

Compact auxiliary power units, using hydrogen gas for both turbine and compressor, shall be used for re-circulation of cryogenic hydrogen leakage in next generation hydrogen fueled turbojet engines.

It is only since about 1950 that the study of gas bearings has been noticeably accelerated. This is because present special-purpose bearing requirements can often best be satisfied by using gas bearings. Gas bearings are useful, both in high-temperature missiles and low-temperature cryogenic applications, because the viscosity does not change much with temperature and retains satisfactory values over wide temperature ranges.

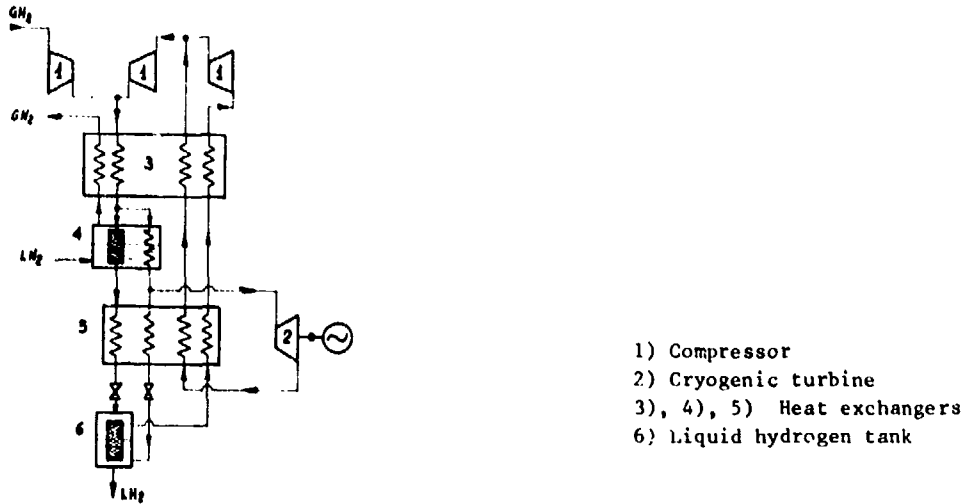


Fig. 1 - Flow chart of a hydrogen liquefaction plant, with cryogenic expansion turbine.

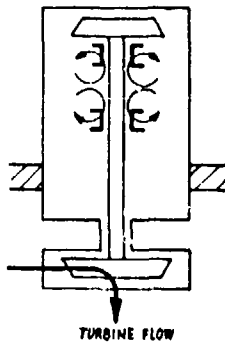


Fig. 2 - Dynamic gas bearing concept.

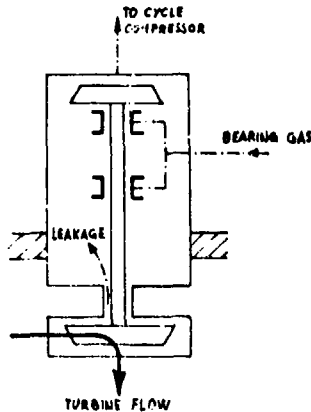


Fig. 3 - Static gas bearing concept.

Gas bearings are used in superconducting alternators, refrigerators and liquefiers. Because of low frictional losses, gas bearings are used for high-speed electrical motors to take advantage of the fact that power equals torque times angular velocity. Thus, higher speeds means smaller sizes to deliver the same horsepower.

Gas bearings are classified as: self-acting, Ref. 5, if the lubricating film exists because of relative tangential motion; and externally pressurized, if due to an external source.

GAS BEARINGS FOR CRYOGENIC PLANTS

Turbines with static gas bearings, figure 3, need a supply of bearing gas from the refrigerator cycle compressor. From the other hand, dynamic gas bearings, figure 2, have no loss in efficiency, caused by bearing gas or leakage stream from the cycle, and improved reliability, because no control system is necessary.

Helium refrigerators normally need two turbines which run at different temperature levels, figure 4.

Figure 5 shows a cooling method for a superconducting magnet. A liquid helium reservoir exists within the refrigerator cold box, where the high pressure helium gas is recooled several times.

As an example of small power device, we consider an electrical alternator which converts the output of an axial helium flow action Laval-turbine into electrical power. The whole engine, including generator and bearings, works at a temperature of 25 K, with: input pressure, 3 000 kPa; pressure ratio, 20; input temperature, 25 K; rotational speed, 160 000 rpm; diameter of the wheel, 20 mm; number of blade, 240.

The Sulzer gas bearing turbine, figure 6 and Ref. 2, is a single-stage inward-flow turbo-expander. The mechanical energy which is withdrawn is transmitted to the brake circuit by a compressor seated on the

same shaft. This brake circuit contains a cooler and a valve. The same medium is contained in the brake circuit and in the process circuit. The two circuits are connected with one another for pressure equalization. The three standard models have the following characteristics: impeller diameter, 9-32 mm; maximum peripheral wheel speed, 460 m/s; performance (helium), 0.1-20 kW; efficiency, 0.58-0.82; maximum rotational speed, 294 000 - 228 000 - 156 000 rpm; shaft diameter in radial bearing, 16-22-32 mm.

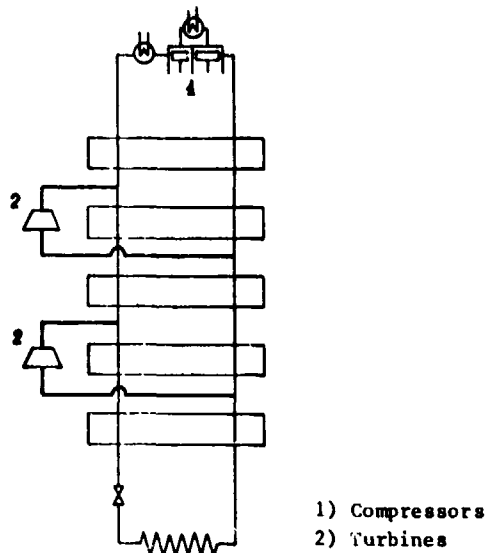


Fig. 4 - Helium liquefaction plant with two cryogenic expansion turbines.

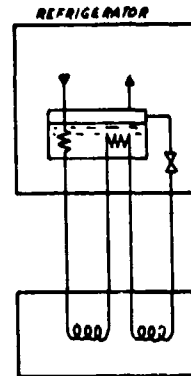


Fig. 5 - Cooling of superconducting magnet.

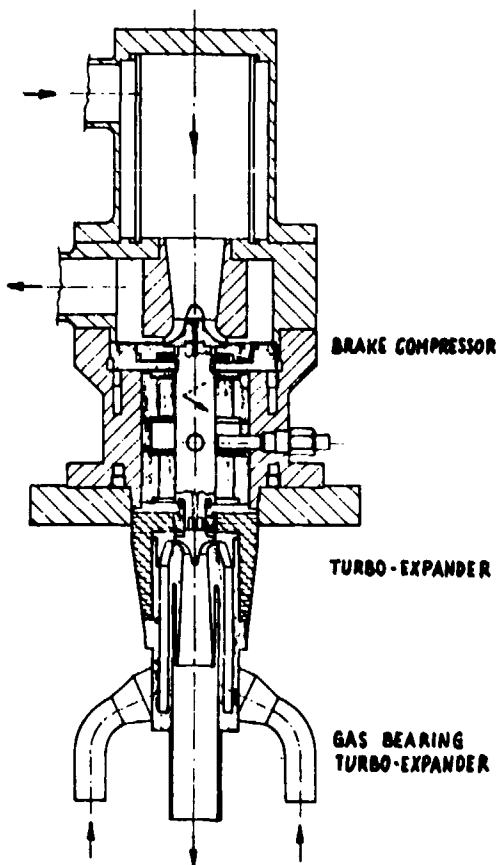


Fig. 6 - Sulzer gas bearing turbo-expander.

The turbine has two radial and two thrust gas bearings, which all operate at ambient temperature. The impeller operates at temperatures of down approximately 6 K. Rotor and bearings are installed in the bearing cartridge. The bearing system has no gas infeed during normal operation, entirely, preventing exchange of hot and cold gas.

An oil-free centrifugal compressor, with gas lubricated bearings, may operate with a single stage pressure ratio of 1.26 at a flow rate of 800 Nm³/h, figure 7 and Ref. 3. As a conventional helium refrigerator operates with a pressure ratio of at least 10, it is necessary to connect a large number of compressor unit in series. All the components from stage to stage are identical except for the impeller, the impeller shroud, the diffuser and the thrust bearing. These components have to be designed to match the volume flow through each stage. The impeller is driven by a 24 m/s, two pole, three-phase induction motor.

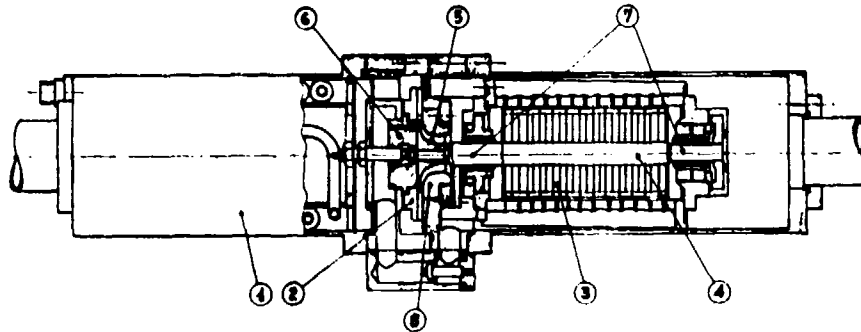
The rotor is supported on tilting pad gas journal bearings. The pads are supported on elastic hinges which limit the motion of each pad to that of rotation in the direction of tilt; they are given a slight bias in the direction of tilt by means of adjustable compression springs. These ensure that the gas films are convergent at all speeds of the shaft. The bearing at the inlet end of the rotor has a nominal diameter of 15.9 mm and the design radial clearance at the hinge line of 0.01 mm. The bearing at the impeller end of the rotor has a nominal diameter of 22.2 mm, and the design radial clearance at the hinge line is 0.015 mm.

The thrust bearing has to support the impeller, with a clearance of order 0.05 mm, over a wide range of operating conditions, including surging.

DYNAMIC GAS BEARING FOR A CRYOGENIC HYDROGEN TURBINE

We refer to a cryogenic expansion turbine, figure 8 and Ref. 4, for a hydrogen liquefaction plant producing 25.74 N/s of LH_2 , corresponding to a power need of $18.35 \cdot 25.74 = 472$ MW (where 18.35 MJ/N = $11.229/0.765 + 3.67$ MJ/N; with the hydrogen low heat of combustion 11.229 MJ/N, the efficiency 0.765 for the gaseous hydrogen production by electrolysis, and the gaseous hydrogen liquefaction energy need 3.76 MJ/N). A liquid hydrogen production of 25.74 N/s is sufficient for 7 flights (each 10 000 km) a day of a 400 passengers subsonic transport plane. As comparison, the present biggest hydrogen liquefaction plant is rated 6.18 N/s.

The thermodynamic liquefaction cycle imposes, figure 1, a pre-cooling by a recycle of gaseous hydrogen, a part of which is flowing through the cryogenic expansion turbine.



- | | |
|--------------------|-------------------|
| 1) Heat exchanger | 2) Diffuser |
| 3) Stator | 4) Rotor |
| 5) Impeller | 6) Thrust bearing |
| 7) Journal bearing | 8) Shroud |

Fig. 7 - Oil-free centrifugal compressor, with gas lubricated bearings.

According to an optimized liquefaction process with ortho-para hydrogen conversion, the weight flow through the turbine is 62.76 N/s, for initial and final pressure, temperature and enthalpy, conditions, respectively, $p_i = 4\ 046$ kPa, $T_i = 80$ K, $i_i = 130.13$ kJ/N, and $p_f = 246.7$ kPa, $T_f = 26$ K, $i_f = 78.93$ kJ/N.

In order to be able to operate a cryogenic plant, like the one in figure 1, it is necessary to reduce the temperature of a gas stream at one or more locations in the plant. In the case of gases which display ideal thermodynamic behaviour, it is not possible to reduce the temperature through throttling. This is the case, within wide ranges, with hydrogen, which is suitable for such plants as a result of its low liquefaction temperature. In such cases, the temperature can only be reduced by removing energy from the gas stream, e.g. through expansion in a full action turbine. Since the expansion occurs at a low temperature level, the volume flow rates and thus the decisive cross sections, are small. The velocity (generally several 100 m/s) of the gas stream leaving the impeller is depending upon the enthalpy drop. In order to achieve a good efficiency there must be a given ratio between the peripheral wheel speed and the gas velocity. This results in relatively high peripheral wheel speeds, which require small dimensions and very high rpm.

Dynamic gas bearings, figure 2, are used because of reduced blow-by losses. The pressurized gas is circulating in a closed cycle without any influence on the expansion process. An outside control system is not needed, and the efficiency is very high. Additional static gas bearings may be used during transient regimes.

Turbines with dynamic gas bearings have been running continuously for more than 50 000 hours in small power cryogenic plants. It is however required high constructive accuracy, to avoid rotor oscillation under a certain value of rotational velocity.

The actual available power at the turbine shaft (27 000 rpm), with an efficiency 0.83, is resulted

$$62.76 (130.13 - 78.93) \cdot 0.82 = 2\ 635 \text{ kW}$$

for the sizes of figure 8.

Even though dynamic gas bearings have been adopted, an auxiliary static gas bearing, figure 3, is provided for near starting and stopping operations. This secondary circuit is using pressurized low temperature gas, to avoid at most heat exchanges.

The low viscosity coefficient of the gas, and the consequent compatibility between load capacity and radial bearing clearance, have imposed high rotating masses and as highest as possible peripheral velocities. The radial gas bearings, containing four tilting pads, are located in two end cartridges filled with low temperature gaseous hydrogen. The auxiliary hydrogen flow, extracted from the cycle, has the only function to recover the blow-by losses through the sealing packing. One major problem with tilting pad bearings

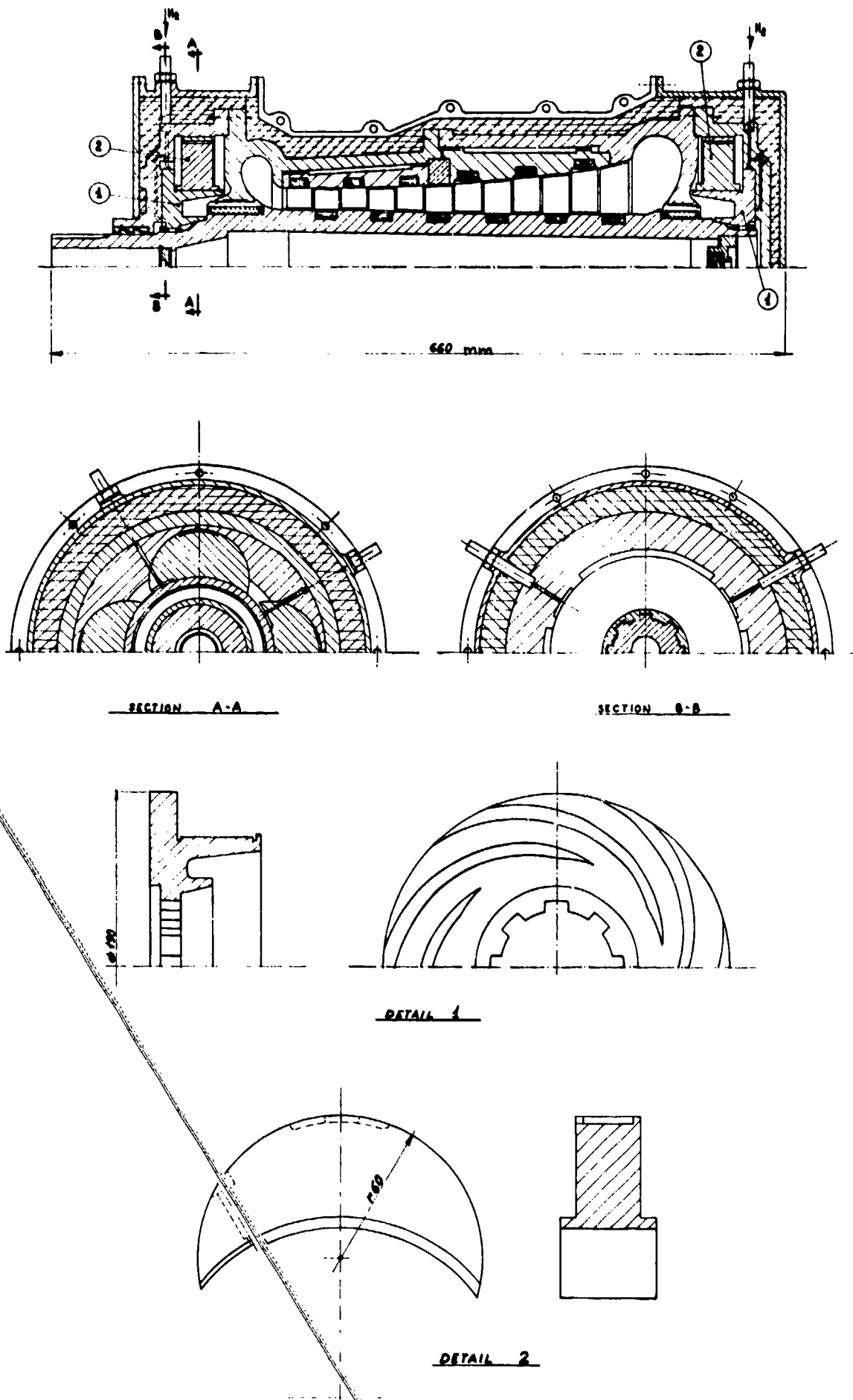


Fig. 8 - Hydrogen cryogenic expansion turbine with dynamic lift and thrust gas bearings: shaft power, 2 365 kW; longitudinal length 660 mm.

is pad friction, which makes them difficult to set. In our case, the bearing surface of the pad is eccentric with reference to the axis of rotation of the pad. A pressure increase is generated in the wedge-shaped gas film between the shaft and the pad. A portion of the gas stream flowing through the wedge is introduced through the pad into the gap between the pad and the gas housing. In this manner, the pressure in the gap is a factor of the pressure in the wedge. The pad is completely surrounded by a gas film. It adjusts itself automatically, in accordance with the equilibrium of the forces. The angle of incidence of the pads is determined by the equilibrium of torques relative to the axis of rotation of the pad. These torques are produced by both the pressure forces normal to the pad surface and by the viscosity forces acting tangential to the surface.

Each oscillating pad has its surface eccentric in respect to the pad rotation shaft. The pressure in the wedge-formed meatus between pin and pad increases, and a small gas flow under pressure fills, through a hole in the pad, the pad/housing hollow space. In such a way, the housing pressure is dependent upon that one existing on the extraction point of the meatus and related to the collecting hole load loss. The pad is completely surrounded by a gas film, so that it may oscillate around its axis according to the acting viscous forces.

Thicknesses and lifts for the pad equilibrium have been carried out on the basis of gas motion in the meatus and in the hollow space. The angle of the resultant load has been carried out from the values of the gas viscosity, the rotational shaft velocity (27 000 rpm), the load of 59 N and relative overload, the maximum length (40 mm) of the pad along the rotational axis, the maximum diameter (140 mm), the radial clearance ($22 \cdot 10^{-3}$ mm), and the gas volumetric flow ($2.40 \cdot 10^{-10}$ m³/s). The maximum relative pressure and the meatus minimum height are resulted, respectively, 35 kPa and 10^{-3} mm, this one requiring a precision grinding (roughness about 0.8 micron).

The pad external surface is assuring equilibrium at pressure 42.17 kPa and 35 kPa, respectively, where the resultant load is applied for zero volumetric flow (pad directly on housing) and $2.04 \cdot 10^{-6}$ m³/s flow (equilibrium).

The pressure drop in the duct, added to the entry and exit losses, is resulted 274.6 kPa. Taking into account the pressure distribution in laminar motion, a minimum hollow space thickness of 4 micron is necessary. In equilibrium conditions, the viscous torque on the pad is $10.3 \cdot 10^{-3}$ Nm, balanced by the torque due to an eccentricity 0.7 mm in respect to the external load.

Both thrust bearings are dynamic gas devices with inwardly pumping spiral grooves. Depending upon the direction of the resultant axial thrust at the rotor, either the right or the left thrust bearing is operative.

This type of bearing has been experimented in the last 50 years, and has been employed to support loads more than a few tons.

The spiral grooves supply a pressurized fluid film, because of viscosity in their inward pumping. High load capacities are developable, but temperature increases are accompanying the low flows pumped by the spirals. The axial load sustained by the bearing is evaluated considering a radial pressure gradient and a flow continuity between spiral and housing.

In sizing the present thrust bearings, with an axial thrust of 24.4 N, is resulted: 15 high pressure labyrinths, with 110 mm diameter and 0.15 mm radial clearance, 2% of total flow as loss, pressure from 3 923 kPa to 98 kPa, and 7 low pressure labyrinths with 103 mm, 0.4 mm, 0.5%, 294 kPa and 98 kPa respectively as diameter, clearance, loss and pressures.

A multi-stage thrust dampers avoid load on the labyrinths. The thrust bearing has the following characteristics: axial load, 93 N; meatus minimum and maximum height, 0.032 and 0.224 mm; spiral groove depth, 0.192 mm.

For that, the tolerable load on the bearing results higher than the turbine axial thrust.

As before considered, a rotor equipped with dynamic gas bearings needs auxiliary startup bearings, also with pressure gas feed, during transient regimes. Pressurized gas is fed in, when the turbine is started and stopped. This auxiliary bearing feed is switched off during normal operation.

Gas static bearings have been chosen, whose lift is generated by pressurized gas impacting a movable slide.

Helium has been used as working fluid, which, besides liquefaction temperature lower than that of hydrogen, is also an inert gas, i.e. such to avoid dangers deriving from mixtures with hydrogen. The system requires an external circuit, for pressure and flow balance, operating at ambient temperature and therefore relatively easy as realization.

Auxiliary lifting bearings must have clearances between static and movable plane higher than that of dynamic gas bearings. This is to avoid mutual sliding between the two auxiliary bearings planes during normal operation. Moreover, the eccentricity, between geometrical axis and bearing pin axis, generated by the load or geometric or pressure distribution errors in presence of more entry ducts, has been less than the dynamic gas bearing clearance, to avoid sliding during transient motion.

The adopted solution, figure 8 (detail 1), consists of three steady sectors located 120° each other, through which pressurized helium impacts the external surface of the thrust bearing disk.

Flow and thrust result meanly, for each sector, 10 dm³/s and 127.5 N, with maximum and minimum clearances, 0.049 and 0.028 mm, between sector and disk. The needed flow results quite high, but it is to be considered its rare use. It is convenient to equip the system with a control circuit for pressure distribution on the three sectors, and with limitation of the eccentricity.

Regarding the auxiliary thrust bearing, it is realizable by introducing gas helium through inlet holes, directly in the hollow space between disk and steady plane of the normal operation thrust bearing.

Dimensions to respect and clearances in whole the bearing system have very stringent tolerances, but it

is to be considered the non-series processing in which every element may be realized with extreme precision and accurate controls. It has to be observed also that the calculated dimensions are the "cold" ones (at cryogenic operating temperatures), while processing is carried out at "warm" conditions (at ambient temperature). For that, materials with very similar (or equal) expansion coefficients have to be adopted, to avoid clearances variations because of temperature gradients.

In order to reduce the control technology required, the auxiliary gas bearing has recently been replaced by an auxiliary magnetic bearing. The magnetic bearing consists of two magnetic rings, which are axially magnetized. Two identical poles work against one another and produce an auxiliary thrust bearing force. Because of the design considerations, the auxiliary magnetic bearing is not arranged in the main thrust bearing, but in the vicinity of one of the radial bearings. The stiffness of the auxiliary magnetic bearing is significantly lower than that of the gas bearing system, so that the latter is not disturbed. In addition, the auxiliary magnetic bearing increases the axial load capacity of the bearing system.

Adopted materials must have, in particular, the following characteristics: compatibility not only with cryogenic temperature hydrogen, but also with external ambient; strength capacity to stresses deriving from thermal contractions during refrigeration cycles; low thermal capacity to avoid cryogenic fluid re-heating; low thermal conductivity, because of the big temperature difference between inside and outside ambient.

Especially at low temperature, thermal fatigue is a possible cause of breaking, particularly for components subjected to temperature variations without their expansions or contractions.

REFERENCES

- [1] D. Dini, G. Nardi and G. Pizzolante Leuzzi, "Turbina in circuito chiuso per espansione di gas idrogeno fino a temperatura criogenica", 36° Congresso Nazionale della Associazione Termotecnica Italiana, 5-9 October 1 981, Viareggio (Italy).
- [2] C.H. Schimid, "Sulzer Gas Bearing Turbines for Cryogenic Plants", International Institute of Refrigeration, 1 976, Münch (Germany).
- [3] R. Sixsmith and M.E. Bland, "An Oil-Free Centrifugal Compressor", International Institute of Refrigeration, 1 976, Münch (Germany).
- [4] D. Dini and G. Nardi, "Design of a Highly Cryogenic Turbine for an Optimized Hydrogen Liquefaction Plant", World Hydrogen Energy Conference IV, 13-17 June 1 982, Jet Propulsion Laboratory Pasadena, California (USA).
- [5] D. Dini, "Self Active Pad Seal Application for High Pressure Engines", AGARD Conference Proceedings No. 237, April 1 978, London (U.K.).

DISCUSSION

W.J. Anderson, Bearings and Lubrication, North Olmsted, Ohio, US
Were the bearings pressurized at startup?

Author's Reply
Yes.

REPORT DOCUMENTATION PAGE

1. Recipient's Reference	2. Originator's Reference	3. Further Reference	4. Security Classification of Document								
	AGARD-CP-323	ISBN 92-835-0318-9	UNCLASSIFIED								
5. Originator	Advisory Group for Aerospace Research and Development North Atlantic Treaty Organization 7 rue Ancelle, 92200 Neuilly sur Seine, France										
6. Title	PROBLEMS IN BEARINGS AND LUBRICATION										
7. Presented at	the 59th Symposium of the AGARD Propulsion and Energetics Panel, held at the Lester E. Pearson Building, Ottawa, Canada, on 31 May -- 3 June 1982.										
8. Author(s)/Editor(s)	Various		9. Date August 1982								
10. Author's/Editor's Address	Various		11. Pages 478								
12. Distribution Statement	This document is distributed in accordance with AGARD policies and regulations, which are outlined on the Outside Back Covers of all AGARD publications.										
13. Keywords/Descriptors	<table border="0"> <tr> <td>Bearings</td> <td>Film thickness in bearings</td> </tr> <tr> <td>Lubrication</td> <td>Hybrid bearings</td> </tr> <tr> <td>Journal bearings</td> <td>Squeeze-film bearings</td> </tr> <tr> <td>Rolling bearings</td> <td>Gas bearings</td> </tr> </table>			Bearings	Film thickness in bearings	Lubrication	Hybrid bearings	Journal bearings	Squeeze-film bearings	Rolling bearings	Gas bearings
Bearings	Film thickness in bearings										
Lubrication	Hybrid bearings										
Journal bearings	Squeeze-film bearings										
Rolling bearings	Gas bearings										
14. Abstract	<p>The Conference Proceedings contain 35 papers and a Keynote Address presented at the AGARD Propulsion and Energetics 59th Symposium on Problems in Bearings and Lubrication which was held in Ottawa, Canada, on 31 May -- 3 June 1982.</p> <p>The Technical Evaluation Report is included at the beginning of the Proceedings. Questions and answers of the discussions follow each paper. The Symposium was arranged into four sessions: Rolling Bearings (5), Lubrication (14), Journal Bearing and Gear Phenomena (6), and Advanced Bearing Applications (10).</p> <p>The purpose of the Symposium was to provide research scientists, development engineers and application specialists with a broad overview of advanced bearing and lubrication technology with emphasis on high speed bearings suitable for aircraft, missiles and aerospace applications.</p>										

<p>AGARD Conference Proceedings No.323 Advisory Group for Aerospace Research and Development, NATO PROBLEMS IN BEARINGS AND LUBRICATION Published August 1982 478 pages</p> <p>The Conference Proceedings contain 35 papers and a Keynote Address presented at the AGARD Propulsion and Energetics 59th Symposium on Problems in Bearings and Lubrication which was held in Ottawa, Canada, on 31 May - 3 June 1982.</p> <p>The Technical Evaluation Report is included at the beginning of the Proceedings. Questions and answers of the discussions follow each paper. The Symposium</p> <p>P.T.O.</p>	<p>AGARD-CP-323</p> <p>Bearings Lubrication: Journal bearings Rolling bearings Film thickness in bearings Hybrid bearings Squeeze-film bearings Gas bearings</p>	<p>AGARD Conference Proceedings No.323 Advisory Group for Aerospace Research and Development, NATO PROBLEMS IN BEARINGS AND LUBRICATION Published August 1982 478 pages</p> <p>The Conference Proceedings contain 35 papers and a Keynote Address presented at the AGARD Propulsion and Energetics 59th Symposium on Problems in Bearings and Lubrication which was held in Ottawa, Canada, on 31 May - 3 June 1982.</p> <p>The Technical Evaluation Report is included at the beginning of the Proceedings. Questions and answers of the discussions follow each paper. The Symposium</p> <p>P.T.O.</p>	<p>AGARD-CP-323</p> <p>Bearings Lubrication Journal bearings Rolling bearings Film thickness in bearings Hybrid bearings Squeeze-film bearings Gas bearings</p>
<p>AGARD Conference Proceedings No.323 Advisory Group for Aerospace Research and Development, NATO PROBLEMS IN BEARINGS AND LUBRICATION Published August 1982 478 pages</p> <p>The Conference Proceedings contain 35 papers and a Keynote Address presented at the AGARD Propulsion and Energetics 59th Symposium on Problems in Bearings and Lubrication which was held in Ottawa, Canada, on 31 May - 3 June 1982.</p> <p>The Technical Evaluation Report is included at the beginning of the Proceedings. Questions and answers of the discussions follow each paper. The Symposium</p> <p>P.T.O.</p>	<p>AGARD-CP-323</p> <p>Bearings Lubrication Journal bearings Rolling bearings Film thickness in bearings Hybrid bearings Squeeze-film bearings Gas bearings</p>	<p>AGARD Conference Proceedings No.323 Advisory Group for Aerospace Research and Development, NATO PROBLEMS IN BEARINGS AND LUBRICATION Published August 1982 478 pages</p> <p>The Conference Proceedings contain 35 papers and a Keynote Address presented at the AGARD Propulsion and Energetics 59th Symposium on Problems in Bearings and Lubrication which was held in Ottawa, Canada, on 31 May - 3 June 1982.</p> <p>The Technical Evaluation Report is included at the beginning of the Proceedings. Questions and answers of the discussions follow each paper. The Symposium</p> <p>P.T.O.</p>	<p>AGARD-CP-323</p> <p>Bearings Lubrication Journal bearings Rolling bearings Film thickness in bearings Hybrid bearings Squeeze-film bearings Gas bearings</p>

<p>was arranged into four sessions: Rolling Bearings (5), Lubrication (14), Journal Bearing and Gear Phenomena (6), and Advanced Bearing Applications (10).</p> <p>The purpose of the Symposium was to provide research scientists, development engineers and application specialists with a broad overview of advanced bearing and lubrication technology with emphasis on high speed bearings suitable for aircraft, missiles and aerospace applications.</p> <p>ISBN 92-835-0318-9</p>	<p>was arranged into four sessions: Rolling Bearings (5), Lubrication (14), Journal Bearing and Gear Phenomena (6), and Advanced Bearing Applications (10).</p> <p>The purpose of the Symposium was to provide research scientists, development engineers and application specialists with a broad overview of advanced bearing and lubrication technology with emphasis on high speed bearings suitable for aircraft, missiles and aerospace applications.</p> <p>ISBN 92-835-0318-9</p>
<p>was arranged into four sessions: Rolling Bearings (5), Lubrication (14), Journal Bearing and Gear Phenomena (6), and Advanced Bearing Applications (10).</p> <p>The purpose of the Symposium was to provide research scientists, development engineers and application specialists with a broad overview of advanced bearing and lubrication technology with emphasis on high speed bearings suitable for aircraft, missiles and aerospace applications.</p> <p>ISBN 92-835-0318-9</p>	<p>was arranged into four sessions: Rolling Bearings (5), Lubrication (14), Journal Bearing and Gear Phenomena (6), and Advanced Bearing Applications (10).</p> <p>The purpose of the Symposium was to provide research scientists, development engineers and application specialists with a broad overview of advanced bearing and lubrication technology with emphasis on high speed bearings suitable for aircraft, missiles and aerospace applications.</p> <p>ISBN 92-835-0318-9</p>